SCHOLARLY PUBLICATIONS

A CURRENT AWARENESS BULLETIN
OF RESEARCH OUTPUT

@DTU

(4rd Edition)

AUGUST 2016

BY: CENTRAL LIBRARY

DELHI TECHNOLOGICAL UNIVERSITY
(FORMERLY *DELHI COLLEGE OF ENGINEERING)*
GOVT. OF N.C.T. OF DELHI
SHAHBAD DAULATPUR, MAIN BAWANA ROAD
DELHI 110042

PREFACE

This is the **Forty four** Issue of Current Awareness Bulletin started by Delhi Technological University, Central Library. The aim of the bulletin is to compile, preserve and disseminate information published by the faculty, students and alumni for mutual benefits. The bulletin also aims to propagate the intellectual contribution of Delhi Technological University (DTU) as a whole to the academia.

The bulletin contains information resources available in the internet in the form of articles, reports, presentations published in international journals, websites, etc. by the faculty and students of DTU. The publications of faculty and student which are not covered in this bulletin may be because of the reason that the full text either was not accessible or could not be searched by the search engine used by the library for this purpose.

The learned faculty and students are requested to provide their uncovered publications to the library either through email or in CD, etc to make the bulletin more comprehensive.

This issue contains the information published during **August 2016**. The arrangement of the contents is alphabetical. The full text of the article which is either subscribed by the university or available in the web is provided in this bulletin.

Central Library

CONTENTS

1. A COMPARATIVE ANALYTICAL AND EXPERIMENTAL ANALYSIS OF SLOSHING WAVES IN RECTANGULAR TANK UNDER SEISMIC CONDITION, Dushyant Kumar Sahu, Hina Gupta, ***3.Nirendra Dev*** and ***3.Alok Verma***, DTU

2. A Hybrid filtering approach of Digital Video Stabilization for UAV using Kalman and Low Pass filter, ***3.Lakshya Kejriwal*** and ***3.Indu Singh***, Computer Science and Engineering, DTU

3. A New Approximate Closed-Form Distribution and Performance Analysis of a Composite Weibull/Log-Normal Fading Channel, ***3.Rupender Singh***, Sanjay Kumar Soni, Ram Shringar Raw and ***3.Sandeep Kumar***, ECE, DTU

4. A retrospective view of noise pollution control policy in India: status, proposed revisions and control measures, N. Garg and ***3.S. Maji***, DTU

5. A Review on Experimental Investigation of Machining Parameters during CNC Machining of OHNS, Surabhi Lata1, Ashish Gupta2, Aditya Jain3, Sonu Kumar4, Anindya Srivastava5, Ramakant Rana6, ***3.Roop Lal*** Department of Mechanical Engineering, DTU

6. Robust Audio Watermarking Technique Using Dual and Hybrid Watermark ***3.Jeebananda Panda, 3.Nitish Goel, 3.Indu Kumari*** and ***3.Asok Bhattarchyya***, ECE, DTU

7. A Social Media Complaint Workflow Automation Tool using Sentiment Intelligence, ***3.Akshi Kumar*** and ***8.Vikrant Dabas***, Computer Science & Engineering, DTU

8. Adsorption of Zn(II) from aqueous solution on mango leaves powder, Achla Kaushala, ***3.S.K.Singh***, Department of Environmental Technology, DTU

9. Alleviation SSR and Low Frequency Power Oscillations in Series Compensated Transmission Line using SVC Supplementary Controllers, Sanjiv Kumar and ***3.Narendra Kumar***, Department of Electrical Engineering, DTU

10. AN EVALUATION OF CONSUMER PERCEPTION AND ATTITUDE TOWARDS THE USAGE OF PLASTIC MONEY IN INDIA, ***7.Anoushka Sharma, 7.Syed Fazal Karim*** and ***7.Vipul Jain***, Delhi School of Management, DTU

11. An Experimental Study of Wireless Transceiver of Modulation Schemes using Software Defined Radio, ***3.P.K. Verma***, S.K. Soni, ***3.Priyanka Jain*** and ***3.Amit Kumar***, ECE, DTU

12. An exploratory study for software change prediction in object-oriented systems using hybridized techniques, ***3.Ruchika Malhotra*** and Megha Khanna, DTU

13. Analysis of ECG Signals using Hybrid Classifier, ***3.Sahil Dalal*** and ***3.Rajesh Birok***, ECE, DTU

14. Automatic Attendance System by Visual Programming Language Lab VIEW, ***3.Amit Kumar, 3.P.K. Verma, 3.Srinivas Perala*** and ***P.R. Chadha***, ECE, DTU

15. BFOA-scaled fractional order fuzzy PID controller applied to AGC of multiarea multi-source electric power generating systems, Yogendra Aryaa and ***3.Narendra Kumar,*** Department of Electrical Engineering, DTU

16. COMBINED CYCLE GAS TURBINE AND GENERATOR MATCHING PERFORMANCE, ***3.Jitendra Nath Rai*** and ***3.Ajendra Singh***, Electrical Engineering, DTU

17. Comparative Study of Load Deformation Behaviour of Silty Clay Bed Reinforced with Stone Column of Different Depth and Gradation, Darin Baruah and ***3.Sahu, Anil Kumar,*** Department of Civil Engineering, DTU

18. Design and analysis of a highly nonlinear composite photonic crystal fiber for supercontinuum generation: visible to mid-infrared, ***3.PURNIYA JAMATIA, 3.THAN SINGH SAINI, 3.AJEET KUMAR*** AND RAVINDRA KUMAR SINHA, Advanced Photonics Simulation Research Lab, Applied Physics, DTU

19. Design and analysis of single-mode tellurite photonic crystal fibers for stimulated Brillouin scattering based slow-light generation, ***3.VARSHA JAIN, 3.SHUBHAM SHARMA, 3.THAN SINGH SAINI, 3.AJEET KUMAR*** and RAVINDRA KUMAR SINHA, Advanced Photonics Simulation Research Laboratory, Department of Applied Physics, DTU

20. Design and modelling of dispersion-engineered rib waveguide for ultra broadband mid-infrared supercontinuum generation, ***3.Than Singh Saini, 3.Ajeet Kumar*** and ***3.Ravindra Kumar Sinha***, Advanced Photonics Simulation Research Laboratory, Department of Applied Physics, DTU

21. Digital Model of Railway Electric Traction Lines, ***3.Rachana Garg***, Priya Mahajan and Parmod Kumar, Electrical Engineering, DTU

22. Effect of aspect ratio on the performance and stability of Hydrodynamic Journal Bearings, ***3.Sachin Dhull*** and ***3.RS Walia***, Precision Engineering Laboratory, Central Workshop, DTU

23. EFFECTS OF DISCRETE DAMPING ON THE DYNAMIC BEHAVIOUR OF ROTATING SHAFT THROUGH EXTENDED LAGRANGIAN FORMULATION, ***3.Vikas Rastogi,*** Department of Mechanical, Production & Industrial and Automotive Engineering, DTU

24. ENERGY AND EXERGY ANALYSIS OF A WASTE HEAT DRIVEN CYCLE FOR TRIPLE EFFECT REFRIGERATION, Manoj Dixit, S. C. Kaushik and ***3.Akhilesh Arora,*** Mechanical Engineering, DTU

25. Energy-Efficient Hierarchical Routing for Wireless Sensor Networks: A Swarm Intelligence Approach, Palvinder Singh Mann and ***7.1Satvir Singh***, ECE, DTU

26. Enhance Bone Strength with Weight Bearing Excerises activities, ***3.Rajiv Chaudhary*** and ***3.Ramesh Chandra Singh***, Mechanical Engineering, DTU

27. EVALUATION OF GREEN HOUSE GASES EMISSIONS FROM SEWAGE TREATMENT PLANTS ***7.Mayank Mrinal, 3.Anubha Mandal, 3.Anunay Gour*** and ***3.Lovleen Gupta***, Department of Environmental Engineering, DTU

28. Experimental Analysis of Surface Roughness During CNC Milling of Brass Using Response Surface Methodology, ***3.Ranganath M. S, 3.Roshan Kumar, 3.Desh Raj*** and ***3.R. S. Mishra***, Mechanical, Production And Industrial Engineering, DTU

29. Experimental Investigation of the Temperature Variation and Vibrations at Different Loads at the , Periphery of Single Cylinder Diesel Engine, ***3.Sumit Chaudhary, 3.Vipin Kumar Sharma, 3.R.C. Singh*** and ***3.Rajiv Chaudhary***, Department of Mechanical Engineering, DTU

30. Experimental Research on MRR in EDM Process Using Regression Modelling, Surabhi Lata, Ravinder Kumar, Ramakant Rana, Ravi Ranjan, Rohit Kumar, ***3.Roop Lal***, Mechanical and Automation Engineering Department, DTU

31. Exploring the flexible chemistry of 4-fluoro-3-nitrophenyl azide for biomolecule immobilization and bioconjugation, ***3.Saroj Kumar*** & Dileep Kumar & Rajesh Ahirwar & Pradip Nahar, Department of Biotechnology, DTU

32. Failure Analysis of First Stage Gas Turbine Blade, ***3.Sushila Rani***, Mechanical, Production Industrial and Automobile Engineering, DTU

33. Frequency Estimation Using Analytic Signal via Wavelet Transform, ***3.Sudipta Majumdar*** and ***Akansha Singh***, ECE, DTU

34. Grey fuzzy optimization of cutting parameters on Material Removal Rate and Surface Roughness of Aluminium, ***3.S. Nanda, 3.Ranganth M.S. 3.S. Singhal*** and ***3.R. Batra***, Mechanical, Production & Industrial and Automobile Engineering, DTU

35. Hybrid filler composition optimization for tensile strength of jute fibre-reinforced polymer composite, ANURAG GUPTA, HARI SINGH1 and ***3.R SWALIA,*** Mechanical Engineering Department, DTU

36. IMPROVING PERFORMANCE OF MESI CACHE COHERENCE PROTOCOL FOR MULTI-CORE PROCESSOR ON MARSSx86 SIMULATOR, ***3.Manoj Kumar, 3.Pooja Arora*** and ***3.Akanksha Bharadwaj***, Computer Engineering Department, DTU

37. IMPROVING THE PERFORMANCE OF MESI PROTOCOL WITH LEVEL 2 CAHCE AS SHARED FOR MULTICORE PROCESSOR ON MARSSx86 SIMULATOR, ***3.Pooja Arora*** and ***3 Manoj Kumar***, Computer Science Department, DTU

38. Kaner biodiesel production through hybrid reactor and its performance testing on a CI engine at different compression ratios, Ashok Kumar Yadav, Mohd Emran Khan and ***3.Amit Pal***, Department of Mechanical Engineering, DTU

39. Mathematical Modeling of Solid Oxide Fuel Cell and Gas Turbine Hybrid System for Enhancing Thermal Performance, ***3.Smita Sharma*** and ***3.R. S. Mishra***, Department of Mechanical Engineering, DTU

40. Methods for Improving Thermodynamic Energy and Exergy Performance of Vapor Compression Refrigeration Systems Using Thirteen Eco-friendly Refrigerants in Primary Circuit and TiO2 Nano Particles Mixed with R718 Used in Secondary Evaporator Circuit for Reducing Global Warming and Ozone Depletion, ***3.RS Mishra***, Department of Mechanical Engineering, Production and Industrial & Automobiles Engineering, DTU

41. Micro-channel fabrication using electrical discharge machining process and optimization of parameters, Urfi Khan, Rituraj Jangid, Harsh Sharma and ***3.Mohd Shuaib***, Department of Mechanical Engineering, DTU

42. Modeling plasma-assisted growth of graphene-carbon nanotube hybrid, ***3.Aarti Tewari***, Department of Applied Physics, DTU

43. Modeling the effect of doping on the catalyst-assisted growth and field emission properties of plasma-grown graphene sheet, ***3.Neha Gupta, 3.Suresh C. Sharma,*** and ***3.Rinku Sharma***, Department of Applied Physics, DTU

44. Nanosilica based electrochemical biosensor: A novel approach for the detection of platelet-derived microparticles, 7.1Priti Singha, Sameer Srivastavaa, Parthasarathi Chakrabartib and Sunil Kumar Singha, Nanoscience and Technology, DTU

45. Numerical Simulation for Dynamic and Chaotic behaviour of Coupled Biological Oscillators through Extended Poincaré-Cartan Invariants, ***3.Vikas Rastogi***, Mechanical Engineering Department, DTU

46. Numerical Study on Response of Laterally Loaded Piles in Soils 7.Amit Jain and 3.A.K. Sahu, Civil Engineering Department, DTU

47. Object Recognition using SIFT Keypoints ***3.Sahil Dalal*** and ***3.Preeti Meena***, Department of ECE, DTU

48. Optimization of high-k and gate metal workfunction for improved analog and intermodulation performance of Gate Stack (GS)-GEWE-SiNW MOSFET, ***3. Neha Gupta*** and ***3.Rishu Chaujar***, Microelectronics Research Lab, Department of Engineering Physics, DTU

49. Performance Analysis of Fuzzy C-Means Clustering Methods for MRI Image Segmentation, ***3.Mahipal Singh Choudhry*** and ***3.Rajiv Kapoor***, DTU

50. Performance and Emission Characteristics of a Transportation Diesel Engine operated with Non-Edible Vegetable oils Biodiesel, Ashok Kumar Yadav, Mohd Emran Khan, Alok Manas Dubey and ***3.Amit Pal***, Mechanical Engineering, DTU

51. Performance Evaluation of Solar Parabolic Trough for Cloths Laundry application, ***3.Shubham Gupta*** and ***3.Prof. R. S. Mishra,*** Mechanical Engineering, DTU

52. Perfortmance evaluations of Concentrated Solar Thermal Power Technology, ***3.Harwinder Singh*** and ***3.R. S. Mishra***, Mechanical Engineering, DTU

53. Preliminary Investigation of Environmental Status of Bhindawas Bird Sanctuary, ***3.A. K. Haritash, 3.Vandana Shan, 3.Priyanka Singh*** and ***3.S. K. Singh***, Environmental Engineering, DTU

54. Prototype Design and Analysis of Controllers for one Dimensional Ball and Beam System, ***3.Sudarshan K Valluru, 3.Madhusudan Singh*** and ***3.Supriya Singh***, Department of Electrical Engineering, DTU

55. Seasonal Assessment of Trophic State of a Palustrine Water Body, ***3.Amit Yadav, 3.Atul Kataria, 3.Kapil Singh, 3.Karamveer Mathur, 3.Sagar Goswami*** and ***3.A. K. Haritash***, Department of Environmental Engineering, DTU

56. Secure Message Transmission Ensuring Authentication Using Digital Signature and Watermarking, ***3.Shivi Garg*** and ***3.Manoj Kumar#***, Computer Engineering, DTU

57. Solar Industrial Process Heating system for Indian Automobile Industry, ***3.Anubhav Uppal*b*3.J.P.Kesari***, Department of Mechanical engineering, DTU

58. Strategic issues in pharmaceutical supply chains: a review, Rajesh Kr Singh, Ravinder Kumar and ***3.Pravin Kumar***, Mechanical Engineering DTU

59. Suppliers' green performance evaluation using fuzzy extended ELECTRE approach, ***3.Pravin Kumar***, Rajesh Kumar Singh and Anurika Vaish, Mechanical Engineering, DTU

60. TARGETED ADVERTISING USING BEHAVIOURAL DATA AND SOCIAL DATA MINING, ***3.Vrinda Bhatia***, Department of Computer Science and Engineering, and ***3.Varun Hasija***, Department of Applied Mathematics, DTU

61. Theoretical Gain in Solar Energy for Different Sun Tracking Systems in Delhi, ***6.Kanav Vij*** and ***3.Rajesh Kumar***, Mechanical Production & Industrial and Automotive Engineering, DTU

62. Thermodynamic (Energy-Exergy) Analysis of Solar Assisted Power-Cooling Combined Generation Systems, ***3.Kaushalendra Kumar Dubey*** and ***3.R. S. Mishra***, Department of Mechanical Engineering, DTU

1. *Chancellor*
2. *Pro Vice Chancellor* — *2.1. Ex Pro Vice Chancellor*
3. *Faculty* — *3.1. Ex Faculty*
4. *Teaching-cum-Research Fellow*
5. *Alumni*
6. *Research Scholar* — *6.1. Ex Research Scholar*
7. *PG Scholar* — *7.1. Ex PG Scholar*
8. *Undergraduate Student* — *8.1. Ex Undergraduate Student*

A COMPARATIVE ANALYTICAL AND EXPERIMENTAL ANALYSIS OF SLOSHING WAVES IN RECTANGULAR TANK UNDER SEISMIC CONDITION

Dushyant Kumar Sahu[1], Hina Gupta[2], Nirendra Dev[3], Alok Verma[4]

[1]*Assistant Professor, ABES Engineering College, Ghaziabad-201009, India*
dushyant.sahu1990@gmail.com
[2]*Scientist, CSIR-Central Building Research Institute, Roorkee-247667, India*
15hinagupta@gmail.com
[3]*Professor, Delhi Technological University, Delhi-110042, India*
nirendra61@gmail.com
[4]*Associate Professor, Delhi Technological University, Delhi-110042, India*
alokverma_dce@hotmail.com

Abstract

Many past earthquakes have witnessed failure of liquid storage tanks in various ways. Sloshing action is one of major kinds of them. Hence it becomes essential to detect the pattern of surface wave and use preventive measures. As we know that the mass of water can be thought of as two parts, impulsive at lower depth and convective at upper depth. This analysis work was primarily focused on convective part. In this experimental study, the earthquake induced waves were analyzed with a representing tank model using shake table facility at DTU, Delhi. Further, the wave patterns and seismic parameters were determined analytically, and results were compared. The work gives a fair idea to study the seismic behavior of liquid storage tanks.

Keywords*: Rectangular Water Tank, Sloshing Waves, Shake Table, Natural Frequency, Fluid-Structure Interaction.*

----------***----------

1. INTRODUCTION

Liquid storage tank is a very important structure to serve normally and even after the disasters like earthquake, fire, etc. Hence it becomes an important structure. At the time of earthquake the container experiences huge hydrodynamic pressure. Thus the understanding of behavior and nature of these pressures becomes more important for the safe design. A lot of works have been carried out to analyze seismically the liquid storage tanks by approaches like finite element techniques[1], computational procedure[2], endurance time method[3], etc. and other traditional approaches which we use for design. All these techniques need the idea about behavior of earthquake induced waves, their natural frequencies, wave patterns, etc.

Tanks that have not designed or detailed adequately may suffer serious damages during earthquake. The various seismic damage modes in liquid storage tanks are buckling of side walls (diamond buckling), failure of tank roof and their junction, failure of anchor bolts, sliding and lifting, elephant foot buckling of tank wall at bottom, and uneven settlement, etc. [4][5]. Most of these failure modes are largely affected by sloshing of liquid and wave induced at the free surface. To safeguard against these, a good idea of sloshing height and sloshing load is required [6], so that we can provide sufficient freeboard or strength to prevent these damages economically.

In this experimental work a model of water tank was used which represents a rigid walled rectangular tank with fixed base over the ground. It was simulated on shake table to study the behavior of earthquake induced waves.

2. FLUID–STRUCTURE INTERACTION

The structure of liquid storage tank is rigid and elastic where as liquid containing in it is fluid and plastic or viscous in nature. When a dynamic force is applied on it, interaction between them takes place making the analysis more difficult. There are many approached to investigate the problem, as discussed in literatures of [7]–[9]. Out of all them the model suggested by Housner[10] was earliest and most accepted by the codes. According to Housner mass of liquid inside the tank can be thought of as two parts, one impulsive (m_i) at the lower part which behaves as rigidly connected with the tank walls and another convective at upper part which oscillates horizontally against a restraining spring. Its mechanical spring-mass model is shown in Fig.1.

3. WAVE PATTERN IN RECTANGULAR TANK

Rectangular tank will have length and width on the plan. Considering the excitation force to be acting along the length, thus its 2-D model is shown in Fig.1(a). The model has length $2l$ (or L) and depth of water h with coordinate axes as shown in the figure. As most of these waves are irrotational [11], thus assuming inviscid and incompressible fluid we can write following differential equation and boundary conditions.

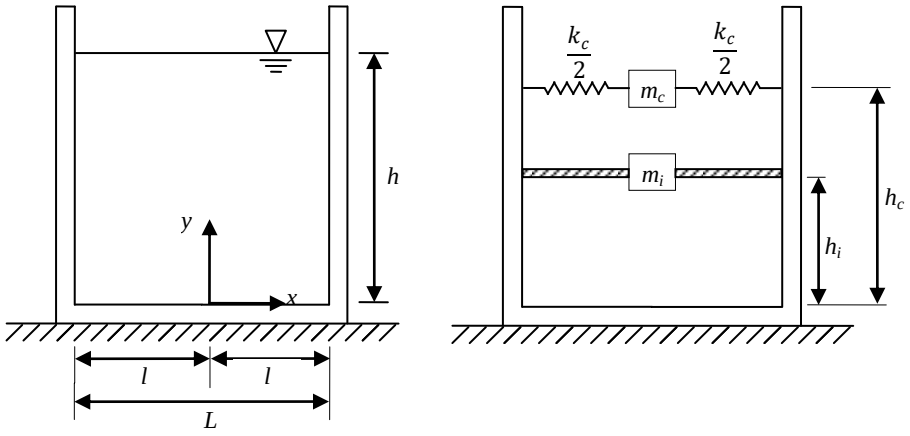

(a) Tank (b) Spring-Mass Model

Fig.1- Housner's Model

$$\frac{\partial^2\phi}{\partial x^2}+\frac{\partial^2\phi}{\partial y^2}=0 \quad (1)$$

$$\frac{\partial^2\phi}{\partial t^2}(x,h,t)+g\frac{\partial\phi}{\partial y}(x,h,t)=0 \quad (2)$$

$$\frac{\partial\phi}{\partial y}(x,0,t)=0 \quad (3)$$

$$\frac{\partial\phi}{\partial x}(\pm l,y,t)=0 \quad (4)$$

Where, $\phi(x,y,t)$ represents velocity potential, g acceleration due to gravity, and t time. Boundary condition (2) is derived from Bernoulli's equation using at free surface. Rest other two boundary conditions (3) and (4) are based on dimensions of tank. After some time of disturbance the wave will attain steady state condition. Thus, we can write velocity potential as, $\phi(x,y,t)=\psi(x,y)\cos\omega t$ and above equations will be modified as,

$$\frac{\partial^2\psi}{\partial x^2}+\frac{\partial^2\psi}{\partial y^2}=0 \quad (5)$$

$$-\omega^2\,\psi(x,h)+g\frac{\partial\psi}{\partial y}(x,h)=0 \quad (6)$$

$$\frac{\partial\psi}{\partial y}(x,0)=0 \quad (7)$$

$$\frac{\partial\psi}{\partial x}(\pm l,y)=0 \quad (8)$$

Solution of $\psi(x,y)$ in variable separable form will be, $X(x)Y(y)$. Thus, from (5)

$$\frac{d^2X}{dx^2}Y+X\frac{d^2Y}{dy^2}=0$$

$$\Rightarrow \frac{1}{X}\frac{d^2X}{dx^2}=-\frac{1}{Y}\frac{d^2Y}{dy^2}=-\lambda^2 \text{ (say)} \quad (9)$$

Here, λ is a constant, because from left side it would be function of *x* only or a constant and from right side it would be a function of *y* only or a constant and both have to be equal in value. And from (6), (7), and (8)

$$-\omega^2\,Y(h)+g\frac{dY}{dy}(h)=0 \quad (10)$$

$$\frac{dY}{dy}(0)=0 \quad (11)$$

$$\frac{dX}{dx}(\pm l)=0 \quad (12)$$

From left side of (9)

$$\frac{d^2X}{dx^2}+\lambda^2X=0$$

$$\Rightarrow X(x)=A\cos\lambda x+B\sin\lambda x \quad (13)$$

A and *B* being arbitrary constants, from boundary condition (12)

$$\lambda\begin{bmatrix}-\sin\lambda l & \cos\lambda l\\ \sin\lambda l & \cos\lambda l\end{bmatrix}\begin{Bmatrix}A\\B\end{Bmatrix}=0$$

Non-trivial solution of above equation would be,

$$-2\lambda\sin\lambda l\cos\lambda l=0$$

This will give two sets of solution in *n* & *m* family as,

$$\lambda_n=\frac{n\pi}{l} \quad ; n=1,2,3,\dots\dots,\infty \quad (14.1)$$

$$\lambda_m=\frac{(2m+1)\pi}{2l} \quad ; m=0,1,2,3,\dots\dots,\infty \quad (14.2)$$

Thus from (13) and (14), solution of $X(x)$ is,

$$X(x)=A\cos\frac{n\pi x}{l} \quad ; n=1,2,3,\dots,\infty \quad (15.1)$$

$$X(x)=B\sin\frac{(2m+1)\pi x}{2l} \quad ; m=0,1,2,3,\dots\dots,\infty \quad (15.2)$$

This is the expression for pattern of standing waves.

Further, from right side of (9)

$$\frac{d^2Y}{dy^2}-\lambda^2Y=0$$

$$\Rightarrow Y(y)=C\cosh\lambda y+D\sinh\lambda y \quad (16)$$

C and D being arbitrary constants, from boundary condition (11)

$$D\lambda = 0 \Rightarrow D = 0 \quad (17)$$

From boundary condition (10) and (17)

$$-\omega^2 C \cosh \lambda h + gC\lambda \sinh \lambda h = 0$$

$$\Rightarrow \omega^2 = g\lambda \tanh \lambda h \quad (18)$$

Substituting value of λ from (14) in (18), we will get two sets of natural frequencies as,

$$\omega_n{}^2 = \frac{n\pi}{l} g \tanh \frac{n\pi h}{l} \quad ; n = 1,2,3, \dots, \infty \quad (19.1)$$

$$\omega_m{}^2 = \frac{(2m+1)\pi}{2l} g \tanh \frac{(2m+1)\pi h}{2l} ; m = 0,1,2,3, \dots, \infty \quad (19.2)$$

This expression will give natural frequency of different modes.

4. EXPERIMENTAL INVESTIGATION

The setup consists of a rectangular water tank model mounted on shake table. The tank wall is made of thick glass encased inside a steel frame to represent a rigid walled liquid storage tank, as shown in Fig.2. The idea about the tank was taken from manual presented by IISc, Bangalore for earthquake engineering education [12]. The tank was rigidly placed over shake table to represent fixed base and hard soil condition. The table can be excited at different frequencies with different amplitudes. Blue trace was added into the water inside the tank so as to visually observe the waves and maximum sloshing height can be marked on paper, while oscillating at various frequencies.

Fig.2- Experimental Model

5. TEST DATA AND CALCULATIONS

5.1. Natural Frequency

Theoretically, natural frequency is determined by (19), with following data-

Length of tank $L = 0.3$ m ($\therefore l = 0.15$ m)
Height of water $h = 0.2$ m
$g = 9.81$ m/s^2

Where, ω is in radian. Thus, $f\,(\text{Hz}) = \frac{\omega}{2\pi}$

Hence, natural frequency for n = 1, 2, 3 and m = 0, 1, 2, 3 respectively are,

f_{n1} = 2.28 Hz	and,	f_{m1} = 1.59 Hz
f_{n2} = 3.23 Hz		f_{m2} = 2.79 Hz
f_{n3} = 3.95 Hz		f_{m3} = 3.61 Hz
		f_{m4} = 4.27 Hz

5.2. Sloshing Wave Height

Height of sloshing wave will depend only on convective mode. it is calculated as per recommendations given in IS-1893 (Part 1 & 2) [13], [14] as follows,

(a) Time Period, $T_c = C_c \sqrt{\frac{L}{g}}$

Where, C_c is a function of h/L ratio.

$$C_c = \frac{2\pi}{\sqrt{3.16 \tanh (3.16\,(h/L))}}$$

For h = 0.2 m, L = 0.3 m, g = 9.81 m/s^2
C_c = 3.59
Thus, T_c = 0.63 s

(b) Design horizontal seismic coefficient

$$(A_h)_c = \frac{Z}{2}\frac{I}{R}\left(\frac{S_a}{g}\right)_c$$

Where,
Z = 0.36 (for zone-V)
I = 1.5 (for post earthquake importance)
R = 2.0 (for fixed base tank)
T_c = 0.63 s
Soil condition- Hard
Damping = 0.5% (for convective mode)
∴ Multiplying Factor = 2.75

Thus, $\left(\frac{S_a}{g}\right)_c = \frac{1}{T_c} \times 2.75 = 4.37$

And, $(A_h)_c$ = 0.59

(c) Maximum Sloshing Wave Height

$$d_{max} = (A_h)_c R \frac{L}{2} = 0.177 \text{ m} \quad (\text{or } 17.7 \text{ cm})$$

6. RESULTS AND DISCUSSION

6.1. Natural Frequency

Variation of natural frequency of different modes with height is shown below in Fig.3, which is obtained from expression (19).

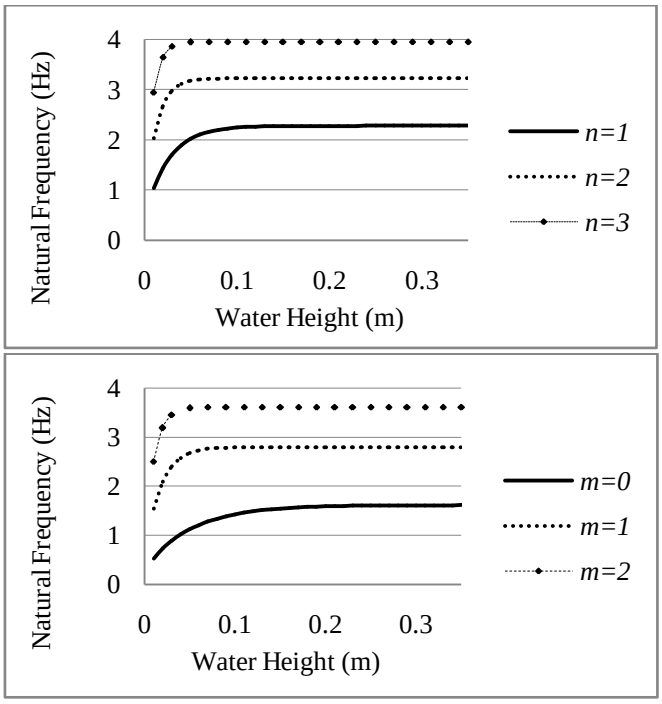

Fig.3 (a) & (b)- Natural Frequency

6.2. Theoretical Wave Pattern

Using expression (15) we can obtain a representative pattern of the induced waves, which is shown below in Fig.4.

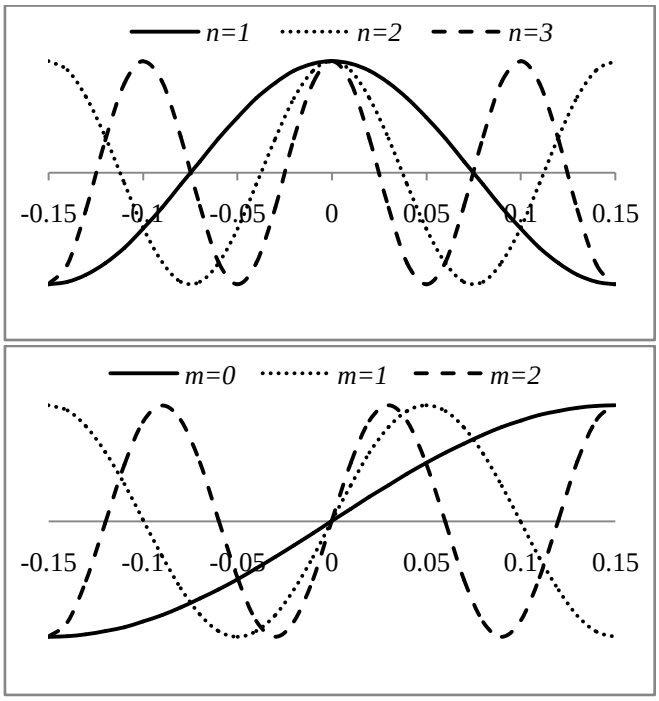

Fig.4 (a) & (b)- Standing Wave Patterns

6.3. Experimental Results

The pattern of induced waves and their trace mark are shown below in figure. Trace mark represents sloshing height of the wave which is indicated in the figures. Fig.5 represents the condition when exciting force is being applied but no resonance is taking place (say, at frequency 1.7 Hz). Others Fig.6-9 shows (a) wave pattern, and (b) trace mark while guiding with natural frequencies at mode 1, 2, 3, and 4 respectively.

Fig.5- No Resonance Condition

(a)

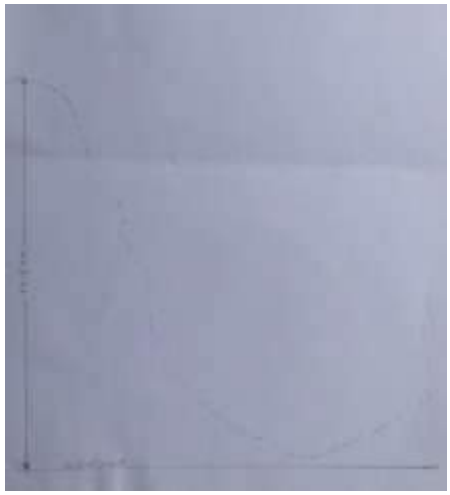

(b)

Fig.6- Mode 1 (1.6 Hz)

(a)

(b)

Fig.7- Mode 2 (2.8 Hz)

(a)

(b)

Fig.8- Mode 3 (3.7 Hz)

(a)

(b)

Fig.9- Mode 4 (4.4 Hz)

Variation of sloshing wave height with different modes can be observed by bar chart, as shown in Fig.10.

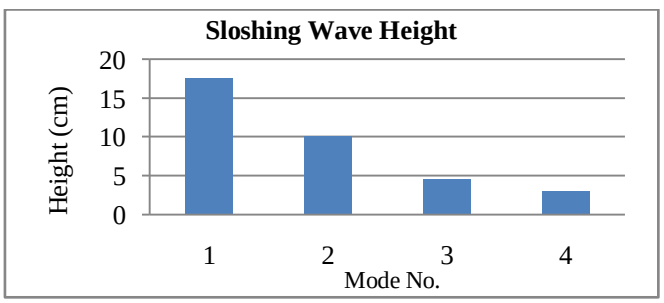

Fig.10- Sloshing Wave Height

For a comparative analysis of results, natural frequencies and sloshing wave heights obtained from experiment and theories are listed below in Table.1.

Table.1- Comparative Results

Mode No.	Experimental Result		Theoretical Result	
	Natural Frequency (Hz)	Sloshing Wave Height (cm)	Natural Frequency (Hz)	Sloshing Wave Height (cm)
1	1.6	17.5	1.59	17.7
2	2.8	10.0	2.79	-
3	3.7	4.5	3.61	-
4	4.4	3.0	4.27	-

7. CONCLUSIONS

It can be easily observed that after a certain height of water the natural frequency becomes almost independent of the height of water. This is the case of convective frequency. Thus convective time period also becomes independent after a certain value which is justified by looking the variation of C_c with h/L ratio in Figure-7 of IS-1893 (Part-2). The natural frequencies getting experimentally and analytically have negligible variation in lower modes but increasing in higher modes. To account for this situation, IS codes recommends a cutoff frequency which is 33 Hz in IS-1893 (Part-1) and 42 Hz in Eurocode 8.

Height of sloshing wave is decreasing with increasing mode number. It should also be observed that the sloshing wave height rises only at natural frequencies. In other frequencies disturbance in water surface occurs but without any significant rise. The sloshing wave height calculated from IS code is almost equal to experimental value. The mathematical model gives a good idea of natural frequency and standing wave patterns. Experimental results are in match with one family of mathematical expression.

REFERENCES

[1] J. R. Cho, J. M. Song, and J. K. Lee, "Finite element techniques for the free-vibration and seismic analysis of liquid-storage tanks," *Finite Elem. Anal. Des.*, vol. 37, no. 6–7, pp. 467–483, 2001.

[2] R. O. Ruiz, D. Lopez-Garcia, and A. a. Taflanidis, "An efficient computational procedure for the dynamic analysis of liquid storage tanks," *Eng. Struct.*, vol. 85, pp. 206–218, 2015.

[3] H. E. Estekanchi and M. Alembagheri, "Seismic analysis of steel liquid storage tanks by Endurance Time method," *Thin-Walled Struct.*, vol. 50, no. 1, pp. 14–23, 2012.

[4] A. Maekawa, "Recent advances in seismic response analysis of cylindrical liquid storage tanks," in *Earthquake-Resistant Structures – Design, Assessment and Rehabilitation*, 2010.

[5] P. K. Malhotra, T. Wenk, and M. Wieland, "Simple

procedure for seismic analysis of liquid-storage tanks," *Struct. Eng. Int. J. Int. Assoc. Bridg. Struct. Eng.*, vol. 10, no. 3, pp. 197–201, 2000.

[6] P. K. Malhotra, "Sloshing loads in liquid-storage tanks with insufficient freeboard," *Earthq. Spectra*, vol. 21, no. 4, pp. 1185–1192, 2005.

[7] R. Livaoglu, "Investigation of seismic behavior of fluid-rectangular tank-soil/foundation systems in frequency domain," *Soil Dyn. Earthq. Eng.*, vol. 28, no. 2, pp. 132–146, 2008.

[8] U. Chaduvula, D. Patel, and N. Gopalakrishnan, "Fluid-structure-soil interaction effects on seismic behaviour of elevated water tanks," *Procedia Eng.*, vol. 51, no. NUiCONE 2012, pp. 84–91, 2013.

[9] J. Z. Chen and M. R. Kianoush, "Generalized SDOF system for seismic analysis of concrete rectangular liquid storage tanks," *Eng. Struct.*, vol. 31, no. 10, pp. 2426–2435, 2009.

[10] G. W. Housner, "The dynamic behavior of water tanks," *Bull. Seismol. Soc. Amerrica*, vol. 53, no. 2, pp. 381–387, 1963.

[11] I. G. Currie, *Fundamental Mechanics of Fluids*, Third., vol. 1. 2003.

[12] C. S. Manohar and S. Venkatesha, "Development of experimental setups for earthquake engineering education," 2006.

[13] "IITK-GSDMA Guidlines for seismic design of liquid storage tanks," 2007.

[14] Bureau of Indian Standards, *IS-1893 (Part 1): 2002 Indian Standard Criteria for Earthquake Resistant Design of Structures, Part 1 General Provisions and Buildings*. 2002.

Wireless Pers Commun
DOI 10.1007/s11277-016-3583-3

A New Approximate Closed-Form Distribution and Performance Analysis of a Composite Weibull/ Log-Normal Fading Channel

Rupender Singh[1] · Sanjay Kumar Soni[2] · Ram Shringar Raw[3] · Sandeep Kumar[1]

© Springer Science+Business Media New York 2016

Abstract The presence of both the fading and shadowing effects (also called composite multipath/shadowed fading) is often encountered in a realistic radio propagation scenario, thus, making it necessary to consider the simultaneous effect of fading and shadowing on the received signal. The multipath effect is captured using models such as Rician, Nakagami-m, Weibull distribution and shadowing effect is modeled using Log-normal distribution. In this paper we present the closed-form expression of composite (Weibull/log-normal shadowed) fading using the efficient tool proposed by Holtzman. Using this result, the closed-form expression of combined (time-shared) shadowed/unshadowed fading is presented. The performance measures of fading communication systems such as probability density function of signal to noise ratio, amount of fading, outage probability (P_{out}) and channel capacity are analyzed and expressed in closed form.

Keywords Combined (time-shared) shadowed/unshadowed fading · Weibull distribution · Log-normal shadowing · Composite PDF

✉ Sanjay Kumar Soni
sanjoo.ksoni@gmail.com

Rupender Singh
Indiarupendersingh04cs39@gmail.com

Ram Shringar Raw
rsrao08@yahoo.in

Sandeep Kumar
sann.kaushik@gmail.com

[1] Department of Electronics and Communication, Delhi Technological University, Delhi, India

[2] Department of Electronics and Communication, G. B. Pant Engineering College, Pauri, UK, India

[3] Ambedkar Institute of Advanced Communication Technologies and Research, Delhi, India

Published online: 08 August 2016

1 Introduction

Wireless communication channels are impaired by detrimental effects such as multipath fading and shadowing [1]. Based on various indoor and outdoor empirical measurements, there is general consensus that shadowing can be modeled using log-normal distribution [2–4] and multipath effect is captured by using distribution such as Nakagami, Rayleigh and Rician distribution [5].

The Weibull distribution plays an important role in several scientific fields, but it has become recently the topic of wireless communications theory [6–8], particularly with mobile radio systems. The Weibull model exhibits an excellent fit to experimental fading channel measurements for both indoor [7] and outdoor [8] environments. Several works [9, 10] have considered Weibull fading channel and analyzed performance metric of communication system. In [9], second-order statistics and channel capacity are analyzed for Weibull fading channel. In [10], the channel capacity in fading channels following distributions such as Nakagamm, Weibull is analyzed for multiple independent channels and the results are expressed in closed-form using Meijer-G function.

Composite multipath/shadowing fading scenarios are often encountered in real scenarios. Modeling of composite fading is important in analyzing the wireless communication system such as Multiple Input Multiple Output (MIMO) and cognitive radio network and in the modeling of interference in cellular system. A composite multipath/shadowed fading environment modeled either as Rayleigh-lognormal, Rician-lognormal, Nakagami-lognormal are considered in [4, 11, 12]. Further, due to mathematical complexity in the closed-form expression of log-normal based composite models, various approximations to log-normal have been suggested. In [13], the gamma distribution is suggested as an alternative approach to log-normal to model shadowing effect. In [14], a composite Weibull/Gamma distrubtion is considered and performance metric such as P_{out} and bit-error rate for receiver are analysed. The work in [15] analyses the composite Nakagami/Log-normal fading approximating Log-normal shadowing as an inverse Gaussian distribution, thus, ensuring the resultant expression in the closed-form. In [16], a composite multipath/shadowing fading is represented as a series of Nakagammi distribution. In [17], considering Weibull/log-normal (WL) composite fading, second-order statistics of fading channel has been studied. However, WL fading scenario has got little attention till date in terms of closed-form PDF andis not reported in literature and thus, hampering further analytical derivation of important performance metric such as AF, P_{out} and average channel capacity.

In the case of mobile user there is the possibility of receiving signal from Line of sight (LOS) and shadowed path both. This concept was discussed in [1, 18]. In early 1990 s, Lutz et al. [19] and Barts and Stutzman [20] found that total fading for land–mobile satellite systems can be viewed as combination of unshadowed fading and a composite multipath/shadowed fading [1]. Statistical modeling of this realistic scenario has also received a little attention in research community till date.

In this paper, our goal is to obtain the closed-form expression of composite WL distribution using Holtzman approximation for the expectation of the function of a normal variant [22]. The closed-form, thus obtained, is mathematically simple and it is expressed as the weighted sum of three Weibull distribution terms with some modifications in shape and scaling parameters. The proposed solution is accurate in severe multipath fading and light to medium shadowing, however, the solution starts deviating from the exact results for higher values of fading and shadowing parameter. The obtained result facilitates to

obtain a simple analytical approximation of the PDF of Combined (time-shared) shadowed (WL)/unshadowed (Rician) fading. Further, the proposed closed-form PDF leads to the derivation of the closed-form solution of the important performance metrics of communication system such as AF, P_{out} and channel capacity using Meijer-G function for both composite multipath/shadowed fading as well as combined (time-shared) shadowed/unshadowed fading channel.

The remaining of the work is organized as follows. In Sect. 2, the closed-form expression of composite WL fading is obtained and using it, the distribution of combined shadowed/unshadowed fading is expressed. In Sect. 3, AF for the composite fading channels is derived followed by combined shadowed/unshadowed fading using Kummer confluent hyper geometric function. In Sect. 4, performance measure such as P_{out} of the communication system is analyzed. In Sect. 5, the derivation of channel capacity using Meijer-G function for both the composite fading as well as combined shadowed/unshadowed fading is derived. Section 6 presents graphical results and some interesting observation. This is followed by conclusion in Sect. 7.

2 The Composite PDF Distribution

2.1 The Probability Density Function of the Composite WL Shadowing

In this section, we derive closed-form of WL composite fading where Weibull represents multipath effect and log-normal model capture the effect of shadowing. PDF of received SNR of composite WL shadowing can be obtained by averaging the conditional PDF of Weibulll distribution over log-normal fading. Conditional Weibull distribution is given by [1, 21]

$$p(\gamma/w) = \frac{c}{2}\left(\frac{\Gamma\left(1+\frac{2}{c}\right)}{w}\right)^{\frac{c}{2}} \gamma^{\frac{c}{2}-1} exp\left[-\left(\frac{\gamma}{w}\Gamma\left(1+\frac{2}{c}\right)\right)^{\frac{c}{2}}\right] \gamma \geq 0 \tag{1}$$

where, c is shape parameter for Weibull fading, w is the average SNR at the receiver, γ is the received SNR and Γ is gamma function. If w is slowly varying, the PDF in (1) becomes statistical terms and its average needs to be computed. Here, the slowly varying fading is modeled using log-normal distribution with PDF given by

$$p(w) = \frac{1}{\sigma w\sqrt{2\pi}} \exp\left(-\frac{(\log_e w - \mu)^2}{2\sigma^2}\right) \tag{2}$$

where, μ, σ are mean and standard deviation of RV $\log_e w$. They can be expressed in dB by $\sigma_{dB} = k\sigma$ and $\mu_{dB} = k\mu$ where $k = 10/\ln(10)$ [2]. Averaging the PDF of (1) w.r.t. to (2), we have,

$$p(\gamma) = \int_0^\infty p(\gamma/w)p(w)dw \tag{3}$$

Substituting (1) and (2), into (3), we have

$$p(\gamma) = \int_0^{\infty} \left\{ \frac{c}{2} \left(\frac{\Gamma\left(1+\frac{2}{c}\right)}{w} \right)^{\frac{c}{2}} \gamma^{\frac{c}{2}-1} exp\left[-\left(\frac{\gamma}{w} \Gamma\left(1+\frac{2}{c}\right) \right)^{\frac{c}{2}} \right] \right\} \left\{ \frac{1}{\sigma w \sqrt{2\pi}} \exp\left(-\frac{(log_e w - \mu)^2}{2\sigma^2} \right) \right\} dw \tag{4}$$

It is difficult to find directclosed-from solution to (4), and therefore, we adopt the efficient tool proposed by Holtzman in, [22, 23] and considering $log_e w = x$ in (4), we obtain

$$p(\gamma) = \int_{-\infty}^{\infty} \psi(\gamma; x) \frac{1}{\sigma\sqrt{2\pi}} e^{-\frac{(x-\mu)^2}{2\sigma^2}} dx \tag{5}$$

Finally, we have PDF of WL fading

$$p_\gamma(\gamma) \approx \frac{2}{3}\psi(\gamma;\mu) + \frac{1}{6}\psi\left(\gamma;\mu+\sqrt{3}\sigma\right) + \frac{1}{6}\psi\left(\gamma;\mu-\sqrt{3}\sigma\right) \tag{6}$$

where,

$$\psi(\gamma; x) = \frac{c}{2} \left(\frac{\Gamma\left(1+\frac{2}{c}\right)}{\exp(x)} \right)^{\frac{c}{2}} \gamma^{\frac{c}{2}-1} exp\left[-\left(\frac{\gamma}{\exp(x)} \Gamma\left(1+\frac{2}{c}\right) \right)^{\frac{c}{2}} \right] \tag{7}$$

Using (6) and (7) and after some mathematical manipulation, we obtain the expression for CDF of composite WL fading channel

$$P_\gamma(\gamma) = \frac{2}{3}\{1-\alpha(\gamma;\mu)\} + \frac{1}{6}\left\{1-\alpha\left(\gamma;\mu+\sqrt{3}\sigma\right)\right\} + \frac{1}{6}\left\{1-\alpha\left(\gamma;\mu-\sqrt{3}\sigma\right)\right\} \tag{8}$$

where,

$$\alpha(\gamma; x) = exp\left[-\left(\frac{\gamma}{\exp(x)} \Gamma\left(1+\frac{2}{c}\right) \right)^{\frac{c}{2}} \right]$$

2.2 The PDF of the Combined (Time-Shared) Shadowed/Unshadowed Fading

Considering the case of moving user there is the possibility of receiving signal from LOS and shadowed path both. Therefore, combined (time-shared) PDF of instantaneous SNR γ is [18]

$$\begin{aligned} p(\gamma; A, K, \mu, \sigma) &= (1-A) \times PDF\ of\ Rician\ fading + A \times PDF\ of\ Composite\ multipath/shadowed \\ &= (1-A) \times p_{rice}(\gamma; K) + A \times p(\gamma; \mu, \sigma) \end{aligned} \tag{9}$$

where, A is shadowing time-share factor, $0 \leq A \leq 1$. Rice distribution of γ (SNR per symbol) is given by [18]

$$p_{rice}(\gamma) = \frac{(1+K)e^{-K}}{\bar{\gamma}} \exp\left(-\frac{(1+K)\gamma}{\bar{\gamma}} \right) I_0\left(2\sqrt{\frac{K(1+K)\gamma}{\bar{\gamma}}} \right) \tag{10}$$

Rice distribution is often used to model the propagation channel consisting of strong line-of-sight (LOS) and some multipath components. Using (6) and (7) into (9) and noting the

Rice distribution of SNR per symbol from (10), we get the PDF of combined shadowed/unshadowed fading

$$p(\gamma;A,K,\mu,\sigma) = (1-A)\frac{(1+K)e^{-K}}{\bar{\gamma}}\exp\left(-\frac{(1+K)\gamma}{\bar{\gamma}}\right)I_0\left(2\sqrt{\frac{K(1+K)\gamma}{\bar{\gamma}}}\right) + A\left(\frac{2}{3}\psi(\gamma;\mu)+\frac{1}{6}\psi\left(\gamma;\mu+\sqrt{3}\sigma\right)+\frac{1}{6}\psi\left(\gamma;\mu-\sqrt{3}\sigma\right)\right) \tag{11}$$

where, $\psi(\gamma;x)$ is defined in Eq. (7).

3 Amount of Fading

AF is a measure of severity of fading of the channel. In this section, we compute AF of the composite WL fading. The AF is given by

$$AF = \frac{E[\gamma^2]}{\{E[\gamma]\}^2} - 1 \tag{12}$$

Closed-form expression used in (6) is nothing but the weighted sum of three Weibull distributions and considering each term separately, we have the kth moment of γ(SNR per symbol) given by

$$E[\gamma^k] = \int_0^\infty \gamma^k \times \frac{c}{2}\left(\frac{\Gamma\left(1+\frac{2}{c}\right)}{\bar{\gamma}}\right)^{\frac{c}{2}}\gamma^{\frac{c}{2}-1}exp\left[-\left(\frac{\gamma}{\bar{\gamma}}\Gamma\left(1+\frac{2}{c}\right)\right)^{\frac{c}{2}}\right]d\gamma \tag{13}$$

where, $\bar{\gamma} = \exp(x)$. Substituting $\left(\frac{\gamma}{\bar{\gamma}}\Gamma\left(1+\frac{2}{c}\right)\right)^{\frac{c}{2}} = R$ in (13) and after some mathematical manipulation, we obtain

$$E[\gamma^k] = \left[\frac{\exp(x)}{\Gamma(1+2/c)}\right]^k\Gamma(1+2k/c) \tag{14}$$

Thus, considering all the three terms of (6), we get the kth moment of γ as given below

$$E[\gamma^k] = \Gamma(1+2k/c)\left\{(2/3)\left[\frac{\exp(\mu)}{\Gamma(1+2/c)}\right]^k + (1/6)\left[\frac{\exp(\mu+\sqrt{3}\sigma)}{\Gamma(1+2/c)}\right]^k + (1/6)\left[\frac{\exp(\mu-\sqrt{3}\sigma)}{\Gamma(1+2/c)}\right]^k\right\} \tag{15}$$

Further using (12) and (15), AF of the composite fading channel is given by

$$AF = \frac{\Gamma(1+4/c)}{\Gamma^2(1+2/c)}\left[\frac{\left\{2/3+(1/6)\exp(2\sqrt{3\sigma})+(1/6)\exp(-2\sqrt{3\sigma})\right\}}{\left\{2/3+(1/6)\exp(\sqrt{3\sigma})+(1/6)\exp(-\sqrt{3\sigma})\right\}^2}\right] - 1 \tag{16}$$

Kth moment of output SNR of combined shadowing/unshadowing fadingis

$$E(\gamma^k) = \int_0^\infty \gamma^k p(\gamma) d\gamma = (1-A) \int_0^\infty \gamma^k p_{rice}(\gamma) + A \int_0^\infty \gamma^k p_{comp}(\gamma) \tag{17}$$

The kth moment of Rice distribution is given by [1]

$$E(\gamma^k)_{rice} = \frac{\Gamma(1+k)}{(1+K)^k} {}_1F_1(-k, 1; -K)\bar{\gamma}^k \tag{18}$$

where, ${}_1F_1(-k, 1; -K)$ is Kummer confluent hyper geometric function. Finally, we get the closed form expression of the kth moment of combined shadowed/unshadowed fading is obtained by substituting (16) and (18) in (17)

$$\begin{aligned} E[\gamma^k] = (1-A)\frac{\Gamma(1+k)}{(1+K)^k} F(-k, 1; -K)\bar{\gamma}^k + A\Gamma(1 \\ + 2k/c)\left\{ \begin{array}{l} (2/3)\left[\dfrac{\exp(\mu)}{\Gamma(1+2/c)}\right]^k \\ + (1/6)\left[\dfrac{\exp(\mu+\sqrt{3}\sigma)}{\Gamma(1+2/c)}\right]^k + (1/6)\left[\dfrac{\exp(\mu-\sqrt{3}\sigma)}{\Gamma(1+2/c)}\right]^k \end{array} \right\} \end{aligned} \tag{19}$$

Therefore, AF of combined shadowed/unshadowed fading can be easily obtained using (19) and (12).

4 Outage Probability

Outage Probability is standard performance criterion of communication systems operating over fading channels and it is defined as the probability that the instantaneous error rate exceeds a specified value, or equivalently, that SNR falls below a predetermined threshold γ_{th}.

$$P_{out}(\gamma_{th}) = P[\gamma \leq \gamma_{th}] \tag{20}$$

Mathematically this can be derived as

$$P_{out}(\gamma_{th}) = \int_0^{\gamma_{th}} p(\gamma) d\gamma \tag{21}$$

Substitution of (10) into (21) yields the P_{out} of Rice-distributed fading channel and it is expressed as

$$P_{out}(\gamma_{th})_{rice} = \int_0^{\gamma_{th}} \frac{(1+K)e^{-K}}{\bar{\gamma}} \exp\left(-\frac{(1+K)\gamma}{\bar{\gamma}}\right) I_0\left(2\sqrt{\frac{K(1+K)\gamma}{\bar{\gamma}}}\right) d\gamma \tag{22}$$

Replacing $I_0(z)$ in (22) from 8.447 tables of integrals [24] by and by assuming $a = (1+K)/\bar{\gamma}$ and using ([25], /0.1.03.21.0058.01), we obtain the expression of P_{out} of Rice-distributed fading channel as follows

$$P_{out}(\gamma_{th})_{rice} = \sum_{n=0}^{\infty} \frac{a^{n+1} e^{-K} K^n}{(n!)^2} \int_0^{\gamma_{th}} \gamma^n \exp(-a\gamma) d\gamma \tag{23}$$

$$P_{out}(\gamma_{th})_{rice} = \sum_{n=0}^{\infty} \frac{a^{n+1} e^{-K} K^n}{(n!)^2} \frac{[\Gamma(1+n) - \Gamma(1+n, a\gamma_{th})]}{a^{(n+1)}} \tag{24}$$

By considering the definition of incomplete gamma function $\int_0^x t^{n-1} \exp(-t) dt = \gamma(n, x)$, and its relation with Kummer' confluent hyper geometric function, the expression (23) can also be expressed in terms of Kummer's confluent function as

$$P_{out}(\gamma_{th})_{rice} = \sum_{n=0}^{\infty} \frac{a^{n+1} e^{-K} K^n}{(n!)^2} a^{(-n-1)} (1+n)^{-1} (a\gamma_{th})^{n+1} {}_1F_1(n+1; 2+n; -a\gamma_{th}) \tag{25}$$

P_{out} of composite WL fading can straightforward be obtained by substituting (6) into (21) which yields

$$P_{out}(\gamma_{th}) = \frac{2}{3}\left(1 - \exp\left(\gamma_{th}^{\frac{c}{2}} b_1^{\frac{c}{2}}\right)\right) + \frac{1}{6}\left(1 - \exp\left(\gamma_{th}^{\frac{c}{2}} b_2^{\frac{c}{2}}\right)\right) + \frac{1}{6}\left(1 - \exp\left(\gamma_{th}^{\frac{c}{2}} b_3^{\frac{c}{2}}\right)\right) \tag{26}$$

where, $b_i = \frac{\Gamma\left(1+\frac{2}{c}\right)}{\exp(x_i)}$, $i = 1, 2, 3$ and $x_1 = \mu$, $x_2 = \mu + \sqrt{3}\sigma$, $x_2 = \mu - \sqrt{3}\sigma$

Finally, we get the closed form expression of P_{out} of combined (time-shared) WL and Rice fading as given below

$$\begin{aligned} P_{out}(\gamma_{th}) = & \sum_{n=0}^{\infty} \frac{(1-A) a^{n+1} e^{-K} K^n}{(n!)^2} [a^{-n-1}(-1)^n \Gamma(1+n, -a\gamma_{th}) - a^{-n-1}(-1)^n \Gamma(1+n, 0)] \\ & + A\frac{2}{3}\left(1 - \exp\left(\gamma_{th}^{\frac{c}{2}} b_1^{\frac{c}{2}}\right)\right) + A\frac{1}{6}\left(1 - \exp\left(\gamma_{th}^{\frac{c}{2}} b_2^{\frac{c}{2}}\right)\right) + A\frac{1}{6}\left(1 - \exp\left(\gamma_{th}^{\frac{c}{2}} b_3^{\frac{c}{2}}\right)\right) \end{aligned} \tag{27}$$

5 Average Channel Capacity

The analysis of channel capacity for fading channel is a significant performance metric as it gives an estimation of the information rate that the channel can support with negligible probability of error. In this section, we obtain the closed-form expression of the average channel capacity of the composite WL fading channel followed by analytical expression of channel capacity of combined (time-shared) multipath/shadowed and unshadowed (Rice) fading channel.

Channel capacity is given by [10]

$$C = B \int_0^{\infty} log_2(1+\gamma) p(\gamma) d\gamma \tag{28}$$

Substituting (10) into (28), the average channel capacity of rice fading channel is given by

$$\frac{C}{B} = \int_0^\infty log_2(1+\gamma)\frac{(1+K)e^{-K}}{\bar{\gamma}}\exp\left(-\frac{(1+K)\gamma}{\bar{\gamma}}\right)I_0\left(2\sqrt{\frac{K(1+K)\gamma}{\bar{\gamma}}}\right)d\gamma \tag{29}$$

Using the 8.447 tables of integrals [24] into (29) and noting the Meijer-G functions from Appendix, the average channel capacity for Rician fading is obtained as

$$\frac{C}{B} = \sum_{n=0}^{\infty}\frac{a^{n+1}e^{-K}K^n}{\ln(2)(n!)^2}\int_0^\infty \gamma^n G_{2,2}^{1,2}\left[\gamma\middle|\begin{matrix}1,1\\1,0\end{matrix}\right]G_{0,1}^{1,0}[a\gamma|0]d\gamma \tag{30}$$

where, $a = (1+K)/\bar{\gamma}$. Replacing n by n-1 in (30) and using ([25], /07.34.21.0011.01) and [10], the average channel capacity of Rician fading channel is given by

$$\frac{C}{B} = \sum_{n=1}^{\infty}\frac{a^n e^{-K}K^{n-1}}{\ln(2)((n-1)!)^2}G_{2,3}^{3,1}\left[a\middle|\begin{matrix}-n,1-n\\0,-n,-n\end{matrix}\right] \tag{31}$$

From (7) and (28), the channel capacity for the composite multipath/shadowed fading is given by

$$\frac{C}{B} = \int_0^\infty log_2(1+\gamma)\left(\frac{2}{3}\psi(\mu) + \frac{1}{6}\psi\left(\mu+\sqrt{3}\sigma\right) + \frac{1}{6}\psi\left(\mu-\sqrt{3}\sigma\right)\right)d\gamma \tag{32}$$

where $\psi(x)$ is given in (7). Substituting $\psi(x)$ in (32) and after some manipulation, we have

$$\frac{C}{B} = \sum_{i=1}^{3}\frac{c}{2}\frac{b_i^{\frac{c}{2}}d_i}{\ln(2)}\int_0^\infty \gamma^{\frac{c}{2}-1}ln(1+\gamma)\exp\left(-\gamma^{\frac{c}{2}}b_i^{\frac{c}{2}}\right)d\gamma \tag{33}$$

where, $d_1 = 2/3$, $d_2 = d_3 = 1/6$ and $b_i = \frac{\Gamma\left(1+\frac{2}{c}\right)}{\exp(x_i)}$ $i = 1,2,3$ with $x_1 = \mu$, $x_{2,3} = \mu \pm \sqrt{3}\sigma$ Using [10, Appendix] we have

$$\frac{C}{B} = \sum_{i=1}^{3}\frac{c}{2}\frac{b_i^{\frac{c}{2}}d_i}{\ln(2)}\int_0^\infty \gamma^{\frac{c}{2}-1}G_{2,2}^{1,2}\left[\gamma\middle|\begin{matrix}1,1\\1,0\end{matrix}\right]G_{0,1}^{1,0}\left[\gamma^{\frac{c}{2}}b_i^{\frac{c}{2}}|0\right]d\gamma \tag{34}$$

The channel capacity of composite WL fading channel is expressed as (for details see Appendix)

$$\frac{C}{B} = \sum_{i=1}^{3}\frac{b_i^{\frac{c}{2}}d_i}{\ln(2)}G_{2,2}^{2,1}\left[b_i\middle|\begin{matrix}-\frac{c}{2},1-\frac{c}{2}\\-c/2,-c/2\end{matrix}\right] \tag{35}$$

Finally, by using (31) and (35), we can get the closed form expression of average channel capacity of the combined (time-shared) shadowed/unshadowed fading channel as

$$\begin{aligned}\frac{C}{B}(I) = &\sum_{n=-1}^{\infty}(1-A)\frac{a^n e^{-K}K^{n-1}}{\ln(2)((n-1)!)^2}G_{2,3}^{3,1}\left[a\middle|\begin{matrix}-n,1-n\\0,-n,-n\end{matrix}\right]\\ &+\sum_{i=1}^{3}\frac{Ab_i^{\frac{c}{2}}d_i}{\ln(2)}G_{2,2}^{2,1}\left[b_i\middle|\begin{matrix}-\frac{c}{2},1-\frac{c}{2}\\-c/2,-c/2\end{matrix}\right]\end{aligned} \tag{36}$$

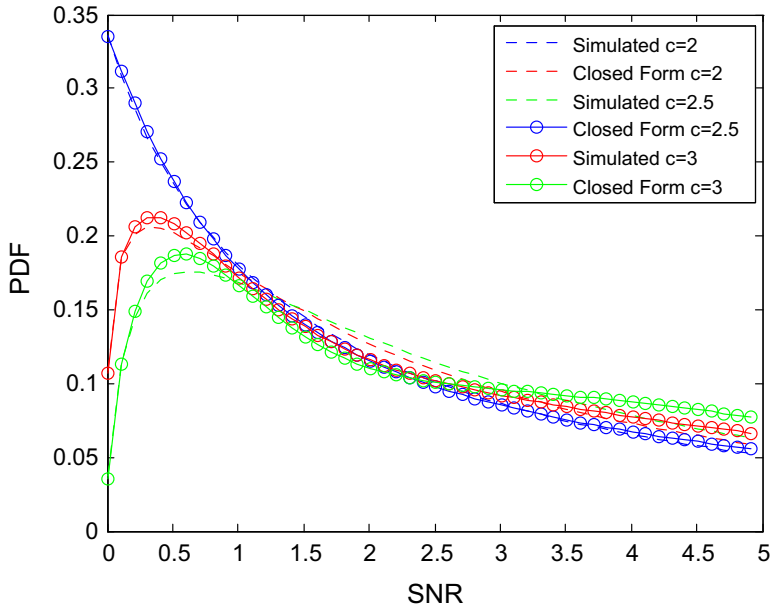

Fig. 1 PDF plots of WL Composite Fading for different values of Weibull fading parameter

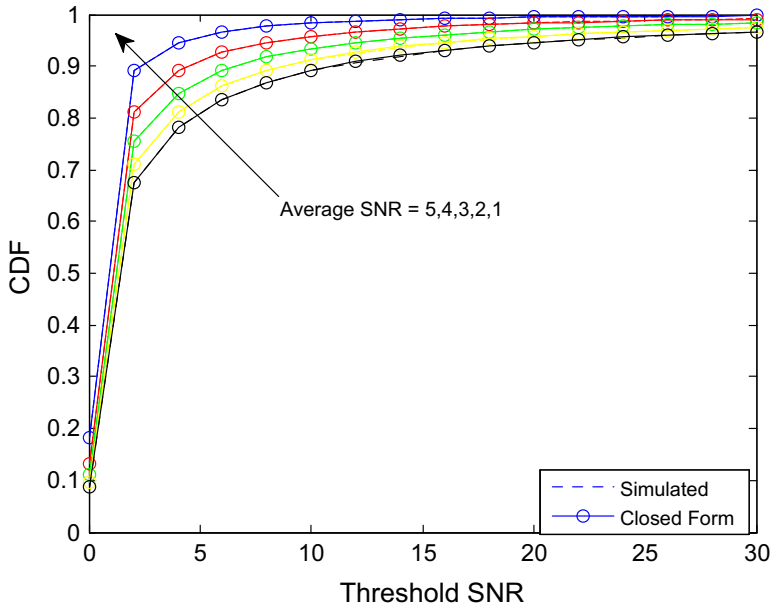

Fig. 2 CDF of composite WL distribution for different values of average SNR

6 Results and Discussion

In this section, we present the graphical results for various performance metrics whose closed-form expressions are obtained in the preceding sections along with the simulation results. The simulation results are obtained by numerically evaluating the exact integrals in MATLAB. Figure 1 depicts the graphical result of composite WL fading (Eq. 6) plotted against SNR (dB) for several values of Weibull fading parameters that is the measure of the severity of the multipath fading. For comparison, the simulated results are also shown. Good agreement confirms the accuracy of the proposed closed-from solution.

In Fig. 2, the CDF of the composite fading is obtained with respect to threshold SNR for several values of average SNR. It is evident from the results that as the average SNR increases, the probability of achieving a given threshold SNR is reduced. Figure 3 illustrates the results of PDF of combined (time-shared) shadowed/unshadowed fading

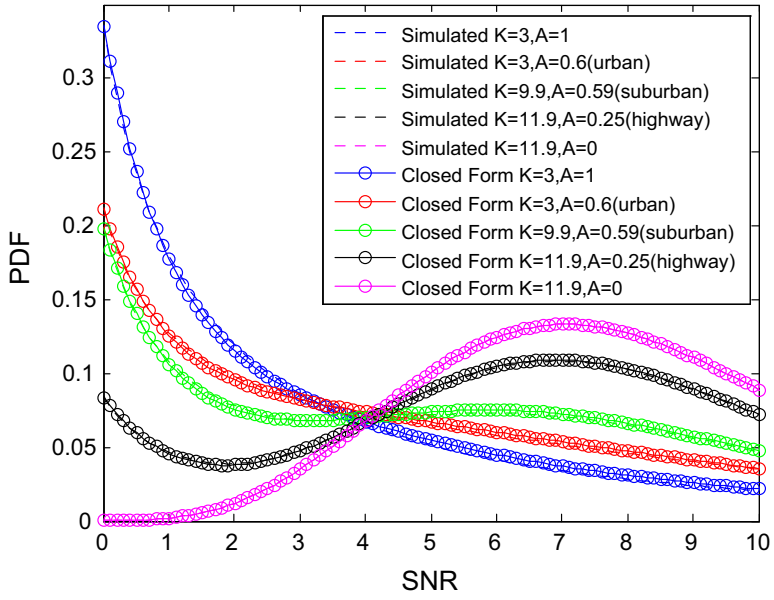

Fig. 3 PDF of combined (time-shared) multipath/shadowing and unshadowing fading for urban, sub-urban and highway [14] for Weibull fading parameter c = 2

Table 1 Parameters A and K for various scenarios [14]

Environment	A	K (dB)
Urban	0.60	3
Suburban	0.59	9.9
Highway	0.25	11.9

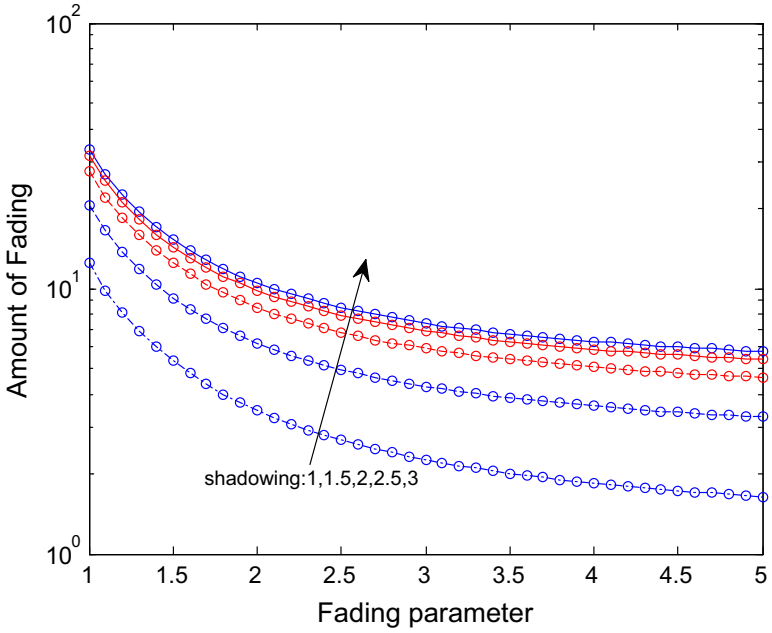

Fig. 4 AF of composite fading against fading parameter for several values of shadowing

(Eq. 11). Several cases of shadowing enlisted in [14] such as urban, sub-urban and highway scenarios have been considered. The corresponding values of *A* (a time-share factor that indicates the probability of occurrence of shadowing and unshadowing) and rice factors for these scenarios are presented in Table 1. It is quite evident from the several PDF distributions of the combined multipath/shadowing and unshadowed fading scenario that as

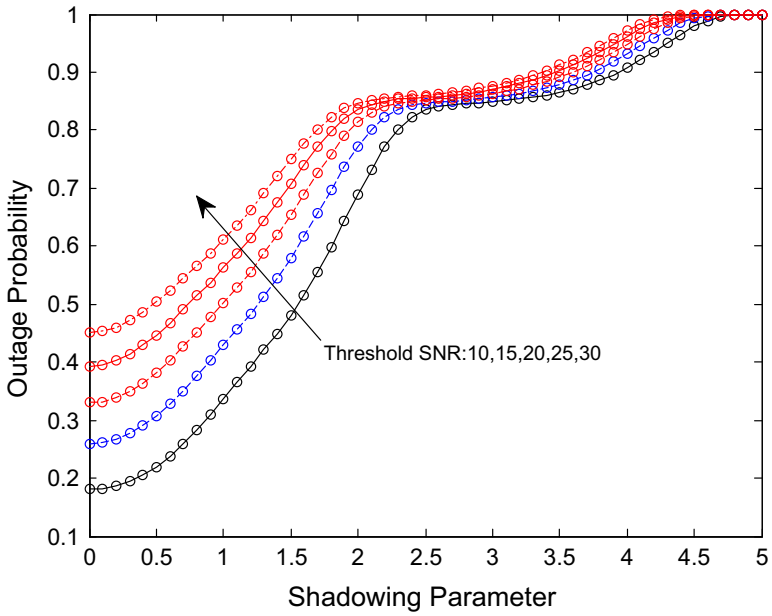

Fig. 5 P_{out} as a function of shadowing parameter

one moves from highway to urban scenario, the PDF moves to left indicating an increase in the randomness of channel. It is also observed that for highway scenario, the fading is dominated by Rician distribution and hence the PDF nearing the perfect Rician curve. Simulated results confirm the accuracy of the results

After discussing the PDF of composite fading, we can use the quantitative measure of AF to compare power fluctuation in the composite fading channel. Figure 4 illustrates the AF of composite WL fading plotted against the multipath fading parameter for several values of shadowing parameters using (12) and (15). The results points out that as the AF decreases with increase in the Weibull fading parameter (It may be noted that the Weibull fading parameter is the measure of severity of multipath and is reduced with increase in the fading parameter). As the severity of shadowing increases, the AF plots of composite fading moves upward indicating an increase in the randomness of channel deteriorating the performance of the receiver.

In Figs. 5, 6 and 7, we have analyzed the performance of the receiver in term of P_{out}. Figure 5 shows the P_{out} as a function of log-normal shadowing parameter for several values

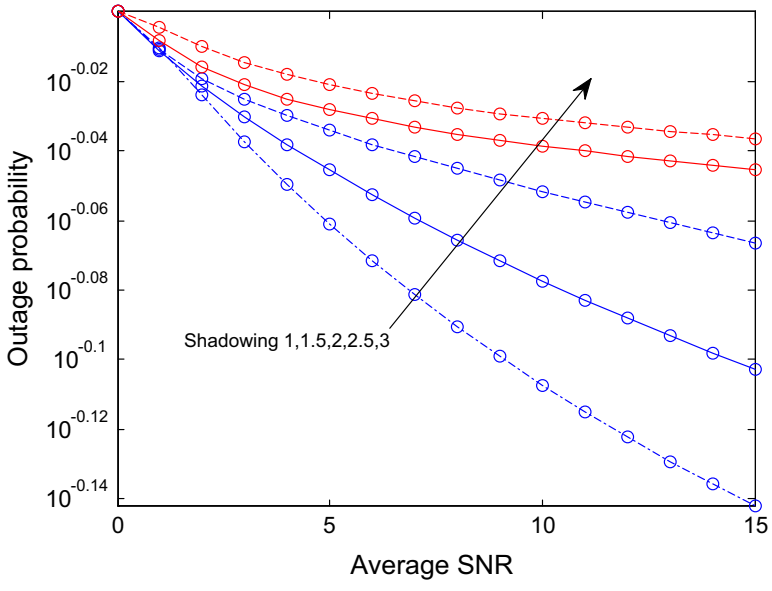

Fig. 6 P_{out} versus average SNR for different values of shadowing parameter σ

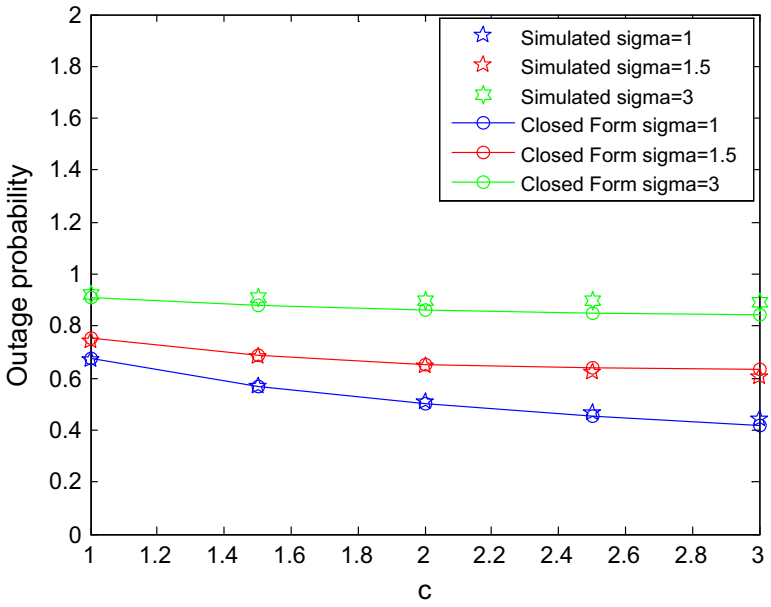

Fig. 7 P_{out} versus fading parameter for several shadowing parameter

Fig. 8 Average channel capacity versus shadowing for varying fading parameter

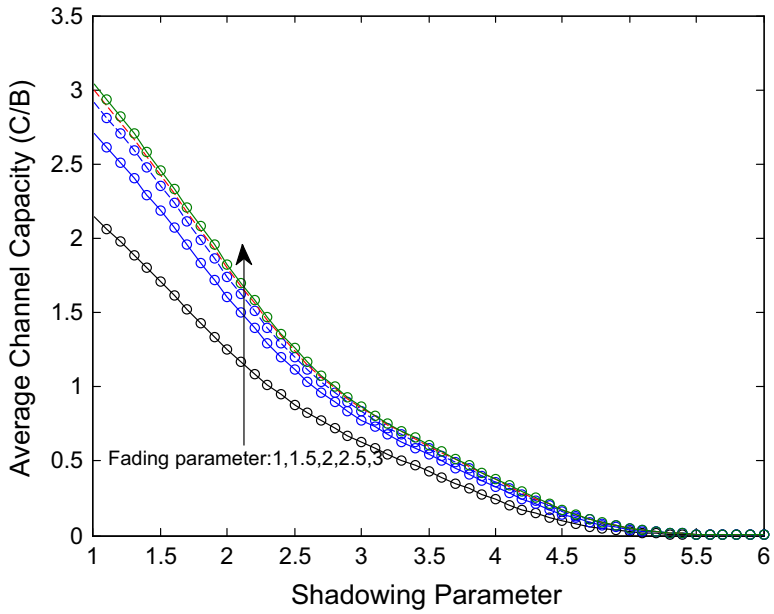

of threshold SNR. It is clear from the results that P_{out} increases with increase in the shadowing parameter indicating the increase in the likelihood of the failure to achieve a given threshold SNR as we move from light shadowing scenario to heavy shadowing scenario. One can seea deleterious effect of shadowing parameter deteriorating the receiver performance, thus, requiring the diversity combining to improve the performance.

In Fig. 6, as expected, P_{out} is shown to decrease with average SNR. Moreover, for a given average SNR, P_{out} increases with moving from light shadowing to medium shadowing, a similar observation as noted in Fig. 5.

In Fig. 7, the results for P_{out} of composite WL fading are illustrated with respect to fading parameter (Eq. 26). The results are obtained for several values of shadowing parameter. It is observed that the increase in the Weibull multipath fading parameter results in the decrease in the P_{out}; a expected results as the decrease in the severity of multipath

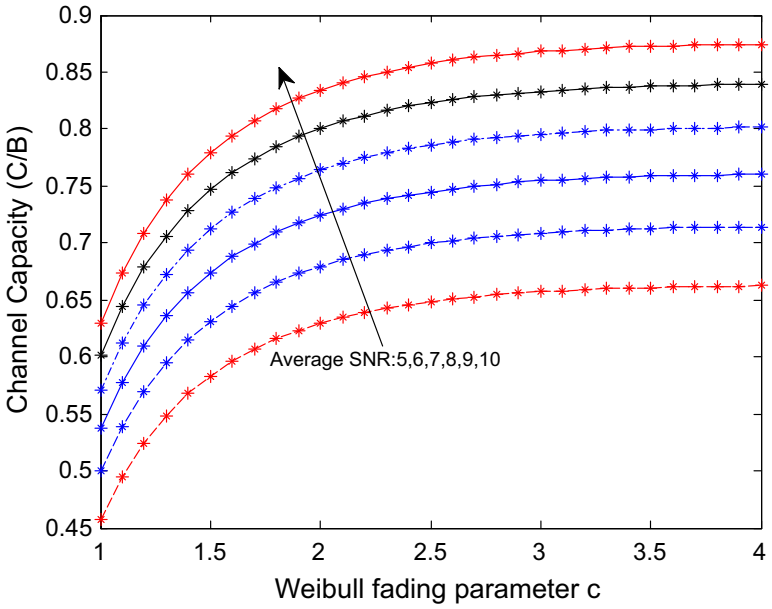

Fig. 9 Average channel capacity versus fading parameter for different average SNR

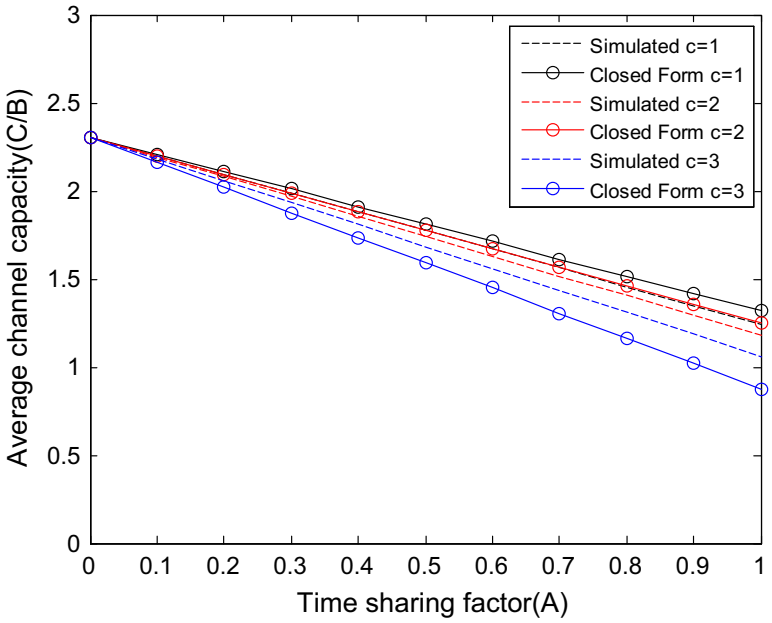

Fig. 10 Average channel capacity against time-sharing factor *A* of combined shadowed and unshadowed fading for several values of fading parameters

should decrease the probability of failure in achieving a given threshold SNR. Further, as we move from average shadowing to heavy shadowing, P_{out} is expected to deteriorate as is obvious from the plot.

Figure 8 and 9 illustrates the average channel capacity of composite WL fading as a function of shadowing parameter and multipath fading parameter respectively. Figure 10 shows the plot of the channel capacity of combined shadowed/unshadowed fading against time-share factor. In Fig. 8, as expected, the average channel capacity is going to decrease with increase in the shadowing parameter; a very obvious deleterious effect of shadowing. The capacity improves with reduction in the severity of the multipath as is obvious from the plot. In Fig. 9, capacity plots are obtained against fading parameter and capacity is, as

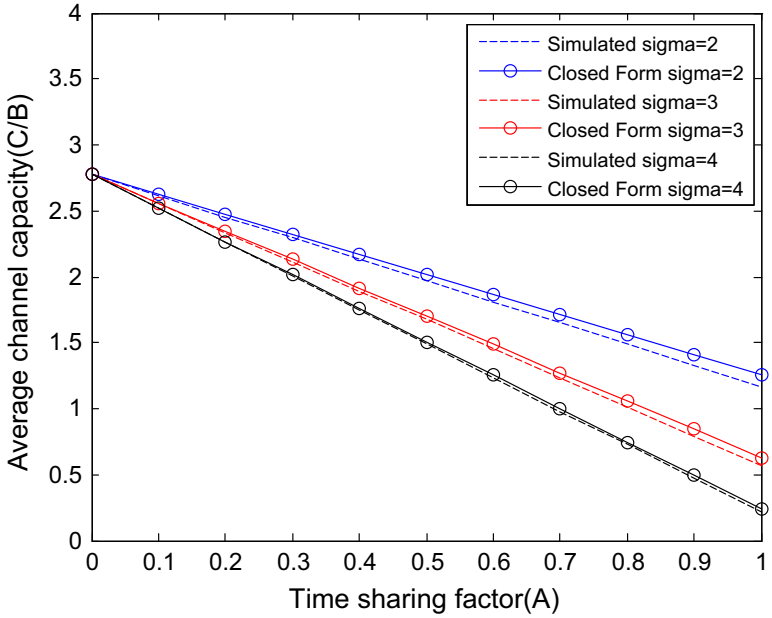

Fig. 11 Average channel capacity against time-sharing factor A of combined shadowed and unshadowed fading for several values of shadowing parameters

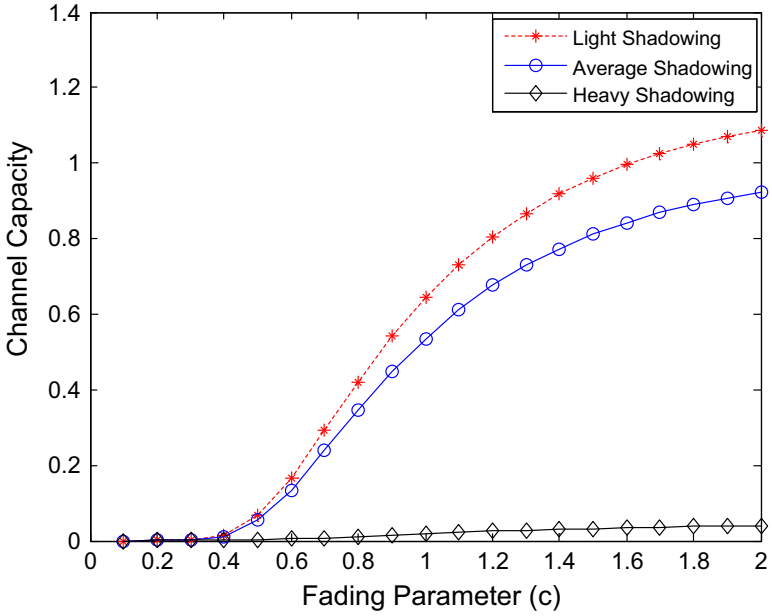

Fig. 12 Comparison of channel capacity for three different shadowing environments: (1) light shadowing (2) average shadowing and (3) heavy shadowing

expected, found to improve with less severe multipath fading condition. Further, an increase in the average SNR improves the average capacity as is shown in the results.

In Figs. 10 and 11, we obtain the channel capacity plots for several values of fading parameter and shadowing parameters respectively against a time-sharing factor which indicates the likelihood of occurrence of unshadowed and shadowed fading conditions. It is observed that as the time-sharing factor increases (indicating a shift from Rice to multipath/shadowed condition), the capacity deteriorates which is quite expected as severity of multipath and shadowing conditions is bound to decrease the capacity. Simulation results are in close agreement with the closed form obtained in this paper. In the last, in Fig. 12, we have provided the comparison of channel capacity for three different scenarios such as light shadowing, average shadowing and heavy shadowing with $\sigma = 0.115, \mu = 0.115$ for

light shadowing, $\sigma = 0.161, \mu = -0.115$ for average shadowing and $\sigma = 0.806, \mu = -3.914$ respectively [15]. The results clearly indicate the extent of channel capacity variation with channel conditions varying from light to heavy shadowing.

7 Conclusion

In this study, we have achieved the closed-form expressions for PDF of instantaneous SNR of the composite WL fading and combined (time-shared) shadowed/unshadowed fading scenario. The procedure uses the Holtzman approximations to estimate the closed-form of composite PDF of WL fading. The solution, thus obtained, is accurate in severe multipath fading with light to medium shadowing conditions. The resulting Holtzman approximation for WL fading has the advantage of being in closed-form, thereby facilitating the analysis of performance parameters such as AF, P_{out} and average channel capacity of the communication links over WL as well as combined (time-shared) shadowed/unshadowing fading channel.

Appendix

Proof of (35)

$$I = \int_0^\infty \gamma^{n-1} G_{2,2}^{1,2}\left[\gamma \middle| \begin{matrix} 1,1 \\ 1,0 \end{matrix}\right] G_{0,1}^{1,0}\left[a\gamma^n \middle| \begin{matrix} 1,1 \\ 1,0 \end{matrix}\right] d\gamma \tag{37}$$

As per Generalization of classical Meijer's integral from two G functions ([25], / 07.34.21.0012.01)

$$\begin{aligned} &\int_0^\infty \tau^{\alpha-1} G_{u,v}^{s,t}\left(\sigma\tau \middle| \begin{matrix} c_1, c_2, \ldots, c_u \\ d_1, d_2, \ldots, d_v \end{matrix}\right) G_{p,q}^{m,n}\left(w\tau^r \middle| \begin{matrix} a_1, a_2, \ldots, a_p \\ b_1, b_2, \ldots, bq \end{matrix}\right) d\gamma \\ &= \sigma^{-\alpha} H_{p+v,q+u}^{m+t,n+s}\left(\frac{w}{\sigma^r} \middle| \begin{matrix} (a_1,1), \ldots, (a_n,1), (1-\alpha-d_1,r), \ldots, (1-\alpha-d_v,r), (a_{n+1},1), \ldots, , (a_p,1) \\ (b_1,1), \ldots, (b_m,1), (1-\alpha-c_1,r), \ldots, (1-\alpha-c_u,r), (b_{m+1},1), \ldots, , (b_q,1) \end{matrix}\right) ./; r > 0 \end{aligned} \tag{38}$$

Using the result of (38), the integral of (37) can be easily written as

$$I = (1)^{-n} H_{2,3}^{3,1}\left[a \middle| \begin{matrix} (-n,n), (1-n,n) \\ (0,1), (-n,n), (-n,n) \end{matrix}\right] \tag{39}$$

For any a, b, c, where $\mathrm{Re}(b) > 0 \,\&\, m \geq 1$; ([26], /Eq. 1.66)

$$H_{p,q}^{m,n}\left[z \middle| \begin{matrix} (a_1,A_1), \ldots, (a_p,A_p) \\ (b,0)(a_1,A_1), \ldots, (a_p,A_p) \end{matrix}\right] = \Gamma(b) H_{p,q-1}^{m-1,n}\left[z \middle| \begin{matrix} (a_1,A_1), \ldots, (a_p,A_p) \\ (a_1,A_1), \ldots, (a_p,A_p) \end{matrix}\right] \tag{40}$$

Using (40), (6) can be easily written as

$$I = \Gamma(1) H_{2,2}^{2,1}\left[a \middle| \begin{matrix} (-n,n), (1-n,n) \\ (-n,n), (-n,n) \end{matrix}\right] \tag{41}$$

Now as per [27, Eq. 3.3],

$$H_{p,q}^{m,n}\left(\begin{matrix}\{(a_j,c)\}_{j=1,\ldots,p}\\ \{(a_j,c)\}_{j=1,\ldots,p}\end{matrix}\middle| z\right)=\frac{1}{c}G_{p,q}^{m,n}\left(\begin{matrix}\{(a_j,c)\}_{j=1,\ldots,p}\\ \{(a_j,c)\}_{j=1,\ldots,p}\end{matrix}\middle| z^{1/c}\right) \tag{42}$$

Using (42), we obtain a simplified form of (41) in terms of Meijer-G function expressed as

$$I=\frac{1}{n}G_{2,2}^{2,1}\left[\begin{matrix}-n,1-n\\ -n,-n\end{matrix}\middle| a^{1/n}\right] \tag{43}$$

References

1. Simon, M. K., & Alouini, M. S. (2004). *Digital communication over fading channels* (2nd ed.). New York: Wiley-IEEE Press.
2. Khandelwal, V., & Karmeshu, (2014). A new approximation for average symbol error probability over log-normal channels. *IEEE Wireless Communications Letters, 3*(1), 58–61.
3. Hashemi, H. (1993). Impulse response modeling of indoor radio propagation channels. *IEEE Journal on Selected Areas in Communications, 11*(7), 967–978.
4. Hansen, F., & Mano, F. I. (1977). Mobile fading—Rayleigh and lognormal superimposed. *IEEE Transactions on Vehicular Technology, 26*(4), 332–335.
5. Al-Ahmadi, S., & Yanikomeroglu, H. (2010). On the approximation of the generalized-K distribution by a gamma distribution for modeling composite fading channels. *IEEE Transactions on Wireless Communications, 9*(2), 706–713.
6. Sagias, N. C., Karagiannidis, G. K., Bithas, P. S., & Mathiopoulos, P. T. (2005). On the correlated Weibull fading model and its applications. *Proceedings of IEEE Vehicular Technology Conference, 4*, 2149–2153.
7. Hashemi, H. (1993). The indoor radio propagation channel. *Proceedings of the IEEE, 81*, 943–968.
8. McConoughey, S. R., Adawi, N. S., Bertoni, H. L., Child, J. R., Daniel, W. A., Dettra, J. E., et al. (1988). Coverage prediction for mobile radio systems operating in the 800/900-MHz frequency range. *IEEE Transactions on Vehicular Technology, 37*(1), 3–72.
9. Sagias, N. C., Zogas, D. A., Karagiannidis, G. K., & Tombras, G. S. (2004). Channel capacity and second-order statistics in Weibull fading. *IEEE Communications Letters, 8*(6), 377–379.
10. El Bouanani, F., Ben-Azza, H., & Belkasmi, M. (2012). New Results for the Shannon channel capacity over generalized multipath fading channels for MRC diversity. *EURASIP Journal on Wireless Communications and Networking, 2012*, 336.
11. Al-Hussaini, E. K., Al-Bassiouni, A. M., Mouradand, H. M., & Al-Shennawy, H. (2002). Composite macroscopic and microscopic diversity of sectorized macro cellular and microcellular mobile radio systems employing RAKE receiver over Nakagami fading plus lognormal shadowing channel. *Wireless Personal Communications, 21*(3), 309–328.
12. Jakes, W. C. (1994). *Microwave mobile communication* (2nd ed.). Piscataway, NJ: IEEE Press.
13. Abdi, A., & Kaveh, M. (1999). On the utility of Gamma PDF in modeling shadow fading (slow fading). *Proceedings of IEEE Vehicular Technology Conference, 3*, 2308–2312.
14. Bithas, P. S. (2009). Weibull-gamma composite distribution: Alternative multipath/shadowing fading model. *IEEE Electronic Letters, 45*(14), 749–751.
15. Laourine, A., Alouini, M.-S., Affes, S., & Stephenne, A. (2009). On the performance analysis of composite multipath/shadowing channels using the G-distribution. *IEEE Transactions on Communications, 57*(4), 1162–1170.
16. Atapattu, S., Tellambura, C., & Jiang, H. (2010). Representation of composite fading and shadowing distributions by using mixtures of gamma distributions. In *Proceedings IEEE WCNC*, pp. 1–5.
17. Miticand, A., & Jakovljevic, M. (2007). Second-order statistics in Weibull-lognormal fading channels. In: *Proceedings of TEKSIKS*, Serbia, Nis.
18. Alouini, M. S., & Smith, G. (1999). A unified approach for calculating error rates of linearly modulated signals over generalized fading channels. *IEEE Transactions on Communication, 47*(9), 1324–1334.
19. Lutz, E., Cygan, D., Dippold, M., Dolainsky, F., & Papke, W. (1991). The land mobile satellite communication channel: Recording, statistics, and channel model. *IEEE Transactions on Vehicular Technology, 40*(2), 375–386.

20. Barts, R. M., & Stutzman, W. L. (1992). Modeling and simulation of mobile satellite propagation. *IEEE Transactions on Antennas and Propagation, 40*(4), 375–382.
21. Lieblein, J. (1955). On moments of order statistics from the Weibull distribution. *The Annals of Mathematical Statistics, 26*(2), 330–333.
22. Holtzman, J. M. (1992). A simple, accurate method to calculate spread multiple access error probabilities. *IEEE Transactions on Communications, 40*(3), 461–464.
23. Khandelwal, Karmeshuand V. (2013). On the applicability of average channel capacity in log-normal fading environment. *Wireless Personal Communications, 68*(4), 1393–1402.
24. Gradshteyn, I. S., & Ryzhik, I. M. Table of integrals, series, and products (7th edn). Academic Press Elsevier.
25. The Wolfram functions site. [Online]. Available: http://functions.wolfram.com.
26. Mathai, A. M., Saxena, R. K., & Haubold, H. J. (2010). *The H-function: Theory and applications*. Berlin: Springer.
27. Coelho, C. A., & Arnold, B. C. (2012). Instances of the Meijer-G and Fox-H functions and of the distribution of the product of independent beta random variables with finite representation. *AIP Conference Proceedings, 1479*, 1133. doi:10.1063/1.4756348.

Rupender Singh has done his M.Tech from Delhi Technological University (Formerly Delhi College of Engineering), Delhi (India). He has received his B.Tech from MJP Rohilkhand University, Bareilly (India). He has published one book with CBS, Delhi (India) and presented 20 research papers in International/National journals/conferences. He is having 6 years of teaching experience in engineering college in Gurgaon (India). His area of interest is wireless communication.

Sanjay Kumar Soni was born in UP, India in 1975. He received his Bachelor of Engineering in electronics engineering from Madan Mohan Malviya Engineering College, Gorakhpur in 1997, the M.Tech., degree in communication engineering from IIT Kanpur in 2004, and Ph.D. in wireless Communication Engineering from IIT Kharagpur in 2011. Currently, he is an Associate Professor in the department of Electronics and Communication in G. B. Pant Engineering College, Pauri (Uttrakhand). He has more than 14 years teaching experience. His research interest includes propagation modelling and characterization of wireless channel, time-domain analysis of propagation channel for UWB signals.

Ram Shringar Raw received his B.E. (Computer Science and Engineering) from G. B. Pant Engineering College, Pauri-Garhwal, UK, India and M.Tech (Information Technology) from Sam Higginbottom Institute of Agriculture, Technology and Sciences, Allahabad (UP), India in 2000 and 2005, respectively. He has obtained his Ph.D. (Computer Science and Technology) from School of Computer and Systems Sciences, Jawaharlal Nehru University, New Delhi, India in 2011. He is currently working as Assistant Professor in the Department of Computer Science and Engineering, Ambedkar Institute of Advanced Communication Technologies and Research, GGSIP University, Delhi, India. He has more than 13 years of teaching and research experience. His current research interest includes Mobile Ad hoc Networks and Vehicular Ad hoc Networks. Dr. Raw has published papers in International Journals and Conferences including IEEE, Springer, Inderscience, Hindawi Publications, American Institute of Physics, AIRCC, etc.

Sandeep Kumar received his B. Tech degree in Electronics and Communication from Kurukshetra University, India in 2004 and M.E. degree in Electronics and Communication from Thapar University, Patiala, India in 2007. He is currently pursuing Ph.D. from Delhi Technological University, India. Presently he is working as Member (Research Staff) at Central Research Laboratory, Ghaziabad, Bharat Electronics Limited. His research interest includes study of wireless channels, performance modeling of fading channels and Radio network Planning.

A retrospective view of noise pollution control policy in India: status, proposed revisions and control measures

N. Garg and S. Maji*

This article provides a retrospective view of noise policies and ordinances in India. It also proposes revisions in them for noise abatement and control based on the available knowledge on noise policies and regulations followed around the world. The work focuses on the inclusion of noise limits for construction activities, household appliances apart from the revision in ambient noise standards and National Building Codes for protection against noise pollution. It is envisaged that the proposed revisions and work plan shall be instrumental in execution of noise abatement action plans for controlling noise pollution in India.

Keywords: Ambient noise standards, control measures, noise pollution, polices and ordinances.

NOISE pollution has become a serious problem for the society. In India, with expanding vehicular population traffic noise levels have increased, which can cause serious health effects. The World Health Organization (WHO) recognized noise as one of the major pollutants affecting the health of the human population[1]. The major sources of noise pollution are: road traffic, rail, aircraft noise, construction noise, noise emitted from the industrial set-ups, honking noise from vehicles, noise emitted from household appliances, loudspeakers, community processions, etc. Road traffic noise has been observed to be the major source of noise pollution in most of these studies carried out in different parts of the world[2–4]. Long-term noise monitoring studies are required not only for ascertaining the magnitude of ambient levels, but also for devising suitable control action plans. The European Environmental Noise Directive 2002/49/EC relating to the assessment and management of environmental noise establishes that the member states should create noise maps for the parts of their territory in terms of single-noise descriptors: day–evening–night level (L_{den}) and night equivalent level (L_{night}) respectively[5]. Implementing long-term and short-term noise monitoring strategies for measuring the ambient noise levels in various part of cities and planning of suitable abatement measures for reducing noise pollution in Indian cities are essential. The Central Pollution Control Board (CPCB), New Delhi, has initiated a National Ambient Noise Monitoring Network (NANMN) with an objective of collecting real-time noise monitoring data from major cities of India[6–8]. The network provides ambient noise level data which can be helpful in identification of noisy spots and adoption of suitable measures of abatement for noise pollution control. A retrospective view of the ambient noise standards and National Building Codes of India is required so as to ensure that the current standards, noise policies and legislations are suitable and effective enough to control noise pollution in India. The development of a validated road traffic noise model[9,10] integrated with a GIS interface for developing noise maps for Indian cities shall be indispensable in conducting Environmental Impact Assessment (EIA) studies especially for new projects and development of 'smart cities' concept implemented recently by the Government of India (GoI).

The objective of the present work is to study the status of policies and ordinances in the Indian scenario, and propose revisions for noise abatement and control based on the available knowledge on noise policies and regulations around the world[11]. This independent study is based on the available knowledge on noise policies and regulations followed around the world. It has nothing to do with any legal or Government body sponsoring the work, or accepting the conclusions of the present work. As such, in India, it is the prerogative of many Government agencies including CPCB, State Pollution Control Boards, Ministry of Environment and Forests (MoEF), GoI in consultation with National Committee on Noise Pollution Control to formulate and revise the ambient noise standards, ordinances and legislations. The Panel for Acoustics, Sound Insulation and Noise Control, CED 46:P20, constituted by the Bureau of Indian Standards

N. Garg is in the CSIR-National Physical Laboratory, New Delhi 110 012, India; S. Maji is in the Delhi Technological University, Delhi 110 042, India.
*For correspondence. (e-mail: ngarg@nplindia.org)

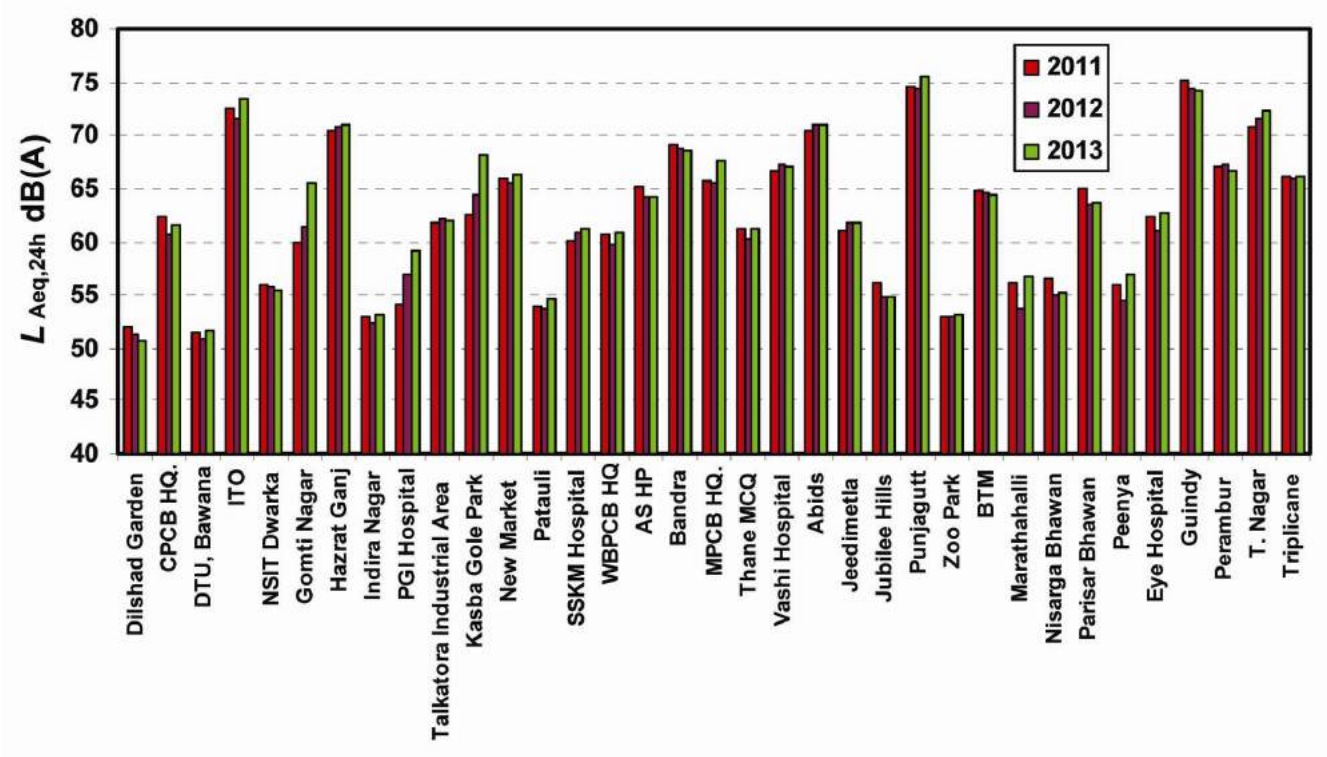

Figure 1. $L_{Aeq,24h}$ at 35 locations spread across seven major cities all over India during 2011–2013.

is responsible for amendments and revisions in National Building Codes of India[12]. Although the proposed revisions in the ambient noise standards and sound regulation requirements have been explicitly discussed earlier[13,14], the objective of the present study is to consider the overall noise pollution control policies, ordinances and measures for all types of noise sources in totality in the Indian scenario and suggesting a road map for developing a 'noise-free community' in Indian cities in the next decades.

NANMN project: status and implications

The NANMN project was established in 2011 by CPCB. Phase I of NANMN covers 35 locations in seven metro cities of India. Among these, 14 locations lie in commercial zones, 5 in industrial, 7 in residential and 9 in silence zones. The details of the project and analysis of available noise data have been discussed elaborately in the literature[8,15–17]. Figure 1 shows the equivalent continuous sound pressure level for 24 h duration, $L_{Aeq,24h}$ levels at 35 locations spread across seven major cities all over India during 2011–2013. It can be observed from the 2013 noise monitoring data that 11 out of the 35 sites (31.4%) have $L_{Aeq,24h}$ levels between 60 and 65 dB(A), while 6 sites (17.1%) have ambient noise levels more than 70 dB(A). Eleven sites have ambient noise levels less than 60 dB(A) $L_{Aeq,24h}$. $L_{Aeq,24h}$ levels varied from 50.8 to 67.1 dB(A) in 2013 for the silence zones, while for residential areas, they varied from 53.1 to 66.1 dB(A). For commercial zones, the $L_{Aeq,24h}$ levels varied from 56.7 to 75.4 dB(A), while for industrial zones, they varied from 57.0 to 74.2 dB(A). The Punjagutta commercial area had maximum $L_{Aeq,24h}$ level of 75.4 dB(A), while the Dilshad Garden had minimum $L_{Aeq,24h}$ level of 50.8 dB(A). Analysis of data also reveals that $L_{Aeq,24h}$ levels have marginally increased in three years, except for the sites Gomti Nagar, PGI Hospital and Kasba Gole Park, where an increase in ambient levels of ≥5 dB(A) is noticed. Thus, the noise monitoring data acquired from these sites are instrumental in analysing the scenario in seven cities of India and adopting suitable noise pollution control measures. The numbers of monitoring stations has increased to 70 in 2014, with each city having ten noise monitoring stations.

Proposed revisions in the ambient standards and National Building Codes

With expanding vehicular population, especially in metro cities, it is necessary to amend the ambient noise standards to reasonable values that can be easily enforced, so as to control the noise pollution levels. Table 1 shows the proposed ambient noise standards[13]. The modified adjustments to ISO 1996-1:2003 (ref. 18) recommendations

are to be added to the measured or predicted $L_{Aeq,24h}$ depending upon the type of sound source and the character of sound as explicitly mentioned in Garg *et al.*[13]. The detailed explanation and basis for selecting a cumulative noise exposure metrics such as $L_{Aeq,24h}$ and modified adjustments proposed can be found in Garg *et al.*[13]. It is proposed that for areas under silence zone, the limit is 55 dB(A); while for commercial area, and mixed residential and commercial zones, the limit is recommended as 65 dB $L_{Aeq,24h}$. The underlying objective behind adding the modified adjustments to ISO 1996-1:2003 to $L_{Aeq,24h}$ sound levels is that it will not only be able to overcome the limitations of tonality and character of sound, but also be applicable to road, rail and aircraft noise. Thus ambient standards shall be applicable for various defined areas, including those prone to aircraft noise. The proposed standards are recommended for various areas categorized under silence, residential, commercial, industrial and mixed type zones and all type of noise sources[13]. A WHO report[19] recommends that noise limits could be relatively high but rigidly enforced, or have a very low value with no legal binding whatsoever. Thus, the ambient standards proposed in the present context recommends reasonable values of ambient noise standards for various areas or zones (Table 1), so as to strictly enforce them for reducing noise pollution in the country[13].

The legal sound insulation requirements are also another important aspect for controlling noise pollution as these are vital to fight against higher ambient noise levels. In view of acoustic comfort, there has been considerable research, particularly in Europe, for better sound insulation criteria to regulate the airborne and impact sound insulation between dwellings and airborne sound insulation of facades. Also, meeting the legal requirements does not guarantee sufficient acoustic comfort. Hence several countries in Europe have adopted classification schemes for better acoustic comfort which are further higher criteria than the legal requirements intended to provide the acoustic comfort. Presently, the National Building Codes of India recommend the sound insulation criteria in terms of weighted sound reduction index (R_w) and minimum sound reduction (D_w) between rooms[12].

Table 1. Proposed ambient noise standards[13]

Area code	Category of area/zone	$L_{Aeq,24h}$ (dB(A))*
A	Industrial area	70
B	Commercial area, mixed zone	65
C	Residential area**	60
D	Silence zone**	55

*The modified adjustment factors to ISO 1996-1:2003 enlisted in Garg *et al.*[13] should be applied to the measured $L_{Aeq,24h}$ in analysis of environmental noise.

**An additional 5 dB(A) relaxation to the existing urban residential area with high population density and existing areas under silence zone may be provided by the competent authority depending upon the situation when there are only few alternatives left for application of noise abatement measures.

However, in the light of many studies conducted in Europe[20,21] and wide usage of spectrum adaptation terms (C, C_{tr}) the National Building Codes have to be amended utilizing the weighted standardized field-level difference, $D_{nT,w}$ as the descriptor used for *in situ* measurement of sound insulation. Table 2 shows the proposed criteria[14] and descriptors for building elements based on the exhaustive literature survey. Class C refers to the minimum criteria that must be followed as chosen in other countries, while Class B is defined for the acoustic comfort having an average noise level reduction of the order of 35 dB. Class A represents the high acoustic comfort levels achieved through a noise level reduction of 40 dB. The $R_w + C_{tr,50\text{-}3150} \geq 50$ dB criterion is chosen for acoustic comfort criteria, when the outdoor noise level is within 70–75 dB(A). The criterion is enhanced by 5 dB (Class A) for an outdoor noise level more than 75 dB(A). The minimum criterion of weighted sound reduction index, R_w of 50 dB is judiciously chosen for new buildings for protection against external noise. The detailed explanation and basis of choosing these values can be found in Garg *et al.*[14]. The choice between the sound insulation criterion down to 50 Hz or the common lower limit of 100 Hz may be exercised[22] depending upon the calibration and measurement capabilities (CMCs) of testing laboratories engaged in sound transmission loss testing in India[23,24]. Thus, in the Indian context, clear-cut guidelines for sound regulation requirements like those in European member states shall not only provide a harmonization of sound descriptors with those followed in other countries, but shall also be helpful in reducing the R&D costs for the building industry in India for development of suitable products or systems with desired noise level reductions[25].

The technological advancement in building sciences adapting for light-weight, dry-wall construction materials with high strength and rigidity and improved sound insulation characteristics has to be thus brought in persistent use in Indian dwellings, rather than relying on massive constructions[26–28]. It is envisaged that stricter building codes with respect to sound insulation requirements of building elements shall be implemented and strictly enforced in National Building Codes of India for new residential projects and 'smart cities' developed in the future to provide acoustic comfort to residents from the outside noise.

Noise pollution control policies and measures

The major objectives of a noise control programme should be to identify areas having high ambient noise levels in each part of the city, and evaluating the efficacy and suitability of noise abatement measures for bringing

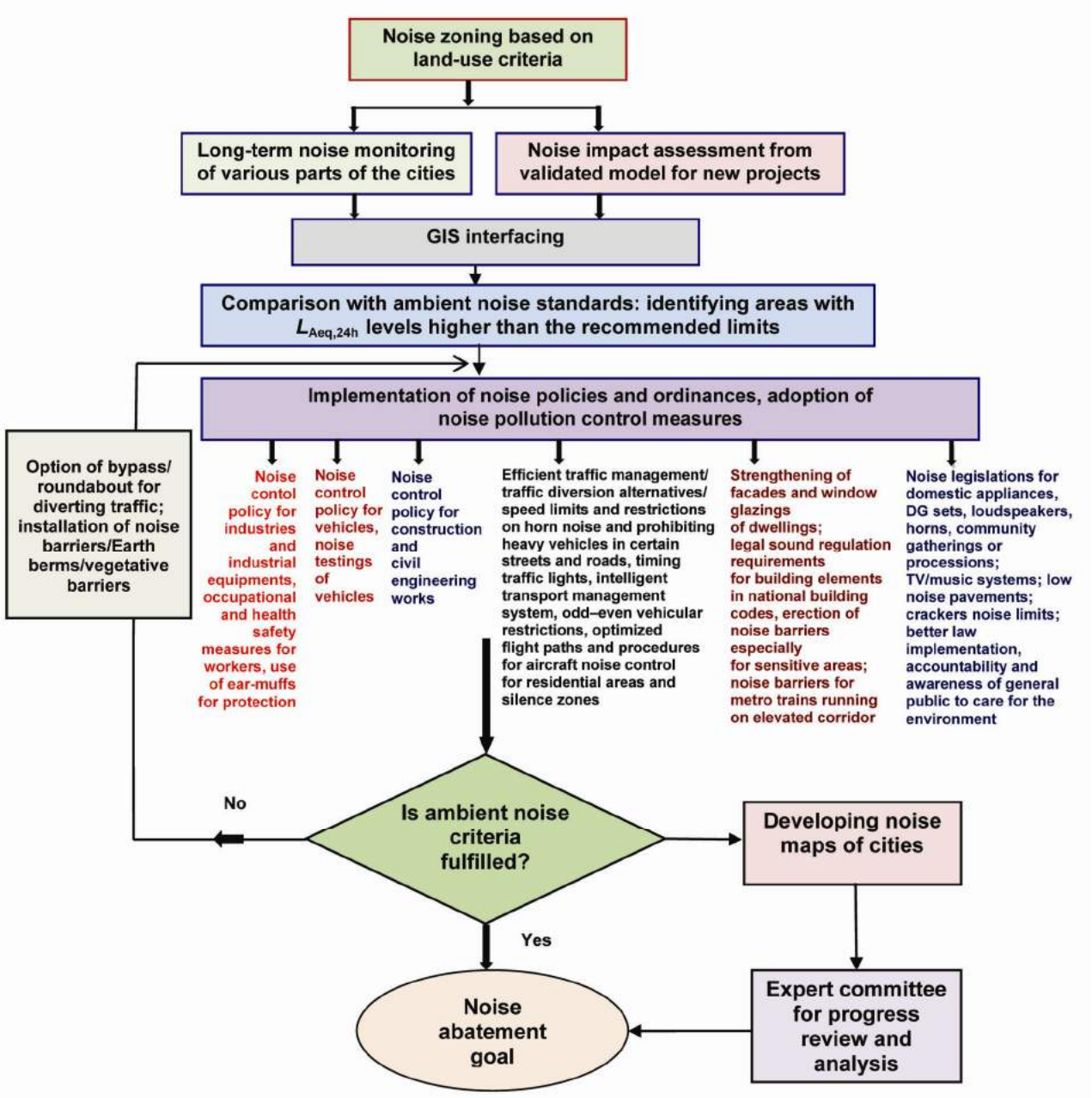

Figure 2. Flow chart of a noise pollution control strategy for reducing ambient noise levels in Indian cities.

these levels below the ambient noise standards. An appropriate noise policy suitable for controlling the noise exposure of various sources is necessary. Figure 2 shows a comprehensive and modified flow chart of a noise pollution control strategy for reducing the ambient noise levels in Indian cities, as discussed previously[13]. Noise zoning based on land-use criteria, noise monitoring and noise impact assessment using a validated model and implementation of policies and ordinances for noise control are the various aspects of the noise control programme to be emphasized. Noise mapping of the cities and ascertaining the compliance of ambient noise standards should be the major objective of such a programme. Adoption of a noise abatement goal as proposed in a Dutch study[29] shall provide a roadmap for execution of such a programme at a diversified scale. However, special fundings, support from local municipal authorities, State Pollution Control Boards, transport and development authority such as Delhi Development Authority, as well as awareness among the general are needed for the accomplishment of targets[30]. For instance, a noise abatement goal may be formulated as follows: decreasing the number of houses exposed to a noise level >75 dB(A) by 100%, >70 dB(A) by 90% and >65 dB(A) by 50% to be realized till 2030.

Table 2. Proposed criteria and descriptors for building elements[14]

Building elements	Prescriptive criteria (dB)		Verification criteria (dB)	
Facades	Class A	$R_w + C_{tr,50\text{-}3150} \geq 55$ when $L_d > 75$ dB(A)	Class A	$D_{nT,w} + C_{tr,50\text{-}3150} \geq 50$ when $L_d > 75$ dB(A)
	Class B	$R_w + C_{tr,50\text{-}3150} \geq 50$ when $70 \leq L_d \leq 75$ dB(A)	Class B	$D_{nT,w} + C_{tr,50\text{-}3150} \geq 45$ when $70 \leq L_d \leq 75$ dB(A)
	Class C	$R_w \geq 50$	Class C	$D_{nT,w} \geq 45$
	Class D	$R_w \geq 45$	Class D	$D_{nT,w} \geq 40$
Between dwellings	Class A	$R_w + C_{50\text{-}3150} \geq 60$	Class A	$D_{nT,w} + C_{50\text{-}3150} \geq 55$
	Class B	$R_w + C_{50\text{-}3150} \geq 55$	Class B	$D_{nT,w} + C_{50\text{-}3150} \geq 50$
	Class C	$R_w \geq 52$	Class C	$D_{nT,w} \geq 47$
	Class D	$R_w \geq 47$	Class D	$D_{nT,w} \geq 42$
Rooms in dwelling units		$R_w \geq 40$		$D_{nT,w} \geq 35$
Classrooms, offices, kitchen and utility rooms		$R_w \geq 45$		$D_{nT,w} \geq 40$
Windows*	Class A	$R_w + C_{tr,50\text{-}3150} \geq 35$	Class A	$D_{nT,w} + C_{tr,50\text{-}3150} \geq 30$
	Class B	$R_w + C_{tr,50\text{-}3150} \geq 30$	Class B	$D_{nT,w} + C_{tr,50\text{-}3150} \geq 25$
	Class C	$R_w \geq 30$	Class C	$D_{nT,w} \geq 25$
	Class D	$R_w \geq 25$	Class D	$D_{nT,w} \geq 20$
Doors*	Class A	$R_w + C_{tr,50\text{-}3150} \geq 30$	Class A	$D_{nT,w} + C_{tr,50\text{-}3150} \geq 25$
	Class B	$R_w + C_{tr,50\text{-}3150} \geq 25$	Class B	$D_{nT,w} + C_{tr,50\text{-}3150} \geq 20$
	Class C	$R_w \geq 25$	Class C	$D_{nT,w} \geq 20$
	Class D	$R_w \geq 20$	Class D	$D_{nT,w} \geq 15$

*If the size of windows and doors is more than 25% of the total area of the facade, the criterion for each class is further enhanced by 5 dB.
Choice between the sound insulation criterion down to 50 Hz, or the common lower limit of 100 Hz may be exercised[22].

Development of noise maps, setting up of expert committee for progress review and analysis like the National Committee for Noise Pollution Control (NCNPC), and targeting a noise abatement goal shall be key steps for controlling the noise pollution levels in the country.

The legal provisions for controlling noise pollution in India are: Indian Penal Code (section 268, 290, 291); Criminal Procedure Code (section 133); Factories Act, 1948; Motor Vehicles Act, 1988; Law of Torts; Air (Prevention and Control of Pollution) Act, 1981 and Environment (Protection) Act, 1986. Under Air (Prevention and Control of Pollution) Act, 1981, noise has been included in the definition of air pollutant[31,32]. The following control measures are suggested for noise emitted by various sources.

Transportation noise control

Transportation noise due to rail, road and aircraft should be specifically dealt with respect to the ambient noise standard proposed. The noise legislations for motor vehicles at the manufacturing stage are essential for controlling transportation noise. The noise limits for vehicles recommended by CPCB as applicable at manufacturing stage from 1 April 2005 should be effectively exercised[33]. Noise regulations should also be planned for future electric and hybrid vehicles. Enforcement of the proposed ambient standards shown in Table 1 valid for all the transportation sources shall be a large step for controlling noise pollution. The 'odd–even restrictions on vehicles' as executed in January and April 2016 in Delhi city can be also a good step for controlling vehicular traffic and noise levels provided that the public transport system is capable of catering to the daily transport needs of the public. Installation of noise barriers for the metro trains running on elevated corridors shall also be helpful in controlling the noise induced due to wheel–rail interaction, especially for dwellings located in the immediate vicinity. The abatement of aircraft noise particularly for the residents living near airports is also to be considered by adopting the noise reduction at source itself, optimized flights paths and procedures such as continuous descent approach, land-use planning and operating instructions for low noise emissions from the aircrafts, especially for the residential areas and silence zones.

Motor vehicle horn noise

Horns should be used only as traffic warning devices. A maximum level, L_{max} of 100 dB(A) for noise made up of a single non-varying loudness is recommended. Experimental studies conducted at various sites in Delhi city have revealed that for areas with traffic noise having dominant horn noise component, octaves in the frequency range 2.5–4 kHz are dominant[34]. Thus, for the abatement of traffic noise with a dominant horn noise component, sound insulation in octaves of 2.5–4 kHz should be higher. However, the coincidence dip observed in sound transmission loss characteristics has to be controlled in this frequency range.

A back pane thickness of 10 mm is recommended to be used in a double glazing with an average air gap of 50 mm for controlling the coincidence dip. A 7 mm laminated glazing (PVB 0.76 mm) in front and 10 mm at the

back with an air gap of 50 mm has $R_w + C_{tr}$ value of 40 dB analytically predicted from Insul software[35], and registers a coincidence dip at 1.6 kHz (mass–air–mass resonance at 63 Hz); it is quite effective for such applications. Garg *et al.*[36] described the analytical formulations that can be readily used by manufacturers and architects to predict sound transmission loss in terms of single-number rating and selection of suitable glazing[34,37,38] for achieving the desired noise-level reductions and reducing the honking noise.

Fire-cracker noise

The manufacture, sale or use of fire-crackers generating noise levels exceeding 125 dB(AI) or 145 dB(C) pk at 4 m distance from the point of bursting shall be prohibited. For individual fire-crackers constituting a series, the above-mentioned limit may be reduced by 5 log 10(N) dB, where N is the number of crackers joined together[6]. The noise from different brands of fire-crackers is tested every year at CSIR-National Physical Laboratory, New Delhi so as to ascertain whether the noise criteria are met or not.

Loudspeaker noise and noise from community processions

The noise level at the boundary of a public place, where a loudspeaker or public address system or any other noise source is being used shall not exceed 10 dB(A) above the ambient noise standards for the area or 75 dB(A), whichever is lower[6]. The peripheral noise level of privately owned sound system shall not exceed by more than 5 dB(A) the ambient air quality standard specified for the area in which it is used, at the boundary of a private place. Night-timing restrictions should be imposed on air shows, public demonstrations, etc. In some cases, wherever appropriate, fines may also be imposed.

Industrial noise

The areas under industrial zone should follow the ambient noise standards recommended for such zones, as described in Table 1. The major noise sources in industrial units, including heavy machinery, power transformers, etc. should be enclosed, if possible, so as to reduce the exposure of workers high noise levels. Exposure to noise in an occupation environmental is recommended to be eight-hour continuous A-weighted sound pressure level, $L_{Aeq,8h}$ less than 85 dB(A). For peak noise, the limit of C-weighted peak sound pressure level, $L_{C,peak}$ of 140 dB(C) is proposed[39]. Isolating the receiver positions from noisy sources by increasing the distance between them and use of source enclosures, control rooms and screen can be helpful in the control of direct field. The reverberant field can be controlled by applying sound absorptive materials to room surfaces[40]. Apart from the implementation of occupational and health safety measures, ear muffs should be provided to workers and other staff in the industry for protecting them against long-term noise exposure.

Diesel genset noise

MoEF notifies that the sale of a product model not having valid type-approval certificate, or not complying with the noise limits as determined by the verification for Conformity of Production (COP), shall be prohibited in India. The noise limit imposed for generator sets run with kerosene or petrol is 86 dB(A) sound power level[41]. The maximum permissible sound pressure level for new diesel generator (DG) sets with rated capacity up to 1000 KVA, manufactured on or after the 1 January 2005 is recommended as 75 dB(A) at 1 m from the enclosure surface[42]. Noise from the DG set shall be controlled by providing an acoustic enclosure or by treating the room acoustically, at the users end. The acoustic enclosure or acoustic treatment of the room shall be designed for minimum 25 dB(A) insertion loss or for meeting the ambient noise standards, whichever is on the higher side. The DG set shall be provided with proper exhaust muffler with insertion loss of minimum 25 dB(A). Six laboratories in India have been authorized by MoEF for carrying out type-approval and COP certification all over the country.

Construction equipment noise

Construction equipment operating in close proximity to residential areas can be of disturbance to the community. Thus, construction noise and vibration limits are essential, particularly those related to digging and piling operations for underground metro stations, etc. Table 3 shows the proposed noise limits for general construction at residential receptors[43]. The piling and digging operations not only cause vibrations which may induce cracks in building, but also produce airborne sound through building

Table 3. Proposed noise limits for commercial activities at residential receptors[43]

	General construction activities $L_{Aeq,15\ min}$ (dB(A))		
	Duration of activity		
Time period	Short term	Medium term	Long term
Daytime	65	60	55
Evening period (6–10 p.m.)	60	55	50
Late night (10 p.m–6 a.m.)	45	45	45

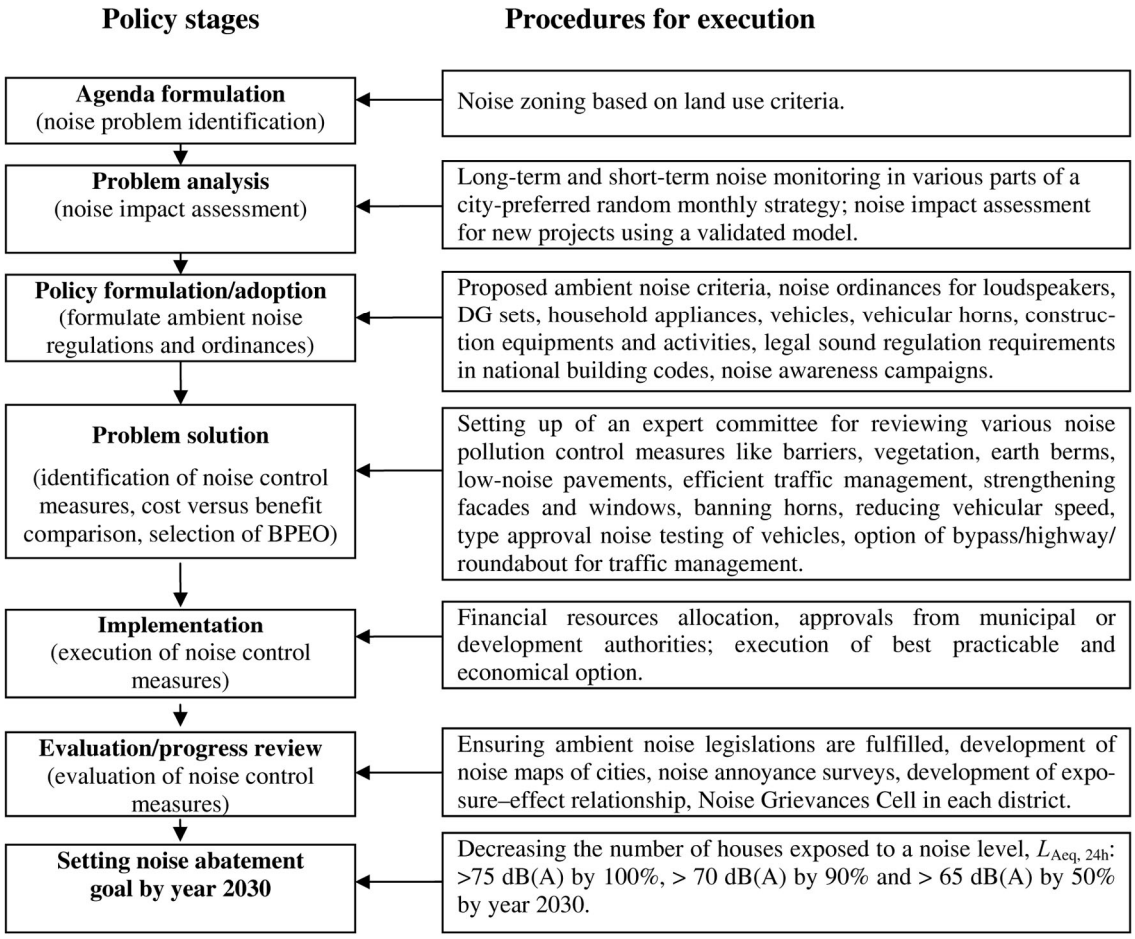

Figure 3. Proposed framework for community noise assessment and abatement in India.

Table 4. Proposed noise limits for domestic appliances and construction equipment at manufacturing stage

Domestic appliance	Maximum permitted sound power level (dB(A))
Refrigerator and freezer	55
Washing machine, spin dry	72
Microwave oven	70
Electrical fan (desk fan, stand fan, wall fan, ceiling fan)	70
Vacuum cleaner and dryer	70
Indoor heater	55
Air conditioners (split, indoor)	72
Air coolers	72
Hair dryer	75
Portable gensets (petrol or kerosene)	86
Food processor	90
Food blender	100
Lawn movers, welding generators, compressors	110
Handheld concrete breakers	120

elements, which can be of annoyance to the residents. The noise labelling of construction equipment should be made mandatory as there are sometimes practical complications involved in enforcement of standard noise limits for construction equipments especially in residential areas.

Noise from domestic appliances

Noise control in home appliances has to be economic, simple and easily implemented as there exists a global competition among manufacturers. An overall reduction of radiated noise levels of 6 and 10 dB have been reported in the domestic dryer and vacuum cleaner respectively, using the developed jute felt acoustical blanket[44]. Sound labelling of appliances shall be a helpful tool for creating awareness amongst manufacturers and customers about increasing the product quality by reducing noise emitted from the domestic appliances[45]. The noise limits should preferably be considered in terms of sound power level[46], which is constant for a given source and is independent of the acoustic environment. Sound power measurements L_{WA} are measured according to ISO 3744 (ref. 47) and ISO 3746 (ref. 48). Table 4 shows the proposed noise limits for domestic appliances and construction equipment at the manufacturing stage.

Figure 4. Illustrative noise ordinance signs for public awareness towards noise pollution control[52,53].

Thus, the noise standards for all the sources in conjunction with the enforcement of the proposed ambient noise standards and legal sound insulation requirements shall be a vital step in fighting the noise pollution in India. Figure 3 assimilates all the measures, policies and discusses a proposed framework for community noise assessment and abatement in India as suggested in some studies[49–51]. Illustrative noise ordinances sign (Figure 4), as suggested by Chanaud[52], can be an effective step for educating about the existence and enforcement of noise ordinances, especially for heavy traffic density areas[53]. Proper measures should be undertaken to avoid long-term noise exposure to school children susceptible to higher noise levels during the mass-drill events, etc. Traffic policeman should be provided with ear-muffs so as to avoid hearing loss due to their prolonged exposure to long-term traffic noise. It is envisaged that awareness among general public in maintaining a 'noise-free community' is a must. Participation of NGOs and social websites[54] in creating awareness and educating people about noise and associated health hazards apart from school and college curriculum shall be a great step in this regard. The noise grievances cell as a part of State Pollution Control Boards should be proactive in receiving, analysing and taking appropriate action on complaints. Such complaints are more particularly on festival days as reported by Mandal and Bandyopadhyay[55]. Establishment of these noise grievance cells in each district and helpline number for easy accessibility and freedom to file a complaint can be a proactive step in this regard. Educative and innovative programmes such as organizing 'Noise Awareness Campaigns', 'Dhwani Pradushan Niyantran Diwas' (noise pollution control day) and integrating 'Noise Pollution Control Mission' as a part of the ongoing 'Swatch Bharat Mission' introduced by the Government of India shall be indispensable in controlling noise pollution in India. Socio-acoustic surveys, noise impact assessment studies due to various noise sources, and noise monitoring during festival days should be conducted in parallel to quantify the noise impact and assessment of induced noise annoyance[56–60].

Conclusion and recommendations

A retrospective view of noise policies and ordinances in India and proposes revisions in them for noise abatement and control based on the available knowledge on noise policies and regulations followed in other countries is provided here. The work focused on inclusion of noise limits for construction activities, and domestic appliances apart from revision in ambient noise standards and National Building Codes for enhancing the sound insulation of building elements for protection against noise pollution. The noise limits for domestic appliances, motor vehicles and construction equipment at the manufacturing stage and enforcement of ambient noise standards shall be helpful in controlling noise pollution in India.

The implementation of noise pollution control measures essentially requires a strategic noise abatement planning with enforcement of proposed ambient standards, revision in National Building Codes, exercising control limits on all the noisy sources and formulation of noise abatement goal. The suggested flow chart for reducing the ambient noise levels and targeting a noise abatement goal shall be a vital step in this regard for environmental protection in future. Identification of noisy hot spots having higher $L_{\mathrm{Aeq,24h}}$ sound levels than the recommended limits and implementing suitable noise abatement measures shall be indispensable for noise pollution control. Provision for the erection of noise barriers, especially for sensitive areas like hospitals, schools, colleges, old-age homes, religious institutions, etc. and other areas lying in the silence zone should be made in future projects planned. Studies on socio-acoustic surveys with an objective of correlating the noise annoyance with exposure, effect of noise levels on the human body and hearing loss, on workers in industry, effect of noise exposure on traffic policeman and workers at construction sites, etc. should also be conducted in parallel for increasing awareness of society towards controlling noise pollution levels in the country. It is envisaged that the proposed standards, revision in National Building Codes and noise control measures shall be indispensable in the development

of 'smart cities' concept proposed by the Government of India.

1. World Health Organization (WHO), Burden of disease from environmental noise, Quantification by healthy life years lost in Europe, WHO Regional Office for Europe, Denmark, 2011.
2. Vijay, R., Sharma, A., Chakrabarti, T. and Gupta, R., Assessment of honking impact on traffic noise in urban traffic environment of Nagpur, India. *J. Environ. Health Sci. Eng.*, 2015, **13**(10), 1–9.
3. Banerjee, D., Research on road traffic noise and human health in India: review of literature from 1991 to current. *Noise Health*, 2012, **14**, 113–118.
4. Martin, M. A., Tarrero, M. A., Gonzalez, A. and Macimbarrena, M., Exposure–effect relationships between road traffic noise annoyance and noise cost valuations in Valladolid, Spain. *Appl. Acoust.*, 2006, **67**(10), 945–958.
5. European Noise Directive, Assessment and Management of Environmental Noise, 2002/49/EU, Official Journal of European Communities, 2002.
6. Noise Pollution (Regulation and Control) Amendment rules, 2010; http://envfor.nic.in/legis/noise.htm
7. National Ambient Noise Monitoring Network, Information Brochure, Central Pollution Control Board, India, March 2011.
8. Central Pollution Control Board, Annual Report, 2011–12.
9. Garg, N. and Maji, S., A critical review of principal traffic noise models: strategies and implications. *Environ. Impact Assess. Rev.*, 2014, **46**, 68–81.
10. Garg, N., Mangal, S. K., Saini, P. K., Dhiman, P. and Maji, S., Comparison of ANN and analytical models in traffic noise modeling and predictions. *Acoust. Aust.*, 2015, **43**, 179–189.
11. Tachibana, H. and Lang, W. W., Final report of I-INCE TSG 3-survey of legislation, regulations and guidelines for control of community noise, I-INCE Publication 09-1, July 2009.
12. National Building Codes of India: Part 8. Building Services: Section 4, Acoustics, Sound Insulation and Noise Control, Bureau of Indian Standards, CED 46 (0072) WD, 2015.
13. Garg, N., Kumar, A., Saini, P. K. and Maji, S., A retrospective view of ambient noise standards in India: status and proposed revision. *Noise Control Eng. J.*, 2005, **63**(3), 1–14.
14. Garg, N., Kumar, A. and Maji, S., Significance and implications of airborne sound insulation criteria in building elements for traffic noise abatement. *Appl. Acoust.*, 2013, **74**, 1429–1435.
15. Central Pollution Control Board, Ambient air quality and noise levels during Deepawali, 2013. Air Laboratory Report, 2013.
16. Garg, N., Saxena, T. K. and Maji, S., Long-term versus short-term noise monitoring: Strategies and implications in India. *Noise Control Eng. J.*, 2015, **63**(1), 26–35.
17. Garg, N., Sinha, A. K., Gandhi, V., Bhardwaj, R. M. and Akolkar, A. B., A pilot study on the establishment of national ambient noise monitoring network across the major cities of India. *Appl. Acoust.*, 2016, **103**, 20–29.
18. ISO 1996-1:2003, Acoustics – description, measurement and assessment of environmental noise – Part 1: Basic quantities and assessment procedures, International Organization for Standardization, Geneva.
19. WHO, Night Noise Guidelines for Europe, Copenhagen, Denmark: The World Health Organization Regional Office for Europe, 2009.
20. Rasmussen, B. and Rindel, J. H., Sound insulation between dwellings – descriptors applied in building regulations in Europe. *Appl. Acoust.*, 2010, **71**, 171–180.
21. Scholl, W., Lang, J. and Wittstock, V., Rating of sound insulation at present and in future. The Revision of ISO 717. *Acta Acust. United Acust.*, 2011, **97**, 686–698.
22. Rasmussen, B., International proposal for an acoustic classification scheme for dwellings-background and perspectives. In Proceedings Internoise, Melbourne, Australia, 2014.
23. Garg, N., Kumar, A. and Maji, S., Measurement uncertainty in airborne sound insulation and single-number quantities: strategy & implementation in Indian scenario. *MAPAN-J. Metrol. Soc. India*, 2016, **31**, 43–55.
24. Garg, N. and Maji, S., On analyzing the correlations and implications of single-number quantities for rating airborne sound insulation in frequency range 50 Hz to 5 kHz. *Build. Acoust.*, 2015, **22**(1), 29–44.
25. Helimäki, H. and Rasmussen, B., Airborne sound insulation descriptors in the Nordic building regulations – overview special rules and benefits of changing descriptor. In Proceedings of Baltic–Nordic Acoustics Meeting (BNAM), Bergen, Norway, 10–12 May 2010, pp. 1–6.
26. Garg, N., Sharma, O. and Maji, S., Design considerations of building elements for traffic and aircraft noise abatement. *Indian J. Pure Appl. Phys.*, 2011, **49**, 437–450.
27. Garg, N., Kumar, A. and Maji, S., Parametric sensitivity analysis of factors affecting the sound insulation of multi-layered building elements. *Arch. Acoust.*, 2014, **39**(2), 165–176.
28. Rasmussen, B. and Machimbarrena, M., *COST Action TU0901 – Building Acoustics throughout Europe. Volume 1: Towards a Common Framework in Building Acoustic throughout Europe*, 2014; http://www.costtu0901.eu/tu0901-e-books
29. Nijland, R., Vos, E. and Hooghwerff, J., The Dutch Noise Innovation Program Road Traffic (IPG). In Proceedings Internoise 2003, Seogwipo, Korea, 2003; http://www.informex.info/IPG_Internoise_203_ppr.pdf
30. Garg, N., Sharma, O., Mohanan, V. and Maji, S., Passive noise control measures for traffic noise abatement in Delhi, India. *J. Sci. Ind. Res.*, 2012, **71**, 226–234.
31. Singal, S. P., *Noise Pollution and Control Strategy*, Narosa Publishing House Pvt Ltd, 2005, pp. 170–203.
32. Yadav, P. and Yadav, R. S., Noise pollution and its enacting laws in India. *G-J. Environ. Sci. Technol.*, 2013, **1**(2), 51–56.
33. ENVIS Centre on Control of Pollution, Water, Air and Noise, Noise limits for vehicles at manufacturing stage; http://cpcbenvis.nic.in/noisepollution/Noise-vehicle.pdf
34. Garg, N., Investigations on modeling transportation noise and passive noise control measures for its abatement. Ph D dissertation, Delhi Technological University, 2016.
35. Insul software, Auckland, New Zealand; http://www.insul.co.nz
36. Garg, N., Kumar, A. and Maji, S., Parametric sensitivity analysis of factors affecting sound insulation of double glazing using Taguchi method. *Appl. Acoust.*, 2013, **74**, 1406–1413.
37. Garg, N., Sharma, O. and Maji, S., Experimental investigations on sound insulation through single, double and triple window glazing for traffic noise abatement. *J. Sci. Ind. Res.*, 2011, **78**, 471–478.
38. Garg, N., Sharma, O. and Maji, S., Design consideration for enhancing sound insulation characteristics of window glazing for traffic noise abatement. *Build. Acoust.*, 2012, **19**(2), 89–98.
39. National Standard for Occupational Noise, NOHSC:1007, National Occupational Health and Safety Commission, Australia, July 2000.
40. Beranek, L. L. and Vér, I. L., *Noise and Vibration Control Engineering: Principles and Applications*, John Wiley, 1992.
41. CPCB, Noise limit for generator run with petrol/kerosene; http://cpcb.nic.in/noise_pollution/NoiseLimit4Genetator-SetsRunwithPetrol.pdf.
42. CPCB, Noise limit for generator sets run with diesel; http://cpcb.nic.in/divisionsofheadoffice/pci2/noiselimit_diesegenset.pdf
43. Roberts, C., Construction noise and vibration impact on sensitive premises. In Proceedings of Acoustics, Australia, 23–25 November 2009.
44. Fatima, S. and Mohanty, A. R., Noise control of home appliances-the green way. *Noise Vibra. Worldwide*, 2012, 26–34.
45. Maluski, S., Churchill, C. and Cox, T. J., Sound quality testing and labeling of domestic appliances in the UK. In Proceedings

Internoise, Prague, Czech Republic, 22–25 August 2004; http://www.salford.ac.uk/_data/assets/pdf-file/0003/392736/maluski-Internoise-2004.pdf
46. Tian, J., Jiao, F. and Lu, Y., The latest development of low noise household appliances in China. In Proceedings International Institute of Noise Control Engineering, Paris, 5–6 July 2011.
47. ISO 3744:2010, Acoustics – Determination of sound power levels and sound energy levels of noise sources using sound pressure – Engineering methods for an essentially free field over a reflecting plane, International Organization for Standardization, Geneva.
48. ISO 3746:2010, Acoustics – Determination of sound power levels and sound energy levels of noise sources using sound pressure – Survey method using an enveloping measurement surface over a reflecting plane, International Organization for Standardization, Geneva.
49. Hede, A., Environmental noise regulation: a public policy perspective. In *Noise as a Public Health Problem* (Noise Effects '98), (eds Carter, N. L. and Job, R. F. S.), Sydney, Australia, 1998, vol. 2, pp. 687–696.
50. Schwela, D., Finegold, L. S. and Stewart, J., A strategic approach on environmental noise management in developing countries. In 9th International Congress on Noise as a Public Health Problem, Foxwoods, CT, USA, 2008.
51. WHO, Guidelines for community noise, World Health Organization, Geneva, 2000.
52. Chanaud, R. C., Noise ordinances, tools for enactment, modification and enforcement of a community noise ordinance, 2014; https://www.noisefree.org/Noise-Ordinance-Manual.pdf
53. Road traffic signs; http://www.roadtrafficsigns.com/truck-sign/quite-please-no-honking-unless-for-danger-sign/sku-k-6179.aspx
54. http://awaaz.org/Awaaz_Foundation/Noise_Press_Coverage/Noise_Press_Coverage.html
55. Mandal, P. K. and Bandyopadhyay, A., Case study from West Bengal, India: management of noise levels during festival time in Kolkata and Howrah Municipal Corporation areas from 2002 to 2011. *Environ. Qual. Manage.*, 2014, **23**(3), 13–32.
56. Banerjee, D., Road traffic noise exposure and annoyance: a cross-sectional study among adult Indian population. *Noise Health*, 2013, **15**(66), 342–346.
57. Garg, N., Sharma, O. and Maji, S, Noise impact assessment of mass rapid transit systems in Delhi city. *Indian J. Pure Appl. Phys.*, 2011, **49**, 257–262.
58. Upadhyay, J. K. and Jain, V. K., Aircraft-induced noise levels in some residential areas of Delhi. *Environ. Monit. Assess.*, 1999, **56**, 195–207.
59. Jamir, L., Nongkyrnuh, B. and Gupta, S. K., Community noise pollution in urban India: need for public heath action. *Indian J. Community Med.*, 2014, **39**, 8–12.
60. Garg, N., Vishesh and Maji, S., Fuzzy TOPSIS approach in selection of optimal noise barrier for traffic noise abatement. *Ach. Acoust.*, 2015, **40**, 453–467.

ACKNOWLEDGEMENTS. We thank the CPCB officials especially A. K. Sinha and R. M. Bhardwaj for sharing their experiences and data in NANMN project. We also thank the Director, CSIR-National Physical Laboratory, New Delhi and the Head, Apex Level Standards and Industrial Metrology Division for their support and providing infrastructural facilities for the study. The views and opinions expressed in this article are those of authors and do not necessarily reflect the official policy or position of any agency of the Government of India.

Received 10 July 2015; revised accepted 29 February 2016

doi: 10.18520/cs/v111/i1/29-38

ResearchGate

See discussions, stats, and author profiles for this publication at: https://www.researchgate.net/publication/305754637

A Review on Experimental Investigation of Machining Parameters during CNC Machining of OHNS

Article · March 2016

READS
8

7 authors, including:

Ramakant Rana
Maharaja Agarsain Institute of Technology
14 PUBLICATIONS **4** CITATIONS
SEE PROFILE

Roop lal Rana
Delhi Technological University
11 PUBLICATIONS **10** CITATIONS
SEE PROFILE

All in-text references underlined in blue are linked to publications on ResearchGate, letting you access and read them immediately.

Available from: Ramakant Rana
Retrieved on: 10 August 2016

RESEARCH ARTICLE OPEN ACCESS

A Review on Experimental Investigation of Machining Parameters during CNC Machining of OHNS

Surabhi Lata[1], Ashish Gupta[2], Aditya Jain[3], Sonu Kumar[4], Anindya Srivastava[5], Ramakant Rana[6], Roop Lal[7]

[1](Department of Mechanical and Automation Engineering, Maharaja Agrasen Institute of Technology, Delhi-86)
[2](Department of Mechanical and Automation Engineering, Maharaja Agrasen Institute of Technology, Delhi-86)
[3](Department of Mechanical and Automation Engineering, Maharaja Agrasen Institute of Technology, Delhi-86)
[4](Department of Mechanical and Automation Engineering, Maharaja Agrasen Institute of Technology, Delhi-86)
[5](Department of Mechanical and Automation Engineering, Maharaja Agrasen Institute of Technology, Delhi-86)
[6](Department of Mechanical and Automation Engineering, Maharaja Agrasen Institute of Technology, Delhi-86)
[7](Department of Mechanical Engineering, Delhi Technological University, Delhi-42)

ABSTRACT
This review paper aims towards the optimization of CNC turning operation when used over an OHNS material. The lathe machine was chosen because of its widespread availability and its ability to perform various tasks without much change in its structure. Also using lathe machines is very cheap and hence it is beneficial from economic point of view as well. The turning operation was specifically chosen because of the various advantages that it offers. It can be used for machining a large variety of materials and it is cheaper than milling. OHNS (Oil Hardened Non Shrinking) tool was chosen due to its hardness. These materials are used only for dies so it was chosen so that its industrial usage could be exploited. To comprehend the usage, all the input and output parameters that could affect the machining process, namely input parameters like feed, cutting conditions, speed, etc. and output parameters like surface roughness, surface finish, material removal rate were analyzed using the researches that had already been done on CNC turning. After careful study of a variety of research papers on this topic, it was decided that several input as well as the output parameters would be considered which included feed, depth of cut and cutting speed were taken as the input parameters whereas Material Removal Rate (MRR) and surface finish were taken as the output parameters. From the results of the research papers, it was concluded that feed, depth of cut and cutting speed could be chosen as input parameters whereas MRR and surface finish would be the output parameters.
Keywords–OHNS, CNC,

I. INTRODUCTION

Today, CNC machining has turned out to be an indispensable part of machining industry. The accuracy and precision achieved through CNC cannot be achieved by the conventional manufacturing machines. Although there is a room for errors in a CNC machine, these errors depend on the skill, experience and the cutting parameters used by the worker to get the proper dimensions. The machine performance and product characteristics are not always acceptable. Out of the various parameters which could be considered as the manufacturing goal, the material removal rate (MRR) was considered for the present work as the factor directly affects the cost of machining and the machining hour rate. Cutting speed, feed rate and depth of cut were considered to be the cutting parameters. The objective was to find the optimized set of values for maximizing the MRR and surface finish using various methodologies proposed by different authors.

In this paper, we have tried to compare various optimization techniques to identify the best among those. The Taguchi method emphasizes over the selection of the most optimal solution (i.e. MRR) over the set of given inputs (i.e. cutting speed, feed rate and depth of cut) with a reduced cost and increased quality.

To diminish the error while using an increased number of inputs, the orthogonal matrix of Taguchi is preferred, this can be selected as per the requirements of the person. In this technique, different levels of Orthogonal Array can be used to obtain optimized and economical results. The Taguchi method for the Design of Experiments also emphasizes over the use of Loss function, which is the deviation from the desired value of the quality characteristics. Based on the obtained Loss functions, the S/N ratio for each experimental set is evaluated and accordingly the optimal results are derived. ANOVA is then generated for the results and finally, the confirmations results are obtained between the experimental values and the determined values.

Response Surface Methodology (RSM) focuses on the optimization of the input parameters models

based on either experimental observations, physical experiments or simulation experiments. These models need to be assessed statistically for their adequacy, and then they can be utilised for an optimisation of the initial model. RSM also quantifies relationships between the controllable input parameters and the obtained response surfaces. The input parameters are called independent variables, and the performance, measure or quality characteristic is the response. By using the results of a numerical experiment in the points of orthogonal experimental design, response surface analysis proves to be less expensive than a solution using the traditional method. With this analytical model, the objective function problem can be easily solved and a lot of time in computation can be saved. Response surface methodology problems have a functional relationship between responses and independent variables, and this relation can be explained using the second-order polynomial model given below:

$$\eta = \beta_0 + \sum_{i=1}^{k} \beta_i X_i + \sum_{i=1}^{k} \beta_{ii} X_i^2 + \sum_i \sum_j \beta_{ij} X_i X_j + \varepsilon \quad (1)$$

Whereη, is the estimated response (surface roughness), β_0 is constant, β_i, β_{ii} and β_{ij} represent the coefficients of linear, quadratic, and cross-product terms, respectively. X reveals the coded variables.

The common approach in the RSM is to use regression methods based on least square methods. The method of least squares is typically used to estimate the regression coefficient, which is shown in the following equation.

$$\beta = \begin{bmatrix} \beta_0 \\ \beta_1 \\ \dots \\ \dots \\ \beta_n \end{bmatrix} = (X^T X)^{-1} X^T \eta =$$

$$\left[\frac{1}{k}\sum_{j=1}^{k} \eta_j, \frac{\sum_{j=1}^{k} X_{1j}\eta_j}{\sum_{j=1}^{k} X_{ij}^2}, \dots, \frac{\sum_{j=1}^{k} X_{nj}\eta_j}{\sum_{j=1}^{k} X_{nj}^2}\right]^T \quad (2)$$

Where η, is the number of objective function and k is the number of factors. The β terms comprise the unknown parameter set which can be estimated by collecting experimental system data. These data can either be sourced from physical experiments or from numeric experiments. The parameter set can be estimated by regression analysis based upon the experimental data.

II. Literature Review

Bagawade and Ramdasi (2014), analyzed the effect of the cutting parameters on the material removal rate (MRR), cutting power and material removal rate per cutting power during turning of AISI 52100 steel when using polycrystalline cubic boron nitride tools (uncoated PCBN (MITSUBISHI) insert). They concluded the following after analyzing the data from their experimentation:

- They found depth of cut to be the most important parameter affecting the material removal rate (MRR), followed by feed rate while cutting speed has the least effect.
- The optimal parameters for maximum MRR, found by them were as follow:
  - Cutting speed 350m/min., feed rate 0.05mm/rev., and depth of cut of 0.3mm.
  - The cutting speed is found to be the most important parameter effecting on cutting power (*PC*), followed by depth of cut while feed rate has the least effect.
- They recommended the following levels of process parameter, to get the good power consumption:
  - The lowest level of cutting speed, 250 m/min, the medium level of feed rate, 0.04 mm/rev and the medium level of depth of cut,0.2 mm.
- The cutting speed was found to be the most important parameter influencing the material removal rate (MRR) per cutting power (*PC*), followed by depth of cut while feed rate has the least effect in the optimization. The optimal parameters for the maximum MRR/cutting power were: Cutting speed 350 m/min., feed rate 0.05mm/rev., and depth of cut of 0.3mm. Machining with lowest cutting speed had a positive effect on material removal rate (MRR) per cutting power (*PC*).

Muthukrishnan et.al (2014), focused their study on optimizing turning parameters for Oil Hardened Non Shrinkable steel (OHNS) steel rod. They made use of the Taghuchi's technique with L9 orthogonal array as the methodology of design of experiment. For process parameters, feed, cutting speed and depth of cut were used as the process parameters. Surface roughness and material removal rate (MRR) were taken as the response parameters. S/N ratio was used for the optimization of process parameters and output results were analyzed using ANOVA.
They identified the problems associated with the turning of OHNS steel rods and listed them as:

- Poor surface finish
- Difficulty in achieving close tolerance
- Machining distortion
- Poor chip breaking
- High cutting pressure for machining.
- High hardness cutting tool required

On the basis of their experimental results the conclusion made was that cutting speed is the most significant parameter while considering surface roughness as a response parameter and feed was the most significant parameter for material removal rate.

K. Saraswathamma and MadhuDurgam (2014), they made a detailed study through a statistical

design of experiments which were carried out to study the effect of machining parameters such as Pulse current, Pulse on time(Ton) and Pulse pause time(T_{off}) on responses variables such as Material Removal Rate(MRR) and Tool Wear Rate (TWR) on OHNS Tool Steel. They designed the experiments using Response surface methodology (RSM) - Central Composite Design (CCD) involving three variables with three levels. They attempted to develop a mathematical model for relating the MRR and TWR to the input parameters.
Separate Analysis of Variance (ANOVA) was conducted and contribution of each parameter affecting improvement in MRR and TWR was calculated. They concluded that MRR and TWR increases with increase in pulse current and pulse on time.

After analyzing the results of the experiments of OHNS tool steel with copper electrode, they concluded:

- The increase in pulse current leads to a sharp increase in the material removal rate. And also it was observed that, tool wear rate are also increases with increasing the current. So, current was the most significant factor in both MRR and TWR.
- The increase in pulse on time leads to an increase in material removal rate and there is slight increase was observed with tool wear rate.
- The increase in pulse pause times both material rate and tool wear was decreasing.

R. Deepak Joel Johnson et.al (2014), they aimed to optimize cutting fluid usage in machining of Oil Hardened Non shrinkable Steel (OHNS) by Taguchi method. There are various methods of application of coolants, the major one being deluge or flood cooling which is essentially an application of cooling fluid in bulk. The huge amount of usage of cutting fluid increases production cost and also puts a pressure on the environment.

The result of the experiments was compared with wet and dry cutting conditions and it was concluded that:

- Cutting performance was improved with minimal cutting fluid application and was comparable to wet and dry turning.
- From their analysis of the results produced by Taguchi method and ANOVA, it was concluded that feed was the prominent factor which influenced surface roughness.
- They observed that surface roughness can be improved by tuning fluid application parameters.
- They also concluded that their experimentation results in lesser usage of cutting fluid which reduced manufacturing costs as well as promoted green shop floor and lesser health hazards to the operators.

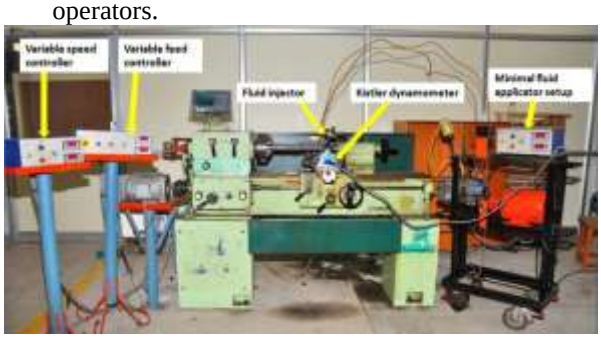

Figure 1- Experimental setup containing lathe and minimal cutting fluid applicator

Aouici et.al (2012), they conducted their experimental investigation to determine the effects of cutting conditions on surf-ace roughness and cutting forces in hard turning of X38CrMoV5-1. This steel was hardened at 50 HRC and machined with CBN tool. Combined effects of three cutting parameters, namely cutting speed, feed rate and depth of cut, on the six performance outputs-surface roughness parameters and cutting force components, are explored by analysis of variance (ANOVA). A relationship between the variables and the technological parameters was determined through the response surface methodology (RSM), using a quadratic regression model.

Their results showed that surface roughness is mainly influenced by feed rate and cutting speed. The depth of cut exhibits maximum influence on cutting force components as compared to the feed rate and cutting speed, whereas the cutting speed has negative effect and depth of cut a negligible influence.

Aggarwal et.al (2008), they experimented on CNC turning of AISI P-20 tool steel considering the effects of cutting environment, cutting speed, nose radius, feed rate, and depth of cut using Tin coated tungsten carbide inserts. Response surface methodology (RSM) and Taguchi's technique were used as design of experiment techniques to accomplish their objective. They used Face Centered Central Composite Design for conducting experiment along with L27 orthogonal array. Their results of 3D surface plots of RSM and Taguchi's technique revealed that the most significant factor in minimizing power consumption was cryogenic environment followed by cutting speed and depth of cut (DOC). On the basis of comparison they found that the effects of nose radius and feed rate were found insignificant. Although their results are predicted by the two techniques used by them were close to each other but, RSM technique was found to be more advantageous over Taguchi's technique.

They concluded after analysis by two techniques that, RSM displayed the significance of all possible

interaction between the parameter and square of individual parameters whereas Taguchi's technique showed the significance of only few interactions thus 3D surface plots helps to analyze the response in the entire limit for an input parameter whereas Taguchi determines only the average values whereas Taguchi's technique is advantageous over RSM only in terms of the number of experiments performed as the number of experiments to be performed in Taguchi is much less than that in RSM.

Figure 2- Photograph of experimental setup

Ahilan et.al (2012) in this paper, they proposed the development of neural network models for optimization of machining input parameters in CNC turning process. Taguchi's Technique was used for the Design of Experiments (DoE) and experiments were conducted by them with feed rate, cutting speed, nose radius and depth of cut as the process parameter and performance parameters were taken as surface roughness and power consumption. Results from experiments were used by them to develop neuro based hybrid models .The influences of input parameters using ANOVA is identified by calculating the responses of Signal-to-noise (S/N) ratios.

Figure 3 -Photograph of CNC experimental set-up

Neural network hybrid model developed and tested were:-

- Back propagation neural network model
- Neural network model trained with genetic algorithm
- Neural network with particle swarm optimization (NNPSO)

They concluded that among the 3 models developed NNPSO requires minimum time for computation as the number of epochs are minimum and is the most accurate, i.e., accuracy of the error is hardly within 2% among the three hybrid neural network models developed as it stores the P_{best} and G_{best} solutions.

Gowd et.al (2014) aimed at finding the optimal process parameters for turning process of EN-31.They chose EN-31 as the work material because of its wide applicability as material and because it has a very high resistance nature against wear and can be used for components subjected to severe abrasion, wear or high surface loading and as material for Ball and roller bearings, spinning tools, Beading rolls, Punches and dies. The experiments were performed as per their design of experiments, that is L-27, and then ANN is applied to predict the models for the chosen output responses. Then the ANOVA Analysis was used to test their adequacy.

Depth of cut, Cutting speed and Feed were taken as process parameters and the output responses were $F_x$and temperature. For different network configurations, as per the value of performance error obtained, the best model was identified and selected. The models were evaluated by calculating the percentage deviation using predicted values and actual values. The models were developed to predict the MRR and tool wear resistance through ANN. Their study optimizes the force and Temperature by adjusting the speed, feed, and depth of cut.
They concluded that:

- The speed and the depth of cut have great significance on the force and Temperature, whereas the feed has less significance on both the outputs.
- The best model was selected based on the best performance error for different network configurations.
- They also concluded that the developed ANN model can be further integrated with optimization algorithms like GA to optimize the turning parameters.

Routara et.al (2012), they used response surface methodology (RSM) to optimize parameters of cutting operation in CNC turning operation on EN-8 steel to minimize surface roughness. On the basis of their experimental results second order mathematical model was developed using RSM methodology. Coated carbide tool was used as tool material. They used the F-Test to check the validation of optimized condition. Optimization of parameters for surface roughness was also achieved with Genetic Algorithm. In the experimental readings the surface roughness of the machined part was checked using three methods i.e.

- Centre line average roughness (R_a)
- Mean line peak spacing (R_{sm})
- Root mean square roughness (R_q)

Surface roughness is a smaller yet better type of parameter in machining operation.
It was finally concluded that with an increase in spindle speed and depth of cut, surface roughness was observed to be decreasing but is increasing with the increase of feed.

Makadia et.al (2012), in their study they chose parameters such as feed rate, tool nose radius, cutting speed and depth of cut on the surface roughness of AISI 410 steel. A mathematical prediction model of the surface roughness was developed in terms of above parameters & their effect on the surface roughness was investigated by using Response Surface Methodology (RSM). They constructed Response surface contours for determining the optimum conditions for a required surface roughness. Their developed prediction equation showed that:

- The feed rate is the main factor followed by tool nose radius influences the surface roughness.
- The surface roughness was found to increase with the increase in the feed and it decreased with increase in the tool nose radius.
- Response surface optimization shows that the optimal combination of machining parameters are(255.75 m/min, 0.1 mm/rev, 0.3 mm, 1.2 mm) for cutting speed, feed rate, depth of cut and tool nose radius respectively.
- They carried out verification experiment to check the validity of the developed model that predicted surface roughness within 6% error.

Mukherjee et.al (2014), they employed Taguchi method with L25 (5^3) Orthogonal Array for three parameters namely Speed, Feed and Depth of cut. For each of these parameters five different levels were used to perform the turning parameters for maximization of material removal rate on an EMCO Concept Turn 105CNC lathe. The material selected for machining was SAE 1020 with carbide cutting tool. The MRR is observed as the objective to develop the combination of optimum cutting parameters.

They produced a predictive equation for determining MRR with a given set of parameters in CNC turning. They concluded that with their proposed optimal parameters it is possible to increase the efficiency of machining process and decrease production cost in an automated manufacturing environment. Their analysis showed that Depth of Cut had the most significant effect on MRR followed by Feed and with an increase in Depth of Cut, MRR increased in the studied range.

Saini et.al (2014), in their research work CNC turning operation is carried out using L27 Taguchi orthogonal arrays on Aluminum alloy 8011 with carbide insert and influence of CNC turning process parameters like Cutting Speed, Feed and Depth of Cut are analyzed for two output objectives like material removal rate and surface roughness. They estimated optimum sets of turning process parameter as well as combined effect of considered response using Taguchi-Fuzzy application. In their analysis they found that feed is the mostsignificant process parameter followed by depth of cut and cutting speed on the selected response parameters.
They calculated SNR of objective functions using Taguchi quality method and amongst selected independent parameters, feed is found to be the most significant parameter followed by depth of cut and spindle speed for surface roughness while depth of cut is most significant parameter for material removal rate followed by feed and spindle speed. They further concluded that, using fuzzy reasoning, surface roughness and MRR which were taken as fuzzy crisp input and COM which was taken as output and the influence of selected independent parameters are estimated on fuzzy crisp output using Taguchi SNR analysis.
They found feed is most significant parameter on COM followed by depth of cut and spindle speed.

Goswami and Kumar (2014), they presented their investigation on wire wear ratio, surface finish and material removal rate using WEDM process taking Nimonic 80A as work piece and Taguchi's technique as design of experiments for planning and designing the experiments. Taguchi method was selected by them as DOE methodology as it tests only pairs of combinations instead of all possible combinations which allow estimation of relevant factors affecting the output, with little experimentation.

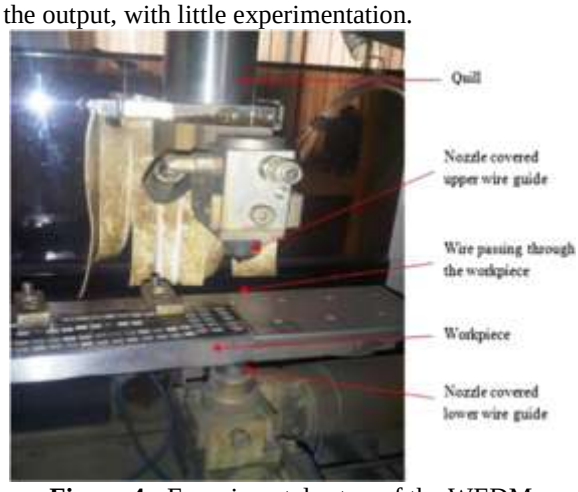

Figure 4 - Experimental setup of the WEDM

Sarikaya and Güllü (2013), studied the effect of cutting environment on the cutting conditions. The adverse effect of cutting fluids has been known on

the environment, productivity and health for machining operations such as turning, facing etc. Surface finish was used as a performance parameter of machining processes and cutting speed, cooling condition, depth of cut and feed rate as process parameters. They used Taghuchi's L16 technique for Design of Experiment & 3 levels of cooling conditions i.e. conventional wet cooling (CC), dry cutting (DC), and minimum quantity of lubrication (MQL). They measured surface roughness using 2 methods mainly Arithmetic average roughness and Average maximum height of the profile (mm). Main effect graphs of means, 3D surface graphs and signal-to-noise ratios (S/N) were used to study the experiment results and optimize the process parameters. Response surface methodology was used to develop the mathematical model for R_z and R_a for optimization.

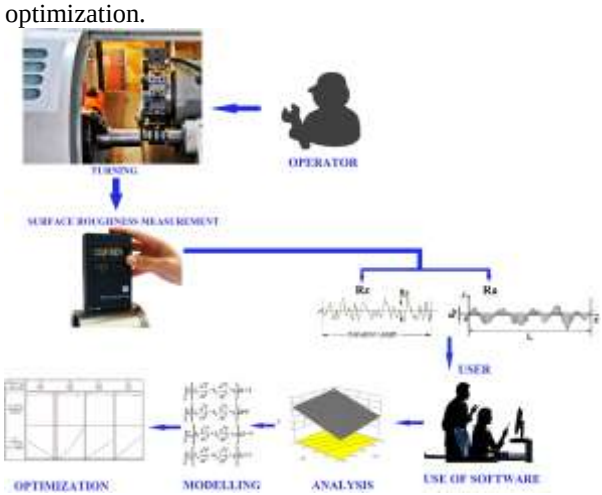

Figure 5- A schematic diagram of the experimental set-up

They concluded that the most effective parameters observed for surface roughness was feed rate. Effect of cooling conditions was also found to be a significant factor on the surface roughness. MQL was observed as an excellent tool to increase of the machined surface quality for machining operations.

AsilturkIlhan and NeseliSuleyman (2011), they checked surface roughness (Ra and Rz) of AISI 304 austenic stainless steel under dry conditions for CNC turning. They considered feed, depth of cut and cutting speed as parameters and tool used was IC 3028 grade carbide insert (SNMG 120408 PP). They designed the experiment by Taguchi method and then response surface analysis was done on it and they proved its adequacy further by ANOVA. S/N ratio was calculated by them and concluded that the plot with steepest ascent was the dominant factor.
They took following process parameters i.e. cutting tool parameters which took into account tool geometry and tool material; work piece parameters, namely metallography and hardness, and cutting parameters which were feed, depth of cut, cutting speed and cutting conditions.
They concluded:

- Feed rate is the dominant factor for surface roughness & its effect lowers when feed & depth of cut lowers and & cutting speed is set to highest level.
- Optimum cutting parameters for Ra were, cutting speed=50mm/min, feed=0.15mm/rev& depth of cut=1.5mm and optimum cutting parameters for Rz were, cutting speed=150mm/min, feed=0.15mm/rev & depth of cut=1mm.

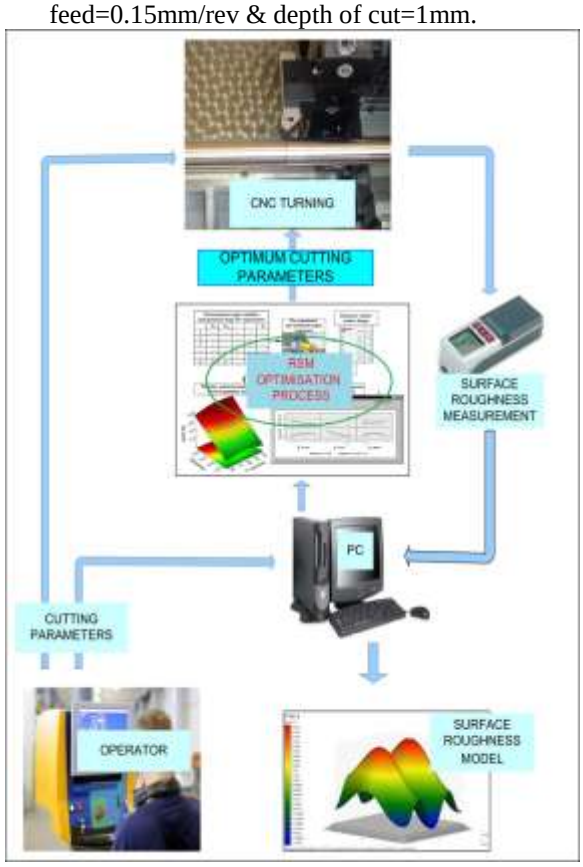

Figure 6- Experimental set up to measure the vibration of the process

KarayelDurmus (2008), they took surface roughness as the primary parameter and initially, the process parameters were kept at their highest values, so they also considered MRR. The experiment was to predict the roughness hence 1 parameter was variable and 2 were kept constant and iterations were done. 8000 iterations were considered and no smoothening was applied to it. They used Neural network approach for Design of experimentation. They used MATLAB for the formulation and tabulation of results. The specifications of the work piece used are 25mm (dia.) x100mm St50.2 steel. They concluded that feed is the most prominent factor in surface roughness followed by cutting speed. Depth of cut shows variable character or rather parabolic as the roughness first reduces and then increases again.

Gupta Anil et.al (2011), they used a hybrid approach of Taguchi and fuzzy logic to make a design of experiment. Work piece used was AISI P-20 tool steel and tool material was a tin coated tungsten carbide inserts. They considered cutting speed, feed, depth of cut, nose radius & cutting environment as machining parameters. The performance parameters were surface roughness, tool life, power consumption, cutting force. For optimum results, they used ANOVA, S/N ratio was calculated and concluded that the optimum values of the machining parameters were cutting speed= 160m/min, nose radius=0.8mm, feed=0.1mm/min, depth of Cut= 0.2mm& cutting environment= Cryogenic.

Raaste d. Koyee et.al (2014), theycombined the Taguchi approach with fuzzy-multiple attribute decision making methods for accomplishing a better surface quality in constant cutting speed face turning of EN 1.4404 austenitic, EN 1.4462 standard duplex and EN 1.4410 super duplex stainless steels. They used two conventional multiple attribute decision making techniques were concurrently to determine multi-surface quality characteristics indices. The distinction in rankings among derived indices are solved through converting each crisp values into trapezoidal fuzzy number and unifying them using fuzzy simple additive weight method. The fuzzy numbers are then deffuzified into crisp values employing techniques like; the spread, mode and area between centroid of centroids. Through this procedure, the decision maker is provided with necessary tools to optimize the cutting conditions with less sensitivity to the change of weights and no dissimilarity in ranking among the deffuzification techniques. Their outcomes of analyses of means and the validation experiments confirm that the optimum cutting conditions resulting from this method produce far better surface finish than the best finish obtained during the experiment. Analyses of variance results have shown the predominant effect of feed rate on surface quality. Finally, the collected chip at regular cutting speed and irregular feed rates and depth of cuts has shown that friendlier-to-machine chips are obtained when machining austenitic stainless steels rather than duplex stainless steel grades.

Zhang and liang (2006), in this paper, they discussed an orderly tactic for designing the optimal tool geometry and cutting conditions for hard turning, integrating the consideration of part finish, tool wear, and material removal rate. Their experiment has demonstrated that optimization scheme is presented at two levels: the first is to authenticate the process prediction results and the second is to validate the optimization results. Hardened AISI 1053 steel was selected as the work piece material in this study and its material property related parameters, including the Johnson–Cook constants and wear coefficients, were determined based on the machining tests. The authors saw that the cutting force and tool wear progression agrees well with the predictions from 3-D oblique cutting model, and the machined surface roughness can be predicted with a surface kinematic model incorporating the plowing effect. Their experiment also demonstrated that the process configuration as derived from the analytical optimization procedure gives superior results in comparison to other experimental results under non-optimal configurations.

In this paper, a systematic methodology to solve for the tooling solution and process planning decisions for finish hard turning process was presented and its validity examined experimentally. Firstly, the process planning problem was formulated and experimental validation scheme introduced. Then, the material property related parameters for hardened AISI 1053 steel were determined based on the machining tests. Afterwards, the process prediction results were compared with the experimental results. The authors found that the 3-D oblique cutting force model and tool flank wear model used gave reasonably good results, while surface roughness values strayed greatly from the measured results if the plowing effect was not accounted for. Also, there were no clear samples for the variation of surface roughness with the progression of the tool wear. An empirical model is established to add to the basic kinematic model in this study in predicting the average surface roughness value. Based on the validated process models, the optimal results are solved by a mixed integer evolutionary algorithm. The optimal configuration was further validated experimentally and found to be the best amongst all the experimental results under various combinations of process parameters.

Mctsai et.al (2003), they believed that the cutting occurs around the cutter contact (CC) point so the efficiency and quality of CNC machining can be improved considerably if the CC velocity along the surface is kept constant. They aimed to develop a real-time interpolation algorithm based on Taylor's expansion to bring to fruition a NURBS (non-uniform rational beta-spline) surface interpolator to achieve high-precision and high-speed CNC machining. The main point of a NURBS surface interpolator is to adjust the NURBS surface segments into each axis' motion command in order to synchronize all axes motion with the desired feed rate (CC velocity). The system's hardware includes a three-axis positioning table maneuvered by three servomotors, with built-in incremental encoders (2500 × 4 pulses/rev) for position feedback, and a PMC32-6000 motion control that incorporates a high

performance DSP, the TI TMS320C32 floating point processor. This setup can implement the following algorithms in real-time: (1) NURBS surface representation; (2) NURBS surface interpolator; and (3) servo controller. Experimental results have indicated that the proposed NURBS surface interpolator is capable of real time generation of CL (cutter location) motion commands for the servo controller and maintains the desired feed rate (CC velocity) along the CC paths and CC path intervals.
The authors have attempted to develop a novel NURBS surface interpolator for real-time CL motion command generation of parts represented in NURBS surface forms. This method was proposed to maintain a constant CC velocity rather than a constant CL velocity, in which an invariable CC velocity along a NURBS surface can enhance the machining efficiency and quality significantly. Their experimental results have signified that the proposed NURBS surface interpolator is competent enough for real time generation of CL motion commands for the servo controller and also maintains the required feed rate (CC velocity) along the CC paths and CC path intervals. Therefore, the machining efficiency and quality can be improved through the use of the proposed novel NURBS surface interpolator

III. Conclusion

This paper reviews the effect of various machining parameters on the performance parameters during turning operation. It further displays modern techniques of optimization as the powerful and popular tools for solving complex engineering problems.

1. In the turning operation, the machining parameters i.e. cutting speed, feed rate and depth of cut play a major role in deciding the performance parameters such as surface roughness, power consumption, tool wear and material removal rate.
2. The material removal rate (MRR) and power consumption shows a significant effect of depth of cut followed by feed rate and then by cutting speed. Increase in any of the input parameter increases the MRR as well as power consumption hence, optimization process requires any of the two performance parameters to be considered in one combination.
3. Surface roughness (SR) was found to be dependent on all these machining parameters. A decrease was exhibited by SR with an increase in cutting speed and feed rate while an increase was noted with the increase in depth of cut.
4. Depth of cut has the major impact on tool wear followed by cutting speed and feed rate.
5. The detailed study of various techniques shows that response surface methodology (RSM) is the most appropriate technique for machining operation because of its high accuracy and ability to consider input parameter in a particular range rather than at specific points for optimization. It further proves to be useful as a lot of information can be derived with few simulations.
6. 3^3 is considered as the most prominent design for experimentation as it has high accuracy within specific limit with minimum number of experiments.
7. The main difficulty was to turn OHNS with high surface finish and low tool wear. The feasible solution to this was the use of either CBN or PCD as turning tool.

In the paper, it was found that machining of OHNS was difficult and was usually carried out for milling operation. Turning of OHNS was done with the help of either CBN or PCD turning tools. Turning of OHNS using carbide tip as turning tool material though decreased the cost of machining but this was achieved at the cost of surface finish. Identifying appropriate combination of machining parameters to optimize turning of OHNS using carbide turning tool can increase the application of OHNS in small industries.

References

[1]. Aggarwal Aman, Singh Hari, Kumar Pradeep, Singh Manmohan, "*Optimizing power consumption for CNC turned parts using response surface methodology and Taguchi's technique—A comparative analysis*", Journal of Materials Processing Technology, 200, 2008, pp. 373–384.

[2]. Ahilan C., Kumanan, Somasundaram, Sivakumaran N., Dhas J. Edwin Raja*," Modeling and prediction of machining quality in CNC turning process using intelligent hybrid decision making tools*", Applied Soft Computing ,13 2013,pp. 1543–1551.

[3]. Gowd G. Harinath, Goud M. Venugopal, Theja K. Divya , Reddy M. Gunasekhar*," Optimal Selection Of Machining Parameters In CNC Turning Process Of EN-31 Using Intelligent Hybrid Decision Making Tools*", Procedia Engineering, 97 2014,pp. 125 – 133.

[4]. Routara B.C., Sahoo A.K., Parida A.K., Padhi P.C., *"Response Surface Methodology and genetic algorithm used to optimize the cutting condition for surface roughness parameters in CNC turning"*, Procedia Engineering ,38 2012, pp.1893 – 1904

[5]. N Muthukrishnan, T M Kannan, M Robert Sahayadoss, J Madhan, P Vijaya Kumar and R Makesk Kumar, "*optimization of turning parameters of ohns (aisi o-1) steel rods*

using taguchi methodology" Int. J. Mech. Eng. & Rob. Res.2014 346-352.

[6]. D. Bagawade, P. G. Ramdasi, "*Effect of cutting parameters on material removal rate and cutting power during hard turning of AISI 52100 steel*", International Journal of Engineering Research & Technology (IJERT) Vol. 3 Issue 1, January – 2014, SSN: 2278-0181.

[7]. AmiteshGoswami, Jatinder Kumar, *"Investigation of surface integrity, material removal rate and wire wear ratio for WEDM of Nimonic 80A alloy using GRA and Taguchi method"*, Engineering Science and Technology, an International Journal 17 (2014) 173-184.

[8]. Anil Gupta, Hari Singh, Aman Aggarwal, "*Taguchi-fuzzy multi output optimization (MOO) in high speed CNC turning of AISI P-20 tool steel*", Expert Systems with Applications 38 (2011) 6822–6828.

[9]. H. Aouici, M. A. Yallese, A Belbah, M. Fameur, M. Elbah, **"***Experimental investigation of cutting parameters influence on surface roughness and cutting forces in hard turning of X38CrMoV5-1 with CBN tool"*, *Sa¯dhana¯* Vol. 38, Part 3, June 2013, pp. 429–445. Indian Academy of Sciences.

[10]. K. Saraswathamma, MadhuDurgam, *"Parametric analysis of CNC EDM on OHNS tool steel"*, 5th International & 26th All India Manufacturing Technology, Design and Research Conference (AIMTDR 2014) December 12th–14th, 2014, IIT Guwahati, Assam, India 561-1 – 561-6.

[11]. Durmus Karayel, *"Prediction and control of surface roughness in CNC lathe using artificial neural network*", journal of materials processing technology 209 (2009) 3125–3137.

[12]. Ashvin J. Makadia, J.I. Nanavati, "*Optimization of machining parameters for turning operations based on response surface methodology*", Measurement 46 (2013) 1521–1529

[13]. Sayak Mukherjee, Anurag Kamal, Kaushik Kumar, "*Optimization of material removal rate during turning of SAE 1020 material in CNC Lathe using Taguchi technique*" Procedia Engineering 97 (2014) 29 – 35.

[14]. Surendra Kumar Saini, Sharad Kumar Pradhan, "*Optimization of Multi-Objective Response during CNC Turning using Taguchi-Fuzzy Application*", Procedia Engineering 97 (2014) 141 – 149.

[15]. Murat Sarıkaya, AbdulkadirGüllü, "*Taguchi design and response surface methodology based analysis of machining parameters in CNC turning under MQL*", Journal of Cleaner Production 65 (2014) 604-616.

[16]. R. Deepak Joel Johnson , K. Leo Dev Wins, Anil Raj , B. Anuja Beatrice, "*Optimization of cutting parameters and fluid application parameters during turning of OHNS steel*", Procedia Engineering 97 (2014) 172 – 177.

[17]. M.C. Tsai, C.W. Cheng, M.Y. Cheng, "*A real-time NURBS surface interpolator for precision three-axis CNC machining*", International Journal of Machine Tools & Manufacture 43 (2003) 1217–1227.

[18]. Rastee D. Koyee, Rocco Eisseler, Siegfried Schmauder, "*Application of Taguchi coupled Fuzzy Multi Attribute Decision Making (FMADM) for optimizing surface quality in turning austenitic and duplex stainless steels*", Measurement 58 (2014) 375–386.

[19]. Jing Ying Zhang & Steven Y. Liang," *Process Optimization of Finish Turning of Hardened Steels*, *Materials and Manufacturing Processes*, 22: 107–113, 2007.

[20]. Ilhan Asiltürk, Süleyman Neseli, "*Multi response optimization of CNC turning parameters via Taguchi method-based response surface analysis*", Measurement 45 (2012) 785–794.

Volume 4, Issue 1 (2016) 301-304 ISSN 2347 - 3258
International Journal of Advance Research and Innovation

Adsorption of Zn(II) from aqueous solution on mango leaves powder

Achla Kaushal[a], S.K.Singh[b]

[a]Chemical Engineering Department, Guru Nanak Dev Institute of Technology, Rohini, Delhi.
[b]Department of Environmental Technology, Delhi Technological University, Delhi, India.

Article Info

Article history:
Received 20 January 2016
Received in revised form
10 February 2016
Accepted 28 February 2016
Available online 15 March 2016

Keywords

Adsorption, Adsorption Isotherms, mango tree leaves, Zn (II), optimum parameters.

Abstract

Since ancient times, it's a common practice in India to use mango tree leaves when there is a large crowd of people to ensure free flow of oxygen, for their ability to absorb excess carbon dioxide. Owing to its purifying nature, it has been studied for waste water treatment also. In the present study, potential of mango tree leaves have been investigated in removing zinc ions from aqueous solution. Batch adsorption studies were conducted to determine the optimum values of solution pH, zinc ion concentration in the solution, adsorbent dose and contact time at 20°C for maximum removal zinc ions from the synthetic solutions. It was observed that Zinc ion removal increased with increase in adsorbent dose and time. Optimum pH was 4. Equilibrium data was well described by the Langmuir, Freundlichand Temkin adsorption isotherm models.

1. Introduction

Increased population, urbanization and industrialization has caused a considerable damage to the environment due to accumulation of pollutants into the surroundings. Presence of heavy and toxic metal ions in water is a major concern today because of their non-biodegradability. Zinc is widely used in various industries such as automobile industry, rubber, paints, pigments and iron and steels, plastics, cosmetics, photocopier paper, wall paper, printing inks, pharmaceuticals and metal industries. Effluents coming out of these industries are contaminated with high amounts of zinc. Accumulation of high levels of zinc in body through contaminated water can result in various ailments such as stomach cramps, skin irritations, anemia, damage pancreas, disturbed metabolism, arteriosclerosis and respiratory disorders etc. Zinc also influences the activity of microorganisms and earthworms, slowing down the breakdown of organic matter, thus interrupting the characteristics of soil [1, 2]. Hence, removal of zinc from waste water is essential till it reaches the permissible levels. Conventional methods for treating effluents, such as precipitation, redox, membrane technologies, electrolysis etc., are costly and have problem of disposal of secondary waste such as toxic sludge [3]. In the light of these facts, adsorption has proven to be a better option as large varieties of adsorbents are available at a very low cost and the sludge formation and disposal is also not a problem of as many of these adsorbents are biodegradable [4]. Thus adsorbents such as activated carbon, zeolites, biosorbents,

Corresponding Author,
E-mail address: achla001@hotmail.com
All rights reserved: http://www.ijari.org

Agricultural waste [5,6,7,8,9,10,11,12,13,14,15,16,17,18] etc., are reported in literature for zinc, other heavy metals and pollutant removal from effluents. The present study was carried out to assess the potential of mango tree leaves as low cost agriculture adsorbents in adsorbing zinc from aqueous samples prepared in lab. The equilibrium data was analysed through adsorption isotherm.

2. Materials and Methods

A. Preparation of Adsorbent

Mango tree leaves were collected from the study area, GNDIT Rohini, Delhi, India. Leaves were Sun dried for 5 days, oven dried at 200°C for six hours in hot air oven. Dried leaves were powdered in a grinder and washed several times with distilled water till the entire colored impurities removed, again dried in hot air oven at 200°C for 8 hours. The powdered bark was sieved (Indian Standard Sieve) and various fractions of adsorbent was separately stored in air tight containers.

B. Preparation of stock solution

Stock solution was prepared by dissolving Zinc metal chips in a few drops of concentrated HCl and then diluting it to a solution of 1000 ml with distilled water. Solutions of required concentrations were prepared by further diluting the stock solution with distilled water. pH of the solutions was adjusted with the help of 0.1N HCl and 0.1N NaOH solutions.

C. Batch Adsorption Studies

Batch experiments were carried out to study the adsorption of zinc ions on mango tree leaves at 22 °C. Aqueous solutions in the concentration range of 10 to 100 ppm with adsorbent dose of 2 to 20 g/L in the pH range from 3 to 8

were agitated at 200 rpm at 22 ºC for 2 hours. The mixture was then filtered and analyzed for zinc ion concentration with the help of AA Susing air-acetylene flame. The amount of metal ions adsorbed on the surface of adsorbent was calculated from the difference between the initial and final concentrations of the solutions. Percentage removal of zinc from the solution after the batch adsorption was calculated as

$$\% \text{ Removal} = [(C_i - C_o)/C_i]*100 \quad (1)$$

Where C_o represents the final zinc ion concentration and C_i represents the initial zinc ion concentration in the solution.

The equilibrium adsorption capacity is calculated as

$$q_e = [(C_i - C_e)V]/m \quad (2)$$

Where V is the volume of the solution in litres and m is the mass of the adsorbent used [13].

3. Results and Discussions

3.1 Effect of pH

Adsorption of zinc on mango tree leaves was investigated in the pH range between 3 and 8.The effect of initial pH on % removal of zinc ions is shown in Fig. 1.Chart suggests that the maximum removal was obtained at pH 5. A maximum of 75% zinc metal ions were removed at this pH at 22ºC. % removal is sufficiently high at pH 4 and 6, but drops sharply at low pH values. Gradually, at higher pH values % removal is lowest at pH 3. % removal increased with increase in pH due to negative charges at active sites on the surface [6].

3.2 Effect of initial zinc ion concentration in the solution

The amount of zinc removed by adsorption on to mango tree leaves depended largely on the initial metal ion concentration, as shown in the fig 2% removal decreased with increase in metal ion concentration. Lower initial

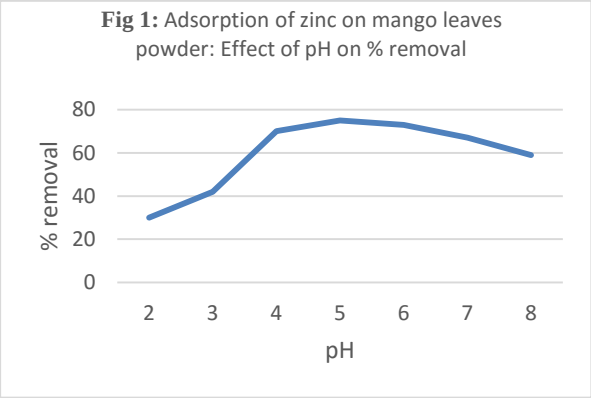

concentration results in higher % removal due large number of available binding sites. As the total number of active sites on the adsorbent are occupied by the heavy metal ions with the course of time, % removal start to decrease.

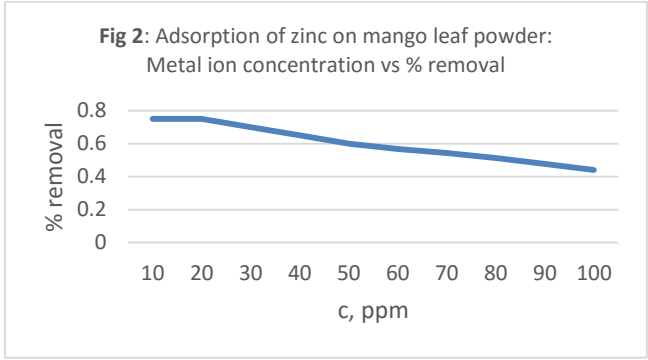

3.3 Effect of adsorbent dose

Results have shown that the amount of zinc adsorbed increased as the amount of adsorbent increased from 2 to 20 g/L, as shown in Fig. 3. This is because the surface area available for adsorption increases to a large extent with increase in adsorbent dose, hence increasing the availability of active sites for the metal ion to adsorb. As the adsorbent dose is increased, the time taken for adsorption also decreases as the metal ions come in contact with freely available active sites, thus increasing the efficiency of the process.

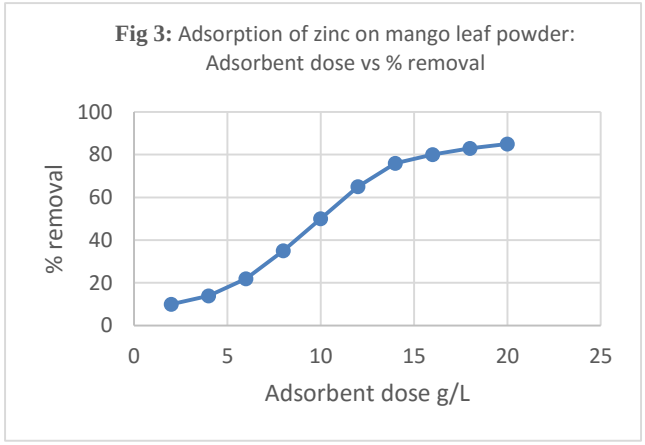

3.4 Effect of Contact Time

During the experiment, it was observed that the % removal increased with time till the equilibrium was reached. Equilibrium was reached in 80 minutes, after which the concentration of zinc ions in the solution became constant. The adsorption of zinc ions was rapid in the beginning, but became gradual with time. The effect of contact time on the amount of zinc ions on adsorbent surface is as shown in Fig.4.

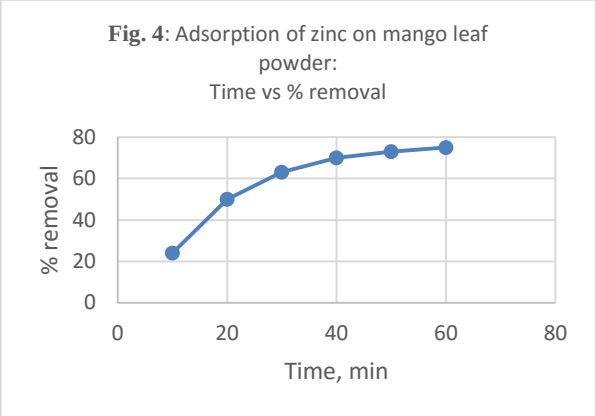

-

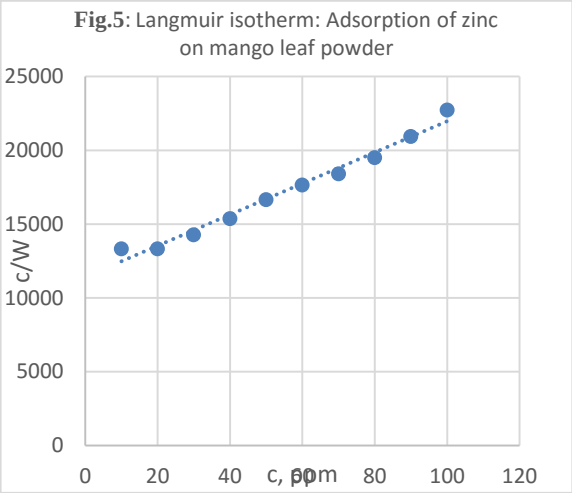

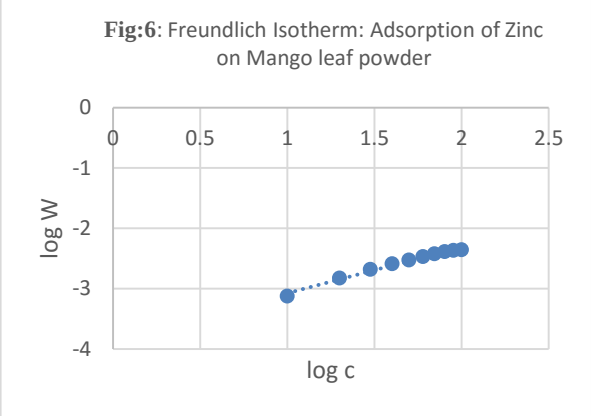

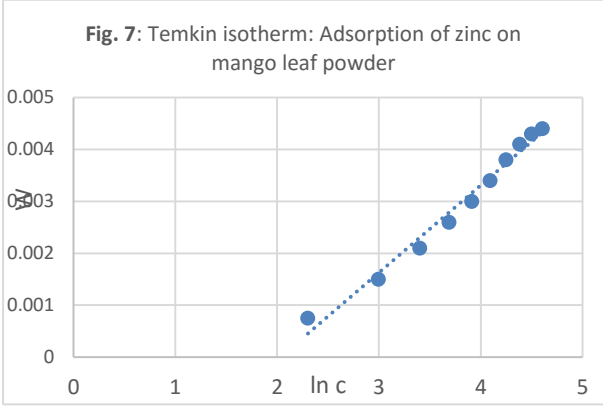

3.5 Adsorption isotherms

The equilibrium data was tested with the help of adsorption isotherms, Langmuir, Freundlich and Temkin isotherms. The data fitted well into the isotherms. Langmuir and Freundlich isotherms gave very good fits as compared to the Temkin isotherm. The Karl Pearson correlation coefficients obtained were .998, .953 and .880 for Langmuir, Freundlich and Temkin isotherms respectively. The adsorption isotherms obtained are shown in fig. 5,6 and 7. The isotherms give a straight line, representing a good fit of the equilibrium data.

4 Conclusions

Mango tree leaves have shown a good potential towards removal of zinc, a heavy metal ion harmful for life when consumed in excess amount, from aqueous solution. The % removal of the zinc metal ion obtained was 75% even at very low temperature i.e. 20^{o}C. The adsorbent can be recommended for treatment of industrial waste water, as it can be a good solution to treat contaminated water when used at optimum conditions given its low cost and ready availability.

References

[1] P.K. Goel, Water Pollution, Causes, Effects and Control, Revised second edition, New Age International Publishers, 2006.
[2] G.L. Rorrer, Heavy Metal Ions In: Removal From Waste Water In: Encyclopedia of Environmental Analysis and Remediation, by RA Meyers (Ed), Wiley, New York, 4 (1998), pp. 2012-2125.
[3] B. Volesky, and Z.R. Holan, Biosorption of heavy metals, Biotechnology Progress 11 (1995), pp. 235-250.
.[4] C. Saka, O.S. Ahin, and M.M. Kucuk, Application on agricultural and forest waste adsorbents for the removal of lead (II) from contaminated waters, Int. J. Environ. Sci. Technol. 9 (2012), pp. 379-394.
[5] K. Mohanty, M. Jha, B.C. Meikap, and M.N. Biswas, Preparation, characterization of activated carbons from terminaliaarjuna nut with zinc chloride activation for the removal of phenol from waste water, Ind. Eng. Chem. Res. 44 (2005), pp. 4128–4138.
[6] H.O. Ali, and K. Abidin, Factors affecting adsorption characteristics of Zn^{2+} on two natural zeolites, Journal of

HazardousMaterials 131 (2006), pp. 59-65.
[7] W.E. Marshall and E.T. Champagne, Agricultural Byproducts as Adsorbents for Metal Ions in Laboratory Prepared Solutions and in Manufacturing Wastewater, Journal of Environmental Science and HealthPart A, Environmental Science and Engineering 30 (1995), pp. 241-261.
[8] P. Kumar and S.S. Dara, Utilization of agricultural wastes for decontaminating industrial/ domestic wastewaters from toxic metals, Agric.Wastes4 (1982), pp. 213-223.
[9] E. Maranon, and H. Sastre, Heavy metal removal in packed beds using apple wastes, Bioresource Technol. 38 (1991), pp. 39-43.
[10] P. Brown, I. Jefcoat, P.D. Atly, S. Gill, and E. Graham, Evaluation of the adsorptive capacity of peanut hull pellets for heavy metals in solution, Advances in Environmental Research 4(2000), pp. 19-29.
[11] K. Conrad, and H.C.B. Hansen, Sorption of zinc and lead on coir,Bioresour. Technol. 98 (2007), pp. 89–97.
[12] S. Qaiser, A.R. Saleemi, and M.M. Ahmad, Heavy metal uptake by agro based waste materials, Electronic J. of Biotech, 10 (2007).
[13] A. Kaushal andS.K.Singh, Removal of Zn (II) from aqueous solutions using agro-based adsorbents, Imperial Journal of Interdisciplinary Research, 2(2016).
[14] A. Kaushal andS.K.Singh, Application of statistical tools and hypothesis testing of adsorption data obtained for removal of heavy metals from aqueous solutions, International Journal of Advanced Research and Innovation, 4 (2016), pp. 82-84.
[15] S.K.Singh and N.Narwal, Assessment of fixed bed column reactor using low cost adsorbent (rice husk) for removal of total dissolved solids, International Journal of Advanced Research and Innovation, 3 (2015), pp. 405-410.
[16] N. Sharma, D.P. Tiwari and S.K. Singh, The Efficiency Appraisal for Removal of Malachite Green by Potato peel and Neem Bark: Isotherm and Kinetic Studies, Int. J. of Chem. and Envi. Engineering 5 (2014) 83-88.
[17] D.P. Tiwari, S.K. Singh and N. Sharma, Sorption of methylene blue on treated agricultural adsorbents, App. Water Sci. 2014, doi 10.1007/S13201-014-0171-0.
[18] N. Sharma, D.P. Tiwari and S.K. Singh, Decolorisation of synthetic dyes by agricultural waste: a review, Int. J. of Sci. Eng. Res. 3 (2012) 1-10.

J. Inst. Eng. India Ser. B
DOI 10.1007/s40031-016-0253-5

ORIGINAL CONTRIBUTION

Alleviation SSR and Low Frequency Power Oscillations in Series Compensated Transmission Line using SVC Supplementary Controllers

Sanjiv Kumar[1] · **Narendra Kumar**[2]

Received: 27 December 2014 / Accepted: 6 July 2016
© The Institution of Engineers (India) 2016

Abstract In this work, supplementary sub-synchronous damping controllers (SSDC) are proposed for damping sub-synchronous oscillations in power systems with series compensated transmission lines. Series compensation have extensively been used as effective means of increasing the power transfer capability of a transmission lines and improving transient stability limits of power systems. Series compensation with transmission lines may cause sub-synchronous resonance (SSR). The eigenvalue investigation tool is used to ascertain the existence of SSR. It is shown that the addition of supplementary controller is able to stabilize all unstable modes for T-network model. Eigenvalue investigation and time domain transient simulation of detailed nonlinear system are considered to investigate the performance of the controllers. The efficacies of the suggested supplementary controllers are compared on the IEEE first benchmark model for computer simulations of SSR by means of time domain simulation in Matlab/Simulink environment. Supplementary SSDC are considered in order to compare effectiveness of SSDC during higher loading in alleviating the small signal stability problem.

Keywords Bus voltage and active power (BVAP) · Bus voltage and reactive power (BVRP) · Series compensation · SSDC · Supplementary controller · Eigenvalue investigation

✉ Sanjiv Kumar
activesanjiv007@rediffmail.com

[1] Department of Electrical Engineering, Institute of Foreign Trade and Management University, Moradabad, UP, India

[2] Department of Electrical Engineering, Delhi Technological University, Bawana Road, Delhi, India

Notations

C_{FC}	Fixed capacitance of SVC branch
C_T	Capacitance of T-circuit
D	Damping constant
H	Inertia constant
K	Spring constant
K_A	Regulator gain, pu
K_B	Gain of SVC auxiliary controller
K_D	Slope of SVC control characteristics
K_E	Exciter gain, pu
K_F	Regulator stabilizing circuit gain, pu
K_I	Integral gain of SVC voltage controller
K_P	Proportional gain of SVC voltage controller
L	Transmission line inductance
t	Time, s
T_A	Regulator amplifier time constant, s
T_D	Thyristor dead time constant
T_e	Electrical torque
T_E	Exciter time constant, s
T_F	Regulator stabilizing circuit time constant, s
T_M	Measurement time constant
T_m	Mechanical torque
T_s	Firing delay time constant
u	Input variable
U	Input variable
V_f	Reference voltage

Greek Symbols

δ	Generator rotor angle
ψ	Flux linkage
θ	Angle
λ	Eigen value
ω	Angular velocity, rad/s
ω_o	Synchronous frequency, rad/s
Δ	Incremental change

Published online: 29 July 2016

Superscripts

T	Transpose

Subscripts

C	SVC supplementary controller
D, Q, 0	D–Q–0 axis variables
d, q, 0	d–q–0 axis variables
f, g, h, k	Field and other rotor coils
G, g	Generator
R, M, E, N	Rotor circuit, mechanical, excitation system, network
0	Initial value or the nominal value at operating point
α, β, 0	α–β–0 axis variables

Introduction

Series capacitor compensation has been widely used to enhance the power transfer capability and improves voltage regulation of the system. Series capacitors expressively increase transient and steady state stability limits. However, series compensation gives rise to dynamic instability and destructive effects of sub-synchronous resonance (SSR) problems [1]. Flexible ac transmission system technology provides unprecedented way for controlling transmission grids and increasing transmission capacity [2]. Flexibility alternating current transmission systems (FACTS) controllers have the flexibility of controlling both real and reactive power which could provide an excellent capability for improving power system dynamics. FACTS controller-based solutions have been proposed to mitigate SSR in series-compensated lines [3].

Three distinct features of SSR analysis have been acknowledged and are referred to as induction generator effect, torsional interaction, and transient torque amplification. Many preventive measures to cope with this dynamic instability problem in series compensated lines have been reported in literature [4, 5]. In the present study, an attempt has been made to evaluate the performance of SVC auxiliary controllers to enhance the dynamic and transient performance of series compensated transmission lines. The first SSR problem was knowledgeable in 1970 ensuing in failure of a 750 MW cross compound turbine-generator shaft damage of Mohave-plant in Southern California. It was until the second shaft failure which again occurred in 1971 [6]. It is learned that series capacitors can create an adverse interaction between the series compensated electrical system and the spring-mass mechanical system of the turbine generators. This effect is known as sub-synchronous resonance [7]. The analysis of transient SSR requires transient simulation of the nonlinear model of the system. For the analysis of SSR, it is adequate to model the transmission line by lumped resistance and inductance where the line transients are also considered [8].

In this work, a detailed system model has been developed using a network model represented by a lumped-parameter T-circuit to investigate the dynamic and transient performance of the transmission line [9–11]. The IEEE first benchmark model [12] is considered for the analysis of SSR. The study is carried out based on damping torque analysis, eigenvalue analysis, and transient simulation. The work is organized for a 400 kV, 600 km, long series compensated (40 %) single-circuit transmission line, and the following studies are accomplished:

- The eigenvalue investigation tool has been employed to ascertain the dynamic performance of the series compensated line and existence of SSR with unstable torsional system modes are investigated.
- The combined BVAP, BVRP, line current and active power (LCAP), line current and reactive power (LCRP) supplementary controllers have been developed and incorporated in the SVC control system. As a result, the unstable torsional modes are stabilized over a wide operating range.
- To elucidate the comparative effectiveness of the various supplementary controllers under disturbance conditions, a digital computer simulation study for a 30 % pulsed torque disturbance using a nonlinear system model is performed. The simulation study exhibits a significant enhancement in the damping of the torsional oscillations in the system [13, 14].

The mathematical modelling of power system including synchronous generator, six mass mechanical system, excitation system, static var compensator (SVC), network system and their overall interconnection by considering IEEE first benchmark model have been depicted in this work.

Power System Modelling

Modeling of the system includes the modeling of synchronous generator, mechanical system, excitation system and the electrical T-network. The study system, as shown in Fig. 1, consists of a steam turbine driven synchronous generator supplying bulk power to an infinite bus over a long transmission line (IEEE first benchmark model) [12]. SVC is located at the middle of the transmission line which provides continuously controllable reactive power at its terminals in response to the supplementary controller. The series compensation is applied at the sending end side of the SVC [15].

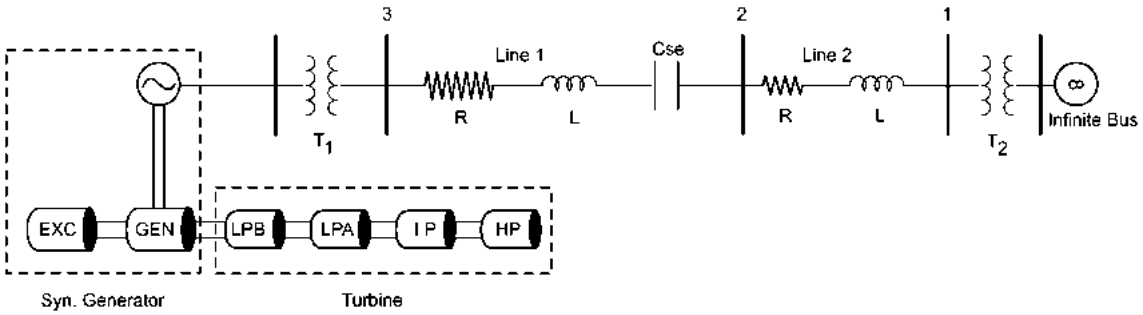

Fig. 1 IEEE FBM of study power system

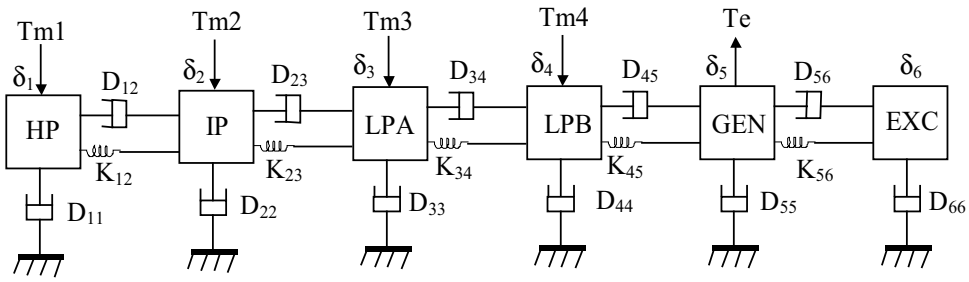

Fig. 2 Six mass-spring mechanical system (typical SSR studies)

Synchronous Generator

In the detailed machine model used in this work, the stator is represented by a dependent current source parallel with the inductance. The generator model includes the field winding f and a damper winding h along d-axis and two damper windings g and k along q-axis [16–18].

The rotor flux linkages 'ψ' associated with different windings are defined by:

$$\left.\begin{aligned}\dot{\psi}_f &= a_1\psi_f + a_2\psi_h + b_1V_f + b_2I_d\\ \dot{\psi}_h &= a_3\psi_f + a_4\psi_h + b_3I_d\\ \dot{\psi}_g &= a_5\psi_g + a_6\psi_k + b_5I_q\\ \dot{\psi}_k &= a_7\psi_g + a_8\psi_h + b_6I_q\end{aligned}\right\} \quad (1)$$

where V_f is the field excitation voltage. Constants a_1 to a_8 and b_1 to b_6 are defined as per the literature [11]. The i_d, i_q are d, and q-axis components, respectively, of the machine terminal current which are defined with respect to machine reference frame. To have a common axis of representation with the network and SVC, these flux linkages are transformed to the synchronously rotating D–Q frame of reference using the following transformation:

$$\begin{bmatrix} I_d \\ I_q \end{bmatrix} = \begin{bmatrix} \cos\delta & -\sin\delta \\ \sin\delta & \cos\delta \end{bmatrix} \begin{bmatrix} I_D \\ I_Q \end{bmatrix} \quad (2)$$

where I_D and I_Q are the respective machine current components along D and Q-axis. δ is the angle by which d-axis leads the D-axis. Currents I_d and I_q, which are the components of the dependent current source along d and q-axis, respectively, are expressed as:

$$I_d = c_1\psi_f + c_2\psi_h; \quad I_q = c_3\psi_g + c_4\psi_k \quad (3)$$

where constants c_1 to c_4 are defined as per the literature [14]. The earlier nonlinear differential equations are used in the power system modelling.

Six Mass Mechanical System

In the mechanical model detailed shaft torque dynamics [19] has been considered for the analysis of torsional modes due to SSR. The mechanical system is described by the six spring-mass model as shown in Fig. 2. This shows the electromechanical mass-spring damper system. It consists of exciter (EXC), generator (GEN), low pressure of two sections (LPA and LPB), intermediate pressure (IP) and high pressure (HP) turbine sections. Every section has its own angular momentum (M) and damping coefficient (D), and every two successive masses have their own shaft stiffness constant (K). The data for electrical and mechanical system are provided in the Appendix. The leading equations, the state and output equations are given as follows [20]:

Where $\delta_i = \omega_{-i}$, $i = 1, 2, 3, 4, 5, 6$

$$\left.\begin{aligned}
\frac{d\omega_1}{dt} &= \frac{1}{M_1}[-(D_{11}+D_{12})\omega_1 + D_{12}\omega_2 - K_{12}(\delta_1-\delta_2) + T_{M_1}] \\
\frac{d\omega_2}{dt} &= \frac{1}{M_2}[D_{12}\omega_1 - (D_{12}+D_{22}+D_{23})\omega_2 + D_{23}\omega_3 - K_{12}(\delta_2-\delta_1) + T_{M_2}] \\
\frac{d\omega_3}{dt} &= \frac{1}{M_3}[D_{23}\omega_2 - (D_{23}+D_{33}+D_{34})\omega_3 + D_{34}\omega_4 - K_{23}(\delta_3-\delta_2) - K_{34}(\delta_3-\delta_4) + T_{M_3}] \\
\frac{d\omega_4}{dt} &= \frac{1}{M_4}[D_{34}\omega_3 - (D_{34}+D_{44}+D_{45})\omega_4 + D_{45}\omega_5 - K_{34}(\delta_4-\delta_3) - K_{45}(\delta_4-\delta_5) + T_{M_4}] \\
\frac{d\omega_5}{dt} &= \frac{1}{M_5}[D_{45}\omega_4 - (D_{45}+D_{55}+D_{56})\omega_5 + D_{56}\omega_6 - K_{45}(\delta_5-\delta_4) - K_{56}(\delta_5-\delta_6) - T_e] \\
\frac{d\omega_6}{dt} &= \frac{1}{M_6}[D_{56}\omega_5 - (D_{56}+D_{66})\omega_6 - K_{56}(\delta_6-\delta_5)] \\
T_e &= -X''_d(i_D I_Q - i_Q I_D)
\end{aligned}\right\} \quad (4)$$

where δ_1, δ_2, δ_3, δ_4, δ_5 and δ_6 are the angular displacements and ω_1, ω_2, ω_3, ω_4, ω_5 and ω_6 are the angular velocities of different shaft segments as shown in Fig. 2.

Excitation System

The IEEE type-1 excitation system is described by the following equations [19]:

$$\left.\begin{aligned}
\frac{dV_f}{dt} &= -\frac{(K_E+S_E)}{T_E}V_f + \frac{1}{T_E}V_r \\
\frac{dV_S}{dt} &= -\frac{K_F(K_E+S_E)}{T_E T_F}V_f - \frac{1}{T_E}V_S + \frac{K_F}{T_E T_F}V_r \\
\frac{dV_r}{dt} &= -\frac{K_A}{T_A}V_S - \frac{1}{T_A}V_r - \frac{K_A}{T_A}Vg + \frac{K_A}{T_A}V_{REF}
\end{aligned}\right\} \quad (5)$$

Electrical T-network System

The ac transmission line in this study system is adapted from the IEEE first SSR benchmark system [12]. The transmission line is represented by standard lumped parameter T-circuit. The network has been represented by its α-axis equivalent circuit, which is identical with the positive sequence network. The governing equations of the α-axis, T-network representation is derived as follows:

$$\left.\begin{aligned}
\frac{di_{1\alpha}}{dt} &= \frac{-R}{L_2}i_{1\alpha} + \frac{1}{L_2}V_{2\alpha} - \frac{1}{L_2}V_{1\alpha} \\
\frac{di_{\alpha}}{dt} &= \frac{1}{L_1}V_{2\alpha} - \frac{R_1}{L_1}i_{\alpha} - \frac{L''_d}{L_1}\frac{di_{\alpha}}{dt} - \frac{1}{L_1}V_{4\alpha} \\
\frac{dV_{2\alpha}}{dt} &= -\frac{1}{C_n}i_{\alpha} - \frac{1}{C_n}i_{2\alpha} - \frac{1}{C_n}i_{1\alpha} \\
\frac{dV_{4\alpha}}{dt} &= \frac{1}{C_{se}}i_{\alpha}
\end{aligned}\right\} \quad (6)$$

where $C_n = C_T + C_{FC}$, $L_A = L_{T1} + L''_n$, $L_1 = L + L_A$, $L_2 = L + L_{T2}$ and $R_1 = R + R_a$.

Similarly, the equations can be derived for the β-network. The α–β network equations are then transformed to *D–Q* frame as per literature [21].

Static Var Compensator

The terminal voltage perturbation ΔV and the SVC incremental current weighted by the factor K_D representing current droop are fed to the reference junction. T_M represents the measurement time constant, which for simplicity is assumed to be equal for both voltage and current measurements. The voltage regulator is assumed to be a proportional-integral (PI) controller. Thyristor control action is represented by an average dead time T_D and a firing delay time T_s. ΔB is the variation in TCR susceptance. ΔV_F represents the incremental supplementary controller [22, 23].

The α–β axes currents entering TCR from the network are expressed as:

$$\left.\begin{aligned}
L_s\frac{di_{2\alpha}}{dt} + R_s i_{2\alpha} &= V_{2\alpha} \\
L_s\frac{di_{2\beta}}{dt} + R_s i_{2\beta} &= V_{2\beta}
\end{aligned}\right\} \quad (7)$$

where R_S and L_S represent TCR resistance and inductances, respectively. The other equations describing the SVC model are:

$$\left.\begin{aligned}
Z_1 &= \Delta V_{\text{ref}} - Z_2 + V_F \\
\dot{Z}_2 &= \frac{1}{T_M}(\Delta V_2 - K_D \Delta i_2) - \frac{1}{T_M}Z_2 \\
\dot{Z}_3 &= -\frac{K_I}{T_3}Z_1 + \frac{K_P}{T_S}Z_2 - \frac{1}{T_s}Z_3 - \frac{K_P}{T_S}\Delta V_{\text{ref}} - \frac{K_p}{Ts}\Delta V_F \\
\Delta B &= \frac{(Z_3 - \Delta B)}{T_D}
\end{aligned}\right\} \quad (8)$$

Table 1 Load flow study of series compensated transmission system with T-circuit network model

Generator bus				SVC bus			Infinite bus		
P_G, MW	Q_G, MVAR	V, pu	δ, °	P_3, MW	Q_3, MVAR	V, pu	θ, °	P, MW	Q, MVAR
100	−12.4858	1.05	6.1411	0	−309.971	1.05	3.8137	−98.5908	−55.5661
200	−20.8733	1.05	12.4655	0	−287.957	1.05	7.8205	−195.127	−37.2716
300	−25.2040	1.05	18.7508	0	−255.292	1.05	11.7941	−289.37	−12.5106
400	−25.4993	1.05	25.0198	0	−212.115	1.05	15.7535	−381.345	18.5991
500	−21.7606	1.05	31.2951	0	−158.455	1.05	19.7177	−471.058	56.0336
600	−13.9696	1.05	37.6001	0	−94.2172	1.05	23.7061	−558.49	99.8655
700	−2.0876	1.05	43.9597	0	−19.1826	1.05	27.7400	−643.6	150.2731
800	13.9450	1.05	50.4019	0	67.0177	1.05	31.8432	−726.317	207.5606
900	34.2107	1.05	56.9595	0	164.9379	1.05	36.0443	−806.538	272.1922
1000	58.8168	1.05	63.6724	0	275.3779	1.05	40.3788	−884.112	344.8493

Table 2 Eigenvalues of T-circuit network without supplementary controller (with series compensation)

Torsional mode	$P = 200$ MW	$P = 500$ MW	$P = 800$ MW
Mode # 5	$-0.0 \pm j\ 298.1$	$-0.0 \pm j\ 298.1$	$-0.0 \pm j\ 298.1$
Mode # 4	$-0.22236 \pm j\ 202.88$	$-0.27157 \pm j\ 202.84$	$-0.33712 \pm j\ 202.78$
Mode # 3	$-0.010518 \pm j\ 160.52$	$-0.047 \pm j\ 160.53$	$-0.09618 \pm j\ 160.52$
Mode # 2	$-0.005104 \pm j\ 126.97$	$-0.0105 \pm j\ 126.96$	$-0.01716 \pm j\ 126.95$
Mode # 1	$-0.026618 \pm j\ 98.757$	$-0.03009 \pm j\ 98.665$	$-0.02494 \pm j\ 98.517$
Mode # 0	$-0.33922 \pm j\ 4.0339$	$-0.09897 \pm j\ 4.2864$	**$0.0787 \pm j\ 4.1284$**
Other modes	$-13.132 \pm j\ 833.01$	$-13.133 \pm j\ 833$	$-13.133 \pm j\ 833$
	$-532.8 \pm j\ 3.3619$	$-532.82 \pm j\ 4.4606$	$-532.83 \pm j\ 4.7221$
	$-12.767 \pm j\ 442.17$	$-12.769 \pm j\ 442.15$	$-12.769 \pm j\ 442.16$
	$-5.4252 \pm j\ 311.97$	$-5.4245 \pm j\ 311.97$	$-5.4245 \pm j\ 311.97$
	$-34.282 \pm j\ 189.06$	$-35.515 \pm j\ 187.54$	$-35.498 \pm j\ 187.12$
	$-3.2239 \pm j\ 187.16$	$-3.2602 \pm j\ 188.75$	$-3.4007 \pm j\ 189.12$
	$-57.127 \pm j\ 86.317$	$-53.469 \pm j\ 85.459$	$-52.804 \pm j\ 85.669$
	$-25.634 \pm j\ 24.258$	$-25.689 \pm j\ 24.357$	$-25.744 \pm j\ 24.309$
	−39.674	−40.643	−40.979
	−27.443	−31.073	−31.573
	−2.5406	−2.8919	−2.9457
	$-0.5906 \pm j\ 0.74682$	$-0.5662 \pm j\ 0.79191$	$-0.66527 \pm j\ 0.84667$

Bold values represent unstable mode

where ΔV_2, Δi_2 are incremental magnitudes of SVC voltage and current, respectively, obtained by linearizing.

$$V_2^2 = V_{2D}^2 + V_{2Q}^2, \quad i_2^2 = i_{2D}^2 + i_{2Q}^2$$

Development of Sub-synchronous Damping Controller

The supplementary controller, U_C is implemented through a first order supplementary controller transfer function G(s), which is assumed to be,

$$G(S) = \frac{\Delta V_F}{\Delta U_C} = K_B\left[\frac{1+sT_1}{1+sT_2}\right] \tag{9}$$

This can be equivalently written as:

$$G(S) = K_B\frac{T_1}{T_2} + K_B\left[\frac{1-T_1/T_2}{1+sT_2}\right] \tag{10}$$

The state and output equations are given by,

$$\left.\begin{aligned}\dot{X}_C &= [A_C]X_C + [B_C]U_C\\ Y_C &= [C_C]X_C + [D_C]U_C\end{aligned}\right\}$$

Table 3 Eigenvalues of T-circuit network with BVAP supplementary controller (series compensated line)

Torsional mode	$P = 200$ MW	$P = 500$ MW	$P = 800$ MW
Mode # 5	$-0.0 \pm j\ 298.1$	$-0.0 \pm j\ 298.1$	$-0.0 \pm j\ 298.1$
Mode # 4	$-0.197 \pm j\ 202.88$	$-0.249 \pm j\ 202.84$	$-0.318 \pm j\ 202.78$
Mode # 3	**$0.002 \pm j\ 160.53$**	$-0.038 \pm j\ 160.56$	$-0.099 \pm j\ 160.58$
Mode # 2	$-0.007 \pm j\ 126.97$	$-0.018 \pm j\ 126.97$	$-0.033 \pm j\ 126.96$
Mode # 1	$-0.072 \pm j\ 98.733$	$-0.132 \pm j\ 98.547$	$-0.153 \pm j\ 98.232$
Mode # 0	$-0.344 \pm j\ 4.0368$	$-0.137 \pm j\ 4.3397$	$-0.006 \pm j\ 4.2983$
Other modes	$-13.25 \pm j\ 833.11$	$-13.275 \pm j\ 833.1$	$-13.304 \pm j\ 833.11$
	-535.63	-539.09	-541.09
	-530.21	-526.93	-525.05
	$-12.66 \pm j\ 441.96$	$-12.689 \pm j\ 441.93$	$-12.712 \pm j\ 441.93$
	$-5.33 \pm j\ 311.81$	$-5.2894 \pm j\ 311.8$	$-5.2609 \pm j\ 311.78$
	$-40.824 \pm j\ 192.39$	$-42.775 \pm j\ 190.9$	$-43.133 \pm j\ 189.9$
	$-2.23 \pm j\ 184.92$	$-1.8689 \pm j\ 186.6$	$-1.7656 \pm j\ 187.03$
	$-24.655 \pm j\ 85.281$	$-21.226 \pm j\ 86.63$	$-21.208 \pm j\ 88.512$
	-110.97	-110.44	-109.98
	-69.725	-71.171	-70.398
	$-25.942 \pm j\ 24.301$	$-25.914 \pm j\ 24.337$	$-25.931 \pm j\ 24.273$
	-33.993	-33.057	-32.605
	-26.744	-30.06	-30.779
	-2.5511	-2.908	-2.9627
	$-0.558 \pm j\ 0.72563$	$-0.528 \pm j\ 0.7664$	$-0.615 \pm j\ 0.81928$

Bold values represent unstable mode

Bus Voltage Supplementary Controller

The SVC bus voltage, V_2 is expressed in terms of its D and Q-axis components as,

$$V_2^2 = V_{2D}^2 + V_{2Q}^2 \tag{11}$$

Magnitude of bus voltage, $V_2 = \sqrt{\left[V_{2D}^2 + V_{2Q}^2\right]}$.

Linearizing earlier equation gives the deviation in bus voltage, ΔV_2 which is selected as supplementary control signal

$$\Delta V_2 = V_{2D0}\frac{\Delta V_{2D}}{V_{20}} + V_{2Q0}\frac{\Delta V_{2Q}}{V_{20}} \tag{12}$$

Line Current Supplementary Controller

The line current entering to SVC bus from generator end is given by,

$$i_2^2 = i_{2D}^2 + i_{2Q}^2 \tag{13}$$

Magnitude of line current, $i_{2D} = \sqrt{\left[i_{2D}^2 + i_{2Q}^2\right]}$.

Linearizing earlier equation gives the deviation in line current, Δi_2 which is selected as supplementary control signal

$$\Delta i_2 = i_{2D0}\frac{\Delta i_{2D}}{i_{20}} + i_{2Q0}\frac{\Delta i_{2Q}}{i_{20}} \tag{14}$$

Active Power Supplementary Controller

The line active power entering to SVC bus from generator end is given by

$$P_2 = V_{2D}i_D + V_{2Q}i_Q \tag{15}$$

where V_{2D} and V_{2Q} are direct and quadrature axis SVC bus voltages and i_D and i_Q are direct and quadrature axis currents.

Linearizing earlier equation gives the deviation in active power ΔP_2 which is selected as supplementary control signal:

$$\Delta P_2 = V_{2D0}\Delta i_D + i_{D0}\Delta V_{2D} + V_{2Q0}\Delta i_Q + i_{Q0}\Delta V_{2Q} \tag{16}$$

Line Reactive Power Supplementary Controller

The transmission line reactive power entering to SVC bus from generator end is given by,

$$Q_2 = -(\mathrm{V}_{2D}i_Q - V_{2Q}i_D) \tag{17}$$

Linearizing earlier equation gives the deviation in line current, ΔQ_2 which is selected as supplementary control signal

$$\Delta Q_2 = -[V_{2D0}\Delta i_Q + i_{Q0}\Delta V_{2D} - V_{2Q0}\Delta i_D - i_{D0}\Delta V_{2Q}] \tag{18}$$

The state and output equations for the combined supplementary controller are obtained as follows:

Table 4 Eigenvalues of T-circuit network with BVRP supplementary controller (series compensated line)

Torsional mode	$P = 200$ MW	$P = 500$ MW	$P = 800$ MW
Mode # 5	$-0.0 \pm j\ 298.1$	$-0.0 \pm j\ 298.1$	$-0.0 \pm j\ 298.1$
Mode # 4	$-0.22033 \pm j\ 202.88$	$-0.26974 \pm j\ 202.84$	$-0.33481 \pm j\ 202.79$
Mode # 3	$-0.0118 \pm j\ 160.52$	$-0.050429 \pm j\ 160.52$	$-0.10365 \pm j\ 160.51$
Mode # 2	$-0.00495 \pm j\ 126.97$	$-0.010415 \pm j\ 126.96$	$-0.016984 \pm j\ 126.95$
Mode # 1	$-0.02881 \pm j\ 98.758$	$-0.035124 \pm j\ 98.66$	$-0.030888 \pm j\ 98.504$
Mode # 0	$-0.34974 \pm j\ 4.0411$	$-0.15041 \pm j\ 4.3884$	$-0.015903 \pm j\ 4.4347$
Other modes	$-13.157 \pm j\ 833.03$	$-13.154 \pm j\ 833.02$	$-13.15 \pm j\ 833.03$
	$-532.8 \pm j\ 1.1197$	$-532.82 \pm j\ 2.3481$	$-532.83 \pm j\ 1.6702$
	$-12.718 \pm j\ 442.17$	$-12.718 \pm j\ 442.16$	$-12.714 \pm j\ 442.17$
	$-5.4227 \pm j\ 311.93$	$-5.4334 \pm j\ 311.93$	$-5.4452 \pm j\ 311.93$
	$-34.237 \pm j\ 190.11$	$-35.165 \pm j\ 188.35$	$-34.83 \pm j\ 187.64$
	$-2.4726 \pm j\ 187.26$	$-2.4573 \pm j\ 188.78$	$-2.5305 \pm j\ 189.12$
	$-60.868 \pm j\ 75.219$	$-57.52 \pm j\ 73.039$	$-58.835 \pm j\ 72.793$
	-86.92	$-69.661 \pm j\ 2.7047$	$-68.254 \pm j\ 13.71$
	-51.075	$-25.738 \pm j\ 24.58$	$-25.824 \pm j\ 24.471$
	$-25.574 \pm j\ 24.584$	-31.342	-31.687
	-28.128	-16.271	-2.9696
	-16.425	-2.9151	$-0.60244 \pm j\ 0.81036$
	-2.5554	$-0.51896 \pm j\ 0.75815$	-16.252
	$-0.551 \pm j\ 0.71829$		

Table 5 Eigenvalues of T-circuit network with LCAP supplementary controller (series compensated line)

Torsional mode	$P = 200$ MW	$P = 500$ MW	$P = 800$ MW
Mode # 5	$-0.0 \pm j\ 298.1$	$-0.0 \pm j298.1$	$-0.0 \pm j\ 298.1$
Mode # 4	$-0.22261 \pm j\ 202.88$	$-0.27174 \pm j\ 202.84$	$-0.33679 \pm j\ 202.78$
Mode # 3	$-0.01037 \pm j\ 160.52$	$-0.046912 \pm j\ 160.52$	$-0.095585 \pm j\ 160.52$
Mode # 2	$-0.00507 \pm j\ 126.97$	$-0.010449 \pm j\ 126.96$	$-0.017573 \pm j\ 126.95$
Mode # 1	$-0.026757 \pm j\ 98.757$	$-0.03019 \pm j\ 98.665$	$-0.025968 \pm j\ 98.514$
Mode # 0	$-0.33913 \pm j\ 4.0336$	$-0.094166 \pm j\ 4.3101$	$-0.8365 \pm j\ 3.7552$
Other modes	$-13.135 \pm j\ 833.01$	$-13.137 \pm j\ 833$	$-13.135 \pm j833$
	$-532.8 \pm j\ 3.6968$	$-532.82 \pm j\ 4.9301$	$-532.84 \pm j\ 4.3843$
	$-12.763 \pm j\ 442.18$	$-12.763 \pm j\ 442.17$	$-12.773 \pm j\ 442.16$
	$-5.4251 \pm j\ 311.97$	$-5.4248 \pm j\ 311.97$	$-5.4199 \pm j\ 311.97$
	$-34.302 \pm j\ 189.15$	$-35.497 \pm j\ 187.66$	$-35.866 \pm j\ 187.04$
	$-3.2247 \pm j\ 187.22$	$-3.2289 \pm j\ 188.8$	$-3.4121 \pm j\ 189.1$
	$-57.047 \pm j\ 85.892$	$-53.426 \pm j\ 84.979$	$-51.232 \pm j\ 85.518$
	-39.728	$-25.687 \pm j\ 24.36$	$-25.767 \pm j\ 24.331$
	$-25.629 \pm j\ 24.26$	-40.74	-42.376
	-27.445	-31.076	-31.595
	-4.9466	-4.981	-5.0682
	-2.5451	-2.9035	-3.0897
	$-0.58208 \pm j\ 0.73535$	$-0.5545 \pm j\ 0.77735$	$-0.26586 \pm j\ 1.6283$
	-1.3895	-1.3909	-0.89987

Table 6 Eigenvalues of T-circuit network with LCRP supplementary controller (series compensated line)

Torsional mode	$P = 200$ MW	$P = 500$ MW	$P = 800$ MW
Mode # 5	$-0.0 \pm j\ 298.1$	$-0.0 \pm j\ 298.1$	$-0.0 \pm j\ 298.1$
Mode # 4	$-0.2272 \pm j\ 202.88$	$-0.27733 \pm j\ 202.84$	$-0.3421 \pm j\ 202.79$
Mode # 3	$-0.0097 \pm j\ 160.51$	$-0.043961 \pm j\ 160.51$	$-0.0894 \pm j\ 160.5$
Mode # 2	$-0.0044 \pm j\ 126.97$	$-0.00898 \pm j\ 126.96$	$-0.014117 \pm j\ 126.95$
Mode # 1	$-0.0262 \pm j\ 98.761$	$-0.027862 \pm j\ 98.67$	$-0.017628 \pm j\ 98.526$
Mode # 0	$-0.3686 \pm j\ 4.1144$	$-0.2827 \pm j\ 4.6113$	$-0.093372 \pm j\ 5.0516$
Other modes	$-13.218 \pm j\ 833.03$	$-13.216 \pm j\ 833.04$	$-13.208 \pm j\ 833.07$
	$-532.78 \pm j\ 8.8444$	$-532.76 \pm j\ 10.951$	$-532.72 \pm j\ 12.713$
	$-12.609 \pm j\ 442.34$	$-12.62 \pm j\ 442.36$	$-12.625 \pm j\ 442.39$
	$-5.4151 \pm j\ 311.94$	$-5.4344 \pm j\ 311.91$	$-5.4604 \pm j\ 311.89$
	$-34.336 \pm j\ 191.15$	$-34.835 \pm j\ 189.67$	$-34.057 \pm j\ 189.3$
	$-2.9071 \pm j\ 188.43$	$-2.7702 \pm j\ 190.02$	$-2.7738 \pm j\ 190.47$
	$-56.412 \pm j\ 77.039$	$-52.792 \pm j\ 75.345$	$-53.062 \pm j\ 74.677$
	-41.808	-44.292	-44.867
	$-25.555 \pm j\ 24.376$	$-25.671 \pm j\ 24.457$	$-25.746 \pm j\ 24.385$
	-27.568	-31.167	-31.61
	$-3.4828 \pm j\ 0.56069$	-4.4628	-5.347
	$-0.61842 \pm j\ 1.0567$	-3.4572	-3.1782
	-1.7605	$-0.45973 \pm j\ 1.1744$	$-0.35791 \pm j\ 1.1512$
		-1.2915	-0.94523

$$\begin{bmatrix} \dot{X}_{C1} \\ \dot{X}_{C2} \end{bmatrix} = \begin{bmatrix} A_{C1} & 0 \\ 0 & A_{C2} \end{bmatrix} \begin{bmatrix} X_{C1} \\ X_{C2} \end{bmatrix} + \begin{bmatrix} B_{C1} & 0 \\ 0 & B_{C2} \end{bmatrix} \begin{bmatrix} U_{C1} \\ U_{C2} \end{bmatrix}$$

$$[Y_C] = [\, C_{C1} \quad C_{C2} \,] \begin{bmatrix} X_{C1} \\ X_{C2} \end{bmatrix} + [\, D_{C1} \quad D_{C2} \,] \begin{bmatrix} U_{C1} \\ U_{C2} \end{bmatrix} \qquad (19)$$

where the state X_{C1} and matrices A_{C1}, B_{C1}, C_{C1} and D_{C1} correspond to bus voltage (BV) supplementary controller and the state X_{C2} and matrices A_{C2}, B_{C2}, C_{C2} and D_{C2} correspond to the line current (LC) supplementary controller. The non-linear differential equations of each subsystem are combined to obtain the mathematical model of the entire system. The order of the overall system model is 35 after adding combined SSDC.

Dynamic Performance

The study system consists of 1110 MVA synchronous generator supplying power to an infinite bus over a 400 kV, 600 km long series compensated single circuit transmission line. The study system is as per the IEEE first benchmark model. The system data and torsional spring mass system data are given in Appendix. Table 1 present the load flow study for the T-circuit model of the ac network at $P = 100$ MW to $P = 1000$ MW of series compensated line. The load flow studies have been carried out by keeping sending end, midpoint and receiving end voltage at 1.05, 1.05 and 1.0 pu, respectively. The SVC reactive power varies from -309.971 MVAR reactive to 275.3779 MVAR capacitive with T-circuit representation. Hence the SVC rating has been chosen to be 200 MVAR reactive to 350 MVAR capacitive. The SVC rating for the line has been chosen to be 100 MVAR inductive to 350 MVAR capacitive. The series compensation is 40 % used at the sending end of the transmission line [14].

Eigenvalue Investigation and Time Domain Simulation

The eigenvalue investigation has been carried using the linearized system modeling of power system. The natural damping has been considered to be zero in order to simulate the weakest system conditions. New supplementary controllers are combined BVAP, BVRP, LCAP and LCRP are investigated and are employed in the SVC control system in order to stabilize the torsional modes over a wide range of generator power. Disturbance is simulated by 30 % sudden increase in input torque for 0.1 s. Table 2 illustrates the complete set of eigenvalues of the system without supplementary controller incorporated in the SVC.

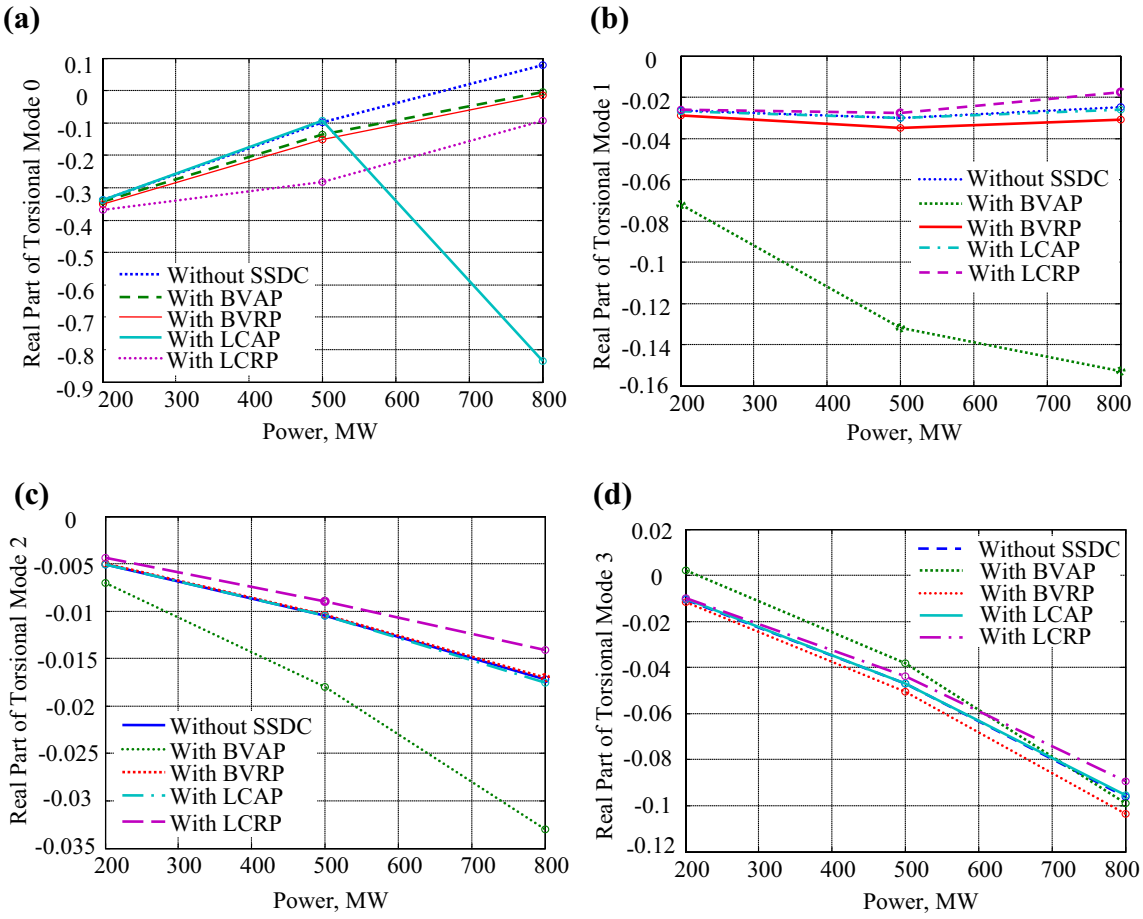

Fig. 3 Real parts of torsional modes with and without SSDC

The eigenvalue investigation show for 40 % compensation level, mode-0 is unstable without supplementary controller of series compensated line. Tables 3, 4, 5 and 6 show the system eigenvalues at $P = 200$, 500 and 800 MW with supplementary controllers of series compensated line. The improvement in the damping of mechanical modes is excellent with SVC supplementary controller. BVRP, LCAP and LCRP supplementary controller stabilizes all the torsional modes over the entire range of generator power considered. Table 3 shows the system eigenvalues at $P = 200$, 500 and 800 MW with BVAP supplementary controller of series compensated line. The BVAP supplementary controller stabilizes all torsional modes at higher generator powers except mode 3. The eigenvalue investigation tool ascertain the LCAP supplementary controller provides the effective damping to the low frequency as well as high frequency torsional mode oscillations. The supplementary controller parameters are selected based on an extensive root locus study and are listed in Appendix. All the electrical and electromechanical modes are found to be stable when the proposed supplementary controllers are applied. Figure 3 shows the behavior of real parts of torsional modes after adding SSDC. The improvement in the damping of mode-0 is excellent. Eigenvalue investigation of the system after accumulation SSDC shows that the incorporated SSDC can damp all torsional modes. Time domain simulations results, when SSDC is implementing to SVC are shown in Figs. 4 and 5. It is seen that the oscillations are sustained and growing and the system is unstable without SSDC. Figure 4 shows that system is stable and oscillation of different shaft sections are damped in a few seconds with the LCAP supplementary controller. The response curves (Fig. 5) of power angle, SVC susceptance, terminal voltage, SVC bus voltage and angular velocity shows the remarkable improvement with the LCAP supplementary controller and oscillations are die out effectively. The result without SSDC is also contained for comparison. As shown in the Figs. 4 and 5 the designed SSDC have successfully stabilized the system even when the large disturbance affected the system. The combined

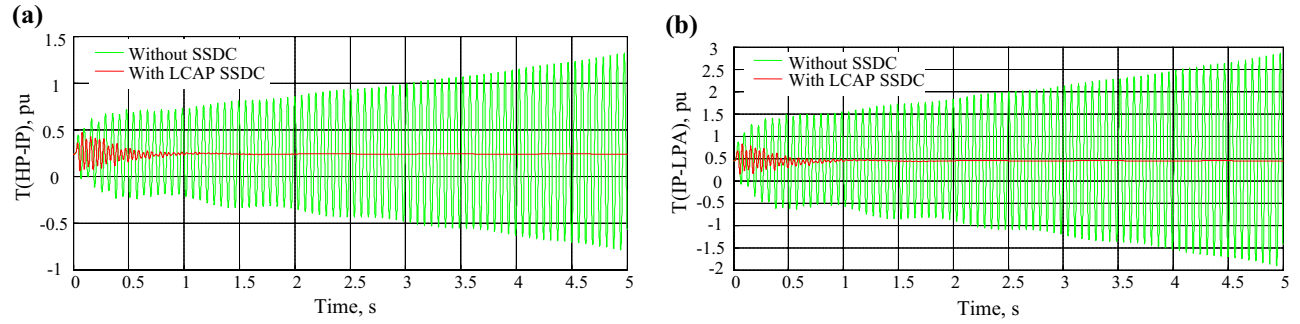

Fig. 4 Variation of torques at different shaft sections with and without SSDC **a** HP-IP, **b** IP-LPA

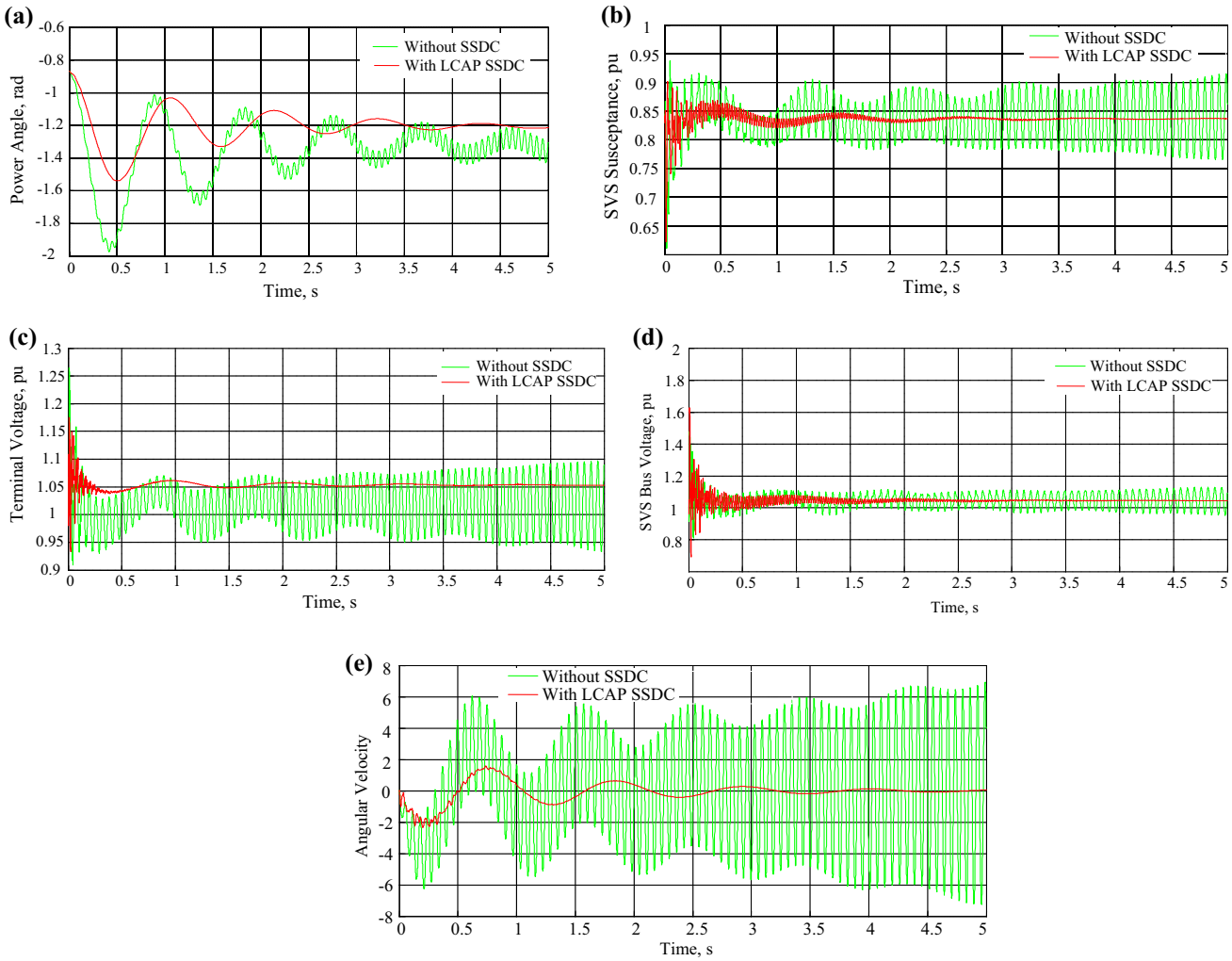

Fig. 5 Variation of **a** power angle, **b** SVC susceptance, **c** terminal voltage, **d** SVC bus voltage, **e** angular velocity, with and without SSDC

reactive power and voltage angle (CRPVA) SVS control strategy effectively stabilized unstable torsional modes and transient performance of series compensated power system is greatly improved [14, 15]. The combined reactive power and frequency (CRPF) auxiliary controller stabilized all the torsional modes over the wide operating range [22]. The result obtained in this paper effectively corroborates the outcome of the eigenvalue analysis and time domain simulation with the proposed SVC supplementary controllers.

Conclusion

The efficacy of combined supplementary controllers has been assessed for improving the transient performance of power system series compensation. The present work has been proposed to use the supplementary controllers to improve the torsional characteristics. Damping of torsional modes for 40 % compensation level of series compensated line is presented in Tables 2, 3, 4, 5 and 6. It can be seen that the presence of the supplementary controllers in the network improves the damping of the lower frequency torsional modes. Eigenvalue investigation demonstrates that the LCAP supplementary controller (as compared to other controllers) improves the damping of the torsional electromechanical oscillations due to sub synchronous resonance of the series compensated power system.

The following conclusions can be drained from the eigenvalue investigation study.

- The unstable torsional modes are stabilized by the BVAP, BVRP, LCAP and LCRP supplementary controllers developed for the SVC located at the middle of the series compensated transmission line, but the effective damping is achieved by the LCAP supplementary controller. The BVAP is not able stabilize mode-3 at low power but become stable at high power.
- The anticipated SSDC has been applied effectively to damping the all unstable torsional modes. The proposed controllers use an ingenuous and easy to implement idea to cope with the SSR phenomenon.
- The enactment of the designed supplementary controllers is corroborated using eigenvalue investigation and time domain simulation. It is found that the damping in the case of the line current active power supplementary controller is highest.
- The BVAP, BVRP, LCAP and LCRP supplementary controllers are developed for the SVC located at the middle of the transmission line improves the dynamic and transient performance of the series compensated line considerably.

Appendix

System Base Quantities

Voltage = 400 kV
Base value MVA = 100
Frequency = 314 rad/s

Synchronous Generator Parameters (on its Own Base)

$S_n = 1110$ MVA	$T'_{do} = 6.66$ s
$V_n = 22$ kV	$T'_{qo} = 0.44$ s
$pf = 0.9$	$T''_{do} = 0.032$ s
$f_n = 50$ Hz	$T''_{qo} = 0.057$ s
$R_a = 0.0036$ pu	$X_d = 1.933$ pu
$X_1 = 0.21$ pu	$X_q = 1.743$ pu
$R_0 = 0$ pu	$X'_q = 0.467$ pu
$X_0 = 0.195$ pu	$X''_q = 1.144$ pu
$H = 3.22$ s*	$X''_d = 0.312$ pu
$D = 0$	$X''_q = 0.312$ pu

* This corresponds to a single generator mass

IEEE Type-1 Excitation System Data

$V_g = 1$ pu	$T_R = 0$ s
$V_f = 1$ pu	$K_A = 400$ pu
$V_{pss} = 0$	$T_A = 0.02$ s
$V_{rmax} = 9.75$ pu	$K_E = 1.0$ pu
$V_{rmin} = -7$ pu	$T_E = 1.0$ s
$V_{fmax} = 5$ pu	$K_f = 0.06$ pu
$V_{fmin} = -7$ pu	$T_F = 1.0$ s
$S_{Emax} = 0.95$	$S_{Emin} = 0$

Static VAR Compensator (SVC) Data

$T_M = 2.4$ ms	$K_I = 950$
$T_S = 5$ ms	$K_P = -1.0$
$T_D = 1.667$ ms	$K_D = 0.01$ pu

Transmission Line Data

Voltage	400 kV
Resistance (R)	0.034 Ω/phase/km
Reactance (X_L)	0.325 Ω/phase/km
Susceptance ($B_C = 1/X_C$)	3.68×10^{-6} ℧/km

Supplementary Controller Parameters

SVC supplementary controller	K_{B1}	T_1	T_2
Bus voltage (BV)	−0.675	0.006	0.45
Line current (LC)	−0.043	0.39	0.02
Active power (AP)	−0.009	0.01	0.009
Reactive power (RP)	−0.009	0.01	0.00989

Torsional Spring-Mass System Data

Inertia H, s	Spring constant K, pu torque/rad
$H_1 = 0.1033586$	
$H_2 = 0.1731106$	$K_{12} = 25.772$
$H_3 = 0.9553691$	$K_{23} = 46.635$
$H_4 = 0.9837909$	$K_{34} = 69.478$
$H_5 = 0.9663006$	$K_{45} = 94.605$
$H_6 = 0.0380697$	$K_{56} = 3.768$

References

1. A.A. Edris, Series compensation schemes reducing the potential of sub synchronous resonance. IEEE Trans. Power Syst. **5**(1), 219–226 (1990)
2. N.G. Hingorani, L. Gyugyi, *Understanding FACTS: Concepts and Technology of Flexible AC Transmission Systems* (IEEE Press, New York, 2000)
3. A.A. Fouad, K.T. Khu, Damping of torsional oscillations in power system with series compensated lines. IEEE Trans. Power Appar. Syst. **97**(3), 744–753 (1978)
4. P.M. Anderson, B.L. Agrawal, J.E. Van Ness, *Subsynchronous Resonance in Power Systems* (IEEE Press, New York, 1990)
5. K.R. Padiyar, *Analysis of Subsynchronous Resonance in Power System* (Kluwer Academic Publishers, Boston, 1999)
6. A. Ghorbani, B. Mozaffari, A.M. Ranjbar, Application of sub-synchronous damping controller (SSDC) to STATCOM. Electr. Power Energy Syst. **43**, 418–426 (2012)
7. E. Lerch, D. Povh, L. Xu, Advanced SVC control for damping power system oscillation. IEEE Trans. Power Syst. **6**(2), 524–535 (1991)
8. K.R. Padiyar, N. Prabhu, Design and performance evaluation of sub-synchronous damping controller with STATCOM. IEEE Trans. Power Deliv. **21**(3), 139–1405 (2006)
9. N. Kumar, M.P. Dave, Application of static VAR system auxiliary controllers to improve the transient performance of series compensated long transmission lines. Electr. Power Syst. Res. **34**, 75–83 (1995)
10. N. Kumar, Damping SSR in a series compensated power system, in *IEEE Proceedings of Power India Conference*, New Delhi, 2006
11. S.K. Gupta, N. Kumar, A.K. Gupta, Damping subsynchronous resonance in power system. IEE Proc. Gener. Transm. Distrib. **149**(6), 679–688 (2002)
12. IEEE Subsynchronous Resonance Task Force, First benchmark model for computer simulation of subsynchronous resonance. IEEE Trans. Power Appar. Syst. **96**(5), 1565–1572 (1977)
13. G.N. Pillai, A. Ghosh, A. Joshi, Torsional interaction studies on power system compensated by SSSC and fixed capacitor. IEEE Trans. Power Deliv. **18**(3), 988–993 (2003)
14. N. Kumar, Development of a new scheme for damping torsional modes in a series compensated power system. J. Ins. Eng. (India) Electr. Eng. Div. Board **87**(3), 23–28 (2006)
15. N. Kumar, M.P. Dave, Application of auxiliary controlled static var system for damping sub synchronous resonance in power systems. Electr. Power Syst. Res. **37**, 189–201 (1996)
16. M.R.A. Pahlavani, H.A. Mohammadpour, Damping of sub-synchronous resonance and low-frequency power oscillation in a series compensated transmission line using gate-controlled series capacitor. Electr. Power Syst. Res. **81**, 308–317 (2011)
17. M. Bongiorno, L. Angquist, J. Svensson, A novel control strategy for subsynchronous resonance mitigation using SSSC. IEEE Trans. Power Deliv. **23**(2), 1033–1041 (2008)
18. R.K. Varma, A. Moharana, SSR in double-cage induction generator-based wind farm connected to series-compensated transmission line. IEEE Trans. Power Syst. **28**(3), 2573–2583 (2013)
19. P. Kundur, N.J. Balu, M.G. Lauby, *Power System Stability and Control* (McGraw Hill Inc., New York, 1994)
20. M. Bongiorno, L. Ängquist, J.S. Lennart, A novel control strategy for subsynchronous resonance mitigation using SSSC. IEEE Trans. Power Electron. **23**(2), 1033–1041 (2008)
21. IEEE Special Stability Control Working Group, Static VAR compensator models for power flow and dynamics performance simulation. IEEE Trans. Power Syst. **9**(1), 229–240 (1984)
22. N. Kumar, A SVS control strategy for damping torsional oscillations due to SSR in a series compensated power system. J. Inst. Eng. (India) Electr. Eng. Div. Board **91**(4), 9–17 (2011)
23. A.E. Hammad, Analysis of power system stability enhancement by static var compensators. IEEE Trans. Power Syst. **1**(4), 222–227 (1986)

ResearchGate

See discussions, stats, and author profiles for this publication at: https://www.researchgate.net/publication/299588332

AN EVALUATION OF CONSUMER PERCEPTION AND ATTITUDE TOWARDS THE USAGE OF PLASTIC MONEY IN INDIA

Article · September 2015

READS

8

3 authors, including:

Syed Fazal Karim

Delhi Technological University

5 PUBLICATIONS **0** CITATIONS

SEE PROFILE

All in-text references underlined in blue are linked to publications on ResearchGate, letting you access and read them immediately.

Available from: Syed Fazal Karim
Retrieved on: 12 August 2016

International Journal of Science Technology and Management
Vol. No.4, Issue 09, September 2015
www.ijstm.com
ISSN 2394 - 1537

AN EVALUATION OF CONSUMER PERCEPTION AND ATTITUDE TOWARDS THE USAGE OF PLASTIC MONEY IN INDIA

Anoushka Sharma[1], Syed Fazal Karim[2], Vipul Jain[3]

[1,2,3]*Student, Delhi School of Management, Delhi Technological University, (India)*

ABSTRACT

Over the past few decades, a small fragment of plastic has revolutionized the way consumers pay.Rise in disposable income, introduction of new products and services, increased travel and growth of the entertainment sector has had an impact on the use of plastic money. With the recent reforms in the banking domain, the marketing of financial products has become quite aggressive, creating a need for maneuvering the marketing efforts. The present paper makes an attempt to understand the consumer preferences and attitude towards the use of plastic money in India. The paper is an exploratory-cum-descriptive research that is primarily based on the data collected from 210 respondents and duly investigates the acceptability of the cards among the Indian consumers and the factors affecting it.

Keywords: Consumer Attitude, India, Plastic Money

I. INTRODUCTION

In India, as in other countries around the globe, an organizedmode of payment has emerged over time from the barter system to the more convoluted forms of monetary arrangements. The prevalent mode of settlement across India in the 20th century has been coins, cash and cheques. As we move ahead into the 21st century, payment through cash and cheques itself has encountered a transfiguration. It has moved from being a physical paper-based transfer of value to a virtual electronic one. This is in line with the introduction of advanced technology based systems in banking services world over which resulted in great modification in terms of how financial organizations provide services to customers purchases such as identification along with that it keeps track of transactions as they are incurred with all the specifics of purchases such as store name, date of purchase, price of the product, purchase place etc. Thus holder has the facility to "retrospect" his memory about his purchases which is denied in the case of paper money holder.

Usage of plastic money has come as a form of amenity to financial institution customers. Electronic service is becoming a feasible option for dealings between financial service providers and their clients [1]. This electronic form of payment has far reaching significance – notably for India. Primarily, it helps aligning with the global financial services business by making the systems more competent and cost effective. It also supports in undertaking the unique challenges India faces – the large unbanked society, the deregulated cash economy and need for monetary clarity. Plastic money yields many more benefits than merely facilitating the replacement of cash and cheques for consumer transactions. It has far-reaching impact on the economy as a whole through low

transaction costs, increased operational competence, improved financial framework and an opportunity for the expeditiously evolving Indian economy to further globalize [2].

In the following sections, existing literature and factors affecting the consumer perception towards the plastic money are discussed. A research design has been used based on the collected data to predict the consumers' acceptance behavior. Finally, the outcomes are analyzed and presented.

II. REVIEW OF LITERATURE

The literature review pointed out that most of the research work in this areadone till now has been only limited to developed countries like United States and other developing countries. But research is still insufficient in case of India. It was also observed that, hardly any extensive study has been carried out in India to examine the insight of cardholders as well as establishments using plastic money. Further, the existing studies have focused their attention predominantly on the usage of either debit cards or credit cards but mostly ignored the joint impact and latest innovative cards. The contemporary studyalso considers the factorslike age, gender, educational qualification, monthly income and occupation. It also evaluates the present status and developments of plastic money in India.

Amongcontemporary monetary theories, there is a strong practice of investigating the coexistence of money and credit. The first model with bargaining, money, and credit shows that money can coexist with credit that yields a higher rate of return [3]. The equilibrium with money and credit can be sustained if individual histories are made public with a lag [4]. In another approach, credits are bank loans in an environment with limited enforcement [5]. However money remains the only means of payment since goods transactions remain private information for banks [6]. Money and credit coexist in a divisible money model with imperfect memory, limited commitment, and theft, while there was a model developed with credit and liquid assets to examine the relationship between unsecured debt and unemployment [7, 8].

The model of costly record-keeping was introduced based on the model of money and costly credit; though it has been observed that debtsare derived under limited commitment instead of assuming that loan repayments can be perfectly enforced [9]. Later, in another costly record-keeping model, focus was on the buyer's choice of payments used in bilateral meetings [10]. The role of money and credit isanalyzed in another model with anonymity, limited commitment, and imperfect record-keeping [11].The key difference in the set-up is that they adopt a different pricing mechanism by assuming abuyer-take-all bargaining solution.

The reputation of plastic money as a payment medium has been associated with the facilitation of not carrying cash and cheques, the limited liability of lost and stolen cards, and additional augmentations, such as dispute resolution services and perks [12, 13, 14].The attitude and the approach of the consumer towards the usage and acceptability of plastic money differ for psychographic reasons [15]. Xiao and Anderson developed a 38-item scale to measure effectiveness, psychological and behavioral attitudes towards plastic money [16].

Many consumers prefer uncollateralized creditwhile purchasing when they are lack liquidity (i.e. before their income arrives), even at comparatively high interest rates. Because of limited choices to short-term uncollateralized credit, demand for such credit would be rather inelastic with respect to price [17]. Consumers may not even acknowledge the interest rates when making purchases because they do not plan to borrow for

aprotracted period when they make purchases. Nonetheless, they may change their thoughts when the bill arrives [18].

Consumers are somewhat subtle not only to fluctuation in the interest rates but also to the value of other enhancements such as frequent-use awards, faster dispute resolutions, extended warranties, and car rental insurance [19]. However, decreasing interest rates may attract less creditworthy customers, therefore discouraging some card issuers from decreasing their interest rates.

As stated by Jeans S. Bowers, low income users of plastic money tends to use their cards for the installment feature instead of service features such as convenience, security or acceptance. It has been suggested that the installment factor of credit is required by the low income consumers to enable purchases such as automobiles, appliances and other consumer durables [20].

Demographics alsoplay an important role in making choice and the use of plastic money as a convenience user. Age and income level has been studied earlier and some indications were suggested for correlation between demographics and the use of plastic money. According to a study, done by Jean Kinsey, the possibility of using plastic money and the number held was highly correlated with age and profession [21]. However these characteristics were less relevant than the place of accommodation, use of cheques and savings accounts and approach towards credit.

III. RESEARCH METHODOLOGY

The paper is based on an empirical study of factors that affect the consumers' perception and usage patterns in case of usage of plastic money (credit cards, debit cards). The paper takes into consideration the positive as well as negative aspects of using plastic money over real money. Primarily, the focus is on recognizing the influential usage reasons that encourage the use of plastic money and the primary concerns that discourage their use.

The data was collected through the source directly, i.e., Primary Data Collection was done. The data that has been collected directly from the source for a study purpose is called Primary Data. The data collected through the source was via a questionnaire or survey format. The questionnaire is one of the most significant and widely used data collection methods. A questionnaire is set of questions used for gathering information and data from individuals. The questionnaire has been designed keeping in view the general uses and problems that a consumer faces when using plastic money. The survey was specifically focused on respondents who carried at least one Debit or Credit Card. Demographic factors such as age, income level, gender and profession have also been considered.

The questionnaire was based on a 5-Point Likert Scale. Likert Scale is a highly common and widely used scale for questionnaires that encourage the respondents to rank the options / quality from either high to low or low to high [22]. The 5-Point Likert Scale chosen for the study has labels attached to each point on the mentioned scale and the mid-point of the scale has been set as the point of neutrality. The label are as follows : 1 : Strongly Disagree ; 2 : Disagree ; 3 : Neutral **;** 4 : Agree ; 5 : Strongly Agree.

The questionnaire was tested through a pilot study on 40 consumers. The pilot study helped in making the needed changes in the questionnaire and allowed the researchers to have a more clear knowledge of what consumers' perception is towards the usage of plastic money, thereby, leading to an improved questionnaire. The refined questionnaire was then sent to 300 eligible respondents out of which only 219 responses came back.

Out of the received 219 responses, 7 responses had missing data. Therefore, only 212 responses qualified for the data analysis done. Therefore, overall response rate was 70.1%.

IV. DATA REPORTING AND ANALYSIS

A total of 212 respondents were finalized for the study. Out of the same, 111 were Male and 101 were Female. The Age division of the respondents is as given in Figure 1. The respondents had a 61% share of people in Service (when divided on basis of their profession). Also, 26% respondents run a business whereas 11% were students. Equal shares of 1% each were freelancers and homemakers. 61% respondents were Graduates (130 in number), 38% were Post Graduates (80 in number) and only 1% (2 in number) was Under Graduates.

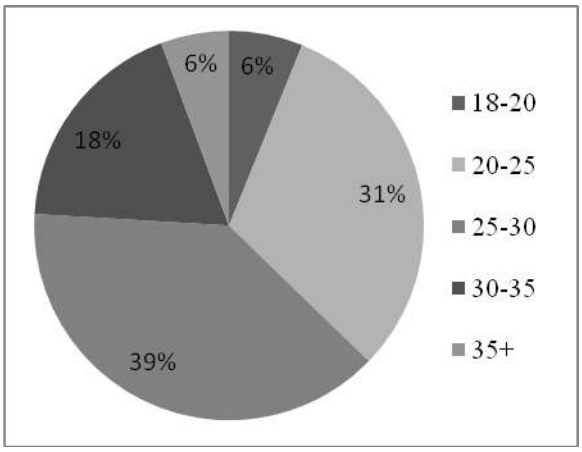

Figure 1 : Age Distribution (In

Additionally, staggering 62% respondents preferred Private Banks whereas only 37% preferred Public Banks. A majority of 57% respondents lie in the Monthly Income section of 25,000 to 50,000. Almost one fourth respondents earn a monthly income of less than 25,000. Below (in Figure 2), a pie-distribution of the cards usage is shown.

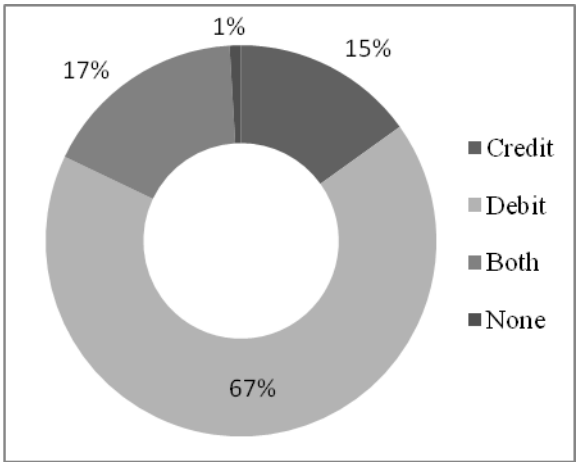

Figure 2: Card Distribution

The analysis of the respondent responses and their subsequent data highlights a few key trends:

ISSN 2394 - 1537

Reporting of data collected through survey indicates that majority (83.49%) of the respondents use plastic money for instant transaction while only (61.32%) uses plastic money because of its ease of use. Around (74.52%) of respondents use plastic because it is less time consuming and a majority (74.52%) of respondents believe that it is more portable and flexible.

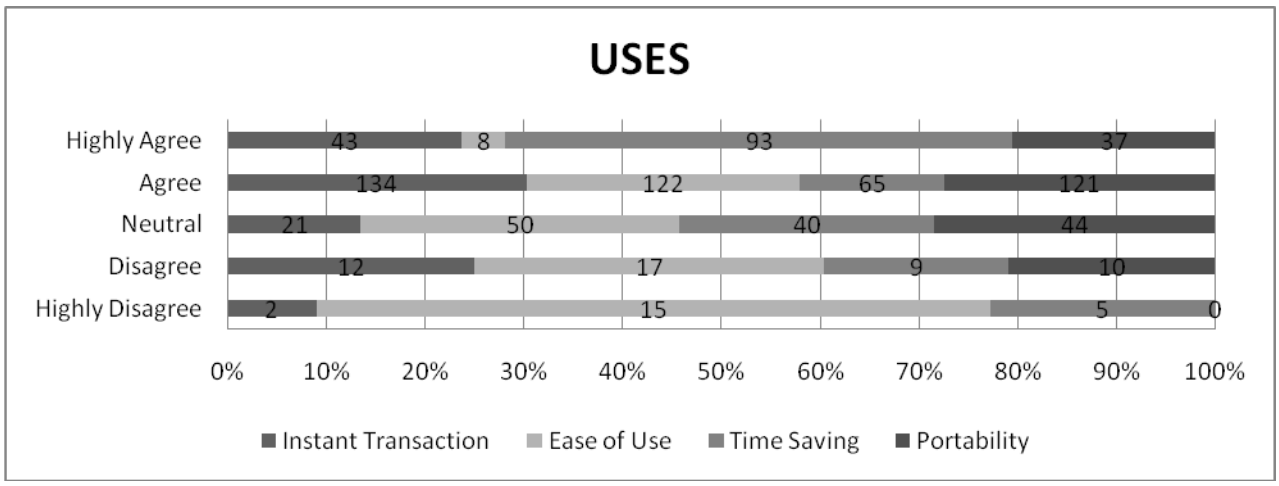

Figure 3: Use of Plastic Money

A staggering percentage (98.11%) of respondents avoids use of plastic money because of fear of losing the card. A very small percentage (12.26%) of the respondents is affected by the processing fee associated with the use of plastic money while (66.98%) of the respondents were neutral about it. A significant percentage (45.28%) of the respondents avoids use of plastic money because they are worried about the transaction charges associated with it while (42.45%) of the respondents were neutral about it. Around (36.79%) of respondents are not affected by documents and form processing associated with the use of plastic money while a very small percentage of respondents (26.88%) are affected by it.

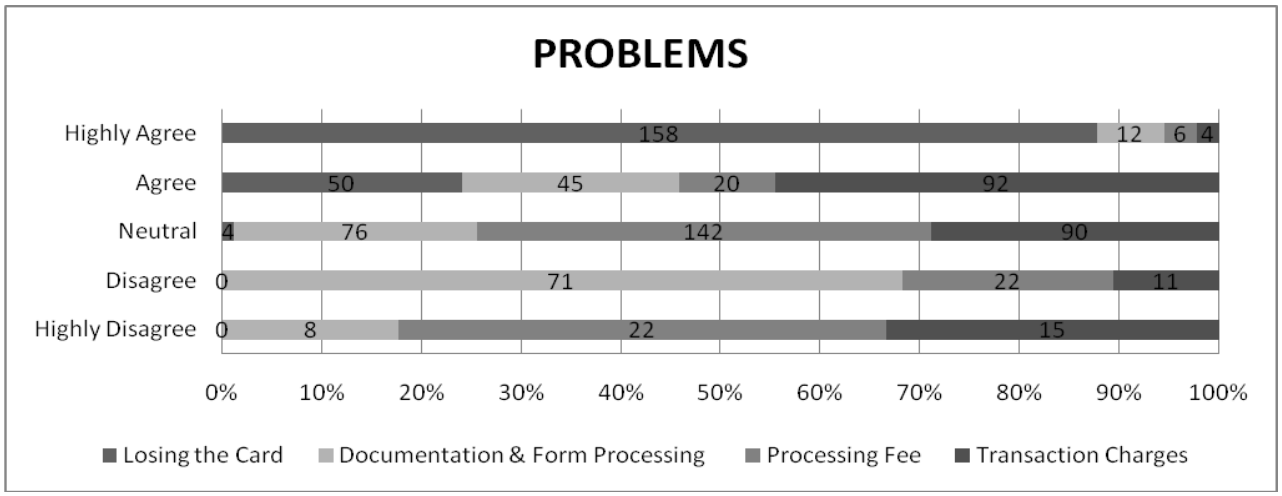

Figure 4: Problems with Plastic Money

V. CONCLUSION

The study has clearly highlighted the advantage of instant transaction as one of the major factors favoring the use of plastic money over real money by the population today. It has already been highlighted by the study of

existing literature that convenience of not carrying cash and ease of transaction is one of the major psychologically influencing factors that encourage the use of plastic money instead of real money. Additionally, the results of the study have also stressed upon the convenience and ease of use while paying or shopping by plastic money. The saving of time and the fact that the plastic money seems to be more portable also seems to further the cause of a possible change in the scenario of money usage in the economy.

On the other hand, plastic money has also raised certain concerns with respect to its usage. Security comes forward as a major cause for concern for the population using plastic money. Security is an integral part of the process of payment via plastic money and the concerns of the people regarding the safety of the transactions need to be handled and solved properly in order to ensure trust amongst the population. The surveyed population is not much concerned with the additional processing fee involved.

Therefore, it is easy to conclude that the population is ready as ever to use plastic money at a greater level due to its high levels of ease and convenience. The issues related to security are proving to be a major hindrance in the acceptance of the concept and usage of plastic money. Security issues, if and when solved, will pave the way for a future Indian economy that is dominated by the use of Plastic money as compared to real money.

VI. FUTURE SCOPE

The study has primarily focused on major factors that are encouraging and hindering the use of plastic money over real money. As a coin always has two sides, both benefits and drawbacks can be associated with any concept or practice. Similar is the case with the use of plastic money.

Future researchers can further dwell upon additional factors that are changing the consumer perception towards the use of plastic money. Future research can also focus on the factors that may positively force the consumers to move towards an extensive use of plastic money.

REFERENCES

[1] **S.** Rotchanakitumnuai, and M. Speece, Corporate customer Perspectives on Business value of Thai Internet Banking. Journal of Electronic Commerce Research, 2004, Vol.5 No.4, p. 270-286

[1] **S.** Rotchanakitumnuai, and M. Speece, 2004. Corporate customer Perspectives on Business value of Thai Internet Banking. Journal of Electronic Commerce Research, Vol.5 No.4, p. 270-286

[3] Shi. Shouyong, Credit and Money in a Search Model with Divisible Commodities.Review of Economic Studies, 1996, 63, 627-652

[4] Kocherlakota, Narayana and Neil. Wallace, Incomplete Record-Keeping and Optimal Payment Arrangements.Journal of Economic Theory,1998, vol. 81(2), 272-289

[5] Berentsen, A., G. Camera and C. Waller, “Money, Credit and Banking", 2004.IEW Working Paper No. 219

[6] Sanches, Daniel and S. Williamson, Money and Credit with Limited Commitment and Theft.Journal of Economic Theory, 2004, Volume 145, 1525-1549

[7] Bethune, Zachary, Ge.Rocheteau, and P. Rupert. (2013). Unemployment and Household Unsecured Debt. Working paper

[8] Gu, Chao and R.Wright. (2011), Endogenous Credit Cycles. Working paper

[9] Nosal, Ed and G,Rocheteau, (2011), Money, Payments, and Liquidity. MIT Press

[10] Dong, Mei (2011), Money and Costly Credit.Working paper

[11] Gomis-Porqueras, Pedro and D. Sanches. Optimal Monetary Policy in a Model of Money and Credit. Journal of Money, Credit, and Banking, 1998

[12] Chakravorti, William R, Sujit and Emmons. Who pays for credit cards? Federal Reserve Bank of Chicago, Policy Studies EPS: 2001

[13] William. C,Whitesell. Deposit banks and the market for payment media. Journal of Money, Credit and Banking,1992,24(4): 246-250

[14] Ausubel and Lawrence M. The failure of competition in the credit card market. American Economic Review, 1991, 81(1): 50-81

[15] Yang, B, James, S and Lester, D, 'Reliability of a Short Credit Card Attitude Scale in British and American Subjects', International Journal of Consumer Studies, 2005, Vol. 29, pp. 41-46

[16] Xiao, J. J.; Noring, F. E. & Anderson, J. G. College students' attitudes toward credit cards. Journal of Consumer Studies and Home Economics, 1995,19: 155–174

[17] Dagobert, Brito L. and Hartley, Peter R. Consumer rationality and credit cards. Journal of PoliticalEconomy, 1995, 103 (2): 400–433

[18] Stavins, Joanna.Can demand elasticities explain sticky credit card rates? Federal Reserve Bank of Boston.New England Economic Review,1996, (July/August): 43–54

[19] Calem, Paul S. and Loretta, J. Mester. Consumer behavior and the stickiness of credit- card interest rates. American Economic Review, 1995,85 (5): 1327–1336

[20] Bowers, Jeans. Consumer credit use by low income consumers who have had a consumer education course: An exploratory study. The journal of consumer affairs,1979, 13(2): 340-341

[21] Kinsey, Jean. Determinants of credit card accounts: An application of Tobit analysis.Journal of consumer Research, 1981, (8): 179-180

[22] Albaum, G. The Likert scale revisited: An alternate version. Journal of the Market Research Society, 1997, 39, 331-349

ResearchGate

See discussions, stats, and author profiles for this publication at: https://www.researchgate.net/publication/303933716

An Experimental study of wireless transceiver of modulation scheme using software defined radio

Conference Paper · July 2016

READS
24

3 authors, including:

P. K. Verma
Delhi Technological University
7 PUBLICATIONS **2** CITATIONS
SEE PROFILE

Priyanka Jain
Delhi Technological University
11 PUBLICATIONS **16** CITATIONS
SEE PROFILE

All in-text references underlined in blue are linked to publications on ResearchGate, letting you access and read them immediately.

Available from: P. K. Verma
Retrieved on: 09 August 2016

An Experimental Study of Wireless Transceiver of Modulation Schemes using Software Defined Radio

P.K. Verma[1], S.K. Soni[2], Priyanka Jain[3] and Amit Kumar[4]
[1,3,4]*Department of Electronics and Communication Engineering, Delhi Technological University, New Delhi, India*
[2]*Department of Electronics and Communication Engineering, G.B. Pant Engineering College, Pauri, UK, India*
E-mail: [1]pappuverma@dtu.ac.in, [2]sanjoo.ksoni@gmail.com, [3]priyajain2000@rediffmail.com, [4]amit.ece.tech@gmail.com

***Abstract*—SDR is nothing but software defined radio technique using laboratory virtual instrument engineering workbench (LabVIEW) as software to mark the radio utilities hardware implemented i.e. universal software defined radio (USRP). In the advancement of SDR implemented LabVIEW to develop as instrument that offers function to support SDR. SDR is the root of innovative wireless communication environment that support both types of fading i.e. short term and long term even composite fading too to create realistic scenario. USRP was a device to develop as a high speed, lower cost and user friendly SRD platform. This paper presents the experimental implementation of LabVIEW and USRP for mounting software and hardware based wireless channel transmission and reception environments for different modulation scheme as constellation diagram, eye diagram and bit error rate (BER), transmitting from TX1 of USRP1 to receiving at RX1 at USRP2. USRP, Software Defined Radio are RF software programmable radio transceiver designed for wireless communication environments.**

Keywords: Modulation Schemes; Software Defined Radio; LabVIEW; Constelletion Daigram; Eye Daigram; Bit Error Rate

I. INTRODUCTION

From the last few years wireless communication system has exponential growth in various fields like image communication, voice communication, text communication and radios. In conventional approach, hardware plays vital role in wireless communication but hardware approach has lots of limitations. So instead of using only hardware, here software is also used in conjugation for wireless communication. By using software in place of hardware our communication systems become more configurable. Traditional communication systems approach has very less adaptation of new technologies. Hardware is designed for very specific band of frequency. So, whenever, it is required to change the frequency, it has to change hardware but in the case of software defined radio, it need to change the parameters only and automatically hardware can change the respective parameters too. Using LabVIEW as software to make radio function with the hardware USRP by the USRP, signal can be transmitted and received and output could be seen on the PC. So, SDR technology [1-2] carries the pliability, lower cost and control to impetus wireless communication by service suppliers and product creators over the users [3]. USRP can be used in the following applications such as SDR, CR (cognitive radio), DSP (digital signal processing), multi-rate DSP, CS (communication systems), FPGA (field programmable gate array) system design and application and widespread verity of additional areas such a homeland security, medical imaging, wildlife tracking, sonar system, radio astronomy, RFID (radio frequency identifications), satellite communication environments and customize test equipment [4]. Transceiver of string type data between two USRPs using GNU technique is implemented [5]. In a multiple input multiple output (MIMO) structure with different h-inputs that a multiple transmit antennas at transmitter h and multiple receive antennas at receiver k, gives the real-time wireless interface implementation of 2×2 MIMO using SDR [6].

In this paper, we transmit different modulation schemes signal (such as QPSK, 8-PSK, 16-PSK, pi/4-PSK, and OQPSK) from TX1 i.e. from USRP1 and received the same to RX1 at USRP2 and their constellation diagram, eye diagram and bit error plots are shown by the LabVIEW. Comparison of BER among different modulation schemes is shown in this paper. Each modulation schemes have certain limitations. So according to application specific modulation scheme can be chosen. In the Software defined system, there is option of changing the types of modulation format from the software called LabVIEW. So, it is general purpose platform for basic communication system. Universal SDR is used as hardware for software defined system. It is the combination of hardware and driver software, which is proficient to transceiver signals in wide range of frequency, 0–5 GHz. However, frequency range depends on the USRP used.

Following sections are given as; in the section II gives details of experimental platform i.e. about the hardware and software. In section III, gives brief discussion on the modulation scheme. Implementation and results illuminated in the section IV and conclude in section V.

978-1-4673-8586-2/16/$31.00 ©2016 IEEE

II. Experimentation Platform

A. *Hardware Platform*

Universal software defined radio (USRP), is nothing but a hardware board for software defined radio [7], consist of USB controller, ADC/DAC and FPGA as shown on Fig. 1 [8]. The hardware i.e. USRP motherboard is positioned in between RF front-end and the host PC as shown in Fig. 2 and the experimental setup of host PC and two USRPs are shown on the Fig. 3.

The USRP board is coupled over Ethernet cable to the hosting PCs [10]. In the experiment, we used two host PC and two USRPs, from USRP1 signal is transmitted through antenna TX1 and received at the receiving antenna RX1 of USRP2 and the these parameters are used: IQ sampling 2M, carrier frequency 915 M, Gain 12dB, transmitter/receiver filter is root raised cosine, host PC IP address is 192.168.10.3 and USRP IP address is 192.168.10.2.

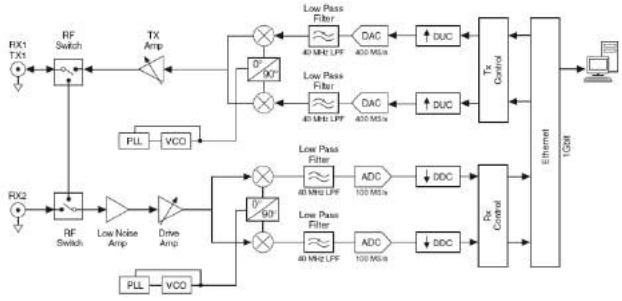

Analog RF Transceiver Fixed Function FPGA PC

Fig. 1: NI USRP Hardware Diagram [9]

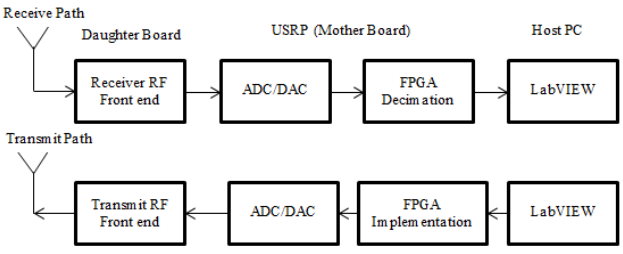

Fig. 2: Basc SDR Architecture [11]

B. *Software Platform*

Fig. 3: Experimental Setup of Software Defined Radio

LabVIEW is visual programming language (i.e. graphical programming) from National Instruments (NI). It is generally used for data acquisition, industrial automation and instrument control. Windows 10 is used as OS (operating system) for the improvement platform. The program is executed from software to hardware through the Gigabit Ethernet cable.

III. Modulation Schemes

Different modulation schemes are transmitted through USRP1 at transmitting antenna TX1 and same signal are received at the RX1 of USRP2. Finite number of phases used in the PSK (phase modulation keying) and each phases allocated a distinctive configuration of binary digits i.e. 0 or 1. Each phase of PSK encodes equal number of bits. Symbols i.e. represented by bits and represented by specific phase. In this paper, constellation diagram, eye diagram and bit error rate of different phase shift keying (PSK) are implemented such as quadrature phase shift keying (QPSK), M-ary phase shift keying (8-PSK, 16-PSK), pi/4-phase shift keying (pi/4-PSK), offset quadrature phase shift keying (OQPSK).

IV. Implementation and Results

The USRP is connected to a host PC to turn as a SDR. Incoming signals are mixed down using DCR (direct conversion receiver) with the help of SMA (subminiature version A) connector to baseband signal i.e. I/Q (in-phase/quadrature) components, that are sampled using 2-channel at the rate of 100 MS/s, 14-bit ADC (analog to digital converter). The encoded I/Q signals tracks parallel routes over DDC (digital down conversion) process. Filter and decimates input baseband signals at the rate of 100 MS/s to user at specific speed. The down converted samples signals passed through the host PV at the rate of 20 MS/s terminated a Gigabit Ethernet cable.

For broadcast, input baseband I/Q sampled signals are produced by host PC and inserted to the NI USRP-2920 (USRP, we have used in our experiment) through Gigabit Ethernet cable, when represented with 32-bits (i.e. 16-bits each for in-phase and quadrature components). USRP intercalates the input baseband signal to 400 MS/s using DUC (digital up conversion) procedure and then convert the incoming baseband signal to analog signal with dual channel, of 16-bit DAC. Then the consequential incoming analog signal mixed with quantified carrier frequency, 915 MHz. An available bit can enable to transfer up to 40 MS/s through Gigabit Ethernet cable between host PC and USRP, then incoming signal can transmitter through the USRP1 from TX1.

For transmitting packets of data frame, it has to be converted the data to specific packet for synchronization. In packet parameter, which include guard band, synchronization sequence, and packet number. All these parameter has to take into consideration while transmitting and receiving data/signal. Signal is transmitted through USRP1 from TX1 and received the same signal through USRP2 at RX1 as shown in the Fig. 3.

From Fig. 4 to Fig. 7, plots the constellation diagram of transmitter, receiver, eye diagram and BER of QPSK respectively. Similarly, from Fig. 8 to Fig. 11, Fig. 12 to Fig. 15, Fig. 16 to Fig. 19 and Fig. 20 to Fig. 23 plots the

978-1-4673-8586-2/16/$31.00 ©2016 IEEE

constellation diagram of transmitter, receiver, eye diagram and bit error rate of 8-PSK, 16-PSK, pi/4-PSK, OQPSK respectively.

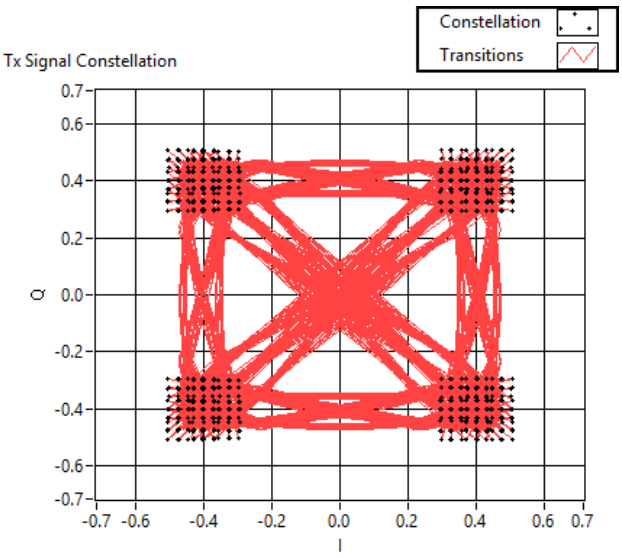

Fig. 4: Constellation Diagram of QPSK at Transmitter from USRP1

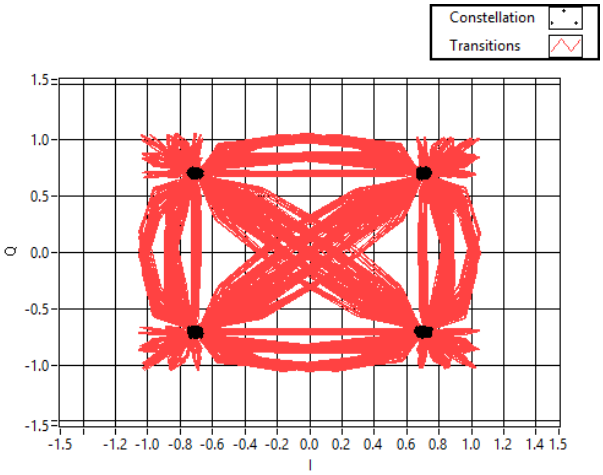

Fig. 5: Constellation Diagram of QPSK at Reciever of USRP2

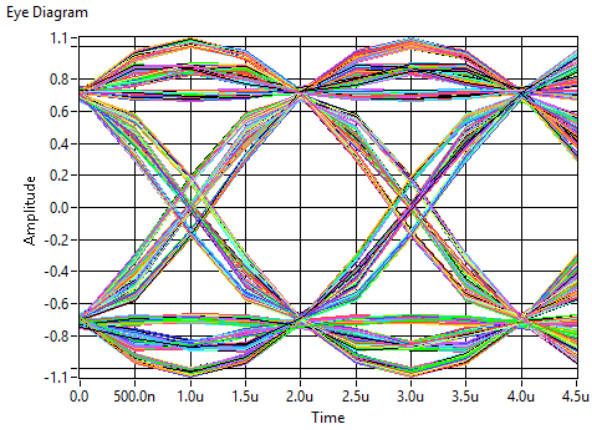

Fig. 6: Eye Diagram of QPSK at Reciever of USRP2

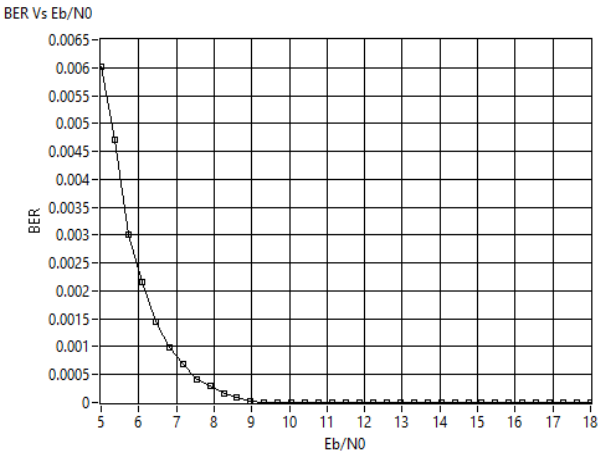

Fig. 7: BER of QPSK at Reciever of USRP2

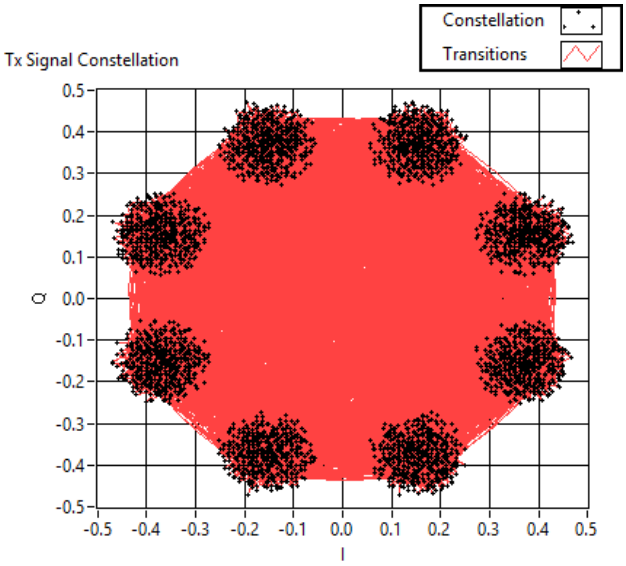

Fig. 8: Constellation Diagram of 8-PSK at Transmitter from USRP1

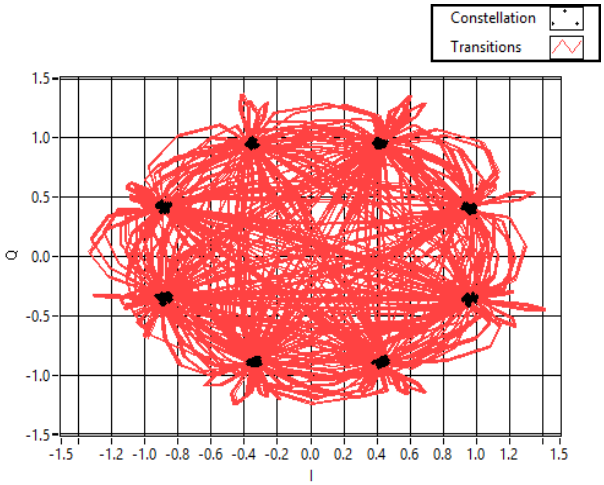

Fig. 9: Constellation Diagram of 8-PSK at Reciever of USRP2

978-1-4673-8586-2/16/$31.00 ©2016 IEEE

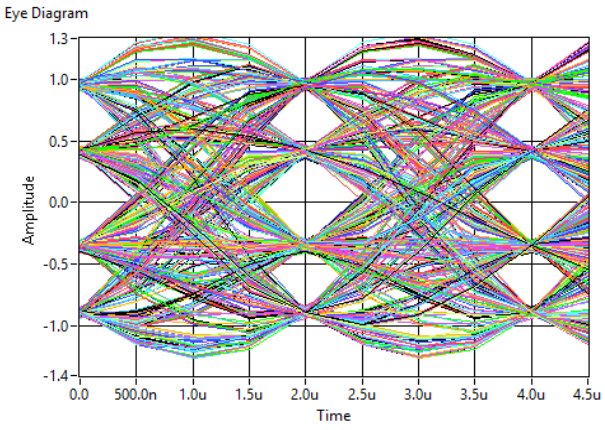

Fig. 10: Eye Diagram of 8-PSK at Reciever of USRP2

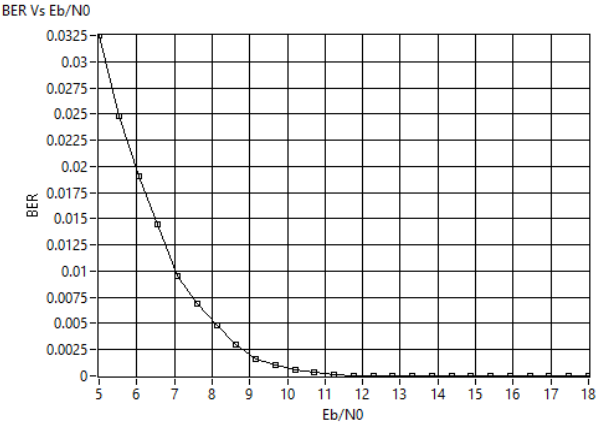

Fig. 11: BER of 8-PSK at Reciever of USRP2

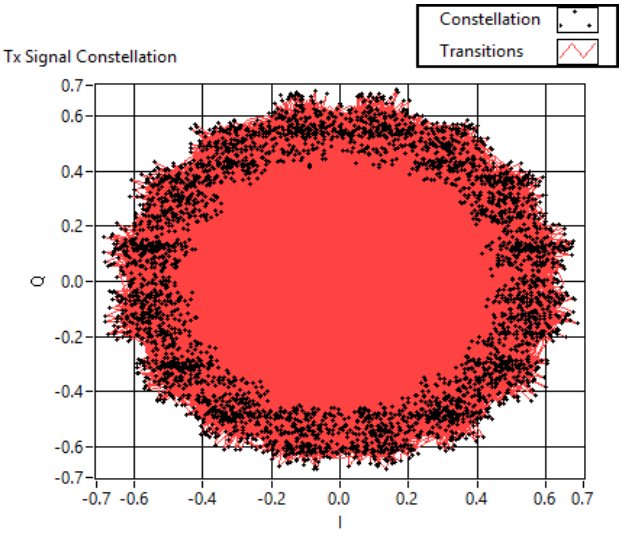

Fig. 12: Constellation Diagram of 16-PSK at Transmitter from USRP1

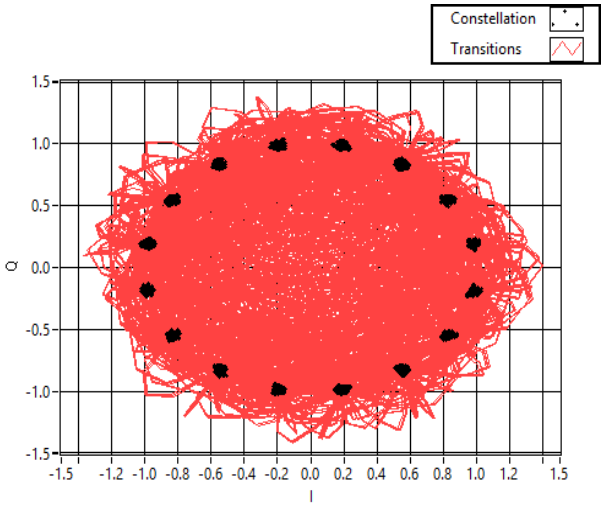

Fig. 13: Constellation Diagram of 16-PSK at Reciever of USRP2

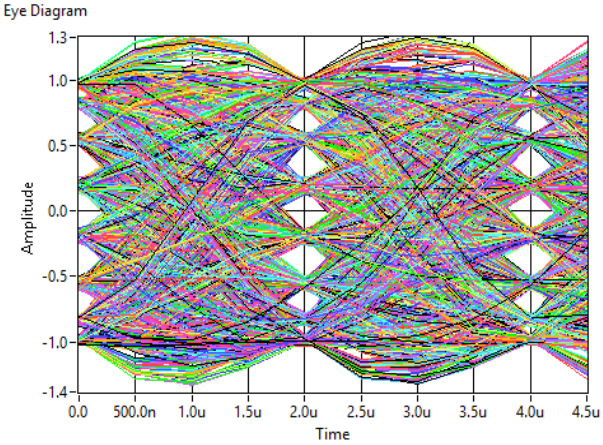

Fig. 14: Eye Diagram of 16-PSK at Reciever of USRP2

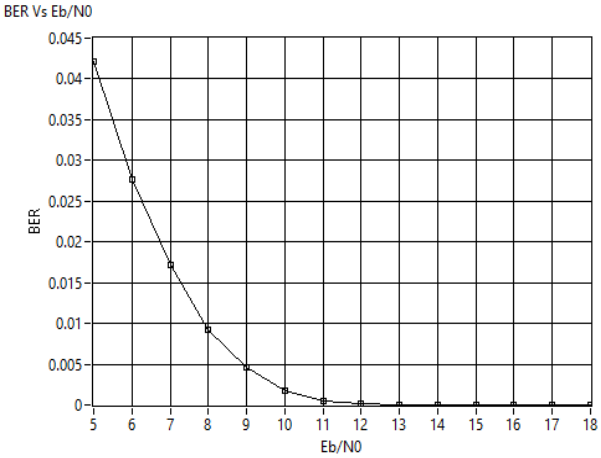

Fig. 15: BER of 16-PSK at Reciever of USRP2

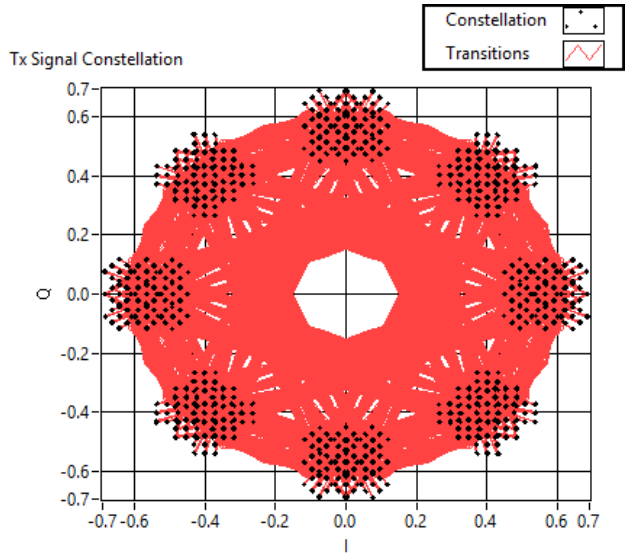

Fig. 16: Constellation Diagram of pi/4-PSK at Transmitter from USRP1

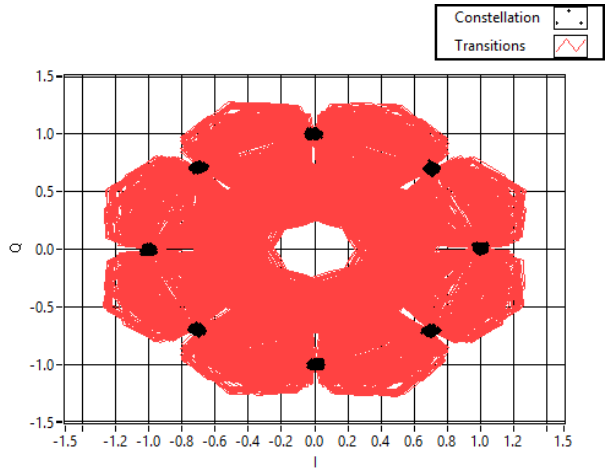

Fig. 17: Constellation Diagram of pi/4-PSK at Reciever of USRP2

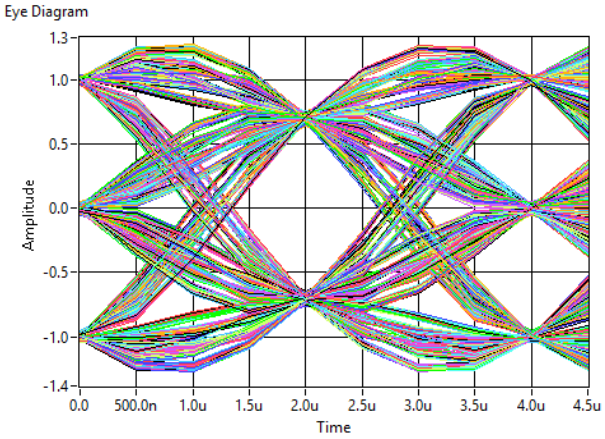

Fig. 18: Eye Diagram of pi/4-PSK at Reciever of USRP2

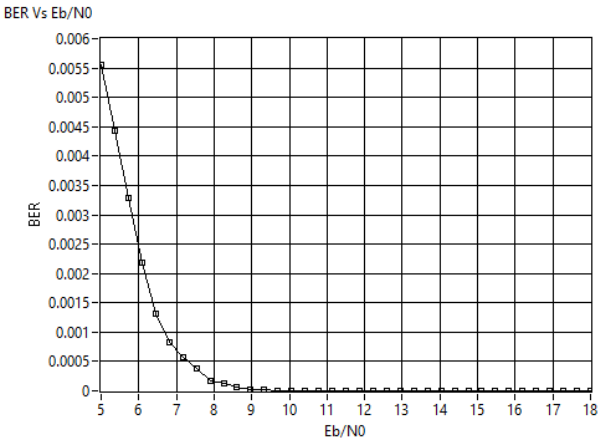

Fig. 19: BER of pi/4-PSK at Reciever of USRP2

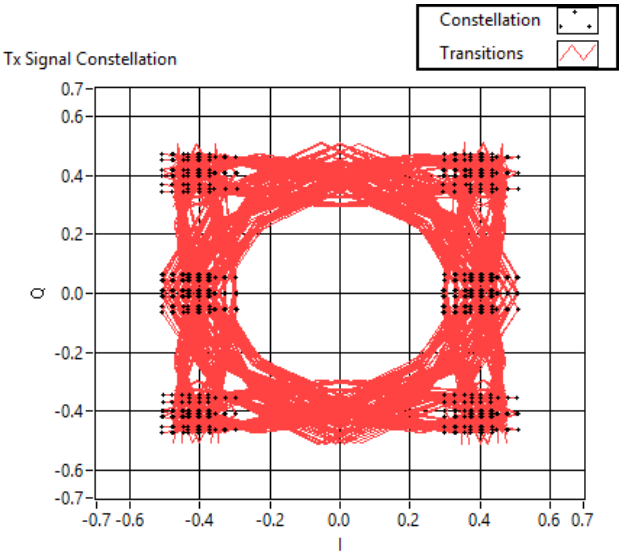

Fig. 20: Constellation Diagram of OQPSK at Transmitter from USRP1

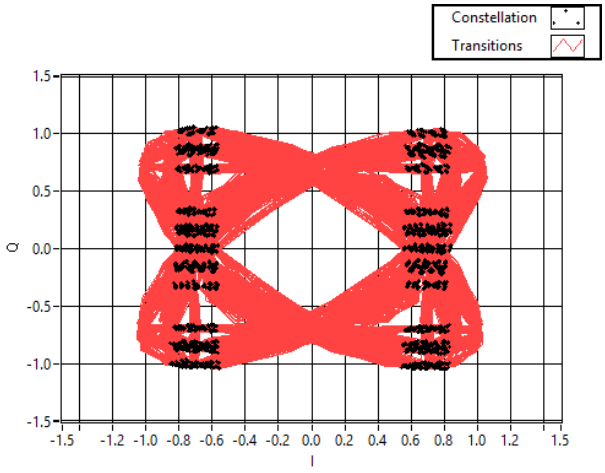

Fig. 21: Constellation Diagram of OQPSK at Reciever of USRP2

978-1-4673-8586-2/16/$31.00 ©2016 IEEE

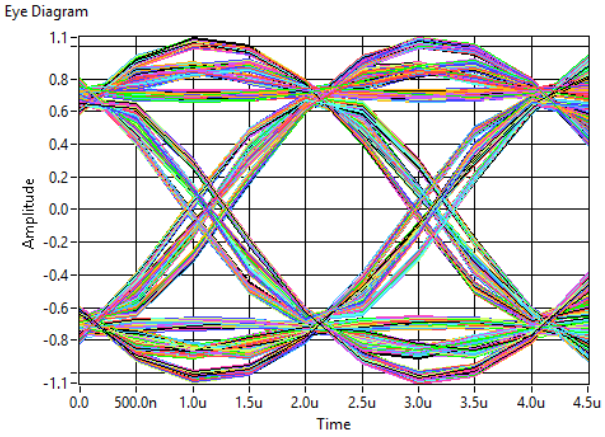

Fig. 22: Eye Diagram of OQPSK at Reciever of USRP2

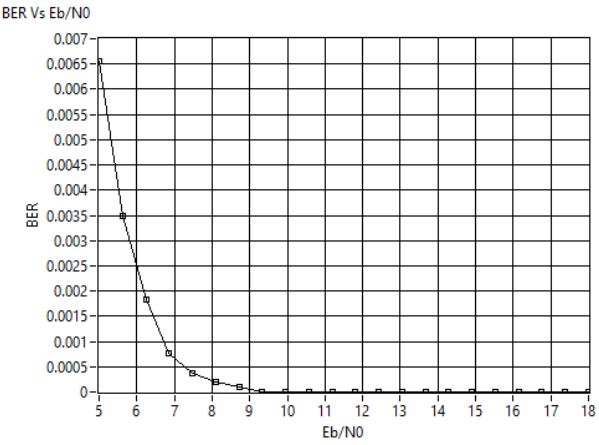

Fig. 23: BER of OQPSK at Reciever of USRP2

V. Conclusion

The experimental setup gives the very accurate plots of constellation diagram, eye diagram and bit error rate of different modulation schemes using LabVIEW as software and USRP as hardware, these combination makes the software defined radio. In this paper, additive white Gaussian noise (AWGN) channel is used and gave the respective results as shown in the different plots. It may be extended to create real time environment i.e. combination of multipath fading and shadowing fading, which is known as the composite fading. Software defined radio also used in cognitive radio to reduce the traffic of the primary used i.e. licensed user.

Acknowledgment

This work was supported by Delhi Technological University, New Delhi, India. I would like to thanks Dr. Sanjay Kumar Soni for their great support.

References

[1] J. Mitola, " Software Radio Survey, Critical Evaluation and Future Directions", *IEEE national Telesystem Conference*, Wasington, DC, May 19-20, 1992.

[2] J. Mitola, "The Software Radio Architecture", *IEEE Communication Magazine*, vol. 33, pp. 26-38, May, 1995.

[3] SDR Forum-Software Defined Radio Forum, "Introduction to SDR" *Citing Internat sources* http://www. sdrforum.org.

[4] Thand B. Welch, Sam Shearam, "Teaching Software Defined Radio Usng the USRP and LabVIEW", *IEEE International Conference on Acoustics, Speech and Signal Processing (ICASSP)*, pp. 2789-2792, 2012.

[5] Shoan Ahmed, S. M. Naviq Iqbal, N. Sakib, Md. R. Islam, "Design and Implementation of Data String Transciever Using GNU Radio", *7th Internatonal Conference on Electrical and Computer Engineering*, pp. 410-404, Dec 20-22, 2012, Dhaka, Bangladesh.

[6] Jackson W. Massey, Jonathan Starr, Seogoo Lee, Dongwook Lee, Andreas Gerstlauer, and Robert W. Heath Jr., "Implemenataion of Real Time Wireless Interface Alignment Network", *IEEE Internation Conference* on Signal, Systems and Computers, pp. 104-108, 2012, Asilomar.

[7] J. N. Laneman, "SDR Documentation", JNL Group, Notre Dame, February 28, 2006, *Citing Internet source* http://www. nd.edu/~jnl/sdr/doc/tutorials/.

[8] M. Ettus, "USRP User's and Developer's Guide", *Ettus Research LLC*, Mountain View, CA.

[9] http://www.ni.com/white-paper/12985/en/

[10] S. M. Shajedul Hasan and P. Balister, "Prototyping a Software Defined Radio Reciever Based on USRp and OSSIE", *Technical Memo*, Virginia Polytechnic Institute & State University, Blacksburg, UA, December 2005.

[11] Z. Tong, M. S. Arifianto and C. F. Liau, "Wireless Transmission using Universal Software Radio Pheripheral", *In Proceeding of the 2009 International Conference on Space Science and Communication*, pp. 19-23, 26-27 October 2009, Port Dickson, Negeri Sembilan, Malaysia.

Autom Softw Eng
DOI 10.1007/s10515-016-0203-0

An exploratory study for software change prediction in object-oriented systems using hybridized techniques

Ruchika Malhotra[1] · **Megha Khanna**[1,2]

Received: 1 April 2015 / Accepted: 2 August 2016
© Springer Science+Business Media New York 2016

Abstract Variation in software requirements, technological upgrade and occurrence of defects necessitate change in software for its effective use. Early detection of those classes of a software which are prone to change is critical for software developers and project managers as it can aid in efficient resource allocation of limited resources. Moreover, change prone classes should be efficiently restructured and designed to prevent introduction of defects. Recently, use of search based techniques and their hybridized counter-parts have been advocated in the field of software engineering predictive modeling as these techniques help in identification of optimal solutions for a specific problem by testing the goodness of a number of possible solutions. In this paper, we propose a novel approach for change prediction using search-based techniques and hybridized techniques. Further, we address the following issues: (i) low repeatability of empirical studies, (ii) less use of statistical tests for comparing the effectiveness of models, and (iii) non-assessment of trade-off between runtime and predictive performance of various techniques. This paper presents an empirical validation of search-based techniques and their hybridized versions, which yields unbiased, accurate and repeatable results. The study analyzes and compares the predictive performance of five search-based, five hybridized techniques and four widely used machine learning techniques and a statistical technique for predicting change prone classes in six application packages of a popular operating system for mobile—Android.

✉ Ruchika Malhotra
ruchikamalhotra2004@yahoo.com

Megha Khanna
meghakhanna86@gmail.com

[1] Delhi Technological University, Delhi, India

[2] Sri Guru Gobind Singh College of Commerce, University of Delhi, Delhi, India

Published online: 17 August 2016

The results of the study advocate the use of hybridized techniques for developing models to identify change prone classes.

Keywords Change proneness · Empirical validation · Hybridized techniques · Predictive modeling · Search-based techniques · Object-oriented metrics

1 Introduction

Change is crucial in any software in order to modify and upgrade it according to changing requirements and technological advancements. Also, corrective maintenance by removing existing defects is another important reason for change (Ouni et al. 2013). Thus, knowledge of change prone classes of a software is important as they are sources of defects and modifications. Identification of change prone classes can assist software developers and project managers in efficient resource allocation of constraint resources like time, effort and cost as more resources should be allocated to these classes for better design and verification during early phases of the software development (Koru and Tian 2005; Koru and Liu 2007). Furthermore, change prone classes should be rigorously monitored and tested in order to plan and execute proper corrective actions, which identifies and eliminates the existent defects. These steps ensure a good quality software product and efficient utilization of limited project resources (Bieman et al. 2003; Elish and Al-Khiaty 2013; Eski and Buzluca 2011; Lu et al. 2012; Malhotra and Khanna 2013). In order to predict change prone classes in the early phases of software development lifecycle, software metrics which represent various characteristics of a software, such as coupling, inheritance etc. can be combined with change data from previous releases to develop change prediction models. These models help in detection of change prone classes in the current and forthcoming releases of a software product (Elish and Al-Khiaty 2013; Lu et al. 2012). A number of studies have been conducted which use statistical (Elish and Al-Khiaty 2013; Lu et al. 2012; Zhou et al. 2009) and machine learning techniques (Giger et al. 2012; Malhotra and Khanna 2013; Romano and Pinzger 2011) for developing models for predicting change prone classes.

However, recently a number of researchers have advocated the use of search-based techniques (SBTs) for developing software engineering predictive models (Clarke et al. 2003; Harman and Jones 2001; Harman 2010a, b; Harman et al. 2012a, b; Malhotra and Khanna 2015). SBT are metaheuristic techniques that enable the search of an optimal or a near-optimal solution in a large solution search space. Each solution is evaluated using a fitness function to ascertain its appropriateness (Harman et al. 2012a). The use of SBT is appropriate because of their inherently parallel and robust nature, which allows effective traversal of a large solution space (Harman et al. 2012a). These techniques attempt to find an optimal solution iteratively in a solution space using a number of operators like mutation, crossover etc. Moreover, these techniques are efficient in handling inaccurate or noisy data (Harman and Jones 2001). Predictive modeling involves efficient balancing of a number of competing constraints to find a good solution. SBT have been found useful in such scenarios where balancing of various conflicting constraints is essential as a change in one parameter may have a significant impact on other related constraints (Clarke et al. 2003). SBT can also

effectively represent the various performance metrics as its fitness functions in predictive modeling, which can be optimized to find the "best solutions" (Harman 2010a). Hence, the use SBT must be explored in software engineering predictive modeling.

Although SBT may be effective in software engineering predictive modeling, Malhotra (2014) advocate the exploration of HyBridized Techniques (HBT) which combine SBT with machine-learning (ML) techniques into a single approach. Such HBT may produce better results by combining the advantages of both ML and SBT. Incorporating the use of SBT as a part of a larger system, may also lead to improvement in predictive performance and the time required for model development. Grosan and Abraham (2007) recognized the importance of hybridized algorithms and stated that their use would pave the way for generating optimal solutions. In predictive modeling, the use of combining ML and SBT may increase the speed of convergence of models under development.

Recognizing the need of effective application of SBT and HBT, we propose a generalized and repeatable approach in this paper. In this work we compare and analyze 15 HBT, SBT and ML techniques. This study provides an effective and repeatable set up for efficient application of SBT and HBT by providing complete description of parameter settings and fitness functions and proper accounting for stochastic nature of these techniques using multiple (30) runs. Moreover, this study provides statistical evidence for comparison amongst different techniques, which strengthens the conclusions of the study. The study evaluates both the CPU time as well as the predictive performance of a specific technique for model development, in order to assess the effectiveness of a technique. Hence, the study explores a trade-off between both these dimensions for effective technique selection for developing change prediction models. The main contributions of the study are summarized as follows:

(i) Evaluation and comparison of five SBT, five HBT along with four ML techniques and a statistical technique for the task of predicting change prone classes. This is important to effectively evaluate and compare a number of techniques on different data sets in order to choose the "best" technique. Moreover, the use of six application packages of popular Android data set for validation of results enhances the repeatability of the study as Android is open source in nature.

(ii) The experimental design of the study ensures easier replicability of the results, low validation bias and effective performance evaluation yielding unbiased results.
   (a) In order to increase the replicability of the study and to understand the impact of parameter settings on the results of the study as noted by Arcuri and Fraser (2011) and Song et al. (2013), the study states complete parameter settings and description of fitness functions for various SBT and HBT.
   (b) Also, since SBT and their hybridized counterparts are stochastic in nature, it is important to perform appropriate number of runs and cross validation for each technique, which reduces result bias. According to Carvalho et al. (2010) and Pai and Dugan (2007), ten-fold cross validation results are widely acceptable and reduce validation bias. Ali et al. (2010) state that it is important to perform more than ten executions in order to effectively handle the stochastic nature of SBTs. This study reports the results of thirty runs for each technique and uses ten-fold cross validation method for model development.

(c) According to He and Garcia (2009), majority of techniques are unable to properly represent the distributive characteristics of imbalanced data, where the number of positive and negative examples are not proportionate. This leads to poor classification accuracies for model development. Therefore, for effective performance evaluation various researchers advocate the use of performance measures such as balance and G-mean to assess models which are developed using imbalanced training data (Harman et al. 2014; He and Garcia 2009; Kubat and Matwin 1997; Menzies et al. 2007; Li et al. 2012). The study evaluates the developed change prediction models using these two performance metrics, in order to yield unbiased results.

(iii) Demšar (2006) advocates the use of statistical tests to statistically compare the predictive performance of various techniques. This study statistically analyses the results of various techniques using Friedman test. Furthermore, the study also performed Wilcoxon test with Bonferroni corrections as a post-hoc test to evaluate the pairwise comparison amongst the results of different techniques.

(iv) Apart from the predictive capability of a technique, it is important to evaluate the CPU time taken by a specific technique for developing change prediction models. This study evaluates a technique on both parameters i.e. predictive performance and CPU time taken and analyzes a trade-off if any to select an efficient technique for model development.

In order to accomplish the above contributions, the following Research Questions (RQ's) will be addressed in this paper:

RQ1: What is the comparative performance of HBT with SBT, SBT with ML/statistical techniques and HBT with ML/statistical techniques for prediction of change prone classes?

It is essential to provide empirical evidence by comparing the predictive capability of different SBT, HBT, ML/statistical techniques for development of effective change prediction models. Researchers and practitioners can use these evidences for selection of effective techniques for model development. This study performs empirical validation on six application packages of open source Android data set and evaluates the results for comparative assessment of predictive capability of different techniques.

RQ2: Which is the best HBT for development of change prediction model? Which techniques perform statistically better or worse than the best chosen HBT?

It is important to statistically assess and establish results, which support and advocate the use of an effective technique for development of change prediction models. The comparison of different techniques should be statistically evaluated in order to ensure effective selection of a good technique for developing change prediction models. The study uses Friedman statistical test for this evaluation. Furthermore, we perform pairwise comparisons of all the other techniques with the best technique to assess which pairs of techniques are statistically significantly different than the chosen best technique using Wilcoxon paired test with Bonferroni corrections.

RQ3: What is the comparative CPU time taken by change prediction models developed using different SBT vs HBT, SBT vs ML/statistical techniques and HBT vs ML/statistical techniques?

The CPU time for model prediction and validation is a crucial factor for selection of an appropriate technique. Thus, it is important to evaluate various techniques according to the CPU time consumed for model prediction and validation.

RQ4: Is there any trade-off between the CPU time and predictive performance of different HBT, SBT and ML/statistical techniques?

The objective of this work is to evaluate both the predictive performance as well as the CPU time consumed by an efficient change prediction model. It is important that an effective technique should have good predictive capability and simultaneously should take low CPU time for model prediction and validation. A technique, which performs very well but consumes a lot of CPU time, may be less favorable over a moderately performing technique that takes very low CPU time.

The results of the study will guide the software community in efficient selection of a technique among a wide array of available techniques.

The various sections of the paper are organized as follows: Sect. 2 summarizes the related work of the study and Sect. 3 describes the empirical design of the study which includes dependent and independent variables of the study, techniques used in the study, subject selection etc. Section 4 describes the experimental design of the study while Sect. 5 states the research methodology. Section 6 reports the results of data-preprocessing and feature selection. Section 7 reports and discusses the obtained results of the study according to each of the specific RQ. Section 8 discusses the various threats to validity of the study. Finally, Sect. 9 reports the conclusions of the study and suggests future work.

2 Related work

This section describes the related work of the study and is sub-divided into three sections. The first section focuses on literature studies which have established the relationship between various software metrics and change proneness attribute of a class in an Object-Oriented (OO) software. The second section discusses the various techniques, which have been used in literature for developing effective models for predicting change prone classes. Finally, the third section briefly states the use of SBT and HBT in different predictive modeling tasks.

2.1 Predicting relationship between software metrics and change proneness

A number of studies in literature have evaluated the change proneness attribute of a class in an object-oriented software. Lindvall (1998) performed an empirical investigation on PMR data set and concluded that large sized classes are more change prone in nature. Bieman et al. (2001) and Bieman et al. (2003) performed an empirical validation for studying the effect of design patterns, inheritance based and size metrics

to ascertain the change prone nature of classes. According to Arisholm et al. (2004) dynamic coupling metrics are effective indicators of change proneness attribute of a class. Koru and Tian (2005) and Koru and Liu (2007) validated a number of OO metrics, which were representative of size, coupling, inheritance and complexity for predicting change prone classes. They concluded that size is a primary indicator for change prone classes prediction. Moreover, Koru and Tian (2005) concluded that highly change prone classes are not the ones, which show highest values of coupling, cohesion, size and inheritance. Zhou et al. (2009) investigated the confounding effect of class size on the relationship among change prone attribute of a class and a number of OO metrics and concluded that confounding effect of class size overestimates the actual relationship among OO metrics and change proneness attribute. Eski and Buzluca (2011) validated the Chidamber and Kemerer (CK) metrics suite and QMOOD metrics suite on three open source software and concluded that a combination of metrics gives the most optimal result for change prediction on a particular data set. Romano and Pinzger (2011) found that cohesion metrics for interfaces are better than CK metrics for predicting change prone java interfaces. Lu et al. (2012) used statistical meta-analysis to investigate the predictive capability of 62 OO metrics by performing empirical validation on 102 java systems. Their study indicates that while size metrics show moderate predictive capability, inheritance based metrics have the least predictive capability for prediction of change prone classes. The predictive ability of coupling and cohesion metrics is lower than size metrics for change prediction tasks. Elish and Al-Khiaty (2013) validated CK metrics in conjunction with a number of evolution based metrics to predict change prone nature of classes and concluded that the best results were provided by using a combination of both metrics suite rather than independently using only CK metrics or only evolution based metrics. Malhotra and Khanna (2013) evaluated 22 OO metrics and Giger et al. (2012) validated the CK metric suite respectively on open source data sets to predict change prone classes. The studies successfully establish the relationship between OO metrics and change proneness attribute of classes. Thus, this study analyzes an effective suite of eighteen OO metrics for developing change prediction models.

2.2 Machine learning techniques for developing change prediction models

A number of studies have used traditional statistical techniques for developing change prediction models (Elish and Al-Khiaty 2013; Lu et al. 2012; Zhou et al. 2009). However, there are also certain studies, which evaluate the performance of ML techniques for developing models for predicting change prone nature of classes. Koru and Tian (2005) and Koru and Liu (2007) used tree-based models for identifying change prone classes in two open source projects Mozilla and KOffice. A number of other ML techniques like support vector machine, bagging, boosting, multilayer perceptrons etc. have been validated by Giger et al. (2012), Malhotra and Khanna (2013) and Romano and Pinzger (2011).

2.3 Applicability of SBT and HBT for software engineering predictive modeling

There have been a number of literature studies, which have evaluated SBT and HBT for developing software engineering predictive models. A recent study by Malhotra and Khanna (2015) extensively reviews 61 primary studies that use SBT for effort estimation, defect prediction and change prediction. According to the review, there were 38 primary studies, which effectively evaluated SBTs for effort estimation, 20 defect prediction studies and only one change prediction study. Some of the prominent effort estimation studies were Bardsiri et al. (2013), Bardsiri et al. (2014), Braga et al. (2008), Burgess and Lefley (2001), Chiu and Huang (2007), Corazza et al. (2013), Dolado (2000), Huang and Chiu (2006), Minku and Yao (2013) and Oliveira et al. (2010). SBT have also been evaluated for developing defect prediction models. Studies by Canfora et al. (2013), Carvalho et al. (2010), Catal and Diri (2009), Di Martino et al. (2011), Harman et al. (2014) and Rodriguez et al. (2012), are some literature studies which effectively establish the use of SBT and HBT for determination of defect prone classes or modules. These literature studies use SBT along with ML techniques for parameter tuning, feature reduction or complete model development in software engineering predictive modeling. As SBT and HBT have been successfully applied in other related predictive modeling domains, it motivates the use of these techniques for development of change prediction studies.

This study extensively evaluates ten SBT and HBT to effectively model change prediction systems. Though, in our previous work (Malhotra and Khanna 2014) we initially evaluated few SBT for development of change prediction tasks, to the best of author's knowledge, there has been no study till date which evaluates the trade-off between the predictive performance and CPU time consumed by a technique for model development. Furthermore, the statistical comparison amongst various investigated techniques and pairwise comparisons using post-hoc tests strengthens the results of a study.

3 Empirical study design

This section states the various design considerations of the study.

3.1 Variables selection

The study finds relationship between OO metrics (independent variables) and change proneness (dependent variable). This study analyzes eighteen OO metrics commonly used for developing software quality predictive models.

3.1.1 Independent variables

Relevant literature reveals wide use of OO metrics for developing models for defect prediction, maintainability prediction or change prediction. These metrics are representatives of various characteristics of a software such as coupling, reusability through inheritance, cohesion, size etc. as shown in Table 1. It is important to monitor and com-

Table 1 OO metrics depicting OO characteristic

OO characteristic	OO metrics
Coupling	CBO, RFC, Ca, Ce, IC, CBM
Cohesion	LCOM, CAM, LCOM3
Inheritance	NOC, DIT, MFC
Size	WMC, NPM, LOC, AMC
Composition	MOA
Encapsulation	DAC

prehend these metrics in order to gain a better understanding and effectively administer and supervise a software product. The OO metrics used in the study are summarized below:

- It includes the Chidamber and Kemerer (CK) metrics suite (1994) consisting of six OO metrics, weighted methods of a class (WMC), number of children (NOC), depth of inheritance tree (DIT), coupling between objects (CBO), lack of cohesion amongst methods (LCOM) and response for a class (RFC). The CK metrics suite is widely used for predictive modeling tasks (El Emam et al. 2001; Elish and Al-Khiaty 2013; Giger et al. 2012; Gyimothy et al. 2005; Kpodjedo et al. 2011; Singh et al. 2009).
- The study also analyses the QMOOD metrics suite, which includes measure of aggression (MOA), data access metric (DAM), method of functional abstraction (MFA), number of public methods (NPM) and cohesion among methods of a class (CAM). This metrics suite has been previously validated by Eski and Buzluca (2011) and Olague et al. (2007) for change prediction and defect prediction tasks respectively.
- Afferent coupling (Ca) and efferent coupling (Ce) metrics proposed by Martin (2002) are also analyzed in the study. Other metrics evaluated in the study are average method complexity (AMC), lines of code (LOC), LCOM3 (proposed by Henderson 1996), inheritance coupling (IC) and coupling between methods of a class (CBM).

A detailed description of these metrics can be obtained from http://gromit.iiar.pwr.wroc.pl/p_inf/ckjm/metric.html.

The primary reason for selection of these OO metrics is that they have been conventionally used and widely accepted for predictive modeling tasks in the software engineering community (El Emam et al. 2001; Eski and Buzluca 2011; Elish and Al-Khiaty 2013; Giger et al. 2012; Gyimothy et al. 2005; Olague et al. 2007; Kpodjedo et al. 2011; Singh et al. 2009). However, there have been only few studies which evaluate the change proneness attribute on the basis of OO metrics. But, a related area with change proneness prediction is prediction of defect prone classes. According to a review conducted by Radjenovic et al. (2013) on 106 defect prediction studies, the most commonly used OO metric suite was the CK metrics suite. Moreover, the study claims that the popularity of CK metric suite has been "evenly distributed over the years and there is no sign that this will change in future." Thus, our study also uses the

CK metrics suite for determining change prone classes. Moreover, an extensive study by Lu et al. (2012) evaluated 62 OO metrics for determining change prone classes and found coupling, cohesion and size metrics like CAM, LCOM, CBO and LOC to be effective predictors of change. Eski and Buzluca (2011) used CK as well as QMOOD metric suite for predicting change and found them to be efficient predictors of change. Therefore, we use an effective group of OO metrics for determining change prone classes.

3.1.2 Dependent variable

As observed in previous studies (Lu et al. 2012; Malhotra and Khanna 2013), while predicting change proneness attribute, this study also deals with prediction of a binary variable, which signifies the change prone nature of a class. A class is termed as "change prone" if there is a change in the class in the two versions which are being evaluated, otherwise, the class is termed as "not change prone". Each class in the data set is labeled as "change prone" or "not change prone". The objective of the study is to build a prediction model that predicts the outcome label for unforeseen classes. The change in each class is computed by taking into account the LOC inserted or deleted from a class. This is because it is important to take a satisfactory and realistic measure of change, which is convenient to compute and is widely acceptable. Measuring change proneness as a probability is cumbersome and theoretical, which cannot be used well for practical and real-life purposes.

3.2 Technique used

The objective of this study is to evaluate the capability of SBT and HBT for developing change prediction models. The study evaluates five HBT and five SBT. The HBT evaluated in the study include genetic fuzzy system Logitboost (GFS_Logit) and hybridized classifier systems which use evolutionary algorithms [hierarchical decision rules (HIDER)]. The study also evaluates two search-based hybridizations of widely used ML techniques, decision trees [decision tress with genetic algorithms (DT_GA)] and neural networks or multi-layer perceptrons [neural net evolutionary programming (NNEP)]. A hybridized version of a search-based technique particle swarm optimization (PSO) with a statistical technique linear discriminant analysis (LDA) is also explored. The various SBT explored in the study include genetic algorithm based classifier algorithm with adaptive discretization intervals (GA_ADI) and memetic Pittsburgh learning classifier system (MPLCS)). Furthermore, the study evaluates X-classifier system (XCS) and SUpervised classifier system (SUCS), which are classifier algorithms using niche based genetic algorithms. Another particle swarm optimization algorithm named constricted particle swarm optimization (CPSO) is also explored. Hence, we evaluate a wide variety of SBT and HBT in order to ascertain their applicability for change prediction tasks. Furthermore, the study compares the results of SBT and HBT with four ML techniques: decision tree (C4.5), support vector machine (SVM), classification and regression trees (CART) and multilayer perceptron (multilayer perceptron with conjugate learning (MLP_CG). These ML techniques

have been commonly explored by various researchers for developing software quality predictive models (Gyimothy et al. 2005; Lessmann et al. 2008; Li et al. 2012). We also evaluated a statistical technique linear discriminant analysis (LDA), for comparative evaluation with different techniques used in the study.

3.3 Subject selection

The study uses six application packages of the Android data set—a popular mobile operating system for empirical validation. Around 70 % of smart phones in the market use Android as a preloaded OS. It is developed by Google and is based on Linux kernel. Android is open source in nature and uses GIT as the version control system. The open source nature of Android increases the replicability of the study. Android forms a unique niche in the operating system market, but the results of the study are also generalizable to iOS, Windows and Unix as they belong to the domain of operating systems. Moreover, the wide use of Android aids the external validity of the study as these results can be effectively used in similar scenarios. The data used in the study is collected by analyzing two versions of Android system—Ice Cream Sandwich and Jelly beans.

3.4 Statistical test selection

The study uses Friedman statistical test along with post-hoc Wilcoxon test to evaluate the predictive capability of various techniques. Both these tests are non-parametric in nature, thus can be used without violating the various underlying data assumptions, which are necessary for use of parametric tests (Demšar 2006). As reported by Lessmann et al. (2008), there is low use of statistical tests for comparing predictive models. Though ANOVA is a good test for determining the differences amongst various techniques but it has very stringent assumptions for normal data distribution and homogeneity of variance. Thus, we refrain from using ANOVA and use its non-parametric equivalent (Demšar 2006; Lessmann et al. 2008). We first compare the predictive performance of all the models using each performance measure independently with the aid of Friedman test to evaluate whether there is any significant difference amongst the performance of various techniques. The Friedman test provides a ranking amongst different techniques according to their predictive performance. In case of rejection of null hypothesis, we employ post-hoc Wilcoxon signed rank test to compare the best performing technique with all the other techniques to determine which pairs of techniques are statistically significantly different from each other.

3.5 Data collection

The data sets used in the study are collected with the help of defect collection and reporting system (DCRS) tool. The tool was developed by undergraduate students of Delhi Technological University in Java language and is used for collecting data from open-source repositories which use GIT as the version control system (Malhotra et al.

Table 2 Software data set details

Software name	Versions analyzed	No. of data points	% of changed classes
Bluetooth	4.3.1–4.4.2	72	19
Contacts	4.3.1–4.4.2	210	48
Calendar	4.3.1–4.4.2	106	19
Gallery2	4.3.1–4.4.2	374	41
MMS	2.3.7–4.0.2	195	30
Telephony	4.2.2–4.3.1	249	63

2014). The DCRS tool analyzes the source code of an open source software from two consecutive versions by extracting change-logs. A change record contains change information such as identifier, commit timestamp, description of the change and a file listing of all the files which are modified including the lines of changed code.

A data point is a combination of change statistics and various OO metrics. The tool uses another open source tool CKJM (http://gromit.iiar.pwr.wroc.pl/p_inf/ckjm/metric.html) for extracting OO metrics. The change statistics include the total LOC added, deleted and the combined LOC changes in a specific class. Each data point contains a binary variable named ALTER, which is assigned a "yes" value if the cumulative LOC changes for a specific class is non-zero, otherwise it is assigned a "no".

This study analyzes the source code of Android OS (https://android.googlesource.com), which uses Git for version control management. The change data is collected from two versions of Android OS i.e. Ice Cream Sandwich and Jelly Bean. It was noted that source code for Android OS was available under many application packages, rather than a single package. The various available application packages include packages for a number of functions such as libraries, kernel, or native applications. This study analyzes six packages of Android OS: Bluetooth, Contacts, Calendar, Gallery2, MMS and Telephony. The Android packages of the study were selected as a representative of Android application as they contained appropriate number of data points i.e. classes which are required for developing effective change prediction models (Elish and Al-Khiaty 2013). Secondly, the selected application packages had sufficient and generally varying degree of percentage of change prone classes i.e. 19–63 %, which would help in developing appropriate prediction models and ascertaining the accuracy of these models when developed using varying degrees of change (Elish and Al-Khiaty 2013). Certain other application packages such as "Desk Clock" and "Email" were also evaluated as candidates for the study between the two Android OS versions but were not found suitable as they did not meet the above criteria.

We extracted only Java source code or class files while ignoring all other layout files, media files etc. The details of classes in each of the packages are given in Table 2 which presents the number of common classes in both the selected versions and the percentage of classes which changed from one version to the next. Figure 1 shows the change statistics of each data set. For example, the Gallery2 data set has 22,177 total changed lines. Amongst these changed lines, 10,499 were inserted LOC and 11,678 deleted LOC.

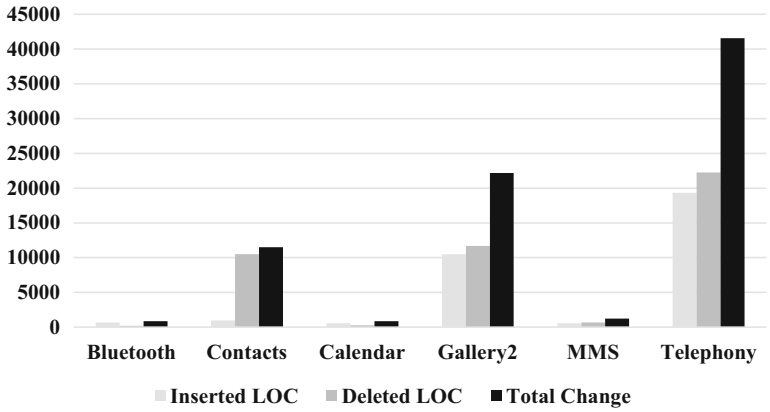

Fig. 1 Change statistics of all data sets

3.6 Performance measures selection

This study reports the true positive rate (TPR) which is also known as probability of detection (PD) and false positive rate (FPR), also known as probability of false alarm (PF). The values of false negative rate can be computed by 100-TPR. An extensive review by Malhotra (2015) reveals that a large number of studies (67 and 32 % respectively) report PD and PF values instead of reporting the actual number of false positives and false negatives. In order, to make our results comparable, we use the above performance metrics.

Furthermore, it is also important to account for imbalance in a data set, when evaluating the prediction model which learns from it. An imbalanced data set is the one that has disproportionate number of change prone and not change prone classes. However, Harman et al. (2014), He and Garcia (2009) and Kubat and Matwin (1997) advocate G-mean as a performance evaluator for imbalanced learning problem. Menzies et al. (2007) and Li et al. (2012) suggest the use of balance for imbalanced data sets. Thus, we evaluate the results of change prediction models using four performance evaluators namely PD, PF, balance and G-mean.

4 Experimental design

The experimental design of the study is described as follows. Figure 2 depicts the diagrammatic representation of the experimental design used in the study.

4.1 Data pre-processing and feature selection

We first analyze the descriptive statistics of various metrics of each data set. This step helps in evaluating the characteristics of each data set. Next, we identify all the outliers in each corresponding data set. It is important for effective model development to remove all the outliers from the data. All the outliers of each of the six data sets were identified and removed using inter-quartile range filter. Also, it is important to eliminate noisy and redundant features to develop a good prediction model.

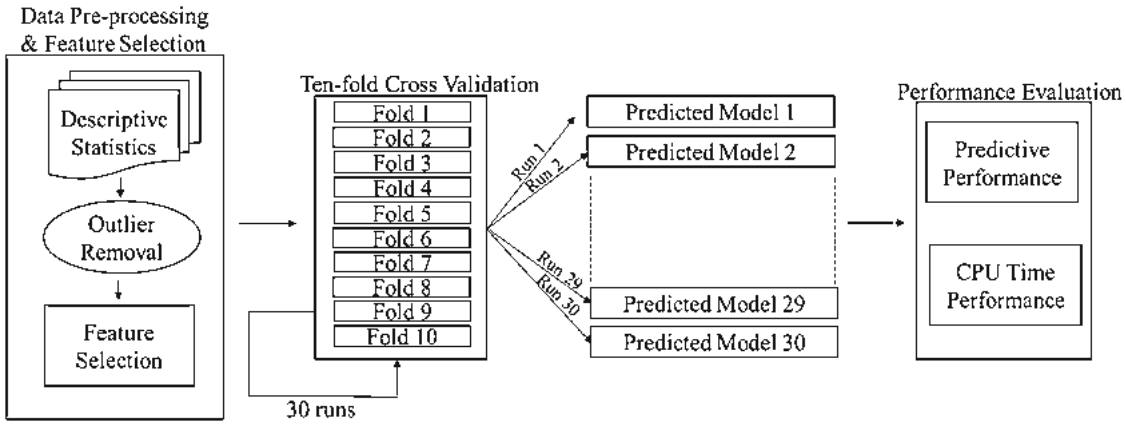

Fig. 2 Experimental design

It is possible that certain independent variables are correlated amongst each other. As suggested by Hall (2000), we use Correlation-based Feature Selection (CFS) method to effectively select the best predictor metrics out of the eighteen OO metrics used in the study. The CFS method scrutinizes all possible combinations of predictor metrics in a specific data set in order to find the best subset of variables for prediction. An effective subset of variables is selected by analyzing their redundancy amongst each other and their individual predictive capability. A number of predictive modeling studies have successfully used CFS method for reducing the dimensionality of the input feature set (Arisholm et al. 2010; Carvalho et al. 2010; Elish and Elish 2008; Malhotra and Khanna 2013).

4.2 Model prediction and validation

Next, we develop change prediction models using all the techniques on the six data sets using ten-fold cross validation method. Use of ten-fold cross validation reduces validation bias (Carvalho et al. 2010; Pai and Dugan 2007). It involves division of all the data points into ten subsets, where nine subsets are used for training the model and the tenth subset is used for model validation (Stone 1974). This process is repeated several times to obtain change prediction values on all the data points. SBT are meta-heuristic algorithms and hence it is important to account for random variation for these algorithms, as their results tend to vary from one execution to the other (Barros and Neto 2011). According, to Ali et al. (2010), each SBT should be run ten or more times to account for the stochastic nature of SBT. We run each technique thirty times in order to account for the randomness of techniques (Arcuri and Briand 2011; Canfora et al. 2013; Harman et al. 2014). Therefore, we perform thirty executions of each technique for developing change prediction models.

4.3 Performance evaluation

The results of change prediction models developed by various techniques are evaluated using PD, PF, balance and G-mean as discussed in Sect. 3.6. We further use the

Table 3 Confusion matrix

		Predicted	
		Change prone	Not change prone
Actual	Change prone	True positive (TP)	False negative (FN)
	Not change prone	False positive (FP)	True negative (TN)

Friedman and Wilcoxon test in order to statistically analyze the results of the study. The different performance measures can be calculated using the confusion matrix, which is described as follows:

A confusion matrix (Table 3) for a binary variable is a 2×2 matrix where each row represents the actual instances and each column represents the predicted instances.

The various performance metrics are defined as follows:

- *Probability of detection (PD)* It is an indicator of percentage of classes, which are correctly classified as change prone. The higher the value of PD, the better is the model.
- *Probability of false alarm (PF)* Probability of False Alarm is also better known as False Positive Rate, which is the ratio of false positives (i.e. incorrectly classified not change-prone classes) to the actual number of not change prone classes (i.e. the sum of false positives and true negatives). The lower the value of PF, the better is the model.
- *Balance* As expected, an ideal value of PD would be 100, i.e. the prediction model should be able to identify all change prone classes correctly. The PF value should be as low as possible as an effective prediction model should never falsely classify a not change prone class as change prone. However, in actual as we try to increase the PD value, the PF value will also increase (Menzies et al. 2007; Misirh et al. 2011). Thus, the balance measure finds the Euclidean distance between the optimum value of PD = 100 and PF = 0 to a specific pair of (PD, PF) (Menzies et al. 2007). Higher balances are desirable for a model.
- *G-mean* It is an indicator of high positive accuracy as well as high negative accuracy and keeps a balance between both the accuracies (Kubat and Matwin 1997). It is the geometric mean of positive accuracy and negative accuracy. A high value of G-mean indicates a good model.

Table 4 states the formulas for computing various performance metrics from the confusion matrix.

Furthermore, we also evaluate the CPU time of a particular algorithm as an important indicator for evaluating the effectiveness of a technique. The CPU time is compared with the predictive capability of a technique in order to analyze the trade-off between the predictive performance and the CPU time taken by a technique to develop change prediction model.

Table 4 Performance metrics

Performance metric	Formula
Probability of detection (PD)	$\frac{TP}{TP+FN} \times 100$
Probability of false alarm (PF)	$\frac{FP}{FP+TN} \times 100$
Balance	$1 - \frac{\sqrt{(0-(PF/100))^2+(1-(PD/100))^2}}{\sqrt{2}}$
G-mean	$\sqrt{\frac{TP}{TP+FP} \times \frac{TN}{TN+FN}}$

5 Research methodology

This section states the description, parameter settings and fitness functions of various techniques used in the study along with the set of hypothesis evaluated to answer RQ2.

5.1 Description of various techniques

The study analyses ten SBT and HBT along with four ML techniques and a statistical technique for developing change prediction models. The aim of the study is to compare the performance of various HBT with SBT, SBT with ML/statistical techniques and HBT with ML/statistical techniques. As noted by Harman et al. (2012a), the choice of fitness function is important as certain fitness functions may lead to ineffective and problematic search of the solution space because they may obtain a large number of plateaus or ridges. Thus, the use of a different fitness function will help in designing the problem effectively with appropriate characterizations. The aim of the study was to explore a good quality effective solution which can useful in guiding software practitioners effectively by developing efficient change prediction models. Thus, we compare various HBT and SBT in their native form. The original authors of each SBT/HBT chose their corresponding fitness function with good reason which are characteristic of each technique. Thus, each SBT or HBT may use different fitness functions in order to analyse the results robustly. As indicated by Ramírez et al. (2015), the "internal characteristics" of an algorithm are crucial for effective conclusion on the outcomes. Thus, a comprehensive study would involve a number of techniques, which may deal with different objectives or fitness for appropriate solution to the problem (Ramírez et al. 2015). In general in the context of this study, the fitness functions aim to maximize the classification accuracy of a classifier which may also be evaluated in terms of PD or (100-PF) and minimize classification error. Moreover, for rule learning algorithms, fitness functions should also appropriately incorporate the rule coverage and rule complexity. A number of studies in literature have compared techniques which use different fitness functions (Gottlieb et al. 2002; Craenen et al. 2003; Ramírez et al. 2015).

We used knowledge extraction based on evolutionary learning (KEEL) tool for simulation. The tool is open source in nature and can be accessed on http://www.keel.es/. In order to effectively tune the parameters of each technique used in the study, a number of variations of different parameters were investigated before selecting the optimum parameters for each technique relative to Android data sets.

The four ML techniques analyzed in the study include decision tree C4.5, support vector machine (SVM), multilayer perceptron with conjugate learning (MLP_CG) and classification and regression tree (CART). Decision tree C4.5 builds accurate and efficient models which are easily interpretable. The parameter settings for C4.5 decision tree method include confidence factor of 0.25, two instances per leaf and prune factor as true. CART involves construction of a decision tree by selecting an appropriate attribute on the basis of Gini index. The parameter settings for CART involves using of a maximum tree depth of 90. SVM technique can be effectively used to encounter problems of redundant features and high dimensionality. It is robust in nature (Malhotra 2015). The parameter settings for SVM method include poly kernel type, a c value of 100, an ε value of 0.001, degree of 1, γ value of 0.01 and v value of 0.1. MLP technique is adaptive in nature and effectively handle non-linear data because of parallel architecture (Malhotra 2015). The conjugate method is used for training the MLP model as it provides better convergence. The MLP topology is used as 10 in KEEL.

Table 5 states a brief description of all the SBT and HBT used in the study. Table 6 reports the fitness functions and parameter settings of SBT and HBT employed in this study.

5.2 Hypothesis for RQ2

This section states the hypothesis evaluated using Friedman test and Wilcoxon test in order to answer RQ2.

5.2.1 Hypothesis for Friedman test

In order to evaluate the best HBT technique, we would evaluate the following hypothesis (H0a and H0b) using Friedman test. We compare the performance of the 15 techniques for two performance indicators, balance and G-mean.

Null Hypothesis H0a Change prediction models developed using all the techniques (GFS_Logit, HIDER, DT_GA, NNEP, PSO_LDA, GA_ADI, CPSO, MPLCS, XCS, SUCS, MLP_CG, SVM, C4.5, CART and LDA) do not show any significant difference when evaluated using the balance measure.

Alternate Hypothesis H0a Change prediction models developed using all the techniques (GFS_Logit, HIDER, DT_GA, NNEP, PSO_LDA, GA_ADI, CPSO, MPLCS, XCS, SUCS, MLP_CG, SVM, C4.5, CART and LDA) show significant difference when evaluated using the balance measure.

Null Hypothesis H0b Change prediction models developed using all the techniques (GFS_Logit, HIDER, DT_GA, NNEP, PSO_LDA, GA_ADI, CPSO, MPLCS, XCS, SUCS, MLP_CG, SVM, C4.5, CART and LDA) do not show any significant difference when evaluated using the G-mean measure.

Alternate Hypothesis H0b Change prediction models developed using all the techniques (GFS_Logit, HIDER, DT_GA, NNEP, PSO_LDA, GA_ADI, CPSO, MPLCS, XCS, SUCS, MLP_CG, SVM, C4.5, CART and LDA) show significant difference when evaluated using the G-mean measure.

Table 5 Technique description

Technique	Description
GFS_Logit	Logitboost combines a number of weak classifiers to formulate a strong performing classifier. The technique is used for learning fuzzy rules for the classification process where the learning process uses a genetic algorithm for searching antecedents in a rule (Otero and Sanchen 2006).
HIDER	The technique produces a hierarchical set of rules by using an evolutionary algorithm. As it is hierarchical in nature, an instance will be correctly classified by the jth rule only if it has not matched any previous (j − 1) rules (Aguilar-Reiz et al. 2003). They are similar to decision lists (Rivest 1987). We first obtain rules which classify larger number of instances.
DT_GA	It is hybrid classification technique which uses C4.5 algorithm in the first phase to identify rules which cover large number of training examples (large disjunct). The second phase uses genetic algorithms to identify rules which cover small number of training examples (Carvalho and Freitas 2004).
NNEP	It is hybrid technique which uses an evolutionary algorithm to design the structure and optimize the weights of a feed-forward neural network which consists of multiplicative nodes called product units (Durbin and Rumelhart 1989; Martinez-Estudillo et al. 2008).
PSO_LDA	It is a hybrid technique which used particle swarm optimization algorithm for feature selection and linear discriminant analysis (LDA) for model development (Lin and Chen 2009).
GA_ADI	It is a Pittsburgh style of technique where structure is similar to that of a decision list. The algorithm represents rules as conjunctive normal form. A number of constant width discretizations are used simultaneously for successful learning and a reduced effective rule set (Bacardit and Garrell 2003).
CPSO	Particle swarm optimization evolves from a population of solutions which are termed as particles. The best solution is obtained by considering both the local best solution of a particle and the best solution of any particle obtained in the neighbourhood. A random velocity is associated with each particle to obtain the global best solution. CPSO involves the use of a constriction factor for the algorithm's convergence (Sousa et al. 2004).
MPLCS	It is a variant of genetic algorithm based classifier combined with a number of local search algorithms. The objective is to obtain a rules set with the smallest number of rules which yields maximum training accuracy (Bacardit and Krasnogor 2009).
XCS	This classifier system is based on reinforcement learning. The system appropriately responds with an action or reward by the environment. It evolves as a classifier's population where each classifier has a rule and certain parameters for ascertaining rule quality. The three major parameters for a rule are prediction payoff, prediction error and fitness. It uses a niche Genetic algorithm (Bernado-Mansilla and Garrell-Guiu 2003).
SUCS	This technique is very similar to XCS except it uses supervised learning paradigm and a different computation for accuracy. It also uses niche based genetic algorithm. However, the niches are correct rule sets abandoning the incorrect rules for exploration (Bernado-Mansilla and Garrell-Guiu 2003).

Table 6 Fitness functions and parameter settings

Technique	Fitness	Parameter settings
GFS_Logit	The fitness of a fuzzy rule "If Attribute^{j}(x) then class(x) = c with confidence s^{j}" is computed as the squared error between the desired output and the logistic transform of the classifier's output. A detailed description is provided by Otero and Sanchen (2006)	Number of label: 5; Number of rules: 25
HIDER	Fitness for rule r: F (r) = 2 (Num – Class Error (r)) + G(r) + Coverage (r) Num is the total number of processed examples, Class error represents the error when an instance does not belong to the same class but is encompassed in the region defined by the rule, coverage represents the proportion of the entire search space which is included by a specific rule r. It is a two-objective optimization which minimize the errors while maximizing the number of correct classifications	Population Size: 100; Number of Generations: 150; Mutation probability: 0.3; Cross percent: 70; Extreme mutation probability: 0.06; Prune examples factor: 0.05; Penalty factor: 2; Error coefficient: 0
DT_GA	$F = \frac{TP}{TP+FN} \times \frac{TN}{FP+TN}$	Instances per leaf: 2; Confidence: 0.20; Threshold for considering small disjunct: 10; Number of total generations for GA: 50; Number of chromosomes in the population: 200; Crossover probability: 0.7; Mutation probability: 0.01
NNEP	$F(x) = \frac{1}{1+l(\theta)}$ $l(\theta)$ is the hessian matrix for error function	Hidden nodes: 6; Transfer: Product unit; Generations: 200
PSO_LDA	$F = \frac{TP+TN}{TP+FN+FP+TN}$	Maximum number of iterations: 400; Number of non-improving iterations: 150; Cognition learning factor: 0.8; Social learning factor: 1.2; Inertial weight (w): 0.5; Number of particles: 15
GA_ADI	$F = \left(\frac{TP+TN}{TP+FN+FP+TN}\right)^2$	Number of iterations: 500; Number of strata: 2; Rule deletion min rules: 14; Size penalty min rules: 4; Number of intervals for uniform discretization: 4, 5, 6, 7, 8, 10, 15, 20, 25

Table 6 continued

Technique	Fitness	Parameter settings
CPSO	$F = \frac{TP}{TP+FN} \times \frac{TN}{FP+TN}$	Number of particles: 25; Convergence radius: 0.1; Weights upper limit: 1.05; Max uncovered instances: 0.1; Indifference threshold: 0.2; Constriction coefficient: 0.83; Convergence platform width: 35
MPLCS	The fitness function is based on minimum description length (MDL) principal which is used to balance both the complexity as well as accuracy of the rule set. The objective is to minimize the following function (Bacardit 2004): F = W*Theory bits + Exception bits Here, W represents the weight for adjusting theory and exception bits, theory bits represent the length of all the alive classification rules and exception bits represent all misclassified or unclassified instances. A detailed description is provided by Bacardit (2004)	Number of iterations: 700; Size of penalty rules: 3; Probability of local search: 0.03; Probability of rule set-wise (RSW) cross-over: 0.2; Number of parents in RSW crossover: 10; Number of rule ordering repetitions: 5
XCS	It is based on accuracy, which is calculated as the inverse function of the error between the reward granted by the environment and the prediction of the classifier. The error can be estimated according to the following formula (Butz et al. 2001): $\text{Error} = 1/\text{R}(\lvert\text{R} - \text{Pred}_{\text{cl}}\rvert * \text{Prob}_{\text{cl}}(\text{c}) + \lvert 0 - \text{Pred}_{\text{cl}}\rvert * (1 - \text{Prob}_{\text{cl}}(\text{c})))$ R represents the reward function, Pred_{cl} represents the classifier's prediction, $\text{Prob}_{\text{cl}}(\text{c})$ represents the probability that the classifier is correct	Number of explores: 100,000; Population size: 6400; $\alpha = 0.1$; $\beta = 0.2$; $\delta = 0.1$; $\mu = 10.0$; $\theta_{\text{ga}} = 50.0$; $\theta_{\text{mna}} = 2$; $\theta_{\text{del}} = 50.0$; €= 1.0; initial prediction: 10.0; Initial fitness: 0.01; Initial prediction error: 0.0; Prediction error reduction: 0.25; GA subsumption: false; Type of selection: roulette wheel selection; Tournament size: 0.4; Type of crossover: 2 point; Crossover probability: 0.8; Type of mutation: free; Mutation probability: 0.03; r = 1.0; m = 0.1
SUCS	$\text{F} = \left(\frac{\text{Number of correct classifications}}{\text{Number of matches for a rule}}\right)^{v}$ Here, v is a constant	Number of explores: 70,000; Population Size: 8400; $\alpha = 0.1$; $\beta = 0.2$; $\delta = 0.1$; $\mu = 10.0$; $\theta_{\text{del}} = 50.0$; € = 1.0; Initial prediction: 10.0; Initial fitness: 0.01; Initial prediction error: 0.0; Prediction error reduction: 0.25; GA subsumption: true; $\theta_{\text{sub}} = 500.0$; Type of Selection: Tournament; Tournament size: 0.4; Type of Crossover: 2 point; Crossover Probability: 0.8; Type of Mutation: Free; Mutation probability: 0.06; $\theta_{\text{ga}} = 50.0$; r=0.6; m=0.1

5.2.2 Hypothesis for Wilcoxon test

If the Friedman test yields significant results, showing technique X as the best technique, we will perform post-hoc Wilcoxon test with Bonferroni correction in order to ascertain the pairwise differences amongst the performances of different techniques. Each technique is compared with technique X for developing change prediction models. The test computes the differences amongst a specific performance measure (balance and G-mean) for the two techniques to be compared. The following set of hypothesis will be evaluated using Wilcoxon test.

Null Hypothesis H1a The performance of change prediction models does not differ significantly, while using technique X as compared to technique A, when evaluated using the balance performance measure.
Alternate Hypothesis H1a The performance of change prediction models differs significantly, while using technique X as compared to technique A, when evaluated using the balance performance measure.
Null Hypothesis H1b The performance of change prediction models does not differ significantly, while using technique X as compared to technique A, when evaluated using the G-mean performance measure.
Alternate Hypothesis H1b The performance of change prediction models differs significantly, while using technique X as compared to technique A, when evaluated using the G-mean performance measure.

Here, technique A corresponds to all other techniques used in the study except the best ranked technique X by the Friedman test. For example, if PSO_LDA (Technique X) is the best ranked technique according to Friedman test, then technique A corresponds to GFS_Logit, HIDER, DT_GA, NNEP, GA_ADI, CPSO, MPLCS, XCS, SUCS, MLP_CG, SVM, C4.5, CART and LDA.

6 Data preprocessing and feature selection results

This section describes the descriptive statistics, outlier removal and feature selection results.

6.1 Descriptive statistics

We analyzed the descriptive statistics of all the data sets (Appendix A) and summarize the following observations:

- The inheritance characteristics was not much used in the data sets analyzed in the study. As the mean of NOC (Bluetooth—1, Contacts—0.9, Calendar—0.95, Gallery2—0.64, MMS—0.85, Telephony—0.97) and DIT (Bluetooth—0, Contacts—0.11, Calendar—0.37, Gallery2—0.35, MMS—0.19, Telephony—0.05) metric was low. A similar trend was shown by CartWright and Shepperd (2000).
- The data sets exhibited very high LCOM mean values (Bluetooth—307, Contacts—104.74, Calendar—244.12, Gallery2—200.85, MMS—153.33, Telephony—

Table 7 Outlier details

Data set name	Number of outliers
Bluetooth	7
Contacts	12
Calendar	6
Gallery2	43
MMS	22
Telephony	37

709.05). The values for LCOM3 metric ranged from 1.26 to 1.39 and that for CAM metric ranged from 0.38 to 0.47.

- The DAC metric had significant values (0.41–0.70) indicating good usage of protected and private attributes in a class. However, the mean values of the MOA metric varied in different data sets indicating varied usage of used defined data types in different data sets. Functional abstraction was hardly used in the data sets as MFA values for all the data sets was quite low.
- The class size of all the data sets varied with a range of 9–718 LOC for Bluetooth data set, 0–422 LOC for Contacts data set, 7–936 LOC for Calendar data set, 8–1507 LOC for Gallery2 data set, 0–882 LOC for MMS data set and 6–1100 LOC for Telephony data sets.

6.2 Outlier analysis

A critical step in data preprocessing involves outlier analysis. In order to provide unbiased results, we effectively identified and removed all the outliers from each data set respectively. The outliers were identified using Inter Quartile Range filter which is based on the inter quartile range metric. The inter quartile range metric is computed as the difference between the upper quartile (Q_3) and the lower quartile (Q_1). A data point will be considered an outlier, if any of its attribute value is an outlier i.e. if the value of any of the OO metric mentioned in Sect. 3.1.1 is an outlier, the data point is termed an outlier. Table 7 below shows the number of outliers identified in each data set.

6.3 Correlation based feature selection results

As explained in experimental design, we use the CFS method for reducing the dimensionality of the input features. However, for model development using the PSO_LDA technique, we use the entire set of features as feature selection is already incorporated in the PSO_LDA technique. Table 8 reports the metrics which were selected after application of CFS on each data set. As the LOC metric and the CAM metrics are selected in five and four data sets respectively, they seem to be highly effective in predicting change prone classes. The WMC, MOA, CBO and Ce are also effective change indicators as they were selected by two data sets each for developing change prediction models. RFC, DIT, NPM, AMC and MFA are the other selected features after application of the CFS method.

Table 8 Metrics selected by CFS method

Data set name	Metrics selected
Bluetooth	WMC, RFC, LOC, CAM
Contacts	DIT, CBO, NPM, LOC
Calendar	CBO, Ce
Gallery2	Ce, LCOM3, LOC, MOA, CAM
MMS	LCOM3, LOC, DAM, MOA, CAM, AMC
Telephony	WMC, LCOM3, LOC, MFA, CAM

7 Results and discussion

This section describes the steps performed for answering a specific RQ and discusses the results. The organization of the results is around specific RQ's.

7.1 What is the comparative performance of different HBT with SBT, SBT with ML/statistical techniques and HBT with ML/statistical techniques for prediction of change prone classes?

In order to perform the comparative evaluation of different techniques, we analyze different performance measures of the change prediction models developed using all the techniques. The values in Figs. 3, 4, 5, and 6 represent the median values of ten-fold cross validation results of all the 30 runs executed using a specific technique. Each bar in the figures corresponds to the performance measure value of a specific technique (color grouped according to the category of the technique) on a specific data set. The HBT are depicted by dark grey bars, the SBT are represented by light grey bars and the ML/statistical techniques by black colored bars.

Figures 3 and 4 shows the PD and PF values of change prediction models developed using all the techniques. As shown in the Fig. 3, the PD values obtained on Bluetooth data set range from 0 to 100 %. The best PD value on Bluetooth data set was given by a ML/statistical (LDA) technique. Similarly, the PD value on Contacts, Calendar and Gallery2 data sets range from 50 to 75 %, 0 to 42 % and 21 to 52 % respectively. The PD values in MMS data set are in the range of 12–65 % and those of Telephony data set range from 72 to 92 %. After analyzing the results obtained on each data sets, it was noted that the best PD value in Calendar, Gallery, MMS and Telephony data sets are given by the PSO_LDA technique, an HBT. The CART technique (an ML technique) gave the best PD value in the Contacts data set. Similarly, as shown in Fig. 4, the PF values obtained on Bluetooth, Contacts, Calendar, Gallery2, MMS and Telephony data sets range from 3 to 100 %, 17 to 27 %, 0 to 12 %, 6 to 27 %, 3 to 15 % and 43 to 51 % respectively. According to the results, SBT's showed best PF values amongst four of the six data sets of the study.

Figure 5 reports the median values of the balance measure for 30 runs with respect to each technique on each corresponding data set. For example, the PSO_LDA technique

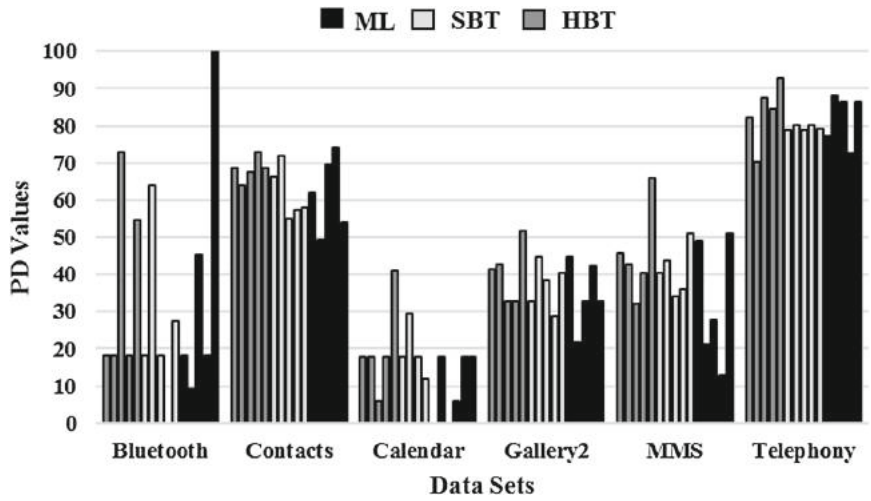

Fig. 3 Median PD values on 30 Runs of different techniques

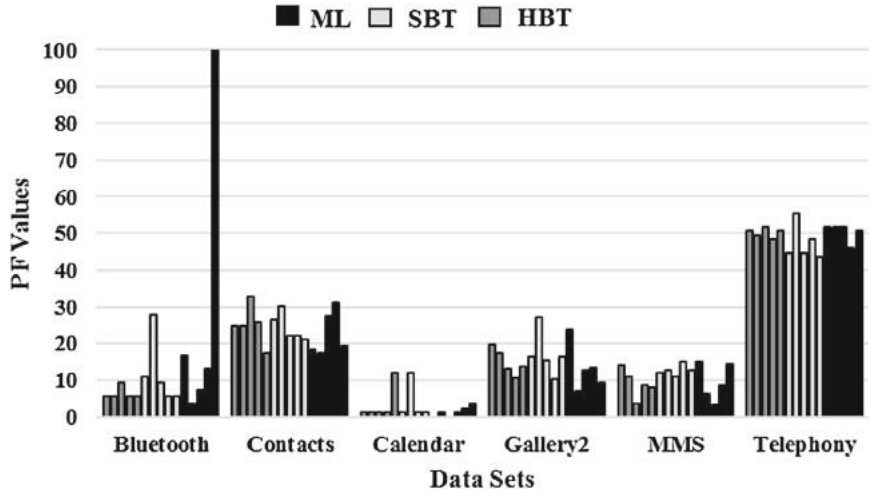

Fig. 4 Median PF values on 30 Runs of different techniques

achieves a median value of 67 % on Bluetooth data set, 74 % on the Contacts data set, 57 % on the Calendar data sets, 64 % on the Gallery2 data set, 75 % on the MMS data set and 64 % on the Telephony data set. As analyzed from the figure, the PSO_LDA technique gave the best cumulative balance values on all the data sets. After analyzing, it was found that the models developed using the PSO_LDA technique gave the best balance values on three data sets of the study. After careful analysis, we could see that the balance values of majority of HBT range from 40 % to 80 %. However, the balance values of majority of SBT range from 40 to 70 %. The balance values of other ML/statistical techniques range from 40 to 75 %.

Figure 6 shows the median G-mean measure values of the ten-fold cross validation results for the 30 runs on all the data sets individually. The HBT are depicted by dark grey bars, the SBT are represented by light grey bars and the ML/statistical techniques by black colored bars. As analyzed from the figure, the best cumulative G-mean values were given by the PSO_LDA technique, which are closely followed by the NNEP technique. The models developed using the PSO_LDA technique showed the best G-mean measure on four data sets of the study. After analyzing, it was noted

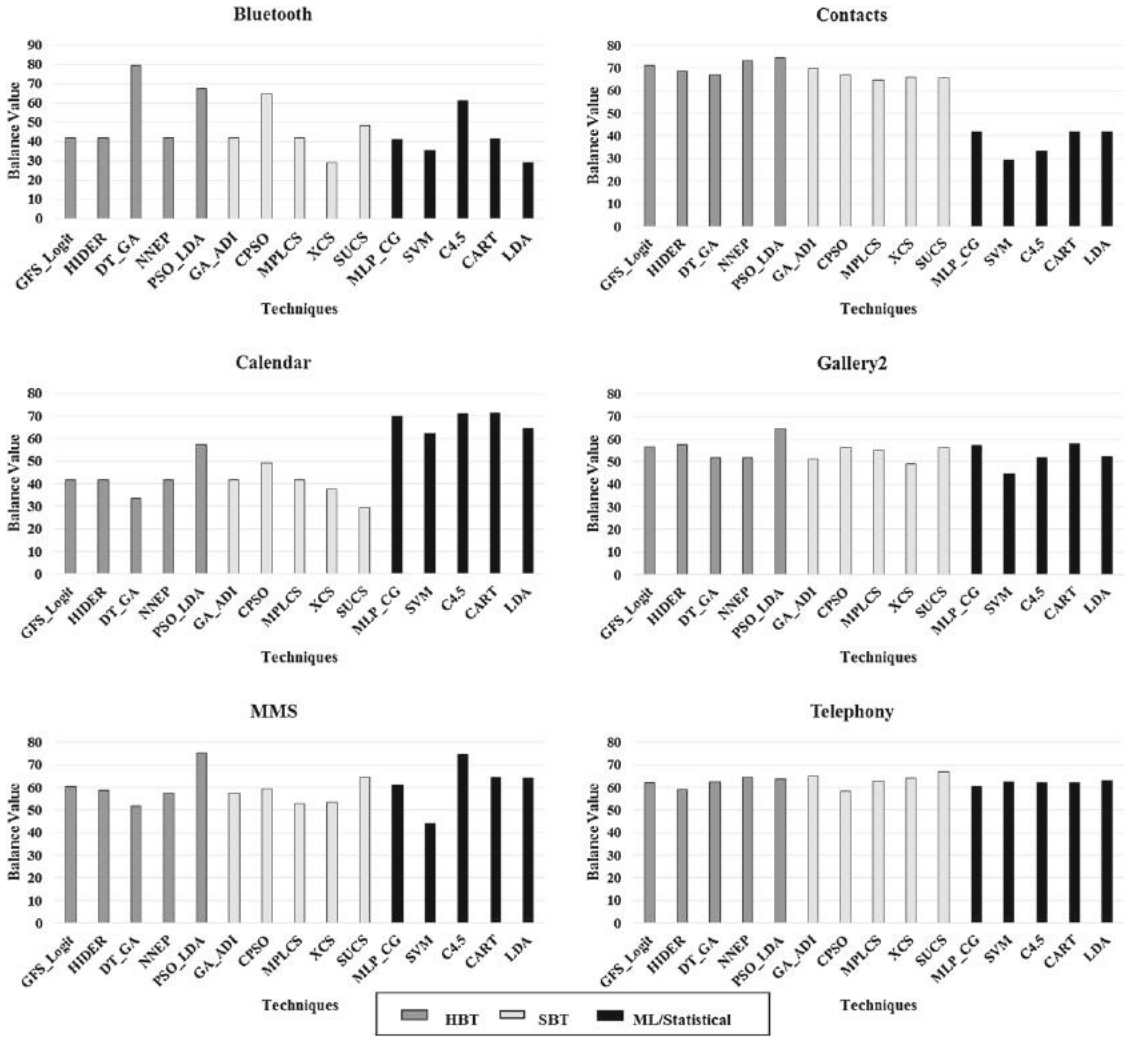

Fig. 5 Median balance values on 30 runs of different techniques

that the average G-mean values of most of the HBT and SBT are in the range of 0.50–0.80 indicating their effectiveness in developing change prediction models. The G-mean values of other ML/statistical range from 0.40 to 0.78.

Figure 7 reports the comparison of different techniques according to the average balance performance measure achieved by the models developed using various techniques. As can be seen from the figure, the HBT (bars with dark grey color) show good values for balance performance measure, which is closely followed by the balance performance values of SBT (bars in light grey). Thus, the predictive performance of SBT and HBT reveal that these techniques are comparable to each other. Apart from the PSO_LDA, an HBT, which shows a very good balance measure and the CPSO technique, an SBT, all other HBT and SBT show very close balance measure values. This could be because, both these sets of techniques performs effective global search and avoid getting trapped in the local maxima. Certain ML techniques like C4.5 and CART shows effective balance measure. However, the SVM technique shows low balance measure when compared to HBT and SBT techniques.

Figure 8 reports the average G-mean values of all the techniques. According to the figure, it can be clearly seen that all HBT techniques perform better than or equivalent

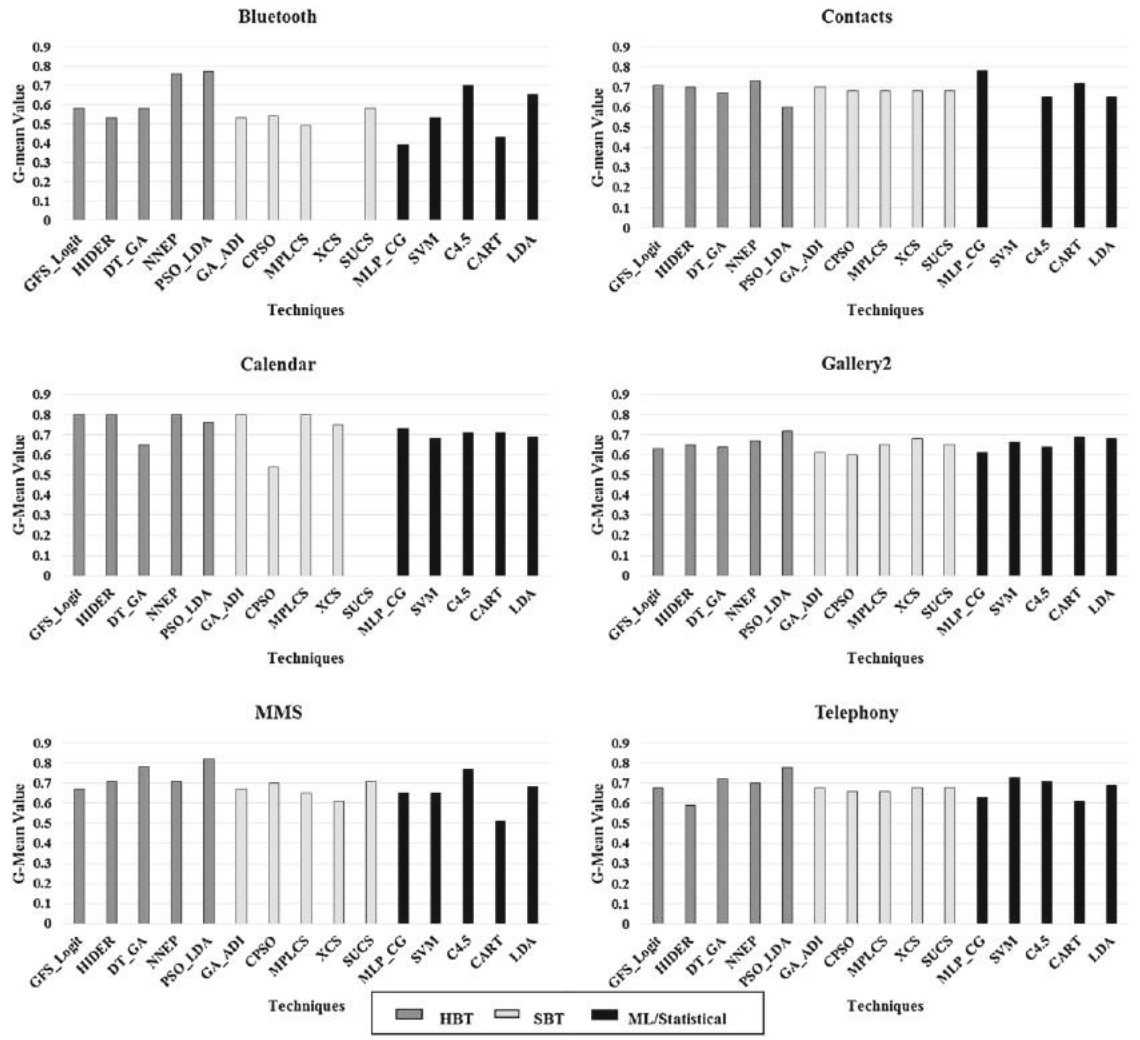

Fig. 6 Median G-mean values on 30 runs of different techniques

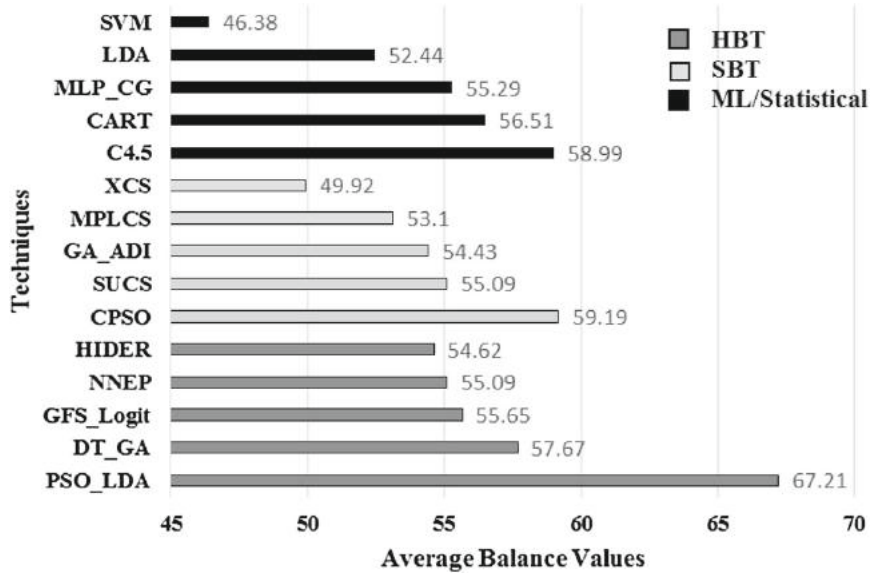

Fig. 7 Average balance values of different techniques

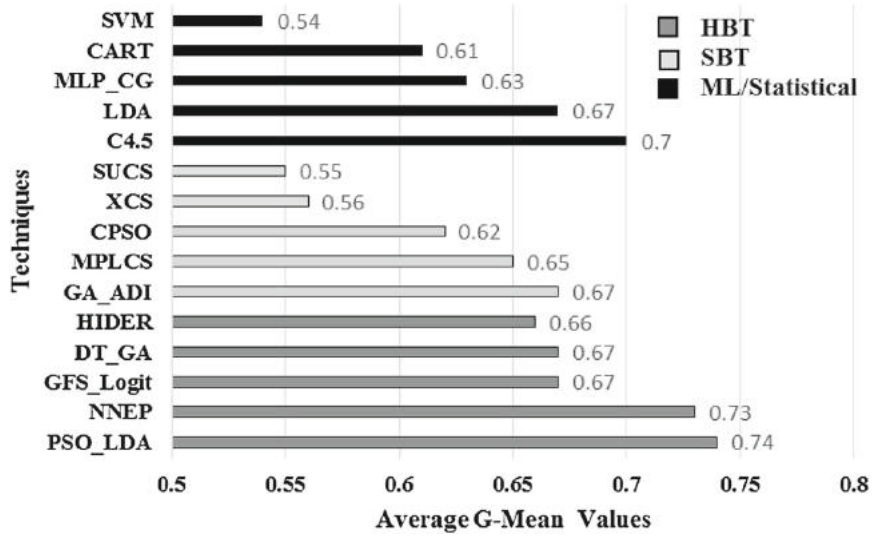

Fig. 8 Average G-mean values of different techniques

SBT and ML techniques. The only exception to this observation was the C4.5 which gave good G-mean values. Moreover, the comparison of the SBT with ML techniques reveal that the SUCS and XCS techniques perform lower than most other SBT and ML/statistical techniques. Other SBT and ML/statistical techniques give comparable performance in terms of G-mean values.

7.1.1 Discussion

After analyzing the performance of various categories of techniques on the basis of balance and G-mean values we can report that the models developed using most of the HBT techniques (DT_GA, GFS_Logit, PSO_LDA, NNEP) are better than those developed by the SBT. Also, HBT's showed best PD values on four of six data sets used in the study. A similar trend can be seen when we compare the results of HBT with the ML/statistical techniques as prediction models developed by most of the HBT (GFS_Logit, PSO_LDA, DT_GA) outperform models developed using the ML and statistical techniques. Also, SBT's showed best PF values on four of six data sets of the study. A comparison of predictive performance of SBT and ML/statistical techniques reveal that most of the SBT (GA_ADI, MPLCS, CPSO) are better than the ML techniques for development of change prediction models. This could be because SBT perform effective search of the whole population to avoid getting trapped in local maxima, thus generating better models with global optimum solutions.

The trends indicate that the value of G-mean and balance for HBT is advantageous when developing change prediction models. This could be because HBT incorporate the advantages of both constituent techniques to perform effectively. Thus, HBT benefits from the favorable properties of its constituent techniques to improve the developed models. For example, the DT_GA technique incorporates the effective pruning of decision trees along with search process of the GA algorithm which helps it to avoid local maxima and perform a global search.

Table 9 Friedman ranks using balance measure

Technique	Rank	Technique	Rank
PSO_LDA	1.83	HIDER	8.00
NNEP	6.00	MLP_CG	8.17
GFS_Logit	6.07	MPLCS	9.50
CART	6.67	LDA	9.50
SUCS	7.08	DT_GA	9.58
CPSO	7.33	XCS	11.17
C4.5	7.42	SVM	13.42
GA_ADI	7.67		

The predictive performance of change prediction models measured in terms of the balance and G-mean measures indicate, that the models developed by most of the HBT are better than those developed by the SBT and the ML/statistical techniques. However, the SBT develop better and effective change prediction models when compared with the change prediction models developed by ML/statistical techniques. The favorable nature of HBT could be due to effective combination of advantages of both its constituent's technique into a single approach.

7.2 Which is the best HBT for development of change prediction model? Which techniques perform statistically better or worse than the best chosen HBT?

Friedman test was used to evaluate the hypothesis stated in Sect. 5.2.1 by computing the mean ranks for each technique over the six Android data sets (Friedman 1937). The lower the rank obtained by the techniques, the better is the given technique.

The test statistic of Friedman test is based on chi square distribution with n-1 degrees of freedom, where n corresponds to the number of compared techniques in this study. As the study compares 15 techniques, the degrees of freedom is 14. The Friedman test is applied by evaluating a specific performance measure of all the techniques on all the six data sets used in the study using the median value of 30 runs. While testing the hypothesis, we calculate the Friedman statistic value and p value and the hypothesis is checked at $\alpha = 0.05$ significance level.

Table 9 states the Friedman mean ranks obtained by different techniques when we evaluated the balance measure of change prediction models developed using all the techniques. As shown in the table, the best rank was obtained by the PSO_LDA technique followed by the NNEP technique. The Friedman test results are significant at $\alpha = 0.05$ as the obtained p value is 0.01. The Friedman test statistic was calculated as 28.30. Thus, we reject Null hypothesis H0a which means that different techniques perform significantly different from each other when evaluated using the balance measure.

Table 10 reports the Friedman mean ranks obtained by different techniques when we assessed the change prediction models using the G-mean measure. According to

Table 10 Friedman ranks using G-mean measure

Technique	Rank	Technique	Rank
PSO_LDA	2.83	SUCS	8.75
NNEP	3.67	CART	9.50
C4.5	6.17	SVM	9.58
LDA	6.17	XCS	9.75
GFS_Logit	7.33	MPLCS	10.08
DT_GA	8.00	MLP_CG	10.33
HIDER	8.08	CPSO	11.17
GA_ADI	8.58		

the table, again PSO-LDA technique achieved the best rank followed by the NNEP technique. As the obtained p value is 0.03, the Friedman results are significant at $\alpha = 0.05$. The Friedman test statistic was computed as 24.55. This leads to acceptance of alternate hypothesis H0b, which states that different techniques are behaviorally significantly different when evaluated using the G-mean measure.

As the Friedman test yields significant results, showing PSO_LDA as the best technique, we performed post-hoc Wilcoxon test with Bonferroni correction to evaluate pairwise differences amongst the performances of different techniques. The set of hypothesis evaluated using Wilcoxon test is stated in Sect. 5.2.2. Here, technique X corresponds to the PSO_LDA technique. The computed differences of Wilcoxon test are ranked according to their absolute values.

An acceptance of Null hypothesis shows that the two techniques do not differ significantly and a rejection reports significant difference amongst the two compared techniques. The pairwise comparison of techniques was performed at chosen significance level $\alpha = 0.05$. Figures 9 and 10 report the pairwise comparison results of Wilcoxon test after Bonferroni correction using the balance and G-mean values. The bars represent the number of data sets which achieve different significance levels. The different colors of the bars indicate different significance level as explained below. It should be noted that the maximum number of data sets achieving a specific significance level would be six as we use six data sets in the study. The Wilcoxon comparison was performed by comparing the performance metrics values of 30 runs. The figures represent the results with four symbols which can be understood as follows:

- S+ $\rightarrow$ Technique X significantly outperforms technique Y on a data set D.
- S− $\rightarrow$ Technique Y significantly outperforms technique X on a data set D.
- NS+ $\rightarrow$ Technique X outperforms technique Y on data set D but not significantly.
- NS− $\rightarrow$ Technique Y outperforms technique X on data set D but not significantly.

According to Fig. 9, the PSO_LDA technique significantly outperforms (S+) all the other techniques on all the data sets except in five cases. These five cases are that of the CPSO technique on the Bluetooth data set and the XCS technique on the Telephony data set which are outperformed by the model developed using the PSO_LDA technique but not significantly. Also, the GA_ADI technique and the SUCS technique on the Telephony data set and the NNEP technique on the Bluetooth data sets significantly outperforms the PSO_LDA technique. It should be noted that there

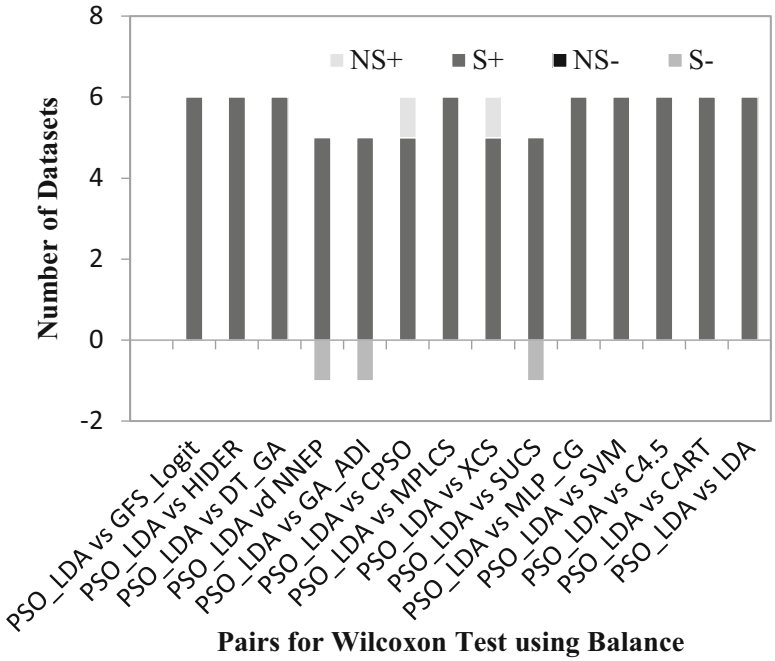

Fig. 9 Pairwise comparison results of Wilcoxon test using balance measure

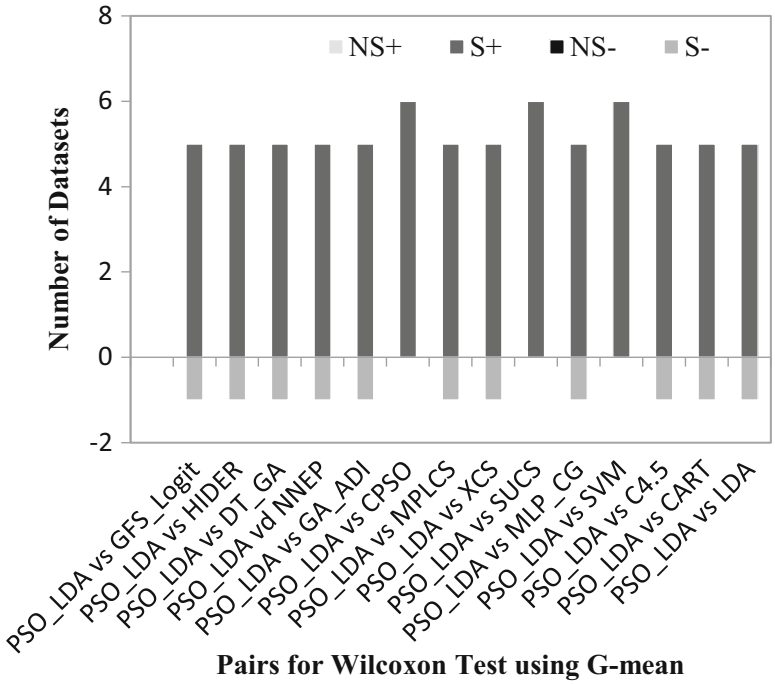

Fig. 10 Pairwise comparison results of Wilcoxon test using G-mean measure

are no NS− cases. The results of the Wilcoxon test with Bonferroni correction accept the alternate hypothesis H1a.

Figure 10 depicts the Wilcoxon results of pairwise comparison of different techniques with the PSO_LDA technique on all the six data sets using the G-mean measure. The PSO_LDA technique significantly outperforms all the other techniques on all the data sets except the Calendar data set. Only three techniques were outperformed by the PSO_LDA technique on the Calendar data set namely CPSO, SUCS and SVM.

It should be noted that there are no NS− or NS+ cases. The results of the Wilcoxon test with Bonferroni correction accept the alternate hypothesis H1b.

7.2.1 Discussion

As reported by the results of Friedman tests, the PSO_LDA technique significantly outperforms all other techniques for developing change-prediction models when evaluated using the balance and G-mean performance measures. The PSO_LDA technique, is a HBT, which incorporates Particle Swarm Optimization (PSO) and a statistical technique Linear Discriminant Analysis (LDA). The PSO technique is used for selecting an effective set of features while the LDA technique is used for model development. The use of PSO technique eliminates all redundant and noisy features, which helps the LDA technique in effective model development. The PSO technique has been advocated by Huang and Dun (2008) and Lin et al. (2008) for effective feature selection. The PSO technique chooses an effective feature set by representing a particle in the population of a D-dimensional space, where D represents the number of features. The fitness i.e. classification accuracy of each particle is calculated to ascertain its fitness for the LDA model. A particle's position is updated if it is better than its global best. As shown by Lin and Chen (2009), the use of PSO for feature selection enhances the effectiveness of LDA technique. Since, LDA is an effective statistical technique for model development, the use of PSO further improves the predictive performance of the model developed using the LDA technique. Similarly, the results of Wilcoxon test reveals that the PSO-LDA technique significantly outperformed all the other techniques when evaluated using the balance and G-mean measure except in very few cases. However, only the results of Calendar data set show that the PSO_LDA was significantly better than only three other techniques namely CPSO, SUCS and SVM. The results undoubtedly advocate that the PSO_LDA technique for development of models to ascertain change prone classes.

The results of statistical tests advocate the use of the PSO_LDA technique, a HBT as the best technique for model development on the investigated data sets. The results of the PSO_LDA technique are closely followed by the NNEP technique which is another HBT. Furthermore, the pairwise comparison results of the PSO_LDA technique with all the other techniques yield significant improvement of models developed using the PSO_LDA techniques. The PSO_LDA effectively combines the capabilities of a SBT named PSO for feature selection and a statistical technique LDA for model development.

7.3 What is the comparative CPU time taken by change prediction models developed using different SBT vs HBT, SBT vs ML/statistical techniques and HBT vs ML/statistical techniques?

In order to assess the comparative CPU time taken by various techniques, we analyzed the minimum (Min), maximum (Max) and the average (mean) CPU time (in seconds)

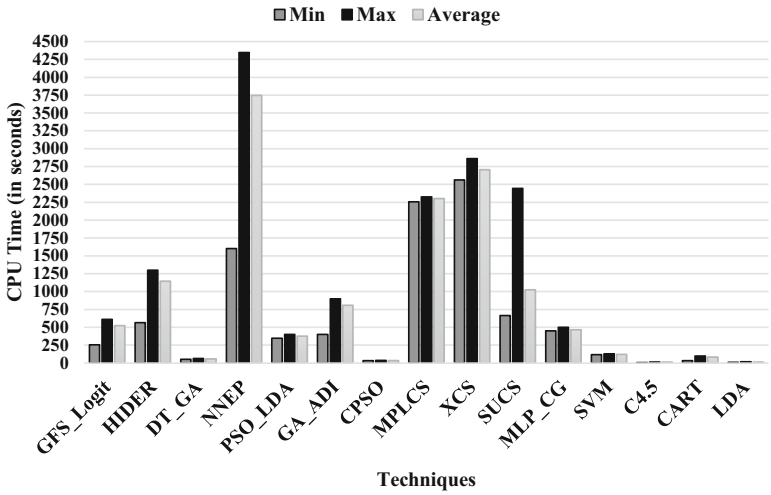

Fig. 11 CPU time taken by different techniques

for 30 runs taken by each technique for developing models on all the combined data sets. These values are depicted in Fig. 11. According to the figure, the largest CPU time is taken by the NNEP technique for model development. However, the least time is taken by the C4.5 technique followed by the LDA technique which is an average CPU time of 13 s each. The SBT which takes the least amount of CPU time is the CPSO technique i.e. 34 s.

The effective time taken by a technique for model development is actually approximately 30 times the average value shown in Fig. 11. For example, the NNEP technique takes an average time of 3746 s to develop change prediction models on all the data sets in a single run. However, we perform 30 runs for effective model development, which means the total time for model development is $3746 \times 30 = 37{,}650$ s, which is approximately 31.21 h.

Figure 12 represents the average CPU time taken by a technique for developing change prediction models on a single data set. According to the figure, the maximum time is taken by the NNEP technique which is close to 624 s. The least time is taken by the C4.5 and LDA techniques which is approximately 2 s. The CPSO and the DT_GA techniques also take very less CPU time which is 6 and 10 s respectively. In general, it can be seen that the ML/statistical techniques take much less time as compared to the SBT and the HBT. However, PSO_LDA, a HBT technique develop change prediction models in about 60 s which is quite competent with other ML techniques like MLP_CG.

7.3.1 Discussion

The following observations can be made after analyzing the average CPU time (computed over all the data sets) of the models developed using the various techniques:

- In terms of average CPU time, most of the ML models are quite effective and fast. It can be seen that the average CPU time taken by the SBT and the HBT is high when compared with the ML/statistical techniques. In order to overcome the problems of high CPU time taken by SBT and HBT, future studies should focus

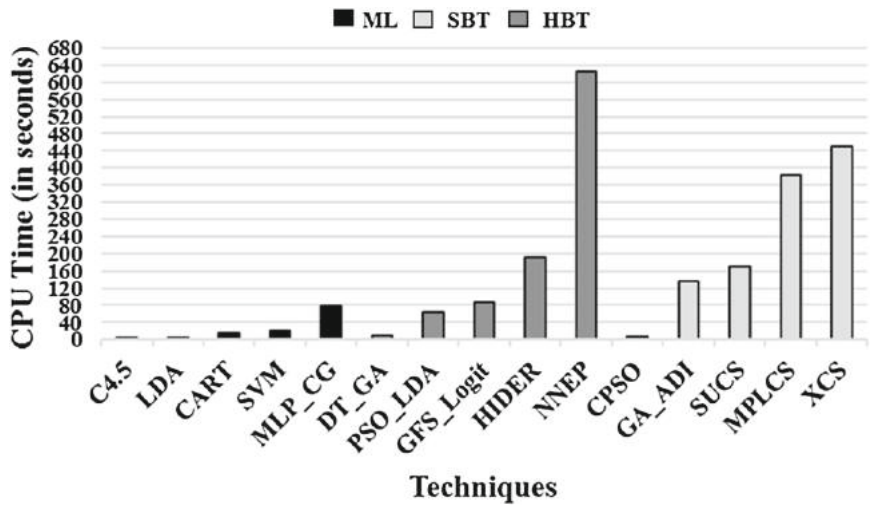

Fig. 12 CPU time taken by different techniques

on increase in efficiency of hardware technology, parallel architecture and cloud computing.

- Hybridization of ML/statistical techniques with the SBT also lowers the average CPU time taken by a technique for model development. This can be seen by the use of the DT_GA and the PSO_LDA technique which are hybridized versions of fast techniques like C4.5 and LDA, which consumed only 2 s of average CPU time for model development. However, the NNEP technique is an exception to this observation. It is observed that one of its similar constituent technique MLP_CG, also takes an effectively high average CPU time (78 s). Thus, hybridization of an ML technique which is itself time consuming with evolutionary programming (NNEP) increases the CPU time for model development exponentially (from 78 to 624 s).
- Though, SBT generally consume high average CPU time when compared with the HBT and ML/statistical techniques, the CPSO technique was an exception to this rule. According to Clerc and Kennedy (2002) the use of constriction factor with the PSO algorithm helps in effective control of the system's explosion and yields efficient convergence to local optima values. Thus, this property helps in effective use of the CPSO technique with low average CPU time.

Thus, it can be seen that the ML/statistical techniques are generally faster in developing change prediction models when compared with the HBT and the SBT. However, the CPU time taken by the HBT on an average is much lower than the CPU time taken by the SBT techniques. Thus, hybridization of a SBT with a fast ML technique effectively lowers the CPU time required for model development by the HBT.

Table 11 CPU time, average balance and average G-mean of different techniques

Technique	CPU time	Average balance	Average G-mean
HBT			
DT_GA	9.5	57.67	0.67
GFS_Logit	87.16	55.65	0.67
PSO_LDA	62.67	67.21	0.74
HIDER	190.83	54.62	0.66
NNEP	624.33	55.09	0.73
SBT			
CPSO	5.67	59.19	0.62
GA_ADI	134.66	54.43	0.67
SUCS	170.83	55.09	0.55
MPLCS	383.66	53.10	0.65
XCS	451.00	49.92	0.56
ML/statistical			
C4.5	2.16	58.99	0.70
LDA	2.16	52.44	0.67
CART	13.83	56.51	0.61
SVM	20.00	46.38	0.54
MLP_CG	77.50	55.29	0.63

The comparative performance of different techniques analyzed in the study varies in terms of CPU time. Most ML/statistical techniques are very fast in terms of developing change prediction models. A number of HBT such as DT_GA, GFS_Logit and HIDER are also quite effective in terms of the CPU time taken for developing change prediction models. However, most of the SBT and certain HBT such as NNEP take high CPU time (more than 100 s) for model development. An exception to this trend is the CPSO technique, a SBT, which takes low CPU time. In general, hybridization of a SBT with a fast performing ML technique decreases the CPU time effectively for model development.

7.4 Is there any trade-off between the CPU time and predictive performance of different HBT, SBT and ML/statistical techniques?

In order to evaluate the trade-off between CPU time and predictive performance, we state the average CPU time (in seconds) and the average balance performance metric as well as the average G-mean metric as shown in Table 11 for each category of techniques (HBT, SBT and ML/statistical). It should be noted that a favorable technique is the one which consumes less CPU time but exhibits high values of balance and G-mean.

According to Table 11, it can be clearly seen that the ML/statistical techniques are effective in terms of average CPU time consumed for model development with only the exception of the MLP_CG technique. However, the performance of the ML/statistical techniques is not exceptional in terms of balance values. The balance values of the models developed using majority of ML/statistical techniques is lower than most of the HBT and certain SBT. The HBT i.e. PSO_LDA and DT_GA show good balance values as compared to the majority of other SBT and ML/statistical techniques. However, though the performance of the NNEP technique is higher than or equivalent to most other techniques in terms of balance measure, the average CPU time taken by the NNEP technique is the highest (624 s). Other HBT such as DT_GA and GFS_Logit showed low average CPU time for model development. The balance value of these techniques ranged from 55 to 58 %. Also, though search-based techniques exhibited good balance measure values (except XCS), the average CPU time taken by them ranges from 60 to 170 s which exhibits moderate to high consumption of average CPU time for model development. Only one SBT, the CPSO technique, showed effective CPU time of about 6 s.

After analyzing the CPU time and average G-mean values shown in Table 11, we see that the HBT shows the best G-mean values. Also, the CPU time consumed by models developed using the HBT techniques is competitive, the only exception being the NNEP technique. According to the table, the DT_GA technique exhibited exceptionally good results with a G-mean value of 67 % and CPU time of about 10 s. The G-mean values of the SBT are lower than the HBT but higher than certain ML/statistical techniques. The C4.5 technique, an ML technique showed effective results with a good G-mean value of 59 % and an average CPU time of 2 s. The CPSO technique takes less CPU time but gives low value for G-mean measure. However, certain SBT techniques like the XCS, MPLCS and the SUCS techniques are quite poor both in terms of low G-mean values and high CPU time consumption.

7.4.1 Discussion

We summarize the trade-off between average CPU time and the predictive performance of various techniques for change prediction model development. Furthermore, we also noted few interesting observations which are summarized below:

- The values stated in Table 11 clearly reports a significant improvement in the G-mean values of the HBT as compared to the other SBT and the ML/statistical techniques. This fact is also reiterated in the comparative performance of the HBT with the SBT and the ML/statistical techniques for most of the compared balance values. It can be seen that the models developed using the DT_GA and the PSO_LDA techniques produced effective values for both the performance metrics as well as take low average CPU time for model development.
- Effective change prediction models developed using various techniques are beneficial in efficient allocation of maintenance and testing resources. Thus, techniques which give very good predictive performance with moderate CPU time such as PSO_LDA may also be used effectively as the average CPU time is compensated

by the cost and time saved by application of the change prediction models developed by these techniques. However, techniques which take large CPU time such as NNEP may be carefully selected, taking into account the large CPU time required by them. We performed cost-benefit analysis in order to evaluate the effectiveness of change prediction models developed using PSO_LDA, NNEP and C4.5 models on all the data sets. The effort gain was calculated according to the following formula (Arisholm and Briand 2006; Misirh et al. 2011):

$$\textit{Effort gain} = \frac{\text{LRT} - \text{LCM}}{\text{LRT}} \times 100$$

Here, LRT denotes the LOC, we need to test if we perform random testing (RT). It is calculated as the product of PD and total LOC of a specific data set. LCM denotes the LOC, we need to test when we use the change model (CM). The effort gain in percentage denotes the percentage of effort reduction for testing. The higher the effort gain, the more effective is the model developed by the technique. We found that the percentage effort gain was approximately between 40 and 60 % when we used HBT techniques (PSO_LDA and NNEP). This effort gain was a 20 % increase from when we used change prediction models developed using the ML method (C4.5). Thus, we note that though there is a trade-off between predictive performance and the average CPU time taken for model development by a technique, we can still use the technique if it balances out the project's costs saved by it by the application of the model developed using the technique.

Thus, after analyzing the trade-off between CPU time and the performance metrics (balance and G-mean), we can conclude that the PSO_LDA, DT_GA, C4.5 and even NNEP are effective techniques for developing change prediction models. The DT_GA technique is comparable to the C4.5 technique in terms of CPU time as well as predictive performance. Though, PSO_LDA technique takes longer CPU time for model development, it is compensated by effective predictive performance of the developed model. Furthermore, we note that the NNEP technique may be carefully selected because it does give an effective percentage gain in effort but takes large amount of CPU time for model development.

The HBT techniques can be effectively used if they balance out the constraints of CPU time and give effectively good performance and effort gain percentage. The use of most of the SBT are not advocated as they take high CPU time and do not produce effective models such that the time factor can be effectively compensated. However, the trade-off between the predictive performance and CPU time of the ML techniques suggest that, though most ML techniques are fast, we should appropriately select an ML technique which develops prediction models giving efficient performance.

There exists a trade-off between the predictive performance of the models developed using various techniques and the CPU time required by them for model development. Though ML/statistical techniques are quite effective in terms of CPU time, they give low predictive performance and effort gain ratio as compared to certain SBT and HBT. The study advocates the use of HBT techniques like PSO_LDA to balance the trade-off between CPU time and predictive performance for developing change prediction models. The trade-off between average CPU time taken can be compensated by the costs and time saved by effective application of the results of change prediction models developed by a specific technique.

8 Validity evaluation

While performing an empirical analysis, it is important to take into account the various threats to validity of the study. The threats could be a possible source of bias to the results of the study. This section states the various threats to validity of the study.

8.1 Conclusion validity

Conclusion validity involves all the threats, which may affect the accurate conclusion of the relationship between the treatment and the outcome (Catal and Diri 2009; Khoshgoftaar et al. 2006). It is also termed as statistical conclusion validity. We have carefully chosen non-parametric tests in the study as they do not require data normality assumptions. Also the significance cut-offs (α values) have been appropriately selected. Furthermore, we perform post-hoc analysis which strengthens the results of the study. The use of ten-fold cross validation and thirty runs eliminates validation bias. As the study uses two performance measures (balance and G-mean) for evaluating the results, it increases the confidence in the results of the study.

8.2 Internal validity

Internal validity concerns itself with the "causal effect" of the independent variables on change proneness attribute (Zhou et al. 2009). In order to determine this effect, it is necessary to conduct controlled experiments, which are difficult in practice (Briand et al. 2001). As the focus of the study, was not to evaluate the causal effect, this threat exists in our study. Also, we used a combination of testing and training data for feature selection as it is not possible to obtain testing data for feature selection. Thus, this threat also exists in the study. According to the results of the study, the best technique for change prediction is PSO_LDA. However, for developing prediction model using PSO_LDA, we did not use CFS technique for selecting features before application of PSO_LDA, in fact the PSO technique itself in PSO_LDA was used for feature selection. This could be a possible reason for the PSO_LDA technique to

perform well. The PSO may have extracted better features and uses LDA for model development. Thus, this threat of feature extraction through PSO exists in our study and could be a reason for very good performance of PSO_LDA.

8.3 Construct validity

"Construct validity is the degree to which the dependent and independent variables accurately measure the concept they purport to measure" (Zhou et al. 2009). Certain researchers have performed experiments to ascertain the accuracy of some of the OO metrics selected in this study (Briand et al. 1998, 1999, 2000). Thus, this threat is reduced in the study. The dependent variable of the study is computed by analyzing the LOC deleted or inserted in a class. As, the DCRS tool is efficient in extracting this information from the change logs, this variable is accurately measured.

8.4 External validity

External validity concerns itself with the generalizability of the results obtained by the study (Zhou et al. 2009). This threat can only be reduced by performing replicated and repeated studies on a number of data sets and comparing the results. Since, the study clearly states the fitness functions and parameter settings, it aids the replicability of the study. Moreover, as we use widely used open-source systems for empirical validation, the results can be effectively applied to similar domains. However, all the evaluated systems are developed in Java language, which may affect the validity of results on different programming language environments. Also, the results may or may not be applicable to other domains such as business, banking, telecommunications etc. The results may only be applicable when the systems are developed using object-oriented paradigms, are of similar sizes and are developed on an industrial scale by experienced programmers such as the Android OS. Thus, in order to increase the applicability of the results, similar studies should be conducted on different applications of different domains. Furthermore, the selected data sets are developed by a group of professionals which increases the external validity of the results (Catal and Diri 2009; Khoshgoftaar et al. 2006).

9 Conclusions and future work

The main aim of the study is to assess the predictive capability of the HBT and the SBT for developing change prediction models. In order to ascertain this, the study analyzed the performance of five HBT, five SBT, four ML techniques and one statistical technique using six application packages of open-source Android data set. The study evaluated various HBT and SBT using an efficient experimental set up which takes into account the stochastic nature of these techniques, imbalanced learning problem, statistical significance of results and provides complete parameter settings and fitness functions for easy replication of the study. The results of the study advocate the effectiveness of HBT over SBT and other ML/statistical techniques

and the use of SBT over ML/statistical techniques used in the study for developing change prediction models. Also, the PSO_LDA technique, a HBT exhibited the best performance among all the investigated techniques of the study, when evaluated statistically. Furthermore, the study also analyzed the CPU time taken for model development using each technique. According to the results, ML/statistical techniques are the fastest in terms of CPU time, which are followed by some effective HBT (DT_GA, GFS_Logit, HIDER). However, SBT and a few HBT (NNEP) take high CPU time for model development as compared to other HBT and ML/statistical techniques. After analyzing the trade-off between CPU time and predictive capability, the study recommends the use of HBT which balances the trade-off between CPU time and predictive performance. Furthermore, the cost and time saved by efficient use of results of developed change prediction models can compensate the trade-off between use of techniques which take moderate CPU times and show good predictive capability.

Change prediction models help software practitioners identify change prone classes. More resources can be allocated to these change prone classes during maintenance and testing in order to improve the quality of the software. Also, these classes should be meticulously verified and tracked in order to remove errors from such classes in the early phases of software development life cycle. These steps save a lot of time and effort and ensure a good quality software product. Thus, this study provides insight to the software practioners and researchers in efficient selection of techniques from a number of techniques available.

Future studies may incorporate the use of these techniques on proprietry and other large sized software. Moreover, replicated studies could also study the effectiveness of a number of other fitness functions on different SBT and HBT.

Appendix

Descriptive statistics

This appendix presents the descriptive statistics of each data set. Tables 12, 13, 14, 15, 16, and 17 report the minimum (Min.), maximum (Max), mean (Mean), standard deviation (SD), 25 % percentile and 75 % percentile for all the OO metrics used as independent variables in the study, for each data set respectively.

Table 12 Descriptive statistics for Android Bluetooth data set

Metric name	Min.	Max.	Mean	SD	Percentile (25 %)	Percentile (75 %)
AMC	1	5	4.93	0.47	5	5
Ca	0	5	0.76	1.15	0	1
Ce	0	10	1.40	2.09	0	2
CAM	0.13	1	0.42	0.24	0.25	0.542
CBM	0	0	0	0	0	0
CBO	0	10	1.94	2.32	0	3
DAM	0	1	0.67	0.39	0.36	1
DIT	1	1	1	0	1	1
IC	0	0	0	0	0	0
LCOM	0	6903	307	1042.07	6	140.25
LCOM3	1.01	2	1.28	0.34	1.06	1.33
LOC	9	718	104.86	127.65	31	116.5
MFA	0	0	0	0	0	0
MOA	0	6	0.72	1.26	0	1
NOC	0	0	0	0	0	0
NPM	0	16	4.51	3.89	1.75	7
RFC	2	119	16	20.24	5	18.25
WMC	1	118	15	20.24	4	17.25

Table 13 Descriptive statistics for Android Contacts data set

Metric name	Min.	Max.	Mean	SD	Percentile (25 %)	Percentile (75 %)
AMC	0	5	4.15	1.78	5	5
Ca	0	15	0.43	1.44	0	0.75
Ce	0	12	0.83	1.49	0	1
CAM	0	1	0.39	0.22	0.21	0.5
CBM	0	1	0	0.06	0	0
CBO	0	15	1.27	2.07	0	2
DAM	0	1	0.65	0.45	0	1
DIT	0	4	0.9	0.42	1	1
IC	0	1	0	0.06	0	0
LCOM	0	1770	104.74	229.76	6	91
LCOM3	0	2	1.39	0.40	1.07	2
LOC	0	422	70.50	69.02	24	91.75
MFA	0	0.96	0.01	0.08	0	0
MOA	0	5	0.19	0.59	0	0
NOC	0	15	0.11	1.06	0	0
NPM	0	43	7.10	6.85	2.25	9
RFC	0	61	11.86	10.14	5	15
WMC	0	60	10.86	10.13	4	14

Table 14 Descriptive statistics for Android Calendar data set

Metric Name	Min.	Max.	Mean	SD	Percentile (25 %)	Percentile (75 %)
AMC	0	5	4.65	1.19	5	5
Ca	0	4	0.56	0.89	0	1
Ce	0	11	1.19	1.84	0	2
CAM	0.05	1	0.38	0.24	0.20	0.5
CBM	0	1	0.01	0.09	0	0
CBO	0	12	1.70	2.12	0	2
DAM	0	1	0.70	0.37	0.44	1
DIT	0	1	0.95	0.21	1	1
IC	0	1	0.01	0.09	0	0
LCOM	0	5995	244.12	755.04	10	148.75
LCOM3	1	2	1.26	0.32	1.05	1.31
LOC	7	936	107.43	134.61	31	133.5
MFA	0	0	0	0	0	0
MOA	0	10	0.55	1.29	0	1
NOC	0	1	0.37	0.19	0	0
NPM	1	65	9.39	10.43	3	11.75
RFC	2	111	15.47	17.20	6	18.75
WMC	1	110	14.47	17.20	5	17.75

Table 15 Descriptive statistics for Android Gallery2 data set

Metric Name	Min.	Max.	Mean	SD	Percentile (25 %)	Percentile (75 %)
AMC	0	5	2.87	2.42	0	5
Ca	0	42	1.35	4.13	0	1
Ce	0	16	1.76	2.17	0	3
CAM	0	1	0.41	0.23	0.25	0.5
CBM	0	4	0.02	0.23	0	0
CBO	0	42	3.06	4.66	1	4
DAM	0	1	0.70	0.42	0.15	1
DIT	0	3	0.64	0.54	0	1
IC	0	2	0.01	0.14	0	0
LCOM	0	31,375	200.85	1646.30	6	91
LCOM3	0	2	1.36	0.38	1.07	1.5
LOC	8	1507	75.46	106.99	24	93
MFA	0	1	0.01	0.07	0	0
MOA	0	8	0.49	1.08	0	1
NOC	0	23	0.35	1.70	0	0
NPM	0	251	8.62	14.94	3	10
RFC	0	252	12.55	16.74	5	15
WMC	0	251	11.55	16.74	4	14

Table 16 Descriptive statistics for Android MMS data set

Metric Name	Min.	Max.	Mean	SD	Percentile (25 %)	Percentile (75 %)
AMC	0	5	3.15	2.23	0.35	5
Ca	0	11	0.89	1.65	0	1
Ce	0	10	1.65	1.39	0	2
CAM	0	1	0.47	0.27	0.25	0.66
CBM	0	5	0.02	0.34	0	0
CBO	0	12	2.00	2.09	0	3
DAM	0	1	0.57	0.45	0	1
DIT	0	4	0.85	0.54	1	1
IC	0	3	0.01	0.21	0	0
LCOM	0	8128	153.33	612.94	3	91
LCOM3	1	2	1.45	0.40	1.08	2
LOC	0	882	66.58	94.75	13	83
MFA	0	1	0.01	0.12	0	0
MOA	0	6	0.23	0.73	0	0
NOC	0	5	0.19	0.72	0	0
NPM	0	53	7.70	9.63	2	8.25
RFC	0	129	11.84	14.17	4	15
WMC	0	128	10.87	14.14	3	14

Table 17 Descriptive statistics for Android Telephony data set

Metric Name	Min.	Max.	Mean	SD	Percentile (25 %)	Percentile (75 %)
AMC	0	5	4.28	1.61	5	5
Ca	0	16	1.29	2.10	0	2
Ce	0	17	1.81	2.72	0	3
CAM	0	1	0.45	0.28	0.21	0.58
CBM	0	1	0.01	0.06	0	0
CBO	0	20	2.84	3.5	1	4
DAM	6	1	0.41	0.43	0	0.95
DIT	0	4	0.97	0.47	1	1
IC	0	1	0.01	0.06	0	0
LCOM	0	22,578	709.05	2569.41	6	190
LCOM3	1	2	1.33	0.37	1.05	1.5
LOC	6	1100	121.78	175.41	26	129
MFA	0	1	0.04	0.20	0	0
MOA	0	37	1.22	3.63	0	1
NOC	0	4	0.05	0.33	0	0
NPM	0	212	14.43	28.91	2	14
RFC	2	214	21.00	32.28	5	21
WMC	1	213	20.00	32.28	4	20

References

Ali, S., Briand, L.C., Hemmati, H., Panesar-Walawege, R.K.: A systematic review of the application and empirical investigation of search-based test case generation. IEEE Trans. Softw. Eng. **36**(6), 742–762 (2010)

Aguilar-Reiz, J.S., Riquelme, J.C., Toro, M.: Evolutionary learning of hierarchical decision rules. IEEE Trans. Syst. Man Cybern. **33**(2), 324–331 (2003)

Arcuri, A., Fraser, G.: On Parameter Tuning in Search Based Software Engineering. Springer, Berlin (2011)

Arcuri, A., Briand, L.C.: A practical guide for using statistical tests to assess randomized algorithms in software engineering. In: International Conference on Software Engineering, pp. 1–10 (2011)

Arisholm, E., Briand, L.C., Foyen, A.: Dynamic coupling measurement for object-oriented software. IEEE Trans. Softw. Eng. **30**(8), 491–506 (2004)

Arisholm, E., Briand, L.C.: Predicting fault-prone components in a java legacy system. In: Proceedings of ACM/IEEE international symposium on empirical software engineering, pp. 8–17 (2006)

Arisholm, E., Briand, L.C., Johannessen, E.B.: A systematic and comprehensive investigation of methods to build and evaluate fault prediction models. J. Syst. Softw. **83**(1), 2–17 (2010)

Bacardit, J., Garrell, J.M. : Evolving multiple discretizations with adaptive intervals for a pittsburgh rule-based learning classifier system. In: Genetic and Evolutionary Computation Conference (GECCO'03), 2724, pp. 1818–1831 (2003)

Bacardit, J.: Pittsburgh genetics-based machine learning in the data mining era: representations, generalization, and run-time. PhD Thesis (2004)

Bacardit, J., Krasnogor, N.: Performance and efficiency of memetic pittsburgh learning classifier systems. Evol. Comput. **17**(3), 307–342 (2009)

Bardsiri, V.K., Jawawi, D.N.A., Hashim, S.Z.M., Khatibi, E.: A PSO-based model to increase the accuracy of software development effort estimation. Softw. Qual. J. **21**(3), 501–526 (2013)

Bardsiri, V.K., Jawawi, D.N.A., Hashim, S.Z.M., Khatibi, E.: A flexible method to estimate the software development effort based on the classification of projects and localization of comparisons. Empir. Softw. Eng. **19**(4), 857–884 (2014)

Barros, M.O., Neto, A.C.D.: Threats to validity in search-based software engineering empirical studies. Technical Report TR 0006/2011, UNIRIO-Universidade Federal do Estado do Rio de Janeiro (2011)

Bernado-Mansilla, E., Garrell-Guiu, J.M.: Accuracy-based learning classifier systems: models, analysis and applications to classification tasks. Evol. Comput. **11**(3), 209–238 (2003)

Bieman, J., Jain, D., Yang, H.: OO design patterns, design structure, and program changes: an industrial case study. In: Proceedings of 17th International Conference on Software Maintenance, pp. 580–589 (2001)

Bieman, J., Andrews, A., Yang, H.: Understanding change-proneness in OO software through visualization. In: 11th IEEE International Workshop on Program Comprehension, pp. 44–53 (2003)

Braga, P.L., Oliveira, A.L., Meira, S.R.: A GA-based feature selection and parameters optimization for support vector regression applied to software effort estimation. In: ACM Symposium on Applied Computing, pp. 1788–1798 (2008)

Briand, L., Daly, J., Wust, J.: A unified framework for cohesion measurement in object-oriented systems. Empir. Softw. Eng. **3**(1), 65–117 (1998)

Briand, L., Daly, J., Wust, J.: A unified framework for coupling measurement in object-oriented systems. IEEE Trans. Softw. Eng. **25**(1), 91–121 (1999)

Briand, L., Wust, J., Daly, J.W.: Exploring the relationship between design measures and software quality in object-oriented Systems. J. Syst. Softw. **51**(3), 245–273 (2000)

Briand, L., Wust, J., Lounis, H.: Replicated case studies for investigating quality factors in object oriented designs. Empir. Softw. Eng. J. **6**(1), 11–58 (2001)

Burgess, C.J., Lefley, M.: Can genetic programming improve software effort estimation? A comparative evaluation. Inf. Softw. Technol. **43**(14), 863–873 (2001)

Butz, M.V., Kovacs, T., Lanzi, P.L., Wilson, S.W.: How XCS evolves accurate classifiers. In: Proceedings of Genetic and Evolutionary Computation Conference, pp. 927–934 (2001)

Canfora, G., De Lucia, A., Di Penta, M., Oliveto, R., Panichella, A., Panichella, S.: Multi-objective cross-project defect prediction. In: 6th International Conference on Software Testing, Verification and Validation, pp. 252–261 (2013)

CartWright, M., Shepperd, M.: An empirical investigation of an object-oriented software system. IEEE Trans. Softw. Eng. **26**(8), 786–796 (2000)

Carvalho, D.R., Freitas, A.A.: A hybrid decision tree/genetic algorithm method for data mining. J. Inf. Sci. **163**(1–3), 13–35 (2004)
Carvalho, A.B.D., Pozo, A., Vergilio, S.R.: A symbolic fault-prediction model based on multi-objective particle swarm optimization. J. Syst. Softw. **83**(5), 868–882 (2010)
Catal, C., Diri, B.: Investigating the effect of dataset size, metrics sets, and feature selection techniques on software fault prediction problem. Inf. Sci. **179**(8), 1040–1058 (2009)
Chidamber, S.R., Kemerer, C.F.: A metrics suite for object oriented design. IEEE Trans. Softw. Eng. **20**(6), 476–493 (1994)
Chiu, N.-H., Huang, S.-J.: The adjusted analogy-based software effort estimation based on similarity distances. J. Syst. Softw. **80**(4), 628–640 (2007)
Clarke, J., Dolado, J.J., Harman, M., Hierons, R., Jones, B., Lumkin, M., Mitchell, B., Mancordis, S., Rees, K., Roper, M., Shepperd, M.: Reformulating software engineering as a search problem. IEEE Proc. Softw. **150**(3), 161–175 (2003)
Clerc, M., Kennedy, J.: The particle swarm—explosion, stability, and convergence in a multidimensional complex space. IEEE Trans. Evol. Comput. **6**(1), 58–73 (2002)
Corazza, A., Di Martino, S., Ferrucci, F., Gravino, C., Sarro, F., Mendes, E.: Using tabu search to configure support vector regression for effort estimation. Empir. Softw. Eng. **18**(1), 506–546 (2013)
Craenen, B.G., Eiben, A.E., van Hemert, J.I.: Comparing evolutionary algorithms on binary constraint satisfaction problems. IEEE Trans. Evol. Comput. **7**(5), 424–444 (2003)
Demšar, J.: Statistical comparisons of classifiers over multiple data sets. J. Mach. Learn. Res. **7**, 1–30 (2006)
Di Martino, S.D., Ferrucci, F., Gravino, C., Sarro, F.: A genetic algorithm to configure support vector machines for predicting fault-prone components. Prod. Focus. Softw. Process Improv. **6759**, 247–261 (2011)
Dolado, J.J.: A validation of component based method for software size estimation. IEEE Trans. Softw. Eng. **26**(10), 1006–1021 (2000)
Durbin, R., Rumelhart, D.: Product units: a computationally powerful and biologically plausible extensions to back-propagation networks. Neural Comput. **1**, 133–142 (1989)
Elish, K.O., Elish, M.O.: Predicting defect-prone software modules using support vector machines. J. Syst. Softw. **81**(5), 649–660 (2008)
Elish, M.O., Al-Khiaty, M.A.: A suite of metrics for quantifying historical changes to predict future change-prone classes in object-oriented software. J. Softw. Evol. Process **25**(5), 407–437 (2013)
El Emam, K., Melo, W., Machado, J.C.: The prediction of faulty classes using object-oriented design metrics. J. Syst. Softw. **56**(1), 63–75 (2001)
Eski, S., Buzluca, F.: An empirical study on object-oriented metrics and software evolution in order to reduce testing cost by predicting change prone classes. In: International Conference on Software Testing, Verification and Validation Workshop, pp. 566–571 (2011)
Friedman, M.: The use of ranks to avoid the assumption of normality implicit in the analysis of variance. J. Am. Stat. Assoc. **32**(200), 675–701 (1937)
Giger, E., Pinzger, M., Gall, H.C.: Can we predict type of code changes? An empirical analysis. In: 9th IEEE Working Conference on Mining Software Repositories, pp. 217–226 (2012)
Gottlieb, J., Marchiori, E., Rossi, C.: Evolutionary algorithms for the satisfiability problem. Evol. Comput. **10**(1), 35–50 (2002)
Grosan, C., Abraham, A.: Hybrid evolutionary algorithms: methodologies, architectures and reviews. Stud. Comput. Intell. **75**, 1–17 (2007)
Gyimothy, T., Ferenc, R., Siket, I.: Empirical validation of object-oriented metrics on open source software for fault prediction. IEEE Trans. Softw. Eng. **31**(10), 897–910 (2005)
Hall, M.A.: Correlation-based feature selection for discrete and numeric class machine learning. In: Proceeding of the Seventeenth International Conference on Machine Learning, pp. 359–366 (2000)
Harman, M., Jones, B.F.: Search based software engineering. Inf. Softw. Technol. **43**(14), 833–839 (2001)
Harman, M.: The relationship between search based software engineering and predictive modeling. In: Proceedings of the 6th International Conference on Predictive Models in Software Engineering (2010a)
Harman, M.: Why the virtual nature of software makes it ideal for search based optimization. In: International Conference on Fundamental Approaches to Software Engineering. Springer, Berlin (2010b)
Harman, M., McMinn, P., Teixeira de Souza, J., Yoo, S.: Search based software engineering: techniques, taxonomy, tutorial. In: Empirical Software Engineering and Verification. Lecture Notes in Computer Science, vol. 7007, pp. 1–59 (2012a)

Harman, M., Mansouri, S.A., Zhang, Y.: Search-based software engineering: trends, techniques and applications. ACM Comput. Surv. **45**(1), 11 (2012b)

Harman, M., Islam, S., Jia, Y., Minku, L.L., Sarro, F., Sirivisut, K.: Less is more: temporal fault predictive performance over multiple hadoop releases. In: 6th International Symposium on Search Based Software Engineering, pp. 240–246 (2014)

He, H., Garcia, E.A.: Learning from imbalanced data. IEEE Trans. Knowl. Data Eng. **21**(9), 1263–1284 (2009)

Henderson-Sellers, B.: Object-Oriented Metrics, Measures of Complexity, Prentice Hall (1996)

Huang, S.J., Chiu, N.H.: Optimization of analogy weights by genetic algorithm for software effort estimation. Inf. Softw. Technol. **48**(11), 1034–1045 (2006)

Huang, C.-L., Dun, J.-F.: A distributed PSO-SVM hybrid system with feature selection and parameter optimization. Appl. Soft Comput. **8**(4), 1381–1391 (2008)

Khoshgoftaar, T.M., Seliya, N., Sundaresh, N.: An empirical study of predicting faults with case-based reasoning. Softw. Qual. J. **14**(2), 85–111 (2006)

Koru, A.G., Tian, J.: Comparing high-change modules and modules with the highest measurement values in two large-scale open-source products. IEEE Trans. Softw. Eng. **31**(8), 625–642 (2005)

Koru, A.G., Liu, H.: Identifying and characterizing change-prone classes in two large-scale open-source products. J. Syst. Softw. **80**(1), 63–73 (2007)

Kpodjedo, S., Ricca, F., Galnier, P., Gueheneuc, Y.G., Antoniol, G.: Design evolution metrics for defect prediction in object-oriented systems. Empir. Softw. Eng. **16**(1), 141–175 (2011)

Kubat, M., Matwin, S.: Addressing the curse of imbalanced training sets: one sided selection. In: Proceedings of 14th International Conference on Machine Learning, vol. 97, pp. 179–186 (1997)

Lessmann, S., Baesans, B., Mues, C., Pietsch, S.: Benchmarking classification models for software defect prediction: a proposed framework and novel finding. IEEE Trans. Softw. Eng. **34**(4), 485–496 (2008)

Li, M., Zhang, H., Whu, R., Zhou, Z.: Sample-based software defect prediction with active and semi-supervised learning. Autom. Softw. Eng. **19**(2), 201–230 (2012)

Lin, S.-W., Ying, K.-C., Chen, S.-C., Lee, Z.-J.: Particle swarm optimization for parameter determination and feature selection of support vector machines. Expert Syst. Appl. **35**(4), 1817–1824 (2008)

Lin, S.-W., Chen, S.-C.: PSOLDA: a particle swarm optimization approach for enhancing classification accuracy rate of linear discriminant analysis. Appl. Soft Comput. **9**, 1008–1015 (2009)

Lindvall, M.: Are large C++ classes change-prone? An empirical investigation. Softw. Pract. Exp. **28**(15), 1551–1558 (1998)

Lu, H., Zhou, Y., Xu, B., Leung, H., Chen, L.: The ability of object-oriented metrics to predict change-proneness: a meta-analysis. Empir. Softw. Eng. J. **17**(3), 200–242 (2012)

Malhotra, R., Khanna, M.: Investigation of relationship between object-oriented metrics and change proneness. Int. J. Mach. Learn. Cybernet. **4**(4), 273–286 (2013)

Malhotra, R.: Search based techniques for software fault prediction: current trends and future directions. In: Proceedings of the 7th International Workshop on Search-Based Software Testing, pp. 35-36 (2014)

Malhotra, R., Khanna, M.: The ability of search-based algorithms to predict change-prone classes. Softw. Qual. Prof. **17**(1), 17–31 (2014)

Malhotra, R., Nagpal, K., Upmanyu, P., Pritam, N.: Defect collection and reporting system for Git based open source software. In: Proceedings of International Conference on Data Mining and Intelligent Computing, pp. 1–7 (2014)

Malhotra, R.: A systematic review of machine learning techniques for software fault prediction. Appl. Soft Comput. **27**, 504–518 (2015)

Malhotra, R., Khanna, M.: Software engineering predictive modeling using search-based techniques: systematic review and future directions. In: Proceedings of 1st American Search-Based Software Engineering Symposium, pp. 1–16 (2015)

Martin, R.C.: Agile Software Development: Principles, Patters, and Practices. Prentice Hall, Upper Saddle River (2002)

Martinez-Estudillo, F.J., Hevas-Martinez, C., Gutierrez, P.A., Martinez-Estudillo, A.C.: Evolutionary product-unit neural network classifiers. J. Neurocomputing **72**(1–3), 548–561 (2008)

Menzies, T., Greenwald, J., Frank, A.: Data mining static code attributes to learn defect predictors. IEEE Trans. Softw. Eng. **33**(1), 2–13 (2007)

Minku, L.L., Yao, X.: Software effort estimation as a multi-objective learning problem. ACM Trans. Softw. Eng. Methodol. **22**(4), 35 (2013)

Misirh, A.T., Bener, A.B., Turhan, B.: An industrial case study of classifier ensembles for locating software defects. Softw. Qual. J. **19**(3), 515–536 (2011)

Olague, H., Etzkorn, L., Gholston, S., Quattlebaum, S.: Empirical validation of three software metric suites to predict the fault-proneness of object-oriented classes developed using highly iterative or agile software development processes. IEEE Trans. Softw. Eng. **33**(10), 402–419 (2007)

Oliveira, A.L.I., Braga, P.L., Lima, R.M.L., Cornelio, M.L.: GA-based method for feature selection and parameters optimization for machine learning regression applied to software effort estimation. Inf. Softw. Technol. **52**(11), 1155–1166 (2010)

Otero, J., Sanchen, L.: Induction of descriptive fuzzy classifiers with the Logitboost Algorithm. Soft. Comput. **10**(9), 825–835 (2006)

Ouni, A., Kessentini, M., Sahraoui, H., Boukadoum, M.: Maintainability defects detection and correction: a multi-objective approach. Autom. Softw. Eng. **20**(1), 47–79 (2013)

Pai, G.J., Dugan, J.B.: Empirical analysis of software fault content and fault proneness using bayesian methods. IEEE Trans. Softw. Eng. **33**(10), 675–686 (2007)

Ramírez, A., Romero, J.R., Ventura, S.: A comparative study of many-objective evolutionary algorithms for the discovery of software architectures. In: Empirical Software Engineering, pp. 1–55 (2015)

Rivest, R.L.: Learning decision lists. Mach. Learn. **1**(2), 229–246 (1987)

Rodriguez, D., Ruiz, R., Riquelme, J.C., Aguluir-Ruiz, J.S.: Searching for rules to detect defective modules: a subgroup discovery approach. Inf. Sci. **191**, 14–30 (2012)

Romano, D., Pinzger, M.: Using source code metrics to predict change-prone java interfaces. In: 27th IEEE International Conference on Software Maintenance, pp. 303–312 (2011)

Singh, Y., Kaur, A., Malhotra, R.: Empirical validation of object-oriented metrics for predicting fault proneness models. Softw. Qual. J. **18**, 3–35 (2009)

Song, L., Minku, L.L., Yao, X.: The impact of parameter tuning on software effort estimation using learning machines. In: Proceedings of the 9th International Conference on Predictive Models in Software Engineering, p. 9 (2013)

Sousa, T., Silva, A., Neves, A.: Particle swarm based data mining algorithms for classification tasks. J. Parallel Comput. **30**(5–6), 767–783 (2004)

Stone, M.: Cross-validatory choice and assessment of statistical predictions. J. R. Soc. Ser. A **36**, 111–114 (1974)

Zhou, Y., Leung, H., Xu, B.: Examining the potentially confounding effect of class size on the associations between object metrics and change proneness. IEEE Trans. Softw. Eng. **35**(5), 607–623 (2009)

IARJSET
ISSN (Online) 2393-8021
ISSN (Print) 2394-1588
International Advanced Research Journal in Science, Engineering and Technology
ISO 3297:2007 Certified
Vol. 3, Issue 7, July 2016

Analysis of ECG Signals using Hybrid Classifier

Sahil Dalal[1], Rajesh Birok[2]

Department of ECE, Delhi Technological University, Delhi, India[1]

Associate Professor, Department of ECE, Delhi Technological University, Delhi, India[2]

Abstract: This research paper describes a novel method in which analysis of the ElectroCardioGraphy (ECG) signals is done using the hybrid classifier. As it is an already known fact that ECG signals are used by doctors to diagnose the heart activity of the subject and on the basis of knowledge about its peaks, treatment of the disease is done. Hence, the purpose of this research work is to identify the Normal, Apnea, Ischemia and Tachycardia signals using the method of Principal Component Analysis (PCA) and Neuro-Fuzzy classifier. PCA algorithm is used to extract the relevant information from the ECG input dataset which are their P-QRS-T parameters values. Then the extracted features data is analyzed and classified using the hybrid of Artificial Neural Networks (ANN) and Fuzzy Logic classifiers i.e. Neuro-Fuzzy classifier. Then these classification results are compared and observed a good accuracy of around 96% in the classification.

Keywords: ANN, ECG, Fuzzy, Neuro-Fuzzy, PCA.

I. INTRODUCTION

There can be so many heart related diseases present in this world among the human beings. So, because of problems in the heart, many people die every year. For this, Electro Cardio Graphy (ECG) is an existing way of measuring the electrical activity of the heart. And Doctors exploits ECG to diagnose and treatment for the related problems.

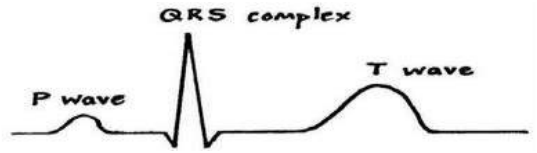

Fig.1. ECG waveform with its characteristic points

This diagnosis can be made automatic if these ECG signals obtained for different subjects can be differentiated on the basis of some pattern. A standard ECG waveform is shown in the Fig.1. In the figure, P-QRS-T waveform is represented and these points can be used as the characteristic points for the ECG signal. For various signals in ECG, variation in the P-QRS-T waveform can be observed. There are so many algorithms already developed for the delineation of the ECG signals.

TABLE.I
SUMMARY OF THE EARLIER PROPOSED METHODS

STUDY	TECHNIQUE	ACCURACY
Shen [3]	HB + WED + NNC	95.3%
Chan et al. [4]	CCORR + NC	90.8%
Chiu et al. [5]	DWT + NC, ED	95.71%
Yao and Wan [6]	DWTMRRS + PCA	91.5%
Boumbarov et al. [7]	PCA + RBFNN	86%
Homer et al. [8]	RARMA + NNC	85.2%
Agrafioti and Hatzinakos [9]	AC + WT + NNC	92.3%
Lourenco et al. [10]	MANRHB + NC	94.3%

Among these algorithms, real time QRS algorithm [11-13], software based algorithm [14-17], CWT [18], matched filters [19], linear predictive coding [20], ECG slope criteria [21], power spectral density [22], second order derivatives [23], DWT [24], wavelet transforms [25-27] are studied. In [1-2], ECG beats were detected using principal component based technique.

And similarly some other beats are selected in other researchers. Now, in this research paper, a novel method is proposed for the classification of the different types of ECG signals i.e.

Apnea, Ischemia, Normal and Tachycardia using the hybrid of Artificial Neural Network and Fuzzy Logic i.e. Neuro-Fuzzy Classifier.

In this, PCA algorithm is utilized to identify the ECG signals. This research paper is organized in the following sections as: Section II tells about the overview of the complete work using a block diagram. Section III tells about the different types of ECG signals used and the proposed method. Then in section IV, results are discussed followed by conclusion in section V.

II. BLOCK DIAGRAM

In the the Fig. 2 shown is the block diagram representing the overview of the work done during this research. In this, four different types of ECG waveforms are taken namely Apnea, Ischemia, Normal and Tachycardia.
Then, as shown in the block diagram, proposed method i.e PCA is applied on these signals and their characteristic points are computed.

After that, on the basis of these characteristic points, ECG signals are classified using the three different classifiers i.e. ANN, Fuzzy and Neuro-Fuzzy classifiers.

Copyright to IARJSET

IARJSET
ISSN (Online) 2393-8021
ISSN (Print) 2394-1588
International Advanced Research Journal in Science, Engineering and Technology
ISO 3297:2007 Certified
Vol. 3, Issue 7, July 2016

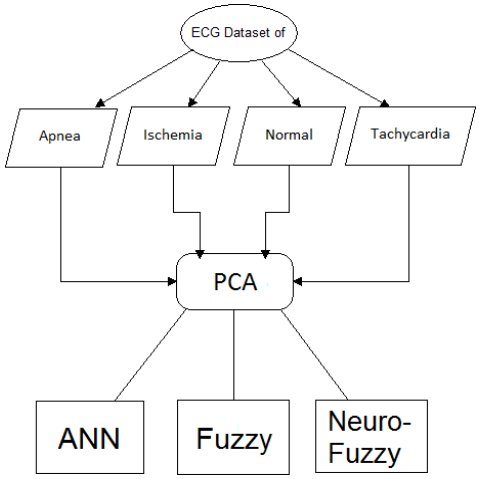

Fig.2. Block Diagram of the Proposed method

III. PROPOSED METHOD

A. Data-Set

Dataset is taken from the MIT-BIH database for the different types of ECG signals utilized during this research. Among these signals, Apnea, Ischemia and Tachycardia are the three types of situations in the subjects having heart related problems with normal signal as the fourth type.

Dataset for ECG detection is loaded from the MIT-BIH database of Physiobank ATM. It is shown below in the Table II. These signals are explained in brief in the sub-sections.

TABLE II
DESCRIPTION OF DATASET USED

ECG Signals	Training	Testing	Total
Apnea	18	12	30
Normal	18	12	30
Ischemia	18	12	30
Tachycardia	18	12	30

a. Normal ECG

Fig.3 represents an ECG waveform showing the heart condition of a normal human being. Comparing with the Fig.1, P-QRS-T points are observable in the Fig.3.

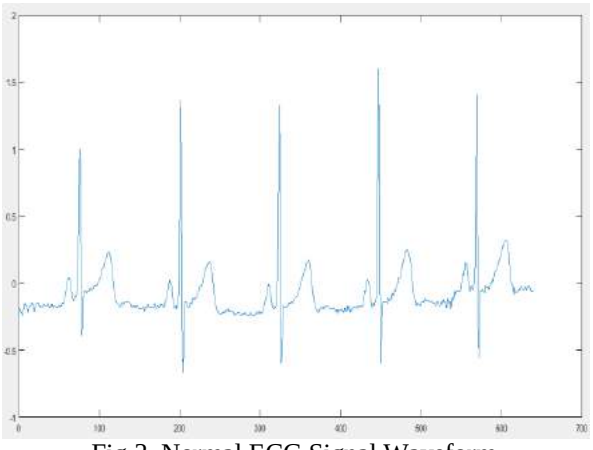
Fig.3. Normal ECG Signal Waveform

TABLE III
DIFFERENT PHASES IN NORMAL ECG

Section of ECG	Source
P-Wave	Record the electrical activity through the upper heart chambers (Atria Excitation)
QRS-Complex	Record the movement of electrical impulses through the lower heart chambers. (Atria repolarization + Ventricle depolarization)
T-Wave	Corresponds to the period when the lower heart chambers are relaxing electrically and preparing for their next muscle contraction. (Ventricle repolarization)
ST Segment	Corresponds to the time when the ventricle is contracting but no electricity is flowing through it.

In the Table III, normal ECG signal is explained that how the peaks in ECG are obtained depending on the different situations in the heart.

b. Apnea

Apnea is defined as ECG waveform obtained during the intermittent halt of breathing in the subject. It is due to the irregular sleep and related to the accrued risks of high pressure level. It is shown in the Fig.4.

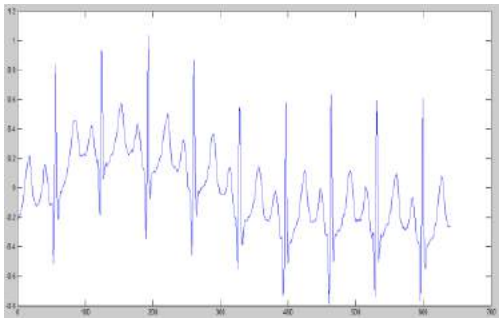
Fig.4. Apnea Signal Waveform

c. Ischemia

Ischemia is a type of ECG signal in which T wave is inverted. In this, sometimes, decrease in the amplitude and disappearance of the R wave may also occur. This type also includes a shift of the ST segment. It is shown in the Fig.5.

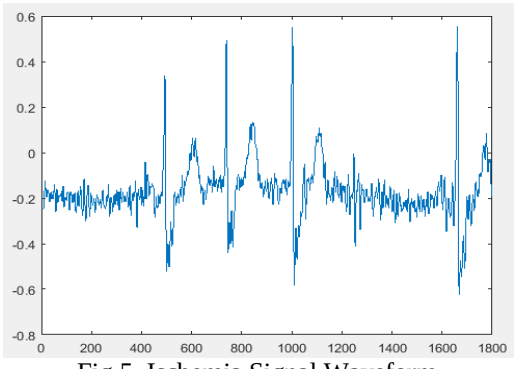

Fig.5. Ischemia Signal Waveform

IARJSET
ISSN (Online) 2393-8021
ISSN (Print) 2394-1588
International Advanced Research Journal in Science, Engineering and Technology
ISO 3297:2007 Certified
Vol. 3, Issue 7, July 2016

d. Tachycardia
Tachycardia is a condition in the ECG in which atrial and ventricular rates are accelerated exceeding the normal ECG rate. Beats in the tachycardia are regular but comparatively faster. It is also observed by the presence or absence of the P or flutter waves in the signal.

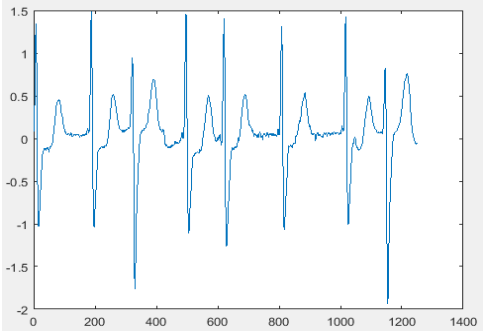

Fig.6. Tachycardia Signal Waveform

B. PCA
PCA is an orthogonal linear transformation. It transfers the data to a new frame of reference such the largest variance of any projection of the information involves lie on the first coordinate (first principal component), the second largest variance lies on the second coordinate (second principal component), and so on. Linear projection method to reduce the number of parameters. Map the data into a space of lower dimensionality.

PCA Algorithm:
Let X be an input data set.
Now, Perform the following steps:

Calculate the mean:

$$m[p] = \frac{1}{Q}\sum_{q=1}^{Q} X[p,q] \qquad (1)$$

Calculate the mean deviation and keep the data in the matrix $D_m[P \times Q]$:

$$D_m = X - m.h \qquad (2)$$

where h is a 1 × Q row vector of all 1's:

h[q] = 1 for n = 1, …....Q

Find the covariance matrix Cv:

$$Cv = D_m.D_m^{\ T} \qquad (3)$$

Find the eigenvectors and eigen values of the covariance matrix $V^{-1}CvV$ where V is the eigenvectors matrix. D is the diagonal matrix of eigen values of Cv.

$$D[m,n] = \lambda_p \qquad (4)$$

for m = n = p is the m^{th} eigen value of the covariance matrix Cv.
Rearrange the eigen values

$$\lambda_1 \geq \lambda_2 \geq \lambda_3 .... \geq \lambda_Q \qquad (5)$$

Choosing components and forming a feature vector: save the first L columns of V as the M × L matrix W,

$$W[m, n] = V[m, n], \qquad (6)$$

for m = 1, . . . ,P
n = 1, . . . , L where $1 \leqslant L \leqslant P$.

Deriving the new data set: The eigenvectors with the maximum eigen values are projected into space. This projection results in a vector represented by fewer dimension (L < P) containing the essential coefficients only.

C. ANN
Firstly, ECG classification is also done using Artificial Neural Network (ANN). In this also, train the network first by using some training data. A suitable training algorithm results in an ANN which is capable of generating a non-linear mapping function with the proficiency of demonstrating relationships between given ECG features and cardiac disorders.

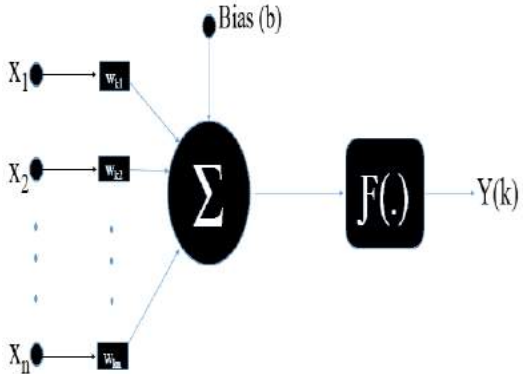

Fig.7. ANN Model

$$u_k = \sum_{j=1}^{n} x_j.w_{kj} \qquad (10)$$

$$v_k = u_k + b_k \qquad (11)$$

A well designed ANN will exhibit good generalization when a correct input output mapping is obtained even when the test input is slightly different from the data used to train the network.

D. FUZZY
Zong and Jiang (1998) described the method of fuzzy logic approach single channel ECG beat and rhythm detection. The method summarized and makes use of the medical knowledge and diagnostic rules of cardiologists. Linguistic

IARJSET
ISSN (Online) 2393-8021
ISSN (Print) 2394-1588
International Advanced Research Journal in Science, Engineering and Technology
ISO 3297:2007 Certified
Vol. 3, Issue 7, July 2016

variables have being used to represent beat features and fuzzy conditional statements perform reasoning. The algorithm can identified rhythms as well as individual beats. This method also handling the beat features and reasoning process is heuristic and seems more reasonable as stated in their paper. It also presented that this method may be of great utility in clinical applications such as multi-parameter patient monitoring systems, where many physiological variables and diagnostic rules exist.

E. NEURO-FUZZY

Neuro-Fuzzy classifier consists of five layers of nodes out of the five layers, the first and the fourth layers consist of adaptive nodes there are Fuzzification and Defuzzification, while the second, third and fifth layers consist of fixed nodes there are Rule, Normalization, and Summation neuron. The Neuro-Fuzzy classifier to implement the Fuzzy rules is shown in Fig.8, in which a circle indicates a fixed node, whereas a square indicates an adaptive node.

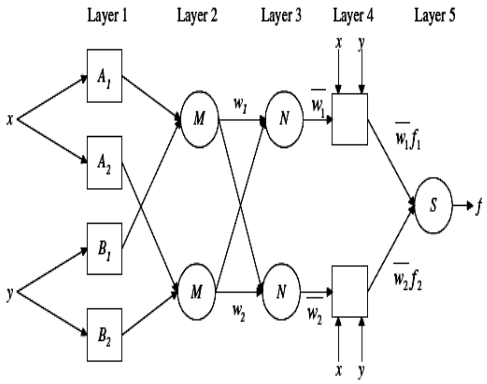

Fig.8. Neuro-Fuzzy architecture

Layer 1: Fuzzification layer Every node I in the layer 1 is an adaptive node. The outputs of layer 1 are the fuzzy membership grade of the inputs, which are given by:

$$O_i^1 = \mu_{A_i}(x), \forall i = 1,2 \quad (12)$$

$$O_i^1 = \mu_{B_{i-2}}(y), \forall i = 3,4 \quad (13)$$

where x and y is the inputs to node i, where A is a linguistic label (small, large) and where $\mu_{Ai}(x)$, $\mu_{Bi\text{-}2}(y)$ can adopt any fuzzy membership function.

Usually we choose $\mu_{Ai}(x)$ to be bell-shaped with maximum equal to 1 and minimum equal to 0, such as:

$$\mu_{A_i}(x) = \frac{1}{1+\{((x-c_i)/a_i)^2\}^{b_i}} \quad (14)$$

where (a_i, b_i and c_i) are the parameters of the membership function. Parameters are referred to as premise parameters.

Layer 2: Rule layer a fixed node whose output is the product of all the incoming signals, The outputs of this layer can be represented as:

$$O_i^2 = w_i = \mu_{A_i}(x).\mu_{B_i}(y), i = 1,2 \quad (15)$$

Layer 3: Normalization layer are also fixed node is a circle node.

$$O_i^3 = w_i = \frac{w_i}{w_1 + w_2}, i = 1,2 \quad (16)$$

Layer 4: Defuzzification layer an adaptive node with a node the output of each node in this layer is simply the product of the normalized firing strength and a first order polynomial.

$$O_i^4 = w_i.f_i = w_i(p_i x + q_i y + r_i), i = 1,2 \quad (17)$$

Layer 5: Summation neuron a fixed node which computes the overall output as the summation of all incoming signals.

$$O_i^5 = \frac{\sum_{i=1}^{2} w_i f_i}{w_1 + w_2} \quad (18)$$

IV. RESULTS & DISCUSSION

Now, in the results, Eigen values computed from the PCA algorithm are utilized to detect the characteristic points in the ECG signals. These characteristic points includes Q, R,S and T peaks of the different types of ECG signals viz. Apnea, Ischemia Normal and Tachycardia signals.

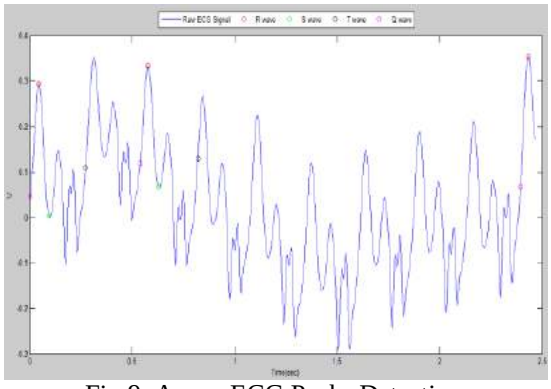

Fig.9. Apnea ECG Peaks Detection

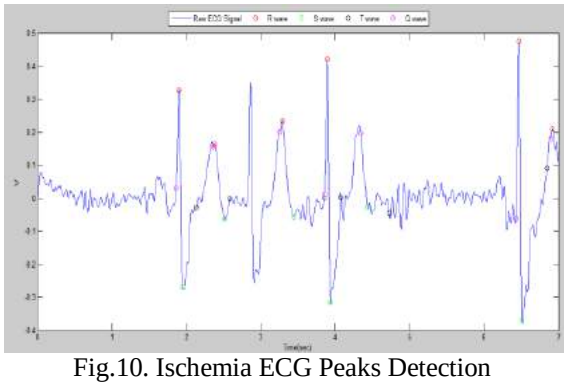

Fig.10. Ischemia ECG Peaks Detection

IARJSET
ISSN (Online) 2393-8021
ISSN (Print) 2394-1588
International Advanced Research Journal in Science, Engineering and Technology
ISO 3297:2007 Certified
Vol. 3, Issue 7, July 2016

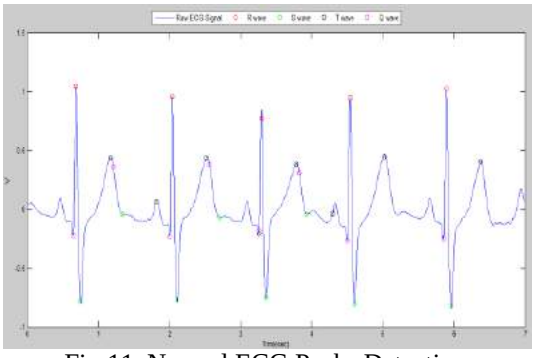

Fig.11. Normal ECG Peaks Detection

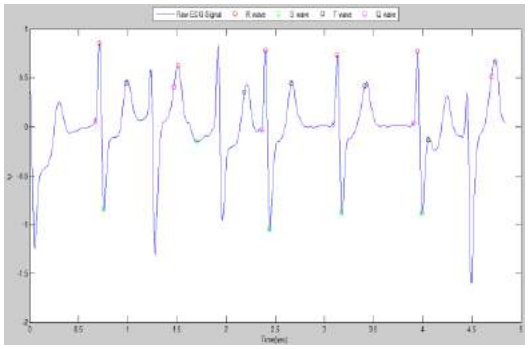

Fig.12. Tachycardia ECG Peaks Detection

In the Fig.9-12 shows the parameter detection in the ECG signals selected as sample from the datasets. It can be observed from the signals figures that variation among the signals can be observed.

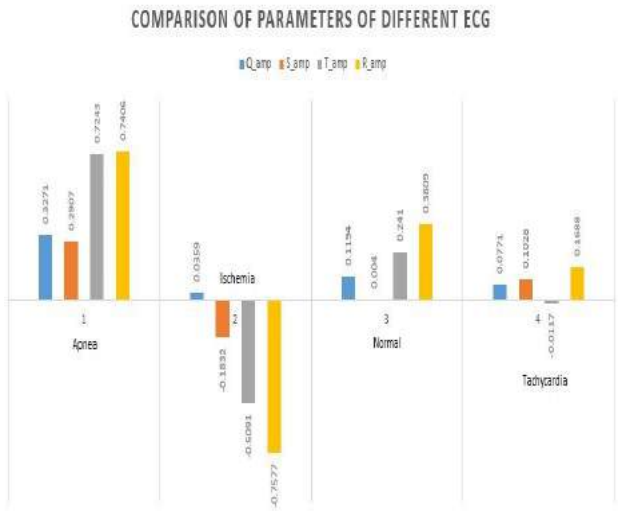

Fig.13. Comparison of characteristic points of different ECGs

Next in the Fig.13 shows is the graph representing the comparison among the feature values extracted using the Principal Component Analysis (PCA) algorithm. And it can be observed from the figure that there is difference among the characteristic points i.e. Q, R, S and T peaks. Now, these parameters obtained, are used in the classifiers for the classification of these ECG signals. For the classification, firstly ANN is used. In this classifier, 120 subjects dataset is used in total. Among these, 72 subjects are used to train the ANN and 48 are tested on this trained classifier as shown in the Fig.14. The results from the ANN classifier are shown in the Table IV which shows a confusion matrix of the tested dataset. In this table, AP, IS, NR and TC represents Apnea, Ischemia, Normal and Tachycardia respectively.

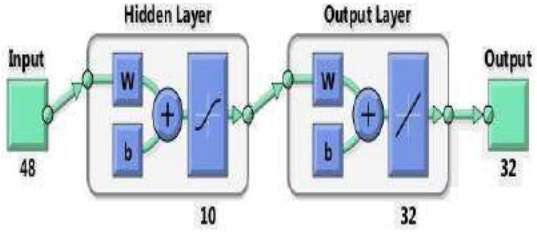

Fig.14. Neural Network

TABLE IV
CONFUSION MATRIX FROM ANN

Targets / Outputs	AP	IS	NR	TC	Accuracy
AP	9/12	1/12	0/12	2/12	75%
IS	0/12	11/12	0/12	1/12	91.67%
NR	0/12	0/12	12/12	0/12	100%
TC	0/12	1/12	1/12	10/12	83.33%

According to this table, an accuracy of 87.5% is observed which is very good and gives only satisfactory results. Next, Fuzzy is applied on these feature values obtained using these ECG datasets.

Now, the dataset is applied on the Fuzzy logic for the classification purpose. Fig.15 shows the modelling of Fuzzy Logic which helps in the classification of the ECG signal classes. Then the Fig.16-17 shows the membership functions for the inputs (Gaussian) and outputs (Triangular) respectively. In the Table V shown is the confusion matrix for the Fuzzy classifier. The table shows good accuracy in classifying the different types of ECG signals used during this project. An accuracy of 91.70% is achieved using this classifier.

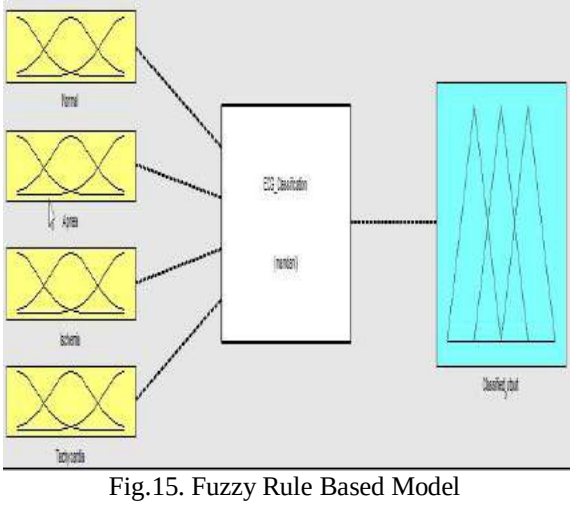

Fig.15. Fuzzy Rule Based Model

Copyright to IARJSET
DOI 10.17148/IARJSET.2016.3717

IARJSET
ISSN (Online) 2393-8021
ISSN (Print) 2394-1588
International Advanced Research Journal in Science, Engineering and Technology
ISO 3297:2007 Certified
Vol. 3, Issue 7, July 2016

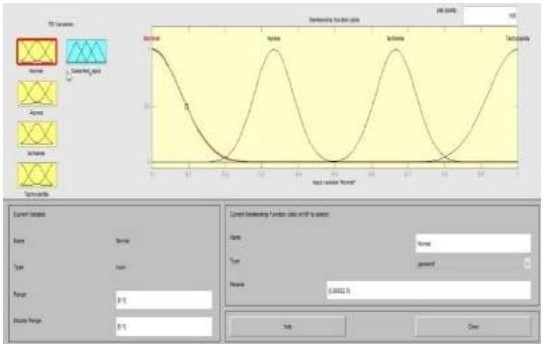

Fig.16. Membership functions for Inputs

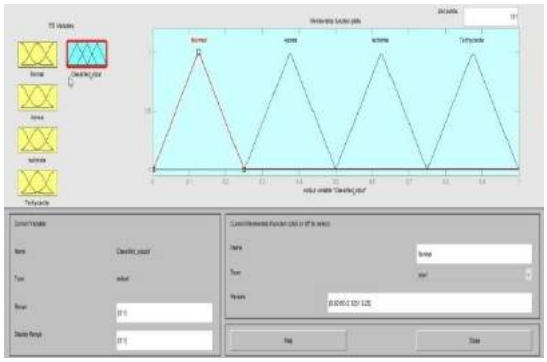

Fig.17. Membership Function for Output

TABLE V
CONFUSION MATRIX FROM FUZZY

Targets / Outputs	AP	IS	NR	TC	Accuracy
AP	10/12	0/12	0/12	2/12	83.33%
IS	0/12	11/12	0/12	1/12	91.67%
NR	0/12	0/12	12/12	0/12	100%
TC	0/12	0/12	1/12	11/12	91.67%

Even now, some signals are mis-classified using this classifiers which is corrected using the hybrid of Neural network and the fuzzy classifiers. Neuro-Fuzzy Classifier. Therefore, next classifier used is the Neuro-Fuzzy classifier for the classification of different types of ECG signals.

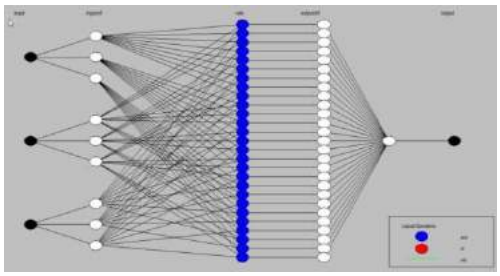

Fig.18. Neuro-Fuzzy Structure

Neuro-Fuzzy Logic is applied on the ECG signals according to the structure shown in the Fig.18. This is a Neuro-Fuzzy structure. It is a multi-layer neural network with fuzzy rules inbuilt in it. In this, Fuzzy rules are used in the hidden layer of the Neural Network and hence, named as Neuro-Fuzzy Classifier.

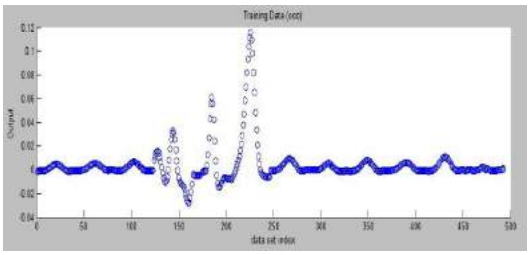

Fig.19. Training data

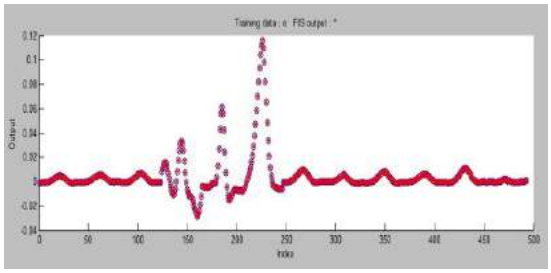

Fig.20. Trained data

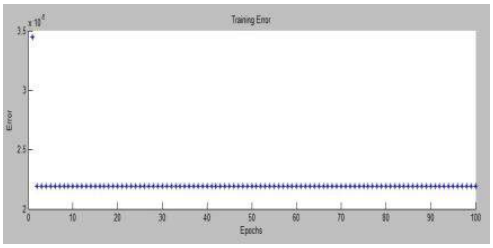

Fig.21. Training error

Now, in Fig.19-21, shows about the training data that how it will look during training (Fig.19), after training (Fig.20) and the error comes during training (Fig.21).

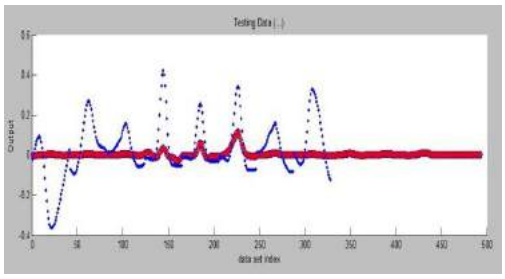

Fig.22. Testing data

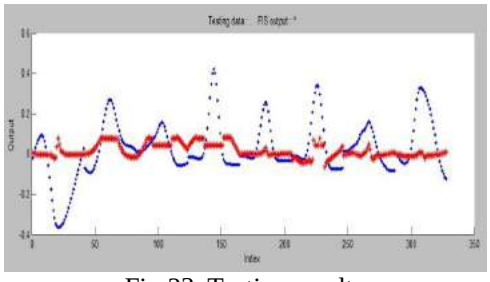

Fig.23. Testing results

Then next figures shows about testing using the Neuro-Fuzzy classifier. Among these figures, Fig.22-23 shows the testing data and testing results. And, Fig.24 represents the rule viewer which are made using the Fuzzy logic in this classifier.

Copyright to IARJSET
DOI 10.17148/IARJSET.2016.3717

IARJSET
ISSN (Online) 2393-8021
ISSN (Print) 2394-1588
International Advanced Research Journal in Science, Engineering and Technology
ISO 3297:2007 Certified
Vol. 3, Issue 7, July 2016

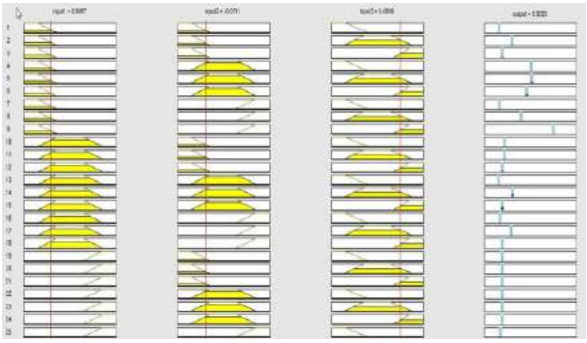

Fig.24. Neuro-Fuzzy rules

Then next, in Table VI, confusion matrix is shown showing the classification using Neuro-Fuzzy classifier. And it can be seen from the table that only 1-1 signals (AP and IS) are misclassified in the other classes but all other signals are accurately classified using this classifier.

TABLE VI
CONFUSION MATRIX FROM NEURO-FUZZY

Targets / Outputs	AP	IS	NR	TC	Accuracy
AP	11/12	1/12	0/12	0/12	91.67%
IS	1/12	11/12	0/12	0/12	91.67%
NR	0/12	0/12	12/12	0/12	100%
TC	0/12	0/12	0/12	12/12	100%

Then in Table VII shown is the comparison of all these classifiers used during this research and it is perceived from the table that Neuro-Fuzzy classifier used gives the best results.

TABLE VII
COMPARISON OF THREE CLASSIFIERS

Classifier Name	Accuracy(%)
ANN	87.5
Fuzzy	91.70
Neuro-Fuzzy	95.83

V. CONCLUSION

The proposed method in this research paper utilizes Principal Component Analysis (PCA) algorithm to classify the different types of ECG signals viz. Apnea, Ischemia, Normal and Tachycardia signals, used during this research which have different characteristic points obtained using the principal component analysis algorithm. Accuracy obtained with the Neuro-Fuzzy classifier is upto 96% (approx.) which is more than the previous methods used and hence, this method can also be utilized by the doctors to classify various ECG signals.

REFERENCES

[1] Sahil Dalal, Rajesh Birok, "ECG Peaks Detection using Principal Component Analysis", International Journal of Innovative Research in Electrical, Electronics, Instrumentation and Control Engineering, Volume 4, Issue 7, pp. 66-70, 2016.
[2] Sahil Dalal, Rajesh Birok, "ECG Signals Analysis using PCA with Neural Network and Fuzzy Logic", International Journal of Advanced Research in Electronics & Communication Engineering (under publication).
[3] T.-W. D. Shen, W. J. Tompkins, and Y. H. Hu, "Implementation of a one-lead ECG human identification system on a normal population," J. Eng. Comput. Innovations, vol. 2, no. 1, pp. 12–21, Jan. 2011.
[4] A. D. C. Chan, M. M. Hamdy, A. Badre, and V. Badee, "Wavelet distance measure for person identification using electrocardiograms," IEEE Trans. Instrum. Meas., vol. 57, no. 2, pp. 248–253, Feb. 2008.
[5] C.-C. Chiu, C.-M. Chuang, and C.-Y. Hsu, "A novel personal identity verification approach using a discrete wavelet transform of the ECG signal," in Proc. 2nd Int. Conf. Multimedia and Ubiquitous Engineering, Busan, Korea, 2008.
[6] J. Yao and Y. Wan, "A wavelet method for biometric identification using wearable ECG sensors," in Proc. 5th Int. Summer School and Symp. Medical Devices and Biosensors, 2008 (ISSS-MDBS 2008), pp. 297–300.
[7] O. Boumbarov, Y. Velchev, and S. Sokolov, "ECG personal identification in subspaces using radial basis neural networks," in Proc. IEEE Int. Workshop on Intelligent Data Acquisition and Advanced Computing Systems: Technology and Applications, 2009 (IDAACS 2009), Sept. 2009, pp. 446–451.
[8] M. Homer, J. M. Irvine, and S. Wendelken, "A model-based approach to human identification using ECG," in Proc. SPIE, Orlando, FL, 2009, vol. 7306.
[9] F. Agrafioti and D. Hatzinakos, "Signal validation for cardiac biometrics," in Proc. 2010 IEEE Int. Conf. Acoustics Speech and Signal Processing (ICASSP), Mar. 2010, pp. 1734–1737.
[10] A. Lourenço, H. Silva, and A. Fred, "Unveiling the biometric potential of finger-based ECG signals," Computat. Intell. Neurosci., vol. 2011, no. 720971, 2011.
[11] B.U. Kohler, C. Hennig, R. Orglmeister, The principles of software QRS detection, IEEE Eng. Med. Biol. Mag. 21 (1) (2002) 42–57.
[12] C. Saritha, V. Sukanya, Y. Narasimha Murthy, ECG analysis using wavelets, Bulg. J. Phys. 35 (2008) 68–77.
[13] P. Ranjith, ECG analysis using wavelet transform: application to myocardial ischemia detection, ITBM-RBM 24 (January) (2003) 44– 47.
[14] J. Pan, W.J. Tomkins, A real time QRS detection algorithm, IEEE Trans. Biomed. Eng. 32 (3) (1985).
[15] O. Pahlm, L. Sörnmo, Software QRS detection in ambulatory monitoring – a review, Med. Biol. Eng. Comput. 22 (July) (1984) 289–297.
[16] F. Gritzali, Toward a generalized scheme for QRS detection in ECG waveforms, Signal Process. 15 (September) (1988) 183–192.
[17] G.M. Friesen, T.C. Jannett, M.A. Jadallah, S.L. Yates, S.R. Quint, H.T. Nagle, A comparison of the noise sensitivity of nine QRS detection algorithms, IEEE Trans. Biomed. Eng. 37 (January) (1990) 85–98.
[18] A. Ghaffari, H. Golbayani, M. Ghasemi, A new mathematical based QRS detector using continuous wavelet transform, Comput. Electr. Eng. 34 (2) (2008) 81–91.
[19] A.S.M. Koeleman, H.H. Ros, T.J. van den Akker, Beat-to-beat interval measurement in the electrocardiogram, Med. Biol. Eng. Comput. 23 (August) (1985) 213–219.
[20] Kang-Ping Lin, Walter H. Chang, QRS feature extraction using linear prediction, IEEE Trans. Biomed. Eng. 36 (10) (1989).
[21] I.K. Daskalov, I.A. Dotsinsky, I.I. Christov, Developments in ECG acquisition, preprocessing, parameter measurement and recording, IEEE Eng. Med. Biol. Mag. 17 (September) (1998) 50–58.
[22] Abdulnasir Hossen, Bader Al-Ghunaimi, A wavelet-based soft decision technique for screening of patients with congestive heart failure, Biomed. Signal process. Control 2 (May) (2007) 135–143.
[23] J.G.C. Kemmelings, A.C. Linnenbank, S.L.C. Muilwijk, A. Sippens-Groenewegen, A. Peper, C.A. Grimbergen, Automatic QRS onsetand offset detection for body surface QRS integral mapping of ventricular tachycardia, IEEE Trans. Biomed. Eng. 41 (September) (1994) 830–836.
[24] E.S. Jayachandran, K. Paul Joseph, R. Acharya U, Analysis of myocardial infarction using discrete wavelet transform, J. Med. Syst. 34 (October) (2010) 985–992.
[25] C. Li, C. Zheng, C. Tai, Detection of ECG characteristic points using wavelet transforms, IEEE Trans. Biomed. Eng. 42 (January) (1995) 21–28.
[26] J.S. Sahambi, S. Tandon, R.K.P. Bhatt, Using wavelet transform for ECG characterization, IEEE Eng. Med. Biol. 16 (1) (1997) 77–83.
[27] Themis P. Exarchos et al., Association rule-mining based methodology for automated detection of ischemic ECG beats, IEEE Trans. Biomed. Eng. 53 (8) (2006).

Copyright to IARJSET

ResearchGate

See discussions, stats, and author profiles for this publication at: https://www.researchgate.net/publication/303933405

Automatic Attendance System By Visual Programming Language LabVIEW

Conference Paper · July 2016

READS
33

4 authors, including:

P. K. Verma
Delhi Technological University
7 PUBLICATIONS **2** CITATIONS

SEE PROFILE

All in-text references underlined in blue are linked to publications on ResearchGate, letting you access and read them immediately.

Available from: P. K. Verma
Retrieved on: 04 August 2016

Automatic Attendance System by Visual Programming Language LabVIEW

Amit Kumar[1], P.K. Verma[2], Srinivas Perala[3] and P.R. Chadha[4]
[1,2,4]*Department of Electronics and Communication Engineering, Delhi Technological University, New Delhi, India*
[3]*Digilogic Systems Pvt. Ltd, Hyderabad, India*
E-mail: [1]amit.ece.tech@gmail.com, [2]pappuverma@dtu.ac.in, [3]srinivaslabview@gmail.com, [4]prchadha@dce.ac.in

***Abstract*—This paper presents an application of LabVIEW and camera interface which is used for taking attendance in classroom. The system use a camera which is connected to PC on USB interface and attached to each and every classroom for taking snap of students presented. LabVIEW graphical programming environment is a tool for realizing the image acquisition and processing. This software has several advantages: simple implementation, modularity, flexibility, attractive user interface and possibility to develop very easy new features. Face recognition and machine vision applications in automatic inspection of various electronic modules can also be implemented using given algorithm.**

Keywords: Pattern Recognition, Image Processing, Image Acquisition, Virtual Instuments(vi), LabVIEW, Digital Image

I. INTRODUCTION

The Prevailing attendance system in the University works manually and is taken by the faculty or the course instructor by the Roll/Registration id call and the attendance is marked for every hour for the students and the responses are saved in an online interface being used for all the University purposes called the UMS or University Management System. This process is taking more time for attendance.

So for reduce this wastage of time this system of taking attendance can be used. Usually 3-5 minutes are wasted in conventional attendance system. But in this new system it is just taking 1-2 seconds in whole process of attendance. So it will to save the time.

In this process a camera is used in every classroom which is connected to PC on USB port. When faculty wants to take attendance he just has to switch on the process [1]. The attached camera will take a snap of whole class. It sends this image to PC and then it is decided that which student is present and who is not. PC operates an algorithm of image processing for taking decision for present and absent students. Using this approach it is allowed to store the captured image for later processing. After taking decision it created a excel sheet of present and absent students or it can also modify exist excel sheet or data.

The applications presented in paper consist in an attendance system which is capable to recognize face and monitor the present and absent students. By the use of modular realization of both software and hardware parts [2], the system can be easily operated with multiple cameras.

In recent years, face recognition becomes very popular [3] and the research on it has rapidly increased by engineers. It has large applications in neuroscience. It has many features in computer vision, machine vision, communication, bio medical and automatic product inspection. Face detection plays critical role in face recognition [4-6]. It is first step for automatic face recognition. But, in case of face detection there are several variations like occlusion, orientation of image, variations of pose, facial expression, and orientation of image.

The organization of the rest of the paper is as follows. In section II, describes the image acquisition. Mathematical representation of digital image is explained in section III. Section IV shows the pattern matching using LabVIEW. Section V, gives the conclusion of proposed system.

II. IMAGE ACQUISITION

Image is generally associated with light incident and reflected from scene. Hence, light distribution in the scene is one of variables information of images. Since the formation of image of any object depends of the interaction of the light with object in any scene and the energy emitted from one or different sources light changes in its trip.

In Fig. 1 it is shown that how to acquire video from a webcam by using LabVIEW and NIVision Acquisition Express located in Vision/Vision Express toolbox. This method is the simplest way to acquire the image or video from camera and also to configure the camera. In NI Vision Acquisition configuration block four sections are there: the first section is the option of "select acquisition source" [1]. Inside this option it shows all the cameras connected with the computer which is used. We can select the required camera used. The second section is "select acquisition type" which determines that what should be the mode of display the image. It has four modes: single acquisition with processing, continuous acquisition with inline processing, finite acquisition with inline processing, and finite acquisition with post processing we can choose any one of these option according to our requirement. The next option corresponds to the "configure acquisition settings" it shows the constraints of camera like size, brightness, contrast, gamma, saturation, etc. of the image taken by camera. The fourth and last section is to select controls and indicators. In Fig. 1 continuous acquisition with inline processing is selected. It will acquire the image

978-1-4673-8586-2/16/$31.00 ©2016 IEEE

and display in continuous mode or video mode. It will keep displaying the real time acquired image until the user presses the stop button.

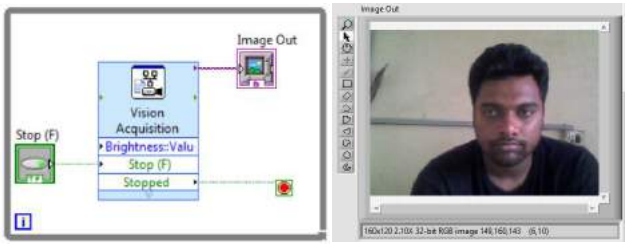

Fig. 1: Video Acquisition using IMAQ Vision Acquisition Express

III. Mathematical Representation of Digital Image

An image is represented as an MxNelementsmatrix [5]. The elements of matrix have a value which is corresponding to pixel values of digitized image of brightness of each and every point in acquired image.

Image can be of resolution in intensity8 bits, 16 bits and so on. An image of 8 bits resolution in intensity has values from 0 to 255. For black and white image the values are either 0 or 1. In general, an image is represented in a bi dimensional matrix as shown in (1).

$$I = \begin{pmatrix} x_{11} & x_{12} \cdots & x_{1n} \\ x_{21} & x_{22} \cdots & x_{2n} \\ \vdots & \vdots \ddots & \vdots \\ x_{n1} & x_{n2} \cdots & x_{nn} \end{pmatrix} \quad (1)$$

According to the depth of acquired image from most of the cameras acquires with a depth of 8 bits so generally the range of gray scale levels is from 0 to 255 for an image so the elements of matrix represented by $x_{ji} \epsilon [0 \ldots 255]$. So from this concept we can say that the acquired RGB format image can easily transformed in gray scale image by using Grassman formula. Grassman formula is:

$$I_{gray} = I_R(0.299) + I_G(.587) + I_B(.114) \quad (2)$$

Where, I_{gray}= Gray scale image, I_R= Red component of color image, I_G= Green component of color image, I_B= Blue component of color image

IV. Pattern Matching using LabVIEW

A. Pattern Recognition

For the recognition and detection of object pattern recognition is a useful technique. This algorithm becomes simple and accurate for finding a template in an image. Along with the searches of exact apparition of image this algorithm also finds a definite status of variation with respect to exact pattern. The simplest method of pattern recognition is the template matching.

Definition of image M is the difference function between segments of the image:

$$M(x.y) = \sum_{a=0}^{w} \sum_{b=0}^{h} (P(a.b) - A(x+a, y+b))^2 \quad (3)$$

Where, M(x, y)= Final Image, P(a, b)= Template pixel values, A(x+a, y+b)=Pixel values of real time image.

In Fig. 2 shows the block diagram of acquiring the video and the pattern recognition system. Here for continuous acquisition from the camera with acquisition option of inline processing was used; hencea while loop is present inside the blocks of video acquisition. First of all the important thing is to transform the acquired video into intensity values or gray scale image. One option is to change RGB values to intensity values is by using IMAQ extract single color plane available in vision utilities/color utilities. The input for pattern recognition function will be always gray scale image.

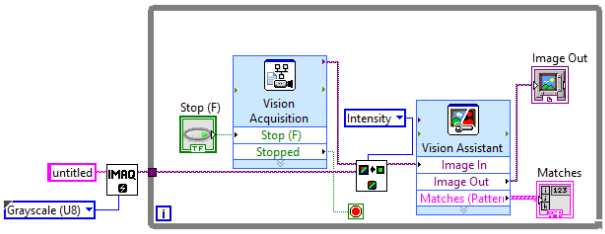

Fig. 2: Block Diagram of Pattern Recognition

For pattern recognition the function available in LabVIEW is vision assistance. As shown in Fig. 3 (a) machine vision function was selected. To create new template click in the option new template and the select required portion of image which we want to use as template as shown in Fig. 3(b).

Fig. 3 (a): Selection of Pattern Matching

In last the vision assistant function which is having the pattern matching algorithm will identifies the desired object according to template in the whole in Fig. 4. At last when program will execute in real time it identifies the desired object in the whole image [1].

A remark is needed to obtain the recognized matches. The checkbox must be selected inside the control parameters. The output of vision assistant is a cluster that contains different information. This cluster can be unbundled to form a rectangular box which can locate the matches.

978-1-4673-8586-2/16/$31.00 ©2016 IEEE

Fig. 3 (b): Creation of New Template

Fig. 4: Recognition of Template in Whole Image

B. *Procedure of Face Detection using LabVIEW*

We easily detect a pattern from an image or a video. For this first of all we take a snap of original image then store the interested part in LabVIEW buffer[6]. In our project we have to detect the face so we take the snap of face of the person as shown in Fig. 5. Store the pattern of that face in LabVIEW function Image Assistant. When we run the program and the same face (Pattern) comes in front of camera then it detects that pattern and gives result in the form of matrix.

Fig. 5: Detecting Key Points of Patterns

C. *Block Diagram of Face Recognition*

The block diagram of face recognition using pattern recognition method is given in Fig. 6 (a) and Fig. 6 (b).

In this paper, we are having all the database of the students in MS-Excel sheet. We store this data base in LabVIEW buffer. For acquire the real time image from camera vision acquisition is used by giving the path of camera. After getting image use vision assistant express VI. Inside vision assistant pattern-matching function is there. Take the key parts of faces of each student inside this express VI [9].

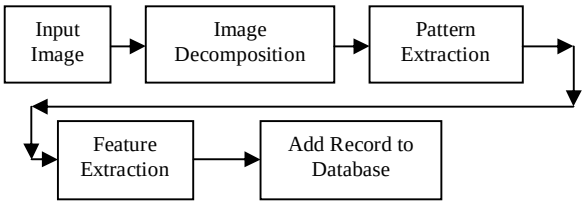

Fig. 6 (a): Procedure for Feature Extraction

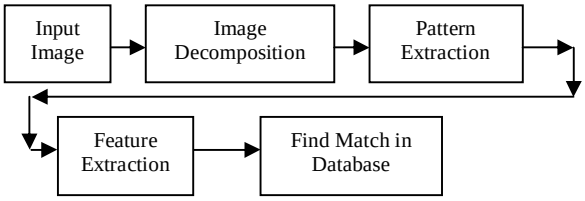

Fig. 6 (b): Procedure for Recognition

At the time of taking the attendance then click the start button, the camera is attached with the vision acquisition and takes the image of the class in top angle view. And after that taking image it sends this to vision assistance where all the reference images are saved. It compares each individual picture to the whole of the image of the class and gives the output as a matrix of 1 and zero with respect to each and every student. By using this matrix LabVIEW decide which student is present and which is not present (absent). The matched patterns of the students are marked as present and rest are marked as absent. After that we use the write to spread sheet, give the output list of present and absent students in an MS-Excel sheet.

D. *Block Diagram of Image Acquisition and Processing*

In the Fig. 7, it is shown that two express VI's used (vision acquisition and vision assistant) [8]. Vision acquisition is used to acquire the real time image from camera. Path of the camera is given inside the configure block of vision acquisition. IMAQ create function is used for giving a name of acquired image and save temporary in LabVIEW buffer.

Acquired image is in the form of color image but pattern matching is done in gray scale image only because pattern matching is based on intensity level of pixel values of image. So we have to convert it into gray scale by using IMAQ extract single color plane. Then gray scale image is given to vision assistant express VI. It finally takes the decision that who is present and who is not.

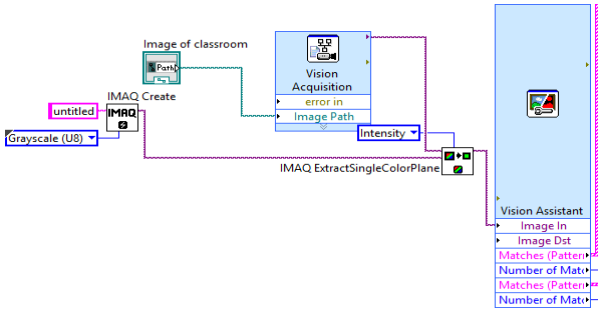

Fig. 7: Block Diagram of Image Acquisition and Processing

978-1-4673-8586-2/16/$31.00 ©2016 IEEE

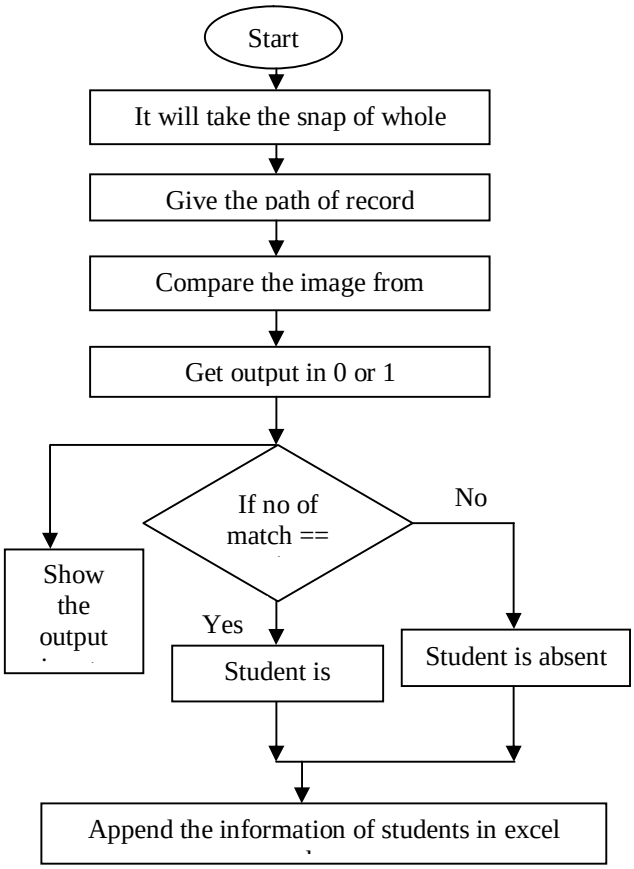

Fig. 8: Flow Diagram of Whole Process

E. *Procedure Involved*

1. Choose the image of class from a particular location.
2. Use a template which occupies the face of each student.
3. Give the Excel sheet path in which the student information will store.
4. The acquired image is in RGB format so convert the image to gray scale format.
5. Take the gray scale image and match it with template.
6. Use the function "no. of matches" which gives the output 1 if pattern match otherwise 0.
7. If output is 1 the student is present otherwise absent.
8. By using this information generate the Excel sheet.

F. *Design Flow Diagram*

This design flow diagram shown in the Fig. 8 represents the whole process from top to bottom.

G. *To Extract Data of Student from Excel Sheet*

For extracting details like roll no, name a function is used called read from spreadsheet. This function extract the excel sheet in rows and column. After extracting software will decide who is present and who is not. Block diagram for the same is shown in Fig. 9.

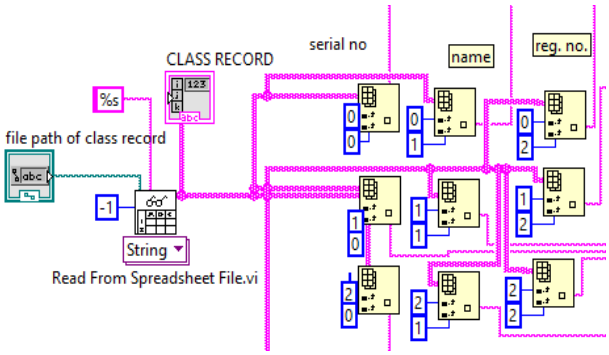

Fig. 9: Block Diagram to Extract Information of Student from Database

H. *Overlay a Rectangular Box over Faces of Present Student*

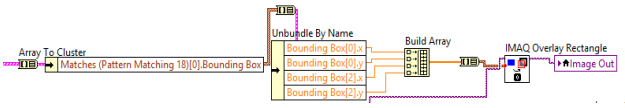

Fig. 10: Block Diagram to Overlay Rectangular Box on Image

At the location of identified student a rectangular box is overlay on the face as shown in Fig. 10. For this a function is used called IMAQ overlay rectangular.

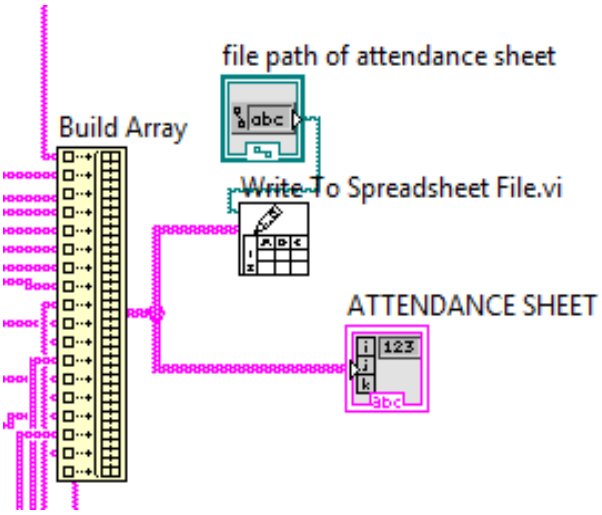

Fig. 11: Block Diagram to Append the Result

I. *Append and Final Result*

Finally append the status of each student and save it into excel sheet. For this we use write to spreadsheet function and block diagram in shown in Fig. 11.

J. *Front Panel*

Front panel is user interface of LabVIEW[10]. All controls and indicators are present in front panel. In this program front panel consist of Image out, 2-D array, image file input, excels file input and outputs are present as shown in Fig. 12.

978-1-4673-8586-2/16/$31.00 ©2016 IEEE

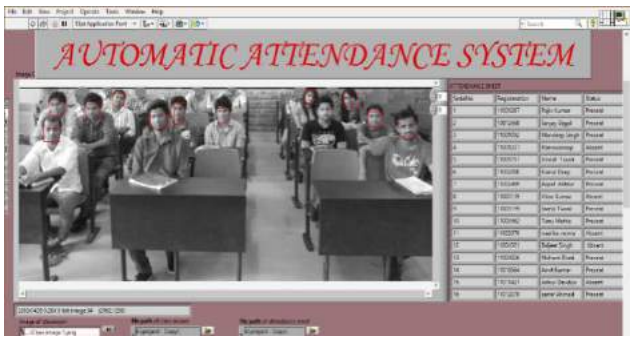

Fig. 12: Front Panel of Final Result

V. Conclusion

Number of modules has been designed and implemented on LabVIEW platform and Image Vision analysis tools in LabVIEW. The objective of automatic attendance system project is to take the students attendance automatically based on face recognition method using NI LabVIEW with Vision toolkit. It would be helpful to reduce the time for taking the attendance and also reduces the manual errors.

Acknowledgment

This work was supported by Delhi Technological University, New Delhi. I would like to thanks Mr. SrinivasPerala for their great support.

References

[1] I. Lita, D. A. Visan, I. B. Cioc, "LabVIEW application for movement detection using image acquisition and processing", *IEEE 16th International Symposium onDesign and Technology in Electronic Packaging (SIITME)*, pp. 225-228. 2010.

[2] Johnson, Gary, "LabVIEW graphical programming", 2nd Edition, *TMH*, 1997.

[3] Caixia Liu, "The Development Trend of Evaluating Face-Recognition Technology", *IEEE International Conference on Mechatronics and Control (ICMC)*, pp. 1540-1544, 2014.

[4] G. Prabhu Teja, S. Ravi, "Face Recognition using Subspaces Techniques", *IEEE International Conference onRecent Trends In Information Technology (ICRTIT)*, pp. 103-107, 2012.

[5] Taketo Horiuchi, Takuro Hada, "A Complementary Study for the Evaluation ofFace Recognition Technology", *IEEE 47th International Carnahan Conference on Security Technology (ICCST)*, pp. 1-5, 2013.

[6] Wuni xu, Lanxiang Zhong, Dingyuan Wang, "Image Processing Based on Seamless Integration Technology Between Lab VIEWandMATLAB", *IEEE International Conference on Information, Networking and Automation (ICINA)*, pp. 219-223, 2010.

[7] Jerome, Jovitha, "Virtual Instrumentation using LabVIEW" 1st Edition, PHI, 2010.

[8] Wang Lei, Shen yuming, "Design of Machine vision applications in Detection ofdefects in high-speed bar copper", *IEEE International Conference on E-Product E-Service and E-Entertainment (ICEEE)*, pp. 1-4, 2010.

[9] I. Laptev, J. Wills, P. Perez, S. J. Belongie, "Periodic Motion Detection and Segmentation via Approximate Sequence Alignment", IEEE International Conference on Computer Vision, vol. 1, pp. 816 – 823, 2005.

[10] P. Surekha, and S. Sumathi, "LabVIEW based Advance Instrumentation" 1st Edition, Springer, 2007.

Author's Accepted Manuscript

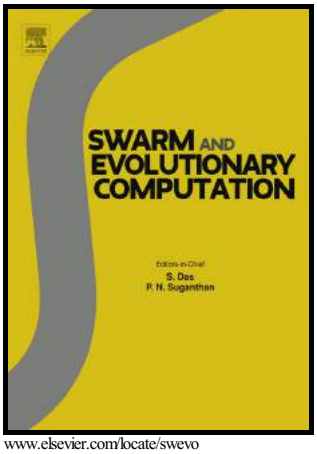

www.elsevier.com/locate/swevo

BFOA-scaled fractional order fuzzy PID controller applied to AGC of multi-area multi-source electric power generating systems

Yogendra Arya, Narendra Kumar

PII: S2210-6502(16)30188-2
DOI: http://dx.doi.org/10.1016/j.swevo.2016.08.002
Reference: SWEVO229

To appear in: *Swarm and Evolutionary Computation*

Received date: 12 March 2016
Revised date: 2 July 2016
Accepted date: 12 August 2016

Cite this article as: Yogendra Arya and Narendra Kumar, BFOA-scaled fractional order fuzzy PID controller applied to AGC of multi-area multi-source electric power generating systems, *Swarm and Evolutionary Computation* http://dx.doi.org/10.1016/j.swevo.2016.08.002

This is a PDF file of an unedited manuscript that has been accepted for publication. As a service to our customers we are providing this early version of the manuscript. The manuscript will undergo copyediting, typesetting, and review of the resulting galley proof before it is published in its final citable form. Please note that during the production process errors may be discovered which could affect the content, and all legal disclaimers that apply to the journal pertain.

ACCEPTED MANUSCRIPT

BFOA-scaled fractional order fuzzy PID controller applied to AGC of multi-area multi-source electric power generating systems

Yogendra Arya[a*], Narendra Kumar[b]

[a]Department of Electrical and Electronics Engineering, Maharaja Surajmal Institute of Technology, Janakpuri, New Delhi, India
[b]Department of Electrical Engineering, Delhi Technological University, Main Bawana Road, Delhi, India

[*]Email: mr.y.arya@gmail.com

Abstract

In the fast developing world of today, automatic generation control (AGC) plays an incredibly significant role in offering inevident demand of good quality power supply in power system. To deliver a quality power, AGC system requires an efficient and intelligent control algorithm. Hence, in this paper, a novel fractional order fuzzy proportional-integral-derivative (FOFPID) controller is proposed for AGC of electric power system. The proposed controller is tested for the first time on three structures of multi-area multi-source AGC system. The gains and fractional order parameters such as order of integrator (λ) and differentiator (μ and γ) of FOFPID controller are optimized using bacterial foraging optimization algorithm (BFOA). Initially, the proposed controller is implemented on a traditional two-area multi-source hydrothermal power system and its effectiveness is established by comparing the results with FOPID, fuzzy PID (FPID) and PI/PID controller based on recently published optimization techniques like hybrid firefly algorithm-pattern search (hFA-PS) and grey wolf optimization (GWO) algorithm. The approach is further extended to restructured multi-source hydrothermal and thermal gas systems. It is observed that the dynamic performance of the proposed BFOA optimized FOFPID controller is superior to BFOA optimized FPID/FOPID/PID and differential evolution/genetic algorithm optimized PID controllers. It is also detected that the dynamic responses obtained under different power transactions with/without appropriate generation rate constraint, time delay and governor dead-zone effectively satisfy the AGC requirement in deregulated environment. Moreover, robustness of the proposed approach is verified against wide variations in the nominal initial loading, system parameters, distribution company participation matrix structure and size and position of uncontracted power demand.

Keywords Multi-area multi-source system; Fractional order PID controller; Fuzzy PID controller; Automatic generation control; PI/PID controller; Restructured power system

Nomenclature

i	subscript referring to area (i = 1,2)	T_{CDi}	gas turbine compressor discharge volume time constant, s

Accepted manuscript

ACCEPTED MANUSCRIPT

F^0	nominal system frequency, Hz	cpf_{ij}	contract participation factor of jth DISCO with ith GENCO
R_i	speed governor regulation parameter, Hz/puMW	ΔP_{Di}^0	initial/nominal loading
D_i	system damping constant, puMW/Hz	ΔP_{gi}	incremental change in area power generation
B_i	frequency bias constant, puMW/Hz	ΔP_{Gi}	incremental change in GENCO power generation
K_{PSi}	power system gain	p	number of parameters to be optimized
T_{PSi}	power system time constant, s	S	number of bacteria
T_{Gi}	speed governor time constant, s	N_S	swimming length after which tumbling of bacteria will be carry out in a chemotactic loop
T_{Ti}	thermal turbine time constant, s	N_C	number of iterations to be undertaken in a chemotactic loop ($N_C > N_S$)
T_{RHi}	hydro turbine speed governor transient droop time constant, s	N_{re}	maximum number of reproduction to be carried out
T_{Ri}	hydro turbine speed governor reset time, s	N_{ed}	maximum number of elimination-dispersal events
T_{GHi}	hydro turbine speed governor main servo time constant, s	P_{ed}	probability with which elimination-dispersal will go on
T_{Wi}	water starting time constant, s	K_{1i}	proportional input scaling factor gain of fuzzy controller
T_{12}	synchronizing coefficient, puMW/rad	K_{2i}	derivative input scaling factor gain of fuzzy controller
X_i	gas turbine speed governor lead time constant, s	γ_i	order of input derivative of fuzzy controller
Y_i	gas turbine speed governor lag time constant, s	K_{Pi}	proportional gain of controller
a_i, c_{gi}	constants of valve positioner	K_{Ii}	integral gain of controller
b_{gi}	time constant of valve positioner, s	K_{Di}	derivative gain of controller
T_{CRi}	gas turbine combustion reaction time delay, s	λ_i	order of output integrator of fuzzy controller
T_{Fi}	gas turbine fuel time constant, s	μ_i	order of output derivative of fuzzy controller

1. Introduction

Increasing load demand in power system insists for interconnection of large number of generating units over existing transmission lines termed as tie-lines. The power transfer over existing interconnected tie-lines operating near their thermal limits results in low frequency power oscillations under sudden variation in power demand. Automatic Generation Control (AGC) is pertinent in order to mitigate these oscillations and to sustain scheduled system frequency of each control area and power flows over high voltage tie-lines during normal operating condition and small perturbations. Frequency depends on the balance in active power demand and generation. Under mismatch of active power in the system, frequency will deviate from its rated value with possibility of amplification of oscillations both of power and frequency. A sizeable fall in frequency might badly affect the timing of electric clocks and magnetizing currents in transformers/induction motors [1]. Additionally, the power system may face a serious instability problem at substantial drop in frequency. In steady state, automatically these variations must be zero. Enhanced power system stability is achieved with proper design of AGC system. However, continuous growth in size and complexity, stochastically changing power demands, system modeling errors and alterations in electric power system structures has turned AGC task a challenging one. Therefore,

Accepted manuscript

ACCEPTED MANUSCRIPT

conventional control strategies may be incompetent to handle such unpredictable variations in an AGC problem. Hence, the researchers over the world are trying to propose several novel control strategies that fuse knowledge, techniques and methodologies from varied sources to tackle AGC of power system. Various optimization and control techniques such as classical continuous-discrete mode I/PI [2], bacterial foraging optimization algorithm (BFOA) based I/PI [3–4], hybrid firefly algorithm-pattern search (hFA-PS) technique based PI/PID [5], grey wolf optimization (GWO) based PI/PID [6], differential evolution (DE) based PID [7], BFOA based fractional order PID (FOPID) [9], conventional FOPID [8,10], imperialist competitive algorithm (ICA) based FOPID [11], chaotic multi-objective optimization based FOPID [12], genetic algorithm (GA) based FOPID [13] and chaotic particle swarm optimization (CPSO) based fractional order fuzzy PID (FOFPID) [14] structured controllers are accessible in the literature. The researches employing fractional calculus based control strategies are gaining escalating interest due to its additional suppleness and superb design performance [8–14]. FOPID controllers have been observed expedient in AGC of different power systems such as single/two-area non-reheat thermal [8], restructured three-area thermal [9], single-area thermal/hydro [10], three-area hydrothermal [11], two-area reheat thermal [12], restructured two-area non-reheat thermal [13] and single-area multi-source renewable power system [14].

In deregulated environment, vertically integrated utilities (VIUs) which generally own generation, transmission and distribution systems do not subsist and numerous independent entities like distribution companies (DISCOs), generation companies (GENCOs), transmission companies (TRANSCOs) and independent system operator (ISO) are introduced [7,9,13,15–18,21–22]. In this scenario, consumers will have prospects to purchase power at reduced rates due to competitive environment among GENCOs. In deregulated environment, various power contracts/transactions between DISCOs and GENCOs may exist such as poolco, bilateral and combination of these two transactions. In poolco, contracts persist between GENCOs and DISCOs of same control area; while in bilateral, DISCOs of one area have contracts with GENCOs of other areas. In open market, both these contracts may be negotiated concurrently. The contracted power wheels between DISCOs and GENCOs via TRANSCOs. All transactions are cleared mandatorily from ISO, which aims to assist system security and stability. AGC is one of the ancillary services managed by ISO. Donde et al., has introduced the concept of DISCO participation matrix (DPM) and area participation factor (apf) for AGC study under deregulated environment [15]. The rows in DPM relates to GENCOs and columns to DISCOs. Each entry of DPM is termed as contract participation factor (cpf). The cpf_{ij} relates to the share of the total power contracted by DISCO-j from GENCO-i. It is to be noted that $\sum_i cpf_{ij} = 0$. With emerging size, complexity, uncertainties and disturbances in the restructured power system under deregulated environment, it is preferred to harness some unique control strategies to attain AGC goals and secure system passably. Literature survey unveils that diverse conventional and intelligent approaches have been implemented effectively by the researchers to solve AGC

Accepted manuscript

ACCEPTED MANUSCRIPT

problem in restructured two/three/four-area thermal/hydrothermal/multi-source power systems [7,9,13,15–18,21–22].

In a practical power system, each control area comprises of a mix of hydro, thermal, gas and nuclear power generations [2]. Owing to high efficiency, nuclear plants generally reserved at base load close to their utmost power output. Gas power plants contribute little percentage of total system generation and are suitable to meet the fluctuating peaking load demands. Thus, the natural alternative for AGC study falls on either thermal/hydro/gas units or multi-source hydrothermal gas units operating in each area of the system [2,5–7,14,17–18,20]. Various control strategies are observed in multi-source systems. A robust PID controller tuned using hFA-PS [5] and GWO [6] is proposed for two-area multi-source hydrothermal systems. Differential evolution (DE) tuned PID controller show ameliorated performance in a deregulated two-area multi-source thermal gas system [7]. Chaotic PSO tuning method is used to optimize controller gains in a single-area multi-source hybrid renewable system [14]. Optimal control strategy is found suitable for restructured multi-source thermal-hydro/gas [17] and hydrothermal [18] systems.

A conventional PI/PID controller tuned at a specific operating condition may not act upon satisfactorily when there is an amendment in operating condition. Because of fluctuations in load demand, the operating point always varies. Hence, the nonlinear environment of AGC problem makes it hard to guarantee stability over the whole operating range with PI/PID controller being tuned at a particular operating condition. Power system configuration and nonlinearity also change over the time and controller parameters are required to be re-tuned to achieve the desired performance, continuously. Recently, fuzzy logic controllers (FLCs) have been gaining more acceptance as an efficient tool to circumvent these drawbacks [13–14,19–22]. FLC is capable to control a process without knowing the information of its underlying dynamics and effectively handles small variations in operating point or system parameters by tuning the controller parameters [14,21]. The membership functions (mfs) and input/output scaling factors of a FLC are tuned using GA for a restructured two-area hydrothermal power system [21]. However, most common technique of FLC tuning is the tuning of gains of input and output scaling factors only since their values influence the performance of FLC extensively [20]. Standard rule base and mfs with optimized input/output scaling factors are exploited in literature to design optimum fuzzy PI/PID controller for various applications [14,20,22]. The input/output scaling factors of a fuzzy PI/PID controller are optimized using hybrid differential evolution-pattern search (DEPS) algorithm for AGC of a two-area non-reheat and multi-source hydrothermal gas systems and it shows enhanced performance over conventional counterparts [20]. For higher order system fuzzy PI controller during the transient phase may not demonstrate fine performance due to its internal integration operation. Hence, to reap improvements, usually fuzzy PID (FPID) structured controllers are recommended. Firefly algorithm (FA) is proposed to tune FPID controller with derivative filter for AGC of a four-area restructured thermal system [22]. Also, BFOA based fuzzy integral double derivative controller is implemented with optimized mfs and output scaling factors on a three-area hydrothermal system [19]. Recently,

Accepted manuscript

ACCEPTED MANUSCRIPT

chaotic PSO optimized FO fuzzy PID (FOFPID) controller is also proposed for AGC of single-area hybrid renewable system; where it shows improved results compared to PID/FPID controller [14].

The literature survey unveils that over the past decade various control strategies have been proposed for AGC of traditional/restructured systems and it is also divulged that the performance of the AGC systems depends chiefly on the sort of intelligent technique exploited and structure of the controller. In context to FLC, a variety of soft computing techniques and FLC structures have been offered [13–14,19–22]. Further, optimized FOPID controllers are also witnessed [8–14]. Additionally, a FOFPID controller is proposed for a single-area renewable multi-source system [14]. Surprisingly, till date, no attempt has been made to design FOFPID structured controller for AGC investigation of multi-area single/multi-source traditional/restructured power systems. Hence, further study of FOFPID controller for AGC of multi-area multi-source traditional/restructured power system is required.

In light of the above, in this paper a maiden attempt has been made to implement FOFPID controller for AGC of multi-area multi-source traditional/restructured power system and BFOA is used to optimize controller parameters like input/output scaling factors, order of integrator (λ) and order of differentiator (μ and γ). The main objectives of this piece of work are:

a) To design BFOA based FOFPID controller for a multi-area multi-source traditional hydrothermal power system.
b) To demonstrate the advantages of BFOA based FOFPID over hFA-PS based PI/PID, GWO based PID and BFOA based FPID/FOPID controller for the same problem.
c) To extend the study to a restructured multi-area multi-source hydrothermal system and to show the superiority of FOFPID over FPID/FOPID/PID controller.
d) To demonstrate the excellent capability of the proposed approach to handle different transactions taking place under deregulated environment and GRC/TD/DZ.
e) To widen the study to a restructured multi-area multi-source thermal gas system and to show the superiority of FOFPID over FPID/FOPID/PID and DE/GA based PID controllers.
f) To perform sensitivity analysis to judge the robustness of the proposed controller under wide variation in the nominal system initial loading, parameters, DPM structure and size and position of uncontracted power demand.

2. Systems investigated

Investigations have been carried out on traditional two-area multi-source hydrothermal system, restructured two-area multi-source hydrothermal and restructured two-area multi-source thermal gas systems. Each area of traditional/restructured hydrothermal system is equipped with one non-reheat thermal and one mechanical governor based hydro unit. Restructured two-area thermal gas system is outfitted with one reheat thermal and one

ACCEPTED MANUSCRIPT

gas plant in its each control area. Frequency bias setting B_i is considered equal to β_i in both areas. Rated area capacity of each system is 2000 MW with initial loading of 1000 MW. The transfer function models of the systems under study are shown in Fig. 1 and Fig. 8. The nominal parameter values of the systems are depicted in Appendix and the list of symbols is given Nomenclature table. MATLAB software version 7.5.0 (R2007b) is utilized to obtain the dynamic responses of the systems under different load perturbations.

3. Controller structures

3.1. FOPID controller

In industry, recently fractional order PID (FOPID) controller has received broad interest and research in comparison to widely accepted classical PID controller. Since introduced by Alomoush [8] firstly in the year 2010 in AGC of power systems, the application of FOPID controller in AGC of different systems has been witnessed broadly in the literature [9–14]. The FO controller concept deals with differential equations via fractional calculus. The fractional calculus is the generalization of the ordinary calculus. It is an extension of $d^n y(t)/dt^n$ concept with n an integer number to the concept $d^\alpha y(t)/dt^\alpha$ with α a non-integer number with prospect to be complex. Many definitions are available in the literature to describe the FO function such as the Cauchy integral formula, the Grünwald-Letnikov definition, the Riemann-Liouville definition and the Caputo definition. However, the Riemann-Liouville definition stated in Eqn. (1) is used mostly in FO calculus.

$$ {}_aD_t^{\alpha} f(t) = \frac{1}{\Gamma(n-\alpha)} \frac{d^n}{dt^n} \int_a^t (t-\tau)^{n-\alpha-1} f(\tau) d\tau \tag{1} $$

where, $n - 1 > \alpha < n$, n is an integer and symbol $\Gamma(\cdot)$ represents Euler's gamma function and is given by

$$ \Gamma(x) = \int_0^{\infty} e^{-t} t^{(x-1)} dt, \; x > 0, \tag{2} $$

with unique case when x = n,

$$ \Gamma(n) = (n-1)(n-2)\cdots(2)(1) = (n-1)!. \tag{3} $$

For expediency, the Laplace domain concept is used to illustrate the fractional differentiation-integration process. The Laplace transformation of Eqn. (1) under zero initial condition for the fractional derivative is given by

$$ \begin{aligned} L\left\{ {}_aD_t^{\alpha} f(t) \right\} &= \int_0^{\infty} e^{-st} {}_aD_t^{\alpha} f(t) dt \\ &= s^{\alpha} F(s) - \sum_{k=0}^{n-1} s^k {}_aD_t^{\alpha-k-1} f(t)\Big|_{t=0} \end{aligned} \tag{4} $$

for $n - 1 \le \alpha \le n$, while $L\{f(t)\}$ indicates the normal Laplace transformation and F(S) is the Laplace transform of f(t).

Accepted manuscript

ACCEPTED MANUSCRIPT

The most common form of FOPID controller is the $PI^{\lambda}D^{\mu}$, where λ and μ are the non-integer order of integrator and differentiator respectively and can be any real numbers. The transfer function has the form given by Eqn. (5)

$$G_c(s) = K_P + \frac{K_I}{s^{\lambda}} + K_D s^{\mu} \tag{5}$$

where, K_P, K_I, K_D are proportional, integral, derivative gains respectively. λ and μ are positive numbers indicating order of integration and differentiation respectively. Hence, $PI^{\lambda}D^{\mu}$ controller structure has five independent knobs to be tuned. For $\lambda = 1$ and $\mu = 1$; the controller structure of Eqn. (5) reduces to the conventional PID controller having parallel structure. Further, if $\lambda = 1$ and $\mu = 0$; then it becomes PI, if $\lambda = 0$ and $\mu = 1$; then it becomes a PD, if $\lambda = 0$ and $\mu = 0$; then it is only P, if $\lambda = 0$; then it becomes PD^{μ}; if $\mu = 0$; then it becomes PI^{λ}, if $\lambda = 1$; then it becomes PID^{μ} and if $\mu = 1$; then it becomes $PI^{\lambda}D$ controller.

In simulations and industrial implementations of transfer functions involving fractional orders of s, it is required to approximate them with usual (integer order) transfer functions. To approximate a fractional transfer function correctly, a usual transfer function would engage an infinite number of poles and zeroes. However, an approximation with a finite number of poles and zeroes can be obtained using the CRONE approximation proposed by Oustaloup [23]. Oustaloup's recursive distribution uses a higher order filter having a order of 2N + 1, and it gives a very good approximation/fitting to the fractional order elements s^{α} given by Eqn. (6) within a selected frequency band $[\omega_L, \omega_H]$ [12,14,23].

$$G_f(s) = s^{\alpha} = K \prod_{k=-N}^{N} \frac{s + \omega_k'}{s + \omega_k} \tag{6}$$

where α is the order of differ-integration and $0 < \alpha < 1$, $(2N + 1)$ is the order of the filter. K is the gain, ω_k' and ω_k are the poles and zeros of the analog filters respectively, and are obtained as follows:

$$K = \omega_H^{\alpha} \tag{7}$$

$$\omega_k' = \omega_L \left(\frac{\omega_H}{\omega_L}\right)^{\frac{k + N + \frac{1}{2}(1+\alpha)}{2N+1}} \tag{8}$$

$$\omega_k = \omega_L \left(\frac{\omega_H}{\omega_L}\right)^{\frac{k + N + \frac{1}{2}(1-\alpha)}{2N+1}} . \tag{9}$$

K is adjusted so that approximation should have unit gain at 1 rad/s frequency [13]. The choice of N is a significant deciding feature in the performance of the approximation. Low values of N may result in simpler approximations and ease in hardware implementation but the approximation performance deteriorates due to ripple formation in magnitude and phase response. Such ripples may be eliminated by raising the values of N but

Accepted manuscript

ACCEPTED MANUSCRIPT

it will turn the approximation difficult and complexity in hardware implementation. In this paper, CRONE approximation is employed with N = 3, while fitting frequency range [ω_L, ω_H] is taken as [0.01, 100].

3.2. FOFPID controller

To solve the AGC problem of traditional/restructured two-area multi-source power systems under study, fractional order fuzzy PID (FOFPID) controller is provided in each area. The dynamic performance of the system with FOFPID controller is compared with PID, fuzzy PID (FPID) and FOPID structured controllers. The FOFPID/FPID controller structure is shown in Fig. 2 [20]. The error input to the controller is the respective area control error (ACE) represented by

$$ACE_1 = \beta_1 \Delta F_1 + \Delta Ptie_{12}, \quad (10)$$

$$ACE_2 = \beta_2 \Delta F_2 + \alpha_{12} \Delta Ptie_{12}. \quad (11)$$

Where, β_i is the area frequency response characteristic (puMW/Hz) and area size ratio, $\alpha_{12} = -P_{r1}/P_{r2}$. P_{ri} is the area capacity (MW). $\Delta Ptie_{12}$ is the deviation in tie-line power (puMW) and ΔF_i is the deviation in area frequency (Hz). However, $Ptie_{12}$ will be termed as $Ptie_{error}$ in restructured system. Fuzzy logic controller (FLC) uses ACE and ACE derivative with fractional order as input signals. The FLC output (i.e., y) is multiplied with FOPID to get output ΔP_{Ci} of the controller. ΔP_{Ci} is the control input to the system. K_1, K_2 (input scaling factors), order of input differentiator (γ), K_P, K_I, K_D (output scaling factors), order of output integrator (λ) and differentiator (μ) are the parameters to be tuned using BFOA to minimize an objective function i.e., Eqn. (13). FLC has four modules i.e., fuzzifier, fuzzy inference engine/system (fis), rule base and defuzzifier. The fuzzifier changes the numeric value into fuzzy sets. The fis performs all the logical operations. The rule base consists of membership functions (mfs) and control rules. The output of fis is a fuzzy set to be converted into numeric value by defuzzification scheme. Commonly, triangular, Gaussian, trapezoidal and bell shaped mfs are favored due to their simple representation, fewer memory necessity for storage and efficient to be handled by the fis. Though, triangular mfs are favorable in FLC designs of real time applications due to of their enhanced and economical performance in comparison to other options [22]. In the current study five triangular mfs are selected with five fuzzy linguistic variables such as MN (more negative), SN (small negative), Z (zero), SP (small positive) and MP (more positive) for inputs and output of FOFPID/FPID controller. The mfs for ACE, fractional rate of ACE derivative and FLC output are shown in Fig. 3 [20]. Identical mfs with identical horizontal range are engaged for inputs and output of the FLC. The two-dimensional rule base for ACE, fractional rate of ACE derivative and FLC output consisting of twenty

Accepted manuscript

ACCEPTED MANUSCRIPT

fives rules is revealed in Table 1. Mamdani fis and centroid defuzzification method are used in this study. Identical controllers are designed for the identical two-area systems.

The control signal of the controller is given by

$$\Delta P_{Ci} = K_p y + \frac{K_I}{s^{\lambda}} y + K_D s^{\mu} y, \ (i = 1, 2 \text{ and } \lambda, \mu > 0). \quad (12)$$

For $\lambda = 1$, $\mu = 1$ and $\gamma = 1$, the FOFPID controller structure shown in Fig. 2 reduces to the integer order FPID controller with parallel structure as shown in reference [20].

4. Optimization problem

The purpose of an optimization problem is to find a solution in the feasible region by curtailing an objective function selected for the system. For AGC problem under study, the objective function is devised integral squared error (ISE) criterion given in Eqn. (13).

$$J = \int_0^T \{\Delta F_1^2 + \Delta F_2^2 + \Delta Ptie_{12}^2\} dt. \quad (13)$$

Here, T is the range of simulation time. $\Delta Ptie_{error}$ will replace $\Delta Ptie_{12}$ in restructured system. The problem constraints are the controller parameter bounds. Consequently, the FOFPID controller design problem can be developed as the subsequent optimization problem. Each FOFPID controller has eight parameters to be tuned. The optimization problem can be defined as to minimize J in view of the following constraints:

$K_{1\,min} \le K_1 \le K_{1\,max}$, $K_{2\,min} \le K_2 \le K_{2\,max}$, $\gamma_{\,min} \le \gamma \le \gamma_{\,max}$, $K_{P\,min} \le K_P \le K_{P\,max}$, $K_{I\,min} \le K_I \le K_{I\,max}$, $\lambda_{\,min} \le \lambda \le \lambda_{\,max}$, $K_{D\,min} \le K_D \le K_{D\,max}$, $\mu_{\,min} \le \mu \le \mu_{\,max}$.

Here, $\gamma_{\,min}$, $\lambda_{\,min}$, $\mu_{\,min}$, $K_{1,2,P,I,D\,min}$ and $\gamma_{\,max}$, $\lambda_{\,max}$, $\mu_{\,max}$, $K_{1,2,P,I,D\,max}$ is the minimum and maximum value of the FOFPID structured controller parameters, respectively. The minimum and maximum values of $K_{1,2,P,I,D}$ parameters are selected as 0.0 and 4.0, respectively. However, γ, λ and μ values are chosen between 0.0 and 1.0. Each bacterium is allowed to take all probable values within this range to minimize Eqn. (13) to derive the optimal parameter values of FOFPID controller. The tunable parameters for FPID (K_1, K_2, K_P, K_I and K_D) and FOPID (K_P, K_I, K_D, λ and μ) controllers would be five; however, their numbers will be three in case of conventional PID (K_P, K_I and K_D) controller.

5. Bacterial foraging optimization algorithm

For the first time, the bacterial foraging optimization algorithm (BFOA) is used to optimize parameters of FOFPID controller in AGC of multi-area traditional/restructured system. Since its development by Passino [24],

Accepted manuscript

ACCEPTED MANUSCRIPT

BFOA is broadly established as a global optimization technique of contemporary interest in AGC of different types of power systems [3–4,9,19]. BFOA is a non-gradient, bio-inspired stochastic search technique based on the natural selection in which animals with deprived foraging strategies eliminate, while survive only those individuals having good foraging strategy signifying survival of the fittest. In BFOA, the foraging behavior of Escherichia coli bacteria residing in human intestine is mimicked [24]. The swarm foraging strategy of E. coli bacteria can be subdivided into four sections viz., chemotaxis, swarming, reproduction, and elimination-dispersal [24]. We briefly introduce them as follows.

5.1. Chemotaxis

Chemotaxis process mimics the movement of E. Coli bacteria through swimming and tumbling via a set of tensile flagella, which makes it swim away from acidic and alkaline regions and nearer to neutral ones. Thus, in the entire life span, the movement of flagella enables bacterium to tumble or swim, which are two basic movements executed by a bacterium during the time of foraging. If the movement follows a predefined way then it is termed swimming; however in random direction it is recognized as tumbling. Mathematically, tumble can be expressed by $\phi(i)*C(i)$; where $\phi(i)$ is unit length of random direction and $C(i)$ is step length of concerned bacterium taken in random direction specified by the tumble (run length unit). Let, $\theta^i(j,k,l)$ represent ith bacterium at jth chemotaxis, kth reproduction and lth elimination-dispersal event; then, ith bacterium movement may be given by

$$\phi(i) = \frac{\Delta(i)}{\sqrt{\Delta^T(i)\Delta(i)}}, \tag{14}$$

$$\theta^i(j+1,k,l) = \theta^i(j,k,l) + C(i)\phi(i) \tag{15}$$

where $\Delta(i) \in R^n$. $\Delta(i)$ is vector whose elements lie in [–1, 1]. If the nutrient amount in the new location is more compared to the last position, it will run one more step in the same direction and will prolong until the nutrient concentration gets lesser or the maximum swim length is reached.

5.2. Swarming

Any one of the bacteria when discovers a better food location, release an attractant aspartate, which helps others to aggregate into groups and thus move as concentric patterns of swarms with high bacterial density. The cell-to-cell signaling in bacteria swarm may be represented mathematically as:

$$J_{cc}(\theta,P(j,k,l)) = \sum_{i=1}^{S} J_{cc}^{i}\left(\theta,\theta^{i}\left(j,k,l\right)\right)$$

$$= \sum_{i=1}^{S}\left[-d_{attract}\exp\left(-w_{attract}\sum_{m=1}^{p}\left(\theta_m - \theta_m^i\right)^2\right)\right] +$$

Accepted manuscript

ACCEPTED MANUSCRIPT

$$\sum_{i=1}^{S}\left[h_{repelent} \exp\left(-w_{repelent} \sum_{m=1}^{p} \left(\theta_m - \theta_m^i \right)^2 \right) \right] \quad (16)$$

where J_{cc} is the objective function value to be added to the actual objective function (to be minimized) to present a time varying objective function or it can also be given as the relative distance of each bacterium from the optimum bacterium. S is the total number of bacteria and p is the total number of parameters to be optimized, which are present in each bacterium, $\theta = [\theta_1, \theta_2, \ldots, \theta_p]^T$ signifies a point in the p-dimensional search domain and $d_{attract}$, $\omega_{attract}$, $h_{repelent}$ and $\omega_{repelent}$ are the various coefficients characterizing swarm behavior and these should be chosen properly.

5.3. Reproduction

In reproduction step, healthiest bacteria (those yielding lower value of objective function) will reproduce themselves after certain number of chemotaxis steps and the least healthy bacteria will die to follow the evolution rule. The bacterium with better health captures the position of bacterium with poor heath in the evolution process. The health of ith bacteria, which is sum of fitness in each chemotaxis including initialization step is represented by

$$J_{health}^i = \sum_{j=1}^{N_C + 1} J(i, j, k, l). \quad (17)$$

The number of bacterial reproduction per generation is given by $S_r = S/2$. Sort bacteria in order of ascending cost J_{health}, the S_r bacteria with the highest J_{health} values will die and the other S_r bacteria with the best values will split in to two. This process keeps the swarm size constant.

5.4. Elimination and dispersal

In the evolution process, gradual or abrupt alterations in the local atmosphere of a region having high concentration of nutrient gradients may eradicate a bacterium population or a cluster of bacteria is dispersed from current location to other regions. The elimination-dispersal events may occur due to environmental changes or some natural disasters like significant increase in heat, flood, Tsunami etc. These events may perhaps destroy the chemotactic progresses, but they may assist the chemotaxis, since dispersal may place bacteria near superior food location. From evolutionary point of view, elimination-dispersal events aid to guarantee diversity of the individuals and reinforce global optimization capability by avoiding stagnation. To simulate this incident in BFOA, some bacteria are liquidated haphazardly with a very small likelihood while the new substitutes are haphazardly initialized over the search space.

The bacterium for which the objective function value of Eqn. (13) is least in the last BFOA iteration estimates the optimized controller parameters to be used in the simulations. In present work, to tune FOFPID controller, the

Accepted manuscript

ACCEPTED MANUSCRIPT

BFOA is implemented with following initialization: (1) no. of parameters to be optimized, p (= 8 (FOFPID), = 5 (FPID/FOPID), = 3 (PID)), (2) no. of bacteria to be used for total search space, S = 6, (3) swimming length after which tumbling of bacteria will be undertaken in a chemotactic loop, N_S = 3, (4) no. of iterations to be undertaken in a chemotactic loop, N_C = 5 ($N_C > N_S$), (5) maximum no. of reproduction steps to be used by bacteria, N_{re} = 15, (6) maximum no. of elimination-dispersal events to be forced on bacteria, N_{ed} = 4, (7) probability with which the elimination and dispersal will prolong, P_{ed} = 0.25, (8) the location of each bacterium p specified by values attained using the trial and error method, (9) the value of step size taken in the random direction, C(i), i = 1,2,⋯,S is assumed to be constant for all bacteria to simplify the design approach, (10) the magnitude of secretion of attractant by a cell, $d_{attract}$ = 0.01, (11) the chemical cohesion signal diffuses (smaller makes it diffuse more), $\omega_{attract}$ = 0.04, (12) the repellant (tendency to avoid nearby cell), $h_{repelent}$ = 0.01 and (13) the width of the repellant, $\omega_{repelent}$ = 10.

The value of $d_{attract}$ and $h_{repelent}$ must be comparable so that the penalty required on the objective function through J_{cc} of Eqn. (16) will be zero when all the bacteria will have alike value i.e., they have converged. In the existing work, we present only a concise outline of BFOA and request the readers to refer [3] for detailed algorithm. In this paper, only the flow chart of BFOA is presented as shown in Fig. 4.

6. Simulation results and discussion

The SIMULINK models and programs of the power system models under consideration are developed on an Intel Core 2 Duo processor of 1.66 GHz and 2 GB RAM computer in the MATLAB version 7.5.0 (R2007b) adopting the system data shown in Appendix to study the dynamic performance of the systems against step load perturbation (SLP) in any control area. The BFOA tuning process for each model under study is repeated 50 times and the best final solution among 50 runs is selected as the controller parameters used in simulations [5,22]. The results indicating superiority are bold faced in the respective tables.

6.1. Traditional two-area multi-source hydrothermal system

A two-area multi-source hydrothermal power system model is simulated considering 1.5% SLP at t = 0 s in area-1. The AGC model is taken from literature [6] and is shown in Fig. 1 (without dotted line connections). Each area has two generating units, one non-reheat thermal and other mechanical governor based hydro plant. The transfer functions of thermal/hydro governor and thermal/hydro turbine are shown and labeled in Fig. 1; while corresponding nominal parameters are declared in Appendix and symbols in Nomenclature table. Each area is rigged with FOFPID/FPID/FOPID controller whose optimized parameters are displayed in Table 2. Regarding this system, $\Delta Ptie_{error}$ signal showed in Fig. 1 will be termed as $\Delta Ptie_{12}$. The system dynamic responses for deviation in frequency of area-1 (ΔF_1), area-2 (ΔF_2), tie-line power ($\Delta Ptie_{12}$) and area control error of area-1

Accepted manuscript

ACCEPTED MANUSCRIPT

(ACE_1) are shown in Fig. 5. To corroborate the advantage of the proposed approach, the simulation results with some newly published approaches like hFA-PS based PI/PID [5] and GWO based PID [6] controller along with FPID/FOPID structured controller tuned in this study using BFOA for the same system are also presented in Fig. 5. Critical analysis of the Figs. 5(a–d) distinctly discloses considerable improvements with the proposed BFOA optimized FOFPID controller compared to FPID/FOPID/PID/PI structured controller in terms of settling times (STs), peak undershoots (PUs) and oscillations. The system performance in terms of numerical values of STs, PUs and different performance indices (PIs) such as ISE (integral of squared error), ITSE (integral of time multiplied squared error), IAE (integral of absolute error) and ITAE (integral of time multiplied absolute error) [5,8] are shown in Table 3. The PIs help in making a clear comparative study of the performance of the proposed technique with that of other techniques. It is perceptible from Table 3 and Figs 5(a–d) that GWO: PID [6] outperforms hFA-PS: PI/PID [5] controller. Table 3 indicates that BFOA: FOPID outperform GWO: PID [6] controller in terms of less STs (FOPID: $\Delta F_1 = 1.20$, $\Delta F_2 = 2.15$, $\Delta Ptie_{12} = 1.678$; GWO: PID: $\Delta F_1 = 1.21$, $\Delta F_2 = 3.50$, $\Delta Ptie_{12} = 2.640$), PUs (FOPID: $\Delta F_1 = 0.0115$, $\Delta F_2 = 0.0046$, $\Delta Ptie_{12} = 0.0015$; GWO: PID: $\Delta F_1 = 0.0149$, $\Delta F_2 = 0.0069$, $\Delta Ptie_{12} = 0.0026$) and PIs (FOPID: ISE = $5.22e^{-05}$, ITSE = $2.14e^{-05}$, IAE =0.0116, ITAE =0.0121; GWO: PID: ISE = $1.47e^{-04}$, ITSE = $9.03e^{-05}$, IAE =0.0233, ITAE =0.0259). However, FPID controller show superior performance compared to FOPID and the proposed FOFPID compared to FPID in terms of least STs (FOFPID: $\Delta F_1 = 0.55$, $\Delta F_2 = 0.98$, $\Delta Ptie_{12} = 0.450$; FPID: $\Delta F_1 = 0.82$, $\Delta F_2 = 1.79$, $\Delta Ptie_{12} = 1.173$), PUs (FOFPID: $\Delta F_1 = 0.0038$, $\Delta F_2 = 0.0007$, $\Delta Ptie_{12} = 0.0003$; FPID: $\Delta F_1 = 0.0065$, $\Delta F_2 = 0.0019$, $\Delta Ptie_{12} = 0.0007$) and PIs (FOFPID: ISE = $2.81e^{-06}$, ITSE = $7.73e^{-07}$, IAE =0.0026, ITAE =0.0035; FPID: ISE = $1.60e^{-05}$, ITSE = $6.07e^{-06}$, IAE =0.0068, ITAE =0.0083). Consequently, enhanced system performance in terms minimum PIs and STs/PUs in frequency and tie-line power deviations is attained with the proposed optimal FOFPID controller compared to others. It is also concluded that the frequency deviation response belonging to area with SLP show more undershoot compared to undisturbed area. Hence, it is established that the effect of SLP reveals local dominance but it also influences the dynamics of other interconnected control area owing to the presence of weak tie-line connecting them.

6.2. Restructured two-area multi-source hydrothermal system

The swell in dimension, complexity, uncertainties and disturbances in restructured power systems adversely affect the performance of systems. Consequently, the controller designed for these systems should adequately cope with such intricacies to achieve AGC goals and secure electric power system, and it is an intriguing task for control engineers. In view of this, to substantiate the capability of the proposed approach in restructured system, the study is further extended from traditional multi-source hydrothermal system to restructured multi-source hydrothermal system whose transfer function model is shown in Fig. 1 (with dotted line connections). GENCO-1 and GENCO-

Accepted manuscript

ACCEPTED MANUSCRIPT

3 are thermal while GENCO-2 and GENCO-4 are hydro generating units. Two DISCOs are assumed in each area i.e., DISCO-1, DISCO-2 in area-1 and DISCO-3, DISCO-4 in area-2. The system parameters are given in Appendix. The optimum parameter values of controllers are obtained by running the BFOA codes written in mfile and models developed in SIMULINK. The optimized values hence find out are shown in Table 4 for FOFPID/FPID/FOPID/PID controller under different transactions, studied next. The computer simulations are carried out using these optimum controller gains. Different contract scenarios are simulated in four numbers of cases to affirm efficacy of the proposed approach in restructured multi-source system.

6.2.1. Case 1: Poolco based transactions

In this type of transactions, DISCOs negotiate power contracts with GENCOs of their own area only [7,15–18,21–22]. It is assumed that the load power is demanded in area-1 only. Hence, the load is demanded by DISCO-1 and DISCO-2. Let $\Delta P_{L1} = \Delta P_{L2} = 0.01$ puMW and $\Delta P_{L3} = \Delta P_{L4} = 0.00$ puMW. Where, ΔP_{Li} denotes the power demand of $DISCO_i$. Hence, ΔP_{D1} ($\Delta P_{L1} + \Delta P_{L2} + \Delta P_{UC1}$) = 0.02 puMW and ΔP_{D2} ($\Delta P_{L3} + \Delta P_{L4} + \Delta P_{UC2}$) = 0.00 puMW. Here, market disturbance signals ΔP_{Di} and ΔP_{UCi} represent the total load demand and uncontracted power, demanded by DISCOs in area-i respectively. The ΔP_{UCi} is assumed equal to zero. The selected DPM structure is given by [7,9,13,15–18]

$$\text{DPM} = \begin{bmatrix} 0.5 & 0.5 & 0.0 & 0.0 \\ 0.5 & 0.5 & 0.0 & 0.0 \\ 0.0 & 0.0 & 0.0 & 0.0 \\ 0.0 & 0.0 & 0.0 & 0.0 \end{bmatrix} \tag{18}$$

Note that DISCOs of area-2 do not demand power from any GENCOs and DISCOs of area-1 do not demand power from GENCOs of area-2; so the related cpfs of DPM are chosen zero i.e., columns 3, 4 and rows 3, 4. The controller output signal (ΔP_{Ci}) is used as the input to ACE participation factor (apf) block of GENCO-i. The apf of a GENCO depends on its participation, profile, bid price and capacity in the generation market. It is assumed that all GENCOs participate equally in the AGC task i.e., $apf_1 = apf_2 = apf_3 = apf_4 = 0.5$. In the steady state, generation of GENCOs necessarily match the demand of the DISCOs in contract with them. The desired generation of a GENCO can be stated in terms of cpfs and the overall demand of DISCOs as:

$$\Delta P_{Gi} = cpf_{i1}\Delta P_{L1} + cpf_{i2}\Delta P_{L2} + cpf_{i3}\Delta P_{L3} + cpf_{i4}\Delta P_{L4},\ i = 1,\cdots,4. \tag{19}$$

Hence, in steady state $\Delta P_{G1} = \Delta P_{G2} = 0.01$ puMW and $\Delta P_{G3} = \Delta P_{G4} = 0.0$ puMW. The scheduled steady state power flow on the tie-line is given as [13,15–18,22]:

$$\Delta Ptie_{scheduled} = \sum_{i=1}^{2}\sum_{j=3}^{4} cpf_{ij}\Delta P_{Lj} - \sum_{i=3}^{4}\sum_{j=1}^{2} cpf_{ij}\Delta P_{Lj},$$

Accepted manuscript

ACCEPTED MANUSCRIPT

$$= [P_{exp1}] - [P_{imp1}]. \quad (20)$$

Where $[P_{exp1}]$ is the net power exported from area-1 and equals the demand of DISCOs in area-2 from GENCOs in area-1, while $[P_{imp1}]$ is the net power imported in area-1 and equals the demand of DISCOs in area-1 from the GENCOs operating in area-2. From Eqn. (20), $\Delta Ptie_{scheduled} = 0$ puMW. The tie-line power flow error is stated as

$$\Delta Ptie_{error} = \Delta Ptie_{actual} - \Delta Ptie_{scheduled}. \quad (21)$$

In steady state $\Delta Ptie_{error}$ ceases to zero as $\Delta Ptie_{actual}$ attains $\Delta Ptie_{scheduled}$. It should be noted that the signal $\Delta Ptie_{12}$ used in Eqns. (10–11) will be replaced with $\Delta Ptie_{error}$ in this new scenario.

Simulations of the system have been carried out with the proposed FOFPID and FPID/FOPID/PID controllers by considering the BFOA optimized gains as shown in Table 4 for poolco based transactions. STs and PUs of ΔF_1, ΔF_2 and $\Delta Ptie_{error}$ and ISE, ITSE, IAE and ITAE for FOFPID/FPID/FOPID/PID controllers are given in Table 5. It is clear from Table 5 that FOFPID is superior to FPID as minimum PIs value is obtained with FOFPID (ISE = $2.04e^{-05}$, ITSE = $7.12e^{-06}$, IAE = 0.0079, ITAE = 0.0147) compared to FPID (ISE = $5.18e^{-05}$, ITSE = $2.07e^{-05}$, IAE = 0.0130, ITAE = 0.0214). Additionally, it is clear that STs and PUs are also less with FOFPID (STs: $\Delta F_1 = 0.79$, $\Delta F_2 = 1.97$, $\Delta Ptie_{error} = 1.19$; PUs: $\Delta F_1 = 0.0085$, $\Delta F_2 = 0.0022$, $\Delta Ptie_{error} = 0.0008$) compared to FPID (STs: $\Delta F_1 = 0.98$, $\Delta F_2 = 2.40$, $\Delta Ptie_{error} = 1.73$; PUs: $\Delta F_1 = 0.0122$, $\Delta F_2 = 0.0035$, $\Delta Ptie_{error} = 0.0014$). Similar trend of improved performance is observed with FPID compared to FOPID and FOPID compared to conventional PID controller. Hence, it can be concluded that the proposed FOFPID controller is superior to all other controllers. The dynamic performance of the system is shown in Figs. 6 and 7. It is clear from Figs. 6(a-d) that improved system dynamic responses in terms minimum STs and PUs in frequency and tie-line power deviations is achieved with the proposed approach compared to FPID/FOPID/PID controller. Further, Figs. 6(a-b,d) and Figs. 7(a-b,d) for Case 1, indicate that FOFPID fulfill AGC requirement as frequency deviation in each area and tie-line power error deviation settle to zero in the steady state. For Case 1, from Figs. 7(e-j), it is observed that steady state simulated values of GENCOs outputs match with desired value obtained using Eqn. (19) and Fig. 6(c)/7(c) validates Eqn. (20).

6.2.2. Case 2: Bilateral based transactions

In this case, all DISCOs have autonomy to be in contracts with GENCOs of its own and other control areas [7,13,15–18,21–22]. It is assumed that each DISCO demand 0.01 puMW power from GENCOs as defined by cpfs in the following DPM [7,13,15]. Hence, $\Delta P_{D1} = \Delta P_{D2} = 0.02$ puMW.

Accepted manuscript

ACCEPTED MANUSCRIPT

$$\text{DPM} = \begin{bmatrix} 0.5 & 0.25 & 0.0 & 0.3 \\ 0.2 & 0.25 & 0.0 & 0.0 \\ 0.0 & 0.25 & 1.0 & 0.7 \\ 0.3 & 0.25 & 0.0 & 0.0 \end{bmatrix} \quad (22)$$

Let each GENCO contribute in AGC as per $apf_1 = 0.75$, $apf_2 = 0.25$, $apf_3 = apf_4 = 0.5$. The apfs do not influence steady state behavior of the system but affect only the transient behavior in the absence of uncontracted power demand. The gain values of FOFPID controller optimized using BFOA technique are given in Table 4. STs, PUs and PIs values are provided in Table 5. From Table 5 it conferred that, for FOFPID controller all these values have been increased in comparison to those obtained in poolco based transaction. Hence, deteriorated performance is observed in bilateral transactions due to extra demand of area-2 DISCOs as shown in Figs. 7(a-j). Using Eqns. (19,22), the desired generations $\Delta P_{G1} = 0.0105$ puMW, $\Delta P_{G2} = 0.0045$ puMW, $\Delta P_{G3} = 0.0195$ puMW and $\Delta P_{G4} = 0.0055$ puMW are validated in Figs. 7(e-j) for Case 2. From Eqn. (20), $\Delta Ptie_{scheduled} = -0.005$ puMW as observed in Fig. 7(c) for Case 2. It is noticed that in restructured system, the proposed controller work well and the type of contract not only affects the area load demand but the scheduled tie-line power flow is also affected.

6.2.3. Case 3: Contract violation

DISCOs in an area may violate a contract by demanding excess power than that specified in the contract. This excess power demand must be supplied by the local GENCOs within the same control area as that of DISCOs [7,9,13,15–18,21–22]. Let us consider Case 2 once again with a variation that DISCO-1 demand 0.01 puMW of excess power i.e., $\Delta P_{UC1} = 0.01$ puMW and $\Delta P_{UC2} = 0.0$ puMW. Hence, $\Delta P_{D1} = 0.02 + 0.01 = 0.03$ puMW and $\Delta P_{D2} = 0.02$ puMW. Optimized parameters of the proposed FOFPID controller for contract violation case are given in Table 4. Figs. 7(a-j) also include the stabilized dynamic responses regarding Case 3. It is observed that, all results in transient state and only area-1 generation output results in steady state are affected due to excess power generated by GENCOs of area-1 to meet excess power demand. Area-1 apfs will decide the distribution of the uncontracted power (ΔP_{UC1}) between GENCO-1 and 2 in steady state. Hence, for Case 3, $\Delta P_{G1} = \{0.0105 + (0.75 \times 0.01)\} = 0.0180$ puMW (Figs. 7(e-f)), $\Delta P_{G2} = \{0.0045 + (0.25 \times 0.01)\} = 0.0070$ puMW (Fig. 7(g)), while ΔP_{G3} (= 0.0195 puMW; Figs. 7(h-i)) and ΔP_{G4} (= 0.0055 puMW; Fig. 7(j)) are invariant. Steady state values of deviation in actual/error tie-line power will be static as shown in Figs. 7(c-d). Compared to Case 2, inferior performance is further obtained in Case 3 in terms of higher values of STs, PUs and PIs as stated in Table 5 for ΔF_1, ΔF_2 and $\Delta Ptie_{error}$ responses, and shown for all responses in Figs. 7(a-j). However, ST for $\Delta Ptie_{error}$ is less in Case 3.

6.2.4. Case 4: Effect of GRC, TD and DZ

Accepted manuscript

ACCEPTED MANUSCRIPT

Electric power generating units cannot change their outputs too rapidly due to the constraint of thermal and mechanical movements. Generation rate constraint (GRC) present major confronts to the control scheme because they influence the dynamic performance of the system considerably. Under the absence of GRC, undesirably, generators are expected to chase large momentary disturbances that may create instability in power system network. In several AGC researches, GRC effect is not considered [4,8,10–11,13,15,21]. For testing the effectiveness of the proposed approach under GRC, the GRC for thermal units is considered ±0.0005 pu/s [2] and for hydro turbine its value is +0.045 pu/s for raising and –0.06 pu/s for lowering generation [2,5,16–20,22]. Schematic diagram of turbine with GRC is shown in [12]. Due to the growing intricacy, time delays (TD) become a notable challenge in the AGC investigation of restructured power systems. TD can mortify a system's performance and even may turn it unstable. A time delay of 50 ms is located in-between controller and apf blocks in each control area [5,20]. Additionally, the speed governor dead-zone (DZ) has enormous impact on the dynamic performance of electric power system. DZ is the amount of a sustained speed variation within which there is no change in the valve position. The speed governor DZ causes the system oscillatory. The maximum value of DZ for speed governors of steam plants is taken as 0.06% [12,16,22]. The block diagram of DZ in thermal speed governor is shown in [12]. In a realistic AGC study the effect of these physical constraints should be incorporated. The FOFPID controller parameters tuned via BFOA are shown in Table 4. Here, Case 3 is again simulated considering appropriate GRC, TD and DZ as stated above. Simulation results for Case 4 are shown in Figs. 7(a–j). For Case 4, it is observed that under the presence of GRC, TD and DZ, system dynamic performance gets deteriorated and all results show larger PUs, longer STs and higher PIs in comparison to Case 3 (Table 5). However, the proposed approach demonstrates stabilized system responses having same steady state values as that of Case 3 and hence satisfy AGC problem requirement efficiently under deregulated environment.

6.3. Restructured two-area multi-source thermal gas system

To evince the scalability and efficacy of the proposed FOFPID controller to cope up with the different restructured systems, the study is further forwarded to a restructured two-area multi-source power system by considering two GENCOs in each control area i.e., thermal and gas plants, as shown in Fig. 8. The thermal plant is provided a single reheat turbine with appropriate GRC of ±0.03%. The test model is taken from [7]. Bilateral case is considered again in which all four GENCOs participate in the AGC task and all four DISCOs for power, contract with the available GENCOs as per apfs and DPM, stated Case 2. It is assumed that a big step load of 0.1 puMW is demanded by each DISCO. Hence, $\Delta P_{D1} = \Delta P_{D2} = 0.2$ puMW. Optimized controller parameters are provided in Table 6. Power system responses with BFOA tuned FOFPID/FPID/FOPID/PID and DE/GA tuned PID controllers are shown in Fig. 9. With the proposed method, ΔF_1, ΔF_2 and $\Delta Ptie_{error}$ signals are hastily driven back to zero with small values of STs/PUs/PIs as indicated in Table 7 and Figs. 9(a-c). Also in the steady state, the tie-line power flow properly converges to the specified value of Eqn. (20) i.e., $\Delta Ptie_{scheduled/actual} = -0.05$ puMW

Accepted manuscript

ACCEPTED MANUSCRIPT

as verified from Fig. 9(c). As shown in Figs. 9(d-f), the actual power generations of some GENCOs, according to Eqn. (19), suitably reach their desired values comparably quickly in the steady state i.e., ΔP_{G1} = 0.105 puMW, ΔP_{G2} = 0.045 puMW, ΔP_{G3} = 0.195 puMW and ΔP_{G4} = 0.055 puMW.

6.4. Sensitivity Analysis

The designed controller is required to perform well in a broad range of operating conditions without significant decline in performance. In other words, the controller should work robustly under changes in system parameters or operating condition [3–6,8–12,14,16–20,22]. Hence, a sensitivity analysis is carried out to verify the robustness of the optimized gains of the proposed FOFPID controller obtained at nominal condition of 50% initial loading for wide changes in initial loading, system parameters, DPM structure and size and location of contract violation. Case 4 of restructured hydrothermal system is considered as the system model in this case is more complex, nonlinear and pragmatic.

The first study is conducted with change in initial loading/parameters. The system responses are shown in Fig. 10 for nominal as well as ±25% change in nominal parameters. Fig. 10(a) shows $\Delta F_{1/2}$ response for change in R parameter and Fig. 10(b) shows $\Delta Ptie_{12}$ response for change in initial loading for traditional multi-source system. Further, Fig. 10(c) shows $\Delta F_{1/2}$ response for simultaneous change in K_{PS}/T_{PS} parameter and Fig. 10(d) shows $\Delta Ptie_{actual/error}$ response for simultaneous change $T_R/T_{GH}/T_G$ parameter for restructured hydrothermal system. Fig. 10(e) shows $\Delta F_{1/2}$ response for simultaneous change in $T_G/b_g/T_{CR}$ parameter for restructured thermal gas system. Critical inspection of all the responses noticeably reveals that the system is stable and responses are almost same. Only nine numbers of responses are shown in five figures to justify the statement.

In restructured power system, with changing market economy, DPM will not remain alike all the time. Adjustment in DPM alters the scheduled tie-line power, generation schedule of the GENCOs and hence the system behavior in the deregulated environment. Consequently, a study is carried out to examine the system conduct in DPM change scenario. In addition to DPM defined in Eqn. (22), two more DPMs i.e. DPMa and DPMb shown in Eqns. (23) and (24) are utilized for the system described in section 6.2.4 i.e., Case 4 considering the same optimized values for DPM (sixth column of Table 4).

$$\text{DPMa} = \begin{bmatrix} 0.4 & 0.3 & 0.0 & 0.2 \\ 0.2 & 0.2 & 0.0 & 0.1 \\ 0.1 & 0.2 & 0.9 & 0.6 \\ 0.3 & 0.3 & 0.1 & 0.1 \end{bmatrix} \tag{23}$$

Accepted manuscript

ACCEPTED MANUSCRIPT

$$\text{DPMb} = \begin{bmatrix} 0.45 & 0.35 & 0.01 & 0.35 \\ 0.25 & 0.2 & 0.05 & 0.05 \\ 0.05 & 0.25 & 0.8 & 0.6 \\ 0.25 & 0.2 & 0.14 & 0 \end{bmatrix} \quad (24)$$

The comparison of dynamic responses corresponding to DPM, DPMa and DPMb are shown in Figs. 10(f-h). Critical inspection of $\Delta F_{1/2}/\Delta Ptie_{error}$ responses of Figs. 10(f-g) shows that responses corresponding to DPM, DPMa and DPMb are more or less same. Thus change in DPMs shows negligible effect on system performance. This statement is similar to the statement postulated in [16]. However, change in DPM structure amends the scheduled tie-line power and power generation of GENCOs as demonstrated in Figs. 10(g) and 10(h), respectively.

Next, in practical power systems, SLP and uncontracted power demands may occur in any one area or in all the areas simultaneously [9]. If controller is not so robust to deal with such situations, system will indeed turn unstable. Again, Case 4 is considered of restructured hydrothermal system. Here, simulations are realized for various combinations of size and locations of ΔP_{UCi}. Evaluation of Fig. 10(i) for ΔP_{G4} response of restructured hydrothermal system and Fig. 10(j) for ΔP_{G3} response of restructure thermal gas system clearly reveal that the designed controller is robust and perform satisfactorily, under different load disturbances under various contract violation scenarios in restructure systems. Thus, K_1, K_2, K_p, K_I, K_D, γ, λ and μ obtained at nominal parameters and initial loading condition of 50% need not be retuned for wide changes in the system loading or parameters or size and location of contract violation. Thus, the main objective of designing a controller to perform satisfactorily under uncertain environment has been fruitfully attained.

7. Conclusions

FOFPID controller is proposed for the first time in AGC of multi-area multi-source traditional and restructured multi-source power systems. The gains and parameters of FOFPID controller are optimized utilizing bacterial foraging optimization algorithm (BFOA). Initially, a traditional two-area multi-source hydrothermal system is considered and superiority of FOFPID controller is demonstrated over BFOA based FOPID/FPID as well as PI/PID controller based on some lately published optimization techniques like hybrid firefly algorithm-pattern search (hFA-PS) and grey wolf optimization (GWO) algorithms. To reveal the effectiveness, the proposed approach is also extended to restructured two-area multi-source hydrothermal and thermal gas electric power systems. Critical analysis of the obtained results reveals the effectiveness of FOFPID controller in comparison to FPID/FOPID/PID controller. It is also observed that the proposed controller satiates the AGC requirement in deregulated environment under varied power transactions taking place with/without considering appropriate GRC, TD and DZ. Sensitivity analysis is carried out to check the robustness of the proposed controller and divulges that the optimum gains of FOFPID controller obtained at the nominal condition are healthy enough and need not

Accepted manuscript

ACCEPTED MANUSCRIPT

be reset for wide variations in nominal system parameters, initial loading, DPM structure and size and position of uncontracted power demands.

Appendix: system data

Traditional/restructured two-area multi-source hydrothermal system [5]:

$P_{r1} = P_{r2}$ = 2000 MW, $Ptie_{max}$ = 200 MW, Base power = 2000 MVA, ΔP_{Di}^{0} = 1000 MW, F^{0} = 60 Hz, α_{12} = –1, β_1 = 0.425, R_1 = 2 Hz/puMW, R_2 = 2.4 Hz/puMW, K_{PSi} = 100, T_{PSi} = 20, T_{Gi} = 0.08 s, T_{Ti} = 0.3 s, T_{RHi} = 48.7 s, T_{Ri} = 5 s, T_{GHi} = 0.513 s, T_{Wi} = 1 s, T_{12} = 0.0707 puMW/rad.

Restructured two-area multi-source thermal gas system [7]:

$P_{r1} = P_{r2}$ = 2000 MW, $Ptie_{max}$ = 200 MW, Base power = 2000 MVA, ΔP_{Di}^{0} = 1000 MW, F^{0} = 60 Hz, α_{12} (= $-P_{r1}/P_{r2}$) = – 1, D_i (= $\partial \Delta P_{Di}^{0}/\partial fP_{ri}$) = 8.33 × 10^{-3} puMW/Hz, H_i = 5 MW s/MVA, T_{Gi} = 0.06 s, T_{Ti} = 0.3 s, K_{ri} = 0.3, T_{ri} = 10 s, R_1 = 3.0784 Hz/puMW, R_2 = 4.9809 Hz/puMW, K_{PSi} (= $1/D_i$) = 120 Hz/puMW, T_{PSi} (= $2H_i/f^0D_i$) = 20 s, β_i (= $D_i + 1/R_i$) = 0.4312 puMW/Hz, T_{12} = 0.02712 puMW/rad, a_i = 1, c_{gi} = 1, b_{gi} = 0.049 s, X_i = 0.6 s, Y_i = 1.1 s, T_{CRi} = 0.01 s, T_{Fi} = 0.239 s, T_{CDi} = 0.2 s.

References

[1] Kothari DP, Nagrath IJ. Modern power system analysis. 3rd ed. New Delhi: McGraw Hill, 2003.

[2] Nanda J, Mangla A, Suri S. Some new findings on automatic generation control of an interconnected hydrothermal system with conventional controllers. IEEE Trans Energy Convers 2006;21(1):187–94.

[3] Nanda J, Mishra S, Saikia LC. Maiden application of bacterial foraging-based optimization technique in multiarea automatic generation control. IEEE Trans Power Syst 2009;24(2):602–9.

[4] Ali ES, Abd-Elazim SM. Bacteria foraging optimization algorithm based load frequency controller for interconnected power system. Int J Elect Power Energy Syst 2011;33(3):633–8.

[5] Sahu RK, Panda S, Padhan S. A hybrid firefly algorithm and pattern search technique for automatic generation control of multi area power systems. Int J Elect Power Energy Syst 2015;64:9–23.

[6] Guha D, Roy PK, Banerjee S. Load frequency control of interconnected power system using grey wolf optimization. Swarm Evolution Comput 2016; 27:97–115.

[7] Hota PK, Mohanty B. Automatic generation control of multi source power generation under deregulated environment. Int J Elect Power Energy Syst 2016;75:205–14.

Accepted manuscript

ACCEPTED MANUSCRIPT

[8] Alomoush MI. Load frequency control and automatic generation control using fractional-order controllers. J Elect Eng 2010;91(7):357–68.

[9] Debbarma S, Saikia LC, Sinha N. AGC of a multi-area thermal system under deregulated environment using a non-integer controller. Electr Power Syst Res 2013;95:175–83.

[10] Sondhi S, Hote YV. Fractional order PID controller for load frequency control. Energy Convers Manage 2014;85:343–53.

[11] Taher SA, Fini MH, Aliabadi SF. Fractional order PID controller design for LFC in electric power systems using imperialist competitive algorithm. Ain Shams Eng J 2014;5(1):121–35.

[12] Pan I, Das S. Fractional order load-frequency control of interconnected power systems using chaotic multi-objective optimization. Applied Soft Comput 2015;29:328–44.

[13] Chathoth I. Ramdas SK, Krishnan ST. Fractional-order proportional-integral-derivative-based automatic generation control in deregulated power systems. Electr Power Compon Syst 2015;43(17):1931–45.

[14] Pan I, Das S. Fractional order fuzzy control of hybrid power system with renewable generation using chaotic PSO. ISA Trans 2016;62:19–29.

[15] Donde V, Pai MA, Hiskens IA. Simulation and optimization in an AGC system after deregulation. IEEE Trans Power Syst 2001;16(3):481–9.

[16] Rahman A, Saikia LC, Sinha N. Load frequency control of a hydro-thermal system under deregulated environment using biogeography-based optimised three-degree-of-freedom integral-derivative controller. IET Gener Transm Distrib 2015;9(15):2284–93.

[17] Arya Y, Kumar N, Ibraheem. AGC of a two-area multi-source power system interconnected via AC/DC parallel links under restructured power environment. Optim Contr Appl Meth 2015; DOI: 10.1002/oca.2181.

[18] Arya Y, Kumar N. AGC of a multi-area multi-source hydrothermal power system interconnected via AC/DC parallel links under deregulated environment. Int J Elect Power Energy Syst 2016;75:127–38.

[19] Saikia LC, Sinha N, Nanda J. Maiden application of bacterial foraging based fuzzy IDD controller in AGC of a multi-area hydrothermal system. Int J Elect Power Energy Syst 2013;45(1):98–106.

[20] Sahu RK, Panda S, Yegireddy NK. A novel hybrid DEPS optimized fuzzy PI/PID controller for load frequency control of multi-area interconnected power systems. J Process Contr 2014;24(10):1596–608.

[21] Bhateshvar YK, Mathur HD, Siguerdidjane H, Bhanot S. Frequency stabilization for multi-area thermal-hydro power system using genetic algorithm-optimized fuzzy logic controller in deregulated environment. Electr Power Compon Syst 2015;43(2):146–56.

[22] Sekhar GTC, Sahu RK, Baliarsingh AK, Panda S. Load frequency control of power system under deregulated environment using optimal firefly algorithm. Int J Elect Power Energy Syst 2016;74:195–211.

[23] Oustaloup A, Mathieu B, Lanusse P. The CRONE control of resonant plants: application to a flexible transmission, Eur J Contr 1995;1(2):113–21.

[24] Passino KM. Biomimicry of bacterial foraging for distributed optimization and control. IEEE Contr Syst 2002;22(3):52–67.

Accepted manuscript

ACCEPTED MANUSCRIPT

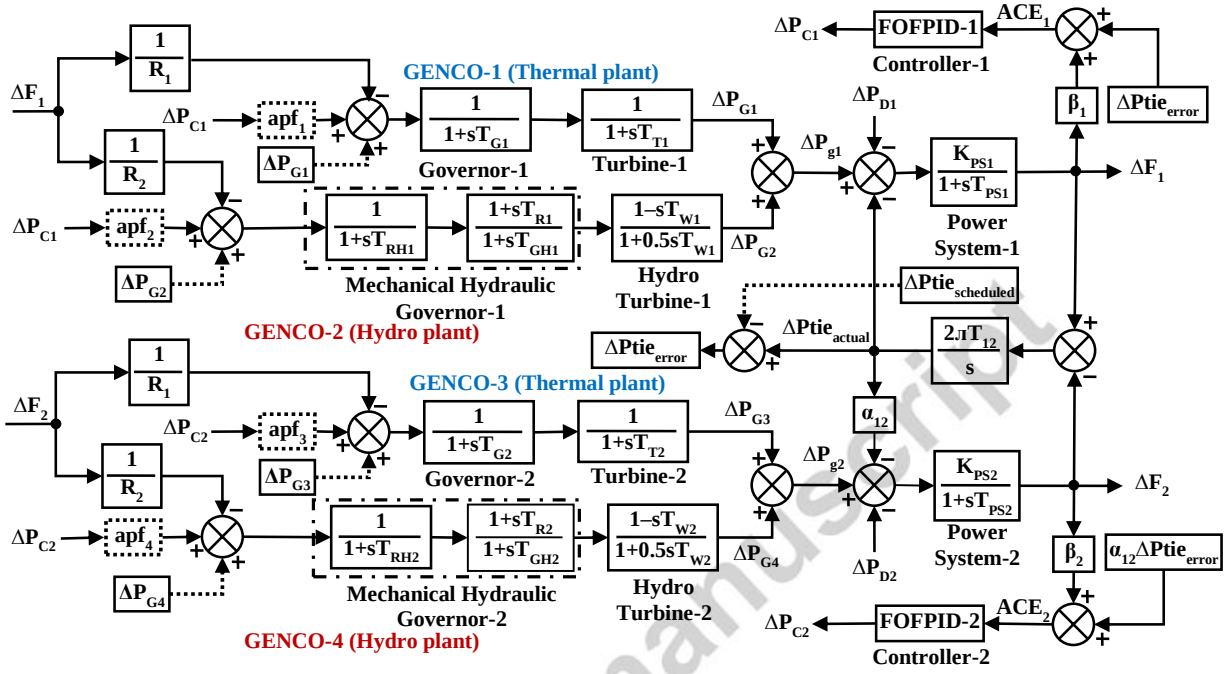

Fig. 1. Transfer function model of multi-area multi-source hydrothermal power system (Traditional: without dotted line connections; Restructured: with dotted line connections).

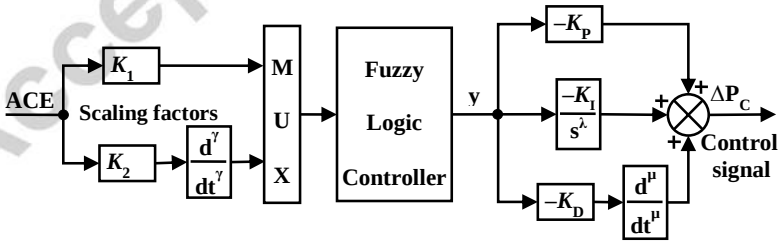

Fig. 2. Structure of FOFPID controller [20].

Accepted manuscript

ACCEPTED MANUSCRIPT

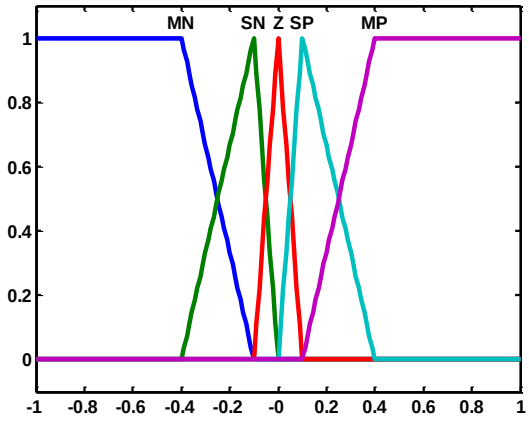

Fig. 3. Membership functions of FOFPID controller for ACE, fractional rate of ACE derivative and FLC output [20,22].

Accepted manuscript

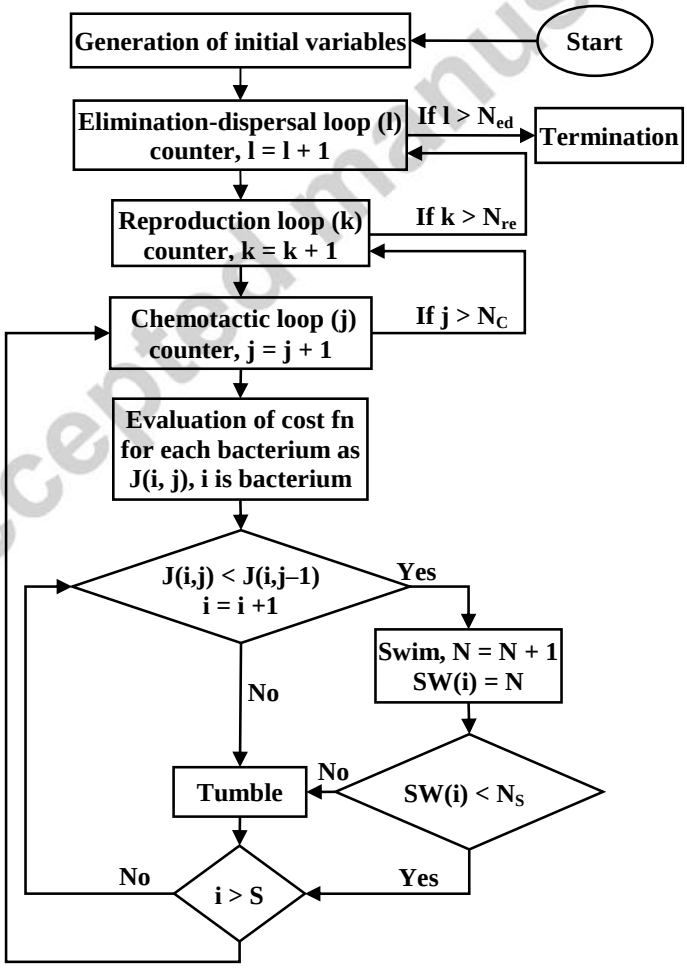

Fig. 4. Flow chart of BFOA for tuning controller parameters.

ACCEPTED MANUSCRIPT

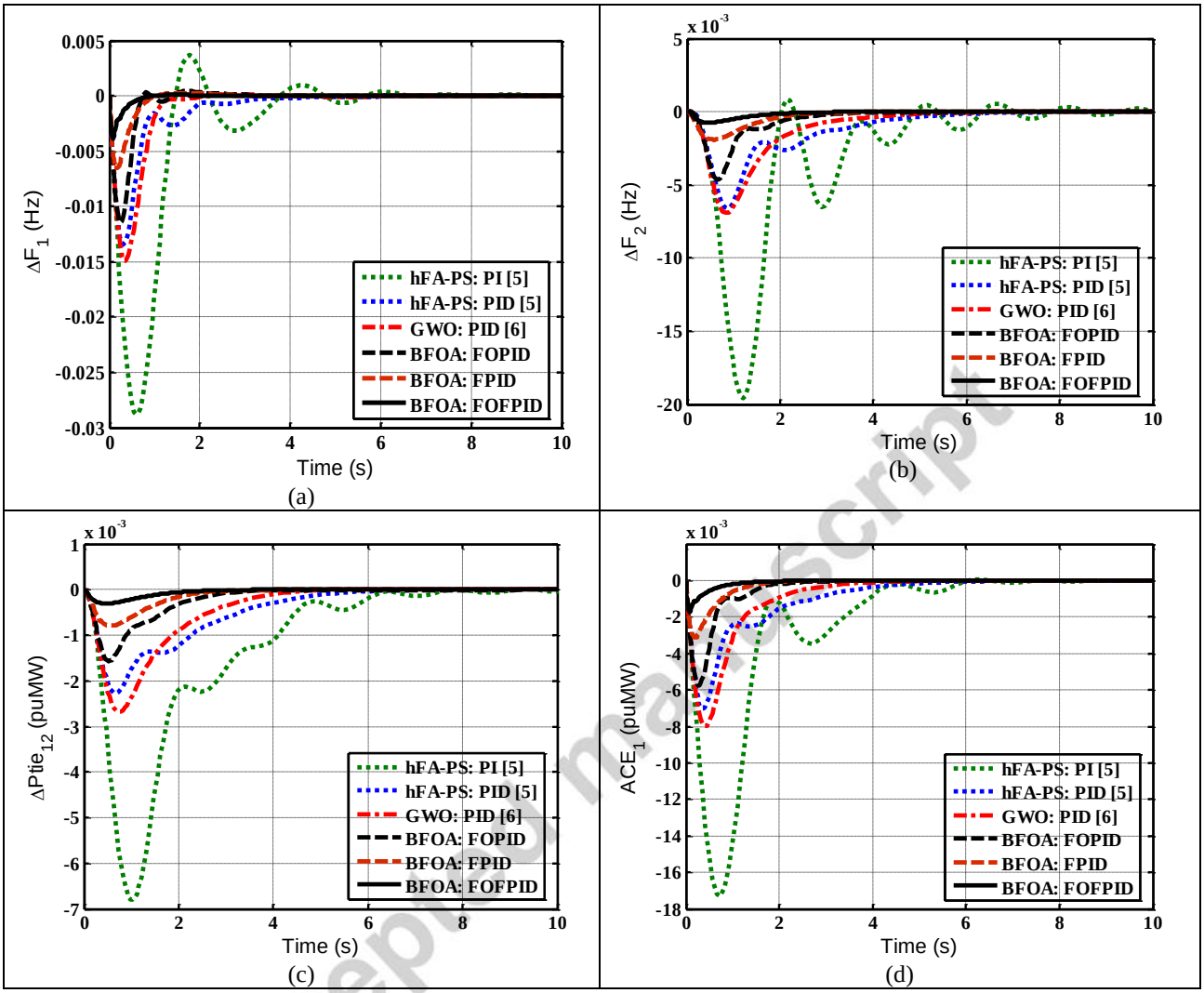

Fig. 5. Dynamic responses of traditional multi-area multi-source system with different controllers for 1.5% SLP in area-1 (a) ΔF_1 (b) ΔF_2 (c) $\Delta Ptie_{12}$ and (d) ACE_1.

Accepted manuscript

ACCEPTED MANUSCRIPT

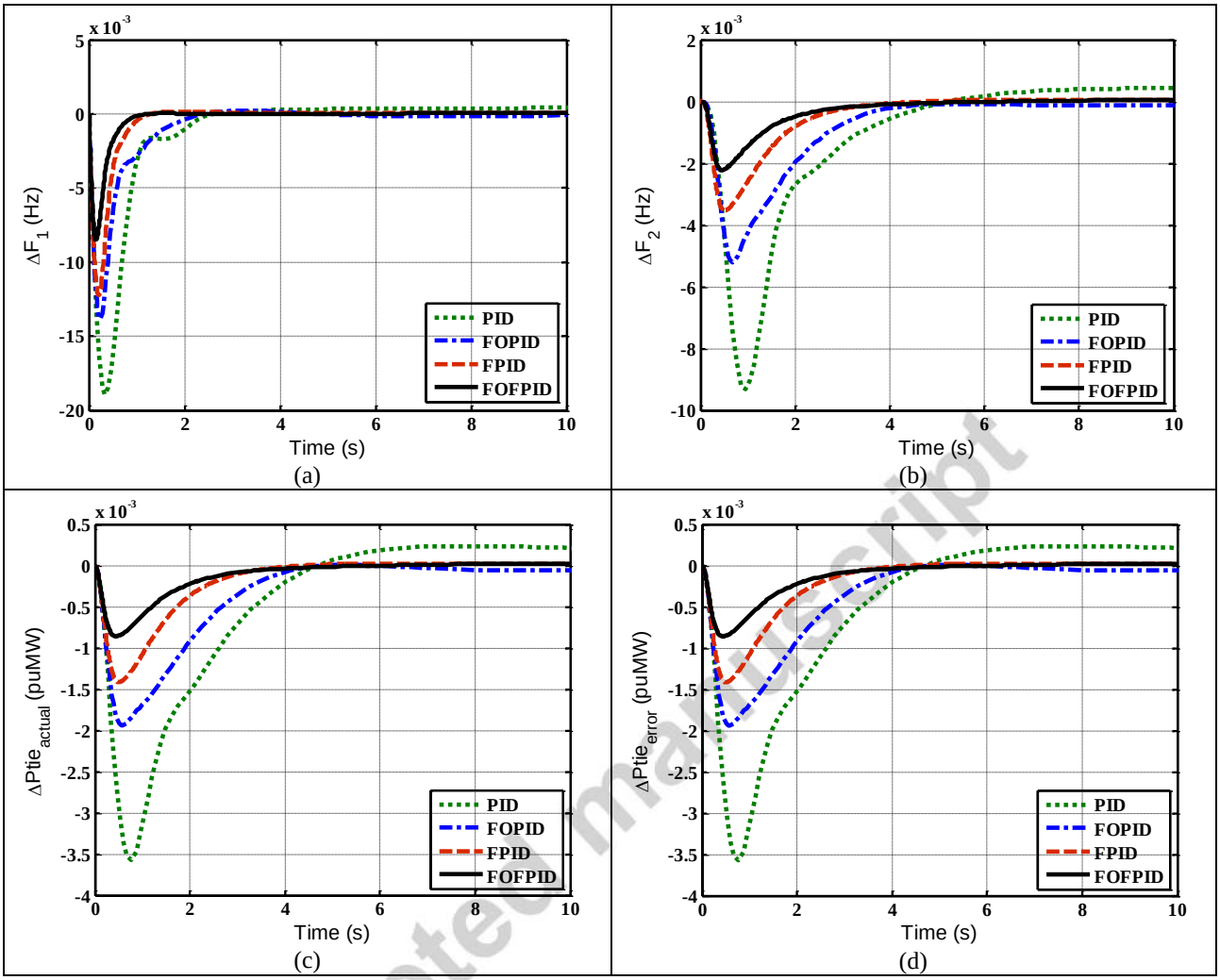

Fig. 6. Dynamic responses of restructured multi-area multi-source hydrothermal system with different controllers for poolco based transactions (a) ΔF_1 and (b) ΔF_2, (c) $\Delta Ptie_{actual}$ and (d) $\Delta Ptie_{error}$.

Accepted manuscript

ACCEPTED MANUSCRIPT

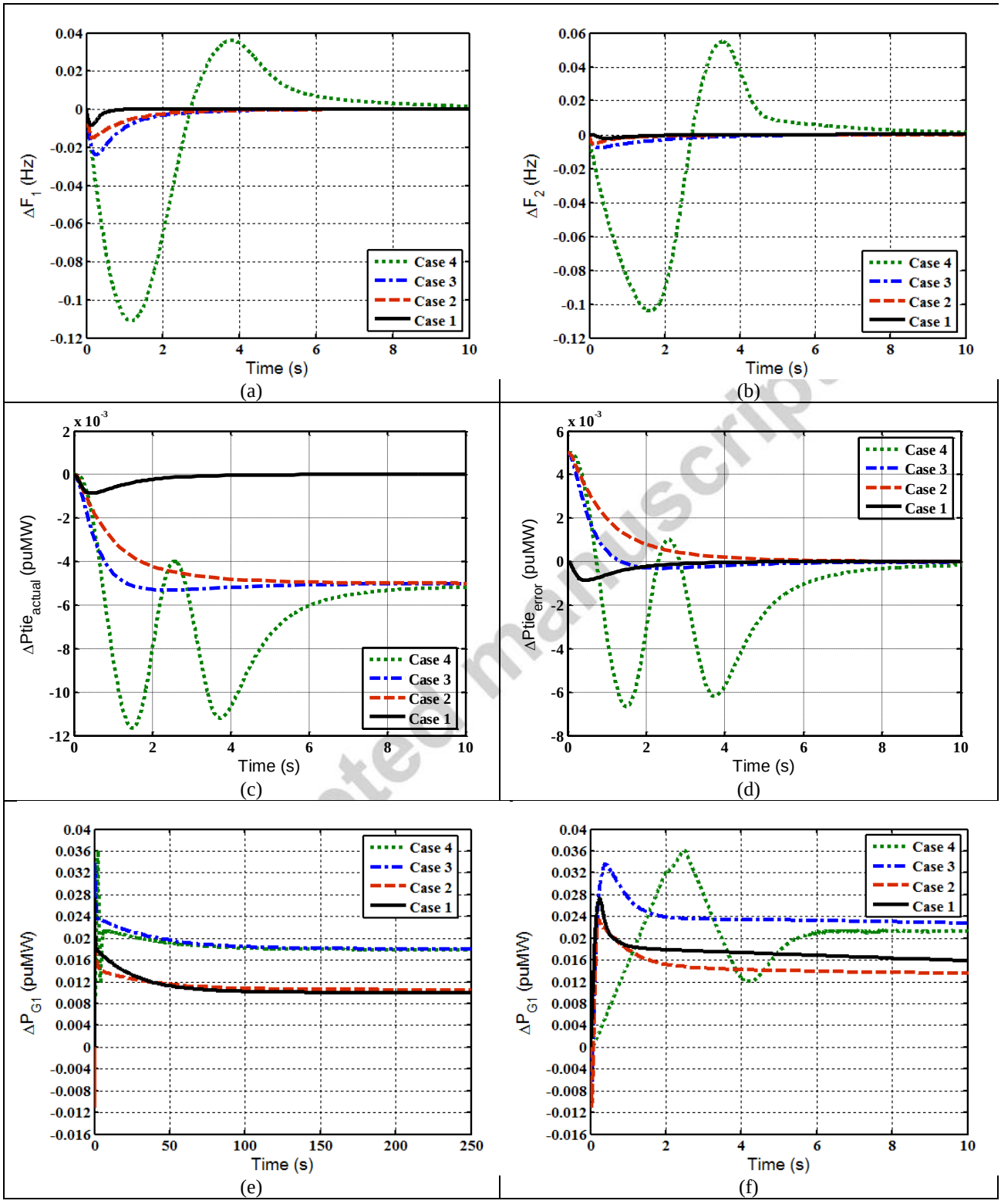

ACCEPTED MANUSCRIPT

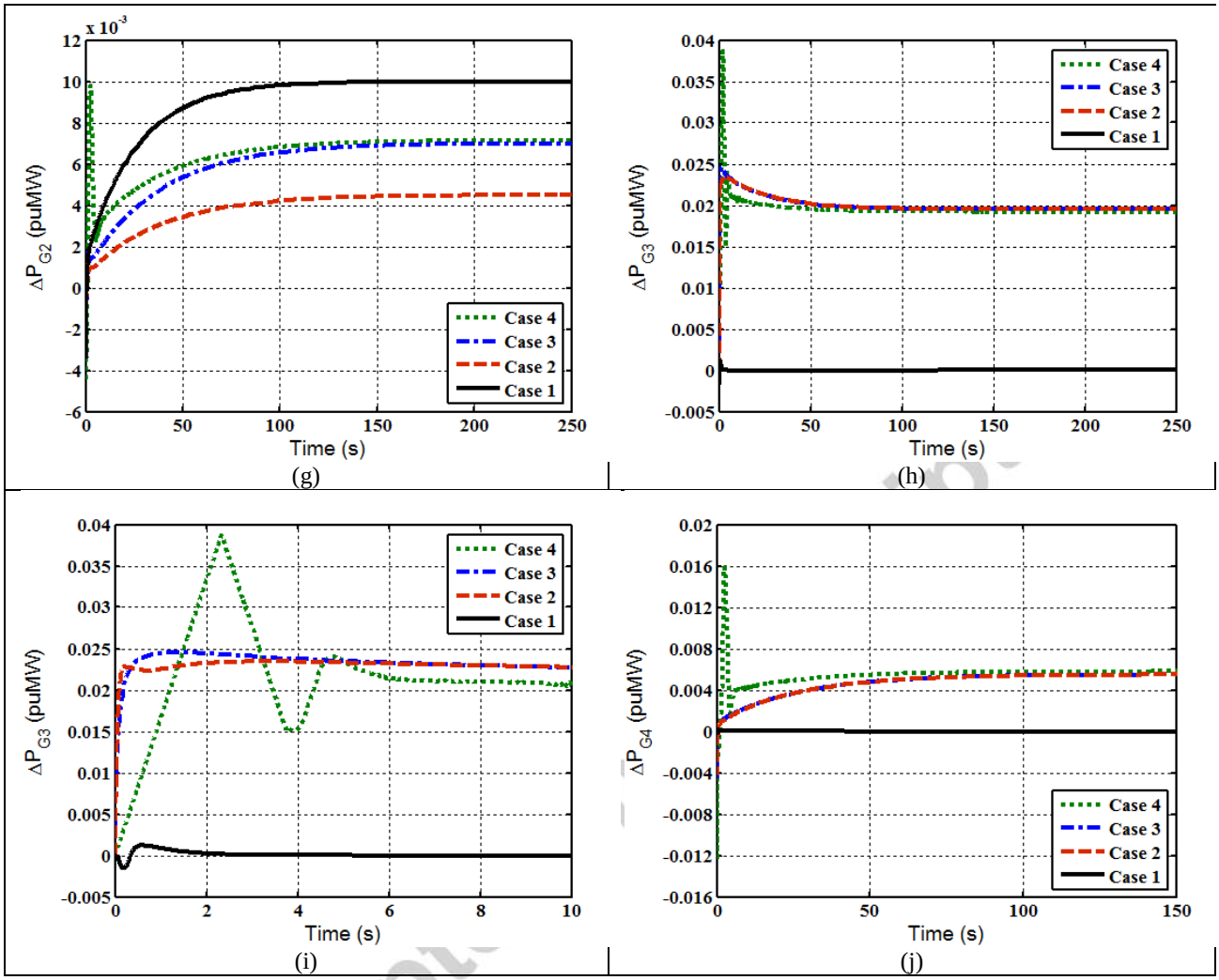

Fig. 7. Dynamic responses of restructured multi-area multi-source hydrothermal system with FOFPID controller for different cases (a) ΔF_1 (b) ΔF_2 (c) $\Delta Ptie_{actual}$, (d) $\Delta Ptie_{error}$, (e) ΔP_{G1}, (f) ΔP_{G1} with t = 0 – 10 s, (g) ΔP_{G2}, (h) ΔP_{G3}, (i) ΔP_{G3} with t = 0 – 10 s and (j) ΔP_{G4}.

ACCEPTED MANUSCRIPT

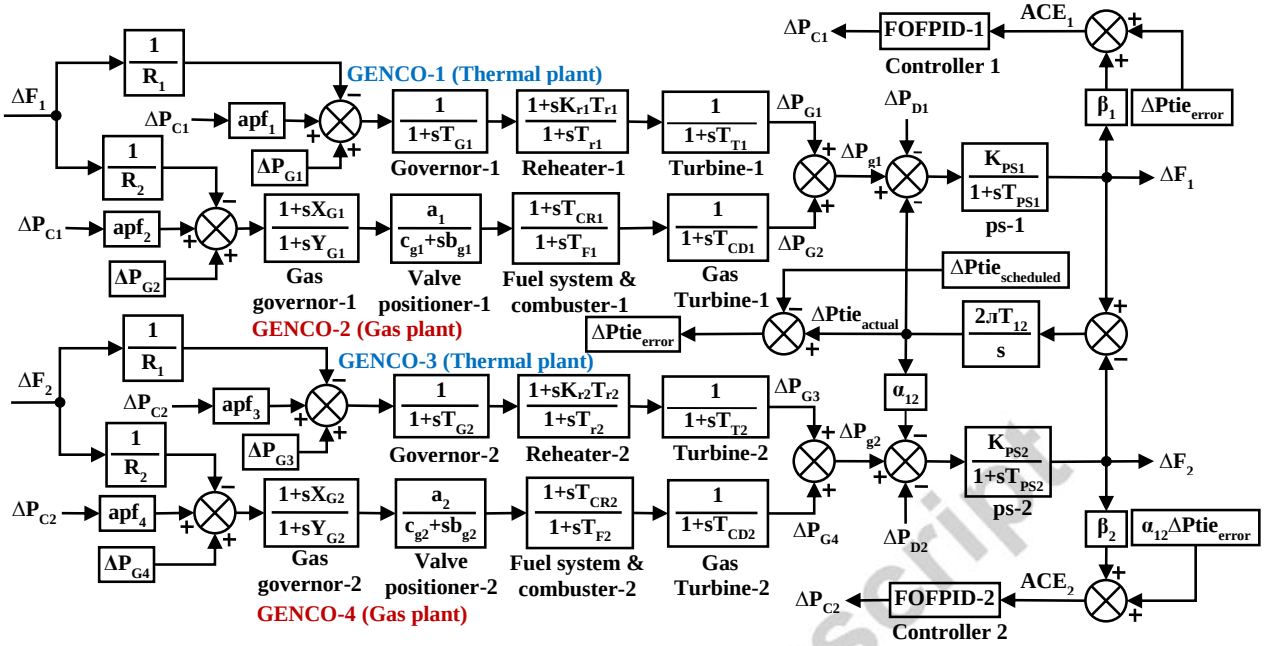

Fig. 8. Transfer function model of restructured two-area multi-source thermal gas system.

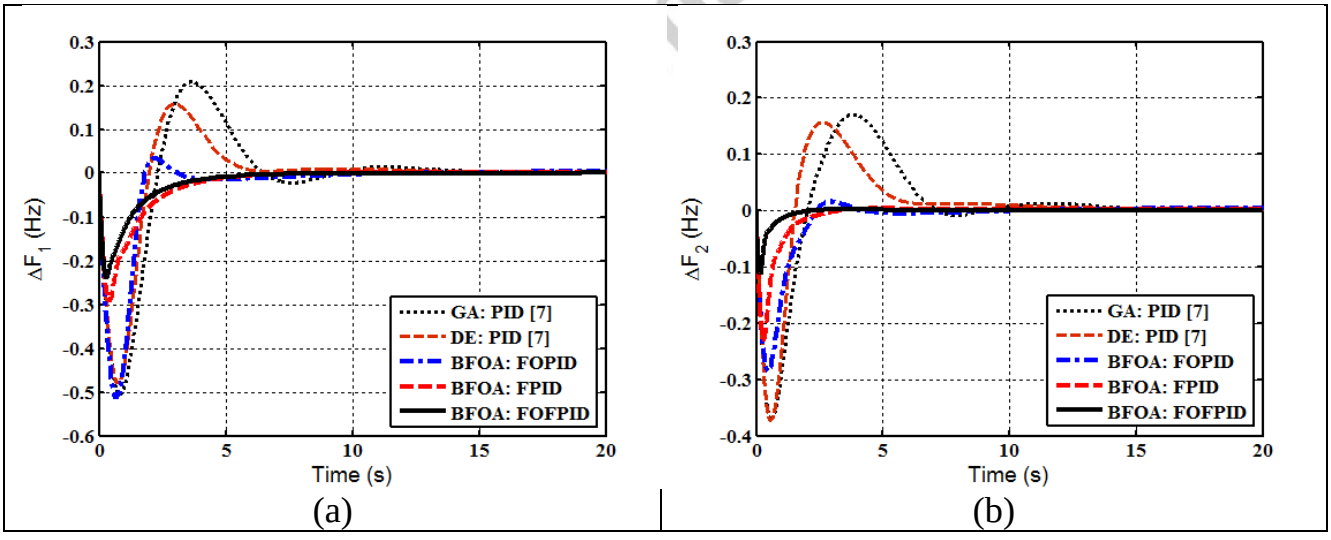

ACCEPTED MANUSCRIPT

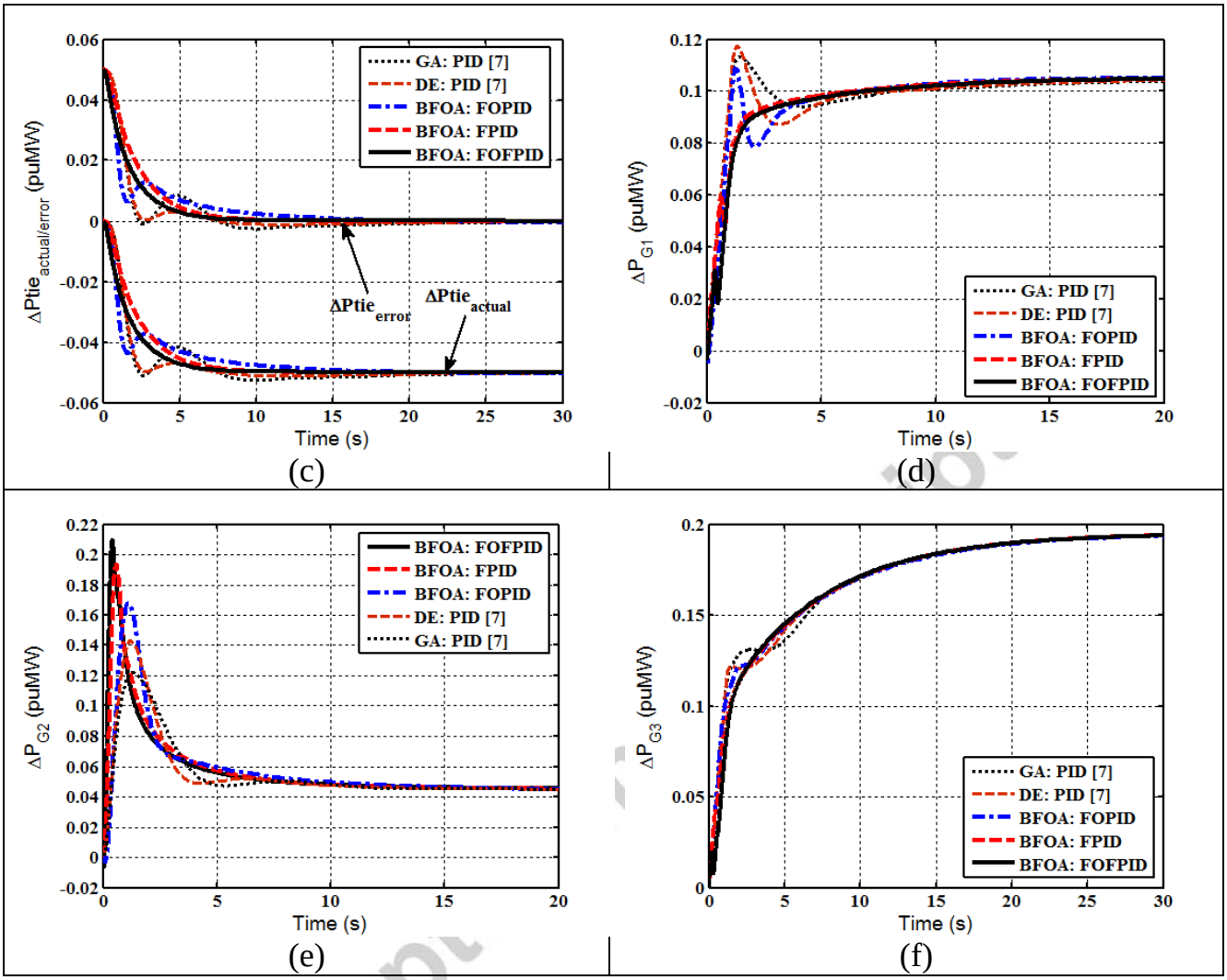

Fig. 9. Dynamic responses of two-area restructured multi-source thermal gas power system with different controllers for bilateral based transactions (a) ΔF_1 and (b) ΔF_2, (c) $\Delta Ptie_{actual/error}$, (d) ΔP_{G1} (e) ΔP_{G2} and (f) ΔP_{G3}.

ACCEPTED MANUSCRIPT

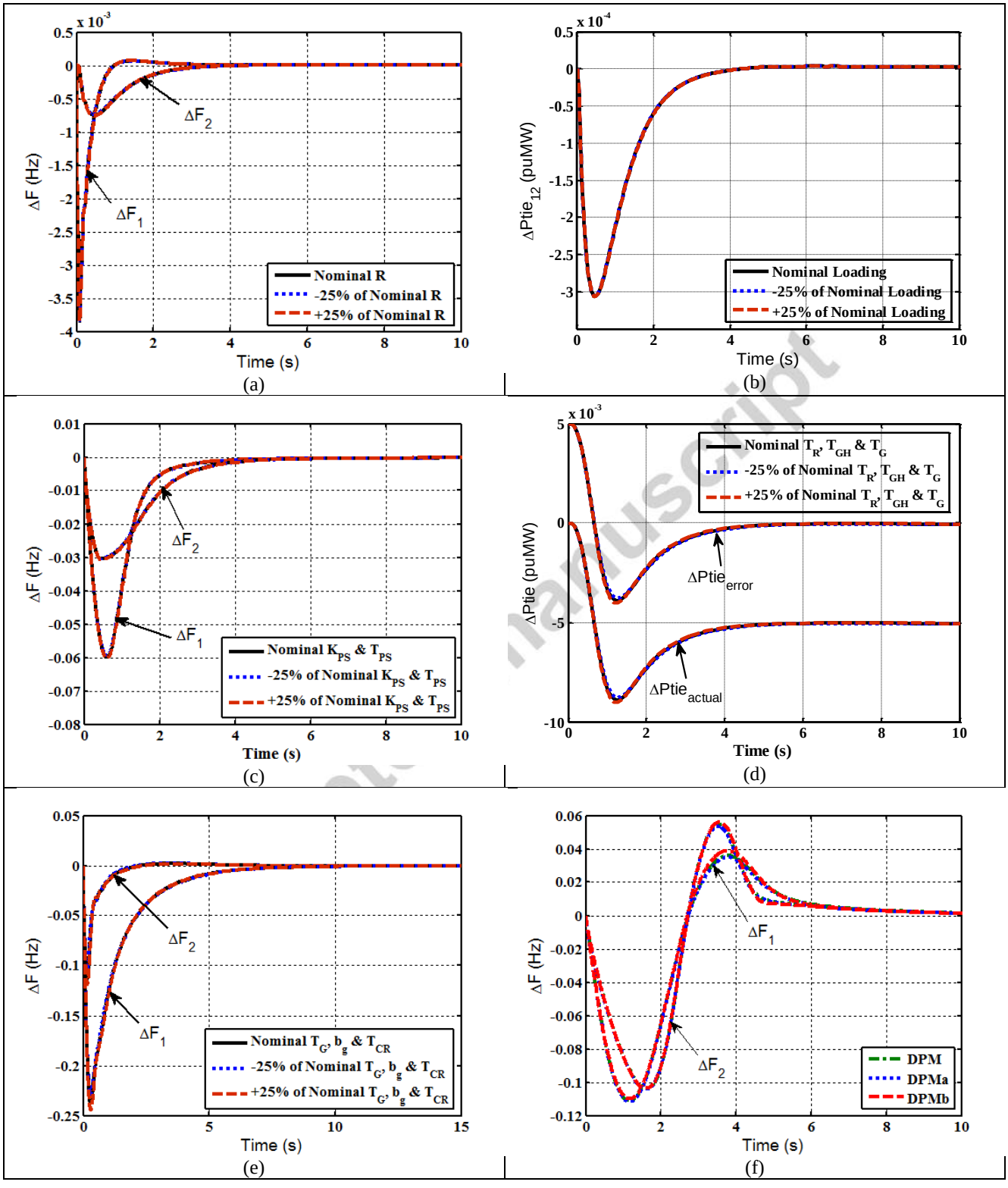

ACCEPTED MANUSCRIPT

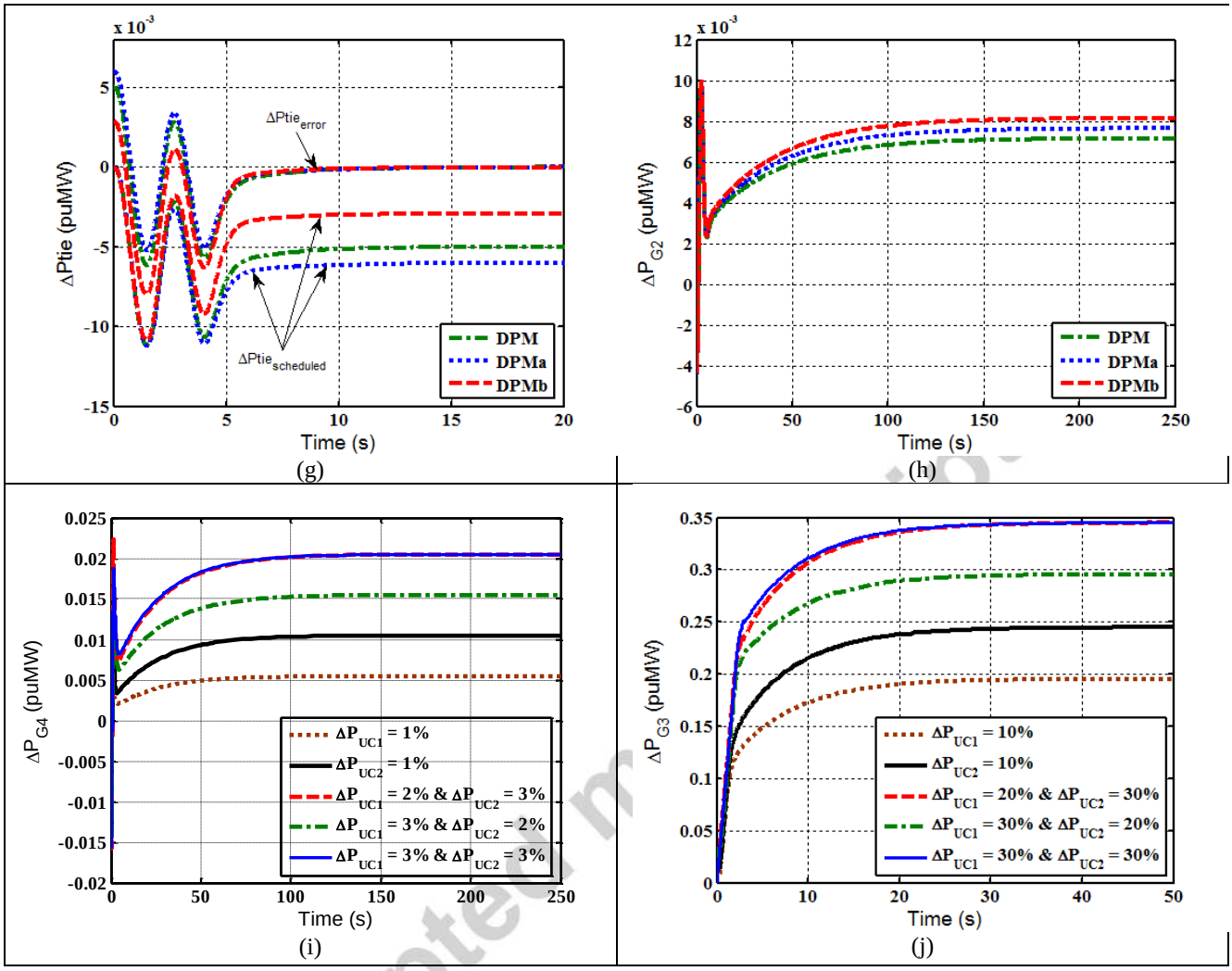

Fig. 10. System dynamic responses with FOFPID controller during sensitivity analysis (a) $\Delta F_{1/2}$ of traditional system, (b) $\Delta Ptie_{12}$ of traditional system, (c) $\Delta F_{1/2}$ of restructured hydrothermal system, (d) $\Delta Ptie_{actual/error}$ of restructured hydrothermal system, (e) $\Delta F_{1/2}$ of restructured thermal gas system, (f) $\Delta F_{1/2}$ of restructured hydrothermal system with various DPMs, (g) $\Delta Ptie_{scheduled/error}$ of restructured hydrothermal system with various DPMs, (h) ΔP_{G2} of restructured hydrothermal with various DPMs, (i) ΔP_{G4} of restructured hydrothermal system under different size and positions of ΔP_{UCi} and (j) ΔP_{G3} of restructured thermal gas system under different size and positions of ΔP_{UCi}.

ACCEPTED MANUSCRIPT

Table 1 Rule base for ACE, fractional rate of ACE derivative and FLC output.

	Fractional rate of ACE derivative				
ACE	MN	SN	Z	SP	MP
MN	MN	MN	MN	SN	Z
SN	MN	SN	SN	Z	SP
Z	MN	SN	Z	SP	MP
SP	SN	Z	SP	SP	MP
MP	Z	SP	MP	MP	MP

Table 2 Optimized controller parameters for traditional multi-source hydrothermal system.

Controller parameters	FOPID	FPID	FOFPID
K_1	-	1.9904	1.9996
K_2	-	1.1099	0.9043
K_P	2.9532	1.1532	1.2192
K_I	3.9172	1.0502	1.9390
K_D	1.0014	0.0719	0.0791
γ	-	-	0.9359
λ	0.9230	-	0.9953
μ	0.9902	-	0.9999

An entry "-" means not applicable.

Table 3 Numerical values of STs (±0.0005 band), PUs and PIs (15 s) with traditional multi-source hydrothermal system.

Controller	STs (s)			PUs (Hz) (–ve)			PIs			
	ΔF_1	ΔF_2	$\Delta Ptie_{12}$	ΔF_1	ΔF_2	$\Delta Ptie_{12}$	ISE	ITSE	IAE	ITAE
hFA-PS: PI [5]	5.35	6.18	4.480	0.0287	0.0195	0.0067	$9.03e^{-04}$	$8.56e^{-04}$	0.0705	0.1177

Accepted manuscript

ACCEPTED MANUSCRIPT

hFA-PS: PID [5]	2.94	4.53	3.300	0.0134	0.0066	0.0022	$1.17e^{-04}$	$8.50e^{-05}$	0.0255	0.0395
GWO: PID [6]	1.21	3.50	2.640	0.0149	0.0069	0.0026	$1.47e^{-04}$	$9.03e^{-05}$	0.0233	0.0259
BFOA: FOPID	1.20	2.15	1.678	0.0115	0.0046	0.0015	$5.22e^{-05}$	$2.14e^{-05}$	0.0116	0.0121
BFOA: FPID	0.82	1.79	1.173	0.0065	0.0019	0.0007	$1.60e^{-05}$	$6.07e^{-06}$	0.0068	0.0083
BFOA: FOFPID	0.55	0.98	0.450	0.0038	0.0007	0.0003	$2.81e^{-06}$	$7.73e^{-07}$	0.0026	0.0035

Table 4 Optimized controller parameters for restructured multi-source hydrothermal system.

Controller parameters	Types of transactions						
	Case-1 (Poolco)				Case-2 (Bilateral)	Case-3 (Contract violation)	Case-4 (Contract violation with GRC, TD and DZ)
	PID	FOPID	FPID	FOFPID	FOFPID	FOFPID	FOFPID
K_1	-	-	1.9598	0.5031	0.5240	0.8931	1.5401
K_2	-	-	1.1839	0.4630	0.6541	0.9924	1.9990
K_P	1.0123	1.2965	0.9469	1.9986	0.9672	0.5534	0.5023
K_I	1.3101	3.0843	0.8042	3.0992	0.8921	0.5746	0.3142
K_D	0.9502	2.9231	0.0259	0.1584	0.1293	0.0558	0.1207
γ	-	-	-	0.9075	0.9999	0.9997	0.9904
λ	-	0.7634	-	0.9563	0.8923	0.9998	0.9912
μ	-	0.8939	-	0.7984	0.7532	0.9642	0.9942

An entry "-" means not applicable.

Accepted manuscript

Table 5 Numerical values of STs (±0.0005 band), PUs and PIs (15 s) with restructured multi-source hydrothermal system.

Case 1 (Poolco based transactions)										
Controller	STs (s)			PUs (Hz) (–ve)			PIs			
	ΔF_1	ΔF_2	$\Delta Ptie_{error}$	ΔF_1	ΔF_2	$\Delta Ptie_{error}$	ISE	ITSE	IAE	ITAE
PID	2.23	4.11	3.34	0.0190	0.0093	0.0035	$2.57e^{-04}$	$2.04e^{-04}$	0.0426	0.1342
FOPID	1.89	3.32	2.68	0.0138	0.0052	0.0019	$9.64e^{-05}$	$5.79e^{-05}$	0.0223	0.0410
FPID	0.98	2.40	1.73	0.0122	0.0035	0.0014	$5.18e^{-05}$	$2.07e^{-05}$	0.0130	0.0214

ACCEPTED MANUSCRIPT

FOFPID	0.79	1.97	1.19	0.0085	0.0022	0.0008	$2.04e^{-05}$	$7.12e^{-06}$	0.0079	0.0147
Case 2 (Bilateral based transactions)										
FOFPID	4.55	3.37	2.61	0.0151	0.0053	0.0000	$1.63e^{-04}$	$9.81e^{-05}$	0.0307	0.0485
Case 3 (Contract violation transactions)										
FOFPID	4.62	5.04	0.99	0.0238	0.0076	0.0003	$4.14e^{-04}$	$2.57e^{-04}$	0.0463	0.0779
Case 4 (Contract violation transactions with GRC, TD and DZ)										
FOFPID	13.09	12.67	6.98	0.1109	0.1039	0.0061	$3.57e^{-02}$	$5.97e^{-02}$	0.5645	1.4050

Table 6 Optimized controller parameters for restructured multi-source thermal gas system.

Controller parameters	FOPID	FPID	FOFPID
K_1	-	1.9290	1.9971
K_2	-	1.9991	1.9990
K_P	1.3972	2.8213	2.2361
K_I	0.9905	0.2705	2.7321
K_D	1.0994	0.0691	0.4179
γ	-	-	0.9973
λ	0.4530	-	0.0993
μ	0.9990	-	0.9992

An entry "-" means not applicable.

Accepted manuscript

Table 7 Numerical values of STs (±0.005 band), PUs and PIs (15 s) with restructured multi-source thermal gas system.

Controller	STs (s)			PUs (Hz) (–ve)			PIs			
	ΔF_1	ΔF_2	$\Delta Ptie_{error}$	ΔF_1	ΔF_2	$\Delta Ptie_{error}$	ISE	ITSE	IAE	ITAE
GA: PID [7]	14.58	14.32	6.158	0.5063	0.3718	0.0000	$5.35e^{-01}$	$9.25e^{-01}$	2.3690	7.0880
DE: PID [7]	13.85	27.16	20.38	0.4790	0.3719	0.0000	$3.93e^{-01}$	$5.03e^{-01}$	1.8500	4.6930
BFOA: FOPID	8.95	5.95	6.450	0.5130	0.2839	0.0000	$2.69e^{-01}$	$2.00e^{-01}$	1.0780	1.8450
BFOA: FPID	6.05	2.70	4.900	0.2906	0.2284	0.0000	$9.29e^{-02}$	$7.08e^{-02}$	0.7576	1.3130
BFOA: FOFPID	5.86	1.55	3.998	0.2374	0.1128	0.0000	$4.67e^{-02}$	$3.43e^{-02}$	0.4901	0.7724

ResearchGate

See discussions, stats, and author profiles for this publication at: https://www.researchgate.net/publication/304996502

COMBINED CYCLE GAS TURBINE AND GENERATOR MATCHING PERFORMANCE

Article · July 2016

READS
5

2 authors, including:

Dr. Jitendra Nath Rai
Delhi Technological University
34 PUBLICATIONS **9** CITATIONS

SEE PROFILE

All in-text references underlined in blue are linked to publications on ResearchGate, letting you access and read them immediately.

Available from: Dr. Jitendra Nath Rai
Retrieved on: 03 August 2016

COMBINED CYCLE GAS TURBINE AND GENERATOR MATCHING PERFORMANCE

Jitendra Nath Rai
Department of Electrical Engineering
Delhi Technological University
Delhi, India
jnrai.phd@gmail.com

Ajendra Singh
Department of Electrical Engineering
Delhi Technological University
Delhi, India
ajendrasingh25@gmail.com

Abstract
Due to ever-increasing demand for power there arise a need for installation of higher efficiency generating stations. This problem of higher efficiency plants can be resolved by the combined cycle power plants which provide a high installation capacity and higher efficiencies, but the installation of newer generating stations affects the stability of grid. The behavior of combined cycle power plants is still a topic of research as none of the models developed yet have been successfully able describe its overall behavior. The following paper studies the behavior of combined cycle generator under various conditions using MATLAB/*Simulink* model.

Key Words
Combined Cycle Gas Turbine, Synchronous Generator, Simulink Model, Stability.

I Introduction

Due to economy and power transmission maximization the present power systems consist of interconnected generating units supplying energy to a common grid [2]. The addition of new units or modifications in existing units requires a careful examination of the system stability as it affects the stability of grid [6-8, 14]. Thus it is required that the operating characteristics of various types generating stations are known so that the stability of the interconnection can be enhanced. The combined cycle gas turbines (CCGT) have a characteristic feature of high efficiency, quick start-up and low emission of greenhouse gases which make them an attractive choice for expansion of power generation [11-13]. As gas turbine operate at high speeds therefore the generator driven by these types of turbines are of cylindrical rotor type of construction. Fig. 1 shows the control equipment of synchronous generator used for controlling the output of the generator.

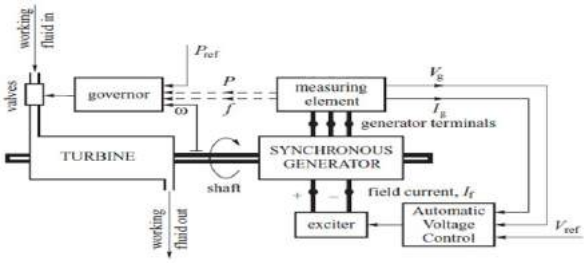

Figure 1: Block diagram of a power generation unit

The generator voltage is controlled by the exciter whose current (excitation current) is controlled by the automatic voltage regulator which produces signals according to the measured value of the generated voltage and current of the generator. The governor of the turbine of the generator adjusts the output of the turbine according to the power and the frequency at which it is produced by the generator by comparing it with a reference frequency and power. The output of the turbine is controlled by the varying fuel flow by the governor. In this paper we have analyzed the behavior of a synchronous generator driven by single shaft combined cycle gas turbine under no load, under load and the effects of excitation control and governor control using MATLAB/*Simulink* for matching performance.

II Cylindrical Rotor Synchronous Generator and CCGT

Synchronous Generator [3]: When in running generator the armature (stator in case of large generators) windings of the generator are open-circuited the generator is said to be operating on no load. The equations describing the operation under such conditions are as follows:

$$e_A = \omega M_f i_f \sin\omega t \quad e_B = \omega M_f i_f \sin(\omega t - 2 * pi/3)$$
$$e_C = \omega M_f i_f \sin(\omega t - 4 * pi/3) \qquad (1)$$

Where e_A, e_B and e_c are the internal voltage (or Excitation EMF) of the generator, M_f is the mutual inductance between the stator and the rotor windings, ω is speed of the rotor in rad/sec and if the field is current.

When the generator is connected to a load armature currents starts to flow and there is a voltage drop in the armature windings due armature resistance and an armature reaction which opposes the field flux. The terminal voltage of the generator under these conditions is given as:

$$V_a = -R_s I_a - (L_s + M_s)\frac{di_a}{dt} + \sqrt{2}|E_i|\cos(\omega t + \delta) \qquad (2)$$

Where R_s is the stator resistance, L_s is the self-inductance of the armature winding, M_s is the mutual inductance between the adjacent pair of windings, i_a is the current in the armature winding of phase 'a' and δ is the load angle.

978-1-4673-8587-9/16/$31.00 ©2016 IEEE

When the system operating under normal conditions i.e. under equilibrium, is disturbed the mechanical torque provided by the turbine is not equal to the electrical torque due to the load, the system under these conditions is described by what is known as the swing equation given as follows:

$$\frac{H}{180f}\frac{d^2\delta}{dt^2} = P_m - P_e = P_a \qquad (3)$$

Where H is the inertia constant, f is the frequency, P_m is the mechanical power and P_e is the electrical power.

2.1 CCGT (Combined Cycle Gas Turbine): The power output of the gas turbine is controlled by varying the fuel flow rate which controlled by the governor of the turbine. An increase in fuel flow causes an increase in the power output and vice versa, but an increase in the fuel flow also causes an increase in the temperature of the turbine which is controlled by increasing the air flow in the turbine [1, 15].

III Simulink Model

The model consists of cylindrical rotor synchronous generator model connected to single shaft CCGT block which provides mechanical energy to the generator. The gas turbine model is based on the Rowen Model [9, 16]. The CCGT block [1, 10] controls the output of the generator on the basis of the speed of the generator provided as an input to the block. There is a separate block for the excitation system consisting of V_{ref}, input voltage that voltage at the terminal of the generator and automatic voltage regulator in conjunction with the power system stabilizer block V_{stab} attached to it for better stabilization of the generated voltage [5]. The input excitation voltage is provided to the generator by the block as a signal V_f to the generator.

The generator model is connected to short length transmission line as depicted by the block consisting of R (resistance) and L (inductance) of the line. A block for the transformer is also provided for stepping up the generated voltage of 11kV of the generator (under normal conditions) to a voltage of 132kV for connection to the grid. A block representing the grid is also present which represents infinite power at 132kV.

A block representing a load of 5MW is connected to the transmission line which is connected to a block which is for measurement of output and provides the voltage and current across the load.

Various scopes have been connected for the graphical display of speed, mechanical power, stator current, voltages, load angle, electrical power, field current, active and reactive power and excitation voltage in continuous mode (represented by powergui).

IV Implementation

(a) *Generator on no load:*

The operation of generator on no load is shown in the graphs of figure 3.This is the case when generator supplied by mechanical power suddenly goes on no load. It can be seen that the voltage and current waveform have a sub-transient and transient period total of about 1 sec. The cause of the high magnitude of the waveforms during the beginning portion is due damper winding reactance and the synchronous transient reactance which causes the reactance of the machine to be lower than the normal value.

It can be seen that when the steady state is attained (i.e. after 1 sec) the voltage waveform is of constant magnitude of about 11kV and the current is of negligible magnitude (small current is present due to the conductance present between the wires of transmission line). The magnitude of the induced voltages in the generator terminals are according to equation (1).Power which is a product of voltage and current is in the range of kW during transient and sub-transient period and then becomes negligible as current becomes near zero.

The Excitation System Implements an IEEE type 1 synchronous machine voltage regulator [5] combined to an Exciter.

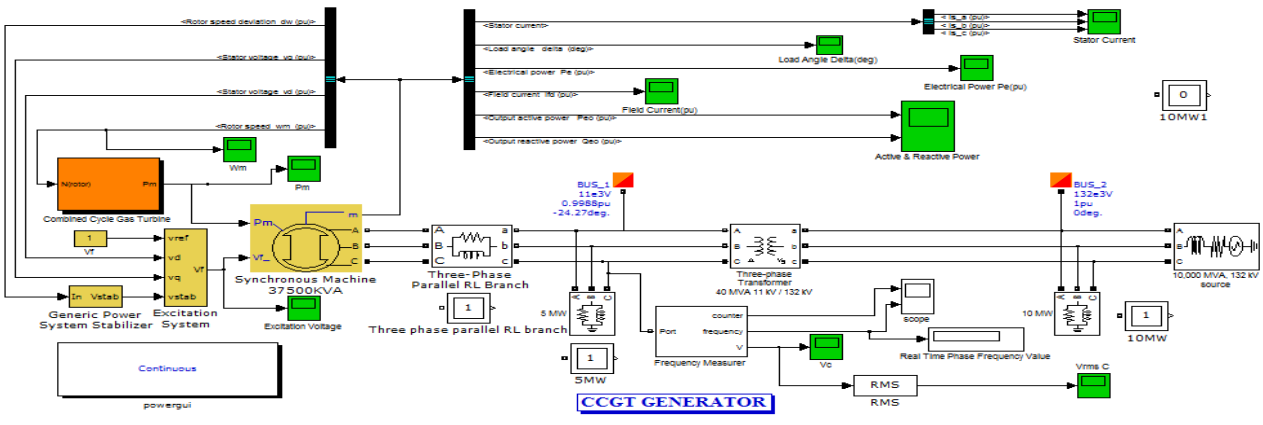

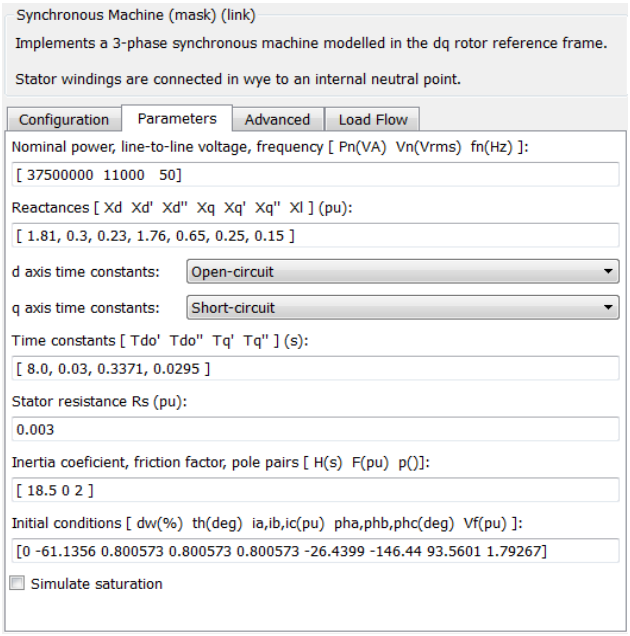

Figure 3. Parameter box of Synchronous Generator in MATLAB

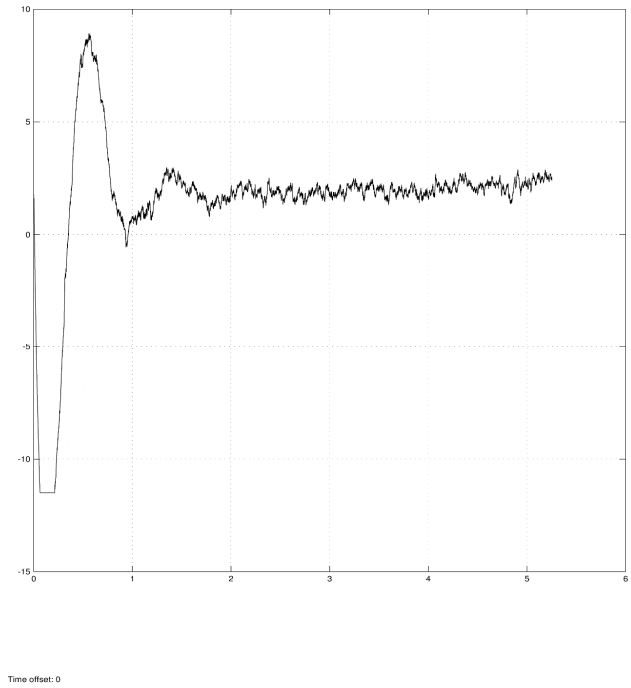

Figure 4. Excitation control of voltage at no load

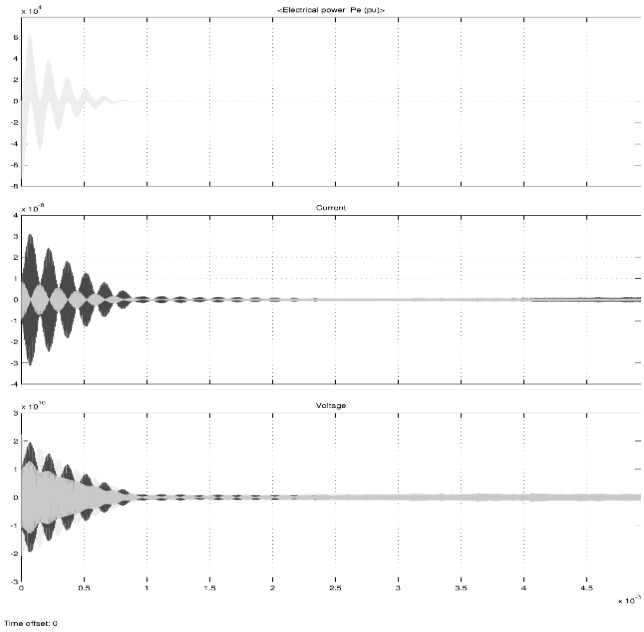

Figure 5. Power, Current and Voltage at no load

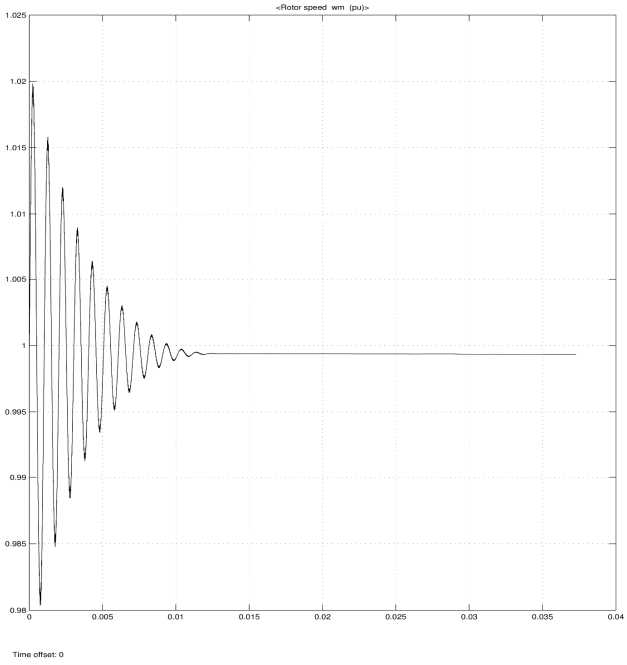

Figure 6. Speed (w) variation

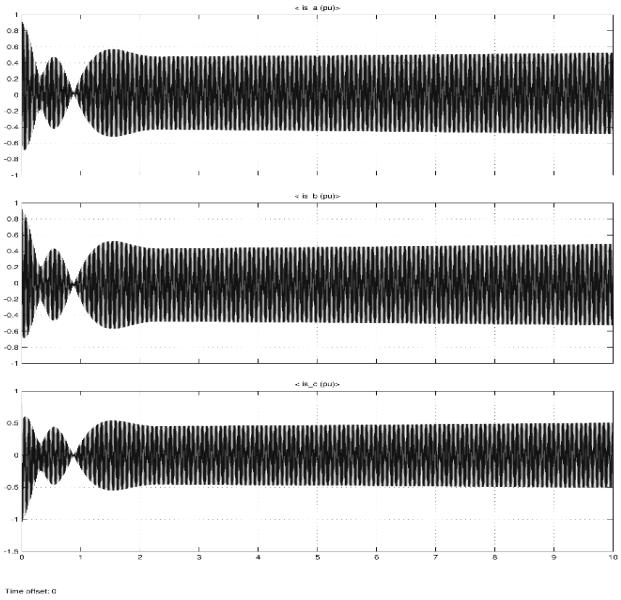

Figure 7. Line currents in the armature (stator) winding

The excitation control of the field winding during no load is as shown in figure 5. The excitation is controlled by the AVR and PSS systems when the machine is suddenly goes at no load. The variation in speed is due sudden changes in electromagnetic torque (and hence power) and according to swing equation (equation (3)) the speed varies as shown in figure 6. The speed of the generator rotor is controlled by the governing system of the turbine.

(b) Generator on Load:

The response obtained when the generator is suddenly connected to load are shown as follows (both steady state and transient state) -

(i) Currents- When generator is suddenly connected to the bus the waveform of currents are shown in figure 7. The Generator first operates in sub-transient and transient state for about 2 to 3 seconds and then attains steady state. Under steady state the terminal voltages have magnitude according to the equation (3) and the developed internal emf, E or no load voltage according to equation (1) which produce steady state currents as can be seen after 2 seconds time in the plot.

(ii) Transmission line currents- The current waveform in the b-phase of the transmission line is shown in figure 8. The magnitude of the transmission line current directly follows form the line current developed in the generator. The current cycle at the beginning is more negative because of the dc offset voltage present at the beginnings which die out eventually according to the current decay rate in an inductive circuit.

(iii) Excitation Control and field control- The excitation control of the generator is shown in figure 9. The excitation is to be reduced at the beginning due to sudden rise in the voltages and currents in the transient phase of generator operation. The sudden increase in the excitation of the rotor above the operating value is due to the transfer function response of the AVR and PSS control system. The waveform of the field current is shown in figure 10 which directly follows the excitation voltage control of the excitation voltage.

(iv) Speed of the rotor- When the generator is loaded there is an increase in an electromagnetic torque which opposes the mechanical torque which causes a reduction in the speed (frequency of generation) of the generator. The speed of the generator is readjusted by the governor system of the turbine. The effect on the speed of the rotor on loading the generator is shown in figure 11. The speed characteristics of the rotor can also be explained by the swing equation [equation (3)].

(v) Input mechanical power- As the speed of the generator drops on application of electrical load the power input from the turbine also drops as shown in figure 12. The balance in electrical power and mechanical power is re-obtained using the turbine governor as explained before.

(vi) Load angle- The load angle of the generator on disturbance is adjusted by the governing system of the generator. It can be seen from figure 13 that the delta comes back to a stable value after the disturbance showing that the system is stable. The stability of the result is in accordance with equation (3) (Swing Equation) which show that the mechanical and electrical power balance each other at constant load angle.

(vii) Active power and Reactive power flow- The active and reactive power flow is shown in figure 14. It can be seen that when there is a reduction in the load angle the active power also reduces as the *sin* of the load angle reduces.

(viii) Turbine governor control of temperature- When the mechanical power from the generator is to balance the electrical power the mechanical power from the turbine is increased by increasing the fuel flow which causes an increase in the temperature of the turbine that is controlled by increasing the airflow as shown in figure 15.

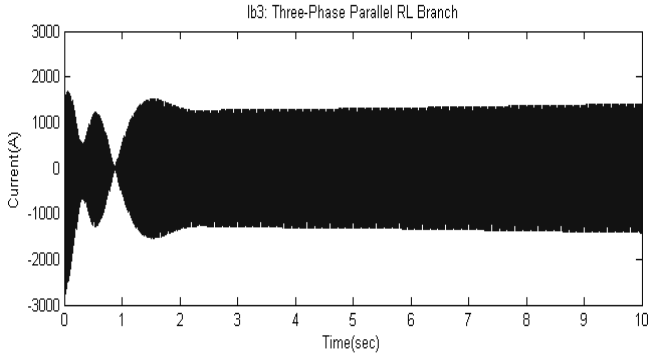

Figure 7.Current in the transmission line of phase b

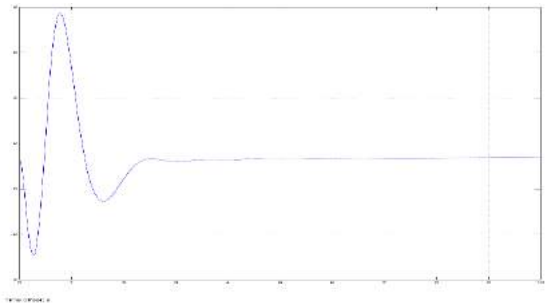

Figure 8. Excitation Control of the field winding

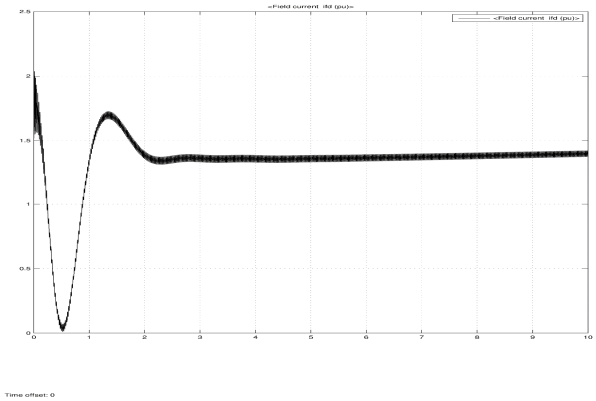

Figure 9. Field Current on excitation control

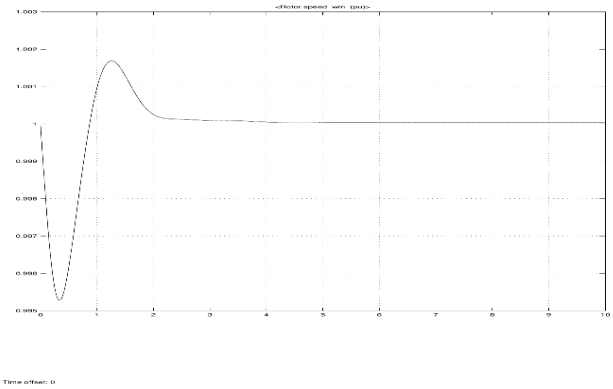

Figure 10. Rotor speed variation

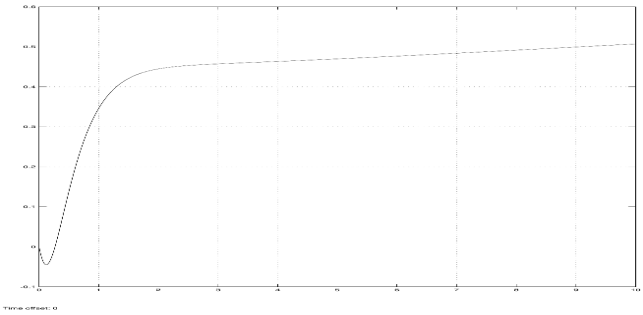

Figure 11. Change in mechanical power (Pm)

V Conclusion

The model setup of CCGT coupled generator was developed and its behavior under various conditions was analyzed. From the implementation results it can be concluded that-

The generated emf of the generator (internal emf) is directly related to the excitation provided to the rotor. (as seen in generator at no load). Effect of sudden changes in load on speed was studied and it is concluded that for system to be able to operate properly the governor system should be such that it is able to balance electrical and mechanical torque after a disturbance has occurred in the system. The changes in the load angle were observed when the generator was suddenly loaded, it showed that the setup is stable for small disturbances as the load angle was able to attain a constant value after some disturbance was applied to the system. The dependence of real power on the load angle delta was observed that as with the decrease in delta active power generated also decreases. The voltages during transient and sub-transient periods are much higher than those during the steady state conditions so the insulation material of the generators should be such that it is able to withstand very high voltages for about 3 to 4 seconds.The current during the transient period is also very high so the thermal properties of the windings and insulators should be such that it is able to withstand the heat generated during that period. From the speed-time graph it can inferred that the rotor inertia should be large so that there is less oscillation about the steady state speed also the strength of the rotor should be such that it does not break due to coupling torque during the period of oscillations in speed. The maximum power input from the turbine i.e. mechanical power, input from the turbine to the generator is limited by the maximum temperature rise in the turbine which rises with the increase in the rate of fuel flow and is controlled by the air flow rate in the turbine.

Figure 12. Load angle (δ) variations versus time

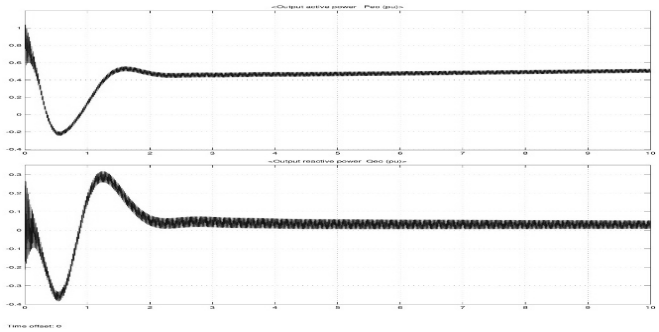

Figure 13. Active and Reactive power output

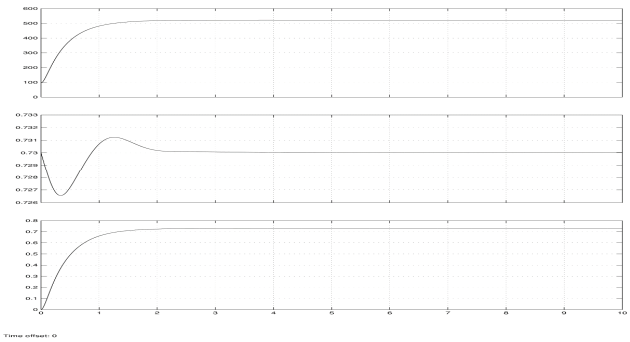

Figure 15. Temperature Exhaust (℃), Air flow (pu) and Fuel flow (pu)

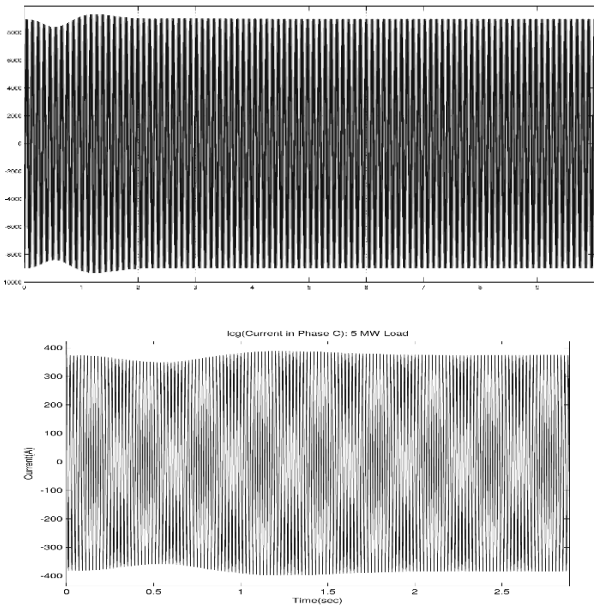

Figure 14. Voltage variation and Current variation of Phase C in 5MW load

(c) Voltages and Currents across 5 MW Load:

From the simulations model it can be seen that the generator is supplying a load of 5 MW. Figure 16 shows the voltage and current across that load, both transient and steady state result.

VI References

[1.] Rai J. N., Hasan Naimul, Arora B. B., Garai Rajesh, Kapoor Rahul, Ibraheem "Performance Analysis Of CCGT Power Plant Using Matlab/Simulink Based Simulation" IJoART Volume 2, Issue 5, May 2013 Issn: 2278-7763

[2.] Rai J. N., Hasan Naimul, Gupta Rishabh K., Kapoor Rahul, Garai Rajesh "Enhancement Of Voltage Profile Of Transmission Line By Using Static Var Compensator-An Overview" IJERT Vol. 2 Issue 5, May - 2013 Issn: 2278-0181

[3.] Krause, P.C., *Analysis of Electric Machinery*, McGraw-Hill, 1986, Section 12.5.

[4.] Kamwa, I., et al., "Experience with Computer-Aided Graphical Analysis of Sudden-Short-Circuit Oscillograms of Large Synchronous Machines," *IEEE® Transactions on Energy Conversion*, Vol. 10, No. 3, September 1995.

[5.] "Recommended Practice for Excitation System Models for Power System Stability Studies,"*IEEE® Standard 421.5-1992,* August, 1992.

[6.] N. Kakimoto, K. Baba, , "Performance of gas turbine-based plants during frequency drops," IEEE Transactions on Power Systems, vol.18, pp. 1110- 1115, Aug. 2003.

[7.] S. Al-Zubaidy, F.S. Bhinder, "Towards optimizing the efficiency of electrical power generation," Energy Conversion Engineering Conference, vol.3, pp. 1857-1862, Aug. 1996.

[8.] K. Kunitomi, A. Kurita, H. Okamoto, Y. Tada, S. Ihara, P. Pourbeik, W. W. Price, A. B. Leirbukt, and J. J. Sanchez-Gasca, "Modeling frequency dependency of gas turbine output," Proc. IEEE/Power Eng. Soc. Winter Meeting, Jan. 2001.

[9.] W. I. Rowen, "Simplified mathematical representations of heavy-duty gas turbines," Trans. Amer. Soc. Mech. Eng., vol. 105, pp. 865–869, Oct. 1983.

[10.] F. P. de Mello and D. J. Ahner, "Dynamic models for combined cycle plants in power system studies," IEEE Trans. Power Syst., vol. 9, pp. 1698–1708, Aug. 1994.

[11.] John H Horlock, "Advanced gas turbine cycles," Pergamon Press, 2003.

[12.] Rolf Kehlhofer, Rukes Bert, Hannemann Frank, and Stirnimann Franz. "Combined-cycle gas & steam turbine power plants," PennWell, 2009.

[13.] F. Drbal Lawrence, G. Boston Patricia, L. Westra Kayla, Black& Veatch. Power Plant Engineering. p. 241 Springer. 1996.

[14.] G. Lalor, M. O'Malley, "Frequency control on an island power system with increasing proportions of combined cycle gas turbines," IEEE Power Tech Conference Proceedings, Bologna , vol.4, pp. 7, June 2003.

[15.] J. N. Rai, Naimul Hasan, B.B. Arora, Rajesh Garai, Rishabh K. Gupta, Rahul Kapoor "Study the Effect of Temperature Control on the Performance of the Output of Combined Cycle Gas Turbine," International Journal of Theoretical and Applied Mechanics. ISSN 0973-6085 Volume 8, Number 1 pp. 15-23 2013.

[16.] William I. Rowen, "Simplified mathematical representations of single shaft gas turbines in mechanical drive service." Turbomachinery International 33.5 (1992).

ResearchGate

See discussions, stats, and author profiles for this publication at: https://www.researchgate.net/publication/303515215

Comparative Study of Load Deformation Behaviour of Silty Clay Bed Reinforced with Stone Column of Different Depth and Gradation

Conference Paper · October 2015

READS
16

2 authors:

Darin Baruah
Manav Rachna International University
1 PUBLICATION **0** CITATIONS
SEE PROFILE

Anil Kumar sahu Sahu
Delhi Technological University,Delhi-110042
6 PUBLICATIONS **2** CITATIONS
SEE PROFILE

All in-text references underlined in blue are linked to publications on ResearchGate, letting you access and read them immediately.

Available from: Darin Baruah
Retrieved on: 11 August 2016

Comparative Study of Load Deformation Behaviour of Silty Clay Bed Reinforced with Stone Column of Different Depth and Gradation

Darin Baruah
Assistant Professor, Civil Engineering, Manav Rachna International University, Faridabad-4, Haryana, India
Sahu, Anil Kumar
Professor, Department of Civil Engineering, Delhi Technological University, New Delhi-42, India

Abstract

Stone column or granular pile is a cost effective measure used to improve the bearing capacity of weak soils. It assists in supporting a wide variety of structures such as residential, commercial and industrial buildings, oil storage tanks, highways to name a few. It also helps in reducing settlements. The stone columns derive its load carrying capacity mainly from confinement of the surrounding soil. In the present investigation, load versus settlement response of silty clay bed is compared with the load versus settlement response of reinforced silty clay bed, with, stone column for different aggregate mixes and different depths, with and without encasement. The plate load tests were carried out on a single column in a large rectangular tank. The test bed was prepared using locally available silty clay soil. Investigations were carried out by varying the size of aggregate in the stone column as well as mixing different size aggregates. The results from the tests indicated a clear improvement in the load carrying capacity of silty clay bed due to the stone columns, as well as reduction in settlement. The bearing capacity improvement factor for stone columns of length/diameter ratio of 2.08, 4.17 and 6.25 have been found to be 11.9%, 23.8% and 66.6% in comparison to unreinforced silty clay bed; and the settlement improvement factor has been found to be 4.1%, 11.28% and 26.4% respectively under a loading of 25kN in comparison to the same.

Keywords: Stone column, ground improvement, silty clay bed

1. Introduction:

With the ever increasing population of the country and the limited land resources, it has become imperative that we develop sites which were previously considered marginal and not viable for construction activities. Although previously it was prohibitively costly but now with the advent of new ground improvement techniques, it has become economically feasible. The high cost of conventional foundations coupled with environmental concerns has made development of weak soil deposits a necessity. For structures which can tolerate settlement to a certain extent, stone columns or granular piles provide a cost effective method for ground improvement. Stone columns are either constructed as fully penetrating the soil layer which is supported on a hard stratum or as floating with their tips embedded in the soil layer itself. Stone columns are primarily composed of granular material compacted in long cylindrical holes and are used for improving strength and consolidation characteristics of soil. Load carrying capacity of a stone column is primarily governed by the frictional properties of stone mass, frictional properties of soil surrounding the stone column, lateral pressure developed on the surrounding soil mass etc. The axial capacity of the stone column is mainly due to passive earth pressure developed due to bulging effect of the column and increased resistance to lateral deformation under superimposed surcharge load. Stone columns on several occasions have been used instead of piles to support many critical structures leading to high degree of economy and speedy construction.

Since 1950s, stone column has been extensively used in Europe to improve soil conditions. But its application has somewhat been limited in India. Infrastructure development in India at present is on full swing. As the availability of good land for construction is depleting fast, hence it is becoming necessary that we develop soils which have low shear strength and bearing capacity as well as high compressibility. Of all the ground improvement techniques, the stone column method provides us with a cheap and fast method through which we can improve ground conditions through increased bearing capacity and reduced settlements.

In this study we have compared load deformational characteristics of untreated silty clay bed with that of silty clay bed reinforced with stone column. The study was being carried out for different column depths having different aggregate gradation. 120mm diameter stone column of varying depths is constructed at the centre of the rectangular tank. The columns were constructed using 10mm, 20mm and a mixture of mixture of 10mm and 20 mm aggregates in a ratio of 1: 1 by weight.

2. Literature Review:

Stone Columns have wide spread application in the field of soil stabilization. They are frequently used for stabilization of soft clay or silts and lose silty sands. Several researchers have worked on stone columns and many field tests, numerical analysis have been carried out to study the effects of stone columns on ground improvement. However, the design of stone columns is mostly based on the empirical approach as the load settlement behaviour of stone columns is influenced by a number of factors. A stone column's load carrying capacity is mainly dependent on the lateral resistance provided by the surrounding soil to the expansion caused by bulging of the aggregates on application of load. The parameters which are used in measuring the load carrying capacity of stone columns are angle of internal friction of stone aggregates in column, diameter of the stone column, undrained shear strength of soil surrounding the stone column, lateral stress in the soil, radial pressure or deformation characteristics of the soil etc.

A number of theories have been presented for predicting the bearing capacity of an isolated single stone column surrounded by soft soil [2], [3], [4], [5], [7]. It was observed that very little of the applied load reaches the bottom of a single column if the column is more than twice its depth. The fact that load applied to a single stone column is transferred to its surroundings was verified [5], [6]. From the latter part of the 20th century researchers have started working on theoretical, experimental and field study on behaviour of stone columns. The information available regarding the design procedure to be adopted for a given situation is sparse. Semi empirical design approach based on the allowable stress on stone columns and the undrained shear strength of clay has been proposed [5], [6], [8], [9]. In 2004, experiments were conducted to determine load versus settlement of clay bed stabilized with stone and reinforced stone columns [10]. They found that on encasing stone columns with geogrids there was an appreciable increase in load carrying capacity of both end bearing and floating columns. The study on behaviour of single and group of geosynthetic encased stone columns found that all round encasement using geosynthetic resulted in increased stiffness and loading capacity of a stone column [11]. The elastic modulus of geosynthetic also played an important role in enhancing capacity and stiffness of encased stone column. From experimental

studies on stone column by varying spacing, shear strength of soft clay, moisture content etc., it was observed that that when column area alone is loaded, the failure is by bulging of the column with maximum bulging at 0.5 to 1 times the column diameter below the top and when the entire area is loaded bulging failure does not take place [1]

3. Materials and Methods:

3.1 Materials:

Soil was excavated from Delhi Technological University campus after removing the surface vegetation. A total quantity of 1.5 cum of soil was excavated, air dried and pulverized. Investigations were subsequently conducted to determine the index properties of soil for its classification. Coarse aggregate of 20mm and 10mm size were used for construction of stone column. A rectangular steel tank of 1.5m×0.6m×0.9m was used for preparation of soil bed. The diameter of stone column was chosen such that the loaded area does not affect the walls of the rectangular tank. Loading frame consisted of a rigid truss which was fixed and anchored to sustain very heavy loading. A hydraulic jack consisting of a loading mechanism fitted with load measuring gauge was used to apply load to the silty clay bed. The jack was supported against the truss and loading was applied. The properties of three basic materials used in the experiment are

Properties of soil			Properties of aggregates		
1	Type of soil	Silty clay	1	Specific gravity	2.72
2	Natural moisture content	5.52%	2	Water absorption	0.68%
3	Average specific gravity	2.69	3	Aggregate impact value	29.95%
4	Clay content	9%			
5	Silt content	54%		Properties of geotextile	
6	Liquid limit	30%	1	Type	Woven
7	Plastic limit	21.45%	2	Material	Polypropylene
8	Plasticity Index	8.55%	3	Thickness in mm	0.58mm
9	Maximum dry density	17.46 kN/m^3	4	Colour	White
10	Optimum moisture content	13.91%	5	Permeability	0.47×10^{-3}m/s
11	Void ratio of soil layer	0.51	6	Ultimate tensile strength	2.86 N/mm^2
12	Angle of internal friction	29.1^0			
13	Shear strength	33.96 kN/m^2			
14	Unconfined compressive strength	118.8 kN/m^2			
15	Cohesion	59.4 kN/m^2			

3.2 Stone Column installation:

The stone column was installed in the centre of the rectangular tank. A PVC pipe of 120mm diameter was placed at the centre of the tank and the silty clay bed was prepared around it. The aggregates were filled in three different layers and each layer was

tamped using a 10mm rod to achieve a density close to 15kN/m^3. For the construction of different types of stone columns, an area greater than the effective area of the stone column was excavated up to full depth and the procedure repeated, and stone columns of different gradation were formed. For encased stone columns, the geotextile was wrapped around the PVC pipe after stitching. Aggregates were charged inside the stone column and the PVC pipe was raised in layers with tamping also being carried out in parallel. The procedure was repeated till the desired depth of stone column is obtained.

3.3 Method Used:

The air dried pulverized silty clay soil was passed through 4.75mm sieve and then filled in three different layers. Each layer was compacted with more than 100 blows with 2.5kg rammer spread over the whole surface. Ramming was also done by wooden rammer to avoid any entrapped air. The soil was filled up to a depth of 750mm. Load was applied gradually and the deformation of the bed at each 5kN increment loading was calculated with the help of dial gauges connected to the base plate. A base plate of size 300mm diameter was used for application of load. Stone column of diameter 120mm was constructed at the centre of the rectangular tank with depths varying from 250mm, 500mm and 750mm; and settlement behaviour of the silty clay bed was observed for each 5kN increment in load. The aggregates used in construction of stone column were of 10mm and 20mm size as well as a mixture of both in the ratio of 1:1 by weight. The stone columns were also encased using woven geotextile and its effect on the load deformation behaviour was observed.

4. Experimental Investigation:

Tests were conducted on a single stone column of diameter 120mm for different length to diameter ratios on a loading frame as stress controlled test. The diameter of the circular steel plate of adequate thickness and rigidity is based on effective tributary soil area of the stone column as per the codal provisions given in IS 15824 (2003). The loading plate used in the test was circular having a diameter of 300mm which is more than twice the diameter of the stone column of 120mm. This size was used so that the loading plate will cover the equivalent circular effective area concentrically. Stone column was prepared by making a circular hole of diameter 120mm with length/diameter ratio 2.08, 4.16 and 5.83. The height of stone column prepared was 250mm, 500mm and 750mm respectively. Sufficient area was provided around the stone column so that there was no effect of loading on the tank walls. The size of aggregate used for the construction of stone column was 20mm, 10mm and a mixture of 10mm and 20mm aggregates in the ratio of 1:1 by weight. Load tests were also carried out on encased stone columns composed of 10mm, 20mm and a mixture of 10mm and 20mm aggregates in the ratio of 1:1 by weight for full depth of 750mm.

Figure 1 Loading applied on silty clay bed

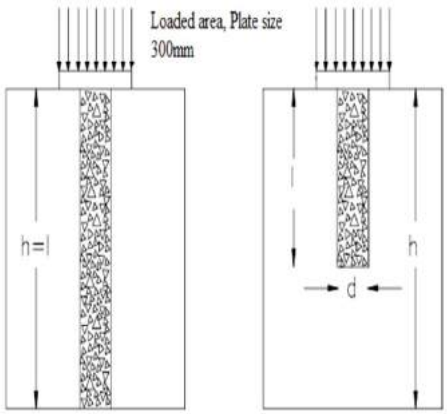

Figure 2 Loading of bed reinforced with stone column

5. Experimental Results:

1. Due to intrusion of stone column of various depths, the settlement increases due to increase in load. However, at any level of load, the settlement of soil with different types of stone column is less as compared to that of silty clay bed. This shows that there is reduction in settlement at any level of load and improvement in bearing capacity at any level of settlement.
2. The percentage increase in load carrying capacity for 250mm, 500mm, and 750mm depth stone column in comparison to soil without stone column are 11.7%, 23.3%, 30.0% for 20mm aggregates; 8.34%, 15.78%, 31.67% for 10mm aggregates and 14.55%, 24.08% and 40.6% for a mixture of 10mm and 20mm aggregates respectively. This may be due to the fact that mixture of 10mm and 20mm aggregates provides better grading and reduce value of void ratio.
3. The percentage increase in load carrying capacity of encased stone columns for full depth i.e. 750 mm is 86.92% for 20mm aggregates, 83.22% for 10mm aggregates and 91.31% for a mixture of 10mm and 20mm aggregates respectively
4. The settlement reduction ratio for stone column of 250mm, 500mm, 750mm depth has been observed to be 0.91, 0.89, 0.86 for 20mm aggregates; 0.95,0.92,0.78 for 10mm aggregates; 0.88,0.82,0.72 for a mixture of 10mm and 20mm aggregates respectively.
5. The settlement reduction ratio for encased stone columns for full depth i.e. 750mm have been found to be 0.5 for 20mm aggregates, 0.52 for 10mm aggregates and 0.47 for a mixture of 10mm and 20mm aggregates respectively.
6. The study on load-settlement behavior is carried out for the stone column of same diameter and various depths such as 250mm, 500mm and 750mm and different gradation of aggregates. Due to increase in depth of stone column, the load carrying capacity is increasing at every level of settlement. It is also observed that there is significant increase in load carrying capacity and reduction in settlement in case of encased stone columns as compared to stone columns without encasement. This may be due to the fact that lateral expansion of stone columns is resisted by the encasement because the geotextile can provide tensile strength.

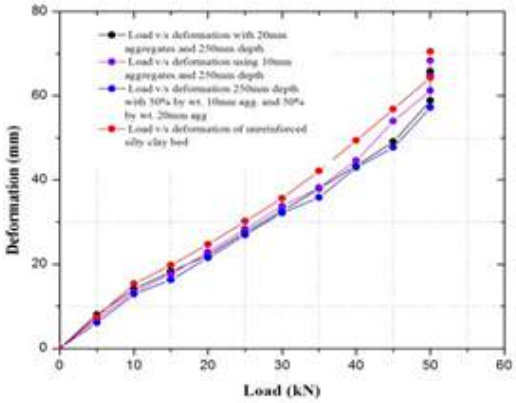

Figure 3 load v/s settlement behaviour for 250mm depth stone column

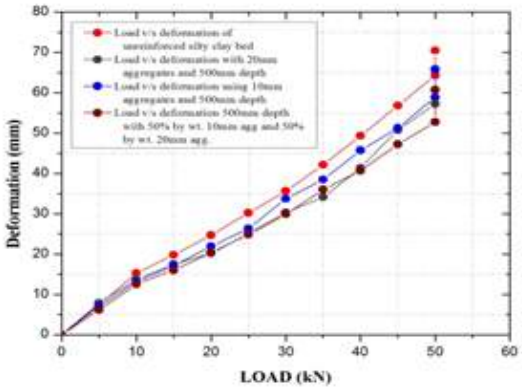

Figure 4 load v/s settlement behaviour for 500mm depth stone column

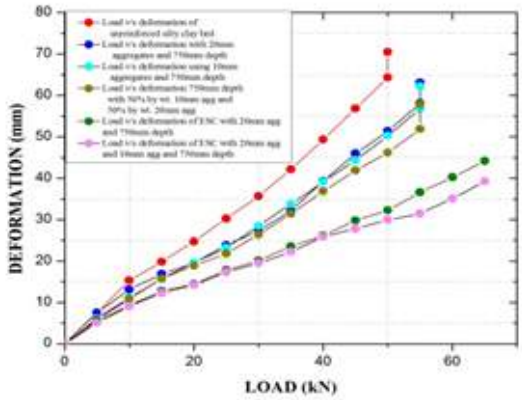

Figure 4 load v/s settlement behaviour for 750mm depth stone column

Table 1
Comparison of load carrying capacity at 25mm settlement for different stone columns

Load at 25mm settlement													
Depth (mm) Pure silty clay bed		Silty clay bed with 20mm aggregates stone column		Silty clay bed with 10mm aggregates stone column		Silty clay bed with mixture of 10mm + 20mm stone aggregates		Silty clay bed + encased stone column with 20mm aggregates (750mm depth)		Silty clay bed+ encased stone column with 10mm aggregates. (750mm depth)		Silty clay bed+ encased stone column with 10mm + 20mm aggregates (750mm depth)	
	Absolute value in kN	Absolute value in kN	% improvement	Absolute value in kN	% improvement	Absolute value in kN	% improvement	Absolute value in kN	% improvement	Absolute value in kN	% improvement	Absolute value in kN	% improvement
250	20.27	22.64	11.7	21.96	8.34	23.22	14.55	37.89	86.92	37.14	83.22	38.78	91.31
500		24.99	23.3	23.47	15.78	25.15	24.08						
750		26.36	30.0	26.69	31.67	28.5	40.6						

Table 2
Comparison of settlements at 50kN load for different stone columns

Depth (mm)	Settlement at 50kN load											
	Pure silty clay bed	Silty clay bed with 20mm aggregates Stone column		Silty clay bed with 10mm aggregates stone column		Silty clay bed with mixture of 10mm + 20mm stone aggregates stone column		Silty clay bed with 750mm depth encased stone column made of 20mm aggregate		Silty clay bed with 750mm depth encased stone column made of 10mm aggregate		Silty clay bed with 750mm depth encased stone column having 50% 20mm + 50% 10mm aggregate by weight	
	Absolute value in mm	Absolute value in mm	Settlement reduction ratio (β)	Absolute value in mm	Settlement reduction ratio (β)	Absolute value in mm	Settlement reduction ratio (β)	Absolute value in mm	Settlement reduction ratio (β)	Absolute value in mm	Settlement reduction ratio (β)	Absolute value in mm	Settlement reduction ratio (β)
250	64.3	58.83	0.91	61.23	0.95	57.21	0.88	32.22	0.50	33.25	0.52	29.92	0.47
500		57.25	0.89	58.91	0.92	52.8	0.82						
750		51.37	0.80	50.28	0.78	46.19	0.72						

6. Conclusion:

1. The experiments carried out on the local soil which is primarily silty clay have highlighted that for a single stone column or granular pile that there is marked decrease in settlement when soil is reinforced with stone column.
2. It is observed that there is reduction in settlement and increase in bearing capacity with increase in depth of stone column.
3. It is also observed that the decrease in settlement is more when the stone column is end bearing instead of floating.
4. It is also found that for encased stone column the percentage increase in load carrying capacity and decrease in settlement is more than that of non-encased stone column.

References:

1. A.P. Ambily and S.R. Gandhi (2004), "Experimental and theoretical evaluation of stone column in soft clay," ICGGE-2004 pp.201-206
2. Baumann, V. and G.E.A. Bauer (1974), "The performance of foundations on various soil stabilized by the vibro-compaction method," Canadian Geotechnical Journal, pp. 509-530
3. Datye, K.R. and Nagaraju S.S. (1981), "Design Approach and Field Control for Stone Columns," Proc. Tenth Int. Conf. On SMFE, Stockholm, Vol. 3, 637 – 640
4. Goughnour, R.R., and A.A. Bayurk. (1979), "Analysis of stone column- Soil

Matrix interaction under vertical load," Proceedings, International Conference on soil reinforcement: Reinforced earth and other techniques, Vol. 1, pp. 271-278
5. Hughes, J.M.O. and Withers, N.J. (1974). "Reinforcing of Soft Cohesive Soils with Stone Columns," Ground Engineering, Vol.7, No.3, pp. 42-49
6. Hughes, J.M.O., Withers, N.J. and Greenwood, D.A. (1975), "A Field Trial of Reinforcing Effect of Stone Column in Soil," Geotechnique, Vol.25, No.1, pp. 32-44
7. Madhav, M.R., N.G.R. Iyenger, R.P. Vitkar, and A. Nandia (1979), "Increased bearing capacity and reduced settlements due to inclusions in soil," Proceedings, International conference on soil reinforcement: Reinforcement and other techniques, Vol. II, Paris, pp. 320-333
8. Saha S. (1992). "Design Approach and Performance of Stone Columns," Proceedings of Indian Geotechnical Conference, Calcutta, pp.195 – 198
9. Saha, S and Roy, A. (2000). "Analysis of Stone Column in Soft Ground," Indian Geotechnical Conference, Bombay, pp.297 – 300
10. S.N. Malarvizhi and K. Ilamparuthi (2004), "Load versus settlement of clay bed stabilized with stone and reinforced stone columns," ICGGE 2004, pp. 322-329
11. S.Murugesan and K. Rajagopal (2010), "Studies on the behavior of single and group of geosynthetic columns," Journal of Geotechnical and Geoenvironmental Engineering, Vol. 136, No.1, January, ASCE
12. Bureau of Indian Standards (1973), ''IS 2720, Part 2: Methods of test for soils: Determination of moisture content''
13. Bureau of Indian Standards (1980), "IS: 2720, Part 7: Methods of test for soils: Determination of water content-dry density relation using light compaction"
14. Bureau of Indian Standards (1985a), ''IS 2720, Part 4: Methods of test for soils: Grain size analysis.''
15. Bureau of Indian Standards (1986), ''IS 2720, Part 13: Methods of test for soils: Direct shear Test''
16. Bureau of Indian Standards (1986), ''IS 2720, Part 2: Methods of test for soils: Determination of specific gravity"
17. Bureau of Indian Standards (1985), ''IS 2720, Part 5: Methods of test for soils: Determination of Atterberg's limits"
18. Bureau of Indian Standards (1991), ''IS 2720, Part 10: Methods of test for soils: Determination of Unconfined compressive strength"
19. Bureau of Indian Standards (2003), ''IS 15284, Part 1: Design and construction for ground improvement"
20. Bureau of Indian Standards (1983), ''IS 2386, Part 3: Methods of tests on aggregate"

Research Article Vol. 55, No. 24 / August 20 2016 / Applied Optics 6775

applied optics

Design and analysis of a highly nonlinear composite photonic crystal fiber for supercontinuum generation: visible to mid-infrared

PURNIYA JAMATIA,[1] THAN SINGH SAINI,[1] AJEET KUMAR,[1,*] AND RAVINDRA KUMAR SINHA[2]

[1]Advanced Photonics Simulation Research Laboratory, Department of Applied Physics, Delhi Technological University, Delhi-110042, India
[2]CSIR-Central Scientific Instruments Organization, Chandigarh-160030, India
*Corresponding author: ajeetdph@gmail.com

Received 15 June 2016; revised 20 July 2016; accepted 30 July 2016; posted 2 August 2016 (Doc. ID 268491); published 18 August 2016

A composite photonic crystal fiber structure has been designed with tellurite as the cladding and chalcogenide as a core material. To increase nonlinearity, rods of the chalcogenide glass material have been inserted around the core region. The reported structure offers very high nonlinearity of 1042 W^{-1} Km^{-1} at 2800 nm pump wavelength with low and flattened dispersion of approximately −11 ps · nm^{-1} Km^{-1}. An effective mode area of 6.46 μm^2 of the propagating mode has been achieved as at pump wavelength. Such a highly nonlinear composite photonic crystal fiber structure is a potential candidate for nonlinear applications, such as slow-light and supercontinuum generation. Pumping at 2800 nm results in a supercontinuum spectrum spanning 0.5–4.7 μm using 8 mm long photonic crystal fiber pumped with femtosecond laser pulses with peak power of 3 kW. © 2016 Optical Society of America

OCIS codes: (190.0190) Nonlinear optics; (060.5295) Photonic crystal fibers; (320.6629) Supercontinuum generation.

http://dx.doi.org/10.1364/AO.55.006775

1. INTRODUCTION

Research based on photonic crystal fiber (PCF) is a great achievement in the field of optics and photonics as PCF is able to guide light not only by refractive index differences but also by structural modifications of the photonic crystals [1]. Higher nonlinearity in these fibers is in much demand, as it has applications in supercontinuum generation (SCG), wavelength conversion, pulse compression, parametric amplification, etc. [2,3]. For achieving high nonlinearity, highly nonlinear glasses such as chalcogenide and tellurite are highly desirable because of their high nonlinear coefficients (i.e., γ) of $\sim 3.0 \times 10^{-18}$ m^2/W [4,5] and $\sim 5.9 \times 10^{-19}$ m^2/W [6,7], respectively. A high nonlinear coefficient counteracts optical losses to a large extent [8,9]. Because of the high nonlinear coefficient, the threshold power requirement is low, so PCF that uses material with a high nonlinear coefficient, such as As_2S_3, is a suitable and attractive medium for SCG [7]. As_2S_3-based chalcogenide glass usually operates in the region of the infrared (IR) [7]. It has a high linear refractive index, high optical nonlinearity, ultrafast nonlinear response, a low to moderate two photon absorption (TPA) effect and long wavelength transparency [7]. Strong vibrational transitions of most of the molecules occur in the IR region, which could be used for aiding in diagnostics dealing with physical, chemical, and biological issues [10].

Supercontinuum (SC) generation is a phenomenon in which extreme spectral broadening of optical pulses occurs because of various nonlinear phenomena, such as self-phase modulation (SPM), cross-phase modulation (XPM), self-steepening, four-wave mixing (FWM), and stimulated Brillouin scattering, stimulated Raman scattering (SRS), along with third-order dispersion and other higher order dispersion [7,11]. It is usually generated by launching ultra short pulses (femtoseconds or picoseconds) in a highly nonlinear PCF with pumping near the zero dispersion wavelength (ZDW). Shifting in the ZDW is achieved with variation in the PCF's geometrical parameters, hence generating a SC in a desired spectral region. SC is popular in the fields of telecommunication, optical metrology, optical coherence tomography, nonlinear microscopy, cosmological studies, and ultrashort pulse generation [12]. PCF is the best choice for SC generation because the group velocity dispersion (GVD) and the zero dispersion wavelength (ZDW) can be engineered over a wide range [11,13]. Dispersion can be designed to facilitate SC generation in a specific region with PCF, which is one of the factors in the generation of a SC spectrum. A low and flattened dispersion curve is desired to have a broader

spectrum, which can be obtained by the geometry in the PCF, including the radius of the core and the radii of air holes.

Non-silica glasses, such as chalcogenide glasses As_2S_3 and As_2Se_3, which are the two most widely used for nonlinear applications as they has very high nonlinear coefficients as compared to silica (~100 times larger) [7,14] and operate in the infrared region [7]. An optical transparency of up to 25 μm can be achieved with these chalcogenide glasses [12]. With silica material, the broadening in the SC spectrum is limited by the material absorption beyond 2.5 μm, which limits the spectrum into the mid-IR region [10]. The propagation losses of silica, ZBLAN, and tellurite fibers are very large beyond 5 μm, so chalcogenide fibers are used instead of these fibers to achieve broadband SC in the mid-IR region [9]. Even though As_2Se_3 has high nonlinearity compared to As_2S_3, it has higher loss compared to the latter, so As_2S_3 is more attractive to be used for nonlinear applications [15]. As_2S_3 glasses also have a lower TPA coefficient in the telecommunication wavelength range and higher material stability compared to As_2Se_3 [7], so As_2S_3 has been chosen as the material in this paper.

Experiments on nonlinear applications in the IR region have already been presented by many researchers [5,8,9–23]. Liao *et al.* [5] modeled a composite PCF structure using As_2S_3 glass and tellurite, resulting in nonlinearity as high as 31.37 $W^{-1}\,m^{-1}$ at 1.55 μm wavelength with a significantly large effective mode area. Feng *et al.* [8] presented the fabrication of holey fiber using tellurite for nonlinear applications, such as SC with a band ranging from 0.9 to 2.5 μm with 9 cm of fiber. Liao *et al.* [9] fabricated and characterized chalcogenide–tellurite composite microstructure fiber and obtained SC spectra in the range of 800–2400 nm. Saini *et al.* [10] reported a triangular core graded-index PCF using As_2Se_3 chalcogenide glass and generating broadband mid-IR SC spectra spanning 2–15 μm. Saini *et al.* [11] generated SC spectrum spanning 1.2–15 μm using an 8 mm long equiangular spiral PCF structure pumped with 50 fs laser pulses of peak power of 500 W. SC generation through dispersion engineering of chalcogenide microstructured fibers was presented by Karim *et al.* [12], producing a spectrum ranging from 1.3 to 11 μm with peak power of 3 kW at a pump wavelength of 3.1 μm. Granzow *et al.* [13] studied SC generation in chalcogenide–silica step index fiber resulting in broadband SC out to 4 μm in a length of 1 cm, pumping at 1550 nm. Xie *et al.* [14] studied and generated spectra covering from 2.1 to 3.2 μm in a 1 mm length of fiber pumped at a wavelength of 2.5 μm using 100 fs pulses. Domachuk *et al.* [15] reported broadband mid-IR SC ranging from 789 to 4870 nm measured at 20 dBm below the spectral power. The ZDW is the most dependent parameter in choosing the pump wavelength for SC generation. Much research on ZDW has already been reported with different materials. Chaudhari *et al.* [16,17] designed a fiber for zero chromatic dispersion using As_2S_3 material and obtained the ZDW at 1.5 μm using a core size of 500 nm.

Much research on SC generation have already been reported using both silica and nonsilica fibers. Ranka *et al.* [18] presented an optical continuum of 550 THz width using air–silica microstructured optical fiber with 100 fs pulse duration with peak power at the kilowatt level near the infrared region. Xia *et al.* [19] proposed SC generation using silica fibers with spectra ranging from ~0.8 to 3 μm in less than 4 mm of fiber using nanosecond pulses. Extensive studies and research that use nonsilica fibers for nonlinear applications have recently been receiving attention. Non-silica fibers such as chalcogenide and tellurite possess high nonlinear coefficients [4–7], making them suitable for broadband SC generation. Tellurite has a nonlinearity coefficient that is lower than that of chalcogenide glasses but higher than that of silica, so this could also be used as the material to obtain SC generation. From these studies it should be noted that wide research on chalcogenide fibers has been fruitful for broadband SC generation, which cannot be achieved with standard fibers. Liao *et al.* [20] designed a fiber using tellurite material with a hexagonal core diameter of 1 μm. Changing the diameter ratio of the holey region to the core (DRHC), Liao *et al.* [20] succeeded in generating a one octave and flattened SC spectrum using the picosecond laser pulses at 1064 nm. Hudson *et al.* [21] demonstrated an octave spanning spectrum in a sulfide-based chalcogenide tapered fiber using only 77 pJ pulse energy. Chaudhari *et al.* [22] presented a design made with a chalcogenide core and tellurite cladding, which generated a SC spectrum of 20 dB ranging from 800 to 2400 nm using a 1.85 μm pump wavelength. Kudlinski *et al.* [23] designed a dispersion-engineered PCF structure and succeeded in generating SC from 650 to 1380 nm with an average power of 19.5 W.

Flat dispersion with small value is desirable for smooth and stable SC generation. SC highly relies on the dispersion curve and has a smooth profile when the PCF has flat dispersion with small slope and a zero crossing wavelength near or at the pump wavelength [11,13]. The need for high power is reduced with a pumping near a ZDW with higher nonlinearity. Generated SC power gets smoothed with pumping near the ZDW [13].

In this paper, we report a highly nonlinear composite PCF structure for SC generation in the visible to mid-infrared region. From the survey of literature, it is noted that visible to near-IR wavelengths are used for several biological applications, because absorption by tissues in this spectral window is relatively low [10,24]. Such a source has potential applications in optical coherence tomography [25] and coherent anti-Stokes Raman spectroscopy [26]. Since the SC spectrum extends to the visible wavelengths, it covers the transparency window of water, which is of much importance for biology. As a result, there are applications in realizing visible broadband sources for Raman spectroscopy [25], optical coherence tomography [25], and frequency metrology. Because chalcogenide has a high nonlinearity coefficient, the desired flattened dispersion curve can be achieved with very high nonlinearity. This resulted in broadening of SC ranging from 0.5 to 6 μm with 3 kW pump power being pumped at 2800 nm with 40 fs pulses in a 8 mm length of fiber.

2. DESIGN OF THE PROPOSED COMPOSITE PCF STRUCTURE

Figure 1(a) illustrates the transverse cross-sectional view of the proposed composited PCF structure.

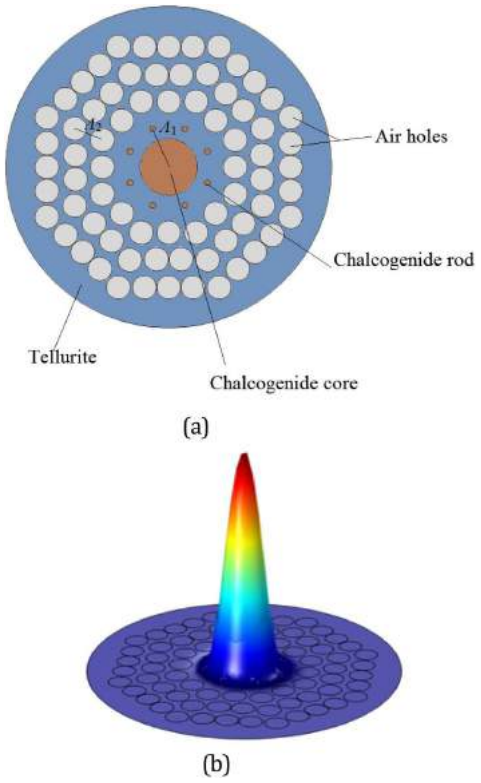

Fig. 1. (a) Transverse cross-sectional view of the proposed PCF. (b) Visualization of the electric field distribution of the propagating mode in the core of the PCF structure.

As shown in Fig. 1(a), it has a chalcogenide core with one ring of small chalcogenide rods around it. In addition to the chalcogenide rods, it consists of three rings of the air holes arranged in a hexagonal lattice pattern in the tellurite material. Introduction of the chalcogenide rods adds to a decrease in effective mode area, resulting in an increase in nonlinearity. Figure 1(b) shows the electric field distribution of the propagating mode in the core of the PCF structure.

As shown in Fig. 1(a), the distance from the centers of the chalcogenide rods (i.e., Λ_1) arranged around the core to the center of the core is taken as 4.375 μm, while the center-to-center distance of the air holes (i.e., Λ_2) in the second, third, and fourth rings has been taken as 3.125 μm. The diameter of the central chalcogenide core (i.e., d_1) is taken as 6 μm. The radius of the central chalcogenide core is denoted by Rc and is $d_1/2$. The diameter of the chalcogenide rods in the first ring around the central core is d_2, which is kept constant at 0.625 μm. The diameter of the air holes in second, third, and fourth rings is represented by d_3 and taken as 2.5 μm. The ratio of the diameter of the air holes to the pitch of the PCF comes out to be 0.8, which is greater than 0.41; hence the PCF is the multimode [27]. From the simulation, it is observed that it is a few-mode fiber supporting five modes.

3. NONLINEAR AND DISPERSION CHARACTERIZATION

Effective measure of the area over which the fundamental mode is confined during its propagation can be calculated from effective area. The effective area equation is given as [5]

$$A_{\text{eff}} = \frac{\left[\iint |E(x,y)\mathrm{d}x\mathrm{d}y|^2\right]^2}{\int |E(x,y)\mathrm{d}x\mathrm{d}y|^4} \ \mu\text{m}^2, \tag{1}$$

where E is the transverse electric field of the fundamental mode.

In this work, tellurite glass and chalcogenide glass have been used as a composite PCF material. The Sellmeier equation is used to calculate the wavelength-dependent refractive index of both materials. The refractive index of the tellurite material is given by the formula [5]

$$n(\lambda) = \sqrt{1 + \frac{b_1\lambda^2}{\lambda^2 - c_1} + \frac{b_2\lambda^2}{\lambda^2 - c_2} + \frac{b_3\lambda^2}{\lambda^2 - c_3}}, \tag{2}$$

where $b_1 = 1.67189$, $b_2 = 1.34862$, $b_3 = 0.62186$, $c_1 = 0.0004665\ \mu\text{m}^2$, $c_2 = 0.0574608\ \mu\text{m}^2$, and $c_3 = 46.72542736\ \mu\text{m}^2$ at 25°C [5,22,28].

The refractive index of the chalcogenide material is given by [5]

$$n(\lambda) = \sqrt{1 + \frac{B_1\lambda^2}{\lambda^2 - C_1^2} + \frac{B_2\lambda^2}{\lambda^2 - C_2^2} + \frac{B_3\lambda^2}{\lambda^2 - C_3^2} + \frac{B_4\lambda^2}{\lambda^2 - C_4^2} + \frac{B_5\lambda^2}{\lambda^2 - C_5^2}}, \tag{3}$$

where, $B_1 = 1.8983678$, $B_2 = 1.9222979$, $B_3 = 0.8765134$, $B_4 = 0.1188704$, $B_5 = 0.9569903$, $C_1^2 = 0.0225\ \mu\text{m}^2$, $C_2^2 = 0.0625\ \mu\text{m}^2$, $C_3^2 = 0.1225\ \mu\text{m}^2$, $C_4^2 = 0.2025\ \mu\text{m}^2$, and $C_5^2 = 750\ \mu\text{m}^2$ at 25°C [5,22,28].

Nonlinearity depends on the nonlinear refractive index of the material. The nonlinearity in a photonic crystal fiber is calculated by the following relation [5,11]:

$$\gamma = \frac{2\pi n_2}{\lambda A_{\text{eff}}} \ \text{W}^{-1}\ \text{m}^{-1}. \tag{4}$$

The nonlinearity coefficient is controlled by two parameters, n_2 and A_{eff}. Figure 2 depicts the spectral variation of the nonlinearity and the effective mode area of the fundamental mode.

For a broader SC spectrum, the nonlinearity coefficient should be as high as possible. Certain materials like soft glass

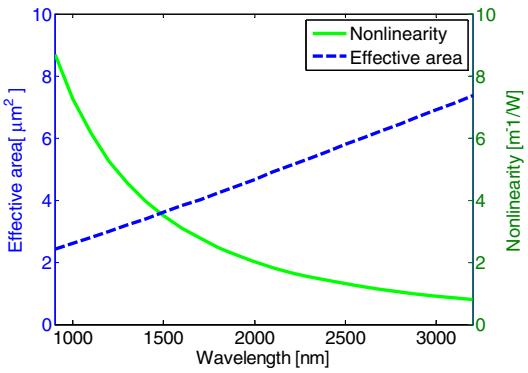

Fig. 2. Effective mode area of the propagating mode and the nonlinear coefficient of the proposed PCF structure versus wavelength.

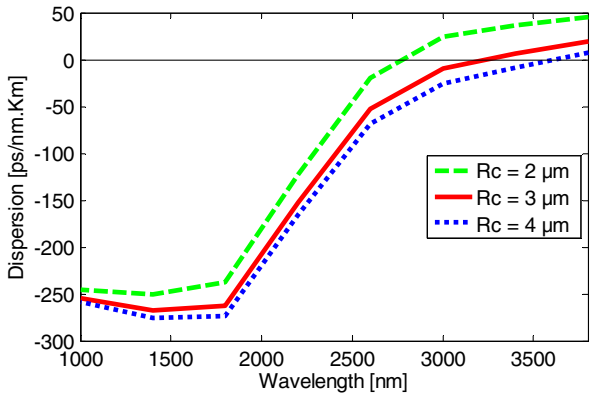

Fig. 3. Chromatic dispersion versus wavelength.

and chalcogenide exhibit a large value of nonlinearity. The value of γ can be enhanced by using the material with a high nonlinear refractive index or by designing a PCF with low effective area. By increasing the nonlinearity value, the proposed PCF structure became suitable for SC generation.

The chromatic dispersion $D(\lambda)$, which is another important factor involved in broadening SC, is calculated from effective index n_{eff} values versus wavelength λ by [5,11]

$$D(\lambda) = -\frac{\lambda}{c}\frac{\partial^2 \operatorname{Re}(n_{\text{eff}})}{\partial \lambda^2}, \tag{5}$$

where c is the velocity of light in vacuum.

Figure 3 describes the effect of change in core radius on dispersion. Changing the radius Rc of the core shifts the ZDW. Figure 3 also depicts the dependence of chromatic dispersion on wavelength.

From the graph it can be concluded that an increase in the radius of the core results in shifting the ZDW at higher wavelengths. Hence, accordingly, a pump wavelength close to the ZDW is usually selected, keeping in mind the availability of the femtosecond laser. In this project, the red curve is selected, taking a pump wavelength of 2800 nm, which is near the ZDW.

4. SUPERCONTINUUM GENERATION

Numerical simulations were performed by solving the following generalized nonlinear Schrödinger equation [11,13]:

$$\frac{\partial A}{\partial Z} + \frac{\alpha}{2}A - \left(\sum_{n\geq 2}\beta_n \frac{i^{n+1}}{n!}\frac{\partial^n A}{\partial t^n}\right) = i\gamma\left(1 + \frac{i}{\omega_0}\frac{\partial}{\partial t}\right) \times \left[A(z,t)\int_{-\infty}^{\infty} R(t')|A(z,t-t')|^2 dt' + i\Gamma_R(z,t)\right]. \tag{6}$$

Equation (6) shows the change in pulse envelope $A(z, t)$ during propagation. The transmission loss of the fiber is α (in units of [1/m]). The attenuation coefficient of the propagation is taken to be ∼30 dB/km [29]. $A(z, t)$ is the envelope of the optical field, T is time, β_n is the nth derivative of the propagation constant β, and γ is the nonlinear coefficient. The nonlinear response function, $R(T)$, is given by [11,13]

$$R(T) = (1 - f_r)\delta(T) + f_r h_r(T), \tag{7}$$

with $f_r = 0.10$, for chalcogenide glass As_2S_3 [7]. The Raman response function h_r can be calculated by the most common and approximate analytic form, which is given by the following relation [11,13]:

$$h_r(t) = \frac{\tau_1^2 + \tau_2^2}{\tau_1 \tau_2^2}\exp\left(-\frac{t}{\tau_2}\right)\sin\left(\frac{t}{\tau_1}\right), \tag{8}$$

where Raman period $\tau_1 = 15.5$ fs and lifetime $\tau_2 = 230.5$ fs for chalcogenide glass [28]. The pump pulses used emerge from the tunable femtosecond laser with hyperbolic secant field profiles. The hyperbolic secant pulse can be expressed as follows [11,13]:

$$A(z = 0, t) = \sqrt{p_0}\,\operatorname{sech}\left(\frac{t}{t_0}\right)\exp\left(-i\frac{C}{2}\frac{t^2}{t_0^2}\right), \tag{9}$$

where $t_0 = T_{\text{FWHM}}/1.7627$, P_0 is peak power, and C is the chirp coefficient. In our calculations we set the pump wavelength to 2.8 μm. Unchirped pulses with full width at half-maximum (FWHM) duration of $T_{\text{FWHM}} = 50$ fs and energy of 120 pJ are chosen to study SC generation.

Figure 4 shows SC broadening with different pump powers of 1, 2, and 3 kW in a length of 8 mm, which is pumped at 2800 nm. Pulse duration is kept fixed, taken as 50 fs. Such an ultrashort pulse is readily available, such as from a Cr:ZnSe/S femtosecond laser operating in the wavelength range of 2–3.5 μm [30,31]. The numerically calculated value of nonlinear length ($L_{\text{NL}} = 1/\gamma P_0$) is 3.2×10^{-4} m. Dispersion length ($L_D = t_0^2/\beta_2$) is calculated using $t_0 = T_{\text{FWHM}}/1.7627$, taking $T_{\text{FWHM}} = 50$ fs. The calculated value of L_D is 4.4×10^{-2} m. The soliton order, $N \approx \sqrt{(L_D/L_{\text{NL}})}$ is ∼12 for this PCF. $L_{\text{fiss}} = L_D/N$ is the soliton fission, with length of 3.67 mm.

As we can see from Fig. 4, most broadening occurs with pump power of 3 kW, and it can be concluded that increase in power results in more broadening of the SC spectrum. Further increase in pump power could destroy the fiber by overheating, e.g., due to absorption at the coating. Higher pump powers are not likely to be incorporated, as higher pump powers are not readily available and energy of very high picojoules is required for spectrum generation.

Figure 5 illustrates the spectral broadening of the SC spectrum in various lengths of the PCF structure when the PCF is pumped with 50 fs laser pulses of peak power of 3 kW at 2800 nm. Initially, the spectrum shows no broadening as it is the input pulse, which when further launched into the length of the nonlinear fiber results in broadening of the spectrum. Broadening in the SC spectrum increases with the length of the PCF. At an 8 mm length of the PCF structure, we are able to get SC broadening from 0.5 to 4.8 μm. After increasing the length above 8 mm, there is no significant change in the broadening of the spectrum because the soliton fission length is limited to 3.67 mm. It is clear from Fig. 5 that the spectral broadening of the SC spectrum at a 8 mm length of fiber is 0.5–4.7 μm at a −30 dB power level. Further increase in the length of the fiber does not provide significant increment in the broadening of SC spectrum.

Initially the spectrum is symmetrical, but as the pump power increases unsymmetrical broadening occurs. Initially

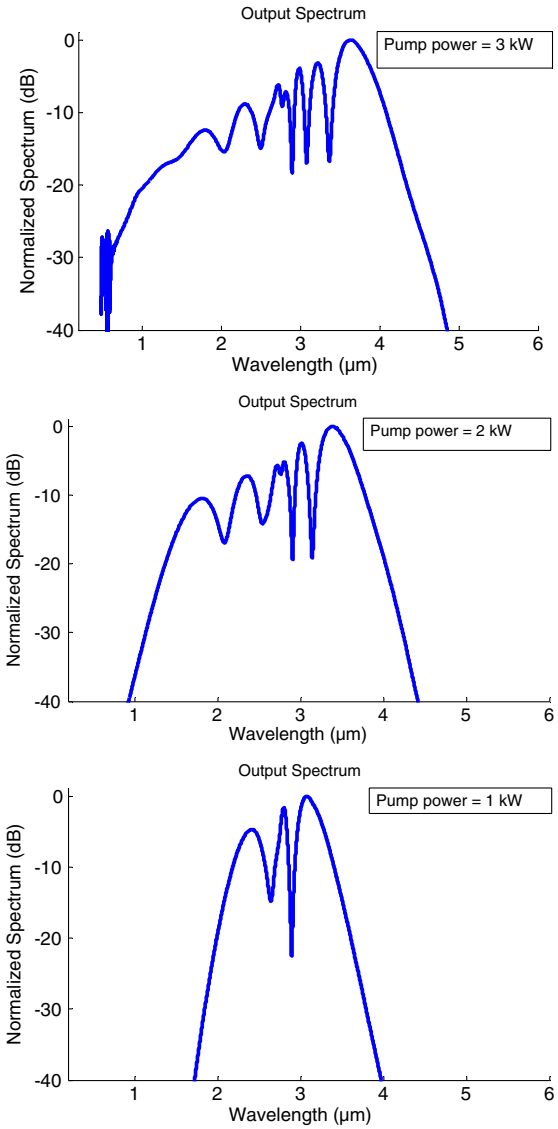

Fig. 4. SC broadening with different pump powers in a fiber length of 8 mm, pumping at 2800 nm.

launching the power at 1 kW, we can see with further increase in pump power to 3 kW that the spectrum broadens to more than 2000 nm. Since femtosecond pulses are being used in this anomalous dispersion regime, the soliton effects come into focus [32].

Figure 6 depicts SC broadening at different pulse durations with pump power of 3 kW in a 8 mm length of fiber. Variations of the parameters responsible in SC generation with respect to the wavelength are studied for nonlinear applications. With increase in pulse duration, the spectrum gets narrower, which is due to the SPM effect. Initially the laser modulates its own phase as it travels through the length of the PCF in the SPM phenomenon [33].

Further propagation adds linear and nonlinear effects, resulting in spectral broadening of the order of hundreds of nanometers [29]. Broadening is also dependent on pulse duration, as the soliton fission length relies on the dispersion length and nonlinear length of the proposed PCF, i.e., indirectly related

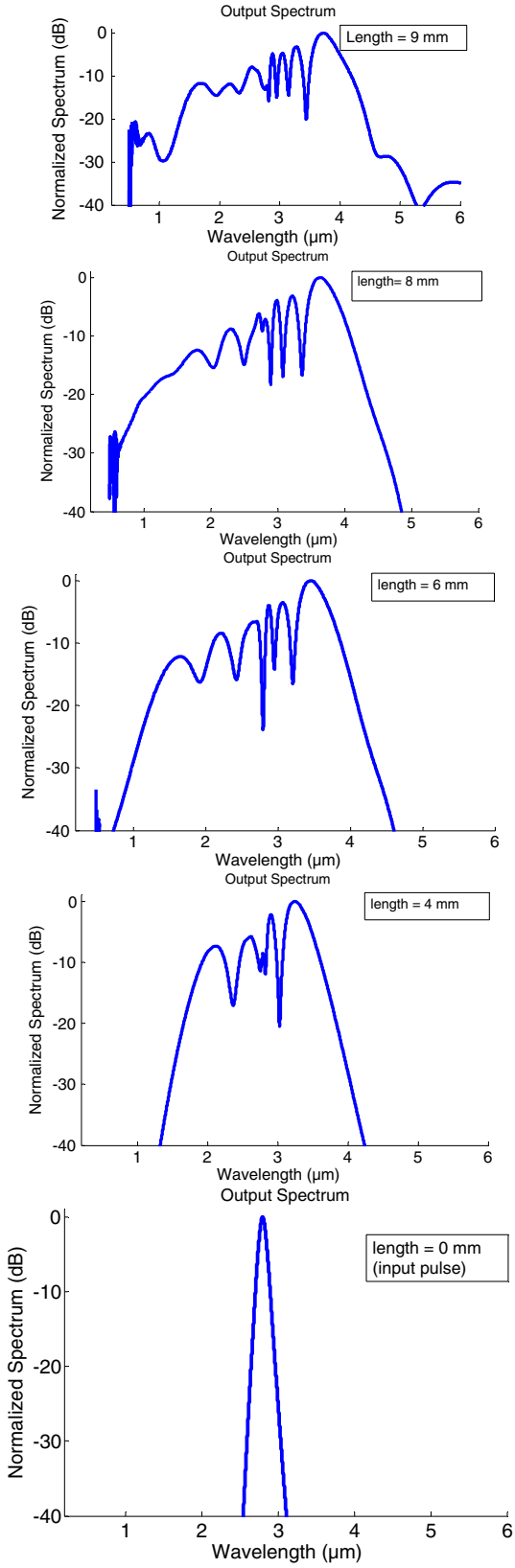

Fig. 5. SC broadening with pump power of 3 kW at different lengths of PCF.

to the T_{FWHM}. Increase in the pulse duration decreases the broadness of the spectrum; hence a laser pulse with smaller pulse duration results in a broader spectrum.

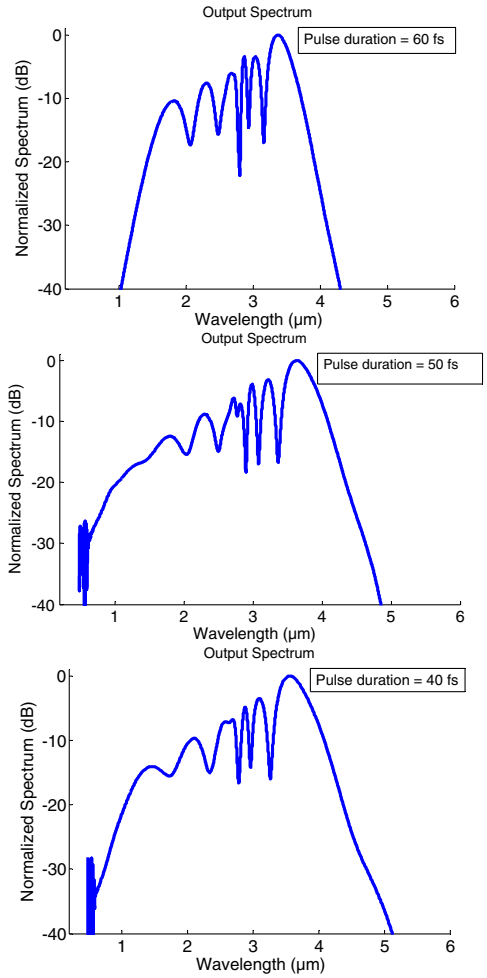

Fig. 6. SC broadening with pump power of 3 kW at different pulse durations.

The simulations suggest that the most effective broadband SC spectrum is obtained by using 3 kW power in an 8 mm length of the fiber with pulse duration of 40 fs, resulting in SC spectrum from 0.5 to 6 μm. Our reported spectral broadening in the SC spectrum is larger than that reported in Ref. [9] or Ref. [13].

For the manufacturing point of view, the designed PCF structure can be fabricated using the pressure-assisted melt filling technique [13]. It can also be fabricated by the method of stack and draw, as presented in Ref. [9].

5. CONCLUSIONS

This proposed composite PCF design results in achieving high nonlinearity of 1042 W^{-1} Km^{-1} with a significantly high effective mode area of 6.46 μm^2. High nonlinearity is desired to generate broad SC spectra with the use of low pump power. The simulations resulted in SC generation ranging from 0.5 to 4.7 μm with an 8 mm length of chalcogenide photonic crystal fiber pumped at a −30 dB power level. This is achieved with low pulse peak power of 3 kW while taking 40 fs as the pulse duration. Broadening of the SC spectrum depends on the dispersion profile of the fiber and its input characteristics, which can be controlled with this design by changing the parameters of the composite PCF. This design is made of very highly nonlinear material, which, along with the flexibility to control chromatic dispersion, made it suitable for realizing compact SC sources. This reported structure can be operated in the visible to IR region. This broadband SC has applications in the fields of telecommunication, optical metrology, cosmological studies, nonlinear microscopy, optical coherence tomography, and ultrashort pulse generation.

Funding. Department of Science and Technology, Ministry of Science and Technology (DST).

Acknowledgment. The authors gratefully acknowledge the Tunisian–Indian bilateral project "Design, modeling and characterization of highly nonlinear fibers for all-optical high bit-rate networks," funded by the Department of Science and Technology, Government of India.

REFERENCES

1. S. Revathi and S. R. Inbathini, "Analysis of propagation characteristics in photonic crystal fiber for large negative dispersion," J. Theor. Appl. Inf. Technol. **36**, 129–133 (2012).
2. G. P. Agarwal, *Nonlinear Fiber Optics*, 4th ed. (Elsevier, 2007).
3. S. P. Singh and N. Singh, "Nonlinear effects in optical fibers: origin, management and applications," Prog. Electromagn. Res. **73**, 249–275 (2007).
4. J. S. Sanghera, L. B. Shaw, P. Pureza, V. Q. Nguyen, D. Gibson, L. Busse, and I. D. Aggarwal, "Nonlinear properties of chalcogenide glass fibers," Int. J. Appl. Glass Sci. **1**, 296–308 (2010).
5. M. Liao, C. Chaudhari, L. Shuo, and L. S. Guang, "Numerical analysis of photonic crystal fiber with chalcogenide core tellurite cladding composite microstructure," Chin. Phys. B. **22**, 074206 (2013).
6. V. V. R. K. Kumar, A. K. George, J. C. Knight, and P. St. J. Russell, "Tellurite photonic crystal fiber," Opt. Express **11**, 2641–2645 (2003).
7. C. Xiong, E. Magi, F. Luan, A. Tuniz, S. Dekker, J. S. Sanghera, L. B. Shaw, I. D. Aggarwal, and B. J. Eggleton, "Characterization of picosecond pulse nonlinear propagation in chalcogenide As_2S_3 fiber," Appl. Opt. **48**, 5467–5474 (2009).
8. X. Feng, W. H. Loh, J. C. Flanagan, A. Camerlingo, S. Dasgupta, P. Petropoulos, P. Horak, K. E. Frampton, N. M. White, J. H. V. Price, H. N. Rutt, and D. J. Richardson, "Single-mode tellurite glass holey fiber with extremely large mode area for infrared nonlinear applications," Opt. Express **16**, 13651–13656 (2008).
9. M. Liao, C. Chaudhari, G. Qin, X. Yan, C. Kito, T. Suzuki, Y. Ohishi, M. Matsumoto, and T. Misumi, "Fabrication and characterization of a chalcogenide-tellurite composite microstructure fiber with high nonlinearity," Opt. Express **17**, 21608–21614 (2009).
10. T. S. Saini, A. Kumar, and R. K. Sinha, "Broadband mid-infrared supercontinuum spectra spanning 2–15 μm using As_2Se_3 chalcogenide glass triangular-core graded-index photonic crystal fiber," J. Lightwave Technol. **33**, 3914–3920 (2015).
11. T. S. Saini, A. Baili, A. Kumar, R. Cherif, M. Zghal, and R. K. Sinha, "Design and analysis of equiangular spiral photonic crystal fiber for mid-infrared supercontinuum generation," J. Mod. Opt. **62**, 1570–1576 (2015).
12. M. R. Karim, B. M. A. Rahman, Y. O. Azabi, A. Agrawal, and G. P. Agrawal, "Ultrabroadband mid-infrared supercontinuum generation through dispersion engineering of chalcogenide microstructured fibers," J. Opt. Soc. Am. **32**, 2343–2351 (2015).
13. N. Granzow, S. P. Stark, M. A. Schmidt, A. S. Tverjanovich, L. Wondraczek, and P. St. J. Russell, "Supercontinuum generation in chalcogenide-silica step-index fibers," Opt. Express **19**, 21003–21010 (2011).

14. D. Xie and J. G. Wen, "Chalcogenide-tellurite composite microstructured fiber for low-threshold mid-IR supercontinuum generation," Adv. Mater. Res. **308–310**, 517–520 (2011).
15. P. Domachuk, N. A. Wolchover, M. Cronin-Golomb, A. Wang, A. K. George, C. M. B. Cordeiro, J. C. Knight, and F. G. Omenetto, "Over 4000 nm bandwidth of mid-IR supercontinuum generation in sub-centimeter segments of highly nonlinear tellurite PCFs," Opt. Express **16**, 7161–7168 (2008).
16. C. Chaudhari, T. Suzuki, and Y. Ohishi, "Design of zero chromatic dispersion chalcogenide As_2S_3 glass nanofibers," J. Lightwave Technol. **27**, 2095–2099 (2009).
17. C. B. Chaudhari, T. Suzuki, and Y. Ohishi, "Chalcogenide core photonic crystal fibers for zero chromatic dispersion in the C-band," in *Optical Fiber Communication Conference* (2009), paper OTuC4.
18. J. K. Ranka, R. S. Windeler, and A. J. Stentz, "Visible continuum generation in air-silica microstructure optical fibers with anomalous dispersion at 800 nm," Opt. Lett. **25**, 25–27 (2000).
19. C. Xia, M. Kumar, M. Y. Cheng, O. P. Kulkarni, M. N. Islam, A. Galvanauskas, F. L. Terry, M. J. Freeman, D. A. Nolan, and W. A. Wood, "Supercontinuum generation in silica fibers by amplified nanosecond laser diode pulses," IEEE J. Sel. Top. Quantum Electron. **13**, 789–797 (2007).
20. M. Liao, C. Chaudhari, G. Qin, X. Yan, T. Suzuki, and Y. Ohishi, "Tellurite microstructure fibers with small hexagonal core for supercontinuum generation," Opt. Express **17**, 12174–12182 (2009).
21. D. D. Hudson, S. A. Dekker, E. C. Mägi, A. C. Judge, S. D. Jackson, E. B. Li, J. S. Sanghera, L. B. Shaw, I. D. Aggarwal, and B. J. Eggleton, "Octave spanning supercontinuum in an As_2S_3 taper using ultralow pump pulse energy," Opt. Lett. **36**, 1122–1124 (2011).
22. C. Chaudhari, M. Liao, T. Suzuki, and Y. Ohishi, "Chalcogenide core tellurite cladding composite microstructured fiber for nonlinear applications," J. Lightwave Technol. **30**, 2069–2076 (2012).
23. A. Kudlinski, G. Bouwmans, M. Douay, M. Taki, and A. Mussot, "Dispersion-engineered photonic crystal fibers for CW-pumped supercontinuum sources," J. Lightwave Technol. **27**, 1556–1564 (2009).
24. J. M. Dudley, G. Genty, and S. Coen, "Supercontinuum generation in photonic crystal fiber," Rev. Mod. Phys. **78**, 1135–1184 (2006).
25. R. Leitgeb, W. Drexler, A. Unterhuber, B. Hermann, T. Bajraszewski, T. Le, A. Stingl, and A. F. Fercher, "Ultrahigh resolution Fourier domain optical coherence tomography," Opt. Express **12**, 2156–2165 (2004).
26. H. Mikami, M. Shiozawa, M. Shirai, and K. Watanabe, "Compact light source for ultrabroadband coherent anti-Stoke Raman scattering (CARS) microscopy," Opt. Express **23**, 2872–2878 (2015).
27. Y. Vidne and M. Rosenbluh, "Spatial modes in a PCF fiber generated continuum," Opt. Express **13**, 9721–9728 (2005).
28. W. S. Rodney, I. H. Malitson, and T. A. King, "Refractive index of arsenic trisulphide," J. Opt. Soc. Am. **48**, 633–636 (1958).
29. G. E. Snopatin, M. F. Churbanov, A. A. Pushkin, V. V. Gerasimenko, E. M. Dianov, and V. G. Plotnichenko, "High purity arsenic-sulfide glasses and fibers with minimum attenuation of 12 dB/km," Optoelectron. Adv. Mater. **3**, 669–671 (2009).
30. I. T. Sorokina and E. Sorokin, "Femtosecond Cr^{2+}-based lasers," IEEE J. Sel. Top. Quantum Electron. **21**, 160159 (2005).
31. S. Vasilyev, I. Moskalev, M. Mirov, S. Mirov, and V. Gapontsev, "Multi-watt mid-IR femtosecond polycrystalline Cr^{2+}:ZnS and Cr^{2+}:ZnSe laser amplifiers with the spectrum spanning 2.0–2.6 μm," Opt. Express **24**, 1616–1623 (2016).
32. R. R. Alfano, *The Supercontinuum Laser Source* (Springer, 1989).
33. A. Ortigosa-Blanch, J. C. Knight, and P. St.J. Russell, "Pulse breaking and supercontinuum generation with 200-fs pump pulses in PCF," J. Opt. Soc. Am. B **19**, 2567–2572 (2002).

To be published in Applied Optics:

Title: Design and analysis of single-mode tellurite photonic crystal fibers for stimulated Brillouin
Authors: Ajeet Kumar,varsha jain,shubham sharma,Than Singh Saini,Ravindra Sinha
Accepted: 03 August 16
Posted 03 August 16
Doc. ID: 264240

Published by

OSA®

The Optical Society

Design and analysis of single-mode tellurite photonic crystal fibers for stimulated Brillouin scattering based slow-light generation

VARSHA JAIN,[1,3] SHUBHAM SHARMA,[1,3] THAN SINGH SAINI,[1] AJEET KUMAR,[1,*] RAVINDRA KUMAR SINHA[2]

[1]*Advanced Photonics Simulation Research Laboratory, Department of Applied Physics, Delhi Technological University, Delhi-110 042, INDIA*
[2]*CSIR-Central Scientific Instruments Organization, Chandigarh-160030, INDIA*
[3]*These authors have contributed equally to this work.*
**Corresponding author: ajeetdph@gmail.com*

Received XX Month XXXX; revised XX Month, XXXX; accepted XX Month XXXX; posted XX Month XXXX (Doc. ID XXXXX); published XX Month XXXX

Published by

We theoretically examine two designs of single-mode (i) Er-doped tellurite and (ii) undoped tellurite photonic crystal fiber for generation of slow-light with tunable features based on stimulated Brillouin scattering. We obtained (i) Brillouin gain up to 91 dB and time-delay of ~145 ns at maximum allowable pump power of ~775 mW in 2 m Er-doped tellurite PCF, and (ii) Brillouin gain up to ~88 dB and time delay of ~154 ns at maximum allowable pump power ~21 mW in 100 m undoped tellurite photonic crystal fiber. Simulated results clearly indicate that the doped tellurite PCF with Er enhances the maximum allowable pump power and comparable time-delay can be obtained even with reduced photonic crystal fiber length. We believe that the carried out examination and simulation has potential impact on design and development of slow-light-based photonic devices applicable in telecommunication systems, enhancement of optical forces, and quantum computing.

OCIS codes: *(290.5900) Scattering, stimulated Brillouin; (060.5295) Photonic crystal fibers; (190.4370) Nonlinear optics, fibers; (060.2370)*

http://dx.doi.org/10

1. Introduction

In last decades, slowing down of light or storing optical pulses by dramatically reducing their group velocity was not feasible. Therefore, processing of optical signal had to be on fly or optical signals had to be converted to electrical domain for buffering purposes. Thus significant efforts have been directed towards varying optical pulse propagating velocity which has applications in optical delay line [1], quantum information processing [2], and optical sensors [3]. In addition, the slow group velocity of light reduces the size of various optical devices [4]. The term "slow light" can be related to reducing the group velocity of optical pulse by interacting with the medium in which light is propagating. Controlling and storing of light offers a promising approach for on-chip integration of slow-light devices in particular photonic crystal devices. Various phenomena have been proposed to slow down the velocity of light such as Electromagnetically Induced Transparency (EIT) [5], Coherent Population Oscillation (CPO) [6], Stimulated Raman Scattering (SRS) [7], Stimulated Brillouin Scattering (SBS) [1], Soliton Collision [8]. Among all these phenomena, Stimulated Brillouin Scattering, has been the attraction of recent research in generation of slow light in optical fibers, due to its potential, flexibility, compatibility with current optical communication, room temperature operation, and tunable working wavelength feature [1,9].

Unlike classical step index fiber, PCFs are inherently single mode for large range of visual and near infrared spectrum. In PCFs, attenuation effect is less than conventional fibers. Small core PCF is an excellent medium to slow down light with a moderate pump power. So there is need to investigate features of tunable slow light in higher refractive index PCF's. Small-core photonic crystal fiber guides light by means of a lattice of hollow microchannel running axially along its length so it has a much larger refractive index contrast than ordinary doped fiber. It can have tighter confinement of both sound and light so as to enhance acousto-optic interaction [10]. Initially, slow light was generated using extremely strong material dispersion, however, use of high refractive index material [11–13] and, the material dispersion that can be modified by artificial photonic cladding with the presence of air-holes arising from engineered structure, in particular, PCF [14] offers a promising approach to shrink the length of fiber and to achieve desired time-delay and Brillouin gain. The shape and strength of Brillouin gain depends on overlap between the optical and acoustic modes. More effective control over acousto-optic interaction can be achieved in photonic crystal fiber geometries.

Earlier, Silica based fibers used for SBS-based slow light application [15] required kilometers of length of fiber for obtaining effective time-delay and gain. Large-delay slow-light based on SBS in a short length of small-core pure silica photonic crystal fiber has been realized by Yang et al. [14]. Woodward et al. [16] characterized the SBS of visible light in silica based small core photonic crystal fiber pumped with 535 nm. A review on various nonlinear phenomenon enhanced by slow light in silicon based photonic crystal waveguides was presented by Monat et al. [17]. Pant et al. reported first time the maximum delay of ~23 ns in 7 cm long chalcogenide rib waveguide [18]. Numerical modeling of SBS in standard silica fibers for slow-light applications has been made earlier in various articles [19].

Tellurite glass has a range of advantages such as high refractive index, good in infrared transmittance, high optical non-linearity and relatively low phonon energy among oxide

glasses. Also, tellurite glasses show higher rare earth solubility than chalcogenide glasses [20]. All these properties make tellurite glass an excellent substance for PCF fabrication. Photonic crystal fibers are produced by several methods that involve preparing a macroscopic meter-length preform with desired transverse crystal lattice and drawing into microscopic scale fibers while preserving the intended cross-section design. Method of fabrication are stack-and-draw, extrusion [21], sol-gel casting [22], drilling [23]. Most common methods for tellurite PCF are extrusion technique [24] and stack-and-draw technique [23], which are fast, clean, low-cost and feasible. It has been confirmed that tellurite fibers are one of the most promising medium for Brillouin fiber laser, amplifiers and slow-light generation [25]. Therefore, features of tunable slow-light are investigated in high refractive index tellurite photonic crystal.

Er-doped fiber amplifiers (EDFAs) are preferred for their excellent behavior under saturated conditions: low-signal distortion and crosstalk at modulation frequencies of interest [26, 27] and high-signal output powers [27, 28]. Erbium-doped fiber amplifiers can efficiently amplify light in the 1.5-μm wavelength region. The noise figure of an Erbium doped fiber amplifier is slightly larger than the theoretical limit of 3 dB for a high-gain amplifier [29]. Thus doping with Erbium enables the production of compact and efficient source. Recent works on tellurite photonic crystal fibers [30] indicate that for SBS, pump powers are between 12.3 and 1100 mW for 2 m long Er-doped tellurite fiber, while for 100 m long undoped tellured fiber the pump powers lie between 1.5 and 23 mW.

In this work, we have designed and analyzed two specialty fiber geometries including (a) Er-doped tellurite photonic crystal fiber; (b) undoped tellurite photonic crystal fiber. We numerically simulated the influences of PCF characteristics such as maximum pump power for undistorted output pulse, Brillouin gain and time-delay experienced by the pulse for both PCF geometries (a) Er-doped tellurite (b) undoped tellurite PCF. Simulated results indicate that time-delay experienced by optical pulse can be tuned with pump power and tunable features can be obtained. Pump power can be tuned between 8.7 mW to 775 mW for 2 m long Er-doped tellurite PCF and between 1.3 to 21 mW for 100 m long undoped tellurite PCF for obtaining desirable time-delay.

2. Theory of Stimulated Brillouin Scattering

Stimulated Brillouin Scattering is one of the most important nonlinear effects that occur in optical fibers which was first observed in 1964 [31] and has since been studied extensively. The process of SBS can be described as a nonlinear interaction between a high intensity pump wave with a signal wave with the help of an acoustic wave, all travelling in the longitudinal direction inside the core of the fiber. The high intensity pump wave and the lower intensity signal waves have unequal frequencies, the difference of which is responsible for the generation of a slowly travelling wave (called acoustic wave) by the phenomenon of electrostriction. This low frequency acoustic wave travels in one direction in the fiber creating travelling modulations of refractive index in the core. These periodic changes in the refractive index of the fiber essentially create a dynamic Bragg grating along the fiber. This travelling grating (moving with acoustic velocity v_A) is responsible for scattering the high power pump wave into a frequency downshifted wave called Stokes wave. When the counter-propagating continuous signal wave has the same downshift as the stokes wave, the signal wave experiences high gains [32].

If the frequencies of the pump wave and signal wave are ω_p and ω_s respectively, and their respective intensities are I_p and I_s, then the coupled non-linear equations for the pump and signal waves are given by equations [33]

$$\frac{dI_p}{dz} = -g_B I_p I_s - \alpha_p I_p \qquad (1)$$

$$\frac{dI_s}{dz} = +g_B I_p I_s - \alpha_s I_s \qquad (2)$$

We can fairly assume the pump wave to be undepleted for the purpose of estimating the Brillouin threshold. Assuming ($\alpha s \approx \alpha p$) $\equiv \alpha$, the result of the above equations (1 & 2) can be given by the following relation

$$I_s(0) = I_s(L)\exp\left(\frac{g_B P_0 L_{eff}}{A_{eff}} - \alpha L\right) \qquad (3)$$

where, L_{eff} is the effective length of the PCF and is given by

$$L_{eff} = \left(1 - e^{(-\alpha L)}\right)/\alpha \qquad (4)$$

Where, α is the attenuation constant (or material loss), L is the real length of the PCF, and L_{eff} is the corresponding effective length.

If E is the electric field distribution inside the core of the PCF, then the effective mode area (i.e. A_{eff}) of the propagating mode is defined as

$$Aeff = \left(\iint_{-\infty}^{\infty} |E|^2\, dx\, dy\right)^2 \Big/ \left(\iint_{-\infty}^{\infty} |E|^4\, dx\, dy\right) \qquad (5)$$

The Brillouin gain of the signal wave for the proposed PCF is characterized by Brillouin gain coefficient, G, which can be calculated using following relation,

$$G = 10\log\left[\exp\left(\frac{g_B K P_0 L_{eff}}{A_{eff}} - \alpha L\right)\right] \qquad (6)$$

where, polarization factor (i.e. K) depends on the polarization properties of the PCF. In our simulation the value of polarization factor (i.e. K) is taken equal to 0.667 [13], [14]. P_0 is the pump wave power and g_B is given by

$$g_B(\Omega) = \frac{g_p(\Gamma_B/2)^2}{(\Omega - \Omega_B)^2 + (\Gamma_B/2)^2} \qquad (7)$$

where g_p is the peak value of Brillouin gain at $\Omega = \Omega_B$, and Γ_B is the Brillouin linewidth.

Γ_B is related to full width at half maximum (FWHM) of the gain spectrum by relation,

$$\Gamma_B = 2\pi\Delta\nu_B \qquad (8)$$

and related to phonon lifetime as [25]

$$\Gamma_B = \tau_{phonon}^{-1} \qquad (9)$$

The power of the pump pulse is limited by the probability of high distortion of the output signal pulse due to backscattered wave generated from the background noise in the fiber when pump power approaches P_{max}. Therefore, the pump power is kept lower than P_{max}. It is related to g_B as [13] , [10],

$$P_{max} = 21\frac{A_{eff}}{K\, g_B\, L_{eff}} \qquad (10)$$

Stimulated Brillouin scattering effect can only occur in a fiber when the total Brillouin gain is larger than the total loss experienced inside

the PCF. For initiating SBS effect the minimum pump power required is given as

$$P_{min} = \alpha \frac{A_{eff} L}{K g_B L_{eff}} \quad (11)$$

The SBS induced time delay per unit length in the PCF is related to the input pump power as follows [9],

$$\frac{\Delta t_d}{L_{eff}} = \left(\frac{K g_0}{\Gamma_B} \right) P_p \quad (12)$$

Unlike conventional fibers the photonic crystal waveguide dispersion can be very strong. Furthermore, the material dispersion is modified by artificial photonic cladding with the presence of air-holes. Dispersion characteristics in PCFs can be easily shaped due to the flexibility of varying air-hole size and the position in the photonic cladding. A key parameter that describes properties of fibers is its dispersion (D). It is given by,

$$D = -\frac{\lambda}{c} \frac{d^2 n_{eff}}{d\lambda^2} \quad (13)$$

where, n_{eff} is given by,

$$n_{eff} = \frac{\beta(\lambda, n_m(\lambda))}{k_0} \quad (14)$$

3. Design of proposed Photonic crystal fiber

To study the generation of SBS based tunable slow-light, we have proposed a single-mode PCF design which consists of array of circular air holes arranged in hexagonal lattice pattern in the cladding region. As shown in Fig. 1, the diameter of the circular air holes is kept identical and is represented by '*d*' while the pitch (i.e. center to center distance between any two consecutive air holes) is represented by '*Λ*'. In our simulation the pitch is kept constant at 2 μm and diameter is varied from 0.6 μm to 1.0 μm to change the effective-mode-area of PCF. For the doped fiber, tellurite glass is doped with rare earth element Erbium(Er) in the entire PCF, i.e. core as well as the cladding.

For (i) Er-doped tellurite PCF, the refractive index has been taken equal to 1.98 at 1.55 μm [34]; and for (ii) undoped tellurite PCF refractive index was calculated to 2.03 at 1.55 μm [35]. In order to ensure single-mode operation in the proposed PCF the value of ratio *d/Λ* must be less than 0.5 [10]. Therefore, we have chosen *d/Λ* equal to 0.4 for ensuring proper single-mode operation.

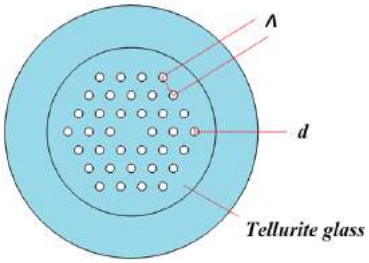

Fig. 1. Transverse 2D cross-sectional view of the proposed photonic crystal fiber structure.

Fig. 2 (a) illustrates 2D surface plot of incident electromagnetic wave in the proposed Er-doped tellurite PCF and Fig. 2 (b) illustrates the 2D surface plot of the incident electromagnetic wave in the proposed undoped tellurite PCF, both with d/Λ = 0.4 at 1.55 μm wavelength.

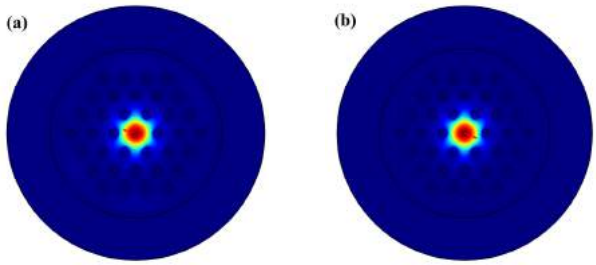

Fig. 2. Electric field distribution of with d/Λ=0.4 at 1.55μm in the proposed (a) Er-doped tellurite PCF and in (b) undoped tellurite PCF.

4. Results and discussions

The simulation of stimulated Brillouin scattering-induced slow-light in Er-doped tellurite PCF is carried out using the following parameters, fiber material loss = 0.51 dB/m (i.e. α = 0.117/m), the polarization factor, K = 0.667, the Brillouin gain coefficient, $g_B = 1.47 \times 10^{-10}$ m/W, Brillouin gain bandwidth, $\Delta\nu_B$ = 23 MHz [13], and the length of the PCF = 2 m. Whereas, for simulation in the proposed undoped tellurite PCF, the following parameters are used, the Brillouin gain coefficient, $g_B = 1.6989 \times 10^{-10}$ m/W, Brillouin gain bandwidth, $\Delta\nu_B$ = 20.98 MHz, the fiber material loss, = 0.0558 dB/m (i.e. α = 0.01354 /m), and the polarization factor, K = 0.667 [25], and the length taken is 100 m.

Using the above parameters, the influence of fraction (d/Λ) on effective mode area (A_{eff}) of propagating mode in (a) Er-doped tellurite PCF and (b) undoped tellurite PCF is illustrated in Fig. 3. As is evident by the figures, the effective mode area (i.e., A_{eff}) deceases on increasing d/Λ because it reduces the core size of the PCF. Thus, effective mode area of PCF can be controlled by tuning the air hole diameter 'd' or pitch 'Λ'. Also, since, nonlinearity is inversely proportional to effective mode area of core, increasing d/Λ effectively increases the nonlinearity of PCF. Simulated results show effective mode area of the fundamental mode is equal to 6.45 μm² at d/Λ = 0.4 for Er-doped tellurite PCF and is equal to 6.29 μm² at d/Λ = 0.4 for undoped tellurite PCF.

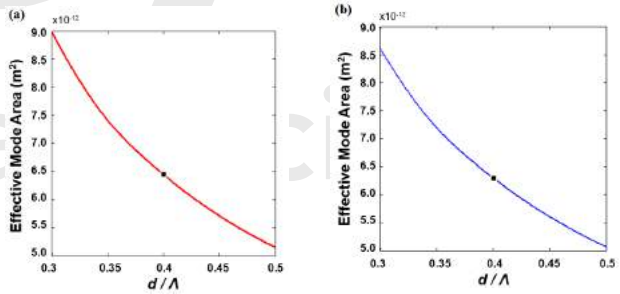

Fig. 3. Effective mode area of propagating mode in (a) Er-doped tellurite PCF and in (b) undoped tellurite PCF.

When the value of the d/Λ increases, the core area decreases, thus confining the field within a smaller region. This decreases the power handling capability of PCF and hence, maximum allowable pump power for the PCF decreases. If the pump power applied is greater than the maximum allowable power, the output pulse obtained will be distorted. The value of P_{max} is equal to (a) 775.3 mW when d/Λ = 0.4 for Er-doped tellurite PCF and is equal to (b) 20.7 mW at d/Λ = 0.4 for undoped tellurite PCF.

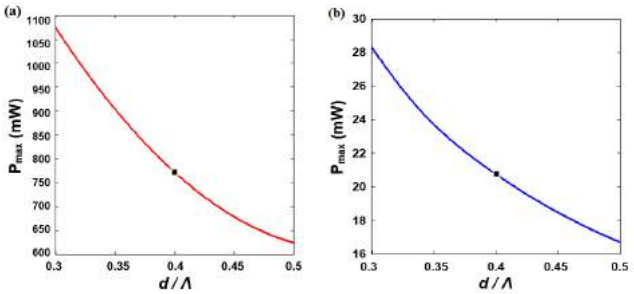

Fig. 4. Maximum allowable pump power as a function of d/Λ for (a) Er-doped tellurite PCF and (b) undoped tellurite PCF.

The minimum pump power indicates the threshold for inducing stimulated Brillouin scattering in the PCF. Below this power the PCF does not show any nonlinear effects. Minimum pump power also decreases when d/Λ increases. The value of P_{min} is equal to (a) 8.7 mW when d/Λ = 0.4 for Er-doped tellurite PCF and is equal to (b) 1.3 mW at d/Λ = 0.4 for undoped tellurite PCF. Fig. 5 shows the relation of minimum pump power with d/Λ.

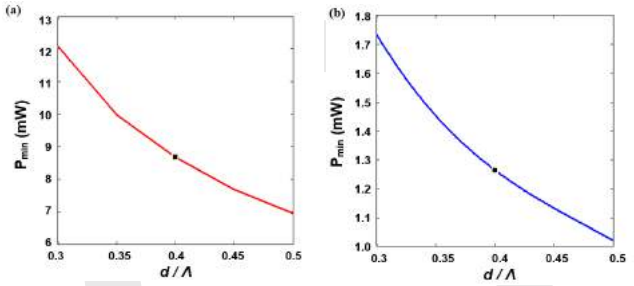

Fig. 5. Threshold power for inducing SBS in (a) Er-doped tellurite PCF and (b) undoped tellurite PCF.

The pump powers indicate the working range of achieving SBS based slow light inside the fiber, thus, an increase in pump powers indicate higher operable range for the fiber in doped fiber as compared to undoped fiber.

A key parameter that describes properties of fibers is Dispersion (D). In order to ensure that the optical signal pulse propagates with minimum distortion, the value of dispersion should be low [36, 37]. Figure 6 shows the dispersion curves for (a) doped and (b) undoped PCF. Dispersion is negative for both doped and undoped tellurite PCFs. Er-doped PCF has -1.247 x 10^{-10} ps/nm-km dispersion and -8.88 ps/nm-km for undoped PCF at communication wavelength (1550 nm).

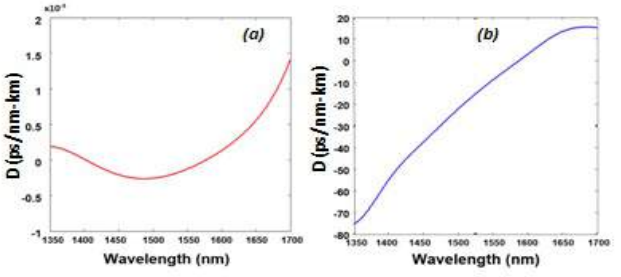

Fig. 6. Group velocity dispersion in (a) Er-doped tellurite PCF and (b) undoped tellurite PCF.

Another important feature of the PCF is the confinement loss, which decreases with increasing d/Λ because as the air hole diameter d increases, the difference between core cladding refractive index increases leading to higher confinement of light in the core. The confinement loss as a function of d/Λ is shown in Fig. 7. Simulation results show that for d/Λ= 0.4, the value of Brillouin gain is (a) ~ 4.6 dB/m for Er-doped tellurite PCF and is equal to (b) ~ 2.8 dB/m for undoped tellurite PCF.

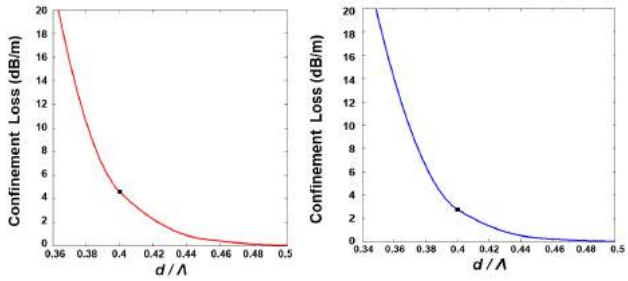

Fig. 7. Confinement losses in (a) Er-doped tellurite PCF and (b) undoped tellurite PCF.

The more is the confinement of field in the core of PCF, greater is the enhancement in Brillouin scattering, which consequently increases the associated Brillouin gain. Variation of Brillouin gain w.r.t. pump power at d/Λ is illustrated in Fig. 8. Simulation results show that for d/Λ= 0.4, the value of Brillouin gain is (a) ~91 dB for Er-doped tellurite PCF and is equal to (b) ~88 dB for undoped tellurite PCF.

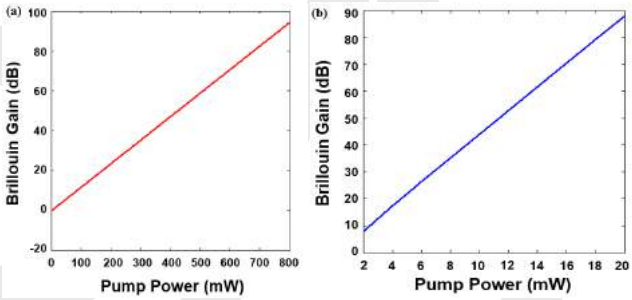

Fig. 8. Variation of Brillouin gain with pump power at d/Λ=0.4 in (a) Er-doped tellurite PCF and (b) undoped tellurite PCF.

The total time-delay with the pump power has been illustrated in Fig. 9. The maximum time-delay using 2 m doped tellurite fiber has been obtained up to 145 ns at 775 mW of maximum allowable pump power. The maximum time-delay of 154 ns at 21 mW of maximum allowable pump power has been obtained using undoped tellurite PCF.

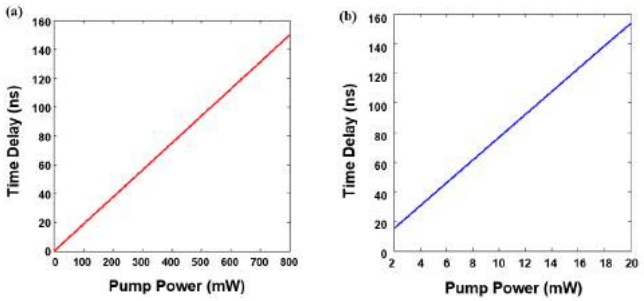

Fig. 9. Dependence of time delay on input pump power in (a) Er-doped tellurite PCF and (b) undoped tellurite PCF.

5. Conclusion

In conclusion, we have reported two different kind of photonic crystal fiber for tunable slow-light generation based on stimulated Brillouin scattering. PCF characteristics for slow-light such as maximum allowable pump power, Brillouin gain, time-delay for both types of PCF have been simulated. Our simulation results indicate that (i) the Brillouin gain up to 91 dB and maximum time-delay of 145 ns can be achieved using 2 m long Er doped tellurite PCF pumped with 775 mW and, (ii) the Brillouin gain up to 88 dB and maximum time-delay of 154 ns can be achieved using 100 m long undoped tellurite PCF pumped with 21 mW. The results of this work found better than earlier reported work in the conventional tellurite fibers [18]. Simulated results indicate that the use of engineered structures like photonic crystal fiber, with the help of doping with tellurite shrinks the length of the fiber used from 100 m to 2 m to obtain desirable time delay. The main advantage of doping the fiber with Er is the significant shortening of length required for similar delay in light signals, enabling realization of ultra- compact optical devices in communication systems. An increase in pump powers indicates higher operable range for the fiber in doped fiber as compared to undoped fiber. Thus, effectively, time delay can be tuned with pump power. The slow light nonlinear enhancement in the designed photonic crystal fibers has the potential to contribute in advancement of the field of integrated nonlinear optics to lower operating powers and ultra-compact devices.

ACKNOWLEDGEMENT

The authors gratefully acknowledge the partially supported by the DST/MHESR Indian/Tunisian bilateral research project.

References

1. Y. Okawachi, M. S. Bigelow, J. E. Sharping, Z. Zhu, A. Schweinsberg, D. J. Gauthier, R. W. Boyd, and A. L. Gaeta, "Tunable all-optical delays via brillouin slow light in an optical fiber," Phys. Rev. Lett. **94**, 1–4 (2005).
2. J. Gao, F. W. Sun, and C. W. Wong, "Implementation scheme for quantum controlled phase-flip gate through quantum dot in slow-light photonic crystal waveguide," Appl. Phys. Lett. **93**, 1–3 (2008).
3. Y. Li and X. Chen, "Theoretic Study of Improving the Sensitivity of Fiber Optic Gyroscope Using Slow light," 9141–9146 (2008).
4. M. Soljačić, S. G. Johnson, S. Fan, M. Ibanescu, E. Ippen, and J. D. Joannopoulos, "Photonic-crystal slow-light enhancement of nonlinear phase sensitivity," J. Opt. Soc. Am. B **19**, 2052 (2002).
5. J. Zhang, G. Hernandez, and Y. Zhu, "Slow light with cavity electromagnetically induced transparency.," Opt. Lett. **33**, 46–48 (2008).
6. S.-W. Chang, P. Kondratko, H. Su, and S. L. Chuang, "Slow Light Based on Coherent Population Oscillation in Quantum Dots at Room Temperature," Quantum Electron. IEEE J. **43**, 196–205 (2007).
7. J. Sharping, Y. Okawachi, and A. Gaeta, "Wide bandwidth slow light using a Raman fiber amplifier.," Opt. Express **13**, 6092–6098 (2005).
8. J. T. Mok, C. M. de Sterke, I. C. M. Littler, and B. J. Eggleton, "Dispersionless slow light using gap solitons," Nat. Phys. **2**, 775–780 (2006).
9. K. Y. Song, M. Herráez, and L. Thévenaz, "Observation of pulse delaying and advancement in optical fibers using stimulated Brillouin scattering.," Opt. Express **13**, 82–88 (2005).
10. R. K. Sinha, A. Kumar, and T. S. Saini, "Analysis and Design of Single-Mode As2Se3-Chalcogenide Photonic Crystal Fiber for Generation of Slow Light with Tunable Features," IEEE J. Sel. Top. Quantum Electron. **22**, 1–6 (2016).
11. K. S. Abedin, "Observation of strong stimulated Brillouin scattering in single-mode As2Se3 chalcogenide fiber.," Opt. Express **13**, 10266–10271 (2005).
12. K. S. Abedin, "Stimulated Brillouin scattering in single-mode tellurite glass fiber.," Opt. Express **14**, 11766–11772 (2006).
13. K. S. Abedin, G.-W. Lu, and T. Miyazaki, "Slow light generation in singlemode Er-doped tellurite fibre," Electron. Lett. **44**, 16 (2008).
14. S. Yang, H. Chen, C. Qiu, M. Chen, M. Chen, S. Xie, J. Li, and W. Chen, "Slow-light delay enhancement in small-core pure silica photonic crystal fiber based on Brillouin scattering.," Opt. Lett. **33**, 95–97 (2008).
15. T. Schneider, D. Hannover, and M. Junker, "Investigation of Brillouin scattering in optical fibers for the generation of Millimeter waves," J. Light. Technol. **24**, 295–304 (2006).
16. R. I. Woodward, E. J. R. Kelleher, S. V. Popov, and J. R. Taylor, "Stimulated Brillouin scattering of visible light in small-core photonic crystal fibers," Opt. Lett. **39**, 2330 (2014).
17. C. Monat, B. Corcoran, D. Pudo, M. Ebnali-Heidari, C. Grillet, M. D. Pelusi, D. J. Moss, B. J. Eggleton, T. P. White, L. O'Faolain, and T. F. Krauss, "Slow Light Enhanced Nonlinear Optics in Silicon Photonic Crystal Waveguides," IEEE J. Sel. Top. Quantum Electron. **16**, 344–356 (2010).
18. R. Pant, A. Byrnes, C. G. Poulton, E. Li, D.-Y. Choi, S. Madden, B. Luther-Davies, and B. J. Eggleton, "Photonic-chip-based tunable slow and fast light via stimulated Brillouin scattering," Opt. Lett. **37**, 969 (2012).
19. Z. Zhu, D. J. Gauthier, Y. Okawachi, J. E. Sharping, A. L. Gaeta, R. W. Boyd, and A. E. Willner, "Numerical study of all-optical slow-light delays via stimulated Brillouin scattering in an optical fiber," J. Opt. Soc. Am. B **22**, 2378 (2005).
20. J. S. Wang, E. M. Vogel, and E. Snitzer, "Tellurite glass: a new candidate for fiber devices," Opt. Mater. (Amst). **3**, 187–203 (1994).
21. V. V. R. Kumar, a George, W. Reeves, J. Knight, P. Russell, F. Omenetto, and a Taylor, "Extruded soft glass photonic crystal fiber for ultrabroad supercontinuum generation.," Opt. Express **10**, 1520–1525 (2002).
22. H. El Hamzaoui, L. Bigot, G. Bouwmans, I. Razdobreev, M. Bouazaoui, and B. Capoen, "From molecular precursors in solution to microstructured optical fiber: a Sol-gel polymeric route," Opt. Mater. Express **1**, 234 (2011).
23. T. a Birks, J. C. Knight, P. S. Russell, and D. M. Atkin, "All-silica single-mode optical fiber with photonic crystal cladding," Opt. Lett. **21**, 1547–1549 (1996).
24. V. V. R. K. Kumar, A. K. George, J. C. Knight, and P. S. J. Russell, "Tellurite photonic crystal fiber," Opt. Express **11**, 2641–2645 (2003).
25. T. Fiber and T. . O. Qin, G.; Sotobayashi, H.; Tsuchiya, M.; Mori, A.; Suzuki, "Stimulated Brillouin Scattering in a Single-Mode Slow Light Generation," Lightwave **26**, 492–498 (2008).
26. C. R. Giles, E. Desurvire, and J. R. Simpson, "Transient gain and cross talk in erbium-doped fiber amplifiers.," Opt. Lett. **14**, 880–2 (1989).
27. E. J. Tarbox, G. Grasso, and D. N. Payne, "High-Power Erbium-Doped-Fiber Amplifiers Operating in the Saturated Regime," IEEE Photonics Technol. Lett. **3**, 253–255 (1991).
28. E. Desurvire, C. R. Giles, J. R. Simpson, and J. L. Zyskind, "Efficient erbium-doped fiber amplifier at a 153-μm wavelength with a high output saturation power," Opt. Lett. **14**, 1266 (1989).
29. R. Mears, L. Reekie, I. Jauncey, and D. Payne, "Low-noise erbium-doped fibre amplifier operating at 1.54μm," Electron. Lett. **23**, 1026–1028 (1987).
30. T. Singh Saini, A. Kumar, and R. Kumar Sinha, "Slow light generation in single-mode tellurite fibers Slow light generation in single-mode tellurite fibers," J. Mod. Opt. **627**, 508–513 (2015).

31. R. Y. Chiao, C. H. Townes, and B. P. Stoicheff, "Stimulated brillouin scattering and coherent generation of intense hypersonic waves," Phys. Rev. Lett. **12**, 592–595 (1964).
32. L. Thévenaz, "Slow and fast light in optical fibres," Nat. Photonics **2**, 474–481 (2008).
33. G. P. Agrawal, "Chapter 9 - Stimulated Brillouin Scattering," Nonlinear Fiber Opt. (Fourth Ed. 329–367 (2006).
34. X. Peng, F. Song, S. Jiang, N. Peyghambarian, M. Kuwata-gonokami, and L. Xu, "Fiber-taper-coupled L-band Er 3 + -doped tellurite glass microsphere laser Fiber-taper-coupled L-band Er 3 ¿ -doped tellurite glass microsphere laser," **1497**, 8–11 (2016).
35. G. Ghosh, "Sellmeier Coefficients and Chromatic Dispersions for Some Tellurite Glasses," J. Am. Ceram. Soc. **78**, 2828–2830 (1995).
36. F. Wang, J. Ma, and C. Jiang, "Dispersionless slow wave in novel 2-D photonic crystal line defect waveguides," J. Light. Technol. **26**, 1381–1386 (2008).
37. A. Di Falco, L. O'Faolain, and T. F. Krauss, "Dispersion control and slow light in slotted photonic crystal waveguides," Appl. Phys. Lett. **92**, 2007–2009 (2008).

Published by
OSA®
The Optical Society

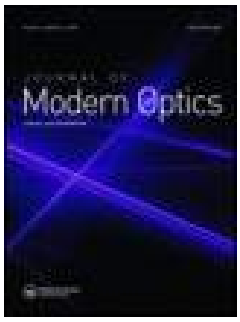

Journal of Modern Optics

ISSN: 0950-0340 (Print) 1362-3044 (Online) Journal homepage: http://www.tandfonline.com/loi/tmop20

Design and modelling of dispersion-engineered rib waveguide for ultra broadband mid-infrared supercontinuum generation

Than Singh Saini, Ajeet Kumar & Ravindra Kumar Sinha

To cite this article: Than Singh Saini, Ajeet Kumar & Ravindra Kumar Sinha (2016): Design and modelling of dispersion-engineered rib waveguide for ultra broadband mid-infrared supercontinuum generation, Journal of Modern Optics, DOI: 10.1080/09500340.2016.1216190

To link to this article: http://dx.doi.org/10.1080/09500340.2016.1216190

Published online: 02 Aug 2016.

Submit your article to this journal

Article views: 10

View related articles

View Crossmark data

Full Terms & Conditions of access and use can be found at
http://www.tandfonline.com/action/journalInformation?journalCode=tmop20

Download by: [Delhi Technological University] **Date:** 05 August 2016, At: 23:29

JOURNAL OF MODERN OPTICS, 2016
http://dx.doi.org/10.1080/09500340.2016.1216190

Taylor & Francis
Taylor & Francis Group

Design and modelling of dispersion-engineered rib waveguide for ultra broadband mid-infrared supercontinuum generation

Than Singh Saini[a], Ajeet Kumar[a] and Ravindra Kumar Sinha[b]

[a]Advanced Photonics Simulation Research Laboratory, Department of Applied Physics, Delhi Technological University (Formerly Delhi College of Engineering), Delhi, India; [b]CSIR-Central Scientific Instruments Organization, Chandigarh, India

ABSTRACT

We report a dispersion-engineered As_2Se_3 chalcogenide glass rib waveguide structure for ultra broadband mid-infrared supercontinuum generation across molecular 'fingerprint region'. The proposed rib waveguide structure offers non-linear coefficient as high as 18,250 W^{-1} km^{-1} at 2.5 μm. Supercontinuum spectrum spanning 2–15 μm, which not only covers the both atmospheric transparent windows (3–5 μm and 8–13 μm) in the mid-infrared domain but also covers the important molecular 'fingerprint domain', is obtained using only 4 mm-long rib waveguide structure. To the best of our knowledge, such broadband mid-infrared supercontinuum spectrum in As_2Se_3-based chalcogenide waveguide geometry is reported for the first time. The proposed design of rib waveguide has potential for robust, integrated and low-cost supercontinuum sources in various applications including frequency comb generation, chemical sensing, food quality control and early cancer diagnostics.

ARTICLE HISTORY
Received 23 February 2016
Accepted 18 July 2016

KEYWORDS
Non-linear optics; highly non-linear rib waveguide; mid-infrared supercontinuum generation

Downloaded by [Delhi Technological University] at 23:29 05 August 2016

1. Introduction

Supercontinuum generation (the creation of broadband spectral components when an intense laser pulse passes through a highly non-linear medium) is one of the most fascinating non-linear effects due to its major impact on spectroscopy, security and molecular sensing (*1*). The phenomenon of supercontinuum generation has been reported first time in crystals in 1970 (*2*). The spectral brightness of supercontinuum is million times brighter than conventional light sources. Supercontinuum generation is the result of combined effect of various non-linear mechanisms including self-phase modulation (SPM), stimulated Raman scattering (SRS), optical wave breaking, four wave mixing (FWM) and cross-phase modulation along with the dispersion properties of the medium. Spectral broadening due to SPM is the result of the maximum phase shift ($\phi_{max} = \gamma P_0 L_{eff}$) induced by SPM, where γ is the non-linear coefficient of the medium; P_0 is the peak power of input pulse; and L_{eff} is the effective length of the medium (*1*). SRS creates new frequency components on the longer wavelength side only. However, FWM is responsible for generating sidebands on both sides of the pulse spectrum when phase matching condition is satisfied.

The choice of the pump wavelength plays a critical role in broadening the supercontinuum generation (*3*). In most of the attempts, spectral broadening is achieved using pump pulses of wavelength near the zero dispersion wavelength in the anomalous dispersion region. When pump wavelength belongs to the anomalous dispersion regime, spectral broadening is due to the solitons fission or modulation instability (MI). The mechanism of solitons fission is highly sensitive to the laser shot noise (*4*). The supercontinuum generation in fibre *or* waveguide exhibiting all-normal dispersion characteristic is another approach (*5*). When we select input wavelength within the normal group velocity dispersion region of the waveguide, the process of solitons fission and broadband noise amplification by modulation instability is absent (*5*). In normal group velocity dispersion region, the FWM process can produce a broadband supercontinuum spectrum (*1*).

The mid-infrared spectral domain ranging from 2 to 15 μm is mainly important because it not only contains two important windows (3–5 μm and 8–13 μm) in which the earth's atmosphere is relatively transparent but also the strong characteristic vibration transitions of most of the molecules in this domain (*6*). Mid-infrared molecular 'fingerprint region' is applicable in various

CONTACT Ajeet Kumar ajeetdph@gmail.com, ajeet.phy@dce.edu

© 2016 Informa UK Limited, trading as Taylor & Francis Group

Downloaded by [Delhi Technological University] at 23:29 05 August 2016

important applications in different diverse fields such as medical, industry, security and astronomy (*7–12*). Therefore, researchers are trying very hard to achieve broadband supercontinuum spectrum in various fibres and waveguides geometries. Foster et al. (*13*) showed that an octave spanning supercontinuum can be generated using sub-wavelength dimension optical waveguides with pulses of 250 pJ energy from a femtosecond mode-locked Ti:sapphire oscillator. Yin et al. (*14*) numerically reported a design of silicon waveguide for supercontinuum spectrum extending over 400 nm using femtosecond laser pulses of low energy. Lamont et al. (*15*) demonstrated experimentally the supercontinuum generation with a –30 dB bandwidth of 750 nm using 610 fs laser pulse with peak power 68 W. Zhang et al. (*16*) reported two octave supercontinuum spectra spanning 630 to 2650 nm using silicon nitride slot waveguides. Halir et al. (*17*) demonstrated supercontinuum spectrum ranging from 665 to 2025 nm using silicon nitride waveguides with pulse energy 160 pJ. Karim et al. (*18*) proposed numerically a design of $Ge_{11.5}As_{24}Se_{64.5}$ nano-wire for supercontinuum spectrum of 1300-nm bandwidth. Hu et al. (*19*) designed and numerically analysed a tapered rib waveguide (air-SF57 glass-SiO_2) for supercontinuum spectrum extending from 1000 to 4600 nm. Safioui et al. (*20*) reported more than 550-nm broad supercontinuum spectrum in 1-cm-long CMOS-compatible hydrogenated amorphous silicon waveguide using picosecond pulses with peak power as low as 4 W. Xie et al. (*21*) demonstrated a 3-mm-long As_2S_3-silica double nanospike waveguide for supercontinuum generation from 0.8 to beyond 2.5 μm in mid-infrared region at 1.55 μm. Karim et al. (*22*) designed a dispersion-engineered air-clad, $Ge_{11.5}As_{24}Se_{64.5}$ chalcogenide glass channel waveguide for mid-infrared supercontinuum spectrum spanning 1800 to 7700 nm using pulse power of 500 W.

For mid-infrared supercontinuum spectrum, chalcogenide fibres *or* waveguides are suitable because they have a number of unique properties such as high linear and non-linear refractive indices, broad infrared transparency, low photon energy and large ultra fast third-order optical non-linearity (*23*). The recent progress in chalcogenide photonics has been extensively reviewed in several research articles (*23–26*). Recently, mid-infrared supercontinuum generation has also been reported in highly non-linear material-based step index fibre as well as photonic crystal fibre geometries (*27–40*).

In this article, design and analysis of a channel rib waveguide have been carried out for mid-infrared supercontinuum generation. The waveguide structure has been engineered to get all-normal dispersion characteristic. The proposed waveguide has high non-linearity with a low negative and flat dispersion profile around pump wavelength. Simulation results indicate that this waveguide structure is capable of achieving ultra broadband mid-infrared supercontinuum spectra using femtosecond laser pulses of relatively low peak power.

There are five sections in this paper. Section 1 gives brief introduction and familiar ideas of previously reported works on the topic. Section 2 gives the design of the proposed rib waveguide. In Section 3, the comprehensive description of the method of analysis is given. Section 4 is devoted to the results and discussion. Finally, the conclusion of the work is summarized in the Section 5.

2. Proposed rib waveguide structure

We report a rib waveguide structure in a highly non-linear material for supercontinuum generation in the mid-infrared region. The transverse cross-sectional view of the proposed waveguide geometry is shown in Figure 1(a). As shown in this figure, 2*a* is the core width, *h* is the core height and $h-t$ represents the trench height. This is an As_2Se_3-based chalcogenide core deposited on a silica substrate. MgF_2 is used as an upper cladding material. All the geometrical parameters of the waveguides have been tailored for getting all-normal dispersion characteristic. Figure 1(b) illustrates the normalized electric field distribution of the propagating mode in the core of the rib waveguide at the pump wavelength. Since the waveguide is going to be used for supercontinuum generation, it is essential to ensure that it will only support single-mode operation to avoid unwanted interaction between the propagating modes. Thus, in order to ensure single-mode operation, we have used the most accurate finite element

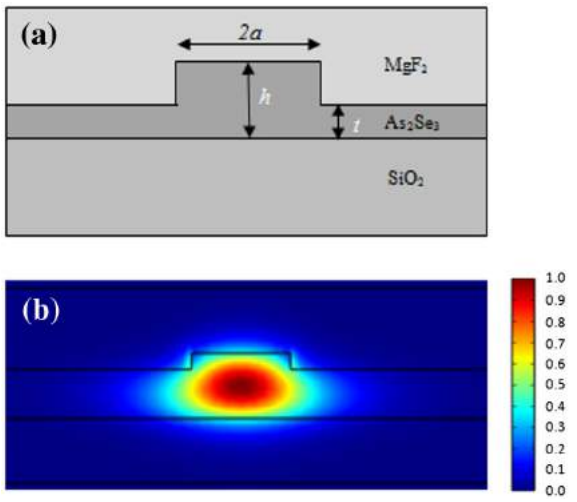

Figure 1. (a) Transverse cross-sectional view of the proposed rib waveguide structure; (b) the normalized electric field distribution of the propagating mode in the core region at the pump wavelength.

Downloaded by [Delhi Technological University] at 23:29 05 August 2016

method which is superior to the approximate method reported in Ref. (*41*).

3. Numerical modelling of supercontinuum generation

Principally, the broadening mechanism of the supercontinuum spectrum mainly depends on two optical parameters: (i) non-linearity and (ii) dispersion characteristic of the structure. To obtain the all-normal dispersion profile of the rib waveguide structure, we have seen the effect of dispersion with geometrical parameters. The chromatic dispersion, $D(\lambda)$, can be calculated from n_{eff} vs. wavelength λ using the equation:

$$D(\lambda) = -\frac{\lambda}{c}\frac{\partial^2 \text{Re}\left(n_{\text{eff}}\right)}{\partial \lambda^2} \tag{1}$$

where c is the velocity of light in vacuum and $\text{Re}(n_{\text{eff}})$ is the real part of the n_{eff}. Since Sellmeier's equation is taken into account while calculating n_{eff}, both the material and waveguide dispersion have been included in the dispersion equation. Various simulations have been performed by shifting the geometrical parameters of the rib waveguide. Careful optimization of this parameter provides better control of the dispersion curve.

The non-linearity coefficient (i.e. γ) can be obtained using the following relation (*1*).

$$\gamma = \frac{2\pi n_2}{\lambda A_{\text{eff}}} \tag{2}$$

where n_2 is the non-linear refractive index of the core and $n_2 = 1.5 \times 10^{-17}$ m^2/W at 2.5 μm for As_2Se_3 glass (*32*). λ is the pump wavelength and A_{eff} is the effective mode area of the propagating mode. For broadband supercontinuum generation, the non-linear coefficient must be as high as possible. The value of the non-linearity coefficient γ can be enhanced by choosing the core material with very high non-linear refractive index or by manipulating the structure having low effective area.

The effective mode area (A_{eff}) of the propagating mode is simulated using the following relation (*1*).

$$A_{\text{eff}} = \frac{\left(\iint |E|^2 \text{d}x\text{d}y\right)}{\left(\iint |E|^4 \text{d}x\text{d}y\right)} \tag{3}$$

where E is the transverse electric field of the propagating mode. The effective mode area of propagating mode can be tuned by changing geometrical parameters of the proposed structure.

The process of supercontinuum generation can be studied by solving the following generalized non-linear Schrodinger equation (GNLSE) for the output pulse envelope $A(z, t)$ (*1*)

$$\frac{\partial A}{\partial Z} + \frac{1}{2}\left(\alpha + i\alpha_1 \frac{\partial}{\partial t}\right)A - \left(i\sum_{m=2}^{M} i^m \frac{\beta_m}{m!}\frac{\partial^m A}{\partial t^m}\right) = i\left(\gamma + i\gamma_1 \frac{\partial}{\partial t}\right)\left[A(z,t)\int_0^\infty \text{R}(t')\left|\left(A(z,t-t')\right)\right|^2 \text{d}t\right] \tag{4}$$

The left side of the equation deals the linear optical effects and the right side of this equation deals with non-linear optical effects of the structure. M represents the order of dispersion effects considered. α gives the losses in the waveguide as the optical pulse travels through it. The term α_1 is included because loss may vary over the entire bandwidth of the supercontinuum. However, for the relatively short length of waveguide, this loss term is neglected in the simulation. In the simulation, a constant material loss coefficient of 0.6 cm^{-1} is considered for the entire range of supercontinuum spectrum (*42*). γ is the Kerr non-linear coefficient of the material. In the simulation, an approximation $\gamma_1 = \gamma/\omega_0$ is employed (*1, 32*). β is the propagation constant. The propagation constant at any frequency around the pulse's central frequency(ω_0), can be expanded as Taylor series expansion (*4*)

$$\beta(\omega) = \beta(\omega_0) + \beta_1(\omega_0)(\omega - \omega_0) + \frac{1}{2!}\beta_2(\omega_0)(\omega - \omega_0)^2 + \frac{1}{3!}\beta_3(\omega_0)(\omega - \omega_0)^3 + \cdots \tag{5}$$

where $\beta_n(\omega_0) = \frac{\text{d}^n \beta}{\text{d}\omega^n}$. We have employed higher order dispersion up to the ninth order from the group velocity dispersion curve. $R(t')$ is the non-linear response function and takes account of the electronic and nuclear contributions and is expressed as follows:

$$\text{R}(t') = (1 - f_{\text{R}})\delta(t' - t_{\text{e}}) + f_{\text{R}} h_{\text{R}}(t') \tag{6}$$

The fractional contribution of the Raman response is $f_{\text{R}} = 0.115$ for As_2Se_3-based chalcogenide glasses (*43*). The Raman response function, $h_{\text{R}}(t')$, gives the information of the vibrations of the molecule of material when light travelled through the waveguide and is given by the subsequent equation:

$$h_{\text{R}}(t') = \frac{\tau_1^2 + \tau_2^2}{\tau_1 \tau_2^2}\exp\left(-\frac{t'}{\tau_2}\right)\sin\left(\frac{t'}{\tau_1}\right) \tag{7}$$

For the As_2Se_3 chalcogenide glasses, the Raman period $\tau_1 = 23.1$ fs and lifetime $\tau_2 = 195$ fs (*43*).

In the simulation, we have considered the hyperbolic secant pulse as an input pulse that is articulated as:

$$A(z=0,t) = \sqrt{P_0} \cdot \mathrm{sech}\left(\frac{t}{T_0}\right) \tag{8}$$

where $t_0 = T_{FWHM}/1.763$ and P_0 is peak power of the input pulse.

To solve the Equation (4), we have used the fourth-order Runge–Kutta interaction picture (RK4IP) method (*44*). In comparison to other numerical methods, this method is most efficient, accurate and achieves faster integration. It is closely related to the split-step Fourier method. The procedure of solving GNLSE using the RK4IP is based on transforming the problem into an interaction picture that allows the use of explicit techniques to progress the solution forward.

To simulate the linear characteristics of the waveguide, we have employed commercially available software 'COMSOL Multiphysics' based on full vectorial finite element method. The wavelength-dependent linear refractive indices of SiO_2, MgF_2 and As_2Se_3 glasses are calculated using the Sellmeier equations given in Ref. (*1, 22, 45*) respectively.

4. Results and discussion

It is well known that the waveguide dispersion strongly depends on the geometry of the waveguide. Thus, the total dispersion of the waveguide can be controlled by tailoring the geometrical parameters of the waveguide. In order to achieve suitable waveguide parameters to achieve the all-normal and flat dispersion, which is desirable for supercontinuum generation (*5*), several simulations have been performed by changing the waveguide geometrical parameters such as *a*, *h* and *t*. The effect of '*t*' on dispersion characteristic has been illustrated in Figure 2 while keeping other parameters fixed as $a = 1$ μm and $h = 1$ μm. From this figure, it is clear that the dispersion profile moves towards the normal dispersion region on increasing the value of '*t*'. The increase in '*t*' decreases the mode index of the fundamental mode and hence tailors the dispersion towards the normal region.

The effect of the core height '*h*' on the chromatic dispersion has been shown in Figure 3. At the larger value of core height, the dispersion curve starts to shift towards anomalous dispersion regions. The increase in '*h*' increases the mode index of the fundamental mode and hence tailors the dispersion towards the anomalous region. Similarly, increase in core width '*a*' also shifts the dispersion towards anomalous region as shown in Figure 4. Thus, by tailoring the geometrical parameters, one can achieve the desired dispersion profile.

We calculate higher order dispersion terms up to the ninth order at the pump wavelength of 2.5 μm. For

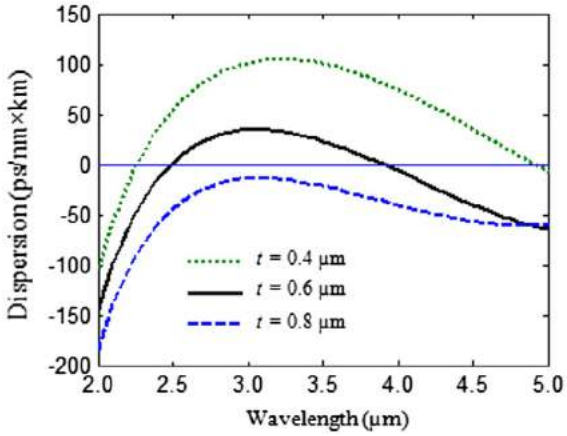

Figure 2. The effect of the geometrical parameter '*t*' on chromatic dispersion profile while keeping other parameters fixed as: $a = 1$ μm, $h = 1$ μm.

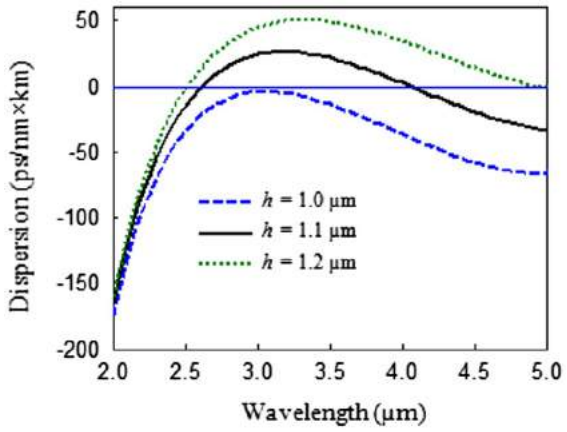

Figure 3. The effect of the core height (i.e. *h*) on chromatic dispersion profile while keeping other parameters fixed as: $a = 1$ μm, $t = 0.75$ μm.

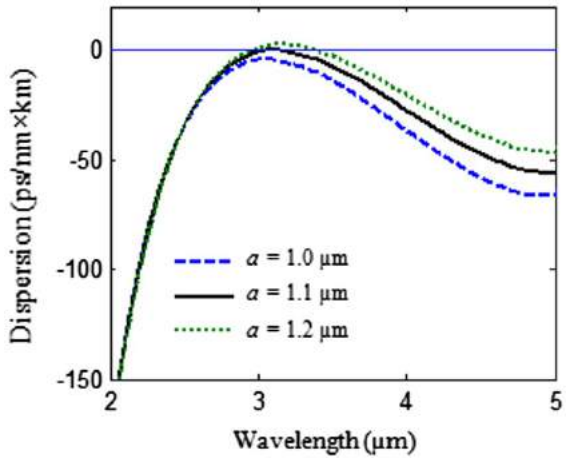

Figure 4. The effect of the core width (i.e. *2a*) on chromatic dispersion profile while keeping other parameters fixed as: $t = 0.75$ μm, $h = 1$ μm.

Downloaded by [Delhi Technological University] at 23:29 05 August 2016

Downloaded by [Delhi Technological University] at 23:29 05 August 2016

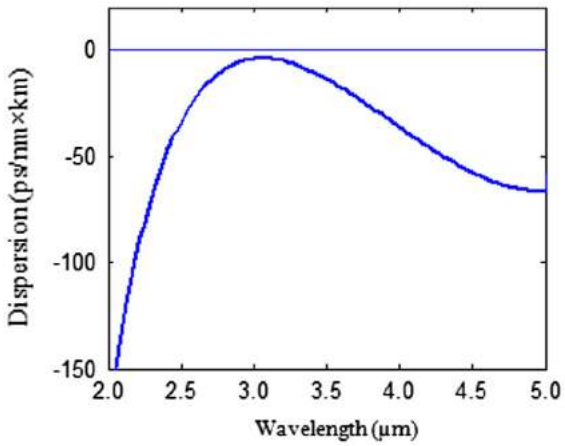

Figure 5. The chromatic dispersion characteristic of the proposed rib waveguide structure with optimized parameters (i.e. $a = 1.0$ μm, $t = 0.75$ μm, $h = 1$ μm).

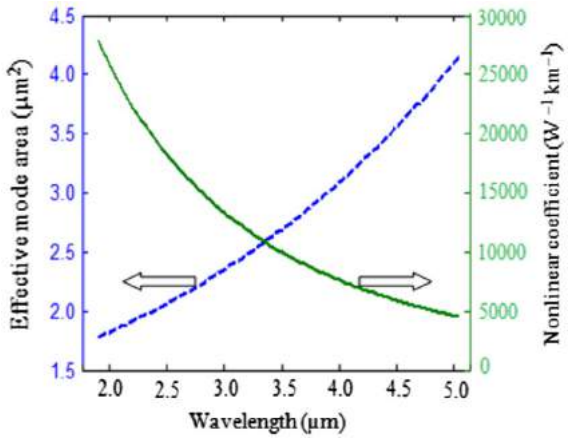

Figure 6. The variation in effective mode area of the propagating mode and corresponding non-linear coefficient of the proposed rib waveguide with optimized parameters (i.e. $a = 1.0$ μm, $t = 0.75$ μm, $h = 1$ μm).

optimized geometrical parameters (i.e. $a = 1$ μm, $h = 1$ μm and $t = 0.75$ μm), the dispersion characteristic of rib waveguide is exposed in Figure 5. It is apparent from the Figure 5 that an all-normal and flat dispersion profile with a dispersion value of about −5 ps/(nm × km) between the spectral range 2.925–3.2 μm is obtained. Flat dispersion profile is critical for producing ultra broadband supercontinuum spectrum at higher wavelengths.

The wavelength-dependent effective mode area of propagating mode is calculated numerically. The effective mode area and corresponding non-linear coefficient are revealed in Figure 6. Simulated results prove that the proposed waveguide structure offers Kerr non-linear coefficient (γ) as high as 18,250 W^{-1} km^{-1} with effective mode area (A_{eff}) of 2.07 μm^2 at the pump wavelength of 2.5 μm. For experimental analysis, the laser source Spectra-Physics OPA-800C can be used at 2.5 μm (*31*). We have performed supercontinuum simulations using the effective mode area obtained at pump wavelength numerically. Insertion of the wavelength dependence of the effective mode area may alter our results quantitatively, but the qualitative performance is expected to remain unchanged.

We carry out numerical simulations by means of Equation (4) for the peak power levels between 0.7 and 1.1 kW and results are revealed in Figure 7. As reported in Figure 7, when we launch the femtosecond laser pulses of appropriate parameters (i.e. pulse width:50 fs, peak power: 1.1 kW, pulse type: hyperbolic secant), a broadband supercontinuum spectrum spanning 2–15 μm at −30 dB power level is obtained in only 4-mm length of proposed rib waveguide structure. The calculated values of non-linear length ($L_{NL} = 1/\gamma P_0$) and dispersion length ($L_D = \frac{T_0^2}{\beta_2}; T_0 = T_{FWHM}/1.763$) for proposed rib waveguide are 4.9×10^{-5} m and 3.89×10^{-2} m, respectively, for 50 fs laser pulse at 2.5 μm. Within 4-mm length of the rib

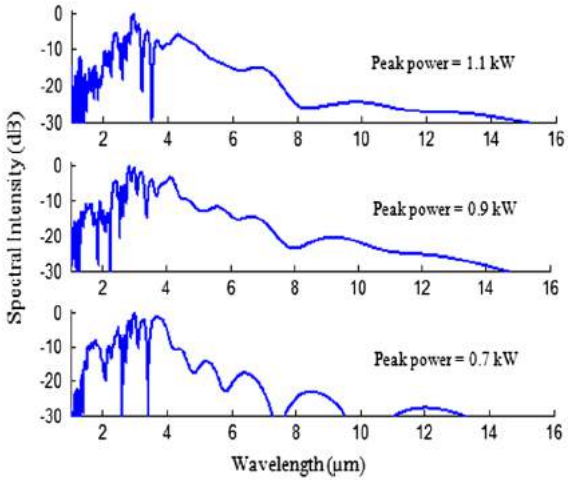

Figure 7. Spectral broadening of supercontinuum spectra from 4 mm-long rib waveguide at different peak powers; when 50 fs laser pulses at 2.5 μm is launched at the proposed rib waveguide structure.

waveguide, an ultra broadband supercontinuum spectrum spanning 2–15 μm is generated by launching a 50 fs laser pulses at peak power 1.1 kW.

The broadening of supercontinuum spectrum also depends on the input pulse width. The influence of the pulse width, i.e. full width at half maximum (T_{FWHM}), on spectral broadening of supercontinuum spectrum in 4 mm-long rib waveguide is revealed in Figure 8. The initial peak power of the pulse is fixed at 1.1 kW. As illustrated in Figure 8, when the value of pulse width increases from 50 to 100 fs, the output spectra start to narrow down. It is clear from this figure that the shorter pulses are better to obtain broader supercontinuum spectrum.

For fabrication purposes, it is very important to investigate the tolerance of the rib waveguide structure with

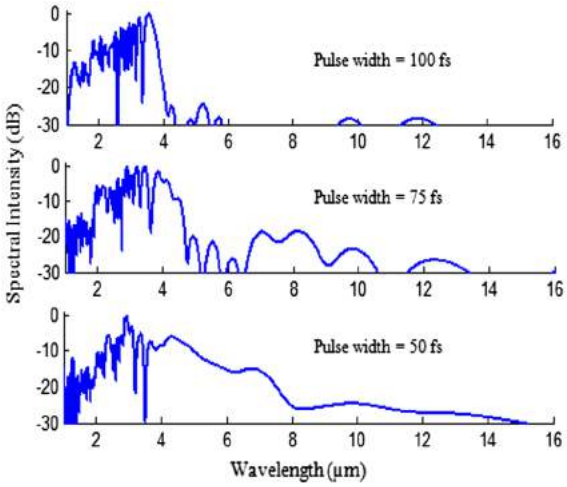

Figure 8. Broadening of output spectra from 4 mm-long rib waveguide obtained at various values of pulse width (T_{FWHM}) when peak power of incident pulses = 1.1 kW.

respect to geometrical parameters. We have found that the magnitude of effective mode area, non-linear coefficient and dispersion are not much sensitive to the structural parameters. For example, at the pump wavelength of 2.5 μm, 1% variation in '*a*' changes the effective mode area by 0.6% and changes non-linear coefficient by 0.4%. These small changes produce only ~1% changes in the spectral width of the supercontinuum spectrum. The proposed rib waveguide structure can be fabricated by photolithography and inductively coupled plasma reactive ion etching techniques (*15, 46*).

5. Conclusions

A dispersion-engineered channel rib waveguide structure is reported for ultra broadband mid-infrared supercontinuum spectrum spanning 2–15 μm at a −30 dB power level. Such broadband spectral range of supercontinuum spectrum is achieved using only 4 mm-long channel rib waveguide when 50 fs laser pulses of 1.1 kW peak power at 2.5 μm are incident on it. Simulated outcomes revealed that the proposed rib waveguide structure offers non-linear coefficient as large as 18,250 W^{-1} km^{-1} at the pump wavelength of 2.5 μm with the effective mode area of 2.07 μm^2. This waveguide structure can be a good candidate for generating efficient supercontinuum that is applicable in various non-linear applications such as frequency comb generation, gas sensing, food quality control and early cancer diagnostics.

Acknowledgement

The authors gratefully acknowledge the (i) TUN-IND bilateral research project 'Design, modeling and characterization of highly nonlinear fibers for all-optical high bit-rate network', funded by Ministry of Higher Education and Scientific Research of Republic of Tunisia and Department of Science and Technology, Govt. of India; and (ii) initiatives and support towards establishment of the 'TIFAC-Center of Relevance and Excellence' in Fiber Optics and Optical Communication at Delhi Technological University (Formerly Delhi College of Engineering) Delhi, through the 'Mission REACH' program of Technology Vision-2020 of the Government of India.

Disclosure statement

No potential conflict of interest was reported by the authors.

Funding

This work was supported by the Ministry of Higher Education and Scientific Research of Republic of Tunisia and Department of Science and Technology, Govt. of India.

References

(1) Agrawal, P. *Nonlinear Fiber Optics*, 5th ed.; Elsevier Academic Press: Oxford, 2013.
(2) Alfano, R.R.; Shapiro, S.L. *Phys. Rev. Lett.* **1970**, *24*, 584–587.
(3) Genty, G.; Lehtonen, M.; Ludvigsen, H.; Broeng, J.; Kaivola, M. *Opt. Express* **2002**, *10*, 1083–1098.
(4) Dudley, J.M.; Genty, G.; Coen, S. *Rev. Mod. Phys*. **2006**, *78*, 1135–1184.
(5) Klimczak, M.; Siwicki, B.; Skibiński, P.; Pysz, D.; Stępień, R.; Heidt, A.; Radzewicz, C.; Buczyński, R. *Opt. Express* **2014**, *22*, 18824–18832.
(6) Schliesser, A.; Picqué, N.; Hänsch, T.W. *Nat. Photonics* **2012**, *6*, 440–449.
(7) Hsiung, P.; Chen, Y.; Ko, T.H.; Fujimoto, J.G.; Matos, C.J.S.de; Popov, S.V.; Taylor, J.R.; Gapontsev, V.P. *Opt. Express* **2004**, 12, 5287–5295.
(8) Takara, H.; Ohara, T.; Yamamoto, T.; Masuda, H.; Abe, M.; Takahashi, H.; Morioka, T. *Electron. Lett*. **2005**, *41*, 270–271.
(9) Sanders, S. *Appl. Phys. B: Lasers Opt.* **2002**, *75*, 799–802.
(10) Seddon, A.B. *Int. J. Appl. Glass Sci*. **2011**, *2*, 177–191.
(11) Ma, P.; Choi, D.Y.; Yu, Y.; Gai, X.; Yang, Z.; Debbarma, S.; Madden, S.; Luther-Davies, B.L. *Opt. Express* **2013**, *21*, 29927–29937.
(12) Gross, S.; Jovanovic, N.; Sharp, A.; Ireland, M.; Lawrence, J.; Withford, M.J. *Opt. Express* **2015**, *23*, 7946–7956.
(13) Foster, M.A.; Gaeta, A.L. *Opt. Express* **2004**, *12*, 3137–3143.
(14) Yin, L.; Lin, Q.; Agrawal, G.P. *Opt. Express* **2007**, *32*, 391–393.
(15) Lamont, M.R.E.; Luther-Davies, B.L.; Choi, D.Y.; Madden, S.; Eggleton, B.J. *Opt. Express* **2008**, *16*, 14938–14944.
(16) Zhang, L.; Yan, Y.; Yue, Y.; Lin, Q.; Painter, O.; Beausoleil, R.G.; Willner, A.E. *Opt. Express* **2011**, *19*, 11584–11590.
(17) Halir, R.; Okawachi, Y.; Levy, J.S.; Foster, M.A.; Lipson, M.; Gaeta, A.L. *Opt. Lett.* **2012**, *37*, 1685–1687.
(18) Karim, M.R.; Rahman, B.M.A.; Agrawal, G.P. *Opt. Lett.* **2014**, *22*, 31029–31040.
(19) Hu, H.; Li, W.; Dutta, N.K. *Opt. Commun.* **2014**, *324*, 252–257.

Downloaded by [Delhi Technological University] at 23:29 05 August 2016

(20) Safioui, J.; Leo, F.; Kuyken, B.; Gorza, S.P.; Selvaraja, S.K.; Baets, R.; Emplit, P.; Roelkens, G.; Massar, S. *Opt. Express* **2014**, *22*, 3090–3097.
(21) Xie, S.; Tani, F.; Travers, J.C.; Uebel, P.; Caillaud, C.; Troles, J.; Schmidt, M.A.; Russell, P.St.J. *Opt. Lett.* **2014**, *30*, 5215–5219.
(22) Karim, M.R.; Rahman, B.M.A.; Agrawal, G.P. *Opt. Express* **2015**, *23*, 6903–6914.
(23) Gai, X.; Han, T.; Prasad, A.; Madden, S.; Choi, D.Y.; Wang, R.; Bulla, D.; Davies, B.L. *Opt. Express* **2010**, *18*, 26625–26646.
(24) Eggleton, B.J. *Opt. Express* **2010**, *18*, 26632–26634.
(25) Yu, Y.; Gai, X.; Wang, T.; Ma, P.; Wang, R.; Yang, Z.; Choi, D.Y.; Madden, S.; Luther-Davies, B.L. *Opt. Mater. Express* **2013**, *3*, 1075–1086.
(26) Eggleton, B.J.; Davies, B.L.; Richardson, K. *Nat. Photonics*. **2011**, *5*, 141–148.
(27) Granzow, N.; Stark, S.P.; Schmidt, M.A.; Tverjanovich, A.S.; Wondraczek, L.; Russell, P.S.J.; *Opt. Express* **2011**, 19, 21003–21010.
(28) Nishizawa, N. *Opt. Fiber Tech.* **2012**, *18*, 394–402.
(29) Saini, T.S.; Kumar, A.; Sinha, R.K. *Frontier in Optics (FiO), paper: FW1D-4*, Tucson, AZ, 2014.
(30) Gao, W.; Amraoui, El.; Liao, M.; Kawashima, H.; Duan, Z.; Deng, D.; Cheng, T.; Suzuki, T.; Messaddeq, Y.; Ohishi, Y. *Opt. Express* **2013**, 21, 9573–18583.
(31) Shaw, L.B.; Nguyen, V.Q.; Sanghera, J.S.; Aggarwal, I.D.; Thielen, P.A.; Kung, F.H. Proceedings of Advanced Solid State Photonics,Vienna, Austria, paper TuC5, **2005**.
(32) Hu, J.; Menyuk, C.R.; Shaw, L.B.; Sanghera, J.S.; Aggarwal, I.D. *Opt. Express* **2010**, *18*, 6722–6739.
(33) Kubat, I.; Agger, C.S.; Moselund, P.M.; Bang, O. *J. Opt. Soc. Am. B* **2013**, *30*, 2743–2757.
(34) Kubat, I.; Rosenberg Petersen, C.R.; Møller, U.V.; Seddon, A.; Benson, T.; Brilland, L.; Méchin, D.; Moselund, P.M.; Bang, O. *Opt. Express* **2014**, *22*, 3959–3969.
(35) Kubat, I.; Agger, C.S.; Møller, U.; Seddon, A.B.; Tang, Z.Z.; Sujecki, S.; Benson, T.M.; Furniss, D.; Lamrini, S.; Scholle, K.; Fuhrberg, P.; Napier, B.; Farries, M.; Ward, J.; Moselund, P.M.; Bang, O.; *Opt. Express* **2014**, 22, 19169–19182.
(36) Petersen, C.R.; Møller, U.; Kubat, I.; Zhou, B.; Dupont, S.; Ramsay, J.; Benson, T.; Sujecki, S.; Abdel-Moneim, N.; Tang, Z.; Furniss, D.; Seddon, A.; Bang, O. *Nat. Photonics* **2014**, *8*, 830–834.
(37) Saini, T.S.; Kumar, A.; Kumar Sinha, R.K. *Opt. Commun.* **2015**, *347*, 13–19.
(38) Saini, T.S.; Kumar, A.; Sinha, R.K. *J. Lightwave Technol.* **2015**, *33*, 3914–3920.
(39) Saini, T.S.; Baili, A.; Kumar, A.; Cherif, R.; Zghal, M.; Sinha, R.K. *J. Mod. Opt.* **2015**, *62*, 1570–1576.
(40) Agrawal, A.; Tiwari, M.; Azabi, Y.O.; Janyani, V.; Rahman, B.M.A.; Grattan, K.T.V. *J. Mod. Opt.* **2013**, *60*, 956–962.
(41) Suzuki, K.; Ogusu, K.; Minakata, M. *Opt. Express* **2005**, *13*, 8634–8641.
(42) Shiryaev, V.; Churbanov, M. *J. Non-Cryst. Solids* **2013**, *377*, 225–230.
(43) Ung, B.; Skorobogatiy, M. *Opt. Express* **2010**, *18*, 8647–8659.
(44) Masip, M.E.; Rieznik, A.A.; König, P.G.; Grosz, D.F.; Bragas, A.V.; Martinez, O.E. *Opt. Lett.* **2009**, *34*, 842–844.
(45) Dantanarayana, H.G.; Abdel-Moneim, N.; Tang, Z.; Sojka, L.; Sujecki, S.; Furniss, D.; Seddon, A.B.; Kubat, I.; Bang, O.; Benson, T.M. *Opt. Mater. Express* **2014**, *4*, 1444–1455.
(46) Madden, S.J.; Choi, D.Y.; Bulla, D.A.; Rode, A.V.; Luther-Davies, B.; Ta'eed, V.G.; Pelusi, M.D.; Eggleton, B.J. *Opt. Express* **2007**, *15*, 14414–14421.

Downloaded by [Delhi Technological University] at 23:29 05 August 2016

J. Inst. Eng. India Ser. B
DOI 10.1007/s40031-016-0256-2

ORIGINAL CONTRIBUTION

Digital Model of Railway Electric Traction Lines

Rachana Garg[1] · Priya Mahajan[1] · Parmod Kumar[2]

Received: 4 February 2014 / Accepted: 8 July 2016
© The Institution of Engineers (India) 2016

Abstract The characteristic impedance and propagation constant define the behavior of signal propagation over the transmission lines. The digital model for railway traction lines which includes railway tracks is developed, using curve fitting technique in MATLAB. The sensitivity of this model has been computed with respect to frequency. The digital sensitivity values are compared with the values of analog sensitivity. The developed model is useful for digital protection, integrated operation, control and planning of the system.

Keywords Railway electric traction lines · Analog model · Digital model · Characteristic impedance · Propagation constant · Sensitivity analysis

Introduction

The analysis and design of power and signal over railway electric traction lines needs mathematical model of the lines. Now-a-days, most of the control algorithms, drives and protection system in railway electric traction system are based on digital technology. The operational data of railway electric traction system including the monitoring of the compartments and engine bogies (safety data, video signal of CCTV, doors status, any hazardous conditions) can be monitored in the control room at traction substation using broad- band over power lines (BPL) which use digital signals. Also, the permeability of power conductor and return rail track are different. Analog model representation of railway traction lines, therefore, is not sufficient and hence it is desired to develop the digital model of characteristic impedance and propagation constant of the electric traction lines which define the transmission system behavior. The digital model of the railway electric traction lines is compatible with the digital controllers, digital protection system and drive control. Further, characteristic impedance and propagation constant depend on the line parameters (R, G, L and C) and the frequency of operation. The digital model can optimize and analyze the traction system under transient and fault conditions in real time mode. Under these situations operating frequency differs from the system frequency and cannot be properly defined. Hence, the sensitivity analysis of digital model of characteristic impedance and propagation constant with respect to frequency plays an important role in analyzing the behavior of the system. In sensitivity analysis, the quantitative aspects of evaluating the deviation of the solution from the reference solution is determined when one or more parameters of the system are given slightly different values. The authors in this paper have developed the digital model of characteristic impedance and propagation constant of contact wire and rail track conductor and carried out the sensitivity analysis of these discretised parameters with respect to frequency first time in the literature. The analog sensitivity analysis with respect to parameters of interest is presented by the authors [1].

The digital mathematical model of railway electric traction lines, which include the contact wire and rail track, has received little attention in the literature. Most of the traction studies are limited to analog railway track modeling. Mahajan et al. [2] has developed the analog model of railway traction lines using multi conductor transmission lines (MTL) theory and computed the characteristic impedance

✉ Priya Mahajan
priyamahajan.eed@gmail.com

[1] Department of Electrical Engineering, Delhi Technological University, New Delhi, India

[2] Maharaja Agrasen Institute of Technology, New Delhi, India

Published online: 22 August 2016

and propagation constant of the lines. Hill and Carpenter [3] have computed frequency dependent self and mutual admittance for a single track power-rail, considering it as a distributed transmission line. Mariscotti and Pozzobon [4] have analyzed the published experimental data and formulae for the determination of the electric parameters of railway traction lines. He observed that the experimental results conform to the calculated results in frequency range of 50 Hz–50 kHz. Mariscotti [5] has also applied MTL theory to railway traction system for finding the distribution of the traction return current in ac and dc electric railway systems and carried out sensitivity analysis of rail current and rail to rail voltage with respect to parameters of interest. Though not much work is done in the digital modeling of railway traction system, Humpage [6–9] is the pioneer in using the z-transformation in power systems. He along with Wong and Nugyen has applied this technique for analysis of the transient in overhead lines and cables. In 1980 [6], they had developed a new electromagnetic transient formulation for multi conductor power transmission lines based on the z-transform. Garg et al. [10] and Garg [11] has developed the digital model of power transmission lines and carried out some studies related to their digital sensitivity analysis.

Analog Model of Railway Traction Lines [2]

Railway electric traction system is a fast and green transportation system with enhanced load carrying capacity. The analysis and design of power and signaling system of railway electric traction system needs mathematical model of the system. The authors have used the multi-conductor transmission line (MTL) theory to develop the mathematical model of the electric traction system and to compute the characteristic impedance and propagation constant of this system [1, 2, 5]. In a railway traction system, the individual lines corresponds to each running rail/rail track conductor and the power conductor or overhead catenary are as shown in Fig. 1. The elements are distributed over length whose values are evaluated per unit length. The current enters through the power conductor and the return is through the rail track conductors. For the MTL theory, power conductor or catenary is termed as cond. 1 whereas the two rail track conductors are termed as cond. 2 and cond. 3, respectively as shown in Fig. 1. The presence of a weak ground effectively completes the circuit for each conductor so that three self and three mutual ground return impedances and admittances can be identified. The MTL model illustrated in Fig. 1 may thus be used for complete equivalent circuit. Accordingly, the series impedance matrix and shunt admittance matrix are formed considering the contact wire and two rail track conductors as the three conductors.

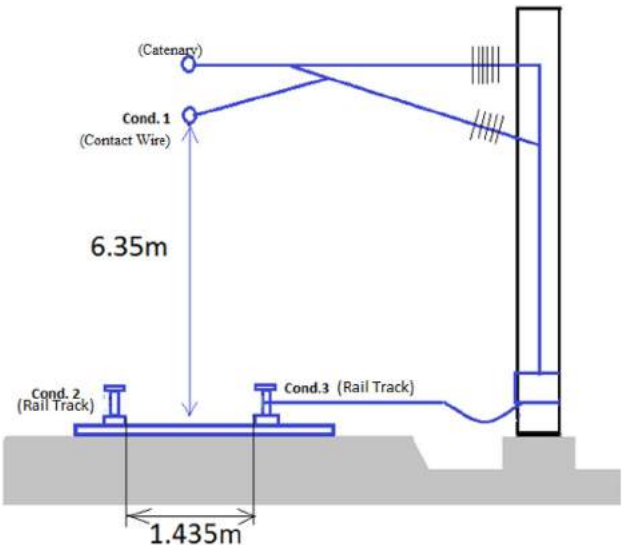

Fig. 1 Multiconductor transmission line model of railway electric traction lines

Series Impedance Matrix

The series impedance matrix, Z, can be given by (1)

$$Z = R_c + R_e + j\left(X_g + X_c + X_e\right) \tag{1}$$

where, suffixes g, e and c represent contribution due to geometry of the contact wire/rail track, earth return path and physical properties of the contact wire/rail track material, respectively.

Shunt Admittance Matrix

The shunt admittance matrix, Y, can be given by (2),

$$Y = G + j\omega C \tag{2}$$

Each of these parameters are defined in Appendix A.

The characteristic impedance, Z_0, and propagation constant, γ, in terms of Z and Y can be given by (3) and (4),

$$Z_0 = \sqrt{\frac{Z}{Y}} \tag{3}$$

$$\gamma = \sqrt{ZY} \tag{4}$$

The series impedance and shunt admittance matrices of railway traction lines are computed by doing programming in MATLAB environment, using MATLAB version 11b.

Digital Model of Railway Traction Lines

Digital model of characteristic impedance and propagation constant is developed by making use of the similarities in the exponential form of the transmission line response in

the frequency domain and frequency to z-domain transformation. The relation between frequency domain and the z-domain is given by (5),

$$e^{st} = z \tag{5}$$

where, $s = j\omega$.

In order to transform characteristic impedance $Z_0(\omega)$ and propagation constant $\gamma(\omega)$ of the system into discrete functions $Z_0(z)$ and $\gamma(z)$, curve fitting methods have been employed using Matlab curve fitting toolbox. The synthesis of these frequency domain functions is first done in s-plane and then transformed from s-plane to z-plane.

At high frequencies, the characteristic impedance of the contact wire and rail track conductor tends to a constant, real value. The variation of modulus of characteristic impedance, $Z_0(\omega)$ with angular frequency can be determined. This variation is then fitted with some known curve and coefficients of the curve are then determined. A first order form in this case is satisfactory in the initial least-squares fitting. The proposed function for characteristic impedance is given by Eqs. (6)–(8):

$$Z_0(s) = Z_{oc} + \frac{Z'}{(1 + \alpha s)} \tag{6}$$

$$\text{For } s = j\omega, \quad Z_0(\omega) = Z_{oc} + \frac{Z'}{(1 + j\omega\alpha)} \tag{7}$$

$$|Z_0(\omega)| = Z_{oc} + \frac{Z'}{\sqrt{1 + \omega^2\alpha^2}} \tag{8}$$

Values of $Z^{'}$ and α can be found using curve fitting for $|Z_0(\omega)|$.

Using bilinear transformation given by (9), (6) is transformed to (10),

$$s = \frac{2}{\Delta t} \times \left(\frac{z-1}{z+1}\right) \tag{9}$$

where, Δt is the sampling time.

$$Z_o(z) = Z_{oc} + \frac{f_o + f_1 z^{-1} + f_2 z^{-2}}{g_o + g_1 z^{-1} + g_2 z^{-2}} \tag{10}$$

Using a similar procedure as used in defining the characteristic impedance, the propagation constant for the power conductor and rail track conductor in the frequency domain are given by (11) and (12), respectively.

$$\gamma_{11}(\omega) = j\omega \times B_0 \tag{11}$$

$$\gamma_{22}(\omega) = \gamma_{33}(\omega) = C_0 \times (j\omega)^{1/2} \tag{12}$$

Values of B_0 and C_0 can be found using curve fitting for $\gamma_{11}(\omega)$ and $\gamma_{22}(\omega)$, respectively.

The flow chart for calculating the digital model of characteristic impedance using curve fitting tool box in MATLAB version 11b is as given in Fig. 2.

Sensitivity Analysis

Sensitivity analysis is the study of the variation (uncertainty) in the output of a mathematical model, qualitatively or quantitatively, to different sources of variation in the input of the model [12, 13].

Parameter Sensitivity

In order to compare the sensitivity values of a quantity with respect to different parameters, the normalized sensitivity of the quantity is evaluated. The normalized sensitivity of a quantity gives directly the percentage change in the value of the quantity for one percent change in the value of the parameter of interest. Thus, normalized sensitivity of any function X with respect to parameter p is evaluated from (13).

$$\hat{S}_p^X = \frac{p}{X}\frac{\partial X}{\partial p} \tag{13}$$

The sensitivity function of characteristic impedance and propagation constant with respect to parameter p can be given by (14) and (15):

$$S_p^{z_0} = \frac{\partial Z_0}{\partial p} = \frac{1}{2Y}\left(\gamma S_p^Z - Z_0 S_p^Y\right) \tag{14}$$

$$S_{\mathrm{p}}^{\gamma} = \frac{\partial \gamma}{\partial p} = \frac{1}{2}\left(\gamma S_p^Z + Z_0 S_p^Y\right) \tag{15}$$

Digital Sensitivity Analysis

Digital model is especially useful in fault analysis, transient analysis and broadband studies. Digital sensitivity analysis is a technique to find out the sensitivity of digital model with respect to parameters of interest. Tomovic [14] and Bekey and Tomovic [15] had applied the method of vector difference equations to carry out the sensitivity analysis of sampled data with respect to sampling rate. A discrete system can be defined by a non linear vector difference equation as given by (16),

$$y(t_{n+1}) = [y(t_n),\, t_n,\, x(t_n)] \tag{16}$$

where, $y(t_n)$ is the R-dimensional state vector; $y(t_0) = y_0$ is the initial condition vector; f is the R-dimensional vector function having partial derivatives with respect to y_r, $r = 1,2,\ldots r$ and $x(t_n)$ is the scalar input function, $n = 1,2,\ldots.N$.

For equidistant sampling given by (17), (16) can be modified as given by (18),

$$T = T_f/N \tag{17}$$

$$y(n+1, T) = f[y(n, T); n; x(n, T); T] \tag{18}$$

Here, N is the number of sampling instants and the observable range is [0 T_f].

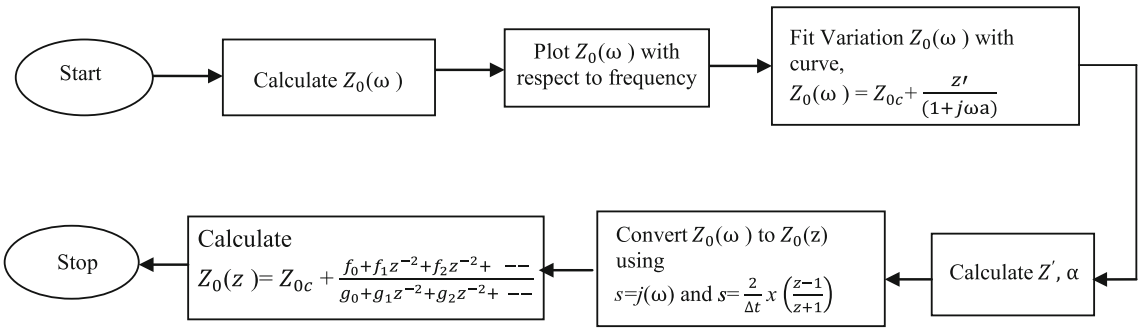

Fig. 2 Flow chart for calculating the digital model of characteristic impedance on MATLAB

To take into account the effect of perturbations in the sampling time, the discrete sensitivity function $u_T(n)$ is defined by (19),

$$u_T(n) \triangleq \frac{\partial y(n,T)}{\partial T} \triangleq \lim_{\Delta T \to 0} \frac{y[n,(T+\Delta T)] - y(n,T)}{\Delta T} \tag{19}$$

here, $y(n,T)$ is a continuous function with respect to time.

Differentiating (19) with respect to T, a vector difference equation is formed whose solution u_T is given by (20)

$$\begin{aligned} u_T &= \frac{\partial}{\partial T} y[(n+1),T] - A(n,T)\frac{\partial y(n,T)}{\partial T} \\ &= a(n,T)\frac{\partial x(n,T)}{\partial T} + \frac{\partial}{\partial T} f(n,T) \end{aligned} \tag{20}$$

where, $A(n,T)$ is a R × R matrix and is given by (21)

$$A(n,T) = \begin{bmatrix} \frac{\partial f_1(n,T)}{\partial y_1} & \cdots & \frac{\partial f_1(n,T)}{\partial y_R} \\ \vdots & \ddots & \vdots \\ \frac{\partial f_R(n,T)}{\partial y_1} & \cdots & \frac{\partial f_R(n,T)}{\partial y_R} \end{bmatrix} \tag{21}$$

and $a(n, T)$ is a column matrix given by (22),

$$a(n,T) = \left[\frac{\partial f_1(n,T)}{\partial x} \cdots \frac{\partial f_R(n,T)}{\partial x}\right]^t \tag{22}$$

using (19), (20) is written as given by (23),

$$u_T(n+1) - A(n,T)u_T(n) = a(n,T)\frac{\partial x(n,T)}{\partial T} + \frac{\partial f(n,T)}{\partial T} \tag{23}$$

with the initial condition $u_T(0) = 0$.

Equation (23) is called as 'sensitivity difference equation' and its solution $u_T(n)$ is called the 'sensitivity sequence'.

In the present studies, the discrete sensitivity model of digital characteristic impedance and propagation constant with respect to frequency has been developed by first deriving the sensitivity functions in frequency domain and then converting them in discrete form. The results are analyzed at different sampling times.

Numerical Results and Discussions

For the system under consideration (Appendix B), the analog values of characteristic impedance and propagation constant obtained are given in Table 1. The corresponding variation of characteristic impedance and propagation constant of catenary and rail track conductors with respect to frequency have been plotted in Figs. 3, 4, 5, 6. These plots are then used to determine the constants of digital model of characteristic impedance and propagation constant of contact wire and rail track conductors.

Table 1 Analog value of characteristic impedance and propagation constant [1]

z_{11}, Ω	$[545.99-57.47j]$
$z_{22} = z_{33}$, Ω	$[7.13 + 6.92j]$
γ_{11} (m^{-1})	$(10)^{-3}[0.0001 + 0.0013j]$
$\gamma_{22} = \gamma_{33}$ (m^{-1})	$(10)^{-3}[0.2497 + 0.2413j]$

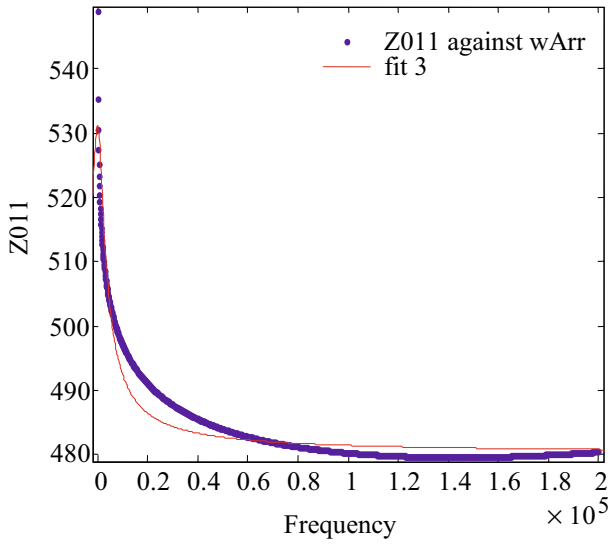

Fig. 3 Characteristic impedance of contact wire against frequency

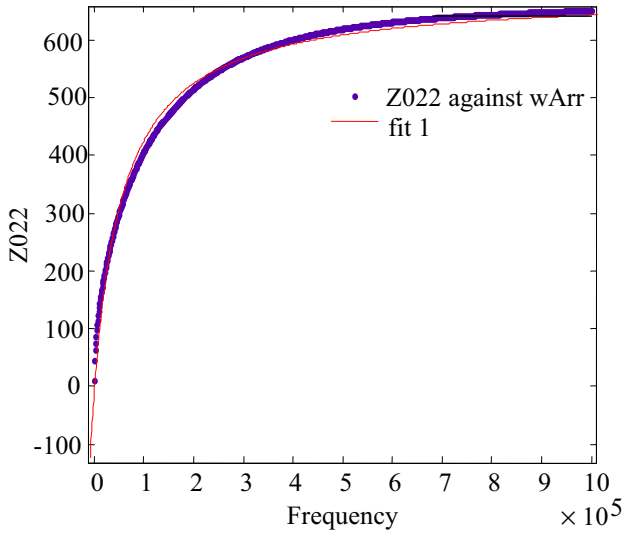

Fig. 4 Characteristic impedance of rail track conductors against frequency

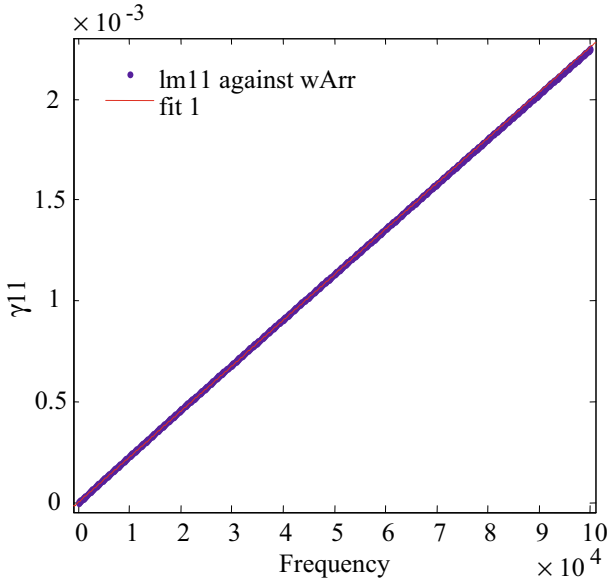

Fig. 5 Propagation constant of contact wire against frequency

Curve fitting toolbox in MATLAB version 11b is used to determine the coefficients of above curves to represent the characteristic impedance and propagation constant in frequency domain which is shown in Table 2. Table 3 represents the digital model of characteristic impedance and propagation constant at different sampling times. The sensitivity of these parameters with respect to frequency

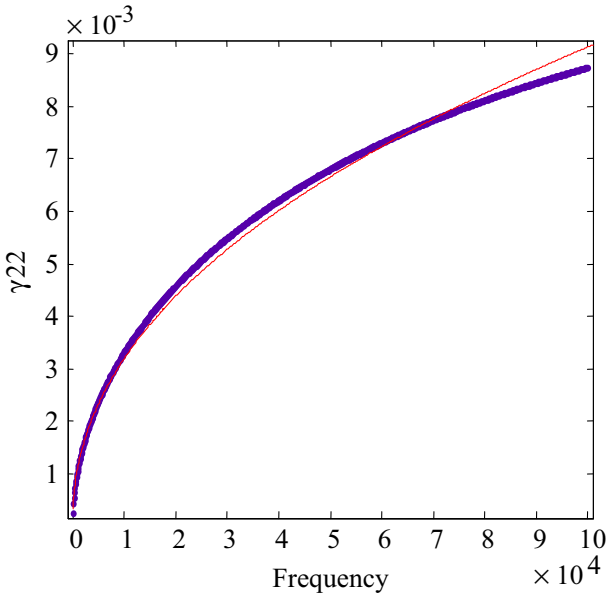

Fig. 6 Propagation constant of rail track conductors against frequency

Table 2 Characteristic impedance and propagation constant in frequency domain

Function	Representation in frequency domain
$Z_{011}(\omega)$	$[481.3 + 51.23/(1 + j\omega \times 3.8 \times 10^{-4})]$
$Z_{022}(\omega) = Z_{033}(\omega)$	$[681 - 672.5/(1 + j\omega \times 2.11 \times 10^{-5})]$
$\gamma_{011}(\omega)$	$[j\omega \times 2.258 \times 10^{-8}]$
$\gamma_{022}(\omega) = \gamma_{033}(\omega)$	$[4.75 \times 10^{-5} \times \sqrt{j\omega}]$

is determined in frequency domain and the results are discretised to evaluate the normalized sensitivity as given in Table 4. These sensitivity functions in z-domain are then compared with the sensitivity functions of analog model [1]. From the Table 3, it is observed that as the sampling time is reduced, more time instants are required for the digital model to approach that of analog model [1], which is the expected behavior. From the Table 4, it is found that the digital sensitivity of characteristic impedance with respect to frequency is approaching the analog sensitivity at smaller sampling time. The digital sensitivity of propagation constant for both rail track and contact wire is found to be independent of the sampling time and hence as almost the same value as the analog sensitivity.

Table 3 Digital model of characteristic impedance and propagation constant

Digital function	Digital form			
	Sampling time, $\Delta t = 3$ ms	Sampling time, $\Delta t = 1$ ms	Sampling time, $\Delta t = 0.3$ ms	Sampling time, $\Delta t = 0.01$ ms
$Z_{011}(z)$	$522.074 + 16.636z^{-1} - 9.91z^{-2} + 5.904\ z^{-3} + \cdots$	$510.41 + 25.14z^{-1} - 3.42z^{-2} + 0.46z^{-3} - 0.006z^{-4} + 0.0082z^{-5} \cdots$	$495.8 + 20.8z^{-1} + 9.01z^{-2} + 3.9z^{-3} + 1.68z^{-4} + 0.732z^{-5} \cdots$	$482.1 + 1.98z^{-1} + 1.93z^{-2} + 1.88z^{-3} + 1.83z^{-4} + 1.78z^{-5} \cdots$
$Z_{022}(z) = Z_{033}(z)$	$18.8 - 22.73z^{-1} + 21.97z^{-2} - 21.23z^{-3} + 20.5z^{-4} - 19.8z^{-5} + \cdots$	$35.73 - 50.9z^{-1} + 46.9z^{-2} - 43.37z^{-3} + 40.0z^{-4} - 36.7z^{-5} + \cdots$	$91 - 144.45z^{-1} + 108.9z^{-2} - 822z^{-3} + 70.7z^{-4} - 53.3z^{-5} \cdots$	$552.17 - 208.3z^{-1} - 128.5z^{-2} - 79.26z^{-3} - 48.9z^{-4} - 30.16z^{-5} \cdots$
$\gamma_{011}(z)$	$1.5 \times 10^{-5}(1 - 2z^{-1} + 2z^{-2} - 2z^{-3} + \cdots)$	$4.5 \times 10^{-5}(1 - 2\ z^{-1} + 2z^{-2} - 2\ z^{-3} + \cdots)$	$1.5 \times 10^{-4}(1 - 2z^{-1} + 2z^{-2} - 2z^{-3} + \cdots)$	$4.5 \times 10^{-3}(1 - 2z^{-1} + 2\ z^{-2} - 2z^{-3} + \cdots)$
$\gamma_{022}(Z) = \gamma_{033}(Z)$	$1.23 \times 10^{-3}(1 - z^{-1} + z^{-2} - z^{-3} + \cdots)$	$2.12 \times 10^{-3}(1 - z^{-1} + z^{-2} - z^{-3} + \cdots)$	$3.87 \times 10^{-3}(1 - z^{-1} + z^{-2} - z^{-3} + \cdots)$	$6.71 \times 10^{-3}(1 - z^{-1} + z^{-2} - z^{-3} + \cdots)$

Table 4 Normalized sensitivity of characteristic impedance and propagation constant, with respect to frequency

Digital function	Normalized digital sensitivity				Normalized analog sensitivity $S_f^{X(\omega)}$
	Sampling time, $\Delta t = 3$ ms	Sampling time, $\Delta t = 1$ ms	Sampling time, $\Delta t = 0.3$ ms	Sampling time, $\Delta t = 0.01$ ms	
$\hat{S}_f^{Z_{011(z)}}$	$-0.016 + 0.012z^{-1} + 0.007z^{-2} - 0.013z^{-3} + 0.0135z^{-4} - 0.0116z^{-5} + 0.009z^{-6} - \cdots$	$-0.024 + 0.0078z^{-1} + 0.0227z^{-2} - 0.007z^{-3} + 0.002z^{-4} - 0.0004z^{-5} + 0.00006z^{-6} - \cdots$	$-0.02 - 0.017z^{-1} + 0.003^{-2} + 0.005z^{-3} + 0.004z^{-4} + 0.0024z^{-5} + 0.0013z^{-6} - \cdots$	$-0.0014 - 0.0026z^{-1} - 0.0023^{-2} - 0.002z^{-3} - 0.0014z^{-4} - 0.0012z^{-5}$	$-0.0715 + 0.0925j$
$\hat{S}_f^{Z_{022(z)}} = \hat{S}_f^{Z_{033(z)}}$	$0.51 - 0.47z^{-1} + 0.961z^{-2} - 0.87z^{-3} + 0.77z^{-4} - 0.412z^{-5} + \cdots$	$0.746 + 0.348z^{-1} - 0.191z^{-2} + 0.0977z^{-3} + 0.036z^{-4} + 0.067z^{-5} - \cdots$	$0.8 + 0.063z^{-1} - 0.28z^{-2} + 0.017z^{-3} - 0.009z^{-4} + 0.01z^{-5} - 0.006z^{-6} + \cdots$	$0.19 + 0.31z^{-1} + 0.18z^{-2} + 0.11z^{-3} + 0.061z^{-4} + 0.039z^{-5} + 0.022z^{-6} + \cdots$	$1.4504 - 0.7840j$
$\hat{S}_f^{\gamma_{11(z)}}$	1	1	1	1	$0.9769 - 0.1527j$
$\hat{S}_f^{\gamma_{22(z)}} = \hat{S}_f^{\gamma_{33(z)}}$	0.5	0.5	0.5	0.5	$0.3953 + 0.0379j$

Conclusions

The characteristic impedance and propagation constant of the contact wire and rail track conductor are the two important parameters that can define the performance of a traction system. The discrete model in z-plane of these parameters in reference to electric railway traction lines has been developed first time in the literature. The digital values of these parameters conform to the analog values. Further, digital sensitivity of characteristic impedance with respect to frequency is observed to be approaching near to analog sensitivity value for the smaller sampling time. These studies will give a greater insight to the designers in designing the traction system and digital protection schemes for the system.

Appendix A: Impedance and Admittance Matrices

Series Impedance Matrix

The resistance of the contact wire,

$$R_{c11} = S \times R_o \tag{24}$$

where R_o is dc resistance of the conductor; and S is skin effect ratio and is given by (25):

$$S = \frac{1 + \sqrt{\left(1 + \frac{x^4}{48}\right)}}{2}, x = \pi d \sqrt{\frac{2f\mu \times 10^{-5}}{\rho}} \tag{25}$$

where d is the diameter of catenary, mm; f, the frequency of supply, Hz; μ, the permeability of conductor material; and ρ is the resistivity of material, $\mu\Omega$ cm.

The resistance of rail track conductors, R_{c22} and R_{c33} is given by (26) [16]:

$$R_{c22} = R_{c33} = \frac{1}{\pi a^2 \sigma_r}\left[\frac{1}{4} + \sqrt{2}\cos\left(\frac{\pi}{4} - \frac{\theta}{2}\right)\right]\left[\frac{a}{2\delta_r} + \frac{3\delta_r}{32a}\right] \tag{26}$$

where, σ_r is the conductivity of rail track; θ is the hysteresis angle; δ_r is skin depth and a is the equivalent radius of rail track and may be calculated considering the rail track as an equivalent I structure [16].

The reactance of contact wire, X_{c11} and rail track conductors X_{c22} and X_{c33} is given by (27) and (28), respectively [16].

$$X_{c11} = \omega \frac{\mu_0}{8\pi} \tag{27}$$

$$X_{c22} = X_{c33} = \frac{1}{\pi a^2 \sigma_r}\left[\sqrt{2}\sin\left(\frac{\pi}{4} - \frac{\theta}{2}\right)\right]\left[\frac{a}{2\delta_r} - \frac{3\delta_r}{32a}\right] \tag{28}$$

The resistance and reactance due to earth path, R_e and X_e, are computed using Carson's formula [17].

Inductive reactance due to geometry of conductors above the ground, X_g is given by (29),

$$X_g = 2\pi f(\mu_0 \mu_r)F \tag{29}$$

where, F is Maxwell's coefficient matrix.

Shunt-Admittance matrix,

$$Y = G + j\omega C \tag{30}$$

where, G is the conductance matrix. The elements of conductance matrix corresponding to the contact wire are zero and the elements corresponding to rail track are given by (31) [18].

$$g_{22} = g_{33} = \frac{\pi\sigma_r}{\ln 2b/a}; g_{23} = g_{32} = \frac{\pi\sigma_r}{\ln 2} \tag{31}$$

where, σ_r is conductivity of rail track, and b is distance between two rail track.

The capacitance matrix [C] is given by (32),

$$[C] = 2\pi\varepsilon_0[F]^{-1} \tag{32}$$

Appendix B: Specifications and Data taken for System under Consideration

Supply frequency = 50 Hz; earth resistivity = 100 Ωm; height of catenary above ground = 6.35 m; height of rail track above ground = 0.75 m; area of catenary conductor = 157 mm^2; radius of rail conductor = 115 mm; permeability of rail conductor material = 18; hysteresis angle = 0.4675 radians; contact wire resistivity = 2.78 $\times$ 10^{-8} Ωm; rail track resistivity = 0.225 $\times$ 10^{-6} Ωm;

References

1. R. Garg, P. Mahajan, P. Kumar, Sensitivity analysis of characteristic parameters of railway electric traction system. Int. J. Electron. Electr. Eng. **2**(1), 8–14 (2014)
2. P. Mahajan, R. Garg, P. Kumar, Sensitivity analysis of railway electric traction system. India Int. Conf. Power Electron. (2011). doi:10.1109/IICPE.2011.5728107
3. R.J. Hill, D.C. Carpenter, Rail track distributed transmission line impedance and admittance: theoretical modeling and experimental results. IEEE Trans. Vehi. Technol. **42**(2), 225–241 (1993)
4. A. Mariscotti, P. Pozzobon, Determination of the electrical parameters of railway traction lines: calculation, measurement, and reference data. IEEE Trans. Power Del. **19**(4), 1538–1546 (2004)
5. A. Mariscotti, Distribution of the traction return current in ac and dc electric railway systems. IEEE Trans. Power Del. **18**(4), 1422–1432 (2003)
6. W.D. Humpage, K.P. Wong, T.T. Nguyen, D. Sutano, Z-transform electromagnetic transient analysis in power systems. Proc. IEE **127**(6), 370–378 (1980)
7. W.D. Humpage, K.P. Wong, T.T. Nguyen, Development of z-transform electromagnetic transient analysis methods for multi node power networks. Proc. IEE **127**(6), 379–385 (1980)
8. W.D. Humpage, K.P. Wong, T.T. Nguyen, D. Sutano, Time convolution and z-transform electromagnetic transient analysis in power systems. Proc. IEE **127**(6), 386–394 (1980)

9. W.D. Humpage, K.P. Wong, T.T. Nguyen, z-transform electromagnetic transient analysis of cross-bonded cable transmission systems. Proc. IEE **128**(2), 55–62 (1981)
10. R. Garg, P. Kumar, M.S. Thomas, Digital sensitivity of transmission lines. Proc. TENCON-2010, 479–482 (2010). ISBN:978-1-4244-6889-8
11. R.Garg, Sensitivity analysis of multiconductor digital transmission lines, Ph.D Thesis, DU, 2009
12. C.S. Indulkar, P. Kumar, D.P. Kothari, Sensitivity analysis of modal quantities for underground cables. Proc. IEE **128**(4), 229–234 (1981)
13. C.S. Indulkar, P. Kumar, D.P. Kothari, Sensitivity analysis of multi conductor transmission line. Proc. IEEE **70**(3), 299–300 (1982)
14. R. Tomovic, *Sensitivity Analysis of Dynamic Systems*. (McGraw-Hill, New York, 1964)
15. G.A. Bekey, R. Tomovic, Sensitivity of discrete systems to variation of sampling interval. IEEE Trans. Autom. Control **11**(2), 284–287 (1966)
16. R.J. Hill, D.C. Carpenter, Determination of rail internal impedance for electric railway traction system simulation. Proc. IEE **138**(6), 311–321 (1991)
17. J.R. Carson, Wave propagation in overhead wires with ground return. Bell Syst. Tech. J. **5**, 539–554 (1926)
18. R.J. Hill, S. Brillante, P.J. Leonard, Railway track transmission line parameters from finite element field modelling: shunt admittance. Proc. IEE Electr. Power Appl. **147**(3), 227–238 (2000)

Volume 4, Issue 1 (2016) 106-113 ISSN 2347 - 3258
International Journal of Advance Research and Innovation

Effect of aspect ratio on the performance and stability of Hydrodynamic Journal Bearings

Sachin Dhull, RS Walia
Precision Engineering Laboratory, Central Workshop, Delhi Technological University, Delhi. India

Article Info
Article history:
Received January 2016
Received in revised form
20 February 2016
Accepted March 2016
Available online June 2016

Keywords
Wear, properties, AFM, forces

Abstract

Abrasive flow machining (AFM), also known as extrude honing, is a method of smoothing and polishing internal surfaces and producing controlled radii. A one-way or two-way flow of an abrasive media is extruded through a work piece, smoothing and finishing rough surfaces. In one-way systems, we flow the media through the work piece, then it exits from the part. In two-way flow, two vertically opposed cylinders flow the abrasive media back and forth. In the paper, the various types of abrasive laden polymer media, their work piece applications as well as the compatibility with the abrasives used is explained. The properties of the polymer used in AFM are compared and the best combination of polymer, abrasive and hydrocarbon oil is selected. Apart from polymer properties, the media flow equations, abrasive wear and forces is also studied.

1. Introduction

With the time, technology is emerging and advancing day by day with the demand for highly accurate, precise and highly efficient machining process for advanced industries from critical aerospace and medical components to mass production automobile parts. This process has capability of finishing even the most areas which are not accessible, processing multiple, slots or edges, holes in one operation [1]. The development of materials having higher strength, hardness, toughness and other desired properties. This also needs to develop the advanced cutting tools material which can ease the process and are economical without compromising productivity

The applications of advanced abrasive finishing technique are increasing so as to get the highly accurate and highly efficient machining of complex shaped 3D components with nano level surface finish. Abrasive finishing can be employed to finish most mechanical parts with shape limitations. Initial surface roughness of 0.25µm R_a can be improved easily to 0.05 µm within a few minutes. In addition AFM process has many attractive advantages, such as self sharpening, self adoptability, controllability and finishing tool requires neither compensation nor dressing. There are various abrasive particles like Al_2O_3, SiC, CBN, diamond powder etc. are available which are being used for abrasive finishing process. To increase the MR and surface roughness, the abrasive are made magnetic in nature with ferromagnetic material by various techniques like sintering, mechanical mixing using ball mill etc. The theoretical and experimental research of thermal properties of media has been carried out by Fletcher et al.

Corresponding Author,
***E-mail address:** sachindhull1989@gmail.com
All rights reserved: http://www.ijari.org

Research reports on AFM are, however, not so enough. Researchers of Indian Institute of Technology have made a progress on AFM theory

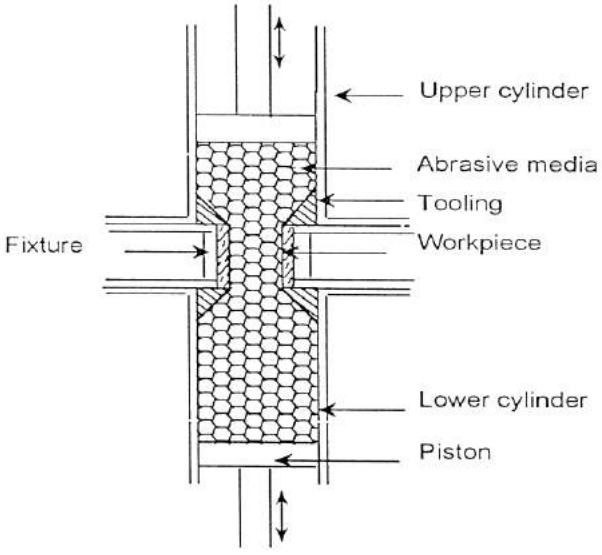

Fig.1: Schematic showing AFM process

Rhoades [2–4] studied the basic principle of AFM and reported that the depth of cut primarily depends upon abrasive grain size, relative hardness and sharpness and extrusion pressure. Przylenk[5] described that with small bore diameter of work piece, more grains come in contact with the wall and material removal increases. The viscosity of this medium is expected to be different as compared to medium used for the industrial purposes. Finished surface characteristics have been studied by Williams and Rajurkar[6]. Three modes of metal deformation so far have

been identified in any abrasive machining processes which are as follows [7]:
1. Elastic deformation associated with rubbing;
2. Plastic deformation or sloughing where majority of the material is displaced without being removed;
3. micro-cutting where removal of material takes in the form of miniature chips.
Gorana et al. [8] further reported that cutting force components and active grain density govern the surface roughness produced during AFM process. Davies [9] experimentally found that viscosity of media is significantly affected by temperature. Jain et al. [10] also reported the effects of specific energy and temperature on AFM. In that report it has been got that work piece temperature increases with cycles and extrusion pressure.

2. Literature Review

An extensive literature review has been done on various types of abrasive laden polymer media, the processing oil and the workpiece used, which is listed below in the table 1and table 2. Magnetic assisted abrasive flow machining has been studied in detail and a number of research papers have been studied on the effect of magnetic field on AFM. Some of the key aspects related to magnetic AFM have been listed in the table 3.

3. Polymer Science

The mechanical properties of polymers used in AFM is explained below:

3.1 Elasticity

3.1.1 Continuous extension

The ratio of stress to strain is called modulus. In the low strain strain region, the stress and strain are directly proportional to each other, as shown in fig.2. When the strain reaches a yield value, the curve becomes non-linear. (a) Soft and weak material such as unfilled silicon rubber- "soft" refers to the fact that initial slope is small, which means low value of modulus. "Weak" refers to low ultimate strength. (b)Hard and brittle (Polystyrene)- "Hard" refers to initial slope or modulus is large. "Brittle" refers to the fact that maximum extensibility is small.

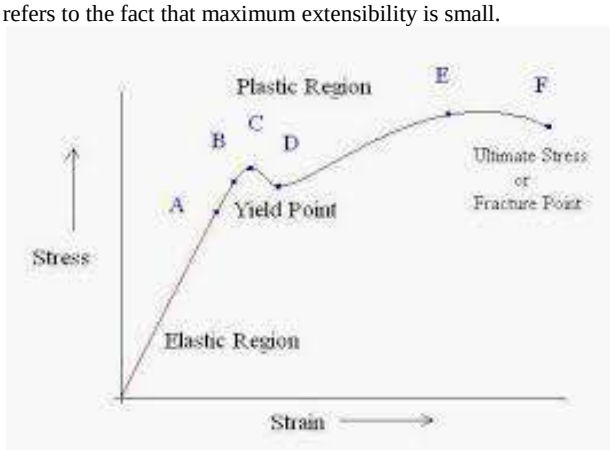

Fig.2: Stress vs strain diagram

3.1.1 Hooks elasticity

Young's modulus $G=\frac{s}{\gamma}$ (1)

Rubber-like elasticity- A good operational definition of rubber-like elasticity is high deformability with essentially complete recoverability. The equation of state is

$$f^* = \frac{f}{A^*} = \vartheta kT(\alpha - \alpha^{-2}) \quad (2)$$

where f^* is nominal stress, f is equilibrium force, A^* is undeformed cross section, ϑ is number density of network chains, k is Boltzmann constant, T is absolute temperature, $\alpha = L/L_i$ is relative length of sample. This equation is similar to ideal gas law P = NkT/V, N is no. of gas molecules, V is volume, p is pressure.

3.2 Viscosity

The viscosity n of a fluid may be defined by the equation

$S = n\frac{dy}{dt} = n\dot{\gamma}$ (3)

Where s is force per unit area, $\dot{\gamma}$is rate of shear.

3.3 Visco-elasticity

It is the combination of viscous characteristics with elastic characteristics to describe the visco-elasticity of polymeric materials. The combination of spring and dashpot in series is called the Maxwell model (fig.3). It is used to describe the visco-elastic behavior of uncrossed-linked polymer.

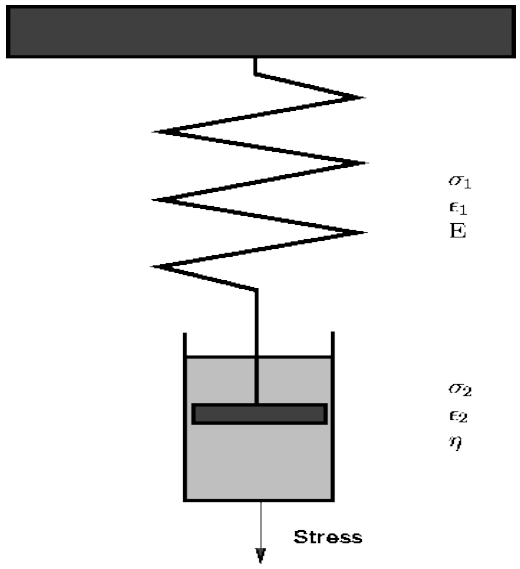

Fig.3: Maxwell model for visco-elasticity

The general differential equation which describes the Maxwell model is

$$\dot{\gamma} = \frac{s}{n} + \left(\frac{1}{G}\right)\left(\frac{ds}{dt}\right) \quad (4)$$

The solution to this equation is

$S = s_0 e^{-t/\tau}$ (5)

Where s_0 is stress at initial t=0 and $\tau = {}^{n}/_{G}$ is relaxation time (the time required for the deformation to decrease to ${}^{1}/_{e}$ of its original value.

Table 1: Abrasive laden polymer media used in AFM:

Author	Abrasive	Carrier medium and processing oil	Work piece
K.K. Kar, N.L. Ravikumar et al (2009) [11]	SiC abrasives (80, 220, 400, ….. mesh size) They constitute 28 to 78% by weight of the medium.	Visco-elastic carrier Natural rubber NR grade RMA-4 Butyl rubber IIR Commercial media is either silicon or poly borosiloxane (i.e. bouncing putty). Its cost is too high. Naphthenic oil is the processing oil.	En8, Al
S. Singh, H.S. Shan et al (2002) [12]	Brown super emery (trade name). It is magnetic in nature. It contains 40% ferromagnetic constituents, 45% Al_2O_3, 15% Si_2O_3.	Silicon-based polymer media. Hydrocarbon gel is the processing oil.	Cylinderical workpiece made of brass.
E. Uhlmann et al (2009) [13]	Polycrystalline diamond PDA311 of company element six ltd., Shannon, Ireland. D46 indicates grain size of abrasive.	MF10 indicates viscosity of polymeric carrier material (silicone basis). Grinding medium: MF10-D46-200 200 signify the weight ratio 1:2 between carrier media and abrasive grain.	Advanced ceramic materials
A.C. Wang, L. Tsai et al (2009)[14]	SiC	Bouncing putty (matrix of abrasive medium) : This is a kind of silicone gel with low flow characteristic and it would not stick on work piece after AFM.	
L. Tsai, A.C. Wang (2012) [15]	SiC or Al_2O_3	Silicone gel is a bonding gel to mix with ferromagnetic particles and abrasives. This gel is a semi-solid polymer and has deformation characteristics. Therefore ferromagnetic particles and abrasives mix with gel uniformly. With flexible property, gel abrasive can wrap around workpiece closely.	
H.J. Tzeng, B.H. Yan (2007) [16]	SiC	Silicone oil Polymer, wax medium	Stainless steel (SUS 304)
R.S. Walia, H.S. Shan, P. Kumar (2009) [17]	Brown super emery (trade name). It is one of the impure forms of conundrum.	The mixture of polymer and gel was used as carrier compound in media. Hydrocarbon oil is the processing oil.	
M. Ravisankar, V.K. Jain et al (2009) [18]	SiC mesh size 220, constituting 66.67% of media by weight.	Styrene Butadiene Rubber SBR is the polymer carrier. Hydrocarbon oil (manufactured by Indian oil). Its composition varies from 2.5 to 17.5% by weight.	Al alloy/SiC MMC (Metal Matrix Composites) with 0%, 10%, 15% SiC.
V.S. Sooraj et al (2014) [19]	Abrasive grits are embedded on polymer beads. The elastic abrasives have flexibility to deform itself in conformity to the shape of the work piece surface.	Elastomeric polymer bead of size (meso-micro range). It exhibits visco-elastic behaviour with low young's modulus and higher resilience, allowing base media to absorb energy when it is deformed elastically and recover it upon unloading.	Hardened steel (440C-58HRC)
S.Rajesha, G.Venkatesh, A.K.Sharma, P.Kumar (2010) [20]	Boron trioxide	Highly viscous and deformable new polymer abrasive carrier media consisting of di-methyl silicon oil and boric trioxide 90:10 by weight ratio respectively and naphthenic based processing oil. Natural rubber mainly contain ester group.	

Table 2: Magnetic assisted AFM study:

Author	Year	Tools and techniques used	Output results
V. Yadava, K.B.Judal [21]	2013	In electrochemical magnetic abrasive machining, the material is removed from the workpiece surface due to simultaneous effect of abrasion and electrochemical dissolution. Finite element method is used to calculate the distribution of magnetic field between the magnetic poles in which cylindrical shaped workpiece is placed. The cutting forces responsible for abrasion are calculated from the magnetic forces due to gradient of magnetic field in the working gap.	A surface roughness model is developed by considering total volume of material removed with the assumption of triangular surface profile.
S.Jha, VK Jain [22]	2009	The three constitutive models, viz. Bingham plastic, Herschel–Bulkleyand Casson's fluid, are used to characterise the rheological behaviour of MRP fluid by fitting the rheological data obtained from capillary magnetorheometer and evaluating respective constants in their constitutive equations.	The fluid flow behavior of MRP fluid exhibits a transition from weak Bingham liquid like structure to a strong gel-like structure on the application of magnetic field. Depending on the size and volume concentration of abrasives and carbonyl iron particles (CIPs) in the base medium, the rheological properties hence, bonding strength gained by abrasives through surrounding CIP chains varies.
H.Yamaguchi, SK Srivastava [23]	2014	The relationships between surface conditions of AlTiN-coated round tools, cutting forces, and wear characteristics were clarified by milling of Ti-6Al-4V alloys.	The roughness of coated tools was improved by 50–60% without deteriorating the cutting edge radius, and the tool life was extended by 150%.
G.Kumar, V.Yadav [24]	2009	From magnetic potential model, the magnetic pressure developed and corresponding heat flux generated on workpiece surface are evaluated. The effects of various operating input parameter on magnetic potential distribution in the gap and temperature rise in the workpiece has been studied.	A mathematical model is developed for the prediction of magnetic potential using Maxwell's equations and finite element method is used to find the magnetic potential distribution within the gap between tool bottom surface and workpiece top surface. Further a mathematical model is developed for heat transfer in the workpiece and again finite element method is used for the prediction of temperature rise in the workpiece.
A.C.Wang,	2009	A novel abrasive medium,using the silicone gel to mix	The results demonstrated that surface

S.J.Lee [25]		the ferromagnetic particles and abrasive,wasdeveloped to enhance the disadvantages in MAF. Magnetic finishing with gel abrasive(MFGA)was utilized in to polish the cylindrical rod of mold steel	roughness of the cylinder part was reduced to 0.1 mm Ra from an initial value of 0.677mmRa within10min, and surface roughness could decrease to 0.038 mm Ra after30min in MFGA. Surface roughness reduction in MFGA was 3 times of surface roughness reduction in MAF using the unbounded magnetic abrasive as medium.
T.A. El Taweel [26]	2008	It emphasizes the features of the development of comprehensive mathematical models based on response surface methodology (RSM) for correlating the interactive and higher-order influences of major machining parameters, i.e. magnetic flux density, applied voltage, tool feed rate and workpiece rotational speed on MRR and SR of 6061 Al/Al2O3 (10% wt) composite.	The results demonstrate that assisting ECT with MAF leads to an increase machining efficiency and resultant surface quality significantly, as compared to that achieved with the traditional ECT of some 147.6% and 33%, respectively.
R.S.Mulik, P.M. Pandey [27]	2011	The experimental studies have been carried out with respect to five important process parameters namely supply voltage, abrasive mesh number, rotation of magnet, abrasive weight percentage, and pulse on time (Ton) of ultrasonic vibrations selected based on literature available in the area of MAF process and ultrasonic generator controls. Percentage change in surface roughness (ΔRa) for AISI 52100 steel workpiece has been considered as response and unbondedSiC abrasives are used in the work.	The surface roughness value obtained by UAMAF was as low as 22 nm within 80 s on hardened AISI 52100 steel workpiece using unbounded SiC abrasives.

Table 3: Abrasive wear

Heat	Electricity	Molecular level	Mechanics	Gas evolution
Diffusion and chemical reactions	Sparc, arc	Cohesion, adhesion	Elastic and plastic strain	Oxygen, hydrogen

Now the variation of Mooney viscosity vs. temperature and the dynamic pressure variation with surface distance is analyzed and discussed as below. Fig 4 shows Mooney viscosity–temperature curves for three medias with different preliminary viscosity. It can be seen that temperature has a great influence on Mooney viscosity values for three medias.

In order to examine the effect of cycle varying on Mooney viscosity during the test, the media temperature after each test is measured, then, Mooney viscosity–temperature curve is used to get Mooney viscosity–cycle curve.

The fig.5 explains that the gradient of the dynamic pressure is also increased with decreasing the media viscosity.

The properties of various polymeric materials are as:

Polyethylene PE- The crystalline , melting point, tensile strength, stiffness, hardness, abrasion resistance, dissolution temp. in benzene, chemical resistance increase with increase in density of PE.

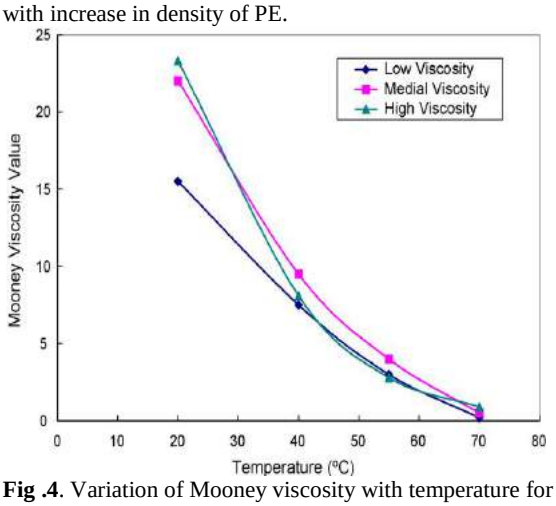

Fig .4. Variation of Mooney viscosity with temperature for three types of suspensions. *L. Fang et al*

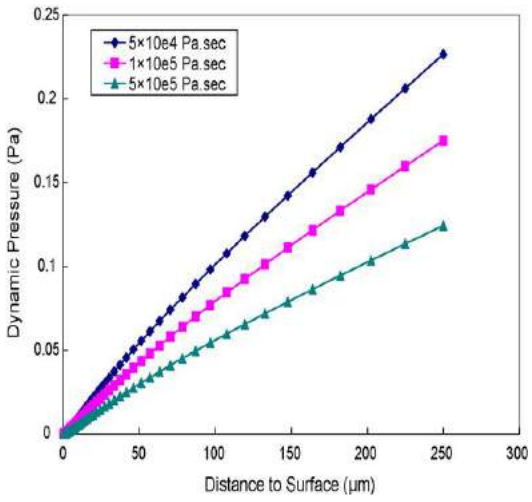

Fig.5 Dynamic pressure distribution normal to specimen surface with different media viscosity for 5MPa extrusion pressure.

Polystyrene PS- It is an amorphous polymer with high degree of branching. It has good chemical stability towards acids, alkalis, water. The most important weaknesses are its brittleness, low thermo stability, low resilience and flammability. The last property can be improved by introduction of halogen atoms in benzene ring [28].

Polymethyl methacrylate PMMA- It is amorphous, has better thermal stability. The solubility and viscosity of this group of polymers depend on the alcoholic group. Polymethacrylates are superior to polyacrylates in chemical stability, thermal stability and stability to water. When heated, polyacrylates soften before the corresponding polymethacrylates.

Styrene butadiene rubber SBR- It is general purpose rubber. Its permeability, heat resistance, resistance to wear, and aging is superior to natural rubber. SBR requires more severe milling than natural rubber, however over milling causes a considerable decrease in tensile strength. Larger amounts of plasticizer and softener are required. At an increased vulcanization temp., a decrease of young's modulus, relative elongation and even abrasion resistance has been observed. [29]

Silicon oils- Silicon oils consist of linear polydimethylsiloxane macromolecules with a MW in the range of 4000-25000. The reason of low viscosity at high MW is low intermolecular force in polydimethylsiloxanes. This also explains the small temperature dependence of silicon oils and elastomers.[30]

Epoxy polymers[31]- have excellent chemical resistance to alkaline environment, outstanding adhesion to variety of substrates, very high tensile, compressive, flexural strengths, low shrinkage on cure, dimensional stability, remarkable resistance to corrosion, a high degree of resistance to physical abuse, ability to cure over a wide range of temperatures, superior fatigue strength.

4. Abrasive Wear and Force Analysis

The mechanical wearing processes consist of separation of particle from the interactive surfaces in the way of micro-machining by loss of micro-roughness or by the loss of abrasive particles. Fatigue of material upper layer caused by the cyclic load is a mechanical cause of wear as well. Physical wear processes are generally connected with adhesion of bodies which rub together.

The volumetric relative wear can be described as volumetric cathode removal divided by machined material.

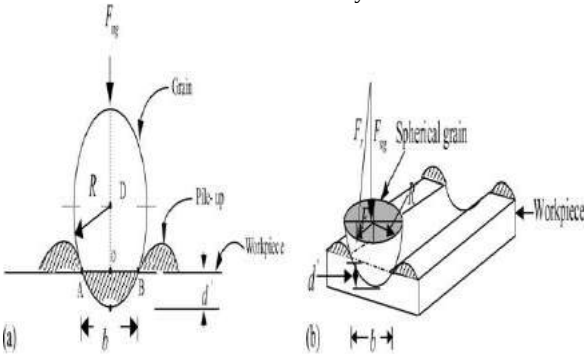

Fig.6: Forces acting on abrasive grain

4.1 Radial force on a single grain

When the radial force is applied during AFM on a grain, it will indent to a depth *d*_ into the work piece (Fig. 6)
With side flow of the material.

$$F_{ng} = \sigma \times A = \sigma \times \pi \times \left(\frac{b}{2}\right)^2 \quad (6)$$

Where b = diameter of projected area
σ =flow stress of workpiece

4.2 Axial force on a single grain

It has two components-

4.2.1 Force P -required to plough the metal from the front of grain [24]

$$P = 0.062 \frac{b^3}{R}\sigma \quad (7)$$

4.2.2 Friction force FR - between the work piece material and abrasive

$$F_R = F_{ng} \times \mu \quad (8)$$

$$F = P + F_R$$

$$= .062 \frac{b^3}{R}\sigma + \sigma \times \pi \times \left(\frac{b}{2}\right)^2 \mu \quad (9)$$

Fig.7 shows a schematic drawing of an active particle acted by several forces. A normal load acted by total pressure in AFM tunnel and a horizontal driving force acted on the profile face of particle. The horizontal driving force is transferred by the media. From fluid dynamics principle, the transferred driving force in the horizontal direction has an uneven distribution.

If a simplified analysis is made, resultant forces acted on a particle can be divided into four concentrated forces as shown in Fig.7, that is, normal force mainly produced by cylinder total pressure, driving force transferred by the pressure of the media and two resistant forces from material surface plastic deformation.

5. ANALYSIS OF SURFACE ROUGHNESS AND WEIGHT LOSS VARIATION WITH NUMBER OF CYCLES

Liang Fang experiments and found that the variation of surface roughness and MRR by number of cycles. Fig. 8 represents the effects of the number of cycles on the surface roughness for AISI 1080, 1045 and A36 steel as test materials It is observed that an increase in the cycles result in an associated decrease in the overall surface roughness. In general, the surface roughness is basically depended on the polishing cycles. It is on the whole insensitive to material hardness. However, the surface roughness is obviously changed only at first 20 cycles no matter what types of steels are used.

Fig. 9 displays the effects of the number of cycles on the wear weight losses for three kinds of steels.

It can be seen from Fig. 9 that wear weight losses increase with increasing the number of cycles. The steel removal efficiency, however, dramatically deteriorates after 20 cycles. It is also shown that the material removal efficiency decreases dominantly with increase of steel hardness for the initial stage of test, which is differ from the effects to surface roughness.

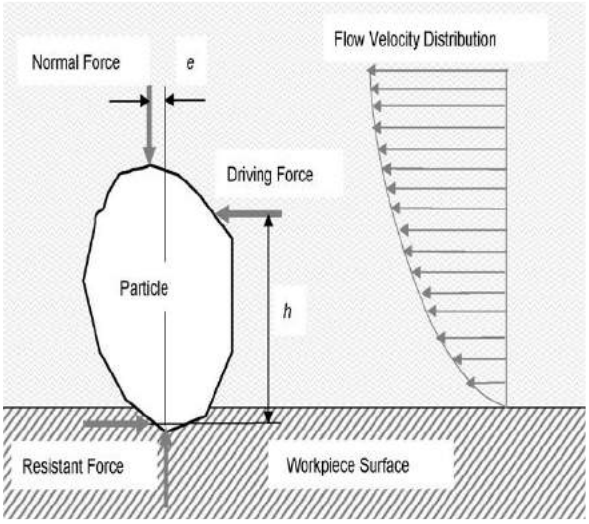

Fig.7 Schematic of force analysis acted on a particle in AFM suspension media.

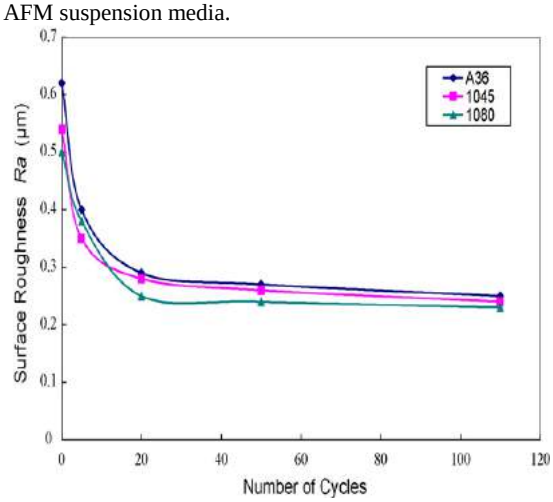

Fig.8 Relation of the number of cycles to surface roughness Ra for AISI 1045, 1080

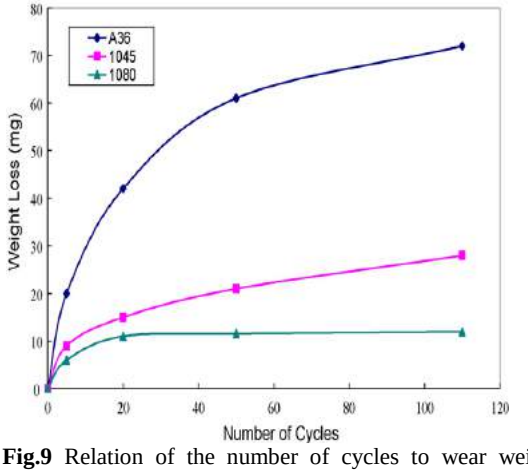

Fig.9 Relation of the number of cycles to wear weight losses for AISI 1045, 1080 and A36 steel.

6. Principle of Abrasive Flow and Governing Equations of the Flow Pattern

The media used in AFM is composed of semisolid carrier mixed with abrasives which exhibits inear viscous flow property [32]. The media is isotropic and homogeneous. Since cylindrical work piece is considered, media flow is taken as axi-symmetric. The media flow is steady.

5.1 Continuity equation

The condition of volume conservation can be expressed as,

$\dot{\epsilon}_{\theta\theta} + \dot{\epsilon}_{rr} + \dot{\epsilon}_{zz} = 0$

where, $\dot{\epsilon}_{\theta\theta}, \dot{\epsilon}_{rr}$ and $\dot{\epsilon}_{zz}$are components of strain rate tensor in azimuthal, radial and axial directions respectively.

5.2 Momentum equation

$$\rho\left[v_r\frac{\partial v_r}{\partial r} + v_z\frac{\partial v_r}{\partial z}\right] + \frac{\partial p}{\partial r} - \left[\frac{1}{r}\frac{\partial(r\tau_{rr})}{\partial r} - \frac{\tau_{\theta\theta}}{r} + \frac{\partial \tau_{rz}}{\partial z}\right] = 0 \quad (10)$$

where, ρ is density of media, p is pressure (hydrostatic stress).

5.3 Constitutive equation

The media behaves as a Newtonian fluid with shear stress being the linear function of shear

rate.The total stress tensor:-

$$\sigma_{ij} = -p\delta_{ij} + \tau_{ij} \quad (11)$$

$$= -p\delta_{ij} + \mu_a \dot{\epsilon}_{ij} \quad (12)$$

Where, μ_a is apparent viscosity and δ_{ij} is identity tensor.

6. Conclusions

Analysis and comparison of various abrasive laden polymer media has been done successfully and their properties have been studied. The compatibility and suitability of the various polymers with different work piece materials has been analyzed. Different abrasive grains, hydrocarbon oil used were studied in detail and the wear and forces acting on abrasive are properly explained in the paper.

References

[1]Rajesha S,Venkatesh G, Sharma A K, Kumar Pradeep (2010), Performance study of a natural polymer based media for abrasive flow maching, Indian Journal of Engineering & materials Sciences, 407-413.

[2] L.J. Rhoades (July, 1987), Abrasive flow machining with not-so-silly putty, Met. Finish. 27–29.

[3] L.J. Rhoades (1988), Abrasive flow machining, Manuf. Eng. 75–78.

[4] L.J. Rhoades (1991), Abrasive flow machining: a case study, J. Mater. Process. Technol. 28 107–116.

[5] K. Przylenk (1986), AFM-A process for surface finishing and deburring of the workpiece with a complicated shape by means of an abrasive laden medium, ASME, New York, , PED, Vol. 22, pp. 101–110.

[6] R.E. Williams, K.P. Rajurkar (1989), Metal removal and surface finish characteristics in AFM, Mechanics of Deburring and Surface Finishing Process, ASME, New York, , PED, Vol. 38, pp. 93– 106.

[7] D. Graham, R.M. Baual (1972), An investigation into the mode of metal removal in the grinding process, Wear 19 ,301–314

[8] V.K. Gorana, V.K. Jain, G.K. Lal,(2004), Experimental investigation into cutting forces and active grain density during abrasive flow machining, International Journal of Machine Tools and Manufacture 44,p.201–211.

[9] P.J. Davies, A.J. Fletcher (1995), The assessment of the rheological characteristics of various polyborosiloxane/grit mixtures as utilized in the abrasive flow machining process, Proceedings of the Institution of Mechanical Engineers 209, p. 409–418.

[10] R.K. Jain, V.K. Jain(2001), Specific energy and temperature determination in abrasive flow machining process, International Journal of Machine Tools and Manufacture 41,p.1689–1704.

[11] K.K. Kar, N.L. Ravikumar (2009), Performance evaluation and rheological characterization of newly developed butyl rubber media for AFM process, Journal of materials processing technology, 209, pp. 2212-2221.

[12] S. Singh, H.S. Shan (2002), Development of magneto AFM process, International Journal of machine tools and manufacture, 42, 953-959.

[13] E. Uhlmann (2009), Modelling the AFM process on advanced ceramic materials, Journal of materials processing technology, 209, 6062-6066.

[14] A.C. Wang, L. Tsa (2009), Uniform surface polished method of complex holes in AFM, Trans. Nonferrous Met Soc. China 19, s250-257.

[15] L. Tsai, A.C. Wang (2012), Investigating of flexible self-sharpening and optimal parameters in magnetic finishing with gel abrasive, International Journal of precision engineering and manufacturing, vol.13, no.5,pp.655-661.

[16] H.J. Tzeng, B.H. Yan (2007), Self-modulating abrasive medium and its application to AFM for finishing micro-channel surfaces, International Journal of advanced manufacturing technology, 32: 1163-1169.

[17] R.S. Walia, H.S. Shan, P. Kumar (2009), Enhancing AFM process productivity through improved fixturing, International Journal of adv. Manufac. Technol., 44: 700-709.

[18] M. Ravisankar, V.K. Jain (2009), Experimental investigation and mechanism of material removal in nano-finishing of MMCs using abrasive flow finishing process, Wear 266: 688-698.

[19] V.S. Sooraj (2014), Fine finishing of internal surfaces using elastic abrasives, International Journal of machine tools and manufacture, 78: pp.30-40.

[20] S.Rajesha, G.Venkatesh, A.K.Sharma, P.Kumar, (2010), Performance study of a natural rubber based media for abrasive flow machining, Indian journal of engineering and materials sciences vol.17, pp.407-413.

[21] Vinod Yadava, K.B.Judal (2013), Modeling and simulation of cylindrical electro-chemical magneticabrasive machining of AISI-420 magnetic steel, Journal of Materials Processing Technology, 213, pp.2089– 2100

[22] S. Jha, V.K. Jain (2009), Rheological characterization of magnetorheological polishing fluid, Int J Adv Manuf Technol ,42, pp.656–668

[23] H. Yamaguchi, S.K. Srivastava, Michael Tan (2014), Magnetic Abrasive Finishing of cutting tools for high-speed machining of titanium alloys, CIRP Journal of Manufacturing Science and Technology 7, pp.299–304

[24] Gurvinder Kumar, V. Yadav (2009), Temperature distribution in the workpiece due to plane magnetic

abrasive finishing using FEM, Int J Adv Manuf Technol 41, pp.1051–1058
[25] A.C. Wang, S.J. Lee (2009), Study the characteristics of magnetic finishing with gel abrasive, International Journal of Machine Tools & Manufacture 49, pp. 1063–1069
[26] T.A., El Taweel (2008), Modelling and analysis of hybrid electrochemical turning magnetic abrasive finishing of 6061 Al/Al2O3 composite, Int J Adv Manuf Technol 37, pp.705–714
[27] R.S. Mulik, P.M. Pandey (2011), Ultrasonic assisted magnetic abrasive finishing of hardened AISI 52100 steel using unbounded SiC abrasives, Int. Journal of Refractory Metals and Hard Materials 29, pp. 68–77
[28] Wang, J.L. and favstritsky N.A. (1994), Polym. Preprints, 35(2) 701
[29] Gharavi, F and Katbab, A.A. (1990), Prog. Rubber Plast.Technology, 6(2), 129.
[30] Bayer AG ,Leverskusen, Th. Goldschmidt AG, Essen (1991), Silicons-Chemistry and Technology, CRC Press, Boca Raton.
[31] Baer, R.S. (1985) Applied Polymer Science, 2nd edn, ACS American Chemical Society, Washington, p.931.
[32] V.K. Jain, C. Ranganatha, Evaluation of properties of media used in abrasive flow machining (to be published).

Journal of Theoretical and Applied Mechanics, Sofia, 2016, vol. 46, No. 3, pp. 35–64

DE GRUYTER
OPEN

DOI: 10.1515/jtam-2016-0015

EFFECTS OF DISCRETE DAMPING ON THE DYNAMIC BEHAVIOUR OF ROTATING SHAFT THROUGH EXTENDED LAGRANGIAN FORMULATION

Vikas Rastogi

Department of Mechanical, Production & Industrial and Automotive Engineering, Delhi Technological University, Delhi-110042, India,

e-mail: rastogivikas@yahoo.com

[Received 26 December 2014. Accepted 20 June 2016]

Abstract. The main focus of the paper is touted as effects of discrete damping on the dynamic analysis of rotating shaft. The whole analysis is being carried out through extended Lagrangian formulation for a discrete - continuous system. The variation formulation for this system is possible, considering the continuous system as one-dimensional. The generalized formulation for one dimensional continuous rotary shaft with discrete external damper has been obtained through principle of variation. Using this extended formulation, the invariance of umbra-Lagrangian density through extended Noether's theorem is achieved. Rayleigh beam model is used to model the shaft. Amplitude equation of rotor is obtained theoretically and validated through simulation results. The simulation results reveal the important phenomena of limiting dynamics of the rotor shaft, which is due to an imbalance of material damping and stiffness of the rotor shaft. The regenerative energy in the rotor shaft, induced due to elasticity/stiffness of the rotor shaft, is dissipated partially through the in-span discrete damper and also through the dissipative coupling between drive and the rotor shaft. In such cases, the shaft speed will not increase with increase in excitation frequency of the rotor but the slip between the drive and the shaft increases due to loading of drive.

Key words: Umbra-Lagrangian density, extended Noether's theorem, dynamic analysis, in-span discrete damping.

1. Introduction

It has been seen in most of the cases of continuous systems that employed methods of Lagrange and Hamilton are basically obtained through the

*This paper is a tribute to late Prof. Amalendu Mukherjee, who has formulated the concept of umbra-Lagrangian; and Prof. Anirvan Dasgupta, Professor, Mechanical Department, IIT, Kharagpur for their valuable suggestions throughout the course of this study.

- 10.1515/jtam-2016-0015
Downloaded from PubFactory at 08/17/2016 09:14:57AM
via Delhi Technological University

variation principle. There are several direct methods available in literature, which approximate the continuous system. In such approach, the system is discretized into finite or discrete particles and equations are obtained, which are finally approached to the continuous limits. However, such methods do not provide generality to the solution. The general relationship between one-parameter continuous symmetry and conserved quantity, specially in field's theory has been achieved by Boyer [1]. Some direct method of associating conserved quantities of Lagrangian system with each dynamical symmetry group has been reported by Sarlet and Cantrijn [2]. Other symmetry aspects of two-dimensional and three dimensional order Lagrangian and Hamiltonian formalism are studied by Katzin and Levine [3] and Damianou and Sophocleous [4]. However, such methods are employed only to a system of some specific configuration; and generality to the application in the interest of science and engineering are quite missing.

A new proposal of umbra-time was made by Mukherjee [5] to extend the scope of Lagrangian-Hamiltonian mechanics. A brief and promising commentary on such extension has been given by Brown [6]. The detailed theory and applications of an extended Lagrangian-Hamiltonian mechanics are presented in various references [7, 8, 10 and 11]. Further, Mukherjee et. al. [9] has applied the extended Lagrangian- Hamiltonian mechanics for a general class of continuous systems, which incorporated gyroscopic coupling and non-conservative fields, including internal and external damping. Both damping were distributed homogeneously throughout the system. However, the methodology and case discussed in ref. [9] did not include the concept of discrete-continuous hybrid system, which is formulated in this research work.

Rotor dynamics is a subject of interest from the middle of 20^{th} Century [12, 13]. This area is consistently in demand and has drawn attentions throughout the globe due to different effects and phenomena [14]. It is a well known fact, that both internal and external damping is significant for rotating shafts. The study of spinning shaft with internal damping was first investigated by Kimball [15]. Although Kimball's study did not specify the type of damping, he stated that internal friction due to bending in a spinning shaft contributes to shaft whirling above the first critical speed. Dimentberg [16] and Gunter [17] illustrated the concepts of the first critical speed due to internal viscous damping, which ultimately led to instability in the rotating shaft. Ehrich [18] studied the stability relationship between internal and external damping and noted that the rotational speed, at which the rotor becomes unstable, is governed by the ratio of internal and external damping. Some interesting results on modelling of internal damping in rotors were reported in the papers of Cran-

- 10.1515/jtam-2016-0015
Downloaded from PubFactory at 08/17/2016 09:14:57AM
via Delhi Technological University

dall [19], Zorzi and Nelson [20], Melanson and Zu [21], Genta [22], and Vance and Lee. [23]. In some of the studies, the instabilities resulting from internal damping are characterized. It is noteworthy that damping inform of material damping contribute the circulatory effects. Internal damping in such cases has a destabilizing influence on the rotor system. The discrete-continuous modelling of a rotor system was presented by Szoic [24]. In this paper, dynamical investigations of a rotor shaft system were performed by means of discrete continuous mechanical models. In such models, a rotating cylindrical shaft was represented as continuous system, whereas bearings were assumed as discrete elements. In another study by Jivkov and Zahariev [25], the stability and non-stationary vibrations of rotor-shaft in elastic-viscous field have been investigated through Bogoliubov–Mitropolski's asymptotical method. Further, Krenk [26] has demonstrated the complex mode analysis of cable and beam problems with concentrated viscous dampers. In these problems, the dissipating effect of the damper is closely linked with the complex character of the modes.

The main focus of this paper includes the extension of Lagrangian-Hamiltonian mechanics for a discrete-continuous hybrid system. In this extension, umbra-Lagrangian density is efficiently used to describe the motion of the system. The invariance of umbra-Lagrangian density (ULD) may be achieved by application of extended Noether's theorem over manifolds. The general formulation for dissipative effects with in-span concentrated discrete damper is developed through extended Lagrangian formulation. A case study of a rotating shaft with in-span discrete damper is analyzed, which shows a significant phenomenon of limiting dynamics of rotor, beyond threshold speed of instability. The effect of discrete external damping is examined and entrainment of critical whirling speeds at natural undamped modes is observed. A simulation rig is also created to animate and visualize the effect of in-span discrete damper on natural modes of rotating shaft.

2. Methodology

2.1. Generalized formulation for one-dimensional discrete-continuous hybrid system through principle of variation

Generalized formulation for one-dimensional discrete-continuous hybrid system shaft may be achieved by defining the system over the closed domain $x_0 \leq x \leq x_1$, as shown in Fig. 1, where t_1 and t_2 are considered as arbitrary times and x is the distance of any material point of the system.

In this generalized formulation of examining the dissipative effects, various gyroscopic forces, rotary inertia, internal damping and in-span dissipation

- 10.1515/jtam-2016-0015
Downloaded from PubFactory at 08/17/2016 09:14:57AM
via Delhi Technological University

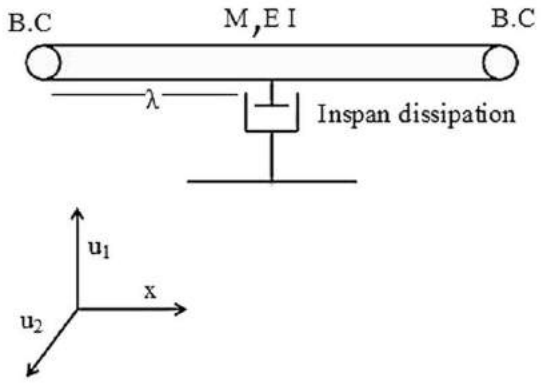

Fig. 1. Schematic diagram of a continuous shaft with uniform mass and constant rigidity with Inspan discrete damper

has been considered. It is assumed, that shaft is rotated at constant speed with ω. Umbra-Lagrangian density may be obtained as:

$$
(1) \qquad L = \left[\begin{array}{l}
\displaystyle\sum_{i=1}^{2} \left\{ \begin{array}{l} \dfrac{1}{2}\rho \left(\dfrac{\partial u_i(\eta,x)}{\partial \eta} \right)^2 - \dfrac{1}{2} EI \left(\dfrac{\partial^2 u_i(\eta,x)}{\partial x^2} \right)^2 \\ \\ +\dfrac{1}{2} I_d \left(\dfrac{\partial^2 u_i(\eta,x)}{\partial \eta\, \partial x} \right)^2 \end{array} \right\} \\
-\omega\, I_p \left(\dfrac{\partial^2 u_1(t,x)}{\partial t\, \partial x} \dfrac{\partial u_2(\eta,x)}{\partial x} - \dfrac{\partial^2 u_2(t,x)}{\partial t\, \partial x} \dfrac{\partial u_1(\eta,x)}{\partial x} \right) \\
+\displaystyle\sum_{i=1}^{2} R_a\, \delta(x-\lambda) \left(\dfrac{\partial u_i(\eta,x)}{\partial \eta} \right)^2 \\
-\mu_i \left\{ \left(\dfrac{\partial^3 u_1(t,x)}{\partial t\, \partial x^2} + \omega \dfrac{\partial^2 u_2(t,x)}{\partial x^2} \right) \dfrac{\partial^2 u_1(\eta,x)}{\partial x^2} \right. \\
\left. + \left(\dfrac{\partial^3 u_2(t,x)}{\partial t\, \partial x^2} - \omega \dfrac{\partial^2 u_1(t,x)}{\partial x^2} \right) \dfrac{\partial^2 u_2\,(\eta,x)}{\partial x^2} \right\}
\end{array} \right] .
$$

In the above Eq. (1), $u_i\,()$ is the displacement coordinates of the rotor in real or umbra time, ρ is the material density of the rotating shaft, EI is the

- 10.1515/jtam-2016-0015
Downloaded from PubFactory at 08/17/2016 09:14:57AM
via Delhi Technological University

rigidity, I_d is the rotary inertia, I_p is the inertia of the rotating shaft through principle axis, ω is the constant angular velocity, μ_i is internal damping of the shaft, R_a is the in-span dissipating element. In Eq. (1), fifth term is umbra-potential, due to In-span external dissipation.

Now, one may take umbra-Lagrangian density variation, which may be expressed as variations in the action integral in homotopic functions notated as $U_i\,(t,x,a)$ and $U_i\,(t,x,b)$, where $i=1,2$:

$$\delta I = \varepsilon \int_{t_0}^{t_1}\int_{x_0}^{x_1}\sum_{i=1}^{2}\left[\begin{array}{l} \left\{\dfrac{\partial L}{\partial U_i(t,x,b)} - \dfrac{\partial}{\partial t}\dfrac{\partial L}{\partial \dot{U}_i(t,x,b)}\right. \\ \left. -\dfrac{\partial}{\partial x}\left(\dfrac{\partial L}{\partial U_{i,x}(t,x,b)}\right)\right\}\hat{U}_i(t,x,b) \\ +\dfrac{\partial}{\partial t\partial x}\left(\dfrac{\partial L}{\partial \dot{U}_{i,x}(t,x,b)}\right)\hat{U}_i(t,x,b) \\ +\dfrac{\partial}{\partial x^2}\left(\dfrac{\partial L}{\partial U_{i,x^2}(t,x,b)}\right)\hat{U}_i(t,x,b) \end{array}\right] dtdx,$$

(2)

$$+\int_{t_0}^{t_1}\sum_{i=1}^{2}\left[\begin{array}{l} \dfrac{\partial L}{\partial U_{i,x}(t,x,b)}\hat{U}_i(t,x,b)\Big|_{x_0}^{x_1} \\ -\dfrac{\partial}{\partial t}\left(\dfrac{\partial L}{\partial \dot{U}_{i,x}(t,x,b)}\right)\hat{U}_i(t,x,b)\Big|_{x_0}^{x_1} \\ +\dfrac{\partial L}{\partial U_{i,x^2}(t,x,b)}\hat{U}(t,x,b)\Big|_{x_0}^{x_1} \\ -\dfrac{\partial}{\partial x}\left(\dfrac{\partial L}{\partial U_{i,x^2}(t,x,b)}\hat{U}_i(t,x,b)\right)\Big|_{x_0}^{x_1} \end{array}\right] dt = 0.$$

Considering variations in U_i as $U_i^* = U_i + \varepsilon\,\hat{U}_i$, one obtains:

- 10.1515/jtam-2016-0015
Downloaded from PubFactory at 08/17/2016 09:14:57AM
via Delhi Technological University

(3)

$$
\begin{aligned}
\delta I = \varepsilon \int_{t_0}^{t_1}\int_{x_0}^{x_1} & \left[\begin{array}{l}
\displaystyle\sum_{i=1}^{2}\left\{\begin{array}{l}\displaystyle\frac{\partial}{\partial t}\left(\rho\dot{U}_i(t,x,b)\right)-\frac{\partial}{\partial x^2}\left(EI\frac{\partial^2 U_i(t,x,b)}{\partial x^2}\right)\\ \displaystyle-\frac{\partial^2}{\partial t\partial x}\left(I_d\frac{\partial^2 U_i(t,x,b)}{\partial t\,\partial x}\right)\end{array}\right\}\hat{U}_i(t,x,b)\\
+(R_a\delta(x-\lambda)\,\dot{U}_i(t,x,b))\hat{U}_i(t,x,b)\\
-\omega I_p\left\{\begin{array}{l}\displaystyle\frac{\partial}{\partial x}\left(\frac{\partial^2 U_1(t,x,a)}{\partial t\,\partial x}\right)\hat{U}_2(t,x,b)\\ \displaystyle-\frac{\partial}{\partial x}\left(\frac{\partial^2 U_2(t,x,a)}{\partial t\,\partial x}\right)\hat{U}_1(t,x,b)\end{array}\right\}\\
-\mu_i\left\{\begin{array}{l}\displaystyle\frac{\partial^2}{\partial x^2}\left(\frac{\partial^3 U_1(t,x,a)}{\partial t\,\partial x^2}+\omega\frac{\partial^2 U_2(t,x,a)}{\partial x^2}\right)\hat{U}_1(t,x,b)\\ \displaystyle+\frac{\partial^2}{\partial x^2}\left(\frac{\partial^3 U_2(t,x,a)}{\partial t\,\partial x^2}-\omega\frac{\partial^2 U_1(t,x,a)}{\partial x^2}\right)\hat{U}_2(t,x,b)\end{array}\right\}
\end{array}\right] dt\,dx\\
&+\int_{t_0}^{t_1}\omega I_p\left\{\frac{\partial^2 U_1(t,x,a)}{\partial t\partial x}\hat{U}_2(t,x,b)-\frac{\partial^2 U_2(t,x,a)}{\partial t\partial x}\hat{U}_1(t,x,b)\right\}\Bigg|_{x_0}^{x_1}\\
&-\left\{\begin{array}{l}\displaystyle\sum_{i=1}^{2}\frac{\partial}{\partial x}EI\frac{\partial^2 U_i(t,x,b)}{\partial x^2}\hat{U}_i(t,x,b)\\
\displaystyle+\frac{\partial}{\partial x}\mu_i\left\{\begin{array}{l}\displaystyle\left(\frac{\partial^3 U_1(t,x,a)}{\partial t\partial x^2}+\omega\frac{\partial^2 U_2(t,x,a)}{\partial x^2}\right)\hat{U}_1(t,x,b)+\\ \displaystyle\left(\frac{\partial^3 U_2(t,x,a)}{\partial t\partial x^2}-\omega\frac{\partial^2 U_1(t,x,a)}{\partial x^2}\right)\hat{U}_2(t,x,b)\end{array}\right\}\\
\displaystyle-\frac{\partial}{\partial t}\sum_{i=1}^{2}\left(I_d\frac{\partial^2 U_i(t,x,b)}{\partial t\partial x}\right)\hat{U}_i(t,x,b)\end{array}\right\}\Bigg|_{x_0}^{x_1}\\
&+\sum_{i=1}^{2}\left\{EI\frac{\partial^2 U_i(t,x,b)}{\partial x^2}\right\}\frac{\partial\hat{U}_i(t,x,b)}{\partial x}\\
&+\mu_i\left\{\begin{array}{l}\displaystyle\left(\frac{\partial^3 U_1(t,x,a)}{\partial t\,\partial x^2}+\omega\frac{\partial^2 U_2(t,x,a)}{\partial x^2}\right)\frac{\partial\hat{U}_1(t,x,b)}{\partial x}\\ \displaystyle+\left(\frac{\partial^3 U_2(t,x,a)}{\partial t\,\partial x^2}-\omega\frac{\partial^2 U_1(t,x,a)}{\partial x^2}\right)\frac{\partial\hat{U}_2(t,x,b)}{\partial x}\end{array}\right\}\Bigg|_{x_0}^{x_1} dt=0
\end{aligned}
$$

- 10.1515/jtam-2016-0015
Downloaded from PubFactory at 08/17/2016 09:14:57AM
via Delhi Technological University

All such notations are changed as $t \times a = t$, $t \times b = \eta$ with $U_i\,(t, x, b) = u_i(\eta, x)$ and $U_i\,(t, x, a) = u_i(t, x)$, where $i = 1, 2$. After equating the coefficients of U_i's, the first part of the Eq. (3) provide umbra-field equations and the second part provide the boundary conditions at two ends of continuous shaft. The first part of the equation may be re-arranged in$\eta - t$ form, one may achieve umbra field after considering the limit $\eta \to t$ as:

$$
\left[\begin{array}{l}
\left\{\begin{array}{l}
\dfrac{\partial}{\partial t}\left(\underset{\eta\to t}{\mathrm{Lim}}\,\rho\dot{u}_1(\eta,x)\right)+\dfrac{\partial}{\partial x^2}\left(\underset{\eta\to t}{\mathrm{Lim}}\,EI\dfrac{\partial^2 u_1(\eta,x)}{\partial x^2}\right)\\
-\dfrac{\partial^2}{\partial t\partial x}\left(\underset{\eta\to t}{\mathrm{Lim}}\,I_d\dfrac{\partial^2 u_1(\eta,x)}{\partial\eta\,\partial x}\right)+
\end{array}\right\}\\
+R_a\delta(x-\lambda)\dfrac{\partial}{\partial t}\left(\underset{\eta\to t}{\mathrm{Lim}}\,\dot{u}_1(\eta,x)\right)\\
-\omega I_p\left\{-\dfrac{\partial}{\partial x}\left(\dfrac{\partial^2 u_2(t,x)}{\partial t\partial x}\right)\right\}\\
-\mu_i\left\{\dfrac{\partial^2}{\partial x^2}\left(\dfrac{\partial^3 u_1(t,x)}{\partial t\partial x^2}+\omega\dfrac{\partial^2 u_2(t,x)}{\partial x^2}\right)\right\}
\end{array}\right]=0, \tag{4a}
$$

and:

$$
\left[\begin{array}{l}
\left\{\begin{array}{l}
\dfrac{\partial}{\partial t}\left(\underset{\eta\to t}{\mathrm{Lim}}\,\rho\dot{u}_2(\eta,x)\right)+\dfrac{\partial}{\partial x^2}\left(\underset{\eta\to t}{\mathrm{Lim}}\,EI\dfrac{\partial^2 u_2(\eta,x)}{\partial x^2}\right)\\
-\dfrac{\partial^2}{\partial t\partial x}\left(\underset{\eta\to t}{\mathrm{Lim}}\,I_d\dfrac{\partial^2 u_2(\eta,x)}{\partial\eta\,\partial x}\right)
\end{array}\right\}\\
+R_a\delta(x-\lambda)\dfrac{\partial}{\partial t}\left(\underset{\eta\to t}{\mathrm{Lim}}\,\dot{u}_2(\eta,x)\right)\\
-\omega I_p\left\{\dfrac{\partial}{\partial x}\left(\dfrac{\partial^2 u_1(t,x)}{\partial t\partial x}\right)\right\}\\
-\mu_i\left\{\dfrac{\partial^2}{\partial x^2}\left(\dfrac{\partial^3 u_2(t,x)}{\partial t\partial x^2}-\omega\dfrac{\partial^2 u_1(t,x)}{\partial x^2}\right)\right\}
\end{array}\right]=0. \tag{4b}
$$

The boundary conditions at each end, which may be expressed after

- 10.1515/jtam-2016-0015
Downloaded from PubFactory at 08/17/2016 09:14:57AM
via Delhi Technological University

taking limit $\eta \to t$ in Eq. (3), which may be represented as:

$$\text{(5a)} \quad \left\{ \begin{array}{l} \omega I_p \left(-\dfrac{\partial^2 u_2(t,x)}{\partial t \partial x} \right) - \dfrac{\partial}{\partial x} \left(\begin{array}{l} EI \dfrac{\partial^2 u_1(t,x)}{\partial x^2} \\ +\mu_i \left(\dfrac{\partial^3 u_1(t,x)}{\partial t\, \partial x^2} + \omega \dfrac{\partial^2 u_2(t,x)}{\partial x^2} \right) \end{array} \right) \\ +\dfrac{\partial}{\partial t} \left(I_d \dfrac{\partial^2 u_1(t,x)}{\partial t\, \partial x} \right) \end{array} \right\} = 0,$$

or $u_1(t,x) = 0$.

$$\text{(5b)} \quad \left\{ \begin{array}{l} \omega I_p \left(-\dfrac{\partial^2 u_1(t,x)}{\partial t \partial x} \right) - \dfrac{\partial}{\partial x} \left(\begin{array}{l} EI \dfrac{\partial^2 u_2(t,x)}{\partial x^2} \\ +\mu_i \left(\dfrac{\partial^3 u_2(t,x)}{\partial t\, \partial x^2} + \omega \dfrac{\partial^2 u_1(t,x)}{\partial x^2} \right) \end{array} \right) \\ +\dfrac{\partial}{\partial t} \left(I_d \dfrac{\partial^2 u_2(t,x)}{\partial t\, \partial x} \right) \end{array} \right\} = 0,$$

or $u_2(t,x) = 0$.

$$\text{(5c)} \quad \begin{array}{l} \left\{ EI \dfrac{\partial^2 u_1(t,x)}{\partial x^2} + \mu_i \left(\dfrac{\partial^3 u_1(t,x)}{\partial t\, \partial x^2} + \omega \dfrac{\partial^2 u_2(t,x)}{\partial x^2} \right) \right\} = 0 \text{ or} \\ \dfrac{\partial u_1(t,x)}{\partial x} = 0, \end{array}$$

$$\text{(5d)} \quad \begin{array}{l} \left\{ EI \dfrac{\partial^2 u_2(t,x)}{\partial x^2} + \mu_i \left(\dfrac{\partial^3 u_2(t,x)}{\partial t\, \partial x^2} + \omega \dfrac{\partial^2 u_1(t,x)}{\partial x^2} \right) \right\} = 0 \text{ or} \\ \dfrac{\partial u_2(t,x)}{\partial x} = 0, \end{array}$$

The different physical conditions at two ends may be reflected by the above boundary conditions. The first part in each of the above four pairs depicts shearing force balance and bending moment balance, and termed as dynamic boundary conditions. The second part in each pair provides displacement or slopes, and termed as geometric or essential boundary conditions.

2.2 Classical Noether's theorem for fields

Noether's theorem may be effectively employed to obtain an invariant of motion or conserved quantities for fields and continuous systems. The Noether's

- 10.1515/jtam-2016-0015
Downloaded from PubFactory at 08/17/2016 09:14:57AM
via Delhi Technological University

theorem [27] for fields states, that any differentiable symmetry of the action of a physical system has a corresponding conservation laws. It can also be defined, that for every differentiable symmetry generated by local actions, there corresponds a constant current. The action of a physical system is the integral over time of a Lagrangian function, from which the system behaviour can be formulated by the least action principle.

2.3. Formulation of Extended Noether's theorem

Formulation of Extended Noether's theorem may be obtained considering the methodology provided in Ref. [9] and briefly presented in Appendix for ready reference of the readers. Some basic concepts of umbra-Lagrangian density have been provided in reference [6, 7, 11].

The prolonged infinitesimal generators [32, 33 and 34] are composed of two parts as

$$p_r^{(3)}V = p_r^{(3)}V_\eta + p_r^{(3)}\,V_t, \tag{6}$$

where, $p_r^{(3)}V_\eta$ and $p_r^{(3)}V_t$ are the prolonged umbra-time and real-time component the infinitesimal generators $p_r^{(3)}V$. One may achieve the invariance of umbra-Lagrangian density, which may now be expressed as:

$$p_r^{(3)}V\,(L) = 0. \tag{7}$$

One may formulate the Extended Noether's theorem through substitution and taking the limit $\eta \to t$,

$$\underset{\eta\to t}{\mathrm{Lim}}\left\{p_r^{(3)}V_\eta(L)\right\} + \underset{\eta\to t}{\mathrm{Lim}}\left\{p_r^{(3)}V_t(L)\right\} = 0. \tag{8}$$

The first term of the Eq. (4a) may be represented as:

$$\begin{aligned}(9)\quad &\underset{\eta\to t}{\mathrm{Lim}}(t,x)p_r^{(3)(t,x)}V_\eta(L)\\ &= \underset{\eta\to t}{\mathrm{Lim}}(t,x)\sum_{i=1}^{2}\left\{\begin{array}{l}\xi_{u_i(\eta,x)}\left(\dfrac{\partial L}{\partial u_i(\eta,x)}\right)+\dot{\xi}_{u_i(\eta,x)}\left(\dfrac{\partial L}{\partial \dot{u}_i(\eta,x)}\right)\\ +\xi'_{u_i(\eta,x)}\left(\dfrac{\partial L}{\partial u'_i(\eta,x)}\right)+\dot{\xi}'_{u_i(\eta,x)}\left(\dfrac{\partial L}{\partial \dot{u}'_i(\eta,x)}\right)\\ +\xi''_{u_i(\eta,x)}\left(\dfrac{\partial L}{\partial u''_i(\eta,x)}\right)+\dot{\xi}''_{u_i(\eta,x)}\left(\dfrac{\partial L}{\partial \dot{u}''_i(\eta,x)}\right)\end{array}\right\},\end{aligned}$$

- 10.1515/jtam-2016-0015
Downloaded from PubFactory at 08/17/2016 09:14:57AM
via Delhi Technological University

All above notions in details are provided in Appendix. Expanding each term with derivatives ofξ's in Eq. (9) yields after simplification as:

$$
\begin{aligned}
(10)\quad & \lim_{\eta\to t} p_r^{(3)}\, V_\eta(L) \\
&= \lim_{\eta\to t} \sum_{i=1}^{2} \left[\begin{array}{l} D_t \left\{ \begin{array}{l} \xi_{u_i(\eta,x)} \left(\dfrac{\partial L}{\partial \dot{u}_i(\eta,x)} \right) + \dfrac{\partial}{\partial x} \left(\xi_{u_i(\eta,x)} \left(\dfrac{\partial L}{\partial \dot{u}_i'(\eta,x)} \right) \right) \\ -\xi_{u_i(\eta,x)} \dfrac{\partial}{\partial x} \left(\dfrac{\partial L}{\partial \dot{u}_i'(\eta,x)} \right) \end{array} \right\} \\ +D_x \left\{ \begin{array}{l} \xi_{u_i(\eta,x)} \left(\dfrac{\partial L}{\partial u_i'(\eta,x)} \right) - \left(\xi_{u_i(\eta,x)} \dfrac{\partial}{\partial t} \left(\dfrac{\partial L}{\partial \dot{u}_i'(\eta,x)} \right) \right) \\ +\xi'_{u_i(\eta,x)} \left(\dfrac{\partial L}{\partial u_i''(\eta,x)} \right) - \xi_{u_i(\eta,x)} \dfrac{\partial}{\partial x} \left(\dfrac{\partial L}{\partial u_i''(\eta,x)} \right) \end{array} \right\} \end{array} \right],
\end{aligned}
$$

where D_t is the total time derivative and D_x is the total space derivatives, respectively and may be mathematically explained as:

$$
(11)\qquad D_t Z_1\,(t, x,\, u,\, u_x) = \frac{\partial Z_1}{\partial t} + \frac{\partial Z_1}{\partial u}\frac{\partial u}{\partial t} + \frac{\partial Z_2}{\partial u_x}\frac{\partial u_x}{\partial t},
$$

$$
(12)\qquad D_x Z_2\,(t, x,\, u,\, u_x, u_{x^2}) = \frac{\partial Z_2}{\partial x} + \frac{\partial Z_2}{\partial u}\frac{\partial u}{\partial x} + \frac{\partial Z_2}{\partial u_x}\frac{\partial u_x}{\partial x} + \frac{\partial Z_2}{\partial u_{x^2}}\frac{\partial u_{x^2}}{\partial x},
$$

and functions Z_1 and Z_2 may explained as:

$$
\begin{aligned}
(13)\quad Z_1 = \lim_{\eta\to t} \sum_{i=1}^{2} \Bigg\{ & \xi_{u_i(\eta,x)} \left(\frac{\partial L}{\partial \dot{u}_i(\eta,x)} \right) + \frac{\partial}{\partial x} \left(\xi_{u_i(\eta,x)} \left(\frac{\partial L}{\partial \dot{u}_i'(\eta,x)} \right) \right) \\
& -\xi_{u_i(\eta,x)} \frac{\partial}{\partial x} \left(\frac{\partial L}{\partial \dot{u}_i'(\eta,x)} \right) \Bigg\},
\end{aligned}
$$

$$
(14)\quad Z_2 = \lim_{\eta\to t} \sum_{i=1}^{2} \left\{ \begin{array}{l} \xi_{u_i(\eta,x)} \left(\dfrac{\partial L}{\partial u_i'(\eta,x)} \right) - \xi_{u_i(\eta,x)} \dfrac{\partial}{\partial t} \left(\dfrac{\partial L}{\partial \dot{u}_i'(\eta,x)} \right) \\ +\xi'_{u_i(\eta,x)} \left(\dfrac{\partial L}{\partial u_i''(\eta,x)} \right) - \xi_{u_i(\eta,x)} \dfrac{\partial}{\partial x} \left(\dfrac{\partial L}{\partial u_i''(\eta,x)} \right) \end{array} \right\}.
$$

Thus, one may re-write Eq. (10) as:

$$
(15)\qquad \lim_{\eta\to t} p_r^{(3)} V_\eta(L) = D_t Z_1 + D_x Z_2.
$$

- 10.1515/jtam-2016-0015
Downloaded from PubFactory at 08/17/2016 09:14:57AM
via Delhi Technological University

After Substitution of Eq. (15) in Eq. (8) finally results in extended Noether's theorem for fields, which may be expressed as:

$$D_t Z_1 + D_x Z_2 + \lim_{\eta \to t} P_r^3 V_t(L) = 0. \tag{16}$$

Where functions Z_1 and Z_2 may be defined as:

$$Z_1 = \lim_{\eta \to t} \left[\sum_{i=1}^{2} \xi_i(\eta) \left\{ \begin{array}{l} \dfrac{\partial L}{\partial \dot{u}_i(\eta, x)} - \dfrac{d}{dx}\left(\dfrac{\partial L}{\partial \dot{u}_{ix}(\eta, x)} \right) \\ + \dfrac{d^2}{dx^2}\left(\dfrac{\partial L}{\partial \dot{u}_{ixx}(\eta, x)} \right) \end{array} \right\} \right], \tag{17}$$

$$\begin{aligned} Z_2 = & \lim_{\eta \to t} \left[\sum_{i=1}^{2} \left(\begin{array}{l} \xi_i(\eta) \dfrac{\partial L}{\partial u_{ix}(\eta, x)} + \xi_i'(\eta) \left(\dfrac{\partial L}{\partial u_{ixx}(\eta, x)} \right) \\ - \xi_i(\eta) \dfrac{d}{dx} \left(\dfrac{\partial L}{\partial u_{ixx}(\eta, x)} \right) \end{array} \right) \right] \\ & + \lim_{\eta \to t} \left[\sum_{i=1}^{2} \left(\begin{array}{l} \dot{\xi}_i(\eta) \dfrac{\partial L}{\partial \dot{u}_{ix}(\eta, x)} + \dot{\xi}_i^{/}(\eta) \left(\dfrac{\partial L}{\partial \dot{u}_{ixx}(\eta, x)} \right) \\ - \dot{\xi}_i(\eta) \dfrac{d}{dx} \left(\dfrac{\partial L}{\partial \dot{u}_{ixx}(\eta, x)} \right) \end{array} \right) \right]. \end{aligned} \tag{18}$$

Equation (16) is represented as an extended Noether's field equation for the umbra-Lagrangian density, where Z_1 may be defined as local density, Z_2 as current or flux density (It is more often defined as Noether's current density) and the last additional term may be defined as the modulatory convection term, which is due to the contribution of nonconservative actions and gyroscopic currents, including the dissipation effects, which may also be assumed as local rate of production.

3. Formulation of continuous rotor shaft with in-span external damping

In this case study, a rotor shaft with in-span concentrated discrete damper has been considered in the system. The rotor shaft material comprises of internal damping and shaft is driven by a constant supply motor. The motor is attached with continuation shaft with an aid of dissipated coupling, as shown in Fig. 2.

- 10.1515/jtam-2016-0015
Downloaded from PubFactory at 08/17/2016 09:14:57AM
via Delhi Technological University

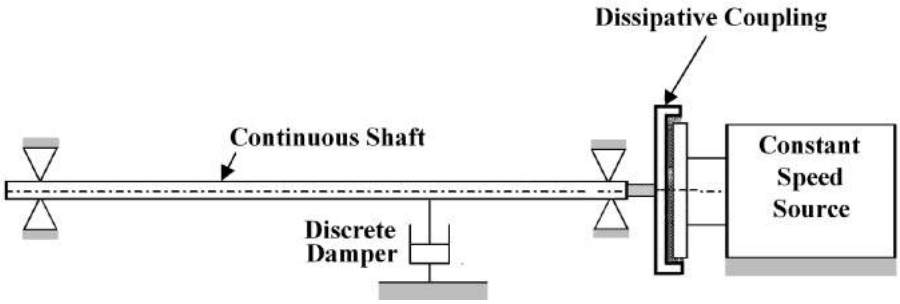

Fig. 2. Continuous rotor shaft with in-span concentrated discrete damper

One may obtain umbra-Lagrangian Density of the system, which may be written as:

$$
\begin{aligned}
L = \int_{x_0}^{x_1} & \left[\sum_{i=1}^{2} \left\{ \begin{array}{l} \frac{1}{2}\rho \left(\frac{\partial u_i(\eta,x)}{\partial \eta} \right)^2 - \frac{1}{2} EI \left(\frac{\partial^2 u_i(\eta,x)}{\partial x^2} \right)^2 \\ -\frac{1}{2} I_d \left(\frac{\partial^2 u_i(\eta,x)}{\partial \eta\, \partial x} \right)^2 \end{array} \right\} \right. \\
& \left. -\mu_i \left\{ \begin{array}{l} \left(\frac{\partial^3 u_1(t,x)}{\partial t\, \partial x^2} + \dot{\theta}(t) \frac{\partial^2 u_2(t,x)}{\partial x^2} \right) \frac{\partial^2 u_1(\eta,x)}{\partial x^2} \\ + \left(\frac{\partial^3 u_2(t,x)}{\partial t\, \partial x^2} - \dot{\theta}(t) \frac{\partial^2 u_1(t,x)}{\partial x^2} \right) \frac{\partial^2 u_2(\eta,x)}{\partial x^2} \end{array} \right\} \right] dx \\
& \int_{x_0}^{x_1} R_a \delta(x-\lambda) \left(u_1 \dot{u}_2 - u_2 \dot{u}_1 \right) dx \\
& - \left[\begin{array}{l} \mu_i \int_{x_0}^{x_1} \left\{ \frac{\partial^2 u_1(t,x)}{\partial x^2} \frac{\partial^3 u_2(t,x)}{\partial t\, \partial x^2} - \frac{\partial^2 u_2(t,x)}{\partial x^2} \frac{\partial^3 u_1(t,x)}{\partial t\, \partial x^2} \right\} dx \\ + R_c \left(\dot{\theta}(t) - \Omega \right) \end{array} \right] \theta(\eta) \\
& + \frac{1}{2} J \dot{\theta}^2(\eta),
\end{aligned}
\tag{19}
$$

where R_c is damping coefficient of a dissipative coupling, R_a is the damping coefficient of in-span external damper, and Ω is the excitation frequency. In Eq. (19), the first term is kinetic energy of the system, the second term is strain energy for small deflections, where E is the Young's modulus of the shaft material, and I is the cross-section moment of inertia, the third term is

- 10.1515/jtam-2016-0015
Downloaded from PubFactory at 08/17/2016 09:14:57AM
via Delhi Technological University

contributed by rotary moments with the angular velocity $\dfrac{\partial^2 u_i(\eta, x)}{\partial \eta \partial x}$, the fourth term is contributed by gyroscopic forces with constant angular velocity ω, the fifth term is contributed by discrete external damper, and the sixth term is umbra-potential, due to internal damping. All terms are in per unit length, In Eq. (19), the fifth term contributed by external damping is very significant. For this system with in-span discrete external damping, the term, which needs special consideration, is:

$$\int_0^L R_a \delta(x-\lambda)\left(u_1 \dot{u}_2 - u_2 \dot{u}_1\right) dx, \quad \text{where} \quad \lambda \in (0, L)\,. \tag{20}$$

In this case, δ is Dirac delta function. It is assumed the following form of motion as:

$$u_1 = \sum_{n=1}^{\infty} A_n \cos \Omega_n t \sin \frac{n\pi}{L} x \quad \text{and,} \quad u_2 = \sum_{n=1}^{\infty} A_n \sin \Omega_n t \sin \frac{n\pi}{L} x, \tag{21}$$

where A_n may be defined as slowly varying function with time.

Substitution of Eq. (21) into Eq. (20) yields:

$$R_a \left(\Omega_n \sum_{n=1}^{\infty} \sum_{m=1}^{\infty} A_n A_m \sin \frac{n\pi}{L}\lambda \ \sin \frac{m\pi}{L}\lambda \right), \tag{22}$$

The above expression may be used in extended Noether's theorem to evaluate the amplitude equation of the system.

3.1 Formulation of extended Noether's theorem for shaft with in-span concentrated discrete damper

The extended Noether's rate with in-span concentrated damping may be written as:

$$\left[\begin{array}{l} \displaystyle\sum_{n=1}^{\infty} \frac{L}{2} \Omega_n A_n \left\{ \dot{A}_n + \frac{1}{2\rho} \left(\mu_i \frac{n^4 \pi^4}{L^4} \right) A_n \right\} - \frac{\mu_i \, n^4 \pi^4}{2\rho \, L^4} \dot{\theta}(t) A_n^2 \\ \displaystyle + \frac{\Omega_n R_a}{2\rho} \sum_{n=1}^{\infty} \sum_{m=1}^{\infty} A_n A_m \sin \frac{n\pi}{L} \lambda \ \sin \frac{m\pi}{L} \lambda \end{array} \right] = 0. \tag{23}$$

- 10.1515/jtam-2016-0015
Downloaded from PubFactory at 08/17/2016 09:14:57AM
via Delhi Technological University

$$(24)\quad \sum_{n=1}^{\infty} A_n \left[\dot{A}_n + \frac{1}{2\rho}\left\{\mu_i \frac{n^4\pi^4}{L^4} - \frac{\mu_i n^4\pi^4}{\Omega_n L^4}\dot{\theta}(t)\right\} A_n\right] \times \frac{L}{2} + \frac{R_a}{2\rho}\sum_{j=1}^{\infty}\sum_{k=1}^{\infty} A_j A_k \sin\frac{j\pi}{L}\lambda \sin\frac{k\pi}{L}\lambda = 0,$$

or it is written as:

$$(25)\quad \frac{L}{2}\sum_{n=1}^{\infty} A_n \left[\dot{A}_n + \frac{1}{2\rho}\left\{\mu_i \frac{n^4\pi^4}{L^4} - \frac{\mu_i n^4\pi^4}{\Omega_n L^4}\dot{\theta}(t)\right\} A_n + \frac{R_a}{\rho L}\sum_{k=1}^{\infty} A_k \sin\frac{n\pi}{L}\lambda \sin\frac{k\pi}{L}\lambda\right] = 0.$$

One may consider independent variations in$A_n + \delta A_n$ and after dropping the factor $^{L}/_{2}$, the variational equation may be expressed as:

$$(26)\quad \begin{aligned} &\sum_{n=1}^{n} \delta A_n \left[\begin{array}{l} \dot{A}_n + \frac{1}{2\rho}\left\{\mu_i \frac{n^4\pi^4}{L^4} - \frac{\mu_i\, n^4\pi^4}{\Omega_n L^4}\dot{\theta}(t)\right\} A_n \\ + \frac{R_a}{\rho L}\sum_{k=1}^{\infty} A_k \sin\frac{n\pi}{L}\lambda\ \sin\frac{k\pi}{L}\lambda \end{array}\right] \\ &+\sum_{n=1}^{n} A_n \delta \left[\begin{array}{l} \dot{A}_n + \frac{1}{2\rho}\left\{\mu_i \frac{n^4\pi^4}{L^4} - \frac{\mu_i\, n^4\pi^4}{\Omega_n L^4}\dot{\theta}(t)\right\} A_n \\ + \frac{R_a}{\rho L}\sum_{k=1}^{\infty} A_k \sin\frac{n\pi}{L}\lambda\ \sin\frac{k\pi}{L}\lambda \end{array}\right] = 0. \end{aligned}$$

One may deduce the symmetry condition, which will be valid for neighbourhood paths. The following conditions are essentially required to be satisfied, given as:

$$(27)\quad \dot{A}_n + \frac{1}{2\rho}\left\{\mu_i \frac{n^4\pi^4}{L^4} - \frac{\mu_i\, n^4\pi^4}{\Omega_n L^4}\dot{\theta}(t)\right\} A_n + \frac{R_a}{\rho L}\sum_{k=1}^{\infty} A_k \sin\frac{n\pi}{L}\lambda\ \sin\frac{k\pi}{L}\lambda = 0.$$

One may examine the condition for entrainment of the n^{th} mode if $A_n \to$ finite limit and $A_k \to 0$. This is possible only if $k \neq n$ for $t \to \infty$, which

- 10.1515/jtam-2016-0015
Downloaded from PubFactory at 08/17/2016 09:14:57AM
via Delhi Technological University

finally resulted into:

$$\frac{1}{2\rho}\left\{\mu_i\frac{n^4\pi^4}{L^4}-\frac{\mu_i n^4\pi^4}{\Omega_n L^4}\dot{\theta}(t)\right\}+\frac{R_a}{\rho L}\sin^2\frac{n\pi}{L}\lambda=0. \tag{28}$$

The value of $\dot{\theta}(t)$ will be obtained from Eq. (28) and written as:

$$\frac{1}{2\rho}\frac{\mu_i n^4\pi^4}{\Omega_n L^4}\dot{\theta}(t)=\frac{1}{2\rho}\mu_i\frac{n^4\pi^4}{L^4}+\frac{R_a\times 2}{\rho L\times 2}\sin^2\frac{n\pi}{L}\lambda\,, \tag{29}$$

or

$$\dot{\theta}(t)=\Omega_n\left[1+\frac{2R_aL^3}{\mu_i n^4\pi^4}\sin^2\frac{n\pi}{L}\lambda\right]. \tag{30}$$

3.2. Umbra-Hamiltonian density of continuous rotor system

It is required to evaluate umbra-Hamiltonian density of the system to achieve the amplitude equation of the shaft, to achieve an amplitude equation of the continuous rotor system with in-span damper. Umbra-Hamiltonian [9] may be expressed as:

$$\begin{aligned}H=&\int_{x_0}^{x_1}\left[\begin{array}{l}\displaystyle\sum_{i=1}^{2}\left\{\begin{array}{c}\displaystyle\frac{1}{2\rho}P_i^2(\eta,x)+\frac{1}{2}EI\left(\frac{\partial^2u_i(\eta,x)}{\partial x^2}\right)^2\\ \displaystyle+\frac{1}{2}I_d\left(\frac{\partial^2u_i(\eta,x)}{\partial\eta\,\partial x}\right)^2\end{array}\right\}\\ \displaystyle+\mu_i\left\{\begin{array}{l}\displaystyle\left(\frac{\partial^3u_1(t,x)}{\partial t\,\partial x}+\dot{\theta}(t)\frac{\partial^2u_2(t,x)}{\partial x^2}\right)\frac{\partial^2u_1(\eta,x)}{\partial x^2}\\ \displaystyle+\left(\frac{\partial^3u_2(t,x)}{\partial t\,\partial x}-\dot{\theta}(t)\frac{\partial^2u_1(t,x)}{\partial x^2}\right)\frac{\partial^2u_2(\eta,x)}{\partial x^2}\end{array}\right\}\end{array}\right]dx\\ &+\int_{x_0}^{x_1}R_a(x-\lambda)\,(u_1\dot{u}_2-u_2\dot{u}_1)\,dx\\ &+\left[\begin{array}{l}\displaystyle\mu_i\int_{x_0}^{x_1}\left\{\frac{\partial^2u_1(t,x)}{\partial x^2}\frac{\partial^3u_2(t,x)}{\partial t\,\partial x^2}-\frac{\partial^2u_2(t,x)}{\partial x^2}\frac{\partial^3u_1(t,x)}{\partial t\,\partial x^2}\right\}dx\\ +R_c\left(\dot{\theta}(t)-\Omega\right)\end{array}\right]\theta(\eta)\\ &+\frac{1}{2J_d}P_\theta^2,\end{aligned} \tag{31}$$

- 10.1515/jtam-2016-0015
Downloaded from PubFactory at 08/17/2016 09:14:57AM
via Delhi Technological University

where $P_i(\eta, x) = \rho \dfrac{\partial u_i(\eta, x)}{\partial \eta}$ and $P_\theta(\eta) = J_d \dot{\theta}(\eta)$.

As discussed in reference [9], one may have the similar theorems for umbra-Hamiltonian density, which may be expressed as:

$$\operatorname*{Lim}_{\eta \to t} \frac{\partial H^*}{\partial \eta} = 0 \Rightarrow \frac{d H_i^*}{dt} = -\operatorname*{Lim}_{\eta \to t} \frac{d H_e^*}{\partial \eta}. \tag{32}$$

Considering the equation (2), one may evaluate exterior umbra-Hamiltonian density, expressed as:

$$\begin{aligned} \operatorname*{Lim}_{\eta \to t} \frac{\partial H_e}{\partial \eta} = \int_{x_0}^{x_1} & \left[\begin{array}{l} R_a(x-\lambda)(u_1 \dot{u}_2 - u_2 \dot{u}_1)\, dx \\ +\mu_i \left[\begin{array}{l} \left\{ \dfrac{\partial^3 u_1(t,x)}{\partial t\, \partial x^2} + \dot{\theta}(t) \dfrac{\partial^2 u_2(t,x)}{\partial x^2} \right\} \dfrac{\partial^3 u_1(t,x)}{\partial t\, \partial x^2} \\ + \left\{ \dfrac{\partial^3 u_2(t,x)}{\partial t\, \partial x^2} - \dot{\theta}(t) \dfrac{\partial^2 u_1(t,x)}{\partial x^2} \right\} \dfrac{\partial^3 u_2(t,x)}{\partial t\, \partial x^2} \end{array} \right] dx \end{array} \right] \\ & + \left[\begin{array}{l} \mu_i \displaystyle\int_{x_0}^{x_1} \left\{ \begin{array}{l} \dfrac{\partial^2 u_1(t,x)}{\partial x^2} \dfrac{\partial^3 u_2(t,x)}{\partial t\, \partial x^2} \\ -\dfrac{\partial^2 u_2(t,x)}{\partial x^2} \dfrac{\partial^3 u_1(t,x)}{\partial t\, \partial x^2} \end{array} \right\} dx \\ +R_c \left(\dot{\theta}(t) - \Omega \right) \end{array} \right] \dot{\theta}(t) = 0. \end{aligned} \tag{33}$$

The end conditions of the continuous shaft have been taken as pin-pin considering self-aligning bearing. After substituting Eq. (21) in Eq. (33), one obtains the following two terms distinguished, as $\{P\}$ and $\{Q\}$:

$$\begin{aligned} \operatorname*{Lim}_{\eta \to t} \frac{\partial H_e}{\partial \eta} = {} & R_a \Omega_n \sum_{n=1}^{\infty} \sum_{m=1}^{\infty} A_n A_m \sin \frac{n\pi}{L} x \, \sin \frac{m\pi}{L} x \\ & + \mu_i \frac{L}{2} \left[\begin{array}{l} \displaystyle\sum_{n=1}^{\infty} A_n^2 \Omega_n^2 \left(\frac{n\pi}{L} \right)^4 \\ +\dot{\theta}(t) \displaystyle\sum_{n=1}^{\infty} A_n^2 \Omega_n \left(\frac{n\pi}{L} \right)^4 + \sum_{n=1}^{\infty} \dot{A}_n^2 \left(\frac{n\pi}{L} \right)^4 \end{array} \right] \\ & \underline{\qquad\qquad\qquad} Term\ \{P\} \underline{\qquad\qquad\qquad} \\ & + \left[\mu_i \left\{ \int_0^L \sum_{n=1}^{\infty} A_n^2 \Omega_n \sin^2 \frac{n\pi\, x}{L} \left(\frac{n\pi}{L} \right)^4 \right\} dx + R_c \left(\dot{\theta}(t) - \Omega \right) \right] \dot{\theta}(t). \\ & \underline{\qquad\qquad\qquad} Term\ \{Q\} \underline{\qquad\qquad\qquad} \end{aligned}$$

- 10.1515/jtam-2016-0015
Downloaded from PubFactory at 08/17/2016 09:14:57AM
via Delhi Technological University

Equating term $\{P\}$ to zero, one obtains the expression:

$$\dot{A}_n^2 + A_n^2\Omega_n\left[\frac{\mu_i\Omega_n n^4\pi^4}{L^4} - \frac{\mu_i n^4\pi^4}{L^4\Omega_n}\dot{\theta}(t) + \frac{2R_a}{L}\sin^2\frac{n\pi}{L}\lambda\right] = 0. \tag{34}$$

Considering independent variations in $A_n + \delta A_n$, the variation equation may be written similar to Eq. (26), after dropping the factor $L/2$. Repeating the same steps from Eq. (27) to (28), one obtains the value of $\dot{\theta}(t)$ as:

$$\dot{\theta}(t) = \Omega_n\left[1 + \frac{2R_aL^3}{\mu_i n^4\pi^4}\sin^2\frac{n\pi}{L}\lambda\right]. \tag{35}$$

The Eq. (35) makes the term $\{P\}$ zero and also resembles with Eq. (30). After equating the second term $\{Q\}$ to zero, one may obtain:

$$\mu_i\sum_{n=1}^{\infty}A_n^2\Omega_n\left(\frac{n\pi}{L}\right)^4\int_0^L\phi_n^2dx + R_c\left(\dot{\theta}(t) - \Omega\right) = 0. \tag{36}$$

Considering the shaft's speed is entrained at

$$\dot{\theta}(t) = \Omega_n\left[1 + \frac{2R_aL^3}{\mu_i n^4\pi^4}\sin^2\frac{n\pi}{L}\lambda\right],$$

then all the amplitudes converge to zero except A_n, thus, the amplitude equation of the shaft with in- span damping may be obtained as:

$$A_n = \sqrt{\frac{2R_c\left(\Omega - \underset{n\in I^+}{\text{Min}}\,\Omega_n\left[1 + \frac{2R_aL^3}{\mu_i n^4\pi^4}\sin^2\frac{n\pi}{L}\lambda\right]\right)}{\mu_i\frac{n^4\pi^4}{L^3}\Omega_n}},$$

or

$$A_n = \sqrt{\frac{2R_c\left(\Omega - \underset{n\in I^+}{\text{Min}}\,\Omega_n\left[1 + \frac{2R_aL^3}{\mu_i n^4\pi^4}\sin^2\frac{n\pi}{L}\lambda\right]\right)}{\zeta_n\Omega_n}}, \tag{37}$$

where $\zeta_n = \mu_i\frac{n^4\pi^4}{L^3}$. The next section presents the modelling simulation of rotating shaft with in span concentrated damper.

- 10.1515/jtam-2016-0015
Downloaded from PubFactory at 08/17/2016 09:14:57AM
via Delhi Technological University

4. Modelling and simulation of rotating shaft with in- span discrete external damping

The physical system of discrete-continuous rotor shaft with in-span discrete external damper has been shown in Fig. 2. The shaft is driven by a constant supply voltage source through dissipative coupling. Any DC motor may qualify as a constant supply voltage source. The self aligning bearing is employed and the coupling of the system is assumed to be flexible in transverse and longitudinal direction, but at the same time, it is torsion rigid, as torsion vibrations are not prominent in comparison to transverse and flexural vibrations. The bond graphs are conveniently used as a modelling technique as it portrays the system from its physical paradigms. The object oriented reusable capsules, called vector bond graphs of the system, shown in Fig. 3 are created with in-span discrete external damping.

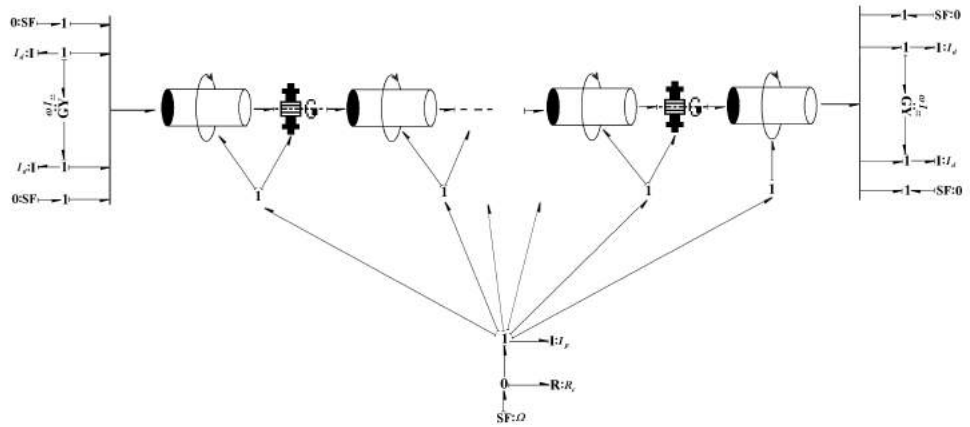

Fig. 3. Bond graph model of integrated system of rotor shaft with in-span concentrated external damper

4.1 Simulation studies

The bond graph model [11, 28, 29] of the continuous shaft with in span concentrated external damping is simulated in SYMBOLS-Sonata [30, 31] software, in order to visualize the complex modes of the system. However, the external damping in sub models of shaft has been considered as discrete or finite. In this case, the effects of concentrated damper are closely linked to the complex character of modes. The simulation rig consists of a hollow rotating shaft with hub elements. In this simulation 10 reticules are used, so that flexural behaviour may be apparent. The two ends are well supported on

- 10.1515/jtam-2016-0015
Downloaded from PubFactory at 08/17/2016 09:14:57AM
via Delhi Technological University

a self-aligning bearing, so as adjust any kind of misalignment. The length of the beam is taken as 5 m long and external and internal diameters are 0.02 m and 0.01 m, respectively. The elasticity of material is taken as $104.5e^9$ N/m^2 and density of material is taken as 4420 kg/m^3. The damping coefficient of dissipative coupling is considered as $R_c = 0.002$ Ns/m. It has been assumed, that in-span discrete damper permits motion to the rotor and at the same time leads to substantial energy dissipation.

Simulation is performed for the parameters, as given in Table-1, considering discrete external damping, $R_a = 0.020$ and excitation frequency, $\Omega = 5$ Hz or 31.41 rad/s. To reduce the simulation time and running the simulation effectively, an initial momentum of 0.001 kg-m^2 was also given to 3$^{\text{rd}}$ reticule. Figure 4 shows the limit orbits of the rotor shaft, due to loading of the motor. The significant feature of the simulation is that the spinning speed of the shaft gets latched at 22.392 rad/s, as the first critical speed of instability, $\dot{\theta}_{1^{\text{st}} \bmod e}$ and matches nearly with the calculated value of shaft spinning speed (latched) $\dot{\theta}(t)$ (Table 1), which is equal to 22.266 rad/s. The analysis has been done at the point of contact with the discrete external damping.

Table 1. Simulation parameters

Parameter	Value
Length of rotor	$L_{\text{beam}} = 5$ m
Number of elements	$N_{\text{elem}} = 10$
Modulus of elasticity for the rotor shaft material	$E = 104.5e9$ N/m^2
Density of the rotor shaft material	$\rho = 4420$ kg/m^3
Internal radius of the shaft	$R_i = 0.01$ m
External radius of the shaft	$\mathrm{R}_o = 0.02$ m
Dissipative coupling coefficient	$R_c = 0.002$ N.m.s
Excitation frequency	$\Omega = 5$H z (for first mode) $\Omega = 30$ Hz (for second mode)
Internal damping coefficient of the rotor shaft	$\mu_i = 1.0e - 4$ Ns/m
Discrete External Damping Coefficient of the rotor shaft	$R_a = 0.020$ Ns/m (for first mode) $R_a = 6.00$ Ns/m (for second mode)
Shaft spinning speed (entrained) calculated	$\dot{\theta}(t) = 22.392$ rad/s, 95.405 rad/s, (For Mode 1, 2, respectively)

Further, coefficient of damping for in-span concentrated discrete damper is increased to 6.0 Ns/m and excitation frequency Ω of the motor is increased to 30 Hz or 188.327 rad/sec. One may achieve the second threshold speed of

- 10.1515/jtam-2016-0015
Downloaded from PubFactory at 08/17/2016 09:14:57AM
via Delhi Technological University

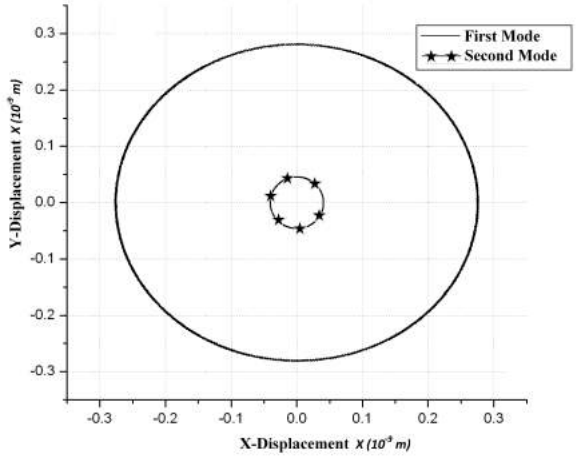

Fig. 4. Limiting orbit of rotating shaft (at point of contact with in span discrete external damping) at first two undamped natural modes

Table 2. Comparison of natural frequency

Description	Calculated Value	Numerical Value	% Error
First mode natural frequency	3.414 Hz	3.400 Hz	0.41%
Second mode natural frequency	13.66 Hz	13.600 Hz	0.44%

the shaft, shown in Fig. 3, as second mode. It is depicted from the figure, that the amplitudes of first two natural modes as trajectories of limit orbits, which are superimposed on the same plot. The simulated value of the natural modes machetes nearly exact to the calculated natural modes, as given in Table 2. The interesting phenomenon, observed from this simulation, is that one obtains the natural undamped modes in this case. The result may also be analysed through Fast Fourier Transform (FFT) analyser tool, as shown in Figs 5(a)–5(b), where first two natural frequencies for natural modes are superimposed.

The animation of the limiting orbits is also carried out to visualize the phenomenon of undamped vibration through animated frames, as shown in Figs 6(a)–6(b). The animation shows, that regenerative energy in the shaft, due to internal damping is dissipated through the discrete damper and the dissipative coupling between drive and the rotor shaft. If excitation frequency is more, then the shaft speed will not increase, but the slip between drive and shaft will increase due to loading of drive.

- 10.1515/jtam-2016-0015
Downloaded from PubFactory at 08/17/2016 09:14:57AM
via Delhi Technological University

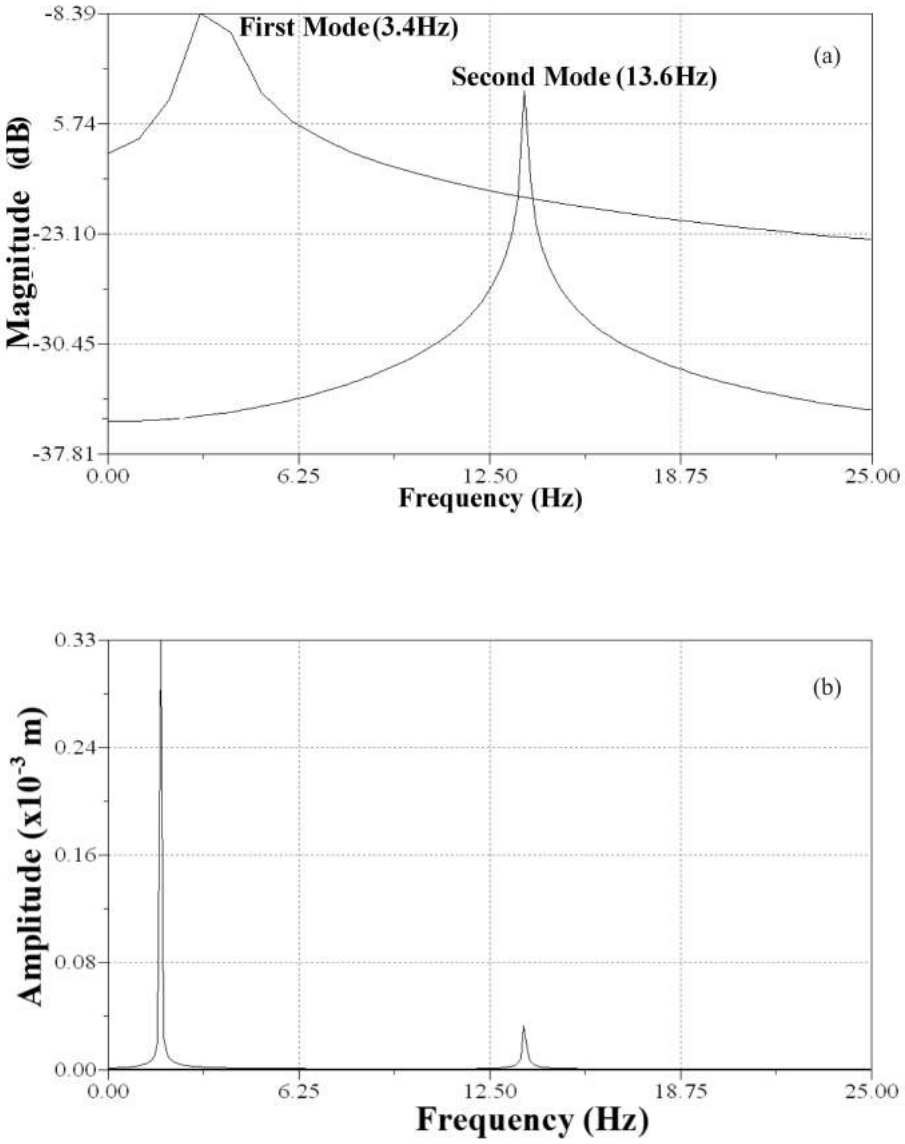

Fig. 5. (a) Superimposed frequency responses at first two undamped natural modes; (b) Amplitude of first two undamped natural modes

- 10.1515/jtam-2016-0015
Downloaded from PubFactory at 08/17/2016 09:14:57AM
via Delhi Technological University

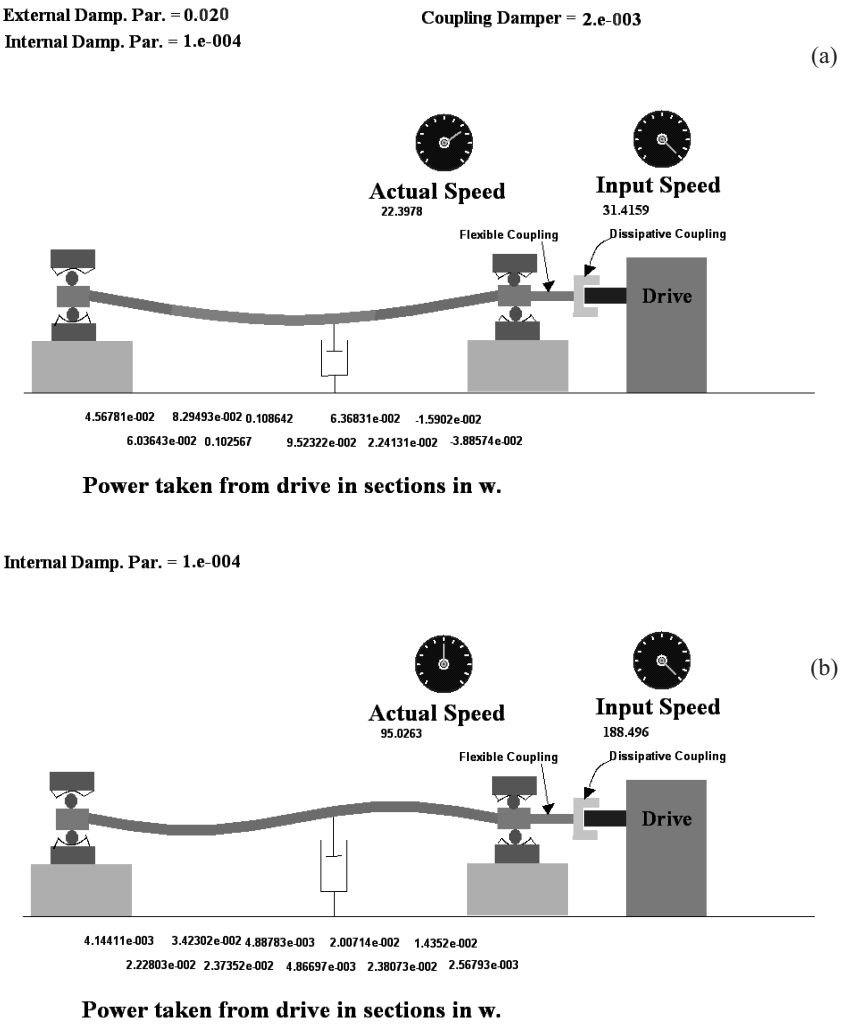

Fig. 6. (a) First mode of vibration of rotor shaft with in- span concentrated external damping $R_a = 0.020$, $\mu_i = 1e-4$, input speed = 31.41 rad/s and actual speed = 22.392rad/s; (b) Second mode of vibration of rotor shaft with in- span concentrated external damping $R_a = 6.00$, $\mu_i = 1e-4$, input speed = 188.496 rad/s and actual speed = 95.490rad/s

- 10.1515/jtam-2016-0015
Downloaded from PubFactory at 08/17/2016 09:14:57AM
via Delhi Technological University

5. Conclusions

It has been demonstrated, that in-span discrete external damping as an isolated damper can be included in the extended Lagrangian-Hamiltonian formulation, that permits a general formulation of the dissipation effects in this new extension. The theory is further used to illustrate the significance of complex modes in vibrations of rotating shafts, which has been taken as a case study. An interesting phenomenon of limiting dynamics of a rotor shaft with in-span external damper through a dissipative coupling has been obtained. The dynamic behaviour has been analysed through extended Lagrangian-Hamiltonain formulation for fields. The case study has been analysed theoretically and numerically. The study has further examined the various aspects of limiting dynamics of the rotor shaft and validated through simulation results. Further, the study demonstrated, that the regenerative energy in the shaft, due to elasticity/stiffness is dissipated partially through in-span external damper and the dissipative coupling. Limiting dynamics basically occurred due to the balance of power imported by internal damping from the shaft spin and dissipation of power by in-span external isolated discrete damper. Some portion of the energy has also been dissipated in the coupling and a part of action of internal damping, which acted as an external damping. The animation frames of the system have depicted the entrainment phenomenon of the whirl speed at different natural frequencies.

This new extension of Lagrangian-Hamiltonian formulation may be further used to illustrate the damped modes in vibration of cables and rods. Moreover, the concepts can also be employed to analyze the cracked beams and structures through this new extension.

Nomenclature:

$A_n =$ Amplitude of n^{th} mode of the rotor

$EI =$ Rigidity of the continuous rotor

$H^* =$ Umbra-Hamiltonian of the system

$I_d =$ Rotary inertia of the rotor

$L_{\text{beam}} =$ Length of beam

$N_{\text{elem}} =$ Number of elements

$D_i =$ Internal Diameter

$D_o =$ External Diameter

- 10.1515/jtam-2016-0015
Downloaded from PubFactory at 08/17/2016 09:14:57AM
via Delhi Technological University

$\rho =$ Material density

$\mu_i =$ Internal Damping Coefficient

$R_a =$ Discrete External Damping Coefficient

$\dot{\theta}(t) =$ Shaft Spinning Speed

$R_c =$ Damping coefficient of dissipative coupling

$V =$ Infinitesimal generator of rotational SO (2) group

$V_t =$ Real time component of infinitesimal generator

$V_\eta =$ Umbra time component of infinitesimal generator

$n =$ Mode number

$p\,(\eta) =$ Umbra-time momentum

$p(t =$ Real-time momentum

$q(t) =$ Generalized displacement in real time

$q\,(\eta) =$ Generalized displacement in umbra-time

$\dot{q}(t) =$ Generalized velocity in real time

$\dot{q}\,(\eta) =$ Generalized velocity in umbra-time

$x_i\,() =$ Linear displacements in real time or umbra-time, where $i = 1, \ldots, n$

$\dot{x}_i\,() =$ Linear velocity in real time or umbra-time, where $i = 1, \ldots, n$

$t =$ Real-time in s.

$\Omega =$ Excitation frequency in rad/s.

$\Omega_n =$ Natural frequency of the rotor shaft in rad/s.

$\eta =$ Umbra-time in s.

$\omega =$ constant angular velocity

$(\ ) =$ Angular displacement in umbra-time or real time in rad.

$\dot{\theta}\,(\ ) =$ Angular velocity of the shaft in umbra-time or real time in rad/s.

$L =$ Umbra-Lagrangian density

$\rho =$ Mass density of rotor shaft

$\mu_a =$ External damping of the beam

- 10.1515/jtam-2016-0015
Downloaded from PubFactory at 08/17/2016 09:14:57AM
via Delhi Technological University

$\mu_i =$ Internal damping of the beam

$\gamma^* =$ Damping ratio

$u_i(t) =$ Real displacement coordinates of beam

$u_i(\eta) =$ Umbra- displacement coordinates of beam

$H =$ Umbra-Hamiltonian density

H_i, $H_e =$ Interior and exterior umbra-Hamiltonian density.

Appendix: Umbra-Lagrangian density and generalized variational formulation

The umbra-Lagrangian density is a function, defined on an extended manifold comprising of real time, umbra and real displacements and velocities, and up to second derivatives of real and umbra displacement with respect to space coordinates x, which may be written as follows:

$$(A1) \quad L = f\left(\begin{array}{l} t, x, U(t,x,a), V(t,x,a), \dot{U}(t,x,a), \dot{V}(t,x,a), \partial_x U(t,x,a), \\ \partial_x \dot{\partial}_x V(t,x,a), U(t,x,a), \partial_x \dot{V}(t,x,a), \partial_{x^2} U(t,x,a), \partial_{x^2} V(t,x,a), \\ U(t,x,b), V(t,x,b), \dot{U}(t,x,b), \dot{V}(t,x,b), \partial_x U(t,x,b), \partial_x V(t,x,b), \\ \partial_x \dot{U}(t,x,b), \partial_x \dot{V}(t,x,b), \partial_{x^2} U(t,x,b), \partial_{x^2} V(t,x,b) \end{array}\right).$$

The Lagrangian density may be written as: $L(t, x, M(t,x,a),\ U(t,x,b),\ V(t,x,b),\ \dot{U}(t,x,b),\ \dot{V}(t,x,b), \dots)$, where a and b are two members of the same homotopic family [29], $M(t,x,a)$is the modulatory part and may be represented as:

$$(A2) \qquad M(t,x,a) \approx \left(\begin{array}{l} U(t,x,a), V(t,x,a), \dot{U}(t,x,a), \dot{V}(t,x,a), \partial_x U(t,x,a), \\ \partial_x V(t,x,a), \partial_x \dot{U}(t,x,a), \partial_x \dot{V}(t,x,a), \partial_x^2 U(t,x,a), \\ \partial_x^2 V(t,x,a) \end{array}\right).$$

Now the action integral may be expressed as:

$$(A3) \qquad I = \int_{t_0}^{t_1} \int_{x_0}^{x_1} L\,(.)\, dtdx.$$

This action integral will be subjected to recursive minimization. The present discussion is illustrated, using a one-dimensional continuous system. For a clear exposition, the variations in variables may be represented as follows:

$$U^*(t,x,b) = U(t,x,b) + \varepsilon \hat{U}(t,x,b), \quad \partial_x U^*(t,x,b) = \partial_x U(t,x,b) + \varepsilon \partial_x \hat{U}(t,x,b),$$

$$V^*(t,x,b) = V(t,x,b) + \varepsilon \hat{V}(t,x,b), \quad \partial_x V^*(t,x,b) = \partial_x V(t,x,b) + \varepsilon \partial_x \hat{V}(t,x,b),$$

$$\partial_{(t,b)} U^*(t,x,b) = \partial_{(t,b)} U(t,x,b) + \varepsilon \partial_{(t,b)} \hat{U}(t,x,b),$$

- 10.1515/jtam-2016-0015
Downloaded from PubFactory at 08/17/2016 09:14:57AM
via Delhi Technological University

$$\partial_{(t,b)}V^*(t,x,b) = \partial_{(t,b)}V(t,x,b) + \varepsilon\partial_{(t,b)}\hat{V}(t,x,b),$$

$$\partial_{x^2}U^*(t,x,b) = \partial_{x^2}U(t,x,b) + \varepsilon\partial_{x^2}\hat{U}(t,x,b),$$

$$\partial_{x^2}V^*(t,x,b) = \partial_{x^2}V(t,x,b) + \varepsilon\partial_{x^2}\hat{V}(t,x,b),$$

It is required to propose a fixed end-points perturbation scheme on the trajectorial function $(U(t,x,b),\dots)$, relating to the modulatory function $M(t,x,a)$ and considering path homotopic loops, based at origins as $J:[t_1,t_2]\times[0,1]\to Y$, such that $J(t_1,\xi)=0$ and $J(t_2,\xi)=0$ with $\xi\in[0,1]$, the action integral with one-dimensional variational problem, may be expressed as:

$$(A4)\qquad I(\varepsilon) = \int_{t_o}^{t_1}\int_{x_o}^{x_1} L\left(t,x,M(t,x,a),U^*(t,x,b),V^*(t,x,b),\dots\right)dt\,dx.$$

Extremization of the action integral implies $\delta I(\varepsilon)_{\varepsilon=0}=0$, which leads to $\nabla_\varepsilon I(\varepsilon)|_{\varepsilon=0}=0$. The condition of extremality results into umbra-Lagrange's field equations and boundary conditions at two ends. Now for detailed proof of umbra-Lagrange's field equation, it is possible to use concise notations as:

$$U(t,x,b)=U_1(t,x,b),\quad V(t,x,b)=U_2(t,x,b),\quad \partial_x U_i(t,x,b)=U_{i,x}(t,x,b),$$

$$\text{and } \partial_{x^2}U_i(t,x,b)=U_{i,x^2}(t,x,b),$$

where $i=1,2$. However, in the above notations, the cognizance of the variance of the vector field is not taken. Let us consider a one-dimensional continuous system, defined over the closed domain $x_0\le x\le x_1$ and, t_1 and t_2 are the times, at which configurations of the system are specified and δ is the variation. On adopting such notational changes, variations in the action integral may be written as:

$$(A5)\quad \delta I = \varepsilon\int_{t_0}^{t_1}\int_{x_0}^{x_1}\sum_{i=1}^{2}\left\{\begin{array}{l}\dfrac{\partial L}{\partial U_i(t,x,b)}\hat{U}_i(t,x,b)+\dfrac{\partial L}{\partial \dot{U}_i(t,x,b)}\dot{\hat{U}}_i(t,x,b)\\ +\dfrac{\partial L}{\partial \dot{U}_{i,x}(t,x,b)}\dot{\hat{U}}_{i,x}(t,x,b)\\ +\dfrac{\partial L}{\partial U_{i,x}(t,x,b)}\hat{U}_{i,x}(t,x,b)\\ +\dfrac{\partial L}{\partial U_{i,x^2}(t,x,b)}\hat{U}_{i,x^2}(t,x,b)\end{array}\right\}\partial t\,\partial x = 0.$$

- 10.1515/jtam-2016-0015
Downloaded from PubFactory at 08/17/2016 09:14:57AM
via Delhi Technological University

Through integration by parts of Eq. (A5), one obtains:

$$\delta I = \varepsilon \int_{t_0}^{t_1}\int_{x_0}^{x_1}\sum_{i=1}^{2}\left[\begin{array}{l}\left\{\begin{array}{l}\dfrac{\partial L}{\partial U_i(t,x,b)} - \dfrac{\partial}{\partial t}\dfrac{\partial L}{\partial \dot{U}_i(t,x,b)} \\ -\dfrac{\partial}{\partial x}\left(\dfrac{\partial L}{\partial U_{i,x}(t,x,b)}\right)\end{array}\right\}\hat{U}_i(t,x,b) \\ +\dfrac{\partial}{\partial t\,\partial x}\left(\dfrac{\partial L}{\partial \dot{U}_{i,x}(t,x,b)}\right)\hat{U}_i(t,x,b) \\ +\dfrac{\partial}{\partial x^2}\left(\dfrac{\partial L}{\partial U_{i,x^2}(t,x,b)}\right)\hat{U}_i(t,x,b)\end{array}\right] dtdx$$

$$+\int_{t_0}^{t_1}\sum_{i=1}^{2}\left[\begin{array}{l}\dfrac{\partial L}{\partial U_{i,x}(t,x,b)}\hat{U}_i(t,x,b)\Big|_{x_0}^{x_1} \\ -\dfrac{\partial}{\partial t}\left(\dfrac{\partial L}{\partial \dot{U}_{i,x}(t,x,b)}\right)\hat{U}_i(t,x,b)\Big|_{x_0}^{x_1} \\ +\dfrac{\partial L}{\partial U_{i,x^2}(t,x,b)}\hat{U}(t,x,b)\Big|_{x_0}^{x_1} \\ -\dfrac{\partial}{\partial x}\left(\dfrac{\partial L}{\partial U_{i,x^2}(t,x,b)}\hat{U}_i(t,x,b)\right)\Big|_{x_0}^{x_1}\end{array}\right] dt = 0. \tag{A6}$$

Considering the following notations as $t \times a = t$, $t \times b = \eta$ with $U_i(t,x,b) = u_i(\eta,x)$ and $U_i(t,x,a) = u_i(t,x)$, where $i = 1,2$, the first part of the Eq. (A6) gives umbra-Lagrange's field equation for one-dimensional continuous systems, when equated to zero. Now re-arranging first part in $\eta - t$ form, umbra field equations may be written after taking the limit $\eta \to t$ as:

$$\frac{\partial}{\partial t}\left\{\lim_{\eta\to t}\left(\frac{\partial L}{\partial \dot{u}_i(\eta,x)} - \frac{\partial}{\partial x}\left(\frac{\partial L}{\partial \dot{u}_{i,x}(\eta,x)}\right)\right)\right\}$$

$$-\lim_{\eta\to t}\left(\begin{array}{l}\dfrac{\partial L}{\partial u_i(\eta,x)} - \dfrac{\partial}{\partial x}\left(\dfrac{\partial L}{\partial u_{i,x}(\eta,x)}\right) \\ +\dfrac{\partial}{\partial x^2}\left(\dfrac{\partial L}{\partial u_{i,x^2}(\eta,x)}\right)\end{array}\right) = 0, \tag{A7}$$

where $i = 1,2$, and $u_{i,x} = \partial u_i/\partial x$.

The second part of Eq. (A6) gives the boundary conditions, when equated to zero, which reflects the physical (geometric) conditions at the two ends and may be expressed as:

$$\lim_{\eta\to t}\left[\frac{\partial L}{\partial u_{i,x}(\eta,x)} - \frac{\partial}{\partial x}\left(\frac{\partial L}{\partial u_{i,x^2}(\eta,x)}\right) - \frac{\partial}{\partial \eta}\left(\frac{\partial L}{\partial \dot{u}_{i,x}(\eta,x)}\right)\right]\hat{u}_i(\eta,x)|_{x_0}^{x_1} = 0 \tag{A8a}$$

- 10.1515/jtam-2016-0015
Downloaded from PubFactory at 08/17/2016 09:14:57AM
via Delhi Technological University

$$(A8b) \qquad \lim_{\eta \to t} \frac{\partial L}{\partial u_{i,x^2}(\eta, x)} \hat{u}_{i,x}(\eta, x) \Big|_{x_0}^{x_1} = 0,$$

where $i = 1, 2$. There exist the following possibilities in the boundary conditions. Either $\lim_{\eta \to t} \left[\frac{\partial L}{\partial u_{i,x}(\eta, x)} - \frac{\partial}{\partial x} \left(\frac{\partial L}{\partial u_{i,x^2}(\eta, x)} \right) - \frac{\partial}{\partial \eta} \left(\frac{\partial L}{\partial \dot{u}_{i,x}(\eta, x)} \right) \right] = 0$ or $u_i(t, x) = 0$, and either $\lim_{\eta \to t} \frac{\partial L}{\partial u_{i,x^2}(\eta, x)} = 0$ or $u_{i,x}(t, x) = 0$, at either of the ends $x = x_0$ and $x = x_1$. Equation (A7) is the dynamical equations, governing the motion of a one-dimensional continuous system (or field) with generalized co-ordinates. The solution of this equation, combined with the appropriate boundary conditions, given by Eqs. (A8a) and (A8b), specify the true motion of such continuous system, the motion that ensures the action integral of Eq. (A4) to be extreme.

REFERENCES

[1] Boyer, T. H. Continuous Symmetries and Conserved Currents. *Annals of Physics,* **42** (1967), No. **3**, 445–466.

[2] Sarlet, W., F. Cantrijn. Generalizations of Noether's Theorem in Classical Mechanics. *SIAM Rev.*, **23** (1981), No. **3**, 467

[3] Katzin, G. H., J. Levine. A Gauge Invariant Formulation of Time-dependent Dynamical Symmetry Mappings and Associated Constants of Motion for Lagrangian Particle Mechanics. *Int. J. Math. Phys.*, **17** (1976). No. **7**, 1345.

[4] Damianou, P. A., C. Sophocleous. Classification of Noether Symmetries for Lagrangians with Three Degree of Freedom. *Nonlinear Dynamics*, **36** (2004), No. **1**, 3–18.

[5] Mukherjee, A. Junction Structures of Bondgraph Theory from Analytical Mechanics Viewpoint, Proc. of CISS-1st Conference of International Simulation Societies, Switzerland, Zurich, 1994, 661-664.

[6] Brown, F. T. Engineering System Dynamics, 2-nd ed, CRC, Taylor & Francis, 2007.

[7] Mukherjee, A., V. Rastogi, A. DasGupta. A Methodology for Finding Invariants of Motion for Asymmetric Systems with Gauge-transformed Umbra Lagrangian Generated by Bond Graphs. *Simulation*, **82** (2006), No. **4**, 207–226.

[8] Mukherjee, A., V. Rastogi, A. DasGupta. A Study of a Bi-Symmetric Electro-mechanical System through Umbra Lagrangian Generated by Bond Graphs, and Noether's Theorem. *Simulation*, **83** (2007), No. **9**, 611–630.

[9] Mukherjee, A., V. Rastogi, A. DasGupta. Extension of Lagrangian-Hamiltonian Mechanics for Continuous Systems-Investigation of Dynamics of a One Dimensional Internally Damped Rotor driven through a Dissipative Coupling. *Nonlinear Dynamics*, **58** (2009), No. **1**, 107–127.

- 10.1515/jtam-2016-0015
Downloaded from PubFactory at 08/17/2016 09:14:57AM
via Delhi Technological University

[10] Mukherjee, A., V. Rastogi, A. DasGupta. Revisiting Umbra-Lagrangian-Hamiltonian Mechanics: Its Variational Foundation and Extension of Noether's Theorem and Poincaré-Cartan Integral. *International Journal of Non-Linear Mechanics*, **46** (2011), No. **5**, 745–757.

[11] Rastogi, V. Extension of Lagrangian-Hamiltonian Mechanics, Study of Symmetries and Invariants, Ph. D. thesis, Kharagpur, Indian Institute of Technology, 2005.

[12] Bogoliubov, N. Perturbation Theory in Nonlinear Mechanics. *Collection of Works of Building Mechanics Institute*, **4** (1950), 9–34, (In Russian).

[13] Meirovitch, L. Elements of Vibration Analysis, McGraw-Hill Book Company,1984.

[14] Krämer, E. Dynamics of Rotors and Foundations, Springer-Verlag, 1993.

[15] Kimball, A. L. Internal Friction Theory of Shaft Whirling. *General Electrical Review*, **27** (1924), 244.

[16] Dimentberg, M. Flexural Vibrations of Rotating Shafts, Butter Worth, London, England, 1961.

[17] Gunter, E. J. Rotor-Bearing Stability, Proceeding of the First Turbo Machinery Symposium, 1972, 119–141.

[18] Ehrich, F. E. Shaft Whirl Induced by Rotor Internal Damping. *Journal of Applied Mechanics*, **31** (1964), 279–282.

[19] Crandall, S. H. The Role of Damping in Vibration Theory, *Journal of Sound and Vibration*, **11** (1970), 3–18.

[20] Zorzi, E. S., H. D. Nelson. Finite Element Simulation of Rotor Bearing Systems with Internal Damping. *Journal of Engineering Power*, *ASME trans.,* **99** (1977), 71–76.

[21] Melanson, J., J. W. Zu. Free Vibration and Stability Analysis of Internally Damped Rotating Shafts with General Boundary Conditions. *J. Vibration Acoustics, ASME Trans.,* **120** (1998), 776–783.

[22] Genta, G. On a Persistent Misunderstanding of the Role of Hysteretic Damping in Rotor Dynamics. *J. Vibration Acoustics, ASME Trans.,* **126** (2004), 459–461.

[23] Vance, J. M., J. Lee. Stability of High Speed Rotors with Internal Friction. *J. of Engineering for Industry, Trans. ASME*, Series B, **96** (1974), No. **3**, 960–966.

[24] Szoic, T. On the Discrete Continuous Modelling of Rotor System for the Analysis of Coupled Lateral Vibration. *Internaltional Journal of Rotating Machinery*, **6** (2000), No. **2**, 135–149.

[25] Jivkov, V., E. Zahariev. Stability and Non-Stationary Vibrations of Rotor in Elasto–Viscous Field, Mechanics Based Design of Structures and Machines. *Taylor & Francis Group,* **42** (2014), No. **1**, 35 – 55.

[26] Krenk, S. Complex Modes and Frequencies in Damped Structural Vibrations. *Journal of Sound and Vibration*, **270** (2004), 981–996.

[27] Noether, E. Invariante Variationsprobleme. *Ges. Wiss. Gottington*, **2** (1918), 235.

- 10.1515/jtam-2016-0015
Downloaded from PubFactory at 08/17/2016 09:14:57AM
via Delhi Technological University

[28] Mukherjee, A., R. Karmakar, A. Samantaray. Modelling and Simulation of Engineering System through Bond Graph, New Delhi, Narosa Publishing House, reprinted by CRC press for North America and by Alpha Science for Europe, 2000.

[29] Karnopp, D. C., R. C. Resenberg, D. L. Margolis. System Dynamics: A Unified Approach, USA, John-Wiley and Sons Inc., 1990.

[30] Mukherjee, A., A. K. Samantaray. SYMBOLS-2000 User's Manual, India, Kharagpur, High-Tech Consultants, STEP Indian Institute of Technology, 2000.

[31] Internet `URL://www.Symbols2000.com`, 2000.

[32] Arnold, V. I. Mathematical Methods of Classical Mechanics, New York – Heidelberg-Berlin, Springer-Verlag, 1974, 88.

[33] Olver, P. Application of Lie Groups to Differential Equations, Springer-Verlag, 1986.

[34] Hassani, S. Mathematical Physics, New York-Heidelberg-Berlin, Springer-Verlag, 1999, 936.

[35] Munkres, J. R. Topology: A First Course, New Delhi, Prentice Hall of India Private Limited, 1994.

- 10.1515/jtam-2016-0015
Downloaded from PubFactory at 08/17/2016 09:14:57AM
via Delhi Technological University

Research Article – JTEN – 2015 – 104

Journal of Thermal Engineering
Yildiz Technical University Press, Istanbul, Turkey
Vol. 2, No. 5, pp. 954-961, October, 2016.

http://eds.yildiz.edu.tr/journal-of-thermal-engineering/Articles
Manuscript Received July 14, 2015; Accepted September 01, 2015

This paper was recommended for publication in revised form by Regional Editor Balaram Kundu

ENERGY AND EXERGY ANALYSIS OF A WASTE HEAT DRIVEN CYCLE FOR TRIPLE EFFECT REFRIGERATION

***Manoj Dixit**
Centre for Energy Studies,
Indian Institute of Technology, Delhi
New Delhi, Delhi, India

Akhilesh Arora
Department of Mechanical Engineering, Delhi Technological University
Delhi, Delhi, India

S. C. Kaushik
Centre for Energy Studies,
Indian Institute of Technology, Delhi
New Delhi, Delhi, India

Keywords: Exergy, Waste heat, triple effect, ejector organic Rankine cycle, absorption refrigeration
** Corresponding author: Phone: 91*-9540660289
E-mail address: mandix@ces.iitd.ac.in

ABSTRACT

In this paper waste heat driven triple effect refrigeration cycle is analyzed from the viewpoint of both energy and exergy concept of thermodynamics. In this cycle ejector organic Rankine cycle, absorption refrigeration cycle and cascade vapour compression refrigeration cycles are integrated in order to obtain a range of temperature for varied simultaneous use. Exergy analysis determines the destruction and losses of exergy in various components and hence in overall system. Exergy efficiencies provide measure of approach to ideality while exergy destruction and losses provide measure of the deviation from ideality. Energy efficiency is found to be around 21.79% while exergy efficiency is 12.91%. The maximum thermodynamic irreversibility occurs in heat recover vapour generator followed by ejector and condenser of combined ejector organic Rankine refrigeration cycle.

INTRODUCTION

Energy plays a significant role in the development of a country. Industries require huge amount of energy which is being presently supplied by fossil fuels. Rapid consumption of primary energy sources like fossil fuels to meet the burgeoning demand of energy is not only causing their fast depletion but also causing global environmental degradation. At the same time, a large amount of low grade waste thermal energy is released in the biosphere by the industries, which further causes ecological imbalance. Up to 70% of energy input in the manufacturing sector is lost in Canada (Galanis et al., 2009). In the US, industrial waste heat amounts to about 20–50% (Inc. BCS. 2008). In the UK heat losses in the industrial sector could represent few tens of TWh (Retting et al., 2011). Therefore, utilization of waste heat for power generation, refrigeration and air conditioning, heating etc. will be beneficial both from the view point of energy as well as environment. Waste heat sources are grouped in three categories based on temperature level (Tchanche BF et al., 2011): low (<230 $^{\circ}C$), medium (230–650 $^{\circ}C$) and high (>650 $^{\circ}C$)

There are many industrial processes where heat is available as low temperature waste heat. Similarly, there are numerous applications which require cooling at different temperatures and at different rates. Thus, there exist an opportunity to utilize the otherwise waste heat to obtain cooling by integration of various cooling technologies.

It is a well proven that absorption refrigeration cycle (ARC) can be operated easily by waste heat. The required temperature of the heat source varies from 60 $^{\circ}C$ to 200 $^{\circ}C$, depending on its configuration. The required generator temperature for single effect cycle is 80-100 $^{\circ}C$(Kaushik et al., 2009), double effect cycle 120-150 $^{\circ}C$ (Arora et al., 2016 a), and half effect 60-75 $^{\circ}C$ (Arora et al., 2016 b). Triple effect cycles require generator temperature even higher than 150 $^{\circ}C$. The Organic Rankine cycle (ORC) are capable of converting low quality thermal energy into high grade mechanical work or

electrical power. Heat source with temperature up to 230 °C can operate an ORC (Tchanche BF et al., 2011). Ejector refrigeration cycle (ERC) can also be operated by a waste heat having temperature up to 65 °C.

Many efforts have been made by researchers to combine various cycles for efficient utilization of waste heat for different purposes. Sun et al. (1996) proposed a combined ejector absorption cycle for refrigeration and air conditioning in order to obtain high coefficient of performance (COP). Hong et al. (2011) proposed the combination of double effect ARC and ejector. The COP of the combined cycle was reported to be 30% higher than that of conventional single effect ARC. Wang et al. (2009) theoretically studied a novel combined power and ejector refrigeration cycle and concluded that heat recovery vapour generator (HRVG) accounts for highest exergy destruction. Dai et al. (2009) combined the ejector refrigeration cycle with the Rankine cycle and found that the exergy loss was maximum in heat addition process, followed by the ejector.

Zheng and Weng (2010) proposed a combined organic Rankine and ejector refrigeration cycle. The turbine of Rankine cycle produced power and its exhaust was used to drive the ejector cycle for refrigeration. Ejector suffered highest irreversibility. Habibzadeh et al. (2013) studied the combined organic Rankine cycle and the ejector refrigeration cycle with various substances like R123, R254fa, R141b, R601a and R600a. For power to refrigeration ratio of 10, R601a showed the highest thermal efficiency and the lowest exergy losses. Many other researchers (Goswami and Xu, 1999; Hasan et al., 2002; Martin and Goswami, 2006) also studied the combined power and ejector refrigeration cycles. Zhang and Lior (2007) proposed many configurations for combined cooling and power applications, having large cooling capacity, but they require high temperature (450 °C).

Although a lot of work is reported in literature on the combined ejector absorption refrigeration system, combined vapour compression ejector refrigeration system for cooling and heating, combined power and refrigeration system etc., yet no/little work is reported that combine ARC, ERC, VCR cascaded and ejector organic Rankine cycle (EORC) for simultaneous production of cooling of wide range using single waste heat source.

In this paper ARC, EORC and VCR cascaded are combined. The waste heat is used to operate EORC and ARC directly while VCR cycle is operated by turbine power. For thermodynamic performance both energy and exergy analysis is carried out. Exergy analysis provides more meaningful information as compared to energy analysis. It helps in identifying site, quantity and source of thermodynamic inefficiency. Exergy destruction in each component is evaluated in order to find out the direction for potential improvement. In order to investigate the influence of various operating parameters on system performance, the parametric analysis is also performed.

SYSTEM DESCRIPTION

The waste heat driven triple effect cycle is shown in fig. 1. The industrial waste heat transfers its heat to HRVG (1-2) and generator (2-12).The working substance used in ORC and ERC is R-141b. The superheated vapour of R-141b (4) is generated in HRVG and expanded in turbine. The turbine exhaust (5) act as a primary motive fluid for ERC (5-6-7-9-10-11). At the exit of the nozzle section of the ejector, the high velocity primary refrigerant vapours create vacuum before mixing section and thereby extracting secondary refrigerant vapour (11) from evaporator. This causes cooling in ejector organic Rankine cycle (EORC). The mixture of primary and secondary fluid (6) is condensed in condenser-1. The work output of turbine is fed to two compressors of VCR cascade cycle (23-24-25-26-27-28-29-30-31-32-33-34). The refrigerant used in both high temperature cycle (HTC) and low temperature cycle (LTC) is nitrous oxide (N_2O). The single effect LiBr-H_2O absorption refrigeration cycle (13-14-15-16-17-18-19-20-21-22) consists of generator, condenser-2, evaporator-2, absorber, solution heat exchanger (SHE), pump-2 (P-2) and throttle valves (TV-2 and TV-3). The description of ARC cycle is given elsewhere (Herold et al., 1996).

THERMODYNAMIC ANALYSIS

To perform the thermodynamic analysis of the triple effect refrigeration cycle, the assumptions made are:

(1) The cycle is under steady state operation.

(2) Pressure drop in pipes is neglected.

(3) Pump work is neglected

(4) The states at the exit of condenser and evaporator are saturated liquid and saturated vapour respectively.

(5) Chemical, kinetic and potential exergies are neglected and only physical exergy is considered.

(6) In order to avoid crystallization, temperature of strong solution exiting the solution heat exchanger is kept 7-8 °C above crystallization temperature.

(7) Lithium bromide solution in the absorber and generator are in equilibrium state at their respective pressure and temperature.

(8) The Lithium bromide solution exiting the generator and absorber are saturated.

(9) Heat loss to the surrounding is neglected.

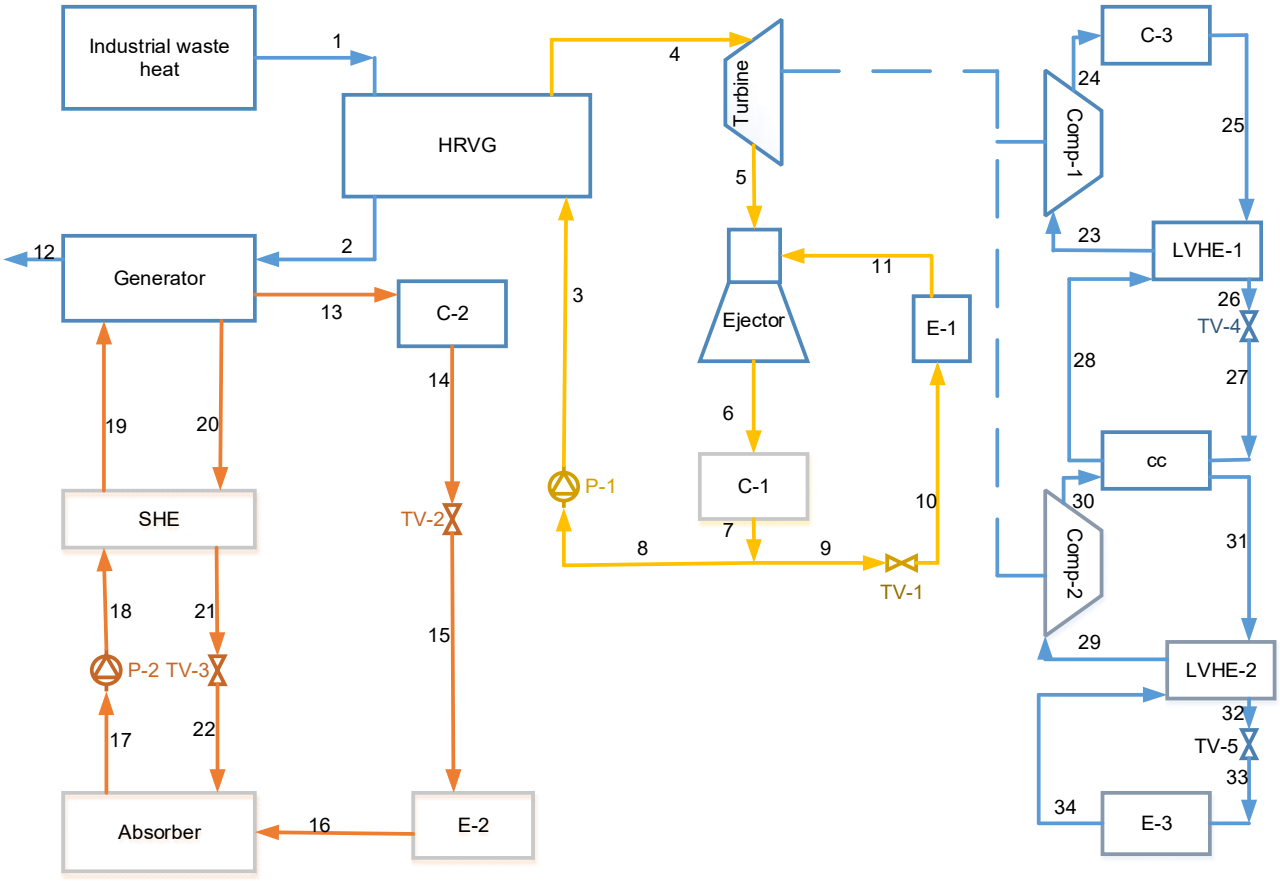

Figure 1 Schematic diagram of waste heat driven triple effect refrigeration cycle

For the thermodynamic analysis, the required parameters are given in Table 1.

The energy and exergy analysis of the refrigeration system incorporates the use of concept of mass and energy conservation and second law of thermodynamics. The performance of the system, based on first law alone, can be evaluated using thermal efficiency (η_{th}) which is defined as the ratio of the cooling effect to the heat input and is described as:

$$\eta_{th} = (\dot{Q}_{e1} + \dot{Q}_{e2} + \dot{Q}_{e3})/\dot{Q}_{in} \quad (1)$$

where $\dot{Q}_{in}$ is the total heat input given by waste heat to the system and $\dot{Q}_{e1}$, $\dot{Q}_{e2}$ and $\dot{Q}_{e3}$ are the refrigeration effect in ERC, ARC and VCR cycle respectively.

The second law of thermodynamics facilitates in assessing the thermodynamic performance of the system based on exergy. For a control volume, the exergy flow rate of a fluid, considering only physical exergy, is expressed as:

$$\dot{E} = \dot{m}[(h - h_0) - T_0(s - s_0)] \quad (2)$$

Exergy balance for a control volume undergoing steady state process is expressed as:

$$\dot{E}D = \sum \dot{E}_{in} - \sum \dot{E}_{out} + (\sum \dot{Q}(1 - {}^{T_0}/_{T})_{in} + \sum \dot{Q}(1 - {}^{T_0}/_{T})_{out} \pm \sum \dot{W} \quad (3)$$

where $\dot{E}D$ is the exergy destruction rate and $\dot{E}$ is the exergy flow rate.

The exergy efficiency is expressed on the basis of second law of thermodynamics as

$$\eta_{ex} = (\Delta\dot{E}_{e1} + \Delta\dot{E}_{e2} + \Delta\dot{E}_{e3})/\dot{E}_{in} \quad (4)$$

where $\dot{E}_{in}$ is the exergy input of waste heat to the system and $\Delta\dot{E}_{e1}$, $\Delta\dot{E}_{e2}$, and $\Delta\dot{E}_{e3}$ are the exergy change in evaporator-1 of ERC, evaporator-2of ARC and evaporator-3 of VCR cycle respectively, which are expressed as:

$$\Delta \dot{E}_{e1} = \dot{E}_{11} - \dot{E}_{10} \quad (5)$$

$$\Delta \dot{E}_{e2} = \dot{E}_{16} - \dot{E}_{15} \quad (6)$$

$$\Delta \dot{E}_{e3} = \dot{E}_{34} - \dot{E}_{33} \quad (7)$$

$$\dot{E}_{in} = \dot{E}_{1} - \dot{E}_{12} \quad (8)$$

Table 1 Parameters used in the modelling

Parameters	Value
Environment temperature (°C)	15
Environment pressure (kPa)	101.35
Waste heat source temperature (°C)	160-180
Turbine inlet pressure (kPa)	900-1700
Turbine back pressure (kPa)	220-300
Turbine isentropic efficiency (%)	85
ERC evaporator temperature (°C)	-1 to -9
ARC evaporator temperature (°C)	5
VCR evaporator temperature (°C)	-85
Condenser-2 temperature (°C)	35
Condenser-3 temperature (°C)	35
Absorber temperature (°C)	35
Mass flow rate of waste flue gas (kg s^{-1})	20
Pump isentropic efficiency (%)	70
HRVG efficiency (%)	100
Pinch point temperature difference (°C)	10
Nozzle efficiency (%)	90
Mixing chamber efficiency (%)	85
Diffuser efficiency (%)	85

The relations obtained by the application of mass, energy and exergy balance to each component are outlined in Table 2.

RESULTS AND DISCUSSION

Based on the thermodynamic relations, a program is developed in engineering equation solver (EES) (Klein and Alvarado, 2005). The results thus obtained are presented and discussed in this section.

Fig. 2 shows the results of energy analysis of triple effect refrigeration cycle. It is found that about 21.79% of total waste industrial heat can be converted into useful output and rest of the energy is lost to environment.

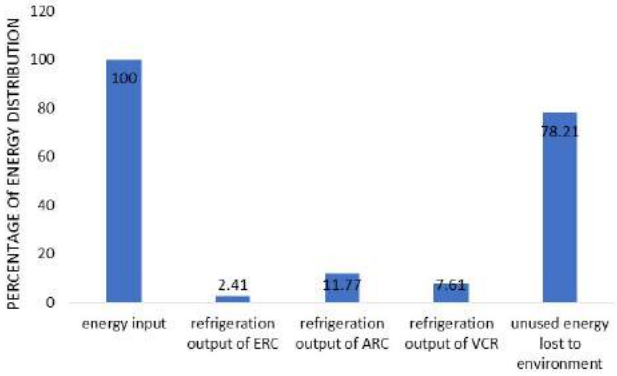

Figure 2 Percentage of energy distribution for the triple effect refrigeration cycle

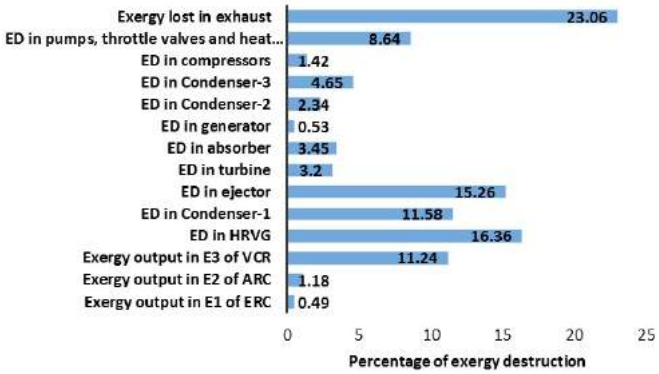

Figure 3 Percentage of exergy distribution in output and destruction for triple effect refrigeration cycle

Fig. 3 shows the result of application of exergy analysis to the triple effect refrigeration cycle. It is found that about 12.91% of the total input exergy is available as useful exergy output. Of the total exergy input, the useful exergy output of VCRC, ARC and EORC accounts for 11.24%, 1.18% and 0.49% respectively. About 23.06% of the input exergy is lost to the environment by hot flue gas and the remaining 64.03% exergy input is destroyed because of irreversibilities associated with various components and exergy loss in absorber and condenser. The second law analysis reveals that the maximum improvement is possible in HRVG as it accounts for highest exergy destruction (16.36%), followed by ejector and condenser of ejector refrigeration cycle. Therefore, from the perspective of second law of thermodynamics, HRVG, ejector and condenser-1 needs expert attention so as to enhance the overall performance of the system.

Table 2 Energy and exergy relations for the sub system of triple effect refrigeration cycle

Component	Energy relations	Exergy relations
HRVG	$\dot{m}_1(h_1 - h_2) = \dot{m}_3(h_4 - h_3)$	$\dot{E}D_{HRVG} = T_0(\dot{m}_2 s_2 - \dot{m}_1 s_1 + \dot{m}_4 s_4 - \dot{m}_3 s_3)$
Turbine	$\dot{W}_T = \dot{m}_4(h_4 - h_5)$	$\dot{E}D_T = T_0(s_5 - s_4)$
Ejector	$\dot{m}_5 h_5 + \dot{m}_{11} h_{11} = (\dot{m}_5 + \dot{m}_{11}) h_6$	$\dot{E}D_{ej} = T_0(\dot{m}_6 s_6 - \dot{m}_5 s_5 - \dot{m}_{11} s_{11})$
	$\mu = [\eta_n \eta_m \eta_d (h_{pf,n1} - h_{pf,n2,s})/(h_{mf,d,s} - h_{mf,m}$	
Condenser-1	$\dot{Q}_{c1} = \dot{m}_6(h_6 - h_7)$	$\dot{E}D_{c1} = T_0(\dot{m}_7 s_7 - \dot{m}_6 s_6 - \dot{Q}_{c1}/T_{c1})$
Evaporator-1	$\dot{Q}_{e1} = \dot{m}_{11}(h_{11} - h_{10})$	$\dot{E}D_{e1} = T_0(\dot{m}_{11} s_{11} - \dot{m}_{10} s_{10} - \dot{Q}_{e1}/T_{e1})$
Generator	$\dot{Q}_g = \dot{m}_f(h_2 - h_{12}) = \dot{m}_{13} h_{13} + \dot{m}_{20} h_{20} - \dot{m}_1$	$\dot{E}D_g = T_0(\dot{m}_{20} s_{20} + \dot{m}_{13} s_{13} + \dot{m}_{12} s_{12} - \dot{m}_{19} s_{19} - \dot{m}_2 s_2)$
Absorber	$\dot{Q}_a = \dot{m}_{16} h_{16} + \dot{m}_{22} h_{22} - \dot{m}_{17} h_{17}$	$\dot{E}D_a = T_0(\dot{m}_{17} s_{17} - \dot{m}_{16} s_{16} - \dot{m}_{22} s_{22} - \dot{Q}_a/T_a)$
Condenser-2	$\dot{Q}_{c2} = \dot{m}_{13}(h_{13} - h_{14})$	$\dot{E}D_{c2} = T_0(\dot{m}_{14} s_{14} - \dot{m}_{13} s_{13} - \dot{Q}_{c2}/T_{c2})$
Evaporator-2	$\dot{Q}_{e2} = \dot{m}_{16}(h_{16} - h_{15})$	$\dot{E}D_{e2} = T_0(\dot{m}_{16} s_{16} - \dot{m}_{15} s_{15} - \dot{Q}_{e2}/T_{e2})$
Compressor-1	$\dot{W}_{comp1} = \dot{m}_{24}(h_{24} - h_{23})$	$\dot{E}D_{comp1} = T_0 \dot{m}_{24}(s_{24} - s_{23})$
Compressor-2	$\dot{W}_{comp2} = \dot{m}_{24}(h_{30} - h_{29})$	$\dot{E}D_{comp2} = T_0 \dot{m}_{30}(s_{30} - s_{29})$
Evaporator-3	$\dot{Q}_{e3} = \dot{m}_{34}(h_{34} - h_{33})$	$\dot{E}D_{e3} = T_0(\dot{m}_{34} s_{34} - \dot{m}_{33} s_{33} - \dot{Q}_{e3}/T_{e3})$
Condenser-3	$\dot{Q}_{c3} = \dot{m}_{24}(h_{24} - h_{25})$	$\dot{E}D_{c3} = T_0(\dot{m}_{25} s_{25} - \dot{m}_{24} s_{24} - \dot{Q}_{c3}/T_{c3})$
CC	$\dot{m}_{30} h_{30} - \dot{m}_{31} h_{31} = \dot{m}_{28} h_{28} - \dot{m}_{27} h_{27}$	$\dot{E}D_{cc} = T_0[\dot{m}_{28}(s_{28} - s_{27}) + \dot{m}_{31}(s_{31} - s_{30})]$
SHE	$\dot{m}_{20} h_{20} - \dot{m}_{21} h_{21} = \dot{m}_{19} h_{19} - \dot{m}_{18} h_{18}$	$\dot{E}D_{she} = T_0[\dot{m}_{19}(s_{19} - s_{18}) + \dot{m}_{21}(s_{21} - s_{20})]$
LVHE-1	$\dot{m}_{25} h_{25} - \dot{m}_{26} h_{26} = \dot{m}_{23} h_{23} - \dot{m}_{28} h_{28}$	$\dot{E}D_{lvhe1} = T_0 \dot{m}_{23}(s_{23} - s_{28} + s_{26} - s_{25})$
LVHE-2	$\dot{m}_{31} h_{31} - \dot{m}_{32} h_{32} = \dot{m}_{29} h_{29} - \dot{m}_{34} h_{34}$	$\dot{E}D_{lvhe2} = T_0 \dot{m}_{34}(s_{29} - s_{34} + s_{32} - s_{31})$
TV-1	$h_9 = h_{10}$	$\dot{E}D_{tv1} = T_0 \dot{m}_{10}(s_{10} - s_9)$
TV-2	$h_{14} = h_{15}$	$\dot{E}D_{tv2} = T_0 \dot{m}_{15}(s_{15} - s_{14})$
TV-3	$h_{21} = h_{22}$	$\dot{E}D_{tv3} = T_0 \dot{m}_{22}(s_{22} - s_{21})$
TV-4	$h_{26} = h_{27}$	$\dot{E}D_{tv4} = T_0 \dot{m}_{27}(s_{27} - s_{26})$
TV-5	$h_{32} = h_{33}$	$\dot{E}D_{tv5} = T_0 \dot{m}_{33}(s_{33} - s_{32})$
Pump-1	$\dot{W}_{p1} = \dot{m}_3(h_3 - h_8)$	$\dot{E}D_{p1} = T_0 \dot{m}_3(s_3 - s_8)$
Pump-2	$\dot{W}_{p2} = \dot{m}_{18}(h_{18} - h_{17})$	$\dot{E}D_{p2} = T_0 \dot{m}_{18}(s_{18} - s_{17})$

Fig. 4 shows the variation of desired refrigeration output with industrial waste heat temperature. It is clear from the figure that increase in temperature of waste heat (flue gas) causes increase in refrigeration output of EORC and VCRC. Increased temperature results in better quality of refrigerant vapour at turbine inlet, thus more power is available from turbine to VCRC, which increases refrigerant mass flow rate in evaporator of VCRC. This results in higher refrigerating effect in vapour compression refrigeration cycle. Improved quality of vapour refrigerant at turbine inlet because of increased waste heat temperature, results in better quality at turbine exit. This causes increase in velocity of primary motive fluid at nozzle exit creating greater vacuum at secondary vapour entrance to ejector. The increased vacuum results in increase in the mass flow rate of the secondary refrigerant through the evaporator of ejector refrigeration cycle and thus higher refrigeration effect in EORC. The decrease in cooling capacity of ARC with the increase in industrial waste heat temperature is because of the decrease in flue gas temperature at the outlet of HRVG. Thus, heat input to the ARC decreases, ensuing decrease in mass flow rate of refrigerant (water) through the evaporator-2. The combined refrigeration output follows the similar declining behaviour with the increase in waste heat temperature because ARC dominates over EORC and VCRC.

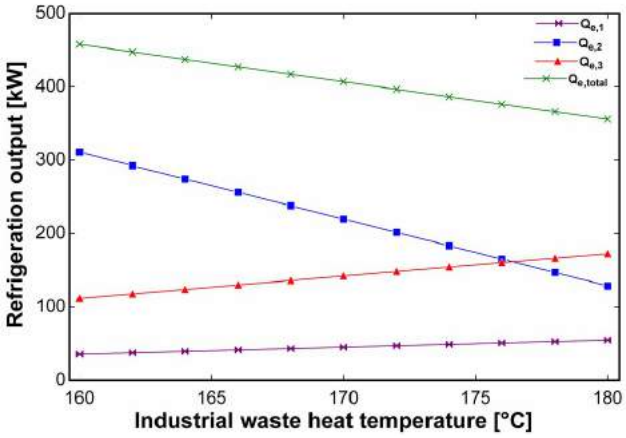

Figure 4 Effect of industrial waste heat temperature on refrigeration output

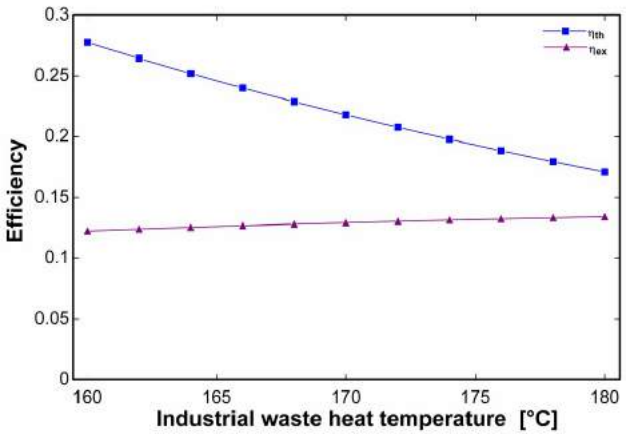

Figure 5 Effect of industrial waste heat temperature on energy and exergy efficiency

Fig. 5 represents the variation of first law based thermal efficiency and second law based exergy efficiency with industrial waste heat temperature. There is appreciable drop in thermal efficiency of the system with the rise in temperature of waste heat. It is because of the dominating nature of absorption refrigeration output over VCR refrigeration output and ejector refrigeration output. In contrast, insignificant increase in exergetic efficiency of the overall system with the increase in waste heat temperature is observed and it is attributed to the fact that the exergy output of VCRC is much higher than that of EORC and ARC. With the rise in flue gas temperature, the exergy output of VCRC exhibits rising behaviour while that of ARC shows declining trend. Hence, the exergetic efficiency of the given system shows minimal increase with the rise in temperature of waste heat.

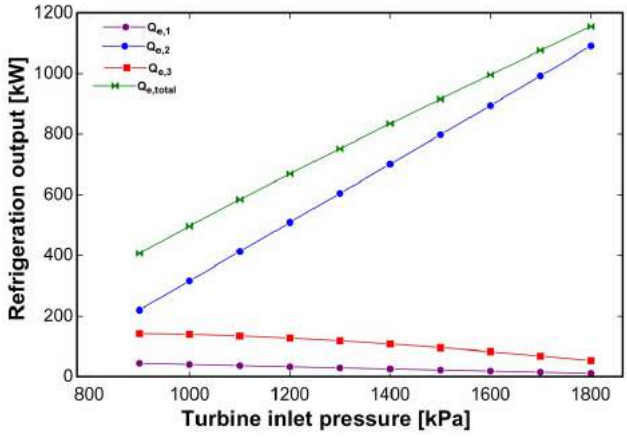

Figure 6 Effect of turbine inlet pressure on refrigeration output

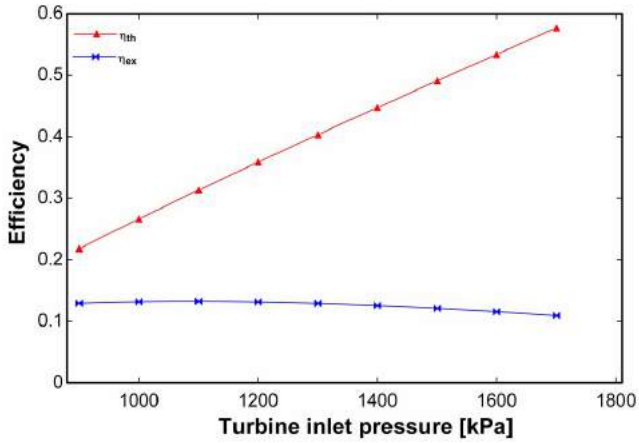

Figure 7 Effect of turbine inlet pressure on energy and exergy efficiency

Fig. 6 shows the effect of turbine inlet pressure on cooling capacity of EORC, ARC and VCRC and on combined cooling capacity. It is found that the cooling capacity of ARC increases considerably with the increase in turbine inlet pressure while cooling capacity of EORC and VCRC decreases with the same. The increase in the turbine inlet pressure lowers the mass flow rate of refrigerant (R141b) vapours generated in the HRVG. This results in reduction in absorption of thermal energy from the flue gas through the HRVG, leading to higher flue gas temperature at HRVG exit (2). This allows higher heat supply to the generator of ARC, causing considerable enhancement in the cooling capacity of ARC due to increased mass flow rate of refrigerant (water) through evaporator-2. The reason for the reduction of refrigeration output of ejector refrigeration cycle is the decrease in the mass flow rate of refrigerant (R141b) vapours through the turbine and the decrease in the turbine exit temperature. The decrease in turbine exit temperature reduces

the velocity of primary fluid at ejector nozzle, resulting in reduced mass flow rate of secondary refrigerant through evaporator-1. Also, the reduced mass flow rate through the turbine causes reduction in power input to the compressors and thus decrease in flow rate of N_2O across evaporator-3. Hence, refrigeration output of both EORC and VCRC decreases with the increase in turbine inlet pressure.

The variation of energy and exergy efficiency with the increase in turbine inlet pressure is shown in fig. 7. With the increase in turbine inlet pressure, the energy efficiency is found to increase significantly while exergy efficiency decreases after initial increase. The rate of increase in refrigeration output of ARC is much higher than the rate of reduction in refrigeration outputs of EORC and VCRC with the increase in turbine inlet pressure. Therefore, variation of energy efficiency follows the pattern of variation of ARC refrigeration output. Initially, the rise in exergy output of ARC surpasses the drop in exergy output of EORC and VCRC, but later, the trend gets reversed. Consequently, the exergy efficiency increases initially and then starts decreasing with the hike in turbine inlet pressure.

CONCLUSIONS

The main conclusion drawn from the energy and exergy analysis of combined ARC, EORC and VCRC triple effect refrigeration cycle are as follows:

✓ Highest irreversibility occurs in HRVG followed by ejector and condenser of ejector Rankine cycle. Therefore, more attention is required to be paid on these components while designing and optimization.

✓ Around 21.79% of the total energy input is available as useful refrigeration output while only 12.91% of the exergy input is available as useful exergy output.

✓ Exergy output of VCR cycle is significantly higher than that of the absorption and ejector refrigeration cycles. It is of the order of 11%, 1% and 0.5%, respectively for VCRC, EORC and ARC.

NOMENCLATURE

ARC	absorption refrigeration cycle
COP	coefficient of performance
C_p	specific heat (kJ/kg.K)
$\dot{E}$	exergy flow rate (kW)
$\dot{E}D$	exergy destruction rate (kW)
EORC	ejector organic Rankine cycle
ERC	ejector refrigeration cycle
EV	expansion valve
h	specific enthalpy (kJ/kg)
HRVG	heat recovery vapour generator
HTC	high temperature cycle
LTC	low temperature cycle
$\dot{m}$	mass flow rate (kg/s)
ORC	organic Rankine cycle
P	pressure (kPa)
$\dot{Q}$	heat transfer rate (kW)
s	specific entropy (kJ/kg.K)
SHE	solution heat exchanger
TV	throttle valve
T	temperature (°C or K)
VCRC	vapor compression refrigeration cycle
$\dot{W}$	work transfer rate (kW)

Subscripts

0	reference state
1, 2…	operating points
a	absorber
c	condenser
cc	cascade condenser
comp	compressor
d	diffuser section
e	evaporator
ej	ejector
ex	exergetic
g, gen	generator
i	inlet, inside
k	any component
lvhe	liquid vapour heat exchanger
max	maximum
m	mixing section
n	nozzle section
o	outlet, outside
p	pump
she	solution heat exchanger
T	turbine
tv	throttle valve
u	useful

Greek symbols

η	efficiency
μ	entrainment ratio
Σ	sum of
ψ	specific exergy

ACKNOWLEDGMENTS

The support of Ministry of New and Renewable Energy (MNRE), Government of India is duly acknowledged.

REFERENCES

Arora, A., Dixit, M., Kaushik, S.C., 2016a. Energy and exergy analysis of a double effect parallel flow LiBr/H2O absorption refrigeration system. Journal of Thermal Engineering 2(1), 541-549.

Arora, A., Dixit, M., Kaushik, S.C., 2016b. Computation of optimum parameters of a half effect water lithium bromide vapour absorption refrigeration system. Journal of Thermal Engineering 2(2), 683-692.

Dai, Y., Wang, J., Gao, L., 2009. Exergy analysis, parametric analysis and optimization for a novel combined

power and ejector refrigeration cycle. Applied Thermal Engineering 29, 1983-1990.

Goswami, D.Y., Xu, F., 1999. Analysis of a new thermodynamic cycle for combined power and cooling using low and mid temperature solar collectors. Journal of Solar Energy Engineering 121 (2), 91-97.

Galanis N, Cayer E, Roy P, Denis ES, Desilets M., 2009. Electricity generation from low temperature sources. J App Fluid Mech 2, 55–67.

Habibzadeh, A., Rashidi, M.M., Galanis, N., 2013. Analysis of a combined power and ejector-refrigeration cycle using low temperature heat. Energy Convers. Manage. 65, 381–391.

Hasan, A.A., Goswami, D.Y., Vijayaraghavan, S., 2002. First and second law analysis of new power and refrigeration thermodynamic cycle using solar heat source. Solar Energy 73 (5), 385-393.

Herold, K.E., Radermacher, R., Klein, S.A., 1996. Absorption chillers and heat pumps. CRC Press, USA.

Hong, D., Chen, G., Tong, L., He, Y., 2011. A novel ejector-absorption combined refrigeration cycle. International Journal of Refrigeration 34, 1596-1603.

Inc. BCS, 2008. Waste heat recovery: technologies and opportunities in U.S. industry. US Dept. of Energy (DOE).

Kaushik, S.C., Arora, A., 2009. Energy and exergy analysis of single effect and series flow double effect water-lithium bromide absorption refrigeration systems. International Journal of Refrigeration 32(6), 1247-1258.

Klein S.A., Alvarado F., 2005. Engineering Equation Solver, Version 7.441, F-Chart software, Middleton, WI.

Martin, C., Goswami, D.Y., 2006. Effectiveness of cooling production with a combined power and cooling thermodynamic cycle. Applied Thermal Engineering 26, 576-582.

Rettig A, Lager M, Li S, Mahadea V, McCllion S, Chernushevich J., 2011. Application of organic Rankine cycles (ORC). World Engineer's convention, Geneva, Switzerland, 4–9 September.

Sun, D., Eames, I.W., Aphornratana, S., 1996. Evaluation of a novel combined ejector refrigeration cycle-I: computer simulation. International Journal of Refrigeration 19, 172-180.

Tchanche BF, Lambrinos Gr, Frangoudakis A, Papadakis G., 2011. Low-grade heat conversion into power using organic Rankine cycles – a review of various applications. Renew Sustainable Energy Rev 15, 3963–79.

Wang, J., Dai, Y., Sun, Z., 2009. A theoretical study on a novel combined power and ejector refrigeration cycle. International Journal of Refrigeration 32, 1186-1194.

Zhang, Na, Lior, Noam, 2007. Methodology for thermal design of novel combined refrigeration/power binary fluid systems. International Journal of Refrigeration 30 (6), 1072-1085.

Zheng, B., Weng, Y.W., 2010. A combined power and ejector refrigeration cycle for low temperature heat sources. Sol. Energy 84 (5), 784–791.

Wireless Pers Commun
DOI 10.1007/s11277-016-3577-1

Energy-Efficient Hierarchical Routing for Wireless Sensor Networks: A Swarm Intelligence Approach

Palvinder Singh Mann[1] · **Satvir Singh**[2]

© Springer Science+Business Media New York 2016

Abstract Energy efficient routing in wireless sensor networks (WSNs) require non-conventional paradigm for design and development of power aware protocols. Swarm intelligence (SI) based metaheuristic can be applied for optimal routing of data, in an energy constraint WSNs environment. In this paper, we present *BeeSwarm*, a SI based energy-efficient hierarchical routing protocol for WSNs. Our protocol consists of three phases: (1) Set-up phase-*BeeCluster*, (2) Route discovery phase-*BeeSearch* and (3) Data transmission phase-*BeeCarrier*. Integration of three phases for clustering, data routing and transmission, is the key aspect of our proposed protocol, which ultimately contributes to its robustness. Evaluation of simulation results show that *BeeSwarm* perform better in terms of packet delivery, energy consumption and throughput with increased network life compared to other SI based hierarchical routing protocols.

Keywords Wireless sensor networks · Swarm intelligence · Energy efficient routing

1 Introduction

Wireless sensor networks (WSNs) contain self-configured, distributed and autonomous sensor nodes (SNs) that monitor physical or environmental activities such as humidity, temperature, sound, vibration or pollutants in a specific area of operation [1]. SNs collect data from their surrounding and forward it to a main location, known as *Sink* or *Base Station* (BS) where data can be monitored and analysed for decision making in variety of applications. A typical WSN scenario is shown in Fig. 1. A WSN may contain hundreds of thousands of such SNs, which can communicate and share data among themselves using

✉ Palvinder Singh Mann
psmaan@hotmail.com

[1] I K Gujral Punjab Technical University, Kapurthala, Punjab 144001, India

[2] S B S State Technical Campus, Ferozepur, Punjab 152004, India

Published online: 08 August 2016

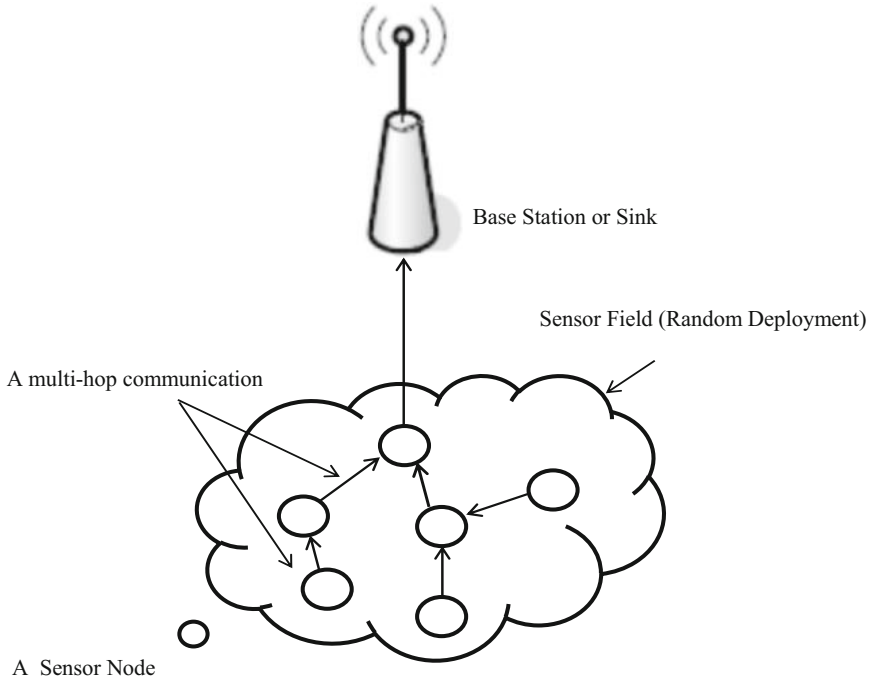

Fig. 1 A typical WSN scenario

radio signals [2]. However, SNs have limited battery life; therefore random deployment of large number of SNs may bring challenges to manage resources for efficient delivery of events in WSNs [3].

Routing of data events in WSNs is one such challenge,that necessitate designing of energy efficient protocols which ultimately results in longer network life and optimal utilization of resources. It is evident form past investigations [4, 5] that cluster based hierarchical routing protocols result in prolonged network life. In this paper, we propose *BeeSwarm*, a SI based, energy-efficient hierarchical routing protocol, which integrates node clustering and data routing in a three phase model to deliver optimal routing with long network life.

1.1 Organization of the Paper

The rest of the paper is organized as follows: In Sect. 2, we review some significant classical and SI based hierarchical routing protocols in WSNs. In Sect. 3, we introduce our proposed protocol *BeeSwarm* and discuss its working in Sects. 4 and 5. Section 6, presents simulation results and analysis of our proposed protocol with existing SI based hierarchal protocols. At last in Sect. 7, a brief conclusion and future work is discussed.

2 Related Work

In the past, advances in sensing devices and wireless networks have build distributed sensor networks (DSNs) [6] to grow from small bunch of sensors to huge swarm of micro-sensors, from fixed sensor networks to dynamic one, from wired topology to wireless topology and from static network configuration to a dynamically changing configuration. In such dynamic environment design and development of efficient routing protocol remain a challenge for researches. Further, Classical as well as SI based approaches used their own

resources and build some efficient solutions for resource constraint WSNs. Below we discuss some of these approaches.

2.1 Classical Routing Protocols

Low-energy adaptive clustering hierarchy (LEACH) [7], is a classical example of cluster based routing which combines energy-efficient cluster-based routing to application specific data aggregation and achieve better lifetime for a micro-sensor network. LEACH remain a guiding force for cluster based routing protocols till date as it remain a high performer under tight constraints of WSNs. De et al. [8] proposed a meshed multi-path routing (M-MPR) protocol based on selective forwarding (SF) scheme of data packets with end-to-end forward error correction (FEC) method, that contributes in reducing the signal overhead of whole network. Mhatre and Rosenberg [9] presents a comprehensive survey on single hop or multi-hop mode of communication for data forwarding along with some results that could serve as procedure to decide which type of communication model should be adopted for given settings in WSNs. Al-Karaki and Kamal [2] presents the architect level challenges for designing protocols for efficient routing in WSNs and a comprehensive survey on routing techniques in WSNs is discussed. Chang and Tassiulas [10] devise the routing problem as a linear programming function, where the focus is to extend the network lifetime and presented two different models for the information exchange and data forwarding. In this paper [11], authors presented a new approach as message-efficient clustering for WSNs, which is based on the allocation of local growth budgets to node neighbours. The proposed algorithm produce clusters of fixed size with low diameter, using minimum number of messages. Abbasi and Younis [4] presents a taxonomy and general classification of existing cluster based routing approaches for WSNs and also put some light on different clustering algorithms for WSNs; highlighting their features, limitations and complexity. Hybrid energy-efficient distributed clustering (HEED) [12], is another classical hierarchical routing protocol for WSNs that periodically selects CHs based on a combination of node residual energy and a secondary parameter. Power-efficient and adaptive clustering hierarchy (PEACH) [13], presents cluster based approach with minimum overhead in network and support multi-level clustering for both location-known and location-unknown WSNs, which helps in minimizing energy consumption for each node thus extends network lifetime compared to its peers. BeamStar [14] is an edge-based routing protocol, which exploits on physical properties associated with directional antenna and power control at the BS with minimum control overhead. They [1] organize the main research problems in WSNs into three different groups: (1) internal platform of WSNs with system software (2) communication protocols used for data transfer and (3) network services with deployment issues. They extensively reviewed all these major development in these three categories and outline new challenges to WSNs. Energy-efficient multi-level clustering (EEMC) [15], is build to achieve optimal energy consumption in WSNs by proposing a multi-level clustering approach in which more time is spend on to transmit data as compared to formation of cluster in order to minimize algorithm overhead. Energy efficient heterogeneous clustered scheme (EEHC) [16], is based on weighted selection probability of each node to become a CH on account of their residual energy and support node heterogeneity in WSNs. Distributed hierarchical agglomerative clustering (DHAC) [17], presents a bottom-up clustering approach with automatic CHs rotation and re-scheduling scheme, it tries to avoid re-clustering of nodes and helps in achieving uniform energy consumption throughout the network. Energy efficient cluster formation protocol (EECF)

[18], works on a hierarchical topology which dynamically selects CHs so that the elected CHs become more adaptive to the frequent change in the residual energies and the network topology, results in minimizing overheads. GEodesic sensor clustering (GESC) [19], exploits the local network information and residual energy of each neighborhood nodes to achieve higher network lifetime. Zhang and Shen [20] proposes an online routing scheme for WSNs named Energy-efficient Beaconless geographic routing (EBGR), which will establish loop-less, stateless, and energy-efficient sensor to BS routing path, at a very less overhead without the help of prior location of neighborhood node. Mobility-based clustering (MBC) protocol [21] is proposed for mobile WSNs, in which a node will elects itself as a CH based on its residual energy plus mobility ratio whereas a non-CH node will aims at its link stability with a CH during clustering for data transfer. Mao et al. [22] focus on prioritizing forwarder list of nodes to minimize energy consumption by all nodes even when the transmission power of each node is supposed to be fixed or adjustable. Energy-aware interference-sensitive geographic routing (EIGR) protocol [23], adaptively make use of an anchor list to direct data delivery of packets, and selects the minimum interference path for data delivery to BS. MUSTER [24], is a routing protocol specifically designed for many-to-many communication channel. They devise an analytical model to compute, a optimal solution to the problem of data routing from multiple sources to multiple sinks. To extend the existing network lifetime, MUSTER reduces the number of nodes involved in many-to-many routing and balances forwarding load. In [25] authors, presents the QoS of an energy-efficient cluster-based routing protocol named as Energy-aware routing protocol (EAP) in terms of network lifetime, delay, packet loss percentage and throughput, later proposes some modifications on it to enhance its performance. Integrated clustering and routing protocol model (ICRP) [26], presents an integrated model for clustering and routing of events. This model differ from others as it eliminates the isolation of clustering and routing. Distributed energy-efficient clustering with improved coverage (DEECIC) [27], works with minimum number of CHs to cover the entire network by giving a unique ID to each node based on local information. It periodically updates CHs according to nodes residual energy and distribution level and by reducing overheads of synchronization and geographic location it prolong the network lifetime and improve network coverage. In [28] author presents a analytical method for computation of the optimal cluster size to reduce the average energy consumption per unit area. In the proposed protocol, authors present a cost metric function that favours those nodes having more energy-redundancy as CHs and select active nodes in a way that it tries to emulate the most efficient solutions for area coverage. Topology aware routing (TAR) protocol [29] effectively manages a network size into virtual coordinate space where hop to hop distances between nodes are preserved and based on that distance, TAR will choose greedy forwarding to find the right neighbour node that is one hop closer to the destination thus achieve good packet delivery ratio without location information of nodes. Anisi et al. [30] put some light on a new promising energy harvesting technology which uses piezoelectric nano-generators to supply power to nano-sensor, along with minimising energy consumption routing strategies are discussed for WSNs. They [31] discussed the architecture of data collection approaches in WSNs and presented a taxonomy of types of data collection approaches in WSNs. They further presented a thematic taxonomy of energy saving techniques used in the various hybrid WSN data collection approaches.

2.2 Swarm Intelligence Based Routing Protocols

T-ANT [32], is a biologically-inspired clustering protocol which exploit different swarm intelligence principles, namely separation and alignment, through a pheromone value control to achieve a optimal and close to uniform selection of CH node. Energy-balanced ant-based routing protocol (EBAB) [33], presents an self-adaptive routing algorithm based on biological species of ants that explore the network to find out routes to destination. It produces clusters of unequal sizes to balance energy consumption for WSNs in order to maximize the network lifetime. Multi-path routing protocol (MRP) [34], is an Ant colony optimization (ACO) based Swarm intelligence (SI) protocol, in which a CH is selected among sensor nodes and an improved ACO algorithm is applied for searching various paths between the CH and BS . MRP extend the network lifetime of the network and minimise the average energy consumption effectively in a WSN. They [35] proposed an effective solution based on a genetic algorithm (GA) for scheduling of relay nodes to collect data, which further can significantly extend the lifetime of a WSN. For small networks, where the global optima can be achieved, this GA based approach is always capable to find the optimal solution. AntSens-Net [36], is based on an ant-based multi-QoS routing metric, which builds a hierarchical class on the network to meet various QoS requirements, thus maximizing network utilization, and improving its performance. In [37], authors proposes cluster based scheme with artificial immune system (AIS) algorithm in WSNs to reduce the energy consumption in nodes and to increase the network lifetime. UCFIA [38], a novel unequal clustering algorithm which combine the characteristics of fuzzy logic and improved ACO, balances the energy consumption in the network and works on prolonging the lifetime of the network. In [39] an extensive survey of SI based protocols is presented with its application to routing. They also introduce a novel taxonomy for routing protocols in WSNs and use it to classify the existing protocols. In [40] authors presented an extensive survey of computational intelligence (CI) based solutions to existing problem domain in WSNs and presents a comprehensive discussion on featuers and shortcomings of existing CI based approaches over traditional WSN solutions. In [41], author's proposes an agent-assisted QoS-based routing algorithm for WSNs with an adaptive value of a particle swarm optimization (PSO) algorithm to improve the overall performance of network. Energy-aware evolutionary routing protocol (ERP) [42], offer better trade-off between lifetime and stability period of a network with efficient energy utilization in the network and is based on evolutionary algorithms (EAs). BeeSensor [43], inspired from the foraging principles of honey-bees is another SI based routing protocol for efficient routing in WSNs. In [44], authors support the use of reinforcement learning (RL) to achieve context aware and intelligent solutions to a variety of problems such as routing, resource utilization and dynamic channel selection in WSNs. This paper [45], presents a survey of intelligent routing protocols which helps to achieve optimization of network lifetime in WSNs and presents a new ideas on the definition of network lifetime in a WSN network. In [46], an integrated platform is presented which enables development of centralized cluster oriented protocols supported by optimization approaches for the WSNs. Based on this platform, Harmony search algorithm (HSA) is proposed which reduces the intra-cluster distances between the nodes and their cluster heads (CHs) and optimize the energy consumption in WSNs. Kuila and Jana [47] presents a linear/nonlinear programming (LP/NLP) formulations of energy efficient clustering and routing problems followed by two algorithms for the same based on a particle swarm optimization (PSO). Their proposed algorithms demonstrate their better working in terms of network life, energy

consumption, dead sensor nodes and delivery of total data packets to the base station. Celal Ozturkand Hancer [48] presents an improved binary artificial bee colony algorithm (IDisABC), which can be used for real world optimization problems of dynamic clustering with hand on experiments conducted on data and image clustering benchmark problems. Kong et al. [49] presents a new approach for obtaining a optimized routing path based on the enhanced parallel cat swarm optimization (EPCSO). EPCSO is employed first time to determine the routing path for the WSNs and it shows its capability of generating a set of the predetermined paths for routing data packets to BS. Hu et al. [50] presents an robust routing recovery protocol with endocrine cooperative particle swarm optimization algorithm (ECPSOA) which is used to establish and optimize the alternative paths based on multi-swarm evolution equation, coupled with endocrine mechanism. This approach can enhance the global search of the proposed protocol and improve the convergence of the algorithm. All of the above discussed algorithms have their own merits and demerits but SI based metaheuristic proved to be better choice for efficient clustering and routing in WSNs. We also took inspiration from the behaviour of SI based metaheuristic and presenting a cluster based energy-efficient and scalable hierarchical routing protocol for WSNs.

3 BeeSwarm-Protocol Description

BeeSwarm is a SI based, energy-efficient hierarchical routing protocol for WSNs inspired from the natural behaviour of honey bees. Honey bees are eco-friendly species on our earth and helped researchers to solve critical optimization problems in the past. Our protocol is based on an integrated three phase layer structure namely (1) Setup phase-*BeeCluster*, (2) Route Discovery phase-*BeeSearch* and finally (3) Data transmission phase-*BeeCarrier*. Below we discuss each phase of our proposed protocol in detail.

4 System Model and Notations

4.1 Energy Model

The proposed model incorporate radio model discussed by Heinzelman et al. [7] for energy consumed by sensor nodes in transmission of data, in which a free space (fs) model is used, when the distance is less than a threshold value d_0, otherwise, multi-path (mp) model is used. Energy consumed by the sensor node radio to transmit an l-bit data over a distance d is given as follows

$$E_{tran}(l,d) = \begin{cases} lE_{elec} + l\epsilon_{fs}d^2 & \text{if } \mathrm{d} < \mathrm{d}_0, \\ lE_{elec} + l\epsilon_{mp}d^4 & \text{if } \mathrm{d} \geq \mathrm{d}_0, \end{cases} \tag{1}$$

where E_{elec}, ϵ_{fs} and ϵ_{mp} be the energy consumed by the electronic devise and by the amplifier in free space and multi-path space respectively. Also the energy consumed in generation of l-bit control messages is given by

$$E_{cont}(l, d) = lE_{elec} \tag{2}$$

E_{elec} depends on various factors such as digital encoding, modulation, filtering, and spreading of the signal.

4.2 Network Model

The proposed WSN model will consists of number of homogeneous sensor nodes randomly distributed over a geographical area with a BS. After cluster formation, which is based on our proposed clustering algorithm, all CHs prepare a TDMA schedule and transmit this schedule to sensor nodes register with them within their cluster. This make sure there will be no collisions among data packets send by various nodes and also allows the radio components of every non-CH node to be turned off at all time except during their transmission time, thus further minimise the energy consumption by individual sensor. After the TDMA schedule is known to all senor nodes, they will be ready to forward events to their respective CHs. Then each node will send data to its respective CH based on proposed routing algorithm using multi-hop communication and CHs forward it to BS after aggregation using single hop communication.

4.3 Notations

We use following notations in our proposed work:

1. Set of Sensor Nodes $S_N = \{ n_1, n_2, \ldots, n_N \}$, are randomly distributed homogeneous nodes over a geographical area of defined dimensions, whereas n_{N+1} denotes the BS.
2. Set of CH's are denoted by $CH_k = \{ CH_1, CH_2, \ldots, CH_k \}$.
3. $D_{n_i}^{BS}(\max)$ denotes the maximum distance between a senor node n_i and BS, is calculated by squared Euclidean distance between them as

$$D_{n_i}^{BS}(max) = Max\{ dis(n_i, n_{N+1}) \quad | \quad \forall\ n_i\ \epsilon\ S_N \tag{3}$$

4. $D_{n_i}^{CH_j}(\max)$ denotes the maximum distance between a senor node n_i and CH_j, is calculated by squared Euclidean distance between them as

$$D_{n_i}^{CH_j}(max) = Max\{ dis(n_i, n_j) \quad | \quad \forall\ n_i,\ n_j\ \epsilon\ S_N \tag{4}$$

5. $D_{CH_j}^{BS}(\max)$ represents the maximum distance between a cluster head CH_j and BS, is calculated by squared Euclidean distance between them as

$$D_{CH_j}^{BS}(max) = Max\{ dis(CH_j, n_{N+1}) \quad | \quad \forall\ j,\ \epsilon\ CH_k \tag{5}$$

6. Residual energy of each senor node n_i is calculated as:

$$E_{res_i} = E_{tot_i} - (E_{tran_i} + E_{cont_i}) \tag{6}$$

where E_{tot_i} is the total initial energy of a sensor node n_i, $E_{tran_i}(1)$ is energy consumed in radio transmission and $E_{cont_i}(2)$ is energy consumed in generating control packets by a sensor node n_i.
7. Life-time of a sensor nodes can be calculated as

$$E_{life_i} = \frac{E_{res_i}}{E_{rd_i}} \tag{7}$$

where E_{rd_i} is energy consumed by a sensor node n_i per round.

8. Set of all nodes which are in communication range of CH are given by

$$R_{CH_j}(max) = Max\{\ n_j \ \mid \ dis(n_i, n_j) \quad \forall\ n_i, n_j\ \epsilon\ S_N. \tag{8}$$

9. Set of maximum number of hop-count required to reach at BS from n_i is given by

$$HC_{n_i}^{BS}(max) = Max\{\ hcount(n_i, n_{N+1}) \ \mid \quad \forall\ n_i,\ \epsilon\ S_N \tag{9}$$

5 Set-Up Phase-BeeCluster

The proposed set-up phase has two main tasks : (1) Cluster Head Selection and (2) Cluster Formation. Firstly, a CH selection algorithm based on ABC metaheuristic is applied to select optimal CHs per round and later on cluster formation phase will be carried out to form clusters of sensor nodes.

5.1 Cluster Head Selection

Cluster head (CH) selection is one of the crucial task in cluster formation as it effect the overall performance of the network. CH will be responsible for collection of data coming from various nodes and transmission of aggregated data to the BS. Handling of large amount of data and performing aggregation require consumption of large amount of energy, therefore we presents an ABC metaheuristic for selection of optimal CHs. Prior to it, BS will broadcast a message to each node, and a volunteer node will act as a CH, which is nearest to BS based on Received Signal Strength (RSS). Further, selection of optimal CHs will be based on following proposed algorithm.

5.1.1 Initialization Phase

We have PN food sources which are randomly placed at a specific geographical area and we initialize each food source (10),i.e., $x_{i,d} = \{\ x_{i,1}, x_{i,2}, \ldots x_{i,D}\},\ 1 \le d \le N$, with a randomly generated uniformly distributed number r, between [0,1].

$$x_{i,d} = x_d^{min} + r \times (x_d^{max} - x_d^{min}), \quad d = 1, 2\ldots, D \tag{10}$$

5.1.2 Fitness Function Derivation

Now, we construct a fitness function to evaluate the fitness of individual food source of the population. We have three objectives in our proposed CH selection algorithm, firstly the node elected as CH, must have maximum residual energy i.e

$$f_i \propto Max(E_{res_i}) \tag{11}$$

Secondly, we need to minimize the maximum distance between elected node as CH and BS, lastly minimize the maximum distance between current CH and newly chosen CH, therefore

$$f_i \propto \frac{1}{Min(D_{n_i}^{BS}(max) + D_{n_i}^{CH_j}(max))} \tag{12}$$

Now aggregating Eqs. (11) and (12) as

$$f_i \propto \frac{Max(E_{res_i})}{Min(D_{n_i}^{BS}(max) + D_{n_i}^{CH_j}(max))} \tag{13}$$

$$f_i = K\frac{Max(E_{res_i})}{Min(D_{n_i}^{BS}(max) + D_{n_i}^{CH_j}(max))} \tag{14}$$

where K is constant of proportionality, assuming K = 1,

Therefore,

$$f_i = \frac{Max(E_{res_i})}{Min(D_{n_i}^{BS}(max) + D_{n_i}^{CH_j}(max))} \tag{15}$$

5.1.3 Employed Bee Phase

Now each employed bee perform a random modification on the existing solution for finding a new solution v_i using Eq. (16).

$$v_{i,d} = x_{i,d} + r' \times (x_{i,d} - x_{k,d}) \tag{16}$$

The obtained value of v_i is evaluated to x_i and if the fitness of v_i is better than x_i, the bee will leave the old solution and memorize the new one. Otherwise, she will keep performing on x_i.

5.1.4 Onlooker Bee Phase

An onlooker bee selects food source x_i based on Eq. (17), and also perform a local search on x_i according to Eq. (16). Now if the new solution has a better fitness, it will replace x_i.

$$p_i = \frac{f_i}{\sum_{n=1}^{SN} f_i} \tag{17}$$

5.1.5 Scout Bee Phase

If the fitness of a solution cannot be improved after a limit called Maximum Cycle Number (MCN), then food source is abandoned. The scout bee will then produce a new food source by using Eq. (10) again as so on.

In this way we select the best optimised node as CH from randomly deployed SNs. After each round the CH will be replaced by a new CH with better fitness values.

The Pseudo-code of the proposed cluster head (CH) selection Algorithm 1 is as follows :

Algorithm 1 Pseudo-code of proposed Cluster Head(CH) Selection Algorithm

Input: Parameter Initialization

a): Population Number (PN)

b): Maximum Cycle Number (MCN)

c): Dimension of Vector to be Optimized (D)

d): Lower bound and Upper bound of each element

1: Generate initial population $x_i \ \forall \ i \ \epsilon \ S_N \ \ 1 \leq i \leq N$

2: Evaluate the aggregate fitness function (f_i)

3: Set round=1

4: **Repeat**

5: **for** each employed bee

6: {Produce new solution v_i using Eq.(16)

7: Evaluate the fitness value of new solution

8: **if** (fitness $x_i <$ fitness v_i)

9: **then** $x_i = v_i$

10: }

11: Calculate the probability p_i for solution x_i using Eq.(17)

12: **for** each onlooker bee

13: {Select a solution x_i based on p_i

14: Produce new solution v_i using Eq.(16)

15: Evaluate the fitness value of new solution

16: **if** (fitness $x_i <$ fitness v_i)

17: **then** $x_i = v_i$

18: }

19: **if**

20: there is a abandoned solution for the scout

21: **then**

22: replace it with a new solution, randomly produced using Eq.(10)

23: Record the best solution so for

24: round=round+1

25: **Until**

26: round = MCN

27: **Stop**

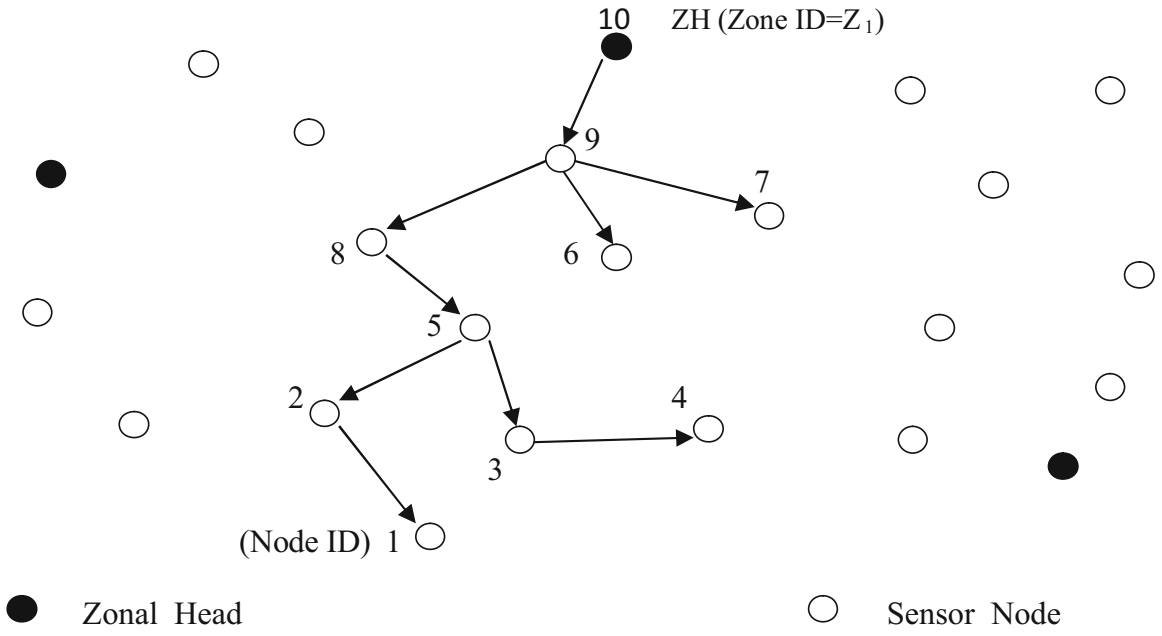

Fig. 2 Route discovery in randomly distributed WSNs

5.2 Cluster Formation

After CH selection, the next big challenge is formation of clusters. Each CH will send a *Join* Request to its nearby nodes in communication range for formation of clusters. After receiving *Join* request from CHs, each node will Join a CH to form a Cluster.

5.3 Route Discovery Phase- BeeSearch

After selection of CHs, the next phase *BeeSearch* will discover routes for event communication through scout bees. BeeSearch is a two way process (1) Forward search and (2) Backward search. Forward Search will explore the network and Backward Search will establish and maintain paths between BS and various nodes. The first event communication is for registration of nodes with respective CHs. Each CH will send a Join-Advertisement (J-ADV) request through scout bees to its neighbours in its Zone as shown in Fig. 2.

The frame formant of J-ADV will contain following fields of 1 byte each as shown in Fig. 3:

SEQN	FS	NS	Z-ID	ZH-ID	SC	CN-ID	PN-ID

SEQN- Sequence No
FS - Frame Status
NS - Node Status
Z-ID - Zone-ID
ZH-ID - Zonal Head ID
SC - Step Count
CN-ID - Current Node ID
PN-ID - Previous Node ID

Fig. 3 Frame format-join-advertisement (J-ADV)

Table 1 Search table (ST)

SEQN	FS	NS	Z-ID	ZH-ID	SC	CN-ID	PN-ID
A0001	0	1	Z_1	10	0	10	–
A0002	0	0	Z_1	10	1	9	10
A0003	0	0	Z_1	10	2	6	9
A0004	0	0	Z_1	10	3	7	9
A0005	0	0	Z_1	10	4	8	9
A0006	0	0	Z_1	10	5	5	8
A0007	0	0	Z_1	10	6	2	5
A0008	0	0	Z_1	10	7	3	5
A0009	0	0	Z_1	10	8	1	2
A00010	0	0	Z_1	10	9	4	3

- Sequence No (SEQN): It contains a unique number for all the event communications.
- Frame Status (FS) : It tells the status of the frame, if the frame contains control packet its value is 0, otherwise 1, in case of data packet.
- Node Status (NS) : NS tells the status of the current Node, if its a CH node then its value is 1, otherwise 0.
- Zone-ID (Z-ID) : It contain the Cluster-ID for which current node belongs.
- Zonal Head ID (ZH-ID): It contain the unique ID for the current CH.
- Step Count (SC) : Step Count will count number of hops for an event communication.
- Current Node ID (CN-ID): It contain node ID, which is communicating an event currently.
- Previous Node ID (PN-ID):It contains the node ID, through which an event is forwarded to current node.

Each CH initiate J-ADV request for its neighbour nodes though scout bees, to join as zonal node under a specific CH. Further each node will forward the J-ADV request to other nodes in their communication range. If a particular node had already received a J-ADV message then it discard the message to eliminate duplicate frames. Now this process will be carried on untill they cover all the surrounding nodes. Simultaneously a Search Table (ST) will be maintained and updated on real time basis as shown in Table 1. ST will contain all information regarding event communication from each node in Forward Search.

After all nodes are discovered in Forward Search, each node will send Join-Acknowledgment (J-ACK) to CH based on Route Table (RT) as shown in Fig. 4. J-ACK will only contain the Node-ID (N-ID) of a particular node under specific Zone. RT will contain

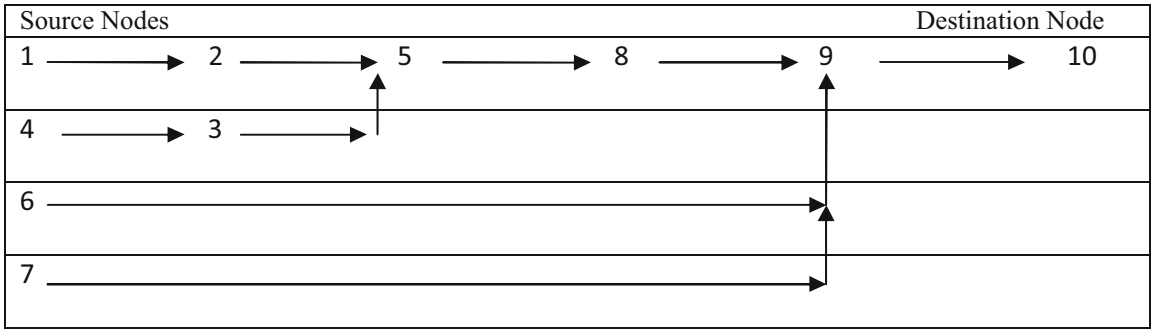

Fig. 4 Route table (RT)

Table 2 Registration table (REG-T)

Z-ID	ZH-ID	N-ID								
Z_1	10	9	6	7	8	5	2	3	1	4
Z_1	25	11	15	17	13	14	18	19	21	23
Z_1	28	13	16	20	22	24	26	27	29	30
Z_1	36	33	31	34	37	35	32	38	40	39

all the routes from various nodes to CH, based on information provided by ST. These routes will be maintained throughout the network life time.

After all nodes send J-ACK to CH, then it reads the Node-ID and accepts its registration. All the registered nodes are maintained in a separate table known as Registration Table (REG-T) as shown in Table 2. If it receives more than one J-ACK of registered nodes, then it simply reject the frame after checking the REG-T entries to avoid duplicate registration.

5.4 Data Transmission Phase-BeeCarrier

Once all the nodes are registered to their respective CHs, scout pass the control to forager which carry the events from various nodes to their respective CHs with the help of RT in data transmission phase known as *BeeCarrier*. The CHs prepare a TDMA schedule [19] and transmits this schedule to its registered nodes in the cluster.The complete Time Line schedule of *BeeSwarm* is shown in Fig. 5, which include time slots for all three phases viz. (1) Set-up phase (2) Route discovery phase and (3) Data transmission phase.

This make sure that there are no collisions among data packets send by various sensor nodes and also allows the radio component of each non-CH node to be turned off at all times except during their transmission time, thus minimize the energy consumed by the individual sensor nodes.

The total time elapsed during all phase of BeeSwarm is calculate as:

$$T_{total} = T_{setup} + T_{route} + T_{tran} \tag{18}$$

further

$$T_{tran} = \sum_{i=1}^{n} T_i \tag{19}$$

After the TDMA schedule is known by all nodes in the cluster, forager will be ready to carry events form nodes to their respective CHs and actual data transmission can begin with the help of real time route search from RT. Now the main objective of forager is to

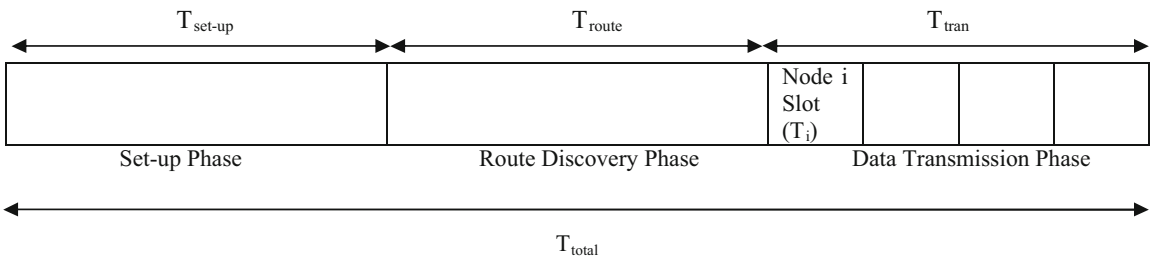

Fig. 5 Time line showing BeeSwarm schedule

Table 3 Simulation parameters

Parameter	Value
Channel type	Wireless channel
Terrain size	100 × 100 m
MAC protocol	802.11
Radio propagation	Free space
Node deployment	Random
Node transmission range	100 m
Packet size	5000 bits
Message size	400 bits

carry event communication through minimum transmission distance by least hop count. After evaluating the optimal path , each forager will carry data from respective nodes to CH and from CHs to BS using multi-hop communication. A proper path maintenance will be done at the source node if it has a forager for it and the best route will remain in the memory of each forager until other optimal path is found. It concludes the whole working of *BeeSwarm* right from clustering to data transmission. This makes our protocol an integrated approach to overcome optimization problem of clustering and routing in WSNs.

6 Simulation Results and Analysis

Our proposed protocol is simulated on *Nature Inspired Tool for Sensor Simulation* (NITSS), a java based platform specially developed to support WSNs environment. To evaluate its performance with other CI based hierarchal routing protocols *MRP* [34] and *ERP* [42] the following parameters are considered (Table 3).

6.1 Performance Matrices

We have evaluated our proposed protocol based on following performance parameters:

6.1.1 Packet Delivery Ratio (PDR)

PDR is a ratio that tells the total sum of packets received at BS to the total sum of packets generated at all sensor nodes in a network, thus provide the percentage of total packets delivered at BS. Simulation results with mean and standard deviation of PDR are shown in Table 4 below:

Table 4 Packet delivery ratio (%)

Number of nodes	BeeSwarm	MRP	ERP	Mean ± SD
25	100	99.92	99.80	99.91 ± 0.10
65	99.98	99.94	99.90	99.94 ± 0.04
120	99.95	99.93	99.87	99.92 ± 0.04
200	99.98	99.97	99.94	99.97 ± 99.97
285	99.97	99.96	99.95	99.96 ± 0.01

Figure 6 shows that our proposed protocol *BeeSwarm* performs better to its peers in delivering packets to BS. At 25 sensor nodes our proposed protocol deliver 100 % packets. Gradually with increasing number of nodes, the PDR is still higher then *MRP* and *ERP*. At 285 nodes *BeeSwarm* delivers the highest PDR with standard deviation of ±0.01. This shows that even on higher node density, PDR of our proposed protocol remains good as compared to other CI based hierarchical protocols.

6.1.2 Total Packet Delivered

This parameter indicate the actual number of packets delivered at BS from various sensor nodes. This parameter is significant as it points to better efficiency of the protocol. Table 5 gives the data packets delivered at BS by *BeeSwarm*, *ERP* and *MRP*.

Figure 7 shows that our proposed protocol, *BeeSwarm* deliver the highest number of packets at BS compared to other protocols, even on high node density. Result shows that our proposed protocol deliver approximately 10 % more packets. This shows the robust information dissemination factor by our proposed protocol, which is very significant in case of data monitoring applications in WSNs.

6.1.3 Average Energy Consumed

This refers to the average energy consumed by all sensor nodes in sending all data packets to BS. The below Table 6, shows the the average energy consumed by various protocols.

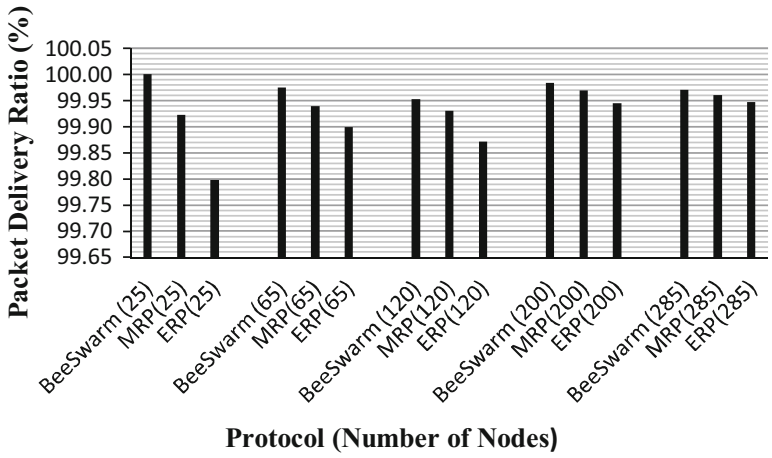

Fig. 6 Packet delivery ratio

Table 5 Total packet delivered

Number of nodes	BeeSwarm	MRP	ERP
25	8092	4904	2811
65	17,105	9762	6928
120	25,153	17,157	14,931
200	28,578	22,412	22,088
285	31,887	28,640	28,555

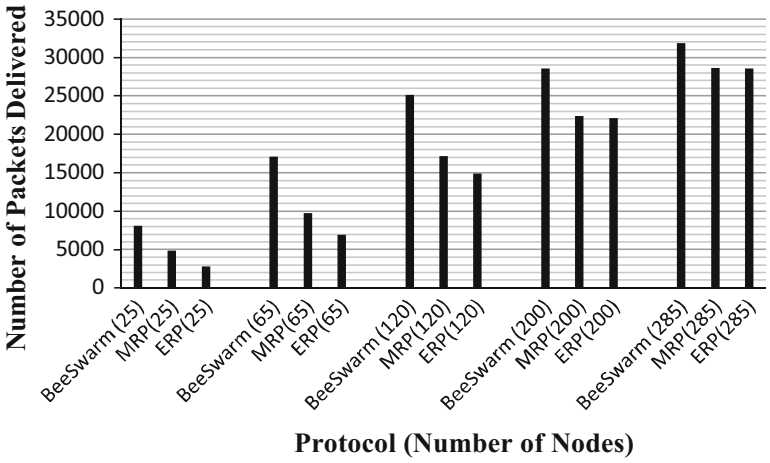

Fig. 7 Total packets delivered

Table 6 Average energy consumed (KJ)

Number of nodes	BeeSwarm	MRP	ERP
25	0.00059	0.00102	0.00108
65	0.00065	0.00106	0.00115
120	0.00094	0.00126	0.00126
200	0.00104	0.00116	0.00012
285	0.00101	0.00112	0.00107

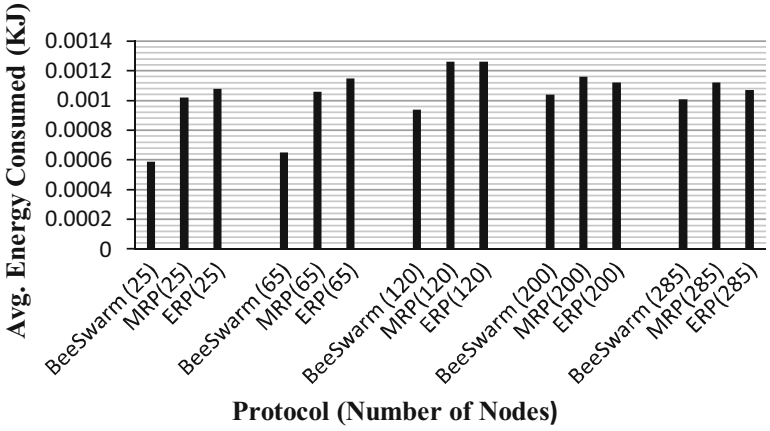

Fig. 8 Average energy consumed

Figure 8 shows that *BeeSwarm* consumed lowest amount of energy as compared to *MRP* and *ERP* even at high density of nodes. On the other hand, *MRP* consumes less amount of energy as compared to *ERP* at low node density but as node density increases, *ERP* deliver better in terms of energy consumption. Other significant factor is that *BeeSwarm* delivers more data packets (as shown in Fig. 7) with less energy consumption compared to *MRP* and *ERP*. The above result prove *BeeSwarm* as energy efficient protocol even for scalable networks.

Table 7 Average throughput ($\times 10^6$ bits/s)

Number of nodes	BeeSwarm	MRP	ERP
25	0.04219	0.03744	0.03463
65	0.08629	0.08171	0.07916
120	0.15123	0.14961	0.14653
200	0.36006	0.35036	0.26867
285	0.36006	0.35262	0.26867

Fig. 9 Average throughput

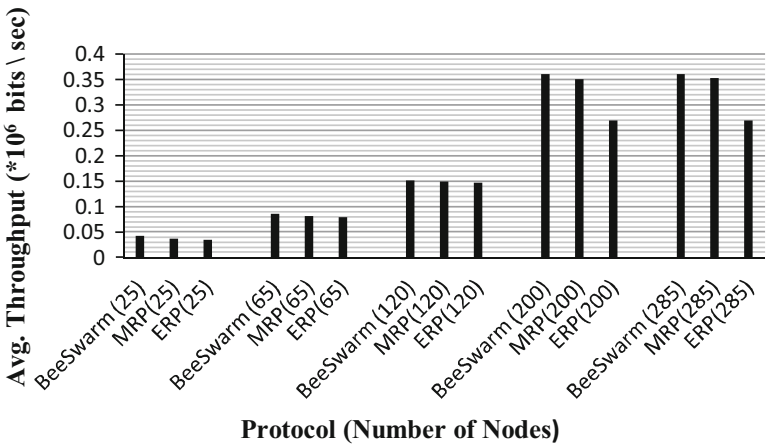

Table 8 Number of rounds

Number of nodes	BeeSwarm	MRP	ERP
25	538	294	169
65	484	285	186
120	374	293	205
200	238	223	216
285	229	217	211

6.1.4 Throughput

Throughput is defined as number of packets delivered at BS per unit time. Throughput is a significant measure of computational and time efficiency of a protocol. Table 7 below shows the results of throughput for *BeeSwarm*, *MRP* and *ERP*.

Figure 9 shows *BeeSwarm* deliver better throughput as compared to *MRP* and *ERP*. At 120 nodes all the protocols have almost same performance but when the node density increases, *ERP* and *MRP* lags behind.

6.1.5 Network Life

Network Life describes the extended lifetime of the network for number of rounds in a specific time, it will ultimately increases the life of the network, hence more data packets can be transmitted at BS for longer duration. The below Table 8, shows the comparative results for number of rounds of *BeeSwarm*, *MRP* and *ERP*.

Figure 10 shows that *BeeSwarm* support almost 50 % more rounds in initial phase of network, moreover when node density increase, it support maximaum number of rounds as

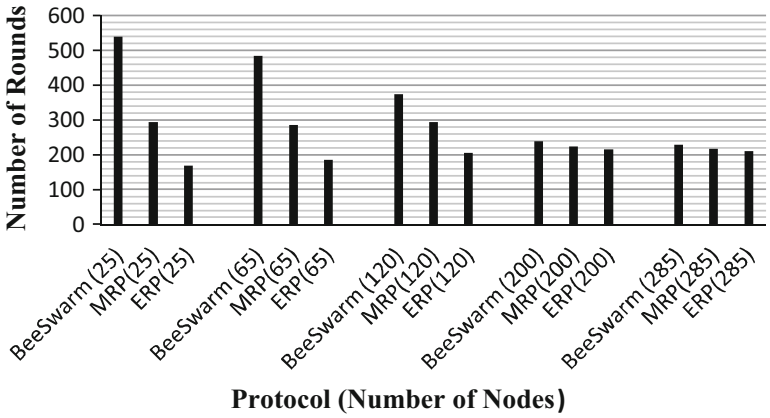

Fig. 10 Network lifetime

compared to *MRP* and *ERP*. This is attributed to *BeeSwarm* efficient clustering phase which choose and rotate ZHs in a way that they deliver maximum data before their exhaust. Hence *BeeSwarm* increases the Network Life by almost 10–15 %.

7 Conclusion and Future Work

In this paper, we proposed *BeeSwarm*, a SI based, energy efficient hierarchal routing protocol for WSNs. *BeeSwarm* offer simple yet robust approach to meet the demands of resource constraint WSNs with wide range of data oriented applications. Our Simulation results prove *BeeSwarm* as an efficient protocol in terms of packet delivery, energy consumption with increased network life over other SI based hierarchal protocols. The reasons behind this improved performance are : (1) SI based hierarchal approach (2) efficient clustering (3) integrated three phase structure and (4) self-organisation. Our results make *BeeSwarm* suitable for large scale deployments with prolonged network life. In future, we want to extent the implementation of *BeeSwarm* on real test-bed of sensor nodes with specific application domain.

Acknowledgments The authors acknowledge I K Gujral Punjab Technical University, Kapurthala, Punjab, India.

References

1. Yick, J., Mukherjee, B., & Ghosal, D. (2008). Wireless sensor network survey. *Computer Networks*, *52*(12), 2292.
2. Al-Karaki, J. N., & Kamal, A. E. (2004). Routing techniques in wireless sensor networks: A survey. *IEEE Wireless Communications*, *11*(6), 6.
3. Akkaya, K., & Younis, M. (2005). A survey on routing protocols for wireless sensor networks. *Ad hoc Networks*, *3*(3), 325.
4. Abbasi, A. A., & Younis, M. (2007). A survey on clustering algorithms for wireless sensor networks. *Computer Communications*, *30*(14), 2826.
5. Tyagi, S., & Kumar, N. (2013). A systematic review on clustering and routing techniques based upon LEACH protocol for wireless sensor networks. *Journal of Network and Computer Applications*, *36*(2), 623–645.
6. Qi, H., Iyengar, S. S., & Chakrabarty, K. (2001). Distributed sensor networks—A review of recent research. *Journal of the Franklin Institute*, *338*(6), 655.

7. Heinzelman, W. B., Chandrakasan, A. P., Balakrishnan, H., et al. (2002). An application-specific protocol architecture for wireless microsensor networks. *IEEE Transactions on Wireless Communications*, *1*(4), 660.
8. De, S., Qiao, C., & Wu, H. (2003). Meshed multipath routing with selective forwarding: An efficient strategy in wireless sensor networks. *Computer Networks*, *43*(4), 481.
9. Mhatre, V., & Rosenberg, C. (2004). Design guidelines for wireless sensor networks: Communication, clustering and aggregation. *Ad Hoc Networks*, *2*(1), 45.
10. Chang, J. H., & Tassiulas, L. (2004). Maximum lifetime routing in wireless sensor networks. *IEEE/ACM Transactions on Networking (TON)*, *12*(4), 609.
11. Krishnan, R., & Starobinski, D. (2006). Efficient clustering algorithms for self-organizing wireless sensor networks. *Ad Hoc Networks*, *4*(1), 36.
12. Younis, O., & Fahmy, S. (2004). HEED: A hybrid, energy-efficient, distributed clustering approach for ad hoc sensor networks. *IEEE Transactions on Mobile Computing*, *3*(4), 366.
13. Yi, S., Heo, J., Cho, Y., & Hong, J. (2007). PEACH: Power-efficient and adaptive clustering hierarchy protocol for wireless sensor networks. *Computer Communications*, *30*(14), 2842.
14. Mao, S., & Hou, Y. T. (2007). BeamStar: An edge-based approach to routing in wireless sensor networks. *IEEE Transactions on Mobile Computing*, *6*(11), 1284.
15. Jin, Y., Wang, L., Kim, Y., & Yang, X. (2008). EEMC: An energy-efficient multi-level clustering algorithm for large-scale wireless sensor networks. *Computer Networks*, *52*(3), 542.
16. Kumar, D., Aseri, T. C., & Patel, R. (2009). EEHC: Energy efficient heterogeneous clustered scheme for wireless sensor networks. *Computer Communications*, *32*(4), 662.
17. Lung, C. H., & Zhou, C. (2010). Using hierarchical agglomerative clustering in wireless sensor networks: An energy-efficient and flexible approach. *Ad Hoc Networks*, *8*(3), 328.
18. Chamam, A., & Pierre, S. (2010). A distributed energy-efficient clustering protocol for wireless sensor networks. *Computers and Electrical Engineering*, *36*(2), 303.
19. Dimokas, N., Katsaros, D., & Manolopoulos, Y. (2010). Energy-efficient distributed clustering in wireless sensor networks. *Journal of Parallel and Distributed Computing*, *70*(4), 371.
20. Zhang, H., & Shen, H. (2010). Energy-efficient beaconless geographic routing in wireless sensor networks. *IEEE Transactions on Parallel and Distributed Systems*, *21*(6), 881.
21. Deng, S., Li, J., & Shen, L. (2011). Mobility-based clustering protocol for wireless sensor networks with mobile nodes. *IET Wireless Sensor Systems*, *1*(1), 39.
22. Mao, X., Tang, S., Xu, X., Li, X. Y., & Ma, H. (2011). Energy-efficient opportunistic routing in wireless sensor networks. *IEEE Transactions on Parallel and Distributed Systems*, *22*(11), 1934.
23. Huang, H., Hu, G., Yu, F., & Zhang, Z. (2011). Energy-aware interference-sensitive geographic routing in wireless sensor networks. *IET Communications*, *5*(18), 2692.
24. Mottola, L., & Picco, G. P. (2011). MUSTER: Adaptive energy-aware multisink routing in wireless sensor networks. *IEEE Transactions on Mobile Computing*, *10*(12), 1694.
25. Mohammad El-Basioni, B. M., Abd El-kader, S. M., Eissa, H. S., & Zahra, M. M. (2011). An optimized energy-aware routing protocol for wireless sensor network. *Egyptian Informatics Journal*, *12*(2), 61.
26. Aioffi, W. M., Valle, C. A., Mateus, G. R., & da Cunha, A. S. (2011). Balancing message delivery latency and network lifetime through an integrated model for clustering and routing in wireless sensor networks. *Computer Networks*, *55*(13), 2803.
27. Liu, Z., Zheng, Q., Xue, L., & Guan, X. (2012). A distributed energy-efficient clustering algorithm with improved coverage in wireless sensor networks. *Future Generation Computer Systems*, *28*(5), 780.
28. Wang, B., Lim, H. B., & Ma, D. (2012). A coverage-aware clustering protocol for wireless sensor networks. *Computer Networks*, *56*(5), 1599.
29. Huang, P., Wang, C., & Xiao, L. (2012). Improving end-to-end routing performance of greedy forwarding in sensor networks. *IEEE Transactions on Parallel and Distributed Systems*, *23*(3), 556.
30. Anisi, M. H., Abdul-Salaam, G., Idris, M. Y. I., Wahab, A. W. A., & Ahmedy, I. (2015). Energy harvesting and battery power based routing in wireless sensor networks. *Wireless Networks*, *22*(1), 1–18.
31. Abdul-Salaam, G., Abdullah, A. H., Anisi, M. H., Gani, A., & Alelaiwi, A. (2016). A comparative analysis of energy conservation approaches in hybrid wireless sensor networks data collection protocols. *Telecommunication Systems*, *61*, 159.
32. Selvakennedy, S., Sinnappan, S., & Shang, Y. (2007). A biologically-inspired clustering protocol for wireless sensor networks. *Computer Communications*, *30*(14), 2786.
33. Wang, L., Zhang, R., & Geng, S. (2009). An energy-balanced ant-based routing protocol for wireless sensor networks. In *5th International Conference on Wireless Communications, Networking and Mobile Computing, IEEE 2009* (pp. 1–4).

34. Yang, J., Xu, M., Zhao, W., & Xu, B. (2009). A multipath routing protocol based on clustering and ant colony optimization for wireless sensor networks. *Sensors*, *10*(5), 4521.
35. Bari, A., Wazed, S., Jaekel, A., & Bandyopadhyay, S. (2009). A genetic algorithm based approach for energy efficient routing in two-tiered sensor networks: A genetic algorithm based approach for energy efficient routing in two-tiered sensor networks. *Ad Hoc Networks*, *7*(4), 665.
36. Cobo, L., Quintero, A., & Pierre, S. (2010). Ant-based routing for wireless multimedia sensor networks using multiple QoS metrics. *Computer Networks*, *54*(17), 2991.
37. Najafi, F., Dezfouli, M. A., & Rostami, H. (2011). Formatting a novel clustering protocol based on artificial immune system algorithm for wireless sensor networks. *International Journal of Advanced Engineering Sciences and Technologies*, *6*(6), 256–260.
38. Song, M. A. O., & Zhao, C. L. (2011). Unequal clustering algorithm for WSN based on fuzzy logic and improved ACO. *The Journal of China Universities of Posts and Telecommunications*, *18*(6), 89.
39. Saleem, M., Di Caro, G. A., & Farooq, M. (2011). Swarm intelligence based routing protocol for wireless sensor networks: Survey and future directions. *Information Sciences*, *181*(20), 4597.
40. Kulkarni, R. V., Forster, A., & Venayagamoorthy, G. K. (2011). Computational intelligence in wireless sensor networks: A survey. *IEEE Communications Surveys and Tutorials*, *13*(1), 68.
41. Liu, M., Xu, S., & Sun, S. (2012). An agent-assisted QoS-based routing algorithm for wireless sensor networks. *Journal of Network and Computer Applications*, *35*(1), 29.
42. Attea, B. A., & Khalil, E. A. (2012). A new evolutionary based routing protocol for clustered heterogeneous wireless sensor networks. *Applied Soft Computing*, *12*(7), 1950–1957.
43. Saleem, M., & Farooq, M. (2012). Beesensor: A bee-inspired power aware routing protocol for wireless sensor networks. In *Applications of Evolutionary Computing* (pp. 81–90). Berlin: Springer.
44. Yau, K. L. A., Komisarczuk, P., & Teal, P. D. (2012). Reinforcement learning for context awareness and intelligence in wireless networks: Review, new features and open issues. *Journal of Network and Computer Applications*, *35*(1), 253.
45. Guo, W., & Zhang, W. (2014). A survey on intelligent routing protocols in wireless sensor networks. *Journal of Network and Computer Applications*, *38*, 185–201.
46. Hoang, D., Yadav, P., Kumar, R., & Panda, S. (2014). Real-time implementation of a Harmony search algorithm-based clustering protocol for energy efficient wireless sensor networks. *IEEE Transactions on Industrial Informatics*, *10*(1), 774–783.
47. Kuila, P., & Jana, P. K. (2014). Energy efficient clustering and routing algorithms for wireless sensor networks: Particle swarm optimization approach. *Engineering Applications of Artificial Intelligence*, *33*, 127.
48. Celal Ozturk, D. K., & Hancer, E. (2015). Dynamic clustering with improved binary artificial bee colony algorithm. *Applied Soft Computing*, *28*, 69–80.
49. Kong, L., Pan, J. S., Tsai, P. W., Vaclav, S., & Ho, J. H. (2015). A balanced power consumption algorithm based on enhanced parallel cat swarm optimization for wireless sensor network. International Journal of Distributed Sensor Networks.
50. Hu, Y. F., Ding, Y. S., Ren, L. H., Hao, K. R., & Han, H. (2012). n endocrine cooperative particle swarm optimization algorithm for routing recovery problem of wireless sensor networks with multiple mobile sinks. *Information Sciences*, *300*, 100–113.

Palvinder Singh Mann received his Bachelor's degree (B.Tech) with Honours (Institute Gold Medal) in Information Technology from Kurukshetra University, Kurukshetra, Haryana, India in the year 2005 and Master's degree (M.Tech) in Computer Science and Engineering from Punjab Technical University, Jalandhar, Punjab, India in the year 2010. He is currently a Ph.D. research scholar at Punjab Technical University, Jalandhar, Punjab, India. He has published more than 40 research papers in various International Journals and Conferences. His research interest includes Wireless Sensor Networks, Computational Intelligence and Cloud Computing.

Satvir Singh received his Bachelor's degree (B.Tech.) from Dr. B. R. Ambedkar National Institute of Technology, Jalandhar, Punjab (India) with specialization in Electronics and Communication Engineering in year 1998, Master's degree (M.E.) from Delhi Technological University (Formerly, Delhi College of Engineering), Delhi (India) with distinction in Electronics and Communication Engineering in year 2000 and Doctoral degree (Ph.D.) from Maharshi Dayanand University, Rohtak, Haryana (India) in year 2011. He is Life Member of ISTE and Corporate Member of IETE. His fields of interest include Evolutionary Algorithms, High Performance Computing, Type-1 and Type-2 Fuzzy Logic Systems, Wireless Sensor Networks and Artificial Neural Networks for solving engineering problems. He has also published nearly 50 research papers in International Journals and Conferences.

JHSS, VOL. 10, NO. 1, HALF YEARLY : JULY 2016

ENHANCING BONE STRENGTH WITH WEIGHT BEARING EXERCISES/ACTIVITIES

Rajiv Chaudhary
Ramesh Chandra Singh
Mechanical Engineering Department,
Delhi Technological University, Delhi 110 042

ABSTRACT

Bones are of great importance to our body, as apart from supporting to our whole body, bones also support many other activities like standing, walking, running, jumping, playing, swimming, dancing and writing etc. Human body is more than 200 bones, which is a complex tissue, made up of several different tissues working together. There are various factors on which strength of bone depends. One such factor is the bone density, which is enhanced by the stress developed in bones. There is a category of sports/activities in which gravitational force or weight acts on bone, developing stress and improving bone density, called Weight-Bearing Activities. Apart from identifying these activities, its mechanism, benefits and other implications have been discussed in this paper.

keywords: Strength, Stresses, Bone Density, Weight-Bearing Activities, Impact,

INTRODUCTION

Strength of bones depend on so many factors. By taking proper diet, having calcium as well other minerals in it and by performing enough physical activities, that supports bone strength. Bones are always growing and these become the strongest in aged 20s, that's why in this period one needs to work hard to build one's bone strength during this age. The category of sports/activities applying gravitational force or weight over bone,

induces stress and by improving bone density, enhances bone strength. Such activities, called Weight-Bearing Activities, have been found to be supportive for bones health.

Bone naturally becomes weaker with age, so exercise is highly desirable for people of all ages, as mass density may be maximized and it therefore prevents poor bone health in elder years. In this paper the mechanism of stress development has been studied and an effort for analysis of stress has been made. Along with the types of the weight-bearing activities, its effects, benefits and other aspects have been discussed in this paper.

WEIGHT-BEARING ACTIVITIES

There is a category of physical activities in which weight is applied o, placed on bone. These activities make our bones work against the pulling force of the ground, and are actually called weight-bearing activities. As the muscles are attached with bones, so the muscles also undergo the pulling and pushing forces along with over bones. Muscles as holding the bones and the Gravitational force together develop the stress in bones and muscles. So with these weight bearing activities bone as well as muscles become stronger. One more thing is noteworthy here that every physical activity can not be brought under weight-bearing activity? For example sports activities like Swimming and Cycling may be one of the best exercises for the heart as well as for the body, but these are not so important from the bone building activity point of view.

SPORTS/ACTIVITIES INVOLVING WEIGHT-BEARING ACTIVITIES

Several weight-bearing activities may be mentioned as Walking, Jogging, Running, Aerobics, Weight Lifting, Climbing, Dancing, Martial art, Push-ups, Hiking and even household/yard work chores etc.

BONE STRENGTH AND WEIGHT-BEARING ACTIVITIES

As muscles grow and get strengthened following exercises and physical activities: bones also respond in same way. Weight bearing activities stimulate the bones in such a way that bones become stronger. On application of weight/load on bones, through various activities, stress would be developed, by which calcium content as well as density of the bone increases. On the other side physical inactivity affects reverse as it causes decrease in bone mass density, making bone weaker. This way Exercise/Physical activity helps in maintaining bone density and reduces possibility of bone weakness with growing age.

BONE STRENGTH AND BONE DENSITY is an important indicator of bone health. Strength of the bones is measured in terms of Bone density. Density of bone being more, means higher proportion of calcium and ultimately representing more strength of bone. As the age grows, bone used to build the strength naturally, by picking up of calcium proportion during their age in twenties. As the age further advances into thirty's, these start losing bone strength, as the body withdraws back calcium, subsequently loosing the strength.

TYPES OF STRESSES

On application of load/gravitational force the bones undergo a kind of stress, that depends on the type of loading taking place over the bone. With weight bearing activities there are three types of stresses may be developed.

GRADUALLY APPLIED LOAD

When a load is assumed to be applied gradually in installments i.e. load of 200 N assumed to be applied in . First a load of 10 N then 20 N, 30 N 40 N.. .up to 200 N is applied. Mostly in static conditions load is assumed to be applied gradually and Stress developed is equal to ratio of Force (F) and normal area (A) over which stress is acting. This causes less stress and less strain as compared to suddenly applied load. (In this case stress strain curve will be a triangle).

$$Stress\ \sigma_2 = \frac{2F}{A}$$

SUDDENLY APPLIED LOAD

When the whole force (F Newton) is applied suddenly i.e. in one installment force of is applied over an area of (A) in one installment. It develops the stress which is two times as compared to when the same load is applied gradually. (In this case stress strain curve will be a rectangle)

$$Stress\ \sigma_1 = \frac{F}{A}$$

IMPACT LOAD

The moving body striking another body creates impact load. It causes many times stress when if the same load is applied gradually. Example: force applied in an accident is an impact load.

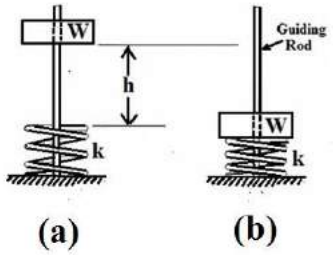

Fig 1: Impact Loading (Load falling from a height)

As shown (Fig 1), a Weight (F) is dropped from a height (h), over an area of (A) to acquire a velocity for impact, with Modulus of Elasticity of the materia1 being (E). So the stress developed may be expressed by the following equation. It is found to be many times more than the value of stress with gradually applied load.

$$Stress\ \sigma_3 = \frac{W}{A}\left[1 + \sqrt{\left(1 + \frac{2hAE}{W}\right)}\right]$$

So through various Weight bearing activities, the degree of stress to be developed may be controlled by different types of loading conditions, that we get in various types of sports/activities under Weight bearing activities.

CONCLUSION:

Through various sports/activities under Weight bearing activities, we have a range of activities developing different degrees of stresses. As these stresses improve bone strength, so we get a variety of activities, to enhance bone strength as desired. So through various Weight bearing activities, the degree of stress to be developed may be controlled by different types of loading conditions, that we get in various types of sports/activities. By Physical activity/exercise strength of bone gets improved. It incorporates balance and develops coordination within muscular mass, which helps in preventing falls & bone fractures and ultimately reduces the risk of weakness of bones. Weight-bearing activities also cause formation of new bone tissues, which further enhances the strength of the bone. During early ages of childhood and adolescence, density as well as strength develops naturally, which does not happen during elder ages. Exercise/physical activities is very beneficial for the people who have been inactive. This way exercise/physical activities become compulsory for people of all ages, in order to strengthen or maintain bone health.

REFERENCES

Currey JD. Bones. Structure and mechanics. Princeton: Princeton University Press; 2002.

Krystyna Ksiezopolska Orfowska Review Article-'Changes in bone mechanical strength in response to physical therapy", Polskie

Archiwum Medycyny Wewnetanej 2010; 120 (9) 389-372

Dempster DW. Structure and function of the skeletal system in adults. Medicographia. 2009; 22: 18-24. Polish.

Smit TH, Burger EH, Huyghe JM. A case for strain induced fluid flow as a regular of BMU-coupling and osteonal alignment. J Bone Miner Res. 2002; 17:2021-2029.

Seeman E, Delmas PD. Bone quality - the material and structural basis of bone strength and fragility. N Engl J Med 2006; 354:2250-2261.

Zebaze RMD, Jones A, Welsh F, et al. Femoral neck shape and the spatial distribution of its mineral mass varies with its size: clinical and biomechanical implications. Bone 2005; 37:243-252.

International Research Journal of Engineering and Technology (IRJET) e-ISSN: 2395 -0056
Volume: 03 Issue: 05 | May-2016 www.irjet.net p-ISSN: 2395-0072

EVALUATION OF GREEN HOUSE GASES EMISSIONS FROM SEWAGE TREATMENT PLANTS

Mayank Mrinal[1], Anubha Mandal[2], Anunay Gour[3], Lovleen Gupta[4]

[1] *M.Tech,Department of Environmental Engineering, Delhi Technological University, Delhi, India.*

[2] *Professor(UGC Scientist 'C'),Department of Environmental Engineering, Delhi Technological University, Delhi,*

[34] *Assistant Professor ,Department of Environmental Engineering, Delhi Technological University, Delhi, India.*

Abstract - *Sewage treatment plants are considered as sources of GHGs (greenhouse gases) production mainly methane, carbon dioxide and nitrous oxide which are produced during biological sewage treatment process and off-site electricity production which is a major source of carbon dioxide generation. Reducing the green house gases from the sewage treatment plants is a major concern. The day to day increase in the global temperature is an alarming situation and the most prominent cause of which is increase in the emission of green house gases. In this study, it has been attempted to evaluate the emissions of green house gases from some of the major sewage treatment plants of Delhi. It has been observed that the indirect GHGs emission because of the generation of power at off-site is much more than the direct on-site GHGs emission as a result of sewage treatment by the Activated Sludge Process. The power consumption of the concerned plants are obtained the respective plants. The total power consumption of Okhla, Keshopur and Yamuna Vihar sewage treatment plants are obtained by the addition of the BSES electricity bills for each month(January-2014 to December-2014) provided by the engineers at the respective plants.*

Key Words: **Green House Gases, Activated Sludge Process, Methane Correction Factor, Methane, Global Temperature.**

.INTRODUCTION

The increasing concentration of GHGs in the atmosphere have led to further studies of GHGs estimation and its source. Waste water is received by wastewater treatment plant and produces treated water by the use of different processes such as aerobic treatment, anaerobic treatment[1]. The GHGs emissions from wastewater treatment processes and operations in recent years have become a significant concern and thus are increasingly measured and also assessed while determining the long term sustainability of a treatment system[2]. The larger minor sources of GHGs emissions are wastewater treatment plants (WWTPs). Both directly and indirectly during the treatment processes these plants produce the three important GHGs namely carbon dioxide (CO_2), methane (CH_4), and nitrous oxide (N_2O). The gaseous byproducts such as CO_2, CH_4, and N_2O results in direct emissions and the indirect emissions are caused due to the use of energy and ancillary activities[3].

1.1 Objectives

In this study, the data from various sources including the sewage treatment plants have been collected for the more accurate and appropriate estimation of GHGs emissions and the objective of the project are:

To evaluate the direct GHGs namely CH_4, N_2O and CO_2 emissions from the four major sewage treatment plants in Delhi namely :

a.) Okhla Sewage Treatment Plant,
b.) Rithala Sewage Treatment Plant,
c.) Keshopur Sewage Treatment Plant and
d.) Yamuna Vihar Sewage Treatment Plant.

To quantify the indirect emissions of green house gases as result of electricity consumption by concerned sewage treatment plants.

2. METHODOLOGY

The data required for the evaluation of green house gases emissions were collected from the respective sewage treatment plants namely Okhla, Rithala, Keshopur and Yamuna Vihar. Also the visits were made to Delhi Jal Board(DJB) and Delhi Pollution Control Committee(DPCC) for obtaining the values for methane correction factor of the concerned treatment plants and other parameters required for estimating GHGs emissions. Procedures and protocols for

quantifying the emissions were followed as per IPCC 2006 guidelines.

2.1 Protocol and Procedure for Evaluating GHGs Emissions

The study is based on GHG protocol and IPCC Guidelines for National Greenhouse Gas Inventories (2006).The Greenhouse Gas (GHG) Protocol, developed by World Resources Institute (WRI) and World Business Council on Sustainable Development (WBCSD), sets the global standard for how to measure, manage, and report greenhouse gas emissions. As per the protocol firstly, the organizational boundary and operational boundary are identified. The organizational boundary includes the STP and the grid from which the electricity is being imported.

The operational boundary includes the emissions associated with operation and the treatment process at STP. The operational boundary includes Scope1,Scope2 and Scope3 emissions.

In scope 1 three gases i.e. CO_2, CH_4 and N_2O are calculated for STP. CO_2 emissions from STP and should not be included in national total emissions. Biogenic origin means short cycle or natural sources of atmospheric CO_2 which cycles from plants to animals to humans as part of the natural carbon cycle and food chain do not contribute to global warming.

In Scope 2 emissions are from import of electricity and in Scope 3 emission other indirect emissions can be calculated but in this study it is not included because of insufficient data.

Secondly, the tracking of emissions over a fixed period of time is done. In this study the GHGs emissions are calculated for a period of one year i.e. from January 2014 to December 2014.

Thirdly, GHGs emissions from STP are calculated. We have followed IPCC 2006 Guidelines for National Greenhouse Gas Inventories for calculating GHG emissions from STPs.

The country specific values for the per capita BOD and methane correction factor is obtained from the Delhi Pollution Control Board and the sewage treatment plants which are established by Delhi Jal Board.

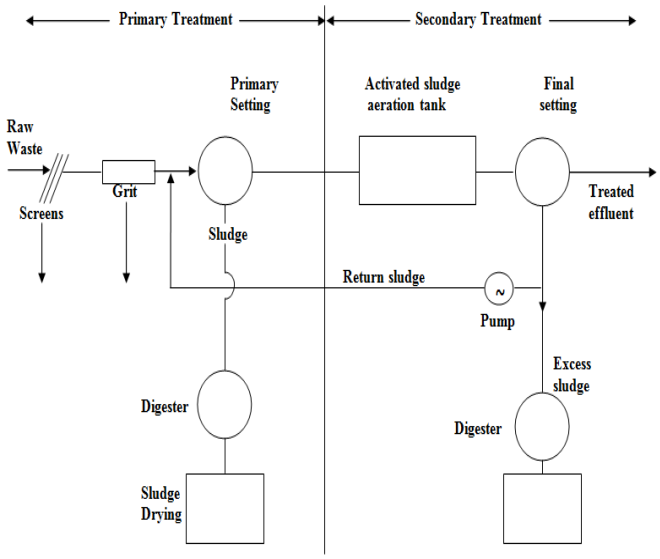

Fig -1: Flow Diagram of Sewage Treatment Plants at Okhla, Keshopur ,Yamuna Vihar and Rithala.

In the sewage treatment plant, the activated sludge process is a biological process that involves air or oxygen being introduced into a mixture of screened, and primary treated sewage combined with organisms to develop a biological floc which reduces the organic content of the sewage. The combination of wastewater and biological mass is commonly known as mixed liquor. In all activated sludge plants, once the wastewater has received sufficient treatment, excess mixed liquor is discharged into settling tanks and the treated supernatant is run off to undergo further treatment before discharge. Part of the settled material, the sludge, is returned to the head of the aeration system to re-seed the new wastewater entering the tank. This fraction of the floc is called return activated sludge.

3. RESULTS AND DISCUSSIONS

3.1 Calculation of Total Organics in Wastewater

TOW (kg BOD/cap/yr)
= P * BOD * 0.001 * I * 365

=16787941*46.8*0.001*1.25*365 (See Table 1)
= 358464510.2 kg BOD/cap/y----------(1)

3.2 Estimation of methane emission factor

Methane Emission factor(EFj)(kg CH4/kg BOD)
= Bo * MCFj
= 0.6*0.001 (See Table 1)
= 0.0006---------- (2)

Bo is the maximum CH_4 producing capacity, kg CH_4/kg BOD

Table -1: Parameter Values for Estimation of Direct GHGs.

Parameter	Value		Source
Per Capita BOD(gBOD/day)	46.8		DPCC
Population(P)	16787941		Statistical Abstract of Delhi 2014 Report, Govt. of NCT of Delhi
Methane correction factor or each treatment system(MCFj),B_0	0.001,0.6 respectively.		DJB, Respective Sewage Treatment Plants, IPCC 2006
Bo, FNPR, FNON-CON, FIND-COM	0.6,0.16,1.4,1.25 respectively.		IPCC 2006
Ui	Rural	0.07	Housing Condition in India NSS Report 2010,MOEF Report 2011
	Urban High	0.66	
	Urban Low	0.27	
Tij	Rural	0.00	Housing Condition in India NSS Report 2010,MOEF Report 2011
	Urban High	0.95	
	Urban Low	0.99	

3.3 Calculation for methane emissions

Type of treatment or discharge is Aerobic.

Fraction of Population income group (Ui) fraction for Delhi is as follows:
Rural = 0.07
Urban High = 0.66
Urban Low = 0.27
Average total = 0.333

Degree of utilization of treatment, discharge pathway or method (Tij) for each income group:
Rural = 0.00
Urban High = 0.95
Urban Low = 0.99
Average Total = 0.65

Using the values of Ui and Tij form Table 1 and TOW and Emission factor from equation(1)&(2) in the governing equation, we get methane emissions as:
Total CH_4 Emissions = [Σi,j(Ui * Ti,j * EFj)](TOW-S)-R
Where,
S = Organic component removed as sludge, kg BOD/yr
R = amount of CH_4 recovered in inventory year, kg CH_4/yr
Default values of S and R are taken as zero as per IPCC 2006 guidelines.

Total CH_4 Emissions(kg CH_4/yr)
= 358464510.2*0.0006*0.65*0.333
= 46553.78.

Global Warming Potential (GWP) for Methane = 25
(Source: IPCC Fourth Assessment Report (FAR),2007)
Total CO_2et = 46.55378*25=**1164 tCO2e/yr**

3.4 Total Nitrogen in the Effluent

Total Nitrogen in the Effluent
= (P*Protein*FNPR*FNON-CON*FIND-COM) - NSLUDGE
= 16787941*0.056*0.16*1.4*1.25 (See Table 1)
= 263234.9 kg N/year ----------(3)
Where:
NEFFLUENT = total annual amount of nitrogen in the wastewater effluent, kg N/yr
P = human population
Protein = annual per capita protein consumption, default=0.056 kg/person/yr
FNPR = fraction of nitrogen in protein, default = 0.16, kg N/kg protein
FNON-CON = factor for non-consumed protein added to the wastewater
FIND-COM = factor for industrial and commercial co-discharged protein into the sewer system
NSLUDGE = nitrogen removed with sludge (default = zero), kg N/yr

3.5 Calculation of N_2O Emissions from the Sewage Treatment Plant

Net N_2O Emission
=NEFFLUENT*EFEFFLUENT*44/28
= 263234.9*.0005*1.57----------from(3)
= **206.6 kg N_2O/year**
Where:
N_2O emissions = N_2O emissions in inventory year, kg N_2O/yr
EFEFFLUENT = emission factor for N_2O emissions from discharged wastewater, kg N_2O-N/kg N
The factor 44/28 is the conversion of kg N_2O-N into kg N_2O.

GWP for N_2O = 298 (IPCC FAR,2007)
Total CO_2e Emission
= 61566.8 kgCO_2e/yr = **62tCO_2/yr**(approx.)

Hence, Total Direct GHGs Emissions(CH_4&N_2O) = (Total CH_4+Total N_2O)Emissions = **1164+62 = 1226tCO_2/yr.**

3.6 Methane Emissions

a.) Net CH_4 Emissions (kg CH_4/yr) from four STPs combined = 186216
b.) Net CH_4 Emissions (tCO_2e/yr) from four STPs combined = 4656

3.7 Nitrous Dioxide Emissions

a.) Net N_2O Emissions (kg N_2O/yr) from four STPs combined = 828
b.) Net N_2O Emissions (tCO_2e/yr) from four STPs combined = 248

The individual methane emissions and nitrous dioxide emissions from all the four STPs are same and the net emissions from all the four STPs are obtained by the addition of emissions by each sewage treatment plants. The methane emissions from each treatment plants is same because of the same MCF values which was provided by the Delhi Jal Board.

3.8 Indirect GHGs Emissions

a.) Emissions from Okhla STP(tCO_2e/yr) = 14240
b.) Emissions from Rithala STP(tCO_2e/yr) = 10560
c.) Emissions from Keshopur STP(tCO_2e/yr) = 17413
d.) Emissions from Yamuna Vihar STP(tCO_2e/yr) = 2933

Table -2 : Total CO_2 equivalent indirect emission from the STPs.

Plant	Power Consumption(MWH/Yr.)	Emission Factor (tCO_2/MWH)	Total CO_2 Equivalent Emission(tCO_2e/yr)
Okhla STP	17365	0.82	14240
Rithala STP	12878	0.82	10560
Keshopur STP	21236	0.82	17413
Yamuna Vihar STP	3577	0.82	2933

The emission factor is available from Central Electricity Authority,CO_2 Baseline Database for Indian Power Sector 2014.
The net green house gases emissions are the sum total of the direct and the indirect emissions from the plants. It is found that Keshopur plant(72MGD) has the highest emissions which is 18640tCO_2/yr and Yamuna Vihar STP has the lowest emission of 4159tCO_2/yr.
The lowest emission of Yamuna Vihar STP is primarily because the volume of the sewage being treated at this plant is less as compared to the other plants. Directions by the Delhi Jal Board have been given to Keshopur plant to reduce the power consumption so that the emission of green house gases can be minimized.

4.CONCLUSION

The direct GHGs emissions from four STPs combined is 4904 tCO_2e/yr while the combined indirect emissions is 45146 tCO_2e/yr. The result indicates that the amounts the indirect green house gases emissions were significantly higher than the direct emissions at all the four STPs.
CH4 production from all the four plants is assessed as 4656 tCO_2e/yr and 248 t CO_2e/yr as N_2O emissions. The four sewage treatment plants which have been studied are the major treatment plants which combined together treats more than 70 percent of the total sewage generated in Delhi.
The Keshopur plant where the actual flow of the sewage to be treated is less as compared to flow at Okhla plant is producing more indirect emissions. The higher emissions from the Keshopur plant can be reduced by reducing the power consumption for various other miscellaneous activities.

REFERENCES

[1] Monteith, H. D., Sahely, H. R., MacLean, H. L., and Bagley, D. M. (2011). A rational procedure for estimation of greenhouse-gas emissions from municipal wastewater treatment plants. Water Environment Research, 77(4), 390-403.

[2] Scanlan, P., Elmendorf, H., Santha, H., and Rowan, J. (2008). How green is your footprint? The impact of greenhouse gas emissions on strategic planning. In Session 12:Climate Change Management, Mitigation, and Adaption. Proceedings of the Water Environment Federation, Sustainability, 10, 783-792.

[3] U.S. EPA (Environmental Protection Agency 2010). U.S. Greenhouse Gas Inventory Report: Inventory of U.S. Greenhouse Gas Emissions and Sinks, 1990–2008. EPA-430-R-10-006.

[4] Penman, Gytarsky, Hiraishi (2006). Intergovernmental Panel on Climate Change Guidelines for National Greenhouse Gas Inventories, Volume 5, Waste.

[5] Frijns, J., Roorda, J., Mulder, M., 2008. Op weg naar een klimaatneutrale waterketen. H2O 10, 36–37.

[6] Ingildsen, P., Jeppsson, U., Olsson, G., (2002). Dissolved oxygen controller based on on-line measurements of ammonium combining feed-forward and feedback. Water Science Technology 46(8-9), 454-465.

[7] Devisscher, M., Bogaert, H., Bixio, D., Van de Velde, J., Thoeye, C., (2002). Feasibility of automatic chemicals dosage control: a full scale evaluation. Water Science Technology 45, 4-5. 448-452.

[8] Olsson, G., Nielsen, M.K., Yuan, Z., Lynggaard-Jensen, A., Steyer, J.P. 2005. Instrumentation, Control and Automation in Wastewater Systems. IWA Publishing, London, UK.

[9] Machado, V.C., Gabriel, D., Lafuente, J., Baeza, J.A., 2009. Cost and effluent quality controllers design based on therelative gain array for a nutrient removal WWTP. Water Res. 43 (20), 5129-5141.

[10] Ayesa, E., De la Sota, A., Grau, P., Sagarna, J.M., Salterain, A., Suescun, J., 2006. Supervisory control strategies for the new WWTP of Galindo-Bilbao: the long run from the conceptual design to the full-scale experimental validation. Water Science Technolnology 53 (45),193-201.

[11] Gujer, W., Erni, P., 1978. The effect of diurnal ammonium load variation on the performance of nitrifying activated sludge processes. Prog. Water Technol. 10 (5/6), 391-407.

[12] Lessard, P., Beck, M.B., 1993. Modelling of the activated sludge process: a case of Norwich plant. Water Res. 27 (6), 963-978.

[13] Jeppsson, U., Pons, M.N., Nopens, I., Alex, J., Copp, J.B., Gernaey, K.V.,Rosen, C., Steyer, J.P., Vanrolleghem, P.A., 2007. Benchmark simulation model no 2 a general protocol and exploratory case studies. Water Sci. Technol. 56 (8), 287-295.

[14] MOEF (Ministry of Environment and Forests) (2010). India Greenhouse Gas Emissions *2*007, Report of Ministry of Environment and Forests, Government of India.

[15] CEA (2014). Central Electricity Authority, Ministry of Power, Govt of India, CO_2 Baseline Database for Indian Power Sector.

[16] Ranganathan, Corbier, Bhatia (2001). World Resources Institute, The Greenhouse Gas protocol: A Corporate Accounting and Reportin Standard, World Business Council for Sustainable Development.

[17] Hiatt, W.C., Grady Jr., C.P.L., 2008b. Application of the activated sludge model for nitrogen to elevated nitrogen conditions.Water Environment Resources 80, 2134-2144.

[18] Sin, G., Kaelin, D., Kampschreur, M. J., Takacs, I., Wett, B., Gernaey, K. V., Rieger, L.,Siegrist, H., Loosdrecht, M.C.M. (2008). Modelling nitrite in wastewater treatment system: a discussion of different modelling concepts. Water Science & Technology , 58, No 6, 1155-1171.

[19] Siegrist, H., & Gujer, W. (1994). Nitrogen removal in activated sludge systems including denitrification in secondary clarifiers. Water Science & Technology , *30*, No 6, 101-111.

[20] National Greenhouse Gas Inventory Committee. (2007). Australian Methodology for the Estimation of Greenhouse Gas Emissions and Sinks 2006: Waste. Australian Government, Department of Climate Change. Department of Climate Change.

[21] Siegrist, H., & Gujer, W. (1994). Nitrogen removal in activated sludge systems including denitrification in secondary clarifiers. Water Science & Technology , 30, No 6, 101-111.

[22] Anthonisen, A., Loehr, R., Prakasam, T., & Srinath, E. (1976). Inhibition of nitrification by ammonia and nitrous acid. Water Pollution Control Federation ,48, 835-852.

[23] Tabrez Khan, S., Hiraishi, A., 2001. Isolation and characterization of a new poly(3-hydroxybutyrate)-degrading, denitrifying bacterium from activated sludge. FEMS Microbiology Letters 205 (2), 253–257.

[24] Zheng, H., Hanaki, K., Matsuo, T., 1994. Production of nitrous oxide gas during nitrification of wastewater. Water Science and Technology 30 (6), 133–141.

[25] J. Foley, D.D. Haas, and Z.G. Yuan, Nitrous oxide generation in full-scale biological nutrient removal wastewater treatment plants, Water Resources 44 (2010), 831–844.

ResearchGate

See discussions, stats, and author profiles for this publication at: https://www.researchgate.net/publication/303738663

Experimental Analysis of Surface Roughness During CNC Milling of Brass Using Response Surface Methodology

Article · May 2016

READS

26

4 authors, including:

Ranganath M Singari

Delhi Technological University, Formerly D…

62 PUBLICATIONS **145** CITATIONS

SEE PROFILE

Radhey SHYAM Mishra

Delhi Technological University

32 PUBLICATIONS **64** CITATIONS

SEE PROFILE

All in-text references underlined in blue are linked to publications on ResearchGate, letting you access and read them immediately.

Available from: Ranganath M Singari
Retrieved on: 10 August 2016

OPEN ACCESS

International
Journal
Of Modern Engineering Research (IJMER)

Experimental Analysis of Surface Roughness During CNC Milling of Brass Using Response Surface Methodology

Ranganath M. S[1], Roshan Kumar[2], Desh Raj[3], R. S. Mishra[4]
[1, 2,3,4]*(Mechanical, Production And Industrial Engineering, Delhi Technological University, Delhi, India.)*

ABSTRACT :- *Optimization of machining parameters need to determine the most significant parameter for required output. The controllable parameters for the CNC milling machine are cutting tool variables, work piece material variables, and cutting conditions whereas the main desired output is surface roughness. Present work discusses the findings of an experimental investigation into the effects of cutting speed, feed rate and tool diameter during CNC milling of Brass keeping depth of cut constant. Response surface methodology (RSM) has been used to accomplish the objective of the experimental study. Face centered central composite design is used for conducting the experiments. The result from RSM revealed that tool dia. is the most significant factor followed by feed.*

Keywords:- *Surface Roughness(Rb); CNC Milling; Experimental Analysis; Brass; Response Surface Methodology;*

I. INTRODUCTION

Surface roughness, used to determine and evaluate the quality of a product, is one of the major quality attributes of a milling product. Previously trial and error approach was followed in order to obtain the optimal machining conditions for particular operations. Brass is specified because of the unique combination of properties, it is stronger and harder than copper, easy to form into various shapes, a good conductor of heat, and is generally resistant to corrosion from salt water. Owing to these properties, brass is usually a first-choice material for many components in equipment made in general.

In the electrical and precision engineering industries, brass is also used to make pipes and tubes, weather stripping, and other architectural trim pieces, screws, radiators, musical instruments, and cartridge casting for firearms. RSM is a collection of mathematical and statistical techniques that are useful for modeling and analysis of problems in which a response of interest is influenced by several variables and the objective is to optimize this response (Montgomery, 1997). RSM also quantifies relationships among one or more measured responses and the vital input factors. The steps in RSM are shown in figure1.

In RSM, polynomial equations, which explain the relations between input variables and response variables, are constructed from experiments or simulations and the equations are used to find optimal conditions of input variables in order to improve response variables. For the design of RSM, central composite design (CCD) is used in this experiment. CCD is widely used for fitting a second-order response surface. CCD consists of cube point runs, plus center point runs, and plus axial point runs. The three factors speed, feed rate, depth of cut, which were selected in the screening experiment, were used in CCD.

The factorial portion is a full factorial design with all factors at three levels, the star points are at the face of the cube portion on the design which correspond to value of -1. This is commonly referred to as a face centered CCD. The center points, as implied by the name, are points with all levels set to coded level 0, the midpoint of each factor range, and this is repeated six times. Twenty experiments to be performed. For each experimental trial, a new cutting edge to be used. The latest version of the Minitab or Design Expert may be used to develop the experimental plan for response surface methodology. The same software can also be used to analyze the data collected.

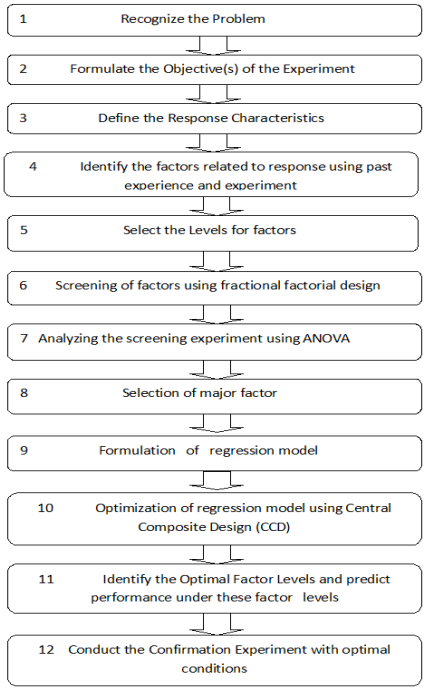

Figure 1. Steps in Response Surface Methodology (RSM).[6]

Present work discusses the findings of an experimental investigation into the effects of cutting speed, feed rate and tool diameter during CNC milling of Brass keeping depth of cut constant. Response surface methodology (RSM) has been used to accomplish the objective of the experimental study. Face centered central composite design is used for conducting the experiments.

II. EXPERIMENTAL SETUP

Experiments were conducted on CNC Milling Machine. Brass is taken as work piece material, HSS end milling cutter is used. Machining has been done as per the Design Matrix. The influencing parameters considered are speed, feed and tool diameter whereas depth of cut are taken constant. Table 1 shows the process parameters and their values.

The process was studied with a standard RSM design called a Central composite design (CCD). The factorial portion is a full factorial design with all factors at three levels, the star points are at the face of the cube portion on the design which correspond to value of -1. This is commonly referred to as a face centered CCD. The center points, as implied by the name, are points with all levels set to coded level 0, the midpoint of each factor range, and this is repeated six times.

Table 1: The process parameters and their values

Levels	Speed (A) (revolution/min)	Feed (B) (mm/min.)	Tool Diameter (C) (mm)	Depth of cut (mm)
1	1400	40	8	0.7
2	1550	55	10	0.7
3	1700	70	12	0.7

Figure 2: CNC Milling Machine

Twenty experiments were performed. For each experimental trial, a new cutting edge was used. The Minitab-17 was used to develop the experimental plan for response surface methodology. The same software was also used to analyze the data collected.

III. RESULTS AND ANALYSIS

The results from the machining trials performed as per the experimental plan are shown in Table 3. These results were used as input in the Minitab Software for further analysis. Without performing any transformation on the response, examination of the fit summary output revealed that the quadratic model is statistically significant for all the conditions and, therefore, it has been used for further analysis. An ANOVA table is commonly used to summarize the tests performed. Table 4 shows the Analysis of Variance (ANOVA). The Model F value of 27.60 implies the model is significant. Significance of Model is desirable as it indicates that the terms in the model have a significant effect on the response. From ANOVA table B, C and CC were found to be significant. From the ANOVA table tool dia. was found to be the most significant factor followed by feed.

Table 2: Central Composite Design Details

Factors: 3	Replicates: 1
Base runs: 20	Total runs: 20
Base blocks: 1	Total blocks: 1
Two-level factorial: Full factorial	
Cube points: 8	
Center points in cube: 6	
Axial points: 6	
Center points in axial: 0	

Table 3: Design Table

S.No	StdOrder	RunOrder	PtType	Blocks	A	B	C	Rb(µm)
1	20	1	0	1	0	0	0	0.458
2	18	2	0	1	0	0	0	0.458
3	1	3	1	1	-1	-1	-1	0.549
4	17	4	0	1	0	0	0	0.458
5	14	5	-1	1	0	0	1	1.5
6	13	6	-1	1	0	0	-1	0.562
7	16	7	0	1	0	0	0	0.458
8	19	8	0	1	0	0	0	0.458
9	9	9	-1	1	-1	0	0	0.382
10	2	10	1	1	1	-1	-1	0.675
11	11	11	-1	1	0	-1	0	0.36
12	15	12	0	1	0	0	0	0.458
13	4	13	1	1	1	1	-1	0.684
14	6	14	1	1	1	-1	1	2.09
15	5	15	1	1	-1	-1	1	1.22
16	8	16	1	1	1	1	1	3.01
17	3	17	1	1	-1	1	-1	0.621
18	7	18	1	1	-1	1	1	3.27
19	12	19	-1	1	0	1	0	0.699
20	10	20	-1	1	1	0	0	0.619

Table 4: Analysis of Variance

Source	DF	Adj SS	Adj MS	F-Value	P-Value
Model	9	13.6145	1.51272	27.60	0.000
Linear	3	7.6549	2.55165	46.55	0.000
A	1	0.1073	0.10733	1.96	0.192
B	1	1.1492	1.14921	20.97	0.001
C	1	6.3984	6.39840	116.73	0.000
Square	3	4.7162	1.57207	28.68	0.000
A*A	1	0.0862	0.08615	1.57	0.238
B*B	1	0.1167	0.11670	2.13	0.175

C*C	1	1.3765	1.37653	25.11	0.001
2-Way Interaction	3	1.2434	0.41445	7.56	0.006
A*B	1	0.1779	0.17791	3.25	0.102
A*C	1	0.0222	0.02216	0.40	0.539
B*C	1	1.0433	1.04329	19.03	0.001
Error	10	0.5481	0.05481		
Lack-of-Fit	5	0.5481	0.10963	*	*
Pure Error	5	0.0000	0.00000		
Total	19	14.1626			

Table 5: Model Summary

S	R-sq	R-sq(adj)	R-sq(pred)
0.234121	96.13%	92.65%	55.78%

Regression Equation

*Rb = 0.4042 + 0.1036 Speed + 0.3390 Feed + 0.7999 Tool diameter + 0.177 Speed*Speed + 0.206 Feed*Feed + 0.707 Tool diameter* Tool diameter - 0.1491 Speed*Feed + 0.0526 Speed* Tool diameter + 0.3611 Feed* Tool diameter*

(Where Rb is Surface roughness of brass.)

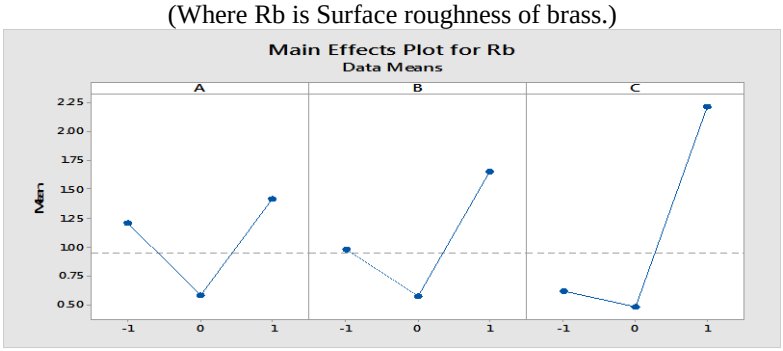

Figure 3: Main Effects Plots for Rb (Data Means)

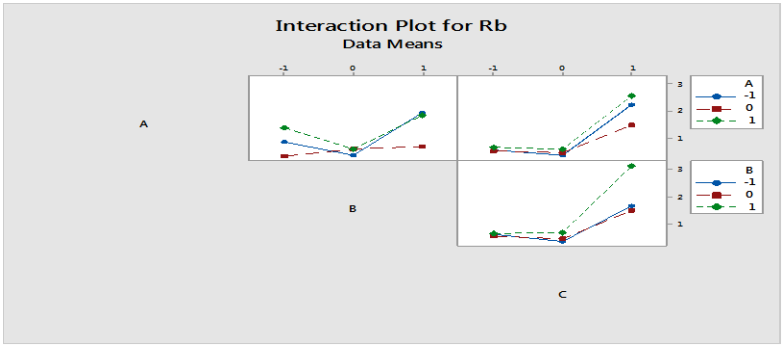

Figure 4: Interaction Plots for Rb (Data Means)

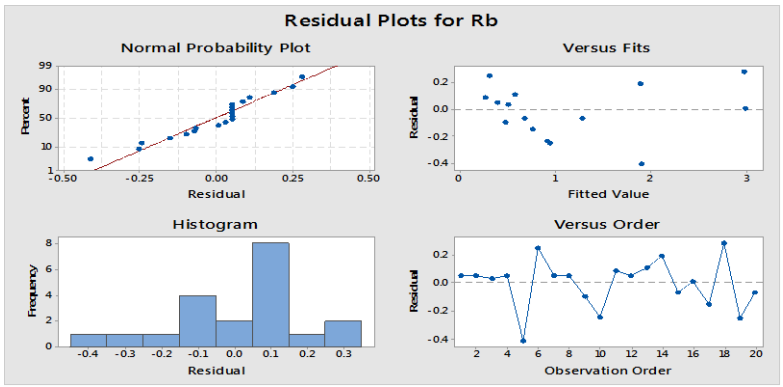

Figure 5: Residual Plots for Rb

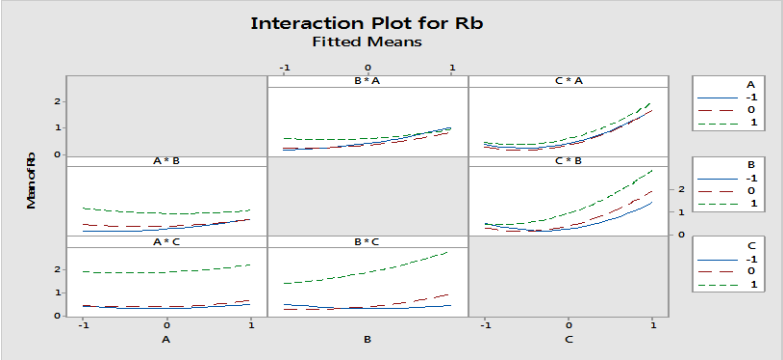

Figure 6: Interaction Plots for Rb

The normal probability plots of the residuals for Rb reveals that the residuals generally fall on a straight line implying that errors are distributed normally. Also in Fig. 5 showing residuals vs order for Rb reveals that they have no obvious pattern and unusual structure. This implies that the models proposed are adequate and there is no reason to suspect any violation of the independence or constant variation assumption. Fig.4 shows the interaction plots of Rb for the parameters.

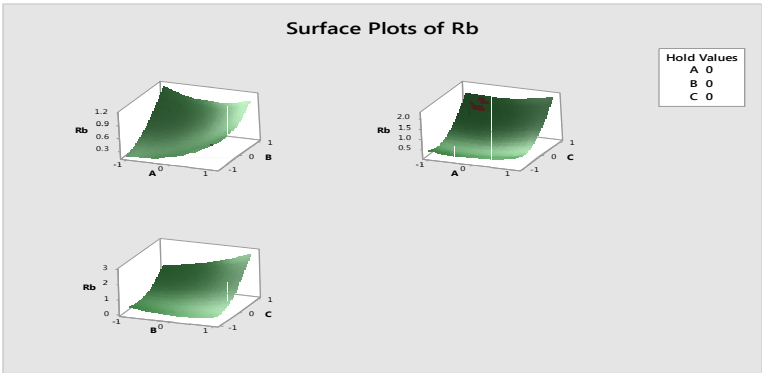

Figure 7: Surface Plots for Rb

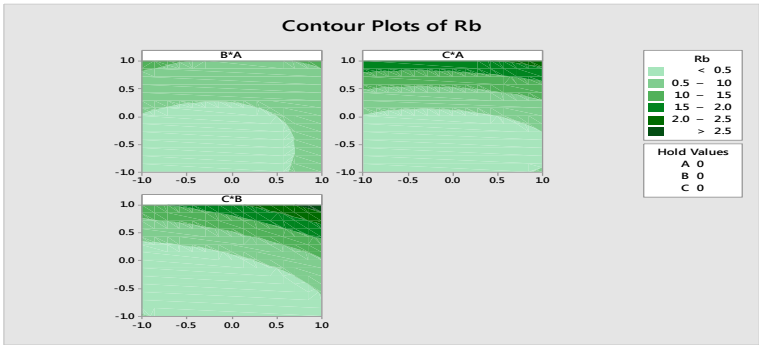

Figure 8: Contour Plots for Rb

The entire 3D surface graph for surface roughness has curvilinear profile in accordance to the quadratic model fitted. Fig-7 shows 3D surface plot graph of the effect of speed and depth of cut on the surface roughness. It has a curve linear shape according to the model fitted. The contour plot for the response, surface roughness is shown in fig-8. The surface roughness increases with increase in feed.

IV. CONCLUSION

The analysis of the results for surface roughness shows that the tool dia is the most significant factor followed by feed. The optimum value of surface roughness in the given range of parameters as depicted by graphs is 55 mm/min. (feed), 10 mm (tool dia) and 1550 rpm (speed). The Response surface methodology shows significance of all possible combinations of interactions and square terms. 3D surfaces generated by Response

surface methodology can help in visualizing the effect of parameters on response in the entire range specified, thus Response surface methodology is a better tool for optimization and can better predict the effect of parameters on response.

ACKNOWLEDGEMENTS

The authors acknowledge with thanks Pankaj Sharma and Roshan Kumar for carrying out the necessary experimental work.

REFERENCES

[1]. IbrahemMaher , M. E. H. Eltaib , Ahmed A. D. Sarhan & R. M. El-Zahry, "Investigation of the effect of machining parameters on the surface quality of machined brass (60/40) in CNC end milling—ANFIS modeling", Int J Adv Manuf Technol (2014) 74:531–537.

[2]. J.Balaraju, K.Srinivas and K.Siva Prasad, " Prediction of Surface Finish by end Milling using Factorial Technique" International Journal of Mathematical Sciences, Technology and Humanities 59 (2012) 647 – 653.

[3]. Ranganath M. S., Vipin, Nand Kumar, Rakesh Kumar, "Experimental Analysis of Surface Roughness in CNC Turning of Aluminium Using RSM Techniques", International Journal of Advanced Research and Innovation,Volume 3, Issue 1, 2015, 45-49.

[4]. Ranganath M. S., Vipin, Nand Kumar, R Srivastava, Surface Finish Monitoring in CNC Turning Using RSM andTaguchi Techniques, International Journal of Emerging Technology and Advanced Engineering Website Volume 4, Issue 9, 2014, 171-179

[5]. Ranganath M. S., Vipin, Harshit, Optimization of Process Parameters in Turning Operation Using Response Surface Methodology: A Review, International Journal of Emerging Technology and Advanced Engineering, Volume 4, Issue 10, 2014, 351-360.

[6]. Ranganath M S, Vipin, Harshit, "Surface Roughness Prediction Model for CNC Turning of EN-8 Steel Using Response Surface Methodology" International Journal of Emerging Technology and Advanced Engineering Website: www.ijetae.com (ISSN 2250-2459, ISO 9001:2008 Certified Journal, Volume 5, Issue 6, June 2015)

[7]. Ranganath M S, Vipin, Bhupendra Singh, "Experimental Investigation and analysis of Surface Roughness in Drilling Operation using Response Surface Methodology" Vth International Symposium on 'Fusion of Science & Technology', New Delhi,India, January 18-22,2016,ISBN: 978-93-84935-64-1.

[8]. Vishal Sardana, Achintya, Ranganath M. S. "Analysis of surface roughness during CNC Turning using Taguchi and Response Surface Methodology" IOSR Journal of Engineering (IOSRJEN) ISSN (e): 2250-3021, ISSN (p): 2278-8719 Vol. 06, Issue 02, 2016 PP 59-70

ISFT 2016

V[th] International Symposium on "Fusion of Science & Technology",
New Delhi, India, January 18-22, 2016

ID: 2016-ISFT-406

Experimental Investigation of the Temperature Variation and Vibrations at Different Loads at the Periphery of Single Cylinder Diesel Engine

Sumit Chaudhary[1], Vipin Kumar Sharma[2], R.C. Singh[3], Rajiv Chaudhary[4]

[1,2,3,4]*Department of Mechanical Engineering, Delhi Technological University, Delhi*
[2]*Department of Mechanical and Automation Engineering, Maharaja Agrasen Institute of Technology, Rohini, Delhi*
[1]*mait.sumit@gmail.com*

Abstract: *Engine head temperature and vibrations has considerable effect on performance, of the 4 stroke diesel engine. Present research work investigates the measurement of piston head temperature, frame temperature and vibration amplitudes at different load values. Thermal Imaging Camera was used to measure the temperature at various load conditions. Results showed that the maximum temperature on engine frame increases very rapidly as the load on the engine increases and engine head temperature along with minimum temperature on frame shows an increment but that is not so significant. In vibration analysis the displacement amplitude goes on increasing as the load on the engine increases. The velocity amplitude and acceleration amplitude both shows a decrement as initially and then increases with increase in load.*

Keywords: *vibration, frame temperature, velocity amplitude*

1. INTRODUCTION

The Engine head temperature is one of the major parameter which influences the performance of the 4 stroke diesel engine. It affects the overall efficiency, BHP, BSFC and the emission from the engine. The vibrations produced during the operation of the 4 stroke diesel engine have a very important impact on the engine stability and engine performance. Therefore for the optimum design of the 4 stroke diesel engine the analysis of these parameters is very important.

1.1 PREVIOUS RESEARCH

Singh R. C. et al.[1] have described the performance behaviors of a commercial diesel engine fueled with diesel and Jatropha based biodiesel (B100) at various loads (up to 100%) and compared using standard (conventional) and three new face profile designs (I, II & III) of piston rings. Face profiles of piston rings has considerable impact on engine's brake thermal efficiency (BTE), brake specific fuel consumption (BSFC), and mass flow rate, irrespective of fuels used. BTE of engine fueled with diesel increases 2-8% with new face profile design (III) of piston rings in comparison to standard (conventional) piston rings. BTE enhances 8-16% when engine is fueled with biodiesel using face profile design (III) on piston rings. Corresponding to increase in BTE, recorded reduction in BSFC (biodiesel) is 28-34%. John B. Heywood [2] explained the basics of Internal Combustion Engines. It contains a broadly based an extensive review of the fundamental principles which governs Internal Combustion Engine design and operation R.B. Gupta[3] elaborates fundamental point of view, how the fuel-air mixture within an Internal Combustion Engine cylinder is ignited and organizes the field. K.Sriniwasan[4] explains the propagation of flame front inside the combustion chamber and it also explains the various parameters are required for proper combustion or normal combustion inside the combustion chamber.

2. EXPERIMENTAL SETUP

The setup consists of single cylinder, four stroke, Diesel engine connected to eddy current type dynamometer for loading. It is provided with necessary instruments for combustion pressure and crank-angle measurements. These signals are interfaced to computer through engine indicator for Pθ–PV diagrams. Provision is also made for interfacing airflow, fuel flow, temperatures and load measurement. The set up has stand-alone panel box consisting of air box, fuel tank, manometer, fuel measuring unit, transmitters for air and fuel flow measurements, process indicator and engine indicator. Rotameters are provided for cooling water and calorimeter water flow measurement. The setup enables study of engine performance for brake power, indicated power, frictional power, BMEP, IMEP, brake thermal efficiency, indicated thermal efficiency, Mechanical efficiency, volumetric efficiency, specific fuel consumption, A/F ratio and heat balance. Labview based Engine Performance Analysis software package "EnginesoftLV" is provided for on line performance evaluation. A computerized Diesel injection pressure measurement is optionally provided. Thermal Imaging Camera used to measure the temperature at various load conditions.

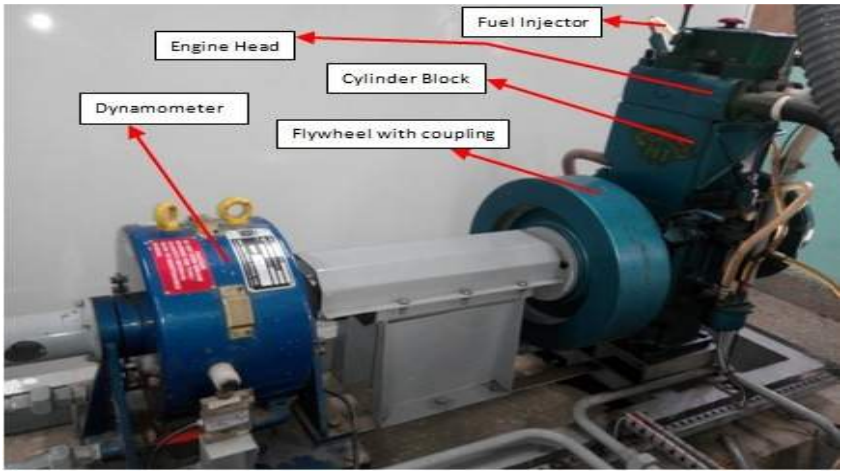

Fig. 1. Test Rig

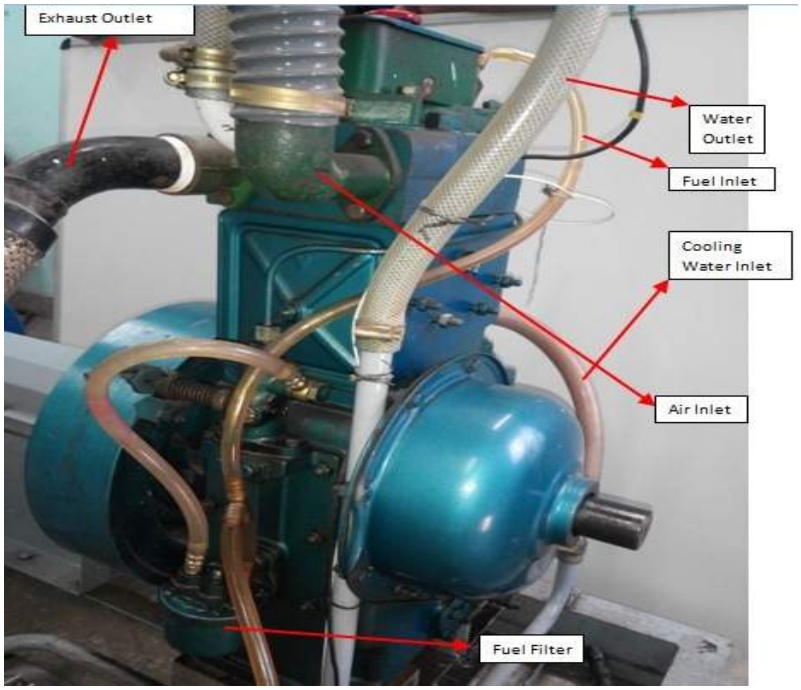

Fig. 2. Engine for experiments

TABLE 1: Specification of Engine Set-up

Engine test set up 1 cylinder, 4 stroke, Diesel engine								
System constants								
Orifice diameter (m)		0.02	Cylinder diameter (m), D				0.088	
Dynamometer arm length (m)		0.185	Stroke(m), L				0.11	
Coeff.of discharge for orifice, Cd		0.6	No of cylinders				1	
Ambient temperature (Deg C)		29	No.of rev./cycle				2	
Fuel density(kg/m3)		830	Specific heat of exhaust(kJ/kg0K)				1.1	
Fuel Calorific value (KJ/kg)		42000						

3. PERFORMANCE GRAPH

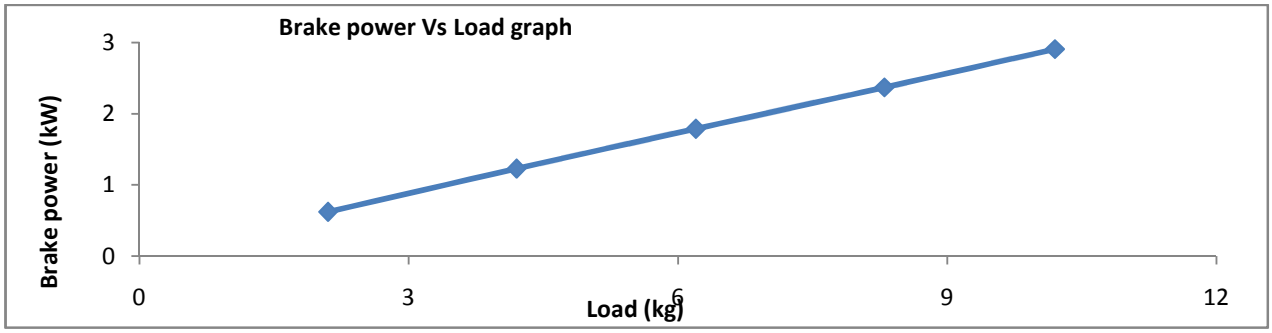

Fig. 3. Brake power vs Load graph

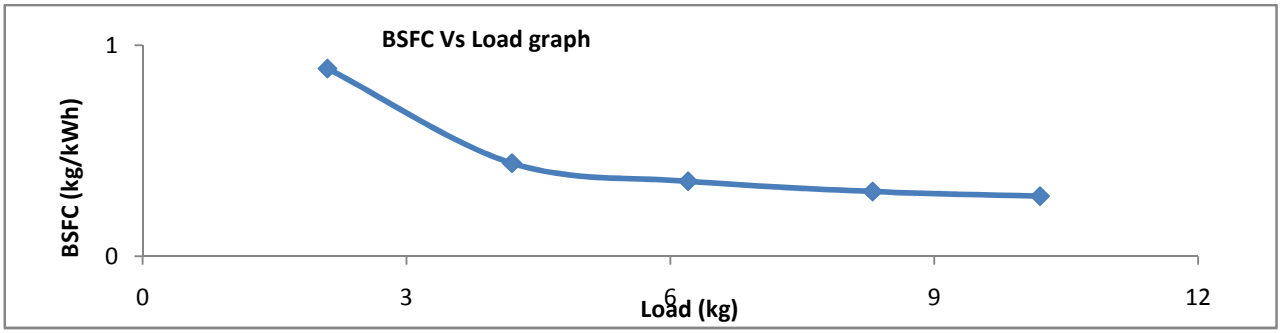

Fig. 4. BSFC vs Load graph

Brake Power is increasing with the increase of Load. BSFC decreases rapidly firstly and afterward decreases but with low rate with the increase of Load.

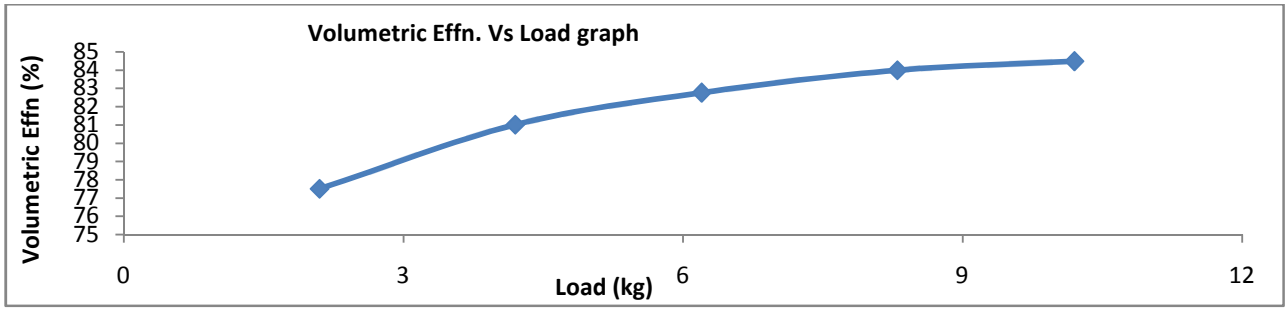

Fig. 5. Volumetric Efficiency vs Load graph

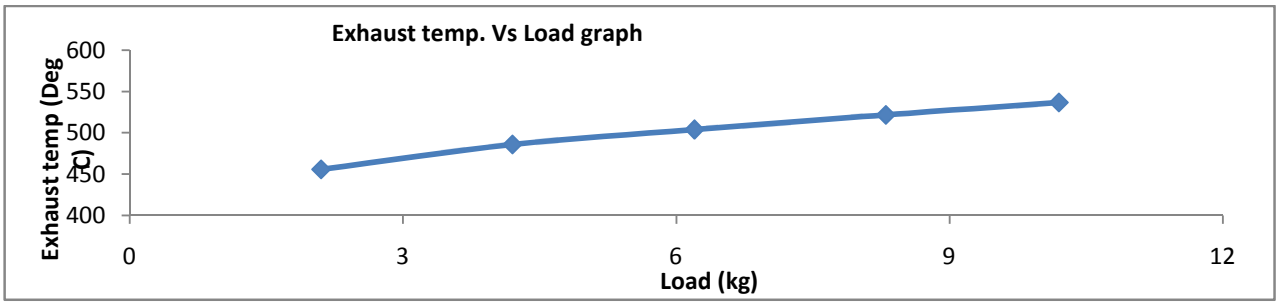

Fig. 6. Exhaust Temperature vs Load graph

- Volumetric Efficiency increases with the increase in Load but rate of increment keep on decreasing. Exhaust Temperature increases with the increase of Load.

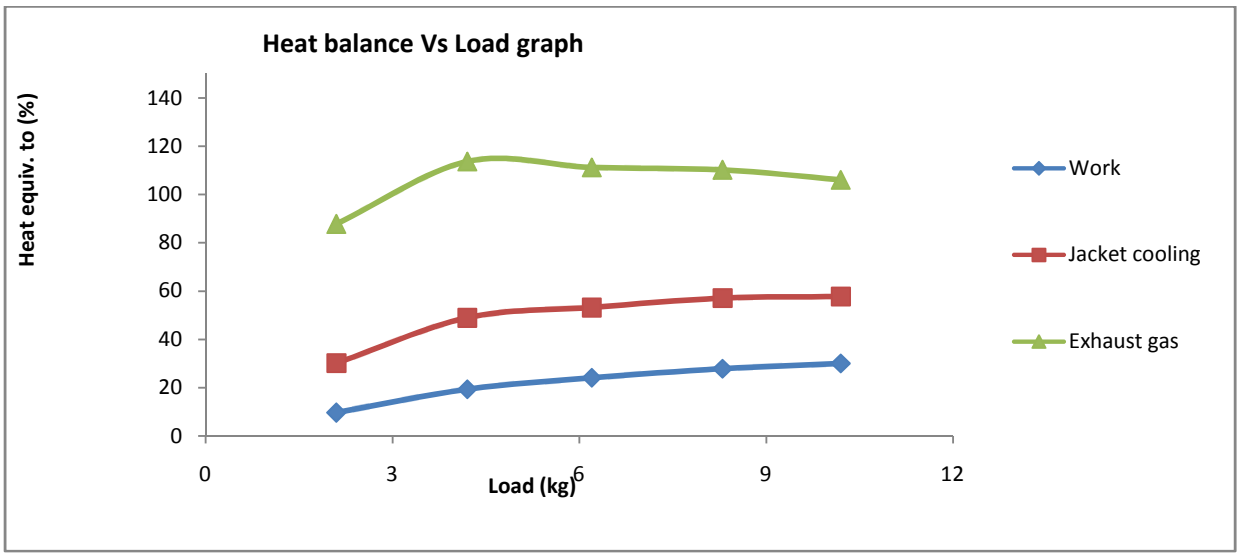

Fig. 7. Heat Balance vs Load graph

Percentage of Heat converted into Work is increases as we raise the load. Percentage of Heat taken by Cooling Jacket is also increases with the increase in Load. Percentage of Heat taken by Exhaust is initially increases with the increase in load up to 4 Kg, but afterward as we increases the load the percentage of heat in exhaust starts decreasing.

4. OBSERVATIONS

4.1 OBSERVATIONS ON THERMAL IMAGING CAMERA

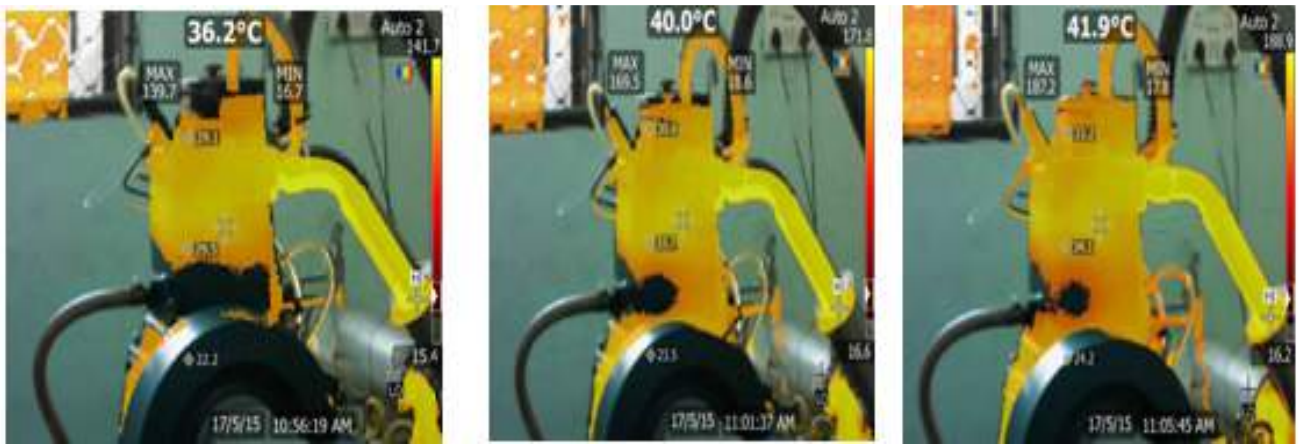

Fig. 8. Load 2.1Kg at 1557 RPM; Load 4.2 Kg at 1539 RPM; Load 6.2 Kg at 1516 RPM

Initially at load of 2.1 kg the temperature of Engine Head was 36.2 ◦C. Highest Temperature in the frame was at Exhaust outlet pipe of Engine which was 139.7◦C.Lowest Temperature in the frame was at Calorimeter, where water is entering into it, i.e 16.7◦C.

At load of 4.2 Kg the temperature of Engine Head was 40.0 ◦C. Highest Temperature in the frame was at Exhaust outlet pipe of Engine which was 169.5◦C.Lowest Temperature in the frame was at Calorimeter, where water is entering into it, i.e 18.6 ◦C.

At load of 6.2 Kg the temperature of Engine Head was 41.9 ◦C. Highest Temperature in the frame was at Exhaust outlet pipe of Engine which was 187.2◦C.Lowest Temperature in the frame was at Calorimeter, where water is entering into it, i.e 17.8 ◦C.

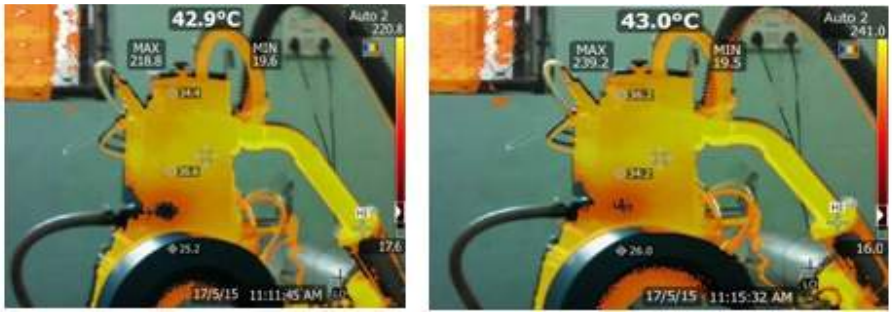

Fig. 9. Load 8.3 Kg at 1503 RPM; Load 10.2 Kg at 1499 RPM

At load of 8.3 Kg the temperature of Engine Head was 42.9 ◦C. Highest Temperature in the frame was at Exhaust outlet pipe of Engine which was 218.8 ◦C. Lowest Temperature in the frame was at Calorimeter, where water is entering into it, i.e 19.6 ◦C.

At load of 10.2 Kg the temperature of Engine Head was 43.0 ◦C. Highest Temperature in the frame was at Exhaust outlet pipe of Engine which was 239.2 ◦C. Lowest Temperature in the frame was at Calorimeter, where water is entering into it, i.e 19.5 ◦C

4.2 OBSERVATIONS ON VIBRATION MEASURING INSTRUMENT

Load 2.1 kg RPM 1557

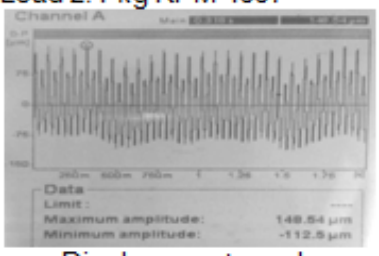

Displacement graph

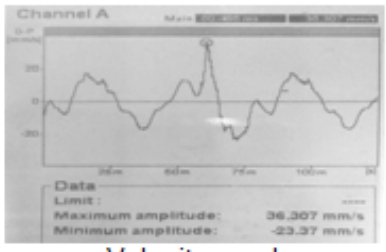

Velocity graph

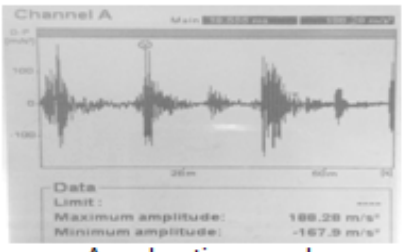

Acceleration graph

Load 4.2 kg and RPM1539:

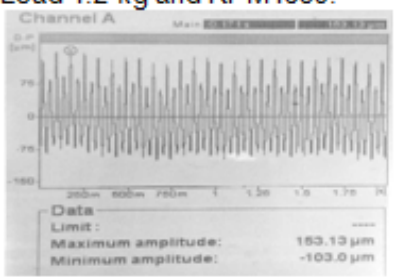

Displacement graph

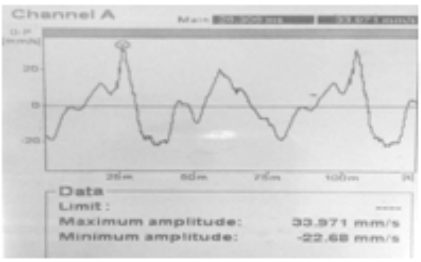

Velocity graph

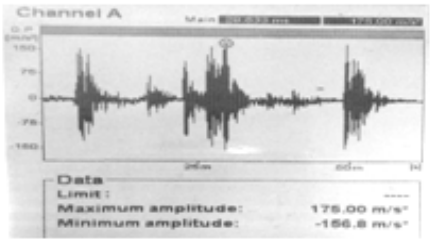

Acceleration graph

Load 6.2 Kg. RPM 1516

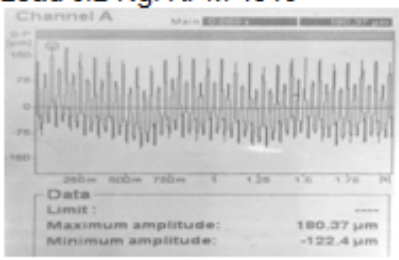

Displacement graph

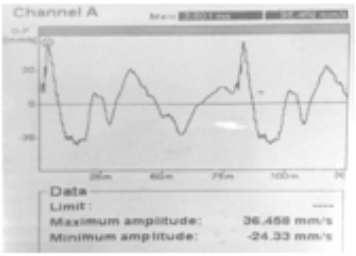

Velocity graph

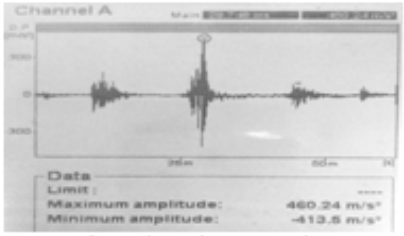

Acceleration graph

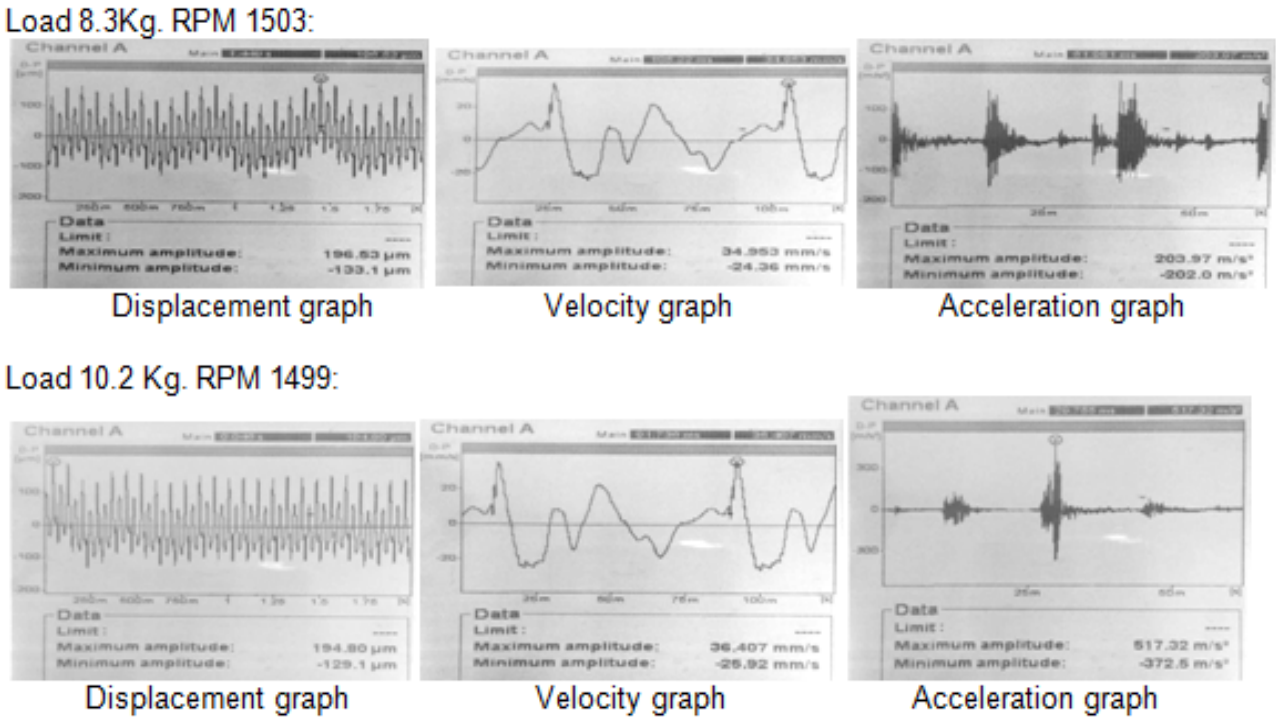

Fig. 10. Results

At load of 2.1 Kg the maximum amplitude on displacement was 148.54 µm. Maximum amplitude on velocity graph was 36.307 mm/s and maximum amplitude on acceleration was 188.28 m/s^2

At load of 4.2 Kg the maximum amplitude on displacement was 153.13µm. Maximum amplitude on velocity graph was 33.971mm/s and maximum amplitude on acceleration was 175.00m/s^2

At load of 6.2 Kg the maximum amplitude on displacement was 180.37µm. Maximum amplitude on velocity graph was 36.458mm/s and maximum amplitude on acceleration was 460.24 m/s^2

At Load of 8.3 Kg the maximum amplitude on displacement was 196.53µm. Maximum amplitude on velocity graph was 34.953mm/s and maximum amplitude on acceleration was 203.97 m/s^2

At Load of 10.2 Kg the maximum amplitude on displacement was 194.80µm. Maximum amplitude on velocity graph was 36.407mm/s and maximum amplitude on acceleration was 571.32 m/s^2

5. CONCLUSIONS

Temperature variation and Vibration in the Internal Combustion Engine with change in load conditions have been investigated. The maximum temperature on engine frame increases very rapidly as the load on the engine increases. The engine head temperature also shows an increment but that is not so significant. The minimum temperature on frame show a very little increment. In vibration analysis the displacement amplitude goes on increasing as the load on the engine increases. The velocity amplitude shows a decrement as the load increases initially then it increases at 6.2 Kg load further as the load is increased the velocity amplitude show a decrement. The acceleration amplitude show a little decrease as the load is increased then at a load of 6.2 Kg there is a sudden increment in the acceleration amplitude further as the load is increased the acceleration amplitude decreases.

REFERENCES

[1] Singh R.C.; Lal, R.; Ranganath M.S.; Chaudhary R. Failure of piston in I C Engines: A Review IJETT Vol-4th (2014) 1-10

[2] Heywood, J.B. Internal Combustion Engine Fundamentals TMH, 8, (2014) 01-37.

[3] Gupta R.B. Automobile Engineering Satya prakashan Vol-8th (2008) 1-88

[4] Sriniwasan, K. Title – Automotive Engines; Publisher- TMH Vol-5th (2002) 1-120

[5] Priest, M.; Taylor, C.M. Automobile engine tribology-approaching the surface, Wear 241 (2000) 193–203

[6] Cerit, M. Thermo mechanical analysis of a partially ceramic coated piston used in an SI engine, Surface & Coatings Technology 205 (2011) 3499–3505

[7] Cerit, M.; Coban, M. Temperature and Thermal Stress analysis of a ceramic-coated aluminium alloy piston used in a diesel engine, International Journal of Thermal Sciences 77, (2014) 11-18

[8] Canakci, M. Combustion characteristics of a turbocharged DI compression ignition engine fueled with petroleum diesel fuels and biodiesel, Bio resource Technology 98 (2007) 1167–1175

[9] Skopp, A.; Kelling, N.; Woydta, M.; Berger, L. M. Thermally sprayed titanium sub oxide coatings for piston ring/cylinder liners under mixed lubrication and dry-running conditions, Wear 262 (2007) 1061–1070

[10] Sreenath, A.V.; Raman, N. Running In Wear Of A Compression Ignition Engine: Factors Influencing The Conformance Between Cylinder Liner And Piston Rings, Wear, 38 (1976) 271 – 289

[11] Zhang, B.; Peng, X.; He, Z.; Xing, Z.; Shu, P. Development of a double acting free piston expander for power recovery in trans critical CO2 cycle, Applied Thermal Engineering 27 (2007) 1629–1636

[12] Friedrich, C.; Berg, G.; Broszeit, E.; Rick, F.; Holland, J. PVD CrxN coatings for tribological application on piston rings, Surface and Coatings Technology 97 (1997) 661–668

[13] Huanga, C.W.; Hsuehb, C.H. Piston on three ball versus piston-on-ring in evaluating the biaxial strength of dental ceramics, Dental materials (2 0 1 1) 117–123

[14] Picken, D.J.; Hassaan, H.A. A Method for Estimating Overhaul Life of Internal Combustion Engines including Engines Operating, J. agric. Engg Res, 28. (1983), 139-147

[15] Li, D.; Wub, H.; Gao, J. Experimental study on stepless capacity regulation for reciprocating compressor based on novel rotary control valve, International journal of refrigeration 36 (2013) 1701-1715

[16] Srivastava, D.K.; Agarwal, A.K.; Kumar, J. Effect of liner surface properties on wear and friction in a non-firing engine simulator, Materials and Design 28 (2007) 1632–1640

[17] Becker, E.P.; Ludema, K.C. A qualitative empirical model of cylinder bore wear, Wear, 225-229 (1999) 387-404

[18] Silva, F.S. Fatigue on engine pistons A compendium of case studies, Engineering Failure Analysis 13 (2006) 480–492

[19] Floweday, G.; Petrov, S.; Tait, R.B. J. Press, Thermo-mechanical fatigue damage and failure of modern high performance diesel pistons, Engineering Failure Analysis 18 (2011) 1664–1674

[20] Sunden, H.; Schaub, R. Piston rings for slow and speed diesel engines, Tribology International February 1979

[21] Willn, J.E. Characterisation of Cylinder Bore Surface Finish A Review Of Profile Analysis, Wear - Elsevier Sequoia S.A., Lausanne - Printed in the Netherlands

[22] Galligan, J.; Torrance, A.A.; Liraut, G. A scuffing test for piston ring bore combinations: Pt. II. Formulated motor lubrication, Wear 236 (1999) 210–220

[23] Milewski, J.; Szabłowski, L.; Kuta, J. Control strategy for an Internal Combustion engine fuelled by Natural Gas operating in Distributed Generation, Energy Procedia 14 (2011) 1478 – 1483

All in-text references underlined in blue are linked to publications on ResearchGate, letting you access and read them immediately.

ResearchGate

See discussions, stats, and author profiles for this publication at: https://www.researchgate.net/publication/283570980

Experimental Research on MRR in EDM Process Using Regression Modelling

Article · October 2015

READS
29

3 authors, including:

Ravinder Kumar
Amity University
13 PUBLICATIONS **23** CITATIONS

SEE PROFILE

All in-text references underlined in blue are linked to publications on ResearchGate, letting you access and read them immediately.

Available from: Ravinder Kumar
Retrieved on: 06 August 2016

OPEN ACCESS

International
Journal
Of Modern Engineering Research (IJMER)

Experimental Research on MRR in EDM Process Using Regression Modelling

Surabhi Lata[1], Ravinder Kumar[2], Ramakant Rana[1], Ravi Ranjan[3], Rohit Kumar[3], Roop Lal[4]

[1]*Assistant Professor, Mechanical and Automation Engineering Department, Maharaja Agrasen Institute of Technology, Delhi, India*
[2]*Associate Professor, Mechanical and Automation Engineering Department, Amity School of Engineering and Technology, Amity University, Noida, India*
[3] *Student, Mechanical and Automation Engineering Department, Maharaja Agrasen Institute of Technology, Delhi, India*
[4]*Assistant Professor, Mechanical Engineering Department, Delhi Technological University, Delhi, India*

ABSTRACT:- *Electric Discharge Machining is used to produce intricate shapes that are difficult-to-machine in conventional machine tools and also to provide good surface finish. In the present research work, the work material used is Stainless Steel 202 which is machined by using EN 31 (AISI 52100) as electrode. This work demonstrates the optimization process of material removal rate (MRR) of electrical discharge machining (EDM) by Response Surface Methodology. The current, pulse on time and machining time were the process control parameters of EDM. RSM method was used to design the experimental model whose adequacy checking was carried out using Minitab software. Regression equations were formulated based on the experimental results. The results evidence that the proposed regression equation can successfully predicted the material removal rate. It was concluded that the analysis carried out yielded the optimum results of material removal rate when the process parameters were current, pulse on time and machining time.*

Keywords:- *EDM, RSM, Design of Experiments, MRR*

I. INTRODUCTION AND LITERATURE REVIEW

Today's technologically advanced world demands materials which are high strength temperature resistant alloys and possess all desired mechanical properties such as high strength, corrosion resistance, toughness, etc. The emerging needs of the automation world led to the development of such difficult-to-machine materials which meets the stringent design requirements and enhance the surface quality. With the advent of these high strength materials, innovation became mandatory in order to search new technologies for machining and processing of the new materials. These materials enhance in terms of thermal, chemical and mechanical properties which are of huge economic benefit to manufacturing industries but defy the traditional machining processes. Therefore, solution is discovered in the advanced machining processes which makes use of different class of energy for material removal using the material properties, like electrical and thermal conductivity, melting temperature, electrochemical equivalent etc.

In today's fast growing technological environment, the advanced industries like aeronautics, automobiles, nuclear reactors, missiles, turbines etc., need materials which are high strength temperature resistant alloys. These alloys possess properties such as high strength, corrosion resistance, toughness, and other diverse properties. To meet the growing demands of the automation world there has been a rapid development in the field of materials. These new developed materials further demand new processes so that they can be utilized to fulfill their desired purpose. The solution is discovered in the new machining processes which are capable of machining these materials conveniently for sustained productivity, high accuracy and versatility at automation. Electrical Discharge Machining is a non-traditional machining technique, which can machine such new materials with ease. It can fulfil the demands of the parts which have intricate and compact shapes as such designs defy machining by conventional methods. It is an electro-thermal non-traditional machining process, where electrical energy is used to generate electrical spark and material removal mainly occurs due to thermal

energy of the spark. The main requirement for the EDM machining process is the electrically conductive nature of the workpiece. It finishes parts through the action of an electrical discharge of short duration and high current density between the tool and work piece. The tool and the work piece do not have any physical contact with each other. Heat resistant steels, super alloys, carbides, heat treated tool steels, composites and ceramics can be easily machined to attain geometrically complex shape through EDM process. Generally the effect of Pulse ON time, Pulse OFF time, Spark gap set Voltage, Peak current, Flushing Pressure, Work piece height, wire tension and wire feed on the material removal rate, surface roughness, kerf and gap current can be investigated.

EDM is a non-traditional machining technique which extensively and effectively machine such materials with ease. It machines electrically conductive materials where material is removed due to the thermal energy of the spark. In this process precisely controlled sparks are generated in the presence of a dielectric fluid between the electrode and the workpiece. The sparks or electrical discharge are of short duration and high current density between the tool and the workpiece. It is assertion that after milling, turning and grinding i.e. conventional machining processes, EDM is the fourth most extensively used machining method. Though efficiency of machining is less but the product quality and productivity in terms of surface finish, geometrical dimensions, process accuracy etc. is high [1]. E. Weingärtner et al. [2] reviewed the paper on Modeling and simulation of electrical discharge machining founding a better correlation with experimental results when the latent heats of fusion and evaporation are taken into consideration, as well as temperature-dependent thermo-physical properties of the workpiece. Input parameters used are short discharge durations and high peak currents. Better simulation results were achieved when considering the material properties as temperature-dependent. Z. Qinjian et al. [3] reviewed the paper on electrical discharge and ultrasonic assisted mechanical combined machining of polycrystalline diamond. The metal bonded diamond grinding wheel was as a tool electrode and the workpiece was supplemented with ultrasonic vibration, electrical discharge and ultrasonic assisted mechanical combined machining achieves efficient precision machining of PCD materials by selecting appropriate combinations of process parameters. The conclusion drawn was that Ultrasonic vibration has chip removal function and it has limited impact on the material removal rate. Karthikeyan et al. [4] used Tungsten carbide/Cobalt (WC–Co) composite and made an attempt to investigate the fracture strength and the reliability of EDMed WC–Co composite using the Weibull distribution analysis. The comparison of results between the machined composites and un-machined composites is carried out and presented in this study. Rajesh et al. [5] optimized the operating parameters for unconventional electric discharge machining through the empirical models developed by conducting a designed experiment based on the Grey Relational Analysis. Genetic Algorithm (GA) based multi-objective optimization for maximization of MRR and minimization of Ra has been done to identify the optimized machining conditions. Jin-Bin et al. [6] analysed the efficiency of traditional cutting processes and found that they are limited by the mechanical properties of the processed material and the complexity of the workpiece geometry, while electrical discharge machining (EDM) being a thermal erosion process, is subject to no such constraints. This paper highlights the development of a comprehensive mathematical model for correlating the interactive and higher order influences of various EDM parameters through RSM, utilizing relevant experimental data as obtained through experimentation. Optimal combination of these parameters was obtained for achieving controlled EDM of the workpieces. Kanlayasiri et al. [7] investigated the following machining variables i.e. pulse-peak current, pulse-on time, pulse-off time, and wire tension. Analysis of variance (ANOVA) technique was used to find out the variables affecting the surface roughness. Results showed that pulse-on time and pulse-peak current are significant variables to the surface roughness of wire-EDMed DC53 die steel. Further, the developed model was validated with a new set of experimental data, and the maximum prediction error of the model was less than 7%. Anand et al. [8] described the selection of machining parameter Discharge current, Pulse on time, Pulse off time in EDM for the machining of AISI 202 Stainless steel material and further using the grey relational analysis for optimizing the machining parameters i.e. material removal rate and surface roughness. Ghoreishi et al. [9] have made a model to optimize process parameters in EDM of tungsten carbide-cobalt composite. Four independent input parameters, viz., discharge current, pulse-on time, duty cycle, and gap voltage were selected to assess the EDM process performance in terms of material removal rate, tool wear rate, and average surface roughness. RSM have been used to plan and analyse the experiments. It has been mainly revealed that all the responses are affected by the rate and extent of discharge energy. The obtained predicted optimal results were also verified experimentally and the values of confirmation errors were computed, all found to be satisfactory, being less than 10%.

The investigation in the non-conventional machining processes is generally related to the effect of Pulse ON time, Pulse OFF time, Spark gap set Voltage, Peak current, Flushing Pressure, Work piece height, wire tension and wire feed on the material removal rate, surface roughness, kerf and gap current. The quality of the surface produced during these processes is of great importance and hence, it is exclusively researched. Surface quality is dependent on the appropriate selection of the machining parameters for any particular material

and also on the operator's experience. These papers present the effect of various process parameters extensively on the surface roughness as the response factor in EDM process [10, 11, 12].

II. METHODOLOGY

Response Surface Methodology is used to model the equations for the process parameters of the Electric Discharge Machining process. Experimental investigation is carried out through the design of experiments and the graphs showing the main and interaction effects of the process parameters on the response factor i.e. material removal rate.

Work Piece and Electrode Material

The work material selected for the experimental work is Stainless Steel 202 which is a difficult-to-machine material. The electrode material are EN 31 (AISI 52100).

Characteristics

Grade 202 stainless steel is a type of Cr-Ni-Mn stainless with similar properties to A240/SUS 302 stainless steel. The toughness of grade 202 at low temperatures is excellent.It is one of the most widely used precipitation hardening grades, and possesses good corrosion resistance, toughness, high harness, and strength.

This chromium- nickel-manganese alloy possesses properties similar to A240/SUS 302 stainless steel. At low temperatures SS 202 exhibits excellent toughness. It is the most widely used precipitation hardening grades possessing high hardness, strength and good corrosion resistant properties. It has good wear resistance and is used in low temperature environments. Typical applications include restaurant equipment, sinks, cooking utensils, automotive trim, architectural structures, railway cars, hose clamps as can be made into plates, sheets and coils.The following datasheet depicts the composition of SS 202 Steel.

Design of Experiments was carried out in order to study and analyse the effect of various process parameters of EDM on response factor i.e. surface roughness. DOE was used to estimate an unknown function for which only a few values were computed while least square error fitting was used to model the generated relations of the response surface [14]. The weight of work piece is measured using digital weighing machine to measure material removal rate and maintain the weight uniformity of the workpiece.

Table I: Composition of SS 202 Steel

Iron (Fe)	Chromium (Cr)	Manganese (Mn)	Nickel (Ni)	Silicon (Si)	Nitrogen (N)	Carbon (C)
68	17- 19	7.50-10	4-6	≤ 1	≤ 0.25	≤ 0.15

Figure 1: Photographic view of SS 202

Figure 2: EDM Machine and Control Panel

III. MATERIAL REMOVAL MEASUREMENTS

A digital weighing machine is used to measure the weight of work piece before and after the machining process to determine the material removal rate.

Figure 3: Weighing machine

Measurement of MRR

$$MRR = \frac{(W_i - W_f)}{t}$$

Where

W_i = weight of work piece in milligrams before machining
W_f = weight of work piece in milligrams after machining
t = period of machining in minutes

IV. RESPONSE SURFACE METHODOLOGY (RSM)

Response surface methodology, or RSM, is a collection of mathematical and statistical techniques useful for the modeling and analysis of problems in which a response of interest is influenced by several variables and the objective is to optimize this response. The objective is to find the correlation between the variables investigated and the response [17, 18].

Design of Experiments (DOE) was used to estimate an unknown function for which only a few values were computed while least square error fitting was used to model the generated relations of the response surface. A Central Composite Design (CCD) gives a comparatively accurate prediction of all response variable averages related to quantities measured during experimentation, hence it was also used [19]. CCD offers the advantage that certain level adjustments are acceptable and can be applied in the two-step chronological RSM. In these methods, there is a possibility that the experiments will stop with few runs and decide that the prediction model is satisfactory [20]. The current, Pulse ON time and processing time are the machining variables selected for this investigation. The different levels taken for this study are depicted in Table II.

Mathematical models are developed on the basis of data obtained through the experiment. The experimental planning is done based on Design of Experiments. The Box Behnken design was used to find the quadratic response surfaces to construct the second order polynomial models. Design of Experiments (DOE) is a method used to obtain useful information about a process by conducting only minimum number of experiments. A Central Composite Design (CCD) gives a comparatively accurate prediction of all response variable averages related to quantities measured during experimentation, hence it was also used. In these methods, there is a possibility that the experiments will stop with few runs and decide that the prediction model is satisfactory. Each controllable variable (T_{on}, I_p, T_{off}) can be set on EDM machine at two consecutive levels and hence the design consisting of 9 experiments was generated. Table III shows the levels used for the design of experiments.

Table II: DIFFERENT VARIABLES USED IN THE EXPERIMENT AND THEIR LEVEL

VARIABLES	UNITS	CODE	LEVELS	
			1	2
CURRENT	Ampere (A)	X_1	3	6
PULSE ON TIME	Micro-seconds (µsec)	X_2	8	11
MACHINING TIME	Minutes (min)	X_3	55	65

Machining was carried out by varying the input process parameters each at a time, two replications of surface roughness measurement were taken, and the planning design matrix of the experiments has been shown in Table III.

Table III: PLANNING MATRIX OF THE EXPERIMENTS WITH THE OPTIMAL MODEL DATA

Trial Runs	Current (Amp)	Pulse on Time (µsec)	Machining Time (min)
R1	3	8	55
R2	3	8	65
R3	3	11	55
R4	3	11	65
R5	6	8	55
R6	6	8	65
R7	6	11	55
R8	6	11	65

The experimental values were analysed and then a mathematical model developed an equation illustrating the relationship between the process response and the variables. The model in equation 1 explains the behavior of the system.

$$y = \beta_0 + \beta_1 x_1 + \beta_2 x_2 + \in \quad \ldots 1$$

Where y = Surface Roughness, x_1 = Current (A), x_2 = Pulse On Time (µsec), x_3 = Machining Time (min) and β_1, β_2, β_3= Partial Regressors.

The equation for calculating the approximate MRR is

$$MRR = -173.6 + 32.24\ X_1 + 18.24\ X_2 + 2.811\ X_3 - 3.217\ X_1X_2 - 0.2877\ X_2X_3 - 0.5070\ X_3X_1 + 0.05051\ X_1X_2X_3$$

Where X_1 is current in amperes, X_2 is Pulse On time in microseconds and X_3 is Machining Time in minutes

V. RESULT AND DISCUSSION

Regression analysis developed the correlation between the process parameters and the response factor i.e. material removal rate (MRR) based on the data acquired from the experiments. In this experimental study, a regression equation have been developed by taking into consideration three process parameters i.e. current, pulse on time and machining time.

The coefficients of regression model were estimated from the experimental outputs. The effects of the process parameters was further studied through the main effects.

Table IV: Plan of Experiments and Output Responses

Trial Runs	Current (X_1)	Pulse on Time (X_2)	Machining Time (X_3)	$X_1 X_2$	$X_2 X_3$	$X_1 X_3$	$X_1 X_2 X_3$	MRR Experimental	MRR Theoretical	% Error
R1	3	8	55	24	440	165	1320	4.80	4.8736	1.11
R2	3	8	65	24	520	195	1560	3.82	3.8704	1.31
R3	3	11	55	33	605	165	1815	6.11	6.16615	0.91
R4	3	11	65	33	715	195	2145	4.65	4.71106	1.31
R5	6	8	55	48	440	330	2640	6.32	6.37048	0.78
R6	6	8	65	48	520	390	3120	4.58	4.64056	1.32
R7	6	11	55	66	605	330	3630	4.89	4.80784	1.43
R8	6	11	65	66	715	390	4290	4.05	4.1254	1.86

Effect of Current on MRR:

The figure 4 shown below indicates that MRR is 4.82 mg/min when the current is 3 amp. It increases steeply to 6.32 mg/min when the current is 6 amps. As the current is increased the MRR increases due to the increase in the number of sparks taking place between the electrode and the work material.

Effect of Pulse ON Time on MRR:

The MRR increases from 4.80 to 4.89 mg/min when the pulse on time increases from 8 µsec to 11µsec. As the pulse on time increases the intensity of spark is affected which is directly influencing the amount of material being removed. Increase in number of sparks leads to increase in MRR.

Effect of Machining Time on MRR:

Figure 6 shows a decrease in MRR value on the increase in the value of machining time. As the machining time increased from 55 min to 65 min a downfall in MRR is experienced due to the increased duration while all other parameters remaining fixed. MRR decreases due to the low range of current on which machining process was carried out.

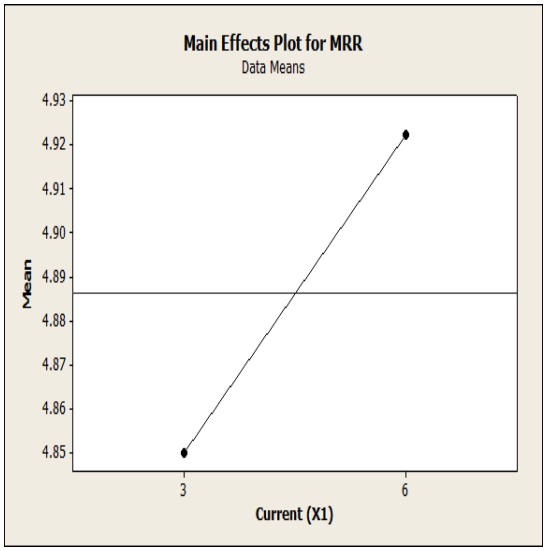

Figure 4: Effect of Current on MRR

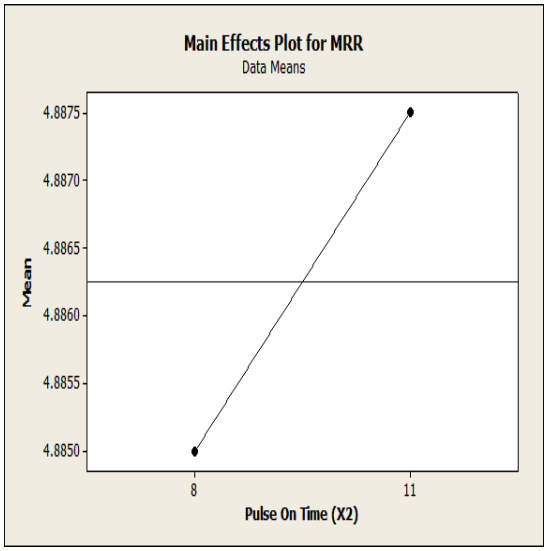

Figure 5: Effect of Pulse ON Time on MRR

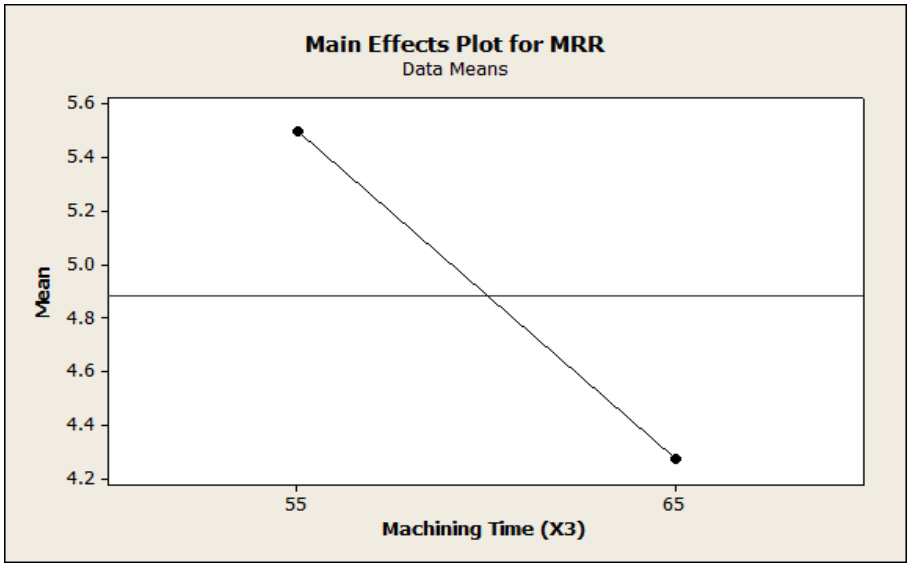

Figure 6: Effect of Machining Time on MRR

Effect of Current and Pulse ON Time on MRR:

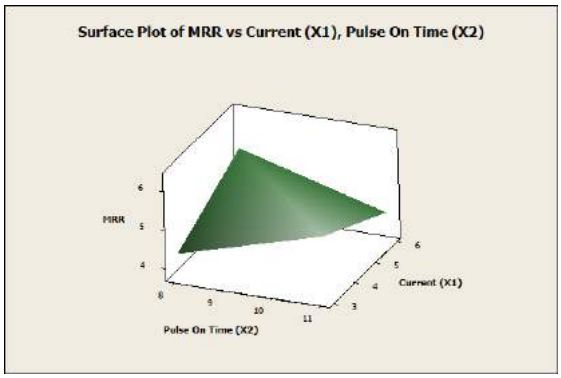

Figure 7: Surface Plot for MRR vs X_1 vs X_2

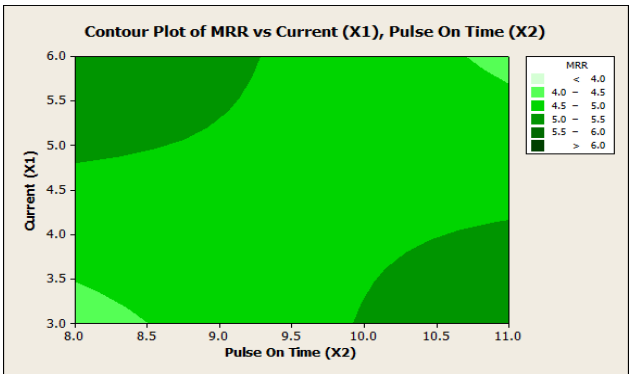

Figure 8: Contour Plot for MRR vs X_1 vs X_2

Figure 7 and 8 shows the estimated response for MRR in relation to the process parameters of current (X_1) and Pulse ON time (X_2) while other parameters remaining constant at their lowest value. It is clear from the above plots that MRR significantly increases with the increase in the value of current for smaller range of pulse ON time. On the same point the effect of pulse on value on MRR increasesit at a higher range of ON time.

VI. CONCLUSION

In this research, regression analysis of process parameters of EDM machining process was carried out. The machining of SS 202 workpiece was done with EN 31 electrode and the following conclusion was drawn from the conducted analysis:

1. It has been confirm that the regression technique can be successfully applied to model the input and output variable of electro discharge machining of SS 202 with EN 31.
2. Within the experimental scope, the MRR value increases with the increase in the value of pulse-on time.
3. Machining rate increases with the increase in current due to predominant increase in spark energy.
4. The proper selection of input parameters can help in achieving a specific output parameter (MRR) and a higher efficiency can be determined by theoretical and experimental characteristic diagrams, especially the two dimensional contour diagrams.

Finally, an attempt has been made to estimate the optimum machining conditions to achieve the best possible outcome of the response factor within the experimental constraints. This study can help in developing a robust, reliable knowledge base and early prediction of MRR without performing the actual experiment with EDM process for EN 31 steel.

REFERENCES

[1]. M. K. Pradhan, and C. K. Biswas, "Modeling and Analysis of process parameters on Surface Roughness in EDM of AISI D2 tool Steel by RSM Approach".

[2]. E. Weingärtner et al. / Procedia CIRP 2 (2012) 74 – 78

[3]. Z. Qinjian et al. / Procedia CIRP 6 (2013) 589 – 593.

[4]. D. Kanagarajan, K. Palanikumar, R. Karthikeyan, "Effect of Electrical Discharge Machining on strength and reliability of WC–30%Co composite", Materials and Design 39 (2012) 469–474.

[5]. R.Rajesha and M. DevAnandb, "The Optimization of the Electro-Discharge Machining Process Using Response Surface Methodology and Genetic Algorithms", Journal of Procedia Engineering 38 (2012) 3941 – 3950.

[6]. Shih Jing-Shiang, TzengYih-Fong, Yang Jin-Bin. "Study of the parameters in electrical discharge machining through response surface methodology approach".Applied Mathematical Modelling 33 (2009) 4397–4407.

[7]. Yan K. Kanlayasiri, S. Boonmungb. "Effects of wire-EDM machining variables on surface roughness of newly developed DC 53 die steel: Design of experiments and regression model.".Journal of Materials Processing Technology 192–193 (2007) 459–464.

[8]. T.M chenthijegan, M.Devanand and D.ravindran, "Determination of electro discharge machining parameter in AISI 202 stainless steel using grey relation analysis", Mater Procedia engineering 38(2012), 4005-4012.

[9]. S. Assarzadeh, M. Ghoreishi, "Statistical modeling and optimization of process parameters in electro-discharge machining of cobalt-bonded tungsten carbide composite (WC/6%Co)", Procedia CIRP 6 (2013), 463 – 468.

[10]. S.H.Tomadi, M.A.Hassan, Z. Hamedon, R.Daud, and A.G.Khalid, "Analysis of the Influence of EDM Parameters on Surface Quality, Material Removal Rate and Electrode Wear of Tungsten Carbide", Proceedings of the International MultiConference of Engineers and Computer Scientists 2009, Vol II IMECS, March 2009.

[11]. S. H. Lee and X. P. Li, "Study of the effect of machining parameters on the machining characteristics in electrical discharge machining of tungsten carbide", The National University of Singapore, 2009.

[12]. R. Snoeys, F. Staelens, and W. Dekeyser, "Current trends in nonconventional material removal processes," Ann. CIRP, vol. 35(2), p. 467 480, 1986.

[13]. H.S. Payal, R Choudhary and S Singh, "Analysis of electro discharge machined surfaces of EN-31 tool steel", Journal of Scientific & Industrial Research, Vol. 67, p. 1072-1077, 2008.

[14]. A Bhatia, S Kumar, and P Kumar, " A study to achieve minimum roughness in wire EDM" ,International conference on advances in manufacturing and materials engineering, Procedia material science 5 p. 2560-2566, 2014.

[15]. I. Puertas, C. J. Luis, and L. Alvarez, "Analysis of the influence of edm parameters on surface quality, mrr and ew of wc-co," Journal of Materials Processing Technology, vol. 153-154, no. 1-3, pp. 1026–1032, 2004.

[16]. G. Petropoulos, N. Vaxevanidis, and C. Pandazaras, "Modeling of surface finish in electro-discharge machining based upon statistical multi-parameter analysis," vol. 155-156, no. 1-3, p

[17]. Korzynski M., "Experiment methodology", WNT Warszawa, 2006.

[18]. Md. A R Khan, and M. M. Rahman, "Development of Regression Equation for Surface Finish and Analysis of Surface Integrity in EDM", International Journal of Mechanical, Aerospace, Industrial and Mechatronics Engineering Vol 7, No. 3, 2013.

[19]. Singaram Lakshmanan, and M Kumar, "Optimization of EDM parameters using Response Surface Methodology for EN31 Tool Steel Machining", International Journal of Engineering Science and Innovative Technology (IJESIT), Volume 2, Issue 5, September 2013.

[20]. S. S. Baraskar, S. S. Banwait, and S. C. Laroiya, "Mathematical Modeling of Electrical Discharge Machining Process through Response Surface Methodology", International Journal of Scientific & Engineering Research, Volume 2, Issue 11, November-2011.

[21]. Mohd B. Ndaliman*, Ahsan A. Khan, and Zakaria M. Zain," Performance of PM Compacted Cu-TaC Electrodes during EDM", Kulliyyah of Engineering International Islamic University Malaysia, 2013.

[22]. Mohammed Yakub Ali, "Development in EDM process variables", International Islamic University Malaysia, 2013.

[23]. Aligiri E., Yeo S.H., and Tan P.C., "A new tool wear compensation method based on real-time estimation of material removal volume in micro-EDM", Journal of Materials Processing Technology 210, p. 2292–2303, 2010.

[24]. Uhlmann E, Roehner M., "Investigations on reduction of tool electrode wear in micro-EDM using novel electrode materials", CIRP Journal of Manufacturing Science and Technology 1, p. 92–96, 2008.

[25]. Uhlmann E., Piltz S., Röhner M., "Influence of Diamond Coatings on Electrode Wear in Mirco-EDM", Proceedings of the 7th Euspen International Conference – Bremen, 2007.

[26]. O. H. Erzurumlu, T., "Comparison of response surface model with neural network in determining the surface quality of moulded parts," Materials and Design, vol. 28, no. 2, pp. 459–465, 2007.

[27]. M. K. Pradhan, R. Das, and C. K. Biswas, "Comparisons of neural network models on surface roughness in electrical discharge machining," Proceedings of the Institution of Mechanical Engineers, Part B: Journal of Engineering Manufacture, vol. 223, p. (In Press), 2009.

Anal Bioanal Chem
DOI 10.1007/s00216-016-9803-6

REVIEW

Exploring the flexible chemistry of 4-fluoro-3-nitrophenyl azide for biomolecule immobilization and bioconjugation

Saroj Kumar[1,2] · **Dileep Kumar**[3] · **Rajesh Ahirwar**[1,4] · **Pradip Nahar**[1,4,5]

Received: 20 May 2016 / Revised: 8 July 2016 / Accepted: 16 July 2016
© Springer-Verlag Berlin Heidelberg 2016

Abstract Bioconjugation and functionalization of polymer surfaces are two major tasks in materials chemistry which are accomplished using a variety of coupling agents. Immobilization of biomolecules onto polymer surfaces and the construction of bioconjugates are essential requirements of many biochemical assays and chemical syntheses. Different linkers with a variety of functional groups are used for these purposes. Among them, the benzophenones, aryldiazirines, and arylazides represent the most commonly used photolinker to produce the desired chemical linkage upon their photo-irradiation. In this review, we describe the versatile applications of 4-fluoro-3-nitrophenyl azide, one of the oldest photolinkers used for photoaffinity labeling in the late 1960s. Surprisingly, this photolinker, historically known as 1-fluoro-2-nitro-4-azidobenzene (FNAB), has remained unexplored for a long time because of apprehension that FNAB forms ring-expanded dehydroazepine as a major product and hence cannot activate an inert polymer. The first evidence of photochemical activation of an inert surface by FNAB through nitrene insertion reaction was reported in 2001, and the FNAB-activated surface was found to conjugate a biomolecule without any catalyst, reagent, or modification. FNAB has distinct advantages over perfluorophenyl azide derivatives, which are contemporary nitrene-generating photolinkers, because of its simple, single-step preparation and ease of thermochemical and photochemical reactions with versatile polymers and biomolecules. Covering these aspects, the present review highlights the flexible chemistry of FNAB and its applications in the field of surface engineering, immobilization of biomolecules such as antibodies, enzymes, cells, carbohydrates, oligonucleotides, and DNA aptamers, and rapid diagnostics.

Keywords 1-Fluoro-2-nitro-4-azidobenzene · Photolinker · Immobilization · Biomolecules · Polymer · Inert surface

Saroj Kumar, Dileep Kumar and Rajesh Ahirwar contributed equally to this work.

✉ Pradip Nahar
pnahar@igib.res.in

[1] CSIR - Institute of Genomics and Integrative Biology, Mall Road, 110007 Delhi, India

[2] Department of Biotechnology, Delhi Technological University, Main Bawana Road, 110042 Delhi, India

[3] Department of Pharmaceutical Sciences, University of Colorado, Denver, Colorado 80045, USA

[4] Academy of Scientific and Innovative Research, Mathura Road, Jasola 110020, New Delhi, India

[5] Present address: Dr. Nahar's New Idea lab, C-202, Ramkrishan Cooperative Group Housing Society, Plot 12, Sector 23, Dwarka, New Delhi, India

Introduction

Bioconjugation is a process that involves cross-linking, immobilization, surface modification, and labeling of biomolecules by a cross-linker that forms a covalent bond between two molecules [1–3]. Bioconjugation is commonly used to modify molecules such as proteins, peptides, nucleic acids, drugs, and solid surfaces for various purposes. Cross-linking reagents, also called linkers, contain reactive groups that bind the target molecules through specific functional groups like primary amines, sulfhydryls, carboxyl group etc. present on them. Some popular linkers include glutaraldehydes [4–6], carbodiimides [7–9], and *N*-hydroxysuccinimide (NHS) esters and imidoesters [10]. Most of these linkers conjugate to amines of the biomolecules either by acylation or alkylation. Aldehydes (formaldehyde and glutaraldehyde) are highly reactive reagents and commonly used to fix and preserve tissues and cells for histochemical

Published online: 02 August 2016

applications [4–6]. Carbodiimides, such as EDC (1-ethyl-3-(3-dimethylaminopropyl)carbodiimide hydrochloride) activate carboxyl groups for conjugation to primary amines [9, 11, 12]. NHS esters and imidoesters are amine-specific functional groups that are incorporated into reagents for protein cross-linking and labeling [13]. The reaction of NHS esters with amines is strongly pH-dependent: at low pH, the amino group is protonated, and no modification takes place. At higher-than-optimal pH, hydrolysis of NHS esters is quick, and modification yield diminishes [14, 15]. All these conventional cross-linking reagents need reactive groups on target surface for conjugation; hence they are not suitable for activation of inert surfaces. On the other hand, photolinkers are a unique class of heterobifunctional cross-linkers with the unique property of activating inert polymers in a photochemical reaction.

In the post-genomic era, applications of photolinkers have increased dramatically in photoaffinity labeling [16–20], organic synthesis [21], conducting polymers [22–24], and lithography and surface modifications [25–30]. Photolinkers can be divided into three major classes depending on generation of reactive intermediates such as (i) nitrine [16–19, 21, 22, 25], (ii) carbene [31, 32], and (iii) oxygen free radicals [33, 34]. Light-induced activation of these photolinkers and their reactions are schematically represented in Fig. 1. Historically, there has been considerable interest in nitrenes that can be generated photochemically either from alkyl or aryl azides. However, biologists preferred aryl azides over alkyl azides because the latter have their absorption maximum at 290 nm, a wavelength that may interfere in monitoring of proteins or nucleic acids.

As the photolysis of phenyl azide is complex, several reaction mechanisms have been proposed to explain the intermediate products formed [35–38]. A general reaction scheme for possible reaction products of phenyl azide **1** are outlined in Fig. 2. Mechanistically, the singlet state nitrene **2** is considered the first intermediate formed when phenyl azide **1** undergoes photolysis with loss of molecular nitrogen. Singlet nitrene **2**, which has a lifetime in the order of nanoseconds, can undergo ring insertion to form bicyclic azirine **3** or ring expansion to generate a didehydroazepine **4** that can be trapped by suitable reagents to give azepine **5**. Singlet nitrene **2** can also deactivate via intersystem crossing (ISC) to the ground state triplet nitrene **6** which predominantly gives C–H or N–H insertion products **8** and C = C addition reaction or azo compound **7**. Although formation of products **2**–**8** is well established, the mechanism of formation of C–H insertion products **8**, whether through singlet nitrine [38] or triplet nitrine [39, 40], is still a matter of debate. The intermediate products formed upon photochemical decomposition of aryl azide strongly depend on the substituents on the benzene ring as well as the temperature of reaction. High temperature usually favors reactions of singlet-state intermediates, while low temperatures favor reactions associated with triplet phenylnitrene [41].

Photolysis of unsubstituated phenyl azide is more prone to ring expansion to create dehydroazepines [39, 42]. Aryl azide with deactivating groups on the benzene ring (chlorinated and fluorinated phenyl azide) have been shown to enhance the stability of the nitrine [43–45]. Photolysis of several fluorophenyl azides has been studied and almost all of them give ring-expanded products except pentafluorophenylazides and 2,6-difluorophenylazides which gave insertion products because of steric and electronic effects of the substituents [46, 47]. Electron-withdrawing substituents (CF_3, $COCH_3$, CN, and NO_2) have a smaller but measurable influence on kinetics of ISC but not enough to form predominantly triplet-state reaction products [48]. Therefore, introduction of nitro group into phenyl azide led to different products upon irradiation, mainly the singlet nitrene, the triplet nitrene, the triplet azide, and the ring-expanded dehydroazepine, depending on the conditions of the experiment [49].

Interestingly, there is no direct report for the photolysis of 4-fluoro-3-nitrophenyl azide (IUPAC: 4-azido-1-fuoro-2-nitrobenzene). This photolinker is historically known as 1-fluoro-2-nitro-4-azidobenzene (FNAB) and we have used this traditional name in this review. FNAB, which has two deactivating groups, fluoro and nitro on the benzene ring, accelerates the rate of ISC and the reaction occurs through a nitrene insertion mechanism. Although a single substituent, either fluoro or nitro, did not make an appreciable difference to the nitrene insertion mechanism, both of them jointly made FNAB an ideal photolinker that forms insertion products probably through the triplet nitrene pathway. Possible photochemical reactions of FNAB are schematically presented in Fig. 3. Unlike pentafluorophenyl azide where several fluoro groups facilitate towards C–H insertion reaction through cumulative inductive and steric effects [50, 51], FNAB does the same by the inductive effect of the fluoro group as well as the strong resonance effect of the nitro group. The mechanism of nitrene insertion into the polymer material is supported by X-ray photoelectron spectroscopy studies on a variety of polymer materials after photochemical reaction with FNAB [52–57].

Thus, from the above discussion, it is clear why FNAB is the most popular heterofunctional photolinker used for photoaffinity labeling, bioconjugation, and surface engineering [58–61]. Another group of nitrene-generating photolinkers which come close to FNAB in terms of usefulness are perfluorophenyl azide derivative [25]. However, one of the advantages of using FNAB over perfluorophenyl azide derivative is its simple and easy preparation from 4-fluoro-3-nitroaniline by a single step diazotization reaction with more than 80 % yield [62]. In brief, preparation of FNAB involves dropwise addition of $NaNO_2$ solution (4.8 g/12 ml of water) to the clear and cooled solution of 10 g of 4-fluoro-3-nitroaniline, dissolved in the mixture of 65 ml warm concentrated HCl and 12 ml water. The reaction mixture is stirred continuously at a temperature of approximate −20 °C.

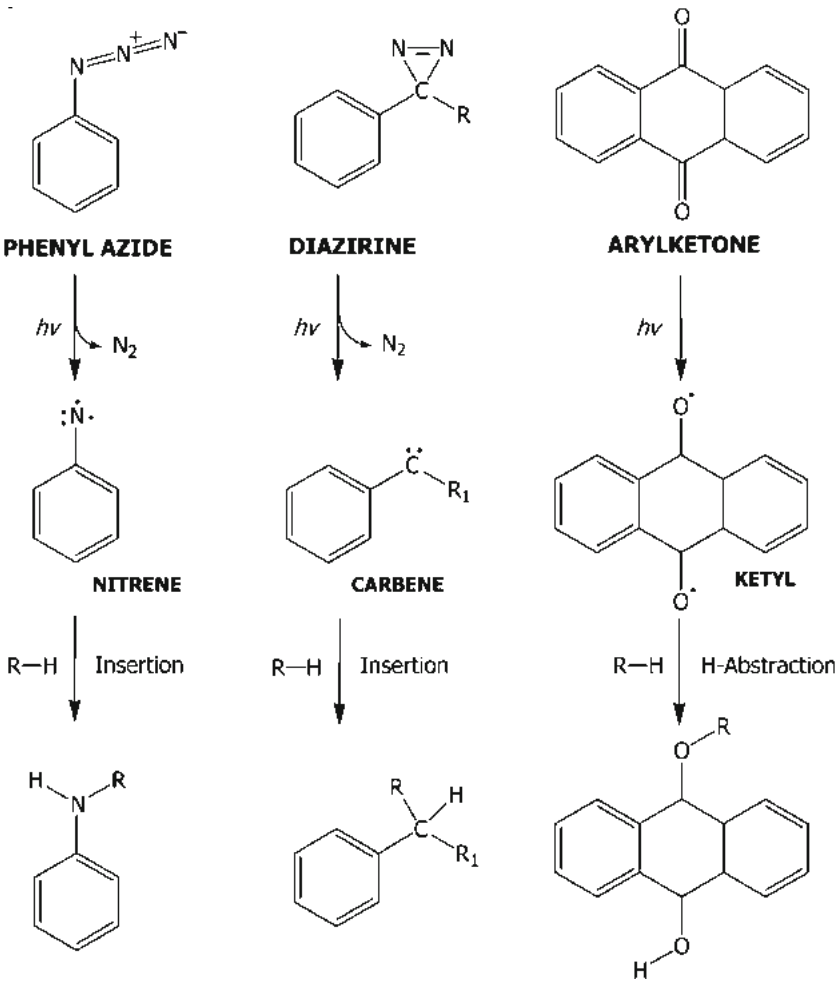

Fig. 1 Light-induced activation and reactions of basic photolinkers aryl azide, diazirine, and arylketone

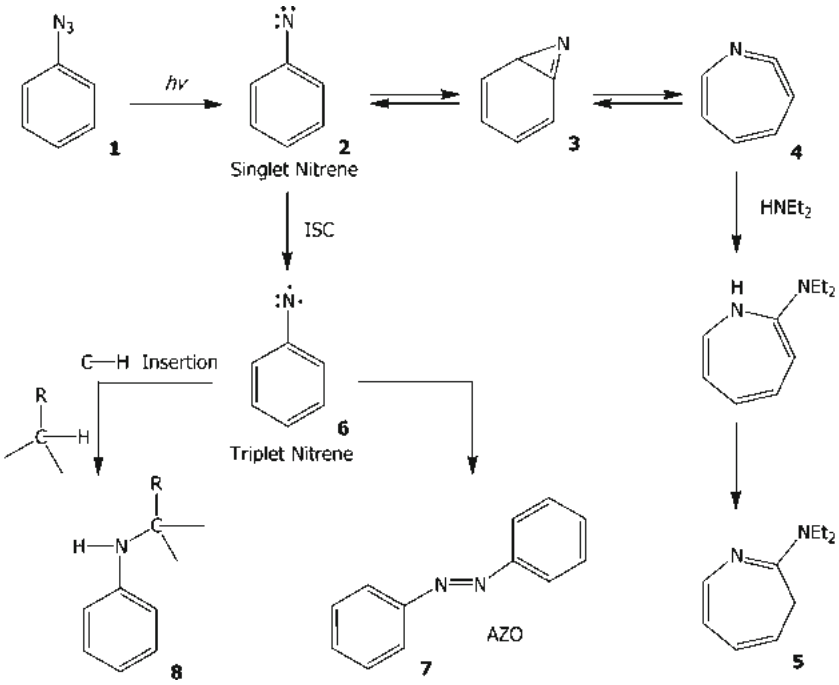

Fig. 2 Formation of nitrenes from aryl azide and some of the important nitrene reactions

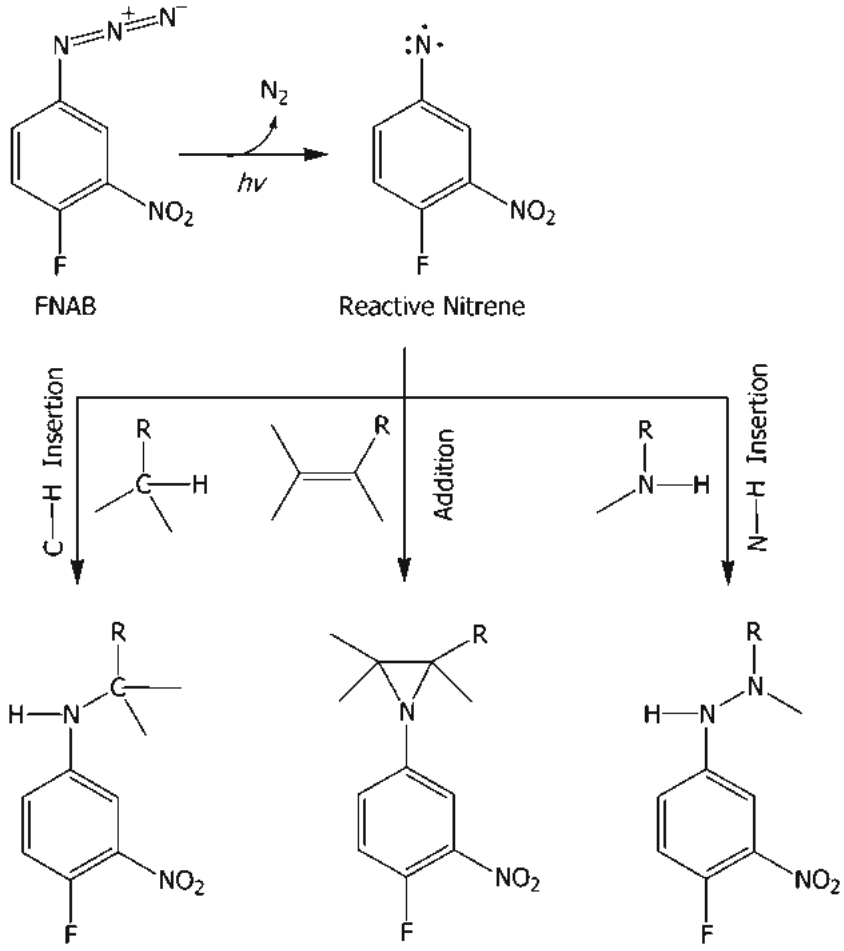

Fig. 3 Possible photochemical reactions of 1-fluoro-2-nitro-4-azidobenzene

After 15 min, NaN_3 (4.4 g/16 ml water) is added dropwise to the reaction mixture at a temperature of −20 °C. After 15 min, the formed yellow precipitate is filtered and washed with ice-cold water. The product is recrystallized from light petroleum to give 7.3 g of 1-fluoro-2-nitro-4-azidobenzene. The melting point of the needle-shaped, straw-colored crystals of FNAB is 52 °C. Diazotization reaction is common in organic chemistry laboratories and needs routine safeguards such as performing the reaction in the fume cupboard and careful handling of acid and flammable solvents. However, once FNAB is formed, filtration and crystallization should be done under dim lighting as it is light sensitive. FNAB belongs to an explosive category of chemicals; nevertheless, we did not encounter any such incident in our decade-long work on it. For the non-expert, it is advisable to prepare it from 1 g or less of starting material. FNAB can be stored safely in the dark in a loosely capped bottle at 4 °C. FNAB is also commercially available from several companies such as Shanghai Aladdin Bio-Chem Technology Co. Ltd., China (catalog no. F131202), Apollo Scientific Ltd. Britain (catalog no. c22209118), and Ryan Scientific, Inc. United States (catalog no. c29689517).

FNAB-mediated activation of different surfaces and molecules is shown schematically in Fig. 4.

In the following sections we focus on possible reaction pathways of FNAB, characterization of FNAB activation, and applications of FNAB.

Reaction pathways of FNAB

FNAB has one photoactivable group—the “azido” group, which is a nitrene precursor. The fluoro group in FNAB is a thermoreactive, a name given to it to differentiate it from

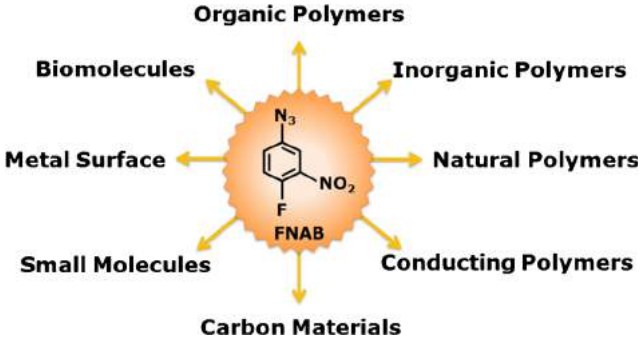

Fig. 4 Engineering of versatile material surfaces and molecules by 1-fluoro-2-nitro-4-azidobenzene

photoreactive groups. Taking advantage of the two distinct functional groups, it is possible to manipulate the attachment of biomolecules to a matrix in a stepwise manner as shown in Fig. 5. There are two possibilities in the first step; either to activate biomolecules (Fig. 5a) or matrix (Fig. 5b). In former case, the biomolecule is activated either thermochemically or photochemically followed by attachment to a matrix. Major drawbacks of this protocol are (i) unreacted FNAB has to be removed completely before immobilization to a matrix, (ii) during photochemical reaction, the reactive nitrene, formed under light exposure, can bind randomly with almost all the species present including the biomolecule or the solvent, resulting in undesirable reactions, which lead to inefficient immobilization. Nevertheless, activation of matrix in the first step (Fig. 5b) becomes more popular because of the easy removal of FNAB from the solid matrix. In this case, the matrix or polymer can be activated either by the thermochemical or photochemical method leading to "photoreactive polymer" and "thermoreactive polymer", respectively. The terms were coined as a result of their modes of immobilization in the subsequent step.

Photoreactive polymer

Thermochemical reaction of FNAB with the matrix (Fig. 5b, pathway III) gives limited choice of the matrix, i.e., the matrix must have a nucleophilic group such as an amino or hydroxyl moiety to form a photoreactive polymer. Onto this polymer, immobilization of a biomolecule is carried out by UV irradiation and this method is known as photo-immobilization. The light-induced immobilization technique is mild, biomolecule friendly, and independent of pH and temperature. The unique advantage of a photoreactive polymer is that it has the potential to immobilize a biomolecule irrespective of its functional group.

Thermoreactive polymer

Surprisingly, photochemical activation of a matrix (Fig. 5b, pathway IV) by FNAB to form a thermoreactive polymer remained unexplored for a long time. Light-induced activation of an inert surface by FNAB was reported for the first time by us in 2001. This pathway is potentially useful for immobilization of biomolecules on inert surfaces as most of them lack active functional groups and are difficult to activate otherwise [63]. In this method, a minimum prerequisite is that the matrix should contain a carbon–hydrogen bond, which is available in most of the polymers. Stepwise photochemical and thermochemical reactions are the main characteristics of a heterobifunctional photolinker like FNAB and are summarized below.

Photochemical reaction

The photochemical activation of polymers can be carried out by pouring a methanolic or ethanolic (most of the polymers are stable in these solvents) solution of FNAB onto the polymer followed by drying and exposing the surface under UV light at a wavelength of 365 nm. The photolinker-coated dry surface excludes undesirable reactions with the highly reactive nitrene, formed by UV irradiation. Thus, the photolinker has better access to the inert surface in the absence of any third ingredient. In the subsequent step, the biomolecule is attached to the active surface through the fluoride-leaving group by a thermochemical reaction [63]. Alternatively, screen printing or similar methods could be used for FNAB coating to the polymer surface. Light-induced activation can also be carried out in solvent without C–H bonds such as carbon tetrachloride, for polymers which are insoluble in it, e.g., polypropylene.

Our group reported an unconventional surface activation of polystyrene, polypropylene, and polyethylene by exposing FNAB-coated surface to sunlight at an intensity of 26,300 lux [64]. Such light intensity is mild (intensity of bright summer sunlight is around 140,000 lux) and may be obtained in most parts of the world. Thus, being a versatile, eco-friendly, and clean energy source, sunlight can be a potential alternative to UV light for photoactivation of a polymer surface as well as photo-immobilization of biomolecules [65].

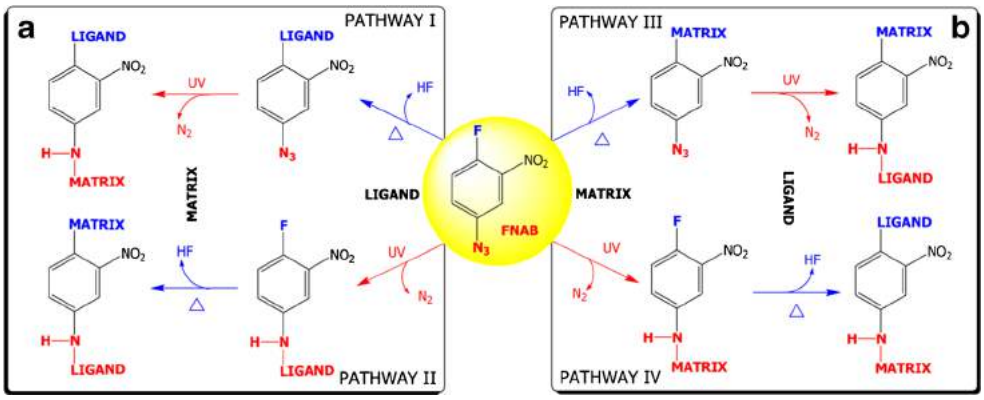

Fig. 5 Different pathways for FNAB-mediated covalent binding of ligands with matrices. **a** FNAB first reacts with ligand thermochemically (pathway I) or photochemically (pathway II) followed by binding with matrix and **b** FNAB first reacts with matrix either thermochemically (pathway III) or photochemically (pathway IV) followed by binding with ligand

Thermochemical reaction

The strong electron-withdrawing nitro group in FNAB makes the adjacent fluoro group highly reactive towards nucleophilic reagents. Thus, thermoreactive polymer binds a protein molecule by displacement of its fluoro group by the amino group of the incoming protein in a thermochemical reaction in 45 min at 37 °C without any additional reagent [63]. Kannoujia et al. [66] covalently immobilized enzymes in 25 min onto FNAB-activated polystyrene microtiter plates kept in a closed steel vessel by applying pressure of 2.0×10^5 Pa by argon gas from a cylinder. Pressure-induced immobilization could be a useful technique in particular for heat-sensitive biomolecules where temperature is a limiting factor. Recently, our group reported another non-conventional method of immobilization of biomolecules onto FNAB-activated solid supports where immobilization was executed in 10 min by ultrasound waves generated in a sonicator bath, operating at a frequency of 40 kHz, and at an ultrasound output power of 120 W [67]. In another advancement, Nahar and Bora [68] covalently immobilized enzymes onto a FNAB-activated polystyrene surface by microwave irradiation for the first time in the 1970s. Thus, the main advantage of FNAB is that it can be used directly without any alteration or activation for rapid binding to a nucleophilic ligand.

X-ray photoelectron spectroscopy of FNAB activation

The photochemical activation of a cellulose membrane through nitrene insertion was characterized by X-ray photoelectron spectroscopy (XPS) which showed characteristic peaks at approx. 684 eV corresponding to F1s of fluorine and a duplex peak at approx. 407 and 401 eV (from core level scans) corresponding to N1s of –NH and N1s of NO_2 respectively (Fig. 6a) [52]. In the thermochemical activation of a cellulose membrane by FNAB, an hydroxyl group of the cellulose displaces the fluorine of FNAB in a nucleophilic reaction to form photoreactive cellulose [69]. In the XP spectra of activated cellulose membrane, the appearance of a duplex nitrogen peak at around 400 eV suggests the incorporation of FNAB and the absence of a fluorine peak confirms the activation of the cellulose surface through displacement of the fluorine of FNAB (Fig. 6b) [69].

Applications of FNAB

At the time of inception, FNAB was mainly used for affinity labeling of protein molecules for biological studies; today FNAB has diverse applications which include surface engineering, biomolecule conjugation, enzyme immobilization, microarray technology, immunodiagnostics, biosensors, bioreactors, affinity chromatography, and many more. The majority of these techniques demand functionalization of versatile solid surfaces or biomolecules.

Photoaffinity labeling

FNAB was first made by Fleet and co-workers [16] in the late 1960s for photoaffinity labeling of antibodies to shed light on the structure and reactivity of macromolecules. Since then, FNAB became more acceptable and popular as a photoaffinity label and a large number of reports were published on the subject [58–61, 70–72].

Immobilization of enzymes

In mid-1970s, Guire et al. activated an aminated matrix by incubating FNAB at 37 °C for 20 h, and in the subsequent step they immobilized enzyme onto the surface of the polymer in a photochemical reaction in 16 h. A similar reaction was carried out by Naqvi and Nahar [62] who substantially reduced the activation time to about 60 s by carrying out the reaction in the presence of microwaves and immobilized protein in 20 min by UV irradiation. Bora et al. [69] chose pathway III (Fig. 5) to immobilize glucose oxidase and horseradish peroxidase on cellulose membrane. Nevertheless, pathway IV (Fig. 5) is the most preferred one for immobilization of enzymes onto inert polymers, like polypropylene, polyethylene, polystyrene, polycarbonate, and cellulose surfaces. Immobilization of enzymes onto inert polypropylene or polyethylene surfaces is of special interest because of their inability to bind through adsorption (unlike polystyrene) and their insolubility in most organic solvents. Enzymes immobilized onto these activated surfaces show enhanced thermal, pH, and storage stability along with improved catalytic activity [52, 53, 73]. A new application of polystyrene cuvettes was demonstrated by Kumar et al. [74] in which they activated disposable cuvettes with FNAB, immobilized oxalate oxidase, and used the system to determine urinary oxalate in a test sample by directly measuring the absorbance in a spectrophotometer. Kumar et al. [75] prepared a flow-through reactor system by covalent linking invertase on the inner surface of an FNAB-activated polyvinyl chloride (PVC) tube to convert sucrose to inverted sugar. FNAB has also been used to immobilize several enzymes for desired applications [76–78]. Recently, Ahirwar et al. has used FNAB for preparation of matrices and surfaces for identification of aptamers and for monitoring of aptamer enrichment during the SELEX process [79, 80].

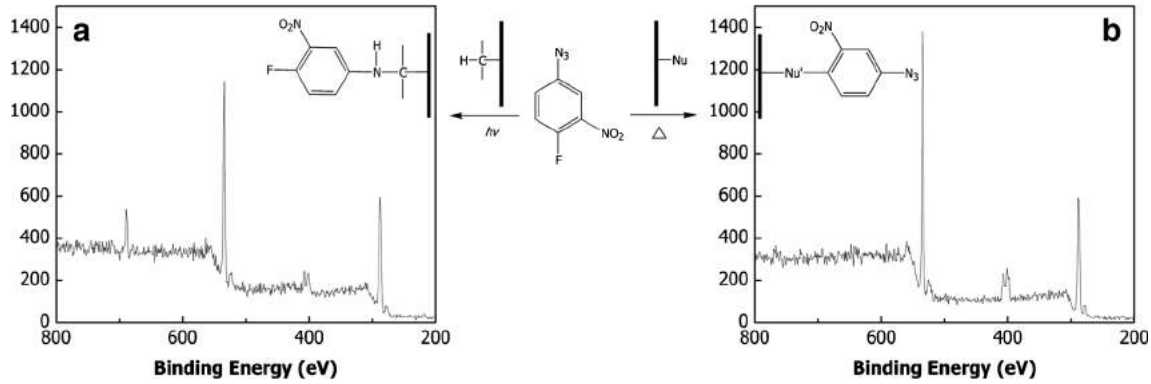

Fig. 6 **a** XP spectra of cellulose membrane after photochemical activation with FNAB. Appearance of fluorine peak at around 684 eV suggests the formation of thermoreactive surface. **b** XP spectra of cellulose membrane after thermochemical activation with FNAB. Appearance of duplex nitrogen peak at around 400 eV suggests the formation of photoreactive surface. Peaks at around 684, 588, 400, and 288 eV correspond to fluorine (F1s), oxygen (O1s), nitrogen (N1s), and carbon (C1s), respectively

Immunodiagnostics

Enzyme-linked immunosorbent assay (ELISA) is a very useful technique for the detection of minute quantities of antigen or antibody for clinical diagnostics and biomedical research [81]. Conventionally, the ELISA procedure is carried out by immobilizing antigen or antibody on a polystyrene microtiter plate through adsorption at 37 °C or less for detection of the target analyte (antibody or antigen) in the sample (Fig. 7). However, immobilization through chemical binding is more attractive as shown by Bora et al. [82] whereby they photoactivated the surface of the wells of a polystyrene microtiter plate with FNAB and covalently immobilized *Epicoccum nigrum* antigen (allergenic antigen) or goat anti-rabbit IgG onto them. Photoactivated microtiter plate gave 1.5–2-fold higher ELISA values for the detection of respective antibodies in less time than the untreated microtiter plate. In one such simple development ELISA was carried out at elevated temperature (50 °C) on a photoactivated microtiter plate and reduced ELISA times from 18 h for conventional setups to around 3 h [83]. The covalently bound antigen was stable enough to withstand subsequent ELISA steps at elevated temperature. Heat-mediated ELISA (HELISA) was also verified by doing cell-ELISA in 3 h with results akin to conventional cell-ELISA carried out in 38 h for detection of cell adhesion molecules (CAMs) on endothelial cells [84]. In another example, autoantibodies from rheumatoid arthritis patient samples was detected by performing the HELISA procedure [85]. HELISA on a photoactivated surface showed 1.5-fold higher ELISA value than those obtained on the untreated surface. In another method ELISA was carried out on FNAB-activated plates in a closed steel vessel by applying pressure of 2.0×10^5 Pa (pressure-mediated ELISA or PELISA) [86], and ultrasound energy (sonication-mediated ELISA or SELISA) [87] to give rapid (in less than 1 h) ELISA with higher sensitivity and specificity. In another breakthrough development, FNAB-activated microtiter plates were used to carry out ELISA by microwave irradiation (MELISA) in less than 5 min [88, 89]. Examples of surface functionalization of polypropylene and polystyrene plates by FNAB for the development of image-based ELISA and aptamer-ELISA were also reported [79, 90].

Microarray fabrication

The post-genome era has witnessed a tremendous advance in microarray technology using different types of photolinkers for binding different sets of biomolecules on versatile materials [91–96]. As FNAB chemistry allows activation of a variety of solid supports without any modification, the technique could be well suited for fabrication of antibody, protein or peptide, DNA, and carbohydrate arrays. Thus, Kannoujia et al. [97] and Ahirwar et al. [98] used photoactivated polymer surfaces for single-step covalent immobilization of amine-modified oligonucleotide probes to fabricate DNA-based biochips. The method shows high selectivity in subsequent

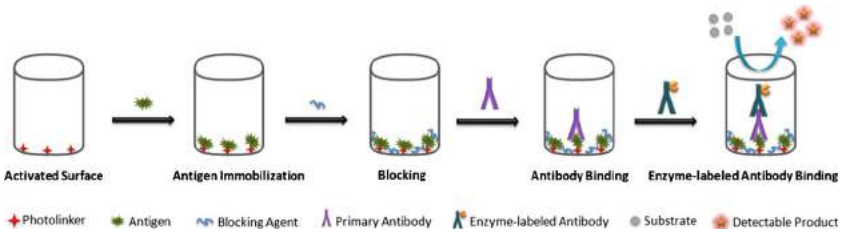

Fig. 7 Rapid ELISA on FNAB-mediated photoactivated polystyrene microtiter plate

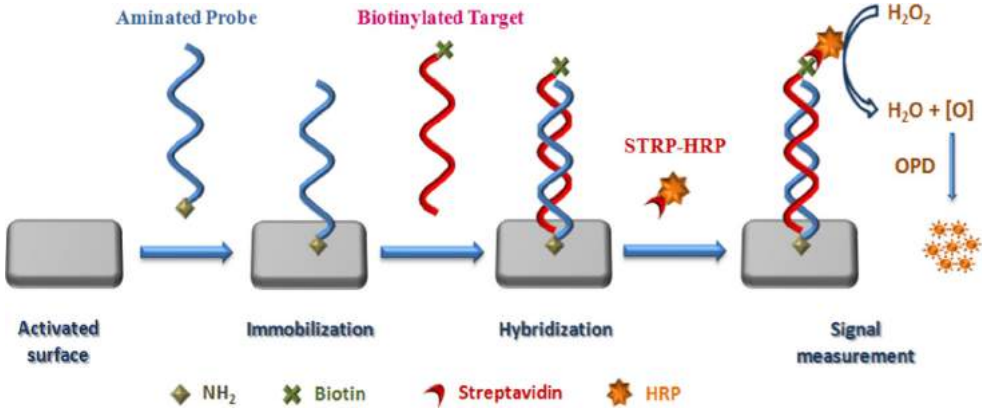

Fig. 8 Immobilization of aminated oligonucleotide probe onto FNAB-activated surface and colorimetric detection of hybridized complementary oligonucleotide target. Adapted with permission from ref. [97]. Copyright 2010 Royal Society of Chemistry

hybridization processes with the complementary target and is able to discriminate even single-base mismatched targets (Fig. 8). Sharma et al. [99] covalently immobilized underivatized (without modification) carbohydrates on photoreactive-cellulose membrane by UV irradiation while retaining their functional activity.

Conducting polymer and biosensor

In recent years, photochemical modification of conducting polymers has received much attention either for controlling the electrochemical properties of the polymers or conjugation of biomolecules for making biosensor and bioelectronics [100, 101]. Chong et al. [54] introduced 1-fluoro-2-nitro-4-azidobenzene into the terminal tail ($-C_6H_{13}$) of poly(3-hexylthiophene) (P3HT) thin layer modified Ag electrode (Ag/P3HT). The FNAB-modified Ag/P3HT anode showed about fourfold higher luminous efficiency than the base device [54]. There are also reports of functionalization of poly(3,4-ethylenedioxythiophene) (PEDOT)-modified films by FNAB in a photochemical nitrene insertion reaction for controlling the redox response of the films [55, 56]. Deepa et al. [55] showed that the FNAB-functionalized PEDOT film allows a reversible insertion and extraction of guest cations and anions, whereas the non-functionalized film is capable of exchanging only anions. Surface morphologies of the functionalized and non-functionalized PEDOT:DSS films are illustrated in Fig. 9, which shows altered morphology of the polymer film after reacting with the highly reactive FNAB molecules [55]. For cholesterol biosensors, self-assembled monolayer (SAM) was prepared on gold-coated glass plates using octadecanethiol (ODT) [102] or P3HT [103] and activated with FNAB by nitrene insertion reaction. The fluoro group of FNAB was further used to bind cholesterol oxidase (ChOx) to make a bioelectrode that was used to estimate cholesterol by a surface plasmon resonance technique. Using the same technique, Pandey et al. [104] developed an electrochemical DNA biosensor for rapid detection of *E. coli*.

PEGylation

PEGylation is important to change the microenvironment of a biomolecule. Recently, Bora et al. activated PEG by a simple photochemical reaction of PEG and FNAB and efficiently conjugated glucose oxidase [105]. PEGylated glucose oxidase was found to have enhanced thermal, pH, and storage stability. The method was found to be useful for PEGylation of biomolecules including proteins and nucleic acids to improve their properties as drugs and also enhance their solubility in organic solvents.

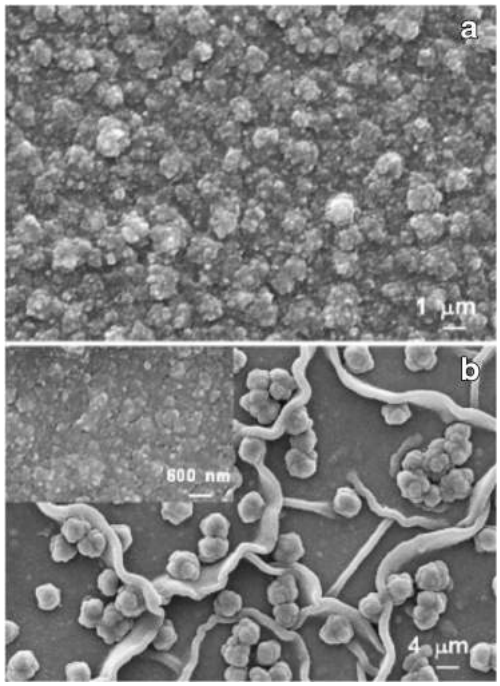

Fig. 9 Scanning electron microscopy images of **a** the non-functionalized (PEDOT:DSS) film and **b** the same film functionalized by 1-fluoro-2-nitro-4-azidobenzene (PEDOT:DSS:FNAB). *Inset* of **b** is a high magnification image of the background. Adapted with permission from ref. [55]. Copyright 2009 Elsevier

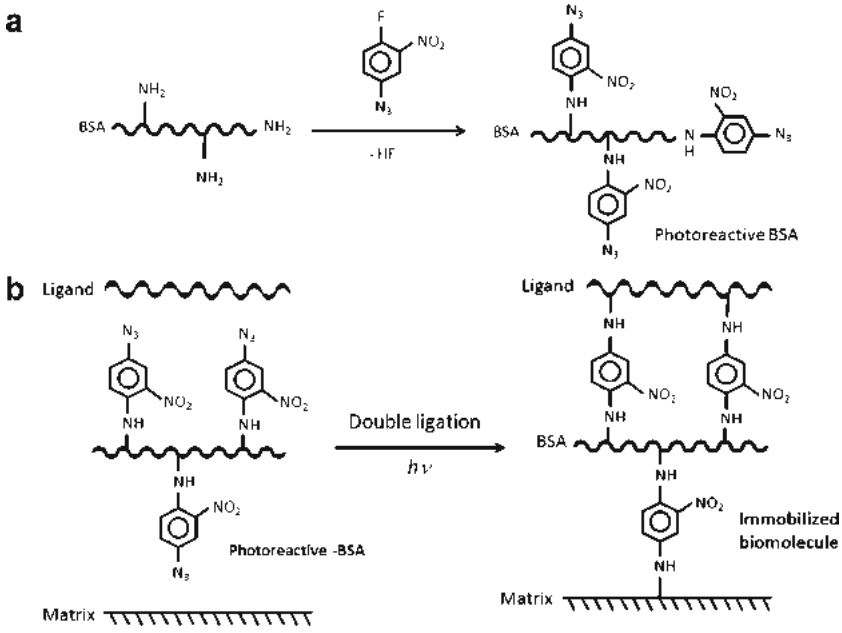

Fig. 10 Double ligation strategy for in situ immobilization. **a** Preparation of photoreactive BSA by thermochemical reaction of BSA and FNAB. **b** The photoreactive BSA having several photoreactive groups was exposed to UV light together with a ligand and a matrix. Photoreactive BSA forms highly reactive nitrenes, some of which attached to the surface and the rest to the ligand by double ligation reaction forming immobilized biomolecule. Adapted with permission from ref. [106]. Copyright 2009 Elsevier

In situ immobilization by double ligation

Recently, we developed a rapid method for the preparation of photoreactive BSA, which is a novel proteinaceous photolinker that binds simultaneously to a biomolecule and a matrix by a double ligation strategy [106]. It is prepared by the reaction of bovine serum albumin (BSA) with excess of FNAB. BSA has several nucleophilic amino groups that react with the fluoro group of FNAB, while the photoreactive azido group, now part of the photoreactive BSA, remains intact. When an enzyme is placed on an inert polystyrene matrix in the presence of photoreactive BSA and exposed to light, the latter forms highly reactive nitrenes, some of which bind to the matrix and the rest to the ligand resulting in simultaneous formation of covalent bonds with the matrix and the enzyme (Fig. 10). The uniqueness of this method is that the binding occurs irrespective of the functional group either on the matrix or on the biomolecule.

Biomedical applications

Chen et al. [57] investigated the in vitro activity of a surface-bound antimicrobial cationic peptide. The antimicrobial cationic peptide was covalently immobilized on a glass surface using two different azide-based photolinkers, FNAB and 4-azidobenzoic acid (ABA). Glass coverslips were activated with photolinkers in UV light for subsequent covalent coupling of the peptide. For the ABA photolinker, EDC was used to activate the free carboxyl terminal for further covalent coupling. This method is potentially useful for antimicrobial coating on desired surfaces for biomedical devices.

Conclusion and future perspectives

FNAB is an efficient heterofunctional photolinker which allows simple and speedy coupling of a biomolecule to a polymer surface or other biomolecules. In this review, we have highlighted the flexible chemistry of FNAB, its reaction mechanism, strategies for surface engineering and biomolecular conjugation, and its versatile applications including diagnostics. The strong resonance effect of the nitro group and inductive effect of the fluoro group make FNAB an attractive molecule for surface engineering of any polymer with C–H or C = C bonds including carbon nanotubes, graphene, graphite, or other carbon materials having an sp^2 configuration by nitrene insertion reaction. The presence of the nitro group in FNAB also makes its fluoro group a good leaving group when attacked by a nucleophile, thereby allowing direct conjugation to a biomolecule without any additional reagent or modification. This allows rapid immobilization of biomolecules on FNAB-activated surfaces. Conjugation of FNAB to bovine serum albumin leads to a photolinker polymer which can bind a matrix and a biomolecule in a double ligation strategy irrespective of their functional groups.

One of the concerns of researchers is that the photochemical reaction of FNAB that generates highly reactive nitrene can undergo highly non-specific reactions. This is a genuine concern; however, this is true for most of the photolinkers. Nevertheless, this concern can be overcome if the photochemical step is carried out with the matrix or polymer. In such cases specificity does not matter much. In a second scenario, when photochemical reaction is carried out with the biopolymer like enzyme, antigen, antibody, and DNA or RNA, there is a small probability that FNAB will attack the reactive center

of the biopolymer as the latter is a huge molecule compared to FNAB. In fact, we have not found this to be a serious practical problem during our decade-long study on protein immobilization. However, for small molecules this may not be a good proposition because nitrene can block the functional group that is needed for further activities. In conclusion, FNAB is a reliable, cheap, and a useful heterofunctional photolinker for surface engineering and biomolecule immobilization and can be further explored for new opportunities.

Acknowledgments This work was supported by the CARDIOMED (BSC0122) project of the Council of Scientific and Industrial Research, New Delhi, India. S.K. thanks the SERB-Department of Science and Technology, Government of India, for the award of Fast Track Young Scientist Fellowship. R. A. thanks the Council of Scientific and Industrial Research, New Delhi, India for the Senior Research Fellowship.

Compliance with ethical standards

Conflict of interest Authors declare no conflict of interests.

References

1. Hermanson GT. Introduction to bioconjugation. In: Bioconjugate techniques. 3rd ed. Boston: Academic. 2013; 1–125. doi:10.1016/B978-0-12-382239-0.00001-7.
2. Kalia J, Raines RT. Advances in bioconjugation. Curr Org Chem. 2010;14(2):138–47.
3. Wong M, Jameson SS. Overview of protein conjugation. In: Chemistry of protein and nucleic acid cross-linking and conjugation. 2nd ed. Boca Raton: CRC. 2011; 18. doi:10.1201/b11175-2.
4. Thavarajah R, Mudimbaimannar VK, Elizabeth J, Rao UK, Ranganathan K. Chemical and physical basics of routine formaldehyde fixation. J Oral Maxillofac Pathol. 2012;16(3):400–5. doi:10.4103/0973-029X.102496.
5. Sewell BT, Bouloukos C, von Holt C. Formaldehyde and glutaraldehyde in the fixation of chromatin for electron microscopy. J Microsc. 1984;136(Pt 1):103–12.
6. Kiernan J. Formaldehyde, formalin, paraformaldehyde and glutaraldehyde: what they are and what they do. Microsc Today. 2000;1:8–12.
7. Khorana HG. The chemistry of carbodiimides. Chem Rev. 1953;53(2):145–66. doi:10.1021/cr60165a001.
8. Kurzer F, Douraghi-Zadeh K. Advances in the chemistry of carbodiimides. Chem Rev. 1967;67(2):107–52. doi:10.1021/cr60246a001.
9. Williams A, Ibrahim IT. Carbodiimide chemistry: recent advances. Chem Rev. 1981;81(6):589–636. doi:10.1021/cr00046a004.
10. Hunter MJ, Ludwig ML. The reaction of imidoesters with proteins and related small molecules. J Am Chem Soc. 1962;84(18):3491–504. doi:10.1021/ja00877a016.
11. Heterobifunctional Cross-Linkers. In: Chemistry of Protein and Nucleic Acid Cross-Linking and Conjugation, Second Edition. CRC Press. 2011; 191–238. doi:10.1201/b11175-7.
12. Monofunctional and Zero -Length Cross -Linking Reagents. In: Chemistry of Protein and Nucleic Acid Cross-Linking and Conjugation, Second Edition. CRC Press. 2011; 265–296. doi:10.1201/b11175-9.
13. Hermanson GT. Chapter 5 - Homobifunctional Crosslinkers. In: Bioconjugate Techniques (Third edition). Academic Press, Boston. 2013; 275–298. doi:10.1016/B978-0-12-382239-0.00005-4.
14. Patil US, Qu H, Caruntu D, O'Connor CJ, Sharma A, Cai Y, Tarr MA. Labeling Primary Amine Groups in Peptides and Proteins with N-Hydroxysuccinimidyl Ester Modified Fe(3)O(4)@SiO(2) Nanoparticles Containing Cleavable Disulfide-bond Linkers. Bioconjugate Chem. 2013; 24 (9). doi:10.1021/bc400165r.
15. Klykov O, Weller MG. Quantification of N-hydroxysuccinimide and N-hydroxysulfosuccinimide by hydrophilic interaction chromatography (HILIC). Anal Methods. 2015;7(15):6443–8. doi:10.1039/C5AY00042D.
16. Fleet G, Porter R, Knowles J. Affinity labelling of antibodies with aryl nitrene as reactive group. Nature. 1969;224(5218):511–2.
17. Bayley H, Knowles JR. [8] Photoaffinity labeling. In: Methods in Enzymology, vol Volume 46. Academic Press. 1977; 69–114. doi:10.1016/S0076-6879(77)46012-9.
18. Brunner J. New photolabeling and crosslinking methods. Annu Rev Biochem. 1993;62:483–514. doi:10.1146/annurev.bi.62.070193.002411.
19. Bayley H. Photogenerated reagents in biochemistry and molecular biology. In Laboratory Techniques in Biochemistry and Molecular Biology, vol 12. Elsevier, New York, Work TS, Burdon RH. Eds. 1983.
20. Liu L, Engelhard MH, Yan M. Surface and interface control on photochemically initiated immobilization. J Am Chem Soc. 2006;128(43):14067–72. doi:10.1021/ja062802l.
21. Brase S, Gil C, Knepper K, Zimmermann V. Organic azides: an exploding diversity of a unique class of compounds. Angew Chem (Int ed Engl). 2005;44(33):5188–240. doi:10.1002/anie.200400657.
22. Meijer EW, Nijhuis S, Van Vroonhoven FCBM. Poly-1,2-azepines by the photopolymerization of phenyl azides. Precursors for conducting polymer films. J Am Chem Soc. 1988;110(21):7209–10. doi:10.1021/ja00229a043.
23. Gomez N, Schmidt CE. Nerve growth factor-immobilized polypyrrole: bioactive electrically conducting polymer for enhanced neurite extension. J Biomed Mater Res Part A. 2007;81(1):135–49. doi:10.1002/jbm.a.31047.
24. Jagur-Grodzinski J. Biomedical applications of electrically conductive polymeric systems. e-Polymers. 2012;12. doi:10.1515/epoly.2012.12.1.722
25. Liu LH, Yan M. Perfluorophenyl azides: new applications in surface functionalization and nanomaterial synthesis. Acc Chem Res. 2010;43(11):1434–43. doi:10.1021/ar100066t.
26. Liu LH, Lerner MM, Yan M. Derivitization of pristine graphene with well-defined chemical functionalities. Nano Lett. 2010;10(9):3754–6. doi:10.1021/nl1024744.
27. Liu L-H, Yan M. Functionalization of pristine graphene with perfluorophenyl azides. J Mater Chem. 2011;21(10):3273–6. doi:10.1039/C0JM02765K.
28. Al-Bataineh SA, Luginbuehl R, Textor M, Yan M. Covalent immobilization of antibacterial furanones via photochemical activation of perfluorophenylazide. Langmuir. 2009;25(13):7432–7. doi:10.1021/la900334w.
29. Yakai FENGHZ, Li ZHANG, Jintang GUO. Surface modification of biomaterials by photochemical immobilization and photograft polymerization to improve hemocompatibility. Front Chem Sci Eng. 2010;4(3):372–81. doi:10.1007/s11705-010-0005-z.
30. Harmer MA. Photomodification of surfaces using heterocyclic azides. Langmuir. 1991;7(10):2010–2. doi:10.1021/la00058a007.
31. Blencowe A, Hayes W. Development and application of diazirines in biological and synthetic macromolecular systems. Soft Matter. 2005;1(3):178–205. doi:10.1039/B501989C.

32. Dubinsky L, Krom BP, Meijler MM. Diazirine based photoaffinity labeling. Bioorg Med Chem. 2012;20(2):554–70. doi:10.1016/j.bmc.2011.06.066.
33. Dorman G, Prestwich GD. Benzophenone photophores in biochemistry. Biochemistry. 1994;33(19):5661–73.
34. Hino N, Okazaki Y, Kobayashi T, Hayashi A, Sakamoto K, Yokoyama S. Protein photo-cross-linking in mammalian cells by site-specific incorporation of a photoreactive amino acid. Nat Methods. 2005;2(3):201–6. doi:10.1038/nmeth739.
35. Borden WT, Gritsan NP, Hadad CM, Karney WL, Kemnitz CR, Platz MS. The interplay of theory and experiment in the study of phenylnitrene. Acc Chem Res. 2000;33(11):765–71.
36. Gritsan NP, Platz MS. Kinetics, spectroscopy, and computational chemistry of arylnitrenes. Chem Rev. 2006;106(9):3844–67. doi:10.1021/cr040055+.
37. Gritsan N, Platz M. Photochemistry of azides: the azide/nitrene interface. Chichester: Wiley; 2010.
38. Platz MS. Comparison of phenylcarbene and phenylnitrene. Acc Chem Res. 1995;28(12):487–92.
39. Dunkin IR, Thomson PC. Pentafluorophenyl nitrene: a matrix isolated aryl nitrene thet does not undergo ring expansion. J Chem Soc Chem Commun. 1982;20:1192–3.
40. Schrock AK, Schuster GB. Photochemistry of phenyl azide: chemical properties of the transient intermediates. J Am Chem Soc. 1984;106(18):5228–34.
41. Leyva E, Platz MS, Persy G, Wirz J. Photochemistry of phenyl azide: the role of singlet and triplet phenylnitrene as transient intermediates. J Am Chem Soc. 1986;108(13):3783–90.
42. Wentrup C, Winter HW. Isolation of diazacycloheptatetraenes from thermal nitrene-nitrene rearrangements. J Am Chem Soc. 1980;102(19):6159–61.
43. Schnapp KA, Poe R, Leyva E, Soundararajan N, Platz MS. Exploratory photochemistry of fluorinated aryl azides. Implications for the design of photoaffinity labeling reagents. Bioconjug Chem. 1993;4(2):172–7.
44. Tate JJ, Persinger J, Bartholomew B. Survey of four different photoreactive moieties for DNA photoaffinity labeling of yeast RNA polymerase III transcription complexes. Nucleic Acids Res. 1998;26(6):1421–6.
45. Smith BA, Cramer CJ. How Do different fluorine substitution patterns affect the electronic state energies of phenylnitrene? J Am Chem Soc. 1996;118(23):5490–1.
46. Leyva E, Sagredo R. Photochemistry of fluorophenyl azides in diethylamine. Nitrene reaction versus ring expansion. Tetrahedron. 1998;54(26):7367–74.
47. Leyva E, Sagredo R, Moctezuma E. Photochemistry of fluorophenyl azides in aniline: asymmetric fluoroazobenzenes by N• H singlet nitrene insertion. J Fluor Chem. 2004;125(5):741–7.
48. Albini A, Bettinetti G, Minoli G. The effect of the p-nitro group on the chemistry of phenylnitrene. A study via intramolecular trapping. J Chem Soc Perkin Trans. 1999;2(12):2803–7.
49. Liang TY, Schuster GB. Photochemistry of 3-and 4-nitrophenyl azide: detection and characterization of reactive intermediates. J Am Chem Soc. 1987;109(25):7803–10.
50. Nina PG, Elena AP. The mechanism of photolysis of aromatic azides. Russ Chem Rev. 1992;61(5):500.
51. Mikhail FB, Kantor MM, Mikhail VA. The photochemistry of phenyl azide. Russ Chem Rev. 1992;61(1):25.
52. Bora U, Kannan K, Nahar P. A simple method for functionalization of cellulose membrane for covalent immobilization of biomolecules. J Membr Sci. 2005;250(1):215–22.
53. Bora U, Sharma P, Kumar S, Kannan K, Nahar P. Photochemical activation of a polycarbonate surface for covalent immobilization of a protein ligand. Talanta. 2006;70(3):624–9.
54. Chong L-W, Chou Y-N, Lee Y-L, Wen T-C, Guo T-F. Hole-injection enhancement of top-emissive polymer light-emitting diodes by P3HT/FNAB modification of Ag anode. Org Electron. 2009;10(6):1141–5.
55. Deepa M, Bhandari S, Kant R. A comparison of charge transport behavior in functionalized and non-functionalized poly 3, 4-(ethylenedioxythiophene) films. Electrochim Acta. 2009;54(4):1292–303.
56. Bhandari S, Deepa M, Srivastava AK, Kant R. Post-polymerization functionalization of poly (3, 4-ethylenedioxythiophene) films by 1-fluoro-2-nitro-4-azidobenzene: electrochromism and redox behavior. J Mater Chem. 2009;19(16):2336–48.
57. Chen R, Cole N, Willcox MD, Park J, Rasul R, Carter E, et al. Synthesis, characterization and in vitro activity of a surface-attached antimicrobial cationic peptide. Biofouling. 2009;25(6):517–24. doi:10.1080/08927010902954207.
58. Fleet GW, Knowles JR, Porter RR. The antibody binding site. Labelling of a specific antibody against the photo-precursor of an aryl nitrene. Biochem J. 1972;128(3):499–508.
59. Guire P. [21] Photochemical immobilization of enzymes and other biochemicals. In: Methods in Enzymology, vol Volume 44. Academic Press. 1976;280–288. doi:10.1016/S0076-6879(76)44023-5.
60. Jacobs S, Hazum E, Shechter Y, Cuatrecasas P. Insulin receptor: covalent labeling and identification of subunits. Proc Natl Acad Sci U S A. 1979;76(10):4918–21.
61. Gorman JJ, Folk JE. Transglutaminase amine substrates for photochemical labeling and cleavable cross-linking of proteins. J Biol Chem. 1980;255(3):1175–80.
62. Naqvi A, Nahar P. Photochemical immobilization of proteins on microwave-synthesized photoreactive polymers. Anal Biochem. 2004;327(1):68–73. doi:10.1016/j.ab.2003.11.026.
63. Nahar P, Wali NM, Gandhi RP. Light-induced activation of an inert surface for covalent immobilization of a protein ligand. Anal Biochem. 2001;294(2):148–53. doi:10.1006/abio.2001.5168.
64. Nahar P, Naqvi A, Basir SF. Sunlight-mediated activation of an inert polymer surface for covalent immobilization of a protein. Anal Biochem. 2004;327(2):162–4. doi:10.1016/j.ab.2003.11.030.
65. Kumar S, Nahar P. Sunlight-induced covalent immobilization of proteins. Talanta. 2007;71(3):1438–40. doi:10.1016/j.talanta.2006.06.029.
66. Kannoujia DK, Ali S, Nahar P. Pressure-induced covalent immobilization of enzymes onto solid surface. Biochem Eng J. 2009;48(1):136–40. doi:10.1016/j.bej.2009.09.005.
67. Sharma P, Kannoujia DK, Basir SF, Nahar P. Rapid immobilization of enzymes onto solid supports by ultrasound waves. Artif Cells Blood Substit Immobil Biotechnol. 2011;39(5):289–92. doi:10.3109/10731199.2011.563361.
68. Nahar P, Bora U. Microwave-mediated rapid immobilization of enzymes onto an activated surface through covalent bonding. Anal Biochem. 2004;328(1):81–3. doi:10.1016/j.ab.2003.12.031.
69. Bora U, Sharma P, Kannan K, Nahar P. Photoreactive cellulose membrane—A novel matrix for covalent immobilization of biomolecules. J Biotechnol. 2006;126(2):220–9.
70. Chen S, Jean Chen S, Xu Q-P. 4-Fluoro-3-nitrophenyl azide, a selective photoaffinity label for type B monoamine oxidase. Biochem Pharmacol. 1985;34(6):781–8. doi:10.1016/0006-2952(85)90758-0.
71. Chen SA, Shih JC, Hsu MC, Xu QP. Photoaffinity labeling of beef liver monoamine oxidase-B by 4-fluoro-3-nitrophenyl azide. Biochem Pharmacol. 1987;36(6):937–43.
72. Hsu MC, Shih JC. Photoaffinity labeling of human placental monoamine oxidase-A by 4-fluoro-3-nitrophenyl azide. Mol Pharmacol. 1988;33(2):237–41.

73. Naqvi A, Nahar P, Gandhi RP. Introduction of functional groups onto polypropylene and polyethylene surfaces for immobilization of enzymes. Anal Biochem. 2002;306(1):74–8. doi:10.1006/abio.2002.5675.
74. Kumar S, Chauhan VS, Nahar P. Preparation of biomolecule-ligated polystyrene cuvets and their applications in diagnostics. Microchem J. 2008;89(2):148–52. doi:10.1016/j.microc.2008.01.009.
75. Kumar S, Chauhan VS, Nahar P. Invertase embedded-PVC tubing as a flow-through reactor aimed at conversion of sucrose into inverted sugar. Enzym Microb Technol. 2008;43(7):517–22. doi:10.1016/j.enzmictec.2008.08.002.
76. Bukhari A, Idris A, Atta M, Loong TC. Covalent immobilization of Candida antarctica lipase B on nanopolystyrene and its application to microwave-assisted esterification. Chin J Catal. 2014;35(9):1555–64. doi:10.1016/S1872-2067(14)60111-X.
77. Pundir S, Gera A, Pundir CS. Photochemical immobilization of cucurbita fruit ascorbate oxidase onto polyethylene disc for determination of ascorbate in serum and foodstuffs. Artif Cells, Blood Substit Biotechnol. 2011;39(5):324–9. doi:10.3109/10731199.2011.573481.
78. Kumar AK, Shamsher S. An efficient immobilization of Streptomyces sp. STL-D8 lipase onto photo-chemically modified cellulose-based natural fibers and its application in ethyl ferulate synthesis. Trends Carbohydr Res. 2012;4(4):13–23.
79. Ahirwar R, Vellarikkal SK, Sett A, Sivasubbu S, Scaria V, Bora U, et al. Aptamer-assisted detection of the altered expression of estrogen receptor alpha in human breast cancer. PLoS ONE. 2016;11(4), e0153001. doi:10.1371/journal.pone.0153001.
80. Ahirwar R, Nahar P. Screening and identification of a DNA aptamer to concanavalin A and its application in food analysis. J Agric Food Chem. 2015;63(16):4104–11. doi:10.1021/acs.jafc.5b00784.
81. Parween S, Nahar P. Image-based ELISA on an activated polypropylene microtest plate–a spectrophotometer-free low cost assay technique. Biosens Bioelectron. 2013;48:287–92. doi:10.1016/j.bios.2013.04.020.
82. Bora U, Chugh L, Nahar P. Covalent immobilization of proteins onto photoactivated polystyrene microtiter plates for enzyme-linked immunosorbent assay procedures. J Immunol Methods. 2002;268(2):171–7. doi:10.1016/S0022-1759(02)00212-0.
83. Bora U, Kannan K, Nahar P. Heat-mediated enzyme-linked immunosorbent assay procedure on a photoactivated surface. J Immunol Methods. 2004;293(1-2):43–50. doi:10.1016/j.jim.2004.06.023.
84. Kumar S, Ghosh L, Kumar S, Ghosh B, Nahar P. A rapid method for detection of cell adhesion molecules (CAMs) on human umbilical vein endothelial cells (HUVECs). Talanta. 2007;73(3):466–70. doi:10.1016/j.talanta.2007.04.016.
85. Sharma P, Gupta B, Farhat Basir S, Rani Das H, Nahar P. Rapid and sensitive detection of autoantibody in rheumatoid arthritis patients by heat-mediated ELISA. Clin Biochem. 2008;41(1-2):97–102. doi:10.1016/j.clinbiochem.2007.09.016.
86. Kannoujia DK, Nahar P. Pressure: a novel tool for enzyme-linked immunosorbent assay procedure. BioTech. 2009;46(6):468–72. doi:10.2144/000113118.
87. Sharma P, Nahar P. Ultrasound wave-mediated enzyme-linked immunosorbent assay technique. Anal Chim Acta. 2009;650(2):241–6. doi:10.1016/j.aca.2009.07.047.
88. Nahar P, Bora U, Sharma GL, Kannoujia DK. Microwave-mediated enzyme-linked immunosorbent assay procedure. Anal Biochem. 2012;421(2):764–6. doi:10.1016/j.ab.2011.09.029.
89. Ahirwar R, Tanwar S, Bora U, Nahar P. Microwave non-thermal effect reduces ELISA timing to less than 5 minutes. RSC Adv. 2016;6(25):20850–7. doi:10.1039/C5RA27261K.
90. Ahirwar R, Nahar S, Aggarwal S, Ramachandran S, Maiti S, Nahar P. In silico selection of an aptamer to estrogen receptor alpha using computational docking employing estrogen response elements as aptamer-alike molecules. Sci Rep. 2016;6:21285. doi:10.1038/srep21285. http://www.nature.com/articles/srep21285#supplementary-information.
91. Ito Y. Photoimmobilization for microarrays. Biotechnol Prog. 2006;22(4):924–32. doi:10.1021/bp060143a.
92. Pei Z, Yu H, Theurer M, Walden A, Nilsson P, Yan M, et al. Photogenerated carbohydrate microarrays. Chembiochem: Eur J Chem Biol. 2007;8(2):166–8. doi:10.1002/cbic.200600447.
93. Rusmini F, Zhong Z, Feijen J. Protein immobilization strategies for protein biochips. Biomacromolecules. 2007;8(6):1775–89. doi:10.1021/bm061197b.
94. Ohyama K, Omura K, Ito Y. A photo-immobilized allergen microarray for screening of allergen-specific IgE. Allergol Int. 2005;54(4):627–31. doi:10.2332/allergolint.54.627.
95. Hook AL, Thissen H, Voelcker NH. Advanced substrate fabrication for cell microarrays. Biomacromolecules. 2009;10(3):573–9. doi:10.1021/bm801217n.
96. Kakiyama T, Usui K, K-y T, Mie M, Kobatake E, Mihara H. A peptide release system using a photo-cleavable linker in a cell array format for cell-toxicity analysis. Polym J. 2013;45(5):535–9. doi:10.1038/pj.2013.20.
97. Kannoujia DK, Ali S, Nahar P. Single-step covalent immobilization of oligonucleotides onto solid surface. Anal Methods. 2010;2(3):212–6.
98. Ahirwar R, Tanwar S, Parween S, Kumar A, Nahar P. Image-based detection of oligonucleotides–a low cost alternative to spectrophotometric or fluorometric methods. Analyst. 2014;139(9):2186–92. doi:10.1039/c3an02402d.
99. Sharma P, Basir SF, Nahar P. Photoimmobilization of unmodified carbohydrates on activated surface. J Colloid Interface Sci. 2010;342(1):202–4.
100. Jenkins ATA. Tutorial Review: Modern Biological Sensors. In: Surface Design: Applications in Bioscience and Nanotechnology. Wiley-VCH Verlag GmbH & Co. KGaA, 2009; 81–101. doi:10.1002/9783527628599.ch4.
101. Park C, Lee C, Kwon O. Conducting Polym Based Nanobiosensors Polym. 2016;8(7):249.
102. Arya SK, Solanki PR, Singh RP, Pandey MK, Datta M, Malhotra BD. Application of octadecanethiol self-assembled monolayer to cholesterol biosensor based on surface plasmon resonance technique. Talanta. 2006;69(4):918–26.
103. Arya SK, Solanki PR, Singh SP, Kaneto K, Pandey MK, Datta M, et al. Poly-(3-hexylthiophene) self-assembled monolayer based cholesterol biosensor using surface plasmon resonance technique. Biosens Bioelectron. 2007;22(11):2516–24. doi:10.1016/j.bios.2006.10.011.
104. Pandey CM, Singh R, Sumana G, Pandey MK, Malhotra BD. Electrochemical genosensor based on modified octadecanethiol self-assembled monolayer for Escherichia coli detection. Sensors Actuators B Chem. 2011;151(2):333–40. doi:10.1016/j.snb.2010.07.046.
105. Bora U, Kannoujia DK, Kumar S, Sharma P, Nahar P. Photochemical activation of polyethylene glycol and its application in PEGylation of protein. Process Biochem. 2011;46(6):1380–3. doi:10.1016/j.procbio.2011.03.004.
106. Kumar S, Kannoujia DK, Naqvi A, Nahar P. A novel proteinaceous photolinker for simultaneous binding to an inert surface and a biomolecule. Biochem Eng J. 2009;47(1–3):132–5. doi:10.1016/j.bej.2009.07.009.

Volume 4, Issue 1 (2016) 274-277 ISSN 2347 - 3258
International Journal of Advance Research and Innovation

Failure Analysis of First Stage Gas Turbine Blade

Sushila Rani
Department of Mechanical, Production, Industrial and Automobile Engineering, Delhi Technological University, Delhi, India

Article Info

Article history:
Received 02 April 2016
Received in revised form
20 May 2016
Accepted 28 May 2016
Available online 15 June 2016

Keywords

Gas Turbine Blade,
Creep,
Corrosion,
Fatigue

Abstract

In last few decades, the operating temperatures of gas turbine engines have been continually increased in order to achieve higher and higher power and efficiency. During the operation of power generation gas turbines, the blade and other components of hot gas path undergoes service induced degradation, which may be neutral or accelerated due to different causes. The degradation or damage may have a metallurgical or mechanical origin and results in reduction of equipment reliability and availability. It also increases risk of failure occurring. Also, due to blade material metallurgical deterioration, the material creep, fatigue, impact and corrosion properties decrease. There are different factors which influence blade lifetime as design and operation conditions but the latter are more critical.

1. Introduction

In order to identify the root causes of blade failures, a complete investigation integrating both mechanical analyses and metallurgical examination has been carried out. In gas power plants, Turbine blades are most critical component of gas turbine. During event of their failure, the power plant shut down. This can cause economic loss. Therefore, it become necessary to conduct the detailed analysis of failure of gas turbine in order to get better understanding of the cause of failure problem and to increase the reliability and efficiency of the system. Turbine blades are subjected to very strenuous environments inside a gas/steam turbine. They face high temperatures, high stresses, and a potentially high vibration environment.The type of damage which occurs in gas turbine blades after a service period can be divided into External and internal surfaces damage (corrosion, oxidation, crack formation, erosion, foreign object damage, fretting) and internal damage of microstructure as γ' phase, Ni_3 [(Al, Ti)], phase aging (rafting), grain growth, grain boundary creep voiding, carbides precipitation and brittle phases formation.

During the operation of power generation gas turbines, the blades and other elements of hot gas path suffer service induced degradation which may be natural or accelerated due to different causes. The degradation or damage may have a metallurgical or mechanical origin and results in reduction of equipment reliability and availability. It also increases risk of failure occurring. Also, due to blade material metallurgical deterioration, the material creep, fatigue, impact and corrosion properties decrease. In service, blade material deterioration is related to the high gas temperature, high steady state load levels (centrifugal load) and high thermal transients loads (trips, start-ups and slowing downs).

Vardar et al. [1] investigated a 40 MW gas turbine blade made of Udimet 500 after 8000 hrs in service and found that the cause of failure are inter-granular cracks which started during exposure to high temperature.

Corresponding Author,
E-mail address: sranidtu@gmail.com
All rights reserved: http://www.ijari.org

The cracks initiated from the grain boundaries and propagated to the critical length to result in catastrophic fracture. Barella et al.[2] has analyzed a third stage turbine blade failure made of nickel-based super-alloy IN738 after 22,400 operating hours in the 150 MW unit of a thermal power plant stated that after observing the turbine blade it was found that the fracture on the turbine blade is located at the top fir-tree root and the fracture surface exhibits two characteristic zones: the first zone shows slow and stable crack growth with crystallographic faceted cracking and striation formation, and the second shows inter-dendritic fracture, typical of final stage failure. This turbine blade failure must be attributed to fretting fatigue phenomena as a result of contact between the nickel-based blade fir-tree and the steel-based rotor disk. Z. Mazur et al. [3] analyzed a 70 MW gas turbine first stage blade made of nickel-base alloy IN738LC after 24,000 hrs of operation conclude that the failure was attributed to thermal fatigue with a significant contribution of creep. Patil et al.[4] has investigated a second stage gas turbine blade made of nickel-base alloy IN738LC after 73,500 hrs in service by metallurgical and mechanical examinations and observed a serious pitting was occurred on the blade surfaces and there were evidence of fatigue marks on fracture surface. Khajavi et al. [5] has reviewed different types of hot corrosion with their microscopic characteristics, and a case study on the first stage blades of a GE-F5 gas turbine. Gallardo et al. [6] has found that first-stage blades of a gas turbine had suffered a severe deterioration after around 10,500 hrs service while the expected service life was 40,000 hrs. FARHANGI et al. [7], has investigated a second stage turbine blade in a 32 MW unit in a thermal power plant. Jianfu et al. [8] has investigated fatigue failures of turbine blades by mechanical analysis. Poursaeidi et al.[9] has investigated a second stage gas turbine blade made of nickel-base alloy IN738LC after 73,500 hrs in service.

The blade failure can be caused by a number of mechanisms under the turbine operating conditions of high rotational speed at elevated temperature. In general, there are three possible damage mechanisms which effect turbine blades are: High temperature corrosion, Fatigue including

both high cycle fatigue (HCF) and low cycle fatigue (LCF), and Creep.

2. Fatigue:

The blade attachment at the fir-tree joint in gas turbine engines is subjected to high cycle fatigue condition that involves high frequencies and vibration type loads, hence failed due to fretting fatigue. During fretting fatigue process, crack will nucleate and propagate according to severe stress gradients that are generated from the effective shape of contact, co-efficient of friction and applied loads. Initially fretting cracks are very small, but lead to catastrophic failure of the components. There are different signs which show the presence of fretting fatigue. These are: presence of wear track on contact surface, formation of wear products on contact surface and at crack opening, micro plastic deformation in nucleation site, nucleation in vicinity of wear tracks, slant orientation of crack in nucleation region. Eliminating or reducing slip between mated surfaces is the only method for preventing fretting fatigue. And it must be accomplished during design process. Another method to reduce fretting fatigue is shot peening, by inducing compressive stress under the surface to increase fatigue strength.

In a study conducted by the Scientific Advisory Board of the US Air Force targeted high-cycle fatigue (HCF) as the single biggest cause of turbine engine failures. HCF results in rapid, essentially unpredictable failure due to fatigue crack propagation under ultrahigh frequency loading. Furthermore, Initiation of cracking takes place due to small defects which are caused by fretting and impact by foreign particles. Gas turbine components experience high frequency (>1 kHz) vibrational loading due to transient airflow dynamics. This vibratory loading is often superimposed on a high mean stress. Because of the very high frequency of loading, even cracks growing at slow per-cycle velocities propagate to failure in a short period of time. For this reason, it is necessary to operate HCF critical gas turbine components below the fatigue crack propagation threshold (ΔK_{TH}), such that crack propagation cannot occur.

To increase the high cycle fatigue (HCF) life of turbine blades against large amplitudes vibrations inter – blade friction dampers are often incorporated into the bladed disks. The principal parameters that govern the performance of friction dampers are: contact load, roughness of rubbing surfaces, level of external excitation, location of contact region, mass and stiffness of the device. Internal material damping has proved to be of less importance in controlling blade vibrations due to low damping ratio of the materials that may be used and is sometimes neglected in the computations. The aerodynamic damping is greatly affected by the aspects of the blade section. This damping may be negative, i.e., adding energy to the motion of vibration, and causing flutter of the blade. The third mechanism of damping is friction damping. Friction damper uses dry friction to dissipate energy and thus reduces the stresses. Friction damping takes place whenever two con tact surfaces experience relative motion. The centrifugal force arising from the rotation of disc forces the damper against the platform and energy is dissipated, when there is slip motion at contact surfaces.

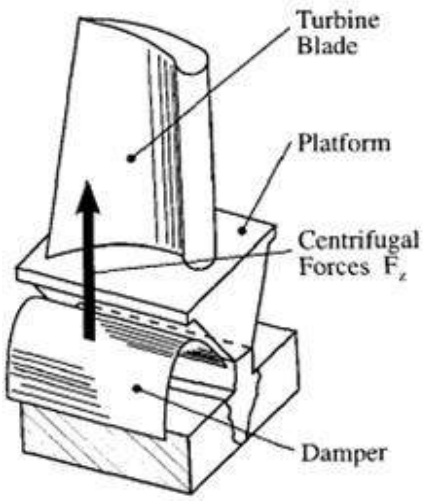

Fig: 1. Gas Turbine Blade

3. Corrosion:

During services of gas turbines, the air and fuel encountered with corrosive contaminants that result in serious hot corrosion problems. A wide range of fuel used in gas turbines ranging from clean gas to crude oil which contains sulphur, sodium, potassium, vanadium, lead, and molybdenum as contaminants. The airborne pollutants entering with the inlet air includes sodium, sulphur, chlorine and calcium. Impurities which are present in the fuel and the air can lead to the deposition of alkali metal sulfates on the blades which results in the hot corrosion attack. When the alkali salt attack on the surface, initially there is no reaction because it is coated with a protective oxide layer. For oxidation, this protective layer must be destroyed. This can be done by four ways: (i) Dissolution of protective oxide layer by using salts, (ii) Mechanical disruption of the oxide either by erosion, thermal cycling and by elastic strain of the substrate putting the oxide in tension, (iii) By diffusion of sulphur through the oxide layer until chromium rich sulfites form within the metal, (iv) A local reducing environment during ignition may form due to incomplete burning of fuel. Such reducing atmosphere can damage the protective oxide layer.

3.1 Hot Corrosion:

Hot Corrosion is defined as an accelerated corrosion which results due to the presence of salt contaminants Na_2SO_4, NaCl, and V_2O_5 that combine to form molten deposits, which further damage protective oxide layer. Hot Corrosion is of two types: (1) High Temperature (Type I) and (2) Low Temperature (Type II).During service, one more type of corrosion is observed which has features of both (HTHC) and (LTHC) and hence the name given is Transition hot corrosion.

3.1.1Hot Corrosion (Type I):

It is an extremely rapid form of oxidation that takes place at temperatures between 815^0C and 950^0C in the presence of sodium sulphate. By the reduction of sodium sulphate, sulphur is released. This sulphur diffuses inward

and then reacts with chromium from the substrate to form chromium sulphides

Sodium sulphate = Sodium + Sulphur + Oxygen (From air and Fuel)

Sulphur + Chromium = Chromium Sulfides

As corrosion proceeds, the sulphides are converted to complex unstable metal oxides and sulphur thus released diffuses more deeply into the substrate where if forms more sulphides. By using an electron beam analyzer, it is found that sulphide particles of chromium and titanium are present in a region below the surface scale which consists of chromium oxide Fig 2(a).

3.1.2 Hot Corrosion (Type II): It takes place in the temperature range of 593^0C to 760^0C. If the conditions are correct, this type of corrosion can be very aggressive. It results due to low melting eutectic compounds which are formed by the combination of sodium sulphate and some of the alloy constituents such as Nickel. Low temperature corrosion characteristically shows no inter-granular attack and no subscale sulfite particles but shows layered type of corrosion scale.

By using an electron beam analyzer, it is found that sulfide particles of chromium and titanium form a continuous layer and the surface scale contains un-protective oxides of Nickel and Cobalt Figure 2(c).

The temperature at the platform region is lower as compare to the airfoil and hence these regions could be prone to type II hot corrosion attack. It is mainly confined to trailing and leading edge regions.

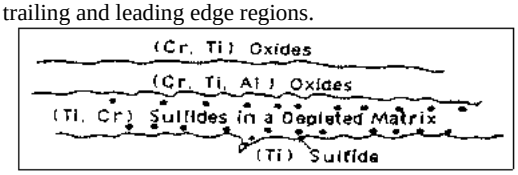

(a) High temperature hot corrosion

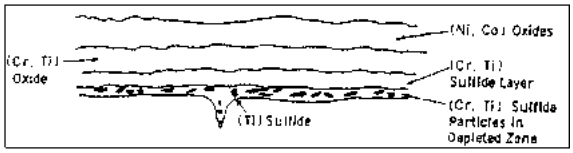

(b) Transition hot corrosion

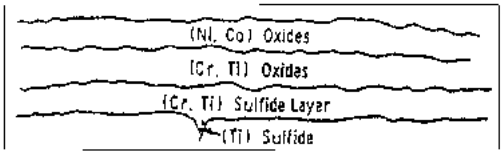

(c) Low temperature hot corrosion

Fig: 2: Types of hot corrosion

3.2 Transition Type:

During services, there are corrosion found which has features of both HTHC and LTHC. Hence the name given to this type of corrosion is Transition Hot Corrosion. By using an electron beam analyzer, It is found that the sulfides of chromium and titanium are increasingly agglomerated into large interconnecting sulfide networks and surface scales contains the oxide of Nickel and Cobalt Fig 2(b).

In order to make gas turbine components oxidation and corrosion resistant, coating must be provided. In accordance to the demand to increase turbine inlet temperatures and thus cycle efficiencies, ceramic insulating coatings can be applied to decrease the temperature of the hottest parts of the turbine components by up to 170^0C. Oxidation and corrosion resistant coatings which are applied to the gas turbine engine components are of two types. These are (1) Diffusion Coating and (2) Overlay Coating.

3.2.1Diffusion Coating:

In diffusion coating, an inter diffusion zone is formed between the substrate and the coating. Diffusion coating is formed by diffusion of one or more elements into the surface of the metal to be protected. Typical diffusion coatings are simple aluminide and chromium or platinum modified aluminide coatings. They are more commonly referred to as diffusion coatings since their application involves inter diffusion between deposited Al or Cr and the substrate onto which they are coated. For example the aluminising of a nickel-based superalloy gives rise to a coating of generic composition NiAl (β-nickel aluminide).

3.2.2 Overlay Coating:

In Overlay coating, no inter diffusion zone is formed between the substrate and the coating as formed in diffusion coating. Overlay coatings are basically coatings of specific composition applied directly on to the surface to be protected. These are deposited by using thermal spray like Argon shrouded plasma spray (APS) or Low pressure plasma spray (LPPS) or Electron beam physical vapor deposition (EBPVD). LPPS gives superior microstructure and mechanical properties but is expensive.

Typical overlay coatings are MCrAlX type where M is usually nickel or cobalt; X is Y, Si, Ta, Hf, etc. which is mostly less than 1% by weight.

4. Creep

Creep behavior is one of the most critical factors determining the integrity of elevated temperature components, because such components can slowly and continuously deform under constant stress over a period of time. The temperature and time dependence of creep deformation indicates that it is thermally activated process. This deformation is the result of Dislocation climb, Vacancy Diffusion, and Grain Boundary sliding. Creep leads to a fracture in components at static stress. Creep is the largest potential problem in applications involving high temperatures and high stress. Betten have described how micro-cracks begin on the surface and propagate until they link into macro-cracks and become visible at the tertiary stage of creep as shown in Fig.[3].

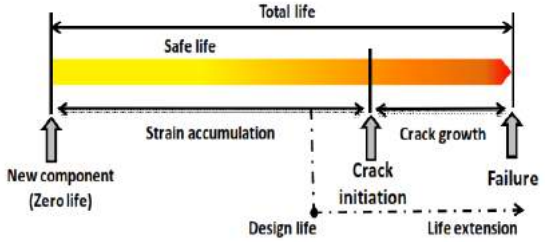

Fig: 3: Creep life span of hot section components due to deformation

The turbine blades made by nickel base super alloy. The Ni-base super alloy has high creep resistance due to precipitation hardening. The micro-structural changes occur due to blade operation at high temperature include irregular growing of γ' particles (rafting) and formation of carbides in grain boundaries and matrix. This leads to alloy creep properties reduction.

References:

[1] Vardar N, Ekerim A., "Failure analysis of gas turbine blades in a thermal power plant" Journal of Engineering Failure Analysis 2007: volume 14,pp 743-9

[2] Barella S, Boniardi M, Cincera S. Failure analysis of a third stage gas turbine blade, Journal of Engineering Failure Analysis 2011: volume 18,pp 386-393.

[3] 3) Mazu Z., Luna Ramirez A., Campus – Amezcua A., "Failure Analysis of a Gas Turbine blade made of Inconel 738LC alloy", Journal of Engineering Failure Analysis 2005: volume 12,pp 474–486

[4] 4) Patil A.A, shirsat U.M. Study of failure analysis of gas turbine blade, IOSR Journal of Engineering 2010;ISBN: 2878-8719, pp 37-43.

[5] 5) Khajavi M.R., Shariat M.H. ,"Failure of first stage gas urbine blade", Journal of Engineering Failure Analysis 2007: volume 11,pp 589-597

[6] 6) Gallardo J.M., Herrera E.J., Rodriguez J.A., "Failure of as Turbine Blades"' Journal of Wear 252 (2002) pp 264-268.

[7] 7) Hassan F, Ali Asghar F.M. Fractographic investigation of the failure of a second Stage Gas turbine blades, proceedings of 8th international conference 2007; pp 577-584.

[8] 8) J.Hou,B.J.Wicks,R.A.Antoniou. An investigation of fatigue failures of turbine blades in a gas turbine engine by mechanical Analysis Journal of Engineering Failure Analysis 2002: volume 9,pp 201-211.

[9] 9) Poursaeidi. E., Aieneravaie M., Mohammadi Arhani M.R., "Failure Analysis of a second stage blade in a Gas Turbine Engine", Journal of Engineering Failure Analysis 2008: volume 15,pp 1111-1129.

ResearchGate

See discussions, stats, and author profiles for this publication at: https://www.researchgate.net/publication/297909286

Grey fuzzy optimization of cutting parameters on Material Removal Rate and Surface Roughness of Aluminium

Conference Paper · March 2016

READS
34

4 authors, including:

Ranganath M Singari
Delhi Technological University, Formerly Del…
62 PUBLICATIONS **145** CITATIONS

SEE PROFILE

All in-text references underlined in blue are linked to publications on ResearchGate, letting you access and read them immediately.

Available from: Ranganath M Singari
Retrieved on: 10 August 2016

Proceedings of the 2016 International Conference on Industrial Engineering and Operations Management
Kuala Lumpur, Malaysia, March 8-10, 2016

Grey fuzzy optimization of cutting parameters on Material Removal Rate and Surface Roughness of Aluminium

S. Nanda[1], Ranganth M.S.[2], S. Singhal[2], R. Batra[2]
Department of Mechanical, Production & Industrial and Automobile Engineering
Delhi Technological University
New Delhi, India
sahilna1@gmail.com

***Abstract*—The research presented successfully applies fuzzy logic and Grey Relational Analysis (GRA) for optimization of turning process carried out on cylindrical bars of Aluminium 6061. Pre-recorded responses (Material Removal Rate & Surface Roughness) subject to three level control factor (Rake Angle, Feed Rate & Speed) variation in accordance with Taguchi's L27 orthogonal array have been utilized for the present research. The data was converted into Grey Relational Coefficients (GRC) using larger-the-better and smaller-the-better techniques for MRR and surface roughness respectively. These GRCs were input into Mamdani type Fuzzy Inference System (FIS) to compute Multi Performance Characteristic Index (MPCI) and Signal to Noise (S/N) Ratios were calculated for each set of responses. Analysis of Variance (ANOVA) was carried out using Main Effects Plot of S/N ratios for MPCI to optimize the cutting parameters by maximization of MRR and minimization of surface roughness. The combination of cutting parameters, A1B3C3 i.e. rake angle of 2°, speed of 710 RPM and feed of 0.4 mm/rev was concluded as the optimum setting if the prime requirement is the maximization of MRR and A1B3C1, i.e. 2º rake angle, 710 rpm and 0.2 mm/rev when the prime requirement is the minimization of surface roughness for the given operation.**

***Keywords*—ANOVA; Fuzzy logic; Grey Relational Analysis; Material Removal Rate; Membership function; S/N Ratio; Surface Roughness.**

I. INTRODUCTION

In any machining process, it is important to determine the cutting parameters for optimal machining performance. In basic turning, a single point cutting tool traverses a helical path to reduce the diameter of the workpiece. The experiments conducted by Ranganath M S et al. (2014) on Aluminium (6061) recorded Material Removal Rate (MRR) and surface roughness (Ra) as responses to variation in cutting parameters in basic turning. Their experiments included variation in Rake Angle, Speed and Feed Rate followed by Analysis of Variance (ANOVA) to the maximum Material Removal Rate and minimum surface roughness. Taguchi's theory on Design of Experiments (DOE) using its orthogonal arrays is widely used owing to its uncomplicated approach to achieve an unbiased and most efficient experimental procedure for a given number of outcomes [1]. It was also used in designing the experiments for the turning operation carried out by the authors. This research paper uses the responses recorded in the same experiment [2] to find the optimum value of cutting parameters using grey fuzzy logic.

The experiments (machining trials) were conducted on a conventional lathe machine (Kirloskar Turnmaster-35) on a cylindrical bar (50mm X 150mm) made out of HINDALCO made Aluminium-6061. The control factors: Rake Angle, Speed and Feed Rate were varied in 3 levels and recorded responses in form of MRR and Surface Roughness (Ra) according to the L27 orthogonal array followed by using Analysis of Variance (ANOVA) to optimize results. Fuzzy logic is a concept largely popularized in the extensive research by Zadeh (1965) wherein he proved the convex theorem for disjoint fuzzy sets. It is now regarded as an essential tool in dealing with uncertain and vague information. In fact, definitions of performance characteristics such as lower the better, higher the better or nominal the better contains to some extent an uncertainty [3]. The fundamental characteristic of uncertain systems is the incompleteness and inadequacy in their information. The research objects of grey systems theory consist of such uncertain systems that they are known only partially with small samples and poor information. Grey system theory thus utilizes this partial information to come up with the complete picture on a subject. On these accounts, this research focuses on the use of fuzzy logic and grey relational analysis for optimization of performance characteristics of turning operation as described above.

The outputs obtained from the experimental data were normalized into Grey Relational Coefficients (GRC) by using concepts derived from Grey Systems Theory. Larger-the-better and smaller-the-better techniques were used for MRR and surface roughness respectively. These GRCs were subdivided into linguistic variables which are the core of any fuzzy logic problem statement and subsequently fed into a specifically modeled Mamdani type Fuzzy Inference System (FIS) in MATLAB. The results attained from FIS were recorded as Multi Performance Characteristic Index (MPCI) for which nominal-the-better type Signal to Noise ratio was computed. Finally, a Main Effects plot for S/N ratios was plotted in Minitab to obtain the optimal cutting parameter setting.

[1]Corresponding Author
[2]Co-Author

978-1-4673-7762-1/16/$31.00 ©2016 IEEE

Balazinski and Bellerose attempted to apply fuzzy set theory to machining processes. They introduced an idea of a fuzzy decision support system (FDSS) working on compositional rule of inference which could be implemented on metal cutting processes. Fang and Jawahir quantified the effects of major influencing factors on the total machining performance (TMP) in finish turning of steels by employing a fuzzy-set method and gave a series of fuzzy-set models which could be used to assess the TMP quantitatively for any provided input conditions. The Machining data Handbook which provided an easy access to an immense collection of machining data was computerized by Bardie which led to the integrated automation of the manufacturing process. He proposed a fuzzy logic model for the selection of machining data for a certain machining process and later himself applied fuzzy logic principles for selection of cutting conditions in machining processes with the aid of Hashmi and Ryan. A new pulse discriminator was developed to classify various discharge pulses in electrical discharge machining (EDM) by utilizing the fuzzy set theory. Automatic synthesis of membership functions of the fuzzy pulse discriminator was made possible by bestowing a machine learning method based on a simulated annealed algorithm. Fuzzy logic was applied coupled with Taguchi dynamic experiments for optimization of EDM process. The fuzzy reasoning of the multiple performance characteristics were performed using fuzzy logic and electrode wear ratio (EWR) and material removal rate (MRR) were considered to optimize machining parameters [4]. The precision and accuracy of the high speed EDM process was optimized using Taguchi fuzzy-based approach [5]. Each process responses were designed according to the Taguchi methodology and their efficiencies were determined by investigating the relationships between the machining precision and accuracy with the help of fuzzy logic system [6]. An attempt was made to improve the machining accuracy at corner parts for wire-EDM without compromising much at the cutting feed rate. A multi-variable fuzzy logic controller was developed and results showed machining error reduction to less than 50% than those in normal machining. A used-friendly intelligent system was established for a more precise selection of EDM parameters. In this system, a compact selection technique was applied based on fuzzy-expert rules which had taken into consideration many parameters that could not be measured easily [7]. An improved approach for optimization of EDM process was implemented based on grey-fuzzy logic. The effects of machining parameters on the multiple process responses in the EDM process were studied and analyzed [3] and later, it was seen that the grey relational analysis method based on the orthogonal array was more straightforward than the fuzzy-based Taguchi method for optimization the EDM process with the multiple process responses. An approach of grey and fuzzy along with Taguchi method was employed to develop a hybrid multi-optimization algorithm. Mamdani type fuzzy inference system was employed to convert the grey relational coefficient (GRC) of these performance parameters into a single multi performance characteristics index (MPCI) [8].

II. THEORY

A. Grey Systems

The grey system theory is employed for explaining the complex co-relationships among the multi-responses involved in the machining process in the form of grey relational coefficients. In grey systems, a color spectrum from black to white is used to describe the degree of clearness of the available information. According to these systems, black represents the systems with completely unknown information, white represents those systems having completely known information, and grey represents the systems with partially known information and partially unknown information. The intensity of the shade of the grey determines the clarity with the available information. Higher the intensity less is the quality of the known information. Developed by Julong Deng in 1982, the grey system theory deals with the uncertain systems with small samples and poor information. Useful information is generated, excavated and extracted from the partially known information available with uncertain systems. It helps in a better study and analysis of operational behavior of the systems.

Grey systems theory attempts to analyze systems and processes incorporating uncertainty and vagueness of information prevalent in most of the scientific scenarios. It defines situations with no information as black, and those with perfect information as white. The situations where there is neither complete presence nor absence of information, it characterizes them as grey. This theory is applied in various ways in different domains like grey relational analysis, grey modelling, grey programming, grey control and grey clustering. This research focuses on just one aspect of the vast theory; Grey Relational Analysis or GRA. Before application of any other attribute of the theory the first step is to normalize the data being input in the system as units of different response attributes might be different and they might also be taking into account different ranges of data.

B. Responses

The responses recorded in the paper are Surface roughness (Ra) and Material Removal Rate (MRR). Surface roughness is the deviation of the surface of the workpiece from its ideal surface. Larger the deviations, more rough is the surface. In the experiment, Surface roughness is an undesirable factor because the surface is desired to be as smooth as possible. MRR is the volume of the workpiece removed per second. Mathematically, MRR is given by (1).

$$MRR = \frac{WRV}{T} \qquad (1)$$

Here, WRV is the workpiece removal volume in mm^3 and T is the machining time in seconds. In the experiment, MRR is desired to be as large as possible because a large MRR means a low total machining time for the same volume of material removed. A compromise has to be made between a low surface roughness and a large MRR. In the experiment, surface roughness is measured in micro meters and material removal rate is measured in mm^3/sec.

C. Taguchi Analysis

Dr. Genechi Taguchi developed a comprehensive quality improvement methodology that included the Design of Experiment (DOE) technique which has now gained popularity as Taguchi's method. The method utilizes a very different approach to DOE as compared to

other methods. Industry welcomed the effort of the scientist for application of DOE which was earlier limited to the academic community. He created a set of orthogonal arrays for direct application in the industry and new methods of analysis for analyzing the responses as measured from experiments. This research primarily relies on L27 array and thorough analysis of Signal to Noise ratio to ensure a design that is immune to the influence of uncontrollable factors. One of the major reasons for the success for the method was the inclusion of loss function. It changed the way quality was normally defined. It describes increment in 'loss' in value due to increase in variation from intended condition. This description was considered a breakthrough in describing quality, and helped the continuous improvement movement that was popularized by Japanese automakers post World War II. Also, in Taguchi's method for DOE the results obtained from experiments are analyzed to either determine the trend of influence of factors and interactions under study or establish the best or the optimum condition for a product or a process. It can also help predict the expected response under optimum experimental conditions that can be identified by studying the main effects of the experiment. This research also includes the main effects plotted using Minitab for the experimental data obtained. Taguchi method recommends majorly two forms of analysis. The first approach, Analysis of Variance (ANOVA) is the most commonly used statistical method to gain in insight into contribution of individual factors in a production process. It should be noted that the desired optimum may not necessarily lie among the many experiments already carried out, as the data represents only a small fraction of all the possibilities. The second one, S/N analysis is recommended for multiple runs, it requires to use the signal-to-noise (S/N) ratio for the same steps in the analysis. It can help identify the most robust set of operating conditions from variations within the results.

D. Grey Relational Analysis

In the analysis of grey systems, the responses are fed in the fuzzy inference system as inputs. But the range of the responses may vary from one case to another. It could extend to thousands or may vary in decimals. This variation between the responses in a single experiment makes it difficult to analyse or compare. Grey Relational Analysis is a method which compares the relational degrees of different responses rather than their absolute values. The relational degrees of the responses are found out by calculating the grey relational coefficients. These coefficients are then inputted into the fuzzy inference system and processed upon. To calculate grey relational coefficients, first the responses (here, Measured Surface Roughness and Material Removal Rate) are normalized between 0 and 1 by using (2) and (3). This step is known as grey relational generating. Equation 2 is used for smaller the better type of responses, here surface roughness as it is an undesirable factor and should be kept as small as possible. Equation 3 is used for larger the better type of responses, here Material Removal Rate as the volume of the material which is removed per second should be as large as possible.

$$x_j(\mathrm{i}) = \frac{\max \eta_j(\mathrm{i}) - \eta_j(\mathrm{i})}{\max \eta_j(\mathrm{i}) - \min \eta_j(\mathrm{i})} \qquad \text{(for smaller the better) (2)}$$

$$x_j(\mathrm{i}) = \frac{\eta_j(\mathrm{i}) - \min \eta_j(\mathrm{i})}{\max \eta_j(\mathrm{i}) - \min \eta_j(\mathrm{i})} \qquad \text{(for larger the better) (3)}$$

Here, $\eta_j(i)$ is i^{th} observation for the j^{th} response, max $\eta_j(i)$ is the maximum value of the observation of the j^{th} response and min $\eta_j(i)$ is the minimum value of the observation of the j^{th} response. The value obtained from grey relational generation is $x_j(i)$. Now, if $x_{0j}(i)$ is the ideal sequence for a response where i= 1,2,3…,27, i.e. $x_{0j}(1)$= 1, $x_{0j}(2)$= 1, $x_{0j}(3)$= 1 and so on because closer the value of $x_j(i)$ to 1, better it is and the ideal situation occurs if every value is equal to 1. Then the grey relational coefficient $\mu_j(i)$ is given by (4).

$$\mu_j(i) = \frac{\Delta_{min} + \xi.\Delta_{max}}{\Delta_j(i) + \xi.\Delta_{max}} \qquad (4)$$

where $\Delta_j(i) = | x_{0j}(i) - x_j(i) |$ i.e. it is the absolute difference between $x_{0j}(i)$ and $x_j(i)$, Δ_{min} is the minimum value and Δ_{max} is the maximum value out of all the $\Delta_j(i)$ for the j^{th} response and ξ is called the distinguishing coefficient. The value of distinguishing coefficient can be anything between 0 and 1. In the paper, value of ξ is taken as 0.5.

E. Fuzzy Inference System

A Fuzzy Inference System (FIS) is a system which maps the inputs (grey relational coefficients) to the outputs (MPCI) using fuzzy logic concepts. The mapping obtained provides a base from which inferences can be made. There are two types of FISs viz Mamdani-type FIS and Sugeno-type FIS. Both type of FISs are similar in the fuzzification processes and in the application of rules. The main difference is in the way the crisp output is computed and displayed. While the output of a mamdani type FIS is calculated by defuzzification of the output, a Sugeno-type FIS computes weighted average of the output and gives either a constant output or a linear mathematical expression. In the paper, Mamdani-type FIS is used. The FIS is made in the fuzzy toolbar of MATLAB software. In a fuzzy inference system, first the grey relational coefficients of the responses are fed into the fuzzifier which uses the membership functions to fuzzify the coefficients. A membership function is a curve which maps the grey relational coefficients to the degree of membership or the membership value between 0 and 1. The membership functions are chosen based on the input responses. In the paper, Gaussian membership function is chosen as it best suits the requirements as per the input data. The three basic steps in fuzzy logic are fuzzification, application of fuzzy rules and defuzzification. Fuzzification means conversion of crisp or numeric value into linguistic variables or fuzzy subsets. The fuzzy subsets are derived from the corresponding membership functions. In the paper, 3 linguistic variables, i.e. low, medium and high are used for both inputs as shown in figure (1) and 5 linguistic variables, i.e. very low, low, medium, high and very high are used for the multi-response output as shown in figure (2). After fuzzification a series of fuzzy rules are applied. Fuzzy rules are If-Then statements which

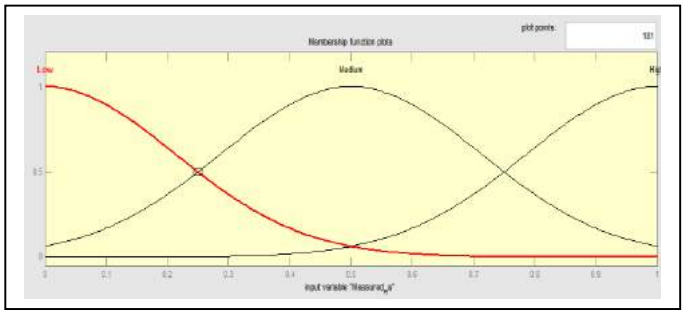

Figure 1. Membership functions of input

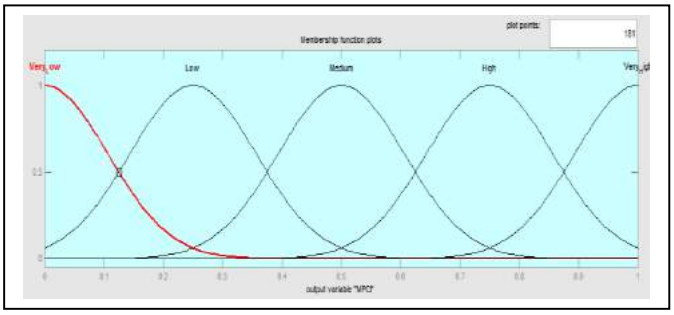

Figure 2. Membership functions of output

specify the conditions between the input space (here two grey relational coefficients) and the output space (here one multi performance characteristic index). For example, If $Ra_x = k_1$ AND $MRRx = k_2$ THEN $MPCI = k_3$, where Ra_x and MRRx are the grey relational coefficients of surface roughness and material removal rate respectively and k_1, k_2 and k_3 are the fuzzy subsets of the respective responses. Nine fuzzy rules are used considering that the larger grey relational coefficient will yield a better or larger output response. A fuzzy multi-response output is calculated by the fuzzy inference system based on the 9 fuzzy rules and recorded as MPCI, i.e. Multi Performance Characteristic Index. The MPCIs are analysed by calculating the S/N ratios and plotting the Main Effects Plots.

F. S/N Ratio

S/N Ratio or Sound to Noise ratio is the ratio of the desired signal to the background noise or the ratio of signal power to the noise power. The signal power is desired to be more whereas the noise power should be as low as possible for maximum efficiency. Hence, higher the S/N ratio, better it is. The noise power can be controlled during the experimentation by varying the control factors setting. An optimum condition will give the least noise or unwanted signals. S/N ratios of the MPCIs are calculated based on the higher the better criteria and given by (5).

$$SNR = - 10 * \log (1/ \alpha^2) \qquad (5)$$

Here, SNR is the sound to noise ratio and α is the MPCI calculated for the corresponding control factor setting. The S/N ratios of the MPCIs obtained are calculated and recorded in table 1.

G. Main Effects Plot

Main Effects Plot is a statistical technique for the analysis of group means with respect to the levels of a factor. It is one of the methods of Analysis Of Variance (ANOVA). It is used to compare the average influence of different levels of a factor on a particular response. A main effects plot computes means of the response corresponding a single level factor and plots them on a graph. The points plotted are connected by straight lines. In the paper, Main Effects Plot for S/N ratios with respect to the control factors is plotted. Since the S/N ratio is desired to be more, the control factor setting corresponding to the maximum S/N ratios is the optimum control factor setting.

III. OBSERVATIONS

TABLE I. TABLE SHOWING THE OBSERVED RA AND MRR BY CHANGING THE CONTROL FACTORS

Expt. No.	Control Factors			Measured Ra (µm)	MRR (mm^3/sec)
	A	*B*	*C*		
1	1	1	1	1.04	18.565
2	1	1	2	2.44	27.869
3	1	1	3	2.06	33.707
4	1	2	1	0.9	46.348
5	1	2	2	1.42	69.613
6	1	2	3	1.74	84.005
7	1	3	1	0.86	68.843
8	1	3	2	1.14	109.88
9	1	3	3	1.2	132.481
10	2	1	1	2.62	18.758
11	2	1	2	5.38	27.97
12	2	1	3	6.34	33.557
13	2	2	1	2.32	46.744
14	2	2	2	3.58	69.746
15	2	2	3	6.24	84.08
16	2	3	1	1.92	73.825
17	2	3	2	3.44	109.857
18	2	3	3	5.18	132.154
19	3	1	1	2.04	18.841
20	3	1	2	4.8	28.136
21	3	1	3	6.06	33.82
22	3	2	1	2.24	47.073
23	3	2	2	3.84	70.221
24	3	2	3	4.66	84.476
25	3	3	1	2.7	74.346
26	3	3	2	3.76	110.817
27	3	3	3	4.28	133.463

Table I depicts the L-27 orthogonal array of the exhaustive set of the three control factors, Rake Angle (A), Speeds (b) and Feed (c), with each of them having three varying values, thus giving a total of 27 experimental readings. Levels 1, 2 and 3 for rake angle represent 2º, 3º and 4º respectively while that for speeds represent 180, 450 and 710 rpm and that for feed represent 0.2, 0.315 and 0.4 mm/rev. The surface roughness and the material removal rate measured from each combination of the control factors is recorded.

IV. CALCULATIONS

TABLE II. TABLE SHOWING THE CALCULATED GRCS, MPCIS AND S/N RATIOS OF MEASURED RA AND MRR

Expt. No.	Grey Relational Coefficients		MPCI	S/N Ratios
	Measured Ra	*MRR*		
1	0.938356	0.333333	0.622	-4.12419
2	0.634259	0.352355	0.495	-6.1079
3	0.695431	0.36544	0.526	-5.58029
4	0.985612	0.397395	0.665	-3.54357
5	0.830303	0.473615	0.634	-3.95821
6	0.756906	0.537374	0.613	-4.25079
7	**1**	**0.470627**	**0.69**	**-3.22302**
8	0.907285	0.708967	0.71	-2.97483
9	**0.88961**	**0.983194**	**0.795**	**-1.99266**
10	0.608889	0.333707	0.477	-6.42963
11	0.37741	0.352573	0.427	-7.39144
12	0.333333	0.365092	0.416	-7.61813
13	0.652381	0.398486	0.52	-5.67993
14	0.501832	0.474135	0.494	-6.12546
15	0.337438	0.537751	0.454	-6.85888
16	0.721053	0.490652	0.583	-4.68663
17	0.515038	0.708766	0.582	-4.70154
18	0.388102	0.977722	0.659	-3.62229
19	0.69898	0.333868	0.514	-5.78074
20	0.41018	0.352933	0.434	-7.25021
21	0.345088	0.365703	0.421	-7.51436
22	0.665049	0.399398	0.526	-5.58029
23	0.479021	0.476001	0.49	-6.19608
24	0.41896	0.539752	0.487	-6.24942
25	0.598253	0.492845	0.527	-5.56379
26	0.485816	0.717261	0.58	-4.73144
27	0.444805	1	0.684	-3.29888

The Grey Relational Coefficients are calculated based on lower the better criteria for the surface roughness and higher the better criteria for the material removal rate and are shown in Table II. The calculated GRCs are put into the Fuzzy Inference System to obtain the Multi Performance Characteristic Index. S/N Ratios of the MPCIs obtained are calculated and recorded for each corresponding pair of surface roughness and material removal rate. The highest S/N ratio obtained from table 2 corresponds to the setting A1B3C3, i.e. 2º rake angle, 710 rpm and 0.4 mm/rev and surface roughness of 1.2 µm and material removal rate of 132.481 mm^3/sec.

TABLE III. TABLE SHOWING THE CALCULATED NORMALIZED VALUES, MPCIS AND S/N RATIOS OF MEASURED RA AND MRR

Expt. No.	Normalized values		MPCI	S/N Ratios
	Measured Ra	*MRR*		
1	0.967153	0	0.492	-6.1607
2	0.711679	0.080976	0.407	-7.80811
3	0.781022	0.131786	0.462	-6.70716
4	0.992701	0.241806	0.594	-4.52427
5	0.89781	0.44429	0.649	-3.75511
6	0.839416	0.569549	0.662	-3.58284
7	**1**	**0.437588**	**0.682**	**-3.32431**
8	0.948905	0.794748	0.748	-2.52197
9	**0.937956**	**0.991453**	**0.814**	**-1.78751**
10	0.678832	0.00168	0.363	-8.80187
11	0.175182	0.081855	0.256	-11.8352
12	0	0.130481	0.206	-13.7227
13	0.733577	0.245252	0.491	-6.17837
14	0.50365	0.445447	0.487	-6.24942
15	0.018248	0.570201	0.327	-9.70904
16	0.806569	0.480948	0.625	-4.0824
17	0.529197	0.794548	0.631	-3.99941
18	0.211679	0.988607	0.578	-4.76144
19	0.784672	0.002402	0.418	-7.57647
20	0.281022	0.0833	0.285	-10.9031
21	0.051095	0.13277	0.228	-12.8413
22	0.748175	0.248116	0.499	-6.03799
23	0.456204	0.449581	0.478	-6.41144
24	0.306569	0.573648	0.451	-6.91647
25	0.664234	0.485483	0.553	-5.1455
26	0.470803	0.802903	0.62	-4.15217
27	0.375912	1	0.661	-3.59597

Table III. shows the S/N ratios calculated from the normalized values of the surface roughness and Material Removal Rate i.e. when fuzzy approach was followed. The optimum setting, i.e the setting with the highest S/N ratio is found to be the same as what we got from grey fuzzy analysis. The optimum condition is A1B3C3, i.e. 2º rake angle, 710 rpm and 0.4 mm/rev and surface roughness of 1.2 µm and material removal rate of 132.481 mm^3/sec.

V. ANALYSIS BY MAIN EFFECTS PLOT

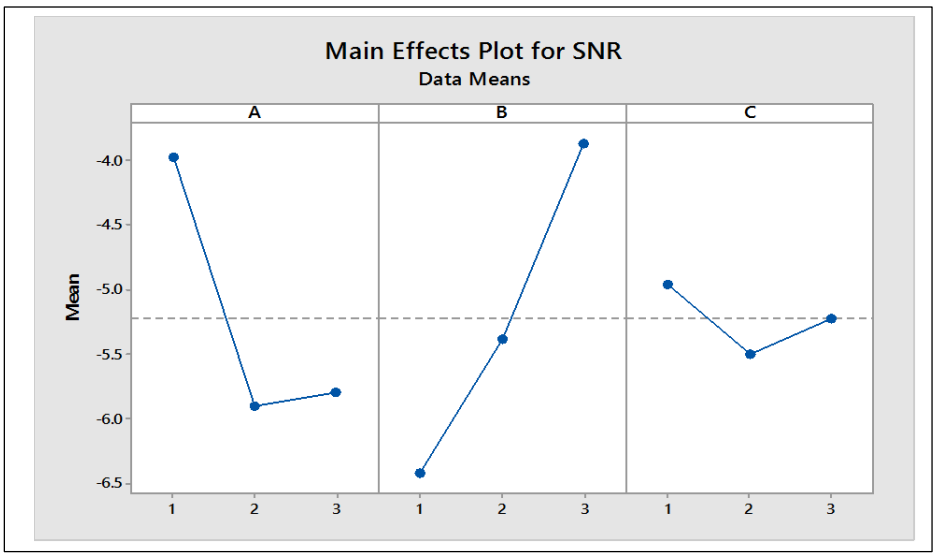

Figure 3. Main Effects Plot of S/N ratios of MPCIs (GRCs)

Main Effects plots of the S/N Ratios are made with respect to the control factors A, B and C, i.e. rake angle, speed and feed respectively. In the paper, Main Effects Plot for S/N ratios with respect to the control factors A, B and C, i.e. rake angle, speed and feed respectively is plotted (fig. 3) with the help of MINITAB software. The control factor setting corresponding to the maximum S/N ratios is the optimum control factor setting. The graphs clearly suggest that the setting of the highest S/N ratios, i.e. the optimum setting of our experiment is A1B3C1 which corresponds to a 2º rake angle, cutting speed of 710 rpm and a feed of 0.2 mm/rev.

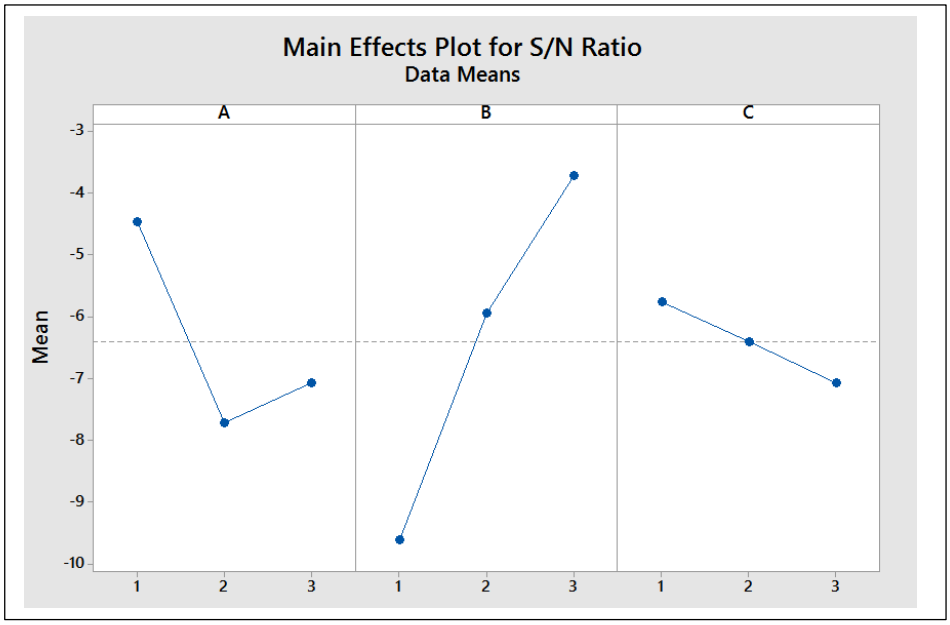

Figure 4. Main Effects Plot of S/N ratios of MPCIs (Normalized)

This is the main effects plot obtained from the S/N ratios of the MPCIs obtained from the normalized value or by applying only fuzzy. As it can be seen the optimal value of the setting remains the same, i.e. A1B3C1 which corresponds to a 2º rake angle, cutting speed of 710 rpm and a feed of 0.2 mm/rev which we got from grey fuzzy analysis.

VI. ANALYSIS BY CLASSICAL TAGUCHI APPROACH

The results obtained from Dr. Ranganath M. S. et al paper titled 'Effect of Cutting Parameters on MRR and Surface Roughness in Turning of Aluminium (6061)' based on classical taguchi approach for the same set of observations are taken for comparison [2]. The S/N ratios obtained from the experiment are as follows-

TABLE IV. S/N RATIOS FOR SMALLER THE BETTER

Rake Angles	Speed	Feed	Ra	MRR	SNRA1	STDE1	MEAN1	CV1
2	180	0.2	1.04	1113.93	-57.9269	786.93	557.49	1.41158
2	450	0.315	1.42	4176.76	-69.4065	2952.41	2089.09	1.41325
2	710	0.4	1.2	7948.86	-74.9958	5619.84	3975.03	1.41379
3	180	0.315	5.38	1678.19	-61.4866	1182.86	841.79	1.40518
3	450	0.4	6.24	5044.8	-71.0466	3562.8	2525.52	1.41072
3	710	0.2	1.92	4429.52	-69.9168	3130.79	2215.72	1.41299
4	180	0.4	6.06	2029.23	-63.1364	1430.6	1017.65	1.40579
4	450	0.2	2.24	2824.41	-66.0083	1995.58	1413.32	1.41197
4	710	0.315	3.76	6649.03	-73.4449	4698.92	3326.4	1.41262

TABLE V. S/N RATIOS FOR LARGER THE BETTER

Rake Angles	Speed	Feed	Ra	MRR	SNRA2	STDE2	MEAN2	CV2
2	180	0.2	1.04	1113.93	3.351	786.93	557.49	1.41158
2	450	0.315	1.42	4176.76	6.0561	2952.41	2089.09	1.41325
2	710	0.4	1.2	7948.86	4.5939	5619.84	3975.03	1.41379
3	180	0.315	5.38	1678.19	17.6259	1182.86	841.79	1.40518
3	450	0.4	6.24	5044.8	18.914	3562.8	2525.52	1.41072
3	710	0.2	1.92	4429.52	8.6763	3130.79	2215.72	1.41299
4	180	0.4	6.06	2029.23	18.6597	1430.6	1017.65	1.40579
4	450	0.2	2.24	2824.41	10.0153	1995.58	1413.32	1.41197
4	710	0.315	3.76	6649.03	14.5141	4698.92	3326.4	1.41262

The optimal solution based on classical taguchi analysis was found out to be 3º rake angle, 180 rpm speed and 0.2 mm/rev feed rate for minimum surface roughness which corresponds to 2.62 µm surface roughness and 18.758 mm3/sec. On the other hand optimal result for maximum material removal rate are found to be 2º rake angle, 710 rpm speed and 0.4 mm/rev feed rate which corresponds to 1.2 µm and 132.481 mm3/sec.

VII. COMPARISON OF GREY FUZZY WITH CLASSICAL TAGUCHI AND FUZZY APPROACH

The result obtained by classical taguchi method for maximizing the material removal rate, i.e. 1.2 µm and 132.481 mm^3/sec is same as that obtained by applying grey fuzzy logic approach. While the result obtained for minimizing surface roughness by following classical taguchi approach are 2.62 µm surface roughness and 18.758 mm^3/sec and that by applying grey fuzzy approach are 0.86 µm surface roughness and 68.843 mm^3/sec material removal rate. The surface roughness obtained by grey fuzzy is 3 times lesser and material removal rate obtained by grey fuzzy is about 6.5 times greater than that obtained from classical taguchi analysis. Thus the results obtained from grey fuzzy analysis are slightly advanced. The conclusions drawn from the results of grey fuzzy and plain fuzzy approach are similar.

VIII. CONCLUSION & FUTURE SCOPE

The research presents a way of optimizing the cutting parameters in a simple machining process like rough turning for double response and single MPCI system wherein the optimum condition set was found to be A1B3C3 (highest S/N ratio), i.e. 2º rake angle, 710 rpm and 0.4 mm/rev which corresponds to surface roughness of 1.2 µm and material removal rate of 132.481 mm^3/sec. This result is ideal when the prime requirement is to maximize the MRR. On the other hand, the optimum setting of the control factors by analysis of main effects plot was found out to be A1B3C1, i.e. 2º rake angle, 710 rpm and 0.2 mm/rev which corresponds to surface roughness of 0.86 µm and material removal rate of 68.843 mm^3/sec. This result is ideal when the prime requirement is to minimize the surface roughness. This could be extended to more number of responses for further increment in operational efficiency. The membership functions for the linguistic variables could also be modelled more carefully. The paper also proves that Fuzzy Inference Systems in combination with Taguchi's DOE & ANOVA can prove to be powerful tools aiding in effective utilization of machining processes.

REFERENCES

[1] R. K. Roy – Design of Experiments using the Taguchi Approach; John Wiley & Sons, April 2001.

[2] Ranganth M. S., Vipin, and R.S. Mishra, "Effect of Cutting Parameters on MRR and Surface Roughness in Turning of Aluminium (6061)", International Journal of Advance Research and Inovation, Vol. 2, Issue 1, pp. 32-39, March 2014.

[3] J. L. Lin and C.L. Lin, "The use of grey-fuzzy logic for the optimization of the manufacturing process", Journal of Materials Processing Technology, pp. 9 – 14, November 2005.

[4] J. L. Lin, K. S.Wang, B. H. Yan, and Y. S. Tarng, ''Op- timization of the electrical discharge machining process based on the Taguchi method with fuzzy logics'' Journal of Materials Processing Technology,Vol.102, pp.48-55, 2000.

[5] Ranganath M. S. - Application of TAGUCHI Techniques in Turning, AKN Learning, September 2015.

[6] Y. F. Tzeng and F. C. Chen, "Multi-objective optimization of high speed electrical discharge machining process using a Taguchi fuzzy-based approach", Materials and Design, Vol. 28, pp. 1159 – 1168, 2007.

[7] O. Yilmaz, O. Eyercioglu , and N. N. Z. Gindy, "A user-friendly fuzzy-based system for the selection of electro discharge machining process parameters", Journal of Materials Processing Technology, Vol. 173, No. 3, pp. 363 - 371, March 2006.

[8] H. Vasudevan, N. C. Deshpande, and R. R. Rajguru, "Grey Fuzzy Multiobjective Optimization of Process Parameters for CNC Turning of GFRP/Epoxy Composites", Procedia Engineering, Vol. 97, pp. 85 – 94, 2014.

BIOGRAPHY

Sahil Nanda is a student of Mechanical Engineering at Delhi Technological University, New Delhi, India. He has done research projects with Indian Railways and many governmental organizations. His research interests inlcude manufacturing, machining, lean transformation, six sigma, SCM, inventory management and optimization. He wishes to pursue his research in Production & Industrial Engineering specializing in Supply Chain Management after graduation. He is a member of IEEE, IET, SAE and IMechE.

Dr. Ranganath M. Singari is currently the Associate Professor, Department of Production & Industrial Engineering, Delhi Technological University. He is a Post Graduate and Doctorate from University of Delhi. He has made contribution in the areas of Production Engineering, Metal Cutting and Automation. He is a Life member of Indian Society of Technical Education, Computer Society of India and Indian Society of Mechanical Engineering. He has published more than 50 research papers in the area of Productio Engineering.

Shubham Singhal is a student of Mechanical Engineering at Delhi Technological University, New Delhi, India. He has been involved in several research projects with Centre for Advanced Studies and Research in Automobile Engineering (CASRAE), DTU and many governmental organizations. His research interests inlcude manufacturing, machining, mechatronics and robotics, six sigma, IC engines and parametric optimization. He wishes to pursue his research in Robotics specializing in Humanoid robots after graduation. He is a member of ASME, IEEE, SAE and IMechE.

Rushil Batra student of Mechanical Engineering at Delhi Technological University, New Delhi, India. He has led the braking system and manufacturing departments in SAE BAJA team of the university. He has done research projects with automobile manufacturers and governmental organizations. His research interests include manufacturing, process engineering, non-conventional machining, lean management, operations management and ergonomics. He wishes to pursue his research in Production & Industrial Engineering after graduation. He is an active member of SAE, SME and IMechE.

Bull. Mater. Sci. © Indian Academy of Sciences.
DOI 10.1007/s12034-016-1248-1

Hybrid filler composition optimization for tensile strength of jute fibre-reinforced polymer composite

ANURAG GUPTA[1,2,*], HARI SINGH[1] and R S WALIA[3]
[1]Mechanical Engineering Department, National Institute of Technology, Kurukshetra 136119, India
[2]Mechanical Engineering Department, Krishna Institute of Engineering and Technology, Ghaziabad 201206, India
[3]Mechanical Engineering Department, Delhi Technological University, New Delhi 110042, India

MS received 23 December 2015; accepted 9 March 2016

Abstract. **In present research work, pultrusion process is used to develop jute fibre-reinforced polyester (GFRP) composite and experiments have been performed on an indigenously developed pultrusion experimental setup. The developed composite consists of natural jute fibre as reinforcement and unsaturated polyester resin as matrix with hybrid filler containing bagasse fibre, carbon black and calcium carbonate ($CaCO_3$). The effect of weight content of bagasse fibre, carbon black and calcium carbonate on tensile strength of pultruded GFRP composite is evaluated and the optimum hybrid filler composition for maximizing the tensile strength is determined. Different compositions of hybrid filler are prepared by mixing three fillers using Taguchi L_9 orthogonal array. Fifteen percent of hybrid filler of different composition by weight was mixed in the unsaturated polyester resin matrix. Taguchi L_9 orthogonal array (OA) has been used to plan the experiments and ANOVA is used for analysing tensile strength. A regression model has also been proposed to evaluate the tensile strength of the composite within 7% error by varying the above fillers weight. A confirmation experiment was performed which gives 73.14 MPa tensile strength of pultruded jute fibre polymer composite at the optimum composition of hybrid filler.**

Keywords. **Composite; pultrusion process; carbon black; bagasse fibre; calcium carbonate; unsaturated polyester resin.**

1. Introduction

It has become a challenging task for researchers all over the world to develop engineering materials with high strength to weight ratio from renewable resources. Environmentally-sound natural fibres having several ecological benefits have been used and established as filler materials in manufacturing automobile parts. Reinforcement of natural fibres like sisal, jute, kenaf, coir and palm has been proved to be good in thermoset and thermoplastic matrices [1–4]. Among various natural fibres, jute fibre seems to be the most promising one and it enjoys the right potential for usage in composites due to its high aspect ratio, toughness, tensile strength and good specific modulus. The jute composites have proved to be very cost-effective materials particularly, for building and construction industry, packaging, railway coach interiors and automobile, and storage devices. In the recent years, lot of work has been done to develop new composites by using different fibres and fillers which have improved strength to weight ratio and better mechanical properties. The composite can be developed by judicious selection of matrix and reinforcing material, which will have comparable or even better strength and modulus than the conventional metallic materials. The addition of filler into polymer resin has been proved to be a better alternative for altering the properties of the resultant composites. Particulate fillers are of considerable interest, not only from an economic viewpoint, but also as modifiers especially for the physical properties of the polymer. It has been found by many researchers that addition of particulate fillers such as $CaCO_3$, glass fibre and carbon black into the polymer matrix can alter stiffness and elastic modulus, and also reduce costs of polymer composite [5–8].

Polymer composites have shown an improved performance by addition of particulate filler materials and thus, attracted the interest of researchers. Specific fillers (additives) are added to enhance and modify the quality of composites. Unsaturated polyester resin (UPR) is a widely used thermoset resin due to its ease of processing, moulding and curing characteristics [9]. Borkar *et al* [10] have shown in their study that the addition of silica and calcium carbonate as filler in the polyester resin matrix reduces the tensile strength in the range of 3–15% for 25–50% fillers in hand layup process.

Sudhir and Chandan [11] have used hybridization of fibre with fillers to investigate the properties of bagasse and jute fibre composites by varying the bagasse loading in composite. Furfuryl alcohol-grafted bagaase fibre loading from 20 to 50% in modified jute fibre epoxy composite shows 43, 52 and 59% improvement in tensile strength, flexural strength and impact strength, respectively. Gupta *et al* [12] have investigated the effect of bagasse fibre, carbon black and calcium carbonate as filler in glass fibre polyester resin composite. It

*Author for correspondence (sky.anurag@gmail.com)

has been observed that as the bagasse fibre content increases, the tensile strength of pultruded glass fibre reinforced polyester (GFRP) composite increases and tensile strength reduces with the increase in content of $CaCO_3$ and carbon black. Murty and De [13] investigated the effect of silica and carbon black to the adhesion between jute and natural rubber and found that minimum loading of jute fibre to achieve reinforcement is reduced in the presence of carbon black. It was also found that clay impairs the properties of jute fibre rubber composites. Abdul Khalil *et al* [14] have shown in their study that the carbon black epoxy composites give better flexural properties than the pure epoxy due to improved adhesion between the carbon black and the epoxy resin. While pultrusion is a very popular method for producing continuous long profile of fibre-reinforced plastic (FRP) composites, but there is very limited work undertaken to study the effect of fillers on tensile strength of pultruded jute composite. Pultruded composite is always associated with high strength and stiffness particularly due to high fibre content, i.e., up to 70%. The advantages of pultrusion over other forms of composite moulding are low capital and operating cost, few finishing and deflashing operations and the better physical properties of product [6,7].

Pultrusion is the combination of two words 'pull' and 'extrusion' and long continuous fibres (jute fibre, glass fibre, carbon fibre, etc.) were wetted in resins, such as polyester, polyurethane, vinyl ester epoxy resins, etc. are pulled through a shaping die. Fibre is wetted or impregnated with resin bath and passed through the cold die for removal of excess resin and initial shaping of profile. Initially, shaped wetted fibre is passed through a precisely machined and chromed heated steel die which cures the thermosetting resin and the cured pultruded FRP composite profile is pulled by pulling mechanism. Generally, additive and fillers are used in the pultrusion process to solve the production difficulty, enhance the physical and mechanical properties and to reduce the production cost [8]. In the present study, the effects of three fillers i.e., carbon black, bagasse fibre and calcium carbonate are investigated on the tensile strength of pultruded jute-reinforced unsaturated polyester resin composite.

2. Experimental

An indigenously designed and developed pultrusion setup is used for experimental work. The complete pultrusion setup for the pultrusion of test specimen is shown in figure 1.

The whole set up is assembled on an 'H' iron section as shown in figure 1 and consists of the following parts:

(1) Preformer: It is a cold die which provides the initial shape to resin impregnated jute fibre; it also squeezes out the extra resin from fibre as shown in figure 1.
(2) Hot die: A stainless steel split die has been used for pultrusion of jute fibre-reinforced composite strip as shown in figure 1. The split die facilitates easy cleaning and maintenance. A protective surface of 25 μm thick hard chrome plating is done to avoid abrasion of die due to the pultrusion of hard filler particles. For heating the die, an electric heater is provided with temperature controller. To measure and control the die temperature, a thermocouple is set at the parting line of the die.
(3) Puller assembly: The puller assembly is shown in figure 1. This assembly consists of four parts:

(i) 1 HP AC motor of 3Φ.
(ii) Arrangement for controlling the speed of pultru-(i)sion.
(iii) (a) AC frequency drive for 1 HP motor and (b) 1:60 speed ratio gear box.
(iv) Pulling rollers: 3 sets.

Figure 1. Indigenously developed pultrusion setup. A: jute fibre; B: resin bath; C: pre-former (cold die); D: heating die; E: steel strip for initial pulling; F: temperature controller; G: A.C. frequency drives for speed control; H: pulling roller; I: speed reducer gear box; J: pulling mechanism assembly.

2.1 *Material used*

(1) Unsaturated polyester resin is used as a matrix.
(2) Jute yarn of Tex unit of 2200 g km^{-1} as reinforcement is used in this experiment.
(3) Fillers:
   (i) Sugar cane Bagasse fibre (13.0 μm in diameter and 60∼30 μm in length),
   (ii) carbon black of 50 μm particle size,
   (iii) $CaCO_3$ of 100 μm particle size.
(4) Cobalt naphthelate of 6% concentration as accelerator.
(5) Methyl ethyl ketone per oxide as catalyst.

The design parameters as well as their chosen levels were decided as per the pilot tests. It was observed during the pilot experiment that high viscosity of the filler-resin blend produces difficulty in impregnation of jute fibre into resin-filler blends. So, the total filler weight content cannot go beyond certain limit. The various process parameters and selected levels for Taguchi L_9 OA experiment are listed in table 1.

The weight fractions of bagasse, carbon black and $CaCO_3$ were selected as variable process parameters to study the effect of filler on tensile strength of jute fibre-reinforced polyester (JFRP) in pultrusion process. The parameters kept constant during the entire experimentation are: pulling speed, 50 mm min^{-1}; die temperature, 190°C; jute fibre to resin ratio by weight, ∼0.95–0.96.

Table 1. Levels of experimental design parameters.

Levels	1	2	3
Variable parameters			
Bagasse (g)	15	25	35
Carbon black (g)	05	10	50
$CaCO_3$ (g)	25	50	75
Constant parameters			
Die temperature		190°C	
Pultrusion speed		50 mm min^{-1}	
Fibre to resin ratio		0.95–0.96	

2.2 *Formation of compound*

The three fillers i.e., bagasse, carbon black and $CaCO_3$ in the particulate forms were properly mixed according to the each experiment run given in table 2. After proper mixing of these fillers, nine compositions of hybrid fillers were prepared and from this 15% of the resin weight is mixed in the resin with the help of hand blender to make resin blend. The jute fibre bundles were wetted in this resin blend bath for pultrusion.

Jute fibre bundles of 1500 mm length and 160–165 g in weight are formed manually instead of using several creels to achieve the thickness of composite and to avoid wastage of fibre as the use of creels causes wastage of certain length of fibre at every new start. After the preparation of these bundles, the pulling speed of the pultrusion setup was adjusted to 50 mm min^{-1} and the hot die temperature was kept 190°C. This setting of the setup is kept constant during the entire experiment. The jute yarn bundles are wetted with resin filler compound by dipping into the resin bath and then pulled against the hot die; thus GFRP composite strip of size 25 × 10 × 1500 mm is formed as shown in figure 2.

2.3 *Testing of specimen*

After manufacturing the composite strip of 1500 mm length, three specimens for testing the tensile strength were prepared according to the ASTM D638 [15] as shown in figure 3.

Tensile tests were conducted according to ASTM D638 on computerized universal testing machine manufactured by Fine Manufacturing Industry Miraj (Maharashtra), India. The

Figure 2. Fibre bundle for pultrusion.

Table 2. Taguchi L_9 OA with responses (raw data and S/N ratios).

	Process parameters						
	Trial condition			Raw data (tensile strength (MPa))			
Run	Bagasse (g)	Carbon black (g)	$CaCO_3$ (g)	R_1	R_2	R_3	Mean S/N ratio (dB)
1	15	5	25	74.8	74.9	74.3	37.46
2	15	10	50	52.4	52.5	52.4	34.39
3	15	15	75	51.7	51.5	51.4	34.24
4	25	5	75	60.51	60.51	60.7	35.65
5	25	10	25	67.7	67.5	67.8	36.61
6	25	15	50	55.4	55.4	55.7	34.89
7	35	5	50	65.3	65.2	65.5	36.30
8	35	10	75	56.67	56.75	56.85	35.08
9	35	15	25	44.4	44.5	44.8	32.98

R_1, R_2, R_3 represent three repetitions of each trial; grand average of tensile strength, $T_{avg} = 58.86$.

results of tensile test are reported in table 2 and figure 4, which shows the average tensile strength and signal-to-noise (S/N) ratio for each experiment.

A jute fibre-reinforced strip is also pultruded with pure polyester resin and tested for reference. The tensile strength of the jute fibre-reinforced composite with pure resin (resin without filler) was found to be 80.7 MPa.

Figure 5 shows the macro aspect of the tensile ruptured pultruded jute fibre-reinforced specimens. The composite specimen with or without hybrid filler shows brittle fracture and also exhibits that the fracture tips are much non-uniform in case of specimen with hybrid filler as compared to the specimen without filler. During the tensile test, it was observed that as the load increases, some of the fibres pop out from the specimen edge due to deboning from polyester resin matrix causing crack propagation at the fibre/matrix interface. As the fibre content in all the specimens is almost the same, hence, the nature of fracture is also the same. This mechanism of fracture is further supported by the scanning electron microscope (SEM) observations.

To estimate the fibre content in pultruded jute-reinforced composite laminates, three pieces of 50 g of composite are cut from the pultruded composite for each sample. ASTM 3171 standard [16] was used for acid digestion test and nitric acid is used as a hot digestion medium to dissolve the resin of the composite specimen. The residue is filtered, dried and weighed. The residue was further rinsed with a water jet and filtered by sintered glass filters, so that all the particulate fillers were washed-out and only jute fibre remains as residue, which is further dried and weighed again. The mass loss of fillers and jute fibre were found to be negligible. The result of digestion tests are given in figure 6. It is clear from figure 6 that the weight% of jute fibre in every specimen is nearly the same. The calculated weight% of the each filler in different experiments is given in figure 7.

Figure 3. GFRP composite tensile test specimen according to ASTM D638.

In the present study, the tensile strength data were analysed to determine the effect of the various design parameters with the help of L_9 Taguchi orthogonal array. The experimental results were then transformed into S/N ratio. According to Taguchi, S/N ratio is the measure of the quality characteristics deviating from the desired values. For the analysis of the S/N ratio, quality characteristics can be divided into three categories i.e., lower-the-better, higher-the-better and nominal-the-best. The greater S/N ratio corresponds to better-quality characteristic regardless of the category of the quality characteristic. Therefore, the greatest S/N ratio corresponds to the optimal levels of the process parameters. The tensile strength as response falls under the category of higher-the-better type and the S/N ratio for the same can be computed as [17,18]:

$$(S/N)_{\mathrm{HB}} = -\log\left[\frac{1}{R}\sum_{k=1}^{R}\left(\frac{1}{Y_k^2}\right)\right],$$

here, Y_k $(k = 1, 2, \ldots, n)$ are the values of response under trial conditions with repeated R times.

Statistically significant process parameters were identified by performing analysis of variance (ANOVA) and main effect plots were used to predict the optimal combinations of the process parameters.

3. Results and discussion

The average tensile strength and the S/N ratio values for each parameter at levels L_1, L_2 and L_3 are calculated and are given in table 3. The ANOVAs for S/N ratio and raw data

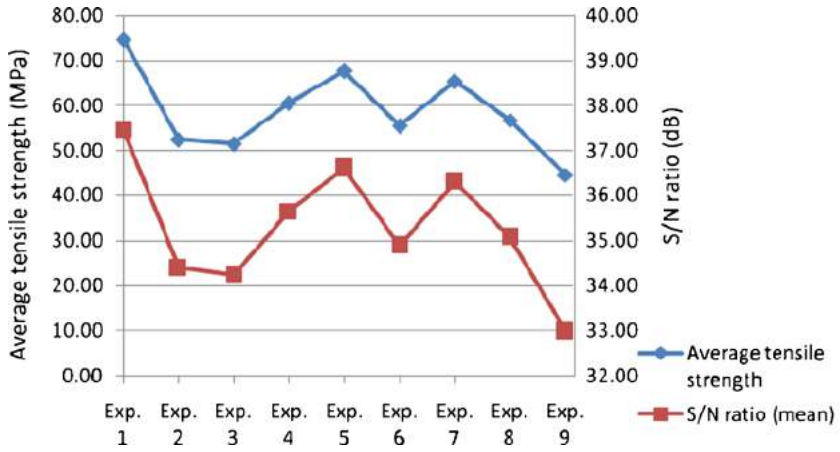

Figure 4. Average tensile strength and S/N ratio of all nine experiments.

are reported in tables 4 and 5, respectively. The values from table 3 have been plotted in figure 8 giving the variations of tensile strength with levels of the process parameters.

Figure 5. JFRP composite tensile test specimen after tensile test.

The properties of composites were highly influenced by loading of short bagasse fibre. The effect of fibre ends plays a significant part in the fracture of hybrid composites. Thus, it becomes necessary to optimize the fibre loading for a particular fibre/matrix system so that the best properties can be achieved. It is evident from figure 8a that as the content of bagasse fibre increases from level 1 to level 2, the tensile strength increases as the short bagasse fibre provides interlocking with jute fibre. This could increase the effective stress transfer at the interface and also reduce the voids in the composite. But tensile strength decreases considerably with increase in content of bagasse fibre from level 2 to level 3. This is due to the fact that higher loading of bagasse fibre leads to greater fibrillation, owing to comparatively larger quantity of fibre ends available for crack initiation. This could lower the effective stress transfer at the interface [11]. This can also be understood with SEM images of specimens 1, 5 and 9 shown in figures 9a, b and c, respectively. It is evident from figure 9a that the bagasse fibre is at level 1 in experiment 1, so there is some cavity and fibre pullout. Figure 9b demonstrates sample of experiment 5, where the bagasse is at level 2; there is no fibre pullout and voids but the fibre filament gets damaged due to erosion by carbon black

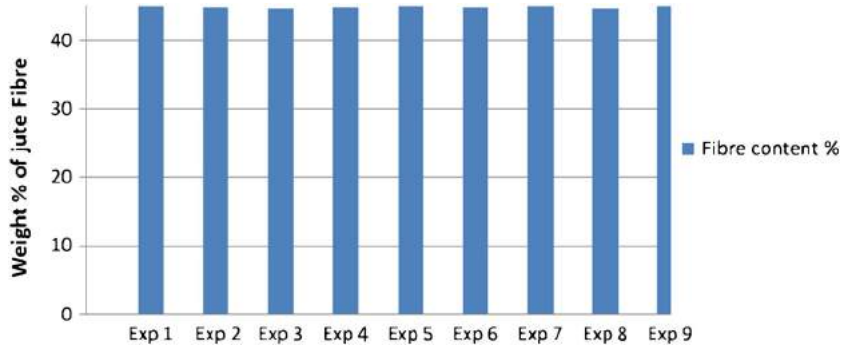

Figure 6. Average weight% of jute fibre in composite specimen in experiment run.

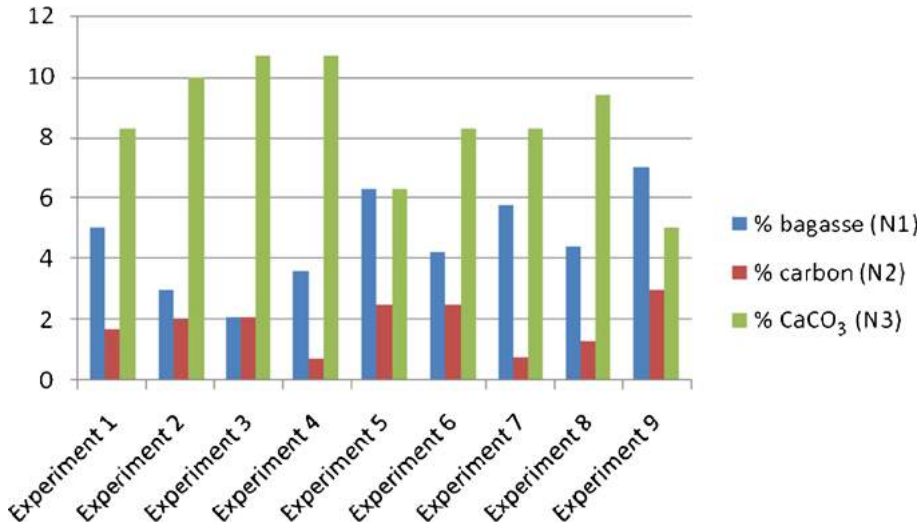

Figure 7. Weight% content of different fillers in each experiment.

Table 3. Average values and main effects of tensile strength of the composite.

		Bagasse		Carbon black		$CaCO_3$	
	Level	Raw data	S/N ratio	Raw data	S/N ratio	Raw data	S/N ratio
Average values (tensile strength MPa)	L_1	59.54	35.37	66.86	36.79	62.30	35.36
	L_2	61.25	35.61	58.95	35.04	57.76	35.30
	L_3	55.55	34.89	50.53	34.04	56.29	35.21
Main effects (tensile strength MPa)	L_2-L_1	1.70	0.25	−7.91	−1.75	−4.54	−0.07
	L_3-L_2	−5.69	−0.72	−8.42	−1.00	−1.47	−0.09

L_1, L_2 and L_3 represent levels 1, 2 and 3, respectively of parameters. L_2–L_1 is the average main effect when the corresponding parameter changes from level 1 to level 2. L_3–L_2 is the average main effect when the corresponding parameter changes from level 2 to level 3.

Table 4. Pooled ANOVA (S/N data).

Source	SS	DOF	*V*	*P*	*F* ratio	*F* ratio table
Bagasse	0.81	2	0.40	5.37	22.48*	19
Carbon black	11.67	2	5.83	77.48	324.31*	19
$CaCO_3$	2.55	2	1.27	16.91	70.79*	19
Error	0.04	2	0.02	0.24	–	–
T	15.0552919	8	–	100	–	–

*Significant at 95% confidence level. SS: sum of square; DOF: degree of freedom; *V*: variance; *P*: percent contribution.

Table 5. Pooled ANOVA (raw data).

Source	SS	DOF	*V*	*F* ratio	*P*
Bagasse	84.95	2	42.48	4.12	4.12
Carbon black	1636.68	2	818.34	79.37	79.37
$CaCO_3$	319.98	2	159.99	15.52	15.51
Error	20.49	20	1.0242	0.99	1.00
T	2062.10	26	–	100	–

SS: sum of square; DOF: degree of freedom; *V*: variance; *P*: percent contribution.

as it is at level 3. The SEM image of sample of experiment 8 shows that there is crack initiation due to hard particles of $CaCO_3$ and more number of bagasse fibre ends.

Figure 8b shows that as the carbon black content increases in the composite, the tensile strength decreases. It is seen in SEM image that the distribution of carbon black filler becomes relatively non-uniform as the carbon black content increases. However, lower carbon black content in the composite shows better carbon black agglomerates dispersion as in figure 9a. The tensile strength of the composite decreases with increase of the carbon black content because the hard particles of carbon black during curing in pultrusion process have damaged some of jute fibre filament. This phenomenon can be seen in SEM image of specimen no. 5 in figure 9c. It is also observed that due to the discontinuity in the matrix produced by carbon black agglomerates causes the stress concentration and hence, decreases the tensile strength of composite.

The tensile strength variation of composite with $CaCO_3$ content is shown in figure 8c. The tensile strength of the

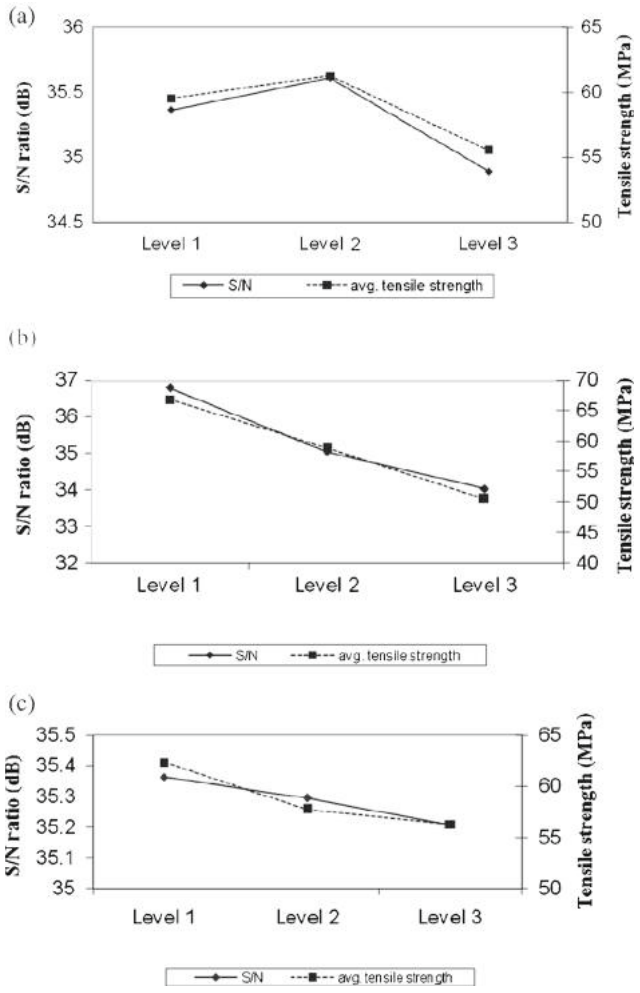

Figure 8. Effect of process parameters on tensile strength and S/N ratio (main effects): (**a**) bagasse content, (**b**) carbon black content and (**c**) $CaCO_3$ content.

composite reduces as the weight content of $CaCO_3$ increases because the particulates of filler practically act as crack initiator and this phenomenon is more pronounced when there is a possibility of clustering of $CaCO_3$ particles. The SEM image shows that the particles of $CaCO_3$ get dissolved partially, but as the $CaCO_3$ content increases the undissolved particles of $CaCO_3$ also increase and cause crack initiation in

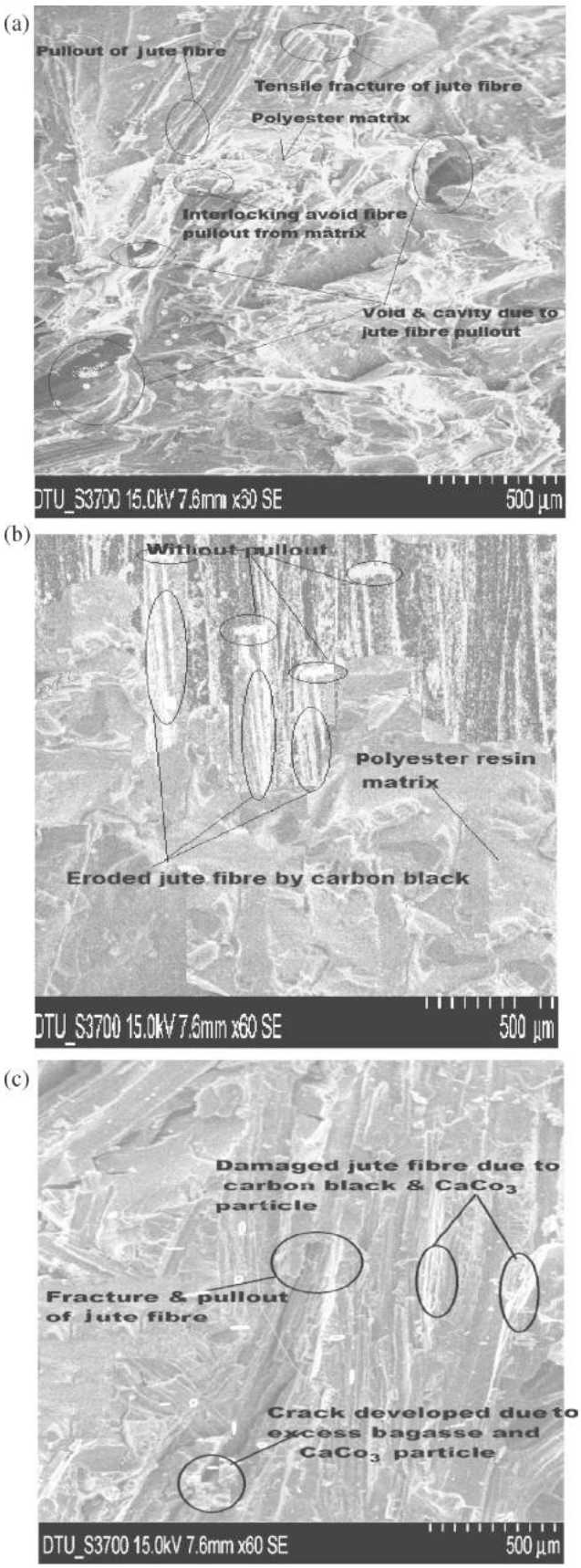

Figure 9. SEM images showing the microstructure of tensile fracture specimens: (**a**) 1, (**b**) 5 and (**c**) 8.

the composite as shown in figures 9b and c. It was observed in the present study that as the content of $CaCO_3$ increases, the shrinkage of composite strip was less and the dimensional stability was better.

It was observed in the present work that the dimensional stability of the pultruded profile is much better as compared with other methods like hand layup, resin transfer molding (RTM) or compression moulding. It was also found that the tensile strength of the pultruded jute fibre polyester resin composite was on the higher side as compared with hand layup or vacuum compression moulding with same fibre content. Desh *et al* [19] have reported in their study that jute polyester resin composite prepared by using solution impregnation and hot curing methods with 60% fibre loading was having highest tensile strength. SEM micrographs of the tensile fracture of the pultruded composite show clearly that the polyester resin has penetrated the jute fibres used as reinforcement material and surrounded each and every fibre causing very less void formation in composite as compared with jute reinforced polyester resin composite manufactured by other methods like hand layup process, resin transfer moulding, vacuum-assisted resin transfer moulding, compression moulding, etc. as reported by different researchers [20–22].

3.1 *Calculation of optimum tensile strength*

The optimum value of tensile strength was predicted at the selected levels of significant parameters A2, B1 and C1 (tables 3 and 5). The estimated mean of the response, i.e., tensile strength was determined as in equation (1):

$$\text{Tensile strength} = T_{A2} + T_{B1} + T_{C1} - 2T_{avg} = 72.8 \text{ MPa}, \quad (1)$$

where T_{avg}, overall mean of tensile strength = 58.78 MPa (table 2); T_{A2} = average tensile strength at the second level of bagasse content (A2) = 61.25 MPa; T_{B1} = average tensile strength at the first level of carbon black content (B1) = 66.86 MPa; T_{C1} = average tensile strength at the first level of $CaCO_3$ (C1) = 62.30 MPa.

Table 6. Observation of confirmation test.

Observation	Trial No. 1	2	3	Avg. tensile strength (MPa)
1	72.81	73.1	73.5	73.14

Table 7. Regression analysis model.

	Coefficients	Standard error	*t* (stat)	*P*
Intercept (*p*)	82.25	5.09	16.17	0.00
Bagasse fibre (*a*)	−0.13	0.21	−0.66	0.53
Carbon black (*b*)	−1.52	0.44	−3.46	0.01
$CaCO_3$ (*c*)	−0.10	0.09	−1.13	0.30

Summary of model $R^2 = 81\%$, adjusted $R^2 = 70.83\%$ and standard error = 6.02%.

Table 8. Result of regression model at optimal level.

	Optimal process parameter settings	Predictive values	Experimental values	Error (%)
S/N ratio (dB)	A2B1C1	36.74	37.30	1.5
Tensile strength (MPa)	A2B1C1	68.74	73.14	6.02

The following equations were used for calculating 95% confidence interval (CI) of confirmation experiments (CI_{CE}) and 95% confidence interval of population (CI_{pop}):

$$CI_{CE} = \sqrt{F_\beta(1,\ f_{error})V_{error}\left[\frac{1}{n_{effective}} + \frac{1}{R}\right]} \tag{2}$$

and

$$CI_{pop} = \sqrt{\frac{V_{error}F_\beta(1,\ f_{error})}{n_{effective}}}, \tag{3}$$

where $F_\beta(1,\ f_{error})$ is the F ratio at the confidence level of $(1-\beta)$ against degree of freedom 1 and error degree of freedom (DOF) f_{error}, N the total number of results = 27 (treatment = 9, repetition = 3), R the sample size for confirmation experiments = 3, V_{error} the error variance = 1.02 (table 5), and f_{error} = error DOF = 20 (table 5).

$$n_{effective} = \frac{N}{1 + [\text{DOF associated in the estimate of mean response}]} = 3.86, \tag{4}$$

$$F_{0.05}(1, 20) = 3.49(F \text{ value tabulated}). \tag{5}$$

So, $CI_{CE} = \pm 5.6$ and $CI_{pop} = \pm 0.96$.

The predicted optimal range for a confirmation run (three repetitions) is: Mean tensile strength $-CI_{CE}$ < tensile strength < mean tensile strength $+CI_{CE}$: 67.25 < tensile strength < 78.45. The predicted optimal range for the population is as follows: mean tensile strength $-CI_{pop}$ < tensile strength < mean tensile strength $+CI_{pop}$: 71.89 < tensile strength < 73.81.

The optimal composition of hybrid filler for the predicted ranges of tensile strength is as follows:

Second level of bagasse content (A2) = 25 g,
First level of carbon black content (B1) = 5 g,
First level of $CaCO_3$ (C1) = 25 g.

3.2 *Confirmation experiments*

All fillers are mixed properly according to the optimum level i.e., bagaase at 2nd level (A2), carbon black 1st level (B2) and $CaCO_3$ 1st level (C1), and 15% of the resin weight of this hybrid filler was mixed in resin. Then keeping the resin and fibre ratio and other process parameters constant, the jute fibre composite strip was pultruded. Three specimens were cut from this strip and tensile tests were performed on universal testing machine. The results are given in table 6.

The average tensile strength of test was found to be 73.14 MPa, which was within the confidence interval of the predicated optima of tensile strength.

3.3 *Regression analysis*

The mathematical model for weight content in grams of bagasse fibre, carbon black and calcium carbonate in the composite as process parameters is obtained from regression analysis using MINITAB 14 statistical software to predict the tensile strength of jute-reinforced composite. Table 7 shows the regression analysis model.

The regression equation is

$$\text{Tensile strength} = 82.25 - 0.135 * a - 1.529 * b - 0.1 * c,$$

where a = bagasse fibre (g), b = carbon black (g) and c = $CaCO_3$ (g). The difference between predicted value of tensile strength by regression model and experimental value of confirmation test at optimal level is shown in table 8.

In this study, the results obtained for final tensile strength are in good agreement with regression model ($R^2 > 0.80$) as R^2 is value of the correlation coefficient and should be between 0.8 and 1 in multiple linear regression analysis.

4. Conclusions

The effect of three fillers bagasse fibre, carbon black and $CaCO_3$ on tensile strength of the jute fibre-reinforced composite was investigated. The following conclusions can be drawn from the study:

(i) The optimum composition of hybrid filler contains: bagasse fibre = 25 g, carbon black = 5 g, $CaCO_3$ = 25 g.
(ii) The tensile strength at the optimum composition of hybrid filler with 15% weight content of filler in resin is 73.12 MPa.
(iii) Experiments also exhibit that within the testing levels the tensile strength decreases with the increasing contents of carbon black and $CaCO_3$.
(iv) The regression model developed to predict the tensile strength of composite with variation of bagasse fibre, carbon black and $CaCO_3$ content is in good agreement with the experimental results. The estimated tensile strength at optimum level was found to be 68.74MPa.
(v) The estimated optimal range for tensile strength is CI_{pop}: 71.89 < tensile strength (MPa) < 73.81.
(vi) The 95% confidence interval of predicted mean for tensile strength is 67.25 < tensile strength (MPa) < 78.45.

References

[1] Joseph K, Thomas S and Pavithran C 1996 *Polymer* **37** 5139

[2] Varma I K, Ananthakrishnan S R and Krishnamoorthi S 1989 *Composites* **20** 383

[3] Geethamma V G, Thomas Mathew K, Lakshminarayanan R and Thomas S 1998 *Polymer* **39** 1483

[4] Sreekala M S, Kumaran M G and Thomas S 1997 *J. Appl. Polym. Sci.* **66** 8

[5] Alamri H and Low I M 2012 *Polym. Test.* **31** 810

[6] Zhou S S, Wu L M, Sun J and Shen W 2002 *Prog. Org. Coat.* **45** 33

[7] Baral D, De P P and Nando G B 1999 *Polym. Degrad. Stab.* **65** 47

[8] Sare I R, Mardel J I and Hill A J 2001 *Wear* **250** 1

[9] Katz H S and Milewskin J V 1978 *Handbook of fillers and reinforcements for plastics* 1st edn (New York: Van Nostrand Reinhold)

[10] Borkar S P, Senthil Kumar V and Mantha S S 2007 *Indian J. Fibre Text. Res.* **32** 251

[11] Sudhir S K and Datta Chandan 2009 *BioResources* **4** 1455

[12] Gupta A, Singh H and Walia R S 2015 *Indian J. Eng. Mater. Sci.* **22** 62

[13] Murty V M and De S K 1982 *J. Appl. Polym. Sci.* **27** 4611

[14] Khalil H A, Firoozian P, Bakare I O, Akil H M and Noor A M 2010 *Mater. Des.* **31** 3419

[15] D638 2010 ASTM International, Standard test method for tensile properties of plastics

[16] D3171-99 2004 ASTM International, Standard test methods for constituent content of composite materials

[17] Ross P J 1998 *Taguchi techniques for quality engineering* (New York: McGraw-Hill Book Company).

[18] Walia R S, Shan H S and Kumar P 2006 *Mater. Manuf. Process.* **21** 907

[19] Dash B N *et al* 1999 *Polym. Compos.* **20** 62

[20] O'Dell and Jane L 1997 *Natural fibres in resin transfer molded composites* Fourth International Conference on Woodfibre-plastic composites

[21] Saravana B D and Mohan K G C 2013 *Proc. World Congress Eng.* **3** 2091

[22] Naveenkumar R *et al* 2015 *Int. J. Appl. Sci. Eng. Res.* **4** 250

ResearchGate

See discussions, stats, and author profiles for this publication at: https://www.researchgate.net/publication/282611600

Improving Performance of MESI Cache Coherence Protocol for Multi-core Processor on MARSSx86 Simulator

Conference Paper · July 2012

READS

3

1 author:

Manoj Kumar

Delhi Technological University

19 PUBLICATIONS **1** CITATION

SEE PROFILE

All in-text references underlined in blue are linked to publications on ResearchGate, letting you access and read them immediately.

Available from: Manoj Kumar
Retrieved on: 03 August 2016

IMPROVING PERFORMANCE OF MESI CACHE COHERENCE PROTOCOL FOR MULTI-CORE PROCESSOR ON MARSSx86 SIMULATOR

Manoj Kumar
Computer Engineering Department
Delhi Technological University
Delhi, India
mkg1109@rediffmail.com

Pooja Arora
Computer Engineering Department
Delhi Technological University
Delhi, India
poojaarora014@gmail.com

Akanksha Bharadwaj
Computer Engineering Department
Delhi Technological University
Delhi, India
akanksha.bharadwaj6@gmail.com

Abstract— **We have conscientiously studied MESI protocol and MARSSx86 (Micro Architectural and System Simulator) simulator whose code is easily available as open source. In this paper we have enhanced the performance in terms of cycle per second and commits per second by modifying the existing Invalid to Invalid (II) in MESI protocol's code of the MARSSx86 simulator. In fact by doing so we have successfully made invalid to invalid transition zero for the programs of PARSEC (Princeton Application Repository for Shared-Memory Computers) benchmark for dual cores. Experiments have shown that for quad cores configuration we have reduced invalid to invalid transition significantly by 99% on an average. When we tested for octet cores configuration invalid to invalid transition is decreased by 99% with CANNEAL, 99% with FERRET and 70% with SWAPTIONS. As shown in experiment's results we are actually depreciating the bus traffic and improving the system performance.**

Keywords- MESI protocol, MARSSx86 simulator, Cache Coherence protocols.

I. INTRODUCTION

MARSSx86 (Micro Architectural and System Simulator) [1] was being developed by Avadh Patel with support from Furat Afram, Hui Zeng and Kanad Ghose [2] at Computer Architecture & Power Aware Systems Research Group (CAPS Research group) at State University of New York at Binghamton (SUNY Binghamton). MARSS used MPTLsim (i.e. a multi-core simulator based on PTLsim) as a root for its development. MARSS is a tool for cycle accurate full system simulation of the x86-64 architecture, especially for multi-core implementations.

The MESI protocol also referred to as the Illinois Protocol [3] makes it possible to maintain the coherence in cached systems. It is based on the four states that a block in the cache memory can have. These four states are the abbreviations for MESI: **M**odified, **E**xclusive, **S**hared and **I**nvalid.

In this paper we have attempted to enhance the system performance by optimizing the MESI protocol implementation for MARSSx86 simulator. For implementing this we modified the existing code so that invalid to invalid transactions can be reduced to almost zero. By doing so we are able to reduce the bus traffic to a great extent.

The organization of this paper is as follows: -Section II represents the basic concepts of MRASSx86 simulator and MESI protocol. Section III represents proposed work, Section IV represents the related work. Section V represents experiment and results. Section VI represents conclusion.

II. MARSSx86 SIMULATOR AND MESI PROTOCOL

A. MARSS x86 SIMULATORS

MARSS–Micro Architectural and System Simulator is a simulator that works only on 64-bit operating system and 64-bit processor. The x86 CPU simulation components of MARSS are based on an extended and modified version of PTLsim [4]. The specific features of MARSS are [2]:

- Cycle-accurate simulation models are being used by CPUs implementing the x86 ISA for out-of-order and in-order single core and multi-core. These are being integrated into QEMU [5] full system emulation environment.
- MARSS allows seamless switching between the cycle-accurate simulation mode and the native x86 emulation mode of QEMU, thus permitting the fast-forwarding of simulation in the above mentioned switching.
- It not only allows the unmodified operating systems to boot on MARSS but also allows us to simulate the execution of unmodified x86 binaries of applications and existing libraries on MARSS.
- MARSS provides detailed, cycle-accurate models of a contemporary memory hierarchy for single-core as well as multi-core processor chips, including coherent caches and a DRAM memory system. 200

to 400K instructions per second of simulation speed are realized in the cycle-accurate simulation mode of multi-core processor chips.

- MARSS permits network packet images, disk block images (i.e. system-level data) to be imported into the simulator from the underlying emulated system. It not only enables the use of realistic data but also allows the users to gauge the effect of core designs on the rest of the system and vice-versa.

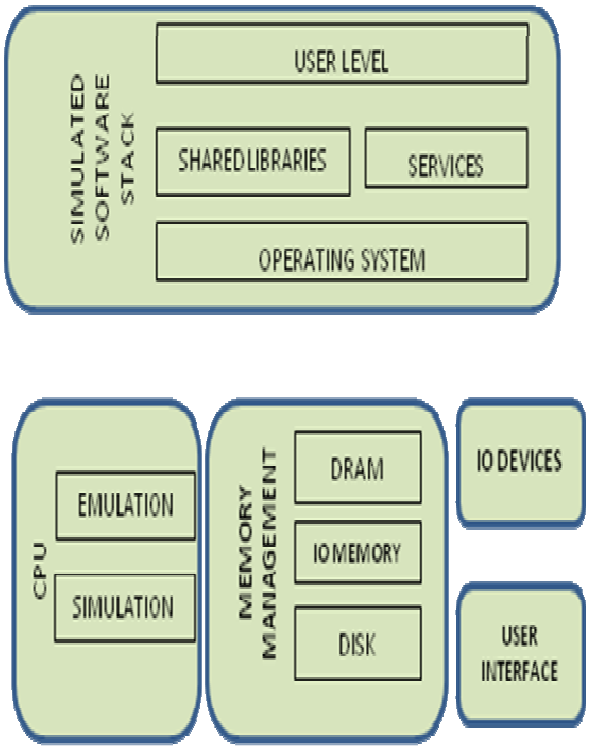

Figure 1: MARSS simulator framework

B. MESI Protocol

MESI protocol [6] also referred to as Illinois protocol due to its development at the University of Illinois at Urbana-Champaign is very renowned cache coherence protocol and it supports write-back cache. In this protocol every cache line can have one of the following states: Modified, Exclusive, Shared, Invalid. There explanation is given below:

Modified: In this the cache line is present only in the current cache, and hence is dirty; also it's been modified from the value available in main memory. So, the cache is required to write the data back to main memory at some time in the future, before permitting any other read of the (no longer valid) main memory state. The write-back will change the state of the line to the Exclusive state.

Exclusive: The cache line is present only in the current cache, but is clean; it matches main memory. It may be changed to the Shared state at any time, in response to a read request. Alternatively, it may be changed to the Modified state when performing write to it.

Shared: Indicates that this cache line may be stored in other caches of the machine as well and is "clean"; it matches the main memory. The line may be discarded (changed to the Invalid state) at any time.

Invalid: Indicates that the cache line is invalid. The detailed explanation is shown in figure 2.

It is better than MSI protocol [7] since for every write operation two transitions are performed, even when the data block taken into consideration is not shared. In the first transition it gets the memory block in the shared state and in second transition causes write, which also changes the state of that data block to shared state from modified state. It adds a new state to MSI protocol i.e. Exclusive state which reduces the traffic because of write operation performed for the shared data block [8].

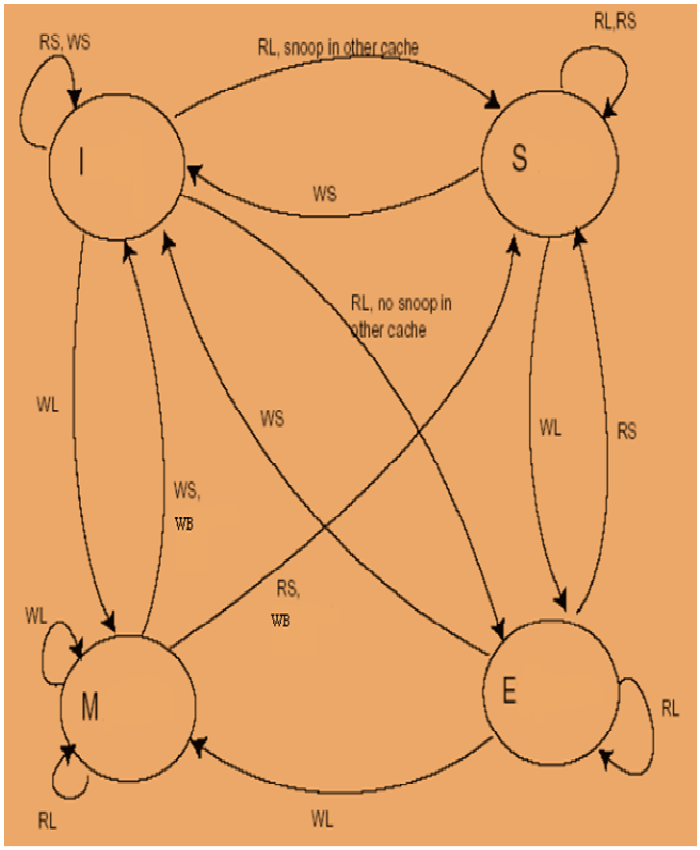

WS: write snoop WL: write local CPU

RS: read snoop RL: read local CPU

WB: write back

Figure 2: State Diagram of MESI Protocol.

For This Experiment we have taken level 2 cache as private, therefore all the results mentioned in below sections are concern with level 2 cache as private only.

III. PROPOSED IDEA

After thoroughly studying the code of MARSSx86 simulator we noticed that in the code of MESI protocol invalid to invalid transition exists there. We thought if we can modify or eliminate this transition in this code then it should increase the system performance by making this transition zero or reducing it to very high extent and in terms of cycles per second and commits per second. In the next section we are showing the experimental work for this proposed idea.

IV. RELATED WORK

The MARSSx86 (Micro Architectural and System Simulator) is a simulator that works only on 64-bit operating system and 64-bit processor. So first we installed LINUX (UBUNTU 11.10) on the system. After successfully installing 64-bit operating system, we installed MARSSx86 simulator. Though we faced lots of problems while compiling and running the MARSSx86 simulator but finally we conquered all the issues. Then we initiated with the standard results, while taking these we kept level-2 cache as private.

We used PARSEC (Princeton Application Repository for Shared-Memory Computers) benchmark for getting all the results. We keep on differing number of cores viz. 2 (dual), 4 (quad), and 8 (octet) for getting standard results and results with modified code. After getting the standard results of our experiment on CANNEAL, FERRET and SWAPTIONS (programs of PARSEC benchmark) we proceeded with the actual task of modifying the code of MESI protocol. After extensive study of MARSSx86 simulator's code which is available without a hitch as open source, we have transformed the code of file mesiLogic.cpp which contains the nitty-gritty of MESI protocol while executing with MARSSx86 simulator. In this file invalid to invalid transitions are present. We have modified the code precisely at this segment. Then again compiled and run this code with CANNEAL, FERRET and SWAPTIONS (programs of PARSEC benchmark) with the variation of number of cores i.e. 2, 4 and 8. After getting experiment results in the form of stats files (results of experiment comes in the form of stats file) we have thoroughly compared them with the standard result's stats files. We have noticed that by keeping number of cores 2 i.e. dual core we have made invalid to invalid transition as zero successfully for all 3 programs of PARSEC benchmark viz. CANNEAL, FERRET and SWAPTIONS.

V. EXPERIMENTS AND RESULTS

We have successfully made reduction in invalid to invalid transition. As visible in table1 results that by keeping number of cores as two we have successfully made invalid to invalid transition directly to zero for all three programs i.e. CANNEAL FERRET and SWAPTIONS of PARSEC benchmark.

Then we compared the experiment's results i.e. stats file for CANNEAL program of PARSEC benchmark, we noticed that with quad cores (i.e. number of cores are 4) we have reduced invalid to invalid transition successfully up to 99% and when we compared the stats file with octet cores (i.e. number of cores are 8) we noticed that then too we are capable in reducing invalid to invalid transition by 99%.

Then we compared results of FERRET program of PARSEC with quad cores configuration, we found that again we have successfully reduced invalid to invalid transition by 99% and with octet core we have decreased invalid to invalid transition by 98%. After this we compared the results of SWAPTIONS program with quad cores configuration. In this we determined that invalid to invalid transitions are reduced up to 70% only. Then we compared for octet cores configuration and in this case too after comparing results with standard results we found that we have reduced invalid to invalid transition till 70% only.

By reducing invalid to invalid transition at huge extent as mentioned in above paragraphs it will reduce the traffic of shared bus so via this we are enhancing the system performance. We have also noticed while analyzing results that with CANNEAL program of PARSEC benchmark we have increased the cycles per second and commits per second at both kernel level and user level for dual cores, quad cores and octet cores configuration.

By taking FERRET program of PARSEC benchmark we have noticed that commits per second are enhanced at both kernel level and user level with core configuration as dual cores, quad cores and octet cores.

Table 1: Comparing results of actual code and modified code

No. of cores	Benchmark	INVALID TO INVALID TRANSITION IN STANDARD CODE RESULT	INVALID TO INVALID TRANSITION IN MODIFIED CODE RESULT
2	CANNEAL	41784	0
	FERRET	28646	0
	SWAPTIONS	4349	0
4	CANNEAL	48865	4031
	FERRET	79300	2658
	SWAPTIONS	6758	2070
8	CANNEAL	233495	2134
	FERRET	16900	1844
	SWAPTIONS	85713	28196

With SWAPTIONS program of PARSEC benchmark we noticed that cycles per second are getting increased with dual cores, quad cores and octet cores as configuration at both user level and kernel level.

VI. CONCLUSION

By modifying the code of MESI protocol present in MARSSx86 (Micro Architectural and System Simulator) simulator we have actualized the invalid to invalid transition as zero for dual cores. When it comes to quad cores and octet cores then too we have attained triumphant by 99% for FERRET and CANNEAL of PARSEC benchmark and 70% for SWAPTIONS of PARSEC benchmark in terms of invalid to invalid transition abatement.

We have also elevated cycles per second and commits per second for CANNEAL eminently. With FERRET cycles per second are escalated and with SWAPTIONS also we have ascended commits per second.

In this way we are escalating the system performance by actualizing invalid to invalid transition as zero or reducing it at very high extent. This will deteriorate the bus traffic deliberately.

REFERENCES

[1] The MARSS website [Online]. Available: http://www.marss86.org/.

[2] Avadh Patel, Furat Afram, Shunfei Chen, Kanad Ghose, "MARSSx86: A Full System Simulator for x86 CPUs", DAC'11, San Diego, California, USA.

[3] Silvia Lametti, "Cache Coherence Techniques", A Technical Report, December 2010

[4] Matt Yourst, "PTLsim: A Cycle Accurate Full System x86-64 Microarchitectural Simulator", Proc. ISPASS 2007.

[5] Fabrice Bellard, "QEMU, a fast and portable dynamic translator", Proc. ATEC 2005.

[6] M. S. Papamarcos and J. H. Patel, "A low-overhead coherence solution for multiprocessors with private cache memories," Proc. 11th Annual Int. Symp. on Computer Architecture, pp. 348-354, June 1984.

[7] Silvia Lametti, "Cache Coherence Techniques", A Technical Report, December 2010.

[8] Manoj Kumar, Pooja Arora, "A Survey of Cache Coherence Protocols in Multiprocessors with Shared Memory", ICACSEE'2012

IMPROVING THE PERFORMANCE OF MESI PROTOCOL WITH LEVEL 2 CAHCE AS SHARED FOR MULTICORE PROCESSOR ON MARSSx86 SIMULATOR

Pooja Arora
Computer Science Department
Delhi Technological University
Delhi, India
poojaarora014@gmail.com

Manoj Kumar
Computer Science Department
Delhi Technological University
Delhi, India
mkg1109@rediffmail.com

***Abstract*— After thoroughly studying about MESI protocol and MARSSx86 (Micro Architectural and System Simulator) simulator, which is an open source therefore its code is available without a hitch. In this paper we have enhanced the performance of the system. We have made existing invalid to invalid transition zero at the Level 1 Data Cache at user level with dual cores and reduced this transition at the great extent when it comes to the FERRET, SWAPTIONS and CANNEAL programs of PARSEC (Princeton Application Repository for Shared-Memory Computers) benchmark. The experiment results have proved that with dual cores we have increased cycles per second for above mentioned programs of PARSEC benchmark and at quad cores we have increased commits per second. When it comes to octet cores we have enhanced the commits per second for FERRET, cycles per second for SWAPTIONS AND CANNEAL program of PARSEC benchmark. By reducing or eliminating completely this invalid to invalid transition we are actually depreciating the traffic at shared bus and enhancing the system performance.**

Keywords- MESI protocol, MARSSx86 simulator, Shared level 2 cache.

I. INTRODUCTION

The MESI protocol which is also referred as the Illinois Protocol [1] made it possible to maintain the cache coherence in systems. This protocol is very renowned, supports write-back cache strategy. It is better than MSI (Modified, Shared, and Invalid) protocol as for every write operation there are two transitions, even when that data block is not shared then too. In the first transition it gets the memory block in shared state and in second transition it causes write, which also changes the state of that data block to shared state from modified state. It adds a new state to MSI protocol i.e. Exclusive state which reduces the traffic because of write operation of shared data block [2]. Its name is suggested by the states where cache block can exist those states are Modified, Exclusive, Shared and Invalid state.

MARSSx86 (Micro Architectural and System Simulator) [3] is developed by Avadh Patel with the support of Furat Afram, Hui Zeng and Kanad Ghose [4] at Computer Architecture & Power Aware Systems Research Group (CAPS Research group) at State University of New York at Binghamton (SUNY Binghamton). MARSS uses MPTLsim (i.e. a multicore simulator based on PTLsim) as nitty-gritty for its development. It is a tool for cycle accurate full system simulation of the x86-64 system architecture, principally for multicore architectures.

In this paper we have made attempt to enhance the system performance by optimizing the existing MESI protocol implementation at MARSSx86 (Micro Architectural and System Simulator) simulator. For doing the same we have modified the existing code of MESI protocol so that invalid to invalid transitions can reach to zero almost. By doing so we have been able to reduce the bus-traffic to the great extent.

The organization of this paper is as follows: Section II represents the basic concepts of MRASSx86 simulator and MESI protocol. Section III represents the proposed idea. Section IV represents the related work. Section V represents experiment and results. Section VI represents conclusion.

II. MARSSx86 SIMULATOR AND MESI PROTOCOL

A. MARSS x86 SIMULATORS

MARSS is a tool which is useful for evaluating and developing products that will use current and emerging single and multicore x86 chips. It is an open source full system simulation tool. The x86 CPU simulation component of MARSS is based on an extended and modified version of PTLsim [5].

There are specific features of MARSS mentioned below as:

- MARSS uses a cycle-accurate simulation models for out-of-order and in-order single core and multicore CPUs implementing the x86 ISA. These are integrated into the QEMU [6] system emulation environment.
- MARSS allows system-level to be imported into the simulator from the underlying emulated system.
- MARSS involves cycle-accurate models of a present memory hierarchy for single-core and multicore processor chips, including coherent caches. Simulation speeds of 200 to 400 kilo instructions per second are realized in the cycle-accurate simulation mode of multicore processor chips [4].
- Unmodified operating systems can be booted on MARSS and the execution of unmodified x86 binaries of applications and existing libraries can be simulated on MARSS. [4]
- MARSS supports consistent switching between the cycle-accurate simulation mode and the native x86 emulation mode of QEMU.

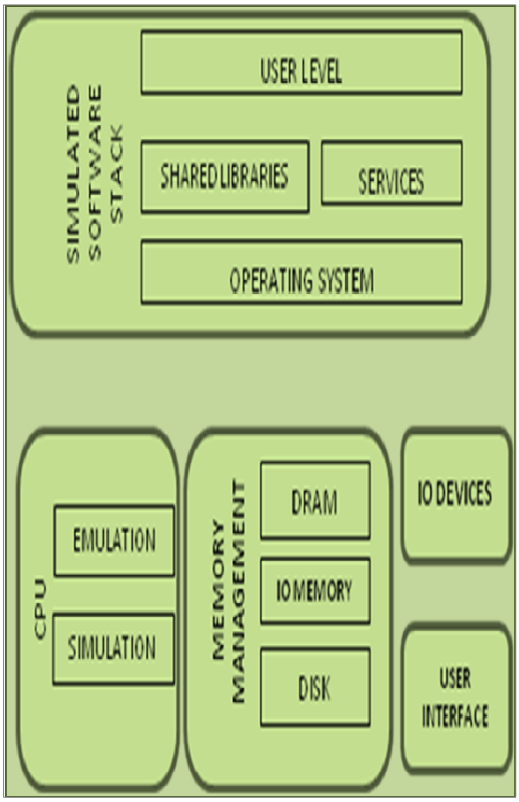

Figure 1: MARSS simulator framework

B. MESI Protocol

MESI protocol [7] also referred to as Illinois protocol as it is developed at the University of Illinois at Urbana-Champaign is very well-known cache coherence protocol and it supports write-back cache strategy. In MESI protocol all the cache lines can have anyone of the states viz. Modified, Exclusive, Shared, Invalid.

Modified: The cache line is present only in the current cache, and it is dirty as it's modified from the value available in main memory. So, the cache is required to write the data back to main memory at some time in the future, before permitting any other read of the main memory state. The write-back will change the state of the line to the Exclusive state.

Exclusive: The cache line is present only in the current cache, is clean and it's same as of main memory. It can be changed to the Shared state at any time, in response to a read request. Alternatively, it may be changed to the Modified state when write operation is done.

Shared: Indicates that this cache line may be stored in other caches of the machine as well and is clean and it matches the main memory. The line may be discarded at any time.

Invalid: Indicates that the cache line is invalid. The detailed explanation is shown in figure 2.

If we compare MESI and MSI protocol then MESI is better than MSI protocol [2] because for every write operation two transitions are performed, even when the data block is just taken into consideration is not shared. In the first transition it places the memory block in shared state and in second transition causes write, which also changes the state of that shared data block from shared state to modified state. It includes a new state to MSI protocol i.e. Exclusive state which reduces the traffic because of write operation performed for the shared data block [2].

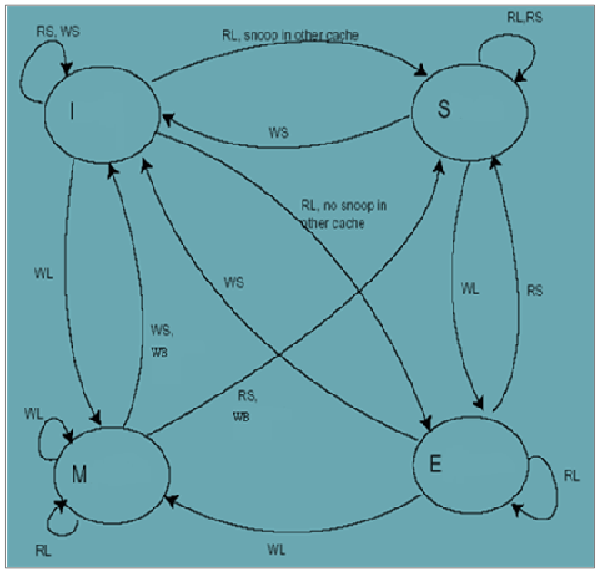

WS: write snoop WL: write local CPU

RS: read snoop RL: read local CPU

WB: write back

Figure 2: State Diagram of MESI Protocol.

For this Experiment we have taken level 2 cache as private, therefore all the results mentioned in below sections are concern with level 2 cache as private only.

III. PROPOSED IDEA

We have intensely studied the code of MARSSx86 simulator and noticed that in the existing code of MESI protocol invalid to invalid transitions are present. We believed that if we can modify or eliminate this transition in this code then it should improve the system performance by making this transition zero or reducing it at very high extent and in terms of cycles per second and commits per second also. In the next section we have mentioned the experimental work for this proposed idea.

IV. RELATED WORK

As mentioned in above sections too that MARSSx86 (Micro Architectural and System Simulator) is a simulator that works only with 64-bit operating system and 64-bit processor. So first of all we have to install LINUX (UBUNTU 11.10) on the system. After getting done with the installation of this operating system successfully, we installed MARSSx86 simulator through the github (used to download the open source code of the software). Though we faced lots of complicated problems while compiling and running the MARSSx86 simulator but at the end we have overcome all of them. Then we started with the standard results and kept level 2 cache as shared.

We used the programs of PARSEC (Princeton Application Repository for Shared-Memory Computers) benchmark for getting all the results viz. FERRET, CANNEAL, SWAPTIONS. We keep on changing number of cores viz. 2 (dual), 4 (quad), and 8 (octet) for getting the standard and the modified results. After getting the standard results of our experiment we continued with our task i.e. modifying the actual code of MESI protocol existing in the MARSS simulator. After extensive study of MARSSx86 simulator's code which is available as open source, we have modified the code of file mesiLogic.cpp which contains the nitty-gritty of MESI protocol while executing with MARSSx86 simulator. In this file there are invalid to invalid transitions. We have modified the code precisely. Then compiled and executed this modified code with CANNEAL, FERRET and SWAPTIONS (programs of PARSEC benchmark) with the variation of number of cores i.e. 2, 4 and 8. After getting experiment results in the form of stats files (results of experiment comes in the form of stats file) for the modified code we carefully compared these files with the standard stats files. We have noticed that by keeping number of cores 2 i.e. dual core we have made invalid to invalid transition as zero successfully for all 3 programs of PARSEC benchmark viz. CANNEAL, FERRET and SWAPTIONS at level 1data cache.

V. EXPERIMENTS AND RESULTS

We have successfully made depreciated invalid to invalid transitions. As visible in table1 results that by keeping number of cores as two we have successfully made invalid to invalid transition directly to zero at level 1 data cache for all three programs i.e. CANNEAL FERRET and SWAPTIONS of PARSEC benchmark.

Then we compared the experiment's results i.e. stats file for CANNEAL program of PARSEC benchmark with the standard results and we noticed that with quad cores (i.e. number of cores are 4) we have depreciated invalid to invalid transition successfully up to 99% and when we compared the stats file with octet cores (i.e. number of cores are 8) we noticed that then too we have in reduced invalid to invalid transition by 99%.

When we compared the results of FERRET program of PARSEC with quad cores configuration, we noticed that in with this program too we have successfully reduced invalid to invalid transition by 92%and with octet core we have decreased invalid to invalid transition by 99%.

After this we compared the results for SWAPTIONS program with quad cores configuration. In this we determined that invalid to invalid transitions are reduced up to 99% only. Then we compared for octet cores configuration and in this case too after comparing results with standard results we found that we have reduced invalid to invalid transitions upto99% only.

By reducing this invalid to invalid transitions at the great extent as mentioned in above paragraphs it will reduce the traffic of shared bus also so in this way we have enhanced the system performance. We have also noticed while analyzing results that with CANNEAL program of PARSEC benchmark we have increased the cycles per second at both kernel level and user level for dual cores and octet cores and commits per second are increased for octet cores configuration.

By taking FERRET program of PARSEC benchmark we have noticed that cycles per second are enhanced at both kernel level and user level with dual cores and with quad cores and octet cores commits per second are increased.

Table 1: Comparing results of actual code and modified code

No. of cores	Benchmark	INVALID TO INVALID TRANSITION IN STANDARD CODE RESULT	INVALID TO INVALID TRANSITION IN MODIFIED CODE RESULT
2	CANNEAL	2113	0
	FERRET	3279	0
	SWAPTIONS	2113	0
4	CANNEAL	13500	307
	FERRET	15320	167
	SWAPTIONS	2976	164
8	CANNEAL	13346	841
	FERRET	32800	327
	SWAPTIONS	62990	5666

With SWAPTIONS program of PARSEC benchmark we noticed that cycles per second are getting increased with dual cores, octet cores and with quad cores as configuration

commits per second are increased at both user level and kernel level.

V. CONCLUSION

By modifying or optimizing the existing code of MESI protocol of the MARSSx86 (Micro Architectural and System Simulator) simulator we have successfully made the invalid to invalid transition as zero for dual cores. When it comes to quad cores and octet cores then too we have attained success by 99% for FERRET and SWAPTIONS of PARSEC benchmark and 99% for SWAPTIONS of PARSEC benchmark in terms of invalid to invalid transitions abatement.

We have also heighten the cycles per second for CANNEAL eminently with dual and octet cores. With FERRET commits per second are escalated and with SWAPTIONS also we have increased cycles per second.

In this way we have optimized the existing MESI protocol and escalating the system performance by actualizing invalid to invalid transition as zero or reducing it at very high extent. This will deteriorate the bus traffic deliberately.

REFERENCES

[1] Silvia Lametti, “Cache Coherence Techniques”, A Technical Report, December 2010

[2] Manoj Kumar, Pooja Arora, “A Survey of Cache Coherence Protocols in Multiprocessors with Shared Memory”, ICACSEE’2012

[3] The MARSS website [Online]. Available: http://www.marss86.org/.

[4] Avadh Patel, Furat Afram, Shunfei Chen, Kanad Ghose, “MARSSx86: A Full System Simulator for x86 CPUs”, DAC’11, San Diego, California, USA.

[5] Matt Yourst, “PTLsim: A Cycle Accurate Full System x86-64 Microarchitectural Simulator”, Proc. ISPASS 2007.

[6] Standard Performance Evaluation Corporation CPU 2006 Benchmarks, http://www.spec.org/.

[7] M. S. Papamarcos and J. H. Patel, "A low-overhead coherence solution for multiprocessors with private cache memories," Proc. 11th Annual Int. Symp. on Computer Architecture, pp. 348-354, June 1984.

[8] Silvia Lametti, “Cache Coherence Techniques”, A Technical Report, December 2010.

All in-text references underlined in blue are linked to publications on ResearchGate, letting you access and read them immediately.

Egyptian Journal of Petroleum (2016) xxx, xxx–xxx

HOSTED BY

Egyptian Petroleum Research Institute

Egyptian Journal of Petroleum

www.elsevier.com/locate/egyjp
www.sciencedirect.com

FULL LENGTH ARTICLE

Kaner biodiesel production through hybrid reactor and its performance testing on a CI engine at different compression ratios

Ashok Kumar Yadav [a,*], **Mohd Emran Khan** [b], **Amit Pal** [c]

[a] *Department of Mechanical Engineering, Raj Kumar Goel Institute of Technology, Ghaziabad 201003, India*
[b] *Department of Mechanical Engineering, Faculty of Engineering & Technology, Jamia Millia Islamia, New Delhi 110025, India*
[c] *Department of Mechanical Engineering, Delhi Technological University, Delhi 110042, India*

Received 9 March 2016; revised 23 June 2016; accepted 25 July 2016

KEYWORDS

Hybrid reactor;
Hydrodynamic cavitation;
Mechanical stirring;
Kaner oil methyl ester (KOME);
CI engine

Abstract The present study deals with development of a hybrid reactor for biodiesel production based on the combined hydrodynamic cavitation and mechanical stirring processes. Biodiesel were produced using Kaner Seed Oil (KSO). The experimental results show that hybrid reactor produces 95% biodiesel yield within 45 min for 0.75% of catalyst and 6:1 M ratio which is significantly higher as compared to mechanical stirring or hydrodynamic cavitation alone. Thus biodiesel production process in hybrid reactor is cheap (high yield), efficient (time saving) and environmentally friendly (lower% of catalyst). Performance study on engine shows that an increase in compression ratios (from 16 to 18) improves the engine performance using biodiesel blends as compared to petroleum diesel.

© 2016 Egyptian Petroleum Research Institute. Production and hosting by Elsevier B.V. This is an open access article under the CC BY-NC-ND license (http://creativecommons.org/licenses/by-nc-nd/4.0/).

1. Introduction

The increasing industrialization and motorization of the world has led to steep rise for the demand of petroleum based fuels. Moreover the finite reserves of crude oil are concentrated in certain regions of the world and most of the developing countries are net importer of the crude oil. Large outflow of foreign exchange and uncertainty in its availability is a matter of great concern for developing countries like India. Diesel engines are more popular for their low fuel consumption and better efficiency. The Road sector diesel fuel consumption in India was 31,378 kT in 2009, according to World Bank Indicators, published in 2010 [1]. As per one of the study within 40 years, the present reserves of petroleum fuel including diesel will deplete at an increased consumption rate estimated to be order of 3% per annum [2]. Excessive use of fossil fuels has led to global environmental degradation effects such as greenhouse effect, acid rain, ozone layer depletion, climate change, etc. The main reason for increased pollution level in spite of stringent emission norms that have been enforced is the increased demand for energy in all sectors and most significantly the transport sector. Depleting reserves of crude petroleum, uncertainty in availability, environmental degradation and rapid hike in petroleum prices have led to search of alternate fuels [3], with

* Corresponding author.
E-mail addresses: ashokme015@gmail.com (A.K. Yadav), mikhan@jmi.ac.in (M.E. Khan), amitpal@dce.ac.in (A. Pal).

Peer review under responsibility of Egyptian Petroleum Research Institute.

http://dx.doi.org/10.1016/j.ejpe.2016.07.006
1110-0621 © 2016 Egyptian Petroleum Research Institute. Production and hosting by Elsevier B.V.
This is an open access article under the CC BY-NC-ND license (http://creativecommons.org/licenses/by-nc-nd/4.0/).

Please cite this article in press as: A.K. Yadav et al., Kaner biodiesel production through hybrid reactor and its performance testing on a CI engine at different compression ratios, Egypt. J. Petrol. (2016), http://dx.doi.org/10.1016/j.ejpe.2016.07.006

particular emphasis on the biofuels that pose the advantage of being renewable and show an ad hoc advantage in reducing CO_2 emissions [4]. Biofuels made from agricultural products (oxygenated by nature) reduce the dependence on oil imports, support local agricultural industries and enhance farming incomes. Moreover they also benefits in terms of reduced smokiness or particulate matter in engine exhausts. There are several factors that need to be taken care before recommending any alternate fuel to be used in existing technologies on a large scale. These factors are extent of modification required in existing hard wares, i.e., if any alternate fuel needs extensive modification in the existing hardware involving huge capital then it may be difficult to implement; investment cost for developing infrastructure to manufacture and supply these alternate fuels i.e. excessive infrastructure cost may act as a constraint for development of the alternative energy resources; environmental compatibility as compared to conventional fuels i.e. if a new fuel is more polluting then it will be unacceptable as a fuel; additional cost to the user in terms of routine maintenance, equipment wear and lubricating oil life i.e. excessive additional cost will have an adverse effect on the wide spread acceptance of this fuel [3]. Ethanol, biodiesel and biogas are the alternate fuels which have a high potential to gradually replace petroleum based fuels as they satisfy most of these parameters.

Biodiesel can be produced from triglycerides present in naturally occurring fats and oils by transesterification with alcohol, usually methanol, in the presence of a catalyst. The feed stocks used for biodiesel production currently are mainly high quality food grade vegetable oils, such as soya bean oil in U.S. A, rapeseed oil in Europe, palm oil in Malaysia [5]. Lower cost feed stocks, such as waste cooking oil, grease, soap stocks are preferred because of their economic viability, since feedstock costs are about more than 85% of the total cost of biodiesel production [6,7]. The non-edible oils like Jatropha, Kaner, Karanja, Mahua, etc. are largely used to produce biodiesel in India.

In mechanical stirring process mixing of oil and alcohol is carried by a motor operated mechanical stirrer. This is the most commonly used conventional technique. It has limitations of the time and capacity. Usually it is time consuming and used for small capacity biodiesel production. In hydrodynamic cavitation method mixing of two liquids is carried out by cavitation conditions, produced by pressure variation, which in turn is obtained using the geometry of system to create velocity variations. Cavitation is generated by the flow of liquid under controlled conditions through simple geometries such as venturi tubes and orifice plates. When the pressure at the throat falls below the vapour pressure of liquid, the liquid flashes, generating a large number of cavities which subsequently oscillate and then give rise to pressure and temperature pulses. These pulses cause the better mixing of immiscible liquids and enhance transesterification process [8]. Principle of ultrasonic cavitation method is the process of creating cavities by the irradiation of power ultrasonic with sufficient energy in immiscible liquid (oil and alcohol are immiscible with each other) as a result micro fine bubbles are formed and these bubbles are collapsing at various place of the reactor and disturb the phase boundary between two immiscible liquid. With the use of ultrasound biodiesel can be produced without heating because the cavitation may lead to a localized increase in temperature at the phase boundary and enhance the reaction [9].

The oxygen content in the fuel facilitates a complete combustion of the fuel even in fuel rich zones during combustion in engine cylinder and thus reducing carbon monoxide (CO) and hydrocarbon (HC) emissions. The higher cetane number of biodiesel reduces the combustion delays and thus the probability of fuel rich zone formation. This led to reduction in HC and CO emissions [10–12]. Biodiesel molecule oxygen content, generates lower stoichiometric requirement of air in case of biodiesel combustion [13,14], which reduces the probability of fuel rich regions and the absence of aromatics in biodiesel fuel, those being considered soot precursors [15], results in reduction of particulate matter (PM) emissions. Nitrogen Oxides (NO_x) formation in engine exhaust is a direct function of combustion temperature. Lower temperature exists in combustion chamber with biodiesel due to overall leaner combustion and its lower LHV. However the higher NO_x values, w.r.t petroleum diesel fuel case, suggest that local oxygen availability has dominant effect [15]. Carbon deposits on cylinder head, piston top and injector tip for biodiesel fuelled engines were 40% less compared to diesel fuelled engines. Carbonization of biodiesel injector after 512 h of operation was far less than the diesel injector after 200 h of engine operation [16].

The details of the hybrid esterification process using enzymes and chemical catalyst for biodiesel production is described by Ting et al. [18]. In the present study a hybrid process reactor has been designed which works on the principle of combined mechanical stirring and hydrodynamic cavitation processes. It is designed to enhance the reliability of the system, as both processes can be simultaneously used to make the biodiesel from Kaner seed oil (KSO). The present hybrid reactor is capable of processing 10–100 kg of oil. This study focuses on Kaner oil conversion into biodiesel. It is evident that most of the work has been focused on edible oils and a small quantum of work has been carried on non-edible oils for biodiesel production and its subsequent utilization. It is also pertinent to note that amongst the non-edible oils, Jatropha, Karanja, Mahua and some other feed stocks have been explored. However, Kaner (Thevetia Peruviana), which is an underutilized non-edible vegetable oil in India, is not adequately studied. The present work deals with the production and optimization of biodiesel production from Kaner oil its physico-chemical characterization and performance testing on a CI engine.

Kaner (Thevetia Peruviana) tree (shown in Fig. 1) is a very drought resistant poisonous plant found throughout India. It is most abundant in north-Indian plains of India, especially in Assam. It contains 52–60% of oil; hence it can be used to produce Bio-diesel in a large scale. It is widespread in American, Asian and African continents. It grows to about 10–18 feet high, the leaves are linear and about 13–15 cm in length arranged spirally and the flowers are funnel like and yellow in colour. An Oleander tree can produce about 800–1000 fruits all the year round depending on the climatic conditions and age of the plant. The fruits are usually green in colour and become black on ripening. Each fruit contains one to four seeds in its kernel and the oil content in the seed is high (60–65%) [19], which makes it a suitable naturally occurring renewable source of non-edible oil. A normal tree produces an average of 40–50 kg of fruit every season. Seeds obtained

Please cite this article in press as: A.K. Yadav et al., Kaner biodiesel production through hybrid reactor and its performance testing on a CI engine at different compression ratios, Egypt. J. Petrol. (2016), http://dx.doi.org/10.1016/j.ejpe.2016.07.006

Figure 1 Kaner plant with fruits.

Figure 2 Kaner kernels.

from the Kaner tree are crushed using a mechanical expeller for oil extraction.

Present research work deals with identifying low cost and potential feedstock for biodiesel production; determination of various physico-chemical properties of biodiesel; and its performance testing. Compression ratio is one of the most important factors affecting engine performance and emission characteristics. Increasing the compression ratio had more benefits with biodiesel than with pure diesel. Due to its low volatility and higher viscosity, biodiesel performs badly at lower compression ratios due to reduced cylinder pressure and temperature. Biodiesel might be performing relatively better at higher compression ratios due to increased pressure and temperature inside the combustion chamber which will result in good droplet atomization and combustion [17]. However, it has been found to be noted that the study on variable compression ratio engine using bio diesel is limited. The effect of compression ratio on engine parameters, emission and combustion characteristics have not been studied extensively. This paper analyses effect of compression ratio on engine performance and emission characteristics for various blends and pure diesel.

2. Materials and method

The Kaner fruits shown in Fig. 1 were collected from plants grown in Delhi Technological University Campus, Delhi, (India). Mature fruits were collected two times a year (summer and winter seasons), pulps removed, seeds dried in sunlight, deshelled and the kernel (Fig. 2) crushed using a grinder prior to oil extraction. A Soxhlet apparatus and *n*-hexane as extraction solvent were used for oil extraction from Kaner seed. Oil extracted by solvent extraction method is shown in Fig. 3. Solvents and other chemicals used were of analytical grade, and they were procured from commercial sources and used as such without further treatment.

3. Experimental work

3.1. Development of the hybrid reactor

The schematic diagram of the hybrid reactor (combined hydrodynamic cavitation and mechanical stirring) is shown in Fig. 4. The set-up consists of a closed loop circuit comprising an oil pre heating tank of approximately 120 l capacity, mechanical stirring tank of approximately 120 l capacity, reciprocating pump (maximum pressure 600 psi, 3HP, 950 RPM), a control valve and a coupling to accommodate the orifice plate. The suction side of the pump is connected to the bottom of the mechanical stirring tank. Discharge from the pump branches into two lines, a bypass line which helps in the control of inlet pressure and inlet flow rate into the main line housing and the orifice with the help of valves. The main line consists of a coupling to accommodate the orifice plate. The diameter of orifice hole was 1 mm passing through an orifice. The liquid in the main line after passing through orifice undergoing cavitation and subsequently processes it is feedback to the mechanical stirring tank where mechanical stirring of rest of the liquid is going on. The remaining liquid again goes to the reciprocating pump and continuous circulation of

Please cite this article in press as: A.K. Yadav et al., Kaner biodiesel production through hybrid reactor and its performance testing on a CI engine at different compression ratios, Egypt. J. Petrol. (2016), http://dx.doi.org/10.1016/j.ejpe.2016.07.006

Figure 3 Kaner seed oil.

liquid takes place in a closed loop circuit. Hydrodynamic cavitation facilitates the transesterification of the reactants liquid. When this high viscosity liquid strikes the remaining liquid in the mechanical stirrer it further increases agitation and the reaction takes place rapidly. There is provision to collect the samples from bottom of the mechanical stirrer frequently during the process. After the completion of reaction, the reactant liquid is pumped to the water washing tank so that next batch may be processed in reactor. The control panel has provision to operate mechanical string and hydro volume cavitation processes separately or together. In water washing tank first, reactant liquid is allowed to settle for about 2 h then from drain valve glycerine is separated then warm water at 70 °C at approx., 30% of the volume of biodiesel formed is mixed and gently stirred. This causes settling of impurities and catalyst in the lower part of the vessel after half an hour. Then this water is removed and remaining biodiesel is drained through the control panel and finally it is heated to a temperature of about 110–120 °C. The test rig also serves the purpose of individual mechanical stirring and hydrodynamic cavitation. In case of individual mechanical stirring the mixture is not allowed to pass through reciprocating pump by closing the valve between mechanical stirring tank and reciprocating pump. In case of individual hydrodynamic cavitation reactor the motor operating mechanical stirrer is switched off.

3.2. Experimental setup for performance testing

The setup consists of single cylinder, four strokes, Diesel engine connected to eddy current type dynamometer for loading. It is used with necessary instruments for combustion

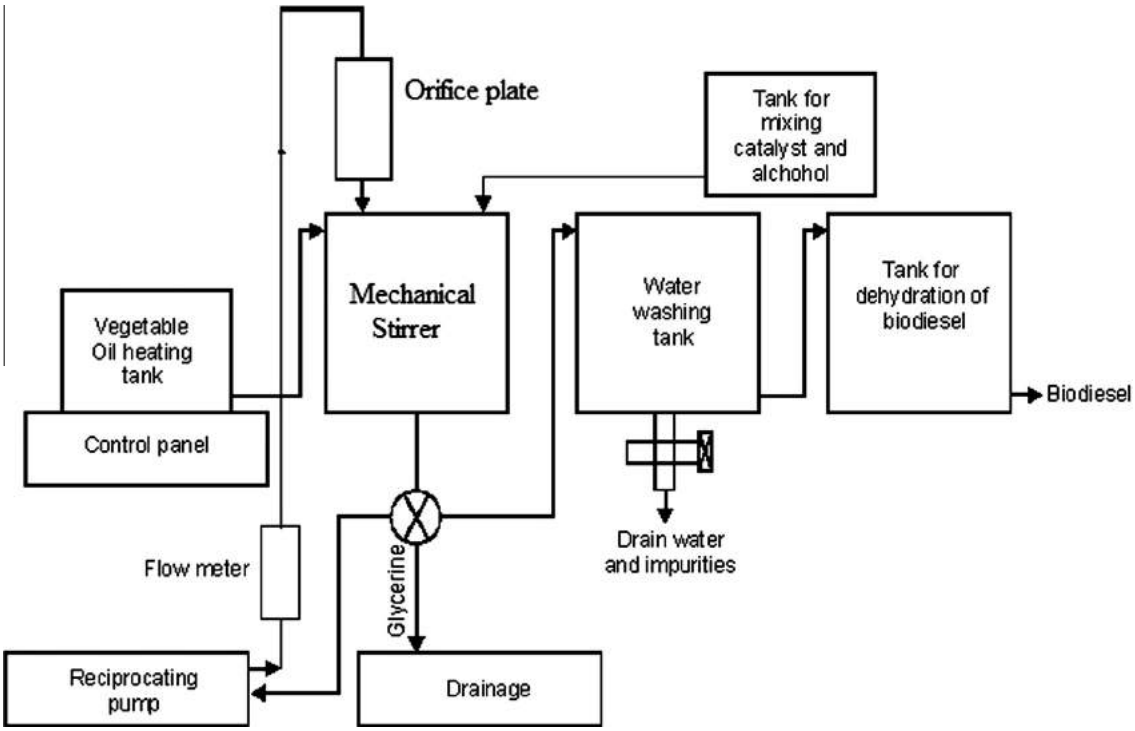

Figure 4 Hybrid reactor for combined hydrodynamic cavitation and mechanical stirring process.

Please cite this article in press as: A.K. Yadav et al., Kaner biodiesel production through hybrid reactor and its performance testing on a CI engine at different compression ratios, Egypt. J. Petrol. (2016), http://dx.doi.org/10.1016/j.ejpe.2016.07.006

pressure and crank-angle measurements. These signals are interfaced to computer through engine indicator for P–θ and P–V diagrams. Sensors are used for interfacing airflow, fuel flow, temperatures and load measurement. The setup has stand-alone panel box consisting of air box, two fuel tanks for duel fuel test, manometer, fuel measuring unit, transmitters for air and fuel flow measurements, process indicator and engine indicator. The engine specifications are given in Tables 1 and 2 shows the range, accuracy and uncertainty of measurements. The setup enables varying the compression ratio for the measurement of engine performance parameters like brake thermal efficiency (BTE) and brake specific fuel consumption (BSFC). Lab view based Engine performance Analysis software package "Engine soft LV" is used for on line performance evaluation. An AVL DIX, (Emission Diagnostic System) were used for measurement of smoke opacity.

4. Results and discussion

Experimental results of biodiesel production and performance testing for a wide range of operating parameters are described below:

4.1. Experimental results of biodiesel production

The filtered Kaner oil is heated up to 120–130 °C and kept on this temperature for about 5–7 min in order to remove the water content of oil to avoid soap formation and then allowed to cool up to 70 °C. Methyl alcohol (CH_3OH) with a molar ratio of 6:1 and sodium hydroxide (1%, 0 .75% and 0.5% by weight of oil), are mixed and stirred till sodium hydroxide dissolves in alcohol. The amount of vegetable oil, alcohol and catalyst taken are given in Table 3. This liquid mixture is supplied to the feed tank of the reactor. During the reaction, temperature of mixture is kept between 50 and 60 °C. After 30 min the first sample of 100 ml was collected from the bottom of the mechanical stirring tank. Samples were further collected after an interval of fifteen minutes.

After 75 min the process is stopped and glycerine was separated from each sample. The glycerine is allowed to settle down in the mixture as it has higher density than methyl esters. A layer of glycerine and methyl esters started to be visible in about 10 min of settling whilst complete settling takes place between 2–3 h duration. After the separation of the glycerine and methyl esters, the methyl esters were washed for all

Table 1 Technical details of the engine.

S. No	Component	Specification
1	Engine make	Kirloskar
2	Engine type	1 cylinder, 4stroke, water cooled
3	Rated power	3.5 kW at 1500 rpm
4	Cylinder volume	661 cc
5	Compression ratio	Variable (12–18)
6	Dynamometer	Eddy current, water cooled
7	Piezo sensors	Range 5000 PSI
8	Crank sensor	Resolution 1 Deg, Speed 5500 RPM
9	Load sensor	Load cell, type strain gauge,
10	Software	"Engine soft LV" Engine Performance analysis software

Table 3 Amount of Kaner oil, alcohol and catalyst used.

Percent catalyst (by weight of oil)	Kaner oil (kg)	Methanol (kg)	Catalyst (kg)
0.5	15	3.312	0.075
0.75	15	3.312	0.112
1	15	3.312	0.15

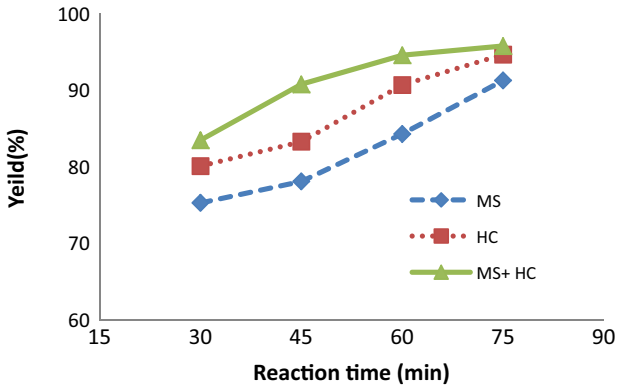

Figure 5 Biodiesel conversion yield at 0.5% NaOH by weight of oil.

Table 2 Range, accuracy and uncertainty of measurements.

Measurements	Instrument	Range	Accuracy
Engine load	Strain gauge type load cell	0–25 kg	±0.1 Kg
Speed	Speed sensor	0–2000 rpm	±20 rpm
Time	Stop watch	–	±0.5%
Exhaust Temperature	K-type thermocouple	0–1000 °C	±1 °C
Smoke density	Smoke metre	0–100%	±2%
Calculated results			Uncertainty
Engine power	–	0–8 kW	±1.0%
Fuel consumption	Level sensor	–	±2.0%
Air consumption	Turbine flow type	–	±1.0%
BTE	–	–	±1.0%
BSEC	–	–	±1.5%

Please cite this article in press as: A.K. Yadav et al., Kaner biodiesel production through hybrid reactor and its performance testing on a CI engine at different compression ratios, Egypt. J. Petrol. (2016), http://dx.doi.org/10.1016/j.ejpe.2016.07.006

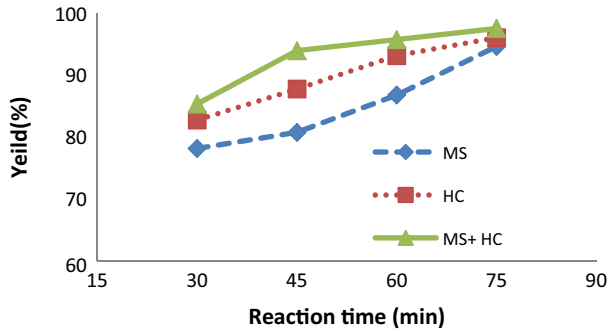

Figure 6 Biodiesel conversion yield at 0.75% NaOH by weight of oil.

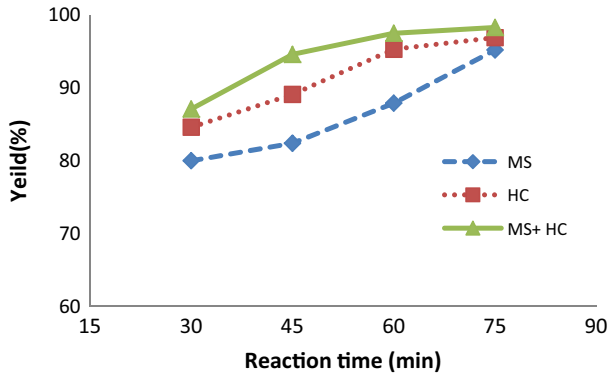

Figure 7 Biodiesel conversion yield at 1% NaOH by weight of oil.

samples to remove residual catalyst or soaps. For washing, first methyl esters and water up to 30% of methyl esters are kept in a separating funnel (at a temperature of 60 °C) and the mixture is stirred for one minutes and then left for settling of water with impurities. After complete settling of water with impurities at the bottom of separating funnel, the same is removed by opening the tab provided at the bottom of separating funnel. Figs. 5–7 represent the comparison of biodiesel yield production for mechanical stirring (MS), hydrodynamic cavitation (HC) and hybrid process (MS plus HC) for different percentages of a catalyst. The experimental data show that hybrid process is the most efficient one for all the observations as compared to other two processes. In the hybrid process, more than 90 percent yield is achieved within 45 min for the three cases compared to other two processes. The increase in the percentage of the catalyst (NaOH) improves the yield of biodiesel production for all three processes. For the hybrid process, the effect of an increase in catalyst on biodiesel yield is only between 0.5% and 0.75% for the duration of 30 to 45 min. Beyond 45 min, further effect of the increase in catalyst percentage is negligible on yield. Therefore, it may safely be concluded from experimental data of hybrid reactor, that 95% biodiesel yield can be achieved within 45 min for 0.75% of catalyst having 6:1 M ratio.

It was observed that higher yield was obtained for combined reactor as compared to hydrodynamic cavitation or mechanical stirring alone at all percentages of catalyst and for all reaction durations as shown. Percentage increase in yield was the maximum for 45 min sample for all the concentrations of catalyst. However percentage increase in yield showed a marginal decreasing trend with increasing reaction time beyond 45 min. Considerable improvement of biodiesel yield is observed when increasing the percentage of catalyst from 0.5% to 0.75% for all the processes. However a small improvement of biodiesel yield is observed when increasing the percentage of catalyst from 0.75% to 1% for all the processes.

4.2. Fatty acid composition

Gas chromatography (GC) analysis of Kaner seed oil revealed that it contains main acids as oleic acid (44.23%), palmitic acid (23.88%) and linoleic acid (21.82%) (Table 4).

4.3. Physico-chemical properties of Kaner seed bio-diesel and its blend

Various physico-chemical properties of Kaner Bio-diesel were determined according to standard methods. Table 5 presents the average values of the physico-chemical properties of Kaner biodiesel and diesel.

4.4. Results of the performance testing

Figs. 8–10 show performance characteristics at variable load conditions at different compression ratios (16 and 18) for neat diesel and diesel-KOME blends (B-20, B-40 and B-60).

4.4.1. Variation of BTE w.r.t. brake power

Fig. 8 shows the variation of BTE v/s brake power for diesel-KOME blends in comparison to petroleum diesel. For compression ratio equal to 16 (Fig. 8(a)), the trend for variation of BTE for petroleum diesel and biodiesel blends are almost coinciding with each other.

On the other hand, for a higher compression ratio (18) (Fig. 8(b)), biodiesel blends show significant improvement in BTE between 2 to 4 kW range of brake power. This gain in BTE as compared to diesel is due to the presence of oxygen in biodiesel molecules and its higher lubricity, which results in better combustion and lower frictional losses. Diesel-KOME blends show poor vaporization and atomization characteristics at lower compression ratios due to higher viscosity and lower volatility. This counteracts the effect of an increase in BTE due to the presence of oxygen in biodiesel molecules and higher lubricity. Similar trends are reported by Dilip Kumar Bora [20] and Hirkude et al. [23] for waste fried oil.

Table 4 Fatty acid composition of Kaner seed oil.

Fatty acids	Chemical formula	Degree of unsaturation	% value
Palmitic	$C_{16}H_{32}O_2$	16:0	23.28
Palmitoleic	$C_{18}H_{36}O_2$	16:1	0.88
Stearic	$C_{18}H_{34}O_2$	18:0	7.3
Oleic	$C_{18}H_{32}O_2$	18:2	44.23
Linoleic	$C_{20}H_{40}O_2$	18:2	21.82
Linolenic	–	18:3	.48
Arachidic	–	20:0	1.8

Table 5 Fuel properties of diesel and biodiesel blends.

Properties	Diesel	B20	B40	B60	B100
Density at 15 °C (kg/m^3)	0.84	0.846	0.845	0.852	0.87
Viscosity at 40 °C (mm^2/s)	3.1	3.3	3.5	3.8	4.2
Gross calorific value (MJ/kg)	43.2	43.04	42.9	42.7	42.4
Flash point (°C)	52 °C	56 °C	61 °C	66 °C	175 °C
Fire point (°C)	68 °C	71 °C	75 °C	78 °C	186 °C
Oxidation stability (h)	–	< 6.5	< 6.5	< 6.5	< 6.5

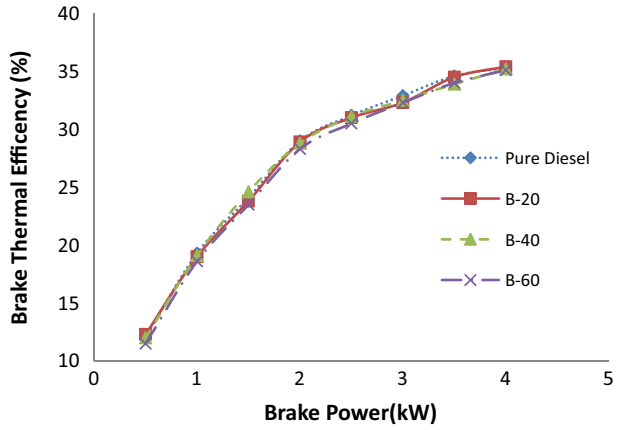

(a) CR = 16

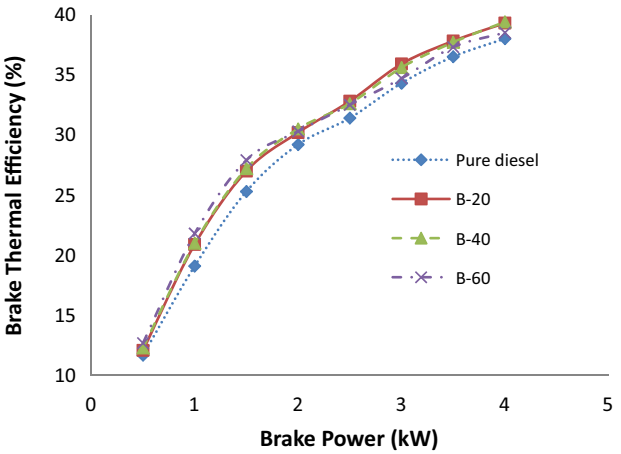

(b) CR = 18

Figure 8 Comparison of BTE v/s Brake Power for petroleum diesel and KOME.

4.4.2. Variation of BSFC w.r.t. brake power

Fig. 9 shows the variation of BSFC v/s brake power for diesel-KOME blends in comparison to neat diesel. Break Specific Fuel Consumption, BSFC is the ratio between mass fuel consumption and brake effective power, and for a given fuel, it is inversely proportional to BTE, for both CR values (16 and 18) (Fig. 9(a) and (b)).

BSFC values were found to be higher for diesel-KOME blends than for neat diesel. This is due to lower heating values

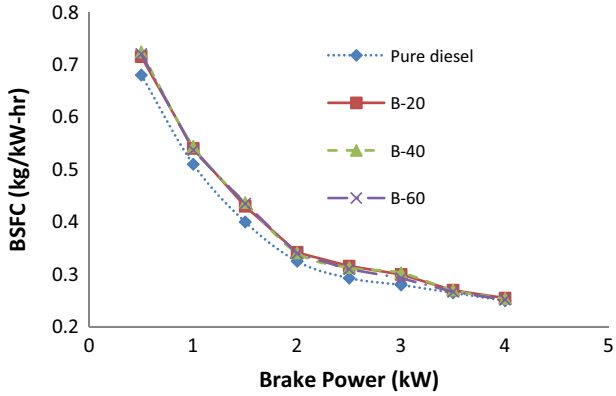

(a) CR = 16

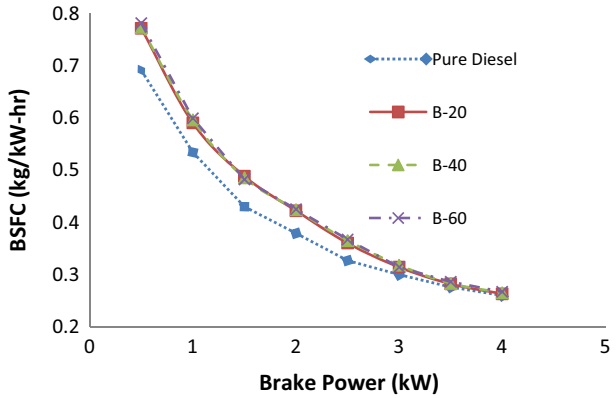

(b) CR = 18

Figure 9 Comparison of BSFC v/s Brake Power for neat diesel and KOME biodiesel.

of diesel-KOME blends and thus relatively higher fuel quantity is required for maintaining constant power output. BSFC reduces for both diesel and biodiesel blends with increase in compression ratio. Similar trend is reported by Muralidharan et al. [21] for waste cooking oil biodiesel.

4.4.3. Variation of smoke opacity w.r.t. brake power

Fig. 10 shows the variation of opacity data with brake power for biodiesel blends in comparison to petroleum diesel for two sets of compression ratio. Fig. 10(a) shows that smoke opacity value for neat diesel is lower as compared to all types of diesel-KOME blends at CR = 16. Biodiesel has about 10% oxygen by weight which results in a decrease of opacity.

However its higher viscosity contributes to the increase in opacity. At lower compression ratio (16) effect of volatility dominates the effect of oxygen content. Probably vaporization and atomization of high viscosity biodiesel fuel becomes difficult at lower compression ratios. Fig. 10(b) shows opacity value for all diesel-KOME blends increases from 1% to 33% between the brake power ranges of 0.5 and 4 kW having CR equal to18. For higher compression ratio, the trends regarding the variation of opacity values w.r.t. brake power is almost similar for all types of blends and the opacity value for petroleum diesel is higher as compared to biodiesel blends. Addition

Please cite this article in press as: A.K. Yadav et al., Kaner biodiesel production through hybrid reactor and its performance testing on a CI engine at different compression ratios, Egypt. J. Petrol. (2016), http://dx.doi.org/10.1016/j.ejpe.2016.07.006

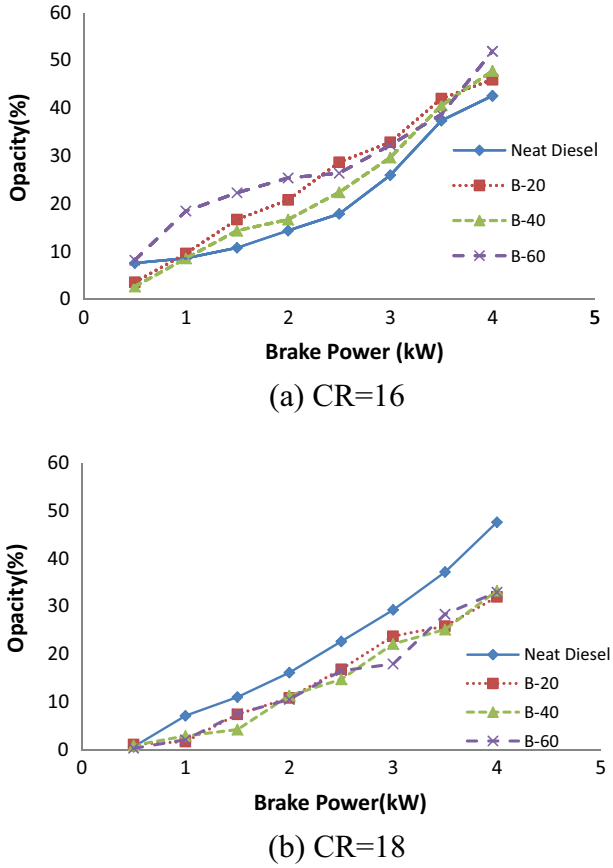

Figure 10 Comparison of smoke opacity v/s Brake Power for petroleum diesel and KOME biodiesel.

of KOME to neat diesel increases the viscosity and oxygen content of fuel. The effect of latter dominates at compression ratio 18 and thus a decrease in opacity is noticed for all diesel-KOME blends. Similar results are reported by previous researchers for different biodiesel blends [22,23].

5. Conclusions

The present study describes the performance of the novel hybrid reactor developed for efficient biodiesel production using Kaner oil. It is compared with conventional mechanical stirring and hydrodynamic process followed by performance testing on a CI engine. The outcome of the experimental results is as follows:

- Hybrid reactor produces 95% biodiesel yield within 45 min for 0.75% of catalyst and 6:1 M ratio which is significantly higher as compared to mechanical stirring and hydrodynamic cavitation.
- Performance study on a CI engine shows that an increase in compression ratio (from 16 to 18) improves the engine performance using biodiesel blends as compared to petroleum diesel.
- Opacity values were lower and BTE values were higher for diesel-KOME blends as compared to neat diesel for compression ratio equal to 18.
- Brake specific fuel consumption for diesel- KOME blends was higher as compared to petroleum diesel in spite of an increase in Brake Thermal Efficiency.

References

[1] World Bank Indicators-India-transportation, available from <www.tradingeconomics.com/india/road-sector-diesel-fuel-consumption-kt-of-oil> equivalent-wb-data.
[2] M.N. Nabi, M.M. Rahman, M.S. Akhtar, Appl. Therm. Eng. 29 (2009) 2265–2270.
[3] L. Lin, Z. Cunshan, S. Vittayapadung, S. Xiangqian, D. Minutesgdong, Appl. Energy 88 (2011) 1020–1031.
[4] A.C. Hansen, D.C. Kyritsis, C.F. Lee, in: A.A. Vertes et al. (Eds.), Biomass to Biofuels – Strategies for Global Industries, John Wiley, New York, 2009.
[5] N.M. Azam, A. Waris, N.M. Nahar, Biomass Bioenergy 29 (2005) 293–302.
[6] M.J. Haas, A.J. McAloon, W.C. Yee, T.A. Foglia, Bioresour. Technol. 97 (2006) 671–678.
[7] Y. Zhang, M.A. Dubé, D.D. McLean, M. Kates, Bioresour. Technol. 90 (2003) 229–240.
[8] A. Pal, A. Verma, S.S. Kachhwaha, S. Maji, Renewable Energy 35 (2010) 619–624.
[9] D.Y.C. Leung, X. Wu, M.K.H. Leung, Appl. Energy 87 (2010) 1083–1095.
[10] K.F. Hansen, M.G. Jensen, Chemical and biochemical characteristics of exhaust emissions from a DI diesel engine fuelled with rapeseed oil methyl esters (RME), SAE paper (1997) 971689.
[11] A.C. Pinto, L.L.N. Guarieriro, J.C. Rezende, N.M. Ribereiro, E.A. Torres, E.A. Lopes, et al, J. Braz. Chem. Soc. 16 (6B) (2005) 1313–1330.
[12] X. Shi, Y. Yu, H. He, S. Shuai, J. Wang, R. Li, Fuel 84 (2005) 1543–1549.
[13] O. Armas, J. Rodriguez, M.D. Cardenas, A.F. Agudelo, Efecto del biodiesel procedente de aceites vegetales usados sobre las emisiones y prestaciones de un motor diesel, Anales del 16 Congreso National de Ingenieria Mecanica, Leon, Spain, 2004.
[14] M. Lapuerta, O. Armas, R. Ballesteros, Diesel particulate emissions from biofuels derived from Spanish vegetable oils, SAE paper (2002) 2002-01-1657.
[15] C.D. Rakopoulos, A.M. Dimartos, E.G. Giakoumis, D.C. Rakopoulos, Appl. Energy 88 (2011) 3905–3916.
[16] A.K. Agarwal, J. Bijwe, L.M. Das, J. Eng. Gas Turbine Power (ASME J.) 125 (3) (2003) 820–826.
[17] M.E.L. Kassaby, M.A. Nemit allah, Alexandria Eng. J. 52 (2013) 1–11.
[18] W.J. Ting, C.M. Huang, N. Giridhar, W.T. Wu, J. Chin. Inst. Chem. Eng. 39 (39) (2008) 203–210.
[19] O.O. Omolara, A.I. Samuel, Afr. J. Biotechnol. 6 (18) (2007) 2166–2170.
[20] Dilip Kumar Bora, J. Sci. Ind. Res. 68 (2009) 960–963.
[21] K. Muralidharan, D. Vasudevan, K.N. Sheeba, Energy 36 (2011) 5385–5393.
[22] T. Murayama, Y. Fujiwara, T. Noto, Inst. Mech. Eng. (2000) 141–148.
[23] Jagannath B. Hirkude, Atul S. Padalkar, Fuel 119 (2014) 266–273.

Please cite this article in press as: A.K. Yadav et al., Kaner biodiesel production through hybrid reactor and its performance testing on a CI engine at different compression ratios, Egypt. J. Petrol. (2016), http://dx.doi.org/10.1016/j.ejpe.2016.07.006

Volume 4, Issue 1 (2016) 136-139 ISSN 2347 - 3258
International Journal of Advance Research and Innovation

Mathematical Modeling of Solid Oxide Fuel Cell and Gas Turbine Hybrid System for Enhancing Thermal Performance

Smita Sharma[1], R. S. Mishra[2*]
[1] Laser Science and Technology Centre (LASTEC), DRDO, Metcalfe House, New Delhi, India
[2] Department of Mechanical Engineering, Delhi Technological University, Delhi, India

Article Info

Article history:
Received 20 January 2016
Received in revised form
10 February 2016
Accepted 28 February 2016
Available online 15 March 2016

Keywords
Gas Turbine,
Solid Oxide Fuel Cell,
Energy

Abstract

Fuel cell systems are environment friendly. It is a clean energy generator but it has a low efficiency when it is used alone. Gas turbine also has a lower efficiency around 30% when working alone. Hybrid system is the combination of gas turbine and fuel cell to achieve a higher efficiency around 60-70%. The fuel cell generates the major portion of the plant power output and the gas turbine generates a fraction of total power output. The major advantage of fuel cell is that it is not a heat engine so its efficiency can be 100 % as it is not limited by the Carnot efficiency. Solid oxide fuel cell (SOFC) combined with gas turbine (GT) hybrid plants produce 50 times less nitrous oxide than current conventional gas turbine and 75% less carbon dioxide than coal- fired power plants. This type of hybrid system has a wide application such as decentralised electricity supply in houses and buildings, heat and cooling energy. The present paper includes reviews of the work done in the field of SOFC/GT hybrid system, mathematical modelling using Methane as a fuel to the hybrid system is presented and future scope of work is discussed.

1. Introduction

There is an ongoing energy crisis due to increasing use and diminishing resources of fossil fuels and another factor is environmental issues such as emission and global warming due to which people are thinking about renewable energy sources and highly efficient energy conversion system. Fuel cells have the potential for high energy conversion. The latest type and probably the best suited for central power generation is the solid oxide fuel cell (SOFC). These cells use a solid ceramic electrolyte of yttrium zirconium which the operating temperature ranges from about 600 to 1000 °C. Hybrid system uses a high temperature fuel cell and gas turbine to achieve higher overall performance than a single mode power plant. Heat can be recovered from the high temperature exhaust gas and used to drive a gas turbine. In the gas turbine exhaust gases expand and produces additional power. This hybrid system is a combination of two systems. One is gas turbine which acts as a heat engine. The other one is fuel cell which is a non heat engine. The efficiency and the performance of this hybrid system are far better than provided by either system alone. Basically in this hybrid system coupling of fuel cell and gas turbine is performed for power generation. Coupling can be performed by two methods by indirect method or integration of a micro gas turbine and SOFC by a heat exchanger and by direct method or integration of micro gas turbine and fuel cell directly.

2. Literature Review

Feasibilities of SOFC/GT hybrid systems have been investigated by numerous researchers. R. A. Roberts and J. Brouwer [1] compared and presented the Results of the dynamic model and experimental data gathered during the operation and testing of the 220kW SOFC/GT at the National Fuel Cell Research Center. Shinji Kimijima and Nobuhide Kasagi[2] investigated a conceptually designed 30 kW capacity SOFC/GT hybrid micro generation system and Result shows that variable speed mode is more advantageous to performance degradation under pert load condition . Denver F. Cheddie, Renique J Murray [3] developed a thermo-economic model for the hybrid power plant, and predicts an optimized power output of 20.6 MW at 49.9% efficiency. Sordi, E. P. da Silva, A. J. M. Neto, D. G. Lopes, C. S. Pinto, P. D. Araújo[4] presented a methodology to simulate a small-scale fuel cell system for power generation using biomass gas as fuel. The comparison with the efficiency of simple gas turbine cycle and regenerative gas turbine cycle shows the superiority of SOFC for the considered electrical power range. Leto, Celidonio Dispenza, Angelo Moreno, Antonio Calabr`o [5] performed the steady state simulation of the Hybrid System shown that the efficiency both of the Electrochemical Unit and of the whole Hybrid System can be higher than that of gas –steam turbine conventional power plant. The overall electrical efficiency could reach a very high value (up to 60%) and total efficiency could be over 70% including the contribution due to heat recovery. Sivan Kartha, Thomas G. Kreutz, and Robert H. Williams [6] calculated the total system efficiency of a power plant in which the fuel cell accounts for approximately three quarter of the generated power (149 kW) and the gas turbine one quarter (50 kW) based upon electrical output of the design. It was calculated to be 43.4%. Senthil V. Vannivedu Umapathi, Kiran Rao Bhimma and Parchuri M. V. Subbarao[7] successfully modeled methane fed hybrid SOFC-GT power generation system of 1.25 MW capacities. It has been demonstrated that SOFC-GT can achieve 60% net electrical efficiencies. Xiao-Juan Wu, Qi Huang Xin-Jian Zhu [8] proposed a least square support vector machine (LS—SVM) identification model based on a improved particle swarm optimization (PSO) algorithm to describe the nonlinear temperature dynamic properties of the SOFC/MGT hybrid system. A

Corresponding Author,
E-mail address: professor_rsmishra@yahoo.co.in
All rights reserved: http://www.ijari.org

SOFC/MGT physical model is established via Simulink toolbox of MATLAB6.5. Compared to the conventional BP neural network and the standard LS-SVM, The simulation results show that the modified LS-SVM model can efficiently reflect the temperature response of the SOFC/MGT hybrid system. Rama S.R. Gorla, Shantaram S. Pai and Jeffrey J. Rusick [9] performed a probabilistic analysis of SOFC/GT hybrid system. The cycle achieved a thermal efficiency of 64.1 percent at a pressure ratio of 14. The specific power output was found to be 520 W/kg s. Said Al-Hallaj, Fuad Alasfour, Sandeep Parekh, Shabab Amiruddin, J.Robert Selman, Hossein Ghezel-Ayagh[10] proposed and investigated a novel concept for integrating fuel cells with desalination systems . Results indicate that such hybrid system could show a 5.6% increase in global efficiency. Bang-Møller Christian, Rokni Masoud [11] presented a system level modelling study of three combined heat and power systems based on biomass gasification. By combining the SOFC and MGT, the unconverted syngas from the SOFC is utilized in the MGT to produce more power and the SOFC is pressurized, which improves the efficiency to as much as 50.3%.

A clean method of power generation is electrochemical extraction of energy from hydrogen via fuel cell. This technology is very suitable for a post fossil fuel based energy economy. But transition from the fossil fuel to hydrogen based system will take time and it is complicated also. There are various types of fuel cell in which solid oxide fuel cell is well suited. The operating temperature of SOFC is very high which facilitates the combination with gas turbine to reach electrical efficiencies beyond the limitations of conventional technologies. Fuel cell is well suited for distributed power generation as it can achieve higher efficiency even for small units. An experimental investigation of this system for design and performance evaluation is very expensive so mathematical modelling of the system and its simulation proves to be inexpensive. In present paper Mathematical modelling is presented for SOFC/GT hybrid system.

3. System Configurations

A schematic diagram of the tubular SOFC/GT hybrid power system using methane as fuel is given in Fig.1. The compressed methane is heated in heat exchanger. In the internal reformer, methane is reformed by using steam and heat from the SOFC. Reforming reaction is as follows:

$CH_4 + H_2O = CO + 3H_2$ & $Co + H_2o = CO_2 + H_2$

The Productions of reforming reaction are then fed to anode of SOFC. Ambient air is compressed by a compressor which is driven by a turbine and then heated in the heat exchanger by the hot gas stream from the turbine exhaust. The hot, high-pressure compressed air is then fed to the cathode section of SOFC. Natural gas and air are streamlined and passes through the anode and cathode sections respectively. The electrochemical reaction results into production of electrical energy and heat. The heat used to reform the natural gas and partly used to heat up the feedstock gases. The high temperature and pressure combustion products are channelled to turbine. In turbine, expansion occurred and pressure and temperature are reduced. The specification of hybrid system components are given in Table 1. The turbine outlet has high temperature and it can be used for increasing of compressor outlet in heat exchanger. Fuel cell electrochemical reaction is as

$½\ O2+2e^-=O^{-2}$ Cathode

$H_2+O^{-2}=H_2O+2e^-$ anode

$H_2+1/2O_2=H_2O$ Overall reaction

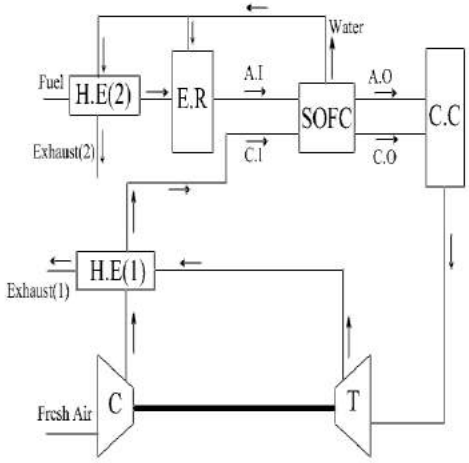

Fig: 1. Schematic Diagram of the Tubular SOFC/MGT Hybrid Power System [14]

Table: 1. Specification of the hybrid SOFC/MGT system [14]

Fuel Inlet Temperature (°C)	20	SOFC Temperature (°C)	800
Fuel Inlet Pressure (kpa)	300	SOFC Pressure (kpa)	300
Air Inlet Temperature(°C)	20	Air Inlet Pressure (kpa)	100
Cell Area (cm^2)	130	Number Of Cells	120
External Reformer Efficiency (%)	80	Air Stoich	6
Internal Reformer Efficiency (%)	80	Combustor Isentropic Efficiency%	98
Compressor Isentropic Efficiency%	87	Combustor Pressure drop%	4
Turbine Isentropic Efficiency (%)	89		

4. Over-potentials in SOFC

Due to irreversibility in the cell operation, the cell voltage, V, is always lower than reversible voltage E. This difference termed polarization and is the sum of three types of losses including, activation, ohmic and concentration.

(1) Activation Losses:

The energy barrier between the electrode and electrolyte results in a loss known as activation loss,

significant at low currents. The activation overvoltage is calculated using the Butler–Volmer equation [12],

$i=i_o[\exp(\alpha nF/RT\ xV_{act})- \exp(-(1-\alpha)nF/RTx\ V_{act})]$

$V_{act}=RT/Fxsinh^{-1}(i/i_o)$

Where α is the charge exchange constant and i_o is the exchange current density.

(2) Ohmic Losses:

The ohmic losses are calculated from following equation:

$V_{ohm}=I\Sigma_j[Ajexp(Bj/T)x\delta i]/Asj$

A, B, δ are the constants which can be taken from [13],

(3) Mass Concentration Losses:

$V_{con}=(RT/2F)\ln(1-i/i_l)$

Where i is the current in the fuel cell and il is the limiting current in that cell. Vcell = E − Vohm − Vconcetration – Vactivation

$P_{SOFC} = nIVcell$

Then the net power from the hybrid SOFC/MGT system is determined by

Pnet + PSOFC + Pturbine + Pcompressor

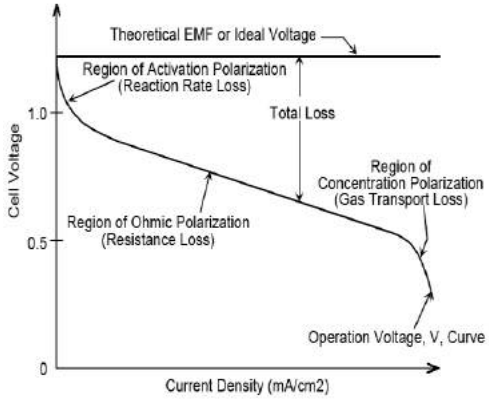

Fig: 2. Polarization curve [12]

5. Result

The effects of pressure of the cell voltage are shown in Fig.3.Improvment in the yield of the cell at higher current densities is clearly visible from the figure. By increasing the fuel mass flow rate, the output current value of the fuel cell increases therefore output power of the cell will be reduced. By increasing the fuel flow rate and therefore flow rate passing through the turbine, the power will increase.

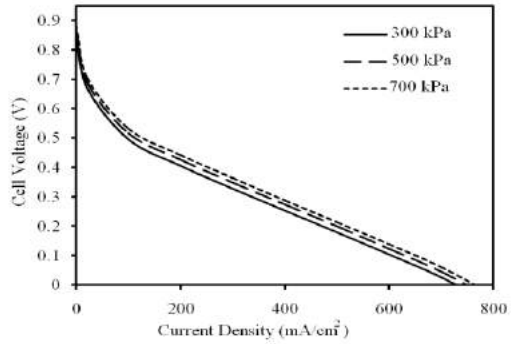

Fig: 3. Polarization Curve at Different Current Density [14]

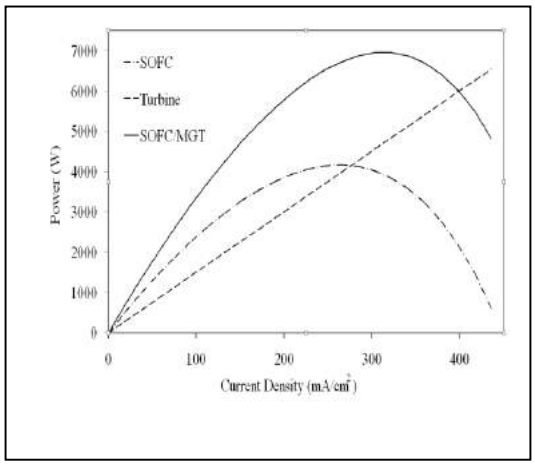

Fig: 4(a). Power produced by SOFC/MGT at different current densities. [14]

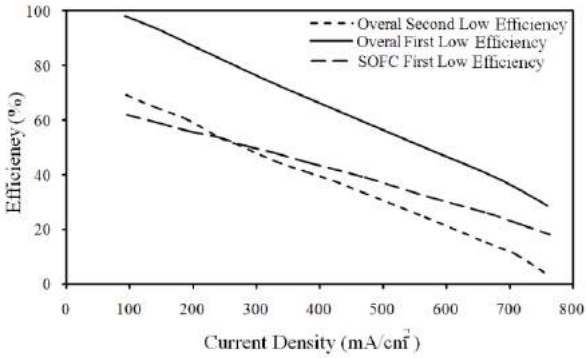

Fig: 4(b). Efficiency produced by SOFC/MGT at different current densities. [14]

6. Conclusions

In this paper, a review study was performed to assess various SOFC/GT hybrid systems. Effect of parameters on performance of a hybrid SOFC/MGT power system was observed. The parameters studied include temperature, pressure, the cathode flow rate, the anode flow rate, and percentage of fuel use. Power production and the first and second law efficiencies of the hybrid SOFC/MGT systems were observed from the literature. It is observed that simulation methods to simulate the SOFC/GT hybrid system are few. It is required to develop a mathematical model and simulate that model by using suitable simulation software.

References

[1] R. A. Roberts, J. Brouwer, Dynamic Simulation of a Pressurized 220kW220kW Solid Oxide Fuel-Cell–Gas-Turbine Hybrid System: Modeled Performance Compared to Measured Results, J. Fuel Cell Sci. Technol 3(1), 18-25

[2] Shinji Kimijima, Nobuhide Kasagi, Performance Evaluation of Gas Turbine-Fuel Cell Hybrid Micro Generation System", ASME Turbo Expo, 2002**,** 3–6, Amsterdam, The Netherlands

[3] Denver F. Cheddie, Renique J Murray, Thermo-economic modeling of an indirectly coupled solid

oxide fuel cell/gas turbine hybrid power plant, Journal Of Power Sources 195(24), 2010, 8134-8140

[4] A. Sordi, E. P. da Silva, A. J. M. Neto, D. G. Lopes, C. S. Pinto, P. D. Araújo, Thermodynamic Simulation of Biomass Gas Steam Reforming for A Solid Oxide Fuel Cell (SOFC) System, Brazilian Journal of Chemical Engineering, 26(04), 2009, 745 - 755

[5] Luigi Leto, Celidonio Dispenza, Angelo Moreno, Antonio Calabr`o, Simulation Model of a Molten Carbonate Fuel Cells - Microturbine Hybrid System, Applied Thermal Engineering, Elsevier, 31(6-7), 2011

[6] Sivan Kartha, Thomas G. Kreutz, Robert H. Williams, Small scal biomass fuel cell/Gas turbine power systems for rural areas, Energy for sustainable Development, 4(1), 2000

[7] Senthil V. Vannivedu Umapathi, Kiran Rao Bhimma and Parchuri M. V. Subbarao, Performance Analysis of Hybrid Solid Oxide Fuel Cell - Gas Turbine Power Generating System, The 2nd Joint International Conference on, Sustainable Energy and Environment (SEE 2006), 21-23 November 2006, Bangkok, Thailand

[8] Xiao-Juan Wu, Qi Huang Xin-Jian Zhu, Thermal modelling of a solid oxide fuel cell and micro gas turbine hybrid power system based on modified LS-SVM, International journal of hydrogen energy 36:885-892, 2011

[9] Rama S.R. Gorla, Shantaram S. Pai, Jeffrey J. Rusick, Probabilistic Analysis of Solid Oxide Fuel Cell Based Hybrid Gas Turbine System, NASA/TM—2003-211995, GT–2003–38046, 2003

[10] Said Al-Hallaj, Fuad Alasfour،,Sandeep Parekh, Shabab Amiruddin, J.Robert Selman, Hossein Ghezel-Ayagh, Conceptual design of a novel hybrid fuel cell/desalination system, Elsevier, Desalination, 164, 19–31

[11] Bang-Møller Christian, Rokni Masoud, Thermodynamic Performance Study of Biomass Gasification, Solid Oxide Fuel Cell and Micro Gas Turbine Hybrid Systems, Energy Conversion and Management, 51, 2010, 2330-2339

[12] J. Larminie, A. Dicks, Fuel Cell Systems Explained, John Wiley, NewYork, 2000

[13] F. Calise, Dentice d'Accadiaa, M. Palomboa A., L. Vanolib, Simulation and exergy analysis of a hybrid Solid Oxide Fuel Cell (SOFC)–Gas Turbine system, Journal of power sources, 158, 2006, 225-244

[14] Ahmad Tahmasebi, Ahmad Sedaghat, Rasool Kalbasi, Mahdi Moghimi Zand, Performance assessment of a hybrid fuel cell and micro gas turbine power system, Energy Equipment and Systems, *1*, (*2013)*, 59-74

Volume 4, Issue 1 (2016) 91-95 ISSN 2347 - 3258
International Journal of Advance Research and Innovation

Methods for Improving Thermodynamic Energy and Exergy Performance of Vapor Compression Refrigeration Systems Using Thirteen Eco-friendly Refrigerants in Primary Circuit and TiO_2 Nano Particles Mixed with R718 Used in Secondary Evaporator Circuit for Reducing Global Warming and Ozone Depletion

RS Mishra
Department of Mechanical Engineering, Production and Industrial & Automobiles Engineering, Delhi Technological University, Bawana Road, Delhi, India.

Article Info
Article history:
Received January 2016
Received in revised form
20 February 2016
Accepted March 2016
Available online June 2016

Keywords
Performance improvement, Vapor compression refrigeration systems, Energy and Exergy Analysis, Nano refrigerants Sustainable Technologies, Green Technologies, Sustainable Development , Alternative refrigerants, Eco-friendly refrigerants, Reduction in global warming , Reduction in ozone depletion

Abstract

The methods for improving energy and exergetic efficiency have been considered in this paper by using water as secondary coolant in evaporator with nano particles of Al_2O_3 and TiO_2 mixed R718 refrigerant is investigated in this paper. Detailed energy and exergy analysis of multi-evaporators at different temperatures in the vapor compression refrigeration systems have been done in terms of performance parameter for R507a, R125, R134a, R290, R600, R600a, R410a, R407c, R404a and R152a refrigerants**.** The numerical computations have been carried out for both systems. The use of nano particles improves the energy and exergy performance significantly. The best thermodynamic performance is found using R152a and worst performance is observed using R410a.

Due to flammable nature of R290, R600, R600a and R152a , the R134a is recommended for domestic applications. The results were compared by using water in secondary circuit with nano refrigerants and without nano-particles used and it was found that use of nano-particles improves thermal performances significantly. The energy performance improvement in terms of COP and exergetic performance in terms of exergetic efficiency (rational efficiency) using TiO_2 is better than using Al_2O_3 with R718 refrigerant in the secondary evaporator circuit.

1. Introduction

An eminent philosopher has defined Science as "TAPASAYA" and Technology as "Bhog" where as science is pure selfless and open to all search for truth where as technology is the exploitation of scientific knowledge for selfish purposes and profit motive and hence it tends to be secretive in this competititive world of today with a throat cutting environment. Sustainable Development is a process in which development can be sustained for generations. It also focuses attention on inter generational fairness in the exploitation of development opportunities while social development is a function of technological advancement, and also the technological advancement, in turn is a function of scientific know how for a streamlined development of the society. Technology is one of the crucial determinants of sustainable development. Technological import through collaborations has been one of the most important sources of technological inputs for Indian conditions. Use of technologies originating in rich countries often ten to create many social, ecological and resource problems in poor countries. The exploitation of the vast natural resources through progressive development of science, engineering and technology that has brought about the vast changes in the civilization and society from the stone age to the present high technology era. In facts, the mad race for industrialization and economic development has resulted in over exploitation of natural resources, leading to a situation where the two worlds of mankind- the biosphere, lithosphere and hydrosphere of his inheritance and the techno sphere of his creation, are out of balance with each other, indeed on a collision path. To facilitate optimal utilization of finite natural resources for ensuring a sustainable benefit steam for better quality of life on the one hand and to simultaneously keep in mind the conservation of natural resources on the other hand, it is essential that the technology conservation process must be made as efficient as possible. Therefore sustainable economic development depends on the careful choice of technologies and judicious management of resources for productive activities to satisfy the changing human needs without degrading the environment or depleting the natural resources base. The efforts under the Montreal protocol to protest the OZONE layer, the alternative refrigerants have been proposed as a substitute for ozone depleting

Corresponding Author, Email address:
professor_rsmishra@yahoo.co.in,
Professor.radheyshyammishra@gmail.com

All rights reserved: http://www.ijari.org

substances. HFCs (Hydro-fluoro carbons) PFCs (Per-fluro carbons) have zero ODP potential but they are producer of green house gases and are subjected to limitation and reduction commitments under UNFCC (United Nations Framework Convention on Climate change). With the entry into force of Kyoto protocol on 16th February 2005 developed countries have already planning and implementing rational measures intended to contribute towards meeting green house gas reduction targets during the first commitment period of Kyoto protocol (2008-2012). The countries have also started together with developing countries to size up projects that qualify under Kyoto clean development mechanism. All Governments will work together over next few years to decide on future intergovernmental action on the climate change. In this light, it is vital that there should be continuous work on the replacement options for ozone depleting substances in way that serve the aim of the Montreal protocol and UNFCC alike. In the developing countries the conversion of CFCs to alternate is still a major issue. In this paper the first law and second law analysis of various eco friendly refrigerants have been carried out which will help in deciding about the path to be followed to satisfy Montreal and Kyoto protocol.

2. Appropriate Vapor Compression Refrigeration Technology

Refrigeration is a technology which absorbs heat at low temperature and provides temperature below the surrounding by rejecting heat to the surrounding at higher temperature. Simple vapor compression system which consists of four major components compressor, expansion valve, condenser and evaporator in which total cooling load is carried at one temperature by single evaporator but in many applications like large hotels, food storage and food processing plants, food items are stored in different compartment and at different temperatures. R-22 is the refrigerant used for window type air conditioning systems long back. Due to Montreal protocol and Kyoto protocol and the provision of 1990 clean air act specifying phasing out the use of R-22 by the year 2030 due to ozone depleting potential around 0.055 as compared to the alternate refrigerants which have zero ozone depleting potential (ODP) and zero global warming potential (GWP).and some other alternate refrigerants which have less ODP & GWP. This paper , energy (first law) analysis and second law (exergy)analysis of vapor compression refrigeration systems have been carried out in terms of performance parameters such as COP, EDR, Exegetic efficiency, percentage of exergy destruction in components (i.e. condenser, compressor, throttle valve and evaporator) to total exergy destruction in the system for air conditioning system of 1.5 ton capacity for seven eco-friendly refrigerants such as (R-134a, R-404a, R-407C, R-502, propane(R-290), isobutene(R-600a), butane (R-600)) . These performance parameters have been evaluated for varying condenser temperatures in the range from 303 K to 333K and evaporator temperatures in the range from 253 to 278K of 1.5 ton capacity of vapor refrigeration systems by using eco friendly refrigerants. It was observed that R-290 (zero ODP & zero GWP) and R-600 (butane of zero ODP and zero GWP) and R-600a (isobutene of zero ODP and zero GWP) are best alternatives if its flammable problem will mitigate and the next option are R-134a (of zero ODP and 1300 GWP), R-407c(of zero ODP and 1530), R-404a (zero ODP and 3260 GWP)and R-410a (of zero ODP & 1730 GWP) for R-22 refrigerant but it needs the some modification in the existing design of components of vapor refrigeration systems (i.e. Larger size of compressors in case of R-134a,which increases the cost of the vapor compression refrigeration system.

3. Use of Multiple Evaporators Vapor Compression Refrigeration Systems.

Vapor compression refrigeration system based applications make use of refrigerants which are responsible for greenhouse gases, global warming and ozone layer depletion. Montreal protocol was signed on the issue of substances that are responsible for depleting Ozone layer and discovered how much consumption and production of ozone depletion substances took place during certain time period for both developed and developing countries. Another protocol named as Kyoto aimed to control emission of green house gases in 1997. The relationship between ozone depletion potential and global warming potential is the major concern in the field of GRT (green refrigeration technology) so Kyoto proposed new refrigerants having lower value of ODP and GWP. Internationally a program being pursued to phase out refrigerants having high chlorine content for the sake of global environmental problems .Due to presence of high chlorine content ,high global warming potential and ozone depletion potential after 90's CFC and HCFC refrigerants have been restricted. Thus, HFC refrigerants are used nowadays, showing much lower global warming potential value, but still high with respect to non-fluorine refrigerants. Therefore there is need of multi evaporator vapor compression refrigeration system. The systems under vapor compression technology consume huge amount of electricity, this problem can be solved by improving performance of system. The use of nano particles improves the first law and second law performance significantly. The best performance is found using R152a and worst performance is observed using R410a. Due to inflammable nature of R290, R600, R600a and R152a.

4. Literature Review

Lots of research work has been done for replacing "old" refrigerants with "new" refrigerants Ahamed et al. [1] emphasized on use of hydrocarbons and mixture compressor shows much higher exergy destruction as compared to rest of components in the vapor compression refrigeration system and this exergy destruction can be minimized by using of nano-fluid and nano-lubricants in compressor. Anand [2] did detailed exergy analysis of 2 ton of refrigeration capacity window air conditioning test rig with R22 as working fluid and reached to the conclusions , that irreversibility in system components will be highest when the system is 100% charged and lowest when 25% charged and irreversibility in compressor is highest among system components Arora et al.[3] developed numerical model of actual vapor compression refrigeration system with liquid vapor heat exchanger and

did energy and exergy analysis on the same in the specific temperature range of evaporator and condenser and concluded that R502 is the best refrigerant compared to R404A and R507A and compressor is the worst component and liquid vapor heat exchanger is best component of the system in case of exergy transfer. Bolaji et al. [4] had done experimentally comparative analysis of R32, R152a and R134a refrigerants in vapor compression refrigerator and concluded that R32 shows lowest performance whereas R134a and R152a showing nearly same performance but best performance was obtained of system using R152aChopra et.al (5) carried out analysis of energetic and exergetic Based comparison Multiple Evaporators with compound compression and flash intercooler with individual and multiple throttle valves and find out the effect of flash intercooler on second law performances. Han et al. [6] Under different working conditions experimental results revealed that there could be replacement of R407C in vapor compression refrigeration system having rotor compressor with mixture of R32/R125/R161 showing higher COP, less pressure ratio and slightly high discharge compressor temperature without any modification in the same system. Mishra et al. [7-9] performed numerical analysis of vapor compression refrigeration system using R134a, R143a, R152a, R404A, R410A, R502 and R507A , and discussed the effect of evaporator temperature, degree of sub-cooling at condenser outlet, superheating of evaporator outlet, vapor liquid heat exchanger effectiveness and degree of condenser temperature on COP and exergetic efficiency. They reported that evaporator and condenser temperature have significant effect on both COP and exergetic efficiency and also found that R134a has the better performance while R404a has poor performance in all respect. Saravana Kumar [10] compared the performance between R134a and R290/R600a mixture on a domestic refrigerator which is originally designed to work with R134a and found that R290/R600a hydrocarbon mixture showed higher COP and exergetic efficiency than R134a. In their analysis, highest irreversibility obtained in the compressor compare to condenser, expansion valve and evaporator. Based on the literature it was observed that researchers have gone through detailed first law analysis in terms of coefficient of performance and second law analysis in term of exergetic efficiency of simple vapor compression refrigeration system with single evaporator. Researchers did not go through the irreversibility analysis (second law analysis) of followings

(i) Simple VCR with nano particles used as secondary evaporator circuit in the water cooled evaporator

(ii) Detailed analysis of vapor compression refrigeration systems using thirteen eco-friendly refrigerants with effect of nano particles for improving their first and second law performances

This paper mainly deals with effect of nano particles (TiO_2 and Al_2O_3) mixed with R718 refrigerants was used in the water cooled evaporator for improving thermal performance of vapor compression refrigeration systems for keeping evaporator size constant due to enhancing heat transfer coefficient in the evaporator.

5. Performance Evaluation of Vapor Compression Refrigeration Systems

The computation modeling of vapor compression refrigeration systems was carried out with the help of EES for first and second law analysis in terms of energetic analysis i.e. COP (First law analysis) and exegetic analysis in terms of exergetic efficiency, exergy destruction ratio (EDR). In this analysis we assumed negligible pressure losses and heat losses. The comparative performance for condenser temperature varying between 320K to 330K, with increment of 2 and evaporator temperature is varying from 265K to 281 K with increment of 4. The energy and exergy change in vapor compression refrigeration cycle have been calculated for various eco friendly refrigerants such asR125, R507, R-134a, R404a, R410a, R407c R-290 (propane), R600 (butane), R-600a (isobutene) for environmental temperature of 298 and results are shown in Table (1-3) respectively. The performance of vapor compression refrigeration system using eco-friendly refrigerants in the primary circuit and TiO2 nano particles mixed in R718 is used in the secondary circuit of evaporators are shown in Table-(1). to Table-(3) respectively. And it was found that maximum First law efficiency in terms of COP and maximum second law efficiency in terms of exergetic efficiency using ecofriendly R152a and minimum first and second law performance using R410a. Due to flammable nature of R152a, and R290, R600 and R600a which can be used by considering safety measure gives better performance. The R407c R134a and R404a also give good performance for replacing R502, R11 and R12 and R22 which produces global warming and ozone depletion

Table-1: Performance prediction of vapor compression refrigeration system using TiO2 in R718 in the secondary circuit and Eco-friendly refrigerants in primary circuit for condenser temperature 48ºC and evaporator temperature of -5ºC

Refrigerant	COP	ETA_II	EDR
R404a	4.36	0.4831	1.694
R410a	2.14	0.2396	6.836
R134a	4.36	0.4880	1.659
R152a	5.169	0.5786	1.143
R507a	4.328	0.4844	1.685
R407c	4.736	0.5301	1.391
R290	4.826	0.5402	1.335
R600	3.605	0.4036	2.429
R600a	4.009	0.4480	1.969
R125	4.03	0.4511	1.949

Table 2 explaining the variation of condenser temperature with first and second law performance parameters and it was observed that increasing condenser temperature reduces first and second law performances and also increases exergy destruction ratio while Table-3shows the variation of evaporator temperature with first and second

law performance parameters and it was found that first law performance in terms of coefficient of performance and second law efficiency increases and exergy destruction ratio of system decreases

Table-2: Variation of performance parameters with condenser temperature in the vapor compression refrigeration system using R-134a in primary circuit and Water in secondary circuit

Condenser temp. (°C)	C.O.P.	η second	EDR
47	2.919	0.3013	0.6987
49	2.825	0.2859	0.7141
51	2.736	0.2713	0.7287
53	2.652	0.2575	0.7425
55	2.572	0.2442	0.7558
57	2.497	0.2316	0.7684

Table-3: Variation of performance parameters with evaporator temperature in the vapor compression refrigeration system using R-134a in primary circuit and water in secondary circuit

Evaporator temp. (°C)	C.O.P.	η second	EDR
-8	2.481	0.3105	0.6895
-4	2.767	0.3000	0.7000
0	3.096	0.2854	0.7146
4	3.467	0.2649	0.7451
8	3.880	0.2369	0.7631
12	4.327	0.1998	0.8002

.

The thermodynamic performance have been obtained using R-152a eco-friendly refrigerant and worst performances were found using R-410a eco-friendly refrigerants. Due to flammable nature of R290, R600, R600a and R152a it is recommended that R407c and R134a are suitable for industrial and commercial applications.

6. Conclusions

In this paper, first law and second law analysis of vapor compression refrigeration systems using multiple evaporators and single compressor and single expansion valve with eco-friendly refrigerants in the system and R718 (water used in secondary circuit with and without nano particles mixed with water used as refrigerant) have been presented. The conclusions of the present analysis are summarized below:

1. The First law efficiency (COP) and Second law efficiency (Exergetic efficiency) of vapor compression refrigeration systems using R718 mixed with nano particles gives better performance is than without nano particles used in the secondary circuit of water cooled evaporator for above mentioned eco-friendly refrigerants.
2. The First law efficiency (COP) and Second law efficiency (Exergetic efficiency) of vapor compression refrigeration systems using R152a refrigerant is higher but is has flammable nature similar to hydrocarbons then safety measures to be taken while using R152a or hydrocarbons (R290, R600 and R600a)
3. The first law performance in terms of Coefficient of performance and second law performance in terms of exergetic efficiency improves using TiO2 in the secondary evaporator circuit as compared to Al_2O_3 in the secondary circuit
4. COP and exergetic efficiency for R507a and R134a are nearly matching the same values are better than that for R125.
5. For practical applications R-407c, R134a and R404a, R125 can be used recommended because it is easily available in the market has second law efficiency slightly lesser than R-152a which was not applicable for commercial applications due to flammable nature and R717 is also toxic nature..
6. The first law performance improvement in terms of COP and second law performance in terms of exergetic efficiency (rational efficiency) using TiO_2 is better than using Al_2O_3 with R718 refrigerant in the secondary evaporator circuit.

Nomenclature

COP	coefficient of performance (non-dimensional)	h	specific enthalpy (kJ/kg)
VCR	vapour compression refrigeration	P	pressure (kPa)
CFC	chlorofluorocarbon	IR	irreversibility (kW)
HCFC	hydrochlorofluorocarbon	E_x	exergy rate of fluid (kW)
Q	rate of heat transfer (kW)	m	mass flow rate (kg/s)
W	work rate (kW)	s	specific entropy (kJ/kgK)
T	temperature (K)	EF	exergy rate of fuel (kW)
δ	efficiency defect (non-dimensional)	EL	exergy loss rate (kW)
ΔT_{sc}	degree of subcooling	η	efficiency (non-dimensional)
EP	exergy rate of product (kW)	r	refrigerant, space to be cooled
EV	Expansion Valve	ex	exergetic
EP	Evaporator	ev	expansion valve
Subscript		c	condenser
e	evaporator		

References

[1.] Ahamed, et.al. A review on exergy analysis of vapor compression refrigeration system. Int J Renewable and sustainable energy reviews. 15, 2011, 1593-1600.
[2.] Anand et.al-Exergy analysis and experimental study of a vapor compression refrigeration cycle .Int J Therm Anal Calorim.. 110, 2012, 961-971.
[3.] Arora, et.al Theoretical analysis of a vapor compression refrigeration system with R502, R404A and R507A. Int J Refrigeration.; 31, 2008, 998-1005.
[4.] B.O. Bolaji et.al. Comparative analysis of performance of three ozone-friends HFC refrigerants in a vapor compression refrigerator. Int J Sustainable Energy & Environment. 2, 2011, 61-64.
[5.] Chopra et.al. Energetic and Exergetic Based Comparison Multiple Evaporators with Compound Compression and Flash Intercooler with Individual or Multiple Throttle Valves International Journal of Advance & Research, 1,2013,73-81
[6.] Han, et.al Cycle performance study on R32/R125/R161 as an alternative refrigerant to R407C. Int J Applied Thermal Engineering.; 27,2007, 20072559-2565
[7.] Mishra RS et.al Methods for improving thermal performances of vapor compression Refrigeration system using eleven eco friendly refrigerants" ISTE conference on "Technological Universities and Institutions in New Knowledge Age: Future Perspectives and Action plan" ISTE paper NO:149, 2013,9.
[8.] Mishra RS. Irriversibility Analysis of Multi-Evaporators Vapor Compression Refrigeration Systems Using New and Refrigerants: R134a, R290, R600, R600a, R1234yf,R502, R404a and R152a and R12, R502" International Journal of Advance Research & Innovations International Journal of Advance Research & Innovations 1, 2013, 180-193.
[9.] Mishra RS Thermodynamic performance evaluation of multiple evaporators , single compressor ,single expansion valve and liquid vapor heat exchanger in vapor compression refrigeration systems using thirteen ecofriendly refrigerants for reducing global warming and ozone depletion" International Journal of Advance Research & Innovations3,2014,163-171
[10.] Mishra RS. Thermodynamic performance evaluation of multiple evaporators , single compressor ,single expansion valve and liquid vapor heat exchanger in vapor compression refrigeration systems using thirteen ecofriendly refrigerants for reducing global warming and ozone depletion" International Research Journal of Sustainable Science & Engineering. 2,(3), 2014,1-10
[11.] R.Saravanakumar, V.Selladurai-Exergy analysis of a domestic refrigerator using eco-friendly R290/R600a refrigerant mixture as an alternative to R134a.Int J Therm Anal Calorim.2013.

Volume 4, Issue 1 (2016) 215-218 ISSN 2347 - 3258
International Journal of Advance Research and Innovation

Micro-channel fabrication using electrical discharge machining process and optimization of parameters

Urfi Khan[1], Rituraj Jangid[1], Harsh Sharma[1], Mohd Shuaib[2,*]
Department of Mechanical Engineering, G.B. Pant Engineering College, Okhla, New Delhi India
Department of Mechanical Engineering, Delhi Technological University, Delhi, India

Article Info

Article history:
Received 20 January 2016
Received in revised form
10 February 2016
Accepted 28 February 2016
Available online 15 March 2016

Keywords
EDM, Die- sink EDM, Electro-discharge machining, microfluidic channel, micromachining, micro fabrication, microchannels, Taguchi, ANOVA, optimization, MEMS

Abstract

In this paper investigation of micro-channels fabrication using electrode sheets in die-sinking electrical discharge machining (EDM) process has been done. The micro-channels were fabricated on AISI D3 die steel using sheets of copper as electrode material. Parametric optimization for process parameters of EDM has been done using Taguchi Method. The control parameters taken were current, pulse-on time, pulse-off time, and voltage. Surface roughness was taken as response parameter.

1. Introduction

In the last few decades, owing to the rapid developments in micro-electronics and biotechnologies, the applied research in micro-coolers, micro-biochips, micro-reactors, and micro-fuel cells has been expanding at a tremendous pace. Among these micro-fluidic systems, micro channels have been identified to be one of the essential elements to transport fluid within a miniature area. In addition to connecting different chemical chambers, micro channels are also used for reactant delivery, physical particle separation, fluidic control, chemical mixing, and computer chips cooling (Jyh-tong Teng et al, 2012).

Micro channels are primarily used in biomedical devices and micro fluidic applications. Fabrication of micro channels has always been a tough task using conventional manufacturing technologies. Various types of materials are in use for fabricating micro channels in different types of applications including metals, polymers and ceramics. A number of methods are in use for fabricating different types of micro channels. These processes include both conventional and nonconventional fabrication techniques (Prakash Shashi, and Subrata Kumar, 2015). Some of the most established techniques include Micro-machining, lithography, Stereo lithography, Diffusion Bonding Chemical Etching, LIGA, embossing processes, and laser ablation processing, etc. In this paper fabrication of micro channels by electro-discharge machining process using copper sheet as electrode has been reported. Electro-discharge machining or EDM is a machining method primarily used for hard metals or those that would be impossible to machine with traditional techniques. So, electro discharge machining (EDM) is one of the most important non-traditional machining processes, which is used for machining difficult to machine materials like composites and inter-metallic materials (Trupti G. Raut and M.Y. Shinde, 2015).

In electro discharge machining the erosive action of an electrical discharge between conductive tool and work-piece is used to remove material. Electro-thermal erosion (material melting and evaporation for every spark) creates small craters both in the piece and in the tool during machining progress, then tool shape is copied in the work piece with a no contact system. With this technique it is possible to machine not only difficult to cut metals (like hardened steels) or carbides but also semiconductors and conductive ceramics. The discharge results from the application of an electrical voltage between electrodes (tool and work piece) with a dielectric flushed fluid interposed (Gentili, E, 2005).

We also used Taguchi method for optimization of EDM process parameters for surface roughness in the machined micro channels. The main disadvantage of this method is that the results obtained are only relative in nature and do not exactly indicate which parameter has the highest effect on the performance characteristic value. Hence, ANOVA is used for finding the most significant parameters. The schematic of the work piece and electrode sheet is shown in Figure 1. This is a fast process for cutting micro channels using electrode sheets as the complete micro channel is made using only the vertical movement of the electrode.

2. Experiments

2.1Materials & Measurements

The experimental studies were performed on EDM Die Sink ECOCUT by Electronica shown in Figure 2. Different settings of Current (Ip), Pulse-on Time (Ton), Pulse-off Time (Toff), and Voltage (Vg) used in the experiments are shown in Table 1. All other factors were kept constant during the experiments. Rectangular micro-channels of size 0.5mm X 0.9mm X 25mm were cut on the

Corresponding Author,
E-mail address: shuaib89141@gamil.com
All rights reserved: http://www.ijari.org

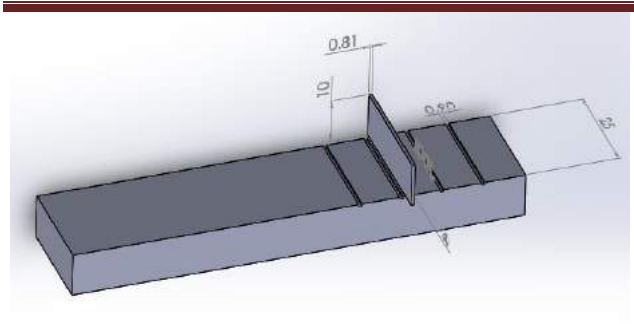

Fig. 1: Schematic of workpiece and electrode sheet

work piece of AISI D3 Die steel with 25mm × 200mm × 10mm size. AISI D3 die steel is one of the most extensively used materials in mould and die-manufacturing industry. The electrode used was copper sheet. Although doped copper may be used as electrode material in EDM because it has very high wear resistance. But for experimental purpose, as to save time and energy, copper sheets were used for better investigation of tool wear rates.

Fig. 2: EDM Set-up

The surface roughness for each micro-channel was measured using Surftest SV-2100 manufactured by MITUTOYO Pvt. Ltd. The Surftest is a high precision, high performance surface roughness tester with dedicated control unit mounted on a heavy-duty granite base with a choice of manual or power drum. The measured values of surface roughness are given in Table 2.

Table 1: Levels of machining parameters as used in experiments

S. No	Machining Parameter	Symbol	Level 1	Level 2	Level 3	Level 4
1	Current (A)	Ip	5	7	9	11
2	Pulse-on Time (µs)	Ton	10	20	30	40
3	Pulse-off Time (µs)	Toff	5	10	15	20
4	Voltage (V)	Vg	30	40	50	60

Table 2 Surface Roughness (Ra) Values

S. No.	**Surface Roughness (in micro-meters)**
1	4.370
2	3.716
3	3.326
4	2.963
5	4.035
6	4.026
7	3.406
8	4.477
9	3.969
10	3.984
11	3.874
12	3.237
13	4.454
14	4.036
15	3.795
16	2.771

2.2 Design of experiments based on Taguchi Method

The experiment was designed using Taguchi's design of experiments (Ross PJ, 1998), (Antony J and Antony FJ, 2001). L16 orthogonal array was chosen. Taguchi method is one of the simple and effective solutions for parameter design and experimental planning (Ross PJ, 1998). Taguchi method is a powerful technique for the design of a high quality system. It provides not only, an efficient, but also a systematic approach to optimize designs for performance and quality (Shahul Backer, 2014), (Siddiquee et al, 2014).

Any man-made system is viewed by Taguchi methods as an engineered system that comprises four main components as illustrated in Figure 3. It is designed to employ energy transformation in converting input signal into specific, intended function requested by customers by applying the laws of physics (Yih-fong Tzeng and Fu-chen Chen, 2007).

Taguchi methods advocate that appropriate design of the control factors makes the system transform energy very efficiently. Unintended effects due to noise factors that are the hardly controllable variables can be minimized. In theory, when all the applied energy is transformed into creating its intended function without any noise effects, a system reaches its ideal function (Yih-fong Tzeng and Fu-chen Chen, 2007) (Khan, Z.A et al, 2014).

The experiments were conducted with four control factors with four levels. Sixteen experimental runs based on the orthogonal array L16 were carried. Table 1 shows the four controlled factors, i.e., current (A (Ampere)), pulse ON time (B (µs)), pulse OFF time (C (µs)), and voltage (D (volts)) with four

levels for each factor. Figure 4 shows working of EDM. Table 3 shows the experimental trials according to the selected orthogonal table. After that the quality objective of the work-pieces was chosen, including the surface roughness Ra (μm). The values of all the parameters namely Current, Pulse ON, Pulse OFF and Voltage were kept at four levels as shown in Table 1.

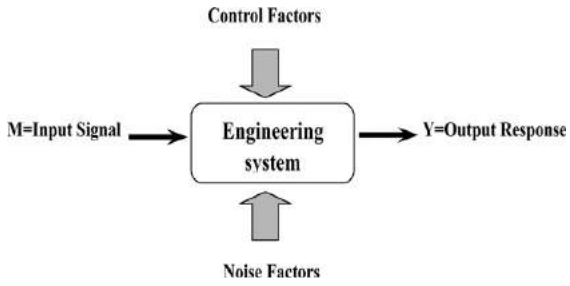

Fig.3: Schematic of an engineering system
Source: (Yih-fong Tzeng and Fu-chen Chen, 2007)

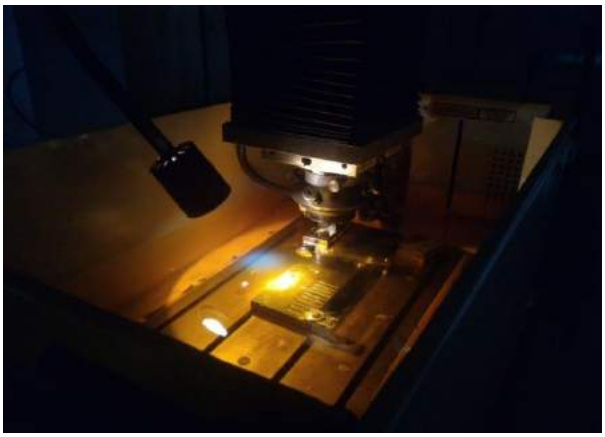

Fig 4: Working of EDM

Table 3 Experimental design using Taguchi L16 Orthogonal Array

S.No.	Current(Ip)	Pulse-on Time(T-on)	Pulse-off Time (T-off)	Voltage(Vg)
1	1	1	1	1
2	1	2	2	2
3	1	3	3	3
4	1	4	4	4
5	2	1	2	3
6	2	2	1	4
7	2	3	4	1
8	2	4	3	2
9	3	1	3	4
10	3	2	4	3
11	3	3	1	2
12	3	4	2	1
13	4	1	4	2
14	4	2	3	1
15	4	3	2	4
16	4	4	1	3

3. Results

3.1 Analysis of experiments

The experiments were conducted based on varying the process parameters, which affect the machining process to obtain the required quality characteristics. Quality characteristics are the response values or the output values expected out of the experiments. As the objective is to obtain best surface finish, we are concerned with obtaining smaller value of surface roughness. Hence, the required quality characteristic for Surface Roughness is smaller the better, which states that the output must be as low as possible. Table 4 shows the signal to noise ratios for the experiments.

ANOVA (Analysis of variance) was performed and the effects of individual parameters are shown in Table 5. And the Main Effect plot is shown in Figure 5.

Where DOF = Degree of Freedom
SS = Sum of Square
MS = Mean of Square

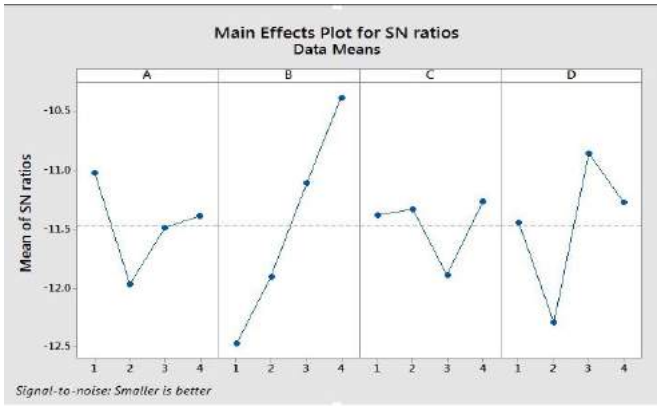

Fig 5: Main Effect Plot

Table 4: S/N Ratios

S.No.	A	B	C	D	Surface Roughness	S/N Ratio
1	1	1	1	1	4.37	-12.8096
2	1	2	2	2	3.716	-11.4015
3	1	3	3	3	3.326	-10.438
4	1	4	4	4	2.963	-9.4346
5	2	1	2	3	4.035	-12.1168
6	2	2	1	4	4.026	-12.0974
7	2	3	4	1	3.406	-10.645
8	2	4	3	2	4.477	-13.0197
9	3	1	3	4	3.969	-11.9736
10	3	2	4	3	3.984	-12.0063
11	3	3	1	2	3.874	-11.7631
12	3	4	2	1	3.237	-10.2028
13	4	1	4	2	4.454	-12.975
14	4	2	3	1	4.036	-12.119
15	4	3	2	4	3.795	-11.5842
16	4	4	1	3	2.771	-8.8527

Table 5: ANOVA table for Surface roughness

Symbol	**Process Parameter**	**DOF**	**Sum of Squares**	**Mean Squares**	**%Contribution**
A	Current	3	1.8206	0.6069	8.026
B	Pulse-on	3	9.0916	3.0305	40.087
C	Pulse-off	3	0.9626	0.3209	4.24
D	Voltage	3	4.0269	1.3423	17.75
Error		3	5.7902	1.9301	
Total		15	22.6833		

4. Conclusions

Micro-channels were fabricated on AISI D3 Die-steel using copper electrodes in the form of sheets. The effects of current, pulse on time, pulse off time, and voltage were experimentally investigated using Taguchi method and ANOVA. The combination of machining parameters $A_1B_4C_4D_3$ i.e. current at 5 A, pulse on time at 40 μs, pulse off time at 20 μs and voltage at 50 V was found to be optimum for minimum surface roughness. In addition, it was also found that pulse on time was the most dominant factor for surface roughness, its percentage contribution is maximum i.e. 40.087%. The level of importance of current, pulse off time and voltage, indicated by percentage contribution, on the surface roughness was observed to be 8.026%, 4.24%, and 17.75% respectively. This paper also demonstrates the effectiveness of the Taguchi approach to optimize machining parameters with minimum number of experiments.

References

[1.] Antony J, Antony FJ (2001) Teaching the Taguchi method to industrial engineers. Work Study 50(4):141–149 doi:10.1108/ 00438020110391873

[2.] Gentili, E., L. Tabaglio, and F. Aggogeri,(2005), " Review on micromachining techniques", Springer Vienna 2005

[3.] Jyh-tong Teng, Jiann-Cherng Chu, Chao Liu, Tingting Xu, Yih-Fu Lien, Jin-Hung Cheng, Suyi Huang, Shiping Jin, Thanhtrung Dang, Chunping Zhang, Xiangfei Yu, Ming-Tsang Lee, and Ralph Greif (2012). Fluid Dynamics in Microchannels, Fluid Dynamics, Computational Modeling and Applications, Dr. L. Hector Juarez (Ed.), ISBN: 978-953-51-0052-2, InTech, Available from: http://www.intechopen.com/books/fluid-dynamicscomputational modeling-and-applications/fluid-dynamics-in-microchannels

[4.] Khan, Z.A., Siddiquee, A.N., Khan, N.Z., Khan, U. and Quadir, G.A., (2014), "Multi response optimization of wire electrical discharge machining process parameters using Taguchi based grey relational analysis", Procedia Materials Science, 6, pp.1683-1695

[5.] Prakash, Shashi, and Subrata Kumar,(2015), "Fabrication of microchannels on transparent PMMA using CO2 Laser (10.6 μm) for microfluidic applications: An experimental investigation." International Journal of Precision Engineering and Manufacturing 16.2 (2015): 361-366.

[6.] Ross PJ (1998) Taguchi techniques for quality engineering. McGraw-Hill, New York

[7.] Shahul Backer, Cijo Mathew and Sunny K. George, (2014), "Optimization of MRR and TWR on EDM by Using Taguchi's Method and ANOVA", International Journal of Innovative Research in Advanced Engineering (IJIRAE) ISSN: 2349-2163, Volume 1 Issue 8

[8.] Siddiquee, Arshad Noor, Zahid A. Khan, Pankul Goel, Mukesh Kumar, Gaurav Agarwal, and Noor Zaman Khan, (2014), "Optimization of deep drilling process parameters of AISI 321 steel using Taguchi method." Procedia Materials Science 6 (2014): 1217-1225.

[9.] Trupti G. Raut and M.Y. Shinde (2015), "A Review on Optimization of Machining Parameters in EDM", International Journal of Innovative Research in Science, Engineering and Technology Vol. 4, Issue 3, DOI: 10.15680/IJIRSET.2015.0403013

[10.] Yih-fong Tzeng and Fu-chen Chen (2007) Multi-objective optimisation of high-speed electrical discharge machining process using a Taguchi fuzzy-based approach, Materials and Design 28 (2007) 1159–1168.

Modeling plasma-assisted growth of graphene-carbon nanotube hybrid

Aarti Tewari

Citation: Physics of Plasmas **23**, 083513 (2016); doi: 10.1063/1.4960328
View online: http://dx.doi.org/10.1063/1.4960328
View Table of Contents: http://scitation.aip.org/content/aip/journal/pop/23/8?ver=pdfcov
Published by the AIP Publishing

Articles you may be interested in

Water-processed carbon nanotube/graphene hybrids with enhanced field emission properties
AIP Advances **5**, 097130 (2015); 10.1063/1.4930966

Effective hybrid graphene/carbon nanotubes field emitters by electrophoretic deposition
J. Appl. Phys. **113**, 174909 (2013); 10.1063/1.4804238

Thermal conductivity of composites with hybrid carbon nanotubes and graphene nanoplatelets
Appl. Phys. Lett. **101**, 211903 (2012); 10.1063/1.4767899

Catalyst-free synthesis of reduced graphene oxide–carbon nanotube hybrid materials by acetylene-assisted annealing graphene oxide
Appl. Phys. Lett. **101**, 123107 (2012); 10.1063/1.4753928

Effects of micro- and macro-plasma-sheath electric fields on carbon nanotube growth in a cross-field radio-frequency discharge
J. Appl. Phys. **96**, 6053 (2004); 10.1063/1.1809777

Reuse of AIP Publishing content is subject to the terms at: https://publishing.aip.org/authors/rights-and-permissions. Downloaded to IP: 14.139.251.107 On: Wed, 17 Aug 2016 07:13:02

PHYSICS OF PLASMAS **23**, 083513 (2016)

Modeling plasma-assisted growth of graphene-carbon nanotube hybrid

Aarti Tewari
Department of Applied Physics, Delhi Technological University, Shahbad Daulatpur, Bawana Road, Delhi 110 042, India

(Received 4 July 2016; accepted 21 July 2016; published online 10 August 2016)

A theoretical model describing the growth of graphene-CNT hybrid in a plasma medium is presented. Using the model, the growth of carbon nanotube (CNT) on a catalyst particle and thereafter the growth of the graphene on the CNT is studied under the purview of plasma sheath and number density kinetics of different plasma species. It is found that the plasma parameter such as ion density; gas ratios and process parameter such as source power affect the CNT and graphene dimensions. The variation in growth rates of graphene and CNT under different plasma power, gas ratios, and ion densities is analyzed. Based on the results obtained, it can be concluded that higher hydrocarbon ion densities and gas ratios of hydrocarbon to hydrogen favor the growth of taller CNTs and graphene, respectively. In addition, the CNT tip radius reduces with hydrogen ion density and higher plasma power favors graphene with lesser thickness. The present study can help in better understanding of the graphene-CNT hybrid growth in a plasma medium. *Published by AIP Publishing.*
[http://dx.doi.org/10.1063/1.4960328]

I. INTRODUCTION

The integration of one dimensional (1D) allotrope of carbon (carbon nanotube) and two dimensional (2D) allotrope (graphene) is of significant interest due to their electrical, mechanical, and optical properties. Both graphene and carbon nanotube (CNT) are promising materials for field emission (FE) devices. While graphene owes it to its atomic thin edges and unique two-dimensional shape, CNT derives its high performance from its high aspect ratio.

Vertically aligned CNTs at preferably low temperatures have been grown extensively via plasma enhanced chemical vapor deposition (PECVD) process[1–8] and vertically aligned graphene too has been synthesized via PECVD process.[9–13] While the field emission (FE) properties of CNT grown via PECVD techniques are exemplary, the FE properties of graphene are still inferior to those of well verified one-dimensional field emitters such as CNT arrays.

Recently, a combination of one dimensional (1D) CNT and two dimensional (2D) graphene to give CNT-graphene hybrid materials has been reported. It is believed that along with reduced agglomeration and high aspect ratio of CNT along with the sharp edges of few layer graphene (FLG) could enhance the electrical properties which otherwise could not be realized using CNT or graphene alone.[14–17] CNT-graphene hybrid materials have been used to fabricate electron field emitters,[18,19] transparent conductors,[20] electrodes for the lithium ion battery,[21,22] and super capacitors.[23,24]

Experimentally CNT-graphene hybrid via arc-discharge,[25] solution process,[26] electrophoretic deposition,[16] chemical vapor deposition (CVD),[16,27] high-energy irradiation,[28] from rice husk by microwave plasma irradiation,[29] and physical vapor deposition[30] among others has been fabricated.

Lv *et al.*[31] have synthesized a novel hybrid structure named "rebar graphene," which is composed of covalently interconnected CNTs with graphene sheets. In this particular configuration, CNTs act as "reinforcing bars" that not only improve the mechanical strength of polycrystalline graphene sheets but also bridge different crystalline domains so as to enhance the electrical conductivity.

Chockalingam *et al.*[32] have synthesized multiwall carbon nanotube (MWCNT)-graphene-like nanocarbon hybrid films on nickel (Ni) substrate without any pre-treatment in a single-step by microwave PECVD technique and investigated the effects of hydrogen partial pressure on the growth of MWCNT-graphene-like nanocarbon hybrid films and analyzed their structural, morphological, and field emission properties.

Deng *et al.*[33] have realized the growth of FLG on CNTs using radio frequency hydrogen plasma sputtering deposition and reason the growth of FLGs on CNTs via defect nucleation mechanism. These hybrids show excellent field emission properties owing to sharp edges protruding over CNT edges, low work function value of hybrid structures and increased effective emission sites.

Kaushik *et al.*[34] have synthesized the hybrid structures of MWCNT and many layer graphene (MLGs) in a two-step process by microwave PECVD technique. They suggest that the dissolution and precipitation of carbon radicals result in the growth of one-dimensional (1-D) CNT, whereas as the catalyst particle saturates, the excess carbon atoms start depositing on the sidewalls of the tubes, thus forming two-dimensional (2D) graphene structure. The electron field emission characteristics of these hybrid structures are found to be better than those of bare MWCNTs and are attributed to factors such as work function, defect concentration and interface.

Deng *et al.*[15] have realized catalyst-free and self-assembled growth of graphene flakes (GFs) on CNT arrays by using the microwave PECVD technique. The GF shapes were seen to depend on the growth time, carbon concentration, and microwave power. The FE properties of GF–CNT composites were strongly influenced by the GF distribution on CNTs.

Pham *et al.*[35] have demonstrated graphene-CNTs (g-CNTs) as catalyst supports for high power output performance in proton

Reuse of AIP Publishing content is subject to the terms at: https://publishing.aip.org/authors/rights-and-permissions. Downloaded to IP: 14.139.251.107 On: Wed, 17 Aug 2016 07:13:02

exchange membrane fuel cell were formed from decomposition of acetylene on the CNTs by two-step processes, including the CVD and radio frequency plasma-enhanced CVD techniques.

Henry *et al.*[36] have produced the g-CNT hybrids, which grew from the decomposition of methane using one-step microwave PECVD system, to exhibit much higher catalytic activity than standard CNTs.

Deng *et al.*[37] have highlighted that the graphene growth on the CNT occurs at the tip because of the densely packed CNT arrays, it is difficult for carbon atoms to go down to the root of CNTs, so the density of the FLGs decreases rapidly from the top to the end of CNTs.

The theoretical models describing the growth of the CNT/CNF[38–41] and graphene[42,43] in the plasma medium have previously been developed. But, as far as the authors' knowledge is concerned, there is presently no theoretical study to underline the growth of graphene-CNT hybrid in a plasma medium.

Under the above mentioned motivation, a numerical model detailing the growth of graphene-CNT hybrid in a plasma medium is developed. The present work includes a theoretical model describing first the growth of CNT on a catalyst-substrate surface and thereafter the growth of the 2-D graphene sheet on CNT. The model incorporates the kinetics of different plasma species such as electrons, ions, and neutrals, and the growth kinetics of both the CNT and graphene to produce graphene-CNT hybrid. The effect of different gas ratios, microwave power, plasma parameter such as ion density on the growth rates of graphene-CNT hybrid is studied.

The paper is organized as follows. In Section II, a numerical model describing the growth of graphene-CNT hybrid is developed. In Section III, a discussion on the numerical results obtained is presented. Finally, the present work is concluded in Section IV.

II. MODEL

The present model details the growth of graphene-CNT hybrid in a plasma medium. In Ar + H_2 + C_2H_2 plasma, acetylene (C_2H_2) acts as a carrier gas, argon (Ar) as a carrier gas, and hydrogen (H_2) as an etching gas. The plasma consisting of electrons, ions of acetylene ($C_2H_2^+$), hydrogen (H^+) denoted as ions of types A and B, and neutrals of type A(C_2H_2) and type B (H_2) is considered. A catalyst of nickel (Ni) is placed over the silicon (Si) substrate.

The present model considers the following processes for the growth of graphene-CNT hybrid in a plasma medium:

(1) First, the applied plasma power dissociates the catalyst particle into catalyst nanoparticle, and also dissociates the feedstock and etching gas into hydrocarbon and hydrogen ions, respectively.
(2) The hydrocarbon and hydrogen ions traverse the plasma sheath and then via thermal dissociation, ion induced dissociation among several other processes, adsorb, diffuse, and accrete to contribute towards the height of the CNT and the hydrogen ions effectively shape CNT tip by etching effects.[38]
(3) As more and more carbon radicals become available, the growth of the CNT ceases due to catalyst–particle saturation.[34]
(4) The excess carbon radicals deposit on the side walls of the tube and these carbon radicals attach to each other to form carbon atom clusters.[42] These carbon clusters on the sidewalls of the tube form the graphene islands and the amalgamation of these graphene islands to form a large graphene island contribute to the perpendicular growth of graphene with respect to CNT.[42]
(5) Finally, the perpendicular growth of graphene on the CNT switches to parallel growth with respect to CNT due to the stress developed at the graphene island boundaries and the electric force generated in the plasma.[44] The main reasons for these stresses are ion bombardment and temperature gradients.[45]
(6) Eventually, the graphene-CNT hybrids are obtained in a plasma medium. It is worth mentioning that the growth of graphene on the CNT is catalyst-free.

Following Tewari and Sharma,[38] Mehdipour *et al.*,[41] Lieberman and Lichtenberg,[46] we investigate the plasma sheath structure around the substrate. We assume that the electric field within the sheath is along the z-axis

$$\left(\hat{i}\frac{\partial}{\partial x}+\hat{j}\frac{\partial}{\partial y}+\hat{k}\frac{\partial}{\partial z}\right).\hat{k}(n_l u_{lz})=\nu_l n_e, \tag{1}$$

$$m_l n_l u_{lz}\frac{du_{lz}}{dz}=en_l E-m_l n_l \nu_{ln} u_{lz}, \tag{2}$$

$$\frac{d^2\phi(z)}{dz^2}=-4\pi\Sigma q_l \xi_l n_l, \tag{3}$$

where Eqs. (1), (2), and (3) represent the continuity equation, ion-momentum balance equation, and Poisson's equation, respectively. l refers to either electron(e), $C_2H_2^+$ or H^+, n_l is their number density, m_l is their mass in plasma, u_{lz} is their fluid velocity, ν_l is the ionization frequency, E is the electric field, ν_{ln} is the collision frequency, ξ_l is the lth ion to electron number density ratio, q_l is the charge of the species, ϕ is the electrostatic potential, $\Sigma_l \xi_l = 1$, and $0 < \xi_l < 1$.

A. Charging of graphene-CNT hybrid

The charge developed on the graphene-CNT hybrid is determined by the accretion of positive ions and electrons on graphene-CNT hybrid surface

$$Z'[\tau]=(I_{iActs}+I_{iActcys}+I_{iAgp})+(I_{iBcts}+I_{iBctcys}+I_{iBgp})-\gamma_e(I_{ects}+I_{ectcys}+I_{egp}), \tag{4}$$

where Z is the amount of charge over graphene-CNT hybrid surface, γ_e is the sticking coefficient of electrons, $I_{ijcts}=\pi r_{ct}^2\left(\frac{8k_BT_i}{\pi m_{ij}}\right)^{\frac{1}{2}}n_{ij}(z)[1-Z\alpha_i]\exp[-\frac{E_b}{k_BT_s}]\exp[-\frac{eU_s}{k_BT_s}]$ is the ion collection current on the spherical CNT tip, $I_{ijgp}=n_{ij}(z)(lt+h't+lh')\left(\frac{k_BT_i}{2\pi^2m_{ij}}\right)^{\frac{1}{2}}\left\{\frac{2}{\sqrt{\pi}}\left(\frac{eV_{sg}}{k_BT_i}\right)^{\frac{1}{2}}+\exp\left[\frac{eV_{sg}}{k_BT_i}\right]erfc\left[\left(\frac{eV_{sg}}{k_BT_i}\right)^{\frac{1}{2}}\right]\right\}\times\exp[-\frac{eU_s}{k_BT_s}]$ is the ion collection current on the graphene

Reuse of AIP Publishing content is subject to the terms at: https://publishing.aip.org/authors/rights-and-permissions. Downloaded to IP: 14.139.251.107 On: Wed, 17 Aug 2016 07:13:02

sheet, $I_{ijctcys} = n_{ij}(z) r_{ct} h (\frac{2\pi k_B T_i}{m_{ij}})^{\frac{1}{2}} \times \left\{ \frac{2}{\sqrt{\pi}} \left(\frac{eV_s}{k_B T_i}\right)^{\frac{1}{2}} + \exp\left[\frac{eV_s}{k_B T_i}\right] erfc\,[(\frac{eV_s}{k_B T_i})^{\frac{1}{2}}] \right\} \exp\left[-\frac{E_b}{k_B T_s}\right] \exp\left[-\frac{eU_s}{k_B T_s}\right]$ is the ion collection current on the cylindrical surface of CNT, $I_{ects} = \pi {r_{ct}}^2 \left(\frac{8k_B T_e}{\pi m_e}\right)^{\frac{1}{2}} n_e(z) \times \exp\left[\frac{Ze^2}{r_{ct} k_B T_e} + \frac{eU_s}{k_B T_s}\right]$ is the electron collection current on the spherical CNT tip, $I_{ectcys} = n_e(z) r_{ct} h \left(\frac{2\pi k_B T_e}{m_e}\right)^{\frac{1}{2}} \exp\left[\frac{eV_s}{k_B T_e} + \frac{eU_s}{k_B T_s}\right]$ is the electron collection current on the cylindrical CNT surface, $I_{egp} = n_e(z)(lt + h't + lh')(\frac{k_B T_e}{2\pi^2 m_e})^{\frac{1}{2}} \exp[\frac{eV_s}{k_B T_e} + \frac{eU_s}{k_B T_s}]$ is the electron collection current on the graphene sheet, T_i is the ion temperature, m_{ij} is the ion mass (j refers to either A(hydrocarbon) or B(hydrogen) positively charged ion), l, t, and h' are the length, thickness, and height of the graphene sheet, respectively, T_s is the substrate or catalyst temperature (assuming catalyst and substrate to be at the same temperature), r_{ct} is the CNT tip radius, h is the height of CNT, and V_{sg} is the surface potential of the graphene sheet.[43]

$$V_{sg} = \frac{1}{(l \times t)} \times 7.2 \times 10^{-10} \left[-8z \tan^{-1}\left(\frac{l \times t}{2z\sqrt{S}}\right) - 2l \log\left(-t + \sqrt{S}\right) + 2l \log\left(t + \sqrt{S}\right) - 2t \log\left(-l + \sqrt{S}\right) + 2t \log\left(l + \sqrt{S}\right) \right],$$

where $S = l^2 + t^2 + 4z^2$; T_e is the electron temperature, m_e is the mass of electron, U_s is the substrate bias; $n_{ij}(z) = n_{ij0}(1 - \frac{2e\phi(z)}{m_{ij} v_{i0}^2})^{-\frac{1}{2}}$ is the ion density in the plasma sheath, v_{i0} is the ion velocity at any point within the plasma; $n_e(z) = n_{e0} \exp[\frac{|e|\phi(z)}{k_B T_e}]$ is the electron density in plasma sheath, $\phi(z)$ is the electrostatic potential, n_{e0} is the electron density in plasma sheath; $\phi(z) = \phi_0 \exp(-\frac{|z|}{\lambda_d})$, ϕ_0 is the negative potential at the surface and k_B is the Boltzmann's constant. A negative bias is applied to the substrate to attract and accelerate the positive ionic species in plasma so that they accrete on growing nanostructures.[47]

B. Balance equation of electron density

Eq. (5) describes the balance of electron number density in the plasma bulk. The processes such as dissociative ionization of neutrals to produce electrons and ions increases electron number density, recombination of electrons with ions reduces electron density in plasma bulk, electron collection current to the graphene-CNT hybrid surface reduces electron density in plasma bulk, and loss of electrons to discharge wall are considered.

$$n_e{}'[\tau] = (\beta_A n_A + \beta_B n_B) - (\alpha_A n_e n_{iA} + \alpha_B n_e n_{iB}) - \gamma_e n_{gcp}(I_{ects} + I_{ectcys} + I_{egp}) - K^e_{wall} n_e, \quad (5)$$

where β_A and β_B are the coefficients of ionization of the constituent neutral atoms of A(hydrocarbon) and B(hydrogen) due to external agency, $\alpha_j(T_e) = \alpha_{j0}(\frac{300}{T_e})^k$ cm^3/s are the coefficients of recombination of electrons and positively charged ions,[48] respectively, where $k = -1.2$ is a constant, n_{gcp} is the graphene-CNT number density, $K^e_{wall} n_e (= \frac{\gamma_e v_{the} S_{surf} n_e}{4V})$ denotes the number of electrons lost on the discharge wall per unit time per unit volume, $v_{the} (= \sqrt{\frac{8T_e}{\pi m_e}})$ is the average thermal velocity of electrons,[49] S_{surf} is the chamber surface area, and V is the volume of the PECVD chamber whose inner diameter R = 16 cm and length L = 23 cm is considered.[49]

The first term on the right side of Eq. (5) is the rate of gain in electron density per unit time because of dissociative ionization of neutral atoms; the second term is the decaying rate of the electron density due to the electron–ion recombination. The third term is the electron collection current at graphene-CNT hybrid surface. The last term denotes the loss of the electrons to the discharge wall.[49]

C. Balance equation of positively charged ion density

Eqs. (6) and (7) describes the balance of positively charged ions in plasma bulk considering dissociative ionization of neutral atoms, recombination of electrons and ions, ion collection current at graphene-CNT hybrid surface, their adsorption, desorption, thermal dehydrogenation, loss to the discharge wall and effects of applied power.

$$n_{iA}{}'[\tau] = \beta_A n_A - \alpha_A n_e n_{iA} - n_{gcp}(I_{iActs} + I_{iActcys} + I_{iAgp}) - J_{aiA} + J_{deiA} - K^{iA}_{wall} n_{iA} + \frac{P}{E_{dCH} \times V}, \quad (6)$$

$$n_{iB}{}'[\tau] = \beta_B n_B - \alpha_B n_e n_{iB} - n_{gcp}(I_{iBcts} + I_{iBctcys} + I_{iBgp}) - J_{aiB} + J_{deiB} + J_{th} - K^{iB}_{wall} n_{iB} + \frac{P}{E_{dH} \times V}, \quad (7)$$

$J_{aij} = \frac{P_i}{(2\pi m_{ij} k_B T_{ij})^{\frac{1}{2}}} \times \frac{n_{ij}}{j_{ij}}$ is the adsorption flux onto the graphene-CNT hybrid surface, P_i is the partial pressure of adsorbing species,[50] $J_{deij} = n_{ij} \nu \exp(-\frac{\varepsilon_{ai}}{k_B T_{ij}})$ is the desorption flux of ions from the graphene-CNT hybrid surface, j refers to either A or B ions, ν is the thermal vibrational frequency, ε_{ai} is the adsorption energy,[50] $J_{th} = n_H \nu \exp(\frac{-\delta\varepsilon_{th}}{k_B T_s})$ is the flux of type B ion (namely, hydrogen) on account of thermal dehydrogenation. $\delta\varepsilon_{th}$ is the activation energy of thermal dehydrogenation, $K^{ij}_{wall} = \frac{\gamma_{ij} v_{thij} S_{surf}}{4V}$ denotes the loss of ions j on the discharge wall per unit time per unit volume, γ_{ij} is the sticking coefficients of ions, $v_{thij} = \sqrt{\frac{8T_{ij}}{\pi m_{ij}}}$ is the average thermal velocity of ions A or B.

The first term in Eqs. (6) and (7) is the gain in ion density per unit time because of ionization of neutral atoms; the second term is loss of ion density in plasma bulk due to electron-ion recombination. The third term is loss of ion density in plasma bulk due to the ion collection current on the graphene-CNT hybrid surface. The fourth term is the loss of ions because of their adsorption to the graphene-CNT hybrid surface and fifth term is the gain in ion density due to desorption of ions from the graphene-CNT hybrid surface into the plasma bulk. The term J_{th} in Eq. (7) describes the increase in hydrogen ion number density in plasma because of thermal

Reuse of AIP Publishing content is subject to the terms at: https://publishing.aip.org/authors/rights-and-permissions. Downloaded to IP: 14.139.251.107 On: Wed, 17 Aug 2016 07:13:02

dehydrogenation. The $K_{wall}^{ij} n_{ij}$ in Eqs. (6) and (7) denotes the loss of the ions to the discharge wall. The last term in Eqs. (6) and (7) is the gain in ion number density due to the dissociation by applied power. The applied power is in Watt and E_{dCH} and E_{dH} are the dissociation energies of hydrocarbon and hydrogen gas, respectively.

D. Balance equation of neutral atoms

Eqs. (8) and (9) describe the balance of neutral species in plasma due to recombination of electrons and ions, dissociative ionization of neutral molecules, ion and neutral collection currents on the graphene-CNT hybrid surface, inflow into and outflow from the chamber

$$\begin{aligned} n_A'[\tau] &= \alpha_A n_e n_{iA} - \beta_A n_A + n_{gcp}(1-\gamma_{iA}) \\ &\quad \times (I_{iActs} + I_{iActys} + I_{iAgp}) \\ &\quad - n_{gcp}\gamma_A (I_{Acts} + I_{Actcys} + I_{Agp}) + I_A - O_A, \end{aligned} \tag{8}$$

$$\begin{aligned} n_B'[\tau] &= \alpha_B n_e n_{iB} - \beta_B n_B + n_{gcp}(1-\gamma_{iB}) \\ &\quad \times (I_{iBcts} + I_{iBctcys} + I_{iBgp}) \\ &\quad - n_{gcp}\gamma_B (I_{Bcts} + I_{Bctcys} + I_{Bgp}) + I_B - O_B, \end{aligned} \tag{9}$$

$I_{jcts} = \pi {r_{ct}}^2 \left(\frac{8k_B T_n}{\pi m_j}\right)^{\frac{1}{2}} n_j$ is the neutral collection current at the surface of the spherical CNT tip, $I_{jctcys} = \pi r_{ct} h \left(\frac{2k_B T_n}{m_j}\right)^{\frac{1}{2}} n_j$ is the neutral collection current on the cylindrical surface of CNT. $I_{jgp} = n_j(lt + h't + lh')\left(\frac{k_B T_n}{2\pi^2 m_j}\right)^{\frac{1}{2}}$ is the neutral collection current at the graphene sheet, $\gamma_{ij} = 1$ is the ion sticking coefficient and $\gamma_{ij} = 1$ is the neutral atom sticking coefficient, T_n is the neutral atom temperature, n_j is the neutral atom density and m_j is the neutral atom mass, $I_j\left(\frac{\text{cm}^{-3}}{\text{s}}\right) = \frac{4.4\times 10^{17} J_j[\text{sccm}]}{\text{V}}$ is the inflow, i.e., the rate at which species j enter the chamber. J_j is the gas inlet flow rate[49] (in standard cubic centimeter per minute), $O_j\left(\frac{\text{cm}^{-3}}{\text{s}}\right) = \frac{\nu_{pump} n_j}{V}$ is the outflow, i.e., the rate at which species j leave the chamber[49] ν_{pump} is the pumping rate. n_j is the number density of species j and V is the volume of the chamber.[49]

The first term in Eqs. (8) and (9) is the gain in neutral atom density per unit time due to electron–ion recombination; the second term is the decrease in neutral density due to dissociative ionization. The third term is the gain in neutral density due to neutralization of the particles collected at the graphene-CNT hybrid surface. The fourth term is the accumulation of neutral atoms of species A and B on the graphene-CNT hybrid surface. The fifth term denotes the increase of neutral density in plasma bulk due to their inflow into the chamber and sixth term denotes the decrease of neutral density in plasma bulk due to their outflow from the chamber.[49]

E. Rate equation for energy of catalyst particle

Initially, a catalyst particle nickel (Ni) of radius 30 nm is considered to be placed over a silicon (Si) substrate surface,

$$\begin{aligned} P(power) &= C_p \frac{d}{d\tau}(m_p T_s) \\ &= \left[I_{iActP}\left(\varepsilon^s_{iAc} + I_{pA}\right) + I_{iBctP}\left(\varepsilon^s_{iBc} + I_{pB}\right)\right] \\ &\quad - \left(\frac{3}{2}k_B\right)[(1-\gamma_{iA})I_{iActP} + (1-\gamma_{iB})I_{iBctP}]T_s, \end{aligned} \tag{10}$$

where $m_p = \frac{4}{3}\pi r_p^3 \rho_p$ is the mass of catalyst particle r_p is the radius of catalyst particle. ρ_p is the mass density of catalyst particle, C_p is the specific heat of catalyst particle (Ni) and is 0.44 kJ/kg°K and T_s is the substrate temperature (in °C). I_{pA} and I_{pB} are the ionization energies of atoms A (acetylene) and B (hydrogen). In the present problem, we have assumed the substrate and catalyst temperature to be the same.

$\varepsilon^s_{ijc}(Z) = \left(\left(\frac{(2-Z\gamma_{ji})}{(1-Z\gamma_{ji})}\right) - Z\gamma_{ji}\right)k_B T_{ij}$ are the mean energy collected by the ions j, (where j refers to ion A or B) at the surface of the catalyst particle[48] and $\gamma_{ji} = \left(\frac{e^2}{r_P k_B T_{ij}}\right)$ $I_{ijctP} = \pi {r_P}^2 \left(\frac{8k_B T_i}{\pi m_{ij}}\right)^{\frac{1}{2}} n_{ij}(z)\left[1 - Z\gamma_{ji}\right]\exp\left[-\frac{E_b}{k_B T_s}\right]\exp\left[-\frac{eU_s}{k_B T_s}\right]$ is the ion collection current at the surface of catalyst particle.

The terms on the right side of Eq. (10) is the rate of energy transferred to the catalyst particle due to the ions collected at the surface of catalyst particle because of ionization of neutral atoms A and B and mean energy collected by the ions at the surface of catalyst particle, and due to the accretion of ions A and B at the catalyst particle site. The resulting value of catalyst nanoparticle at time τ serves as the initial base radius of the cylindrical part of nanotube.

F. Growth rate equation of CNT

Following Tewari and Sharma[51]

$$\begin{aligned} 2\pi r_P G_h(\tau) &= \left(\left\{2n_{CH}\nu\exp\left(\frac{-\delta E_t}{k_B T_s}\right) + 2\theta_{CH} j_{iA} y_d + 2j_{iA}\right. \right. \\ &\quad \left. + \frac{j_{iA}\sigma_{ad} j_{iB}}{\nu} + j_{carbon}\right\} m_{carbon} \\ &\quad + \left\{j_{iA} + \frac{j_{iA}\sigma_{ad} j_H}{\nu} + j_{iA}\exp\left(\frac{-\delta E_t}{k_B T_s}\right)\right\} m_{iA}\Bigg) \\ &\quad \times \frac{D_s \times 2\pi r_p}{\pi r_p^2 \rho_p}\left(\frac{1}{I_{iActcys}}\right) + \gamma_{C_2H_2}\pi r_P^2 I_{C_2H_2} ctcys. \end{aligned} \tag{11}$$

$G_h(\tau)\left(= \frac{dh}{d\tau}\right)$ is defined as the growth rate of height of the CNT.

$$\begin{aligned} 4\pi G_r(\tau) &= \left\{j_{iB}\exp\left(\frac{-E_b}{k_B T_s}\right) + j_{iB}\exp\left(\frac{-\delta E_{th}}{k_B T_s}\right)\right. \\ &\quad + j_{iB}(1-\theta_t) + j_{iB} \\ &\quad \left. + \theta_{CH}\left(j_{iB} y_d + \nu_0 \nu \exp\left(\frac{-\delta E_i}{k_B T_s}\right)\right)\right\} \\ &\quad \times \frac{h(\tau)}{n_{iB}} - \frac{1}{4}(1-\theta_t)\nu_0 \nu \sigma_{ad} J_{iB}. \end{aligned} \tag{12}$$

Reuse of AIP Publishing content is subject to the terms at: https://publishing.aip.org/authors/rights-and-permissions. Downloaded to IP: 14.139.251.107 On: Wed, 17 Aug 2016 07:13:02

TABLE I. Explanation for the terms used in Eq. (11).

S. No.	The mathematical expression for terms in Eq. (11)	The detailed explanation for terms in Eq. (11)
1.	$2n_{CH}\nu \exp\left(\frac{-\delta E_t}{k_B T_s}\right)$	The generation of carbon atoms on the catalyst surface due to thermal dissociation of acetylene ions[41]
2.	$2\theta_{CH} j_{iA} y_d$	Ion-induced dissociation of C_2H_2[41]
3.	$2j_{iA}$	Decomposition of positively charged hydrocarbon ions
4.	$\frac{j_{iA}\sigma_{ad} j_{iB}}{\nu}$	Interaction of hydrocarbon ions with hydrogen ions[39]
5.	j_{carbon}	Incoming flux of carbon atoms
6.	j_{iA}	Incoming flux of hydrocarbon ions per unit time onto the catalyst particle
7.	$\frac{j_{iA}\sigma_{ad} j_H}{\nu}$	Interaction of adsorbed type A ions with atomic hydrogen from plasma[41]
8.	$j_{iA}(1-\theta_t)$	Adsorption of hydrocarbon ions onto the catalyst-substrate surface[39]
9.	$j_{iA}\exp\left(\frac{-\delta E_t}{k_B T_s}\right)$	Thermal dissociation of C_2H_2[41]
10.	$\frac{D_s \times 2\pi r_p}{\pi r_p^2 \rho_p}$	The surface diffusion of various species onto the catalyst surface across the catalyst nanoparticle per unit area per unit mass density[39]
11.	$\gamma_{C_2H_2}\pi r_P^2 I_{C_2H_2} ctcys$	Accretion of neutral acetylene atoms to the cylindrical surface of CNT

In Eq. (12), the area of the tip of CNT is $4\pi r^2_{ct}$ where $G_r(\tau)(=\frac{dr_{ct}^2}{d\tau})$ is defined as the growth rate for CNT tip radius.

Eqs. (11) and (12) trace the development of the CNT on the catalyst nanoparticle. The height of cylindrical CNT surface is obtained from Eq. (11) in which we consider the growth of the cylindrical part of the CNT and the value of the height of the cylindrical CNT surface at time τ is then fed into Eq. (12) to determine the radius of spherical CNT tip (r_{ct}). Eq. (12) specifically calculates the curved surface area of the spherical CNT tip. Eq. (12) accounts only for the nanoparticle tip radius as bottom area is already determined by the catalyst nanoparticle because they seed nanoparticle growth on them. $h(\tau)$ is the height of the CNT at a time τ.

The terms in Eqs. (11) and (12) are explained in Tables I and II, respectively.

G. Graphene growth equation

Once the catalyst-particle saturates and the CNT growth ceases, the excess carbon radicals starts depositing on the sidewalls of the tube to form carbon clusters and then the graphene islands.[34] These graphene islands first grow perpendicular to the tube, but thereafter due to stress generated by ion bombardment, temperature gradients,[45] and the electric field directed from plasma bulk to sheath,[44] the graphene islands grow parallel with respect to CNT to form a graphene sheet. The effect on the thickness of graphene sheet due to etching by the incoming hydrogen ions is also accounted for

$$l\frac{d(h'\times t)}{d\tau} = \left(\frac{n_A}{\nu}\times D_A \exp\left(-\left\{\frac{E_d + E_{inc}}{k_B T_s}\right\}\right) \times \frac{\pi r_{ct}^2 M_{gp}}{2\pi r_{ct}\rho_{gp}} \times (I_{iAgp})\right) + l\gamma_{C_2H_2}\pi r_{ct}^2 I_{C_2H_2 cts}, \tag{13}$$

$$\left[h'(\tau)+l\right]\frac{d(t)}{d\tau} = \left\{ j_{iB}\exp\left(\frac{-\delta E_{th}}{k_B T_s}\right) + j_{iB}(1-\theta_t) + j_{iB} + \theta_{CH}\left(j_{iB}y_d + \nu_0\nu\exp\left(\frac{-\delta E_i}{k_B T_s}\right)\right)\right\} \times \frac{h(\tau)}{n_{iB}} + \gamma_{H_2}\pi r_{ct}^2 I_{H_2 cts} - \frac{1}{4}(1-\theta_t)\nu_0\nu\sigma_{ad} j_{iB}. \tag{14}$$

Eq. (13) describes the increase in the area of the graphene sheet due to diffusion of carbon atoms, and ion and neutral collection current to the sidewalls of the CNT. The first term

TABLE II. Explanation for all the terms used in Eq. (12).

S. No.	The mathematical expression for terms in Eq. (12)	The detailed explanation for terms in Eq. (12)
1.	$j_{iB}\exp\left(\frac{-E_b}{k_B T_s}\right)$	Hydrogen atom diffusing into catalyst—substrate surface [39]
2.	$j_{iB}\exp\left(\frac{-\delta E_{th}}{k_B T_s}\right)$	Incoming flux of hydrogen due to the dehydrogenation of C_2H_2[41]
3.	$j_{iB}(1-\theta_t)$	Adsorption of hydrogen ions to the catalyst—substrate surface[39]
4.	j_{iB}	Decomposition of hydrogen ions
5.	$\theta_{CH} j_{iB} y_d$	Ion induced dissociation of C_2H_2[41]
6.	$\theta_{CH}\nu_0\nu\exp\left(\frac{-\delta E_i}{k_B T_s}\right)$	Incorporation of hydrogen ions due to thermal decomposition of hydrocarbon ions[39]
7.	$h(\tau)$	Height of CNT at time τ
8.	n_{iB}	Number density of type B ions, i.e., hydrogen ions
9.	$\frac{1}{4}(1-\theta_t)\nu_0\nu\sigma_{ad} j_{iB}$	Etching due to hydrogen ions[63]

Reuse of AIP Publishing content is subject to the terms at: https://publishing.aip.org/authors/rights-and-permissions. Downloaded to IP: 14.139.251.107 On: Wed, 17 Aug 2016 07:13:02

on the right side of Eq. (13) describes the diffusion and incorporation of carbon atoms to the sidewalls of the CNT. The second term accounts for the sticking of neutral atoms of acetylene on the CNT tip.

Eq. (14) details the decrease in thickness of graphene sheet. In Eq. (14), the first term on the right hand side refers the incoming hydrogen flux due to the thermal dehydrogenation of acetylene ions;[52] second term denotes the adsorption of hydrogen ions to the surface. The third term[52] is the decomposition of positively charged hydrogen ions, fourth term[52] describes ion induced dissociation of acetylene, and fifth term[52] is due to the incorporation of hydrogen ions due to thermal dissociation of acetylene ions. The sixth term denotes the sticking of neutrals of hydrogen on the surface of the graphene sheet. The last term describes the etching of graphene thickness by incoming hydrogen ions.

III. NUMERICAL RESULTS AND DISCUSSION

The present work serves an analytical model for the growth of graphene-CNT hybrid in a plasma medium. In this section, the numerical solutions of the plasma sheath and graphene-CNT hybrid growth equations developed in Section II are presented. The dependence of growth rates of graphene and CNT for different plasma parameters, gas ratios, and microwave power is studied using the present model. In a plasma-assisted and catalyst aided growth of the nanostructures, a plasma sheath is formed around the catalyst-substrate surface that separates it from plasma bulk. The electric field directed from the bulk to the sheath directs the ion currents to the catalyst-substrate surface that then participates in nanostructure growth. The variations in plasma parameter and other external parameters changes the thickness of plasma sheath and the electric field within the sheath, to result a change in ion fluxes to the catalyst-substrate surface to eventually modify the growth profiles of nanostructures.

In the present model describing the growth of graphene-CNT hybrid, we assume that the applied plasma power ionizes the feedstock and etching gas and fragments the catalyst particle into catalyst nanoparticles. The hydrocarbon and hydrogen ions undergo numerous processes such as adsorption, desorption, ion induced dissociation, thermal dissociation, dehydrogenation among others to contribute towards graphene-CNT hybrid growth. In the first stage of graphene-CNT hybrid growth, it is assumed that the catalyst-nanoparticle seed the nanotube growth on them such that the hydrocarbon ions contribute to the height of CNT and hydrogen ions shapes the CNT tip radius through etching (see Ref. 38). Afterwards, the CNT growth stops due to catalyst-particle saturation (see Ref. 34). Thereafter, the incoming carbon radicals deposit on the sidewalls of the tube and these carbon radicals through covalent-bonding form carbon clusters on the CNT sidewalls. These carbon clusters then form the graphene-islands and then amalgamate to form large graphene islands on the CNT sidewalls. Finally, due to factors such as ion bombardment, temperature gradients, and electric field, the graphene growth switches to vertical graphene growth on CNT sidewalls. It should also be pointed that the growth of the graphene on the CNT occurs around the tip region of the CNT because of the densely packed nature of the CNT arrays, it is difficult for carbon radicals to trip down to the roots of the CNT (see Ref. 37). The growth in the dimensions of graphene, i.e., height and thickness of graphene occur via ion accretion currents and surface diffusion. Moreover, the hydrogen ions terminate the thickness of the graphene due to etching.

The numerical calculations have been formed to investigate the growth rate of height of the CNT for different values of the hydrocarbon ion density, radius of CNT for varying hydrogen density, height, and thickness of graphene for different concentrations of gas ratio and source power. Using the MATHEMATICA software, Eqs. (1)–(14) are simultaneously solved at appropriate boundary conditions, i.e., at $\tau = 0$, ion number density of hydrocarbon $(n_{iA0}) = 0.5\ n_{e0}$, ion number density of hydrogen $(n_{iB0}) = 0.5 n_{e0}$, electron number density $(n_{e0}) = 1.12 \times 10^9\ cm^{-3}$,electron temperature $(T_{e0}) = 1.5\,eV$, ion temperature $(T_{i0}) = 2200\,K$, neutral temperature $(T_{n0}) = 2000\,K$, mass of hydrocarbon ion $(m_{iA}) = 26\,amu$, mass of hydrogen ion $(m_{iB}) = 1\,amu$, coefficient of recombination of electrons and ions $(\alpha_A = \alpha_B) = 1.12 \times 10^{-7}\ cm^3/s$, substrate temperature $(T_s) = 400\,^{\circ}C$, energy barrier for bulk diffusion of carbon into nickel $(E_b) = 1.6\,eV$, cross section for the reactions of atomic hydrogen with adsorbed particles $(\sigma_{ad}) \approx 6.8 \times 10^{-16}\,cm^2$, energy due to thermal dissociation of acetylene ions $(\varepsilon_{th}) = 4.2\,eV$, chamber surface area $(S_{surf}) = 3918.72\,cm^2$, chamber volume $(V) = 1.85 \times 10^4\ cm^3$, thermal velocity of hydrogen ion $(v_{thi}H^+) = 69.52 \times 10^4\,cm/s$, thermal velocity of electron $(v_{the}) = 5.13 \times 10^7\ cm/s$, thermal vibrational frequency $(\nu) = 10^{13}\ Hz$, initial radius of catalyst particle $(r_P) = 30\,nm$, energy barrier for carbon atom diffusion[53] $(E_d) \approx 0.13\,eV$, energy barrier for carbon atom incorporation[54] $(E_{inc}) \approx 0.4eV$.

Fig. 1 is a schematic representation of the growth stages of graphene-CNT hybrid in a plasma medium assisted by catalyst. The figure shows the different stages of graphene-CNT hybrid growth from fragmentation of catalyst particle to CNT growth on them and eventually the growth of graphene on CNT sidewalls to form graphene-CNT hybrid.

Fig. 2 shows the growth rate of the height of the CNT $G_h(\tau)$ (in $\mu m\ s^{-1}$) with parameter $\Omega[=(1000/T_s)]$ for different values of hydrocarbon ion density ($n_{iA0} = 1 \times 10^{11}\ cm^{-3}$, $5 \times 10^{12}\ cm^{-3}$, and $7 \times 10^{13}\ cm^{-3}$). From Fig. 2, it can be seen that the growth rate of the height of the CNT increases with hydrocarbon ion density. This is imputable to the fact that as the hydrocarbon ion density (n_{iA0}) increases, the thickness of plasma sheath increases and ions gain more energy on traversing the sheath, and consequently, the diffusion of these energized ions to the catalyst particle increase, thereby contributing to enhanced growth rates of the CNT. The observations of Fig. 2 are in accordance with the theoretical findings of Mehdipour *et al.*[41] and with experimental observations of Aksak *et al.*[55] and Loffler *et al.*[56] According to Mehdipour *et al.*,[41] the growth rate at low and intermediate temperatures increase with ion density due to stronger effective carbon flux to the catalyst surface. Moreover, Loffler *et al.*[56] have reasoned that at higher temperatures facilitate faster diffusion of hydrocarbon gas which then contributes to longer CNTs.

Reuse of AIP Publishing content is subject to the terms at: https://publishing.aip.org/authors/rights-and-permissions. Downloaded to IP: 14.139.251.107 On: Wed, 17 Aug 2016 07:13:02

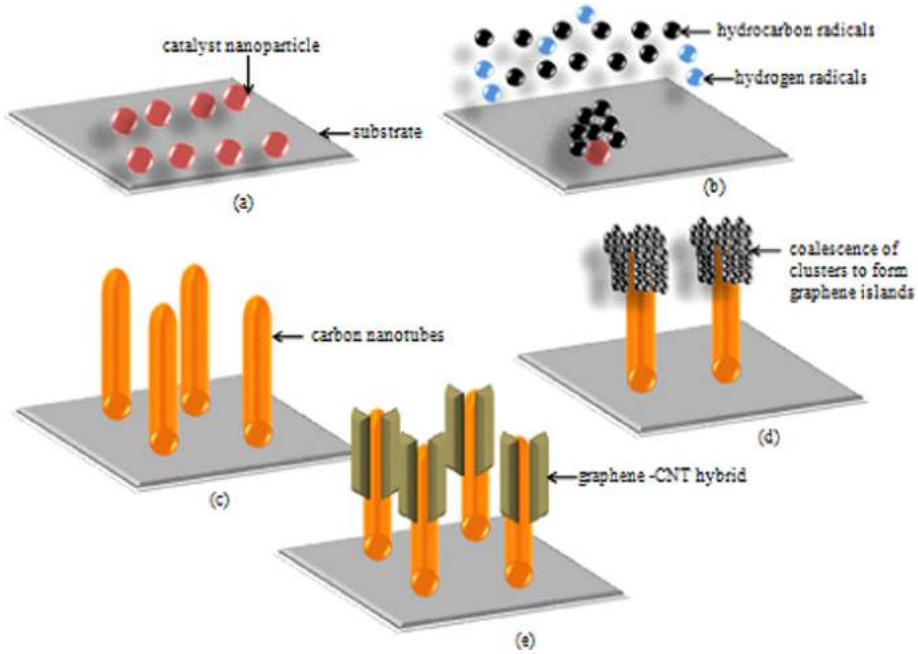

FIG. 1. Schematic of the graphene-CNT hybrid growth process in plasma where (a) is the fragmentation of catalyst particle into nanoparticles, (b) advent of hydrogen and hydrocarbon ions on the catalyst nanoparticle, (c) CNT formation on catalyst nanoparticle, (d) coalescence of clusters on the CNT sidewalls, (e) graphene-CNT hybrid.

Fig. 3 displays the variation of the radius of CNT with time for different values of hydrogen ion density ($n_{iB0} = 10^9\,cm^{-3}$, $10^{10}\,cm^{-3}$, and $10^{11}\,cm^{-3}$). Fig. 3 indicates that the radius of CNT decreases as the hydrogen ion density increases. This is because with the increase in hydrogen ion density the etching of the CNT tip by hydrogen ion attains prominence and the radius of CNT tip decreases. The results of Fig. 3 comply with the findings of Mehdipour *et al.*[41] and Denysenko and Ostrikov.[54]

Fig. 4 illustrates the time evolution of height of graphene for different values of gas ratio, i.e. ($n_{A0}/n_{B0} = 1/10$, 3/10, and 5/10). It can be seen from Fig. 4 that as the gas ratio is increased the height of graphene increases. This is answerable to the fact that as the gas ratio increases, there is faster generation and consequently enhanced diffusion of carbon radicals to the sidewalls of CNT thereby, contributing to the increased height of graphene. The results of Fig. 4 are in accordance with Deng *et al.*[15] According to Deng *et al.*,[15] the GFs of sample with gas ratio 1/15 are extremely sparsely distributed and their sizes are less than 100 nm while for sample with gas ratio 0.1, the GFs are densely distributed on the surface of CNT arrays and their sizes reach 1 μm. In the present work, the height of graphene sheet obtained at 100 s for n_{A0}/n_{B0} is nearly 120 nm.

Fig. 5 shows the thickness of graphene sheet with time for different values of source power. It can be seen that as the source power is increased the thickness of graphene sheet decreases. This is because as the source power is increased, more hydrogen ions are created because of dissociation of hydrogen gas and the etching of the edges of graphene sheet by hydrogen ions increases thus decreasing the thickness of graphene. The results of Fig. 5 comply with the works of Deng *et al.*,[15] Nang and Kim,[57] and Liu *et al.*[58] According to

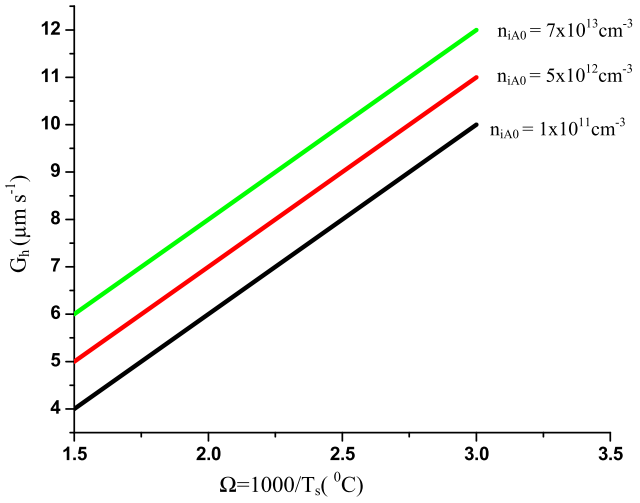

FIG. 2. Display the growth rate of the height of the CNT $G_h(\tau)$ (in μm s^{-1}) with parameter $\Omega[=1000/T_s\,(^\circ C)]$ for different values of hydrocarbon ion density ($n_{iA0} = 1 \times 10^{11}\,cm^{-3}$, $5 \times 10^{12}\,cm^{-3}$, and $7 \times 10^{13}\,cm^{-3}$).

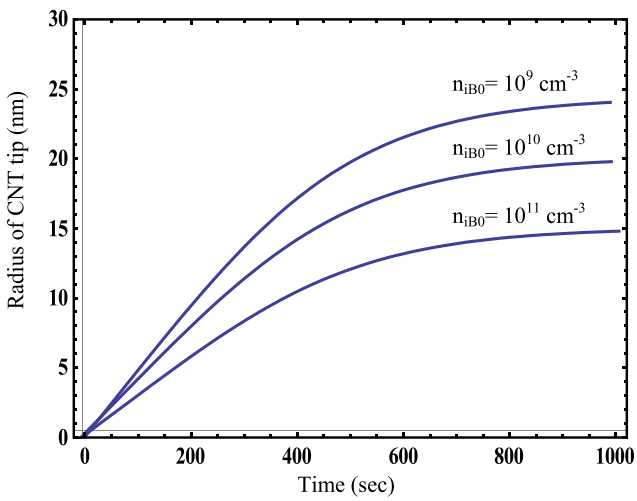

FIG. 3. Illustrates the variation of radius of CNT with time for different values of hydrogen ion density ($n_{iB0} = 10^9\,cm^{-3}$, $10^{10}\,cm^{-3}$, and $10^{11}\,cm^{-3}$).

Reuse of AIP Publishing content is subject to the terms at: https://publishing.aip.org/authors/rights-and-permissions. Downloaded to IP: 14.139.251.107 On: Wed, 17 Aug 2016 07:13:02

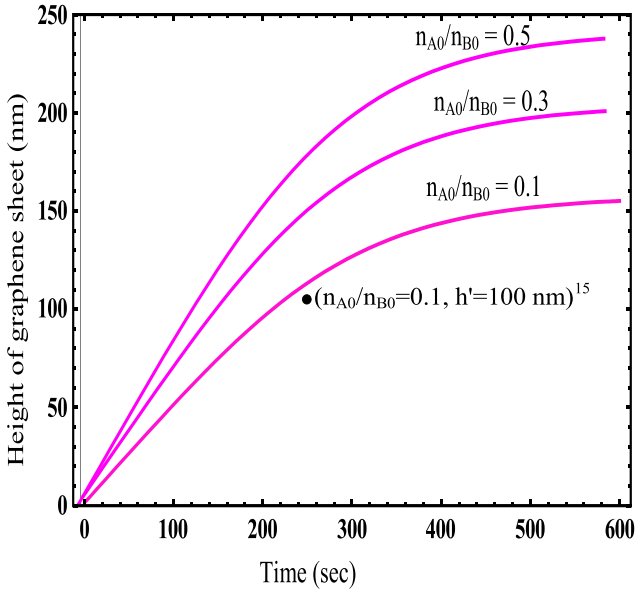

FIG. 4. The time evolution of the height of graphene for different values of gas ratios, i.e. (n_{A0}/n_{B0} = 1/10, 3/10, and 5/10). The experimental data point for height of graphene for n_{A0}/n_{B0} = 1/15 of Deng *et al*. is marked.

Deng *et al*.,[15] both the density and the size of GFs together with the amount of amorphous carbon on the surface of CNTs decrease with the increase of microwave power from 100 to 400 W. The result in Fig. 5 is qualitatively similar to Deng *et al*.[15] but since the actual dimensions of graphene at different source power are not given in Ref. 15 a direct quantitative comparison with the results obtained in the present work is not possible.

The findings of the above work may be employed to obtain the desired dimensions of graphene-CNT hybrid in a plasma medium. By manipulating the plasma parameters, gas ratio, and source power, one can obtain graphene-CNT hybrid of varied dimensions. The plasma and process parameters are seen to affect graphene-CNT hybrid growth and this fact can be used in graphene-CNT hybrid based field emission devices. One should expect enhanced field emissions from graphene-CNT hybrid grown in plasma because

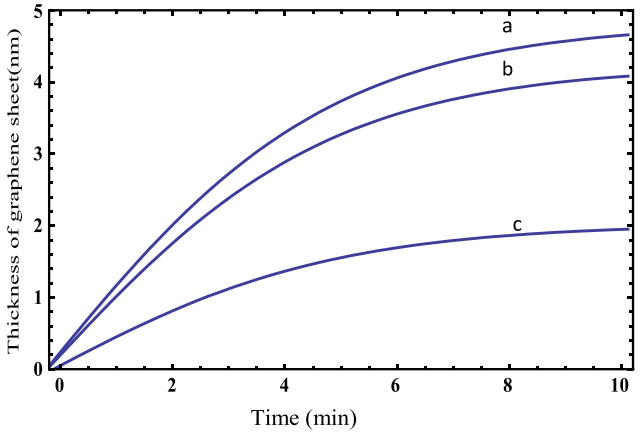

FIG. 5. The variation of thickness of graphene sheet with time for different values of source power, where a, b, and c correspond to power (P) = 100 W, 400 W, and 700 W, respectively.

the radius of CNT tip and thickness of graphene sheet decrease if plasma parameters are increased.

Since the field enhancement factor of CNT[59] is $\beta(\approx \frac{h}{r_{ct}}$, where h is the height and r_{ct} is the radius of CNT) and graphene[60] is $\beta(\approx \frac{h'}{t}$, where h' is the height and t is the thickness of graphene sheet), both are inversely proportional to radius of CNT and thickness of graphene sheet, respectively. Therefore, any decrease in CNT radius and graphene thickness should give better field emissions from graphene-CNT hybrids.

Moreover, the field enhancement factors of heterostructures of graphene and silicon nanowires (SiNW)[61,62] are given as $\beta_{heterostructures} = B_{SiNWs}\beta_{graphene}$.

So, if dimensions of heterostructures (in the present case of graphene and CNT) decrease with plasma and process parameters, the consecutive field emissions from them should be high.

The increase in field emission characteristics of the graphene-CNT hybrid grown in plasma has also been suggested by Deng *et al*.,[33] Kaushik *et al*.,[34] and Deng *et al*.[15]

A more realistic expression for the field enhancement factor of graphene-CNT hybrid is underway and would form a part of future work.

IV. CONCLUSION

A numerical model is developed to study the growth of graphene-CNT hybrid in a plasma medium assisted by catalyst. The plasma sheath kinetics, balance equations for the plasma species and the growth of the CNT on a catalyst particle and thereafter the growth of graphene sheet on CNT sidewalls to form graphene-CNT hybrid is presented. It is found from the present work that by suitably manipulating plasma parameters such as ion densities, gas ratios, and plasma power the graphene-CNT hybrids of desired dimensions can be obtained. The results of the present study can be extended to realize the many practical applications of graphene-CNT hybrids.

[1]V. I. Merkulov, A. V. Melechko, M. A. Guillorn, D. H. Lowndes, and M. L. Simpson, Appl. Phys. Lett. **79**, 2970 (2001).
[2]M. S. Bell, K. B. K. Teo, and W. I. Milne, J. Phys. D: Appl. Phys. **40**, 2285 (2007).
[3]M. Su, B. Zheng, and J. Liu, Chem. Phys. Lett. **322**, 321 (2000).
[4]L. Delzeit, B. Chen, A. Cassell, R. Stevens, C. Nguyen, and M. Meyyappan, Chem. Phys. Lett. **348**, 368 (2001).
[5]L. Delzeit, I. McAninch, B. A. Cruden, D. Hash, B. Chen, J. Han, and M. Meyyappan, J. Appl. Phys. **91**, 6027 (2002).
[6]S. K. Srivastava, V. D. Vankar, and V. Kumar, Nano-Micro Lett. **2**, 42 (2010).
[7]G. Burmaka, I. B. Denysenko, K. Ostrikov, I. Levchenko, and N. A. Azarenkov, Plasma Processes Polym. **11**, 798 (2014).
[8]K. B. K. Teo, D. B. Hash, R. G. Lacerda, N. L. Rupesinghe, M. S. Bell, S. H. Dalal, D. Bose, T. R. Govindan, B. A. Cruden, M. Chhowalla, G. A. J. Amaratunga, M. Meyyappan, and W. I. Milne, Nano Lett. **4**, 921 (2004).
[9]I. Levchenko, O. Volotskova, A. Shashurin, Y. Raitses, K. Ostrikov, and M. Keidar, Carbon **48**, 4570 (2010).
[10]Y. Kim, W. Song, S. Y. Lee, C. Jeon, W. Jung, M. Kim, and C.-Y. Park, Appl. Phys. Lett. **98**, 263106 (2011).
[11]T.-o. Terasawa and K. Saiki, Carbon **50**, 869 (2012).
[12]A. Malesevic, R. Kemps, A. Vanhulsel, M. P. Chowdhury, A. Volodin, and C. V. Haesendonck, J. Appl. Phys. **104**, 084301 (2008).
[13]S. K. Srivastava, A. K. Shukla, V. D. Vankar, and V. Kumar, Thin Solid Films **492**, 124 (2005).

Reuse of AIP Publishing content is subject to the terms at: https://publishing.aip.org/authors/rights-and-permissions. Downloaded to IP: 14.139.251.107 On: Wed, 17 Aug 2016 07:13:02

[14]J. Y. Kim, J. J. Wook, Y. D. Hyun, J. Y. Kim, E. S. Kim, and J. S. Lee, RSC Adv. **2**, 9415 (2012).
[15]J. H. Deng, G. A. Cheng, R. T. Zheng, B. Yu, G. Z. Li, X. G. Hou, M. L. Zhao, and D. J. Li, Carbon **67**, 525 (2014).
[16]X. Dong, B. Li, A. Wei, X. Cao, M. B. C. Park, H. Zhang, L. J. Li, W. Huang, and P. Chen, Carbon **49**, 2944 (2011).
[17]Y. Hu, Y. Zhao, G. Lu, N. Chen, Z. Zhang, H. Li, H. Shao, and L. Qu, Nanotechnology **24**, 195401 (2013).
[18]J. Gong, H. Yang, and P. Yang, Composites, Part B **75**, 250 (2015).
[19]A. T. T. Koh, T. Chen, L. Pan, Z. Sun, and D. H. C. Chua, J. Appl. Phys. **113**, 174909 (2013).
[20]C. Li, Z. Li, H. Zhu, K. Wang, J. Wei, X. Li, P. Sun, H. Zhang, and D. Wu, J. Phys. Chem. C **114**, 14008 (2010).
[21]C. Tang, Q. Zhang, M.-Q. Zhao, J.-Q. Huang, X.-B. Cheng, G.-L. Tian, H.-J. Peng, and F. Wei, Adv. Mater. **26**, 6100 (2014).
[22]M.-Q. Zhao, X.-F. Liu, Q. Zhang, G.-L. Tian, J.-Q. Huang, W. Zhu, and W. Fei, ACS Nano **6**, 10759 (2012).
[23]Y. S. Kim, K. Kumar, F. T. Fisher, and E. H. Yang, Nanotechnology **23**, 015301 (2012).
[24]C. Kang, R. Baskaran, J. Hwang, B. C. Ku, and W. Choi, Carbon **68**, 493 (2014).
[25]Y. Wu, T. Zhang, F. Zhang, Y. Wang, Y. Ma, Y. Huang, Y. Liu, and Y. Chen, Nano Energy **1**, 820 (2012).
[26]Z. J. Fan, J. Yan, T. Wei, G. Q. Ning, L. J. Zhi, J. C. Liu, D. X. Cao, G. L. Wang, and F. Wei, ACS Nano **5**, 2787 (2011).
[27]V. C. Tung, L. M. Chen, M. J. Allen, J. K. Wassei, K. Nelson, R. B. Kaner, and Y. Yeng, Nano Lett. **9**, 1949 (2009).
[28]H. Sharma, D. C. Agarwal, M. Sharma, A. K. Shukla, D. K. Avasthi, and V. D. Vankar, J. Phys. D: Appl. Phys. **46**, 315301 (2013).
[29]Z. Wang, H. Ogata, S. Morimoto, J. Ortiz-Medina, M. Fujishige, K. Takeuchi, H. Muramatsu, T. Hayashi, M. Terrones, Y. Hashimoto, and M. Endo, Carbon **94**, 479 (2015).
[30]N. Chiodarelli, C. Xu, O. Richard, H. Bender, A. Klekachev, M. Cooke, M. Heyns, S. De Gendt, G. Groeseneken, and P. M. Vereecken, J. Nanomater. **2012**, 130725.
[31]R. Lv, E. Cruz-Silva, and M. Terrones, ACS Nano **8**, 4061 (2014).
[32]S. Chockalingam, A. Bisht, O. S. Panwara, A. K. Kesarwani, B. P. Singh, J. Chand, and V. N. Singh, Mater. Chem. Phys. **156**, 38 (2015).
[33]J.-h. Deng, R.-t. Zheng, Y.-m. Yang, Y. Zhao, and G.-a. Cheng, Carbon **50**, 4732 (2012).
[34]V. Kaushik, A. K. Shukla, and V. D. Vankar, Appl. Phys. A: Mater. Sci. Process. **117**, 2197 (2014).
[35]K. C. Pham, D. H. Chua, D. S. McPhail, and A. T. Wee, ECS Electrochem. Lett. **3**, F37 (2014).
[36]P. A. Henry, A. S. Raut, S. M. Ubnoske, C. B. Parker, and J. T. Glass, Electrochem. Commun. **48**, 103 (2014).
[37]J.-h. Deng, R.-t. Zheng, Y. Zhao, and G.-a. Cheng, ACS Nano **6**, 3727 (2012).
[38]A. Tewari and S. C. Sharma, Phys. Plasmas **21**, 063512 (2014).
[39]I. Denysenko, K. Ostrikov, M. Y. Yu, and N. A. Azarenkov, J. Appl. Phys. **102**, 074308 (2007).
[40]I. Levchenko, K. Ostrikov, J. Khachan, and S. V. Valdimirov, Phys. Plasmas **15**, 103501 (2008).
[41]H. Mehdipour, K. Ostrikov, and A. E. Rider, Nanotechnology **21**, 455605 (2010).
[42]H. Mehdipour and K. Ostrikov, ACS Nano **6**, 10276 (2012).
[43]S. C. Sharma and N. Gupta, Phys. Plasmas **22**, 123517 (2015).
[44]K. Yu, G. Lu, Z. Bo, S. Mao, and J. Chen, J. Phys. Chem. Lett. **2**, 1556 (2011).
[45]J. Chen, Z. Bo, and G. Lu, *Vertically-Oriented Graphene: PECVD Synthesis and Applications* (Springer International Publishing, Switzerland, 2015).
[46]M. A. Lieberman and A. J. Lichtenberg, *Principles of Plasma Discharges and Materials Processing* (Wiley Interscience Publication, USA, 1994).
[47]K. Ostrikov and S. Xu, *Plasma Aided Nanofabrication: From Plasma Sources to Nanoassembly* (Wiley-VCH, Weinheim, Germany, 2007).
[48]M. S. Sodha, S. Misra, S. K. Mishra, and S. Srivastava, J. Appl. Phys. **107**, 103307 (2010).
[49]I. B. Denysenko, S. Xu, J. D. Long, P. P. Rutkevych, N. A. Azarenkov, and K. Ostrikov, J. Appl. Phys. **95**, 2713 (2004).
[50]O. A. Louchev, C. Dussarrat, and Y. Sato, J. Appl. Phys. **86**, 1736 (1999).
[51]A. Tewari and S. C. Sharma, Phys. Plasmas **22**, 043501 (2015).
[52]I. Denysenko and K. Ostrikov, J. Phys. D: Appl. Phys. **42**, 015208 (2009).
[53]M. Zhu, J. Wang, B. C. Holloway, R. A. Outlaw, X. Zhao, K. Hou, V. Shutthanandan, and D. M. Manos, Carbon **45**, 2229 (2007).
[54]I. Denysenko and N. A. Azarenkov, J. Phys. D: Appl. Phys. **44**, 174031 (2011).
[55]M. Aksak, S. Kir, and Y. Selamet, J. Optoelectron. Adv. Mater. - Symp. **1**, 281 (2009).
[56]R. Loffler, M. Haffner, G. Visanescu, H. Weigand, X. Wang, D. Zhang, M. Fleischer, A. J. Meixner, J. Fortagh, and D. P. Kern, Carbon **49**, 4197 (2011).
[57]L. V. Nang and E.-T. Kim, J. Electrochem. Soc. **159**, K93 (2012).
[58]W. Liu, T. Dang, Z. Xiao, X. Li, C. Zhu, and X. Wang, Carbon **49**, 884 (2011).
[59]Z. Xu, X. D. Bai, and E. G. Wang, Appl. Phys. Lett. **88**, 133107 (2006).
[60]S. Watcharotone, R. S. Ruoff, and F. H. Read, Phys. Procedia **1**, 71 (2008).
[61]S. Lv, Z. Li, J. Liao, G. Wang, M. Li, and W. Miao, Sci. Rep. **5**, 15035 (2015).
[62]R. Khanna, S. J. Pearton, F. Ren, I. Kravchenko, C. J. Kao, and G. C. Chi, Appl. Phys. Lett. **87**, 052110 (2005).
[63]F. Abild-Pedersen, J. K. Norskov, J. R. Rostrup-Nielsen, J. Sehested, and S. Helveg, Phys. Rev. B **73**, 115419 (2006).

Reuse of AIP Publishing content is subject to the terms at: https://publishing.aip.org/authors/rights-and-permissions. Downloaded to IP: 14.139.251.107 On: Wed, 17 Aug 2016 07:13:02

Modeling the effect of doping on the catalyst-assisted growth and field emission properties of plasma-grown graphene sheet

Neha Gupta, Suresh C. Sharma, and Rinku Sharma

Citation: Physics of Plasmas **23**, 083509 (2016); doi: 10.1063/1.4960562
View online: http://dx.doi.org/10.1063/1.4960562
View Table of Contents: http://scitation.aip.org/content/aip/journal/pop/23/8?ver=pdfcov
Published by the AIP Publishing

Articles you may be interested in

Theoretical modeling of the plasma-assisted catalytic growth and field emission properties of graphene sheet
Phys. Plasmas **22**, 123517 (2015); 10.1063/1.4938506

Publisher's Note: "Effect of plasma parameters on growth and field emission properties of spherical carbon nanotube tip" [Phys. Plasmas18, 063503 (2011)]
Phys. Plasmas **18**, 109902 (2011); 10.1063/1.3641489

Effect of plasma parameters on growth and field emission properties of spherical carbon nanotube tip
Phys. Plasmas **18**, 063503 (2011); 10.1063/1.3595636

Remarkably low turn-on field emission in undoped, nitrogen-doped, and boron-doped graphene
Appl. Phys. Lett. **97**, 063102 (2010); 10.1063/1.3464168

Improved field emission property of graphene paper by plasma treatment
Appl. Phys. Lett. **97**, 033109 (2010); 10.1063/1.3467042

Reuse of AIP Publishing content is subject to the terms at: https://publishing.aip.org/authors/rights-and-permissions. Downloaded to IP: 14.139.251.107 On: Wed, 17 Aug 2016 06:59:12

PHYSICS OF PLASMAS **23**, 083509 (2016)

Modeling the effect of doping on the catalyst-assisted growth and field emission properties of plasma-grown graphene sheet

Neha Gupta, Suresh C. Sharma, and Rinku Sharma
Department of Applied Physics, Delhi Technological University (DTU), Shahbad Daulatpur, Bawana Road, Delhi-110042, India

(Received 10 May 2016; accepted 23 July 2016; published online 8 August 2016)

A theoretical model describing the effect of doping on the plasma-assisted catalytic growth of graphene sheet has been developed. The model accounts the charging rate of the graphene sheet, kinetics of all the plasma species, including the doping species, and the growth rate of graphene nuclei and graphene sheet due to surface diffusion, and accretion of ions on the catalyst nanoparticle. Using the model, it is observed that nitrogen and boron doping can strongly influence the growth and field emission properties of the graphene sheet. The results of the present investigation indicate that nitrogen doping results in reduced thickness and shortened height of the graphene sheet; however, boron doping increases the thickness and height of the graphene sheet. The time evolutions of the charge on the graphene sheet and hydrocarbon number density for nitrogen and boron doped graphene sheet have also been examined. The field emission properties of the graphene sheet have been proposed on the basis of the results obtained. It is concluded that nitrogen doped graphene sheet exhibits better field emission characteristics as compared to undoped and boron doped graphene sheet. The results of the present investigation are consistent with the existing experimental observations. *Published by AIP Publishing.*
[http://dx.doi.org/10.1063/1.4960562]

I. INTRODUCTION

Since its discovery,[1] graphene has gained a heightened interest among both theoretical and experimental researchers due to its exotic physical, thermal, mechanical, and electrical properties. The unique two-dimensional structure with atomic thickness and high aspect ratio, high specific area, and high electrical conductivity endow graphene to be a propitious candidate for field emission applications in flat panel field emission displays (FEDs), vacuum microelectronic devices, such as electron guns and microwave power amplifiers, electron source for electron microscopy, illumination, and many others.[2] In addition, owing the sp^2 bonded carbon atoms, graphene emitters are expected to possess strength to endure the stress and ion-bombardment effects produced by the electrostatic field during field emission.[3]

Since electrons are primarily emitted from the graphene sheet (GS) edges,[4] the fabrication of vertically aligned GS with sharp edges is prerequisite for highly efficient graphene emitter. Among myriad of synthesis techniques, plasma-enhanced chemical vapor deposition (PECVD) method is viewed as a standout for growing vertical GS as it exhibits better control over the GS structure at relatively low temperatures and in many cases demonstrates superior properties as compared to other nanoscale synthesis methods.[5] Several theoretical models have been developed to study the growth of carbon nanostructures in plasma.[5–7]

Denysenko and Azarenkov[5] have suggested that it is possible to grow nanostructures at higher rates through PECVD in comparison to thermal CVD. They recognized that by appropriately controlling the ion and etching fluxes on the catalyst nanoparticles, the high aspect ratio carbon nanostructures can be obtained at low substrate temperature than that of CVD.

Mehdipour *et al.*[6] have investigated the effect of variations in plasma parameters and substrate potential on the carbon nanofiber growth parameters with an emphasis on the effect of the substrate temperature. They established that an increase in the etching gas (hydrogen gas) supply, the growth rate decreases at almost all surface temperatures.

Recently, we have also shown theoretically that by tuning the plasma parameters, one can selectively control the height and thickness of the GS and thereby its field emission characteristics.[7]

Plasma treatment also offers the advantage of material modification by the introduction of foreign atoms or groups, and thereby altering the material electronic properties.[8] In general, doping with foreign atoms is considered one of the effective methods to intrinsically modify the properties and structure of the GS, and thus expanding the field emission characteristics. Among the several heteroatoms available for doping, nitrogen and boron are the most frequently used candidates for doping of graphene as they have similar atomic radii size as that of carbon and ability to induce n- and p-type conduction in graphene. The nitrogen atoms replace the carbon atoms on the carbon nanostructure and function as donors which eventually boost the electron field emission properties whereas the boron atoms reduce the electron concentration due to the formation of electron holes and, therefore the electron field emission decreases.[9] The similar effect of nitrogen and boron doping on the field emission characteristics of carbon nanotubes has been shown theoretically by Sharma *et al.*[10] Numerous works have been performed to show that nitrogen and boron doping can effectively change the structure, growth rate, number density, and dimensions of graphene.[11–14]

Seo *et al.*[11] have investigated the effect of nitrogen concentrations on the dimensions and structure of vertical

Reuse of AIP Publishing content is subject to the terms at: https://publishing.aip.org/authors/rights-and-permissions. Downloaded to IP: 14.139.251.107 On: Wed, 17 Aug 2016 06:59:12

graphene nanosheets (VGS) using low-temperature plasma-based process. They observed that upon addition of nitrogen to the $CH_4/Ar/H_2$ gas mixture, the VGS length decreases and their number density increases. They also found that the thickness of nanosheets decreases with nitrogen concentration.

Koos *et al.*[12] have synthesized nitrogen doped graphene using methane and ammonia gases and found that the growth rate of graphene decreases by increasing the ammonia gas flow rate. They observed that upon increasing the synthesis temperature and ammonia gas flow rate, the concentration of nitrogen dopants increases.

Tang *et al.*[13] have found that boron doping increases the thickness of graphene (cf. Fig. S2 in the supplementary material of Tang *et al.*[13]). They also revealed that boron content in graphene increases on increasing the ion reaction time of trimethylboron decomposed by microwave plasma.

Jin *et al.*[14] have fabricated nitrogen doped graphene using CVD method with pyridine as both carbon and nitrogen sources. Their results indicate that dopant nitrogen atoms substitute for carbon atoms in the graphene lattice and the synthesized nitrogen doped graphene is monolayer and exhibits n-type behavior, different from pristine graphene.

Moreover, the influence of nitrogen and boron doping on the field emission characteristics of the graphene has also been studied widely.[3,15–18]

More *et al.*[15] have analyzed the field emission current fluctuations of mulitwalled carbon nanotubes, undoped, nitrogen, and boron doped graphene and polyaniline nanotubes. They have shown that amongst these materials, nitrogen doped graphene exhibits low turn-on field and highest field enhancement factor β. The highest β of nitrogen doped graphene has been attributed to the sharp edges of the graphene.

Takeuchi *et al.*[16] have observed that the electron emission current from the carbon nanowalls (CNWS) increases after the nitrogen plasma treatment. Their findings reveal that incorporation of N atoms increase the nanodomain size, electrical conductivity, and field emission characteristics.

Palnitkar *et al.*[17] used the boron and nitrogen doping to tailor the turn-on voltage and found that the nitrogen doped graphene exhibits the lowest turn on voltage, relative to undoped graphene. They also calculated the field enhancement factor β from the Fowler–Nordheim (FN) plot and found β to be largest for nitrogen-doped graphene followed by undoped and boron doped graphene (cf. Fig. 2 of Palnitkar *et al.*[17]). They accredited this observation to the nanometric features and resonance tunneling.

The low turn-on voltage and increase in the field emission current were also reported by Kashid *et al.*[3] and Soin *et al.*[18] They explained this behavior on the basis of change in the structure, improved electrical conductivity, and upshift of the Fermi level with nitrogen doping.

Using above mentioned motivation, we try to model the effect of different heteroatoms such as nitrogen and boron on the dimensions of GS (i.e., height and thickness) and their repercussion on the GS field enhancement factor. Moreover, as far as authors' knowledge is concerned, yet no theoretical model has been developed to study the effect of doping of heteroatoms on the growth and field emission properties of GS. In order to elucidate this effect, we develop a phenomenological model describing the surface deposition kinetics as well as the gas-phase processes of the species responsible for GS growth. The present theoretical model includes the charging rate of the GS; kinetics of various species in plasma, i.e., electrons, ions, and neutral atoms including doping species of nitrogen and boron; and the growth rate equation of the GS due to diffusion of carbon clusters on the catalyst surface.

The remainder of the paper is organized as follows: In Sec. II, we present the details of the GS growth model. Results and discussion are given in Sec. III. Finally, conclusion is given in Sec. IV.

II. MODEL

In the present paper, the catalytic growth of GS and typically a PECVD case is examined through a model that accounts acetylene, hydrogen, and ammonia/diborane as reaction gases. Fig. 1 shows the schematic of GS growth on the

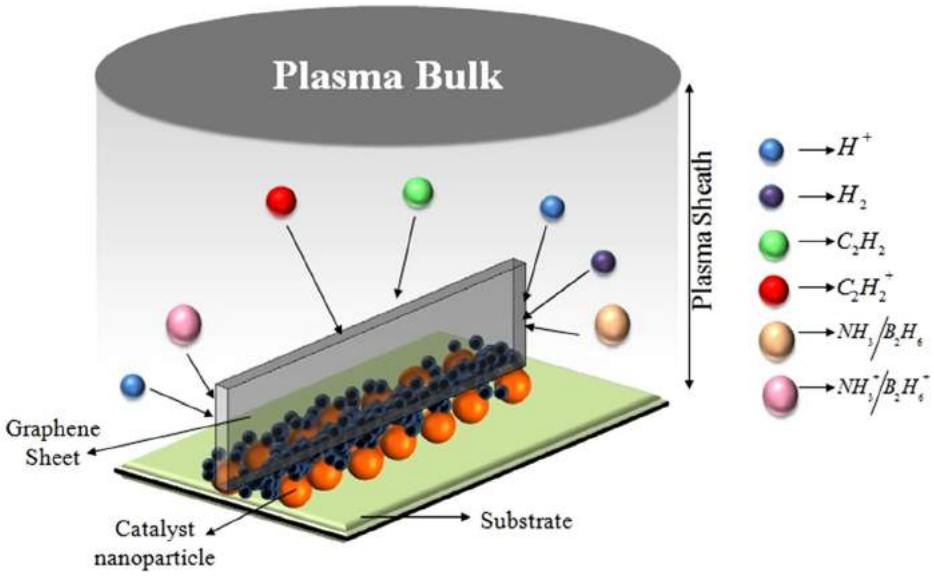

FIG. 1. Schematic of particle deposition on the graphene sheet and the catalyst nanoparticles.

Reuse of AIP Publishing content is subject to the terms at: https://publishing.aip.org/authors/rights-and-permissions. Downloaded to IP: 14.139.251.107 On: Wed, 17 Aug 2016 06:59:12

catalyst copper (Cu) over the silicon (Si) substrate surface, subjected to the incoming neutral and ionic species from the reactive plasma of $C_2H_2 + H_2 + NH_3/B_2H_6$ gas mixture. In reality, reactive plasma contains a plethora of different ions.[5] However, for simplicity, and following the experimental observations[19] and theoretical works,[5,6] the present model considers a plasma consisting of electrons, ions of acetylene ($C_2H_2^+$), hydrogen (H^+), doping ions of $NH_3^+/B_2H_6^+$ denoted as ions of type 1, 2, and 3, respectively, and neutrals of type 1, (acetylene, C_2H_2), type 2 (hydrogen, H_2), and type 3 (NH_3/B_2H_6). Among these, ammonia and diborane ions serve the purpose of nitrogen and boron doping, respectively, of the GS.

The stages for the catalyst-assisted growth of doped GS in plasma environment considered in the present model are as follows:

(i) Fragmentation of catalyst film into catalyst nanoparticles.
(ii) Nucleation of graphitic CN_x/CB_x clusters at the catalyst surface on account of reactive acetylene and doping species generated due to ionization of gas within the chamber.[20]
(iii) Formation of doped graphene islands due to diffusion and agglomeration of these clusters.[21]
(iv) Lateral extension or parallel growth of doped GS due to coalescence of the doped graphene islands.[21]
(v) The upward bending of the GS on account of stress generated at the graphene island boundaries.
(vi) The vertical growth of GS via delivery of carbon atoms at the graphene island boundaries.

More specific details of the GS growth process can be found elsewhere.[7] In a typical PECVD,[22–24] plasma sheath (areas with uncompensated surface charge) is formed near the boundaries of plasma-exposed substrate-catalyst surface. The GS is thus produced in the plasma sheath (rather in the plasma bulk) where the microscopic electric fields near the surface accelerate the ions towards the plasma-exposed surface. In the present model, we consider the sheath electric field (due to space-charge variation) to be directed along the z-axis which accelerates all ions toward the substrate.[6] To investigate the sheath structure, fluxes, and energy of the plasma generated species, the sheath kinetics are considered.

Following Mehdipour *et al.*[6] and Sharma and Gupta,[7] the sheath equations used are described by the continuity equation

$$\frac{d}{dz}(n_p v_{pz}) = f_{iz} n_e, \tag{1}$$

and the ion-momentum balance equation

$$M_p n_p v_{pz} \frac{dv_{pz}}{dz} = e n_p \frac{d\phi}{dz} - M_p n_p f_{pn} v_{pz}, \tag{2}$$

where p denotes either e, $C_2H_2^+$, H_2^+, or $NH_3^+/B_2H_6^+$. M_p, n_p, and v_{pz} are the mass, number density, and fluid velocity of the charged species p, respectively. Furthermore, f_{iz} and f_{pn} are the ionization frequency and collision frequency of the electrons and ion species with neutrals, respectively.

The sheath potential ϕ is determined by the Poisson's equation which relates the densities of charge particles to the electrostatic potential

$$\frac{d^2\phi}{dz^2} = -4\pi e \sum_p \xi_p n_p, \tag{3}$$

where ξ_p is the pth ion to electron number density ratio and is supplemented by the condition $\sum_p \xi_p = 1$, and $0 < \xi_p < 1$.

A. Charging of the graphene

Equation (4) describes the charge developed on the GS due to accretion of electrons and positively charged ions on the surface of the GS

$$Q'[\tau] = \sum_{j=1}^{3} I_{ijgn} - \gamma_e I_{egn}, \tag{4}$$

where Q is the charge over the GS, j refers to 1, 2, and 3 type of positively charged ions, and γ_e is the sticking coefficient of the constituent electrons, $I_{ijgn} = n_{ij}(x)(lt + ht + lh)\left(\frac{k_B T_{ij}}{2\pi^2 m_{ij}}\right)^{\frac{1}{2}} \left\{\frac{2}{\sqrt{\pi}}\left(\frac{eV_s}{k_B T_i}\right)^{\frac{1}{2}} + \exp\left[\frac{eV_s}{k_B T_{ij}}\right] erfc\left[\left(\frac{eV_s}{k_B T_{ij}}\right)^{\frac{1}{2}}\right]\right\} \times \exp\left[-\frac{eU_s}{k_B T_s}\right]$, $I_{egn} = \left(\frac{k_B T_e}{2\pi^2 m_e}\right)^{\frac{1}{2}} n_e(x)(lt + ht + lh)\exp\left[\frac{eV_s}{k_B T_e} + \frac{eU_s}{k_B T_s}\right]$ are the ion and electron collection current at the GS surface, respectively.[7] l, t, and h are the length, thickness, and height of the GS, respectively. T_{ij} is the ion temperature, m_{ij} is the ion mass (subscript j refers to either 1, 2, or 3 type of positively charged ion as explained earlier). $n_{ij}(x) = n_{ij0}\left(1 - \frac{2e\phi(x)}{m_{ij} v_{i0}^2}\right)^{-1/2}$ is the ion density at any point within the plasma sheath, where v_{i0} is the ion velocity, $\phi(x) = \phi_0 \exp\left(-\frac{|x|}{\lambda_d}\right)$ is the electrostatic potential, where ϕ_0 is the negative potential at the surface and λ_d is the Debye length, T_s is the substrate or catalyst temperature (assuming catalyst and substrate to be at the same temperature), V_s is the surface potential of the GS (Refer Eq. (A2) of Sharma and Gupta[7]), $n_e(x) = n_{e0} \exp\left[\frac{|e|\phi(x)}{k_B T_e}\right]$ is the electron density in plasma sheath, T_e is the electron temperature, m_e is the mass of electron, U_s is the substrate bias, and k_B is the Boltzmann constant.

In Eq. (4), the first term on the right hand side describes the charge developed on the graphene surface due to accretion of positively charged ions of types 1, 2, and 3. The last term indicates the reduction in charge on account of accretion of electrons at the surface of the GS.

B. Kinetic equation of electron density

Equation (5) describes the growth rate of electron density in plasma

$$n_e'[\tau] = \sum_{j=1}^{3} \beta_j n_j - \sum_{j=1}^{3} \alpha_j n_e n_{ij} - \gamma_e n_{gn} I_{egn}, \tag{5}$$

where β_j is the coefficient of ionization of the constituent neutral atoms due to external field, n_e is the electron number

Reuse of AIP Publishing content is subject to the terms at: https://publishing.aip.org/authors/rights-and-permissions. Downloaded to IP: 14.139.251.107 On: Wed, 17 Aug 2016 06:59:12

density, $\alpha_j(T_e) = \alpha_{j0}(\frac{300}{T_e})^k \mathrm{cm}^3/\mathrm{s}$ is the coefficient of recombination of electrons and positively charged ions,[25] $k = -1.2$ is a constant, and j refers to 1, 2, and 3 types of ions.

In Eq. (5), the first term on the right side is the gain in electron density per unit time because of ionization of neutral atoms of types 1, 2, and 3. The second term and third term display the decaying rate of the electron density due to electron–ion recombination and the electron collection current at the surface of the GS, respectively.

C. Kinetic equation of positively charged ion density

Equations (6a)–(6c) refer to the growth rate of positively charged ions of types 1, 2, and 3, respectively, in plasma

$$n'_{i1}(\tau) = \beta_1 n_1 - \alpha_1 n_e n_{i1} - n_{gn} I_{i1gn} - J_{ai1} + J_{desorpi1} + \sum_i k_{i1} n_1 n_{i3}, \tag{6a}$$

$$n'_{i2}(\tau) = \beta_2 n_2 - \alpha_2 n_e n_{i2} - n_{gn} I_{i2gn} - J_{ai2} + J_{desorpi2} + J_{th} + \sum_i k_{i2} n_2 n_{i3}, \tag{6b}$$

$$n'_{i3}(\tau) = \beta_3 n_3 - \alpha_3 n_e n_{i3} - n_{gn} I_{i3gn} - J_{ai3} + J_{desorpi3} + \sum_i k_{i1} n_1 n_{i3} + \sum_i k_{i2} n_2 n_{i3}, \tag{6c}$$

where $J_{aij} = \frac{P_i}{(2\pi m_{ij} k_B T_{ij})^{\frac{1}{2}}} \times \frac{n_{ij}}{J_{ij}}$ is the adsorption flux onto the catalyst substrate surface;[26] P_i is the partial pressure of adsorbing species; J_{ij} and n_{ij} are the ion flux and ion number density at the catalyst-substrate surface, respectively, j refers to either 1, 2, or 3 type of ions, $J_{desorpij} = n_{ij}\nu \exp(-\frac{\varepsilon_{ai}}{k_B T_{ij}})$ is the desorption flux from the catalyst-substrate surface;[26] ν is the thermal vibration frequency, ε_{ai} is the adsorption energy, $J_{th} = n_H \nu \exp\left(\frac{-\delta\varepsilon_{th}}{k_B T_s}\right)$ is the flux of type 2 ion (namely, hydrogen) on account of thermal dehydrogenation; $\delta\varepsilon_{th}$ is the activation energy of thermal dehydrogenation, and n_H is the hydrogen ion number density at catalyst-substrate surface.

The first term on the right hand side in Eqs. (6a)–(6c) describes the gain in ion density per unit time on account of ionization of neutral atoms. The second and third term represents the rate of decrease in positively charged ion density due to electron-ion recombination and ion collection current at the surface of the graphene, respectively. The next two terms denote the adsorption and desorption of ions to/from the catalyst-substrate surface, respectively. The term J_{th} in Eq. (6b) represents the increase of hydrogen ion number density in plasma because of thermal dehydrogenation.[7] The last term in Eqs. (6a)–(6c) accounts for the gain of ion density due to ion-neutral reactions[27] and their reaction rate coefficients[28,29] are $k_{i1} = 1.4 \times 10^{-9}\,\mathrm{cm}^3/\mathrm{s}$ and $k_{i2} = 7.8 \times 10^{-9}\,\mathrm{T_n}^{-0.39} \exp(-14.8/\mathrm{T_n})\,\mathrm{cm}^3/\mathrm{s}$.

D. Kinetic equation of neutral atoms

Equations (7a)–(7c) refer to the growth rate of neutrals of types 1, 2, and 3, respectively, in plasma

$$n'_1(\tau) = \alpha_1 n_e n_{i1} - \beta_1 n_1 + n_{gn}(1-\gamma_{i1}) I_{i1gn} - n_{gn}\gamma_1 I_{1gn} - \sum_i k_{i1} n_1 n_{i3}, \tag{7a}$$

$$n'_2(\tau) = \alpha_2 n_e n_{i2} - \beta_2 n_2 + n_{gn}(1-\gamma_{i2}) I_{i2gn} - n_{gn}\gamma_2 I_{2gn} - \sum_i k_{i2} n_2 n_{i3}, \tag{7b}$$

$$n'_3(\tau) = \alpha_3 n_e n_{i3} - \beta_3 n_3 + n_{gn}(1-\gamma_{i3}) I_{i3gn} - n_{gn}\gamma_3 I_{3gn} - \sum_i k_{i1} n_1 n_{i3} - \sum_i k_{i2} n_2 n_{i3}, \tag{7c}$$

where $I_{jgn} = n_j(lt + ht + lh)(\frac{k_B T_n}{2\pi^2 m_j})^{\frac{1}{2}}$ is the neutral collection current at the surface of graphene, j refers to either 1, 2, or 3 type of neutral atom, T_n is the neutral temperature, m_j is the mass of neutral atom, n_j is the neutral atom density, γ_j and γ_{ij} are the sticking coefficients of the corresponding neutral atoms and ions, respectively.

The first term on the right side in Eqs. (7a)–(7c) denotes the gain in neutral atom density per unit time due to electron–ion recombination. The next two terms represent the decaying rate of neutral atom density due to ionization, gain in neutral density due to neutralization of ions collected at the graphene surface, respectively. The fourth term is the accretion of neutral atoms of species 1, 2, and 3 on the graphene surface,[7] and the last term is the decay in neutral atom density on account of neutral-ion reactions.[27]

E. Kinetic equation for the growth of graphene nuclei

Initially, the applied plasma power fragments the catalyst film into catalyst nanoislands. We consider the size of the catalyst nanoparticle to be 40 nm.[30] Various processes such as thermal and ion-induced dissociation of hydrocarbon gas; adsorption and decomposition of acetylene ions; decomposition, interaction of adsorbed acetylene ions with hydrogen; thermal dissociation of carbon source gas of acetylene ions, surface diffusion; accretion and other processes leads to the formation of C-atom clusters. The surface diffusion (with energy barrier E_{sdCl}) and agglomeration of these C-clusters lead to the formation of graphene island (with radius R_g).[7]

Following Sharma and Gupta[7]

$$\frac{d}{d\tau}\left(\pi R_g^2\right) = \left[\left\{2n_{CH}\nu \exp\left(\frac{-\delta E_i}{k_B T_s}\right) + 2\theta_{CH} J_{i1} y_d + 2J_{i1} + \frac{J_{i1}\sigma_{ads} J_{i2}}{\nu} + J_c\right\} m_c + \left\{J_{i1}(1-\theta_t) + \frac{J_{i1}\sigma_{ads} J_H}{\nu} + J_{i1}\exp\left(\frac{-\delta E_i}{k_B T_s}\right)\right\} m_{i1}\right] \times \frac{2\pi R_{cat}}{\pi R_{cat}^2 \rho_{cat}}\left(D_1 \exp\left(\frac{-E_{sdC}}{k_B T_s}\right) + D_2 \exp\left(\frac{-E_{sdCl}}{k_B T_s}\right)\right) \times \left(\frac{1}{I_{i1g}}\right) + \gamma_{C_2H_2}\pi R_{cat}^2 I_{C_2H_2 g} + \gamma_d \pi R_{cat}^2 I_{dg}, \tag{8}$$

Reuse of AIP Publishing content is subject to the terms at: https://publishing.aip.org/authors/rights-and-permissions. Downloaded to IP: 14.139.251.107 On: Wed, 17 Aug 2016 06:59:12

where R_g is the radius of the graphene nuclei, R_{cat} is the radius of the catalyst nanoparticle, ρ_{cat} is the mass density of the catalyst particle, $n_{CH}(=\theta_{CH}\nu_0)$ is the surface concentration of CH; θ_{CH} is the surface coverage by C_2H_2 species[6] and $\nu_0(\approx 10^{15}\text{cm}^{-2})$ is the number of adsorption sites per unit area,[6] δE_i is the thermal energy barrier ($\approx$1.87 eV),[21] $y_d(\approx 2.49 \times 10^{-2} + 3.29 \times 10^{-2} \times E_i$; where E_i is the ion energy in eV) is the stitching probability,[31] $J_{ij} = \left(n_{ij}\left(\frac{k_B T_e}{m_{ij}}\right)^{\frac{1}{2}}\right)$ is the flux of type j ion[7] (where, j refers to 1 or 2 type of ion, $\sigma_{ads}(\approx 10^{-16}\text{cm}^2)$ is the cross-section for the reactions of atomic hydrogen,[6] $J_\alpha = (n_\alpha v_{th\alpha}/4)$ is the flux of impinging species α (where $\alpha = C, H$); C and H stands for carbon and hydrogen species, respectively, n_α and $v_{th\alpha}$ are the number density and thermal velocity of α species, respectively,[6] $\nu(=10^{13}\text{Hz})$ is the thermal vibration frequency,[6] $m_C(=12$ a.m.u) is carbon atom mass, $m_{i1}(=26$ a.m.u for $C_2H_2^+$) is the mass of type 1 ions, $D_1\exp\left(\frac{-E_{sdC}}{k_B T_s}\right)$ and $D_2\exp\left(\frac{-E_{sdCl}}{k_B T_s}\right)$ are the surface diffusion coefficients of carbon monomers and C-atom clusters, respectively, with corresponding activation energies, E_{sdC}= 0.1 eV and E_{sdCl} = 0.82 eV, respectively.[21] $I_{ijg} = \left(\pi {R_g}^2\left(\frac{8k_B T_i}{\pi m_{ij}}\right)^{\frac{1}{2}} n_{ij}(x)\left[1 - Q\gamma_{ji}\right]\exp\left[-\frac{eU_s}{k_B T_s}\right]\right)$ is the ion collection current at the surface of the graphene nuclei, (where j refers to either 1 or 2 type of ion); $\gamma_{ji} = \frac{e^2}{R_g k_B T_s}$, $I_{jg} = \left(\pi R_g^2\left(\frac{8k_B T_n}{\pi m_j}\right)^{\frac{1}{2}} n_j\right)$ is the neutral collection current at the surface of the graphene nuclei,[7] j refers to neutral atom of types 1, 2, or 3, $I_{C_2H_2 g}$ and I_{dg} corresponds to the collection current of acetylene and doping neutral atom, respectively, and $\gamma_{C_2H_2}$ and γ_d are the sticking coefficients of neutrals of types 1 and 3, respectively.

Equation (8) outlines the growth of graphene island on the catalyst nanoparticle. Here, the first term and second term in the first bracket on the right side[6] indicates the generation of carbon atoms on the catalyst surface due to thermal dissociation of acetylene ions (with activation energy of thermal dissociation, δE_i) and ion induced dissociation of C_2H_2, respectively;[6] third term denotes the decomposition of positively charged hydrocarbon ions, i.e., $C_2H_2^+$; fourth term is the interaction of adsorbed type 1 ions with hydrogen ions;[6] fifth term denotes the rate of the incoming flux of carbon atoms onto the catalyst particle.[6] The terms in the second bracket refers to the adsorption flux of type1 ions to the catalyst surface, interaction of adsorbed type 1 ions with atomic hydrogen from plasma, and thermal dissociation of hydrocarbon source gas C_2H_2, respectively.[6] The factor I_{i1g} accounts for the collection current of type1 ion on the growing graphene island. The last two terms denote the accretion of neutral acetylene and doping gas atoms to the graphene island.

F. Growth rate equation for the graphene sheet

$$l\frac{d(h\times t)}{d\tau} = \left(\left(\frac{n_1}{\nu}\times D_1\exp\left\{\frac{E_d + E_{inc}}{k_B T_s}\right\}\right)\frac{\pi R_g^2}{2\pi R_g} \times (I_{i1gn}) + (\gamma_{C_2H_2} I_{C_2H_2 gn}) + (\gamma_d I_{dgn})\right) \times \frac{M_{gn}}{\rho_{gn}}, \quad (9)$$

$$[h(\tau) + l]\frac{d(t)}{d\tau} = \left\{J_{i2}\exp\left(\frac{-\delta E_{sdh}}{k_B T_s}\right) + J_{i2}(1-\theta_t) + J_{i2} + \theta_{CH}\left(J_{i2} y_d + \nu_0\nu\exp\left(\frac{-\delta E_i}{k_B T_s}\right)\right) + \theta_{NH}\left(J_{i2} y_d + \nu_0\nu\exp\left(\frac{-\delta E_i}{k_B T_s}\right)\right)\right\}\frac{h(\tau)}{n_{i2}} + \gamma_{C_2H_2}\pi R_g^2 I_{C_2H_2 gn} + \gamma_d \pi R_g^2 I_{dgn}, \quad (10)$$

where ρ_{gn} is the GS density, M_{gn} is the mass of the growing GS ($M_{gn} \approx 12g$), θ_{CH}, and θ_{NH} are the surface coverage by C_2H_2 and NH_3, respectively.

The growth of graphene island results in the formation of planar GS. Due to influence of stress and/or localized electric field due to plasma at the graphene island boundaries, the initial planar growth of GS eventually switches to the vertical growth of GS. At this stage, GS grows due to continuous delivery of dissociated carbon species from the plasma (i.e., due to ion and neutral collection current) at the surface of the growing doped GS.[32] The last two terms in Eq. (9) represent the sticking of neutral atoms 1 and 3 at the GS and the factor I_{i1gn} corresponds to the ion collection on the growing doped GS. The diffusion (with energy barrier, $E_d \approx 0.13$eV) and attachment of carbon atoms (with energy barrier, $E_{inc} \approx 0.4$ eV) at the peripherals of the growing graphitic platelets also contribute to the growth of GS.[33] The similar effect has been incorporated in the first term of Eq. (9). Moreover, in Eq. (9), length (l) of the doped GS has been presumed to be 0.81 μm[11] as we believe that the length of the GS progresses during the planar growth of the GS. Finally, the growing edges of the GS are terminated by the etching of carbon atoms.[32] This effect has been accounted in Eq. (10) which describes the decrease in thickness of GS due to etching of carbon atoms. In Eq. (10) the first term on the right hand side refers the incoming flux of type 2 ions, i.e., hydrogen due to thermal dehydrogenation of type 1 ions (see Ref. 6) and second term accounts the adsorption of type 2 ions to the surface. The third term is the decomposition of positively charged ions of type 2 (see Ref. 6); the fourth term describes ion induced dissociation of acetylene (see Ref. 6); and the fifth term (see Ref. 6) is due to the incorporation of hydrogen ions due to thermal dissociation of acetylene ions. The next two terms describe the generation of hydrogen due to ion induced dissociation of ammonia[29] and thermal decomposition of ammonia ions.[34] The last two terms denote the sticking of neutrals of types 1 and 3, respectively, on the surface of the GS.

III. RESULTS AND DISCUSSION

In the present paper, a theoretical model has been invoked to understand the growth and field emission characteristics of the GS on account of effect of doping of heteroatoms such as nitrogen and boron. In particular, we investigate the effect of nitrogen and boron doping on the dimensions, i.e., thickness and height of the GS through the catalyst-assisted PECVD process. The charging rate of the GS, kinetics of the electrons, ions, and neutrals; adsorption,

Reuse of AIP Publishing content is subject to the terms at: https://publishing.aip.org/authors/rights-and-permissions. Downloaded to IP: 14.139.251.107 On: Wed, 17 Aug 2016 06:59:12

surface diffusion, and accretion of carbon species via several processes on the catalyst surface; formation of clusters and graphene islands; vertical growth of GS in the presence of doping species has been incorporated in the model.

Using the analytical equations presented in Section II, we will now investigate the influence of doping on the dimensions (i.e., height and thickness) of GS with time and its repercussions on the field enhancement factor of GS. To elucidate this effect, we have simultaneously solved first order differential Eqs. (1)–(10) numerically with the aid of MATHEMATICA software using typical glow discharge parameters, i.e., at appropriate boundary conditions, viz., at $\tau = 0$, electron number density $n_{e0}(=10^{10}\,\mathrm{cm}^{-3})$, ion number density of ion 1 $n_{i10}(=0.8n_{e0})$, ion number density of ion 2 $n_{i20}(=0.7n_{e0})$, and ion number density of ion 3 $n_{i30}(=0.5n_{e0})$, number density of neutral atom j $n_{j0}(=5\times10^{12}\,\mathrm{cm}^{-3})$, where j = 1, 2, and 3, electron temperature $T_{e0}(=1.6\,\mathrm{eV})$, ion temperature $T_{i0}(=2400\,\mathrm{K})$, neutral temperature $T_{n0}(=2000\,\mathrm{K})$, charge on the GS surface Q_0 $(=-1\,\mathrm{stat\,C})$, mass of ion 1 $m_{i1}(=26$ a.m.u for $C_2H_2^+)$, mass of ion 2 $m_{i2}(=1$ a.m.u for $H^+)$, mass of ion 3 $m_{i3}(=17$ a.m.u for NH_3^+ and 27.62 a.m.u for $B_2H_6^+)$, radius of graphene nuclei $R_{g0}(=80\,\mathrm{nm})$,[35] density of catalyst Cu $\rho_{ct}(=8.96\,\mathrm{g/cm}^3)$, coefficient of recombination of electrons and ions $\alpha_{10}\approx\alpha_{20}(=1.12\times10^{-7}\,\mathrm{cm}^3/\mathrm{s})$, $\kappa=-1.2$, and substrate temperature $T_s(=550\,^\circ\mathrm{C})$. Other parameters used in the calculations are sticking coefficient of electron $\gamma_e(=1)$, sticking coefficient of ion γ_{ij} $(=1)$, thermal energy barrier on the catalyst surface $\delta E_i(=1.87\,\mathrm{eV})$, energy barrier for diffusion of carbon monomers $E_{sdC}(=0.1\,\mathrm{eV})$ and for carbon clusters $E_{sdCl}(=0.82\,\mathrm{eV})$, and energy due to dehydrogenation of C_2H_2 $\delta E_{sdh}(=1.7\,\mathrm{eV})$.

Fig. 2 shows the variation of thickness of undoped, nitrogen-doped, and boron-doped GS with time. From Fig. 2, it can be seen that doping of GS with heteroatoms such as nitrogen decreases the thickness of GS and boron increases the thickness of GS. The decrease in thickness of nitrogen doped GS can be explained in many ways. One such explanation is that the introduction of ammonia in the chamber produces nitrogen and hydrogen species in the plasma which leads to the etching of the GS edges. Moreover, several researchers have reported that addition of ammonia results in the generation of cyanide species (due to reaction of nitrogen species with hydrocarbon species) which further augments the etching of the GS and thereby leads to thinning of the GS.[11,19,36,37] It has also been reported that NH_3 is more effective source of atomic hydrogen than H_2; therefore, the etching effect of hydrogen is more pronounced in nitrogen doped GS as compared to undoped GS.[36] Furthermore, as ammonia ions contain nitrogen which is pentavalent, the presence of nitrogen atom on the GS surface produces an extra electron which increases the ionization of neutral atoms; therefore, the number density of neutral atoms available for accretion decreases and eventually lead to GS with reduced thickness. However, in the case of boron doped GS, boron captures an electron from the GS surface, which decreases the electron density, and hence, ionization of neutral atoms reduces. Thus, the thickness of boron doped GS is high due to the reduced ionization and increased number density of neutral atoms available for accretion. The results of Fig. 2 are in compliance with the experimental observations of Seo *et al.*[11] and Tang *et al.*[13] (cf. Fig. S2 in the supplementary material of Tang *et al.*[13]).

Fig. 3 illustrates the variation of height of undoped, nitrogen doped, and boron doped GS with time. Fig. 3 indicates that the height of GS shortens with nitrogen doping and increases upon doping with boron. This is because the neutral atoms available for accretion is less in the case of nitrogen doping as compared to boron doping, as explained above for Fig. 2. The similar effect can be seen from Fig. 4 which indicates that the hydrocarbon density decays faster for nitrogen-doped GS followed by undoped and boron-doped GS. In addition, the Fig. 4 also displays that at a particular time, the hydrocarbon density is least for nitrogen doped GS followed by undoped and boron doped GS. It is believed that upon doping with nitrogen, the generation of cyanide and hydrogen species increases which form a barrier for GS growth. These species act as the sink for carbon that might otherwise participated in the GS growth.[31] The reduction in number density of hydrocarbon species upon addition of ammonia is in compliance with the results of Bell *et al.*,[19] Woo *et al.*,[36] and Smith *et al.*[37]

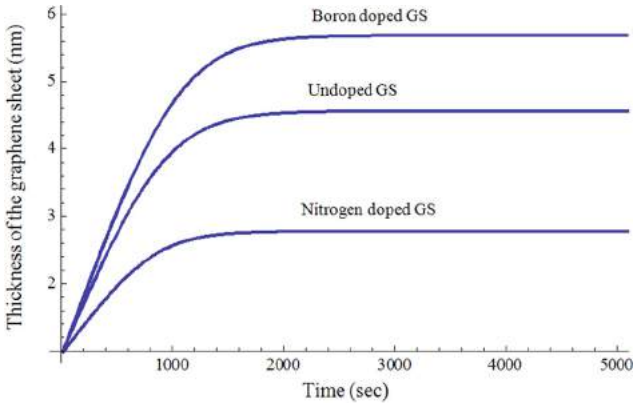

FIG. 2. This figure illustrates the time variation of the thickness (in nm) of undoped, nitrogen doped, and boron doped graphene sheet. The other parameters are given in the text.

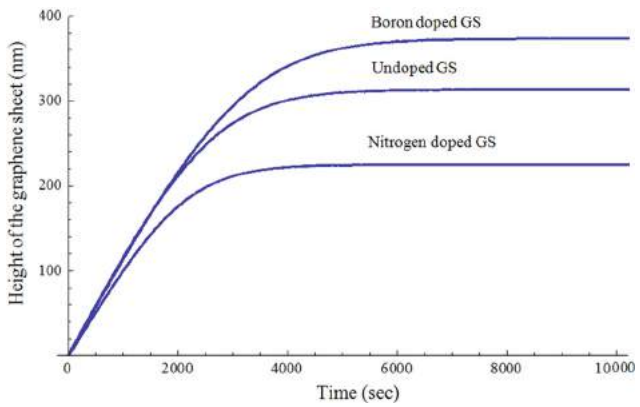

FIG. 3. This figure illustrates the time variation of the height (in nm) of undoped, nitrogen doped, and boron doped graphene sheet. The other parameters are given in the text.

Reuse of AIP Publishing content is subject to the terms at: https://publishing.aip.org/authors/rights-and-permissions. Downloaded to IP: 14.139.251.107 On: Wed, 17 Aug 2016 06:59:12

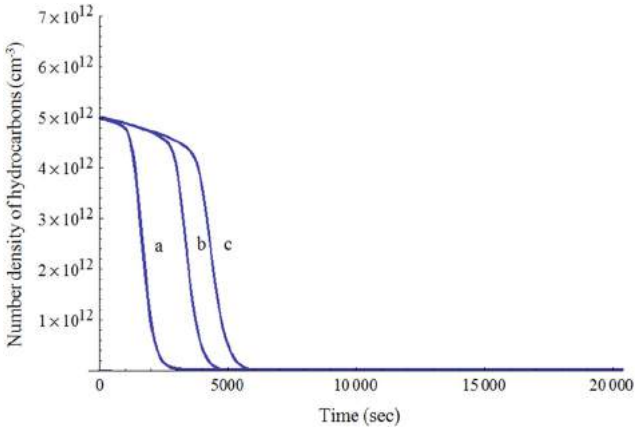

FIG. 4. This figure illustrates the time variation of hydrocarbon number density (in cm^{-3}) for undoped (b), nitrogen doped (a), and boron doped (c) graphene sheet. The other parameters are given in the text.

The results of Fig. 3 are in accordance with the experimental works of Koos *et al.*[12] (cf. Fig. 4 of Koos *et al.*[12]). The similar effect of nitrogen and boron doping on the height was observed by Sumpter *et al.*[38] and Blase *et al.*[39] in their nitrogen and boron mediated growth of carbon nanotubes, respectively.

Fig. 5 depicts the time evolution of charge on undoped, nitrogen, and boron doped GS. From Fig. 5, it can be seen that the charge developed on the nitrogen doped GS is more followed by undoped and boron doped GS. This is ascribed to the fact that upon nitrogen doping the electron number density increases whereas upon doping with boron, the concentration of electron holes increases that engulfs the electron and consequently retards the electron density. The n and p type feature of nitrogen doped and boron doped GS, respectively, can be accredited to this observation.

The field emission characteristics are primarily characterized by the field enhancement factor β that specifies the amplification of electric field at the tip of the emitters. The field enhancement factor $\beta\left(\approx\frac{h}{t}\right.$, where h is the height and t is the thickness of GS$)$[40,41] of GS is mainly dependent on the geometry of the GS. From the above results obtained, we found that the height and thickness of GS changes with the effect of doping. Thus, in order to study the effect of

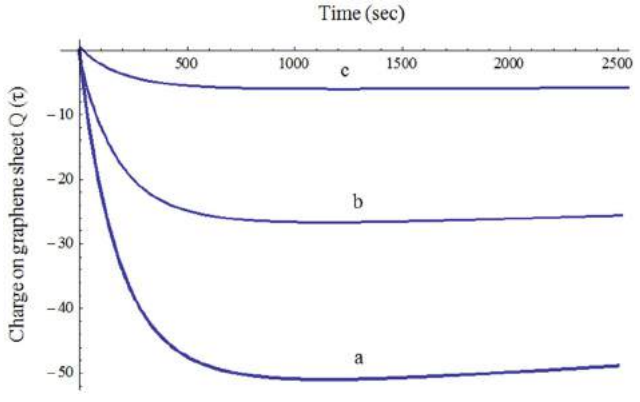

FIG. 5. This figure illustrates the time variation of charge for undoped (b), nitrogen doped (a), and boron doped (c) graphene sheet.

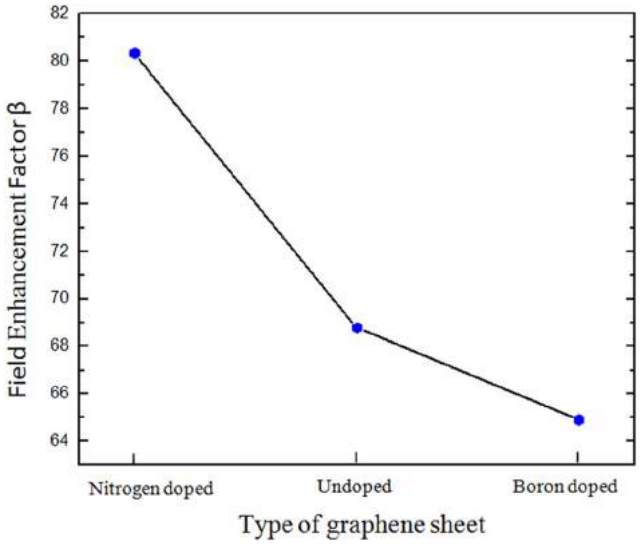

FIG. 6. This figure illustrates field enhancement factor β for undoped, nitrogen doped, and boron doped graphene sheet.

doping on the field emission characteristics of GS, we calculated the field enhancement factor corresponding to saturated value of thickness (i.e., 4.4 nm for undoped GS, 2.65 nm for nitrogen doped GS and 5.6 nm for boron doped GS) and height (i.e., 300 nm for undoped GS, 215 nm for nitrogen doped GS and 360 nm for boron doped GS) for all three types of GS. The variation of field enhancement factor β for the undoped, nitrogen doped, and boron doped GS is illustrated in Fig. 6. It is found that nitrogen doped GS has highest field enhancement factor followed by undoped and boron doped GS. This result is attributed to the fact that nitrogen doped GS has least thickness followed by undoped and boron doped GS. Moreover, it can also be seen from Figs. 2 and 3 that the effect of nitrogen doping is more pronounced on the thickness of GS than on the height of the GS. The results of Fig. 6 are similar to the experimental observations of More *et al.*,[15] Takeuchi *et al.*,[16] Palnitkar *et al.*,[17] Kashid *et al.*,[3] and Soin *et al.*[18] Hence, doping of GS with nitrogen improves the field emission characteristics of GS, and boron doping hampers the field emission from GS.

IV. CONCLUSION

A theoretical model to investigate the effect of nitrogen and boron doping on the growth of GS by a PECVD process has been developed and its field emission properties have been estimated. It is observed from our study that on nitrogen addition, the thickness and height of the GS decreases and with boron doping, the thickness and height of the GS increases. These results have been explained on the basis of decrease and increase of hydrocarbon density on nitrogen and boron doping of the GS, respectively. The field enhancement factor β estimated from these results reveals that the nitrogen doped GS has highest field enhancement factor followed by undoped and boron doped GS. The present work would pave the way for highly efficient graphene based field emitters.

Reuse of AIP Publishing content is subject to the terms at: https://publishing.aip.org/authors/rights-and-permissions. Downloaded to IP: 14.139.251.107 On: Wed, 17 Aug 2016 06:59:12

ACKNOWLEDGMENTS

This work has been partially supported by the Department of Science and Technology (DST), Government of India.

[1]K. S. Novoselov, A. K. Geim, S. V. Morozov, D. Jiang, Y. Zhang, S. V. Dubonos, I. V. Grigorieva, and A. A. Firsov, Science **306**, 666 (2004).
[2]W. Choi, I. Lahiri, R. Seelaboyina, and Y. S. Kang, Crit. Rev. Solid State Mater. Sci. **35**, 52 (2010).
[3]R. V. Kashid, M. Z. Yusop, C. Takahashi, G. Kalita, L. S. Panchakarla, D. S. Joag, M. A. More, and M. Tanemura, J. Appl. Phys. **113**, 214311 (2013).
[4]M. Araidai, Y. Nakamura, and K. Watanabe, Phys. Rev. B **70**, 245410 (2004).
[5]I. Denysenko and N. A. Azarenkov, J. Phys. D: Appl. Phys. **44**, 174031 (2011).
[6]H. Mehdipour, K. Ostrikov, and A. E. Rider, Nanotechnology **21**, 455605 (2010).
[7]S. C. Sharma and N. Gupta, Phys. Plasmas **22**, 123517 (2015).
[8]Y. Wang, Y. Shao, D. W. Matson, J. Li, and Y. Lin, ACS Nano **4**, 1790 (2010).
[9]L. H. Chan, K. H. Hong, D. Q. Xiao, W. J. Hsieh, S. H. Lai, H. C. Shih, T. C. Lin, F. S. Shieu, K. J. Chen, and H. C. Cheng, Appl. Phys. Lett. **82**, 4334 (2003).
[10]S. C. Sharma, A. Tewari, and R. Gupta, J. At. Mol. Condens. Nanophys. **2**, 195 (2015), available at: <http://www.rgnpublications.com/journals/index.php/jamcnp/article/view/342>.
[11]D. H. Seo, S. Kumar, A. K. Rider, Z. Han, and K. Ostrikov, Opt. Mat. Express **2**, 700 (2012).
[12]A. A. Koos, A. T. Murdock, P. Nemes-Incze, R. J. Nicholls, A. J. Pollard, S. J. Spencer, A. G. Shard, D. Roy, L. P. Biro, and N. Grobert, Phys. Chem. Chem. Phys. **16**, 19446 (2014).
[13]Y.-B. Tang, L.-C. Yin, Y. Yang, X.-H. Bo, Y.-L. Cao, H.-E. Wang, W.-J. Zhang, I. Bello, S.-T. Lee, H.-M. Cheng, and C.-S. Lee, ACS Nano **6**, 1970 (2012).
[14]Z. Jin, J. Yao, C. Kittrell, and J. M. Tour, ACS Nano **5**, 4112 (2011).
[15]M. A. More, R. V. Kashid, S. S. Patil, D. R. Shinde, and D. S. Joag, in *Proceedings of the 25th International Vacuum Nanoelectronics Conference, Jeju* (2012), pp. 1–2.
[16]W. Takeuchi, H. Kondo, T. Obayashi, M. Hiramatsu, and M. Hori, Appl. Phys. Lett. **98**, 123107 (2011).
[17]U. A. Palnitkar, R. V. Kashid, M. A. More, D. S. Joag, L. S. Panchakarla, and C. N. R. Rao, Appl. Phys. Lett. **97**, 063102 (2010).
[18]N. Soin, S. S. Roy, S. Roy, K. S. Hazra, D. S. Misra, T. H. Lim, C. J. Hetherington, and J. A. McLaughlin, J. Phys. Chem. C **115**(13), 5366 (2011).
[19]M. S. Bell, R. G. Lacerda, K. B. K. Teo, N. L. Rupesinghe, G. A. J. Amaratunga, and W. I. Milne, Appl. Phys. Lett. **85**, 1137 (2004).
[20]D. Wei, L. Peng, M. Li, H. Mao, T. Niu, C. Han, W. Chen, and A. T. S. Wee, ACS Nano **9**, 164 (2015).
[21]H. Mehdipour and K. Ostrikov, ACS Nano **6**, 10276 (2012).
[22]Y. Ma, H. Jang, S. J. Kim, C. Pang, and H. Chae, Nanoscale Res. Lett. **10**, 1 (2015).
[23]Y. Zhang, Q. Zou, H. S. Hsu, S. Raina, Y. Xu, J. B. Kang, J. Chen, S. Deng, N. Xu, and W. P. Kang, ACS Appl. Mater. Interfaces **8**, 7363 (2016).
[24]S. Kumar and K. Ostrikov, Nanoscale **3**, 4296 (2011).
[25]M. S. Sodha, S. Misra, S. K. Misra, and S. Srivastava, J. Appl. Phys. **107**, 103307 (2010).
[26]O. A. Louchev, C. Dussarat, and Y. Sato, J. Appl. Phys. **86**, 1736 (1999).
[27]I. B. Denysenko, S. Xu, J. D. Long, P. P. Rutkevych, N. A. Azarenkov, and K. Ostrikov, J. Appl. Phys. **95**, 2713 (2004).
[28]See http://www.udfa.net/ for database of neutral-ion reactions rate coefficients.
[29]D. B. Hash, M. S. Bell, K. B. K. Teo, B. A. Cruden, W. I. Milne, and M. Meyyappan, Nanotechnology **16**, 925 (2005).
[30]J. Li, J. Chen, B. Shen, X. Yan, and Q. Xue, Appl. Phys. Lett. **99**, 163103 (2011).
[31]N. V. Mantzaris, E. Gogolides, A. G. Boudouvis, A. Rhallabi, and G. Turban, J. Appl. Phys. **79**, 3718 (1996).
[32]M. Cai, R. A. Outlaw, S. M. Butler, and J. R. Miller, Carbon **50**, 5481 (2012).
[33]Z. Bo, S. Mao, Z. J. Han, K. Cen, J. Chen, and K. Ostrikov, Chem. Soc. Rev. **44**, 2108 (2015).
[34]M. Grunze, C. R. Brundle, and D. Tomanek, Surf. Sci. **119**, 133 (1982).
[35]Z. Bo, K. Yu, G. Lu, P. Wang, S. Mao, and J. Chen, Carbon **49**, 1849 (2011).
[36]Y. S. Woo, D. Y. Jeon, I. T. Han, N. S. Lee, J. E. Jung, and J. M. Kim, Diamond Relat. Mater. **11**, 59 (2002).
[37]J. A. Smith, J. B. Wills, H. S. Moores, A. J. Orr-Ewing, and M. N. R. Ashfold, J. Appl. Phys. **92**, 672 (2002).
[38]B. G. Sumpter, V. Meunier, J. M. Romo-Herrera, E. Cruz-Silva, D. A. Cullen, H. Terrones, D. J. Smith, and M. Terrones, ACS Nano **1**, 369 (2007).
[39]X. Blase, J.-C. Charlier, A. De Vita, R. Car, P. Redlich, M. Terrones, W. K. Hsu, H. Terrones, D. L. Carroll, and P. M. Ajayan, Phys. Rev. Lett. **83**, 5078 (1999).
[40]S. Watcharotone, R. S. Ruoff, and F. H. Read, Phys. Procedia **1**, 71 (2008).
[41]R. Miller, Y. Y. Lau, and J. H. Booske, Appl. Phys. Lett. **91**, 074105 (2007).

Reuse of AIP Publishing content is subject to the terms at: https://publishing.aip.org/authors/rights-and-permissions. Downloaded to IP: 14.139.251.107 On: Wed, 17 Aug 2016 06:59:12

Accepted Manuscript

Title: Nanosilica based electrochemical biosensor: A novel approach for the detection of platelet-derived microparticles

Author: Priti Singh Sameer Srivastava Parthasarathi Chakrabarti<ce:author id="aut0020" biographyid="vt0020" orcid="0000-0001-6603-6282"> Sunil Kumar Singh

PII: S0925-4005(16)31369-7
DOI: http://dx.doi.org/doi:10.1016/j.snb.2016.08.136
Reference: SNB 20817

To appear in: *Sensors and Actuators B*

Received date: 10-5-2016
Revised date: 22-8-2016
Accepted date: 24-8-2016

Please cite this article as: Priti Singh, Sameer Srivastava, Parthasarathi Chakrabarti, Sunil Kumar Singh, Nanosilica based electrochemical biosensor: A novel approach for the detection of platelet-derived microparticles, Sensors and Actuators B: Chemical http://dx.doi.org/10.1016/j.snb.2016.08.136

This is a PDF file of an unedited manuscript that has been accepted for publication. As a service to our customers we are providing this early version of the manuscript. The manuscript will undergo copyediting, typesetting, and review of the resulting proof before it is published in its final form. Please note that during the production process errors may be discovered which could affect the content, and all legal disclaimers that apply to the journal pertain.

ACCEPTED MANUSCRIPT

Nanosilica based electrochemical biosensor: A novel approach for the detection of platelet-derived microparticles

Priti Singh[a], Sameer Srivastava[a], Parthasarathi Chakrabarti[b] and Sunil Kumar Singh[a *]

[a] Department of Biotechnology, Motilal Nehru National Institute of Technology, Allahabad-211004 Uttar Pradesh, India.

[b] Indian Institute of Technology (BHU), Department of Electronics Engineering, Varanasi-221005, India[**]

priti656@gmail.com, sameers@mnnit.ac.in, pchakrabarti.ece@itbhu.ac.in

[*]Corresponding author, E-mail: singh.sunil06@gmail.com, +919450950549, Fax: 0091-532-2545341

[**]The author is currently on deputation as Director, Motilal Nehru National Institute of Technology Allahabad, Allahabad-211004, India

Research Highlights:

1. Nanosilica-based electrochemical biosensor has been developed for the detection of platelet-derived microparticles.
2. Electrochemically deposited thionine doped silica and horseradish peroxidase entrapped mesoporous silica was utilized for detection of membrane activation markers.
3. Simultaneous detection of microparticles through two different antibodies enhances the specificity of the sensor, minimizing the chance of false detection.
4. Detection and quantification of microparticles will provide information about platelet quality over storage i.e. platelet storage lesion to overcome adverse clinical outcomes associated with the transfusion.
5. Developed sensor proved to be highly specific in identifying PMPs in plasma and offers highly biocompatible, label-free, cost-effective, ease of miniaturization, short analysis time and simple instrumentation for the detection of biomarkers for a variety of diseases.

ACCEPTED MANUSCRIPT

Abstract

Elevation of platelet-derived microparticles (PMPs) in blood plasma has a strong correlation with the pathogenesis of diseases like thrombosis, diabetes, cancer and considered as a potential biomarker. The article presents a novel method of fabrication of an electrochemical biosensor to detect PMPs in a blood using nanosilica. Electrochemically deposited thionine doped silica nanoparticles (Th@SiNPs) and horseradish peroxidase entrapped amine functionalized mesoporous silica nanoparticles (NH_2-MSNs) was utilized for conjugation with antibodies recognizing active confirmation of platelet glycoprotein GPIIb/IIIa and P-selectin expressed on PMPs respectively. Cyclic voltammetric analysis showed a progressive increase in reduction peak current on PMPs binding with the fabricated electrode in the presence of peroxide. The response of the sensor was linear in the range from 490 to 4080 PMPs μL^{-1} and could detect PMPs with a detection limit of ~96 PMPs μL^{-1}. Developed sensor proved to be highly specific in identifying PMPs in plasma and offers highly biocompatible, label-free, cost-effective, ease of miniaturization, short analysis time and simple instrumentation for the detection of biomarkers for a variety of diseases. The novel sensor is expected to find widespread applications in clinical point-of-care testing

Keywords: Platelets; Microparticles; Nanosilica; Electrochemical sensor; Mesoporous; Cyclic voltammetry.

1. Introduction

Platelet-derived microparticles (PMPs) are small membrane-bound vesicles (0.1 to 1.0 μm in size) formed by budding of plasma membrane during platelet activation or apoptosis [1,2]. PMPs represents about 70–90% of all circulating microparticles (MPs) [3]. PMPs elevation in blood shows strong correlation with the pathogenesis of diseases including atherosclerosis [4], arterial thrombosis [5], acute coronary syndrome [6], sepsis [7], cancer [8], hypertension [9] and diabetes [10]. PMPs highly express phosphatidylserine, platelet-specific glycoproteins

ACCEPTED MANUSCRIPT

GPIIb/IIIa & GPIb/IX, P-selectin on their surface and have strong procoagulant nature [11,12]. Recent reports revealed an increased incidence of adverse clinical outcomes associated with the blood transfusion due to increase in the number of MPs during storage including risk of infection, with multiple organ failure and death [13-16]. Thus, the clinical importance of PMPs is increasingly recognized for early detection to mark the risk state of progression of a particular disease in a patient and potentially pathogenic effects during blood storage.

Flow cytometry is the most widely used approach for detecting PMPs that integrates light scattering and fluorescence signals derived from particles, thereby generating extensive statistical data on size, shape and internal characteristics [17]. But studies revealed that approach cannot easily resolve particles smaller than 500 nm [18]. In view of the above, a reliable and robust technique is required for estimating level of PMPs in blood circulation.

Electrochemical immunosensors finds great potential in biomedical field as they are highly sensitive, label-free, portable, inexpensive and also provide ease of miniaturization, short analysis time as compared to conventional immunoassay techniques [19]. For enhancing the sensitivity of these sensors electron transfer mediators like different organic dyes such as methylene blue [20], methylene green [21], prussian blue [22], phenazines [23] and thionine [24] are generally employed. Further improvement in sensitivity and stability of electrode is done using different nanomaterials such as gold nanoparticles [25], carbon nanotubes [26], metallic oxides [27] and semiconductors [28]. Silica nanoparticles or nanosilica (SiNPs) based solid support are also being widely utilized for the immobilization of various biomolecules such as enzymes, proteins, and DNA due to its inherent biocompatible nature, large surface area, ordered uniform pore structure and unique environment for electron transfer [29]. Nanosilica based three-dimensional network is highly suited for the encapsulation of different biomolecules, but it cannot directly transfer an electron from biomolecules to electrodes. To overcome this shortcoming, a new kind of organic–inorganic nanocomposite material composed of SiNPs and

ACCEPTED MANUSCRIPT

thionine has been proposed. Nanosilica will provide high surface area for interaction with biomolecules as a bioreceptor and thionine act as mediator of electron transfer to the electrode. To the best of our knowledge, there are only very few reports available that make use of dye-SiNPs nanocomposite as a mediator for electrochemical analysis [30,31]. Recently, poly (methylene blue) encapsulated SiNPs composite have been developed for the electrochemical detection of glucose [32].

A novel approach for electrochemical detection of PMPs level in blood plasma using SiNPs fabricated electrode (filed Patent no.1687/DEL/2015) is proposed [33]. Earlier, our group have shown electrochemical detection of PMPs through graphene oxide [34]. In the present study, we have used for the first time two different types of SiNPs both solid as well as mesoporous and two different PMPs specific markers (PAC1 & P-selectin) which will further enhance the specificity of the sensor. Enhanced cyclic voltammetry signal was obtained due to increase in the concentration of anti-P-Selectin conjugated HRP encapsulated in amine functionalized mesoporous silica nanoparticles (NH_2-MSNs) with the increase in PMPs counts in the presence of fixed concentration of hydrogen peroxide (see Fig. 1). This mode of detection is expected to offer a cost effective, highly specific, label-free sensor which provides qualitative as well as quantitative method for the detection PMPs, a key player behind pathogenesis of various diseases.

2. Materials and methods

2.1. Materials

Analytical grade tetraethyl orthosilicate (TEOS), ammonium hydroxide (NH_4OH), hexanol, Triton X-100, cyclohexane, (3-Aminopropyl) triethoxysilane (APTES), thionine, ethylene diamine tetraacetic acid (EDTA), acetylsalicylic acid (aspirin), 4-(2-hydroxyethyl)-1-piperazineethanesulfonic acid (HEPES), methylene glycol tetraacetic acid (EGTA), calcium ionophore (A23187), bovine serum albumin (BSA), horse radish peroxidase (HRP) all purchased

ACCEPTED MANUSCRIPT

from Sigma-Aldrich (St. Louis, MO, USA); PAC1 and P-selectin were from BD Biosciences (San Jose, CA); Cetyl trimethyl ammonium bromide (CTAB), ethanol, sodium dihydrogen phosphate (NaH_2PO_4), sodium hydroxide (NaOH), sodium chloride (NaCl) potassium chloride (KCl), magnesium chloride ($MgCl_2$), calcium chloride ($CaCl_2$), glutaraldehyde and disodium hydrogen phosphate (Na_2HPO_4) from Merck (USA) were used as primary chemicals in the processing. Indium Tin oxide (ITO) glass was a product of Techinstro (Maharashtra India). All other chemicals were also of analytical grade.

2.2. Preparation and deposition of thionine doped silica nanoparticles (Th@SiNPs)

Triton X-100, hexanol, cyclohexane (volume ratio 1:1:4.2; final volume 25 mL) was mixed and stirred for 1 hr to form emulsion. When the solution becomes clear, 0.02M thionine (250 µL of 2M) and 100 µL of TEOS was added slowly to the mixture and sonicated for 1 hr. After that, 28% aqueous NH_4OH (60 µL) was added which serves the purpose of reactant and catalyst both for the hydrolysis of TEOS. The mixture was further kept for 24 hrs stirring. Finally, ethanol was added to release SiNPs from the microemulsion [35]. SiNPs were separated by centrifuging the mixture at 4000 rpm for 15-30 mins and washing by ethanol followed by water. Particles were then suspended in 10 mL of phosphate buffer (6.5 pH) for electrochemical deposition on ITO. Deposition process was carried out in two steps (a) Chronoamperometry (holding ITO under constant potential of -1.5V for 5 mins in the above solution); (b) Cyclic voltammetry (CV) (potential cycling of 50 cycles at 100 mV/sec between -0.4 to 0.6 V) (see supporting Fig. S1) [36].

2.3. *Synthesis of NH_2-MSNs*

NH_2-MSNs were synthesized *via* co-condensation method where surfactant (CTAB) was used as liquid crystal templating, TEOS as silica precursor, APTES as surface modifier and alkali as catalyst followed by the template removal [37]. NH_2-MSNs was prepared by dissolving 0.2 gm of CTAB in 96 mL of deionised water (DI) along with 0.7 mL NaOH (2M) and stirred

ACCEPTED MANUSCRIPT

vigorously at 80°C. Silica precursor TEOS was added to this mixture followed by APTES (2.6 mM) and stirred for 2 hrs. NPs were collected by centrifugation and washing several times by ethanol and water. After that, acid refluxing of NH_2-MSNs (1.5 mg) in a solution of 9.00 mL of HCl (37.4%) and 160.00 mL of methanol was done for 24 hrs to remove surfactant template from NH_2-MSNs.

2.4. *Characterization of deposited thin film and synthesized NH_2-MSNs*

The deposited thin film and synthesized particles were characterized by SEM (Zeiss EVO Series), FESEM (Zeiss EVO Series) and AFM (Agilent Technologies 5500 model) to examine the morphological structure, size and distribution pattern of the particles. Brunauer–Emmett–Teller (BET) was done to know about the mesoporous nature of particles that was determined from nitrogen adsorption/desorption isotherms using an Autosorb 1C (Quantachrome, USA) instrument.

2.5. *Platelet preparation*

Blood (10 ml) was collected from healthy volunteers, under informed consent as per the Institute Ethical Committee recommendation, in citrate-phosphate-dextrose-adenine buffer (80 µL) and centrifuged at *180 g* for 20 mins. Platelet rich plasma (PRP) having straw color was separated and mixed with 1 µL mL^{-1} aspirin and kept at 37°C in water bath for 15 mins. After that EDTA 10 µL mL^{-1} (5 mM) was added and centrifuged at 800 *g* for 15 mins. Dense white pellet was found to settle at the bottom, discard supernatant i.e. platelet poor plasma (PPP) and resuspended in 5 mL buffer A (20 mM HEPES, 138 mM NaCl, 2.9 mM KCl, 1 mM $MgCl_2$, 0.36 mM NaH_2PO_4, 1 mM EGTA, supplemented with 5mM glucose) and centrifuged at *800 g* for 15 mins. The supernatant was discarded and the pellet was resuspended in buffer B (5 mL) which was same as buffer A but without EGTA [38].

2.6. *Generation of PMPs*

ACCEPTED MANUSCRIPT

Isolated platelets were induced to shed MPs by 1 mM A23187 at room temperature (300 K) for 30 mins in the presence of 2 mM $CaCl_2$. The solution was centrifuged to pellet down platelets and supernatant containing PMPs were collected [34].

2.7. *Flow Cytometry*

For absolute counting of PMPs through flow cytometry, samples were serially diluted in a ratio (1:1, 1:10, 1:100, 1:1000) (200 µL each in buffer B) and incubated with PE-P-selectin antibody (4 µL each) for 30 mins in dark. At the time of analysis, an appropriate gate on MP population was drawn to differentiate it from platelets and also to exclude background noise. Forward scatter (FSC) and side scatter (SSC) was plotted on logarithmic scale. Events were acquired using collection criteria of the software to stop acquisition after 10,000 events (event limit) or after 20 s has elapsed (time limit). To acquire true events of MPs and separate it from background noise, MPs labelled with PE-P-selectin were run and positive fluorescence data was collected using four-quadrant logarithmic amplification with the flow cytometer (BD Accuri C sampler). In parallel, set up was prepared to specifically acquire PMPs in plasma (normal) and PMPs enriched plasma samples (200 mL each). Both the samples were incubated with FITC-annexinV/PE-P selectin for 30 mins in dark.

2.8. Electrode modification for the electrochemical detection of PMPs

A set of five electrochemically modified ITO electrodes were utilized for sensing of PMPs. The films were firstly kept under shaking condition for 1 hr with glutaraldehyde (2.5%) [32]. After that, 20 µL of PAC1 antibody (0.1µg $100\mu L^{-1}$) was adsorbed on the surface followed by blocking with 2% BSA. Modified electrodes were used for sensing different concentrations/counts of PMPs by keeping it for 2 hrs. The samples were washed to remove any unspecific binding. In parallel set up synthesized NH_2-MSNs was used for antibody/enzyme

ACCEPTED MANUSCRIPT

conjugation for that 1 mg of SiNPs was suspended in phosphate buffer (pH 7.4) and 2.5% glutaraldehyde. After that P-selectin antibody (2 µg 100 μL^{-1}) was added and incubated for 1 hr followed by mixing HRP (1 mg 100 μL^{-1}). Modified particles were then immobilized on the surface coated by PMPs, subjecting it for 1 hr incubation. The samples were washed and kept at 4°C.

2.9. Electrochemical analysis

CV was performed on Autolab potentiostat-galvanostat model PGStat101 (Metrohm Autolab B.V, The Netherlands) employing a three-electrode system (modified ITO glass as working electrode, platinum wire as counter electrode and Ag/AgCl as reference electrode) utilizing software Nova 1.1. Each experiment was repeated for at least 3–5 times to verify the results.

3. Results and discussion

3.1. Characterization of deposited Th@SiNPs and NH_2-MSNs

Fig. 2a-d show the SEM and AFM images, which clearly depict the change between the bare ITO plate and ITO-Th@SiNPs coated thin film. The ITO-Th@SiNPs film was found to be composed of numerous tight packing spherical nanoparticles. It looks as if some cages were crosslinked to each other. This grape-like aggregation indicates that Th@SiNPs were linked with each other, and the nanoscale silica cages were firmly fixed on the electrode surface in thionine polymerization process. This tightly-packaged nanostructure provides a large effective area for antibody loading.

The characterization results of NH_2-MSNs were done through BET and FESEM as shown in Fig. 2e-f. The images clearly confirm the mesoporous nature, shape and size of the particles. The adsorption isotherms of the prepared mesoporous particles depict that the volume of adsorbed nitrogen gradually increases with pressure. As per BET classification, Type IV Adsorption isotherm was obtained showing mesoporous nature of synthesized SiNPs [39]. The hysteresis loops were observed due to capillary condensation in mesopores. *Barrett-Joyner-Halenda* (BJH)

ACCEPTED MANUSCRIPT

analysis was carried out to measure pore size and surface area of the particles. Results showed pores size of ~2 nm, having pore volume of 2.4 cm^3/g and surface area ~1297 m^2/g. FESEM micrograph clearly showed the presence of hollow structures on SiNPs surface that can be effectively employed for encapsulation of enzymes.

3.2. *Redox behavior of thin film*

To confirm surface confined current response of Th@SiNPs fabricated ITO electrode, we examined peak currents response with scan rate (20, 40, 60, 80, 100 mVs^{-1}) in 0.1 M phosphate buffer solution (PBS) (pH 6.5) (see Fig. 3). The redox peak current increased gradually with the rise of the scan rate and it was observed that the anodic peak shifted positively but the cathodic peak moved negatively. Both the anodic and cathodic peak currents were directly proportional to the scan rate in the range of 20–100 mVs^{-1}, indicating a surface-controlled electrode process. The peak separation of the redox was increased about three fold on increasing the scan rate from 20-100 mVs^{-1} indicating good redox reversibility of the modified film.

3.3. *PMPs counting using flow cytometry and count dependent response of sensor*

MPs obtained from platelets were counted with the help of flow cytometer using PE-P-selectin antibody (CD62P). Firstly, platelet population was acquired to locate their position on FSC-SSC dot plot, after that PMPs were run to get their exact location on plot, by setting a proper threshold to avoid the background noise. As the size of MPs are smaller in comparison to platelets we observed two set of population in FSC/SSC dot plot, shown in Fig. 4a. The MP population was properly gated and run again to acquire 10,000 events of that population, containing MPs alone. In order to identify microparticles of platelet origin specifically, PE-P-selectin labeled population was acquired on FL1/FL2 channel, FL2 signals were again gated to obtain 10,000 positive P-selectin events (Fig. 4b). For further confirmation of the origin of MPs in gated population, we serially diluted the sample in ratio (1:1, 1:10, 1:100, 1:1000) and events were acquired for 20 s at each dilution (see Fig. 4c-f). It was observed that on increasing dilution the number of positive P-

ACCEPTED MANUSCRIPT

selectin events μL^{-1} goes on declining progressively due to decrease in PMPs concentration, confirming it as real signals of platelet microparticles and not the background noise [40]. Fig. 4g depicts the quantification of PMPs with increasing dilution when samples were analyzed for 20 s.

The quantified PMPs samples were then immobilized on the fabricated electrode surface and analyzed through cyclic voltammetry. To make the sensor specific for the detection of PMPs, NH_2-MSNs encapsulating HRP and tagged by P-selectin (CD62P) antibody were used (specifically bind on the surface of PMPs), making a sandwich structure. When a fixed concentration of H_2O_2 (10 μM) was added to the buffer solution, H_2O_2 gets reduced due to immobilized encapsulated HRP in NH_2-MSNs on working electrode. The cyclic voltammetry detects a sharp increase in reduction of peak current with the increasing count of the PMPs (see Fig. 5a). This strongly correlates with the fact that the increase of HRP molecules on the fabricated electrode is directly proportional to the count of PMPs in the sample. Fig. 5b represents a linear dose-dependent response of sensor with increasing PMPs count *versus* current. The response of the sensor was linear in the range from 490 to 4080 PMPs μL^{-1} and detection limit was found to be ~96 PMPs μL^{-1}. PMPs count detected through the modified electrode is comparable with other existing methods such as flow cytometer which can detect 1500-2000 PMPs μL^{-1} [41,42] and enzyme-linked immunoassay method having detection limit of 200-500 PMPs μL^{-1} [43,44]. This indicates that developed electrochemical method could provide suitable platform and better sensitivity for the detection of PMPs within clinically relevant range (100-4000 PMPs μL^{-1}) in blood plasma [42].

3.4. *Specificity of the sensor for PMPs*

In order to test sensor specificity, plasma sample that possesses MPs from other cells e.g. red blood cells, leukocytes etc. and plasma enriched with PMPs were subjected to analysis firstly by flow cytometry [45]. The presence of dual stained FITC-annexinV (binds to different MPs)/ PE-

ACCEPTED MANUSCRIPT

P-selectin (specifically recognizes PMPs) reflects the number of MPs derived from platelets alone (Fig. 6b) while both the samples possessed microparticles derived from non-platelet sources (PE-P-selectin negative, FITC-annexin V-positive, as shown in Fig. 6a upper left quadrant (green)). The same plasma sample, with and without PMPs, was then added onto the PAC1-modified electrodes and subjected to electrochemical analysis. Strikingly, electrodes coated with plasma hardly exhibited any change in reduction peak current while plasma sample enriched with PMPs, responded well by giving an enhanced reduction peak current as shown in Fig. 6c. This clearly demonstrates that sensor surface was able to exclusively bind and detect PMPs having integrins $\alpha_{IIb}\beta_3$ active conformation with selective P-selectin marker present on their surface.

3.5. Stability of the sensor

Stability is one of the major parameter of concern for a successful biosensor. In order to check the stability of our developed immunosensor, we have continuously monitored the electrochemical reponse of the fabricated SiNPs electrode for a month. Only 5% reduction in electrochemical reponse was observed as compared to initial measurement. This can be further improved by proper passivation.

4. Conclusion

It is well understood that MPs act as markers of various diseases like cancer, diabetes, thrombosis and have prognostic potential. We developed a novel approach for the electrochemical detection of PMPs using nanosilica. Th@SiNPs was electrochemically deposited on ITO-coated glass serving as an excellent sensing platform having large surface area and huge active sites for immobilization of PAC1 antibodies. Besides, NH_2-MSNs was utilized for conjugating antibodies targeted against other selective marker P-selectin expressed on PMPs. The simultaneous detection of microparticles through two different antibodies enhances the

ACCEPTED MANUSCRIPT

specificity of the sensor, minimizing the chance of false detection. Developed sensor showed detection limit of ~96 PMPs μL^{-1} and linearity in the range from 490 to 4080 PMPs μL^{-1} The results revealed that our biosensor has many advantages over conventional flow cytometry as it offers label-free detection, wide linear range, ease to operate, excellent accuracy free of any background noise and cost effective tool towards analysis of tested samples. Detection and quantification of MPs will provide information about platelet quality over storage i.e. platelet storage lesion to overcome adverse clinical outcomes associated with the transfusion. The sensor proved to have promising potential for its efficient application in clinical testing of various pathological conditions. The work related to the development of a miniaturized sensor prototype is currently underway.

Acknowledgements

The authors gratefully acknowledge the Department of Science and Technology for providing INSPIRE Faculty Research grant (No. IFA-LSBM-31) and Defense Research and Development Organization (DRDO), Government of India for research grant support (No. ERIP/ER/0803699/M/01/1423). The authors are thankful to the Centre for Interdisciplinary Research (CIR), Motilal Nehru National Institute of Technology Allahabad for providing the experimental facilities.

Supporting Information

Figure S1 (a) deposition of Th@SiNPs thin film through chronoamperometry (b) cyclic voltammetry at scan rate of (100 mVs^{-1}).

Competing financial interest statement

The authors declare no competing financial interests.

References

ACCEPTED MANUSCRIPT

1. O. Morel, L. Jesel, J.M. Freyssinet, F. Toti, Cellular mechanisms underlying the formation of circulating microparticles. Arterioscl. Throm. Vas. 31 (2011), 15-26.
2. C. Laresche, F. Pelletier, F. Garnache-Ottou, T. Lihoreau, S. Biichlé, G. Mourey, F. Aubin, Increased levels of circulating microparticles are associated with increased procoagulant activity in patients with cutaneous malignant melanoma. J. Invest. Dermatol. 134 (2014), 176-182.
3. L. Burnier, P. Fontana, B.R. Kwak, A. Angelillo-Scherrer, Cell-derived microparticles in haemostasis and vascular medicine. Thromb. Haemost. 101 (2009), 439–451.
4. K.T. Tan, G.Y. Lip, The potential role of platelet microparticles in atherosclerosis. Thromb. Haemost. 94 (2005), 488-492.
5. S. Nomura, Function and clinical significance of platelet-derived microparticles. Int. J. Hematol. 74 (2001), 397-404.
6. L. Bernal-Mizrachi, W. Jy, J.J. Jimenez, J. Pastor, L.M. Mauro, L.L. Horstman, E. de Marchena, Y.S. Ahn, High levels of circulating endothelial microparticles in patients with acute coronary syndromes. Am. Heart. J. 145 (2003), 962-970.
7. K. Osumi, Y. Ozeki, S. Saito, Y. Nagamura, H. Ito, Y. Kimura, H. Ogura, S. Nomura, Development and assessment of enzyme immunoassay for platelet-derived microparticles. Thromb. Haemost. 85 (2001), 326-330.
8. O. Dashevsky, D. Varon, A. Brill, Platelet-derived microparticles promote invasiveness of prostate cancer cells via upregulation of MMP-2 production. Int. J. Cancer. 124 (2009), 1773-1777.
9. P. Diehl, M. Aleker, T. Helbing, V. Sossong, M. Germann, S. Sorichter, C. Bode, M. Moser, Increased platelet, leukocyte and endothelial microparticles predict enhanced coagulation and vascular inflammation in pulmonary hypertension. J. Thromb. Thrombolys. 31 (2011), 173-179.

ACCEPTED MANUSCRIPT

10. F. Lovren, S. Verma, Evolving role of microparticles in the pathophysiology of endothelial dysfunction. Clin. Chem. 59 (2013), 1166-1174.

11. M. Hou, D. Stockelberg, J. Kutti, H. Wadenvik, Antibodies against platelet GPIb/IX, GPIIb/IIIa, and other platelet antigens in chronic idiopathic thrombocytopenic purpura. Eur. J. Haematol. 55 (1995), 307-314.

12. A.D. Blann, S.K. Nadar, G.Y. Lip, The adhesion molecule P-selectin and cardiovascular disease. Eur. Heart. J. 24 (2003), 2166-2179.

13. J.F. Keuren, E.J. Magdeleyns, J.W. Govers-Riemslag, T. Lindhout, J. Curvers, Effects of storage-induced platelet microparticles on the initiation and propagation phase of blood coagulation. Brit. J. Haematol. 134 (2006), 307-313.

14. A.S. Amlt, K.E. Nollet, K. Yajima, Preventing platelet-derived microparticle formation-and possible side effects-with prestorage leukofiltration of whole blood. Arch. Pathol. Lab. Med. 134 (2010), 771.

15. M.A. Refaai, R.P. Phipps, S.L. Spinelli, N. Blumberg, Platelet transfusions: impact on hemostasis, thrombosis, inflammation and clinical outcomes. Thromb. Res. 127 (2011), 287-291.

16. E. Maurer-Spurej, K. Chipperfield, Past and future approaches to assess the quality of platelets for transfusion. Transfus. Med. Rev. 21 (2007), 295-306.

17. R. Flaumenhaft, J.R. Dilks, J. Richardson, E. Alden, S.R. Patel-Hett, E. Battinelli, M. Sola-Visner, J.E. Italiano, Megakaryocyte-derived microparticles: direct visualization and distinction from platelet-derived microparticles. Blood 113 (2009), 1112-1121.

18. M.D. Shah, A.L. Bergeron, J.F. Dong, J.A. López, Flow cytometric measurement of microparticles: pitfalls and protocol modifications. Platelets 19 (2008), 365-372.

19. Y. Wan, Y. Su, X. Zhu, G. Liu, C. Fan, Development of electrochemical immunosensors towards point of care diagnostics. Biosens. Bioelectron. 47 (2013), 1-11.

ACCEPTED MANUSCRIPT

20. M. Arvand, S. Sohrabnezhad, M.F. Mousavi, M. Shamsipur, M.A. Zanjanchi, Electrochemical study of methylene blue incorporated into mordenite type zeolite and its application for amperometric determination of ascorbic acid in real samples. Analytica. Chimica. Acta. 491 (2003), 193-201.
21. Q. Chi, S. Dong, Electrocatalytic oxidation of reduced nicotinamide coenzymes at Methylene Green-modified electrodes and fabrication of amperometric alcohol biosensors. Analytica. Chimica. Acta. 285 (1994), 125-133.
22. A.A. Karyakin, E.A. Puganova, I.A. Budashov, I.N. Kurochkin, E.E. Karyakina, V.A. Levchenko, V.N. Matveyenko, S.D. Varfolomeyev, Prussian blue based nanoelectrode arrays for H_2O_2 detection. Anal. Chem. 76 (2004), 474-478.
23. M.M. Barsan, E.M. Pinto, C.M. Brett, Electrosynthesis and electrochemical characterisation of phenazine polymers for application in biosensors. Electrochimica. Acta. 53 (2008), 3973-3982.
24. S.A. John, R. Ramaraj, Microenvironment effects on the electrochemical and photoelectrochemical properties of thionine loaded Nafion® films. J. Electroanal. Chem. 561 (2004), 119-126.
25. J. Wang, Nanomaterial-based electrochemical biosensors. Analyst 130 (2005), 421-426.
26. A. Merkoçi, M. Pumera, X. Llopis, B. Pérez, M. del Valle, S. Alegret, New materials for electrochemical sensing VI: carbon nanotubes. TrAC 24 (2005), 826-838.
27. A. Salimi, R. Hallaj, S. Soltanian, H. Mamkhezri, Nanomolar detection of hydrogen peroxide on glassy carbon electrode modified with electrodeposited cobalt oxide nanoparticles. Analytica. Chimica. Acta. 594 (2007), 24-31.
28. E. Katz, I. Willner, J. Wang, Electroanalytical and bioelectroanalytical systems based on metal and semiconductor nanoparticles. Electroanal. 16 (2004), 19-44.

ACCEPTED MANUSCRIPT

29. H. Yao, N. Li, S. Xu, J.Z. Xu, J.J. Zhu, H.Y. Chen, Electrochemical study of a new methylene blue/silicon oxide nanocomposition mediator and its application for stable biosensor of hydrogen peroxide. Biosens. Bioelectron. 21 (2005), 372-377.

30. M. Yang, H. Li, A. Javadi, S. Gong, Multifunctional mesoporous silica nanoparticles as labels for the preparation of ultrasensitive electrochemical Immunosensors. Biomaterials 31 (2010), 3281-3286.

31. H. Yao, J.M. Hong, N. Li, S. Xu, J.J. Zhu, Homogenous thionine-SiO_2 nanocomposite spheres: sonochemical preparation, characterization, and application in H_2O_2 biosensor. J. Nanosci. Nanotech. 9 (2009), 2421-2425.

32. X. Xiao, B. Zhou, L. Tan, H. Tang, Y. Zhang, Q. Xie, S. Yao, Poly (methylene blue) doped silica nanocomposites with crosslinked cage structure: Electropolymerization, characterization and catalytic activity for reduction of dissolved oxygen. Electrochimica. Acta. 56 (2011), 10055-10063.

33. S.K. Singh, P. Singh, P. Chakrabarti, Electrochemcial process of immuno-based thionine doped nanosilica electrode modification and its use as an enzymatic sensor for electrochemical detection of platelet hyperactivity. Patent File No. 1687/DEL/2015.

34. J. Kailashiya, N. Singh, S.K. Singh, V. Agrawal, D. Dash, Graphene oxide-based biosensor for detection of platelet-derived microparticles: A potential tool for thrombus risk identification. Biosens.Bioelectron. 65 (2015), 274-280.

35. R.P. Bagwe, C. Yang, L.R. Hilliard, W. Tan, Optimization of dye-doped silica nanoparticles prepared using a reverse microemulsion method. Langmuir 20 (2004), 8336-8342.

36. R. Yang, C. Ruan, W. Dai, J. Deng, J. Kong, Electropolymerization of thionine in neutral aqueous media and H_2O_2 biosensor based on poly(thionine). Electrochimica. Acta. 44 (1999), 1585-1596.

ACCEPTED MANUSCRIPT

37. F. Tang, L. Li, D. Chen, Mesoporous silica nanoparticles: synthesis, biocompatibility and drug delivery. Adv. Mater. 24 (2012), 1504-1534.

38. S.K. Singh, M.K. Singh, M.K. Nayak, S. Kumari, S. Shrivastava, J.J. Grácio, D. Dash, Thrombus inducing property of atomically thin graphene oxide sheets. Acs Nano 5 (2011), 4987-4996.

39. P.J. Branton, P.G. Hall, K.S. Sing, H. Reichert, F. Schüth, K.K. Unger, Physisorption of argon, nitrogen and oxygen by MCM-41, a model mesoporous adsorbent. J. Chem. Soc. 19 (1994), 2965-2967.

40. S.K. Singh, M.K. Singh, M.K. Nayak, S. Kumari, J.J. Grácio, D. Dash, Size distribution analysis and physical/fluorescence characterization of graphene oxide sheets by flow cytometry. Carbon 49 (2011), 684-692.

41. J. Pereira, G. Alfaro, M. Goycoolea, T. Quiroga, M. Ocqueteau, L. Massardo, D. Mezzano, Circulating platelet-derived microparticles in systemic lupus erythematosus. Thromb. Haemost. 95 (2006), 94-99.

42. S. Robert, P. Poncelet, R. Lacroix, L. Arnaud, L. Giraudo, A. Hauchard, F. Dignat-George, Standardization of platelet-derived microparticle counting using calibrated beads and a Cytomics FC500 routine flow cytometer: a first step towards multicenter studies?. *J. Thromb. Haemost. 7* (2009), 190-197.

43. A. Andoh, T. Tsujikawa, K. Hata, Y. Araki, K. Kitoh, M. Sasaki, Y. Fujiyama, Elevated circulating platelet-derived microparticles in patients with active inflammatory bowel disease. Am. J. Gastroentero. 100 (2005), 2042-2048.

44. T. Shirafuji, H. Hamaguchi, F. Kanda, Measurement of platelet-derived microparticle levels in the chronic phase of cerebral infarction using an enzyme-linked immunosorbent assay. *Kobe J Med Sci*, 54(2009) E55-61.

ACCEPTED MANUSCRIPT

45. W. Jy, M.E. Johansen, C. Bidot, L.L. Horstman, Y.S. Ahn, Red cell-derived microparticles (RMP) as haemostatic agent. Thromb. Haemos. 110 (2013), 751-760.

ACCEPTED MANUSCRIPT

Priti Singh received her Master of Technology degree in Nanoscience and Technology from the Delhi Technological University in 2013. She is a PhD scholar at the Department of Biotechnology, Motilal Nehru National Institute of Technology (MNNIT) Allahabad. Her current research is focused on prospective biomedical nanomaterials.

Dr. Sameer Srivastava is currently working as an Assistant Professor at Motilal Nehru National Institute of Technology (MNNIT) Allahabad. He received his PhD degree in Biotechnology from the National Chemical Laboratory (NCL) Pune in 2009. He received the Endeavour Award from the Australian Government and DBT Research Associate Fellowship from the Department of Biotechnology, India. His main research interest is focused on biochemistry including molecular biology.

Prof. P. Chakrabarti, Professor and former Head of the Department of Electronics Engineering, IIT(BHU), Varanasi and presently Director of Motilal Nehru National Institute of Technology, Allahabad, India on deputation. He earned his B.Tech., and M.Tech., degrees from the University of Calcutta, Kolkata. He received his Ph.D. degree in Electronics Engineering from the Indian Institute of Technology (BHU). He has made a significant contribution in experimental and theoretical research in the areas of Microelectronics and Photonics. He is a recipient of Indian National Science Academy (INSA) Visiting Fellowship and Senior Visiting Fellowship of Engineering and Physical Sciences Research Council (EPSRC), UK.

Dr. Sunil Kumar Singh is currently an Assistant Professor (INSPIRE Faculty) at the Motilal Nehru National Institute of Technology (MNNIT) Allahabad. He received his PhD in Biotechnology from the Institute of Medical Science, Banaras Hindu University in 2012. He received the DST-INSPIRE Faculty Award from the Department of Science and Technology (DST) India. He is also awarded with the INSA Medal for Young Scientists from the Indian National Science Academy India, NASI-Young Scientist Platinum Jubilee Award from The National Academy of Sciences Allahabad, India, India and Foundation of Science and Technology (FCT) Postdoctoral Fellowship, Portugal. His main research interests include the biomedical application of nanomaterials, thrombus biology, electrochemical biosensor, and nanomaterials-cell interactions.

ACCEPTED MANUSCRIPT

FIGURE CAPTIONS

Figure 1: Schematic showing preparation and functioning of Si-NPs based elctrochemical biosensor for the detection of platelet hyperactivity

Figure 2: SEM and AFM micrograph of (a,c) Bare ITO (b,d) thin film of Th@SiNPs on ITO, (e, f) BET and FESEM of NH_2-MSNs respectively.

Figure 3: Cyclic voltammograms of Th@SiNPs modified ITO plate in 0.1 M phosphate buffer (pH 6.5) at scan rates of 20, 40, 60, 80, 100, 200 mVs^{-1}. Inset showing the variation in peak current at cathodic and anodic potential (-0.3V and 0.3V) at different scan rates.

Figure 4: Absolute counting of microparticles through flow cytometry (a) microparticles population (red) (b) gated PE-P-selectin population to count PMPs (c, d, e, f) increasing dilution of PMPs (g) quantification of P-selectin labeled PMPs population μl^{-1}.

Figure 5: (a) Cyclic voltammograms of PMPs detection in 0.1 M phosphate buffer solution (pH 6.5) in the presence of 10 µM H_2O_2. (b) Standard dose-response relationship between PMPs μl^{-1} and current (average of 4 repeat experiment results) with standard deviations at constant potential (-0.2 V).

Figure 6: PMPs detection through flow cytometry (a) in plasma (b) plasma enriched with PMPs (c) detection through electrochemical biosensor.

ACCEPTED MANUSCRIPT

Figure 1

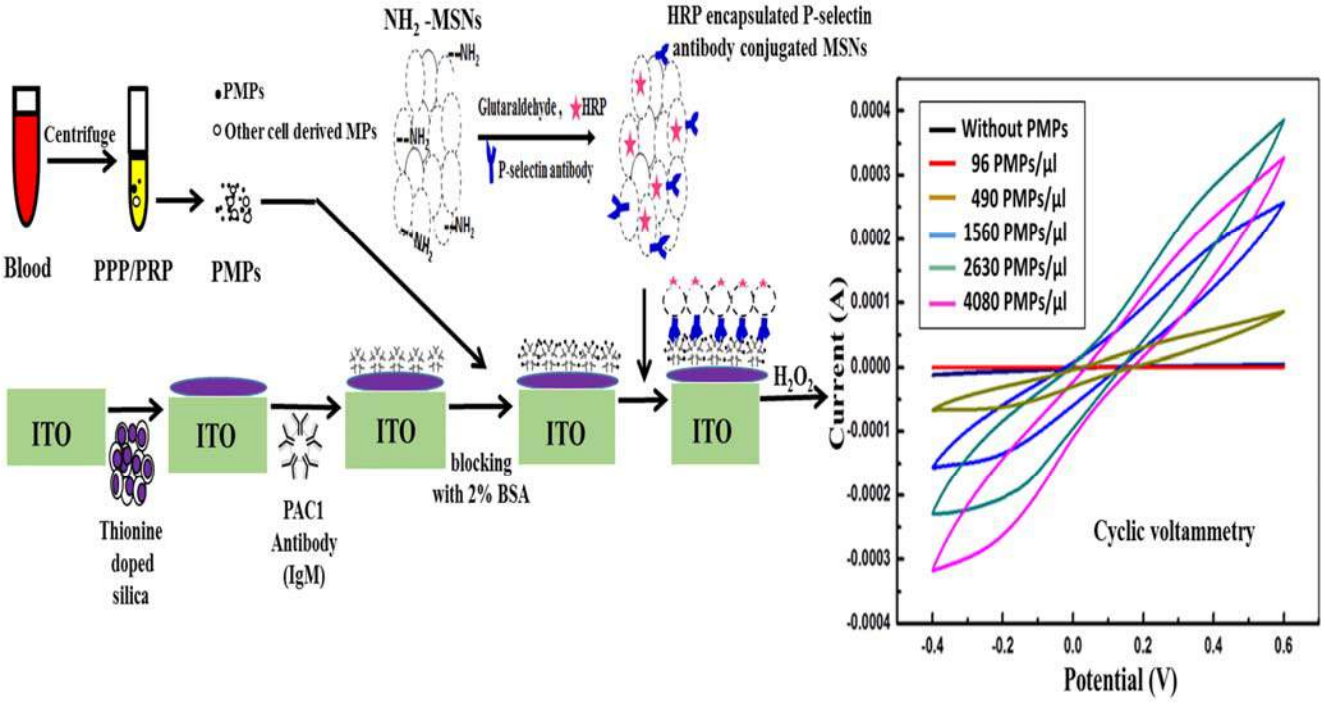

ACCEPTED MANUSCRIPT

Figure 2

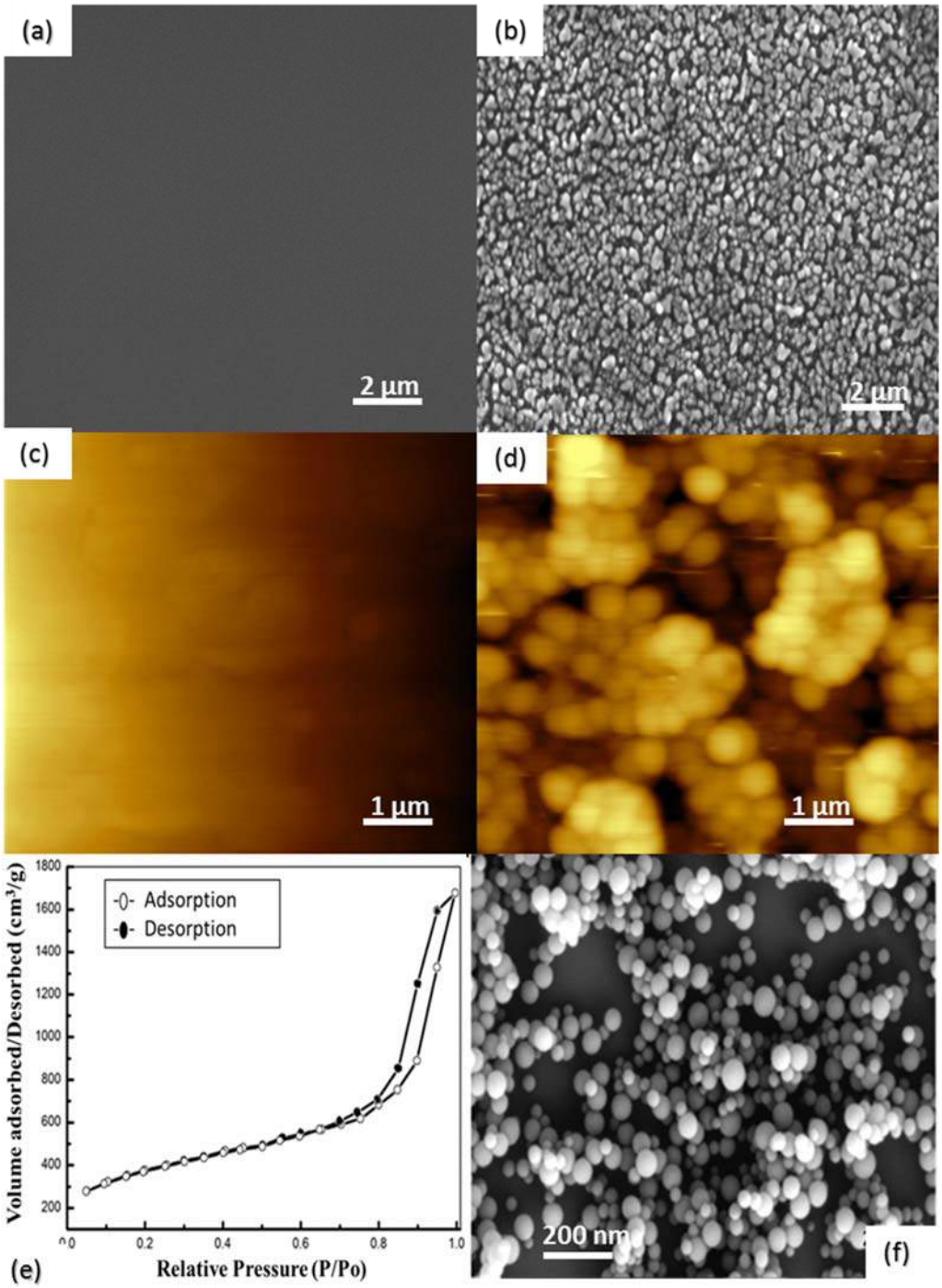

ACCEPTED MANUSCRIPT

Figure 3

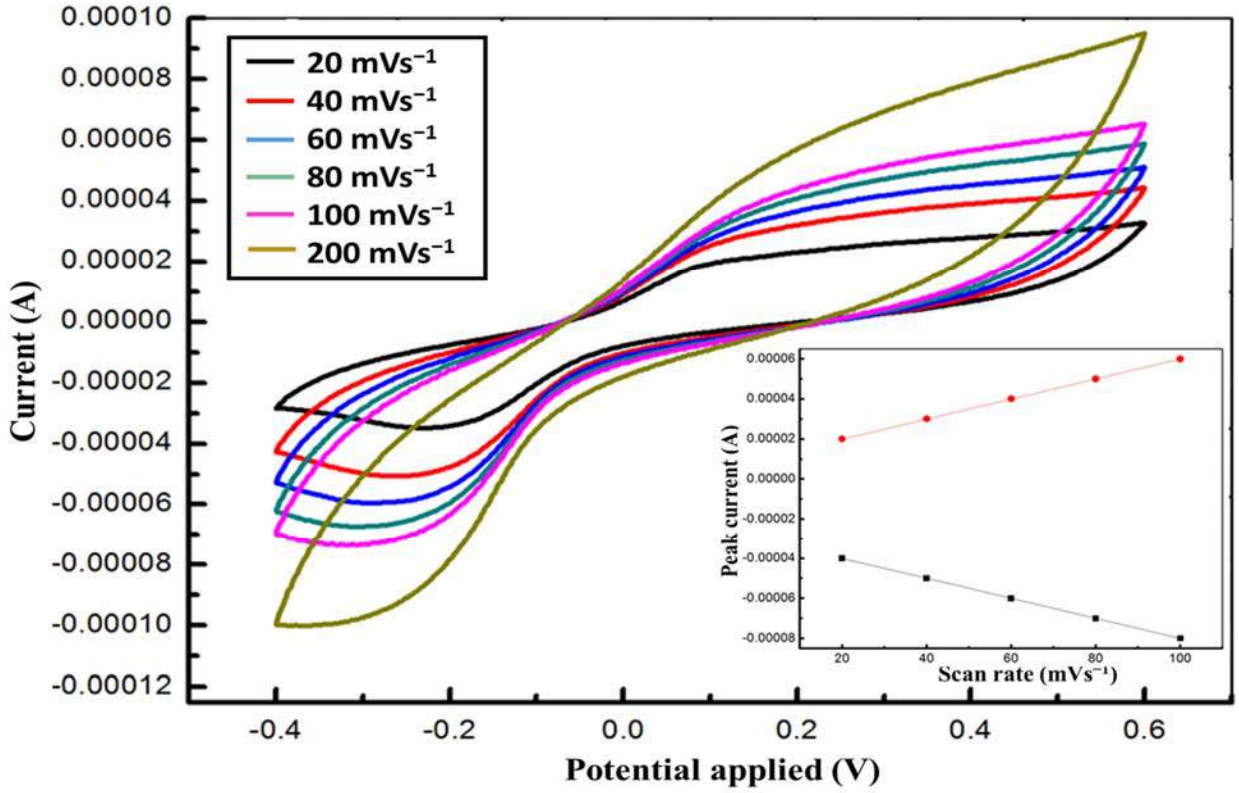

ACCEPTED MANUSCRIPT

Figure 4

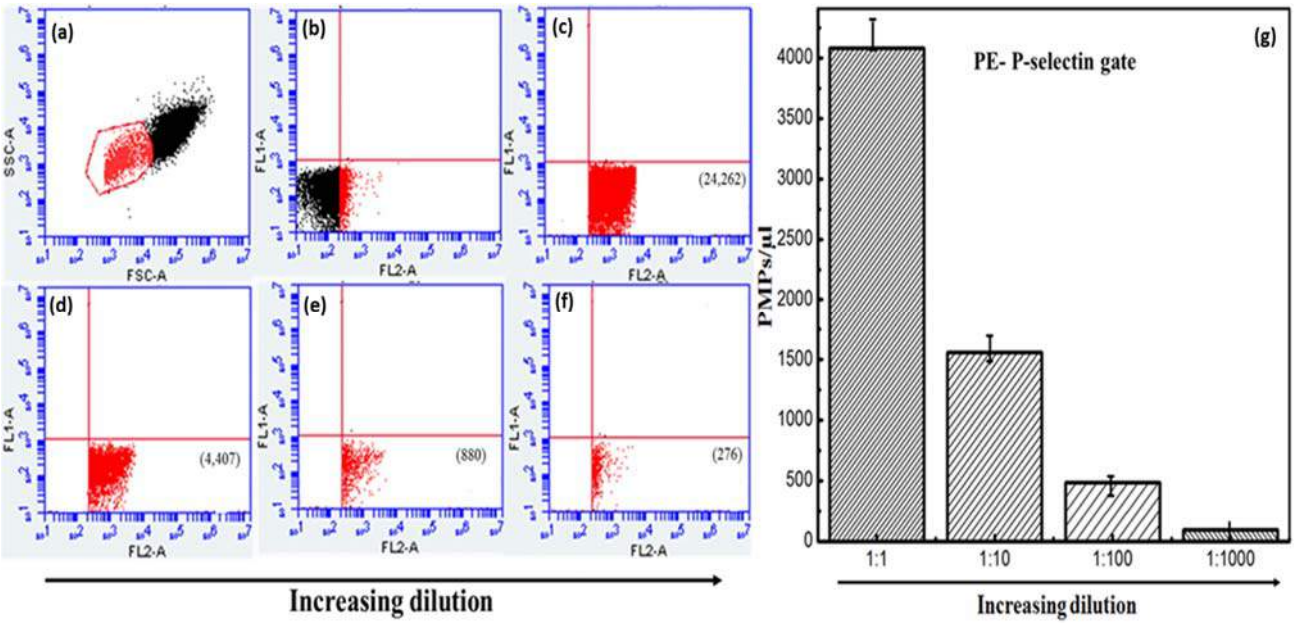

ACCEPTED MANUSCRIPT

Figure 5

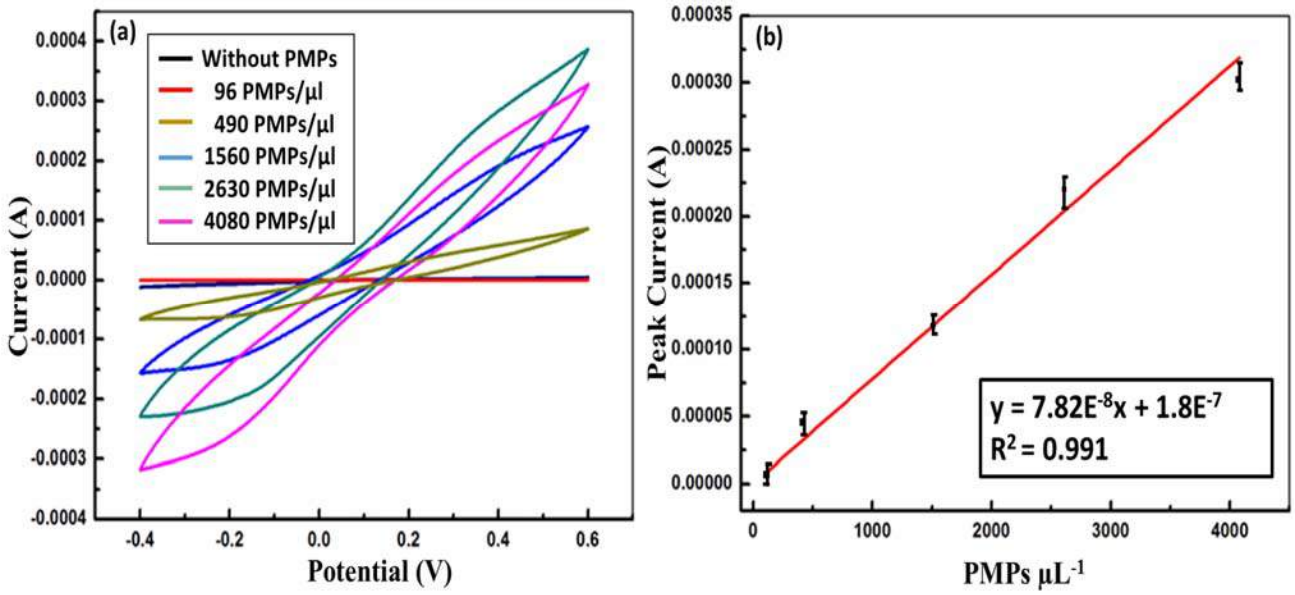

ACCEPTED MANUSCRIPT

Figure 6

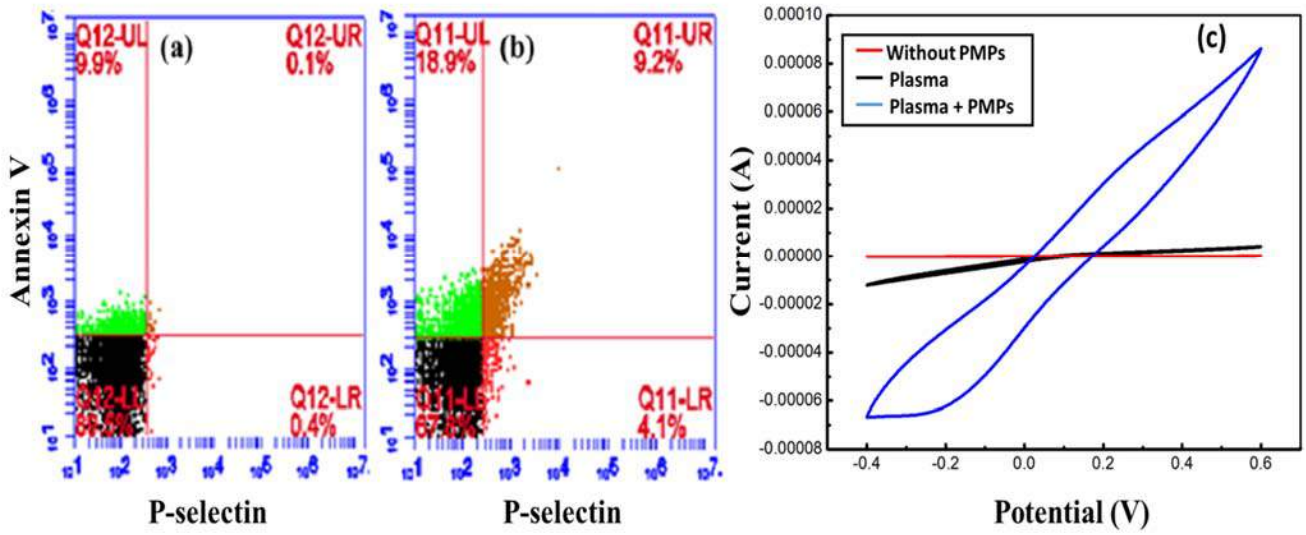

Chaotic Modeling and Simulation (CMSIM) **3: 333-354, 2016**

Numerical Simulation for Dynamic and Chaotic behaviour of Coupled Biological Oscillators through Extended Poincaré-Cartan Invariants

Vikas Rastogi[1]
[1]Mechanical Engineering Department
Delhi Technological University
Delhi-110042, India
(E-mail: rastogivikas@gmail.com)

Abstract: This article deals with the numerical analysis of linearly coupled oscillators, which are connected in the form of a ring. This system is being used as a model of biological system of intestine or may be the liver tissues exhibiting a tube of oscillators having cells both around the periphery and along the axis of the tube. The biological oscillators may be represented as Van der Pol oscillators, which are coupled with non-trivial couplings, where damping parameters are also included in system. The dynamics is determined analytically through extended Poincaré -Cartan theorem of umbra-Lagrangian theory, which examines the invariance of Poincare integral in *m*-dimensional phase space. The synchronization dynamics is achieved with full and cluster mode in terms of coupling parameters. The effects of injected signal on the stability boundaries of the synchronized states are analyzed using numerical simulations, which exhibit interesting beating phenomena. This analysis is corroborated with simulation results to visualize the chaotic behaviour of the coupled oscillator.

Keywords: Coupled oscillators, Umbra-Lagrangian theory, Biological system, Poincaré – Cartan Invariant, Chaotic behaviour.

Notation:

q_i	Generalized displacement
$\dot{q}_i =$	Generalized velocity
t =	Real-time
x_i =	Concentration of the oscillator, where $i = (1,2,3,4)$
$\dot{x}_i$ =	Rate of concentration of the oscillator, where $i = (1,2,3,4)$
$A_{K_{ij}}$ =	Kinematic area projection in $i-j$ *th* plane
$A_{P_{ij}}$ =	Phase area projection in $i-j$ *th* plane
$A_{T_{ij}}$ =	Trajectorial area projection $i-j$ *th* plane
K =	Solute concentration gradients of all oscillators

Received: 20 October 2015 / Accepted: 29 June 2016
© 2016 CMSIM
ISSN 2241-0503

K_{cp}^{A} =	Solute concentration gradients of the inhibitory coupling
K_{cp}^{B} =	Solute concentration gradients of the excitatory coupling
L =	Lagrangian of the system
L_* =	Umbra-Lagrangian of the system
m=	Mass of the all oscillators
R_{cp} =	Resistance to the flow of solute
μ =	Nonlinear damping coefficient
η =	Umbra-time

1. Introduction

The dynamics of non-linearly coupled oscillators has received much attention around the world and dynamical systems are currently the most popular and complex research areas. This is specifically true that non-linear dynamics of these systems have been widely investigated by [1-3] and now a day, attention is focused on dissipative dynamical systems [4-5]. Coupled non-linear oscillators have been source of growing interest in different research areas, ranging from physics, chemistry, engineering to biology and even in social sciences [6-7]. Non-linearity in these systems is essential to attain self-sustained characteristics. These systems reach as stable oscillatory dynamics as consequences of an internal balance between amplification and dissipation. The one of the most interesting features displayed by coupled oscillators is synchronization, due to an adjustment of rhythms due to weak interactions. This phenomenon of synchronization is observed in nature and offers the possible applications in electronics, communications engineering, information technology, biological and chemical structures. Wang et. al.[8] have studied the synchronous bursts on scale-free neuronal networks considering an attractive and repulsive coupling. In another research, Want et al [9] also investigated synchronization transitions on scale-free neuronal networks. In this study, they considered the transitions due to finite information transmission delays. In similar study by Sun et. al.[10], the burst synchronization has been attempted in neuronal networks. In another study by Volman et. al.[11], the gap junctions and epileptic seizures were analyzed in view of synchronization of neuronal ensembles. All such studies have attempted the synchronization phenomena in neuronal networks of brain.

The synchronization phenomena have been successfully applied in chemical cells as revealed in the study of Perc et. al. [12], where periodic calcium waves in coupled cells due to internal noise has been investigated. In another study by Gosak et. al. [13], spatial coherence resonance in excitable biochemical media induced by internal noise has been examined.

Recently, research has shifted towards the study of dynamical behaviour of a system of coupled limit cycle oscillators forming a ring with main focus of synchronization criteria [14-15]. The behaviour of a pair of coupled limit cycle oscillators display a

significant wider range of phenomenon than a single limit cycle oscillators and may be used to model systems such as cardiac cells, gas flux control in plant, vibrations of heat exchangers, human body, biomedical engineering etc. Many researchers have contributed in these areas. Bi [16] studied the dynamical behaviour of two coupled parameter excited Vander Pol's oscillators. Leung [17] investigated the dynamics process of synchronizing chaotic Vander Pol systems driven periodic force. Such situations are very prominent in biological systems such as animal and human bodies. Collins and Richmond [18] have shown that quadrupedal mammals, the four oscillators controlling the limb of animals may be coupled to form a ring. Similarly McClellan [19] has also provided the organization of spinal locomotors networks. A lot of works in this field are contributed by Woafo and his team [20]. Woafo and Enjieu Kadji [21] had investigated the synchronized states in a ring of mutually coupled self –sustained electrical oscillators and later Enjieu Kadji et al. [22] have applied the same theory in human intestine. But their model has several constraints, as they have not considered the damping coefficient of the coupling, which otherwise, in biological systems find wider applications from duodenum, liver tissues, kidney, and heartbeat, and also affects the synchronization dynamics of the oscillators. Present paper deals with the synchronization dynamics through a novel approach of extended Poincare-Cartan invariant, which was not attempted in any archival literature.

Integral invariants of dynamical systems play an important role in mechanics. Primarily, the study of integral invariants is limited only to conservative systems. Some researchers have tried to extend the applications of integral invariants to non-conservative systems and non-holonomic systems [23]. However, they introduced integral invariants of Poincaré-Cartan's type for non-holonomic constrained systems by extending the Hamilton's stationary principle to nonholonomic-constrained systems. Benavent and Gomis [24] had extended the Poincaré-Cartan integral to constrained systems and found sufficient conditions for systems whose equations of motion contain arbitrary functions to be Hamiltonian. Liu et al. [25] reported that no basic integral invariants exist for non-conservative systems from traditional viewpoint and put forward the integral variants of the non-conservative system.

Some significant works in this direction were reported by Gou et al. [26, 27, 28] in their several papers. They have proposed the Poincaré-Cartan integral invariants for non-conservative dynamical systems on an extended

phase space, where the set of dynamical equations and their adjoint equations are canonical. In another work, Gou et al. [27] further constructed Poincaré and Poincaré-Cartan integral invariants of a generalized Hamiltonian system and also for non-holonomic constrained system [28], where non-holonomy of the constraints and non conservative forces acting on the system is derived from D'Alembert-Lagrange principle.

The key to the generalization of integral invariants to other systems lies in the search for new Lagrangian or Hamiltonian for those systems. Apart from all previous extensions of classical Lagrange's equation, Mukherjee [30] suggested an alternative method for finding invariants of motion or possible invariant trajectories for dynamical systems. Mukherjee *et al.* [31] proposed a modified Lagrange's equation introducing an additional time like variable called 'umbra time'. This notion was extended to all type of energies as well as the Lagrangian itself, which was termed as the "umbra-Lagrangian". The umbra-Lagrange's equation for general class of systems with *n* generalized co-ordinates [29, 33] and [34] may be written as

$$\frac{d}{dt}\left[\underset{\eta\to t}{Lim}\frac{\partial L^*}{\partial \dot{q}_i(\eta)}\right]-\underset{\eta\to t}{Lim}\frac{\partial L^*}{\partial q_i(\eta)}=0\text{ ,for } i=1..n\,. \tag{1}$$

where L^* is umbra-Lagrangian, t and η are real and umbra time respectively and q_i and $\dot{q}_i$ are generalized displacements and velocities. Umbra-Lagrangian may be given as

$$L^*\left(t,\boldsymbol{q}(t),\dot{\boldsymbol{q}}(t),\boldsymbol{q}(\eta),\dot{\boldsymbol{q}}(\eta)\right)=T_C^*\left(t,\dot{\boldsymbol{q}}(\eta)\right)-V^*\left(t,\boldsymbol{q}(t),\dot{\boldsymbol{q}}(t),\boldsymbol{q}(\eta)\right), \tag{2}$$

where a bold face letter represents a vector quantity, with $T^*(...)$ as the umbra – co-kinetic energy and $V^*(...)$ as the umbra-potential energy. The details expression of umbra-co kinetic energy and umbra-potential energy has been outlined in ref. [33, 34] and briefly presented in *Appendix 'A'*.

In present work, the model of Collins and Richmond [18] and Enjieu Kadji et al. [22] have been refined by incorporating the damping parameter in the system for modeling the duodenum or intestine. This ring model has been investigated through extended Poincare-Cartan theorem [29] of umbra-Lagrangian theory formulated by Mukherjee [30] and Mukherjee et. al. [33, 34]. A candid commentary on this umbra-Lagrangian theory has been given by Brown [31]. The intestine model comprises a tube of oscillators having cells both around the periphery and along the axis of the tube. In this physiological model, the enzyme does not migrated in the product, so that it may be separated easily. In this model, the ring connections of these four oscillators have been considered with four protomers of the oligomer of an allosteric enzyme. The coupling parameters have been considered non-identical between the oscillators enrolled in the process. Moreover, earlier model of promoters [22] is also refined by incorporating damping coefficient of the coupling, which also contributes some interesting results as a promoter may also bind a single molecule of an effector ligand present in the surrounding solution and molecule may also exert some resistance to the flow of solute.

In this paper, different aspects of the dynamical behaviour of coupled oscillators are discussed. In section two, Poincaré-Cartan theorem of umbra-Lagrangian theory is presented and mathematical analysis of coupled biological oscillators is obtained. Section three presents the dynamical behaviour of the coupled biological oscillators. This behaviour is quite obvious through simulation results with changing the value of coupling parameters. One may also obtain the chaos conditions and beating phenomena, when local injected signals in forms of irregularity are incorporated in the model and analyzed using numerical simulations.

2. Poincaré -Cartan Theorem for umbra-Lagrangian theory

To enlarge the scope of Lagrangian-Hamiltonian mechanics, a new proposal of additional time like variable 'umbra-time' was made by Mukherjee [30] and this new concept of umbra-time leads to a peculiar form of equation, which is termed as umbra-Lagrange's equation [31]. The details of this theory are reported in reference [33-34]; however some specific proof may be reproduced here. This theorem is an extension of Poincare-Cartan theorem, which has an action integral, where initial and terminal terms are varied as functions of a parameter α [35]. The modulatory and the trajectories displacements are also varied through the variation of the indices, which select the members of the homotopic family of these functions. The homotopy may now be extended up to the varied initial and terminal instants of time.
The integral may be written as

$$W = \int_{t_0(\alpha)}^{t_1(\alpha)} L\left(\bar{q}(\xi, a+\alpha), \dot{\bar{q}}(\xi, a+\alpha), \bar{q}(\xi, b+\alpha), \dot{\bar{q}}(\xi, b+\alpha), \xi\right) d\xi. \tag{3}$$

The index *a* corresponds to modulatory and *b* corresponds to trajectorial member. The parameter α=0 corresponds to unvaried function with initial and terminal time. Assuming δt as a small variation in the parameter α from the zero value, one may write

$$\Delta W = \int_{t_0(\alpha)}^{t_1(\alpha)} L(...) d\xi - \int_{t_0(0)}^{t_1(0)} L(...) d\xi, \tag{4}$$

After following the procedure as in reference [35], one obtains integral invariant as

$$\frac{dI(t)}{dt} = -\oint_{C_t} \sum_{i=1}^{n} \left[\left(Lim_{\eta \to t} \frac{\partial L^*}{\partial \dot{q}_i(t)} \right) \delta \dot{q}_i + \left(Lim_{\eta \to t} \frac{\partial L^*}{\partial q_i(t)} \right) \delta q_i \right]. \tag{5}$$

Applying Green's theorem, Eq. (5) may be rewritten by taking $\dot{q}_i$ and q_i in cyclic order as

$$\frac{dI(t)}{dt} = -\sum_{i=1}^{n}\sum_{j=1}^{n}\iint_{A_{K_{ij}}}\left\{\frac{\partial}{\partial\dot{q}_i(t)}\left(Lim_{\eta\to t}\frac{\partial L^*}{\partial\dot{q}_j(t)}\right)-\frac{\partial}{\partial\dot{q}_j(t)}\left(Lim_{\eta\to t}\frac{\partial L^*}{\partial\dot{q}_i(t)}\right)\right\}\delta\dot{q}_i\,\delta\dot{q}_j$$
$$-\sum_{i=1}^{n}\sum_{j=1}^{n}\iint_{A_{P_{ij}}}\left\{\frac{\partial}{\partial\dot{q}_i(t)}\left(Lim_{\eta\to t}\frac{\partial L^*}{\partial q_j(t)}\right)-\frac{\partial}{\partial q_j(t)}\left(Lim_{\eta\to t}\frac{\partial L^*}{\partial\dot{q}_i(t)}\right)\right\}\delta\dot{q}_i\,\delta q_j$$
$$-\sum_{i=1}^{n}\sum_{j=1}^{n}\iint_{A_{T_{i,j}}}\left\{\frac{\partial}{\partial q_i(t)}\left(Lim_{\eta\to t}\frac{\partial L^*}{\partial q_j(t)}\right)-\frac{\partial}{\partial q_j(t)}\left(Lim_{\eta\to t}\frac{\partial L^*}{\partial q_i(t)}\right)\right\}\delta q_i\,\delta q_j\,. \tag{6}$$

gives the rate of change of a Poincaré integral and contains three area projections in *i- j*th plane, which are, the velocity-velocity area projection $A_{K_{ij}}$ termed as the *kinematic projection*, velocity-displacement area projection $A_{P_{i,j}}$ termed as the *phase projection*, and displacement-displacement area projection $A_{T_{i,j}}$ termed as the *trajectorial* or *orbital projection*. For purely Hamiltonian systems with no dissipative, gyroscopic or regenerative forces and fields, the right hand side terms vanish, and lead to the classical result as

$$\frac{dI(t)}{dt} = 0\,. \tag{7}$$

2.1 Physical Model and Problem Statement

Any biological system can be easily model with Ferro-electricity behaviour in brain waves [36-37] and may be represented by classical Vander Pol equation as

$$m\ddot{x} - \mu\left(x^2 - 1\right)\dot{x} + Kx = 0\,. \tag{8}$$

In this paper, a general approach for analyzing ring structure of coupled biological oscillators is presented. The study may be applied to mammalian intestinal activity and how the enzymes flow from one cell to other cells. However, four coupled oscillators are presented in context of animal locomotion [43]. Quadruped gaits closely resemble the natural patterns of four oscillators systems. As example of rabbit bounds its move its front leg together then its back legs. There is a phase difference of zero between the two front legs and one half between the front and back legs. Four oscillators may be coupled in

seven ways such as (a) Synchrony each one fourth of a cycle out of phase with the others (b) Three synchronous and one with unrelated phase (c) Peculiar rhythm of two oscillators, anti-synchronous with each other.

As already stated that this system is already interacting with their surroundings and neighboring enzymes, so there will be cooperating interactions between them. In this problem, coupled enzymes with ring connection consisting of four mutually coupled Vander Pol oscillators can be shown in Fig.1, which may be expressed by following equations:

$$\begin{aligned}
m\ddot{x}_1 - \mu\left(x_1^2 - 1\right)\dot{x}_1 + Kx_1 &= K_{cp}^A\left(x_4 - x_1\right) + K_{cp}^B\left(x_2 - x_1\right) + R_{cp}\left(\dot{x}_4 - \dot{x}_1\right) + R_{cp}\left(\dot{x}_2 - \dot{x}_1\right) \\
m\ddot{x}_2 - \mu\left(x_2^2 - 1\right)\dot{x}_2 + Kx_2 &= K_{cp}^A\left(x_3 - x_2\right) + K_{cp}^B\left(x_1 - x_2\right) + R_{cp}\left(\dot{x}_3 - \dot{x}_2\right) + R_{cp}\left(\dot{x}_1 - \dot{x}_2\right) \\
m\ddot{x}_3 - \mu\left(x_3^2 - 1\right)\dot{x}_3 + Kx_3 &= K_{cp}^A\left(x_2 - x_3\right) + K_{cp}^B\left(x_4 - x_3\right) + R_{cp}\left(\dot{x}_2 - \dot{x}_3\right) + R_{cp}\left(\dot{x}_4 - \dot{x}_3\right) \\
m\ddot{x}_4 - \mu\left(x_4^2 - 1\right)\dot{x}_4 + Kx_4 &= K_{cp}^A\left(x_1 - x_4\right) + K_{cp}^B\left(x_3 - x_4\right) + R_{cp}\left(\dot{x}_1 - \dot{x}_4\right) + R_{cp}\left(\dot{x}_3 - \dot{x}_4\right)
\end{aligned} \tag{9}$$

In this set of equation, the over dot denotes the time derivative, μ, the parameter of non-linearity and $x_i(1,2,3,4)$ the concentration of i^{th} biological system. It is a fact when two or more oscillators are coupled, the equation governing the behaviour tends to become intractable and possible behaviour becomes much more complex. In this formation of a ring, each oscillator may be coupled only to a few immediate neighbours. This ring may be the same as the neuro-muscular oscillators in the small intestine. The force of coupling between the oscillators is significant parameter to decide the synchronization behaviour. In this system, there is one positive and one negative direction of the solute flow, which represents the inhibitory and excitatory couplings. In this way, the directions of the solute flow may be represented as K_{cp}^A and K_{cp}^B, which may be positive or negative. R_{cp} in the model represents the resistance to solute flow due to any irregularity and may be expressed as damping coefficient of couplings. Now, from these equations, one may easily obtain Umbra-Lagrangian Equation [33-34], which may be written as

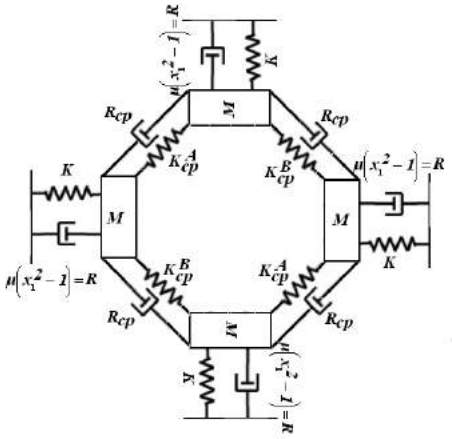

Fig.1: Four Biological oscillators connected in a ring with non-trivial coupling

$$
\begin{aligned}
L^{*} = {} & \frac{1}{2}m\dot{x}_1^2(\eta)+\frac{1}{2}m\dot{x}_2^2(\eta)+\frac{1}{2}m\dot{x}_3^2(\eta)+\frac{1}{2}m\dot{x}_4^2(\eta)-\frac{1}{2}Kx_1^2(\eta)-\frac{1}{2}K_{cp}^{A}\{x_4(\eta)-x_1(\eta)\}^2 \\
& -\frac{1}{2}K_{cp}^{B}\{x_2(\eta)-x_1(\eta)\}^2-\frac{1}{2}Kx_2^2(\eta)-\frac{1}{2}K_{cp}^{A}\{x_3(\eta)-x_2(\eta)\}^2-\frac{1}{2}K_{cp}^{B}\{x_1(\eta)-x_2(\eta)\}^2 \\
& -\frac{1}{2}Kx_3^2(\eta)-\frac{1}{2}K_{cp}^{A}\{x_2(\eta)-x_3(\eta)\}^2-\frac{1}{2}K_{cp}^{B}\{x_4(\eta)-x_3(\eta)\}^2 \\
& -\frac{1}{2}Kx_4^2(\eta)-\frac{1}{2}K_{cp}^{A}\{x_1(\eta)-x_4(\eta)\}^2 \\
& -\frac{1}{2}K_{cp}^{B}\{x_3(\eta)-x_4(\eta)\}^2-\mu(x_1^2-1)\dot{x}_1(t)x_1(\eta)-\mu(x_2^2-1)\dot{x}_2(t)x_2(\eta)-\mu(x_3^2-1)\dot{x}_3(t)x_3(\eta) \\
& -\mu(x_4^2-1)\dot{x}_4(t)x_4(\eta)-R_{cp}\{\dot{x}_2(t)-\dot{x}_1(t)\}\{x_2(t)-x_1(t)\}-R_{cp}\{\dot{x}_3(t)-\dot{x}_2(t)\}\{x_3(t)-x_2(t)\} \\
& -R_{cp}\{\dot{x}_4(t)-\dot{x}_3(t)\}\{x_4(t)-x_3(t)\}-R_{cp}\{\dot{x}_1(t)-\dot{x}_2(t)\}\{x_1(t)-x_2(t)\}
\end{aligned}
\tag{10}
$$

Now through Eq. (6), one may finally obtains

$$
\frac{dI}{dt}=\begin{bmatrix}
-\mu\iint\limits_{A(P\dot{x}_1x_1)}(x_1^2(t)-R_{cp}-1)\,\delta\dot{x}_1(t)\delta x_1(t)-\mu\iint\limits_{A(P\dot{x}_2x_2)}(x_2^2(t)-R_{cp}-1)\,\delta\dot{x}_2(t)\delta x_2(t) \\
-\mu\iint\limits_{A(P\dot{x}_3x_3)}(x_3^2(t)-R_{cp}-1)\,\delta\dot{x}_3(t)\delta x_3(t)-\mu\iint\limits_{A(P\dot{x}_4x_4)}(x_4^2(t)-R_{cp}-1)\,\delta\dot{x}_4(t)\delta x_4(t) \\
-\iint\limits_{A(P\dot{x}_1x_2)}R_{cp}\,\delta\dot{x}_1(t)\delta x_2(t)-\iint\limits_{A(P\dot{x}_2x_1)}R_{cp}\,\delta\dot{x}_2(t)\delta x_1(t)-\iint\limits_{A(P\dot{x}_2x_1)}R_{cp}\,\delta\dot{x}_2(t)\delta x_3(t) \\
-\iint\limits_{A(P\dot{x}_3x_2)}R_{cp}\,\delta\dot{x}_3(t)\delta x_2(t)-\iint\limits_{A(P\dot{x}_3x_4)}R_{cp}\,\delta\dot{x}_3(t)\delta x_4(t)-\iint\limits_{A(P\dot{x}_4x_3)}R_{cp}\,\delta\dot{x}_4(t)\delta x_3(t) \\
-\iint\limits_{A(P\dot{x}_4x_1)}R_{cp}\,\delta\dot{x}_4(t)\delta x_1(t)-\iint\limits_{A(P\dot{x}_1x_4)}R_{cp}\,\delta\dot{x}_1(t)\delta x_4(t)
\end{bmatrix}
\tag{11}
$$

Equation (11) gives the oscillations of coupled Vander Pol's oscillators in a 12 dimensional phase space. When the coupling terms R_{cp} and K_{cp} are equal to zero, the system consist of four independent oscillators each evolving on a limit cycle that is orbitally stable. In this way, Equation (11) just reduces to

$$
\frac{dI}{dt}=\begin{bmatrix}
-\mu\iint\limits_{A(P\dot{x}_1x_1)}(x_1^2(t)-1)\,\delta\dot{x}_1(t)\delta x_1(t)-\mu\iint\limits_{A(P\dot{x}_2x_2)}(x_2^2(t)-1)\,\delta\dot{x}_2(t)\delta x_2(t) \\
-\mu\iint\limits_{A(P\dot{x}_3x_3)}(x_3^2(t)-1)\,\delta\dot{x}_3(t)\delta x_3(t)-\mu\iint\limits_{A(P\dot{x}_4x_4)}(x_4^2(t)-1)\,\delta\dot{x}_4(t)\delta x_4(t)
\end{bmatrix}. \tag{12}
$$

It is assumed that the coupled oscillators are identical and let any stage of time t, the system be initiated on a circle of radius r as $x(t), y(t) = r\cos t$ and $\dot{x}(t), \dot{y}(t) = r\sin t$, after simplification, it yields

$$
\frac{dI}{dt}=2\left[\mu r^2\pi\left(1-\frac{r^2}{4}\right)\right]. \tag{13}
$$

It is clear that $\frac{dI}{dt} = 0$ if $r=2$, $\frac{dI}{dt} < 0$ if $r>2$ and $\frac{dI}{dt} > 0$ if $r<2$. Therefore, $r=2$ leaves the Poincare-Cartan integral I invariant and hence is the radius of the limit cycle as shown in *Fig. 2 a-2d*.

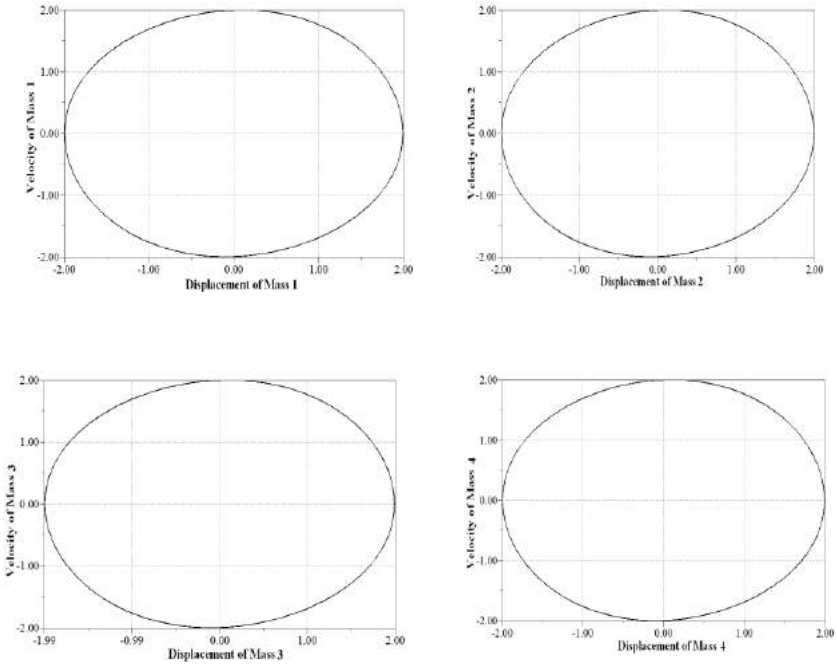

Fig.2 (a-d): Limit cycle of first, second, third and fourth biological oscillator at $\mu = 0.05$

When non-trivial couplings exists due to some internal parameters of the system, it is possible that the nearest neighbouring oscillator are coupled to a considered oscillator through the same or different energy activation due to a conformational spread. In this way, coupled oscillators interact altogether resulting in trajectories embedded in 12 dimension phase space, which may be obtained as Eq. 11.

3. Dynamics of Coupled Oscillators

First of all, it is considered that the coupled oscillators are identical i.e. $x_1(t) = x_2(t) = x_3(t) = x_4(t)$, and there is no coupling between the oscillators, then one may easily obtain in phase mode to be exist in the system by simple inspection of Eq. (12)

$$\frac{dI}{dt}=\begin{bmatrix}-\mu \iint\limits_{A(P\dot{x}_1x_1)}(x_1^2(t)-1)\delta\dot{x}_1(t)\delta x_1(t)-\mu \iint\limits_{A(P\dot{x}_1x_1)}(x_1^2(t)-1)\delta\dot{x}_1(t)\delta x_1(t)\\ -\mu \iint\limits_{A(P\dot{x}_1x_1)}(x_1^2(t)-1)\delta\dot{x}_1(t)\delta x_1(t)-\mu \iint\limits_{A(P\dot{x}_1x_1)}(x_1^2(t)-1)\delta\dot{x}_1(t)\delta x_1(t)\end{bmatrix}, \quad (14)$$

which reduces into four uncoupled Vander Pol equations. In this way, the in phase mode gives an exact solution to the coupled equations.The dynamic behaviour of coupled oscillators include in phase/full synchronization and cluster synchronization. This synchronization phenomenon is of great interest in neural systems and related with several important issues in neurology and science. Moreover, these results are well proven by experiments and analysis in several neurological and heart disease [38-39]. The other significant characteristics of these oscillators lie in the fact that they are highly sensitive to their initial conditions. If these four oscillators are excited at different initial conditions, their trajectory finally circulates on the same limit cycle but with different phase, which is termed as phase synchronization. Simulation results also reveal that there exits a very small region in the coupling parameter space, where the synchronization dynamics are found to be chaotic. The next subsection provides the detailed analysis of in phase or full synchronization.

3.1. In-Phase synchronization / Full Synchronization

In-phase mode is a periodic motion and satisfies the condition $x_1(t)=x_2(t)=x_3(t)=x_4(t)$. Substituting $x_1(t)=x_2(t)=x_3(t)=x_4(t)$ into Eq. (11), one may find the integral invariant as

$$\frac{dI}{dt}=-4\left[\mu \iint\limits_{A(P\dot{x}_1x_1)}(x_1^2(t)-R_{cp}-1)\delta\dot{x}_1(t)\delta x_1(t)+2\iint\limits_{A(P\dot{x}_1x_1)}R_{cp}\,\delta\dot{x}_1(t)\delta x_1(t)\right]. \quad (15)$$

In phase mode, if it exists, resides in the 2-dimensional space $x_1-\dot{x}_1$, which is itself as invariant manifold in 12-dimensional space $x_1-\dot{x}_1-x_2-\dot{x}_2-x_3-\dot{x}_3-x_4-\dot{x}_4$. This mode gives four similar limit cycles oscillating in two dimensional phase space. Thus in-phase mode can further be visualized for any value of R_{cp} and any of the coupling parameter K_{cp}^{A} or $K_{cp}^{B}>0$. Numerical simulation may be advantageous to visualize the phase synchronization as shown in Fig.3, where time history of biological oscillators is shown at value

($\mu = 2.03, R_{cp} = 0.06, K_{cp}^{A} = -0.294, K_{cp}^{B} = 0.294$). The initial conditions for all such oscillator are assumed to the same or $x_{01} = x_{02} = x_{03} = x_{04} = 0.0$.

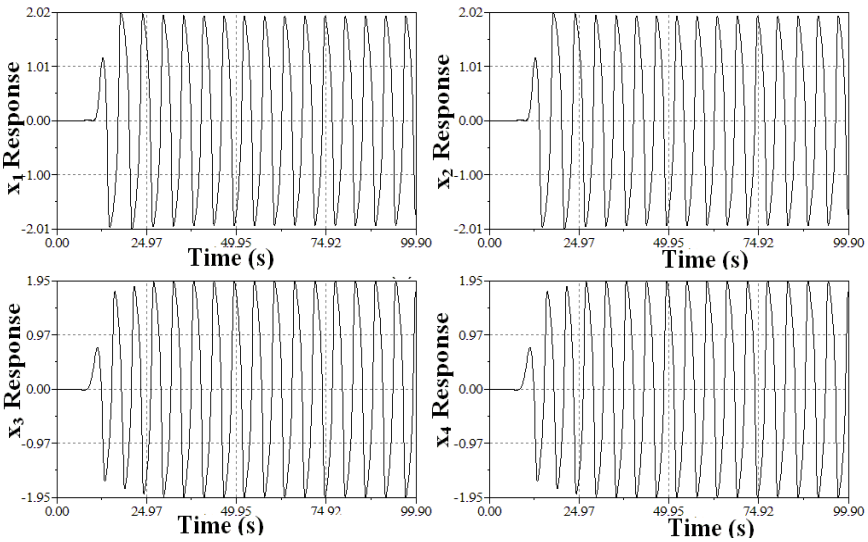

Fig. 3: Time history of oscillators at

$\mu = 2.03, R_{cp} = 0.06, K_{cp}^{A} = -0.294, K_{cp}^{B} = 0.294$

The Fig. 4 and Fig. 5 reveal that all oscillators cross zero (with a positive slope or negative slope) at the same time, which indicates that all oscillators are in–phase synchronization. The full synchronization is also apparent either in positive or negative direction, which means that the full synchronization is having full phase identical whenever the solute flow in positive direction or vice versa. The four biological oscillators display same dynamics at this instant. In the process of phase synchronization, the oscillators oscillate with a repeating sequence of relative phase angles. It may be concluded that the all four oscillators are synchronized having the identical phase.

3.2 Cluster Synchronization

The out of phase is a periodic motion, which satisfy $x_1(t) = x_2(t)$ *and* $x_3(t) = x_4(t)$. Putting this condition into Eq. (11), one obtains

$$\frac{dI}{dt} = -2\left[\begin{array}{l}\mu \iint\limits_{A(P\dot{x}_1x_1)} (x_1^2(t) - R_{cp} - 1)\,\delta\dot{x}_1(t)\delta x_1(t) + \mu \iint\limits_{A(P\dot{x}_3x_3)} (x_3^2(t) - R_{cp} - 1)\,\delta\dot{x}_3(t)\delta x_3(t) \\ + \iint\limits_{A(P\dot{x}_1x_1)} R_{cp}\,\delta\dot{x}_1(t)\delta x_1(t) + \iint\limits_{A(P\dot{x}_2x_3)} R_{cp}\,\delta\dot{x}_3(t)\delta x_3(t)\end{array}\right] \tag{16}$$

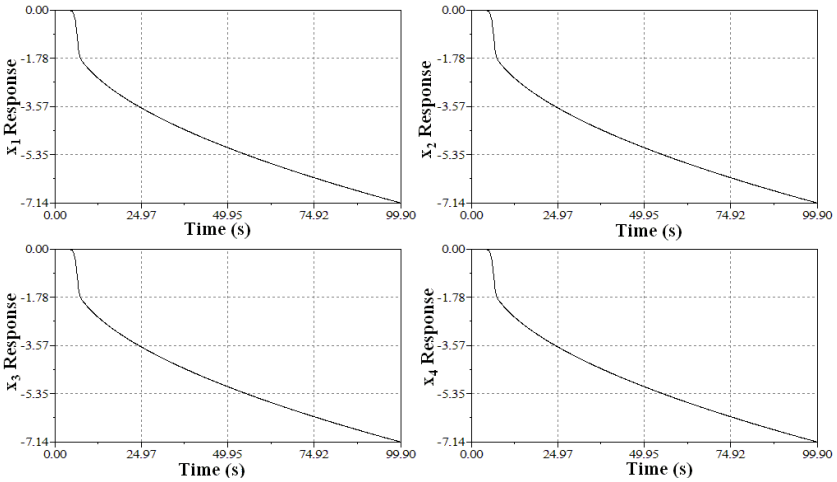

Fig.4: Full synchronization in negative direction at

$\mu = 0.84, R_{cp} = 0.954, K_{cp}^{A} = -1.064, K_{cp}^{B} = -0.316$

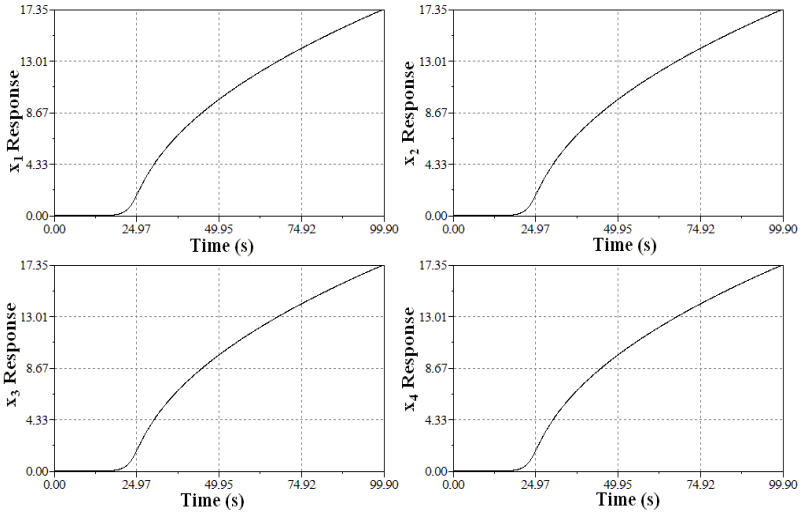

Fig.5: Full synchronization in positive direction at

$\mu = 2.03, R_{cp} = 0.06, K_{cp}^{A} = -1.064, K_{cp}^{B} = 0.316$

Here the two oscillators in group are shifted with the zero crossings at a constant time. This phase lag φ may be defined as

$$\varphi = \frac{\Delta t}{T}.2\pi$$

where Δt is the time difference between the zero crossings. The two oscillators are out of phase, when φ =180°. The equation (16) determines that two oscillators $x_1(t)$, $x_2(t)$ and $x_3(t)$, $x_4(t)$ will synchronize together and this group of two oscillators will oscillate in out of phase synchronization with phase lag of 180°. This phenomenon is termed as cluster synchronization, where oscillators cleave such that all oscillators within one cluster move in perfect synchrony but the motion of two clusters is not synchronized at all. This phenomenon of cluster may also be achieved with $x_1(t) = x_4(t)$ *and* $x_2(t) = x_3(t)$.

The reason is quite oblivious for oscillator with neighboring interactions. However, it will not be achieved with the configuration $x_1(t) = x_3(t)$ *and* $x_2(t) = x_4(t)$ due to non interacting coupling between them. It may be shown in Figure 6 the time history of out of phase motion corresponding to the value ($\mu = 2.03, R_{cp} = 0.30, K_{cp}^{A} = -0.28, K_{cp}^{B} = -1.4$). The two oscillators are shifted with the zero crossings at a constant time. This phase lag ϕ may be 180 during out of phase synchronization.

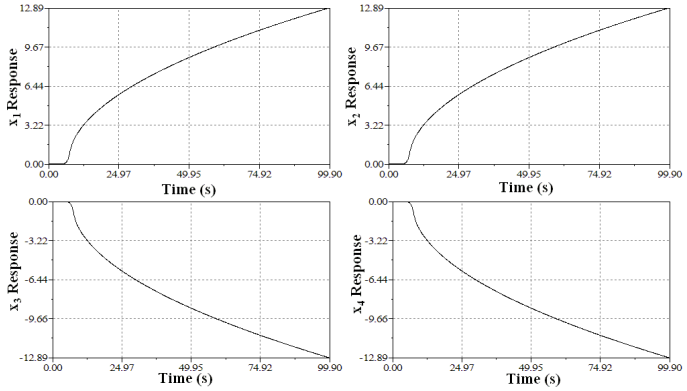

Fig.6: Cluster synchronization of oscillators at

$$\mu = 2.03, R_{cp} = 0.30, K_{cp}^{A} = -0.28, K_{cp}^{B} = -1.4$$

The ranges of coupling parameter including damping coefficient leading to full synchronization and lack of synchronization can be shown in the Fig.7, where the regions of in-phase and out of phase are clearly marked to obtain the optimal output of synchronization phenomena.

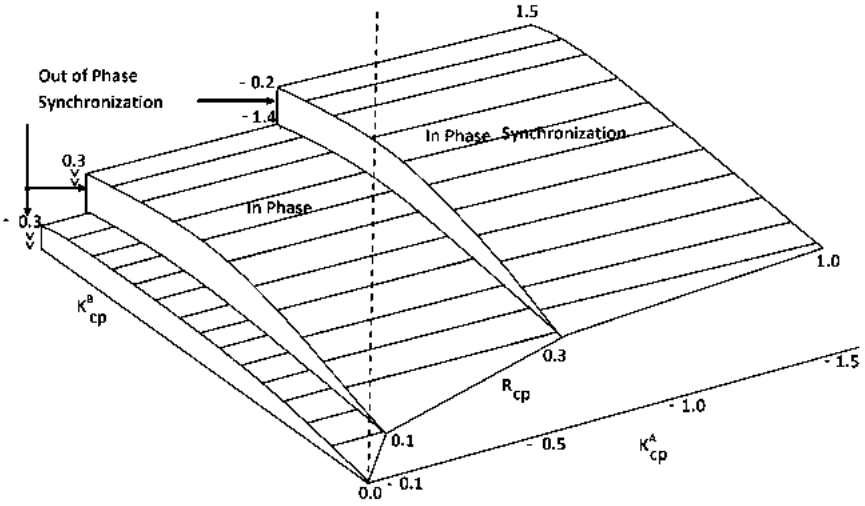

Fig.7: Reigns of in phase and out of phase synchronization of oscillators

4. Influence of Locally Injected Signal on Synchronization Phenomena

As mentioned in previous subsections that different dynamical states are observed in several identical coupled biological oscillators like clustering synchronization (synchronization in sub groups) or complete synchronization (in phase synchronization). But there are some situations in nature in which the complete system may be coupled with an external independent oscillator or excitation. This is a matter of fact that all real system contains impurity, irregularity in the form of natural fluctuations,

which is associated with dissipation as well as random external environment.

In self-sustained oscillators are always prone to different causes of irregularity in a form of some external strength like ΔK (sometime termed as detuned parameter). This example may be further ascertained by considering the example of cardio-vascular system of humans, displaying self-sustained vibration. When there is any impact of any irregularity, the cardiac vibrations [40-41] are not perfectly periodic. That is why some locally injected signal in the form of ΔK may be added in the systems in first biological oscillator. Present case of biological system deals with an impulse transmission in neurons and their synchronization dynamics is analyzed further. Including the locally injected parameter ΔK , one may obtain the equations as

$$\begin{aligned}
&m\ddot{x}_1 - \mu\left(x_1^2 - 1\right)\dot{x}_1 + Kx_1 = K_{cp}^A(x_4 - x_1) + K_{cp}^B(x_2 - x_1) + R_{cp}(\dot{x}_4 - \dot{x}_1) + R_{cp}(\dot{x}_2 - \dot{x}_1) + \Delta K(x_1 - x_c)\\
&m\ddot{x}_2 - \mu\left(x_2^2 - 1\right)\dot{x}_2 + Kx_2 = K_{cp}^A(x_3 - x_2) + K_{cp}^B(x_1 - x_2) + R_{cp}(\dot{x}_3 - \dot{x}_2) + R_{cp}(\dot{x}_1 - \dot{x}_2)\\
&m\ddot{x}_3 - \mu\left(x_3^2 - 1\right)\dot{x}_3 + Kx_3 = K_{cp}^A(x_2 - x_3) + K_{cp}^B(x_4 - x_3) + R_{cp}(\dot{x}_2 - \dot{x}_3) + R_{cp}(\dot{x}_4 - \dot{x}_3)\\
&m\ddot{x}_4 - \mu\left(x_4^2 - 1\right)\dot{x}_4 + Kx_4 = K_{cp}^A(x_1 - x_4) + K_{cp}^B(x_3 - x_4) + R_{cp}(\dot{x}_1 - \dot{x}_4) + R_{cp}(\dot{x}_3 - \dot{x}_4)
\end{aligned} \tag{17}$$

In Eq. (17), x_c represents the dynamic parameter of the external oscillator and also defined as controlling signal.

The umbra-Lagrangian equation for Eq.(17) may be written as

$$\begin{aligned}
L^* = {} & \frac{1}{2}m\dot{x}_1^2(\eta) + \frac{1}{2}m\dot{x}_2^2(\eta) + \frac{1}{2}m\dot{x}_3^2(\eta) + \frac{1}{2}m\dot{x}_4^2(\eta) - \frac{1}{2}Kx_1^2(\eta) - \frac{1}{2}K_{cp}^A\{x_4(\eta) - x_1(\eta)\}^2\\
& - \frac{1}{2}K_{cp}^B\{x_2(\eta) - x_1(\eta)\}^2 - \frac{1}{2}\Delta K\{x_c(\eta) - x_1(\eta)\}^2 - \frac{1}{2}Kx_2^2(\eta) - \frac{1}{2}K_{cp}^A\{x_3(\eta) - x_2(\eta)\}^2\\
& - \frac{1}{2}K_{cp}^B\{x_1(\eta) - x_2(\eta)\}^2 - \frac{1}{2}Kx_3^2(\eta) - \frac{1}{2}K_{cp}^A\{x_2(\eta) - x_3(\eta)\}^2 - \frac{1}{2}K_{cp}^B\{x_4(\eta) - x_3(\eta)\}^2\\
& - \frac{1}{2}Kx_4^2(\eta) - \frac{1}{2}K_{cp}^A\{x_1(\eta) - x_4(\eta)\}^2 - \frac{1}{2}K_{cp}^B\{x_3(\eta) - x_4(\eta)\}^2 - \mu(x_1^2 - 1)\dot{x}_1(t)x_1(\eta)\\
& - \mu(x_2^2 - 1)\dot{x}_2(t)x_2(\eta) - \mu(x_3^2 - 1)\dot{x}_3(t)x_3(\eta) - \mu(x_4^2 - 1)\dot{x}_4(t)x_4(\eta) - R_{cp}\{\dot{x}_2(t) - \dot{x}_1(t)\}\\
& \{x_2(t) - x_1(t)\} - R_{cp}\{\dot{x}_3(t) - \dot{x}_2(t)\}\{x_3(t) - x_2(t)\}\\
& - R_{cp}\{\dot{x}_4(t) - \dot{x}_3(t)\}\{x_4(t) - x_3(t)\} - R_{cp}\{\dot{x}_1(t) - \dot{x}_2(t)\}\{x_1(t) - x_2(t)\}
\end{aligned} \tag{18}$$

Now through Eq. (6), one may finally obtains Poincaré-Cartan integral invariant similar to Eq. (11) as coupling parameter does not appear in the mathematical expression of the integral invariant. One may visualize the parametric variation of coupling and injecting signal parameter to obtain the significant dynamics, which may be explained in next subsections.

4.1 Beating Phenomena

When the value of injecting signal ΔK is very small, $\Delta K < 0.1$, the four oscillators are in phase to some extent as observed in Fig. 8.

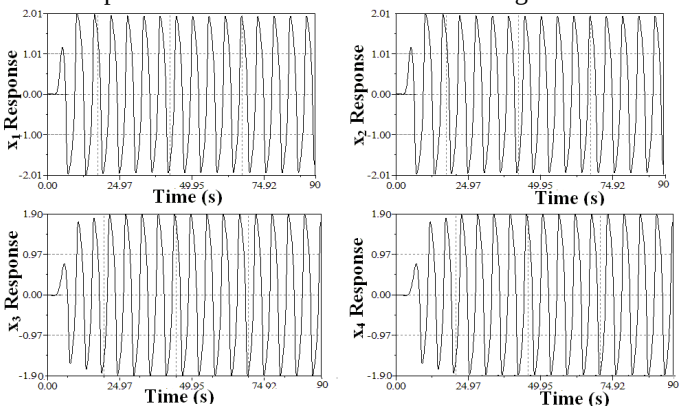

Fig.8: In phase synchronization with local injected signal at

$$\mu = 0.426, R_{cp} = 0, K_{cp}^{A} = -3.16, K_{cp}^{B} = 1.208, \Delta K = 0.08$$

However, at the larger value of ΔK, $\Delta K > 0.1$, in phase mode of vibration vanishes and amplitude of each oscillators beats while the general motion of the response remains similar to in-phase mode. This phenomena is beating phenomena as shown in Fig.9 at $\Delta K = 0.396$. This beating phenomenon may be observed for a bigger time window also.

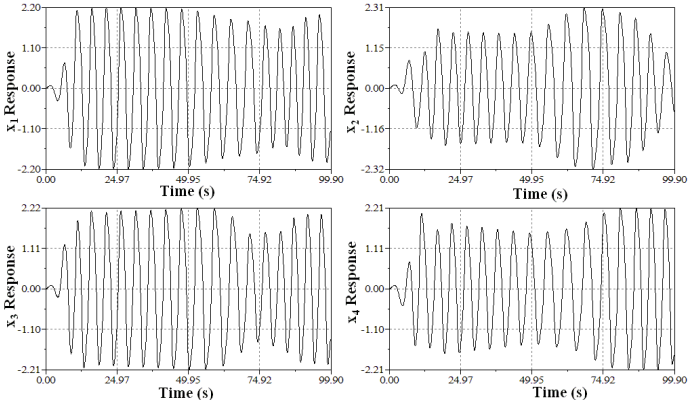

Fig.9: Beating Phenomenon with local injected signal at

$$\mu = 0.426, R_{cp} = 0, K_{cp}^{A} = -3.16, K_{cp}^{B} = 1.208, \Delta K = 0.396$$

4.2 Chaotic behaviour

Chaotic behaviour is also obtained in the system of coupled oscillators, when the strength of local injection signal is enhanced. In this case, damping effect is not taken into consideration because it has a very limited role in determining the chaotic behaviour. As shown in Fig. 10, the phase plot of first oscillator is showing the chaotic behaviour for the value of $\mu = 1.6, R = 0, K_{cp}^{A} = -.172, K_{cp}^{B} = 0.1728, \Delta K = .761.$

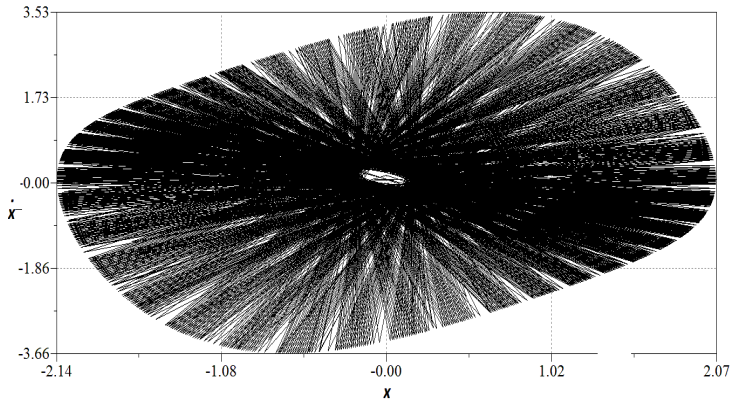

Fig.10: Phase plot of first biological oscillators with $\Delta K = 0.761$

The chaotic behaviour may also be determined by showing the Poincaré maps of the all oscillators as shown in Fig.11, which shows that the chaos is dependent on initial conditions of the oscillators and this sensitive dependency on initial conditions has been verified by computational methods.

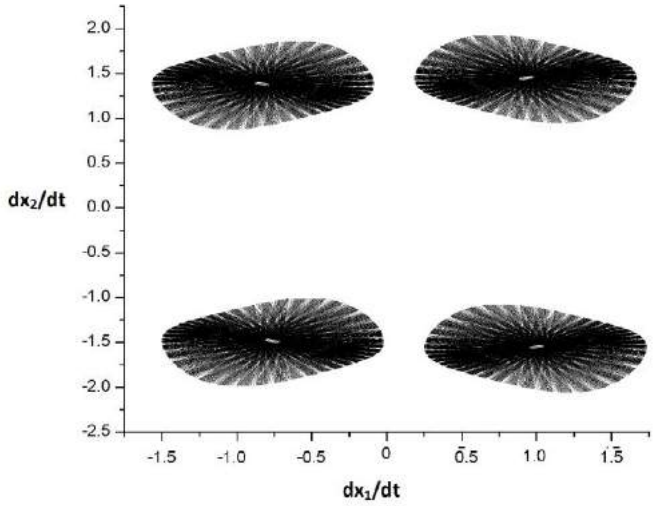

Fig. 11: Projections of second Poincaré map for the section $x_1=0$, and $x_2=0$ for the first oscillators with $\Delta K = 0.761$

The chaotic behaviour may also be shown, when the time step used is reduced at the order of 10^{-1} to 10^{-2}. The Poincaré session contains a series of points by which the periodicity is entrained. But as soon as the pattern vanishes and leads to a structure, which is known as torus. In this case, the overall periodicity of the oscillator is totally disappeared and a torus is achieved as shown in Fig.12.

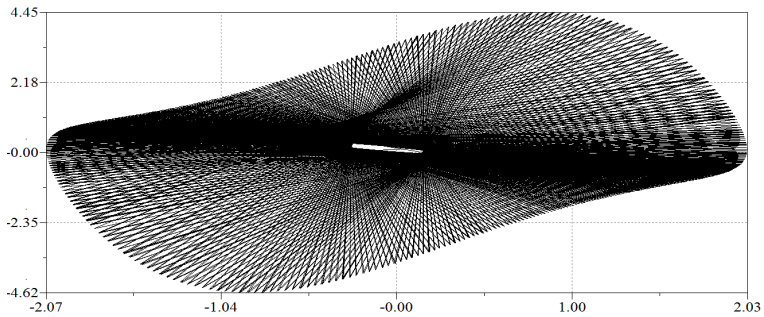

Fig. 12: Torus structure for one oscillators, when simulation time $t>10^5$ with $\Delta K = 0.761$

The chaotic behaviour may also be visualized by Lorenz maps, which are drawn for all the oscillators as shown in Fig. 13. The trajectory leaves one spiral only

after exceeding some critical distance from the centre point. In this case, the intensity of injecting signal is kept at 0.761.

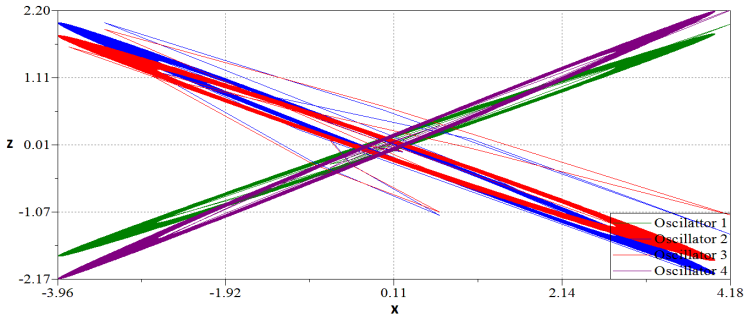

Fig. 13: Phase plot for all the oscillators, when simulation time $t>10^5$ with $\Delta K = 0.761$

5. Conclusions

In this paper, the analysis of mutually coupled oscillators has been obtained theoretically and numerically. The extended Poincaré-Cartan theorem has been applied in theoretical analysis. It has been shown that in absence of any kind of non-trivial coupling, oscillators oscillate in stable and independent limit cycle. However, presence of this coupling, the oscillators interact resulting in trajectories in 12-dimensional phase spaces, which has been supported by the mathematical formulation of integral invariant. Beside this theoretical analysis, full and cluster synchronization of biological oscillator are also discussed, which has been supported by simulation study of the system. These results relate to phenomena occurring in physiological experiments, such as the periodic stimulation of neural and cardiac cells and in the non-regular function of organs and organism. The effect of local injected signal has been presented, which shows the beating phenomena and chaotic behaviour of the oscillators. The phenomena of stability and bifurcation may also be deal in near future as a separate case to show the chaos control of oscillators.

Acknowledgements:

This paper is a tribute to late Prof. Amalendu Mukherjee, who has formulated the concept of umbra-Lagrangian. Special thanks to Dr. Pravir Kumar, Associate Professor, Biotechnology Department, DTU, Delhi for their valuable suggestions throughout the course of this study.

References

[1] G.M. Mahmoud, "Approximate solutions of a class of complex non-linear dynamical systems", Physica A, 253, pp.211-222, 1998.

[2] A. Maccari, "Periodic and quasi-periodic motion for complex non-linear

systems," Inter. J. Non-linear Mech, 38, pp. 575-584, 2003.

[3] G.M. Mahmoud and S.M. Aly, " On periodic solutions of parametrically excited complex non-linear dynamical systems", Physica A, 278, pp.390-404. 2000.

[4] G.M. Mahmoud and S.M. Aly, " On periodic attractors of complex damped non-linear systems", Inter. J. Non-linear Mech, 35, pp. 309, 323, 2000.

[5] G.M. Mahmoud and AAM Faraglay , " Stabilization of unstable periodic attractors of complex damped non-linear dynamical systems," Chaos, Soliton and Fractals, 17, pp. 105-112, 2003.

[6] R.H. Rand and P. Holmes., " Bifurcation of periodic motions in two coupled Vander Pol Oscillators," Inter. J. Non-linear Mech, 15, pp. 387-399, 1980.

[7] J. Kozolowski , U. Parlitz , W. Lauterborn, , "Bifurcation analysis of two coupled Periodically driven Duffings oscillators," Physics Review E, 51, pp. 1861-1867, 1995.

[8] Q. Wang, G. Chen and M.Perc, "Synchronous bursts on scale-free neuronal networks with attractive and repulsive coupling," , PLoS ONE 6, e15851, 2011.

[9] Q.Wang,M.Perc, Z.Duan and G.Chen, "Synchronization transitions on scale-free neuronal networks due to finite information transmission delays," Phys. Rev. E, 80, 026206 2009.

[10] X. Sun, J. Lei, M. Perc, J. Kurths and G. Chen, "Burst synchronization transitions in a neuronal network of subnetworks, Chaos 21, 016110, 2011.

[11] V. Volman, M.Perc and M. Bazhenov "Gap junctions and epileptic seizures - Two sides of the same coin?", PLoS ONE 6, e20572, 2011.

[12] M. Perc , M. Gosak, and M. Marhl, "Periodic calcium waves in coupled cells induced by internal noise," Chem. Phys. Lett.. 437, 143-147 , 2007.

[13] M. Gosak, M. Marhl and M. Perc, "Spatial coherence resonance in excitable biochemical media induced by internal noise, Biophys. Chem. 128, 210-214, 2007.

[14] D. W. Storti, and R. H. Rand, "Dynamics of two strongly coupled Van der Pol oscillators, International Jr. of Non-Linear Mechanics, 17,pp.143-152, 1982.

[15] D.W. Storti, C. Nevrinceanu, and P. G. Reinhall, "Perturbation solution of an oscillator with periodic Van der Pol damping," Dynamics and Vibration of Time-varying systems and Structures (ASME), 56,pp.397-402, 1993.

[16] Q. Bi, "Dynamical analysis of two coupled parametrically excited Van der Pol oscillators," International Jr. of Non-Linear Mechanics, 39, pp.309-323, 2004.

[17] H. K. Leung, "Synchronization dynamics of coupled Van der Pol systems," Physics *A*, 321, pp. 248-255, 2003.

[18] J. J. Collins and S. A. Richmond, "Hard wired central pattern generators for quadrupedal locomotion" Biology and Cybernetics, 71, pp.371-385, 1994.

[19] A. D. McClellan "Organization of spinal locomotor networks: Contributions from Model System," Comments Theoretical Biology, 4, pp 63-91, 1996.

[20] Y. Chembo Kouomou and P. Woafo " Generalized correlated states in a ring of coupled non-linear oscillators with a local injection, Physics Rev. E, 66, pp-66201. 2002.

[21] P. Woafo, H. G. Enjieu Kadji " Synchronized states in a ring of mutually coupled self sustained electrical oscillators," Physics Rev. E, 69, pp. 66206, 2004.

[22] H. G. Enjieu Kadji, J. B. Chabi Orou., and P. Woafo, " Synchronization dynamics in a ring of four mutually coupled biological systems", Communications in Non-linear Science and Numerical Simulation, 13 (7), pp.1361-1372, 2008.

[23] Z. P. Li, and X. Li, 1990, Generalized Noether Theorem and Poincare Invariant for Nonconservative Nonholonomic Systems, International J. Theoretical Physics, 29, pp.765-771.

[24] F. Benavent and J. Gomis, 1979, Poincare-Cartan Integral Invariant for Constrained Systems, Annals of physics, 118(2), pp.476-489.

[25] D. Liu, Y. Luo, S. Y. Xin, 1991, About the Basic Integral Variants of Holonomic Nonconservative Dynamical systems, Acta Mechanica Sinica, 7, pp.178-185.

[26] Y.X. Guo, M. Shang, F.X. Mei, 1999, Poincare-Cartan Integral invariants of Nonconservative Dynamical Systems, International J. Theoretical Physics, 38(3), pp.1017-1027.

[27] Y.X. Guo, L. Jiang , and Y. Yu , 2001, Poincare and Poincare-Cartan integral Invariants of a generalized Hamiltonian System, Communications in Nonlinear Science and numerical Simulation, 6(1), pp. 45-49.

[28] Y.X. Guo, M. Shang , S.K. Luo, F.X. Mei., 1999, Poincare-Cartan Integral Variants and Invariants of Nonholonomic Constrained Systems, International J. Theoretical Physics, 40(6), pp.1197-1205.

[29] V. Rastogi, "Extension of Lagrangian-Hamiltonian mechanics, study of symmetries and invariants", Ph.D. thesis, Indian Institute of Technology, Kharagpur, 2005.

[30] A. Mukherjee, "Junction Structures of Bondgraph Theory from Analytical Mechanics Viewpoint", Proc. *of CISS-1st Conference of International Simulation Societies*. Zurich, Switzerland, pp. 661-666, 1994.

[31] Amalendu Mukherjee, Vikas Rastogi, Anirvan Dasgupta, "*Revisiting umbra-*

Lagrangian-Hamiltonian mechanics: Its Variational foundation and extension of Noether's theorem and Poincaré-Cartan Integral, International Journal of Non-Linear Mechanics, *745-757, Vol.46 (5), 2011.*

[32] A. Mukherjee, "The Issue of Invariants of Motion for General Class of Symmetric Systems through Bond Graph and Umbra-Lagrangian," Proc. of Int. Conf. of Bond Graph Modelling and Simulation ICBGM'01, Phoenix, Arizona, USA, 295,2001.

[33] A. Mukherjee, V. Rastogi, and A. Das Gupta, "A Methodology for finding Invariants of Motion for Asymmetric Systems with Gauge-transformed Umbra Lagrangian Generated by Bond Graphs," Simulation, Vol. 82(4), pp. 207-226, 2006.

[34] A. Mukherjee, V. Rastogi, and A. Das Gupta, "A Study of a Bi-Symmetric Electro-mechanical System through Umbra Lagrangian Generated by Bond Graphs, and Noether's Theorem," Simulation, Vol. 83(9), pp. 611-630, 2007.

[35] F. Gantmachar, Lectures *in Analytical Mechanics*, Mir Publication, Moscow, 1970.

[36] F. Kaiser, "Coherent oscillations in biological systems, I, bifurcations phenomena and phase transitions in an Enzyme-subtrate reaction with ferroelectric behaviour," Z Naturforsh A, 294, pp.304-333, 1978.

[37] H. Frohlich , " Long range coherence in biological and energy storage in a biological systems," International Jr. of Quantum Chemistry, 641, pp. 649-652, 1968.

[38] B. Schecheter , " Now the brain gets rhythm," Science, 274, pp. 339-340, 1996.

[39] L. Glass, " Synchronization and rhythmic process in physiology," Nature, 410, pp. 277-284, 2001.

[40] T.E. Vadivasova, G.I. Strelkova, V.S. Anishchenko, " Phase frequency synchronization in a chain of periodic oscillators in the presence of noise and harmonic forces," Physics Review E, 63, pp. 36225, 2001.

[41] L.A. Low, P.G. Rein hall, D.W. Storti, " An investigations of coupled Vander Pol oscillators" ASME Transactions of Journal of Vibration and Acoustics, 125, pp.162-169, 2003.

[42] A. Mukherjee, and A.K. Samantaray, *SYMBOLS-shakti User's Manual,* High-Tech Consultants, STEP Indian Institute of Technology, Kharagpur, India, 2006.

[43] S.H. Strogatz and I. Stewart, " Coupled Oscillators and Biological Synchronization, Scientific American Journal, pp. 102-109, Dec. 1993.

Imperial Journal of Interdisciplinary Research (IJIR)
Vol-2, Issue-8, 2016
ISSN: 2454-1362, http://www.onlinejournal.in

Numerical Study on Response of Laterally Loaded Piles in Soils

Amit Jain[1] & A.K. Sahu[2]
[1]Civil Engineering Department, Delhi Technological University
[2]Professor, Department of Civil Engineering, Delhi Technological University, Delhi

Abstract: *Parametric studies are done to examine the influence of soil layering, pile slenderness ratio and cross-sectional shape on the response of piles of laterally loaded in homogeneous and heterogeneous soil in which the soil shear modulus varies discretely with depth. Numerical method such as finite element method is used for presenting the analysis of laterally loaded piles with circular and rectangular cross section. The analysis is developed by solving the displacement of the pile-soil system derived. The Abaqus software is used for estimating the pile-head deflection and development of stresses which is mainly used in design purposes. The result shows that the soil layering with different soil shear modulus influences the lateral response of pile. The lateral response in the homogeneous soil system is affected by the cross-sectional shape of the pile. The lateral responses of piles in soil layered systems were mostly affected by the stiffness and thickness of the top soil layer. The pile head deflection varies in the cases in which the pile slenderness ratio was less than twenty-five in different layered soil system. Using this analysis, deflection in pile, stress profiles and curve of the lateral displacement and the stress variation in the pile can be obtained quickly along the entire pile length. Also, the stresses developed in the surrounding soil of the pile were analyzed. Various numerical examples based on this analysis are provided.*

Keywords*: Circular pile; Rectangular pile; Lateral Load; Continuum-based mechanism; Heterogeneous soil; Numerical Solution; Abaqus Software.*

1. Introduction

Some ground surfaces have weak or poor soil conditions as soil may be composed of clay, loose saturated sand on the construction site. So it may be necessary to transmit the building loads to deeper more stable soil and for that purpose we mainly use piles. Piles are widely used to transfer vertical and lateral loads to the ground. In many structures like in tall buildings, bridges, dams, offshore platforms the major problem arises due to the lateral load as wind gust, seismic activity, wave action, etc. For solving this problem, laterally loaded piles in homogeneous or heterogeneous soils in which the properties of soils vary with depth are analyzed either by using the p-y method, which is mainly based on the beam-on-foundation concept or by using continuum-based numerical methods, such as finite element method, finite-difference method and the boundary element method. Reese and Matlock (1956) worked on the laterally loaded piles in heterogeneous soil and presented the non-dimensional curve which can be used to obtain deflections, moments, shear at any point along the length of the pile. Broms (1964) worked on lateral resistance of vertical piles and concluded that it can be used for short and long piles and for both cohesion and cohesion less soil but not applicable to layered soil and c-□ soils. Reese and Welch (1974) worked on dry and stiff clay and obtained p-y curves and bending moment curves. The p-y curves determine the relation between the lateral pile displacement y and the resistance p offered by the soil. The results are obtained easily and quickly because of the one-dimensional differential equation of pile that is solved with the nonlinear p-y curves taken as input. But the major drawback of this method is that they can't provide accurate predictions and actual mechanism about their results because the 3D pile-soil interactions are different for different pile-soil conditions (Li Yan and P.M. Byrne 1992).

While, in continuum-based numerical mechanism, finite element method can provide accurate solutions for the 3D pile soil interaction. The solutions obtained from this approach are quick as variables required for the geometry and numerical mesh is less. In this paper, analytical approach is used for analyzing the pile-soil interaction to determine the pile head deflection and stress variation in the pile and the soil. Here, main contributions for the analysis are the cross-sectional shape of the pile, study of responses of pile in heterogeneous soil with variation of soil modulus with depth. Numerical examples are provided for analyzing the problem of pile-soil model with the help of ABAQUS 6.10 software.

2. Numerical Analysis

2.1 Pile-Soil Interaction

The behaviour of the pile supported structure mainly depends on the type of pile-soil interaction. The contact between the pile and the soil surface can be both normal and tangential. A relatively small sliding is present in between pile and soil in the tangential direction and no slippage is observed in the normal direction along the pile-soil surface. For analyzing the response of the pile in the homogeneous and heterogeneous soil, finite element method is used in which the soil is treated as continuum.

2.2 Finite Element Method

Finite Element method is a versatile method. It's greatest advantage is that the analyst has complete freedom to analyze the structure to any degree of refinement by increasing the no of elements, number of nodes in an element etc. and test all possible configurations to arrive at the final solution. It can be ideally used in the cases involving the complicated geometrics, loadings and boundary conditions. The main concept in the FEM involves division of given structure into smaller elements for analysis called finite elements and these elements are interconnected at a discrete number of joints/nodes. For analysis purpose, we combine each and every finite element equations to obtain the solution of the whole structure in the form of simultaneous equations. The main advantage of FEM is the ability to accommodate different boundary and loading conditions, can model composite structure involving regions with different properties. Here, for analyzing the problem of pile-soil model, we are using ABAQUS 6.10 software. It is a simulation program that can solve the problem ranging from relatively simple linear analysis to the most challenging non-linear simulations.

2.3 Parametric Study

A parametric study is done to examine the effects of the stiffness of the layered soil, cross-sectional shape of the pile and the slenderness ratio on the pile response. For getting the response, the soil layer is to be consider as discrete with depth.
To perform the parametric study, normalized pile-head deflection caused by the lateral force F_a defined as "U" for layered soil profiles with different value of soil shear modulus "G" is considered (G_i for the i_{th} soil layered medium). The dimension of the sides of the rectangular pile is taken as "W" that produces the same area as that of a circular pile ($W=2\ r_p$). The length of the pile is taken as L_p.

3. Finite Element Modelling

The references for the properties of the soil and the pile, which are used in the numerical problems, are taken from engineersedge.com, geotechdata.info, supercivilcd.com.

3.1 Analysis of different shape of piles

A finite element model of the pile-soil interaction was developed using the finite element software Abaqus/CAE.
In this, an elastic model was adopted for modelling the pile with the modulus of elasticity 30GPa and Poisson ratio 0.15. Rectangular and circular pile is considered in this analysis. The cross sectional dimension of the rectangular pile is 0.36m x 0.36m. The circular pile has a cross sectional diameter of 0.4m (both the piles have the same cross-sectional area approximately). The length of both the piles is taken same as 15m.
A single layer soil profile is considered with length 14.85m, breadth 10m, modulus 60 MPa and Poisson ratio 0.4. The section taken for both the pile and soil is solid and homogeneous. The tangential movement between the two parts, surrounding soil and pile, is provided with a friction value of 0.36. The outer surface of the pile is chosen as the master surface (because of more stiffness) and the inner surface of the soil medium which has been in contact with the pile is considered to be the slave surface. A relatively small sliding is taken in between the contact of two surfaces.
A relatively fine mesh is used for the pile than that of soil. In this model, the pile and the soil are modelled using eight-nodded solid continuum elements (C3D8R) to explain the continuum nature of the soil. In the FE model, the bottom of the pile is fixed to imitate the embedment of the pile and the outer surface of the soil medium is fixed to simulate the confinement of the soil. The boundary conditions and the load are step dependent. The lateral load (30kN) is applied in (-) x direction at the cited point that defines the rigid body motion at the top of the pile to examine the effect of the lateral load on the induced stress developed along the length of the pile and the soil and lateral displacement of the pile. Figure shows the lateral displacement and stress developed along the length of the pile.

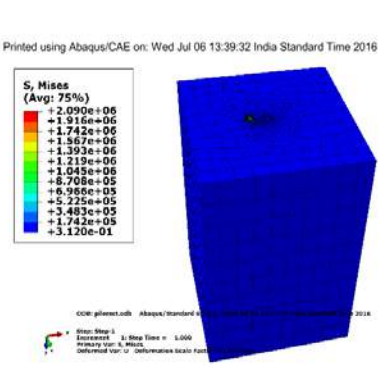

Fig.1. Rectangular pile soil model

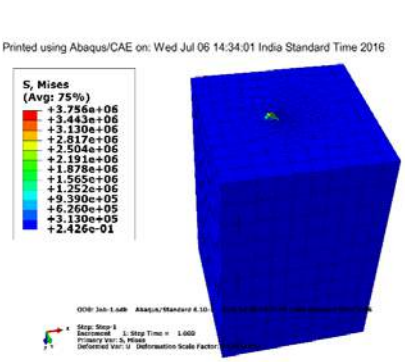

Fig.2. Circular pile-soil model

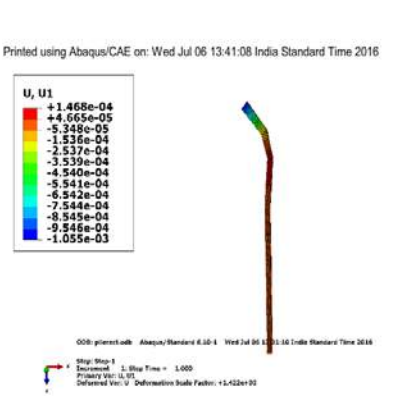

Fig.3. Deflection in Rectangular pile

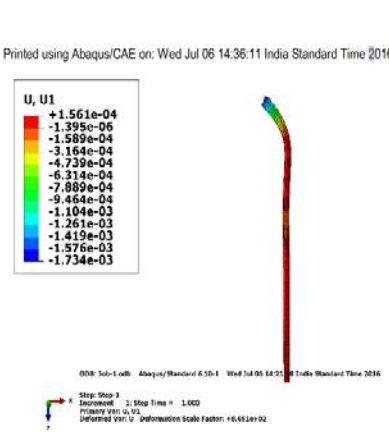

Fig.4. Deflection in Circular pile

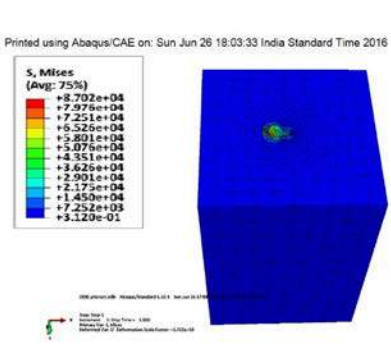

Fig.5 Stress developed in Rectangular soil

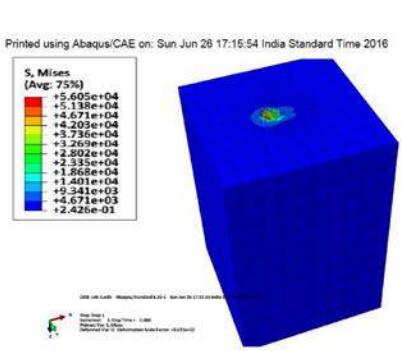

Fig.6 Stress developed in Circular soil

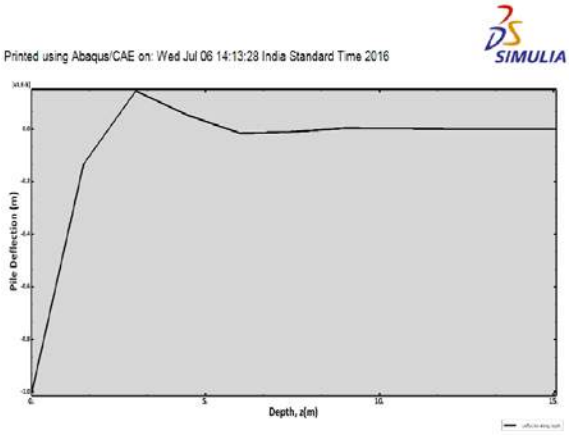

Fig.7. Deflection along depth in rectangular pile

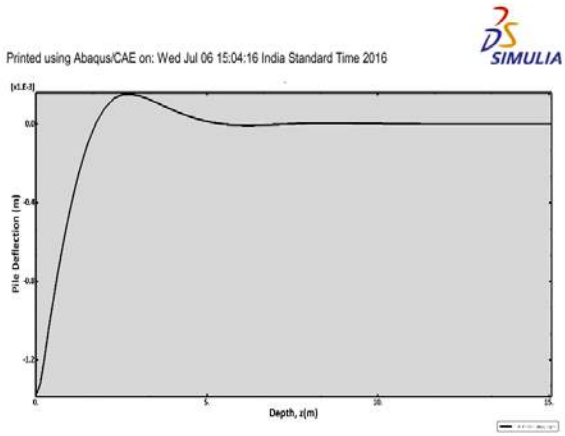

Fig.8. Deflection along depth in circular pile

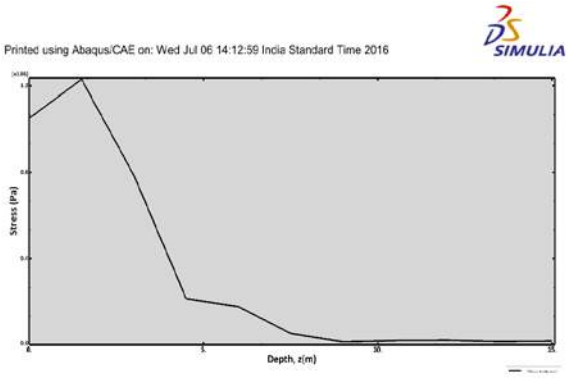

Fig.9. Stress along depth in rectangular pile

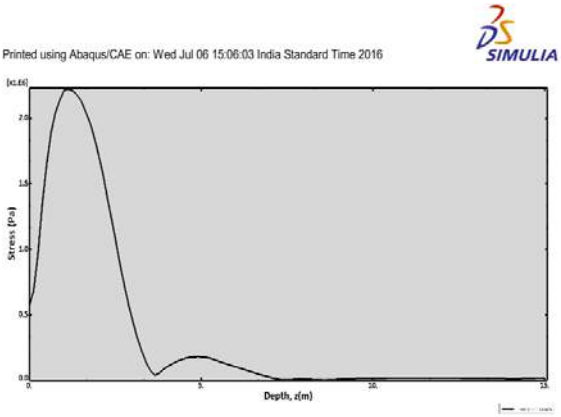

Fig.10. Stress along depth in circular pile

The observation about the maximum pile deflection and the maximum stress developed are recorded for both, Rectangular and Circular pile.

Table 1. Response of Different Shape of the pile

Pile Shape	Maximum pile deflection (in mm)	Maximum stress produced (in MPa)
Rectangular	1.055	2.090
Circular	1.734	3.756

In analysis, it is found that the different cross-sectional shapes of the pile, as here rectangular and circular pile, with same area have different responses when we applied lateral load (assume all other factors are same).

3.2 Analysis in two-layered soil

Here, the response of the circular pile in a two-layered soil profile is observed. In this, two cases have been taken in which the breadth and the Poisson ratio is taken same as 10m and 0.40, respectively. The different properties taken for the top and the bottom layer of the soil are mentioned in Table 2.

Table 2. Properties in two-layered soil system

Case	Length of the soil (in m)		Soil modulus (in MPa)	
	Top (H_1)	Bottom (H_2)	Top (G_1)	Bottom (G_2)
1	4.5	10	30	70
2	10	4.5	30	70

The cross sectional diameter of the circular pile is 0.40m. Length of the pile is 15m. The young modulus of the pile is 30 GPa and Poisson ratio 0.15. The section taken for both the pile and soil is solid and homogeneous. The tangential movement between the two parts, surrounding soil and pile, is provided with the friction value of 0.36. In the direction which is normal to the surface, a hard contact behaviour (no separation) is taken. The outer surface of the pile is chosen as the master surface and the inner surface of the soil mass which is contact with the pile is considered to be the slave surface. Tangential movement between the two layers of the soil is provided with the friction value of 0.001 and in radial (normal) direction, a hard surface contact behavior is taken. A relatively fine mesh is used for the pile than that of soil. In this model, the pile and the soil were modelled using eight-nodded solid continuum elements (C3D8R) to explain the continuum nature of the soil. In the FE model, the bottom of the pile was fixed to imitate the embedment of the pile and the outer surface of the soil medium was fixed to simulate the confinement of the soil. The lateral load (40kN) was applied in (-) x direction at the cited point defining the rigid body motion at the top of the pile to examine the effect of the lateral load on the induced stress developed along the length of the pile and the soil and lateral displacement of the pile. Figure shows the lateral displacement and stress developed along the length of the pile.

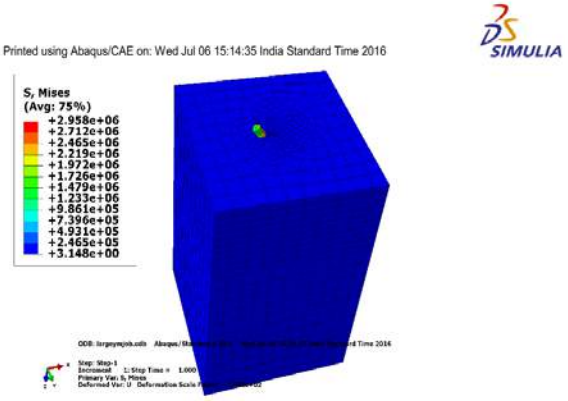

Fig.11. Stress in pile-soil model in CASE 1

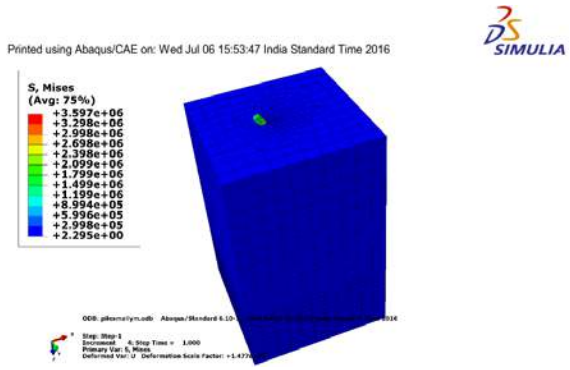

Fig.12. Stress in pile-soil model in CASE 2

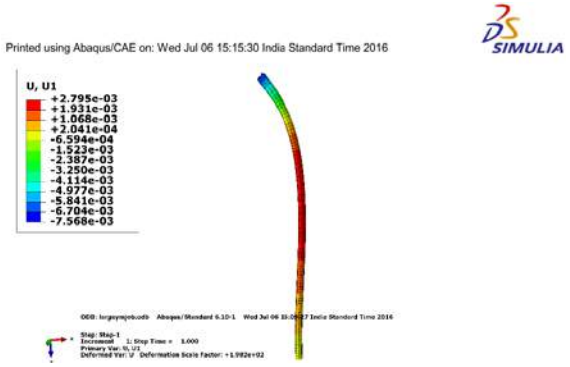

Fig.13. Displacement in pile in CASE 1

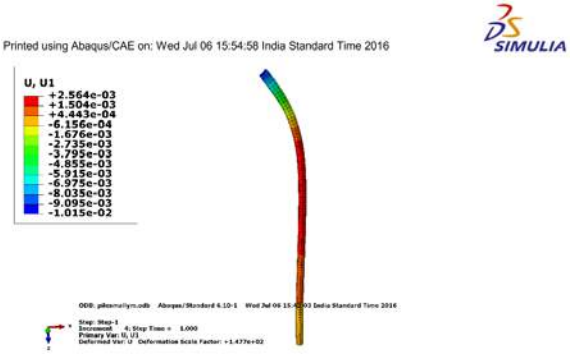

Fig.14. Displacement in pile in CASE 2

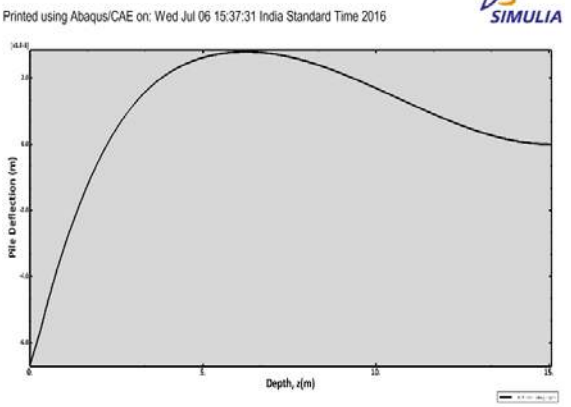

Fig.15. Curve between Pile Deflection (m) vs Depth (m) in CASE 1

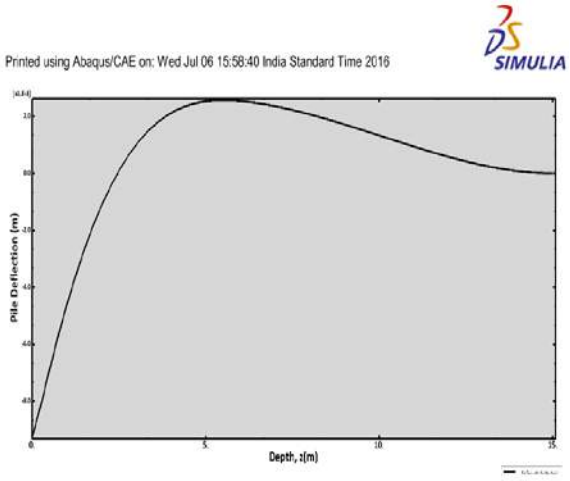

Fig.16. Curve between Pile Deflection (m) vs Depth (m) in CASE 2

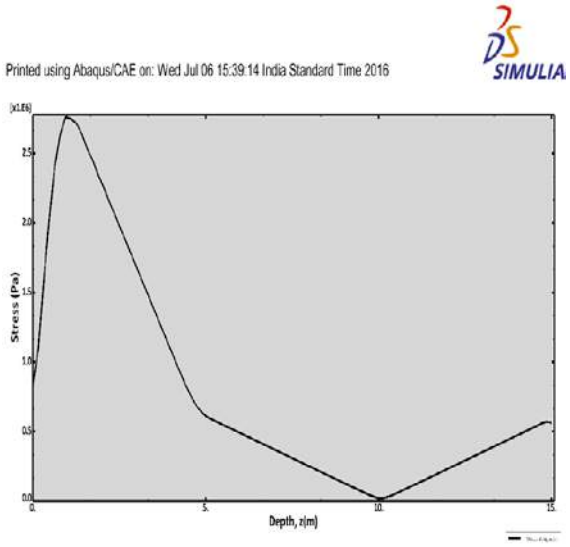

Fig.17. Curve between Stress (Pa) vs Depth (m) in CASE 1

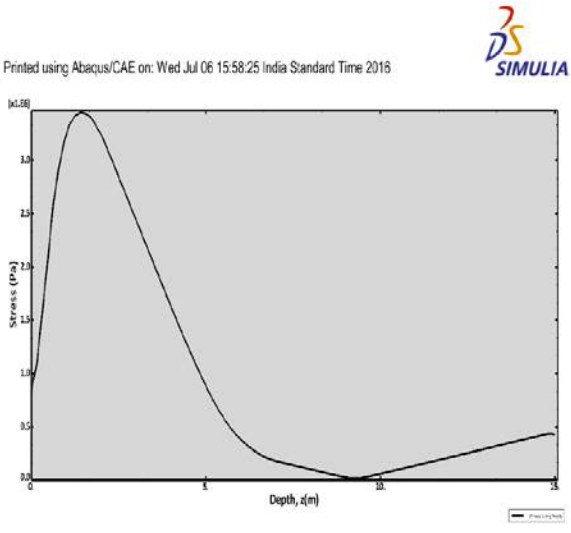

Fig.18. Curve between Stress (Pa) vs Depth (m) in CASE 2

The observation for both the cases is mentioned in the Table 3.

Table 3. Observation of the output result

Case	Maximum pile deflection (in mm)	Maximum stress developed in pile (in MPa)
1	7.568	2.958
2	10.15	3.597

After analyzing, the magnitude of the pile deflection and stress developed in Case 1 is less than that of Case 2.
The result shows that in the layered soil system, here two-layered soil system, the lateral behaviour of the pile is mainly affected by the stiffness (soil modulus) and thickness of the top soil layer. The normalized head deflection and the stress developed in the pile is dependent on the soil modulus of the top soil layer in the layered soil system.

3.3 Analysis in three-layered soil

For analyzing the lateral-load response of the pile in three-layered sol profiles, three different soil layering cases (Case 1-3) are considered. Each layer of the soil profiles have different young modulus such that the average shear modulus is the same for all the cases.
For Case 1, soil modulus increases with depth, whereas for Case 3, it decreases with depth. In Case 2, the intermediate layer has the least value of soil modulus. The thickness for all the three layers of the soil is taken equal. Some properties of the three-layered soil profile in all the cases are given in the Table 4.

Table 4. Properties in three-layered soil system

Case	Length of the soil (in m)			Soil modulus (in MPa)		
	Top (H_1)	Mid (H_2)	Bottom (H_3)	Top (G_1)	Mid ($G_{2)}$	Bottom (G_3)
1	4.95	4.95	4.95	10	15	30
2	4.95	4.95	4.95	30	15	10
3	4.95	4.95	4.95	15	10	30

The breadth and the Poisson ratio of the soil is taken as 10m and 0.25 for all the three layers of the soil.
The cross-sectional diameter and the length of the circular pile is 0.6m and 15m, respectively. The properties used for the pile is that of concrete with Young modulus of 30 GPa and Poisson ratio 0.15.
The section is taken for the pile and soil is solid and homogeneous. The analysis that is performed on the pile-soil model consists of an initial step and one general analysis step which is Static, General.
The tangential friction coefficient between the surrounding soil and the circular pile is provided as 0.55 and hard contact behaviour is taken normally.
The interaction properties in different layers of soil is also provided with a friction value of 0.001 in tangential direction and hard contact in normal direction. The elements used for the meshing is of hexahedron shape and eight noded solid continuum (C3D8R) to explain the continuum nature of the soil. The circular pile and the soil medium is meshed by providing 10 elements to the selected edges. The lateral load of 30kN is applied in (-) x direction to the pile. The bottom of the pile and the outer surface of the soil are fixed with Encastre conditions. After giving the properties and conditions, the model is run in Abaqus. Following figures are obtained after analysis.

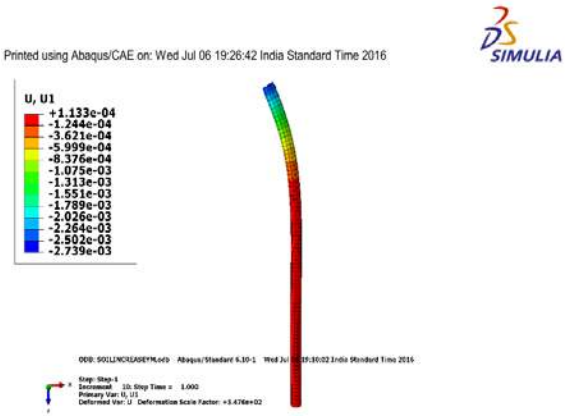

Fig.19. Deflection in pile in CASE 1

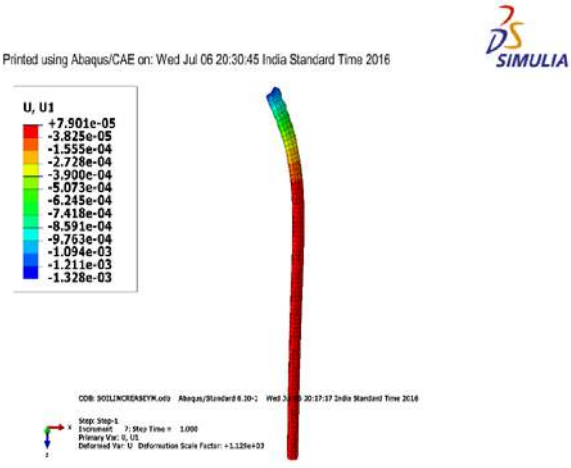

Fig.20. Deflection in pile in Case 2

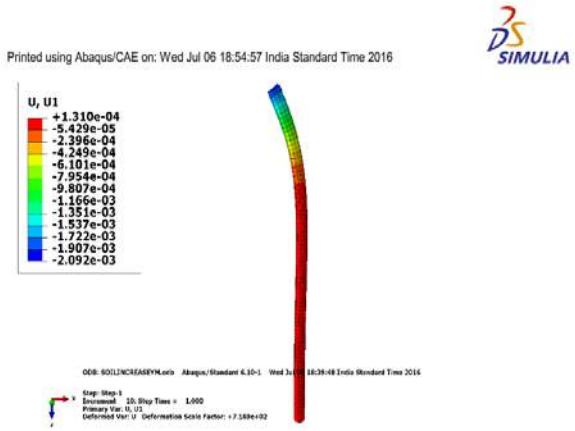

Fig.21. Deflection in pile in CASE 3

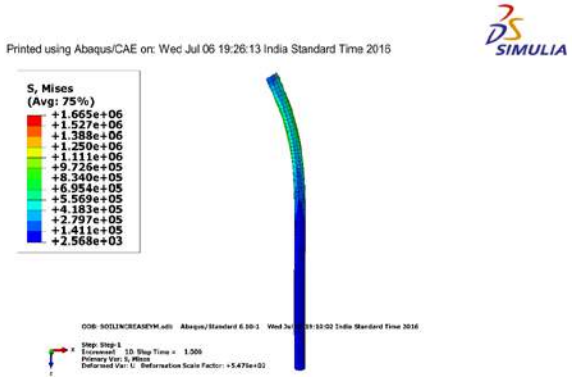

Fig.22. Stress developed in pile

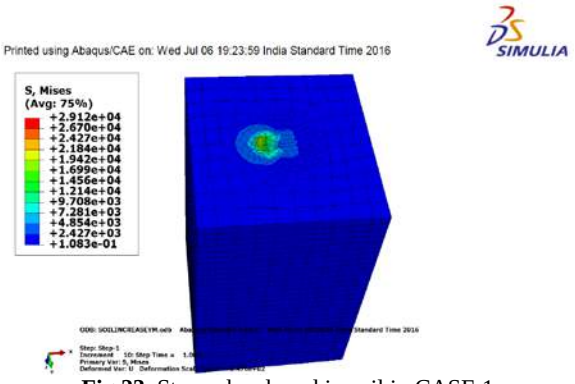

Fig.23. Stress developed in soil in CASE 1

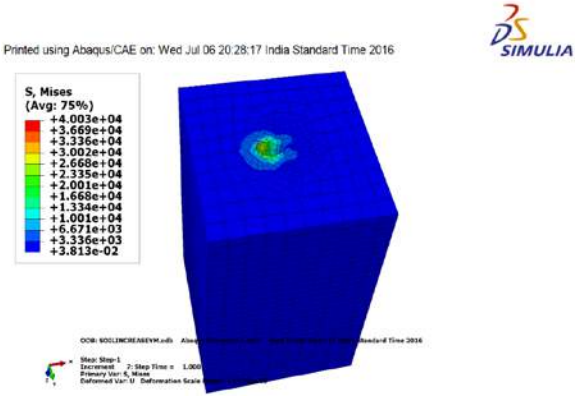

Fig.24. Stress developed in soil in CASE 2

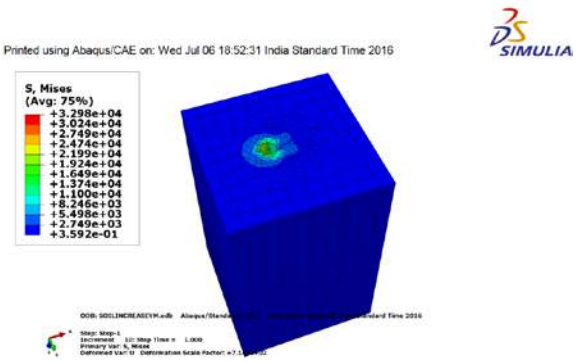

Fig.25. Stress developed in soil in CASE 3

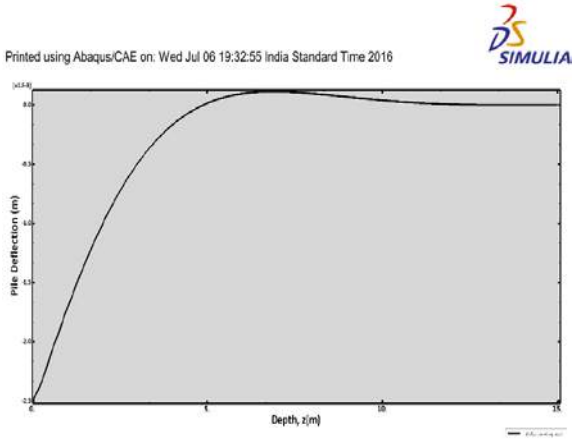

Fig.26. Deflection along depth in CASE 1

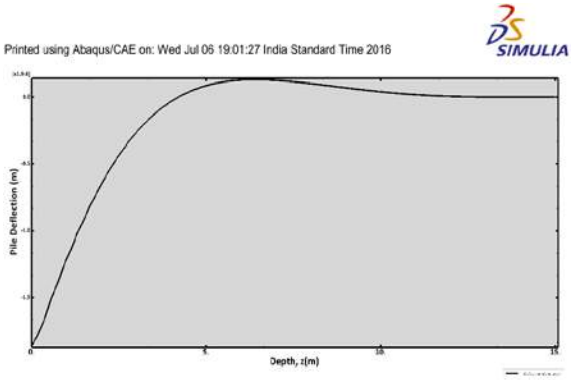

Fig.27. Deflection along depth in CASE 2

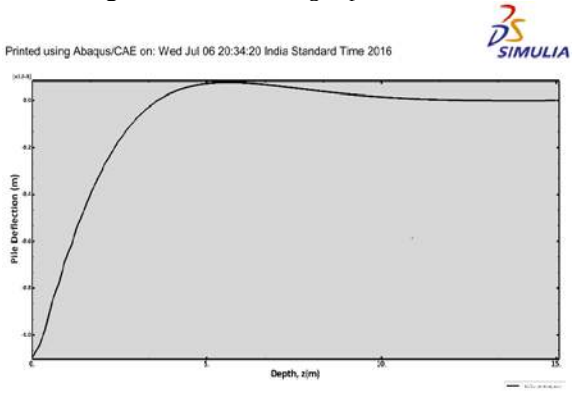

Fig.28. Deflection along depth in CASE 3

The observations are taken into account in Table 5.

Table 5. Observation of the output result

Case	Maximum Pile Deflection (in mm)	Maximum Stress developed in pile (in MPa)
1	2.739	1.665
2	1.328	1.665
3	2.092	1.665

After observing the result, it is found that the normalized head deflection is minimum in Case 2. The maximum stress developed in all the three cases is same as 1.665 MPa.
In the above problem, in which the average soil shear modulus were same in all the cases, the head deflection was found to be minimum in which the soil modulus decreases with depth.

3.4 Analysis with varying Pile slenderness ratio

The response of long and short piles is different under lateral loads. Therefore, it is necessary to examine the effect of the slenderness ratio on the response of the laterally loaded piles. For analyzing different layered soil profiles with varying pile slenderness ratio, different cases are taken.

A four layered soil profile of 16m (H_1=4m, H_2= 4m, H_3=4m, H_4=4m) is considered with the shear modulus of the soil (G_1=10 MPa, G_2=15 MPa, G_3=25 MPa, G_4=40 MPa) is increasing with depth and the Poisson ratio of the soil is 0.25 for all the layers. The cross-sectional diameter of the circular pile is 0.6m and the applied lateral force in (-) x direction at the top of the pile is 30kN. The same above properties is used for the circular pile. The cross-sectional diameter of the circular pile is 0.6m. Length of the pile is different for different cases as mentioned in Table 6.

Table 6. Different pile slenderness ratio

Case	Length of the pile (L_p) (in m)
1	8.15
2	10.15
3	12.15
4	15.15

The section taken for the pile and the soil is solid and homogeneous. The elements used for the meshing is of hexahedron shape and eight noded solid continuum (C3D8R) to account for the continuum nature of the soil. The circular pile is meshed by providing 8 elements and different layers of the soil medium is meshed with 11, 10, 9, 8 elements to the selected edges, respectively. The model is run in Abaqus for analysis after completion. Figure shows the lateral displacement and stress developed along the length of the pile.

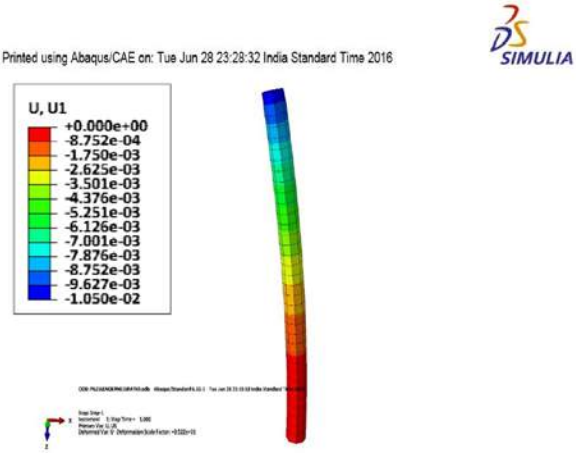

Fig.29. Deflection in pile in CASE 1

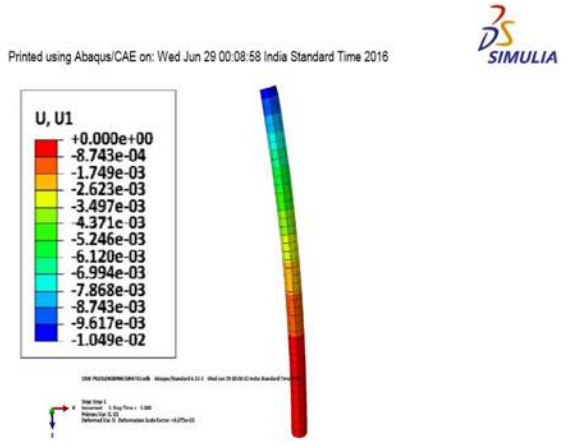

Fig.30. Deflection in pile in CASE 2

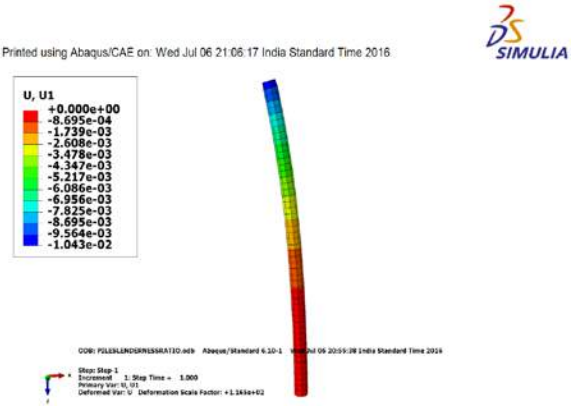

Fig. 31. Deflection in pile in CASE 3

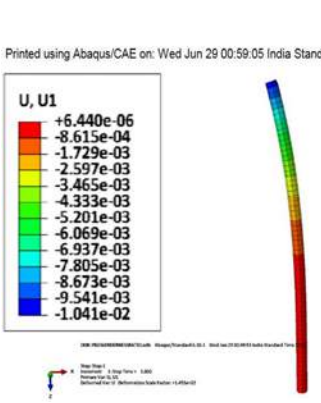

Fig.32. Deflection in pile in CASE 4

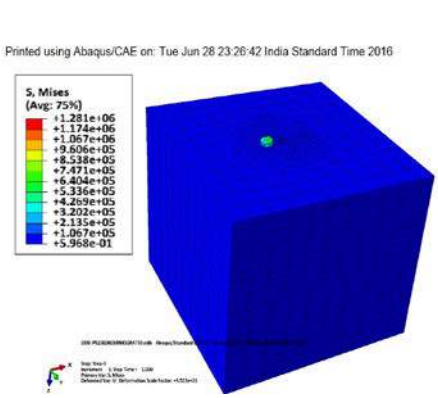

Fig.33 Stress Developed in pile in CASE 1

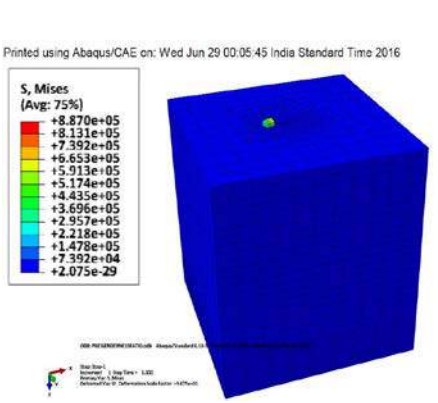

Fig.34 Stress Developed in pile in CASE 2

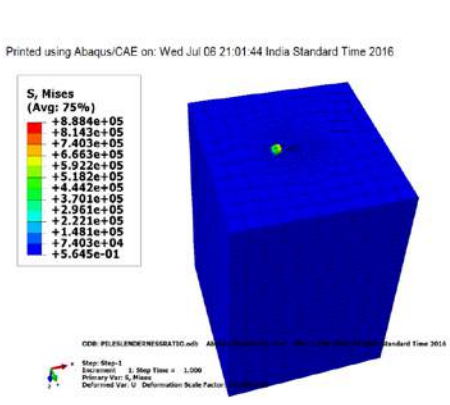

Fig.35 Stress Developed in pile in CASE 3

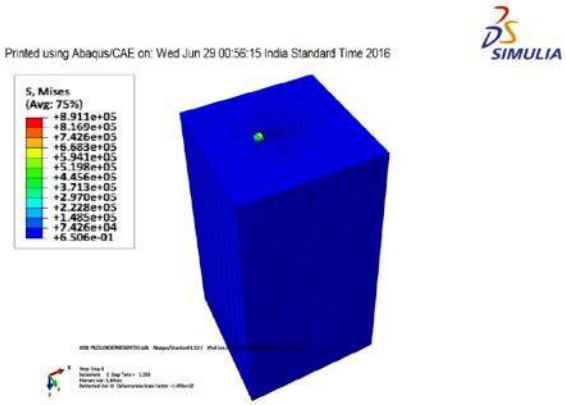

Fig.36 Stress Developed in pile in CASE 4

The observations of the result are taken into account in Table 7.

Table 7. Observation of the output result

Case	Maximum Pile Deflection (in mm)	Maximum Stress Developed in pile (in MPa)
1	10.50	1.281
2	10.49	0.8870
3	10.43	0.8840
4	10.41	0.8911

While analyzing the laterally loaded pile, it was observed that when the pile slenderness ratio was increased but less than twenty-five in layered soil system, the pile head deflection in the pile decreased.

4. Conclusions

In this report, an analysis is done to formulate the response of the load applied laterally on the circular and rectangular piles in the homogeneous and heterogeneous soil deposits. In heterogeneous soil deposits, soil shear modulus increases linearly with depth or discrete values of shear modulus is taken for distinctly different layers.

Through this analysis, deflection in pile, shear stress profiles, slope of the deflected and shear curve can be quickly obtained along the entire pile length. From this analysis, the stresses developed in the surrounding soil of the pile were also obtained. The input values required for the analysis are that of pile geometry, thickness of the soil layers and the elastic constant of the pile and soil.

Parametric studies were done to evaluate the effect of pile cross-sectional shape, pile slenderness ratio and soil heterogeneity and layering on the lateral loaded piles, namely lateral deflection and development of the stresses. The lateral response is affected by the

cross sectional shape of the pile. For piles in layered soil system, the thickness and stiffness of the top soil layer mainly affects the lateral behavior of the pile. Various graphical representations were obtained after the analysis of the respective problem.

5. Acknowledgements

The authors of this paper are grateful to Prof. Vijay Gautam, Department of Mechanical Engineering and Ankur Mudgal, Department of Civil Engineering for their immense support.

6. References

[1] ABAQUS 6.10 [Computer software]. Providence, RI, Dassault Systems.

[2] Appendix A: Broms method for analysis of single piles under lateral loading.

[3] Banerjee,P.K. and Davies , T.G. (1978) .Geotechnique 28, No.3 , 309-326 "The behavior of axially and laterally loaded single piles embedded in nonhomogeneous soils".

[4] Barry J. Meyer and Lymon C. Reese (1979), "Analysis of single piles under lateral loading", Research Report 244-1, Department of Highway and Public Transport.

[5] Broms, B. B. (1964). "Lateral resistance of piles in cohesionless soils." J. Soil Mech. And Found. Div., 90(3), 123-156.

[6] Getting Started with Abaqus ,Help Manual , Abaqus Software.

[7] Indian standard code , Design and construction of pile foundation , ICS 91.100.30 : 93.020 , IS 2911:2010 , ANNEX C (Clause 6.5.2) ,"Analysis of laterally loaded piles".

[8] P.N. Godbole(1923) , "Introduction to Finite Element Method"

[9] Poulos, H.G.(1971). "Behaviour of laterally loaded piles: I-Single piles." J.Soil Mech. and Foundation Div. 97(5), 711-731

[10] Reese L.C. and Welch,R.C.(1975) "Laterally loading on deep foundation in stiff clay" .J.Geotech. Engrg. Div. 101(7),633-649

[11] Verruijt,A. and Kooijman,A.P.(1989). Geotechnique 39, No. 1, 39-46 "Laterally loaded piles in a layered elastic medium".

[12]W.Jerin Wiba, V.Jeyanthi Vineetha (1990) "Behaviour of laterally loaded piles in cohesionless soils ",eISSN :2319-1163.

IJIREEICE

ISSN (Online) 2321 – 2004
ISSN (Print) 2321 – 5526

INTERNATIONAL JOURNAL OF INNOVATIVE RESEARCH IN ELECTRICAL, ELECTRONICS, INSTRUMENTATION AND CONTROL ENGINEERING
Vol. 4, Issue 7, July 2016

Object Recognition using SIFT Keypoints

Sahil Dalal[1], Preeti Meena[1]

Department of ECE, Delhi Technological University, Delhi, India[1]

Abstract: This research paper presents a novel method for the identification of some object in a video using the distinctive invariant features from images. This method uses reliable matching between different views of an object or scene. The features shows a robust matching across a particular range of affine distortion, change in 3D viewpoint, addition of noise, invariant to image scale and rotation and change in illumination. In this, the recognition for the object proceeds by matching individual features to a database of features from known objects using a technique called as scale invariant feature transform. This approach to recognition can robustly identify objects among clutter and occlusion while achieving near real-time performance.

Keywords: Difference of Gaussian, Keypoint descriptor, Object, SIFT.

I. INTRODUCTION

Object recognition is an important aspect of many problems in computer vision for 3D structure from multiple images, stereo correspondence, and motion tracking. This research paper describes image features that have many properties which make them suitable for detecting different images of an object or scene. The features are invariant to image scaling and rotation, and partially invariant to change in illumination and 3D camera viewpoint.

Large numbers of features can be extracted from typical images with efficient algorithms. In addition, the features are highly distinctive, which allows a single feature to be correctly matched with high probability against a large database of features, providing a basis for object and scene recognition.

The development of image matching by using a set of local interest points can be traced back to the work of [1] on stereo matching using a corner detector. The Moravec detector was improved by [2] to make it more repeatable under small image variations and near edges. Harris also showed its value for efficient motion tracking and 3D structure from motion recovery [3], and the Harris corner detector has since been widely used for many other image matching tasks. While these feature detectors are usually called corner detectors. [4] showed that it was possible to match Harris corners over a large image range by using a correlation window around each corner to select likely matches. The ground-breaking work of [5] showed that invariant local feature matching could be extended to general image recognition problems in which a feature was matched against a large database of images. Earlier work by the author [6] extended the local feature approach to achieve scale invariance. Then, there has been an impressive body of work on extending local features to be invariant to full affine transformations [7]. Now, in recent years, wide range of techniques are utilized for object recognition. These are color descriptors [8], genetic [9], unsupervised scale invariant learning [10], appearance information [11]. Some of the other techniques were also used in [12-17].

For image matching and recognition, SIFT features are first extracted from a set of reference images and stored in a database. A new image is matched by individually comparing each feature from the new image to this previous database and finding candidate matching features based on Euclidean distance of their feature vectors. This paper will discuss fast nearest neighbour algorithms that can perform this computation rapidly against large databases.

This research paper is organised in the following sections as: Section II tells about the overview of the complete work using a block diagram. Section III tells about the different types of ECG signals used and the proposed method. Then in section IV, results are discussed followed by conclusion in section V.

II. BLOCK DIAGRAM

Following are the major stages of computation used to generate the set of image features:

Scale-space extrema detection: The first stage of computation searches over all scales and image locations. It is implemented efficiently by using a difference-of-Gaussian function to identify potential interest points that are invariant to scale and orientation.

Keypoint localization: At each candidate location, a detailed model is fit to determine location and scale. Keypoints are selected based on measures of their stability.

Orientation assignment: One or more orientations are assigned to each keypoint location based on local image gradient directions. All future operations are performed on image data that has been transformed relative to the assigned orientation, scale, and location for each feature, thereby providing invariance to these transformations.

Keypoint descriptor: The local image gradients are measured at the selected scale in the region around each keypoint.

Copyright to IJIREEICE

IJIREEICE

ISSN (Online) 2321 – 2004
ISSN (Print) 2321 – 5526

INTERNATIONAL JOURNAL OF INNOVATIVE RESEARCH IN ELECTRICAL, ELECTRONICS, INSTRUMENTATION AND CONTROL ENGINEERING
Vol. 4, Issue 7, July 2016

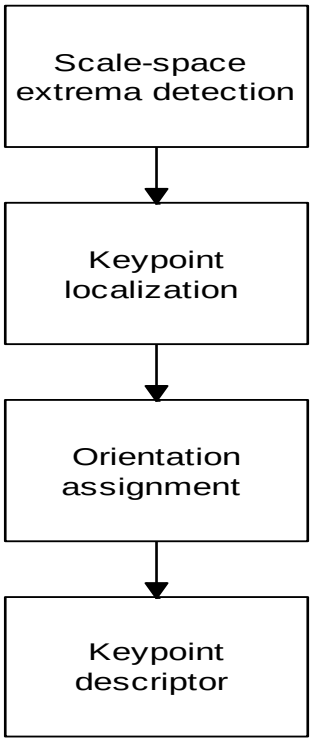

Fig.1. Block Diagram of the proposed work

These are transformed into a representation that allows for significant levels of local shape distortion and change in illumination.

These steps are also shown in the form of a block diagram in the Fig.1.

This approach has been named the Scale Invariant Feature Transform (SIFT), as it transforms image data into scale-invariant coordinates relative to local features.

III.PROPOSED METHOD

A. Scale-space extrema detection
The scale space of an image is defined as a function, S(w, z, σ), that is produced from the convolution of a variable-scale Gaussian, g(w, z, σ), with an input image, i(w, z):

$$S(w, z, \sigma) = g(w, z, \sigma) * i(w, z) \qquad (1)$$

where $*$ is the convolution operation in g and i, and

$$g(w, z, \sigma) = \frac{1}{2\pi\sigma^2} e^{-\frac{w^2+z^2}{2\sigma^2}} \qquad (2)$$

To efficiently detect stable keypoint locations in scale space, we have proposed (Lowe, 1999) using scale-space extrema in the difference-of-Gaussian function convolved with the image, DoG(x, y, σ), which can be computed from the difference of two nearby scales separated by a constant multiplicative factor n:

$$DoG(w, z, \sigma) = (g(w, z, n\sigma) - g(w, z, \sigma)) * i(w, z)$$
$$= S(w, z, n\sigma) - S(w, z, \sigma) \qquad (3)$$

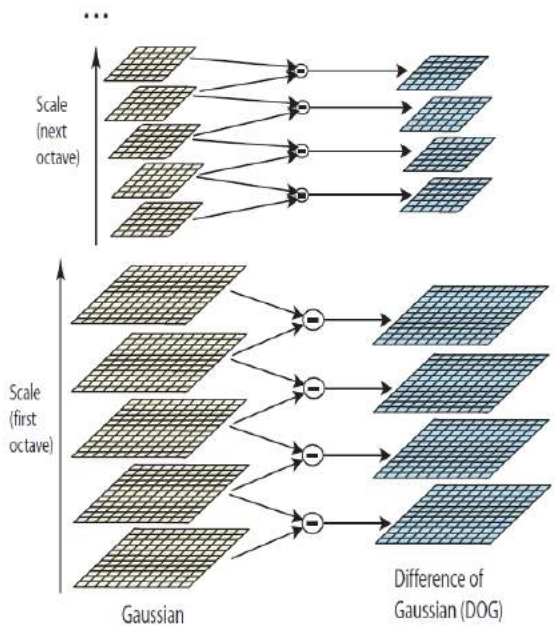

Fig.2. Difference of Gaussian in an image

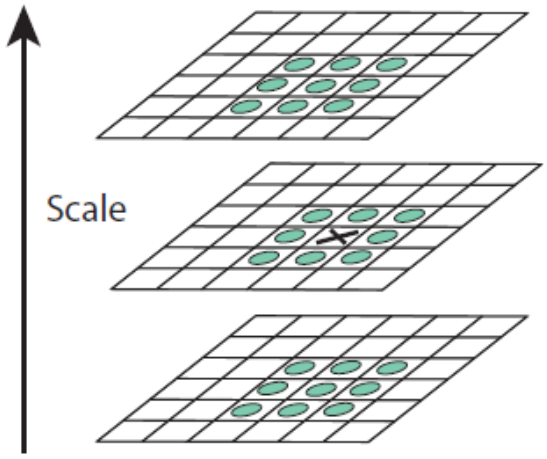

Fig.3. Detection of maxima and minima from DoG

B. Keypoint localization
Once a keypoint candidate has been found by comparing a pixel to its neighbours, the next step is to perform a detailed fit to the nearby data for location, scale, and ratio of principal curvatures. This information allows points to be rejected that have low contrast (and are therefore sensitive to noise) or are poorly localized along an edge.

For fitting a 3D quadratic function to the local sample points to determine the interpolated location of the maximum, scale-space function, D(x, y, σ), is shifted as:

$$DoG(x) = DoG + \frac{\partial DoG^T}{\partial x} x + \frac{1}{2} x^T \frac{\partial^2 DoG}{\partial x^2} x \qquad (4)$$

where DoG and its derivatives are evaluated at the sample point and $X = (w, z, \sigma)^T$ is the offset from this point. The location of the extremum, $\hat{X}$, is determined by taking the derivative of this function with respect to X and setting it to zero, giving

IJIREEICE

ISSN (Online) 2321 – 2004
ISSN (Print) 2321 – 5526

INTERNATIONAL JOURNAL OF INNOVATIVE RESEARCH IN ELECTRICAL, ELECTRONICS, INSTRUMENTATION AND CONTROL ENGINEERING
Vol. 4, Issue 7, July 2016

$$\hat{X} = -\frac{\partial^2 DoG^{-1}}{\partial x^2}\frac{\partial DoG}{\partial x} \qquad (5)$$

The function value at the extremum, DoG ($\hat{X}$), is useful for rejecting unstable extrema with low contrast. This can be obtained by substituting equation (3) into (2), giving

$$DoG(\hat{X}) = DoG + \frac{1}{2}\frac{\partial DoG}{\partial x}\hat{X} \qquad (6)$$

For the experiments in this paper, all extrema with a value of |D($\hat{X}$)| less than 0.04 were discarded (as before, we assume image pixel values in the range [0,1].

C. Orientation assignment

By assigning a consistent orientation to each keypoint based on local image properties, the keypoint descriptor can be represented relative to this orientation and therefore achieve in-variance to image rotation. Fig.4 represents this orientation assignment.

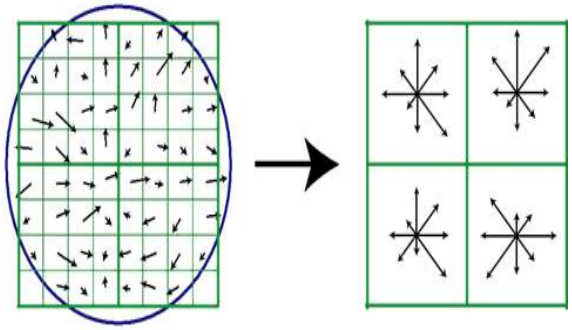

Fig.4. Orientation assignment in image gradient using keypoint descriptor

Following experimentation with a number of approaches to assigning a local orientation, the following approach was found to give the most stable results. The scale of the keypoint is used to select the Gaussian smoothed image, S, with the closest scale, so that all computations are performed in a scale-invariant manner. For each image sample, S(w, z), at this scale, the gradient magnitude, d(w, z), and orientation, φ(w, z), is pre-computed using pixel differences:

$$d(w,z) = \sqrt{(S(w+1,z)-S(w-1,z))^2 + (S(w,z+1)-S(w,z-1))^2} \quad (7)$$

$$\varphi(w,z) = \tan^{-1}\left(\frac{S(w,z+1)-S(w,z-1)}{S(w+1,z)-S(w-1,z)}\right) \quad (8)$$

D. Keypoint descriptor

The local image gradients are measured at the selected scale in the region around each keypoint.

These are transformed into a representation that allows for significant levels of local shape distortion and change in illumination. Fig.5 shows the object which is to be find out in the video.

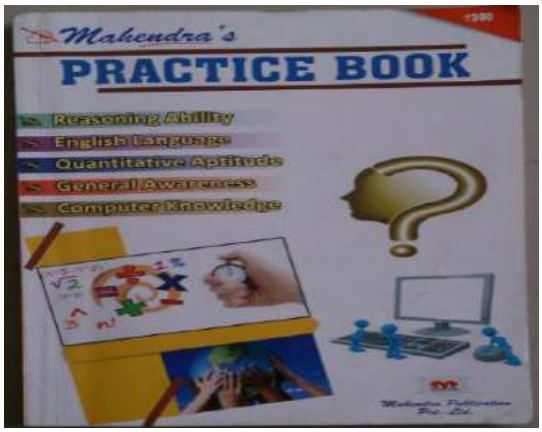

Fig.5. Object to be identified in the video

IV. RESULTS & DISCUSSION

Now, in the results, frames of the video are shown in the Fig.6-12. In the figures, the object i.e., a book, whose keypoints are detected are shown in various positions and it can be observed that, using this method, the object is detected in all respects.

Fig.6. Frame 1

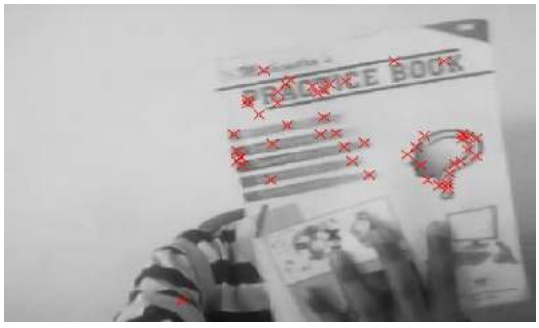

Fig.7. Frame 2

Fig.8. Frame 3

DOI 10.17148/IJIREEICE.2016.4742

IJIREEICE

ISSN (Online) 2321 – 2004
ISSN (Print) 2321 – 5526

INTERNATIONAL JOURNAL OF INNOVATIVE RESEARCH IN ELECTRICAL, ELECTRONICS, INSTRUMENTATION AND CONTROL ENGINEERING
Vol. 4, Issue 7, July 2016

Fig.9. Frame 4

Fig.10. Frame 5

Fig.11. Frame 6

Fig.12. Frame 7

From these figures, recognition of the object is obtained with a successful recognition rate of more than 90%. Hence, the proposed technique of the novel method is helpful in detecting objects in videos.

V. CONCLUSION

The SIFT keypoints described in this paper are particularly useful due to their distinctive-ness, which enables the correct match for a keypoint to be selected from a large database of other keypoints. These keypoints are then utilized to recognise an object in a video. And it can be concluded that the object is recognised efficiently. Hence, for the future work, recognition rate can be increased using some classifier and some more features of the object.

REFERENCES

[1] Moravec, H. 1981. Rover visual obstacle avoidance. In International Joint Conference on Artificial Intelligence, Vancouver, Canada, pp. 785-790.

[2] Harris, C. and Stephens, M. 1988. A combined corner and edge detector. In Fourth Alvey Vision Conference, Manchester, UK, pp. 147-151.

[3] Harris, C. 1992. Geometry from visual motion. In Active Vision, A. Blake and A. Yuille (Eds.), MIT Press, pp. 263-284.

[4] Zhang, Z., Deriche, R., Faugeras, O., and Luong, Q.T. 1995. A robust technique for matching two un-calibrated images through the recovery of the unknown epipolar geometry. Artificial Intelligence, 78:87-119.

[5] Schmid, C., and Mohr, R. 1997. Local grayvalue invariants for image retrieval. IEEE Trans. on Pattern Analysis and Machine Intelligence, 19(5):530-534.

[6] Lowe, D.G. 1999. Object recognition from local scale-invariant features. In International Conference on Computer Vision, Corfu, Greece, pp. 1150-1157.

[7] Baumberg, A. 2000. Reliable feature matching across widely separated views. In Conference on Computer Vision and Pattern Recognition, Hilton Head, South Carolina, pp. 774-781.

[8] Koen E.A. van de Sande, Theo Gevers and Cees G.M. Snoek, "Evaluating Color Descriptors for Object and Scene Recognition," IEEE Transactions on Pattern Analysis and Machine Intelligence, Vol. 32, No. 9, pp. 1582-1596, September 2010.

[9] George Bebis, Sushil Louis, Yaakov Varol and Angelo Yfantis, "Genetic Object Recognition Using Combinations of Views," IEEE Transactions on Evolutionary Computation, Vol. 6, No. 2, pp. 132-146, April 2002.

[10] R. Fergus, P. Perona and A. Zisserman, "Object Class Recognition by Unsupervised Scale-Invariant Learning," in Proceedings of CVPR, pp. 264-271, 2003.

[11] Zachary Pezzementi, Erion Plaku, Caitlin Reyda and Gregory D. Hager, "Tactile-Object Recognition from Appearance Information," IEEE Transactions on Robotics, Vol. 27, No. 3, pp. 473-487, June 2011.

[12] Bjorn Ommer and Joachim M. Buhmann, "Learning the Compositional Nature of Visual Object Categories for Recognition," IEEE Transactions on Pattern Analysis and Machine Intelligence, Vol. 32, No. 3, pp. 501-516, March 2010.

[13] Jialue Fan, Xiaohui Shen and Ying Wu, "What Are We Tracking: A Unified Approach of Tracking and Recognition," IEEE Transactions on Image Processing, Vol. 22, No. 2, pp. 549-560, February 2013.

[14] Joseph L. Mundy, "Object Recognition in the Geometric Era: A Retrospective," J. Ponce et al. (Eds.): Toward Category-Level Object Recognition, LNCS 4170, pp. 3–28, 2006.

[15] Gyuri Dorko and Cordelia Schmid, "Object Class Recognition Using Discriminative Local Features," Submitted to IEEE Transactions on Pattern Analysis and Machine Intelligence, October 2004.

[16] K. Matusiak, P. Skulimowski and P. Strumillo, "Object recognition in a mobile phone application for visually impaired users," IEEE HSI 2013, Vol. 978-1-4673-5637-4, No. 13, pp. 479-484, June 2013.

Copyright to IJIREEICE

ResearchGate

See discussions, stats, and author profiles for this publication at: https://www.researchgate.net/publication/305518683

Optimization of high-k and gate metal workfunction for improved analog and intermodulation performance of Gate Stack (GS)-GEWE-SiNW MOSFET

Article *in* Superlattices and Microstructures · July 2016

DOI: 10.1016/j.spmi.2016.07.021

READS

15

2 authors:

Neha Gupta

Delhi Technological University

18 PUBLICATIONS **23** CITATIONS

SEE PROFILE

Rishu Chaujar

Delhi Technological University

88 PUBLICATIONS **201** CITATIONS

SEE PROFILE

All in-text references underlined in blue are linked to publications on ResearchGate, letting you access and read them immediately.

Available from: Neha Gupta
Retrieved on: 20 August 2016

Accepted Manuscript

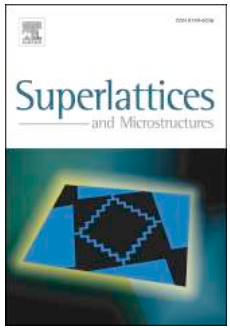

Optimization of high-k and gate metal workfunction for improved analog and intermodulation performance of Gate Stack (GS)-GEWE-SiNW MOSFET

Neha Gupta, Rishu Chaujar

PII: S0749-6036(16)30511-0

DOI: 10.1016/j.spmi.2016.07.021

Reference: YSPMI 4425

To appear in: *Superlattices and Microstructures*

Received Date: 24 May 2016

Revised Date: 7 July 2016

Accepted Date: 19 July 2016

Please cite this article as: N. Gupta, R. Chaujar, Optimization of high-k and gate metal workfunction for improved analog and intermodulation performance of Gate Stack (GS)-GEWE-SiNW MOSFET, *Superlattices and Microstructures* (2016), doi: 10.1016/j.spmi.2016.07.021.

This is a PDF file of an unedited manuscript that has been accepted for publication. As a service to our customers we are providing this early version of the manuscript. The manuscript will undergo copyediting, typesetting, and review of the resulting proof before it is published in its final form. Please note that during the production process errors may be discovered which could affect the content, and all legal disclaimers that apply to the journal pertain.

ACCEPTED MANUSCRIPT

Optimization of High-k and Gate Metal Workfunction for Improved Analog and Intermodulation Performance of Gate Stack (GS)-GEWE-SiNW MOSFET

Neha Gupta[1] and Rishu Chaujar[2]

Microelectronics Research Lab, Department of Engineering Physics,
Delhi Technological University, Bawana Road, Delhi-110042, India[1]
E-Mail: nehagupta@dtu.ac.in[1] and rishu.phy@dce.edu[2]

***Abstract*—This work optimizes the gate engineering scheme (both gate stack and gate metal workfunction engineering) of Stacked Gate (SG) Gate Electrode Workfunction Engineered (GEWE)-Silicon Nanowire MOSFET at 300K for improved analog and intermodulation performance. This has been done by evaluating and analyzing the metrics such as Switching Ratio, Subthreshold Swing (SS), Device Efficiency, channel and output resistance, VIP3, IIP3, 1-dB Compression Point, IMD3, HD2 and HD3. Simulation results exhibit that HfO_2 as a gate stack exhibit high linearity at a comparatively low gate bias of 0.56V with higher IIP3 (6.21dBm) and low IMD3 (9.6 dBm). Further, the characteristics/performance is modulated by adjusting the workfunction difference of metal gate. This study demonstrates that SiNW MOSFET modeled with HfO_2 as a gate stack over SiO_2 interfacial layer, and gate metal workfunction difference (ΔW) of 4.4 eV can be considered as a promising potential for low power switching component in ICs and Linear RF amplifiers.**

***Keywords*—Gate Stack, Gate Electrode Workfunction Engineering, Analog, Linearity, Harmonic Distortion, Silicon Nanowire**

I. INTRODUCTION

According to Moore's Law, the transistor size has shrunk to get higher device performance and reduce its cost, but short channel effects (SCEs) such as DIBL, HCEs, Punchthrough, V_{th} roll-off, etc., hinders its performance. To overcome such limitations, various device designs and engineering schemes are reported in literature such as Dual Gate [1], Recessed channel [2], Multi-Gate [3], CNT FET [4], Nanowire FET [5], etc. Among them, Silicon Nanowire (SiNW) emerged as a most promising in electronic devices because its properties such as concentration, dopant type can be changed during synthesis. Also, its mobility is higher than bulk silicon due to stronger quantum confinement. The body thickness (diameter) of the nanowire can readily be reduced to a few nanometers in size scale that is challenging to obtain using bulk silicon [6] and to get further improvement against SCEs the concept of SiNW MOSFET was put forward by Cui et al. [7] in 2003 concluded that silicon nanowires MOSFET as building blocks for future nano-electronics.

Moreover, the most common issue of scaling is oxide thickness. As oxide thickness scales down to 1.5nm or below, the leakage current increases up to $1A/cm^2$ at 1V due to direct tunneling of carriers which, consequently increases the static power and hence affect the circuit operation as reported by [8-9]. High-k films are proved to be the most promising solution. However, these films result in high fringing fields from gate to source/drain regions and thus degrading the device performance. This constraint can be overcome by using gate stack architecture consisting of SiO_2 layer as a passivation between high-k films and bulk by keeping the effective oxide thickness (EOT) constant, high-k dielectrics permit the increase in physical oxide thickness to prevent gate tunneling [10-11] and thus improves the carrier efficiency but at the same time, gate capacitance increases. Therefore, for selection of high-k materials relationship between dielectric constant and band-offset must be considered. The excessive high-k constant is generally undesirable owing to a tradeoff between dielectric constant and band-offset. Hence, selection of metal material becomes necessary. This work is an extension of [12], mainly focusing on effect of high-dielectric constant (such as Si_3N_4, HfO_2, ZrO_2) and gate metal

workfunction in terms of Analog and Intermodulation metrics, since linearity plays an important role in RFIC designing and high-frequency systems because nonlinearity causes harmonic generation, gain compression, desensitization etc. [13-14]. A high linearity with low distortion is preferred in modern communication systems even while working with a weak signal. Thus, previously performed analysis has been extended with an aim to optimize the value of high-dielectric constant and gate metal workfunction difference (ΔW) which can be used as a reference tool for designing circuits for different analog and RF applications where linearity is a major concern.

II. Device Structure and its Description

Fig.1 (a-b) shows the 3D and 2D cross-sectional view of gate stack (GS) GEWE SiNW MOSFET. The channel length of the device is 30nm and radius of SiNW is 5nm. The length of region 1 (L_1) and region 2 (L_2) are 15nm each which is towards the 45nm node CMOS technology as stated in ITRS Roadmap[15]. The Source/Drain region is heavily doped with an n-type impurity of 1×10^{19} $cm^{-3}$of 5nm long, while the SiNW is doped with a p-type impurity of 1×10^{16} $cm^{-3}$and effective oxide thickness is 1.5nm. The gate metal work function at the source end (Φ_{m1}) is 4.8 eV (Au) and metal gate work function at the drain end (Φ_{m2}) is 4.4 eV (Ti) as shown in Fig. 1. In this analysis, all the junctions are assumed as abrupt, and the doping profiles are uniform. All simulations have been performed using ATLAS and DEVEDIT 3D device simulator [16].

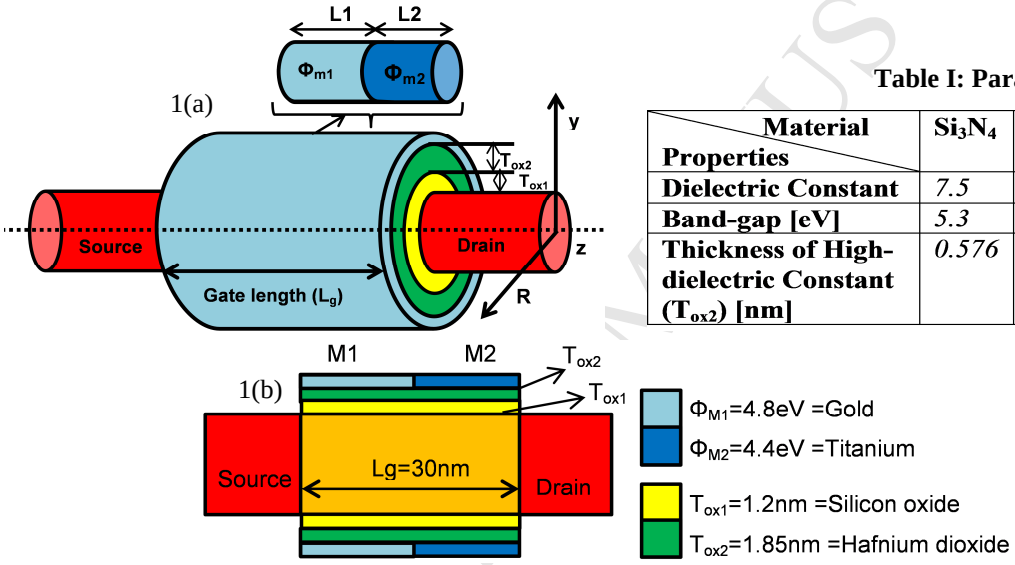

Table I: Parameters

Material / Properties	Si_3N_4	HfO_2	ZrO_2
Dielectric Constant	*7.5*	*24*	*30*
Band-gap [eV]	*5.3*	*5.8*	*5-7*
Thickness of High-dielectric Constant (T_{ox2}) [nm]	*0.576*	*1.85*	*2.3*

Fig.1 (a-b): Schematic Representation and its 2D cross-sectional view of GS-GEWE-SiNW MOSFET, Table I show the default parameters of high-k.

III. Simulation Methodology

All the simulations have been executed using physical models accounting for the electric field-dependent and concentration-dependent carrier mobilities, Shockley–Read–Hall (SRH) recombination/generation with doping dependent carrier lifetime, inversion layer Lombardi CVT mobility model, wherein concentration-dependent mobility, high field saturation model are all included [15]. To incorporate all non-local effects, we have adopted the quantum mechanical models which are more accurate than drift-diffusion method. To characterize the device performance accurately, it is very important to define the carrier transport with proper models. The quantum confinement effect in the deep scaled device may not be negligible [17]. Since the inversion charge layer thickness in the conducting silicon nanowire channel is comparable to the nanowire dimension, thus the effect of quantum confinement in the sub-nm device may not be negligible. The Bohm Quantum Potential (BQP) model [18] can also be used with Energy balance and hydrodynamic models, where the semi-classical potential is modified by the quantum potential in a similar way as for the continuity equations. The model introduces a position dependent quantum potential, Q, which is added to the Potential Energy of a given carrier type. This quantum potential is derived using the Bohm interpretation of quantum mechanics [19] and is described below:

Time-independent Schrodinger equation can be written as:

$$\left(\frac{-\hbar}{2m^*}\nabla^2 - V\phi\right)\psi_j = E_j\psi_j \quad \text{..... (1)}$$

According to Bohm's interpretation of quantum mechanics, the wave function in a polar representation can be written as:

$$\psi = R.\exp\left(\frac{iS}{\hbar}\right) \quad \text{..... (2)}$$

where R is probability density per unit volume, S has dimensions of action (energy×time)
By substituting equation 2 in 1, the Schrodinger equation can be written as:

$$\frac{\hbar^2}{2}\nabla\left\{M^{-1}\nabla\left[R.\exp\left(\frac{iS}{\hbar}\right)\right]\right\} + V.\mathrm{Re}\,xp\left(\frac{iS}{\hbar}\right) = E.R.\exp\left(\frac{iS}{\hbar}\right) \quad \text{..... (3)}$$

Where M^{-1} is the inverse of effective mass tensor and $M^{-1}\nabla S$ is the local velocity of particle associated to wave function. Real part of Eq. 3 is interpreted as continuity equation of probability density while imaginary part states that the total energy, E is conserved and equal to the sum of potential (V) and kinetic energy ($0.5\, M^{-1}\nabla S$). Therefore, Quantum potential is defined as:

$$V = \frac{-\hbar^2}{2}\frac{\nabla\left(M^{-1}\nabla R\right)}{R} \quad \text{..... (4)}$$

Potential V is obtained by the single particle Schrodinger equation and use "*mean field approximation*" and consider an effective quantum Bohm Potential defined as the weighted average potential for all carriers constrained in confining potential. Effective Quantum Potential is written as:

$$Q_{eff} = \frac{-\hbar^2}{2}\gamma\nabla\frac{[M^{-1}\nabla\left(n^{\alpha}\right)]}{n^{\alpha}} \quad \text{..... (5)}$$

where α and γ are two adjustable parameters, M^{-1} is the inverse effective mass tensor, n is the electron (or hole) density and h is a Planck's constant.

Bohr Quantum Potential (BQP) Model with alpha=0.5 and gamma=1.2 was used to take quantum mechanical effects into consideration. Additionally, numerical methods such as BICGST (bi-conjugate gradient stabilized) have been considered to obtain the solutions with improved convergence in 3D device structure [16]. Default simulator coefficients for all parameters have been employed. In order to fairly analyze the device performances, all the three devices are optimized to have the same threshold voltage, i.e., 0.32V by changing channel doping. The calibration of model parameters used in simulation has been performed according to the experimental results [20] and closed proximity of simulated results with the experimental results as shown in Fig. 2 validates the choice of parameters invoked during simulation. A proposed summary of the process flow, outlining the fabrication process of GEWE-SiNW MOSFET is shown in Table II.

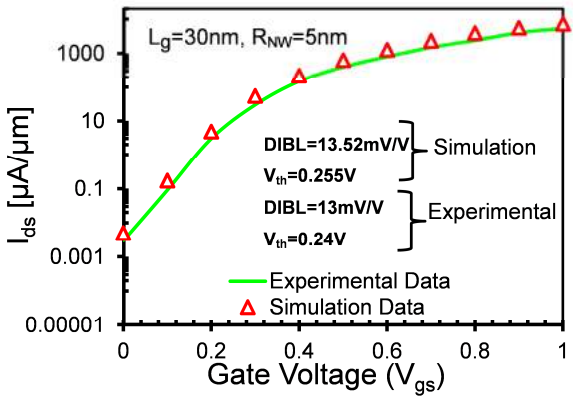

Fig.2: Calibration of simulated models with experimental results with L=30nm, R=5nm and V_d=1.0V.

Table II: Process Flow of GEWE-SiNW MOSFET

P-type SiNWs synthesized by LPCVD with silane as the silicon precursor and gold as the catalyst [21]

↓

SiNWs were oxidized in CVD reactor at 800° C in O_2 atmosphere to obtain uniform SiO_2 shell of t_{ox}=1.5-5nm, wrapping SiNW [22]

↓

Gate, Source and Drain regions with desired lengths are defined by E. beam lithography [23]

↓

S/D regions doped with Arsenic through implantation at a dose of 5×10^{19} cm^{-2}

↓

Deposit Gate Metal 1 by Precise Tilt angle evaporation and Gate Metal 2 by Normal Evaporation [24]

↓

Metal Electrodes deposited using thermal evaporation in ultra-high-vacuum and anneal

↓

GEWE-SiNW is formed and Continue Processing

IV. Results and Discussion

A. Analog Figure of Merits (FOMs)

In this subsection, the effect of dielectric constant and gate metal workfunction engineering are examined in terms of switching ratio, subthreshold slope (SS), device efficiency, channel resistance and output resistance as analog FOMs.

1. Switching Ratio and Device Efficiency

As is evident from Fig. 3(a), on-current is higher in the case of HfO_2 due to lowering of tunneling current owing to higher band-gap and band-offset in comparison to Si_3N_4 and ZrO_2. Consequently, a switching ratio which is an important criterion for any analog application also enhances in HfO_2 due to reduced off-current as indicated by Fig. 3(a). Further, as high-k dielectric increases, the threshold voltage (V_{th}) increases due to a reduction in off-current but subthreshold swing (SS) decreases as shown in Fig, 3(b).

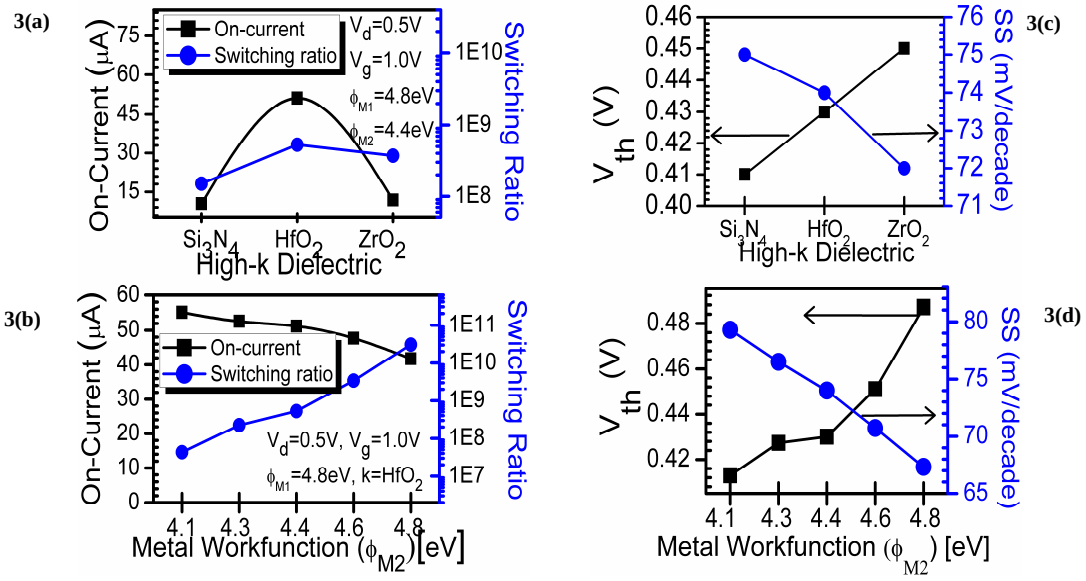

Fig. 3: (a-d) On-Current, switching ratio and Threshold Voltage, Subthreshold Swing for different high-dielectrics and metal gate workfunction (Φ_{M2}) at V_d=0.5V and V_g=1.0V.

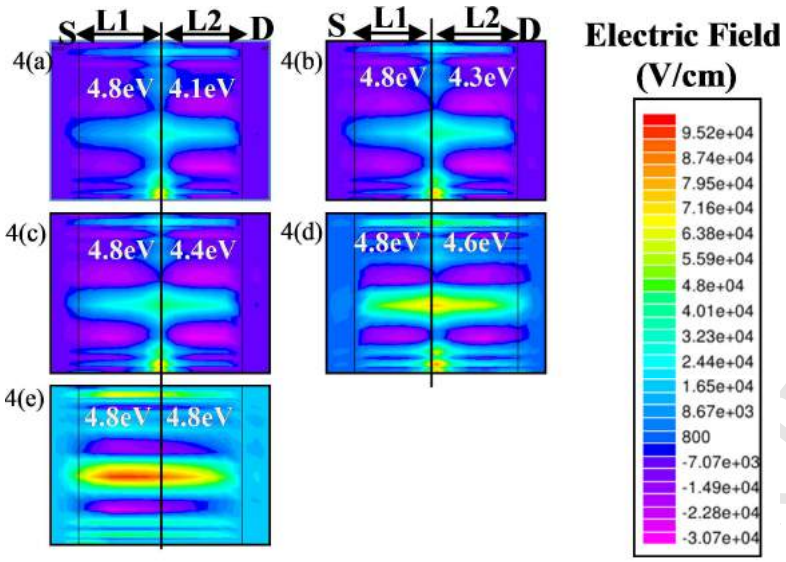

Fig. 4: (a-e) Electric Field Distribution for different metal gate workfunction (Φ_{M2}) at $V_{d;}$=0.5V and V_g=1.0V.

Moreover, the effect of workfunction difference is also examined by considering HfO_2 as a gate-stack and varying the workfunction at the drain end (Φ_{M2}) by keeping source side metal workfunction constant (Φ_{M1}). As gate metal workfunction at the drain end (Φ_{M2}) decreases or workfunction difference increases (ΔW), on-current rises significantly as shown in Fig. 3(b) due to redistribution of the electric field in the channel region owing to step potential due to workfunction difference which enhances carrier transport efficiency and thus current driving capability as is manifest from contour plots shown in the Fig. 4(a-e) and this effect is more apparent if workfunction difference increases as stated in [25], thus, also signifying the suppression of short channel effects. On the contrary, switching ratio reduces with increase in workfunction difference as exhibited in Fig. 3(c). This reduction is due to workfunction engineering scheme in which there is a high electric field in the channel that results into tunneling of carriers and causes higher off-current and thus degrades switching ratio. Hence, the trade-off between on-current and off-current is required to optimize the switching ratio depending upon the applications. Moreover, V_{th} rises with an increase in workfunction at the drain end. As workfunction difference decreases, the efficacy of GEWE scheme reduces and thus reduces the on-current as shown in Fig. 3(c) thereby enhancing threshold voltage as reported in Fig. 3(d). As revealed by Fig. 3(c) that sub-threshold current (off-current) decreases as workfunction difference increases due to which subthreshold swing reduces as demonstrated in Fig. 3(d).

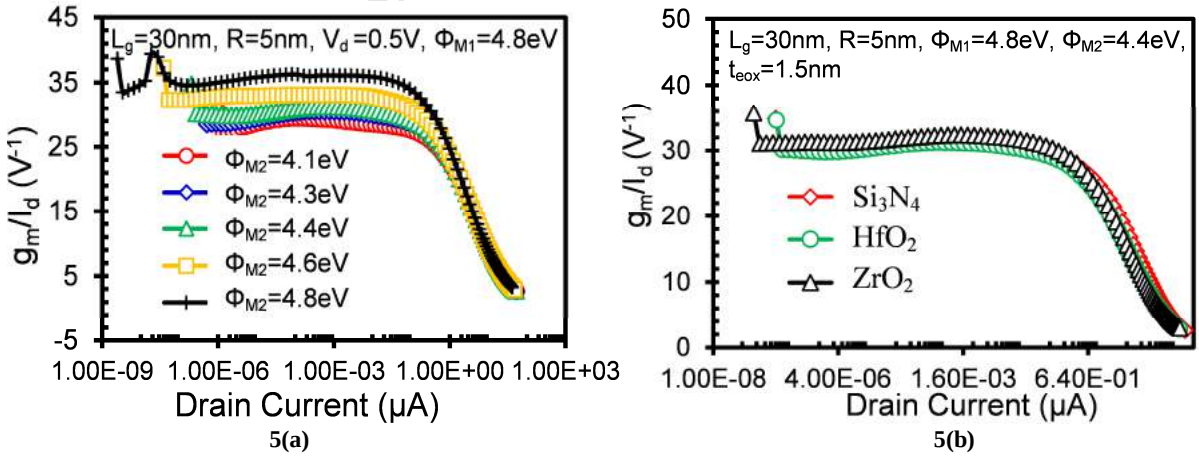

Fig. 5: Device Efficiency as a function of drain current for different high-dielectrics and metal gate workfunction (Φ_{M2}) at V_d=0.5V and V_g=1.0V.

Also, device efficiency [D.E] (g_m/I_d) is an important parameter in the design of analog circuits, which offers the measure of efficiency to convert power into speed. Fig.5 (a) shows the device efficiency as a function of drain current for different high-k materials. It is clearly shown that the variation of D.E occurs mainly at the weak-

inversion region of operation and in the saturation region, device efficiency reduces due to a reduction in transconductance and increment in on-current. The decrease in D.E. with HfO_2 is due to large deviation in drain current as compared to transconductance. Further, with the tuning of workfunction difference of metal gates, D.E. of HfO_2 gate stack increases as revealed by Fig. 5(b) owing to enhanced transconductance with an increase in workfunction difference.

2. Output Resistance and Channel Resistance

The output resistance (R_{out}) of a MOSFET is the inverse of the output conductance. The most important characteristics of R_{out} in the circuit design are maximum R_{out} which decides the maximum available power gain for the device. Fig. 6(a-d) shows that in the linear region (V_d=0-0.2V), R_{out} decreases, and it is desirable when the circuit is to act as an ideal voltage source, and as drain bias reaches to saturation region (V_d=0.4-0.8V) R_{out} rises due to increasing drain current. This effect is more pronounced for HfO_2 in comparison to other high-k dielectrics.

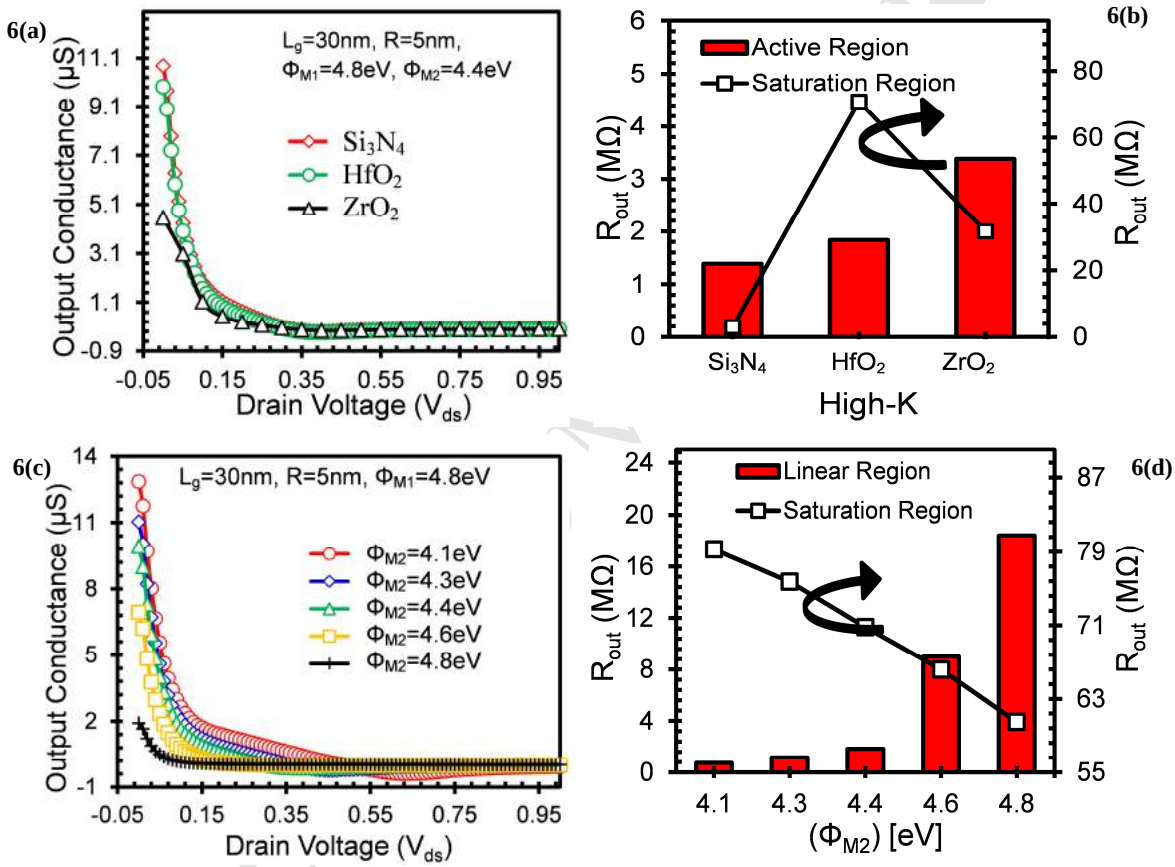

Fig. 6(a-d): Output conductance as a function of drain voltage for different high-dielectrics and metal gate workfunction (Φ_{M2}) at V_g=1.0V

As ΔW increases, output resistance (=1/g_D) reduces in the linear region, and as drain bias increases to saturation, its value increases as evident from Fig. 6(c). Thus, higher ΔW (approx. 0.7eV) of GS-GEWE-SiNW is beneficial for analog applications. Likewise, channel resistance (R_{ch}) of a MOSFET reveals the resistance of carriers in the channel region. As is clearly shown in Fig. 7(a) that with the incorporation of HfO_2 as a high-k layer onto the interfacial layer, R_{ch} decreases and as V_{gs} increases, electrostatic gate control enhances and thus reduces channel resistance. This region is called linear, ohmic or triode region. On the other hand, as workfunction at the drain end increases, carrier concentration decreases in the channel as is evident in contours of Fig. 8(a-e), due to which R_{ch} increases as shown in Fig. 7(b) which implies enhancement in the current driving capability of GS-GEWE-SiNW as ΔW increases. Thus, we have to choose optimum values of both high-k and workfunction difference for improved analog performance.

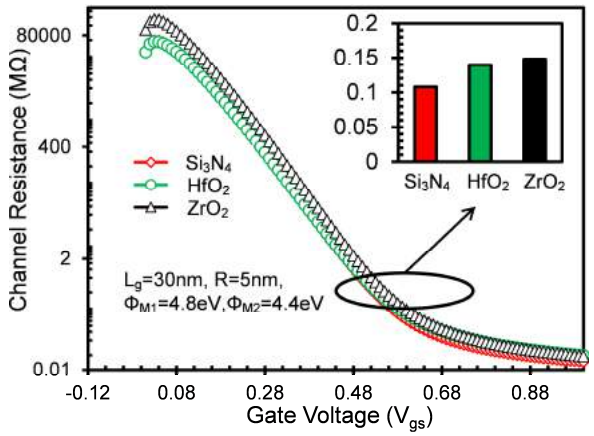

7(a)

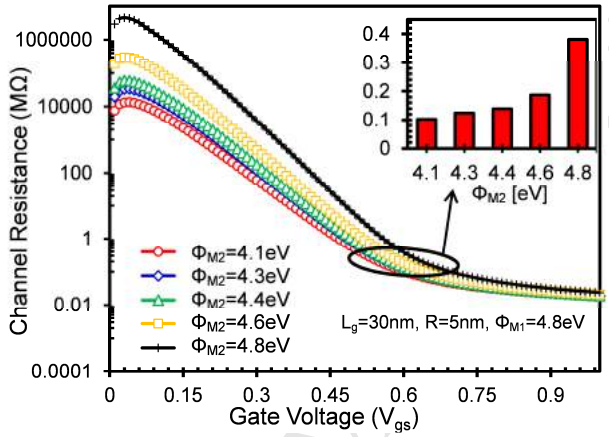

7(b)

Fig. 7(a-b): Channel Resistance as a function of gate voltage for different high-dielectrics at V_d=0.5V.

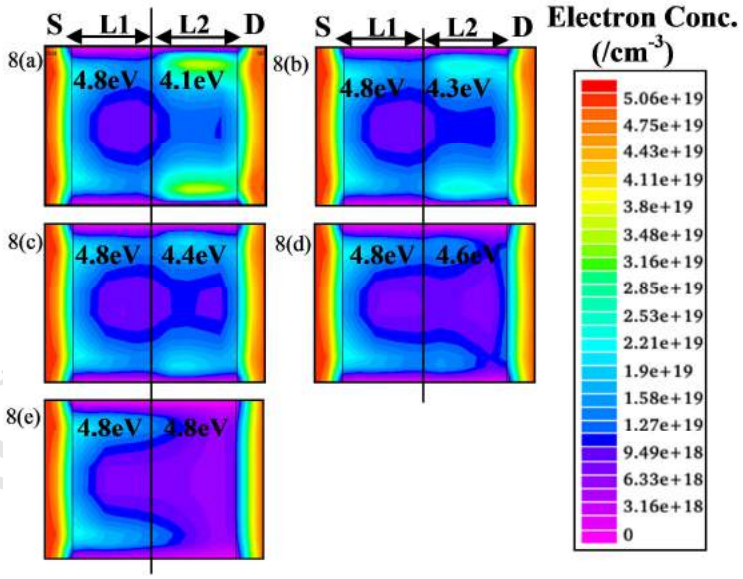

Fig. 8: (a-e) Electron Concentration Distribution for different metal gate workfunction (Φ_{M2}) at V_d=0.5V and V_g=1.0V.

B. Linearity and Harmonic Distortion Analysis

In this sub-section, linearity and distortion performance of GS-GEWE-SiNW MOSFET is investigated with an aim to find optimum high-k and gate workfunction difference for highly linear performance with low harmonic distortion. Non-linearity of MOS amplifiers is mainly from transconductance higher order harmonics (g_{m3}) that may interfere with the fundamental frequency and causes non-linearity. The metrics used in this work to evaluate the device linearity performance and intermodulation distortion are higher order transconductance

coefficients, *V*IP3, third-order input intercept point (IIP3), 1-dB intercept point and distortion such as second and third order harmonic distortion (HD2, HD3), third-order intermodulation distortion (IMD3) [26-27] which are defined as follows:

$$VIP3 = \sqrt{\frac{24 \times g_{m1}}{g_{m3}}} \quad \text{..... (6)}$$

$$IIP3 = \frac{2}{3}\frac{g_{m1}}{g_{m3} \times Rs} \quad \text{.... (7)}$$

$$1-dB\ Compression\ Point = 0.22 \times \sqrt{\frac{g_{m1}}{g_{m3}}} \quad \text{.... (8)}$$

where $g_{m1} = \frac{\partial I_d}{\partial V_{gs}}$, $g_{m3} = \frac{\partial^3 I_d}{\partial V^3{}_{gs}}$ and $R_S = 50\Omega$

g_{m3} is a high-order derivative of I_d-V_{gs} characteristics and their amplitudes should be minimized for lower distortion. The value of V_{GS} at which the higher order of transconductance parameters (g_{m3}) becomes zero is known as zero crossover point (ZCP) which decides the optimum DC bias point for device operation. Higher gain can be realized by setting DC bias point close to V_{th}. Fig. 9(a-b) shows the variation of g_{m3} as a function of gate overdrive voltage (V_{gs}-V_{th}) and the results indicate that incorporation of GS over GEWE-SiNW MOSFET lowers the amplitude of g_{m3} in comparison to GEWE-SiNW due to lowering of tunneling current which improves gate controllability and hence, transconductance and its harmonic distortion.

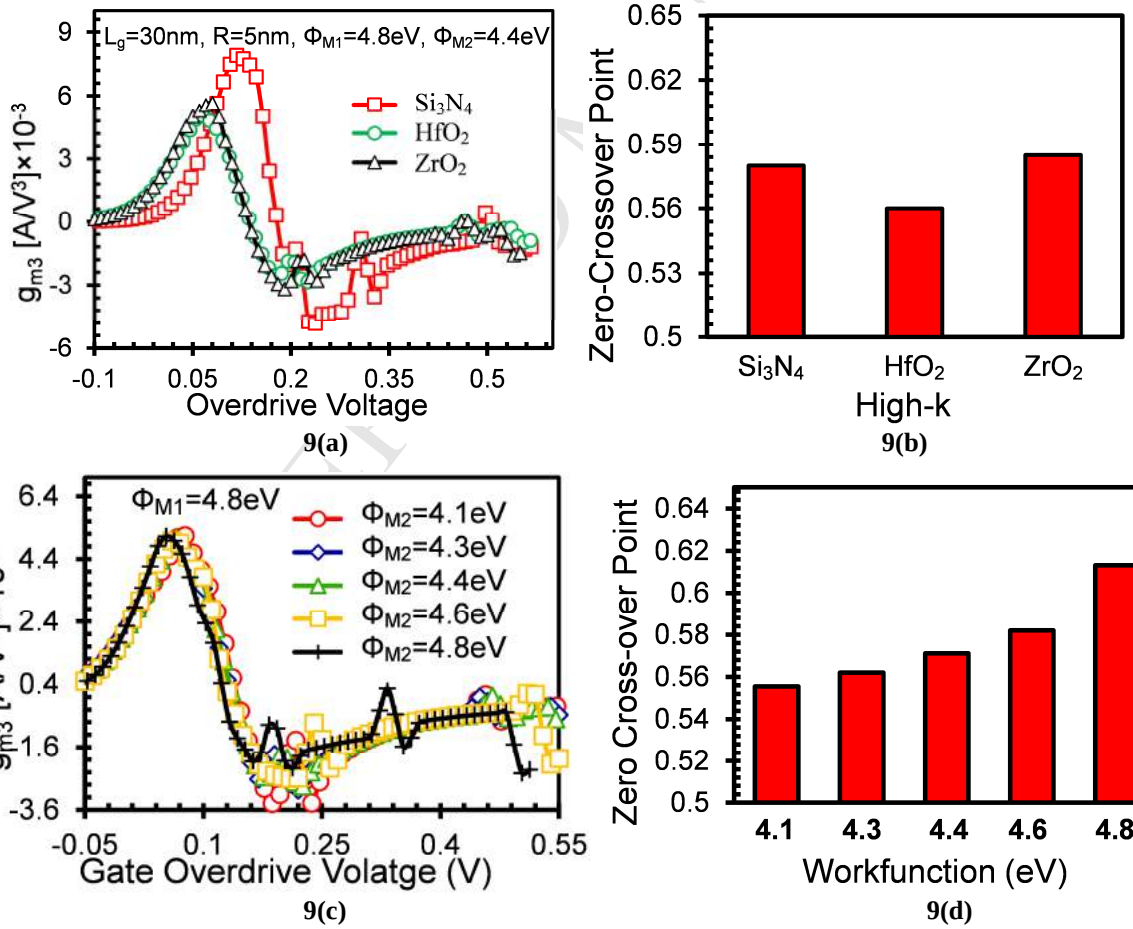

Fig. 9(a-d): Higher order transconductance coefficients g_{m2} and g_{m3}, (c) Zero-Crossover Point for different high-dielectric materials at V_d=0.5V.

Also, the DC bias points shifts towards lower V_{gs} by changing the dielectric constant as shown in Fig. 9(b). Among all dielectrics, HfO_2 shows better improvement in terms of lower distortion (g_{m3}) and lower bias point in comparison to other high-k. With the increase in metal gate workfunction at the drain end (or reduces ΔW), there is not as much change in amplitude of g_{m3} as is evident from Fig. 9(c) due to change in on-current as reflected by Fig. 3(c) but the DC bias point shifts towards lower V_{gs} if ΔW increases as shown in Fig. 9(d).

1. VIP3/IIP3 and 1-dB Compression Point

In all linearity FOMs, generally two peaks are appearing: one at a lower gate bias and maxima at higher gate bias for GS-GEWE-SiNW MOSFET. However, for analog circuit applications, it is desired that device should operate in moderate inversion region and not in the saturation region where power dissipation is more. So, in this analysis, a maximum appearing at a lower value of V_{gs} is considered for comparison. VIP3 represents extrapolated input voltage at which first and third order harmonics of drain current are equal and expressed as in Eq. 1. The peak of VIP3 reveals the cancellation of third-order nonlinearity coefficient by device internal feedback around second-order nonlinearity. Fig 10(a) shows that peak value of VIP3 increases significantly in the case of gate-stack architecture at lower V_{gs}-V_{th} due to lowering of g_{m3} as given by eq.1 and enhancement in transconductance (g_{m1}) owing to high on-current and improvement in carrier mobility. The peak value of VIP3 increases by 34% in HfO_2 in comparison to Si_3N_4 and is observed at lower bias voltage as shown in Fig. 10(a). Moreover, there are two important FOMs which govern amplifier's efficiency and linearity i.e. third-order intercept point (IIP3) and 1-dB compression point (1dB CP). In general for MOS based amplifiers, higher the output at the intercept, the better the linearity. Third-order intercept is a theoretical point at which the third-order distortion signal amplitudes equal the input signals, and it is useful in determining the linearity condition of an amplifier. IIP3 increases to a peak value (i.e. g_{m3}=0) and IIP3 peak enhances with the incorporation of gate stack scheme, and its magnitude is higher in the case of HfO_2 due to high band offset which reduces the off-current, improves transconductance and thus enhances IIP3 as shown in Fig, 10(c).

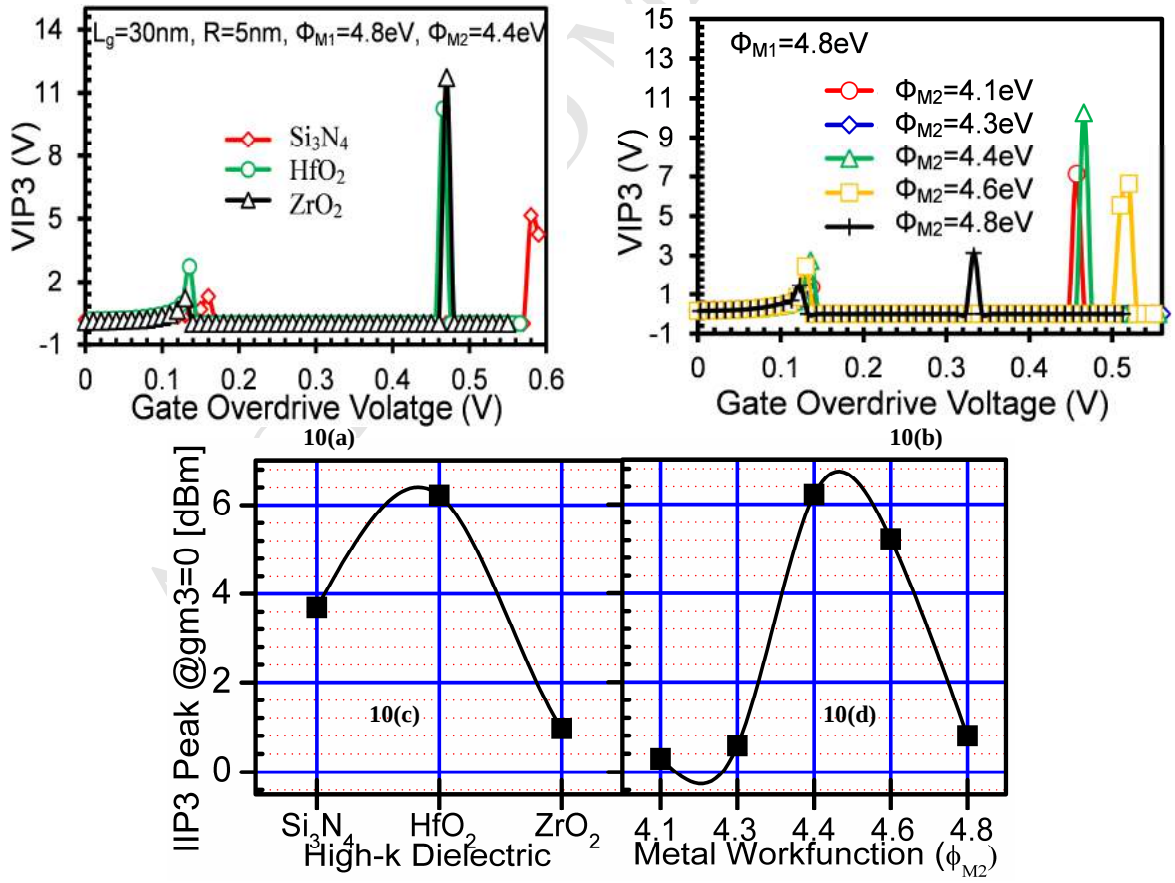

Fig. 10 (a-d): VIP3 as a function of gate overdrive voltage and Peak value of IIP3 for different high-k and gate metal workfunction at the drain end (Φ_{M2}) at V_d=0.5V and V_g=1.0V

The 1-dB compression point is the parameter that describes a circuit's tolerance to desensitization. It is essential to identify at what point compression occurs so that input levels can be limited to prevent distortion. It is usually the input power that causes the gain to decrease 1 dB from the normal linear gain specification. This parameter signifies the maximum input power that the amplifier circuit can handle by providing a fixed amount of gain, and if the input power surpasses the compression point, the gain starts falling. Hence, it is desirable that a 1-dB compression point should be as high as possible for the high linear amplifier. The effect of high-dielectrics on 1-dB compression point is presented in Fig. 11(a). The result shows 1-dB compression point in case of HfO_2 enhances by 1.4 and 2.3 times in comparison to Si_3N_4 and ZrO_2 respectively owing to reduced signal distortions and transconductance as stated in Eq. 4. Moreover, by modulating ΔW, linearity improves appreciably in terms of high VIP3, IIP3 and 1-dB CP peak in comparison to other cases due to a reduction in higher order harmonics and improvement in on-current as evident from Fig.10 (b), 10(c) and 11(b).

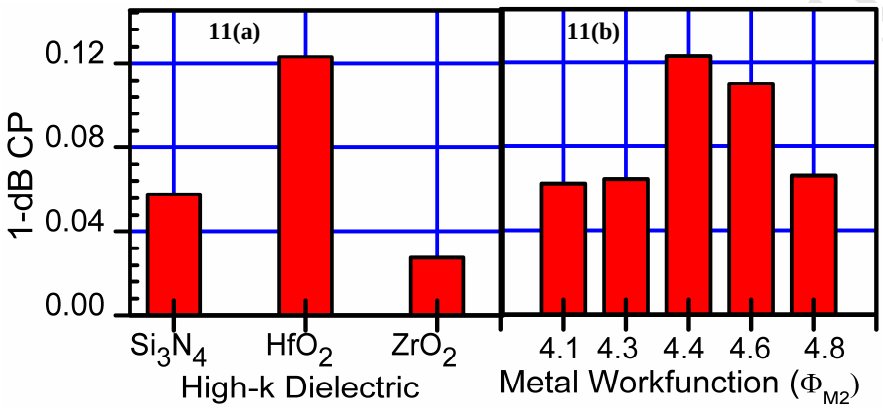

Fig. 11 (a-b): 1-dB Compression Point for different high-dielectrics and metal gate workfunction (Φ_{M2}) at V_d=0.5V and V_g=1.0V

2. Harmonic Distortions

Harmonic distortion (HD) is an essential reliability issue in analog and RF circuit applications that arises owing to the non-linear performance of devices. Nonlinearity may induce intermodulation (IM), which generate signals with frequencies different from the input ones. These unwanted signals may fall into the band of interest, interfering or even corrupting the desired components [28]. Therefore, improved linearity performance of GEWE-SiNW MOSFET with HfO_2 as a gate stack is observed in the previous sub-section. In the following sub-section, Harmonic Distortion FOMs such as 2nd order HD (HD2), 3rd Order HD (HD3) and 3rd Order Intermodulation Distortion (IMD3) for the device are analyzed considering the effect of the gate stack and workfunction engineering. The distortion has been calculated through the integral function method (IFM) since this approach permits the distortion extraction from DC measurements without the need of an AC characterization, contrary to Fourier-based methods [29-30]. The approximate analytical expressions for HD2, HD3 and IMD3 are given as:

$$HD2 = 0.5V_a \frac{\left(\frac{dg_{m1}}{dV_{GT}}\right)}{2g_{m1}} \quad \text{.... (9)}$$

$$HD3 = 0.25V_a^2 \frac{\left(\frac{d^2 g_{m1}}{dV^2{}_{GT}}\right)}{6g_{m1}} \quad \text{.... (10)}$$

$$IMD3 = \left(\frac{9}{2} \times (VIP3)^3 \times g_{m3}\right)^2 \times R_S \quad \text{.... (11)}$$

Where V_a is the amplitude of AC signal and considered to be very small, of about 50mV for the IFM analysis. Fig.12 (a) shows HD2 and HD3 as a function of gate overdrive voltage for GEWE-SiNW incorporating different high-k as a gate stack. It is observed that HD2 and HD3 are significantly reduced in HfO_2 at lower V_{GT} in comparison to other high-k materials. This reduction is due to higher transconductance owing to high on-current

and is in accordance with Eq. 4 and 5. IMD3 denotes the intermodulation harmonic power at which the first and third order intermodulation harmonic powers are equal. IMD3 plays a major role in determining intermodulation distortion in CMOS RF amplifiers, since these applications make use of both phase and amplitude modulation. Therefore, reduction of IMD3 in the RF front-end transceiver parts is of great importance for maximizing overall system performance and minimizing distortions.

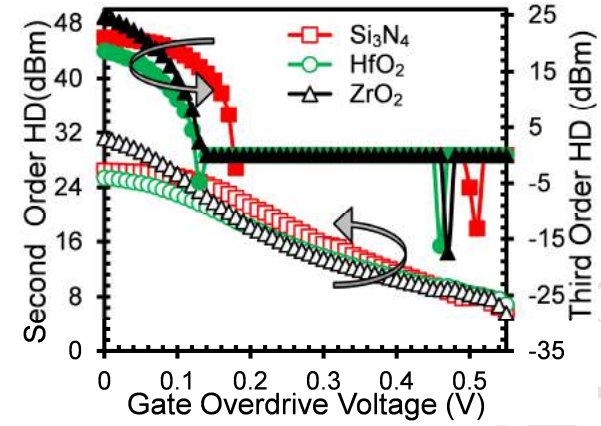

12(a)

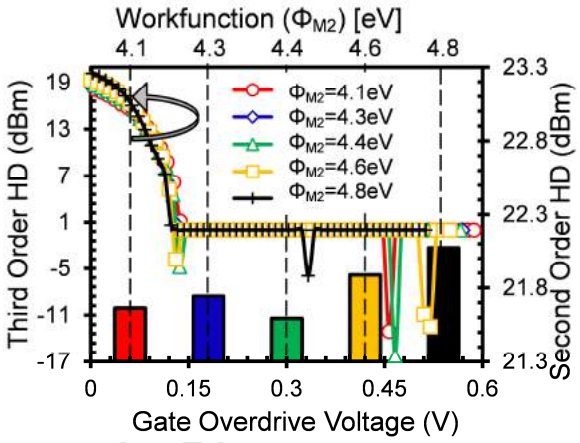

12(b)

Fig. 12(a-b): 2nd order Harmonic Distortion and 3rd Order Harmonic Distortion as a function of V_{GT} for different high-k and metal gate workfunction (Φ_{M2}) at V_g=1.0V, V_d=0.5V.

Fig 13(a) exhibits that IMD3 reduces with the incorporation of gate-stack design on GEWE-SiNW MOSFET, and this decrement is due to a reduction in higher order harmonics (g_{m3}) which originates from the non-linear transistor's I_d-V_{gs} characteristic according to Eq. 6. Moreover, distortions in GS (HfO_2+SiO_2)-GEWE-SiNW is further reduced by tuning gate metal workfunction as indicated by Fig. 12(b) and 13(b). As ΔW increases, gate controllability improves due to enhancement in carrier velocity which enhances g_{m1} and so from Eq. 4-6 again, it is reflected that HD2, HD3 and IMD3 reduces. Thus, by appropriate selection of high-k material and gate metal workfunction, GS-GEWE-SiNW achieves high linearity with minimum distortion for RF amplifier.

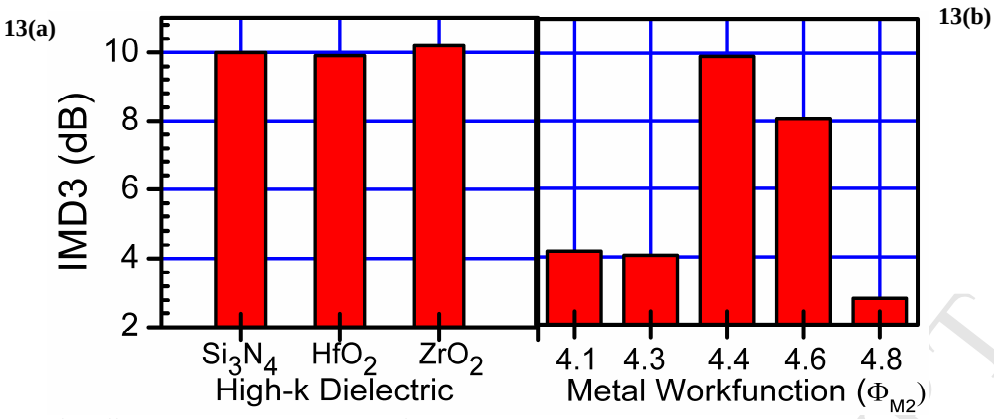

Fig. 13(a-b): IMD3 for different high-k and metal gate workfunction (Φ_{M2}) at V_g=1.0V, V_d=0.5V

V. CONCLUSION

In this work, improved analog and intermodulation performance of GS-GEWE-SiNW MOSFET is demonstrated by considering the effect of both high-k materials and metal gate workfunction difference. It is observed that high-k material (HfO_2) as a gate stack over SiO_2 interfacial layer in GEWE-SiNW significantly influence the analog performance of the device by enhancing the current driving capability and lowering of leakage current owing to large band-gap of HfO_2. Moreover, reduction in the electric field at the drain end and high carrier concentration in the channel region is achieved by tuning of gate workfunction difference which results in improved analog metrics such as switching ratio, channel resistance, device efficiency for low power analog applications. The enhancement in on-current and lowering of g_{m3} results into 2.14 and 2.28 times improvement in VIP3 in comparison to Si_3N_4 and ZrO_2 respectively and the input power rises to 0.128 dB in HfO_2 with ΔW=0.4eV, which the device can handle without compression. It is also examined that the DC bias point is shifted towards lower input voltage which indicates lowering of dynamic power consumption for circuit applications.

ACKNOWLEDGMENT

The authors would like to thank the Microelectronics Research Lab, Department of Engineering Physics, Delhi Technological University (formerly DCE) and one of the authors (Neha Gupta) is grateful to the University Grant Commission (UGC) for providing the necessary financial assistance to carry out this research work.

REFERENCES

[1] R.M. Barsan, “Analysis and Modeling of Dual- Gate MOSFETs”, IEEE Transactions on Electron Devices, Vol. 28, pp. 523-534, 1981.

[2] A. Kumar, N. Gupta and R. Chaujar, “Power gain assessment of ITO-based Transparent Gate Recessed Channel (TGRC) MOSFET for RF/wireless applications”, Superlattices and Microstructures, Vol. 91, pp. 290-301, 2015.

[3] C. P. Auth and J. D. Plummer, “Scaling Theory for Cylindrical, Fully-Depleted, Surrounding-Gate MOSFET’s”, IEEE Electron Device Letters, vol. 18, pp. 74-76, 1997

[4] E. Gnani, A. Marchi, S. Reggiani, M. Rudan and G. Baccarani, “Quantum-mechanical analysis of the electrostatics in silicon-nanowire and carbon nanotube FETs”, Solid-State Electronics, Vol.50, pp. 709-715, 2006.

[5] W. Xu, H. Wong, K. Kakushima and H. Iwai, “Quasi-analytical model of ballistic cylindrical surrounding gate nanowire MOSFET”, Microelectronic engineering, Vol. 138, pp. 111- 117, 2015.

[6] X. Chen and C. M. Tan, “Modeling and analysis of gate-all-around silicon nanowire FET”, Microelectronics Reliability, vol. 54, no. 6-7, pp. 1103-1108, July 2014.

[7] Y. Cui, Z. Zhong, D. Wang, W.U. Wang, C.M. Lieber, “High performance silicon nanowire field effect transistors”, Nano Lett., Vol. 3, pp. 149–152, 2003.

[8] S.H. Lo, D. A. Buchanan, Y. Taur, and W. Wang, “Quantum-Mechanical Modeling of Electron Tunneling Current from the Inversion Layer of Ultra-Thin-Oxide nMOSFET’s,” IEEE Electron Device Letters, vol. 18, no. 5, pp. 209-211, 1997

[9] G. Ribes, J. Mitard, M. Denais, S. Bruyere, F. Monsieur, C. Parthasarathy, E. Vincent, and G. Ghibaudo, “Review on High-k Dielectrics Reliability Issues”, IEEE Transactions on Device and Materials Reliability, Vol. 5 (1), 2005

[10] B.H. Lee, J. Oh, H.H. Tseng, R. Jammy and H. Huff, “Gate stack technology for nanoscale devices”, Materials today, Vol. 9, pp. 32-40, 2006.

ACCEPTED MANUSCRIPT

[11] R. Chau, S. Datta, Member, M. Doczy, B. Doyle, J. Kavalieros, and M. Metz "High-k/Metal–Gate Stack and Its MOSFET Characteristics" IEEE ELECTRON DEVICE LETTERS, Vol. 25, pp. 408-410, 2004.
[12] N. Gupta, A.Kumar and R. Chaujar, "Effect of Dielectric Engineering on Analog and Linearity performance of Gate Electrode Workfunction Engineered (GEWE) Silicon Nanowire MOSFET", Proceedings of the 15th IEEE International Conference on Nanotechnology, pp. 928-931, 2015.
[13] C. Yu, J.S. Yuan, H. Yang, MOSFET linearity performance degradation subject to drain and gate voltage stress, IEEE Trans. Device Mater. Rel. 4 (4) (2004) 681–689.
[14] A. Razavieh, D. B. Janes, and J. Appenzeller, "Transconductance Linearity Analysis of 1-D, Nanowire FETs in the Quantum Capacitance Limit", IEEE Transactions on Electron Devices, Vol. 60, pp. 2071-2076, 2013
[15] C. Hu, "Modern Semiconductor Device for Integrated Circuit", Prentice Hall, pp. 261–274, 2009.
[16] ATLAS User's Manual. SILVACO Int. Santa Clara, CA (2014)
[17] A. Chaudhry and J. N. Roy, "Mosfet Models, Quantum Mechanical Effects and Modeling Approaches: A Review", Journal of Semiconductor Technology and Science, Vol.10: 20-27, 2010.
[18] V. S. Patnaik, A. Gheedia and M.J. Kumar, "3D Simulation of Nanowire FETs using Quantum Models", 2008, http://web.iitd.ac.in/~mamidala/HTMLobj 1227/jul_aug_sep08
[19] G. Iannaccone, G. Curatola and G. Fiori, "Effective Bohm Quantum Potential for device simulators based on drift-diffusion and energy transport", Simulation of Semiconductor Processes and Devices (SISPAD), 275-278, 2004
[20] S. D. Suk et al, "High performance 5 nm radius twin silicon nanowire MOSFET (TSNWFET): fabrication on bulk Si wafer, characteristics, and reliability", IEEE IEDM Tech Digest, pp. 717-720, 2005.
[21] O. Shirak, O. Shtempluck, V. Kotchtakov, G. Bahir and Y. E. Yaish "High performance horizontal gate-all-around silicon nanowire field-effect transistors", Nanotechnology, Vol. 23, pp. 395202 (8pp), 2012.
[22] D. Moon, S-J. Choi, J. P. Duarte and Y-K. Choi, "Investigation of Silicon Nanowire Gate-All-Around Junctionless Transistors Built on a Bulk Substrate", IEEE Trans. Electron Devices, Vol. 60, pp. 1355-1360, 2013.
[23] J-H. Lee, B-S. Kim, S-H. Choi, Y. Jang, S. W. Hwangc and D. Whang, "A facile route to Si nanowire gate-all-around field effect transistors with a steep subthreshold slope", Nanoscale, Vol. 5, pp. 8968–8972, 2013.
[24] W. Long, H. Ou, J. M. Kuo, and K. K. Chin, "Dual-material gate (DMG) field effect transistor," IEEE Trans. Electron Devices, vol. 46, no. 5, pp. 865–870, May 1999.
[25] W. Long and K. K. Chin, "Dual material gate field effect transistor (DMGFET)," in IEDM Tech. Dig., 1997, pp. 549–552.
[26] R. Chaujar, R. Kaur, M. Saxena, M. Gupta, and R. S. Gupta, "Intermodulation distortion and linearity performance assessment of 50-nm gate length L-DUMGAC MOSFET for RFIC design," Superlattices Microstruct., vol. 44, no. 2, pp. 143–152, August 2008.
[27] Ó. Breandán and T. J. Brazil, "An Accurate Nonlinear MOSFET Model for Intermodulation Distortion Analysis," IEEE Microwave and wireless Components Letters, vol. 14, pp. 352–354, 2004.
[28] A. Dutta, K. Koley, and C. K. Sarkar, "Analysis of Harmonic distortion in asymmetric underlap DG-MOSFET with high-k spacer," Microelectron. Reliab., vol. 54, pp. 1125–1132, 2014.
[29] A. Cerdeira, M. A. Alemán, M. Estrada, and D. Flandre, "Integral function method for determination of nonlinear harmonic distortion," Solid. State. Electron., vol. 48, pp. 2225–2234, 2004.
[30] R. T. Doria, A. Cerdeira, J. P. Raskin, D. Flandre, and M. A. Pavanello, "Harmonic distortion analysis of double gate graded-channel MOSFETs operating in saturation," Microelectronics J., vol. 39, pp. 1663–1670, 2008.

ACCEPTED MANUSCRIPT

ACCEPTED MANUSCRIPT

HIGHLIGHTS

1. Optimizes the Gate Engineering Scheme for enhanced Analog and Intermodulation Performance

2. HfO_2 as a gate stack exhibit high linearity at comparatively low gate bias of 0.56V with higher IIP3 (6.21dBm) and low IMD3 (9.6 dBm).

3. It is also observed that the DC bias point shifted towards lower input voltage which indicates lowering of dynamic power consumption for circuit applications.

4. Characteristics/performance of GS-GEWE-SiNW is further improved by modulating the workfunction difference of metal gate (ΔW).

5. SiNW MOSFET modeled with HfO_2 as a gate stack and ΔW of 4.4 eV can be considered as a promising potential for low power switching component in ICs and Linear RF amplifiers.

ACCEPTED MANUSCRIPT

Available online at www.sciencedirect.com

ScienceDirect

Procedia Computer Science 89 (2016) 749 – 758

Twelfth International Multi-Conference on Information Processing-2016 (IMCIP-2016)

Performance Analysis of Fuzzy C-Means Clustering Methods for MRI Image Segmentation

Mahipal Singh Choudhry* and Rajiv Kapoor

Delhi Technological University, Delhi, India

Abstract

MRI is one of the most eminent medical imaging techniques and segmentation is a critical stage in investigation of MRI images. FCM is most usually used techniques for image segmentation of medical image applications because of its fuzzy nature, where one pixel can belong to multiple clusters and which lead to better performance than crisp methods. Conventional FCM fail to perform well enough in the presence of noise and intensity inhomogeneity in MRI images. Various FCM variations like BCFCM, PFCM, SFCM, FLICM, MDFCM, FCM_S1, FCM_S2, TEFCM, RFCMK, WIPFCM and KWFLICM, have been proposed to overcome these predicament by using the spatial statistics available in the images. In this paper all these techniques, used for segmentation, are implemented and compared in terms of two classes of cluster validity functions, fuzzy partition and feature structure, on the basis of their performance for the noisy MRI images. All these FCM variants are analyzed in terms of Partition Coefficient, Partition Entropy, Time Complexity and Segmentation Accuracy.

© 2016 Published by Elsevier B.V. This is an open access article under the CC BY-NC-ND license (http://creativecommons.org/licenses/by-nc-nd/4.0/).
Peer-review under responsibility of organizing committee of the Organizing Committee of IMCIP-2016

Keywords: Fuzzy C-Means (FCM); Image Segmentation; Magnetic Resonance Imaging (MRI); Medical Imaging.

1. Introduction

Medical images characteristically comprise complex configurations and their accurate segmentation is crucial for quantifiable diagnosis[1]. Image segmentation and contour extraction are the utmost instinctive techniques for medical image visualization[21]. Image segmentation is a thought provoking assignment in medical image investigation as the images contain complex boundaries and often affected by noise. FCM is most frequently used technique in medical image applications[1]. Most of the times, MRI images, contains noise and intensity inhomogeneity. Conventional FCM couldn't dealt with these effects[4] so many FCM variations like BCFCM, PFCM, SFCM, FLICM, MDFCM, FCM_S1, FCM_S2, TEFCM, RFCMK, WIPFCM and KWFLICM are proposed in the recent years to overcome limitations of conventional FCM by using the spatial information or by estimating the bias field for inhomogeneity or by making changes to the cost function. These methods are validated by their performance on real MRI images as well as synthetic images. Validation of these methods is done by using cluster validity functions for real MR images. Two types of cluster validity functions, fuzzy partition and feature structure, are used to evaluate the efficiency of clustering[19,20].

*Corresponding author. Tel: +91-9911811500.
E-mail address: msc_1976@yahoo.com

1877-0509 © 2016 Published by Elsevier B.V. This is an open access article under the CC BY-NC-ND license (http://creativecommons.org/licenses/by-nc-nd/4.0/).
Peer-review under responsibility of organizing committee of the Organizing Committee of IMCIP-2016
doi:10.1016/j.procs.2016.06.052

Effectiveness of the discussed methods is evaluated in terms of Segmentation Accuracy (SA)[6] for synthetic image tainted by Gaussian noise (For noise density, $\sigma = 0$ to 0.1).

The main contributions of the paper are as follows:

- FCM and 09 latest variants are validated by implementation of real MRI images as well as synthetic images.
- Performance comparison of FCM and variants is done in terms of Partition Coefficient Partition Entropy and Time Complexity for real MRI images.
- Performance comparison of FCM and variants is done in terms of Segmentation Accuracy for synthetic image corrupted by Gaussian noise.

Section-2 of the research paper deals with literature survey in this field. This includes background and latest related work. FCM and variants are explained in terms of mathematical and system model with their strength and limitations in section-3. Section-4 includes results/performance analysis with algorithm and implementation issues. Conclusion, which is follow by references, is explained in section-5.

2. Literature Survey

FCM finds its applications in variety of problems varying from data analysis to segmentation of images. K. Xiao *et al.*,[11] performed Gaussian smoothing on input image and proposed a method to find the weightage for each feature using bootstrapping technique when dealing with multiple features. To deal with intensity in homogenities, Pham *et al.*[12] proposed Adaptive FCM. In this case, the centroids are multiplied by unknown multiplier filed, which represents the inhomogeneity. First and second order regularization terms are included in the cost function to make the multiplier field varying slowly and smoothly.

Jude *et al.*[13] used multidimensional features formed by GLCM feature generation model to include spatial information into FCM. Extra dimensions make the process time consuming so to overcome this, distance metric based compression is proposed to selects the representative pixels of the groups and perform clustering on them, which resulted in fast and effective clustering. Enhanced FCM is proposed by Szilagyi *et al.*,[14] to fasten the segmentation process as well as to reduce the noise effect. For achieving this, a new factor which includes the pixel intensity along with mean of neighborhood pixels is calculated in advance of the segmentation process and computational complexity is condensed by considering the histogram count of the voxels into the cost function.

Noise inhomogeneity effect is reduced in a faster way by GCFFCM proposed by Jingjing Song *et al.*,[15]. GCFFCM algorithm uses a gain field to deal with inhomogeneity and uses the histogram of the image to reduce the computational time. Abbas Biniaz *et al.*,[16] proposed Gaussian spatial FCM, in which the membership function is updated twice in the algorithm to reduce the noise effect. First update is similar to the conventional FCM but in the second update, a spatial factor is included which contains the Gaussian average of neighborhood membership values. Another method to deal with noise affect is proposed by Shan Shen *et al.*,[17] called as Improved FCM (IFCM). In IFCM the distance term of FCM is modified by including two terms, feature attraction and distance attraction, which are calculated by considering weighted average of neighborhood intensity differences and weighted average of spatial difference respectively. The parameters that are giving weightage to these terms are optimized at every step by using a simple artificial neural network model.

A prior probability and fuzzy spatial information are used in ISFCM, proposed by Zulaikha Bevi *et al.*,[18] to minimized the noise affect in MRI images. In this method, cluster centers are initialized using histogram based FCM in the first step to achieve faster convergence and the membership updating equation is modified in a way to use probability obtained by the proportion of amount of pixels belongs to the cluster with pixels in the neighborhood and spatial information.

3. FCM and Various FCM Based Techniques

In FCM, it is possible for a data sample to belong to multiple clusters at the same time. The similarity is indicated by the membership value. In FCM a data sample is assigned with a membership value based on its similarity with the cluster center. The membership values are between 0 to 1 and more the similarity, higher the membership value.

Defuzzification is applied at the end of the clustering process to decide the clustering. FCM is a repetitive algorithm and the solution is achieved by repetitively updating the cluster center and membership value. These updating equations are obtained by solving the cost function. Let $X = \{x_1, x_2, x_3, \ldots, x_N\}$ denotes the data with N data samples. It has to be partitioned into c-clusters by minimizing the subsequent cost function

$$J = \sum_{j=1}^{N} \sum_{i=1}^{c} u_{ij}^{m} \|x_j - v_i\|^2 \tag{1}$$

where, u_{ij} represents the membership of x_j with the i^{th} cluster, v_i is the i^{th} cluster center, $\|\cdot\|$ is a norm metric and 'm' is a constant. The parameter m decides the fuzziness of the consequential partition. By taking the derivative of the equation and make it equal to zero by using Lagrange method, the following equations are achieved

$$v_i = \frac{\sum_{j=1}^{N} u_{ij}^{m} x_j}{\sum_{j=1}^{N} u_{ij}^{m}} \tag{2}$$

$$u_{ij} = \sum_{k=1}^{c} \left(\frac{\|x_j - v_i\|}{\|x_j - v_k\|} \right)^2 \tag{3}$$

Many variations to the FCM have been proposed because conventional FCM couldn't perform well in the presence of noise and intensity inhomogeneity. These FCM variants are discussed as

3.1 Bias-Corrected Fuzzy C-Means (BCFCM)

Ahmed *et al.*,[2] proposed a bias field estimation based FCM, known as BCFCM. In BCFCM, voxel is modal as the sum of observed intensity and a bias field term to deal with intensity inhomogeneity intensity of MRI. The objective function of FCM is modified by including neighborhood information. It acts as regularization term and helps to reduce the effect of salt and pepper noise. The modified objective function used in BCFCM is given by

$$J = \sum_{j=1}^{N} \sum_{i=})^{c} u_{ij}^{m} \|y_j - \beta_j - v_i\|^2 + \frac{\alpha}{N_R} \sum_{j=1}^{N} \sum_{i=1}^{c} u_{ij}^{m} \left(\sum_{k \in N(x_j)} \|y_k - \beta_k - v_i\|^2 \right) \tag{4}$$

Here, β_i is the bias field value at the j^{th} voxel, N_R represents size of neighborhood to be considered. β_i helps in removing the inhomogeneity effect in segmentation. The neighborhood effect on objective function is controlled by the parameter α. Selection of the parameter α heavily affects the accuracy of results, for example small value of α for low Signal to Noise Ratio (SNR) resulted in leakage of boundaries in the segmented image. This method cannot be applied when multiple features have to be considered as input.

3.2 Possibilistic Fuzzy C-Means (PFCM)

Yang *et al.*,[3] introduced a penalty term to the FCM objective function which is inspired by Neighborhood Expectation-Maximization (NEM) algorithm to decrease the effect of noise in the segmentation process. The penalty is formed by using the neighborhood information and few changes are made to it to satisfy the criterion of FCM. The modified objective function used in PFCM is given by

$$J = \sum_{j=1}^{N} \sum_{i=1}^{c} (u_{ij})^m d^2(x_j, v_i) + \gamma \sum_{j=1}^{N} \sum_{k=1}^{N} \sum_{i=1}^{c} (u_i j)^m (1 - u_{ik})^m w_{jk} \tag{5}$$

where, w_{jk} represents the neighborhood region, γ is the controlling parameter similar to α in BFCM. If x_k is neighbor of x_j then $w_{jk} = 1$ else $w_{jk} = 0$. In PFCM cluster center updating equation hasn't affected by the changes made to objective function, only membership updating will change. This will result in less computational complexity. Like BFCM, PFCM also gives satisfactory results for low SNR data and it can be applied even for multidimensional input feature data also. But it deals only with noise and it can't reduce the effect of intensity inhomogeneity.

3.3 Spatial Fuzzy C-Means (SFCM)

To overcome the noise effect on the segmentation phase, Chuang *et al.*,[4] used spatial information while updating the membership function in the repetitive FCM algorithm because the neighborhood pixels possess same properties as the centre pixel. In contrast to BCFCM and PFCM, the objective function is not changed in the Spatial FCM (SFCM) instead the membership function is updated twice. The first updation is similar to the conventional FCM but in the second step, a spatial function is defined as sum of the membership values in spatial domain in the entire neighborhood around the pixel under consideration. It is define as

$$h_{ij} = \sum_{k \in N(x_j)} u_{ik} \tag{6}$$

where, $N(x_j)$ is the neighborhood under consideration around x_j. The spatial function is used in updating membership function again given by the equation

$$u_{ij} = \frac{u_{ij}^p h_{ij}^q}{\sum_{k=1}^{c} u_{kj}^p h_{kj}^q} \tag{7}$$

when surrounding pixels belongs to the same cluster as the centre pixel, the membership function will gain larger values. In smooth regions clustering remains unchanged because spatial function will just strengthens the membership function. The correction of misclassified pixels from noisy regions will happen when spatial function decreases the weight of a noisy pixel by considering its neighborhood pixels. The Spatial FCM works well for high as well as low density noise. It can be applied for single and multiple feature data. Compared to other methods; it gives superior results without any boundary leakage even at high density noise, when $\boldsymbol{q}$ value is carefully selected. Parameter (p, q) selection is very crucial in SFCM. High value of $\boldsymbol{q}$ may results in blurring of fine details.

3.4 FCM_S1 & FCM_S2

Chen and Zhang *et al.*,[7] suggested a novelsystem to reduce the computational complexity taken by BCFCM. The noise reduction is taken care by taking the neighborhood information but in contrast to BCFCM, it computes the spatial term prior to the repetitive FCM algorithm. The variations of FCM proposed here are FCM_S1, FCM_S2. The modified cost function is specified as

$$J = \sum_{i=1}^{C} \sum_{k=1}^{N} u_{ik}^m \|x_k - v_i\|^2 + \alpha \sum_{i=1}^{C} \sum_{k=1}^{N} u_{ik}^m \|\bar{x}_k - v_i\|^2 \tag{8}$$

where, $\bar{x}_k$ is mean or median of neighborhood pixels for FCM_S1, FCM_S2, respectively. This algorithm work well in the presence of noise also since it used spatial information also in the cost function. It can be used for multidimensional data. The computational complexity will be less as the spatial term is computed only once.

3.5 Fuzzy Local Information C- Means (FLICM)

The limitations faced by most of the variations of FCM techniques, which are trying to use the spatial information, are due to their dependence on noise density. FLICM algorithm is suggested by Krinidis and Chatzis[5] to overcome the usage of the parameter selection when dealing with segmentation of noisy images. A fuzzy factor G is introduced into the objective function of conventional FCM. G is defined as

$$G_{ki} = \sum_{j=N_i \& i \neq j} \frac{1}{d_{ij}+1} (1 - u_{kj})^m \|x_j - v_k\|^2$$

The objective function of FLICM is given as

$$J = \sum_{i=1}^{N} \sum_{k=1}^{C} u_{ki}^m \|x_i - v_k\|^2 + G_{ki} \tag{9}$$

where, d_{ij} is the spatial Euclidean distance from pixel i to j so pixels near to the center pixel will affect the fuzzy factor most. The objective function looks like a small change to BCFCM but it resulted in better approach. When a centre pixel is a noisy pixel, it will belong to a noisy cluster but the neighborhood forces the noisy pixel to their cluster in order to minimize the objective function. FLICM can be used when the prior knowledge of noise is not available. It is independent of any parameter selection. It can be used for multidimensional data but can't deal with intensity inhomogeneity.

3.6 Multi-dimensional Fuzzy C-Means (MDFCM)

Jamal *et al.*,[6] introduced a new method to reduce the noise effect by using spatial information. The segmentation is carried by considering the multiple features like mean, standard deviation, singular value and intensity of the pixel hence called multi-dimensional FCM. The features used in FLICM are pixel intensity mean, largest singular value of local window with standard deviation. Before the segmentation, instead of using all the features, different combination of features can be formed. The feature set selection depends on the requirement. If accuracy is the constraint, considering all the features gives better results. If computational cost is the criteria, then selection of few important features like, Eigen value, pixel intensity is recommended. In MDFCM by considering the spatial information, in terms of different features, result in improved efficiency compared to most of the variations of FCM. Even with the images, despoiled by high density noise, MDFCM resulted in clear boundaries and noise free clustering. The main disadvantage of this method is computational complexity because of multidimensional data.

3.7 Weighted Image Patch Based FCM (WIPFCM)

A new approach to use the spatial information in FCM process was introduced by ZexuanJi *et al.*,[9]. In this method, image patches are considered instead of just pixels, which add additional information to the data. Weight vectors are assigned to every image patch based on their variance with respect to their neighboring pixels. The expression to carry out this weight assignment is given by

$$\zeta_{kr} = \exp\left[-\left(\sigma_{kr} - \frac{\sum_{r\in N_k}\sigma_{kr}}{n_k}\right)\right] \tag{10}$$

where, $\zeta_{kr}c$ and σ_{kr} represent the weight and variance of r^{th} pixel in k^{th} patch respectively, later it is normalized to make the sum of the weights equal to one. The weight vector assigned here results in removing effect of edges and noisy pixel on clustering process by assigning less weight to them. The objective function for WIPFCM is given by

$$J = \sum_{i=1}^{C}\sum_{k=1}^{N} u_{ik}^{m} \sum_{r\in N_k} w_{kr}\|I_{kr} - v_{ri}\|^2 \tag{11}$$

where, I_k represents the image patch of size $q \times q$ around the pixel, x_k, v_i represents the cluster center of size $q \times q$. In this method noise is handled effectively by utilizing the spatial information. There is no external parameter to be selected like in other methods. This method increase computational burden because each pixel need to be represented by a patch and additional step of calculation of their weights is required.

3.8 Kernel Weighted Fuzzy Local Information C- Means (KWFLICM)

Maoguo Gong *et al.*,[10] proposed kernel weighted variation of FLICM. In this approach they have introduced trade off weights to the pixels and replaced the Euclidean distance with kernel metric based distance. In FLICM a factor is introduced which utilizes spatial distance and Euclidian distance of neighboring pixels from the centre pixels but it fails to analyze the neighboring pixels when the centre pixel itself is noisy. To overcome this disadvantage of FLICM, KWFLICM utilizes more local information by utilizing spatial variance instead of Euclidian distance. The weight

assigning technique is similar to the one used in WIPFCM, here in addition to that, it utilizes spatial distance also and it can be explained by these equations

$$w_{ij} = w_{gc} \cdot w_{sc} \tag{12}$$

$$w_{gc} = \begin{cases} 2 + \beta_{ij}\sigma_j < \bar{\sigma} \\ 2 - \beta_{ij}\sigma_j \geq \bar{\sigma} \end{cases} \tag{13}$$

$$w_{sc} = 1/(d_{ij} + 1) \tag{14}$$

where, β_{ij} is the weight obtained using the formula given in WIPFCM after normalization, w_{gc} is made positive by keeping these conditional statements, $\bar{\sigma}$ is the average variance in the local window. The objective function is given by

$$J = \sum_{i=1}^{N}\sum_{k=1}^{C} u_{ik}^{m}(1 - K(x_i, v_k)) + G'_{ki} \tag{15}$$

and the fuzzy factor G'_{ki} is given by

$$G'_{ki} = \sum_{i=1}^{N}\sum_{k=1}^{C} u_{ik}^{m} \sum_{i\neq j \& j\in N_i} w_{ij}(1 - u_{ki})^m [1 - K(x_i, v_k)] \tag{16}$$

where, N represents the local window around the pixel, $K(x_i, v_k)$ is the kernel based distance measure. The kernel used in this method is Gaussian radial basis function (GRBF). For this Gaussian kernel, the bandwidth parameter is estimated using the variance of the zero-mean input data. It can be expressed by the following relations

$$\sigma = \left(\frac{1}{N-1} \sum_{i=1}^{N} (d_i - \bar{d})^2 \right)^{\frac{1}{2}} \tag{17}$$

$$d_i = \|x_i - \bar{x}\| \tag{18}$$

The kernel distance is obtained by bulging the input data into a high dimensional space by using the kernel. KFLICM is independent of any external parameter selection and it utilizes local information in an effective way by using the spatial variance and spatial positioning. Kernel metric distance used here leads better clustering performance in the presence of image artifacts, noise and outliers.

3.9 Strong FCM

The data given to FCM is projected into a high dimensional space using kernels and distance between the cluster centre and data points is calculated in that domain. It leads to better clustering of complex noised data. This technique is proposed by S. R. Kannan *et al.*,[8]. In this he has proposed two techniques based on this approach and also a new method to initialize the cluster centres to improve the performance of FCM. First FCM technique proposed is **Robust Fuzzy C-means Based Kernel Function (RFCMK)** algorithm. In proposed technique the modified cost function is given by

$$J = 2\sum_{i=1}^{N}\sum_{k=1}^{C} u_{ik}^{m}(\beta - K(x_i, v_k)) \tag{19}$$

and kernel function is expressed as

$$K(x_i, v_k) = -\frac{\|x_i - v_k\|^2}{\alpha} + \beta, \quad \beta > 0 \tag{20}$$

Cost function here is obtained by projecting the data into higher dimensional space by non-linear transformation and it is minimized using the properties of kernel functions. The updating expressions for membership function and cluster centres can be obtained by differentiating the cost function and making it equal to zero using Lagrange multiplier technique as done in the conventional FCM. Second FCM technique proposed is **Tsallis Entropy Based Fuzzzy C-Means (TEFCM)** algorithm. This is an extension to the previous technique, because previous technique cannot distinguish similar intensity objects of different clusters. To overcome this problem an extra term is introduced into the cost function and modified cost function is

$$J = 2\sum_{i=1}^{N}\sum_{k=1}^{C} u_{ik}^{m}\beta K(x_i, v_k) + \frac{\alpha_i}{\gamma - 1}\left(\sum_{i=1}^{N}\sum_{k=1}^{C} u_{ik}^{m} - 1\right) \tag{21}$$

where, $\alpha_i = \frac{n}{\zeta}(x_i + ((n/c)/N_R)\sum_{j\in N_i} x_j)$ is a term which will include data from neighborhood and ζ is a factor which regulates the outcome of neighborhood terms. By including this extra term, spatial information is also included in the objective function, which leads to improved performance. Time consumption is less because neighborhood term is calculated only once and it is utilized in the clustering process.

4. Results

FCM and variants are validated by their performance on real MRI images as well as synthetic images by using cluster validity functions. Two forms of cluster validity functions, fuzzy partition and feature structure, are commonly applied to estimate the efficiency of clustering. The characteristics terms for the fuzzy partition are Partition Coefficient, Vpc[19] and Partition Entropy, Vpe[2]. They are defined as

$$V_{pc} = \frac{\sum_{j=1}^{N}\sum_{i=1}^{C} u_{ij}^{2}}{N} \tag{22}$$

$$V_{pe} = \frac{-\sum_{j=1}^{N}\sum_{i=1}^{C}[u_{ij}\log u_{ij}]}{N} \tag{23}$$

The fuzzy partition validity functions are indication of fuzziness means and partition, with less fuzziness means better performance. As a result, the best clustering is achieved when the value **Vpc is maximal** or **Vpe is minimal**. V_{pc} and V_{pe} measure only the fuzzy partition and lack a direct connection to the featuring property so another validity function, **Vxb**, is also used. It is based on the feature structure and defined as

$$V_{xb} = \frac{-\sum_{j=1}^{N}\sum_{i=1}^{C} u_{ij}\|x_j - v_i\|^2}{N * (\min_{i\neq k}\{\|v_k - v_i\|^2\})} \tag{24}$$

A worthy clustering outcome produces samples that are compressed within one cluster and disconnected between diverse clusters. **Minimizing Vxb** is desired for good clustering. Figure 1 shows the resultant images after applying the various FCM based techniques for MRI image.

By Fig. 1, it is observed that BCFCM successfully removed the noise but it lost some of the edge information giving very smooth edges. PFCM shows good clustering irrespective of noise and contains edge details. FLICM also gave good clustering, which is independent of noise and also doesn't lost edge details. RFCMK is successful in removing noise but mixed two clusters into one cluster. Results of SFCM, FCM_S1 & S2, MDFCM, KWFLICM, TEFCM and WIPFCM contain a little noise in the clustered image but remains edge information. The performance of the discussed methods is evaluated in terms of the parameters Vpc, Vpe, Vpx and time complexity (time taken by these methods). The values of these parameters for real MRI image are shown in Fig. 2 to 5. In these Figs, X-axis represents performance in the presence of different noise densities.

The performance of FCM and variants is evaluated in terms of Segmentation Accuracy (SA) for synthetic image corrupted by Gaussian noise (For noise density, $\sigma = 0$ to 0.1). The values of SA are shown in Table 1 and SA is defined as[2]

$$\text{SA} = \frac{\text{Number of Correctly Classified Pixels}}{\text{Total Number of Pixels}}$$

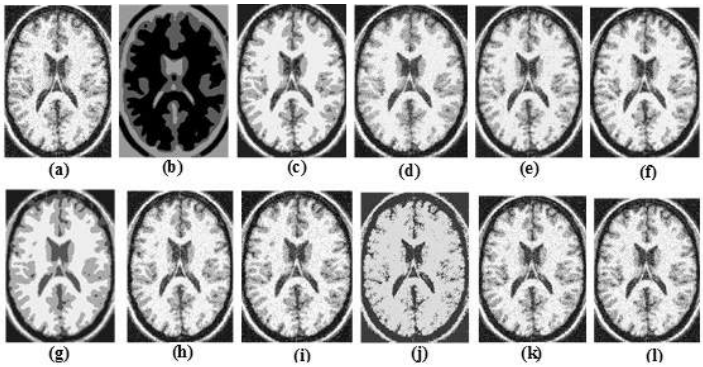

Fig. 1. (a) MRI Image with Gaussian Noise Density $\sigma = 0.03$ and K Value (no of clusters) $= 4$, De-Noised Images using; (b) BCFCM; (c) PFCM; (d) SFCM; (e) FCM_S1; (f) FCM_S2; (g) FLICM; (h) MDFCM; (i) KWFLICM; (j) RFCMK; (k) TEFCM and (l) WIPCM.

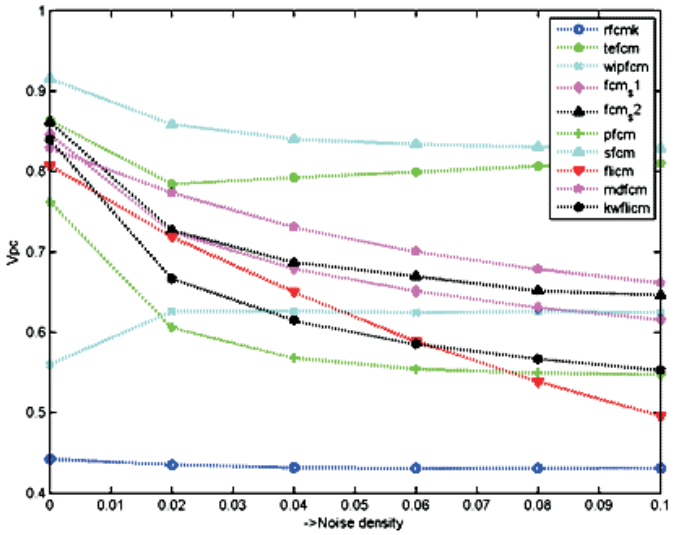

Fig. 2. Comparison of Various FCM based Techniques based on V_{pc}.

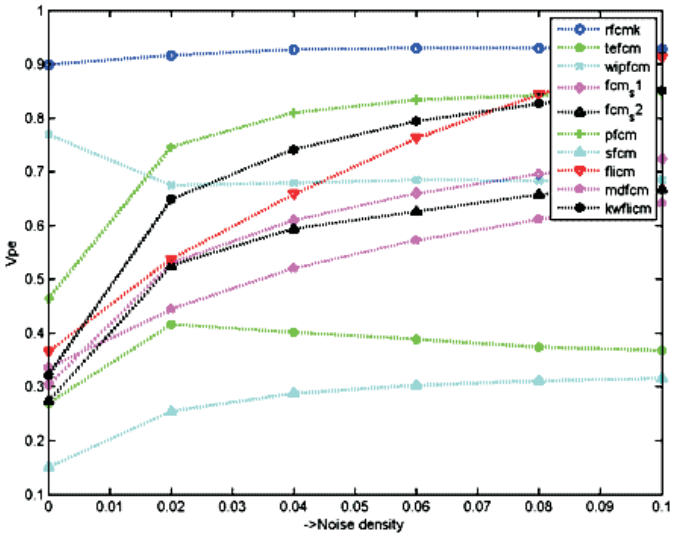

Fig. 3. Comparison of Various FCM based Techniques based on V_{pe}.

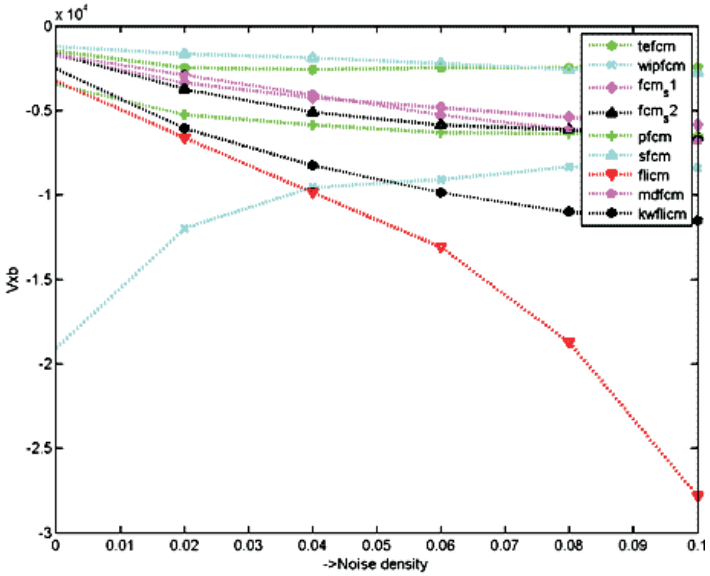

Fig. 4. Comparison of Various FCM based Techniques based on V_{xb}.

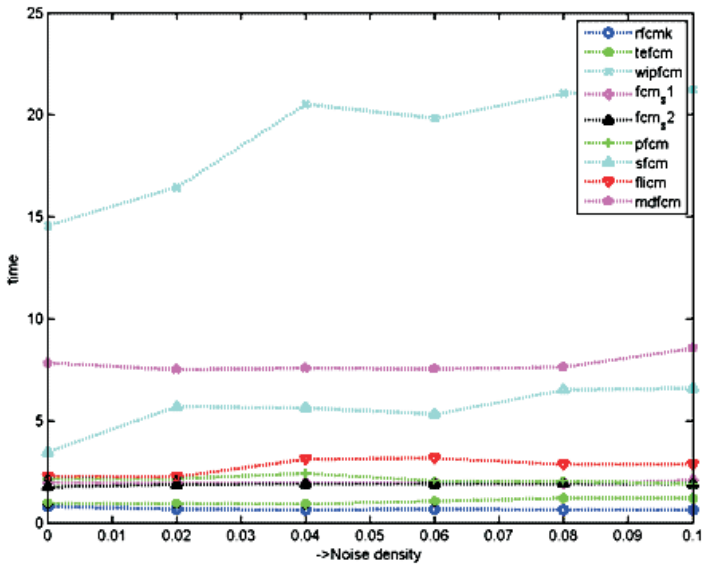

Fig. 5. Time Complexity (in seconds) of Various FCM based Techniques.

Table 1. 1SA for Synthetic Image Corrupted by Gaussian Noise.

	Noise density					
Method	0	0.02	0.04	0.06	0.08	0.10
RFCMK	100	92.90	84.12	78.06	73.93	70.53
TEFCM	100	92.84	84.26	78.27	73.91	70.43
WIPFCM	100	99.65	99.37	98.47	97.43	95.91
FCM	100	92.83	84.17	78.15	74.02	70.49
FCM−S1	100	98.73	94.31	89.76	85.72	82.27
FCM_S2	99.99	99.01	95.36	90.94	87.33	84.04
PFCM	100	100	99.95	99.72	98.88	97.62
SFCM	100	99.78	99.41	99.41	98.38	91.11
FLICM	99.55	99.54	99.52	99.50	99.42	99.28
MDFCM	99.77	99.74	99.18	97.91	96.43	95.05
KWFLICM	100	96.70	89.90	83.98	79.51	75.78

5. Conclusions

High value of Partition Coefficient (Vpc) implies better performance since it is calculated on the basis of membership values and high membership value for a single cluster implies better clustering. Similarly low value of Partition Entropy (Vpe) implies better clustering. SFCM, TEFCM and MDFCM resulted in high Vpc and low Vpe values. Low value of Vxb represents better clustering since it is computed by taking the difference between data and cluster prototypes and more number of good clustered samples implies that sum of their difference will be less so it will results in lesser value of Vxb. When considering Vxb, RFCMK gives best result and WIPFCM, MDFCM, KWFLICM give good results. When it comes to time complexity, RFCMK, TEFCM, FCM_S1 & S2 gain advantage. All the methods leading to good SA, when applied on image without noise but when the image is corrupted by noise, FLICM gives results with consistent accuracy, followed by PFCM, WIPFCM and MDFCM.

References

[1] L. O. Hall, A. M. Bensaid, L. P. Clarke, R. P. Velthuizen, M. S. Silbiger, J. Bezdek, A Comparison of Neural Network and Fuzzy Clustering Techniques in Segmenting Magnetic Resonance Images of the Brain, *IEEE Transaction Neural Network*, vol. 3, pp. 672–682, (1992).

[2] Mohamed N. Ahmed, Sameh M. Yamany, Nevin Mohamed, Aly A. Farag and Thomas Moriarty, A Modified Fuzzy C-Means Algorithm for Bias Field Estimation and Segmentation of MRI Data, *IEEE Transition of Medical Imaging*, vol. 21(3), March (2002).

[3] Y. Yang, Ch. Zheng and P. Lin, Fuzzy C-Means Clustering Algorithm with a Novel Penalty Term for Image Aegmentation, *Opto-Electronics Review*, vol. 13(4), pp. 309–315, (2001).

[4] Keh-Shih Chuang, Hong-Long Tzeng, Sharon Chen, Jay Wu and Tzong-JerChen, Fuzzy C-Means Clustering with Spatial Information for Image Segmentation, *Journal of Computerized Medical Imaging and Graphics*, vol. 30, pp. 9–15, (2006).

[5] Stelios Krinidis and Vassilios Chatzis, A Robust Fuzzy Local Information C-Means Clustering Algorithm, *IEEE Transaction on Image Processing*, vol. 19(5), May (2010).

[6] Jamal Ghasemi, Reza Ghaderi, Mohamad Reza Karamimollaei and Ali Hojjatoleslami, Separation of Brain Tissues in MRI based on Multi-Dimensional FCM and Spatial Information, *Eighth International Conference on Fuzzy Systems and Knowledge Discovery (FSKD)*, (2011).

[7] Songcan Chen and DaoqiangZhang, Robust Image Segmentation using FCM with Spatial Constraints Based on New Kernel-Induced Distance Measure, *IEEE Transactionon Systems*, Man and Cybernetics-Part B, vol. 34(4), August (2004).

[8] S. R. Kannana, S. Ramathilagamb, R. Devia and E. Hinesc, Strong Fuzzy C-Means in Medical Image Data Analysis, *The Journal of Systems and Software*, pp. 2425–2438, (2012).

[9] A. Zexuan Ji, Yong Xiab, Qiang Chena, QuansenSuna, Deshen Xiaa and David Dagan Feng, Fuzzy C-Means Clustering with Weighted Image Patch for Image Segmentation, *Applied Soft Computing*, vol. 12, pp. 1659–1667, (2012).

[10] Maoguo Gong, Member, Yan Liang, Jiao Shi, Wenping Ma and JingjingMa, Fuzzy C-Means Clustering With Local Information and Kernel Metric for Image Segmentation, *IEEE Transaction on Image Processing*, vol. 22(2), February (2013).

[11] Kai Xiao, Sooi Hock Ho and AndrzejBargiela, Automatic Brain MRI Segmentation Scheme Based on Feature Weighting Factors Selection on Fuzzy C-Means Clustering Algorithms with Gaussian Smoothing, *International Journal of Computer Intelligence in Bioinformatics and Systems Biology*, vol. 1(3), (2010).

[12] Dzung L. Pham and Jerry L. Prince, An Adaptive Fuzzy C-Means Algorithm for Image Segmentation in the Presence of Intensity Imhomogeneities, *Pattern Recognition Letter*, vol. 20, pp. 57–68.

[13] L. Szilagyi, Z. Benyol, S. M. Szilagy and H. S. Adam, MR Brain Image Segmentation using an Enhanced Fuzzy C-Means Algorithm, *Proceedings of the 25th Annual International Conference of the IEEE EMBS Cancun*, Mexico, pp. 17–21, September (2003).

[14] Jingjing Song, Qingjie Zhao, Yuanquan Wang and JieTian, Gain Field Correction Fast Fuzzy C-Means Algorithm for Segmenting Magnetic Resonance Images, *PRICAI 2006, LNAI 4099*, pp. 1242–1247, (2006).

[15] Abbas Biniaz1 and Ataollah Abbassi, Medical Image Segmentation with FCM Based on Gaussian Spatial Neighborhood Information.

[16] Shan Shen, William Sandham, Member, Malcolm Granat and Annette Sterr, MRI Fuzzy Segmentation of Brain Tissue using Neighborhood Attraction with Neural-Network Optimization, *IEEE Transaction on Information Technology in Biomedicine*, vol. 9(3), September (2005).

[17] Bing Nan Li, Chee Kong Chui, Stephen Chang and S. H. Ong, Integrating Spatial Fuzzy Clustering with Level Set Methods for Automated Medical Image Segmentation, *Computers in Biology and Medicine*, vol. 41, pp. 1–10, (2011).

[18] S. Zulaikha Beevi, M. Mohammed Sathik and K. Senthamaraikannan, A Robust Fuzzy Clustering Technique with Spatial Neighborhood Information for Effective Medical Image Segmentation, *International Journal of Computer Science and Information Security*, vol. 7(3), March (2010).

[19] J. C. Bezdek, Cluster Validity with Fuzzy Sets, *J Cybern*, vol. 3, pp. 5–73, (1974).

[20] JC. Bezdek, Mathematical Models for Systematic and Taxonomy, *Eight International Conference on Numerical Taxonomy*, San Francisc; pp. 14–66, (1975).

[21] Jagadish H. Pujar, Pallavi S. Gurjal, D. S. Shambhavi and Kiran S. Kunnur, Medical Image Segmentation based on Vigorous Smoothing and Edge Detection Ideology, *International Journal of Electrical and Computer Engineering*, vol. 5, pp. 2, (2010).

Author's Accepted Manuscript

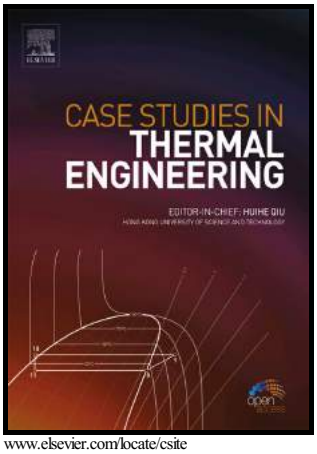

www.elsevier.com/locate/csite

Performance and Emission Characteristics of a Transportation Diesel Engine operated with Non-Edible Vegetable oils Biodiesel

Ashok Kumar Yadav, Mohd Emran Khan, Alok Manas Dubey, Amit Pal

PII: S2214-157X(16)30073-9
DOI: http://dx.doi.org/10.1016/j.csite.2016.08.001
Reference: CSITE139

To appear in: *Case Studies in Thermal Engineering*

Received date: 12 April 2016
Revised date: 1 August 2016
Accepted date: 1 August 2016

Cite this article as: Ashok Kumar Yadav, Mohd Emran Khan, Alok Manas Dubey and Amit Pal, Performance and Emission Characteristics of a Transportation Diesel Engine operated with Non-Edible Vegetable oils Biodiesel *Case Studies in Thermal Engineering* http://dx.doi.org/10.1016/j.csite.2016.08.001

This is a PDF file of an unedited manuscript that has been accepted for publication. As a service to our customers we are providing this early version of the manuscript. The manuscript will undergo copyediting, typesetting, and review of the resulting galley proof before it is published in its final citable form. Please note that during the production process errors may be discovered which could affect the content, and all legal disclaimers that apply to the journal pertain.

ACCEPTED MANUSCRIPT

Performance and Emission Characteristics of a Transportation Diesel Engine operated with Non-Edible Vegetable oils Biodiesel

[1] Ashok Kumar Yadav[*], [2] Mohd Emran Khan, [3]Alok Manas Dubey [4]Amit Pal

[1]Assistant Professor, Department of Mechanical Engineering, Raj Kumar Goel Institute of Technology, Ghaziabad, 201003, India

[2] Professor, Department of Mechanical Engineering, Faculty of Engineering & Technology, Jamia Millia Islamia, New Delhi – 110025, India

[3]Professor, Department of Mechanical Engineering, Raj Kumar Goel Institute of Technology, Ghaziabad, 201003, India

[4]Associate Professor, Department of Mechanical Engineering, Delhi Technological University, Delhi 110042, India

[*]Corresponding author ; Email: ashokme014@gmail.com

: mikhan@jmi.ac.in

: alokmanas28@rediffmail.com

Abstract

In this study, production, performance and emission characteristics of methyl esters of Oleander, Kusum and Bitter Groundnut oil in a transportation diesel engine were studied. Oleander oil methyl esters (OOME), Kusum oil methyl esters (KOME), and bitter Groundnut Oil Methyl Esters (BGOME) were prepared by transesterification process. The effects of three methyl esters on engine performance and exhaust emissions were examined at different engine speed and full load condition. Experimental results showed that the brake thermal efficiency of OOME is found higher and brake specific fuel consumption lower compared to KOME and BGOME. BGOME shows less emissions compared to OOME and KOME. In short, it may be concluded from the experimental investigations that biodiesel from different non-edible oils (Oleander, Kusum, and Bitter Groundnut) can become an alternative source of fuel in the future.

Keywords: Non-Edible Oils; Biodiesel; Diesel Engine; Performance & Emissions.

1. Introduction

Many reports project that India will double its fuel consumption by 2030 (Hebbal et al., 2006). Biodiesel from non-edible vegetable oils appears to be an attractive source of energy in India. Currently, more than 95% of the world biodiesel is produced from edible vegetable oils such as rapeseed, soybean,

ACCEPTED MANUSCRIPT

palm and sunflower oils (Likozarand Levec, 2014). Biodiesel production on a large scale is a cause of concern due to food vs. fuel competition in the long term (Chhetri et al. 2008). Therefore the use of non-edible vegetable oils like Karanja, Mahua, Kusum, Oleander and Calophyllum inophyllum oil (Silitonga etal. 2015, Dhar and Agarwal 2014, Raheman and Ghadge 2007, Ong et. al. 2014) can not only can skip the food vs. fuel concerns, but also decrease the final biodiesel cost.

Significant research work has been reported with regards to the production, and performance of biodiesel derived from a variety of vegetable oils. Dharand Agarwal, 2014, reported maximum torque for 10% and 20% KOME blends which were higher than mineral diesel. Similarly, Rahemanand Ghadge, 2007, found the comparable performance of Mahua biodiesel and its blends with petroleum-based diesel. Ong et al. 2014, reported an optimum yield of C. inophyllum biodiesel at 9:1 methanol to oil ratio with 1% wt. NaOH catalyst at 50^{o}C for 2h. The performance and emission of 10% C. inophyllum biodiesel blends (CIB10) gave a satisfactory result in diesel engines. Khiari et al. 2016, reported a maximum increase of 3.1% at full engine load condition for pistacialentiscus biodiesel. Carbon monoxide and unburned hydrocarbon are significantly reduced whereas, higher NOx levels.

Yadav et al. 2015, studied engine performance with used transformer oil and reported that the retarded injection timing of 20^{o} before TDC resulted in decreased oxides of nitrogen, carbon monoxide and unburned hydrocarbon by 11.57%, 17.24%, and 10% respectively while the brake thermal efficiency and smoke increased under all the load conditions when compared to that of standard injection timing. Yang et al. 2013 and Sharon et al. 2012 carried out the investigations on diesel engine with methyl esters of Jatropha and used cooking oil as fuels. The efficiencies with the above said two biodiesels are lower than that of diesel fuels. Utlua and Kocak (2008) conducted an experimental study on a four cylinder, direct injection, turbocharged, intercooled diesel engine using waste frying oil methyl ester and reported that the brake specific fuel consumption was 14.34% higher than that of diesel fuel. They concluded that the low heating value and the higher density of waste frying oil methyl ester were responsible for the increased fuel consumption rate.

Puhanetal. 2009 noted a slight decrease in brake thermal efficiency with linseed biodiesel compared to mineral diesel. Linetal. 2009 observed that when fueled with various vegetable oil methyl esters; the smoke emission from the engine was reduced compared to petroleum diesel, due to the uniform air–fuel mixing and the extra oxygen content in vegetable oil. J. Kakati and T.K. Gogoi (2016) reported that Kutkura fruit seed contains 35.45% oil with 3.1% FFA. Engine BTE and ITE were higher

Accepted manuscript

ACCEPTED MANUSCRIPT

with the biodiesel blends and it was the maximum for B20 at all BMEPs. B10 and B20 produce less smoke compared to diesel fuel and the smoke was the minimum with B10.

It is found that there are about 300 varieties of oil seeds but only 10-15 varieties have been tapped so far, amongst which “Oleander”, “Bitter Groundnut” and “Kusum”, the non-edible vegetable oils can be considered as a potential alternative fuel for CI engines. These have been chosen in the present study to explore their possibility for use as fuel because no substantial work has been done on utilization of these oils as a fuel for CI engine. From literature review it is also found that many researchers have done work on edible oils or very costly oils. The higher price, in many countries is offset by legislative and regulatory incentives or subsidies in the form of reduced excise taxes. However, the higher price can also be (partially) offset by the use of less expensive feed stocks, which has sparked interest in oils such as “Oleander”, “Bitter Groundnut” and “Kusum”.

In India, diesel costs are about Rs.45 per liter. But in India, petro- diesel is a highly subsidized fuel due to its vast use in agriculture. If there were no subsidies given to diesel by the Government of India, the price of diesel would have jumped over the price of even petrol, which is around Rs.80 per liter now-a-days. On the other hand the cost of Oleander, bitter Groundnut and Kusum oil is less because they are generally treated as waste in India. This waste can be collected and oil is extracted at a very low cost. Biodiesel is then prepared and blended with petrol diesel, thus reducing the price of the fuel to about Rs.50 per liter.

From the literature it is found that most of the test have been done on stationary diesel engines (Khiari et al. 2016; Hebbal et al. 2006; lin et al 2009; Sharon et al. 202; Atabani et al. 203;Puhan et al 2009; Raheman et al 2007; Datta and mandal2016;Avinash Kumar Agarwal, 2007; Kakati, J. and Gogoi, T.K 2016.).Stationary diesel engine is usually designed for optimum/constant speed as the load in such case is usually fixed. Stationary engines are used largely in rural areas for irrigation. Very less work has been done on "Transportation Engine"(Dhar et al. 2014 and Chuah et al. 2015). In transportation engine the loads vary w.r.t. loading condition of the vehicle. Loading of vehicle may be fully loaded/half loaded or move empty. To achieve the variation of power required the speed of a transport engine has to be varied. So the present investigation focuses on the experimental study on Transportation Engine.

Oleander is a very drought resistant poisonous plant found throughout India especially in Assam. An Oleander plant produces, more than 400 -800 fruits annually (Fig 1a). The plant has annual seed yield of 52.5 t/ha and about 1750 L of oil can be obtained from a hectare of waste land. It has high oil content which is around 60% in its kernel (Atabani and Silitonga, 2013). Hence, it can be used to

ACCEPTED MANUSCRIPT

produce bio-diesel on large scale. India ranks second in Groundnut production in the world next to China. It produces an average 3, 00,000 tonnes of groundnut oil every year. Out of this, approximately 10 % could not be utilized due to its bitterness and is generally treated as waste, which is can be used as novel feedstock for biodiesel production.The production of Kusumseed (Fig1c) is 66000 tonnes per year in India. It is mainly produced in sub-Himalayan tracts in the north, central parts of eastern India. It contains about 51%–62 % oil (Silitonga et al., 2015).The objective of the present study is to investigate performance and emission characteristics of a transportation engine operated with biodiesel derived from Oleander, Kusum and bitter Groundnut oil.

2. Materials and method

2.1 Materials

The Oleanderand Kusum seed used in the present study for biodiesel production were collected from their plants available on the campus of Delhi technological university and bitter Groundnut collected from an oil mill available locally. Oil from the seeds was obtained by means of mechanical extraction. Anhydrous methanol (99.8% min.) and Potassium hydroxide (85% min.) were purchased from a local chemical store.

2.2 Production and Characterization of Biodiesel

Chemical transesterification of Oleander/Kusum/bitter Groundnut oil was done, to produce their methyl esters (biodiesel) and physico-chemical properties of the all the three biodiesel samples were evaluated experimentally and compared with that of base diesel.

2.3 Experimental Engine Setup

The setup consists of four cylinders, four stroke Diesel engine connected to eddy current type dynamometer for loading. Provision is also made for interfacing airflow, fuel flow, temperatures and load measurement. The setup has stand-alone panel box consisting of air box, fuel tank, manometer, fuel measuring unit, transmitters for air and fuel flow measurements, process indicator and engine indicator. Rotameters are provided for cooling water and calorimeter water flow measurement.Windows-based engine performance analysis software package “Engine soft” is used for on-line performance evaluation. An AVL DIX Emission diagnostic system was used for engine exhaust measurement. Specification of test engine and Emission diagnostic system is shown in table 1and table 2 with present range, accuracy and uncertainty of measurements.

Accepted manuscript

ACCEPTED MANUSCRIPT

3. Results and discussion

3.1Physico-chemical properties

Physico-chemical properties of different biodiesel and diesel fuel are presented in table 3.

3.2 Fatty acid composition

Fatty acid composition of different oil used in this work were determined by Gas chromatography (GC) analysis, in Intertek India Pvt. Ltd. Chemical Testing Lab (Food Services), and shown in table 4.

3.3Engine Performance

Figures 3 to 4 show the percentage change in the performance parameters with respect to engine speed considering diesel as a baseline. All observations are taken in the speed range of 1500 to 5000 rpm with an increment of 500 rpm. Brake thermal efficiency is a vital engine performance parameter. It is the ratio of mechanical work obtained at the engine shaft and the total energy supplied by the injected fuel, which is the product of fuel heating value and mass flow rate (Lapuerta et al 2008).The variation of the engine BTE obtained for all the tested biodiesels and diesel fuel with respect to engine speed is shown in Fig. 3.For all biodiesels brake thermal efficiency is lower as compared to pure diesel over the entire range of engine speed at full load. This was attributed to increased brake power and reduced wall heat losses at higher engine loads (Chauhan et. al.2012). The BTE in general, was found to decrease with increased volume fraction of biodiesel in the blends. This is due to a number of factors like lower heating value, higher viscosity and density of the biodiesel resulting in poor atomization/vaporization, and increased fuel consumption. Among the tested biodiesels, KOME showed the least BTE (19.7%), while OOME the maximum efficiency (20.20%) at a speed of 2900 rpm. compared to diesel (22.5%). Further increase in rpm decreases the brake thermal efficiency for a wide range of engine rpm.These results are supported by literature (Hirkude & Padalkar, 2012; Lapuerta et al., 2008; Nabi et al., 2009 ; Dharand Agarwal, 2014, Ong et al. 2104 ,Kakati and. Gogoi, 2016).

The BSFC of diesel engine depends mainly on the relationship between fuel density, viscosity and energy content (Qi, Chen, Geng, & Bian, 2010).The variation of brake specific fuel consumption for OOME, KOME and BGOME compared to diesel fuel is shown in figure 4. The BSFC initially decreases sharply with an increase in rpm up to 2900 and then increases suddenly with an increase in speed. The BSFC for all biodiesels and pure diesel is least at 2900 rpm. OOME, however, showed less brake specific fuel consumption compared to KOME and BGOME. The brake specific fuel consumption values were 0.314 ,0.331 and0.345 kg/kWh for OOME, BGOME, and KOME, respectively, and with

ACCEPTED MANUSCRIPT

diesel fuel, it was 0.221 kg/kWh at a speed of 2900 rpm. Similar trends of BSFC with different biodiesel blends were also reported by other researchers (Dhar and Agarwal, 2014, Ong et.al. 2104).The reason for the higher BSFC of biodiesels blends is mainly due to the higher density and lower energy content of biodiesel-diesel blends (Mofijur et al., 2013). Any fuel is delivered to the engine on a volumetric basis. For the same fuel volume, an increase in fuel density would imply a larger mass flow rate to the cylinders and this would increase the BSFC to produce the same power (Tsolakis et al., 2007). KOME showed least brake thermal efficiency (19.7%) compared to OOME and BGOME due to high viscosity and low volatility. The biodiesels exhibited more brake specific fuel consumption compared to diesel fuel, as calorific value is less hence, more fuel is needed for the same power output. At higher speed beyond 2900 rpm, BSFC goes on increasing for all tested fuels.

3.4 Engine emissions

Fig 5 to 8 shows emission characteristics of different biodiesels and diesel at different engine speed. The amount of CO produced by using diesel, OOME, KOME, and BGOME is shown in Figure 5.Carbon monoxide (CO) is a toxic gas formed due to the incomplete combustion of any fuel which does not contain oxygen. Several factors such as engine speed, air-fuel ratio, injection pressure, injection timing and type of fuel used have an effect on CO emission.A similar trend was found for CO in biodiesel blends and diesel fuel, which steeply decreased as the engine speed increased from 1,500 rpm to 2,900 rpm and then increases up to 5000rpm. It was noticed that CO emissions of diesel fuel are higher than all the biodiesel fuels at all speed of the engine. This was due to biodiesel containing more oxygen element, which gave better combustion.Therefore, as the percentage of biodiesel increases in the blend, the higher oxygen contents of biodiesel allow more carbon molecules to burn and combustion is completed. Moreover, low aromatics in the blends may be an additional reason for reducing CO emission.Onget.al. 2104 claimed that there was lower CO emission during combustion using biodiesel as compared to the diesel fuel. OOME, on the other hand, exhibited higher CO emissions compared to KOME and BGOME at maximum speed (5000 rpm), due to incomplete combustion. CO emissions of diesel, OOME, KOME, and BGOME were 0.19, 0.15, 0.14, and 0.13 % at rated speed.

Figure 6 shows a variation of HC emissions for OOME, KOME, BGOME and diesel with engine speed. The HC emissions were less compared to diesel fuel at all speeds. For efficient combustion of a fuel, the fuel has to atomize, mix with air and ignite properly. Atomization and mixing of fuel depends on the physical property of the fuel. Viscosity and surface tension affect the penetration rate, maximum

Accepted manuscript

ACCEPTED MANUSCRIPT

penetration and droplet size of the fuel. Cetane number of the fuel plays a vital role in ignition process. As cetane number of biodiesel is higher than diesel, it exhibits a shorter ignition delay period and permits the fuel for better combustion. The oxygen content of biodiesel enhances the combustion process. Therefore the net result of oxygen content and cetane number of the biodiesel is low HC emission compared to diesel. The lowest UHC emission was observed for BGOME. The HC emission increases as speed increases for all tested fuels. The decreased trend of HC emission for all biodiesel fuel compared to diesel might be due to the presence of oxygen molecules in the biodiesels that helped for complete combustion (Chuah et al., 2015).

Among the tested biodiesels, the HC emissions were 70, 60 and 55 ppm for OOME, KOME and BGOME, respectively, compared to a value of 100 ppm for diesel at maximum speed. This is in line with the findings reported by many other researchers (Ong et.al. 2104, Chuah et. al., 2015) while fueling diesel engines with different biodiesels. The variation of nitrogen oxides (NOx) emissions w.r.t engine speed is shown in Figure 7.The presence of oxygen in biodiesel blends caused higher NOx formation and it is indicated that exhaust gas temperature was increased as well (Celikten et al 2012). Furthermore, Ozsezen and Canakci (2011) mentioned that the oxygen content is affected in NOx formation due to high exhaust gas temperatures caused excess hydrocarbon oxidation. Lin et al. (2009) observed that higher EGT leads to increase in NOx emission. In general, NOx formation depends on temperature and presence of oxygen (Avinash Kumar Agarwal 2007).It was observed that NOx emissions were higher for all biodiesels, compared to diesel fuel . NOx emissions were 1923, 1887, and 1750 ppm for BGOME, KOME and OOME and respectively, compared to a value of 1532 ppm for diesel. Similar results are reported by previous researchers (Dhar and Agarwal, 2014, Chuah et. al., 2015).

Smoke opacity is a measure of soot content in the exhaust gases. Figure 8 shows the variation of opacity vs. speed for OOME, KOME and BGOME in comparison to pure diesel. It was observed that smoke opacity for OOME, KOME and BGOME was 28.2 %, 27.3% and 25.9 respectively at 2900 rpm. However, the highest smoke opacity was found 35.3% for diesel fuel at the same speed. The trend regarding the variation of opacity with respect to speed is almost similar for all type of fuels. However, the highest smoke opacity was 41.4% for diesel fuel at 5000rpm.The BGOME has lower smoke opacity than diesel because of the oxygen content present in biodiesel fuel (Datta and Mandal 2016).This is agreed by Raheman and Ghadge, (2007) who reported that smoke emissions for biodiesel blends decreased due to increase of oxygen content in the fuel. Moreover, many researchers were agree that the higher oxygen content in biodiesel reduces smoke opacity (Chattopadhyay and Sen .2013; Panwaret.al

ACCEPTED MANUSCRIPT

2010). Another reason of smoke emissions reduction for biodiesel is the lower carbon to hydrogen ratio and absence of aromatics compounds. The lower carbon and higher oxygen content decrease the tendency of fuel for soot production and thus reduce smoke opacity (2010). It was agreed by Gumus and Kasifoglu (2010) that biodiesel rich in oxygen can decrease smoke formation. On the other hand, Zhang et al. (2008) observed that start of combustion for biodiesel blends is earlier than diesel. The early start of combustion for biodiesel blends and advanced injection timing can reduce the smoke emission. On other hand, high smoke opacity of diesel fuel was due to higher sulfur content compared to biodiesel (Usta N.2005).

4. Conclusions

Biodiesels were produced by chemical transesterification method and different properties of biodiesel were determined. The performance and emission characteristics were studied for a transportation engine. The biodiesels, such as oleander oil (OOME), Kusum oil (KOME) and bitter Groundnut oil (BGOME), show poor performance compared to diesel fuel. The CO, HC emissions and smoke opacity of OOME, KOME, and BGOME were found to be slightly less than that of the diesel fuel. The NOx emissions were slightly more than that of the diesel. Overall engine operation with all three biodiesels (OOME, KOME, and BGOME) was smooth. All tested biodiesels (OOME, KOME, and BGOME) exhibited reduced brake thermal efficiency and exhaust emissions (CO and HC and smoke opacity) except NOx emissions. The engine could be operated with these biodiesels without major modifications.

Accepted manuscript

ACCEPTED MANUSCRIPT

5. References

Agarwal, A. K., 2007. Biofuels (alcohols and biodiesel) applications as fuels for internal combustion engines. Progress in Energy and Combustion Science, 33: 233-271.

Agarwal, Avinash Kumar. Biofuels (alcohols and biodiesel) applications as fuels for internal combustion engines, Progress in Energy and Combustion Science 33 (2007) 233–271.

An H, Yang W M, Maghbouli A, Li J, Chou S K, Chua K J. Performance, combustion and emission characteristics of biodiesel derived from waste cooking oils. Appl Energy2013;112:493–9.

Atabani, A.E. and Silitonga, A.S., 2013. Non-edible vegetable oils: a critical evaluation of oil extraction fatty acid compositions, biodiesel production, characteristics, engine performance and emissions production. Renewable Sustainable Energy Review. 18:211-245

Celikten I, Mutlu E, Solmaz H. Variation of performance and emission characteristics of a diesel engine fueled with diesel, rapeseed oil and hazelnut oil methyl ester blends. Renew Energy 2012;48: 122–6.

Chattopadhyay S, Sen R. Fuel properties, engine performance and environmental benefits of biodiesel produced by a green process. Appl Energy 2013;105:319–26.

Chauhan B.S, Kumar N, Cho HM. A study on the performance and emission of a diesel engine fuelled with Jatropha biodiesel oil and its blends. Energy 2012;37:616–22.

Chhetri A. B., Tango M. S., Budge S. M., Watts K. C. and Islam M. R. 2008. Non-edible plant oils as new sources for biodiesel production. International Journal of Molecular Science. 9: 169–180.

Chuah, L. F., Rashid, A., Aziz, A.,Yusu, S., Bokhari, A., Jarom, J., and Abdullah, K. Z. 2015. Performance and emission of diesel engine fuelled by waste cooking oil methyl ester derived from palm oil using hydrodynamic cavitation. Clean Technology Environment Policy. 15: 957-2

Datta , Ambarish. , Mandal Bijan Kumar, A comprehensive review of biodiesel as an alternative fuel for compression ignition engine, Renewable and Sustainable Energy Reviews 57(2016)799–821

Dhar A and Agarwal AK. 2014. Performance, emissions and combustion characteristics of Karanja biodiesel in a transportation engine. Fuel. 119: 70–80.

Accepted manuscript

ACCEPTED MANUSCRIPT

Gumus M, Kasifoglu S. Performance and emission evaluation of a compression ignition engine using a biodiesel (apricot seed kernel oil methyl ester) and its blends with diesel fuel. Biomass Bioenergy 2010;34:134–9.

Hebbal, O. D., Reddy V. K. and Rajagopal, K. 2006. Performance characteristics of a diesel engine with deccan hemp oil. Fuel. 85:2187–2194.

Hirkude, J. B., & Padalkar, A. S. (2012). Performance and emission analysis of a compression ignition: Engine operated on waste fried oil methyl esters. *Applied Energy, 90*(1), 68-72.

Kakati, J. Gogoi, T.K., Biodiesel production from Kutkura (Meyna spinosa Roxb. Ex.) fruit seedoil: Its characterization and engine performance evaluation with 10% and 20% blends, Energy Conversion and Management 121 (2016) 152–161

Khiari ,K., Awad , S. , Loubar ,k. , Tarabe, L. , Mahmoud ,R , Tazerout ,M. , experimental investigation of pistacia lentiscus biodiesel as a fuel For direct injection diesel engine, energy conversion and management 108 (2016) 392–399

Lapuerta M, Jose OA, Ferna´ndez R. Effect of biodiesel fuels on diesel engine emissions.Progr Energy Combust Sci 2008;34:198–223.

Likozar B and Levec J. 2014. Transesterification of canola, palm, peanut, soybean and sunflower oil with methanol, ethanol, isopropanol, butanol and tert-butanol to biodiesel: modelling of chemical equilibrium, reaction kinetics and mass transfer based on fatty acid composition. Applied Energy. 123:108–120.

Lin B F, Huang J H, Huang DY. Experimental study of the effects of vegetable oil methyl ester on DI diesel engine performance characteristics and pollutant emissions. Fuel 2009; 88: 1779–85.

Maleki, E, Aroua M.K. and Sulaiman, N. M. N. 2013. Improved yield of solvent free enzymatic methanolysis of palm and jatropha oils blended with castor oil. Applied Energy. 104: 905–909.

Mofijur, M., Masjuki, H. H., Kalam, M. A., & Atabani, A. E. (2013). Evaluation of biodiesel blending, engine performance and emissions characteristics of Jatropha curcas methyl ester: Malaysian perspective. *Energy, 55*(15), 879-887.

Nabi, M. N., Hoque, S. M. N., & Akhter, M. S. (2009). Karanja (Pongamia Pinnata) biodiesel production in Bangladesh, characterization of karanja biodiesel and its effect on diesel emissions. *Fuel Processing Technology, 90*(9), 1080-1086.

Ong, H. C., Masjuki H.H. , Mahlia T.M.I. , Silitonga A.S. , Chong W.T. and Leong K.Y. 2014. Optimization of biodiesel production and engine performance from high free fatty acid

Accepted manuscript

ACCEPTED MANUSCRIPT

Calophyllum inophyllum oil in CI diesel engine, Energy Conversion and Management. 81: 30–40.

Ozsezen AN, Canakci M. Determination of performance and combustion characteristics of a diesel engine fueled with canola and waste palm oil methyl esters. Energy Convers Manage 2011;52:108–16.

Panwar NL, Shrirame HY, Rathore NS, Jindal S, Kurchania AK. Performance evaluation of a diesel engine fueled with methyl ester of castor seed oil. Appl Therm Eng 2010;30:245–9

Puhan S, Jegan R, Bala subbramanian K, Nagarajan G. Effect of injection pressure on performance, emission and combustion characteristics of high linolenic linseed oil methyl ester in a DI diesel engine. Renew Energy 2009;34: 1227–33.

Qi, D. H., Chen, H., Geng, L. M., & Bian, Y. Z. (2010). Experimental studies on the combustion characteristics and performance of a direct injection engine fueled with biodiesel/diesel blends. Energy Conversion and Management, 51(12), 2985-2992.

Raheman H. and Ghadge S. V. 2007. Performance of compression ignition engine with mahua (Madhuca indica) biodiesel. Fuel. 86: 2568–2573.

Sharon H, Karuppasamy K, Kumar D R S, Sundaresan A. Ateston DI diesel engine fueled with methyl esters of used palm oil. Renew Energy 2012;47:160–6.

Silitonga , A.S., Masjuki, H.H., Mahlia T. M. I., Ong Hwai Chyuan., Kusumo, F., Aditiya, H. B., and Ghazali, N. N. N. 2015. Schleichera oleosa L oil as feedstock for biodiesel production, Fuel 156: 63–70.

Srivastava, A. and Prasad, R. 2000. Triglycerides based diesel fuels. Renewable Sustainable Energy Review. 4: 111–133.

Tsolakis, A., Megaritis, A., Wyszynski, M. L., & Theinnoi, K. (2007). Engine performance and emissions of a diesel engine operating on diesel-RME (rapeseed methyl ester) blends with EGR (exhaust gas recirculation). Energy, 32(11), 2072-2080.

Usta N. An experimental study on performance and exhaust emissions of a diesel engine fuelled with tobacco seed oil methyl ester. Energy Convers Manage 2005;46:2373–86.

Yadav ,S. Prasanna Raj , Saravanan ,C.G., Kannan ,M., Influence of injection timing on DI diesel engine characteristics fueled with waste transformer oil, Alexandria Engineering Journal (2015) 54, 881–888

Accepted manuscript

ACCEPTED MANUSCRIPT

Zhang X, Gao G, Li L, Wu Z, Hu Z, Deng J. Characteristics of combustion and emissions in a DI engine fueled with biodiesel blends from soybean oil. SAE technical paper, vol. 1; 2008. p. 1832–5.

Fig.1. Picture of (a) Oleander Seed (b) Bitter Groundnut Seed and (c) Kusum Seed

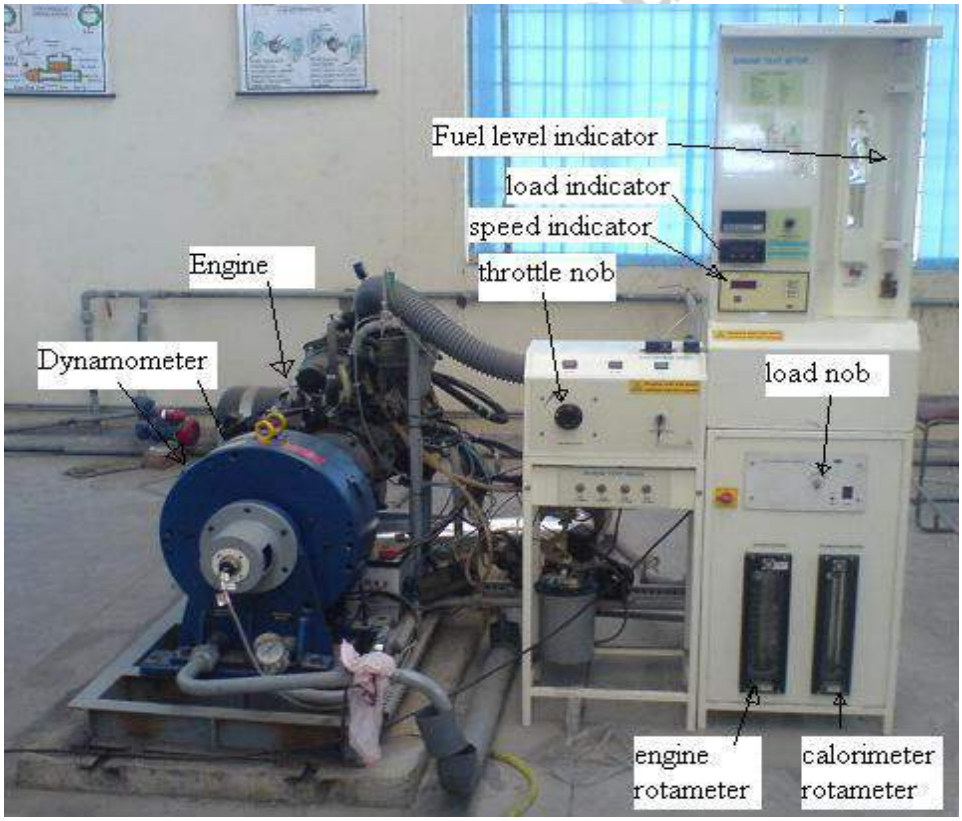

Fig.2. Tata Indica Diesel Engine Test Rig

ACCEPTED MANUSCRIPT

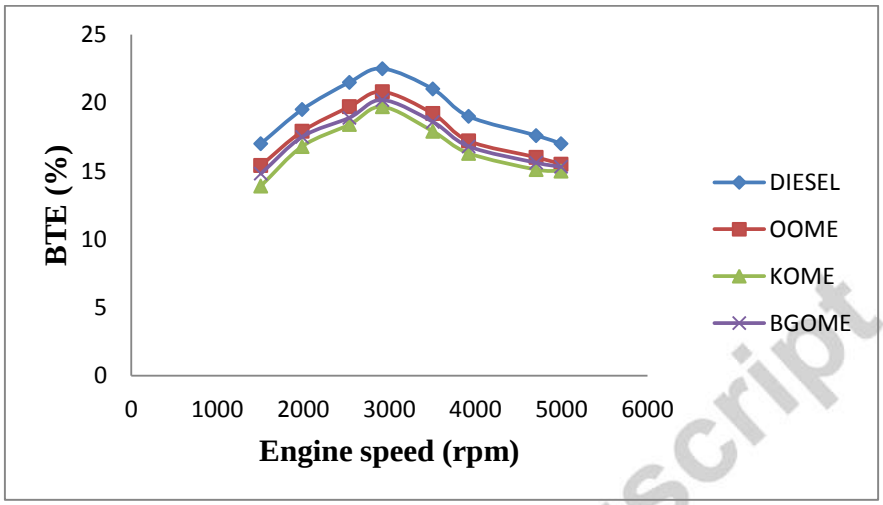

Figure 3: Variation of Brake thermal efficiency (BTE) with Engine speed

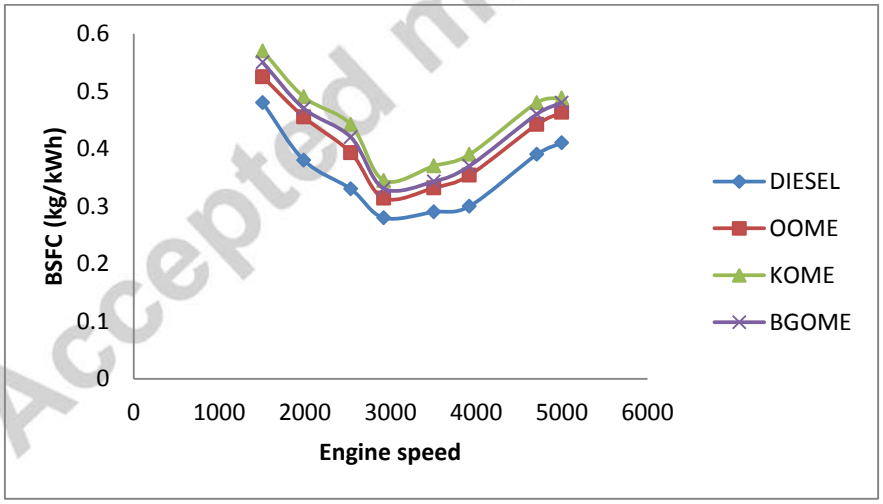

Figure 4: Variation of Brake specific fuel consumption (BSFC) with Engine speed

Accepted manuscript

ACCEPTED MANUSCRIPT

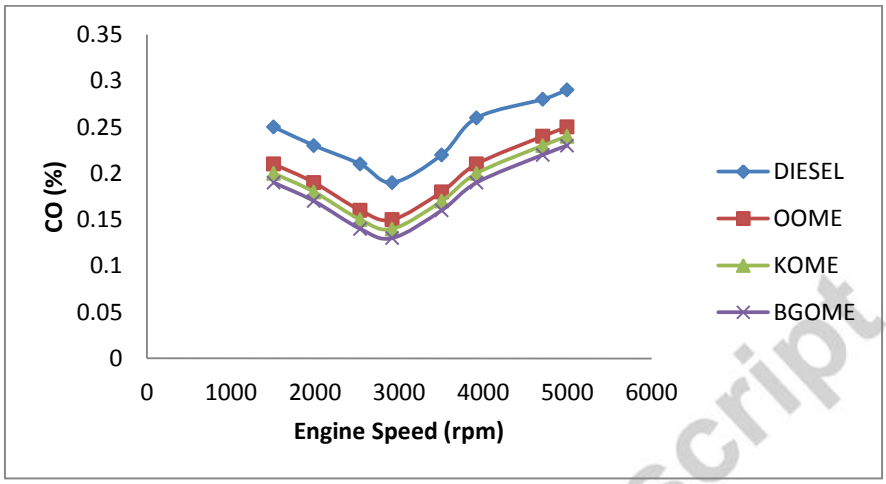

Fig. 5. Variation of carbon mono oxide (CO) with Engine speed

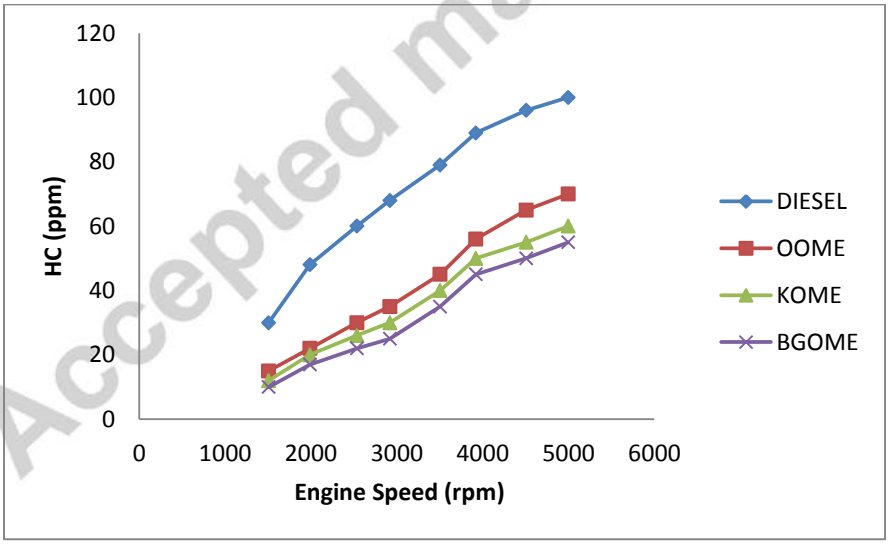

Fig. 6. Variation of hydrocarbon(HC) with Engine speed

Accepted manuscript

ACCEPTED MANUSCRIPT

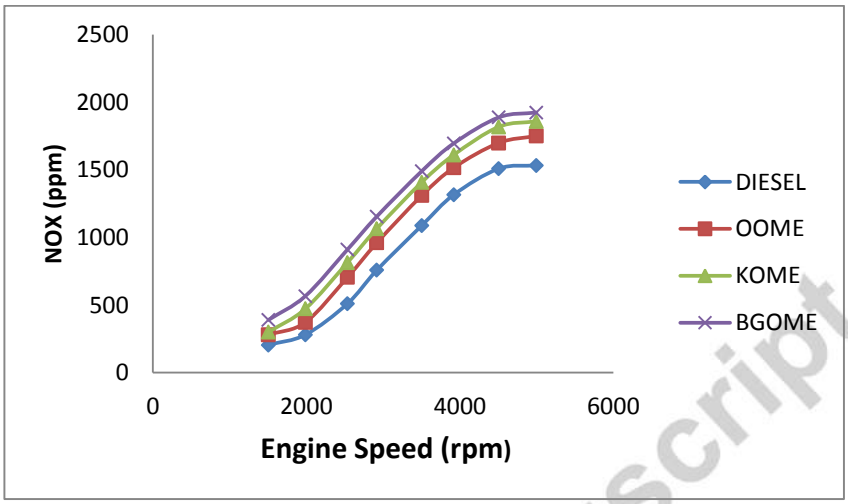

Fig. 7. Variation of Oxides of nitrogen (NO_X) with Engine speed

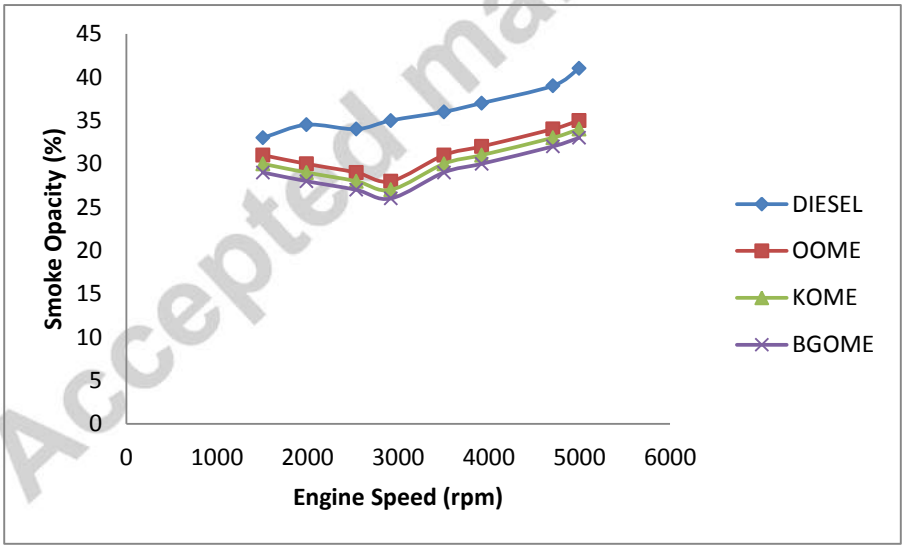

Figure 8: variation of Smoke Opacity with Engine speed.

Accepted manuscript

ACCEPTED MANUSCRIPT

Table 1: Technical specification of the Test engine and emission diagnostics system

Make	Telco, Model Tata Indica,
Type	4 Cylinder, 4 Stroke, Diesel water cooled,
Rated Power	39 kW at 5000 rpm,
Torque	85 Nm at 2500 rpm,
Cylinder volume	1405 cc
Compression ratio	22:1
Dynamometer	Type eddy current, water cooled, with loading unit
Load sensor	Load cell, type strain gauge
Software	Engine soft Lab view, Engine performance analysis software
Emission Diagnostic	
Make	AVL; model: DI-Gas 480

Exhaust Emissions	Measurement range	Resolution	Accuracy
CO	0–10 vol. %	0.01 vol. %	<0.6% vol.: ±0.03% vol.
HC	0–20,000 ppm	<2000: 1 ppm vol. >2000: 10 ppm	<200 ppm vol.: ±10 ppm vol. P200 ppm vol.: ±5% of ind. val.
CO_2	0–20 vol.%	0.1 vol.%	<10% vol.: ±0.5% vol.
NO	0–5000 ppm	1 ppm vol.	<500 ppm vol.: ±50 ppm vol.
Opacity	0-100%	0.001	±2%

Accepted manuscript

ACCEPTED MANUSCRIPT

Table 2: Range, Accuracy and uncertainty of measurements

Measurements	Instrument	Range	Accuracy
Engine load	Strain gauge type load cell	0–25 kg	±0.1Kg
Speed	Speed sensor	0-10000rpm	±20 rpm
Time	Stop watch	–	±0.5%
Exhaust Temperature	K-type thermocouple	0–1000 ^{0}C	±1 ^{0}C
Smoke density	Smoke meter	0–100%	±2%
Calculated results			Uncertainty
Engine power	–	0–8 kW	±1.0%
Fuel consumption	Level sensor	–	±2.0%
Air consumption	Turbine flow type	–	±1.0%
BTE	–	–	±1.0%
BSEC	–	–	±1.5%

Accepted manuscript

ACCEPTED MANUSCRIPT

Table3. Properties of Oleander, Kusum and Bitter Groundnut oil methyl esters compared with diesel

Properies	Biodiesel			Diesel	ASTM Limit
	OOME	KOME	BGOME		
Density at 15 ^{0} C (g/cc)	0.874	.857	.866	.840	.86 -.90
Viscosity at 40^{0}C(cst)	4.2	4.5	4.1	3.0	2.52 – 7.5
Flash point (^{0}C)	175	138.5	148	51	Min 130
Fire point ^{0}C	186.2	147	152.8	58	Min 53
Pour Point (^{0} C)	3	-2	6	-6	-15 - 16
CFPP (^{0} C)	7	- 4	5	-9	Max 19
Cetane number	75	52.4	49	50.3	Min. 47
Calorific Value (MJ/kg)	42.35	39.07	41.05	44.47	Min. 33

Accepted manuscript

ACCEPTED MANUSCRIPT

Table 4. Fatty acid composition of different selected oils

Type of fatty acids	Oleander Oil	Bitter Groundnut Oil	Kusum Oil
Myristic (14:0)	-	-	-
Palmitic (16:0)	23.88	10.42	6.73
Stearic (18:0)	7.46	1.9	5.81
Palmitoleic (16:1)	-	1.2	2.88
Oleic (18:1)	44.23	49.3	48.51
Linoleic (18:2)	21.82	33.76	6.57
Linolenic (18:3)	0.48	1.4	0.21
Arachidic(20:0)	1.8	1.1	27.21
∑ Saturated fatty acids	33.14	4.4	40.64
∑ Unsaturated fatty acids	66.53	94.88	58.17

Accepted manuscript

ACCEPTED MANUSCRIPT

Abbreviations used

BGOME	Bitter Groundnut Oil Methyl Ester
OOME	Oleander Oil Methyl Ester
KOME	Kusum Oil Methyl Ester
C.I	Compression Ignition
CO	Carbon Monoxide
UHC	Unburnt Hydrocarbons
NOx	Oxides of Nitrogen
BTE	Brake Thermal Efficiency
BSFC	Brake Specific Fuel Consumption
ppm	Parts Per Million
cSt	Centi Stoke
kW h	Kilo-Watt-Hour
rpm	Rotations Per Minute

Accepted manuscript

International Journal of Engineering Research and General Science Volume 4, Issue 4, July-August, 2016
ISSN 2091-2730

Performance Evaluation of Solar Parabolic Trough for Cloths Laundry application

Shubham Gupta*, Prof. R. S. Mishra

Department of Mechanical Engineering Delhi Technological University,

Delhi-110042.

guptashubham@outlook.in , *Post Graduate Student

Abstract- Solar thermal technology installation has enabled to use a completely free and clean form of energy. Because of this diesel consumption in many industries can be saved and hence can positively affect the environment. In this paper particularly laundry of cloths application is evaluated as this process conventionally used diesel in large quantities and hence makes suitable for the use of solar thermal technology.

Key Words: Solar Thermal, Parabolic Trough, Collector, Laundry, Steam, Renewable energy, Solar Energy

Introduction

Thermal or heat energy from the sun can be utilized or converted in one form or another to meet the suitable requirement or application such as cooking, electricity generation, etc. there are two types of radiation that we deal in Solar Thermal Designing: DNI (Direct Normal Incidence) & GHI (Global Horizontal Incidence). Water Heating Parabolic-trough is a proficient technology of renewable energy for heating applications. In India Direct Normal Incidence is also high which makes this technology much more suitable. Hot water applications can be used at various places such as temples (Meal preparation), Hotels, Cloths laundry, etc. This technology has a good payback as compared to Solar PV technology. There are various types of Solar concentrating thermal technologies which includes Linear Fresnel, compound parabolic, paraboloid dish, solar tower, flat plate collector.

Solar Concentrator Parabolic Trough

Solar thermal collectors can be considered as a heat exchanger which transforms solar direct irradiation to enthalpy of the fluid medium in the tube. Following are the main components of Solar Thermal Collector

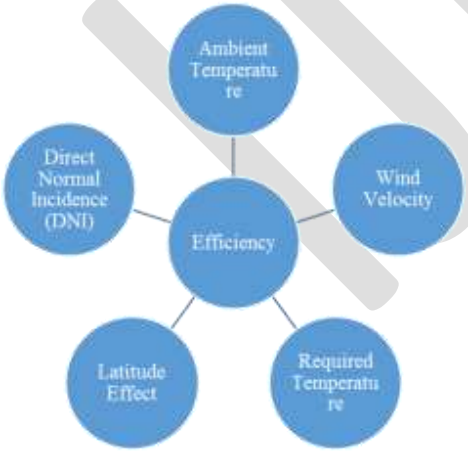

Fig 1: Factors effecting Efficiency of Solar Thermal Technology

- **Collector:** Receives or collects the sun radiation convert it to heat and directs or concentrates it to the receiver
- **Receiver**: It is a glass tube in working fluid which circulates and gains the heat from the collectors and transfers it to the desired equipment or heat storage tank
- **Fluid:** It can be organic fluids, water, heating oil, etc.
- **Tracking:** E-W tracking or N-S tracking or both can be done to increase the efficiency of parabolic trough
- **Storage tank**: In case of cloudy, rainy & non-sunshine conditions heat can be stored in a storage tank.

Literature Review

A. Valan Arsau et.al (2007) [1] designed the parabolic trough with rim angle 90^o with the use of reinforced fibreglass and provide the manufacture techniques. This modal has very low drag coefficient in the acceptable range. Standard deviations of the of the parabolic surface error distribution was in the limit range of accuracy. Kalogirou et.al (2004) [2] Explains the importance of renewable energy considering environmental factors as a major issue. Author also discussed various solar thermal technologies such as flat plate collector, parabolic troughs, etc. and their applications. Krishnamurthy et.al (2012) [3] Focuses on economic evaluation of the solar thermal parabolic trough technology considering various factors such as rate of equity, discount rate, capital cost, generation cost, solar insolation and various models are compared. Omid karimi sadaghiyani et.al (2014) [4] Designed two solar collectors and evaluate and compared performance characteristics by using CFD and MATLAB. S. D.Odeh (1998) [5] Evaluate the performance characteristics of parabolic trough by considering absorber wall temperature instead of fluid bulk temperature to provide flexibility of use of any working fluid. Author used Syltherm 800 as a working fluid for experimental work. Vinay V Gadikar et.al (2016) [6] Assesses the Solar concentrator technology use in laundry purposes at Goa by detail specification discussion and also discussed about the problems and challenges faced and performance evaluation is also done. Richter et.al (1996) [7] provides the methods to improve the optical efficiency of parabolic trough which plays a great role in overall efficiency of the solar thermal technology. Price.H et.al (2002) [8] stated at low working temperature difference Concentrating solar thermal technology works with high efficiency. Many design considerations can also be improved to improve the efficiency.

Case study undertaken

Gandhinagar city is considered for the case study. It has good DNI. An industry of approximately load of 2000 cloths per day for dry cleaning is considered for the case study in this paper.

Methodology

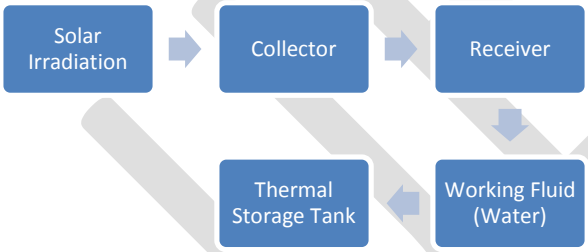

Fig 2: Methodology used in Solar Parabolic Trough

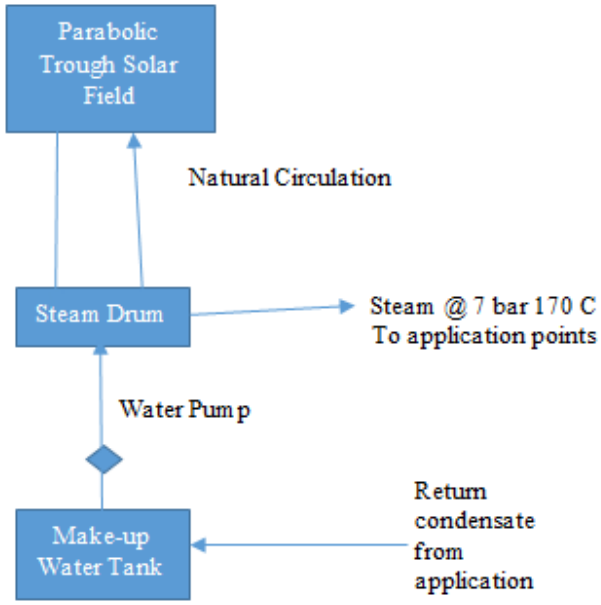

Fig 3: Schematic of Solar Parabolic Trough system

Design Considerations

Longitude: 23.2^{o} N

Latitude: 72.6^{o} E

No. of cloths: 2000-2500

Steam required: 2000 Kg/day

Shade free Area available for Solar Concentrator Technology installation: 80 square meters

No. of operational Hours in a year: 2700

Operating temperature: 170^{o} C

Operating pressure: 7 bar

Table 2: Ambient Conditions Considered

Ambient Conditions		
Parameters	**Units**	
Wind Speed	m/s	3
Irradiation	W/m2	1000
Tilt Factor		1.02

Table 3: Fluid Specifications Considered

Fluid Specifications		
Parameters	**Units**	**Vapour**
Mass Flow Rate	Kg/s	0.25
Density	Kg/m3	5.147
Heat Capacity	KJ/Kg-K	2.5944

Thermal Conductivity	W/m-k	0.0364
Kinematic Viscosity	m2/s	2.91948E-06
Dynamic Viscosity	Kg/m-s	1.50E-05

Table 4: Parabolic Trough Specifications Considered

Parabolic Trough Specifications		
Parameters	**Units**	
Outer Diameter	m	0.025
Inner Diameter	m	0.022
Outer Diameter Glass Cover	m	0.055
Inner Diameter Glass Cover	m	0.05
Aperture	m	2
Length	m	4
Aperture Area	m2	7.9
Avg. Value transmissivity-Absorbivity product for beam radiation		0.9
Specular Reflectivity of the concentrator Surface		0.95
Intercept factor (The fraction of the reflected radiation intercepted by the absorber tube)		0.95
Temperature Outlet	Celsius	65
Temperature Inlet	Celsius	30

Computation of energy potential

Table 5: Monthly Thermal Output Generation

Parameters	**Units**	**Jan**	**Feb**	**Mar**	**Apr**	**May**	**Jun**	**Jul**	**Aug**	**Sep**	**Oct**	**Nov**	**Dec**
Incident Beam radiation	W/m2	1000	1000	1000	1000	1000	1000	1000	1000	1000	1000	1000	1000
DNI	KWh/day	3.2353	4.9237	6.3184	5.7870	5.3760	4.1276	2.7863	3.4971	4.6744	4.2386	3.4537	3.1160
Overall Loss Coefficient	W/m2-K	24.8	24.8	24.8	24.8	24.8	24.8	24.8	24.8	24.8	24.8	24.8	24.8
Useful Heat Gain	W	3907	3907	3907	3907	3907	3907	3907	3907	3907	3907	3907	3907
Thermal Units/Day	KWh	12.64	19.24	24.69	22.61	21.01	16.13	10.89	13.66	18.27	16.56	13.50	12.18
No. of Modules		8	8	8	8	8	8	8	8	8	8	8	8
Total Thermal Units	KWh/day	101	154	198	181	168	129	87	109	146	132	108	97

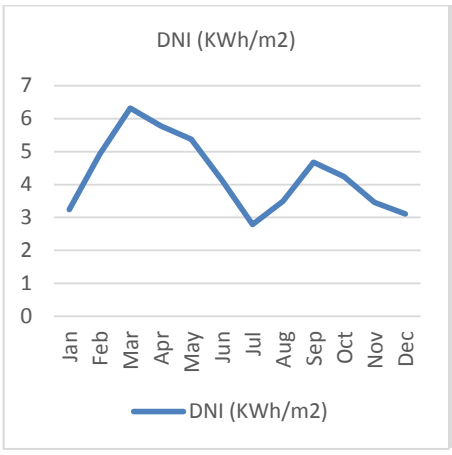

Fig 4: DNI variation with Month

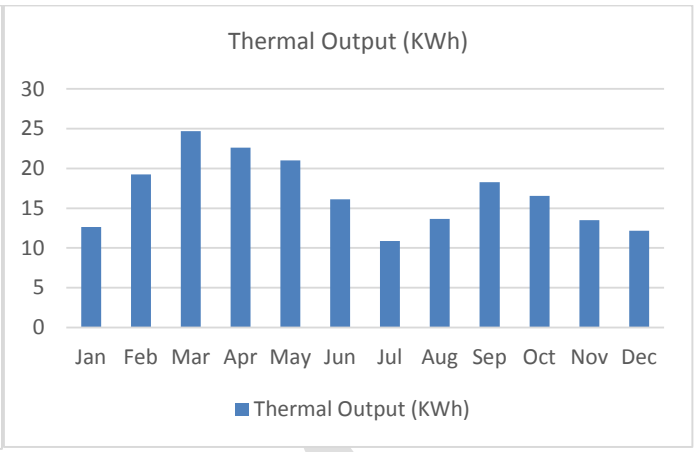

Fig 5: Thermal Output with Month

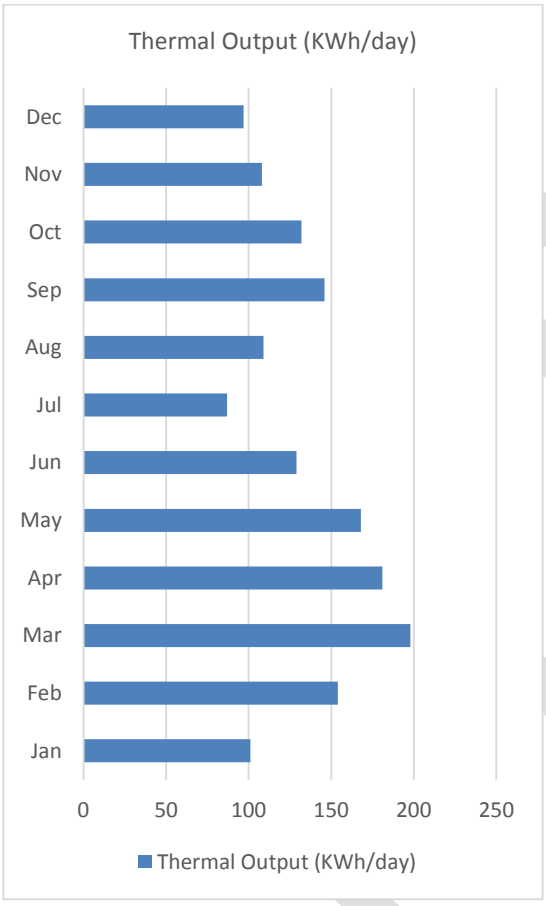

Fig 6: Thermal Output with Month

Results & discussion

15 KWh/day is produced from 8 parabolic troughs with 64 square meters of reflective area. Collector efficiency is 45 %. Concentration ratio is 27. This energy is enough to carry out laundry operation of around 2000 cloths per day. In overall 20 litres/day of Diesel is saved which provides of annual saving of 6000 Kg of LPG gas.

Conclusion

New concept of solar thermal technology has the potential to improve the efficiency of energy (i.e. the thermodynamically efficient use of fuel) supply systems, while at the same time integrate seamlessly with the use of renewable energy sources, for the delivery of the required energy in different forms in industries. Since because of various factors like clouds, dust, etc. Sun's rays reach the earth in a diffuse manner a less Direct rays is received. Solar PV technology works on GHI. While Solar thermal works on DNI. So if we use the Solar thermal output as a heat it will be more useful gain as in converting electricity much more losses occur in concentrating solar thermal technology. A fluid run through a pipe line continuously and gain heat from concentrated sun's rays by parabolic trough. Parabolic trough concentrator is such designed to achieve desire temperature difference. This fluid after gaining heat moves to storage tank where it can be utilized. After utilization again it moves to make up tank then to inlet of Parabolic Trough.

REFERENCES:

1. A. Valan Arsau, T. S. (2007). Design, manufacture and testing of fiberglass reinforced parabola trough for parabolic trough solar collectors. Solar Energy, 1273-1279.
2. Kalogirou, S. A. (2004). Solar thermal collectors and applications. Progress in Energy and combustion science, 231-295.
3. Krishnamurthy, P. M. (2012). An analysis of costs of parabolic trough technology in India. Energy Policy, 407-419.
4. Omid KARIMI SADAGHIYANI, M. B. (2014). Two new designs of Parabolic solar collectors. Thermal Science, 323-334.
5. S. D. ODEH, G. L. (1998). Modelling of parabolic trough through direct steam generation solar collectors. Solar Energy, 395-406.
6. Vinay V Gadikar, S. D. (2016, Jan-Mar). CST BEING USED IN LAUNDRY AT LAKAKI DRYCLEANERS, GOA . Sun Focus, pp. 15-17.
7. Richter, J. L. (1996), Optics of a Two-trough Solar Concentrator, Solar Energy, pp. 191-198
8. Price, H., et al. (2002), Advances in Parabolic Trough Solar Power Technology, Journal of Solar Energy Engineering, pp. 109-125

Volume 4, Issue 1 (2016) 145-150 ISSN 2347 - 3258
International Journal of Advance Research and Innovation

Perfortmance evaluations of Concentrated Solar Thermal Power Technology

Harwinder Singh*, R. S. Mishra
Department of Mechanical Engineering, Delhi Technological University, Delhi, India

Article Info

Article history:
Received 20 January 2016
Received in revised form
10 February 2016
Accepted 28 February 2016
Available online 15 March 2016

Keywords
Solar Energy,
Concentrated Solar Power,
Thermal Performance,
Solar Thermal Collector,
Electric Power Generation

Abstract

This review work consists of detailed description on various types of research in the field of solar thermal systems and various methods to improve the performance of the collector systems. Concentrated solar thermal systems are the highly advanced and large scale technology, which is used to generate the thermal energy and converted it in to electric energy through the application of power producing device coupled with the collector systems, therefore from the research point of view improvement in the working performance of the solar thermal system is highly important to achieve the better efficient device.

1. Introduction

Solar energy is a renewable and green resource of energy. Solar energy has several advantages over other alternative or renewable energy sources. All the primary or conventional energy resources are continuously depleting the environment of earth and are giving harmful effect to human health. Among all alternative sources of energies solar energy has great potential and India receives great amount of solar energy as compare to many other developed countries throughout the year. Concentrated solar thermal power is the most prominent and highly proven technology, which is used to generate electric power on large basis. Concentrating collectors are also known by focusing type collectors. Radiations coming from sun are falling on the collector and concentrating on the absorber area by reflected through mirrors. Continuous falling of radiations on receive per unit area can increase the temperature of receiver or absorber surface of collector. There are some losses which also accounts in the working mechanism of concentrating solar collectors and those losses are reflection losses from mirror and energy absorption losses on concentrating surface i.e. absorber copper tube. There are some advantages of concentrating collector over flat plate collector like achievement of higher temperature in receiver tube, which results in higher thermodynamic efficiency and further requirement of material in concentrating collectors are also less as compare to non concentrating collector due to which cost reduction in fabrication of solar concentrating collector can be achieved. Solar concentrators can be classified in different ways or methods. Solar concentrators can have reflecting surface or refracting type surface and it completely depends upon the concentrating device used to concentrate the sun's radiation on the absorber surface, reflecting surface are further classified into flat, spherical or parabolic type. Solar concentrators can be of imaging and non-imaging concentrators and further imaging type can be classified into line or point focussing solar concentrators. Concentrator's classification also depends upon the amount of temperature requirement for various applications. High concentration ratio means achievement of high temperature. Efficient working of concentrating collector also depends upon adopted tracking mechanism. Tracking can be done on intermittent and on continuous basis. Further tracking can be possible about one axis and two axes also. Flat plate collector along with mirror adjusted at edges has a capability to reflect and concentrated solar radiation on collector's absorber plate. It has low concentration ratio approximately unity, can achieve higher temperature as compare to flat plate collector alone. Compound parabolic concentrating collector have curved parts of two parabolas, it is also a type of non-imaging collector. This type collector possess moderate concentration ratio for e.g. 3 to 10. Apart from these advantage of compound parabolic collector having higher acceptance angle, which means that collector are adjusted on occasional basis. Another important type of collector known by cylindrical parabolic collector, sun rays are concentrated or image formation on the focal axis of the parabolic collector. Lenses are also used to concentrate sun light like Fresnel lens. Line concentrating collector like cylindrical, Fresnel lens having concentration ratio vary from 10 to 80 and range of temperature achieved between $150°C$ to $400°C$. Point focussing collector like parabolic dish collector can achieve higher concentration ratio and temperature as compare to line focussing collector and point focussing collector can achieve concentration ratio from 100 to 1000 and temperature up to approximately $2000°C$. For concentration of high amount of energy on a point, a new concept called as central receiver has been used on a large scale in the world. In this type of concentrating system a large number of mirrors also known as heliostats are used to concentrate the sun light on the central receiver which is situated at the top of tower [16].

Corresponding Author,
E-mail address: harrymehrok14@gmail.com
All rights reserved: http://www.ijari.org

2. Literature Review

[1] Jan Fabian feldoff et al. (2012) conclude that Level zed Electricity Cost of a Direct Solar Generation plant

could be higher than that of synthetic oil plant and both the power generation systems have a 100 MWe gross turbine and a 9 hours storage capacity. They also conclude that without the application of thermal storage system, the Direct Solar Generation plant could show lower Level zed Electricity Cost. They analyze both synthetic oil power plant with molten salt two tank storage system and Direct Solar Generation system uses phase change material. It has been seen that application of Thermal Energy Storage influence the cost of Direct Solar Generation plant up to very high level. Therefore investment cost is higher about 10% and efficiency is about 8% better and finally they concluded that direct solar generation have higher levelized electricity costs are about 6%, which is due to the specific solar field costs and thermal storage costs. [2]Xiang-Qi Wang et al. (2007) conclude that with the change in geometry of flow, boundary conditions and by enhancing thermal conductivity of fluid, convective heat transfer can be increased. They describe that nano fluids also has capability to enhance heat transfer or thermal characteristics as compare to liquids, base or conventional fluids and superior in thermo physical properties as compare to mixture containing micro particles with base fluid. They also conclude that due to suspension of any type of nano particles, surface area can be enhanced and results in increase in amount of thermal conductivity of working fluid. Wang et al use the method of steady state parallel plate for measurement of the thermal conductivity of nano fluids. Suspension of Al_2O_3 and CuO nano particles with average diameter of 28 and 23nm in base or conventional fluids (like H_2O and ethylene glycol ($C_2H_6O_2$)), they evaluate from experimental results that nano fluids posses' higher amount of thermal conductivity than base fluids and also evaluate that thermal conductivity can be increased with decreasing of particle size. It has been seen that thermal conductivity of suspended carbon nano tubes can show higher thermal conductivity among all other nano particles and CNT also have very high aspect ratio. [3] Soteris A. Kalogirou et al. (2004) They discussed about different type of solar thermal collectors like flat plate, compound parabolic solar thermal, cylindrical parabolic or parabolic trough (PTC), Fresnel lens reflector system (LFR), parabolic dish and heliostats for different applications like water and space heating and cooling also, industrial heat process and also in thermal power plants. Further they also analyze the effect of using conventional fuel sources on environment of earth, which is associated with the Problem (like pollution), they also analyze that Industrialization is also a big cause for degradation of environment. They gave the brief description on solar energy collectors and its different types. Solar collector is an instrument used to extract the sun's energy from incoming solar radiations, this energy convert directly into heat or thermal energy and further this heat or thermal energy transfer to fluid like water following through collector system. Basically two type of solar collector are available like Non concentrating and concentrating collector, apart from this solar collectors are further classified according to motion like stationary collector, single axis collector and two axis collector. [4]T. Yousefi et al. (2012) they examine the effect of variation in pH of MWCNT-H_2O based nanofluid on the flat plate collector's efficiency experimentally and they take volume concentration 0.2 wt. % MWCNT with the application of Triton X-100 and also with various pH values, 3.5, 6.5, and 9.5. They concluded from the ASHRAE standard that increasing or decreasing the pH values with respect to the pH of isoelectric point, the efficiency of solar collector can be increased. [5]R. Saidur et al. (2012) they examine the effect of nanofluid on the performance of direct solar collector by using nanofluid as a working fluid. They investigate about extinction coefficient of Al-H_2O nanofluid has been experimentally and they found that particle size has minute effect on the optical properties of nanofluid. They observed enhancement in optical and thermal properties due to the use of nanofluids as volumetric absorber in Direct Solar Generation system. They finally conclude that water behaves like a transparent for incoming visible light but it has a greater absorption capacity at longer wavelength and Aluminum nanoparticle showed high extinction coefficient at small wavelength. On the contrary a lower extinction coefficient possessed longer wavelength, therefore for this reason aluminum nanoparticle can be used to increase absorption ability of water at the visible and small wavelength of light. [6]Alibakhsh Kasaeian et al. (2015) they describes the ways to enhance the working performance of solar parabolic trough collector system. For the purpose of investigation or inspection they employed four different types of receivers like evacuated steel tube with painted black, bare copper tube with painted black, non evacuated copper tube with glass envelop along with painted black and evacuated copper tube with painted black to examine and compare the optical and thermal efficiency of solar parabolic trough collector system. They take Volume concentration of nano particles is decided as 0.2% and 0.3% in oil base fluid for preparation of the working fluid for testing of these four different types of receiver. Finally they conclude from research work that efficiency of evacuated tube shows 11% higher than the bare tube efficiency due to convection losses and also conclude that time response is an important factor for evaluation of performance because it tells us that how much time needed by the system to stabilize it. It has been seen that evacuated copper tube showed greater time response due to minimum heat loss as compare to heat losses in evacuated steel tube with painted black due to radiations. They observed that efficiency of solar trough collector system with volume concentration 0.2% and 0.3% can be enhanced 4-5% and 6-7% with the help of MWCNT and mineral oil based nano fluid as comparison to efficiency achieved from pure oil only. It has also been found that black coated copper tube possesses high absorptive and thermal conductivity. [7]Nor Azwadi Che Sidik et al. (2014) this paper is review study, which is concentrated on methods to prepare the nano fluids along with challenges due to nano fluids. They describe all methods of preparation given by different investigators or researchers. They conclude that metallic and non metallic particles can be used to fabricate nano particles. They also describe the synthesis process for nano fluids along with characterization of nano fluids. They also includes some challenges comes in the synthesis process. Further they found that non metallic particles like silicon dioxides, titanium dioxides, aluminium oxide, iron oxide, aluminium nitride and carbon nano tubes. Further metallic

particles like gold, silver and copper can be use for fabrication of nano fluids. They also concluded that effect on properties like thermal conductivity of nano particles, Brownian motion of particles, thermo physical properties along with change in temperature are due to factors like poor dispersion or suspension of nano particles and lack of knowledge in understanding of mechanism that all are responsible. They also observed that increasing concentration of nano particles results in viscosity increases; this became also a challenge due to more requirement of pumping power to operate the system. They noticed that thermal conductivity of pure metallic particle based nano fluids will be higher as comparison to nano fluid containing oxide nano particles and also noticed that nano fluids posses less specific heat as comparison to base fluids. Further they observed that viscosity of nano fluids generally higher than the base fluids and it depends upon type of particles and also depends upon particle volume concentration. They also evaluate that homogeneous and stable dispersion of nano particles in conventional fluid are always a challenge for investigators. They conclude in his review study that preparation of nano fluids is followed by three common methods like sonication, PH control and surfactants. Cost comes on synthesis of nano particles and stability of nano particle in base fluid; both are the major factors that prevent the use of nano fluid on commercial basis. [8]Zhongyang Luo et al. (2014) they construct a simulation model of solar collector using nanofluid based on concept of Direct absorption collector by understanding the radiative transfer equations of particulate media and by combining both conduction and convection heat transfer. They concluded from the results of simulation model that nanofluids improved the outlet temperature by 30–100 K and system efficiency by 2–25% than the base fluid flowing through the system. They also found that photo thermal efficiency of graphite based nanofluid with 0.01wt% flowing through a coating absorbing collector is measured 122.7% and they finally conclude that nanofluids with in small concentration have a good ability to absorb the solar radiation, and also has an ability to improve the outlet temperatures and efficiency of system. [9]John Philip et al. (2012) they describe the developments and advances in the field of nano fluids applications and also they found their effect on the thermal characteristics of nano fluids. They gave an approach to achieve better thermal conductivity of nano fluids or heat transfer fluid. Enhancement in k is due to weight fraction of nano particles in base fluid like in water and ethylene glycol/MWCNT based nano fluid showed an increase in 'k' with an increment in $'\varphi'$. Water based CNT describe a non linear behavior between k and φ. They also found that thermal conductivity also affected by size of nano particles like dispersion of Al_2O_3 nano particles in water with different diameter i.e. 20, 50 and 100nm determine an increment in thermal conductivity with the reduction in the size of nano particles. It has been seen that 'k' for Al_2O_3 in water and E.G. based nano fluid increases with the reduction of size of nano particles. Apart from this some kind of nano fluids showed different characteristics and behaviour like SiC and water based nano fluid with different diameters of 16, 29, 66 and 99nm determine an increment in 'k' with an enhancement in size of particle. It has also been seen that in metallic dispersion like gold nano particle in water based nano fluids determine a decrement in 'k' with decrease in size of particle within the range of 2 to 40nm. Metal nano fluids like Cu with particle diameter 80nm dispersed in water and E.G also show an incremental change in 'k' with an enhancement in temperature. Ag in water based nano fluid show an incremental change in 'k' approximately 3.2% at 30℃ temperature and increment of 4.5% at temperature 60 ℃ at volume concentration 0.001%. Water based Al_2O_3 with diameter 36nm showed an increment in 'k' at temperature range between 2 to 50℃. For MWCNT and water based nano fluid showed an enhancement in 'k' is independent on the temperature at low concentration of MWCNT. Some nano fluid like TiO_2 with diameter 21nm and water based nano fluid show and decrement in 'k' with increment in temperature over a range of 15-35℃. In CNT and water based nano fluids an increment in 'k' with length of the nano tubes like at $0.5\mu m$ length of nano tube increment in 'k' was estimated to 14% and 45% increment was estimated in 'k' with length of 5 μm. The incremental behaviour of 'k' was found to be increased with increase of aspect ratio of nanotubes in water based CNT nano fluids. Water based nano fluid also show less enhancement in k as compare to E.G based nano fluids. To maintain the stability of nano particles, there is a requirement of surfactants, because they prevent the agglomeration of nano particles. SEM results show that water based CNT show reduction in 'k' with increase in ultra sonication time due to the reduction in the length of the nano tubes, while in E.G based CNT show an incremental change in 'k' with increase in ultra sonication time. They described that some change in temperature can become a cause of large error in thermal conductivity, apart from this agglomeration and settle down of nano particles in base fluid can affect to the results of experiment. [10]G.C. Bakos et al. (2001) They concluded from Simulation results that variations of parabolic trough collector's efficiency is a function of some important parameters like heat transfer fluid, pipe diameter, intensity of solar radiations as well as exposed area of the collector and it has also been seen from the results that with increase of flux of heat transfer fluid, there is a noticed incremental change in efficiency. However they also noticed that flux of flowing fluid cannot increase continuously because of decreasing solar flux with the change in time due to this decrement shown in temperature of fluid. Further with the increment in pipe length there is an effective decrease in efficiency value. [11]Tooraj Yousefi et al. (2012) they performed an experimental study with Al_2O_3-H_2O nano fluid as working fluid is used for investigate the efficiency of flat plate collector. They decided to take Volume fraction or concentration of nano particles as 0.2wt% and 0.4wt% with the particle diameter of 15nm along with the application of surfactant Triton X-100. Selective mass flow rates are 1, 2 and 3Lit/min. they found from results that nano fluid show an enhancement in efficiency as comparison to water. They concluded that heat removal factor (F_R) value for nano fluid is 0.6194 and 0.6086 with and without surfactant. They also concluded that adding surfactant into nano fluid has a positive effect seen on the efficiency of flat plate collector. It has also been seen that efficiency of flat plate collector increasing

by increase in mass flow rate. Results from performed experiments concluded that efficiency enhancement in collector is 28.3% at 0.2% weight fraction of nano particles along with the 15.63% efficiency enhancement with the application of surfactant due to enhancement in heat transfer. [12]K. Vignarooban et al. (2015) they found the effect of different types of heat transfer fluids available like air, water and thermal Oils, organic fluids, molten-salts and liquid metals etc on solar thermal collector system components. They concluded in his review study that it is highly important to evaluate the stability of used stainless steels and nickel based alloys for piping and container materials because heat transfer fluids, while flowing through the piping system show high impact on these materials and stability of these material while in contact with heat transfer fluids is very important from research point of view for the long life of concentrating solar power systems. [13]Gianluca Coccia et al. (2015) they found that industrial process heat applications ranging from 70 to 250DegC has been possible by the manufacture of low-cost parabolic trough collectors (PTCs), therefore in this construct a prototype of PTC with a 90Deg rim angle and a small concentration ratio of 9.25 built along with Fiberglass is used as the external shell and polystyrene used for inside fill component. They used receiver is of circular cross section and made up of aluminum, which is covered or evacuated with glass envelope. They also used the application automatic tracking system, which is based on a solar-position computer program. They evaluate the main features of prototype are its less cost, low weight and ease of manufacture. [14] J. Paetzold et al. (2014) they concluded that flowing wind is greatly affect to performance of parabolic trough collector system. They also concluded that increasing concentration ratio, results in higher temperature achieved from receiver tube and concentration ratio is also increased due to increment in aperture area. They found that heat losses by convection increased due to high wind speed flowing over the collector. They evaluated data from the series of test performed in wind tunnel and also from previous research work related to PTC. They performed total 17 types of simulation for every geometry of parabolic trough by using CFD program with variable parameter i.e. depth of trough system with the variation in pitch angle i.e. -90° to 90° also with an increment of 15°. They evaluate that high quantity of aerodynamic forces and larger vortex are formed on backside of of trough, when pitch angle posses higher value above 15° and smaller from -60°. Forces exerts on PTC collector affect to the working performance of solar PTC system. It has been seen that with incremental change in depth of trough, results in incremental change in aerodynamic forces also measured in the PTC system. [15]Harwinder singh (2015) performed an experimental study on the prototype of parabolic trough collector using MWCNT based nanofluid. He takes different volume concentrations of 0.01% and 0.02% along with different volume flow rates i.e. 160L/h and 100L/h. He also evaluates the thermo physical properties of MWCNT based nanofluid theoretically and he compared the thermal performance due to water and MWCNT based nanofluid, while used as working fluid in parabolic trough collector system. Finally he concluded that MWCNT based nanofluid at 0.02wt% and at 160L/h showed higher thermal performance as comparison to other fluids at various concentrations and volume flow rates.

3. Outcome from Literature/ Research Gap

1 Nano fluid has an ability to show higher efficiency along with high outlet temperature, while working as a working fluid in solar thermal collector.
2 Phase change material can be used for thermal storage for a long period.
3 Agglomeration of nano particles can be avoided by using surfactants and by sonication method.
4 pH value of nanofluid highly affect to the efficiency of collector system.
5 Top covered along with different receiver materials and selective receiver coating has an ability to increase the life of reflecting surfaces and also help to minimize the heat losses from the receivers.
6 It has been studied that low cost parabolic trough collector system can be used for industrial process heat applications.
7 Efficiency of solar thermal collector highly depend upon various kind of working fluid used like conventional, micro fluid as well as nano fluid and further efficiency also depend upon the parameter of the collector design along with tracking mechanism i.e. automatic or manual. It has also been seen that size of nanoparticles, viscosity of fluid and thermo physical properties if nanofluid has a high impact on the collector performance.

4. Objective of Research Work

1. Evaluation of the performance of concentrated solar thermal collector on commercial basis with the help of various types of fluids with different volume flow rates and at different concentration and further comparison between the results outcome from the collector system theoretically and experimentally later.
2. Evaluation and comparison of the performance by using different receiver material and different glazing materials for solar concentrator.
3. Storage capability of the solar thermal power plant for the storage of heat for the usage of non sun shine hours can be increased by the phase change materials.
4. Various types of evacuation tubes around receiver and metal glass seal at the end of the receiver can be used for the prevention of heat loss from the receiver. Further insulated material can be used to prevent the heat loss from the pipes in which fluid is flowing.
5. Evaluation of the various thermal properties of various fluids used as a working fluid like thermal conductivity, viscosity, density along with the evaluation of various flow parameters, which are responsible for better thermal performance of collector during their working in the system

5. Experimentation & Data Collection

This section is deals with the experimental as well as theoretical data, which comes out from the evaluation of performance of solar thermal collector system by using different fluids and different collector receiver material along with different type concentrator glazing. Further this section also contains the experimental results for the

different types of storage medium used for increasing the heat storage capability of the thermal power plant and it will be discussed later in brief. This section includes the results of experimental study, which is based upon the analysis of parabolic trough collector system using nanofluid [15].

1. Some results are concluded during the experimental study, which was held on PTC prototype in Thapar university and finally evaluates that thermo physical properties of MWCNTs based nano fluid far expressive than base or conventional fluids like water, ethylene glycol. Further it has also been seen in this study that MWCNT and water based nano fluid with volume concentration i.e. 0.01% and 0.02% showed less value of important thermo physical properties specific heat and density. While thermal conductivity of MWCNT based nano fluids is always seems to be higher than water at the decided concentration.
2. It has also been seen that useful heat gain by nano fluid and water, while used as working fluid in collector system is fully dependent upon the volume flow rate, specific heat and also upon temperature difference measured during experimental working. It has also been observed by the author of thesis that in case of nano fluid mixture highest dominant factor is temperature difference, which is dependent upon incoming solar intensity throughout the experimental time and higher solar intensity results in higher amount of temperature difference. It has been concluded from figure that nano fluid mixture with 0.02% volume concentration and at 160L/h volume flow rate showed maximum useful heat gain overall among other fluids [15].

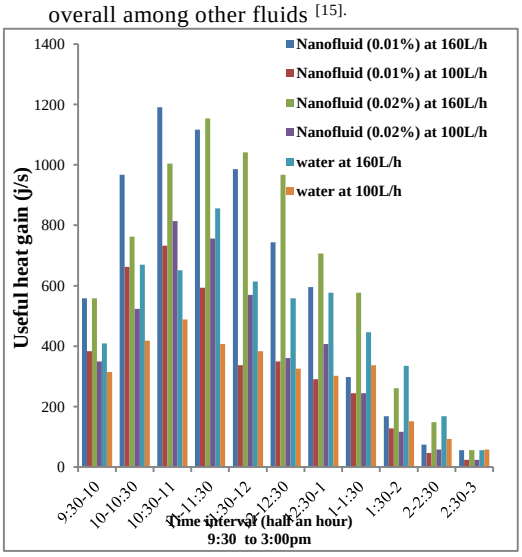

Fig: 1. Experimental variation in useful heat gain by nano fluid and water at different conc and volume flow rates [15]

3. Experimental work concluded that obtained maximum value of instantaneous efficiency for MWCNT based nano fluid mixture at 0.01% and 0.02% vol. concentration and at 160L/h volume flow rate is 96.49% and 96.46%[15]. It has been observed during experimental work maximum instantaneous efficiency possessed by nano fluid mixture with 0.01% and 0.02wt% at 160L/h volume flow rate among other fluids. It has been also been observed from experimentation that water at 160L/h also showed highest value of instantaneous efficiency at some points as compare to other fluids like water at 100L/h and nano fluid with different volume flow rates i.e. 160L/h & 100L/h[15]. It has been concluded from experimental work that maximum thermal efficiency for nano fluid mixture with at 100L/h volume flow rate is 11.36% and 10.31% measured. It has been also concluded that nano fluid mixture with 0.01% volume concentration at 100L/h possessed higher value of overall thermal efficiency as comparison to nano fluid mixture with same concentration and at 160L/h. Further nano fluid mixture 0.02% vol. concentration showed different behaviour, it means that nano fluid mixture at 160L/h showed higher value of overall thermal efficiency as comparison to thermal efficiency possessed by nano fluid mixture with same concentration (0.02%) at 100L/h and thermal efficiency achieved by nano fluid mixture with 0.01% vol. concentration at different volume flow rates. Thermal efficiency dependent upon the important parameters like temperature difference, total mass of liquid fluid through receiver collector system, specific heat of the fluid and most important total solar global radiation comes on the collector system. The changes come in all these parameters results in the changes come out in the performance of thermal efficiency.

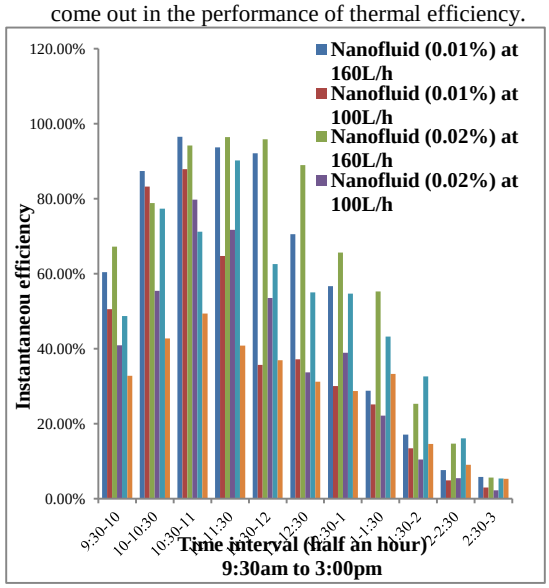

Fig: 2. Experimental variations of instantaneous efficiency [15]

6. Future Scope

Solar concentrating collectors can be used for the electricity generation on large scale and in various applications like industrial process heat. Therefore improvement in the solar thermal collector performance is highly important from research point of view so that an efficient solar thermal device can be developed. Further

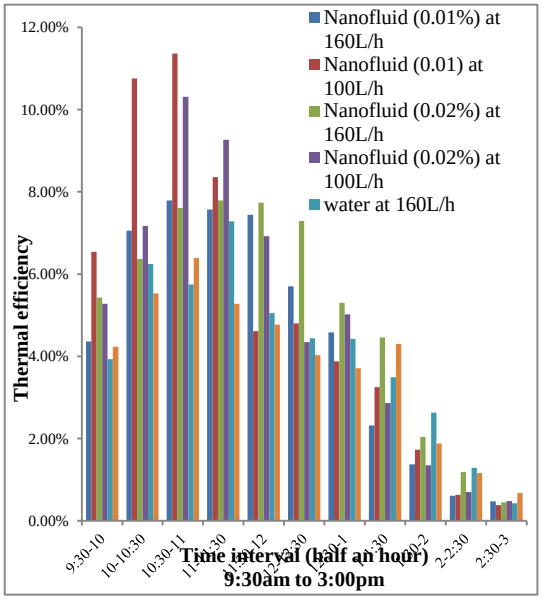

Fig: 3. Experimental variations in overall thermal efficiency for different fluids

Improvement in thermal storage device for the use in night or cloudy days also an important aspect for the construction of efficient solar thermal power plant in future. Nanofluids are the efficienct fluids, which have a capability to enhance the thermal performance of every solar thermal collector systems due to greater thermo physical properties of nanofluids like thermal conductivity so it is possible to enhance the efficiency of the hybrid as well as simple collector system by the combination of various types of nanofluids, which are made up of mixing the nano particles with different base fluids or conventional fluids like water, ethylene glycol, synthetic oil and combination of both water and ethylene glycol.

7. Conclusion

Concentrated solar thermal power is a highly prominent and proven technology to meet the current world's electricity demand, therefore advancements in the technology is greatest requirement for the better performance. Many aspects like different fluids conventional as well as nano fluid along with the improvement in thermal collector design parameters can show high thermal performance. Improvement in the thermal storage system by using phase change material is very important aspect from the research point of view because it has an ability to decrease down the cost of overall solar thermal power plant.

References

[1] Jan Fabian Feldhoff, Kai Schmitz, Markus Eck, Lars Schnatbaum-Laumann, Doerte Laing, Francisco Ortiz-Vives, Jan Schulte-Fischedick, Comparative system analysis of direct steam generation and synthetic oil parabolic trough power plants with integrated thermal storage, Solar Energy, 86, 2012, 520-530

[2] Xiang-Qi Wang, Arun S. Mujumdar, Heat trabsfer characteristic of nano fluids: a review, International Journal of Thermal Science, 46, 2007, 1-19

[3] Soteris A. Kalogirou, Solar thermal collector and applications, Progress in Energy and Combustion Science, 30, 2004, 231–295

[4] T. Yousefi, E. Shojaeizadeh, F. Veysi, S. Zinadini, An experimental investigation on the effect of pH variation of MWCNT–H_2O nanofluid on the efficiency of a flat-plate solar collector, Solar Energy, 86, 2012, 771-779

[5] R. Saidur, T. C. Meng, Z. Said, M. Hasanuzzaman, A. Kamyar, Evaluation of the effect of nanofluid-based absorbers on direct solar collector, International Journal of Heat and Mass Transfer, 55, 2012, 5899–5907

[6] Alibakhsh Kasaeian, Samaneh Daviran, Reza Danesh Azarian, Alimorad Rashidi, performance evaluation and nano fluid using capability study of a solar

parabolic trough collector, Energy Conversion and Management, 89, 2015 368–375

[7] Nor Azwadi Che Sidik, H.A. Mohammed, Omer A. Alawi, S. Samion, A review paper on preparation methods and challenges of nanoluids, International Communications in Heat and Mass Transfer, 54, 2014, 115–125

[8] Zhongyang Luo, Cheng Wang, Wei Wei, Gang Xiao, Mingjiang Ni, Performance improvement of a nanofluid solar collector based on direct absorption collection (DAC) concepts, 75, 2014, 262-271

[9] John Philip, P. D. Shima, Thermal properties of nanofluids, Advances in Colloid and Interface Science, 183–184, 2012, 30–45

[10] G. C. Bakos, I. Ioannidis, N. F. Tsagas, I. Seftelis, Design, optimisation and conversion-efficiency determination of a line-focus parabolic-trough solar-collector (PTC), Applied Energy, 68, 2001, 43-50

[11] Tooraj Yousefi, Farzad Veysi, Ehsan Shojaeizadeh, Sirus Zinadini, An experimental investigation on the effect of Al_2O_3-H_2O nanofluid on the efficiency of flat-plate solar collectors, Renewable Energy, 39, 2012, 293-298

[12] K. Vignarooban, Xinhai Xu, A. Arvay, K. Hsu, A.M. Kannan, Heat transfer fluids for concentrating solar power systems – A review, Applied Energy, 146, 2015, 383-396

[13] Gianluca Coccia, Giovanni Di Nicola, Marco Sotte, Design, manufacture, and test of a prototype for a parabolic trough collector for industrial process heat, 74, 2015, 727-736

[14] J. Paetzold, S. Cochard, A. Vassallo, D. F. Fletcher, Wind engineering analysis of parabolic trough solar collectors: the effects of varying the trough depth, journal of wind engineering and industrial aerodynamics, 135, 2014, 118–128

[15] Harwinder Singh, Pushpendra Singh, Performance Analysis of Parabolic Trough Collector System Using Nano fluid" Delhi Technological University Delhi, An Unpublished M.tech Thesis, 2015

[16] S. P. Sukhatme, J. K. Nayak, Solar Energy principles of thermal collection and storage, Mc Graw Hill,

ResearchGate

See discussions, stats, and author profiles for this publication at: https://www.researchgate.net/publication/295363103

Preliminary Investigation of Environmental Status of Bhindawas Bird Sanctuary

Article · November 2015

READS
40

4 authors, including:

A.K. Haritash
Delhi Technological University
19 PUBLICATIONS **970** CITATIONS
SEE PROFILE

Vandana Shan
Delhi Technological University
1 PUBLICATION **0** CITATIONS
SEE PROFILE

S. K. Singh
Delhi Technological University
95 PUBLICATIONS **220** CITATIONS
SEE PROFILE

All in-text references underlined in blue are linked to publications on ResearchGate, letting you access and read them immediately.

Available from: S. K. Singh
Retrieved on: 12 August 2016

Preliminary Investigation of Environmental Status of Bhindawas Bird Sanctuary

A. K. Haritash*, Vandana Shan, Priyanka Singh, S. K. Singh
Department of Environmental Engineering
Delhi Technological University, Bawana Road,
Shahbad, Delhi (110 042)

Abstract- **− Bhindawas wetland is located between 28˚28' to 28˚36' North latitude and between 76˚28' to 76˚38' East longitude in Jhajjar district of Haryana state. It was declared as a bird sanctuary by MoEF in 1986. Due to the dropping water levels at Bharatpur Bird Sanctuary (Rajasthan), the Bhindawas wetland attracts migratory birds during winter season. There have been only a few studies on seasonal variations in quality, contribution from different sources, loading of nutrients by different activities and in depth studies on determination of trophic status and ecological productivity of the wetland. This study is a preliminary investigation of water quality, trophic state index, productivity and proliferation of weeds in the wetland. The growth of weeds is observed to be maximum during summer since the temperature for growth is favourable and photoperiod is longer. The proliferation is restricted during winter since the availability of sunlight and nutrients, alongwith volume of water is less. The investigation reveals fairly high average concentration of total phosphate (5.2 mg/L) and nitrate (48 mg/L) resulting in conditions favourable for eutrophication. Based on the results obtained, the water of Bhindawas wetland was designated as eutrophic with a Trophic State Index value of 127 for TSI-TP and 63.95 as TSI-SD. The gross primary productivity in water was 2.2 mg/L/day (as O_2). The average concentration of Dissolved organic carbon (DOC), Biological oxygen demand (BOD), Chemical oxygen demand (COD), and Total Kjeldahl's Nitrogen (TKN) was 17.5 mg/L, 5.2 mg/L, 187.1 mg/L, and 4.2 mg/L, respectively. It was observed that though the water is eutrophic, algal growth is limited possibly due to zooplankton grazing, or excessive growth of macrophytes like water hyacinth, salvinia, vallisneria, hydrilla etc.**

Keywords: Bhindawas wetland, eutrophic, productivity, nutrients

I. INTRODUCTION

Freshwater ecosystems are known as the most important natural resources for survival of variety of organisms, and water quality has become a major global concern due to increasing human development activities near water bodies. Increasing pollution due to overpopulation and unprecedented development create extreme pressure on the ecological health of water bodies [1]. Excess input of nutrients in surface water bodies (lakes, rivers ad ponds) deteriorate the quality of water and interfere with recreational uses of lakes and adversely affect the biodiversity of that region. Nitrates and phosphates are two major nutrients which are responsible for choking several lakes to death due to excess growth of algal blooms and consequently depleting dissolved oxygen level [2]. These constituents also help in the speedy growth of the macrophytes like water hyacinth which is the most troublesome aquatic weed in many parts of the world. Such changes in aquatic ecosystems have resulted in alteration of conditions favourable for maintaining good water quality, maintenance of biodiversity, and conservation of water resources. There have been several reports on deteriorating water quality, reduced biodiversity and fishing, shoreline erosion, and water shrinkage in water bodies around the world [3-6]. Reduced levels of water in Bharatpur bird sanctuary has forced even migratory birds to look for alternate bodies for their nesting. Bhindawas Lake (Haryana) is a preferred alternate site for nesting of migratory birds and endemic avian fauna. It is located at 28˚32' North latitude and 76˚32' East longitude in Jhajjar district with an area of 1074 acres. It is a natural depression with manmade earthen impoundments around to store the stormwater and agricultural runoff. It gets water from rainfall (during monsoon) and mostly from excess spilling over from JLN Canal and drains its water into drain no. 8. Bhindawas wetland also collects water from the vast stretches of agricultural field of twelve villages namely a few Bhindawas, Redhuwas, Chhadwana, Nawada, Bilochpura etc. The water depth in lake actually ranges from 1 foot to 6 feet, and its water holding capacity has been enhanced with construction of earthen embankment all along its boundary. The lake serves as a buffer during floods and lean season/drought. Realizing the environmental significance and ecological services of the lake, MoEF declared it as a bird sanctuary in 1986. Since then the wetland has emerged as an important ecological habitat and place of recreation attracting a good number of tourists. Recently, some of the studies [7-8] have reported the problem of weed infestation in the wetland resulting in reduced sunlight penetration, lower dissolved oxygen levels, mobilization of problematic chemical species like phosphate, eutrophication, and reduced aesthetics. The

present study, therefore aims to study spatial variations of water quality, proliferation of weeds, and identification of major sources/processes resulting in degeneration of water quality.

II. MATERIALS AND METHODS

In order to determine the spatial variation of water quality, the wetland was divided into grids of equal size. Twenty (20) representative samples of water were collected from each grid in Polypropylene-grade plastic bottles pre-rinsed with ultrapure (Type-1) grade water. The area under the cover of *Eichhornia* was inaccessible and no sample could be collected from that region (Fig. 1).

Fig. 1. Sampling locations in Bhindawas bird sanctuary

Temperature, pH, Electrical conductivity (EC), Total Dissolved Solids (TDS), Dissolved Oxygen (DO), and Oxidation-Reduction Potential (ORP) were measured on the site using Orion make Star A329 model multiparameter meter. The gross primary productivity (GPP), and transparency were determined using DO levels under light and dark conditions, and sechhi-disc depth, respectively. Other parameters were determined within 24 hours after transporting the preserved samples to laboratory using standard methods of APHA [9]. Total phosphate (TP), sulfate (SO_4^{2-}), nitrate (NO_3^-), and ammonia (NH_3) were determined spectrophotometrically, and sodium (Na), potassium (K), calcium (Ca), and lithium (Li) were determined on Systronics make 128 μC model flame photometer. Dissolved Organic Carbon (DOC) was determined on Analytil-Jena make multi N/C2100 model TNC analyzer. The statistical analysis of values obtained was done on MS-Excel software. The eutrophication status of a wetland is usually measured using one of several trophic state indexes (TSI) of algal weight (biomass): water transparency (Secchi Depth, TSI-SD), algal chlorophyll (TSI-Chl), and total phosphorus (TSI-TP) [10]. The following equations can be used to compute the Carlson's TSI.

$$TSI\ (SD) = 60 - 14.41\ \ln(SD)$$
$$TSI\ (CHL) = 9.81\ \ln(Chl) + 30.6$$
$$TSI\ (TP) = 14.42\ \ln(TP) + 4.15$$

Where, SD is sechhi depth (m), Chl is chlorophyll (μg/L), and TP is total phosphorus (μg/L).

III. RESULTS AND DISCUSSION

Based on the results obtained, spatial variations of nutrients (CNP) and other parameters were observed (Table 1). The measurement of area in a satellite image revealed that 0.98 Km^2 of area was under clear water as against 1.344 Km^2 under intensive weed growth. Since more than half of the water surface remains covered with weeds, an adverse effect over water quality is very likely. The average pH (8.0) was reported to be slightly alkaline ranging from 7.1 to 9.6. It was observed that the pH of water was less alkaline or near neutral at sampling locations near to weed-cover and shoreline. Similar trend was observed for DO with lower values near to weed cover and shoreline. The probable reasons are restricted penetration of sunlight, limited photosynthesis, and so lower DO levels.

Average DO in the wetland was 8.0 mg/L ranging from 5.3 to 13.3 mg/L. Concurrent values of ORP were observed representing oxidizing conditions in exposed water of the wetland. The mean value of ORP was 92 mV ranging from 30 to 126 mV. The exposed water favors photosynthesis by algae and submerged vegetation resulting in higher ORP levels, thus confirming the earlier observations of higher DO values in sunlight exposed water than in vicinity to weed cover. Average TDS concentration was 234 mg/L with slight variations between 203 and 250 mg/L. It reflects that the water quality *w.r.t.* dissolved solids is almost the same throughout, and there is minimum possibility of different sources to the wetland. Further, the almost constant value of bicarbonate species, and absence of carbonate ions throughout represents uninterrupted cycling of inorganic carbon with no precipitation/fixation of carbonates in sediments. Relatively lower values of chloride and sulphate reveal that there is no input of sewage or domestic wastewater into the wetland since excess of these species is related to domestic activities of cleaning and washing. On the other hand, nutrients like nitrate and phosphate were present in excess with an average concentration of 50.5 and 4.9 mg/L, respectively. The probable source of nutrients in wetland water is agricultural runoff. The agricultural runoff and water-logging is usually pumped into Drain No. 8 and the wetland, adding the nutrients to it. The cations Na, K, Ca, and Mg were present in moderate concentration with average levels of 31.4, 2.4, 18.8, and 17.3 mg/L, respectively.

TABLE I. RANGE, MEAN (N = 20), AND STANDARD DEVIATION OF PARAMETERS MONITORED IN WATER OF BHINDAWAS BIRD SANCTUARY

Parameter	Range		Mean	SD (±)
	Min.	Max.		
pH	7.1	9.6	8.0	0.6
EC (µS/cm)	403.0	508.0	472.5	26.2
Temp (˚C)	32.3	33.9	33.0	0.5
DO (mg/L)	5.3	13.3	8.0	2.1
ORP (mV)	29.7	126	92.1	23.3
TDS (mg/L)	203	250	234.3	9.6
HCO_3^- (mg/L)	92.7	117.1	105.6	6.3
Cl^- (mg/L)	52.0	88.0	58.2	7.6
SO_4^{2-} (mg/L)	26.8	239.9	85.2	51.0
PO_4^{3-} (mg/L)	0.4	10.6	4.7	2.9
NO_3^- (mg/L)	BDL	380.1	48.0	107.4
Na (mg/L)	29.8	34.3	31.4	1.3
K (mg/L)	1.1	3.0	2.4	0.4
Ca (mg/L)	15.4	20.2	18.8	1.0
Mg (mg/L)	6.8	28.3	17.3	6.2
BOD (mg/L)	3.0	10.0	5.0	1.5
COD (mg/L)	186.0	190.0	187.0	2.0
DOC (mg/L)	8.7	38.8	17.5	5.5
NH_3 (mg/L)	0.2	1.4	0.5	0.3
TKN (mg/L)	1.4	22.4	4.2	4.6

Lower levels of the cations also confirm to the speculation of absence of domestic wastewater as source. Mean BOD_5 in the lake water was 5.0 mg/L ranging from 3.0 to 10.0 mg/L classifying Bhindawas lake as moderately polluted *w.r.t.* organic pollution. The death and decay of phytoplanktons and macrophytes in eutrophic lakes has been identified as major contributor of organic pollution. It, inturn, scavenges dissolved oxygen of water thereby affecting fish and other sensitive organisms. COD values varied between 186 to 190 mg/L with an average of 187 mg/L signifying that the oxygen demand of water is almost the same throughout the region studied. The dissolved organic carbon content varied between 8.7 and 38.8 mg/L with most of the values around the mean value of 17.5. The concentration of dissolved ammonia in water was also high with an average of 0.5 mg/L, ranging from 0.2 to 1.4 mg/L. Most of the fish and aquatic organisms are reported to be sensitive to dissolved ammonia levels higher than 0.2 mg/L in water. Toxic levels are both pH and temperature dependent, and it increases as pH decreases and as temperature decreases. Plants are more tolerant of ammonia than animals, and invertebrates are more tolerant than fish. Hatching and growth rates of fishes may be affected by higher dissolved ammonia [11]. Similarly high concentration of total Kjeldahl's nitrogen (TKN) was observed with an average of 4.2 mg/L ranging from 1.4 to 22.4 mg/L. Very high levels of TKN, nitrate, and phosphate are a testimony to eutrophicated status of Bhindawas.

IV. TRANSPARENCY, PRODUCTIVITY, AND EUTROPHIC STATUS

Secchi depth transparency is the simplest, most extensive and appropriate parameter for determination of ecosystem health. In present study, average (n = 5) secchi depth was recorded as 0.76 metres. As per Nurnberg (1996) [11], lakes with sechhi transparency depth <1 metres are classified as hypereutrophic lakes. Bhindawas lake is classified as a highly eutrophic lake based on sechhi disc transparency. The trophic state index was calculated as 63.95 based on sechhi depth (TSI-SD), and 127 based on total phosphate (TSI-TP). Since TSI-TP>TSI-SD, it may be concluded that overgrazing by zooplanktons and excessive growth of macrophytes limits the growth of algae.

V. CONCLUSION

Based on the results obtained, it is observed that water in Bhindawas lake has high concentration of nitrogen and phosphorus and is eutrophic in nature. Despite excess of nutrients, overgazing by zooplanktons complemented by excessive growth of macrophyte weeds is assumed to be associated with limited growth of algae. Based on the values of cations and anions, it is observed that pumping from water-logged areas and agricultural runoff around the wetland is major source of nutrients (nitrogen and phosphorus). The water of lake is slightly alkaline and there is no precipitation/deposition of inorganic carbon in the form of carbonates. The organic carbon resulted in moderate organic pollution, but was autochthonous since death and decay of algae and weeds resulted in addition of organic carbon to the lake. The DO levels were sufficiently good to support normal growth of aquatic life forms.

VI. REFRENCES

[1] R. Chandra, K.A. Nishdh, P.A. Azeez, "Monitoring water quality of Coimbatore wetlands, TamilNadu, India," Envciron. Monit. Assess., Vol. 169, pp. 671-676, 2010.
[2] R. Upadhyay, A.K. Pandey, S.K. Upadhyay, "Assessment of lake water quality by using Palmer and Trophic State Index- a case study of upper Lake, Bhopal, india," International Research journal of Environmental Sciences, Vol. 2(5), pp. 1-8, 2013.
[3] A.A. Ayoade, N. aggarwal, "Preliminary analyses of physical and chemical parameters of Tehri dam reservoir, Garhwal himalaya, India," Zoology and Ecology. Vol. 22(1), pp. 72-77, 2012.
[4] O. Singh, C.K. Jain, "Assessment of water quality and eutrophication of lakes," Journal of Environmental and Nanotechnology, Vol. 2, pp. 46-52, 2013.

[5] J.A. Shah, A.K. Pandit, "Physico-chemical characteristics of water in Wular lake-A Ramsar site in Kashmir Himalaya," International Journal of Geology, vol. 2, pp. 257-265, 2012.

[6] S. Singh, R. Kumar, "Changes in land use pattern of Bhindawas wetland in Haryana," International journal of Informative & Futuristic Research, vol. 2, pp. 346-349, 2014.

[7] S. Kumar, R. Dhankhar, "Trophic State Index and assessment of water quality for domestic and agriculture purpose of Bhindawas wetland, Jhajjhar, Haryana (India)," Annals of Biology, vol. 28, pp. 144-151, 2012.

[8] R. Saluja, J. K. Garg, "Surface water quality assessment of Bhindawas Lake (Haryana, India) using Multivariate Statistical Techniques," Journal of Global Ecology and Environment, vol. 2, pp. 2454-2644, 2014.

[9] American Public Health Association: Standard Methods for the Examination of Water and Wastewater, 21st Edn. APHA-AWWA, Washington DC, USA, 2005.

[10] R.E. Carlson, "A trophic state index for lakes," Limnology and Oceanography, vol.2, pp. 361-369, 1977.

[11] G.K. Nurnberg, "Trophic state of clear and colored, soft- and hardwater lakes with special consideration of nutrients, anoxia, phytoplankton and fish," J. Lake and Reservoir Management, vol. 12, pp. 432-447, 1996.

ResearchGate

See discussions, stats, and author profiles for this publication at: https://www.researchgate.net/publication/305395518

Prototype Design and Analysis of Controllers for one Dimensional Ball and Beam System

Conference Paper · July 2016

READS
7

3 authors, including:

Sudarshan Valluru
Delhi Technological University
13 PUBLICATIONS **6** CITATIONS

SEE PROFILE

All in-text references underlined in blue are linked to publications on ResearchGate, letting you access and read them immediately.

Available from: Sudarshan Valluru
Retrieved on: 19 August 2016

Prototype Design and Analysis of Controllers for one Dimensional Ball and Beam System

Sudarshan K Valluru, Madhusudan Singh, Supriya Singh
Department of Electrical Engineering
Delhi Technological University
Delhi-110042, India
E-mail: sudarshan_valluru@dce.ac.in, madhusudan@dce.ac.in, sups.singh28@gmail.com

***Abstract*— Ball and Beam structure is an under actuated nonlinear unstable electro-mechanical system and it is one of the robotic benchmark problem in control engineering. This paper addresses the control and real time modelling of ball and beam system. Different types of controllers are being used to balance a ball on a beam at a pre-defined location with precise amount of force and torque in minimum time for stable operation of the system. The accurate control of ball position on beam is a challenging task. The performance analysis of ball and beam system is carried out using PID, state space, lag-lead, robust LQR, observer based LQG controllers, and performance characteristics of the system is presented. Lyapunov direct method is used describe the unstable behaviour of ball and beam system.**

Keywords— PID, state space, lag-lead, LQR, LQG, Lyapunov stability.

I. INTRODUCTION

The study of system dynamics and control is essential for analyzing and design of automatic control systems. Most of the physical systems display nonlinear dynamics and require a complex nonlinear analysis methods to investigate their performance. In recent years many nonlinear controllers are suggested to improve the performance of nonlinear system. A ball and beam system is a nonlinear unstable system, where control problem is to automatically control the angle of the beam in order to obtain the required position of the ball on the beam by applying an appropriate torque to the joint. This task is difficult because the ball moves with an acceleration that is proportional to the tilt angle of the beam and ball does not stay at one location on the beam[1]. There are two degrees of freedom in this system. One is the ball rolling up and down the beam, and the other is beam rotating through its central axis.

Numerous studies have been conducted on a ball-beam system and various controllers have been proposed for control of this under actuated mechanism. The ball-beam system is a bench mark example in control systems but unlike other models, a stepper motor pivoted at the center of the beam is used here to control the position of the ball along with an accelerometer sensor which provides information related to the orientation of the beam. Thus, as the ball moves to an external disturbance, the angle of the beam is changed to counteract this change[2]. The current orientation of the beam and the position of the ball is displayed serially to a terminal window[3]. This paper presents a comprehensive modelling of ball and beam system and design of different controllers such as PID, state space, lag-lead, robust LQR and observer based LQG controllers for positioning control of ball on the beam. A linearized model of ball and beam system is derived for testing of controllers and dynamic performance of ball position is determined through simulation study in MATLAB. Stability of open loop unstable ball beam system is also described using Lyapunov Direct method.

This research paper is organized in four sections: Section II briefly describes the mathematical model for the ball beam system and transfer function deduction. Section III deals with the design of different controller's viz. PID, state space controller, lag-lead compensator, robust LQR and observer based LQG controller. Section IV consists of prototype implementation of ball beam system followed by the conclusion in Section V.

II. MODELLING AND IDENTIFICATION OF BALL ON A BEAM SYSTEM

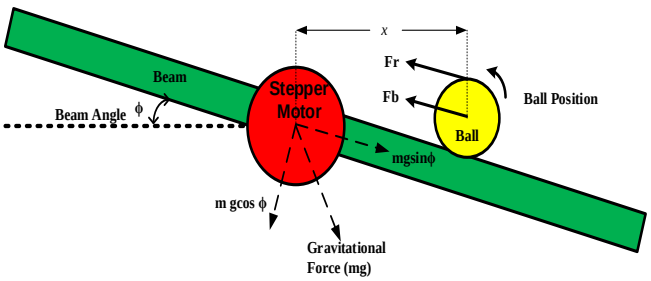

Fig.1 A schematic diagram of ball and beam system

The Fig.1shows the schematic representation of a ball and beam system, here the beam is mounted on the output shaft of a stepper motor that can be tilted about its centre axis by applying an electrical actuating signal to the motor. The system is open loop unstable in control system terminology because the system output (the ball position) increases without limit for a fixed input (motor angle). To keep the ball in a desired position on the beam feedback controllers are used, so that the ball is positioned accordingly to desired position[4].

978-1-4673-8587-9/16/$31.00 ©2016 IEEE

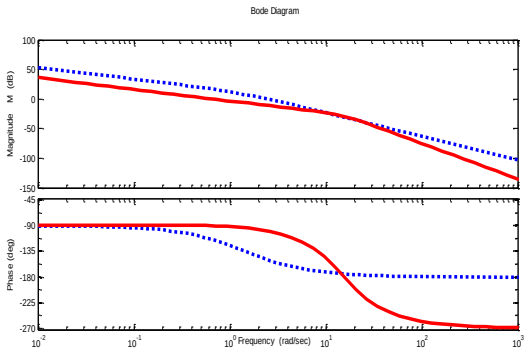

Fig.8(c) Bode plot for observer based LQG

III. PROTOTYPE IMPLEMENTATION OF BALL BEAM SYSTEM

The system includes a beam made up of polyvinyl chloride sheet which is rotated about its center by a 12 V permanent magnet stepper motor as per desired motion and a ball which is an unconstrained object as it rolls freely unless acted by an external force. Basically a high voltage and high current Darlington array IC ULN 2003 is used as a driver IC to give full strength and speed to stepper motor. The IC is connected to Arduino UNO microcontroller with ATMEGA328 as processor. The position of ball is sensed by an ultrasonic sensor HC-SR04 fixed at one end of beam which works on SONAR principle. Further the tilt sensor ADXL-335 keeps a track on tilt of beam. By locating the position of ball and tilt of beam, signals could be sent to move the beam clockwise or anticlockwise accordingly so as to keep ball at the center of the beam. The beam tilt angle is compared with the definite angle of zero degrees and PID controller is used to minimize the error. The prototype of ball beam is shown in Fig.9. The unique features of our ball-on-beam system are as follows:

1. First, it is inexpensive compared to those commercially available.
2. Second, the position of ball is sensed by using ADXL-335 sensor. There is no tear and wear by the ball movement.
3. Third, it uses a microcontroller for the implementation of the control algorithm. It enjoys all the convenience that comes with a microcontroller.

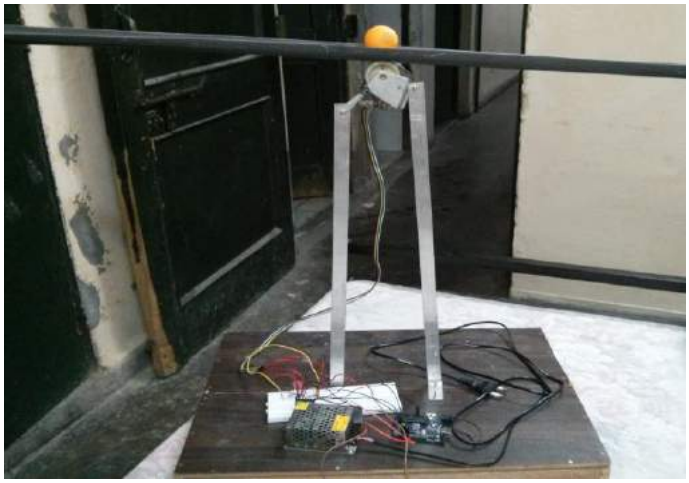

Fig.2 Proto type of ball beam system

IV. CONCLUSION

In this paper, the basic design of a one dimensional ball beam system using different controllers has been illustrated. This system emulates real control problems such as horizontal stabilization of an aircraft during landing and while experiencing turbulence. The MATLAB simulation results along with the graphs for the controllers have been included. From output graphs it can be seen that robust LQR controller approaches the desirable performance when compared with other controllers. Unlike other systems, here the motor being used is a stepper motor instead of a servo makes the system more economical one.

REFERENCES

[1] J. Hauser, S. Sastry, and P. Kokotovi, "Nonlinear Control Via Approximate Input-Output Linearization: The Ball and Beam Example," *IEEE Trans. Automat. Contr.*, vol. 37, no. 3, pp. 392–398, 1992.

[2] D. J. S. Ruth, K. Dhanalakshmi, and S. S. Nakshatharan, "Interrogation of Undersensing for an Underactuated Dynamical System," *IEEE Sens. J.*, vol. 15, no. 4, pp. 2203–2211, 2015.

[3] H. Sira-ramirez, "On the Control of t.he 'Ball and Beam' System: A," in *39th IEEE conference on Decision and control*, 2000, pp. 4042–4047.

[4] M. Amjad, M. I. Kashif, S. S. Abdullah, and Z. Shareef, "Fuzzy logic control of ball and beam system," in *2nd International Conference on Education Technology and Computer*, 2010, vol. 3, pp. 489–493.

[5] W. Chen, X. Sui, and Y. Xing, "Modeling and Modulation of Nonlinear Ball-beam System Controller Based on Matlab," in *Proceedings of 9th international conference on fuzzy systems and knowledge discovery*, 2012, vol. 5, no. Fskd, pp. 2388–2391.

[6] B. C. Chang, H. Kwatny, and S.-S. H. S.-S. Hu, "An application of robust feedback linearization to a ball and beam control problem," in *Proceedings of the IEEE International Conference on Control Applications*, 1998, vol. 1, no. September, pp. 694–698.

[7] C. Aguilar-ibañez and C. Aguilar-iban, "The Lyapunov direct method for the stabilisation of the ball on the actuated beam," *Int. J. Control I*, vol. 7179, no. April, pp. 2169–2178, 2016.

[8] K. T. Prasad and Y. V. Hote, "Optimal PID controller for Ball and Beam system," in *International Conference on Recent Advances and Innovations in Engineering, ICRAIE 2014*, 2014, pp. 1–5.

[9] P. Rapp, O. Sawodny, and C. Tar, "An Immersion and Invariance based Speed and Rotation Angle Observer for the Ball and Beam System," in *proceedings of American control conference*, 2013, pp. 1069–1075.

[10] N. Hara, M. Takahashi, and K. Konishi, "Experimental Evaluation of Model Predictive Control of Ball and Beam Systems," in *proceedings of the American Control Conference*, 2011, no. 4, pp. 1130–1132.

ResearchGate

See discussions, stats, and author profiles for this publication at: https://www.researchgate.net/publication/299562399

Seasonal Assessment of Trophic State of a Palustrine Water Body

Article · January 2015

READS
17

6 authors, including:

A.K. Haritash
Delhi Technological University
19 PUBLICATIONS **968** CITATIONS

SEE PROFILE

All in-text references underlined in blue are linked to publications on ResearchGate, letting you access and read them immediately.

Available from: A.K. Haritash
Retrieved on: 09 August 2016

Seasonal Assessment of Trophic State of a Palustrine Water Body

Amit Yadav, Atul Kataria, Kapil Singh,
Karamveer Mathur*, Sagar Goswami, A. K. Haritash
Department of Environmental Engineering
Delhi Technological University, Bawana Road,
Shahbad, Delhi (110 042)

Abstract- **− Most of the water bodies around human habitations are observed to be moderately to severely polluted. Inflow of sewage, addition of domestic waste water, and run off from neighbouring areas has resulted in increase in dissolved solids, salinity, and eutophication of most of the Palustrine water bodies. Therefore, the present study was undertaken to determine the nutrient status and trophic state of a sacred groove village pond. It is observed that the water body is eutrophic with an increasing Carlson's Trophic State Index (CTSI) with time. The concentration of Total Phosphate (TP) increased from 14.6mg/l to 17.3mg/l within six months of time. It resulted in more than 4 times increase in Gross Primary Productivity (GPP) (12.7mg/l/day-54.7mg/l/day), which was also confirmed by an increase in Chlorophyll concentration from 2.88mg/l to 3.25mg/l. Although, the secchi depth decreased from 26 cm to 21 cm resulting in decreased penetration of sunlight and limiting the photic Zone. The dissolved oxygen too decreased from 7.3mg/l to 2.1mg/l, although the variation in average temperature of surface water was negligible. The concentration of Total Dissolved Solids (TDS) and Salinity increased during the period confirming to addition of nutrient/pollutants and a gradual deterioration of water quality. In the light of above mentioned facts it is important to monitor the health of pond water ecosystems; restrict the discharge of waste water without pre treatment; and to adopt suitable interventions and management practices to improve the health of water bodies.**

Keywords: Palustrine, Eutrophication, CTSI, GPP

I. INTRODUCTION

Palustrine ecosystems are micro environments having significant ecological, environmental, social, and economic benefits particularly in rural areas of developing countries. These are not only the storage reservoirs but are also the systems to recharge ground water, sources to drinking water and irrigation, conserve soil quality, and maintain aquatic diversity. Since most of the rural and remote areas lack proper drainage system most of the domestic waste water, agricultural and storm water run off finds its way into the ponds. During the process a considerable amount of nutrients like carbon, nitrogen, and phosphorus (CNP), and pollutants like dissolved metals, pesticides, organic matter, and other dissolved impurities are carried to the ponds. Most of the village ponds, therefore, suffer from the problem of excessive algal growth, intensive weed proliferation, reduced dissolved oxygen (DO) levels, production of obnoxious odour, and reduced aesthetics resulting in overall degradation of environmental quality [1]. Excess of nutrients leach through the soil and may contaminate ground water, and indirectly affect health, agricultural production, and soil quality as well. High concentration of organic impurities (specifically carbonaceous and nitrogenous) results in decreased DO particularly in bottom layers [2], and increased levels of nitrate and phosphate in sediments. Excess of anions like chloride (Cl^-), sulphate (SO_4^{2-}), nitrate (NO_3^-), and phosphate (PO_4^{3-}) may also interfere with the DO levels in hypolimnion [3]. Formation of reducing or anoxic conditions in bottom sediments may render the insoluble phosphate soluble and further increase the intensity of eutrophication [4]. Turbidity of lakes and ponds is an important parameter to determine the water quality, and most of the eutrophicated lakes have low transparency because of algal growth and dead and decomposing organic matter this reduces sunlight penetration, reduced photosynthesis, and low productivity of the lake. Such water bodies are prone to stratification during summer and winter, whereas spring and fall may coincide with algal bloom [5]. There have been number of studies to determine water quality of lakes and rivers [6-10], but the studies on monitoring of ponds are limited. Though the size and volume of ponds is smaller compared to lakes but the number is considerably high. Monitoring and management of pond ecosystems at local level can result in significant improvement in soil and water quality of the region. Owing to lack of awareness, and disposal of waste water, such water bodies are gradually turning useless with more frequent algal blooms. In order to meet the water demand, dependence on ground water has increased and ground water table in such areas is gradually depleting. Realizing their importance, village ponds have been restored and declared as sacred grooves in many villages. The present study is an attempt to monitor the water quality of a sacred groove declared village pond; identification of major sources and parameters of concern; and classify the water body based on its trophic status.

II. MATERIALS AND METHODS

A. Study Area and sample collection

The study area is located at 28º44′20″ N longitude and 77º2′6″ E latitude in Karala village of North-west district of Delhi (Fig. 1). It is a natural depression having an area of around 10 acres. The source to the pond is domestic wastewater, agricultural runoff, and rainfall. It has an average

depth of 5 feet in summer and winter, and 8 feet during monsoon. It is surrounded by agricultural fields on North and village temples in southern direction. It has been declared as a sacred groove for more than 50 years. It was exclusively used for bathing, irrigation, and cattle earlier. But in the past two decades the village has registered significant growth in population, and a few industries. Since then it is receiving domestic waste water and industrial effluent resulting in an increase in concentration of nutrients as well as pollutants in order to determine the water quality the study area was divided into 10 grids of equal size, and representative water sample was collected from each grid in the month of September 2014 and February 2015 representing an interval of 6 months. Temperature, pH, Electrical conductivity (EC), Total Dissolved Solids (TDS), and Dissolved Oxygen (DO), were measured on the site using Orion make Star A329 model multiparameter meter. The gross primary productivity (GPP), and transparency were determined using DO levels under light and dark conditions, and sechhi-disc depth, respectively. Other parameters were determined within 24 hours after transporting the preserved samples to laboratory using standard methods of APHA [11]. Total phosphate (TP), sulfate (SO_4^{2-}), and nitrate (NO_3^-) were determined spectrophotometrically, and sodium (Na), potassium (K), calcium (Ca), and lithium (Li) were determined on Systronics make 128□□C model flame
analysis of values obtained was done on MS-Excel software. The eutrophication status of a wetland is usually measured using one of several trophic state indexes (TSI) of algal weight (biomass): water transparency (Secchi Depth, TSI-SD), algal chlorophyll (TSI-Chl), and total phosphorus (TSI-TP) [12]. The following equations can be used to compute the Carlson's TSI.

$$TSI(SD) = 60 - 14.41 \ln(SD)$$

$$TSI(CHL) = 9.81 \ln(Chl) + 30.6$$

$$TSI(TP) = 14.42 \ln(TP) + 4.15$$

Where, SD is sechhi depth (m), Chl is chlorophyll (mg/L), and TP is total phosphorus (mg/L).

$$CTSI = \{(TSI\text{-}SD)+(TSI\text{-}Chl)+(TSI\text{-}TP)\}/3$$

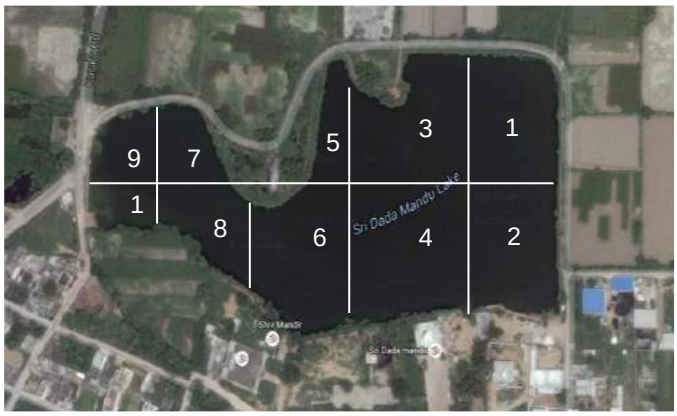

Fig. 1. Sampling locations in the village pond

III. RESULTS AND DISCUSSION

Based on the analysis of samples, there were slight spatial variations except at the inlet, but the temporal variations represented a significant increase in concentration of pollutants (Table 1). The pH of water was observed to slightly alkaline in range during September 2014 (post-monsoon), whereas it was slightly acidic with an average value of 6.3 during February, 2015 (winter). It shows significant variation of chemical composition and the chemical stress the water body goes through. The acidic pH may be correlated to anoxic and reducing conditions formed in the pond during winter, apart from the possibility of addition of some acidic waste into the water body. The later period of winter represented higher concentration of dissolved solids (TDS) and electrical conductivity (EC) owing to higher import of pollutants and reduced volume of water during winter. The difference in temperature in the two seasons was marginal with average values of 24.1˚**C** and 26.8˚**C.** Although the temperature difference is marginal, there was significant difference of DO with average values of 7.0 mg/L and 2.0 mg/L during post-monsoon and winter, respectively. Reduced DO in winter further strengthens the assumption that reducing conditions in bottom layer had resulted in formation of acids, thus leading to lowering of pH. Another important aspect related to DO is survival of fish and other aquatic life. Most of the sensitive species fail to survive at DO level of 2.0 mg/L; low temperature and reduced photoperiod during winter decreases overall productivity resulting in death of flora and fauna of the pond. This further adds dead biomass resulting in increased oxygen demand and reduced DO levels. The lowering of pH in water reverses carbonate cycle. The same is confirmed in our study with the absence of carbonates in winter since the average pH had dropped to 6.3 resulting in conversion of carbonate to bicarbonate. An increase in bicarbonate concentration was also reported which supports the results. High concentration of anions like chloride and sulphate is an indication of addition of domestic wastewater in a water body. In the present study, average chloride concentration was 1245.5 and 563.0 mg/l in post monsoon and winter, respectively. Concurrent trend for sulphate was observed in the seasons. Higher levels during post monsoon may be correlated to higher water demand and more wastewater production compared to winter. Phosphate and nitrate are important parameters to regulate algal growth in a water body. Average concentration of phosphate was 15.5 mg/L initially, and increased to 17.3 mg/L in a period of six months.

TABLE 1. RANGE (MIN.-MAX.), MEAN, AND STANDARD DEVIATION OF CONCENTRATION OF VARIOUS PARAMETERS

Parameter	September 2014				February 2015			
	Range		Mean	SD (±)	Range		Mean	SD (±)
	Min.	Max.			Min.	Max.		
pH	8.1	8.5	8.3	0.12	6.1	6.7	6.3	0.18
EC (mS/cm)	3.0	3.51	3.45	0.16	3.5	3.6	3.5	0.05
Temp (˚C)	23.5	24.8	24.1	0.45	25.5	27.7	26.8	0.69
DO (mg/L)	3.0	13.0	7.0	3.35	1.0	4.0	2.0	0.96
TDS (mg/L)	1460	1720	1690	90	1750	1770	1760	10
HCO_3^- (mg/L)	384.3	683.2	503.3	82.7	414.8	610.0	502.6	61.9
CO_3^{2-} (mg/L)	BDL	78.0	41.0	16.6	BDL (*Below the detection limit*)			
Cl^- (mg/L)	1050.0	1345.0	1245.5	80.7	490.0	660.0	563.0	56.8
SO_4^{2-} (mg/L)	138.5	163.7	150.8	8.93	112.8	144.9	132.4	10.8
PO_4^{3-} (mg/L)	14.5	18.4	15.5	1.15	11.8	27.8	17.3	14.5
NO_3^- (mg/L)	2.4	24.5	16.5	7.43	0.77	4.7	2.9	1.2
Na (mg/L)	227.4	438.4	336.9	86.6	373.6	463.5	401.6	29.0
K (mg/L)	97.7	163.5	128.8	24.9	145.2	193.6	157.5	17.0
Ca (mg/L)	35.4	42.9	38.7	1.98	150.8	177	158.5	9.13
CTSI	87.0				92.0			
GPP (mgO_2/L/day)	12.65				54.65			

As discussed earlier, formation of reducing/acidic conditions result in mobilization of phosphate, which otherwise remains in bound form with sediments. The calcium and ferric-ion bound inorganic phosphate gets mobilized/soluble in water with the lowering of pH, and reduction of ferric ions to ferrous, respectively. Dissolution of calcium carbonate sediments increases calcium concentration as observed in our study, representing an increase of average calcium concentration from 38.7 to 158.5 mg/L, thus confirming our speculation. Similar increase in concentration of other cations (Na, K) was observed. An increase in dissolved solids, phosphate, and nitrate results in increased frequency and intensity of eutrophication. The trophic status of the water body was calculated based on Carlson's Trophic State Index (CTSI) to classify the water body. CTSI was 87.0 during post-monsoon and 92.0 during winter classifying the lake as a hypereutrophic water body [13], which is heading towards more frequent and intense cycles of eutrophication. In order to confirm it, the productivity of water body was also calculated. With an increase in CTSI value, the gross primary productivity (GPP) increased from 12.65 mgO_2/L/day to 54.65 12.65 mgO_2/L/day from post monsoon to winter season. Significant increase in GPP confirms that the water body is going through increased intensity of algal bloom. Based on the results obtained, it is concluded that discharge of domestic wastewater in village ponds may result in eutrophication and poor state of health of the water body. There is an urgent need to regularly monitor the status of palustrine water-bodies, and take necessary measures to restore the already eutrophicated ponds.

IV. REFRENCES

[1] S. Tamot, P. Sharma, "Physico-chemical status of Uper Lake (Bhopal, India) water quality with special reference to phosphate and nitrate concentration and their impact on lake ecosystem," Asian Journal of Experimental Science, Vol. 20(1), pp. 151-158, 2006.

[2] C.H. Sujatha, N. Benny, R. Raveendran, C.L. Fanimol, N.K. Samantha, "Nutrient dynamics in two lakes of Kerala, India," Indian Journal of Marine Sciences, Vol. 38(4), pp. 451-456, 2009.

[3] O. Singh, C.K. Jain, "Assessment of water quality and eutrophication of lakes," Journal of Environmental and Nanotechnology, Vol. 2, pp. 46-52, 2013.

[4] L.H. Kim, E. Choi, M.K. Stenstrom, "Sediment characteristics, phosphorus types and phosphorus release rates between river and lake sediments," Chemosphere, Vol. 50, pp. 53-61, 2003.

[5] J.A. Shah, A.K. Pandit, "Physico-chemical characteristics of water in Wular lake-A Ramsar site in Kashmir Himalaya," International Journal of Geology, vol. 2, pp. 257-265, 2012.

[6] R. Chandra, K.A. Nishadh, P.A. Azeez, "Monitoring water quality of Coimbatore wetlands, TamilNadu, India," Envciron. Monit. Assess., Vol. 169, pp. 671-676, 2010.

[7] A.A. Ayoade, N. aggarwal, "Preliminary analyses of physical and chemical parameters of Tehri dam reservoir, Garhwal himalaya, India," Zoology and Ecology. Vol. 22(1), pp. 72-77, 2012.

[8] S. Singh, R. Kumar, "Changes in land use pattern of Bhindawas wetland in Haryana," International journal of Informative & Futuristic Research, vol. 2, pp. 346-349, 2014.

[9] S. Kumar, R. Dhankhar, "Trophic State Index and assessment of water quality for domestic and agriculture purpose of Bhindawas wetland, Jhajjhar, Haryana (India)," Annals of Biology, vol. 28, pp. 144-151, 2012.

[10] R. Saluja, J. K. Garg, **"**Surface water quality assessment of Bhindawas Lake (Haryana, India) using Multivariate Statistical Techniques," Journal of Global Ecology and Environment, vol. 2, pp**.** 2454-2644, 2014**.**

[11] American Public Health Association: Standard Methods for the Examination of Water and Wastewater, 21st Edn. APHA-AWWA, Washington DC, USA, 2005.

[12] R.E. Carlson, "A trophic state index for lakes," Limnology and Oceanography, vol.2, pp. 361-369, 1977.

[13] R.E. Carlson, J. Simpson, "A Coordinator's Guide to Volunteer Lake Monitoring Methods," *North American Lake Management Society*, pp. 96, 1996.

ResearchGate

See discussions, stats, and author profiles for this publication at: https://www.researchgate.net/publication/296384779

Secure Message Transmission Ensuring Authentication Using Digital Signature and Watermarking

Conference Paper · February 2016

READS
10

2 authors:

Shivi Garg
Delhi Technological University
1 PUBLICATION **0** CITATIONS
SEE PROFILE

Manoj Kumar
Delhi Technological University
19 PUBLICATIONS **1** CITATION
SEE PROFILE

All in-text references underlined in blue are linked to publications on ResearchGate, letting you access and read them immediately.

Available from: Shivi Garg
Retrieved on: 10 August 2016

ISSN:0975-9646

Secure Message Transmission Ensuring Authentication Using Digital Signature and Watermarking

Shivi Garg[#1], Manoj Kumar[#2]

[#]*Computer Engineering Department,*
Delhi Technological University
Delhi, India

Abstract— **This paper presents a system that allows the users to securely transfer the messages by embedding them in the digital images. The information, which is to be sent to the receiver, is made to be more secure in spite of simple plain text. The message is hashed and digitally signed to provide authentication. The Quick Response (QR) Code for this secured information is generated. This QR Code image is accommodated in the original cover image by the embedding algorithm. This system uses the watermarking scheme. To accommodate the messages the original cover image is modified by the embedding algorithm to obtain the stego image. At the receiving end, the message is decoded using the other key value pair. The proposed system is not hacked by any intended user thereby ensuring authentication and non-repudiation.**

Keywords— **Digital Signature, Hash, QR code, Watermarking.**

I. INTRODUCTION

Many methods exist to make the information secure. Information security is the method of protecting information which protects its availability, privacy and integrity [1]. For providing secure message transmission cryptography is used in both wireless and wired network.

Cryptography is the study of techniques and methods for secure communication in the presence of third parties known as adversaries. Cryptography is a process of converting a plain text into cipher text (Encryption) and cipher text into a plain text (Decryption) [2]. Cryptography is mainly of two types: Symmetric key cryptography (or secret key cryptography) and Asymmetric key cryptography (or Public key cryptography). Secret-key cryptography is encryption method or a technique where both the sender and receiver share the same key. The sender uses an encryption algorithm and the key to encrypt the data; the receiver uses the corresponding decryption algorithm and this same key to decrypt the data. Public-key cryptography uses different set of keys for encryption (Public key) and decryption (Private Key).

In computer science and cryptography there is a type of function known as Hash function that plays a very important role in making messages secure. The predicate hash function is easy to compute whereas it is hard to invert, i.e., for a given output it is hard to find an input that maps to that output [3]. After the message is hashed, key pairs are generated to form digital signature. The encrypted hash is then embedded in the QR Codes, which is then hidden behind the cover image to form the watermarked image.

II. DIGITAL CERTIFICATE GENERATION

A. Key Pair Generation

The key-pair generation is based on RSA Algorithm. RSA is a public key cryptosystem having two keys: public key and the private key [4]. Here, encryption is done using the private key and decryption is done using the public key. An RSA public-private key pairs can be generated by the steps mentioned as follow:

1. Generate a pair of large, random prime numbers: p and q.
2. Compute the modulus n such that n = p * q.
3. Compute $\varphi(n) = (p-1) * (q-1)$.
4. Chose ‘e’ such that $1 < e < \varphi(n)$ and e & n are co-primes.
5. Compute a value for ‘d’ such that $(d*e) \% \varphi(n) = 1$.
6. The public key is the number (e, n) & private key is (d, n).

To encrypt a message, M, with the public key, creates the cipher, C, using the equation: $C = M^e \bmod n$.

The receiver then decrypts the cipher, C, with the private key using the equation: $M = C^d \bmod n$.

B. Digital Signature Algorithm

A digital signature is a mathematical and computational scheme for representing the authenticity of a digital information or document. It ensures non-repudiation i.e., the sender of the message cannot later on deny having sent the message and that the receiver cannot deny having received the message and that maintains the integrity of the message i.e. it is not altered in transit [5].

A digital signature scheme generally consists of three algorithms:

1) A key generation algorithm, which chooses a private key uniformly at random from a set of possible private keys. This algorithm then produces the private key and a corresponding public key

2) A signing algorithm when, given a message and a private key, produces a signature

3) A signature verifying algorithm, which when given a message, public key and a signature, either accepts or discards the message's claim to authenticity

III. PROPOSED SYSTEM

This system helps to merge the concepts of cryptography and watermarking. In this system payload is being inserted in the QR Code image which consists of the hash value of patient information. The payload is encrypted using a key (provided by the user) based on the digital signature algorithm before embedding. This digitally signed information is encoded into QR Code. This secure code is then embedded in an image to form the watermarked image. In case where the number of pixel pairs free for inserting the watermark outnumbers the length of the payload, then payload is repeated several times according to the requirement.

IV. METHODOLOGY

C. Embedding Process

1) The In this process patient information like-Name, Age and Sex are stored in the text file patient.txt.

2) Compute the hash of the patient information.

3) This hash is encrypted with the private key of the sender and digital signature is then generated. The key generation is based on RSA Algorithm. RSA is a public key crypto-system having two keys-Public Key and the Private Key.

4) The digitally signed information is encoded into the QR Code.

5) The secured code is then embedded in an image to form the watermarked image.

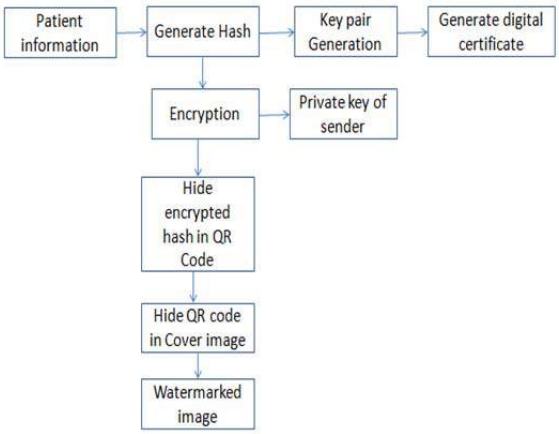

Fig. 1 Flowchart of Embedding Process

D. Restoration Process

1) In the restoration process we apply the extraction process of Coltuc et al. scheme and extract the encrypted QR Code.

2) To decode the QR Code any QR code decoder can be used and encrypted hash of the patient information is obtained.

3) To recover the original patient information it is decrypted by using the public key and the digital signature.

4) If some different QR code is decrypted, then this information will not match and it is rejected.

5) Or if the hash is not matched, then also it will be rejected confirming that the sender is not authentic and the image has been tampered.

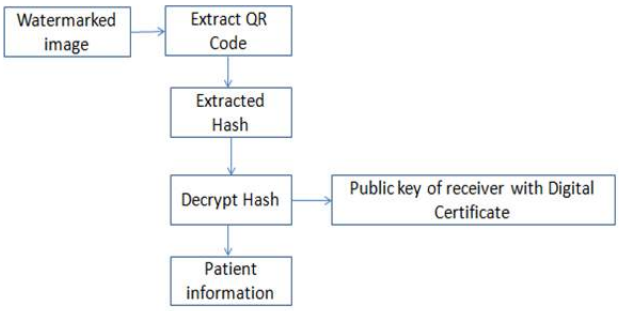

Fig. 2 Flowchart of Restoration Process

V. RESULTS AND ANALYSIS

A. Patient Information

Patient information is a simple text file as patient.txt which contains the attributes like-Name, Age and Sex of the patient. Fig. 3 shows the patient.txt file.

Fig. 3 Patient information in patient.txt file

B. Hash Generation

Hash of the patient information is generated using MD-5 (Message Digest). It produces 128 bit hash value and normally expressed in text format as a 32 digit hexadecimal number format [6]. Fig. 4 shows the hash of the patient information.

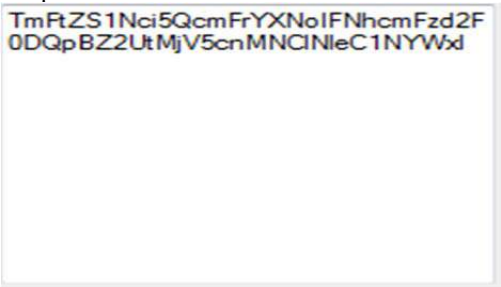

Fig. 4 Hash of patient information

C. Key Pair Generation

Key pair generation is based on RSA algorithm. It is a public key cryptosystem which has two set of keys: private key and public key. Encryption is done using private key and decryption is done by public key [7]. Key pair generation is shown in the Fig. 5.

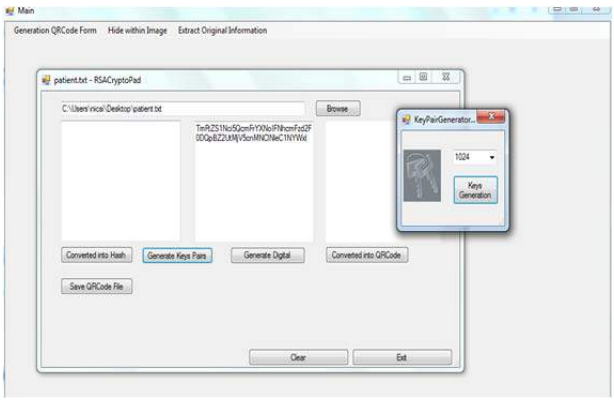

Fig. 5 Key pair (public and private key) generation

D. Digital Certificate Generation

Digital certificates (also known as Public key Certificate) connect the identity of an individual or an institution to a digital public key, i.e., to a pair of keys that can be used to encrypt and sign digital information. The arrangement of principles, protocol standards and software that assist digital certificates is known as a public key infrastructure, or PKI. The software, which supports this infrastructure, generates a set of public-private key pairs. [8]. Fig. 6 shows the digital certificate generation.

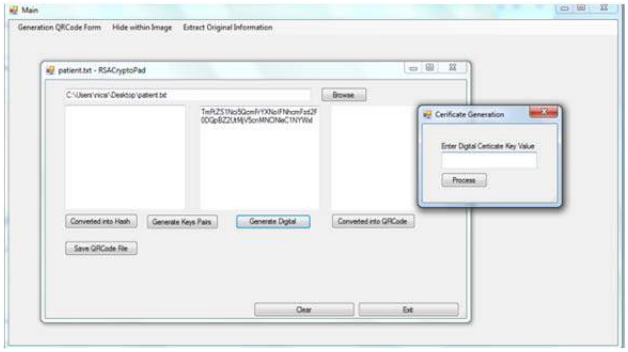

Fig. 6 Digital certificate generation

E. QR Code Generation

QR code (Quick response) is a two dimensional information storage tool. The length of the stored information depends on: Data type/Mode, Version (ranging from 1 – 40) and Error Correction Levels (L, M, Q, and H) [9]. The hashed information is encrypted using the Private key, which is then encoded to QR Code as shown in the Fig. 7.

Fig. 7 Hash Encrypted with Private key and encoded to QR Code

F. Watermark Generation

The QR Code is then embedded in the cover image to generate the watermarked image. This is done by using Coltuc et al. scheme of reversible watermarking.[10]. Fig. 8 shows embedded QR code in the cover image to form watermarked image.

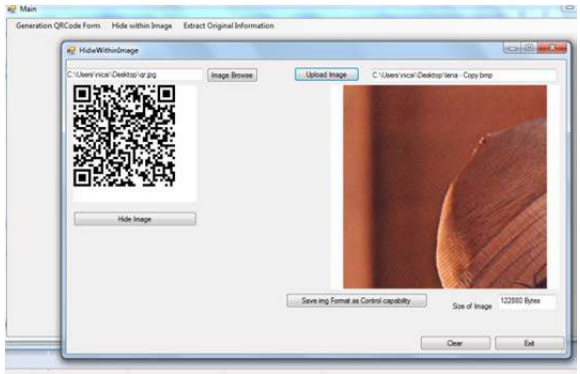

Fig. 8 QR Code hidden behind a cover image to get watermarked image

G. Receivers' End

To extract the original information, public key of the receiver is used to decrypt the hashed information along with the digital certificate as shown in the Fig. 9.

Fig. 9 Decryption of hash using public key with digital certificate

If the key pairs match, then QR code is decoded to correct patient information as shown in the Fig. 10.

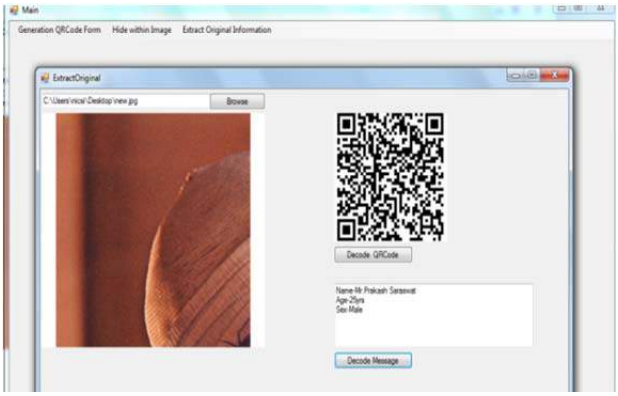

Fig. 10 QR Code decoded to correct patient information

If the key pairs do not match, then QR code cannot be decrypted to the original information as in Fig. 11.

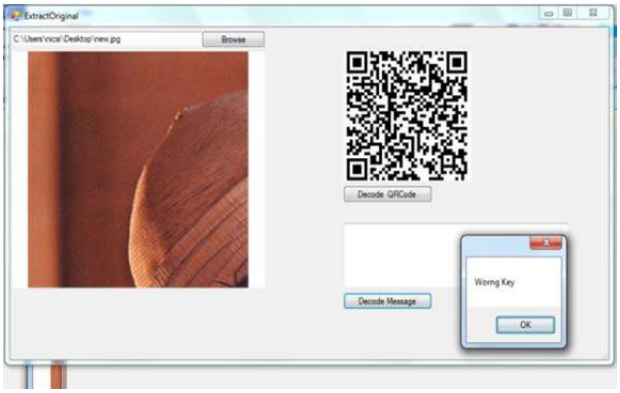

Fig. 11 QR Code decoded to wrong patient information

VI. Conclusions

The proposed scheme is robust to all the attacks. In this system the hash of the patient information is encrypted using the RSA encryption algorithm along with the generation of digital signature. This signed and encrypted hash is then embedded in the QR Code. This QR Code then embedded in the cover image using Coltuc et al. scheme. The embedding algorithm is made to work in feedback mode so that if a single bit of data gets changed, then following data gets changed too. And in that case the recovered hash and the hash of the recovered image will never match resulting in a rejected image.

Acknowledgment

It is a pleasure to acknowledge Dr. O.P. Verma (HOD computer engineering department) for the conversations and ideas that led to this research on secure message transmission. We would like to thank Dr. Seba Susan and Mrs. Ritu Agarwal for their important advice, corrections, and valuable suggestions, and for devoting their precious time on our research.

References

[1] Vishwa Gupta, Gajendra Singh and Ravindra Gupta, *Advance cryptography algorithm for improving data security*, vol. 2, issue 1, January 2012

[2] Sangeet Saha, Chandrajit pal, Rourab paul, Satyabrata Maity and Suman Sau, *Encryption using different techniques: a review,* vol. 2, no. 1, January-February-2013.

[3] Marc Stevens, *Attacks on Hash Functions and Applications*, 2012.

[4] Sonal Sharma, Jitendra Singh Yadav, Prashant Sharma *Modified RSA Public Key Cryptosystem Using Short Range Natural Number Algorithm* vol. 2, issue 1, August 2012.

[5] D. Shiva Rama Krishna, *Providing security to confidential information using digital signature,* vol. 3, issue 11, November 2015.

[6] Xiaoyun Wang and Hongbo Yu, *How to break MD5 and other hash functions*, pp. 19–35, 2005.

[7] Amare Anagaw Ayele1, Dr. Vuda Sreenivasarao, *A Modified RSA Encryption Technique Based on Multiple public keys*, vol. 1, issue 4, June 2013.

[8] Dr. Ali M. Al-Khouri., *The role of digital certificates in contemporary government systems: the case of UAE identity authority*, 2010.

[9] Peter Kieseberg, Sebastian Schrittwieser, Manuel Leithner, Martin Mulazzani, Edgar Weippl, Lindsay Munroe and Mayank Sinha, *Malicious pixels using QR Codes as attack vector*, 2012.

[10] Dino Coltuc, and Alain Treméau, Simple *reversible watermarking schemes*, January, 2005.

Volume 4, Issue 1 (2016) 278-282 ISSN 2347 - 3258
International Journal of Advance Research and Innovation

Solar Industrial Process Heating system for Indian Automobile Industry

Anubhav Uppal, J.P.Kesari
Department of Mechanical engineering, Delhi Technological University, Delhi, India

Article Info

Article history:
Received 02 April 2016
Received in revised form
20 May 2016
Accepted 28 May 2016
Available online 15 June 2016

Keywords

Automobile Industries

Heat Energy

Solar Thermal technology

Abstract

Indian automobile industry is one of the largest in the world. To match production with demand, many automobile makers have started to invest heavily in various parts in the industry. Automobile industries have number of different production that needs large amounts of energy in form of electricity or heat. In automobile industry over 65% of the energy demand is for heating. Possible integration with proper solar thermal technology depending on the temperature range achieved by different solar collectors and temperature needed for process provided by heat application media. It also shows the current energy source or fuel being used to achieve these processes. Proposed system combines the direct steam generation concentrating collectors with the fossil fuel fired high pressure boiler. Solar thermal technology can be installed in the most automobile industrial sectors to lower consumption of fossil fuels, cut production costs, preserve environment by lessening CO_2 emissions. Concentrating solar collector field is mounted on the roof of an industrial production site to Solaris the supply of saturated steam into steam network

1. Introduction

Demand of heat energy accounts for around 70% of total energy consumption in any industry, therefore solar heat for industry can be perfect application of solar thermal technology as solar collectors can provide most of this heat energy demand. Also the India has a great potential for solar industrial heat because of high solar irradiation for almost 300+ sunny days in year. Apart from these reasons, Shortage of fossil energy sources such as oil, gas or coal with rapidly rising energy consumption in developing countries like India have result in hike in energy prices. From now integration of solar thermal technology with industrial heat sources will increase India's independence from future energy price hikes and help to lessen industrial production costs. Now a day, the automobile industry is under great strain to make their products more environmentally sound in this 21st century especially after C02 emission laws made in Kyoto protocol. Not only the automobiles themselves, but the whole production has to become more sustainable. Therefore there is urgent need for more sustainable automobile production with lessened demand for energy, materials and as well as emissions.

2. Performance of Indian automobile Industry in 2014-15

The Indian automobile industry is one of the largest in the world with an annual production of 2,33,66,246 automobiles including passenger vehicles, commercial vehicles, three wheelers and two wheelers in fiscal year 2014-15 as compared to 2,15,00,165 vehicles produced in year 2013-14 with a annual growth of 8.68 % . [1] The automobile industry has a very high share in the country's manufacturing gross domestic product (Gross Domestic Product). India is also a major automobile exporter, with huge export growth expectations in the near future. Sales of passenger automobiles in India grew by 3.90 percent 2014-15 from a previous year ago, according to data given by Society of Indian Automobile Manufacturers (Society of Indian Automobile Manufacturers). Sales of cars also grew at 4.99 % in 2014-15 over the last period. Figure 1 [2] shows the production trend of automobile industry in India for year 2009-2010 to 2014-15.

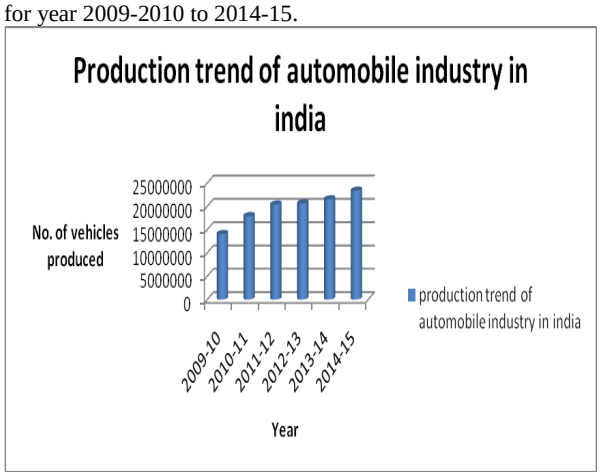

Fig: 1. Production trend of automobile industry in India

To match production with demand, many automobile makers have started to invest heavily in various parts in the

Corresponding Author,
E-mail address: Anubhav3365@gmail.com
All rights reserved: http://www.ijari.org

industry in the last few months. The industry has attracted foreign direct investment worth United States $ 12,232.06 million during the period April 2000 to February 2015, according to the data released by Department of Industrial Policy and Promotion. Also The Government of India encourages foreign investment in the automobile and allows 100 percent Foreign Direct Investment under the automatic route. From now the vision of government of India is to make India as the top destination in the world for make of automobiles and auto parts.

3. Energy Demand in Automobile industry

The Automobile industry has a very high energy demand. According to a study over 65% of the energy demand is for heating. The three major production shops in automobile manufacturing are:-

(i) Paint shop
(ii) Body shop
(iii) Assembly shop

Most automobile factories have a central steam system for producing steam at around 180°C – 200°C which supplies all processes.

Automobile industries have number of different production that needs large amounts of energy in form of electricity or heat. Various energy sources used in Automobile for different production are mainly electricity with major share, followed by petroleum products like natural gas as second largest source and followed by others sources also. [3] Figure 2 shows to divide various energy sources used in automobile industry.

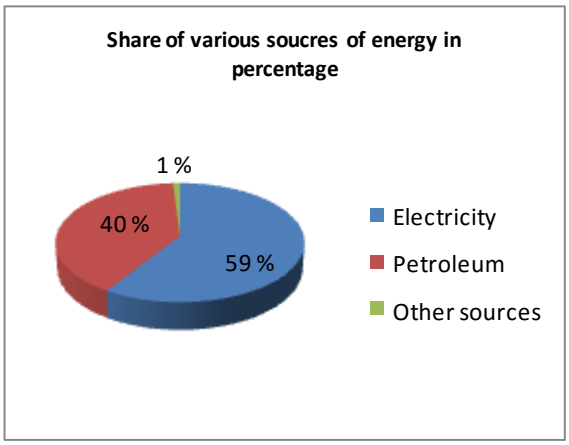

Fig: 2. Composition of energy sources used in automobile industry

Total energy consumed in automobile industry for automobile production divided in three Areas named Body shop, Paint shop and Assembly shop where different production takes place in a well-defined sequence leading to product. Figure 3 shows to divide total energy consumption in an automobile production in various shops like Paint shop, Assembly shop and Body shop.

The following analysis can made from figure 3 on pattern of energy consumption in automobile industry that 73 % of total energy consumed in Paint shop, followed by 17% consumption in paint shop and 10%in Assembly shop. [4] Two major sources of total energy consumption are an Electricity and petroleum product that is natural gas in automobile. Electricity is consumed mainly in Paint shop with 45%share, followed by 35% share in body shop and rest 20% in assembly shop as shown in figure 4.

Other source of energy is Natural gas which consumed in Paint shop with High share of 92 %, small shares of 4% in Body shop and 4% in Assemble shop as shown in figure 5.

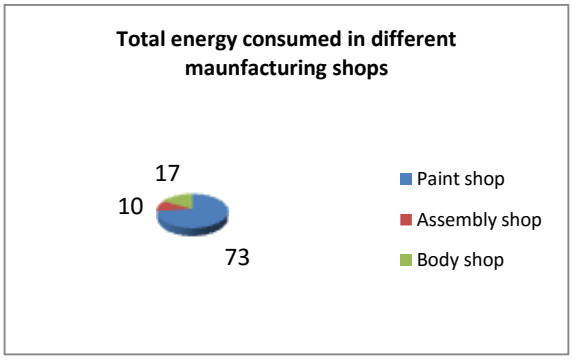

Fig: 3. Pattern of energy consumption in Different shops in Automobile industry

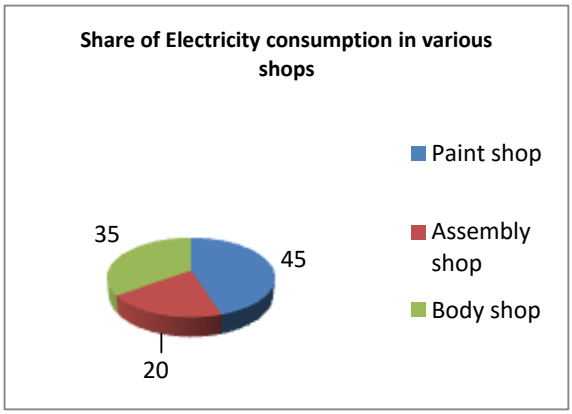

Fig: 4. Pattern of Electricity consumption in Different shops in Automobile industry

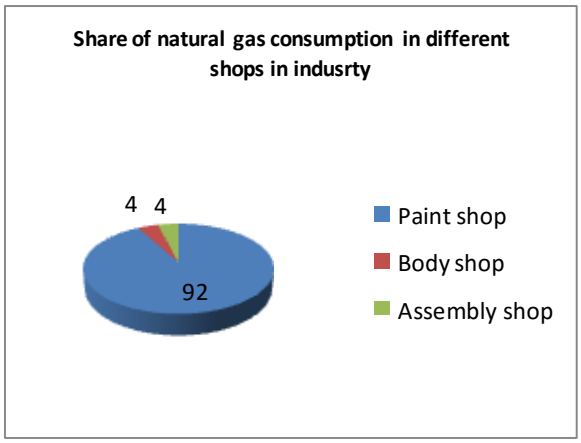

Fig: 5. Pattern of Petroleum products (natural gas) consumption in Different shops in Automobile industry

4. Production processes requiring thermal energy in automobile industry

Manufacturing automobile includes many that need thermal energy either in the low temperature range (60 – 100°C) or medium temperature range (100 – 200°C). These are suitable for integration with solar thermal Technologies to provide industrial heat. Figure 6 shows the entire flow diagram for an Automobile manufacturing. Processes marked with * need thermal energy at temperature range. Body shop includes process needing thermal energy like Drying of castings and parts, part cleaning, etc. Paint shop includes processes like Dip Zinc phosphate or 7 tank processes, baking of paint in ovens, etc.

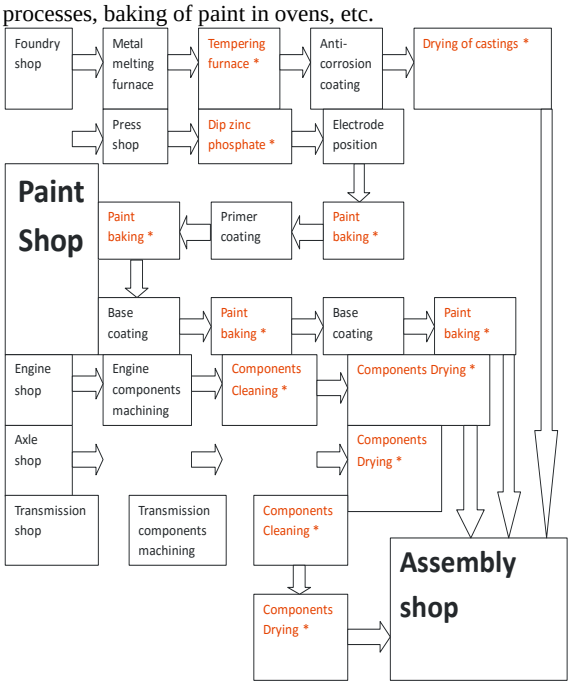

Fig: 6. Different processes needing thermal energy marked in automobile industry

5. Solar Thermal technology Applications in Automobile industry

Some of the typical processes in the automobile manufacturing industry needing thermal energy as shown in figure 4 now explain below in some details with temperatures needed in process and application media used like Hot water, hot air or pressured steam. [5] Figure 7 shows the temperature associated with different thermal processes in automobile manufacturing on a temperature scale.

5.1 Part Cleaning, washing or Degreasing

Pressured Hot water at a temperature of about 90°C sprays over the automobile engine parts to remove the dust content. The hot water needed for spraying is heated either by electrical heaters or natural gas based heating sources.

5.2 Drying of washed parts after Degreasing

The cleaned parts from Degreasing are dried in the hot air chamber in which the hot air is blown at 90°C. The hot air used is heated by using electrical coil heaters or natural gas based burners. The heating cycle depends on the size of the part to be dried.

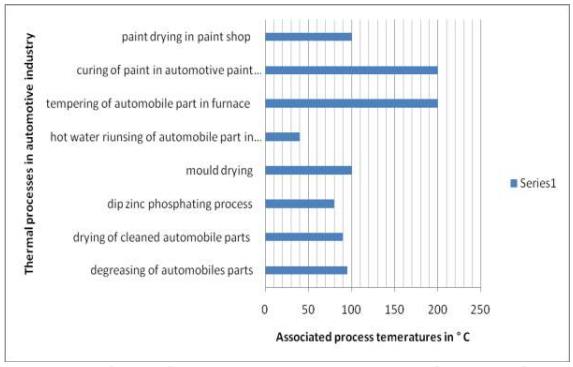

Fig: 7 thermal processes in automotive industry with associated process temperatures

5.3 Mould Drying

The casted or moulded automobile parts are coated with anticorrosion coatings for improving life and overall performance. These parts are then dried by hot air blown by hot air blower at high temperature of 100°C.

5.4 Paint curing process in baking ovens

After each coat of paint on automobile, the paint is baked in baking oven using hot air heated either by electrical coils or gas burners. The temperatures needed in baking ovens range around 200 °C.

5.5 Dip zinc Phosphating or 7 tank process

A standard 7 tanks or DIP ZINC PHOSPHATING process is used to achieve good paint adhesion and corrosion resistance on automobile body before painting is done. All heated tanks are heated directly by electrical immersion hot water heaters or closed steam coils. Table 1 shows the 7 processes involved in the 7 tank process with the Temperature involved and Dip time needed.

Table: 1. Steps involved in 7 tank process with temperature and dip time needed

Step	Temperature in °C	Dip time in seconds
Degrease	95	15
Cold water rinse	25	5
Derust	70	10
Cold water rinse	25	5
Zinc phosphate dip	80	5
Cold water rinse	25	5
Passivation	70	10

5.6 Tempering of parts in a Furnace

Hardening and tempering are normally done to improve the wear resistance, strength and toughness of the automobile parts. Some typical application of tempering in automobile industry are low temperature tempering (150°C-200°C) of steel bearing, medium temperature tempering (350°C-550°C) of carbon steel and high temperature tempering (550°C-650°C) of medium carbon alloy steel.

Table 2 shows the process with possible integration with proper solar thermal technology depending on the

temperature range achieved by different solar collectors and temperature needed for process provided by heat application media. It also shows the current energy source or fuel being used to achieve these processes.

Table: 2. Applications of solar thermal technology in different automobile production process

Process steps	Energy or fuel being used	Application media	Temperature need °C	Recommended solar technology
Degreasing of automobile parts or part cleaning	Natural gas	Pressured Hot water	90	Evacuated tube collectors
Drying of cleaned parts	Natural gas	Hot air	90	Parabolic trough collectors with air as working medium
Dip zinc phosphating process	Electricity	Hot water	80	Flat plate collector
Mould drying	Electricity	Hot air	100	Solar air heaters
Tempering in furnace	Natural gas	Hot air	200	Solar air heaters with Concentrating collectors
Paint shop Preconditioning that is Hot water rinsing of automobile body in paint shop	Electricity	Hot water	40	Flat plate collector
Paint shop that is curing of automobile paint in paint baking ovens	Natural gas	Hot air	200	Linear Fresnel concentrating collectors
Paint shop air-conditioning of wet paints in the paint shop	Natural gas	Hot or Cold air supply	50	Evacuated tube collectors based chillers
Paint shop evaporation drying	Natural gas	Hot air supply	100	Solar air heating

6. Proposed SIPH system for automobile industry

Proposed system combines the direct steam generation concentrating collectors with the fossil fuel fired high pressure boiler. Two main components of the proposed system are steam boiler and a concentrating collector field. Tubular steam boiler is used for steam generation with fossil fuel firing in case of non sunshine hours to give system high reliability. Concentrating solar thermal collector foiled is used as solar boiler for industrial process heat applications. [6]

The efficiency of these collectors depends upon various factors like:-

(i) Geographic location
(ii) Operating conditions i.e. operating temperature and corresponding heat losses
(iii) Field layout
(iv) Orientations of collector field

Concentrating solar collector field is mounted on the roof of an industrial production site to solarise the supply of saturated steam into steam network. Figure 8 shows the layout of the proposed system for integration of solar with fossil fuel fired steam generation system for industrial process heat application in automobile industry.

Concentrating solar collector field supply saturated steam to steam lines which supply heat to various thermal loads. For producing saturated steam, liquid water enters solar field, is heated up to boiling point and beyond also and stars evaporating. Water steam mixture leaving the solar field enters the steam drum where separation of steam from liquid water takes place. A pump recirculates the liquid water out of the steam drum back to the solar field. Evaporated water is being replaced by feed water pump from the feed water tank. The water is circulated until the pressure and the related temperature) is sufficient enough for the application. Then Steam supply starts. The main steam line supplies various thermal loads in the automobile production line for degreasing of automobile parts, heat treatment in furnace , curing of paint in paint shop,etc. [7]

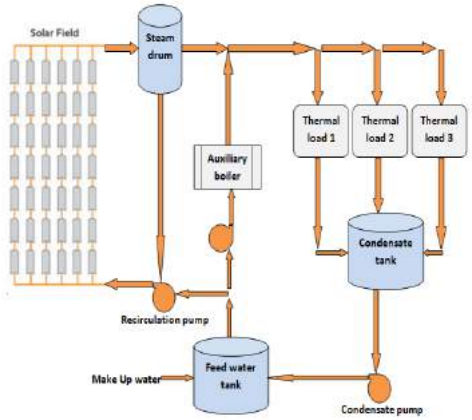

Fig: 8 layout of the proposed SIPH system for automobile industry

7. Conclusions

Thus solar thermal technology can be installed in the most automobile industrial sectors to lower consumption of fossil fuels, cut production costs, preserve environment by lessening CO2 emissions. Also Commercial viability of solar technologies is much higher for industries using furnace oil, coke or captive diesel based electricity. However Major challenges before solar industrial process heat market development in India are like:-

(i) Low payback period usually expected by the industry
(ii) Missing awareness about this technology in industry

(iii) Lack of solid policy by the government
(iv) Missing pilot projects showing these technologies success here in India.

Aim of this paper is to develop solar-fossil fuel steam generation system for industrial applications for a more sustainable production in sectors such as automobile, food, textile, pharmaceutical and many others. This system consists of two main components: a solar concentrating collector field and a conventional steam boiler. With this system, integration of saturated steam supply for process heat applications in a reliable, energy efficient and cost effective way is possible.

References

[1] Society of Indian automotive manufacturers http://www.siamindia.com/statistics.aspx?mpgid=8&pgidtrail=9
[2] Society of Indian automotive manufacturers http://www.siamindia.com/statistics.aspx?mpgid=8&pgidtrail=13
[3] Zahler, C., & Iglauer, O. Solar process heat for sustainable automobile manufacturing. Energy Procedia, 30,2012, 775-782.
[4] Presentation of india clean tech summit Day 3 http://www.indiacleantechsummit.com/presentations/day3/ParallelSessionV_RETThermalApps/Veena_Sinha.pdf
[5] Clique solar thermal solutions for industrial process heat http://www.cliquesolar.com/AutomobileSolution.aspx
[6] Hafner, B., Stoppok, O., Zahler, C., Berger, M., Hennecke, K., & Krüger, D. Development of an integrated solar-fossil powered steam generation system for industrial applications. Energy Procedia, 48, 2014, 1164-1172.
[7] Krüger, D., Lichtenthäler, N., Dersch, J., Schenk, H., Hennecke, K., Anthrakidis, A., & Wirth, H. P. Solar steam supply: initial operation of a plant. ISES.2011

Emerald Insight

International Journal of Pharmaceutical and Healthcare Marketing

Strategic issues in pharmaceutical supply chains: a review
Rajesh Kr Singh Ravinder Kumar Pravin Kumar

Article information:

To cite this document:
Rajesh Kr Singh Ravinder Kumar Pravin Kumar , (2016),"Strategic issues in pharmaceutical supply chains: a review", International Journal of Pharmaceutical and Healthcare Marketing, Vol. 10 Iss 3 pp. -
Permanent link to this document:
http://dx.doi.org/10.1108/IJPHM-10-2015-0050

Downloaded on: 02 August 2016, At: 23:17 (PT)
References: this document contains references to 0 other documents.
To copy this document: permissions@emeraldinsight.com
The fulltext of this document has been downloaded 3 times since 2016*

Access to this document was granted through an Emerald subscription provided by emerald-srm:544911 []

For Authors

If you would like to write for this, or any other Emerald publication, then please use our Emerald for Authors service information about how to choose which publication to write for and submission guidelines are available for all. Please visit www.emeraldinsight.com/authors for more information.

About Emerald www.emeraldinsight.com

Emerald is a global publisher linking research and practice to the benefit of society. The company manages a portfolio of more than 290 journals and over 2,350 books and book series volumes, as well as providing an extensive range of online products and additional customer resources and services.

Emerald is both COUNTER 4 and TRANSFER compliant. The organization is a partner of the Committee on Publication Ethics (COPE) and also works with Portico and the LOCKSS initiative for digital archive preservation.

*Related content and download information correct at time of download.

Downloaded by Delhi Technological University At 23:17 02 August 2016 (PT)

Strategic issues in pharmaceutical supply chains: a review

1. Introduction

The pharmaceutical industry can be defined as a combination of processes, organizations and operations involved in the development, design and manufacturing of useful pharmaceutical drugs (Shah, 2004). According to Xie and Breen (2012, pharmaceutical supply chain is a special supply chain in which drugs are produced, transported and consumed. Papageorgiou (2009) has observed that enterprises cannot be competitive without considering supply chain management activities. According to Lee (2002) management of supply chains is a complex and challenging task, because of the changing trends in expanding variety of products, short product life cycles, increased outsourcing, continuous advances in information technology, and globalization of businesses. It also includes expenditure of high cost and time in conducting clinical trials with low success rate in product discovery and clinical development, generic competition at the end of product patent life followed by high uncertainties in demands and capacity planning (Lainez et al., 2012). Narayana et al. (2012) have concluded that slow growth for the industry had also been a major challenge in the recent past. Talias (2007) has observed that innovation rates in the industry have shown considerable decline, due to the long time of 15-30 years spent in the development of new drugs. WHO (2009) has noticed that drug prices rises as high as 650 percent than the acceptable international standard in under developed countries in addition to the low availability of cheap medicines in the market. Insufficient funding, inability to forecast accurately, lack of incentives for maintaining stocks, inefficient distribution systems and pilferage of medicines for private resale have led to the low availability of cheap medicines that are essential for primary healthcare sector (WHO, 2009). Porter, (1980) has considered input pricing, uncertainty in product demand, actions of competitors, actions of governmental bodies, bargaining power of suppliers and buyers, threat of new drugs in the field and global economic dynamics as the major challenges for the pharmaceutical industries.

To meet challenging requirements, companies must find new sources of competitiveness and engage in developing unceasing innovation techniques (Ageron et al., 2013). Srivastava (2008) pointed out risks and uncertainties related to the recovery of pharmaceutical drugs such as timing, quality, quantity, and variety of returns; estimation of operation and cost-related parameters for reverse supply networks; customer behavior and preferences; decisions resolution for product returns; and cost of co-ordination along the reverse supply chain. Grossmann (2004) has observed that product discovery, design, supply chain optimization and global life cycle assessment are likely to be the major challenges in the pharmaceutical sector over the next few decades. Pisano (2000) have felt the need for the pharmaceutical industry to learn from other industries that how to manage operational excellence in terms of cost-effective development and faster lead-times, in the field of product obsolescence and price competition.

Bhakoo and Chan (2011) have considered pharmaceutical supply chain more complex because it requires the participation of different stakeholders such as pharmaceutical manufacturers, wholesalers, distributors, customers, information service providers, and regulatory agencies. Due to these complexities, pharmaceutical sector is not widely researched. It is also felt that due to lack of research, pharmaceutical sector in developing countries are not able to contribute significantly in global markets. Such as in context to India, Mahajan et al. (2015) have observed that pharmaceutical industry has largely capitalised on its low-cost production of generic drugs

Downloaded by Delhi Technological University At 23:17 02 August 2016 (PT)

© Emerald Group Publishing Limited
This is a pre-print of a paper and is subject to change before publication. This pre-print is made available with the understanding that it will not be reproduced or stored in a retrieval system without the permission of Emerald Group Publishing Limited.

and in domestic market. Therefore the present study will try to identify existing research gaps in this sector on the basis of past literature available. For literature review, authors have developed a framework as shown in figure 1. The framework consists of mainly three strategic issues such as resources, process and performance. Remaining part of the paper is organised as follows. Second section discusses the literature review on different issues of pharmaceutical supply chain. Third section discusses the summary and gaps identified from literature review. Finally the fourth section discusses the conclusion.

2. Strategic issues in pharmaceutical supply chains

All over the globe pharmaceutical organisations are facing challenges like global quality standards, healthcare reform, patent expiries and increased service requirements. To meet these challenges, pharmaceutical firms have to reduce costs, increase agility and improve speed to market. To get success in global and volatile market strategic planning is very important. Shah (2004) has defined the key issues which play an important role in the design and development of pharmaceutical supply chain such as process development, capacity planning, network design, plant design and pipeline and development management. Perez-Escobedo et al. (2012) have studied that development of decision support strategies and systems for managing new product portfolios are necessary to minimize risk while optimizing an objective or a set of objectives i.e. maximization of expected net present value, minimization of time to market, etc. Wan et al. (2006) have worked to accommodate the higher level of complexity required by time dependent strategic decisions such as capacity contraction/ expansion. Jain and Grossmann (1999) have developed an operational decision support systems exclusively based on quantitative information and with a dynamic character at the operational level.

Ageron et al. (2013) have focused on the different practices and collaboration issues of suppliers and customers for improving the competitiveness of the whole supply chain. This can only be achieved by best use of limited resources available to obtain the high profitability and effective decisions involved in the presence of significant uncertainty (Levis and Papageorgiou, 2004). Health action international and WHO (2009) have also observed that insufficient funding, lack of incentives for maintaining stocks, inability to forecast accurately, inefficient distribution systems and pilferage of medicines for private resale have led to the low availability of cheap generic drugs that are required especially in primary healthcare. Governments and other private agencies have to become more concerned at increasing cost of healthcare drugs. Shah (2004) has observed that strict measures should be taken for controlling the prices of new drugs and encouragement of the use of generic alternatives should be promoted. For structured literature review in this study, strategic issues have been classified into three major categories i.e. resources, processes and performance. Singh and Sharma (2015) have also used assets, processes and performance in their framework to analyse competitiveness of supply chains. It is observed that effectiveness of strategy depends mainly upon these strategic issues. Resources consisted of factors related to assets of a organisation such as new product development capabilities, new process development capabilities, capacity development & planning, plant & network design, pipeline & development management, e-business capability, research and development capabilities and processes consisted of other value adding activities such as inventory management, outsourcing logistics activities, reverse logistics processes, lean manufacturing

Downloaded by Delhi Technological University At 23:17 02 August 2016 (PT)

© Emerald Group Publishing Limited
This is a pre-print of a paper and is subject to change before publication. This pre-print is made available with the understanding that it will not be reproduced or stored in a retrieval system without the permission of Emerald Group Publishing Limited.

process, green scm processes and quality management. While developing strategies, these are important attributes and are shown as a framework in Figure 1.

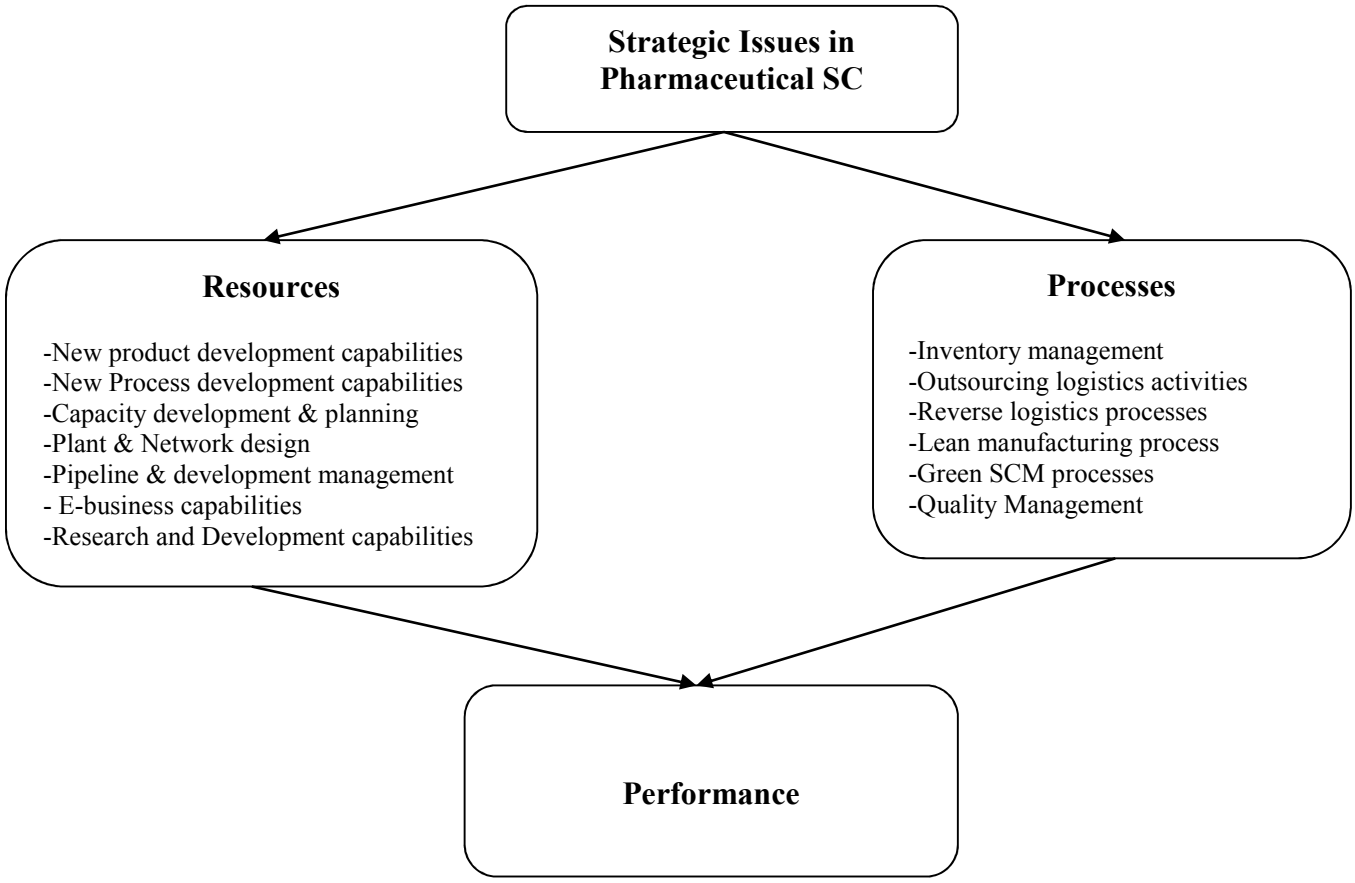

Figure1. Research Framework for the present study

Downloaded by Delhi Technological University At 23:17 02 August 2016 (PT)

2.1 Resources of pharmaceutical supply chain

Resources are assets, which a particular organization has. Effective utilization of resources for developing different capabilities plays very important role in ensuring competitiveness of any supply chain. Different organizational resources are discussed in following section:

2.1.1 New product development capabilities

The concept of NPD (new product development) has been characterized by many factors such as increased competition, rapid technological advances, higher costs, shorter product life cycles (Gupta and Wilemon, 1990). Levis and Papageorgiou (2004) have found that since the effective patent life is diminishing and generic drugs will inevitably enter the market, there is a valid threat to the profitability of the new products, therefore it is mandatory for the company to

© Emerald Group Publishing Limited
This is a pre-print of a paper and is subject to change before publication. This pre-print is made available with the understanding that it will not be reproduced or stored in a retrieval system without the permission of Emerald Group Publishing Limited.

decide on its capacity investment plan so as to guarantee the availability of the necessary manufacturing capacity resources to produce the new products in near future. Sustainable competitive advantage requires capabilities that provide enduring benefits and are not easily copied by competitors (Kwak and Anbari, 2009). Other issues i.e. continuous hike in drug prices and need for new product development are driving the way pharmaceutical supply chain work. Narayana et al. (2012) have studied that growing lifestyle diseases like obesity and the evolution of new viral strains have placed pressures on the industry to adapt rapidly to risks and uncertainty.

According to Chiesa and Toletti (2004), pharmaceutical industries should benchmark its performance against other industries, and adopt similar practices to improve the way they develop new products (NPD). Nonaka and Takeuchi (1995) have observed that many pharmaceutical companies are considering NPD as more important issue than the accepted need of high quality, low cost, and differentiation to excel in today's competitive market. Scott (2000) conducted a study on those activities that are perceived by NPD practitioners and academic researchers as being in greatest need of improvement in many high-tech companies. Pisano and Wheelwright (1995) have also emphasized that shorter product life cycles, increasingly hard-to manufacture product designs, fragmented markets, and growing technological advancements are changing the nature of competition in pharmaceutical industries. Iacocca et al. (2015) have observed that customers are ready to pay more for branded products. Therefore research scope lies in strategy formulation for branded drugs and generic drugs under dynamic environment.

2.1.2 New process development capability

Various strategies have been discovered for the survival of pharmaceutical industry. These strategies include strategic imperatives, commercial initiatives and finally adoption of a new drug development process (Baker et al., 2002). Efficient process development may provide better performance and improve the productivity of pharmaceutical drugs. Application of optimal process can also help in reducing manufacturing costs and improving the quality of medicines. Narayana et al. (2012) have considered process development crucial because research in any field generally involves a cyclic process, beginning with exploratory studies using interviews/surveys, followed by case studies and theoretical formulations. According to Perez-Escobedo et al. (2012), optimal process planning and scheduling is crucial for the development of new product in order to achieve better product discovery, process development and plant design in pharmaceutical industries. Crosby (1979) has observed that creation of both operating procedures and processes is necessary for producing defect-free products. Process development work can also be conducted for testing of drugs as well as for construction and design of a commercial plant if the product is to be launched (Perez-Escobedo et al., 2012). Gray et al. (2011) have found that distinct language, beliefs and values encountered in different countries are the major challenges that pharmaceutical companies have to face for the development of their process especially in offshore manufacturing. Therefore researchers should explore strategies to overcome on different challenges for offshore manufacturing and new process development.

2.1.3 Capacity planning

Shah (2004) has observed that capacity planning has gained some attention due to the problems associated with clinical trials uncertainty. Various theories have been formulated in order to

Downloaded by Delhi Technological University At 23:17 02 August 2016 (PT)

© Emerald Group Publishing Limited
This is a pre-print of a paper and is subject to change before publication. This pre-print is made available with the understanding that it will not be reproduced or stored in a retrieval system without the permission of Emerald Group Publishing Limited.

create consistent capacity planning models. Samuelsson (1999) has developed both a deterministic and a stochastic single-site capacity planning model. Blau et al. (2000) considered the decision-making process involved in the development of the product portfolio under uncertainty of a pharmaceutical company. Papageorgiou et al. (2001) have developed a multi-site, multi-period capacity planning model incorporating the internal trading structure of the company. Gatica et al. (2001) described a stochastic single-site capacity planning model considering multiple clinical trials outcomes per candidate product. Shah (2004) has observed that capacity planning decisions is subject to considerable risks. These include product failures during trials, product withdrawal during sales due to side effects, uncertainties about final dosage and treatment regimes, competition from similar products, etc. Requirement of medicines is not certain and at uniform rate. Therefore capacity planning and its effective utilization is major challenge for pharmaceutical sector. Researchers should develop certain framework for ensuring effective capacity planning under uncertain and dynamic environment.

Downloaded by Delhi Technological University At 23:17 02 August 2016 (PT)

2.1.4 Plant and Network design

Plant design plays an important role in improving the profitability of pharmaceutical supply chain. Recent trends in global sourcing, production and distribution have considered supply network strategies and practices as essential elements of business strategy (Arshinder et al., 2008). Drug distribution is concerned with bringing a medicine from the manufacturer to the patient (Quick et al., 1997). This includes the ordering, transportation and storage of the pharmaceutical drugs with the involvement of manufacturers, wholesalers and distributors as well as the prescribers and dispensers (Patel et al., 2009). Papageorgiou (2009) has recognized the need for efficient integrated approaches to reduce capital and operating costs, increase supply chain productivity and improve business responsiveness. This can be achieved by considering various levels of enterprise management, plant-wide coordination and plant operation, in a systematic way (Grossmann 2005). Supply chain network design can be used for the determination of the optimal levels of capacity and operational product flows associated with supply chain activities of manufacturing, storage, and distribution at minimal total cost. Their importance to the timely and efficient delivery of products such as food, energy and pharmaceuticals has fueled an immense interest in their analysis on the part of both researchers and practitioners (Nagurney, 2010). Several network models have been proposed by researchers from all over the world. Jin-Kwang et al. (2000) have created a multi period optimization model for continuous process networks focusing on the main operational decisions over short time horizons (1week to 1 month) taking into consideration only special features of the supply chain such as sales, production shortfalls, intermittent deliveries, inventory profiles, delivery delays and job changeovers. Tsiakis et al. (2001) presented a mixed integer linear programming model to determine production capacity allocation among different products, optimal layout and flow allocations of the distribution network by reducing an annualized network cost to minimum. Mousazadeh, et al. (2015) have suggested bi-objective mixed-integer programming model (MILP) for a pharmaceutical supply chain network design problem. Mousazadeh et al., (2014) have observed that dynamic and imprecise nature of quantity and quality of manufactured products in the pharmaceutical industry network results in a high degree of uncertainty in

© Emerald Group Publishing Limited
This is a pre-print of a paper and is subject to change before publication. This pre-print is made available with the understanding that it will not be reproduced or stored in a retrieval system without the permission of Emerald Group Publishing Limited.

required data when designing such supply chains. Network optimization problems may change from country to country due to variation in infrastructure and lack of connectivity. Researchers should explore optimal network under dynamic operational conditions with reference to different regions.

2.1.5 Improvement in Research& Development capabilities

The pharmaceutical industry devotes significant resources to research and development (R&D). In 2011, the industry spent USD 92 billion on R&D (OECD, 2015). Pharmaceutical and biotechnology companies need R&D at larger extent to meet new health care issues. Pharmaceutical industries receives R&D tax credits in many countries, and the development of medicines draws heavily on knowledge and innovation derived from other sectors including higher education and NGOs (Kezselheim et al., 2015). In 2011, the pharmaceutical industry spent close to USD 50 billion for R&D in the United States, 11.5 billion in Japan, 5.2 in Germany and 3.7 in France. As a share of GDP, pharmaceutical industry R&D spending is highest in Switzerland (0.63%), Belgium (0.45%), Slovenia (0.45%) and Denmark (0.36%). In the United States and Japan, the percentages were 0.30 and 0.26 respectively (OECD, 2015). Banerjee (2012) observed that the cost of new drug development is increasing every year. Pharmaceutical companies use R&D joint ventures, mergers, and outsource different stages of pharmaceutical R&D activities for a faster and cost minimizing method of innovation. Simango (2000) discussed the extent to which American, European and Japanese pharmaceutical multinational enterprises (MNE) with subsidiaries in the Republic of Ireland have localized specific forms of R&D and contributed to technology transfer. Pharmaceutical companies' investment in research has gone up resulting in higher number of application for new drug approvals. In India, pharmaceutical companies have significantly increased their research investment. However, the NME pipeline is still slim though there has been a significant surge in generic filings (Dubey and Dubey, 2010). Therefore researchers can explore for major areas of R&D investment and their impact on performance of organisations in global and domestic markets.

2.1.6 Pipeline and development management

The order in which drugs are released in the pipeline is of great importance as it helps in scheduling problems effectively (Perez-Escobedo et al., 2012). This involves the selection of potential drugs to develop further, and the planning of the development activity (Shah 2004). Subramanian et al. (2000) have developed a computing architecture based on mathematical programming in order to address the combinatorial nature of the R&D product pipeline problem and discrete-event system simulation so as to facilitate decision-making for new product development. Schmidt and Grossmann (1996) considered the problem of sequencing of testing tasks where unlimited resources are assumed to be available. Jain and Grossmann (1999) developed a methodology for the sequencing and scheduling of testing tasks under resource constraints. In this approach, each product has a specified set of testing tasks and each task is characterized by duration, cost, precedence constraints, resource requirements and probability of success. Scheduling of different tasks across pipeline under dynamic market requirements is a challenging task. Further research can be done in this direction.

Downloaded by Delhi Technological University At 23:17 02 August 2016 (PT)

© Emerald Group Publishing Limited
This is a pre-print of a paper and is subject to change before publication. This pre-print is made available with the understanding that it will not be reproduced or stored in a retrieval system without the permission of Emerald Group Publishing Limited.

2.1.7 E-business capabilities

According to Gimenez and Lourenco (2008), recent technological developments in information systems and information technologies have facilitated the coordination and integration of the entire supply chain. Bhakoo and Chan (2011) have identified the key issues in the implementation of e-business practices in the healthcare supply chain such as lack of consistency and poor data quality and global nature of suppliers. Bhakoo and Chan (2011) have also observed that e-business technologies can be used to support critical supply-chain functions such as procurement, distribution and inventory management. Burns (2002) has found that the majority of hospitals seem to have outdated information systems with inter-organizational connectivity as the major IT investment has largely centered on improving health care delivery mechanisms rather than information systems integration that enables the implementation of e-business processes. Bartezzaghi and Ronchi (2003) and Presutti (2003) have suggested that the use of e-business processes i.e. e-procurement can be used to reduce transaction costs by aggregating demand, improving operational efficiencies, enabling an organisation to gain access to a wider supplier base and facilitating the analyses of procurement patterns across different functional departments. Retailers in developing countries such as India are reluctant for online retailing or e- business. Therefore research scope lies in formulating effective strategies for encouraging IT applications in Pharmaceutical sector especially in context to developing countries.

2.2 Processes of pharmaceutical supply chain

Next step in strategic planning for a pharmaceutical firm is the effective scheduling of all processes in its supply chains. Effective planning of processes improves responsiveness and agility of overall supply chain. Different supply chain processes are discussed in following sections.

2.2.1 Inventory management

Drug products made of synthetic or natural organic compounds contain active and sensitive molecular entities that can degrade with time even with superior packaging and careful control of environmental conditions, which imposes special constraints for inventory management and the additional risk of loss of product value to the enterprise (Laínez et al., 2012). Inventory management has become essential for healthcare organizations in order to fulfill the demands of hospitals carrying large amounts of a great variety of medicines for emergency needs (Nicholson et al., 2004). According to Jarett (1998), inventory costs in the health care sector are substantial and are estimated to be between 10% and 18% of net revenues. Jan deVries (2011) have studied that large numbers of health-care organisations have started with projects in the area of inventory management in order to reduce costs and improve service levels. Shang et al. (2008) have observed that determining optimal inventory levels in the pharmaceutical supply chain is a complex problem due to the involvement of various stochastic variables. They emphasized to provide a high service level (SL) to customers, while keeping inventory levels low to save the cost. They also concluded that high level of inventory is not suitable for an enterprise, because it

Downloaded by Delhi Technological University At 23:17 02 August 2016 (PT)

© Emerald Group Publishing Limited
This is a pre-print of a paper and is subject to change before publication. This pre-print is made available with the understanding that it will not be reproduced or stored in a retrieval system without the permission of Emerald Group Publishing Limited.

represents an investment with very low return. Researchers can explore most appropriate inventory management model for pharmaceutical sector after considering different risks in supply chain related to product varieties, product life cycle and delivery time.

2.2.2 Outsourcing logistics activities

According to Chase et al. (2004), outsourcing as an "act of moving some of a firm's internal activities and decision responsibilities to outside providers". In today's highly competitive environment, which demands cost effectiveness, many pharmaceutical companies are looking forward at gaining a share of the global market and taking benefit of improved production and sourcing efficiencies by outsourcing their business activities to specialized suppliers known 3PLs (third-party logistics) (Aktas et al. 2011). Gadde and Hulthen (2009) have observed that the use of 3PLs, had been previously involved in warehousing and transportation only, but now they have extended their capabilities to serve a broad range of functions. Graf and Mudambi (2005) showed that outsourcing allows a firm to not only cut costs, but also focus on its core competences and helps in speeding up its innovation processes in pharmaceutical industries. Harris et al. (1998) have observed that a firm that engages in outsourcing may lose control and flexibility, and potentially causing a risk of disclosing the proprietary knowledge to suppliers, who may emerge as its competitors in the future. Bolumole (2001) have identified the factors which influence outsourcing decisions and the implications of outsourcing strategies. Deavers (1997) have identified five main reasons for outsourcing: improving company focus, accessing world-class capabilities, acceleration of benefits from reengineering, sharing of risk, and freeing of resources for other purposes. Boulaksil and Fransoo (2010) has observed that outsourcing activities and outsourced supply chains have not been documented yet but now they are rapidly developing in pharmaceutical industry. Survey conducted by Business Insights (2005) has shown that total revenues of contract manufacturers in the pharmaceutical industry rise on average by approximately 13 percent per year, which shows that outsourcing is increasing in this industry. According to research executed by the World Bank (2007), logistics costs constitute 30% of the total GDP in some of the developing economies, while this ratio is only about 10% in the developed economies which clearly represents the importance of logistics for the economic growth of developing countries. Sundaramoorthy and Karimi (2004) have presented a model in which they considered production outsourcing in the pharmaceutical industry, but they addressed the strategic question whether to undertake the production of a new product in-house or whether to outsource it to a contract manufacturer. Kremic et al. (2006) has given an explicit review of the literature on outsourcing and developed a framework to classify whether the considered papers address outsourcing benefits, risks, motivations, or factors.

Mathematical models have been developed by Tsai and Lai (2007) in order to evaluate the benefits of expanding the various kinds of capacity and outsourcing simultaneously. Boulaksil and Fransoo (2010) have specifically analysed the distinction between strategic decisions, which are related to whether to outsource or not. Outsourcing sometimes becomes risky option also therefore appropriate decision framework for outsourcing options can be proposed by researchers specifically for pharmaceutical sectors.

2.2.3 Reverse logistics

Downloaded by Delhi Technological University At 23:17 02 August 2016 (PT)

© Emerald Group Publishing Limited
This is a pre-print of a paper and is subject to change before publication. This pre-print is made available with the understanding that it will not be reproduced or stored in a retrieval system without the permission of Emerald Group Publishing Limited.

Kara and Onut (2010) have observed that due to the national, international regulations and legislations governing waste management; waste minimization, reuse, and material recycling have received increased attention over the last decade. According to Chen et al. (2007), a physical distribution process is implemented by which all the recycled materials are processed into various forms in order to eliminate either hazardous materials before the final disposition into landfills or to extract precious substances for reselling back to market. Xie and Breen (2012) have emphasized to create a channel through which expired medicines can be sent back to manufacturers, and can be reused. They also observed that logistics providers or wholesalers can play the role of collecting pharmaceutical waste from the community pharmacy and transporting to manufacturers or suitable places for disposal.
Krumwiede and Sheu (2002) have suggested that logistics providers or wholesalers should get involved in the system by acting as independent operators and carry out functions such as collecting, sorting, recycling and disposing, or cooperating with other actors in the system. Biehl et al. (2007) have observed that unlike forward supply chains, reverse supply-chain operations are more complex and prone to a high degree of uncertainty, affecting collection rates, the availability of recycled production inputs, and capacities in the reverse channel. Listes and Dekker (2005) have suggested that Stochastic programming models can be employed for solving the problem of uncertainty by considering real information based on the uncertain characteristics of the problem. Designing a reverse logistic network is a costly and challenging project for pharmaceutical sector due to high level of unpredictability in supply chain. Therefore researchers can explore reverse logistic optimisation problems for pharmaceutical sectors.

Downloaded by Delhi Technological University At 23:17 02 August 2016 (PT)

2.2.4 Lean Manufacturing

The principles of lean manufacturing have become state-of-the-art in modern manufacturing design and its implementation has become a vital pre-requisite in global competition (Matt, 2008). Lean manufacturing is based on the fundamental goals of Toyota Production System (TPS), which is aimed at continuously minimizing waste to maximize flow (Vinodh et al., 2010). According to TPS, the seven most common wastes are overproduction, waiting, transport, inappropriate processing, unnecessary inventory, waste of motion and defects (Ohno, 1988). Companies recognize that consistent and disciplined application of lean manufacturing strategies with the emphasis on waste elimination and process streamlining can lead to business excellence (Rahman et al., 2010). According to Mehralian et al. (2015), achieving supply chain agility is dependent on other capabilities; including flexibility, responsibility, competency and quickness. Chowdary and George (2012) have observed that integrated current good manufacturing practices (CGMP) and lean environment create an environment of clear communication and provide a system that allows a simple flow of products to reduce production time and cost. In order to achieve product and process quality in pharmaceutical plants, Miller (2008) have recommended a holistic and systematic approach in incorporating lean manufacturing principles. Leanness is associated with reducing lead times in production (Rahman et al., 2010). Main lean manufacturing techniques are 5S, Kanban, Kaizen, total productive maintenance, total quality management, failure mode and effect analysis, quality function deployment (QFD), value stream mapping (VSM), cellular manufacturing (CM), etc. (Vinodh et al., 2010). Among various lean techniques available in the literature, VSM and CM are the most popular tools and widely accepted by pharmaceutical sector (Chowdary and George, 2012). VSM is a micro-level analysis of material and information flow through the various levels of a manufacturing set up (Vinodh et

© Emerald Group Publishing Limited
This is a pre-print of a paper and is subject to change before publication. This pre-print is made available with the understanding that it will not be reproduced or stored in a retrieval system without the permission of Emerald Group Publishing Limited.

al. 2010), while CM includes cell design which is purely a process of selecting and grouping of machines into cells (Angra et al., 2008). It is observed that pharmaceutical industry is still in nascent stage in implementing lean manufacturing initiatives. Therefore researchers should explore level of lean manufacturing in pharmaceutical sector and its impact on operational performance.

2.2.5 Quality Management

Quality means that medicines meet all prescribed standards. According to WHO (2003), substandard medicines are defined as "products whose composition and ingredients do not meet the correct scientific specifications and which are consequently ineffective". Quick et al. (1997) has defined quality of medicines in terms of compliance with pharmacopoeial specifications with respect to the product's identity, purity, potency, uniformity of dosage form, bioavailability, and increased public awareness about counterfeit medicines (Newton et al., 2006). Effective drug regulation through an independent, honest, accountable and competent national drug regulatory authority are two key strategies proposed to control quality and safety of drugs (WHO, 2006). Newton et al. (2006) have considered effective medicines regulation as a challenging task due to limited resource availability in the developing countries. In pharmaceutical industry, quality standards are very stringent as good manufacturing practices focuses mainly on the manufacturing of safe and quality products (Greene and O'Rourke, 2006). According to Patel et al. (2009), limited emphasis on the enforcement of the distribution of medicines could potentially lead to increased access to substandard and counterfeit medicines. Drug distribution is concerned with bringing a medicine from the manufacturer to the patient (Quick et al., 1997). Pharmaceutical sector in developing counties is facing many challenges in context to quality issues. Therefore researchers should suggest a strategic framework to overcome on such kind of quality issues.

2.2.6 Green Supply Chain Management

According to Xie and Breen (2012), environmental issues such as global warming, carbon emissions, toxic substance usage, and resource scarcity have escalated awareness all over the world during the past decades. Therefore policy makers and activists have started emphasizing on green operations and many organizations throughout the world have responded to this by applying green principles. According to Zhu and Sarkis (2004) the concept of green supply chain management (GSCM) has emerged in the late 1990s. It is reactive monitoring of general environmental management programs, and moving towards more proactive practices such as the recycling, reclamation, reverses logistics (RL) and remanufacturing in addition to implementing innovation practices. GSCM has been adopted by many companies to lower the environmental risks and raise ecological efficiency, in order to achieve higher profits and increased market share (Van Hoek, 1999). Disposal of expired/unwanted medication can be very costly and harmful to the environment.

With the increasing focus on pharmaceutical waste management (Breen and Xie, 2009), it has become necessary to green the pharmaceutical supply chain by correctly disposing of expired/unwanted medications and reducing the level of preventable pharmaceutical waste. The Department of Health has produced a set of practices for efficient waste management in order to help healthcare organizations and other producers meet legislative environmental requirements

Downloaded by Delhi Technological University At 23:17 02 August 2016 (PT)

© Emerald Group Publishing Limited
This is a pre-print of a paper and is subject to change before publication. This pre-print is made available with the understanding that it will not be reproduced or stored in a retrieval system without the permission of Emerald Group Publishing Limited.

e.g. “Disposal of Pharmaceutical Waste in Community Pharmacies” (Department of Health, 2007a), and “Safe Management of Healthcare Waste” (Department of Health, 2006). There is emerging concern about the potential impact of pharmaceuticals that reaches lakes and rivers via sewage plants and other sources (New Hampshire Department of Environmental Services, 2009). Investigation done in the disposal habits of the American public says that, only 1.4 per cent of people return unused drug to the pharmacy, while 54 per cent throw them away and 35.4 per cent flush them into the sink or toilet (Kuspis and Krenzelok, 1996). Further it has been found that in 2003 at least £0.56 billion worth of unused medications were flushed down in the toilet all over the world (Van Eijken et al., 2003). Sustainability is the need of the day for pharmaceutical sector. Therefore researchers can explore different issues such as challenges, constraints, strategy development and performance frameworks for green pharmaceutical supply chains.

Downloaded by Delhi Technological University At 23:17 02 August 2016 (PT)

2.3 Performance Management

The pharmaceutical industries are under severe pressure, all over the globe. Research & development (R&D) costs are increasing, product life cycle is reducing and consumers awareness is increasing. Performance criterions are changing on day to day bases. According to Kim (2009), SCM seeks to enhance competitive performance by closely integrating the internal functions within a company and effectively linking them with the external operations of suppliers, customers, and other channel members. There are numerous theoretical arguments describing the role of SC integration for the improvement of business performance and competitive capabilities (Powell, 1995; Johnson, 1999; Stank et al., 2001; Tracy, 2004; Koufteros etal., 2005; Sanders and Premus, 2005; Vachon and Klassen, 2008). Narasimhan and Carter (1998) have noticed that supply chain strategies and operational resources can be used to support business strategies and help in improving the competitive capabilities of the firm. Dangayach and Deshmukh (2001) have observed that those firms that can manage their practical resources in a supply chain more efficiently are likely to gain competitive capabilities. They also concluded that developing world-class SCM practices can help them achieving superior performance and increased competitiveness. Fleury and Fleury (2003) have emphasized that the definition of competitive capabilities should begin with a thorough understanding of the strategic activities characterised by physical, financial, organizational and human resources on a supply chain.

According to Olavarrieta and Ellinger (1997) and Shang and Sun (2004), competitive capabilities are required to build a strong strategic SCM. Morash (2001) have classified supply chain capabilities into supply-side capabilities and demand-side capabilities. Rosenzweig et al. (2003) have observed that by developing a high level of supply chain integration, manufacturers will be able to overcome non-value-added activities in order to improve their product quality and delivery reliability capabilities, thereby providing a growth to their sales.

Stank et al. (2001) have observed that supply chain integration synchronizes the core competencies and capabilities of all supply chain participants to jointly achieve improved service capabilities at lower total supply chain cost. Ragatz et al. (1997) have also observed that using the knowledge and expertise of all supply chain members to complement internal capabilities, can help reduce concept-to- customer cycle-time and improve the overall design efforts. Droge et al. (2004) indicates that the extent of use of external and internal integration practices has a positive effect on flexibility factors such as product development time, product cycle time and

© Emerald Group Publishing Limited
This is a pre-print of a paper and is subject to change before publication. This pre-print is made available with the understanding that it will not be reproduced or stored in a retrieval system without the permission of Emerald Group Publishing Limited.

responsiveness. Narasimhan and Jayaram (1998) have proposed that SC integration impacts customer responsiveness and manufacturing performance. Fawcett et al. (2000) have concluded that flexibility, quality and cost are important capabilities that can help pharmaceutical industries to enhance their performance and manage their resources and markets worldwide. Curkovic et al. (2000) have observed that both product quality and service quality are related to overall firm performance, regardless of whether investment - based, asset -based, or market-based measures are considered. For improving overall performance, organisations need to work on all fronts i.e. social, environmental and economical. For this, they need to integrate their resources and processes with performance measures. Taking these factors into consideration, researchers can develop a framework and validate with empirical or case based studies.

3. Summary and research findings

About one hundred and thirty six research papers have been reviewed and the key strategic issues related to pharmaceutical supply chains are analyzed to create a strategic framework (figure 1) for performance improvement. Major issues emerging after review of these 136 papers are product and process development, capacity planning, plant and network design, e- business and IT applications, inventory management, outsourcing and reverse logistic, lean and green supply chain issues and performance measures etc. All issues are classified into three broad categories i.e. Resources, Processes and Performance. These issues considered for review are summarized in table 1. Papers have been considered from different countries. Country wise division of papers is shown in figure 2. It has been observed that USA, UK and Australia are leading in terms of research publications in pharmaceutical sector. Detailed spectrum of reviewed papers by year wise has been shown in figure 3. Intensity of research varies from year to year. On the basis of this exhaustive literature review, major research findings can be summarized as follows.

- Most of the drugs have specific patent life. Strategy formulation for new drugs and generic medicines under sustainable environment specifically in context to developing countries is a major challenge.
- For expansion of business in other countries, cultural and other local issues are major challenges. Most of the firms are not able to cope up with these challenges and mainly they are dealing with active pharmaceutical ingredients (APIs) not final formulations.
- Due to lot of uncertainties and unpredictability, capacity planning and inventory management is a big challenge for pharmaceutical sector.
- In many developing countries pharma firms are reluctant for IT applications and e-business.
- Due to lack of R&D, many firms are not able to compete in developed countries. They have a lack of motivation to increase investment in R&D.
- Quality is a major concern for pharmaceutical sectors. Firms are not able to maintain process capability as per global standards. Due to this, major share in global market is occupied by few developed countries.
- Most of the pharma firms are lacking in terms of lean and green operations. They are unaware of sustainability issues.
- Rate of innovations in pharma sector is not at par with new market requirements and price control is another challenge for pharmaceutical sector.

Downloaded by Delhi Technological University At 23:17 02 August 2016 (PT)

© Emerald Group Publishing Limited
This is a pre-print of a paper and is subject to change before publication. This pre-print is made available with the understanding that it will not be reproduced or stored in a retrieval system without the permission of Emerald Group Publishing Limited.

- Lack of performance frameworks, which could measure performance in holistic manner i.e. triple bottom line approach consisting of social, economical and environmental measures.

Based on these research findings, researchers can explore different research areas for future research.

Table 1: Summary of research issues

Research Issues	References
Strategy development Concepts	Shah (2004), Perez-Escobedo et al. (2012), Wan et al. (2006), Jain & Grossmann, (1999), Ageron et al.,(2013), Levis and Papageorgiou (2004), Health Action International and WHO (2009), Rossetti et al. (2011), Dadfar and Brege (2012), Sweet (2010), Goncharuk and Getman (2014),Kumar et al.(2014), Singh and Sharma (2015).
Resources of Pharmaceutical SC	
New product development capabilities	Gupta and Wilemon (1990), Chiesa and Toletti (2004), Nonaka and Takeuchi (1995), Scott (2000), Pisano and Wheelwright (1995), Baker et al. (2002), Iacocca et al. (2015)
New process development	Narayana et al.(2012), Perez-Escobedo et al. (2012), Crosby (1979), Gray et al. (2011), Dadfar and Brege (2012), Goncharuk and Getman (2014)
Capacity planning	Shah (2004), Samuelsson (1999), Blau et al. (2000), Papageorgiou, Rotstein, and Shah (2001), Gatica, Shah and Papageorgiou (2001), Bhatti et al. (2015)
Plant & Network design	Nagurney , (2010), Jin-Kwang et al. (2000), Tsiakis et al. (2001), Hira (2009), Yu et al. (2014), Papageorgiou (2009), Grossmann (2005), Tsiakis et al. (2001), Nagurney, (2010), Mousazadeh, et al. (2015)
Pipeline and development management	Perez-Escobedo et al. (2012), Shah (2004), Subramanian et al. (2000), Schmidt and Grossmann (1996), Jain and Grossmann (1999), Yu et al. (2014)
e-business capabilities	Gime´nez and Lourenco (2008), Bhakoo and Chan (2011), Bartezzaghi and Ronchi (2003), Presutti (2003), Kanungo (2004), Kumar et al. (2009).
Processes of Pharmaceutical SC	
Inventory management	Nicholson et al., (2004), Jarett (1998), Jan deVries (2011), Shang et al., (2008)
Outsourcing logistics activities	Chase et al. (2004), Aktas et al. (2011), Gadde and Hulthen (2009), Graf and Mudambi (2005),Harris et al. (1998), Bolumole (2001), Deavers (1997), Boulaksil and Fransoo (2010), Business Insights (2005),World Bank (2007), Sundaramoorthy and

Downloaded by Delhi Technological University At 23:17 02 August 2016 (PT)

© Emerald Group Publishing Limited
This is a pre-print of a paper and is subject to change before publication. This pre-print is made available with the understanding that it will not be reproduced or stored in a retrieval system without the permission of Emerald Group Publishing Limited.

	Karimi (2004), Kremic et al. (2006), Tsai and Lai (2007), Kumar et al.(2015a).
Reverse logistics	Kara and Onut (2010), Chen et al. (2007), Biehl et al. (2007), Srivastava (2008), Listes & Dekker (2005), Xie and Breen (2012), Krumwiede and Sheu (2002), Kumar et al. (2009)
Lean manufacturing	Matt (2008), Vinodh et al., (2010), Ohno, (1988), Rahman et al., (2010), Miller (2008), Angra et al. (2008), Chowdary and George (2012), Mehralian et al. (2015)
Green SC Management	Xie and Breen (2012), Zhu and Sarkis (2004), Van Hoek (1999), Breen and Xie (2009), Department of Health (2007a), Department of Health (2006), New Hampshire Department of Environmental Services (2009), Kuspis and Krenzelok (1996), Van Eijken et al. (2003)
Performance issues in Pharmaceutical SC	
Improvement in financial capabilities	Kim(2009),Powell(1995),Johnson(1999), Stank et al. (2001),Tracy (2004), Vachon and Klassen(2008), Droge et al.(2004),Kumar et al.(2015b).
Improvement in R & D capabilities	Banerjee (2012), Simango(2000), Dubey and Dubey (2010), Kezselheim et al. (2015), OECD (2015).

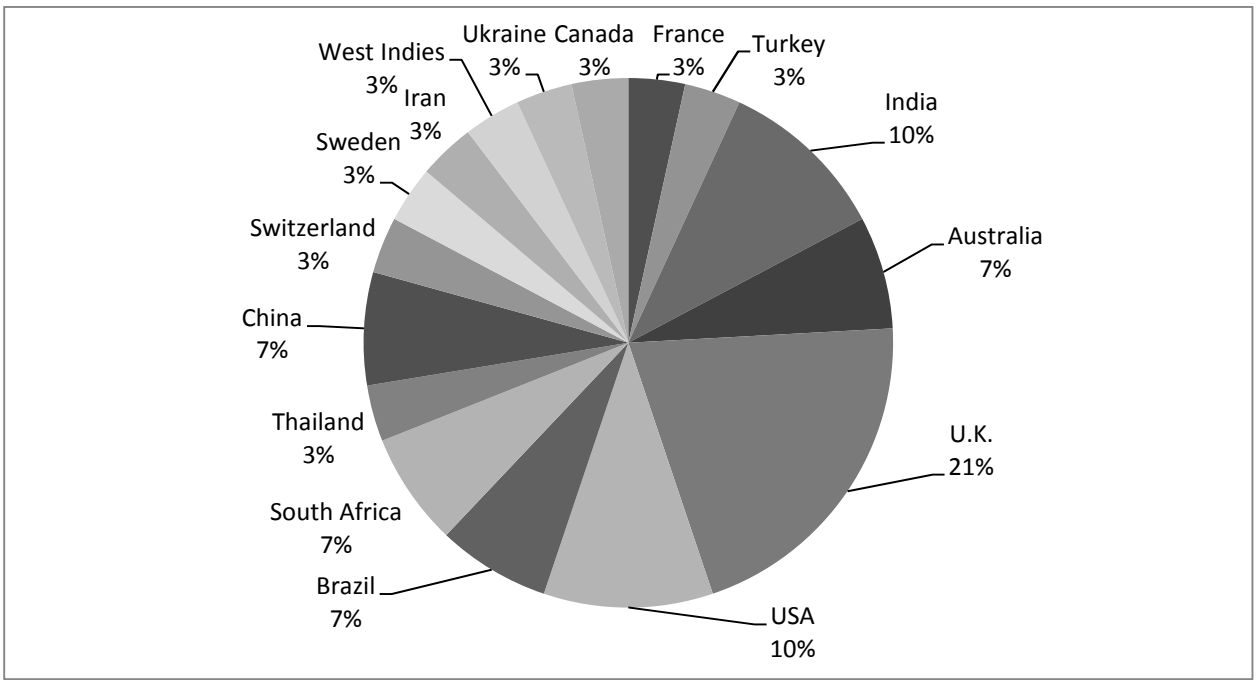

Figure 2: Reviewed papers from different countries

Downloaded by Delhi Technological University At 23:17 02 August 2016 (PT)

© Emerald Group Publishing Limited
This is a pre-print of a paper and is subject to change before publication. This pre-print is made available with the understanding that it will not be reproduced or stored in a retrieval system without the permission of Emerald Group Publishing Limited.

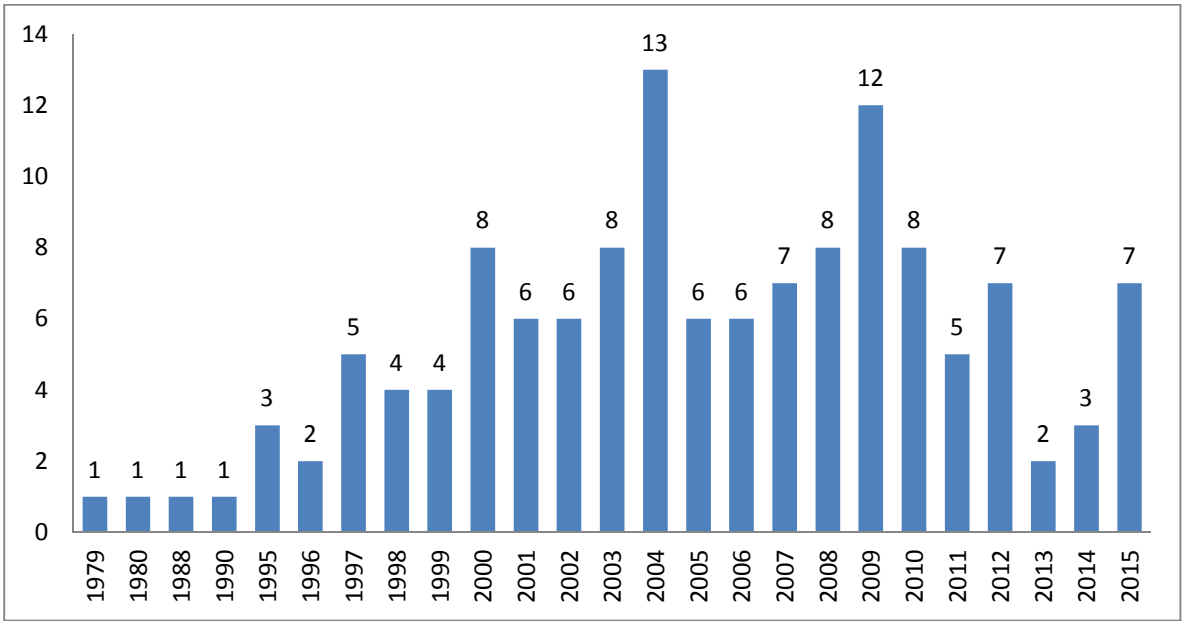

Figure 3: Year wise distribution of reviewed papers (X-axis-Year of Publication, Y-axis –No. of papers)

4. Conclusion

The pharmaceutical sector plays crucial role in economic growth and social welfare of any country. Being capital and research intensive, this sector has not been widely covered and researched by researchers in developing countries. Total one hundred thirty six research papers are reviewed in this study. Major issues discussed in this paper are inventory management, new product development, process development, capacity planning, network design, plant design, pipeline and development management, outsourcing logistics activities, reverse logistics, lean manufacturing, green supply chain management and implementation of e-business processes. Based on gaps identified from this study, it is observed that this sector is not widely researched in developing countries. Findings also imply that developing countries are not investing much on R &D, use of electronic media for health awareness, process and capacity building, sustainability and quality issues. Due to this contribution of developing countries in global market in this sector is not significant. Therefore there is urgent need to strengthen pharmaceutical sector in such developing countries. This paper will help the supply chain managers from the pharmaceutical sector to understand the market conditions in the present scenario and also assist them in building better strategic policies for their firms. The findings of the paper will also help researchers in setting the future research agenda in this sector.

References

Ageron B., Lavastre O and Spalanzani A. (2013), "Innovative supply chain practices: the state of French companies", Supply Chain Management: An International Journal, Vol.18 No.3, pp.265–276.

Aktas E, Agaran B, Ulengin F and Onsel S (2011), "The use of outsourcing logistics activities: The case of turkey", Transportation Research, Part C, No. 19, pp. 833–852.

Downloaded by Delhi Technological University At 23:17 02 August 2016 (PT)

© Emerald Group Publishing Limited
This is a pre-print of a paper and is subject to change before publication. This pre-print is made available with the understanding that it will not be reproduced or stored in a retrieval system without the permission of Emerald Group Publishing Limited.

Angra, S., Sehgal, R. and Noori, Z.S. (2008), "Cellular manufacturing – a time based analysis to the layout problem", International Journal of Production Economics, Vol. 112, pp. 427-38.
Arshinder, Kanda, A., and Deshmukh, S.G., (2008), "Supply chain coordination: Perspectives, empirical studies and research directions", International Journal of Production Economics, No. 115, pp. 316–335.
Banerjee,T. (2012), "Aspects of Research and Development Contract Terms in the Bio/Pharmaceutical Sector, in Kristian Bolin", Robert Kaestner (ed.) The Economics of Medical Technology (Advances in Health Economics and Health Services Research, Volume 23) Emerald Group Publishing Limited, pp.1 – 33.
Bartezzaghi, E. and Ronchi, S. (2003), "Internet supporting the procurement process: lessons from four case studies", Integrated Manufacturing Systems, Vol. 14 No. 8, pp. 632-41.
Bhakoo, V. and Chan, C. (2011), "Collaborative implementation of e-business processes within the health-care supply chain: the Monash Pharmacy Project", Supply Chain Management: An International Journal, Vol. 16 No. 3,pp. 184–193.
Bhatti, S.K., Singh, R.P. and Singh, I. (2015), "Analytical model for performance measurement in healthcare sector of Punjab", Journal of Modelling in Management, Vol. 10 No. 2, pp.226 – 237.
Biehl, M., Prater, E., & Realff, M. J. (2007), "Assessing performance and uncertainty in developing carpet reverse logistics systems", Computers and Operations Research, Vol. 34 No. 2, pp. 443–463.
Blau, G., Mehta, B., Bose, S., Pekny, J. F., Sinclair, G., and Keunker, K (2000), " Risk management in development of new products in highly regulated industries", Computers & Chemical Engineering, 24, 659–664.
Bolumole, Y.A. (2001), "The supply chain role of third-party logistics providers", The International Journal of Logistics Management, Vol. 12 No. 2, pp. 87–102.
Boulaksil, Y and Fransoo, J.C (2010), "Implications of outsourcing on operations planning: findings from the pharmaceutical industry", International Journal of Operations & Production Management, Vol. 30 No. 10, pp. 1059-1079
Breen, L. and Xie, Y. (2009), "Examining the role of the customer in facilitating reverse logistics system in NHS community pharmacy in the UK", Proceeding of the Logistics Research Network Annual Conference, 9-11 September, 2009, Cardiff, UK, pp. 588-91.
Burns, L.R. (2002), The Health Care Value Chain, Jossey-Bass, San Francisco,USA.
Chase, R.B., Jacobs, F.R. and Aquilano, N.J. (2004), "Operations Management for Competitive Advantage", 10th ed., Irwin/McGraw-Hill, Boston, MA.
Chen, H.K., Chou, H.W and Chiu, Y.C. (2007), "On the modeling and solution algorithm for the reverse logistics recycling flow equilibrium problem", Transportation Research Part C, No. 15, pp. 218–234.
Chiesa, V and Toletti, G. (2004), "Network of collaborations for innovation: the case of biotechnology", Technology Analysis and Strategic Management, Vol.16 No. 1, pp. 73–96.
Chowdary, B.V. and George, D. (2012), "Improvement of manufacturing operations at a pharmaceutical company: A lean manufacturing approach", Journal of Manufacturing Technology Management, Vol. 23 No.1, pp.56 – 75.
Crosby, P.B., (1979), Quality is Free. McGraw-Hill, New York.

Downloaded by Delhi Technological University At 23:17 02 August 2016 (PT)

© Emerald Group Publishing Limited
This is a pre-print of a paper and is subject to change before publication. This pre-print is made available with the understanding that it will not be reproduced or stored in a retrieval system without the permission of Emerald Group Publishing Limited.

Curkovic,S.,Vickery,S.K. and Droge,C.,(2000) “An empirical analysis of the Competitive dimensions of quality performance in the automotive supply industry”, International Journal of Operations and Production Management, Vol 20 No.3,pp.386–403.
Dadfar, H. and Brege, S. (2012), "Differentiation by improving quality of services at the last touch point: The case of Tehran pharmacies", International Journal of Quality and Service Sciences, Vol. 4 No. 4, pp.345 – 363.
Dangayach, G.S. and Deshmukh, S.G. (2001), “Manufacturing strategy: literature review and some issues”, International Journal of Operations and Production Management, Vol 21 No 7, pp. 884–932.
De la Fuente, M.V., Ros, L. and Cardo´ S, M. (2007), “Integrating forward and reverse supply chains: application to a metal-mechanic company”, International Journal of Production Economics, Vol. 111 No. 2, pp. 782-92.
De Treville, S., Shapiro, R.H. and Hameri, A.P., (2004), “From supply chain to demand chain: the role of lead time reduction in improving demand chain performance”, Journal of Operations Management, Vol. 21, pp.613–627.
Deavers, K.L. (1997), “Outsourcing: a corporate competitiveness strategy, not a search for lower wages”, Journal of Labor Research, Vol. 18 No. 4, pp. 503-19.
Department of Health (2006), “Memorandum 07-01: safe management of healthcare waste”,availableat:www.dh.gov.uk/prod_consum_dh/groups/dh_digitalassets/documents/digitalasset/dh073328.pdf (accessed 6 April 2010).
Department of Health (2007a), Environment and Sustainability Health Technical Memorandum 07-06: Disposal of Pharmaceutical Waste in Community Pharmacies, Department of Health, London.
Ding and Eliashberg (2002) approach the problem of determining how many projects, that are assigned to develop the same product, have to be included in the pipeline in order to maximize the profitability.
Ding, M., and Eliashberg, J. (2002), “Structuring the new product development pipeline”, Management Science, Vol.48, pp.343–363.
Dobrzykowski, D.,(2013), “A structured analysis of operations and supply chain management research in healthcare (1982–2011)”, International Journal of Production Economics , http://dx.doi.org/10.1016/j.ijpe.2013.04.055
Droge,C.,Jayaram,J., and Vickery, S.K.,(2004), “The effects of internal versus External integration practices on time-based performance and Overall firm performance”, Journal of Operations Management, Vol. 22, pp. 557–573.
Dubey, J. and Dubey, R. (2010), "Pharmaceutical innovation and generic challenge: recent trends and causal factors", International Journal of Pharmaceutical and Healthcare Marketing, Vol. 4 No. 2, pp.175 – 190.

Fawcett, S.E.,Calantone, R.J., and Roath,A.,(2000), “Meeting quality and cost imperatives in a global market”, International Journal of Physical Distribution and Logistics Management, Vol. 30 No.6,pp.472–499.
Fleury, A. and Fleury, M.T. (2003), “Competitive strategies and core competencies: perspectives for the internationalization of industry in Brazil”, Integrated Manufacturing Systems, vol.14 No.1, pp.16–25.
Gadde, L.E. and Hulthen, K. (2009), “Improving Logistics Outsourcing through increasing buyer-provider interaction”, Industrial Marketing Management, Vol. 38, pp. 633–640.

Downloaded by Delhi Technological University At 23:17 02 August 2016 (PT)

© Emerald Group Publishing Limited
This is a pre-print of a paper and is subject to change before publication. This pre-print is made available with the understanding that it will not be reproduced or stored in a retrieval system without the permission of Emerald Group Publishing Limited.

Gatica, G., Papageorgiou, L. G. & Shah, N, (2003), "Capacity planning under uncertainty for the Pharmaceutical industry", Chemical Engineering Research & Design, Vol.81 No.6, pp.665-678.
Gimenez C and Lourenco H.R (2008),"e-SCM: internet's impact on supply chain processes", The International Journal of Logistics Management, Vol. 19 No. 3, pp. 309-343.
Goncharuk, G.A. and Getman, M. (2014), "Benchmarking to improve a strategy and marketing in pharmaceuticals", Benchmarking: An International Journal, Vol. 21 No. 3, pp.364 – 385.
Graf, M., and Mudambi, S.M., (2005), "The outsourcing of IT-enabled business processes: a conceptual model of the location decision", Journal of International Management, Vol. 11 No. 2, pp. 253–268.
Gray, J.V., Roth, A.V. and Leiblein, M.J. (2011), "Quality risk in offshore manufacturing: Evidence From the pharmaceutical industry", Journal of Operations Management, Vol. 29, pp. 737-752
Greene, A. and O'Rourke, D. (2006), "Lean manufacturing practice in a CGMP environment", Pharmaceutical Technology Europe, Vol. 18 No. 10, pp. 33-40.
Grossmann, I. E. (2005). Enterprise-wide optimization: A new frontier in process systems engineering. AICHE Journal, 51, 1846–1857.
Grossmann, I.E. (2004),"Challenges in the new millennium: product discovery and design, enterprise and supply chain optimization, global life cycle assessment", Computers and Chemical Engineering, Vol. 29,pp29–39
Gupta, A.K. and Wilemon, D.L. (1990), "Accelerating the development of technology-based new products, California Management Review (Winter issue), pp. 24–44.
Harris, A., Giunipero, L.C. and Hult, T.M. (1998), "Impact of organizational and contract flexibility on outsourcing contracts", Industrial Marketing Management, Vol. 27, pp. 373–384.
Health Action International and WHO (2009), "Medicine prices, availability, affordability and price components", available at: www.haiweb.org/medicineprices/15072009/Bulletin5final.pdf (accessed March 16, 2010).
Hira, A. (2009), "The political economy of the global pharmaceutical industry: Why the poor lack access to medicine and what might be done about it", International Journal of Development Issues, Vol. 8 No. 2, pp.84 – 101.
Hugos, M. (2003). Essentials of supply chain management. John Wiley & Sons.
Iacocca, K. Sawhill, J. and Zhao, Y. (2015), "Why brand drugs priced higher than generic equivalents", International Journal of Pharmaceutical and Healthcare Marketing, Vol. 9, No. 1, pp. 3 – 19.
Jain, V., and Grossmann, I. E. (1999), "Resource-constrained scheduling of tests in new product development", Industrial Engineering and Chemical Research, Vol.38,pp. 3013–3026.
Jan deVries, J.D. (2011), "The shaping of inventory systems in health services: A stake holder analysis", International Journal of Production Economics, Vol. 133, pp. 60–69
Jarett, P.G. (1998), "Logistics in the health care industry", International Journal of Physical Distribution and Logistics Management, Vol. 28 No. (9/10), pp. 741–742.
Jin-Kwang, B., Grossmann, I. E., and Park, S. (2000), "Supply chain optimization in continuous flexible process networks", Industrial & Engineering Chemistry Research, Vol.39,pp.1279–1290.

Downloaded by Delhi Technological University At 23:17 02 August 2016 (PT)

© Emerald Group Publishing Limited
This is a pre-print of a paper and is subject to change before publication. This pre-print is made available with the understanding that it will not be reproduced or stored in a retrieval system without the permission of Emerald Group Publishing Limited.

Johnson, J.L., (1999), "Strategic integration in industrial distribution channels: managing the inter firm relationship as a strategic asset", Journal of the Academy of Marketing Science, Vol. 27 No.1, pp. 4–18.
Kanungo, R.P. (2004), "E-commerce in the pharmaceutical industry: threshold of innovation", Management Research News, Vol. 27 No. 8/9, pp.98 – 108.
Kara, S.S. and Onut, S. (2010), "A two-stage stochastic and robust programming approach to strategic planning of a reverse supply network: The case of paper recycling", Expert Systems with Applications, No. 37, pp. 6129–6137.
Kezselheim, A., Y. Tan and J. Avorn (2015), "The Roles of Academia, Rare Diseases, and Repurposing in the Development of the Most Transformative Drugs", Health Affairs, Vol. 34, pp. 286-293.
Kim S.W. (2009), "An investigation on the direct and indirect effect of supply chain Integration on firm performance", International Journal of Production Economics, Vol. 119, pp.328–33.
Koufteros, X.A., Vonderembse, M. and Jayaram, J. (2005), "Internal and external Integration for product development: the contingency effects of uncertainty, equivocality, and platform strategy", Decision Sciences, Vol. 36, No. 1, pp. 97–133.
Kremic, T., Tukel, O.I. and Rom, W.O. (2006), "Outsourcing decision support: a survey of benefits, risks, and decision factors", Supply Chain Management: An International Journal,Vol. 11 No. 6, pp. 467-82.
Krumwiede, D.W. and Sheu, C. (2002), "A model for reverse logistics entry by third-party providers", OMEGA: International Journal of Management Science, Vol. 30, No. 5, pp. 325-33.
Kumar, R., Singh, R.K. and Shankar, R. (2014), "Strategy development by Indian SMEs for improving coordination in Supply chain: An Empirical study", Competitiveness Review, Vol. 24, No.5, pp. 414-432.
Kumar, R., Singh, R.K. and Shankar, R. (2015a), "Study on collaboration and information sharing practices for SCM in Indian SMEs", International Journal of Business Information Systems, (In Press).
Kumar, R., Singh, R.K. and Shankar, R. (2015b), "Critical success factors for implementation of Supply Chain Management in Indian SMEs and their impact on performance", IIMB Management Review, Vol. 27, No.2, pp.92-104.
Kumar, S., Dieveney, E. and Dieveney, A. (2009) "Reverse logistic process control measures for the pharmaceutical industry supply chain", International Journal of Productivity and Performance Management, Vol. 58, No. 2, pp.188 – 204.
Kuspis, D.A. and Krenzelok, E.P. (1996), "What happens to expired medications? A survey of community medication disposal", Veterinary & Human Toxicology, Vol. 38, No. 1, pp. 48-9.
Kwak, Y.H. and Anbari, F.T. (2009), Analyzing project management research: perspectives from top management journals. International Journal of Project Management 27, 435–446.
Laínez, J.M., Schaeferb, E. and Reklaitis, G.V. (2012), "Challenges and opportunities in enterprise-wide optimization in the pharmaceutical industry", Computers and Chemical Engineering, No. 47, pp. 19-28.
Lee, H. (2002), "Aligning supply chain strategies with product uncertainties", California Management Review, Vol. 44, No. 3, pp. 105-19.

Downloaded by Delhi Technological University At 23:17 02 August 2016 (PT)

© Emerald Group Publishing Limited
This is a pre-print of a paper and is subject to change before publication. This pre-print is made available with the understanding that it will not be reproduced or stored in a retrieval system without the permission of Emerald Group Publishing Limited.

Levis A.A, Papageorgiou L.G (2004) “A hierarchical solution approach for multi-site capacity planning under uncertainity in pharmaceutical industry” Computers and Chemical Engineering,Vol.28, pp.707–725.
Listes, O., and Dekker, R. (2005), “A stochastic approach to a case study for product recovery network design”, European Journal of Operations Research, Vol.160, No.1, pp.268–287.
Mahajan, V., Nauriyal, D.K. and Singh S P., (2015), "Trade performance and revealed comparative advantage of Indian pharmaceutical industry in new IPR regime", International Journal of Pharmaceutical and Healthcare Marketing, Vol. 9 No. 1, pp. 56 – 73.

Matt, D.T. (2008), “Template based production system design”, Journal of Manufacturing Technology Management, Vol. 19, No. 7, pp. 783-97.
Mehralian, G., Zarenezhad, F. and Ghatari, A.R. (2015), "Developing a model for an agile supply chain in pharmaceutical industry", International Journal of Pharmaceutical and Healthcare Marketing, Vol. 9, No.1, pp.74 – 91.
Mehralian, G., Zarenezhad, F., and Ghatari, A. R., (2015),"Developing a model for an agile supply chain in pharmaceutical industry", International Journal of Pharmaceutical and Healthcare Marketing, Vol. 9 Iss 1 pp. 74 – 91.
Miller, G. (2008), Ensuring Product and Process Quality by Utilising Lean Manufacturing In Your Plant, Pharmaceutical Manufacturing Conference on “Ensuring Compliance And Efficiency for Pharmaceutical Manufacturers”, Johannesburg, June 23-25.
Morash, E.A. (2001), “Supply chain strategies, capabilities, and performance”, Transportation Journa, Vol. l41, No. 1, pp. 37–54.
Mousazadeh M, Torabi SA, Pishvaee MS (2014), “Green and reverse logistics management under fuzziness” In: Kahraman C, Öztaysi B, editors. Supply chain management under fuzziness, Studies in fuzziness and soft computing, Vol. 313. Berlin/Heidelberg: Springer-Verlag; p. 607–37.

Mousazadeh, M, Torabi, S.A., and Zahiri, B. (2015), “A robust possibilistic programming approach for pharmaceutical supply chain network design” Computers and Chemical Engineering, Vol. 82, pp. 115–128.
Nagurney A (2010),”Optimal supply chain network design and redesign at minimal total cost and with demand satisfaction”, Int. J. Production Economics 128 200–208
Narasimhan, R., and Carter, J.R., (1998), “Linking business unit and material sourcing strategies”, Journal of Business Logistics, Vol. 19, No. 2, pp. 155–171.
Narasimhan, R.,1997.Strategic supply management: a total quality Management imperative. Advances in the Management of Organizational Quality2, pp.39–86.
Narayana, S.A., Pati R.P., Vrat, P. (2012), “Research on management issues in the pharmaceutical industry: a literature review”, International Journal of Pharmaceutical and Healthcare Marketing, Vol. 6, No. 4, pp. 351-375
New Hampshire Department of Environmental Services (2009), “How to address unwanted medicine disposal in New Hampshire”, available at: http://des.nh.gov/organization/commissioner/pip/publications/wmd/documents/unused_ medicine.pdf (accessed 28 May 2009).
Newton, P.N., Green, M.D., Fernandez, F.M., Day, N.P.J. and White, N.J. (2006), “Counterfeit anti-infective drugs”, Lancet Infectious Diseases, Vol. 6, pp. 602-13.

Downloaded by Delhi Technological University At 23:17 02 August 2016 (PT)

© Emerald Group Publishing Limited
This is a pre-print of a paper and is subject to change before publication. This pre-print is made available with the understanding that it will not be reproduced or stored in a retrieval system without the permission of Emerald Group Publishing Limited.

Nicholson, L., Vakharia, A.J. and Erenguc, S.S. (2004), "Outsourcing inventory management decisions in healthcare: models and applications", European Journal of Operations research, Vol. 154, pp. 271–290.
Nonaka, I., and Takeuchi, H., (1995), The knowledge-creating company: how Japanese companies create the dynamics of innovation. Oxford University Press, New York.
OECD (2015), "Research and development in the pharmaceutical sector", in Health at a Glance 2015: OECD Indicators, OECD Publishing, Paris.
Ohno, T. (1988), Toyota Production System, Productivity Press, Cambridge, MA, pp. 1-44.
Olavarrieta, S., and Ellinger, A.E., (1997), Resource-based theory and strategic logistics research. International Journal of Physical Distribution and Logistics Management,Vol. 27, No. 9/10, pp.559–587.
Papageorgiou L.G (2009), "Supply chain optimisation for the process industries: Advances and opportunities", Computers and Chemical Engineering , Vol.33, pp.1931–1938
Papageorgiou, L., Rotstein, G., and Shah, N. (2001). Strategic supply chain optimization for the pharmaceutical industries. Industrial & Engineering Chemistry Research, Vol. 40, pp. 275–286.
Patel A, Norris P, Gauld R, Rades T (2009), "Drug quality in South Africa: perceptions of key players involved in medicines distribution", International Journal of Health Care Quality Assurance, Vol. 22, No. 5, pp.547-560.
Pedroso, M.C. and Nakano, D. (2009), "Knowledge and information flows in supply chains: A study on pharmaceutical companies", Int. J. Production Economics, No. 122, pp. 376–384.
Perez-Escobedo, J.L., Azzaro-Pantel, C. and Pibouleau, L. (2012), "Multiobjective strategies for New Product Development in the pharmaceutical industry", Computers and Chemical Engineering, Vol. 37,pp 278-296.
Pisano, G.P. (2000), "The Molecular Biology Revolution: How Can We Turn Promise Into Reality", Available at: http://www. thebiotechclub.org / industry / articles / transforming_econ.php, (accessed February 2005)
Pisano, G.P., Wheelwright, S.C., 1995. The new logic of high-tech R&D. Harvard Business Review September–October, 93–105.
Porter, M. E. (1980). Competitive strategy. New York, NY: The Free Press.
Powell, T.C. (1995), "Total quality management as competitive advantage: a Review and empirical study", Strategic Management Journal, Vol.16, pp. 15–37.
Presutti,W.D. (2003), "Supply management and e-procurement: creating value added in the supply chain", Industrial Marketing Management, Vol. 32 No. 3, pp. 219-26.
Quick, J.D., Rankin, J.R., Laing, R.O. and O'Connor, R.W. (1997), Managing Drug Supply: The Selection, Procurement, Distribution and Use of Pharmaceuticals, 2nd ed, revised and expanded, Kumarian Press, Bloomfield, CT.
Ragatz, G.L.,Handfield,R.B., and Scannell,T.V.,(1997), "Success factors for Integrating suppliers in to new product development" Journal of Product Innovation Management, Vol.14, pp.190–202.
Rahman, S., Laosirihongthong, T. and Sohal, A.S. (2010), "Impact of lean strategy on operational performance: a study of Thai manufacturing companies", Journal of Manufacturing Technology Management, Vol. 21, No. 7, pp. 839-52.
Rosenzweig, E. D., Roth,A.V.,DeanJr.,J.W., (2003), "The influence of an Integration strategy on competitive capabilities and business performance: an exploratory study of consumer products manufacturers" Journal of Operations Management, Vol. 21, pp.437–456.

Downloaded by Delhi Technological University At 23:17 02 August 2016 (PT)

© Emerald Group Publishing Limited
This is a pre-print of a paper and is subject to change before publication. This pre-print is made available with the understanding that it will not be reproduced or stored in a retrieval system without the permission of Emerald Group Publishing Limited.

Rossetti, C.L., Handfield, R. and Dooley, K.J. (2011), "Forces, trends, and decisions in pharmaceutical supply chain management", International Journal of Physical Distribution & Logistics Management, Vol. 41 No. 6, pp.601 – 622.
Samuelsson, J. (1999), "Pharmaceutical capacity planning", M.Sc, Thesis, London: Imperial College.
Sanders, N.R., Premus, R. (2005), "Modeling the relationship between firm it capability,collaboration and performance", Journal of Business Logistics, Vol. 26, No. 1, pp. 1–23.
Schmidt, C. W., & Grossmann, I. E. (1996). Optimization models for the scheduling of testing tasks in new product development. Industrial Engineering of Chemical Research, 35, 3498–3510.
Scott, G.M., 2000. Critical technology management issues of new product development in high-tech companies. Journal of Product Innovation Management, Vol.17, pp.57–77.
Shah, N. (2004), "Pharmaceutical supply chains: key issues and strategies for optimization",Computers and Chemical Engineering, No. 28, pp. 929–941
Shang, J., Tadikamalla, P.R., Kirsch, L.J, Lawrence Brown L (2008), "A decision support system for managing inventory at GlaxoSmithKline", Decision Support Systems, Vol. 46, pp. 1–13
Shang, K.C. and Sun, L.F. (2004), "Taxonomy in logistics management: a resource-based perspective", International Journal of Management, Vol. 21, No. 2, pp. 149–165.
Simango, C.C.B. (2000) "Corporate strategy R&D and technology transfer in the European pharmaceutical industry: research findings", European Business Review, Vol. 12, No. 1, pp.28 – 33.

Singh, R.K and Sharma, M.K (2015), "Selecting competitive supply chain using Fuzzy-AHP and Extent analysis", Journal of Industrial and Production Engineering (Tayler and Francis), Vol. 31, No. 8, pp. 524-538.

Srivastava, S. K. (2008). Network design for reverse logistics. Omega-International Journal of Management Science,Vol. 36, No.4,pp. 535–548.
Stank, T.P., Keller, S.B. and Closs, D.J. (2001), "Performance benefits of supply chain logistical integration", Transportation Journal, Vol. 41, No. 2/3, pp. 32–46.
Subramanian, D., Pekny, J. F., and Reklaitis, G. V. (2000), "A simulation-optimization framework for addressing combinatorial and stochastic aspects of an R&D pipeline management problem", Computers & Chemical Engineering, Vol. 24, pp. 1005–1011.
Sundaramoorthy, A. and Karimi, I.A. (2004), "Planning in pharmaceutical supply chains with outsourcing and new product introductions", Industrial & Engineering Chemistry Research, Vol. 43 No. 2, pp. 8293-306.
Sweet, C. (2010), "Indian pharmaceuticals in Brazil: emerging multinationals in emerging markets", International Journal of Emerging Markets, Vol. 5, No. 3/4, pp.398 – 422.
Talias, M. (2007), "Optimal decision indices for R&D project evaluation in the pharmaceutical industry: Pearson index versus Gittins index", European Journal of Operational Research, Vol. 177, pp. 1105-12.
Tracy, M. (2004), "A holistic approach to new product development: new insights", Journal of Supply Chain Management, Vol. 40, No. 4, pp. 37–55.

Downloaded by Delhi Technological University At 23:17 02 August 2016 (PT)

© Emerald Group Publishing Limited
This is a pre-print of a paper and is subject to change before publication. This pre-print is made available with the understanding that it will not be reproduced or stored in a retrieval system without the permission of Emerald Group Publishing Limited.

Tsai, W.H. and Lai, C.W. (2007), "Outsourcing or capacity expansions: application of activity-based costing model on joint products decision", Computers & Operations Research, Vol. 34, No. 12, pp. 3666-81.
Tsiakis, P., Shah, N., and Pantelides, C. C. (2001), "Design of multi-echelon supply chain networks under demand uncertainty", Industrial & Engineering Chemistry Research, No. 40, pp. 3585–3604
Vachon, S. and Klassen, R.D (2008), "Environmental management and manufacturing performance: the role of collaboration in the supply chain", International Journal of Production Economics, Vol.111, No. 2, pp. 299–315.
Van Eijken, M., Tsang, S., Wensing, M., De Smet, P.A.G.M. and Grol, R.P.T.M. (2003), "Interventions to improve medication compliance in older patients living in the community: a systematic review of the literature", Drugs & Aging, Vol. 20, No. 3, pp. 229-40.
Van Hoek, R.I. (1999), "From reversed logistics to green supply chains", Supply Chain Management, An International Journal, Vol. 4, No. 3, pp. 129-35.
Vinodh, S., Arvind, K.R. and Somanaathan, M. (2010), "Application of value stream mapping in an Indian camshaft manufacturing organization", Journal of Manufacturing Technology Management, Vol. 21, No. 7, pp. 888-900.
Wan, X., Pekny, J., and Reklaitis, G. (2006). Simulation based optimization for risk management in multi-stage capacity expansion. In Computer-aided chemical engineering, 16th European symposium on computer aided process engineering and ninth international symposium on process systems engineering Vol. 21.
WHO (2003), Substandard and Counterfeit Medicines, available at: www.who.int/mediacentre/factsheets/fs275/en/ (accessed 31 January 2006).
WHO (2006), Public Health, Innovation and Intellectual Property Rights: Report of the Commission on Intellectual Property Rights, Innovation and Public Health, WHO, Geneva.
WHO (2009), World Health Statistics – 2009, available at: www.who.int/entity/whosis/whostat/EN_WHS09_Full.pdf (accessed December 15, 2009).
WHO (2010), "Who expert committee on specifications for pharmaceutical preparations", Technical Report Series, WHO Technical Report Series 957, WHO, Geneva, available at: www.who.int/medicines/publications/TRS957_2010.pdf
World Bank, 2007, Connecting to Compete, Trade Logistics in the Global Economy. <http://siteresources.worldbank.org/INTTLF/Resources/lpireport.pdf>.
Xie, Y, Breen, L. (2012), "Greening community pharmaceutical supply chain in UK: a cross boundary approach Supply Chain Management", An International Journal, Vol. 17 No.1, pp. 40–53.
Yu, Y., Ma, Z., Hu, H. and Wang,Y., (2014) "Local government policies and pharmaceutical clusters in China", Journal of Science and Technology Policy Management, Vol. 5, No. 1, pp.41 – 58.

Zhu, Q.H. and Sarkis, J. (2004), "Relationships between operational practices and performance among early adopters of green supply chain management practices in Chinese manufacturing enterprises", Journal of Operations Management, Vol. 22, No. 12, pp. 265-89.

Downloaded by Delhi Technological University At 23:17 02 August 2016 (PT)

© Emerald Group Publishing Limited
This is a pre-print of a paper and is subject to change before publication. This pre-print is made available with the understanding that it will not be reproduced or stored in a retrieval system without the permission of Emerald Group Publishing Limited.

About the authors

Dr Rajesh Kr Singh, is Professor at the Management Development Institute, Gurgaon, India. His areas of interest include Competitiveness, Small Business Management, Quality Management and Supply chain management. He has about 125 research papers published in reputed international/national journals and conferences. He has published papers in journals such as *Resources, Conservation and Recycling, Industrial Management and Data Systems, Production planning and Control, Singapore Management Review, International Journal of Productivity and Performance Management, Benchmarking: An International Journal, Journal of Modelling in Management, Competitiveness Review: An International Business Journal, Global Journal of Flexible Systems and Management, International Journal of Productivity and Quality Management, International Journal of Services and Operations Management, International Journal of Automotive Industry and Management, International Journal of Logistic Systems Management, IIMB Management Review and Productivity* Promotion. Email: rksd ce@yahoo.com

Dr Ravinder Kumar holds a bachelor's degree with honors in Mechanical Engineering, Master's degree and Ph.D. in Production Engineering from Faculty of Technology, University of Delhi, India. He has more than fourteen year of teaching experience in reputed organizations. Currently he is working as Associate Professor at Amity school of Engineering & Technology, Amity University, Noida (India). His main research area is supply chain management, small business management and quality management. He has published about 20 research papers in reputed international journals and conferences. He has published papers in journals such *Competitiveness Review: An International Journal, Global Journal of Flexible Systems Management, International Journal of Manufacturing Research, International Journal of Business Information Systems (IJBIS)* and *IIMB Management Review*. Email: ravinderkumar.ap@gmail.com

Dr Pravin Kumar is an Assistant Professor in Mechanical Engineering Department, Delhi Technological University, Delhi, India. He has a Ph.D. in supply chain Management from IIT Delhi and M. Tech in Industrial Management from I.T., BHU, Varanasi (Now IIT BHU Varanasi). He has published many research papers in international and national journals and conferences. His area of research is supply chain and logistics management. He has more than 14 years of teaching and research experience. He has authored the books on *Engineering Economics and Industrial Engineering and Management* by Wiley India and Pearson Learning respectively. Email-pravin.dce@gmail.com

Downloaded by Delhi Technological University At 23:17 02 August 2016 (PT)

© Emerald Group Publishing Limited
This is a pre-print of a paper and is subject to change before publication. This pre-print is made available with the understanding that it will not be reproduced or stored in a retrieval system without the permission of Emerald Group Publishing Limited.

Clean Techn Environ Policy
DOI 10.1007/s10098-016-1268-y

ORIGINAL PAPER

Suppliers' green performance evaluation using fuzzy extended ELECTRE approach

Pravin Kumar[1] · **Rajesh Kumar Singh**[2] · **Anurika Vaish**[3]

Received: 6 June 2016 / Accepted: 13 August 2016
© Springer-Verlag Berlin Heidelberg 2016

Abstract In the present context of the globalized market, sustainable manufacturing has become a major concern for all organizations. The sustainable manufacturing system includes economic, environmental, and social sustainabilities. Green manufacturing enhances the environmental sustainability but, it also affects the economic and social sustainabilities. The compulsion to follow the environmental rules and regulation in any business activity has increased the awareness for the use of green products, recyclable materials for packaging, reduction of carbon emission, etc. Due to the involvement of extra costs in green manufacturing, some ignorance in the implementation of green practices may be observed. To ensure sustainable systems, selection of suppliers based on green performance measures is very important. This study evaluates the suppliers' performances based on Green Practices as follows: environmental management and pollution control, cost, quality, and flexibility using the fuzzy-extended Elimination and Choice Expressing Reality approach. This approach helps the managers to incorporate the linguistic decision of the decision makers and convert it into quantitative scale. This method is used to eliminate and outrank the poor performers. As poor performers are outranked, this approach helps to select the most suitable green suppliers as per organization's requirement.

Keywords Green supply chain management · Sustainability · Supplier evaluation · Outranking · Fuzzy sets · ELECTRE

Introduction

In the recent past, climate change and its impacts on the society had been gaining momentum; and managing pollution-free environment is becoming very important in today's business scenario (Mangla et al. 2014). Therefore, business managers/practitioners are under immense pressure to lessen the harmful ecological and social impacts in their supply chains (Ağan et al. 2016). Sancha et al. (2015) established the relationship between institutional pressures and the sustainable supplier development in various locations. Mansi (2015) discussed sustainable disclosure practices in the purchasing activities of Indian government's public sector enterprises. Green manufacturing is concerned with the replacement of hazardous or nonrenewable inputs by less-hazardous materials or renewable materials, respectively; better control of operations at higher efficiency; equipment modification; technology change; and product modification for minimization of the waste and the emission. The compulsion of linking the green practices

Electronic supplementary material The online version of this article (doi:10.1007/s10098-016-1268-y) contains supplementary material, which is available to authorized users.

✉ Pravin Kumar
pravin.dce@gmail.com

Rajesh Kumar Singh
rksdce@yahoo.com

Anurika Vaish
anuriaka.vaish@gmail.com

[1] Department of Mechanical Engineering, Delhi Technological University, Shahbad-Daulatpur, Bawana Road, Delhi 110042, India

[2] Department of Operations Management, Management Development Institute, Mehrauli Road, Sukhrali, Gurgaon 122001, Haryana, India

[3] Department of Management Studies, Indian Institute of Information Technology, Devghat Jhalwa, Allahabad 211012, India

with corporate strategies has attracted the attention of researchers and practitioners toward sustainable manufacturing and green supply chain management (Gunasekaran and Gallear 2012; Brockhaus et al. 2013). For ensuring green manufacturing, effective management of green supply chain activities is very important.

The concepts of green supply chain management have been evolved through a number of stages—from its inception to empirical studies (Fu et al. 2012). Many terms in green supply chain are concerned with sustainable supply chain concepts (Bai and Sarkis 2010), such as supply chain environmental management (Sharfman et al. 2009); green logistics (Murphy and Poist 2000); closed-loop supply chain (Zhu and Sarkis 2006); sustainable supply network management (Cruz and Matsypura 2009); and green procurement (Gunther and Scheibe 2006). Reverse logistics consists of a collection of discarded products, inspection, sorting, and recovery activities like recycling, remanufacturing, reuse, disposal, etc. (Govindan et al. 2015).

Amindoust et al. (2012) used fuzzy inference systems for sustainable supplier selection. They divided the selection criteria into three classes: economic, environmental, and social sustainabilities. For economic sustainability, they considered profit, quality, delivery and services as the subcriteria. For environmental sustainability, they considered environmental management systems and environmental competencies as the subcriteria. Similarly, for social sustainability, they considered the rights of stakeholders, work safety, and labor health as the subcriteria.

Büyüközkan and Ciftci (2012) observed that most of the adverse effects of the product on the environment can be eliminated during the design phase of the product development. According to Eltayeb et al. (2011), eco-friendly design (known as ecodesign) process consists of design for reduction of environmentally hazardous substances, design for reuse of a product, design for recycling waste material, and design for remanufacturing. Green purchasing covers the area of waste reduction, environmental material substitution, minimization of hazardous material, etc. Hence, companies have to take care of suppliers' environmental performance and ensure that purchased materials are environmentally friendly for cleaner production (Lin 2013).

The World Business Council for Sustainable Development (WBCSD) and the World Resources Institute in 2009 have observed that at least 80 % of carbon emissions were produced through supply chains (Hsu et al. 2013). Wittneben and Kiyar (2009) emphasized on the importance that the supplier declare the exact figure of greenhouse gas emissions and that of the objective to reduce their carbon emissions. Hsu et al. (2013) summarized the main attributes for green supplier selection in carbon management. Supplier environmental collaboration covers activities that enhance supplier's environmental performance related to joint planning, shared knowledge, green product development, and innovations (Eltayeb et al. 2011). Environmental collaboration helps companies to assure that the purchased materials are environment-friendly and produced using green processes (Zhu and Sarkis 2007).

Environmental management systems (EMS) should include policies, procedures, and audit procedures to evaluate the environmental impact of an organization's operations. One of the most popular EMS is the International Organization for Standardization (ISO) 14000 series (Nawrocka et al. 2009). ISO 14001 directs all supply chain partners to select more environmentally friendly practices. It develops a systematic approach to reduce the negative environmental effects of organizations, decreases resource consumption and waste, and contributes to quality improvement (Eltayeb et al. 2011; Xu and Shen 2014).

This paper consists of four sections. The first section introduces the green supply chain management; the second section outlines the literature on the attributes for evaluation of supplier's green performance; the third section deals with the proposed methodology; the fourth section illustrates this approach with a case study, i.e., green supplier selection; and the fifth section concludes the research work.

Literature review

The green approach toward supply chain management ensures green manufacturing for sustainable performance. The operative GSCM (Green Supply Chain Management) performance leads to the decline of the solid/liquid wastes, reduction in emission levels, the use of hazardous and toxic materials, and improvement in the health-related concerns of employees and the community (Eltayeb et al. 2011). As suppliers can contribute significantly to ensuring a supply chain green, the environmental aspect of green supplier selection has gained more importance nowadays.

Supplier selection criteria and methodologies

In earlier research works, cost (Awasthi et al. 2010), delivery (Kuo et al. 2010), quality (Shaik and Abdul-Kader 2011), service (Buyukozkan 2012), strategic alliance (Awasthi et al. 2010), pollution control (Lee et al. 2009), green product (Awasthi et al. 2010), and environmental management (Kuo et al. 2010) are considered as the main factors in the green supplier selection.

It has been observed that a number of criteria have been used by the researchers to evaluate the suppliers. Some of the environmental factors are considered with other factors, such as cost, quality, reliability, flexibility, etc., of the

suppliers for performance measurement of suppliers or their selection. No reference has been found, which had used environmental factors in isolation for supplier selection. Thus, the review analysis shows that nowadays buyers are environmentally conscious in purchasing the goods/services, but other factors are equally important for them. In those references, no supplier is outranked, and all suppliers are considered for quota allocation as per their ranking and capacity constraints. Liu and Zhang (2011) used Elimination and Choice Expressing Reality (ELECTRE III) as an outranking method for supplier selection, but they have not considered the environmental factor at all in this process. However, they have used 19 criteria for supplier selection. Sevkli (2010) used fuzzy ELECTRE for supplier selection, but without giving any consideration to environmental factors. Tsui et al. (2015) used PROMETHEE for performance measurement of green suppliers in TFT-LCD industry and considered the environment and green management as factors with other factors for performance evaluation. Kuo et al. (2015) used DANP and VIKOR techniques to prioritize the 17 criteria and rank the suppliers. They have considered many environment-related criteria for supplier evaluation, and some criteria are related to management systems.

To incorporate all subcriteria individually in the analysis of supplier selection may be very complex; therefore, there is the need to show the overall impact of these subfactors in a broader perspective. For example, if cost is considered as one of the criteria for supplier selection, then it means that the different types of costs related to material processing, manufacturing, testing and inspection, packaging, transportation, etc. form parts of the main cost criteria. Similarly, in this paper, a total of 38 subfactors have been considered in supplier rating. These subfactors are grouped into six main clusters such as cost, quality, flexibility, service, green practices, environmental management, and pollution control, as shown in Fig. 1.

Cost

Cost components related to suppliers are purchasing, transportation, inventory, operation, maintenance, energy, inspection, delivery, security, ordering, holding, etc. (Ghodsypour and O'Brien 2001). There are some limitations of this process because all the performances should be measured in the same unit and there is complexity in developing a cost-accounting system (Petroni and Braglia 2000). Transportation cost is an important component of the logistics costs. It includes the cost of fuel or lubricants, penalties, driver salaries, maintenance costs, failure of the vehicle (Ongkunaruk and Piyakarn 2011). At the microlevel a number of cost components are there; it is very difficult to consider all the components at a time for supplier selection. Therefore, only the macrolevels of the cost components are highlighted in the decision-making problem.

Quality

It deals with quality control and assurance. Quality assurance deals with the fulfillment of customer demands with optimal utilization of resources and to coincide with the firm's policy (Manning et al. 2006). "Business Process Reengineering (BPR)" and "Total Quality Management (TQM)" are two basic components of process organization, control, and improvement. There are many performance attributes such as certifications and awards that have been applied by the companies to benchmark the performance. ISO 9000, ISO 14000, EN 29000, and BS 5750 are some of the performance certifications and Quality improvement awards (Kardaras and Mentzas 1997).

Service

Nowadays, companies are able to provide products of a high quality, but high responsiveness, stock management, design capability, and low price, are some crucial issues in the improvement of service level to the customer. Suppliers play a crucial role in the supply chain; they provide a number of services such as assurance of fast deliveries, quick response, logistics Service, vendor managed inventory (VMI), and product design including components. Firms can improve their logistics performance through fast deliveries, quick response, low stocks, no damage, low costs, high productivity, fewer mistakes, minimum wastage, the high morale of staff, and so on. In order to meet customer's specific and rapidly changing needs, a firm is required to be more responsive (Gunasekaran et al. 2008). The success of order-fulfillment solutions depends on the integration of order-fulfillment planning, product execution, distribution management, and cross-application integration.

Flexibility

Flexibility is an important part of the supply chain to meet the changing business requirements. Kumar et al. (2008) discussed the various types of flexibility and relationship among the variables of flexibility for global supply chain. Flexibility includes the ability to change the systems as per the requirement of the buyer. In this paper, the authors have incorporated different attributes of the flexibility for the supplier rating, which are technological change, material change, equipment upgradation, process improvement, volume flexibility, and design flexibility to reduce the use of hazardous materials, to minimize the consumption of

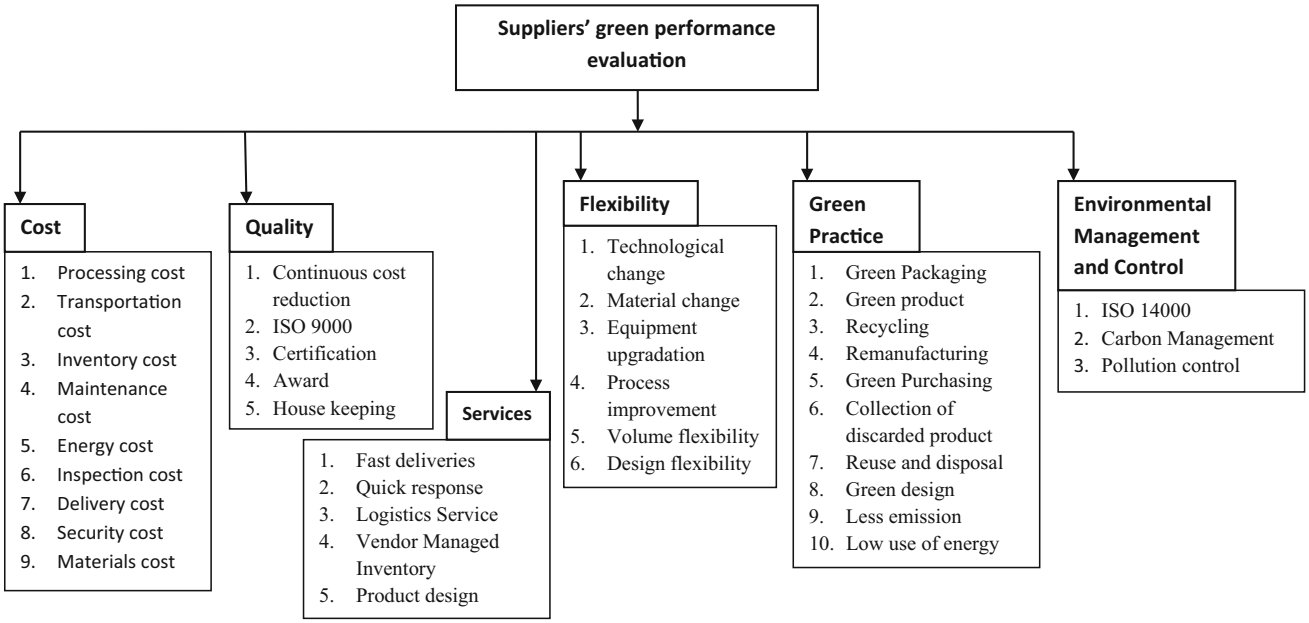

Fig. 1 A framework for Supplier performance evaluation for cleaner production

energy, and to control the pollution and wastes during the usage of the products.

Green practice

Green practice is a very broad term and covers a number of activities of green supply chain, such as green purchasing, green packaging of the product, green product, recycling of wastes and end products, remanufacturing, collection of discarded product, reuse and disposal, green design, less emission, and low use of energy. In the recent years, a "green" competency between vendors and suppliers has increased the value of the company in the market. Green packaging aims to use environmentally friendly packaging material to protect the environment. Its main characteristic is to get dissolved or degraded in nature rapidly without harming the environment. Green packaging can be explained in terms of 4R1D (reduce, reuse, reclaim, recycle, degradable) (Zhang and Zhao 2012). Another important green practice is *recycling*. It is a process in which the used product is reduced to its raw materials and new and different products are generated from them. Recycling can be implemented if the scrapped product could not be reused again. Recycling needs a few processes, such as extraction, separating, etc., which require energy and harm the environment (Zhang and Zhao 2012). *Reuse* of a product is the extension of its life at the end with little or no treatment. Reuse can also be explained utilizing the material for a second or further time. There is no addition of any new value to the product. It is the process of getting a green product (Ke et al. 2011). *Remanufacturing* is also considered an important green practice. It is a process of restoring a large quantity of the products to a new state. Damaged components are repaired, but it does not ensure attaining the same performance level as the original product. The manufacturers can add some values or features to the product. It can be seen similar to the recycling, but it differs from it. Recycling is concerned with the raw materials, but remanufacturing is concerned with the original function (Zhang and Zhao 2012).

Environmental management and pollution control

Recently, the environmental obligation has been added to the procurement processes. Due to the high stress on Environmental Management Systems (EMS) and the increasing awareness of the negative impacts of productions to the environment, buyers have started to evaluate the green performance of suppliers. It influences the decision-making process, and many buyers expect from their supplier for applying EMS (Handfield et al. 2002). Ozonedepleting chemicals (ODCs) such as CFC (chlorofluorocarbon) and NOxs are the human-made chemical compounds which are responsible for the depletion of the ozone layer (Ravishankara et al. 2009). International Organization for Standardization (ISO 14001) is an institution for producing guidelines to provide certification to the firm based on "environmental aspects." All policies, regulations, goals, and targets are reassessed and reevaluated for the continuous improvement (Bansal and Bogner 2002). Supplier's attitude toward the pollution control is very important for the buyer to work together. With the growing production rate, energy

consumption grows rapidly, and the pollution is the byproduct of energy use. Therefore, pollution-control programs that imply a proper usage of energy consumption are propagated (Yanqing and Mingsheng 2012).

Shaw et al. (2012) have used fuzzy Analytic Hierarchy Process (FAHP) and multiobjective goal programming for supplier selection and quota allocation. They laid emphasis on the development of low-carbon supply chain. For supplier selection, they gave the importance to greenhouse gas emission with some of the other criteria, such as cost, quality, lead time, and demand. The quota allocation among the shortlisted suppliers is based on four objective functions: the minimization of total purchasing cost, minimization of rejection due to quality problem, minimization of late delivery, and minimization of carbon footprints.

Chaharsooghi and Ashrafi (2014) used a risk-management system, transparently, and culture and strategy in addition to economic, environmental, and social sustainabilities as the criteria for sustainable supplier evaluation and selection. They used neofuzzy TOPSIS (Technique for Order Preference by Similarity to Ideal Solution) as the methodology for supplier selection. Deviating from simple fuzzy TOPSIS, they inserted two absolute conditions (Bad and Good) in the decision-making matrix in neofuzzy TOPSIS methodology. Neofuzzy TOPSIS compares the candidates (suppliers) with these two standards, so the distance between candidates becomes real.

It has been observed that the environmental sustainability strongly influences the economic and social sustainabilities in terms of cost- and health-related issues. Most of the researchers have talked about the environmental sustainability with economic and social sustainabilities and some other factors for supplier selection. The uniqueness of this paper is that the authors have given weights to the green practices and environmental management systems and control with some other conventional factors, such as cost, quality, flexibility, services, etc. for supplier evaluation.

Research methodology

For the ranking of suppliers for green supply chain, the Fuzzy ELECTRE approach has been applied in this paper. A number of variants of ELECTRE method have been in use for the decision-making process. In this paper, the concept of decision making with the help of fuzzy ELECTRE has been taken from the research work of Hatami-Marbini et al. (2013). Basic steps of this approach will be described in this section.

Definition 1 Let X be a universe set. The fuzzy set $\tilde{A}$ is defined by a membership function, $\mu_{\tilde{A}}(x) = [0, 1]$, where $\mu_{\tilde{A}}(x)$, $\forall x \in X$, indicates the degree of membership of $\tilde{A}$ to X(Zadeh 1965).

Definition 2 A triangular fuzzy number $\tilde{A}$ is defined as (a^l, a^γ, a^u), $a^l \le a^\gamma \le a^u$. The membership function $\mu_{\tilde{A}}(x)$ is defined as (Zimmerman 1991; Kahraman et al. 2004)

$$\mu_{\tilde{A}}(x) = \begin{cases} 0 & x \le a^l \\ \dfrac{x - a^l}{a^\gamma - a^l}, & a^l < x < a^\gamma \\ \dfrac{a^u - x}{a^u - a^\gamma}, & a^\gamma < x < a^u \\ 0, & x \ge a^u \end{cases} \tag{1}$$

Definition 3 The mathematical operations of TFN (Triangular Fuzzy Number) can be done using the following equations (Chen 2014):

$$\tilde{A} + \tilde{B} = (a^l + b^l, a^\gamma + b^\gamma, a^u + b^u)$$
$$\tilde{A} - \tilde{B} = (a^l - b^l, a^\gamma - b^\gamma, a^u - b^u)$$
$$\tilde{A}/\tilde{B} = (a^l/b^u, a^\gamma + b^\gamma, a^u + b^l)$$
$$\tilde{A} \otimes \tilde{B} = (a^l \times b^l, a^\gamma \times b^\gamma, a^u \times b^u)$$
$$\text{Reciprocal of } \tilde{A} = (1/a^u, 1/a^\gamma, 1/a^l).$$

Definition 4 Hamming distance between two fuzzy numbers $(\tilde{A},\tilde{B})$ is defined as (Hamming 1950)

$$\int_R \left|\mu_{\tilde{A}}(x) - \mu_{\tilde{B}}(x)\right| \tag{2}$$

where R is the set of real numbers.

However, for simplicity in calculation, the distance between two fuzzy numbers (Chen 2000; Li and Yang 2004), especially in ELECTRE method can be represented by

$$d(\tilde{A}, \tilde{B}) = \sqrt{\sum_{k=1}^{3} (A_k - B_k)^2}. \tag{3}$$

Definition 5 Standard intersection, $A \cap B$ and standard union, $A \cup B$ of two fuzzy sets, $\tilde{A}$ and $\tilde{B}$ are defined as $(\tilde{A} \cap \tilde{B})(x) = \min[\tilde{A}(x), \tilde{B}(x)]$ and $(\tilde{A} \cup \tilde{B})(x) = \max[\tilde{A}(x), \tilde{B}(x)]$ respectively.

Definition 6 Comparison of fuzzy numbers on the basis of outranking

The outranking relations in ELECTRE are shown as S,which means ''at least as good as.'' Considering two alternatives A_f and A_g, four situations may arise (Hatami-Marbini and Tavana 2011):

- A_f S A_g and not A_g S A_f (A_f is strictly preferred to A_g),
- A_gS A_f and not A_fS A_g (A_g is strictly preferred to A_f),
- A_f S A_g and A_g S A_f (A_f is indifferent to A_g)
- Not A_f S A_g and not A_g S A_f (A_f is incomparable to A_g).

Fuzzy ELECTRE

Fuzzy ELECTRE is a process of multicriteria decision making. In this process, poor performers are outranked, and only comparable performers are ranked. This outranking is based on the concordance and discordance values. Fuzzy sets are used to incorporate the linguistic variables or vague state of mind of the decision-makers. The major steps of the fuzzy TOPSIS are discussed as follows (Pl refer Appendix 1 for framework):

Step 1: Preparation of fuzzy decision matrix

To prepare a fuzzy decision matrix of 'm' alternatives and 'n' attributes, first, the fuzzy importance of the attributes is determined. The decision makers are given different weightages on the basis of their respective experiences and levels in organization hierarchy, e.g., the first, second, and third decision makers among the three levels are assigned with the weights of 40, 35, and 25 % respectively.

After deciding the weights for the decision makers, the fuzzy importance(s) of attributes is(are) decided by a weighted average of the ratings of attributes by the decision makers using the following formula:

$$\tilde{w}_j = \frac{1}{K}\left(\sum_{k=1}^{3} \tilde{w}_{jk}\right), \tag{4}$$

where $k = 1,2,\ldots,K$ is the number of decision makers; $j = 1,2,\ldots,n$ is the number of attributes; and $\tilde{W}_{jk}$ is the importance of jth attributes assigned by kth decision makers.

After deciding the importance(s) of the various attributes, various alternatives are rated against each attribute by all the K decision makers, and the final fuzzy rating of alternatives is determined by weighted average using the following formula:

$$\tilde{x}_{ij} = \frac{1}{K}\left(\sum_{k=1}^{3} \tilde{x}_{ijk}\right), \tag{5}$$

where $k = 1,2,\ldots,K$ is the number of decision makers; $i = 1,2,\ldots,m$ is the number of alternatives; $j = 1,2,\ldots,n$ is the number of attributes; and $\tilde{x}_{ijk}$ is the rating of ith alternative against the jth attributes by the kth decision maker.

The decision matrix can be represented as

$$\tilde{U} = \begin{array}{c} \begin{matrix} \tilde{W}_1 & \tilde{W}_2 & \ldots & \tilde{W}_n \end{matrix} \\ \begin{bmatrix} \tilde{x}_{11} & \tilde{x}_{12} & \ldots & \tilde{x}_{1n} \\ \tilde{x}_{21} & \tilde{x}_{22} & \ldots & \tilde{x}_{2n} \\ . & . & \ldots & . \\ \tilde{x}_{m1} & \tilde{x}_{m2} & \ldots & \tilde{x}_{mn} \end{bmatrix} \end{array} \tag{6}$$

Step 2: Preparation of normalized decision matrix

Linear-scale normalization is applied to ensure that all values of the elements in the decision matrix have homogeneous and comparable units. Moreover, this transformation guarantees that every triangular fuzzy number belongs to [0,1] which reduces the complexity in the mathematical operations. The normalized fuzzy decision matrix is shown below:

$$\tilde{R} = \left[\tilde{r}_{ij}\right]_{m \times n}. \tag{7}$$

$$\tilde{r}_{ij} = \left(r_{ij}^{l}, r_{ij}^{\gamma}, r_{ij}^{u}\right) = \left(\frac{x_{ij}^{l}}{c_j^*}, \frac{x_{ij}^{\gamma}}{c_j^*}, \frac{x_{ij}^{u}}{c_j^*}\right) \tag{8}$$
$$c_j^* = \max_i (x_{ij}^{u}), j \in B,$$

where B is the set of benefit attributes; $i = 1,2\ldots,m$; and $j = 1,2,\ldots,n$.

$$\tilde{r}_{ij} = \left(r_{ij}^{l}, r_{ij}^{\gamma}, r_{ij}^{u}\right) = \left(\frac{a_j^-}{x_{ij}^{u}}, \frac{a_j^-}{x_{ij}^{\gamma}}, \frac{a_j^-}{x_{ij}^{l}}\right) \tag{9}$$
$$a_j^- = \min_i (x_{ij}^{l}), j \in C,$$

where C is the set of cost attributes; $i = 1,2\ldots,m$; and $j = 1,2,\ldots,n$.

Step 3: Computing the weighted normalized matrix

Multiply the standard rating of the alternatives with the importance of corresponding attributes to compute the weighted normalized matrix using the following formula:

$$\tilde{v}_{ij} = \left(\tilde{r}_{ij}\right) \times \left(\tilde{w}_j\right) = \left(r_{ij}^{l}, r_{ij}^{\gamma}, r_{ij}^{u}\right) \times \left(w_j^{l}, w_j^{\gamma}, w_j^{u}\right). \tag{10}$$

Step 4: Calculating the distance between any two alternatives

The concordance and discordance matrices are prepared using the weighted normalized fuzzy decision matrix and pairwise comparison of the alternatives. Considering two alternatives A_x and A_y, the concordance set is formed as $J^C = \{J|\tilde{v}_{xj} \geq \tilde{v}_{yj}\}$ where J^C is the concordance coalition of the attributes and the assertion is A_xSA_y. The discordance set is defined as $J^D = \{J|\tilde{v}_{xj} \leq \tilde{v}_{yj}\}$ where J^D is the discordance coalition, and it is against the assertion, A_xSA_y. Note that S is the outranking relation, and A_xSA_y means that ''A_x is at least as good as A_y.''

In order to compare any two alternatives A_x and A_y, with respect to each attribute, and to define the concordance and discordance sets, we specify the least upper bound of the alternatives, max $\left(\tilde{v}_{xj}, \tilde{v}_{yj}\right)$), and then, the distance is used with the following assumptions:

$$\tilde{v}_{xj} \geq \tilde{v}_{yj} \Leftrightarrow d(\max(\tilde{v}_{xj}, \tilde{v}_{yj}), \tilde{v}_{yj}) \geq d(\max(\tilde{v}_{xj}, \tilde{v}_{yj}), \tilde{v}_{xj}), \text{ and} \tag{11}$$

$$\tilde{v}_{xj} \leq \tilde{v}_{yj} \Leftrightarrow d(\max(\tilde{v}_{xj}, \tilde{v}_{yj}), \tilde{v}_{yj}) \leq d(\max(\tilde{v}_{xj}, \tilde{v}_{yj}), \tilde{v}_{xj}). \tag{12}$$

Step 5: Constructing the concordance and discordance sets, and concordance and discordance matrices

The concordance set is the set of attributes for which $\tilde{v}_{xj} \geq \tilde{v}_{yj}$ and the discordance set is the set of the attributes for which $\tilde{v}_{xj} \leq \tilde{v}_{yj}$. The following concordance matrix is formed in which the elements are the fuzzy summation of the fuzzy importance weights for all the attributes in the concordance set.

$$\tilde{C} = \begin{bmatrix} \tilde{c}_{11} & \cdots & \tilde{c}_{1x} & \cdots & \tilde{c}_{1(m-1)} & \tilde{c}_{1m} \\ \cdots & \cdots & \cdots & \cdots & \cdots & \cdots \\ \tilde{c}_{x1} & \cdots & \cdots & \cdots & \tilde{c}_{x(m-1)} & \tilde{c}_{xm} \\ \cdots & \cdots & \cdots & \tilde{c}_{xy} & \cdots & \cdots \\ \tilde{c}_{(m-1)1} & \cdots & \tilde{c}_{(m-1)y} & \cdots & \cdots & \cdots \\ \tilde{c}_{m1} & \cdots & \cdots & \cdots & \tilde{c}_{m(m-1)} & \tilde{c}_{mm} \end{bmatrix}, \tag{13}$$

where $\tilde{c}_{xy} = \left(c^l_{xy}, c^\gamma_{xy}, c^u_{xy}\right) = \left(\sum_{J\in J^c} w^l_j, \sum_{J\in J^c} w^\gamma_j, \sum_{J\in J^c} w^u_j\right)$.

Now, we determine the concordance level as

$$\bar{\tilde{c}} = \sum_{x=1}^{m} \sum_{y=1}^{(m-1)} \frac{\tilde{c}_{xy}}{m(m-1)}. \tag{14}$$

The discordance matrix is prepared as

$$\tilde{D} = \begin{bmatrix} \tilde{d}_{11} & \cdots & \tilde{d}_{1x} & \cdots & \tilde{d}_{1(m-1)} & \tilde{d}_{1m} \\ \cdots & \cdots & \cdots & \cdots & \cdots & \cdots \\ \tilde{d}_{x1} & \cdots & \cdots & \cdots & \tilde{d}_{x(m-1)} & \tilde{d}_{xm} \\ \cdots & \cdots & \cdots & \tilde{d}_{xy} & \cdots & \cdots \\ \tilde{d}_{(m-1)1} & \cdots & \tilde{d}_{(m-1)y} & \cdots & \cdots & \cdots \\ \tilde{d}_{m1} & \cdots & \cdots & \cdots & \tilde{d}_{m(m-1)} & \tilde{d}_{mm} \end{bmatrix}, \tag{15}$$

where

$$d_{xy} = \frac{\max_{j\in J^D} \left|\tilde{v}_{xj} - \tilde{v}_{yj}\right|}{\max_j \left|\tilde{v}_{xj} - \tilde{v}_{yj}\right|} = \frac{\max_{j\in J^D} \left|d(\max(\tilde{v}_{xj}, \tilde{v}_{yj}), \tilde{v}_{xj}\right|}{\max_j \left|d(\max(\tilde{v}_{xj}, \tilde{v}_{yj}), \tilde{v}_{yj})\right|}. \tag{16}$$

Now, we determine the disconcordance level as

$$\bar{d} = \sum_{x=1}^{m} \sum_{y=1}^{(m-1)} \frac{d_{xy}}{m(m-1)}. \tag{17}$$

Step 6: Preparing the Boolean matrices E and F for the concordance and discordance matrices

$$E = \begin{bmatrix} e_{11} & \cdots & e_{1x} & \cdots & e_{1(m-1)} & e_{1m} \\ \cdots & \cdots & \cdots & \cdots & \cdots & \cdots \\ e_{x1} & \cdots & \cdots & \cdots & e_{x(m-1)} & e_{xm} \\ \cdots & \cdots & \cdots & e_{xy} & \cdots & \cdots \\ e_{(m-1)1} & \cdots & e_{(m-1)y} & \cdots & \cdots & \cdots \\ e_{m1} & \cdots & \cdots & \cdots & e_{m(m-1)} & e_{mm} \end{bmatrix}, \tag{18}$$

where

$$\begin{cases} \tilde{c}_{xy} \geq \bar{\tilde{c}} \Leftrightarrow e_{xy} = 1 \\ \tilde{c}_{xy} \leq \bar{\tilde{c}} \Leftrightarrow e_{xy} = 0 \end{cases}$$

$$F = \begin{bmatrix} f_{11} & \cdots & f_{1x} & \cdots & f_{1(m-1)} & f_{1m} \\ \cdots & \cdots & \cdots & \cdots & \cdots & \cdots \\ f_{x1} & \cdots & \cdots & \cdots & f_{x(m-1)} & f_{xm} \\ \cdots & \cdots & \cdots & f_{xy} & \cdots & \cdots \\ f_{(m-1)1} & \cdots & f_{(m-1)y} & \cdots & \cdots & \cdots \\ f_{m1} & \cdots & \cdots & \cdots & f_{m(m-1)} & f_{mm} \end{bmatrix}, \tag{19}$$

where

$$\begin{cases} d_{xy} \geq \bar{d} \Leftrightarrow d_{xy} = 0 \\ d_{xy} \leq \bar{d} \Leftrightarrow d_{xy} = 1 \end{cases}$$

Step 7: Preparing the final matrix

A final matrix G is prepared by peer-to-peer multiplication of the elements of the matrices, E and F, which can be represented as

$$G = E \otimes F. \tag{20}$$

Step 8: Constructing a decision graph and ranking the alternatives

A decision graph is drawn using the final matrix G in order to determine the ranking order of the alternatives. Let A_x and A_y be two alternatives. There is an arc between the two alternatives from A_x to A_y if alternative A_x outranks A_y; there is no arc between the two alternatives if alternatives A_x and A_y are incomparable; and there are two arcs between the two alternatives in both directions if these alternatives are not different.

Case illustration

In an automotive supply chain, supplier plays an important role, and the success of the supply chain depends on the performance of the supplier. Only a few parts of the automobile are of strategic importance and produced in-house. Most of the components are outsourced, and the buyer depends on his supplier for those components. Therefore, the buyer develops a strategic relationship with the supplier. Some of the autocomponents are supplied in the integrated form to the OEM or assembler. These components may be supplied by the tier-1 or tier-2 suppliers. A detailed structure of a typical automotive supply chain is shown in Fig. 2. It has been observed that many components, such as tires, tubes, and electric, and electronic parts are directly supplied or supplied from the regional distributors to the assembler.

In this research, about twenty autocomponent suppliers were considered for green performance evaluation at the initial stage, but finally, eight suppliers were shortlisted on the basis of their market shares. These suppliers are supplying the autocomponents to the world's leading car manufacturers in India and abroad. All the suppliers are certified by the ISO certification and awarded with different quality awards. Some suppliers are more concerned with the environment and pollution. However, most of the suppliers in developing countries have a lack of awareness and show ignorant behavior toward the green product, carbon footprint, and the emission control. This ignorance may be due to lack of infrastructure, intention to provide the products at low cost to meet the competition, no strict control of the government over the implementation of environmental management systems, etc. In the developed nation, implementation of the environmental rules and regulation is more strict in comparison with developing nation due to the availabilities of infrastructure and technology, awareness among the buyers and suppliers related to environmental rules and regulations, strict control of the government over the implementation of the green practices in manufacturing, mandatory nature of ISO 14000 certification, social health awareness, etc.

Therefore, to know the suppliers' efforts toward the green supply chain management, a framework has been proposed to evaluate the suppliers' green performance. To gather the exact information about the suppliers, all the three levels of management of a buyer company were consulted for their opinion. The decision maker from the top-level management is given the highest weightage (40 %), from middle-level management is given the moderate weightage (35 %), and from lower-level management is given less weightage (25 %). On the basis of these decision makers, total six groups of attributes were shortlisted to rate the suppliers. These attributes are cost, quality, services, flexibility, green practice, environmental management, and pollution control. The importance of these attributes is based on the weighted average of the ratings of the decision makers. Table 1 shows the linguistic and the fuzzy quantitative scales that are used in this paper. In this table, the first column shows the linguistic scale for the importance ratings of the criteria; the second column shows the linguistic scale for the performance ratings of the alternatives with respect to the various criteria, and the last column shows the fuzzy quantitative scale for the corresponding linguistic scale. Since the linguistic scale cannot be directly used in mathematical operations, it is converted to fuzzy quantitative scale.

The final weights of the attributes for supplier evaluation are calculated using a weighted average of the opinion given by the decision makers: for example, the first decision maker, second decision maker, and the third decision maker rate the importance of the attributes 'cost' as very high, high, and very high, respectively. The weighted average of the importance of cost can be calculated using Eq. (4). The importance ratings of the attributes by these three decision makers and their weighted averages are shown in Table 2.

After finding the weighted average of the importance of all the attributes, suppliers are evaluated by these decision makers against all the attributes on a linguistic scale as shown in Table 1. The ratings of suppliers by all the three decision makers against the various attributes are shown in Table 3.

Then the weighted average of the ratings of the suppliers for all the decision makers is calculated using Eq. (5). The fuzzy decision matrix is prepared using the weighted average of ratings of suppliers against the various attributes. The elements of the fuzzy decision matrix are normalized using Eqs. (8) and (9) to represent the elements on a uniform scale, i.e., on the scale between 0 and 1. Equation (8) is used for the benefit attributes, and Eq. (9) is used for the cost Attributes.

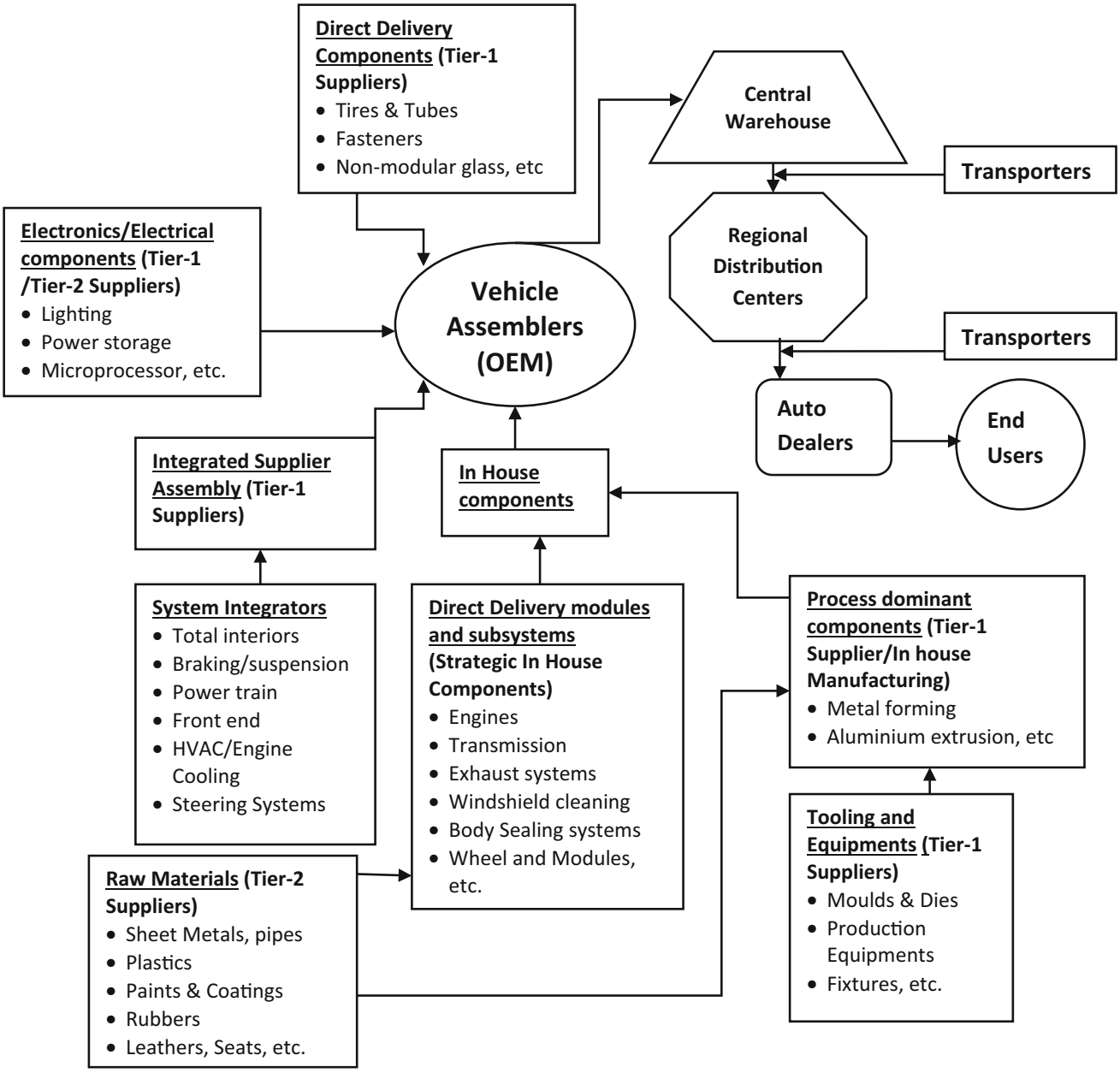

Fig. 2 A structure of automotive supply chain

Table 1 Lingusitic and Fuzzy quantitative scales for importance ratings of criteria and performance ratings of alternatives

Linguistic Scale for the importance of criteria	Linguistic scale for the rating of alternatives	Fuzzy quantitative scale
Very low (VL)	Poor (P)	(1, 1, 3)
Low (L)	Satisfactory (S)	(1, 3, 5)
Medium (M)	Good (G)	(3, 5, 7)
High (H)	Very good (VG)	(5, 7, 9)
Very high (VH)	Excellent (EX)	(7, 9, 9)

Table 2 Importance ratings of Attributes by three decision makers

Attributes	Decision Makers			Fuzzy weight
	D1 (0.4)	D2 (0.35)	D3 (0.25)	
C1 (cost)	VH	H	VH	(2.10, 2.77, 3.00)
C2 (quality)	VH	VH	VH	(2.33, 3.00, 3.00)
C3 (services)	H	H	VH	(1.67, 2.33, 3.00)
C4 (flexibility)	VH	VH	H	(2.17, 2.83, 3.00)
C5 (green practice)	M	M	L	(0.83, 1.50, 2.17)
C6 (environmental management and pollution control)	M	M	H	(1.17, 1.83, 2.50)

Table 3 Ratings of suppliers by three decision makers against the various attributes

Attributes	Decision Makers (weight)	Alternatives							
		A1	A2	A3	A4	A5	A6	A7	A8
C1	D1 (0.4)	H	M	L	H	VL	M	M	H
	D2 (0.35)	H	M	L	M	VL	L	H	M
	D3 (0.25)	M	H	M	M	M	M	H	H
C2	D1 (0.4)	G	EX	G	VG	Ex	G	VG	G
	D2 (0.35)	G	VG	G	VG	EX	G	VG	VG
	D3 (0.25)	VG	VG	VG	G	VG	VG	EX	VG
C3	D1 (0.4)	VG	VG	VG	VG	Ex	VG	VG	VG
	D2 (0.35)	G	G	VG	VG	VG	VG	G	G
	D3 (0.25)	G	G	G	VG	VG	G	VG	G
C4	D1 (0.4)	S	G	VG	G	VG	EX	G	G
	D2 (0.35)	S	VG	G	VG	G	VG	VG	VG
	D3 (0.25)	G	VG	G	VG	G	VG	VG	G
C5	D1 (0.4)	G	VG	S	VG	G	G	VG	VG
	D2 (0.35)	VG	VG	S	VG	VG	G	EX	VG
	D3 (0.25)	G	G	S	EX	VG	S	G	G
C6	D1 (0.4)	G	VG	S	VG	VG	S	VG	VG
	D2 (0.35)	G	VG	S	VG	G	S	VG	G
	D3 (0.25)	S	VG	G	VG	G	G	EX	G

After the preparation of fuzzy normalized matrix, the elements of the fuzzy normalized matrix are multiplied by the weights of corresponding attributes using the Eq. (10). Thus, the weighted normalized matrix is prepared.

From the weighted normalized matrix, the distance between two alternatives such as $\tilde{v}_{A1C1}$ and $\tilde{v}_{A2C1}$ for an attribute C_1, is calculated using Eq. (3). Similarly, distance matrices of all the alternatives for each attribute are prepared using Eqs. (11) and (12).

Now concordance sets of the attributes are prepared for all the attributes based on the distance matrix. The jth attributes will be the elements of the respective concordance sets of attributes, x and y, if $\tilde{v}_{xj} \geq \tilde{v}_{yj}$. A concordance matrix is prepared based on the weights of the attributes of the concordance set. For example, the concordance set between the alternatives A1 and A3 is represented as {2, 5, 6}. The elements for A1 and A3 in the concordance matrix will be the fuzzy sum of the importance weights of attributes 2, 5, and 6.

Now discordance matrix is also prepared from the distance matrix. Considering two alternatives, i.e., suppliers A_x and A_y, the jth attribute is placed in the discordance set assuming that A_xSA_y, where S is the outranking relation, if and only if A_x is preferred to A_y. In the fuzzy environment, the discordance set is formed as $\mathrm{J}^{\mathrm{D}} = \{\mathrm{J}|\tilde{v}_{xj} \leq \tilde{v}_{yj}\}$ where J^{D} is the discordance coalition of the attributes. The discordance matrix is constructed using Eq. (16).

For example, let us consider Suppliers, A1 and A2. In the evaluations of A1 and A2, the distances in terms of each attribute are (0.21, 0), (1.09, 0), (0, 0), (1.39, 0), (0.24, 0), and (0.92, 0), respectively, in the distance matrix, and the all the pair values satisfy the definition of the

discordance set. Therefore, the discordance set includes all the pairs and the corresponding discordance levels by means of Eq. (16) as follows:

$$\frac{\max|(0-1.39)|}{\max(|0-0.21|,|0-1.09|,|0-0|,|0-1.39|,|0-0.24|,|0-0.92|)} = 1.$$

After preparing the concordance and discordance matrices, we prepare the Boolean matrices E and F for the both concordance and discordance matrices, respectively. The values of $\tilde{\bar{C}}$ are calculated as (5.62, 7.68, 8.98) from concordance matrix using Eq. (14). If the individual element of concordance matrix is greater than or equal to $\tilde{\bar{C}}$, then the value of that element in Boolean matrix will be 1, and if the individual element of concordance matrix is less than $\tilde{\bar{C}}$, then the value of that element in Boolean matrix will be 0.

The value of $\bar{D}$ is calculated as (0.7) from discordance matrix using Eq. (17). If the individual element of disconcordance matrix is greater than or equal to $\bar{D}$, then the value of that element in Boolean matrix will be 0, and if the individual element of concordance matrix is less than $\bar{D}$, then the value of that element in Boolean matrix will be 1. Detailed analysis of above-mentioned steps in tabular forms is given in Appendix 2.

Both the Boolean matrices derived from concordance and discordance matrices are aggregated by peer-to-peer multiplication of their elements to capture their simultaneous effects, and the constructed general matrix G thus is presented in Table 4.

Finally, the decision graph is constructed based on the final matrix G as shown in Fig. 3. The decision graph enabled us to identify the ranking order of the Suppliers. The outgoing arc shows the domination of one supplier over another, and the incoming arc shows the domination of other suppliers over the arrow-headed supplier.

A's are shown in this decision graph (Fig. 3):

Table 4 General matrix G

	A1	A2	A3	A4	A5	A6	A7	A8
A1	–	0	0	0	0	0	0	0
A2	1	–	0	0	0	0	0	1
A3	1	0	–	0	0	0	0	0
A4	1	0	0	–	0	0	1	1
A5	1	1	0	1	–	1	0	1
A6	0	0	1	0	0	–	0	0
A7	1	1	0	0	0	0	–	1
A8	0	0	0	0	0	0	0	–

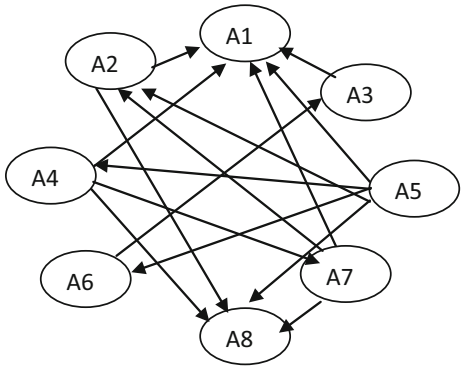

Fig. 3 Decision graph for ranking of suppliers

Supplier A1 is dominated by Suppliers A2, A3, A4, A5, A6, A7, and A8.
Supplier A2 dominates A1 and A8, while it is dominated by Suppliers A5 and A7.
Supplier A3 dominates Supplier A1, while it is dominated by A6.
Supplier A4 dominates Suppliers A1, A7, and A8, while it is dominated by Suppliers A5.
Supplier A5 dominates Suppliers A1, A2, A4, and A8.
Supplier A6 dominates Supplier A3, while it is dominated by A5.
Supplier A7 dominates Suppliers A1, A2, and A8, while it is dominated by Supplier A4.
Supplier A8 is dominated by A2, A4, A5, and A7.

From Fig. 3, It can be observed that A5 is the first-ranked supplier as it dominates the suppliers A1, A2, A4, A6, and A8. Supplier A4 dominates Suppliers, A1, A7, and A8 and Supplier A6 dominates A3. Thus, indirectly, Supplier A5 dominates all the other suppliers and has the first rank. Similarly, Supplier A4 gets the second rank; Supplier A7 gets the third rank. Suppliers A6 and A2 have the fourth and fifth ranks, respectively. Suppliers A1 and A8 are outranked as they do not show domination over any supplier.

This method leads us to the other multicriteria decision-making methods such as AHP, TOPSIS, ANP (Analytic Network Process), etc. where outranking of the poor performers is not possible. These methods provide ranks to all the alternatives or DMUs (Decision-making Units); even poor performers get some ranks. In the ELECTRE method, the decision maker uses concordance and discordance indices to analyze outranking relations among different alternatives and to choose the best alternative. The poor performers are outranked by all the good performers and do not get any rank. Thus, it may help the manager to eliminate and shortlist only comparable performers or suppliers.

There are some limitations of the ELECTRE method. The lowest performances under certain criteria are not

displayed due to the way preferences are incorporated. The outranking method prevents the strengths and weaknesses of the alternatives from being directly identified, nor results and impacts to be verified (Konidari and Mavrakis 2007). ELECTRE has been used in energy, economics, environmental, water management, transportation problems, etc. Like other methods, it also takes the uncertainty and vagueness factors into account.

Conclusions

Nowadays, sustainability has become a major concern for all organizations to survive in global markets. Organizations have become very particular in the procurement of raw materials and selection of suppliers accordingly. Supplier selection is usually done in terms of traditional measures without considering sustainability perspective. This paper has tried to illustrate an approach for supplier selection to ensure environmental sustainability with other factors in the whole value chain. This study considers thirty-eight factors which are grouped into six clusters such as cost, quality, flexibility, service, green practice, environmental management, and pollution control. Suppliers are evaluated and ranked using fuzzy outranking approach.

The fuzzy ELECTRE, a fuzzy outranking approach of supplier evaluation/selection is a very effective multiattribute decision-making tool which is used to outrank the suppliers having poor performance. The uniqueness of this approach is that it eliminates the suppliers performing very poorly, whereas, in other multiattribute decision-making tools, each alternative has some rank. Thus, using the fuzzy ELECTRE method, the decision makers can discard many suppliers who are not performing up to a certain minimum level. By following this approach, decision makers can concentrate only on selected top ranked suppliers for further development as per their business requirement. Moreover, suppliers also know their relative performance with respect to other suppliers. Therefore outranked suppliers can also work on their performance improvement to meet emerging requirements of the market. The findings of the paper will also motivate suppliers to adopt green initiatives in their processes. However, findings may further be validated with some cases and empirically based studies.

Future scope of the research

The future work related to supplier selection may be more focused on green production and green practices such as solid waste, chemical waste, air emission, water waste, energy, environmental friendly materials, redesign of product, staff training, recycling, reuse, remanufacturing, disposal, environmental policy, training, ISO 14001, top management commitment, etc. to improve the environmental sustainability and its relationship with economic and social sustainability. This approach can be applied for selection of sustainable supplier in other sectors also, where the number of suppliers is more and difficult to choose. As it outranks poor performers, therefore buyers would be able to focus on performing suppliers only.

Acknowledgments Authors express sincere thanks to Chief editor of the journal and reviewers for their constructive and valuable suggestions to improve the quality and content of the paper.

References

Ağan Y, Kuzey C, Acar MF, Açıkgöz A (2016) The relationships between corporate social responsibility, environmental supplier development, and firm performance. J Clean Prod 112:1872–1881

Amindoust A, Ahmed S, Saghafinia A, Bahreininejad A (2012) Sustainable supplier selection: a ranking model based on fuzzy inference system. Appl Soft Comput 12(6):1668–1677

Awasthi A, Chauhan SS, Goyal SK (2010) A fuzzy multicriteria approach for evaluating environmental performance of suppliers. Int J Prod Econ 126(2):370–378

Bai C, Sarkis J (2010) Integrating sustainability into supplier selection with gray system and rough set methodologies. Int J Prod Econ 124(1):252–264

Bansal P, Bogner WC (2002) Deciding on ISO 14001: economics, institutions, and context. Long Range Plan 35(3):269–290

Brockhaus S, Kersten W, Knemeyer AM (2013) Where do we go from here? Progressing sustainability implementation efforts across supply chains. J Bus Logist 34:167–182

Buyukozkan G (2012) An integrated fuzzy multi-criteria group decision-making approach for green supplier evaluation. Int J Prod Res 50(11):2892–2909

Büyüközkan G, Ciftci G (2012) A combined fuzzy AHP and fuzzy TOPSIS based strategic analysis of electronic service quality in healthcare industry. Expert Syst Appl 39(3):2341–2354

Chaharsooghi SK, Ashrafi M (2014) Sustainable supplier performance evaluation and selection with neofuzzy TOPSIS method. Int Sch Res Not. doi:10.1155/2014/434168

Chen C-T (2000) Extensions of the TOPSIS for group decision-making under fuzzy environment. Fuzzy Sets Syst 114:1–9

Chen T-Y (2014) An ELECTRE-based outranking method for multiple criteria group decision making using interval type-2 fuzzy sets. Inf Sci 263:1–21

Cruz JM, Matsypura D (2009) Supply chain networks with corporate social responsibility through integrated environmental decision-making. Int J Prod Res 47(3):621–648

Eltayeb TK, Zailani S, Ramayah T (2011) Green supply chain initiatives among certified companies in Malaysia and environmental sustainability: investigating the outcomes. Resour Conserv Recycl 55(5):495–506

Fu X, Zhu Q, Sarkis J (2012) Evaluating green supplier development programs at a telecommunications systems provider. Int J Prod Econ 140(1):357–367

Ghodsypour SH, O'Brien C (2001) The total cost of logistics in supplier selection, under conditions of multiple sourcing, multiple criteria and capacity constraint. Int J Prod Econ 73(1):15–27

Govindan K, Azevedo SG, Carvalho H, Machado VC (2015) Lean, green and resilient practices influence on supply chain

performance: interpretive structural modeling approach. Int J Environ Sci Technol 12(1):15–34
Gunasekaran A, Gallear D (2012) Special issue on sustainable development of manufacturing and services. Int J Prod Econ 140(1):1–6
Gunasekaran A, Lai KH, Cheng TCE (2008) Responsive supply chain: a competitive strategy in a networked economy. Omega Int J Manag Sci 36(4):549–564
Gunther E, Scheibe L (2006) The hurdle analysis. A self-evaluation tool for municipalities to identify, analyze and overcome hurdles to green procurement. Corp Soc Responsib Environ Manag 13(2):61–77
Hamming RW (1950) Error detecting and error correcting codes. Bell Syst Tech J 26:147–160
Handfield R, Walton SV, Sroufe R, Melnyk SA (2002) Applying environmental criteria to supplier assessment: a study in the application of the Analytical Hierarchy Process. Eur J Oper Res 141(1):70–87
Hatami-Marbini A, Tavana M (2011) An extension of the ELECTRE I method for group decision-making under a fuzzy environment. Omega Int J Manag Sci 39:373–386
Hatami-Marbini A, Tavana M, Moradi M, Kangi F (2013) A fuzzy group Electre method for safety and health assessment in hazardous waste recycling facilities. Saf Sci 51:414–426
Hsu CW, Kuo TC, Chen SH, Hu AH (2013) Using DEMATEL to develop a carbon management model of supplier selection in green supply chain management. J Clean Prod 56(1):164–172
Kahraman C, Cebeci U, Ruan D (2004) Multi-attribute comparison of catering service companies using fuzzy AHP: the case of Turkey. Int J Prod Econ 87:171–184
Ke Q, Zhang H, Liu G, Li B (2011) Remanufacturing engineering literature overview and future research needs. In: glocalized solutions for sustainability in manufacturing, pp. 437–442
Konidari P, Mavrakis D (2007) A multi-criteria evaluation method for climate change mitigation policy instruments. Energy Policy 35(12):6235–6257
Kumar P, Shankar R, Yadav SS (2008) Flexibility in global supply chain: modeling the enablers. J Model Manag 3(3):277–297
Kuo RJ, Wang YC, Tien FC (2010) Integration of artificial neural network and MADA methods for green supplier selection. J Clean Prod 18(12):1161–1170
Kuo TC, Hsu C-W, Li J-Y (2015) Developing a green supplier selection model by using the DANP with VIKOR. Sustainability 7:1661–1689
Lee AHI, Kang H-Y, Hsu C-F, Hung H-C (2009) A green supplier selection model for high-tech industry. Expert Syst Appl 36(4):7917–7927
Li D-F, Yang J-B (2004) Fuzzy linear programming technique for multiattribute group decision making in fuzzy environments. Inf Sci 158:263–275
Lin RJ (2013) Using fuzzy DEMATEL to evaluate the green supply chain management practices. J Clean Prod 40:32–39
Liu P, Zhang X (2011) Research on the supplier selection of a supply chain based on entropy weight and improved ELECTRE-III method. Int J Prod Res 49(3):637–646
Mangla SK, Kumar P, Barua MK (2014) Flexible decision approach foranalysing performance of sustainable supply chains under risks/uncertainty. Glob J Flex Syst Manag 15(2):113–130
Manning L, Baines R, Chadd S (2006) Quality assurance models in the food supply chain. Br Food J 108(2):91–104
Mansi M (2015) Sustainable procurement disclosure practices in central public sector enterprises: evidence from India. J Purch Supply Manag 21(2):125–137
Kardaras D, Mentzas, G (1997) Using fuzzy cognitive maps to model and analyze business performance assessment. Published in Chen J, Mital A (eds). Advances in Industrial Engineering Applications and Practice II, pp. 63–68
Murphy PR, Poist RF (2000) Green logistics strategies: an analysis of usage patterns. Transp J 40(2):5–16
Nawrocka D, Brorson T, Lindhqvist T (2009) ISO 14001 in environmental supply chain practices. J Clean Prod 17(16):1435–1443
Ongkunaruk P, Piyakarn C (2011) Logistics cost structure for mangosteen farmers in Thailand. Systems Engineering Procedia 2:40–48
Petroni A, Braglia M (2000) Vendor selection using principal component analysis, vendor selection using principal component analysis. J Supply Chain Manag 36(2):63–69
Ravishankara AR, Daniel JS, Portmann RW (2009) Nitrous Oxide (N_2O): the dominant ozone-depleting substance emitted in the 21st century. Science 326(5949):123–125
Sancha C, Longoni A, Giménez C (2015) Sustainable supplier development practices: drivers and enablers in a global context. J Purch Supply Manag 21(2):95–102
Sevkli M (2010) An application of the fuzzy ELECTRE method for supplier selection. Int J Prod Res 48(12):3393–3405
Shaik M, Abdul-Kader W (2011) Green supplier selection generic framework: a multi-attribute utility theory approach. Int J Sustain Eng 4(1):37–56
Sharfman M, Shaft T, Anex R (2009) The road to cooperative supply-chain environmental management: trust and uncertainty among proactive firms. Bus Strategy Environ 18(1):1–13
Shaw K, Shankar R, Yadav SS, Thakur LS (2012) Supplier selection using fuzzy AHP and fuzzy multi-objective linear programming for developing low carbon supply chain. Expert Syst Appl 39(9):8182–8192
Tsui C-W, Tzeng G-H, Wen U-P (2015) A hybrid MCD M approach for improving the performance of green suppliers in the TFT-LCD industry. Int J Prod Res 53(21):6436–6454
Wittneben Bettina BF, Kiyar D (2009) Climate change basics for managers. Manag Decis 47(7):1122–1132
Xu J, Shen F (2014) A new outranking choice method for group decision making under Atanassov's interval-valued intuitionistic fuzzy environment. Knowl Based Syst 70:177–188
Yanqing X, Mingsheng X (2012) A 3E model on energy consumption, environment pollution and economic growth an empirical research based on panel data. Energy Proced 16:2011–2018
Zadeh LA (1965) Fuzzy sets. Inform Control 8:338–353
Zhang G, Zhao Z (2012) Green packaging management of logistics enterprises. Physics Proced 24:900–905
Zhu Q, Sarkis J (2006) An inter-sectoral comparison of green supply chain management in China: drivers and practices. J Clean Prod 14(5):472–486
Zhu Q, Sarkis J (2007) The moderating effects of institutional pressures on emergent green supply chain practices and performance. Int J Prod Res 45(18–19):4333–4355
Zimmerman HJ (1991) Fuzzy set theory and its applications, 2nd ed. Kluwer Academic Publishers, Boston, MA

IARJSET
ISSN (Online) 2393-8021
ISSN (Print) 2394-1588
International Advanced Research Journal in Science, Engineering and Technology
ISO 3297:2007 Certified
Vol. 3, Issue 7, July 2016

Theoretical Gain in Solar Energy for Different Sun Tracking Systems in Delhi

Kanav Vij[1], Rajesh Kumar[2]

Student, Mechanical Production & Industrial and Automotive Engineering Department,

Delhi Technological University, Delhi, India[1]

Assistant Professor, Mechanical Production & Industrial and Automotive Engineering Department,

Delhi Technological University, Delhi, India[2]

Abstract: Solar energy is now one of a major source of energy, which is clean and environmental friendly. The challenge arises to convert solar energy into useful energy using devices. These devices have low conversion efficiency. The seasonal and diurnal movement of earth affects the radiation falling on solar collectors. Sun tracking devices move these collectors to compensate the motion of the earth and maintain the best orientation with respect to sun. In this paper, we have discussed about different tracking systems and their theoretical gain as compared to fixed horizontal system by considering a location as Delhi (ϕ=28.6^o North).

Keywords: solar energy, sun tracking, sunpath, azimuth, gain, cosine.

I. INTRODUCTION

Energy has been universally recognized as one of the most important inputs for economic growth and human development. There is a strong two-way relationship between economic development and energy consumption. On one hand, growth of an economy, with its global competitiveness, hinges on the availability of cost-effective and environmentally benign energy sources, and on the other hand, the level of economic development has been observed to be reliant on the energy demand. One such source of energy can help significantly to meet this surging demand, viz. solar energy. Solar energy is radiant light and heat from the sun. Source of the radiant light and heat energy of the sun is nuclear fusion reaction. The energy due to nuclear fusion reaction taking place at the sun reaches earth by radiative heat transfer. Amount of energy reaching earth is around **1367 W/m^2** (Solar Constant). Solar radiation is energy in the form of electromagnetic radiation which are characterized by wavelengths and frequencies. Use of solar energy requires devices to extract energy and use it for different applications. These devices are also known as solar collectors. Alternative renewable energy sources such as sun energy can be substituted for exceeding human energy needs. Covering 0.16% of the land on earth with 10% efficient solar conversion systems would provide 20 TW of power, nearly twice the world's consumption rate of fossil energy [1].

A. Nomenclature

β = inclination of plane
ϕ = Latitude position of site
δ = Declination of earth
γ = surface azimuth angle of plane
γ_s = solar azimuth angle
ω = hour angle
θ = angle of incidence
θ_z= zenith angle
α = solar altitude angle
I_{rr} = irradiation received
C = cosine factor

II. TRACKING

Searching for clean energy sources is one of the biggest challenges for society. Even availability of energy is not sufficient, but, to make the available energy sustainable is major challenge. Solar Energy, one of alternative renewable energy source, can substitute the human energy needs. The potential for solar energy is enormous, with covering just 0.16% of land on earth and using 10% efficient solar energy conversion device, 20TW of power can be generated, which is nearly double the power required by the world [2]. But, solar energy falling on a surface is not constant because of movement of the sun in sky.

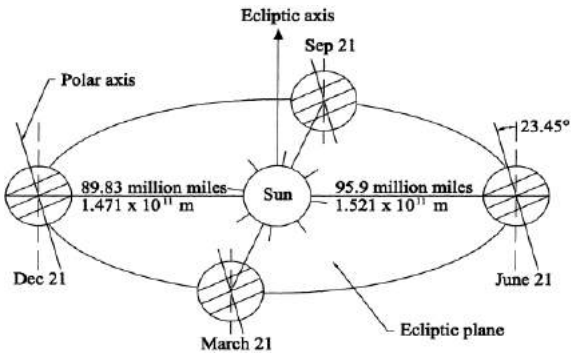

Figure 1: Motion of Earth about sun

IARJSET
ISSN (Online) 2393-8021
ISSN (Print) 2394-1588
International Advanced Research Journal in Science, Engineering and Technology
ISO 3297:2007 Certified
Vol. 3, Issue 7, July 2016

The earth revolves around the sun, the orbit of revolution is elliptical in shape, with sun at one of the foci. The time taken by the earth to complete one revolution of its orbit defines a year. The plane in which earth's orbit is part of, is known as elliptic plane. With revolution around the sun, earth is also rotating about its own axis. Earth's axis is tilted by 23.45^o to the axis of elliptic plane. The angle made by; a line joining the centers of earth and sun and the equatorial plane of earth is called **declination angle (δ).**

As shown in Figure 1, declination angle changes from -23.45^o on December 21st (also known as winter solstice) to $+23.45^o$ on June 21st (also known as summer solstice). Declination angle is zero on March 21st (venal) and September 21st (autumnal), these days are known as equinoxes. As the earth rotates about its own axis, the instantaneous position of sun can be described by **hour angle (ω)**. Hour angle is angle between meridian passing through sun and the meridian of location or site of study. Hour angle is zero when meridian passing through sun is same as that of the site, this time is known as solar noon. Hour angle is negative before solar noon viz. when sun is rising in the East and it is positive after solar noon, in the west. Rate of change of hour angle (ω) is 15^o per hour.

To define any location of site on earth's surface, one needs two parameters, those are **latitude (ϕ)** and longitude of that location. Latitude is a geographic coordinate defined by an angle between a radial line made by joining the point of site and the centre of earth and plane of equator. Lines of constant latitude, also known as parallels run from east to west. The range of latitude is 0^o for equator, $+90^o$ for North Pole and -90^o for South Pole. Longitudes are meridian lines running from the North Pole to the South Pole. The intersection of longitudes and latitudes will give location of any site on earth's surface. Latitude have importance to understand the movement of sun.

III. ANGLES FOR TRACKING SURFACE

There are several angles to describe position of the sun relative to any plane situated at any point on surface of the earth. The plane can be fixed or moving (in case of tracking).

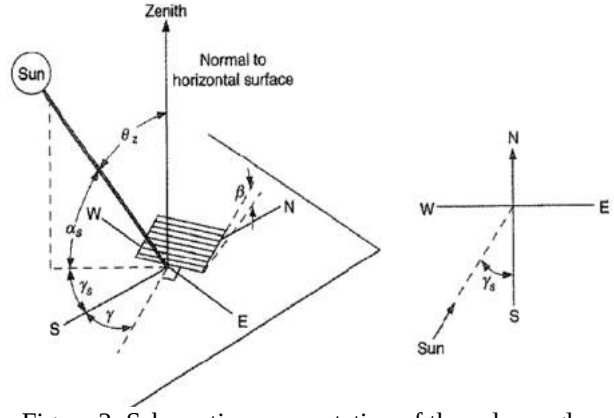

Figure 2: Schematic representation of the solar angles

These angles will help us understand the motion of sun which will give direction of beam (or direct) radiation. Beam radiation have major role in working of any solar technology and without beam radiation no concentrated solar technology will work. For a tracking system, sun direction is necessary because surface has track the sun directly.

Following are some of important angles to describe sun's position with respect to any plane on earth's surface:

Figure 2 represents few angles to describe position of sun with respect to any plane or surface.

ϕ = **Latitude**, Location of a point on a surface, described by angle. $-90^o \le \phi \le 90^o$.

δ = **Declination**, The angle made by; a line joining the centers of earth and sun and the equatorial plane of earth, $-23.45^o \le \delta \le 23.45^o$.

β = **Slope of surface**, it is the angle between surface plane and the horizontal surface at that location. $0^o \le \beta \le 180^o$

γ = **Surface azimuth angle**, made by projection of normal of plane on horizontal surface and local meridian. Ranges from $-180^o \le \gamma \le 180^o$ with south as zero, east negative and west positive.

ω = **Hour angle** is angle between meridian passing through sun and the meridian of location or site of study

θ = **Incident angle**, angle between normal of surface and beam radiation.

θ_z = **Zenith angle**, angle made by a vertical line at location and the beam radiation.

α_s = **Sun Altitude angle**, angle between beam radiation and horizontal surface

γ_s = **Sun azimuth angle**, it is the angle made by local meridian and projection of beam radiation on a horizontal plane or deviation of the projection from south direction. East is negative and west is positive.

The sun motion is divided in two directions; first is **Azimuth motion** and **Altitude Motion**. In the following relationships, we will know the details of each azimuth and altitude motion.

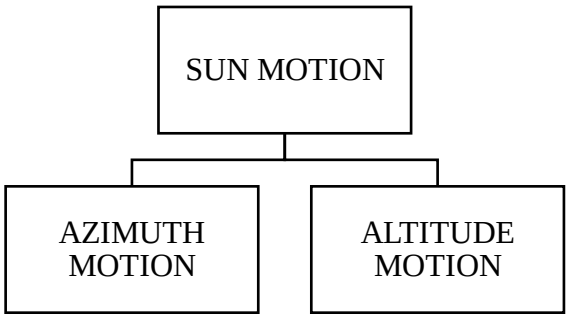

IARJSET
ISSN (Online) 2393-8021
ISSN (Print) 2394-1588
International Advanced Research Journal in Science, Engineering and Technology
ISO 3297:2007 Certified
Vol. 3, Issue 7, July 2016

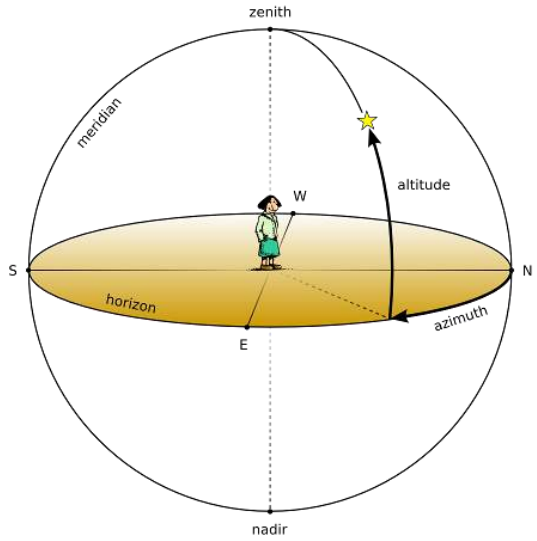

Figure 3: azimuth and altitude for a coordinate on earth.

A. Important Relations

We know that earth revolves around the sun, on its elliptic orbit. But to study angles, we assume that earth is stationary and relatively sun moves. Before proceeding with the study, there are few trigonometric relations relating earth's movement with respect to sun. These relations are important because sun's position changes with respect to a point located on earth and therefore changes energy input to the collector surface [3]. Declination angle can be found from the following relationship:

$$\sin\delta = \sin(23.45)\sin[360\,\frac{(284+n)}{365}] \qquad (A)$$

Where n is the day number during a year with January 1 being n=1

$$\cos\theta = \sin\delta\sin\phi\cos\beta - \sin\delta\cos\phi\sin\beta\cos\gamma + \cos\delta\cos\phi\cos\beta\cos\omega + \cos\delta\sin\phi\sin\beta\cos\gamma\cos\omega + \cos\delta\sin\beta\sin\gamma\sin\omega \qquad (1)$$

From equation (1), we can see that, incident angle (θ) is a function of day (n), on which we are observing, location (ϕ) of site, angles of plane (β and γ) and hour angle (ω). Hour angle changes at 15^{o}/hr. For a particular day, sunrise and sunset time is determined as:

cos ω = - (tan ϕ tan δ)
(sunrise)
cos ω = (tan ϕ tan δ)
(sunset)

Hour angle also helps to determine the length of day. At solar noon, hour angle is zero.

B. Variation of Solar Altitude and Solar Azimuth Angle With Respect to Hour Angle

Solar elevation and solar azimuth angle give us information about the position of sun in sky as viewed from a point on earth. To track sun we should know these angles. These angles act as guides for tracking systems.

$$\sin\alpha = \cos\phi\cos\delta\cos\omega + \sin\phi\sin\delta \qquad (2)$$

$$\cos\gamma_s = \frac{\sin\alpha\sin\phi - \sin\delta}{\cos\alpha\cos\phi} \qquad (3)$$

C. Energy estimation on a surface

Cosine Factor (C)

$$= \frac{\text{Direct radiation received perpendicular to the surface (D)}}{\text{Incoming Radiation (Irr)}}$$

Energy for small fraction of time

$$= (\text{Cosine factor}) * (\text{incoming direct radiation from sun}) * (\text{small interval of time})$$

$$\text{Insolation} = \int_{t1}^{t2} C.\,Irr.\,dt \qquad (4)$$

Where t1 and t2 are sunrise and sunset time, dt is small change in time. This small change in time is proportional to hour angle and t1 and t2 can be written as in terms of hour angle. Assuming irradiation (I_{rr}) to be constant. After integration we get the value of insolation for a particular day.

Therefore, equation (4) can be written as:

$$\text{Insolation} = \int_{\omega1}^{\omega2} C.\,Irr.\,d\omega$$

$$= Irr\int_{\omega1}^{\omega2} C.\,d\omega$$

$\int_{\omega1}^{\omega2} C.\,d\omega$ Gives the value of equivalent sunshine hours for a day.

Direct radiation (D) collected by any surface is given by the product of cosine factor (C) and incoming solar radiations (I_{rr}). The value calculated will be a theoretical maximum value for a particular day. Practical value of radiation received by a surface depends on various atmospheric conditions. To know the benefit of using tracking system, we will compare theoretical values for each tracking arrangements.

IV. SUNPATH

Sun path is a path followed by sun in sky, with hourly and seasonal variations in its position. As earth rotates the sun apparently travels in sky and with revolution of earth around sun, seasonal variations occur. A diagram made of curve showing sun's position i.e. solar azimuth and solar altitude, is known as sunpath diagram. Sunpath diagram is also known as solar position plot. Sun path finder is a device which is used to trace these curves, however, these curves can be plotted on MATLAB or Excel from the relations discussed above. The position of sun is an important factor to evaluate heat gain for a building and performance analysis of solar energy technologies. Knowledge of sunpath and local climatic conditions are necessary inputs to make economic decisions for any solar energy technology. Sunpath is not

IARJSET
ISSN (Online) 2393-8021
ISSN (Print) 2394-1588
International Advanced Research Journal in Science, Engineering and Technology
ISO 3297:2007 Certified
Vol. 3, Issue 7, July 2016

just necessary for tracking systems, it is also necessary for fixed systems for which shadow analysis is crucial [4].
Sunpath acts as the guiding path for the tracker. Therefore, solar tracker should follow the sunpath in order to receive maximum radiation. The actual movement for solar tracker is different for its application. For example, solar tracker used for photovoltaics follows sunpath completely; but for heliostat mirror, the tracker follows different path which depends on its position in the field and height of the tower. Due to this fact, it becomes necessary to use tracking mechanism for heliostats. Sunpath diagrams are also used in passive air-conditioning design, to reduce the direct radiation by the help of shades. Sunpath diagram for each can be drawn in MATLAB, using relations (1) and (2). A script file was created to draw sunpath for a particular day. **Error! Reference source not found.** Shows the sunpath for Delhi (ϕ=28.6^o), for summer and winter solstice, i.e. 21st of June and 21st of December.

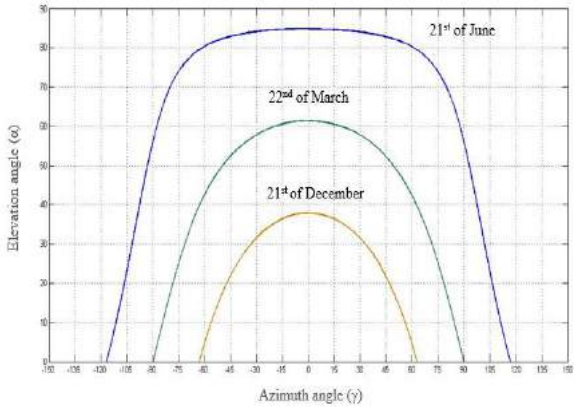

Figure 4: Sunpath diagram for Delhi (ϕ = 28.6^o)

V. SUN-TRACKING DRIVING METHODS

Solar trackers require external driving force to track the sun. There are three driving methods used to track sun:

A. Passive Trackers
Passive solar trackers work on the principle of thermal expansion. The driving material could be a gas or a metal. When gases are heated, the pressure increases and this rise in pressure drives the solar tracker. Two gas cylinders are placed against each other, when sunlight falls on any one of the cylinder, the thermal energy in solar radiation raises the temperature of the gas, a pressure difference is created and tracker moves with the path of sun [5]. Shape Memory alloys are sensitive to temperature, when they are heated they form different shape. This sensitive material can also be used to drive tracking system. Passive trackers do not require external power source to operate, but, their only drawback is that they are sensitive to irradiation, which always varies due to local weather conditions such as clouds.

B. Active Trackers
Active sun trackers are categorized as optical sensor and microprocessor based, chronological data based and an auxiliary bifacial solar cell based systems. Active trackers follow the sun actively with the help of low speed motors (called actuators). The actuators can be guided by a optical sensor or by a program based on dates (chronological inputs). Active system require an external source of power to operate them. Advantage of active trackers over passive trackers is that, these are very accurate, their working does not depend on weather conditions, and their structure is solid.

VI. TYPES OF SUN TRACKING

We have seen that sun uniformly travels in sky, or it changes its apparent position with respect to earth. This change affects the energy captured by any solar energy device (cosine effect). To minimize this loss of energy, solar energy collectors have an integrated arrangement to track the sun's apparent position. The principle to maximize beam radiation is by minimizing the angle of incidence (θ). These integrated devices are called sun trackers. Though these tracking arrangements have some drawbacks, such as, require external power to drive the tracking mechanism, require maintenance. But, the benefit of using these systems is economical. In this section, we will understand different types of tracking systems classified by their motions, also we will know the benefit of using each tracking systems.

A. Single Axis Tracking
In this type of tracking systems, the orientation of the collector (surface) is changed about a single axis, therefore, in this system, only one parameter is required to control movement of the collector to get maximum incident radiation. These systems are widely used with large photovoltaic plants and concentrated collectors. Concentrated solar thermal technology; linear Fresnel collector and parabolic trough collectors use single axis tracking systems. From relations (2) and (3) it can be seen that there are two sun angles viz. sun azimuth angle and sun altitude angle, so we can control any one angle. Based on the angle controlled, single axis tracking is divided in two categories [6]:

1.) North South Tracking:

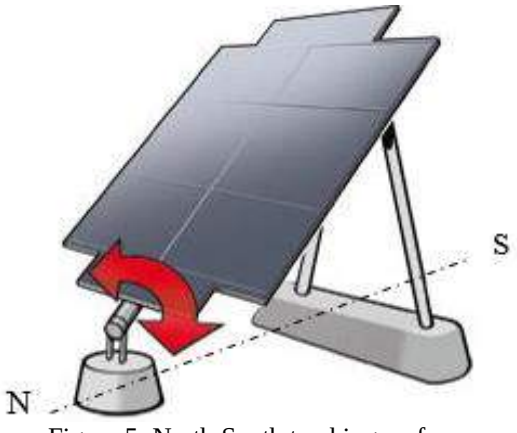

Figure 5: North South tracking surface.

IARJSET
ISSN (Online) 2393-8021
ISSN (Print) 2394-1588
International Advanced Research Journal in Science, Engineering and Technology
ISO 3297:2007 Certified
Vol. 3, Issue 7, July 2016

In this type of single axis tracking system, the movement of collecting surface is adjusted by rotating the surface about an axis which is drawn from North to South of that location or the normal drawn to collector surface is rotated about a NS line, however the axis can be parallel or inclined to the N-S axis. Sun azimuth angle (γ_s) is tracked continuously for a day to get the maximum input of direct solar radiations. Cosine factor for NS tracking surface is given by the following relationship:

$$C = \sqrt{(\cos^2 \theta z + \cos^2 \delta \sin^2 \omega)} \qquad (5)$$

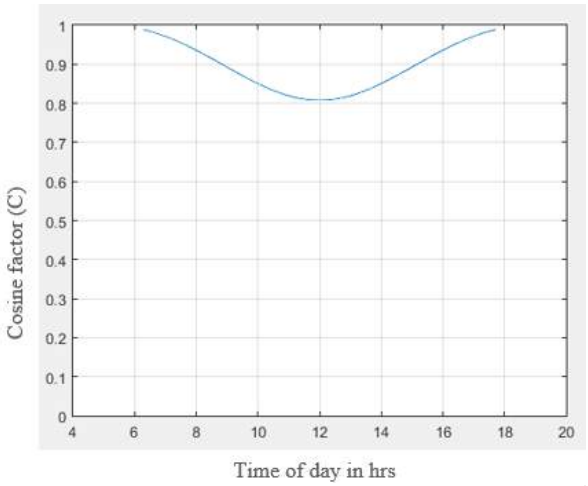

Figure 6: cosine curve for N-S tracked surface ($\phi = 28.6^o$)

A curve (figure 6) of equation (5) is drawn in MATLAB to show an example of cosine factor, location selected is Delhi (ϕ=28.6^o), date is 10th of October. Area under this curve will give us equivalent sunshine hours for that day. Area can also be found by integrating the equation with respect to hour angle. By evaluating the curve for each day and calculating the sunshine hours for each day, for a complete year we add all the values for different days, therefore, we get total equivalent sunshine hours =3972 hrs.

2.) East West Tracking:
In this type of tracking system, the movement of collecting surface is adjusted by rotating the surface about an axis which is drawn from East to West of that location. The normal of plane rotates about E-W axis. Altitude angle (α) is tracked to get maximum input.

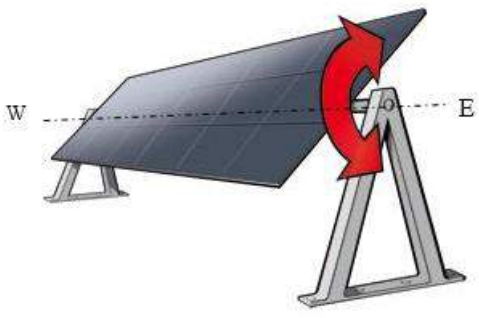

Figure 7: East West tracking surface.

The adjustment can be made in two ways:

a. Daily single adjustment:
The collector surface is rotated about horizontal east-west axis with a single daily adjustment so that the beam radiation is normal to the surface at solar noon each day. Cosine factor for EW single daily tracking surface is given by the following relationship:

$$C = \sin^2 \delta + \cos^2 \delta \cos \omega \qquad (6)$$

b. Daily continuous adjustment:
The collector surface is rotated about horizontal east-west axis with continuous adjustment. Cosine factor for EW daily continuous tracking surface is given by the following relationship:

$$C = (1 - \cos^2 \delta \sin^2 \omega)^{1/2} \qquad (7)$$

A plot of curve (7) for date 10th October for Delhi (ϕ=28.6^o) is shown in figure 8.

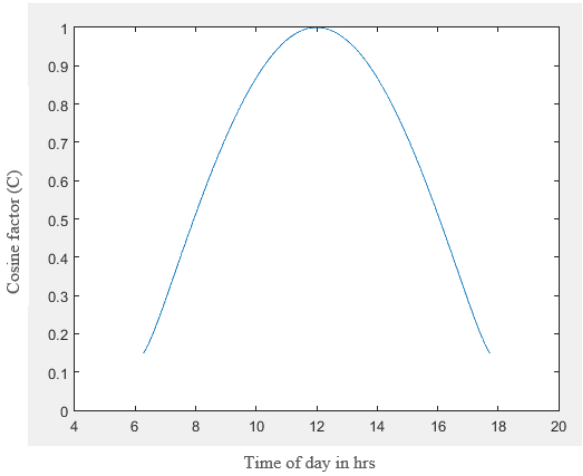

Figure 8: Cosine curve for E-W tracked surface (ϕ=28.6^o)

Area under this curve will give us equivalent sunshine hours for that day. Area can also be calculated by integrating the equation with respect to hour angle. By plotting the curve for each day and calculating the sunshine hours for each day, for a complete year we add all the values for different days, therefore, we get total equivalent sunshine hours =3016.3 hrs.

B. Two Axis Tracking:
Two axis tracking system involves tracking the sun's movement completely. The tracking system has to track both the motion of sun viz. Azimuth motion and altitude motion. For this tracking, two actuators are used to control the motion of system in two axis. Therefore, this system is also known as 2 degree of freedom tracking. For these systems, cosine factor is always unity.

$$C = 1$$

For this type of tracking we get a straight line ideally and maximum sunshine hours is equal to sun hours for that particular day. For a complete year we add all the values

IARJSET
ISSN (Online) 2393-8021
ISSN (Print) 2394-1588
International Advanced Research Journal in Science, Engineering and Technology
ISO 3297:2007 Certified
Vol. 3, Issue 7, July 2016

for different days and we get total sunshine hours= 4380 hrs.

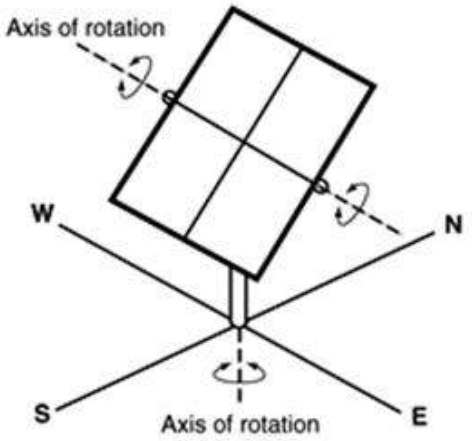

Figure 9: dual axis tracking

VII. GAIN IN ENERGY BY USING TRACKING SYSTEMS (A CASE STUDY OF DELHI)

A case study is done for Delhi (latitude location 28.6° north). A comparison of different tracking systems stated above is done graphically to know the advantage of tracking systems over fixed mounted systems. This comparison study does not include any losses due to atmosphere reflection and absorption nor loss due to weather conditions. Therefore, this study is just ideal case study and compare the maximum availability of sun for a particular location with different system arrangements (tracking systems). Figure 10, shows a plot made by evaluating ideal energy output for each day, for each tracking system with equivalent sunshine hours on y-axis and months on x-axis.

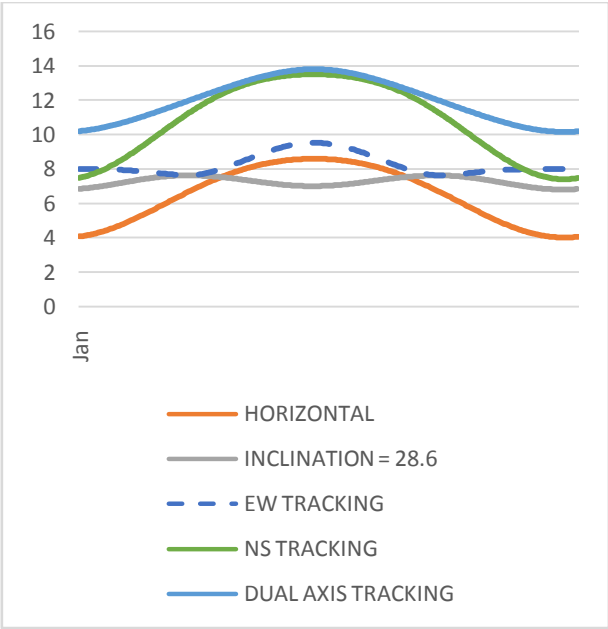

Figure 10: A comparison of output of different tracking systems for Delhi (ϕ=28.6)

VIII. CONCLUSION

We have discussed about different tracking situations for a particular location (Delhi, ϕ=28.6°). The study done is for ideal case in which no weather conditions are considered. We have calculated equivalent sunshine hours for a year for each tracking arrangement. For dual axis tracking, equivalent sunshine hours were equal to 4380, therefore, maximum capacity factor is 50%. For single axis, N-S tracking arrangement, equivalent sunshine hours is 3972, capacity factor is 45.3%. For single axis, E-W tracking arrangement, Equivalent sunshine hours is 3016.3, capacity factor is 34.4%. For a plane inclined at an angle equal to latitude (ϕ=28.6°), equivalent sunshine hours are 2656.8, capacity factor is 30.3%. For a horizontal plane, equivalent sunshine hours are 2379, capacity factor is 27.1%. Therefore, we can say by comparing each arrangement with horizontal arrangement; dual axis arrangement has 84.11% more output; N-S tracking arrangement has 67% more output; E-W tracking has 26.7% more output. These calculations are purely for ideal case. The output for solar energy largely depends on location (ϕ) and local weather conditions.

REFERENCES

[1]. Liu, L., Xiaoqing, H., Liu, C., & Wang, J. (2013). The influence factors analysis of the best orientation relative to the sun for dual-axis sun tracking system. Journal of Vibration and Control, 1077546313488988.
[2]. Mousazadeh, H., Keyhani, A., Javadi, A., Mobli, H., Abrinia, K., & Sharifi, A. (2009). A review of principle and sun-tracking methods for maximizing solar systems output. Renewable and sustainable energy reviews, 13(8), 1800-1818.
[3]. Goswami, D. Y., Kreith, F., & Kreider, J. F. (2000). Principles of solar engineering. CRC Press.
[4]. Khavrus, V., & Shelevytsky, I. (2010). Introduction to solar motion geometry on the basis of a simple model. Physics Education, 45(6), 641.
[5]. Passive Solar Tracking System. Parmar, Naraendrasinh J., Parmar, Ankit .N. and Gautam, Vinod .S. 1, s.l. : International Journal of Emerging Technology and Advanced Engineering, 2015, Vol. 5. ISSN 2250-2459.
[6]. Duffie, J. A., & Beckman, W. A. (1980). Solar engineering of thermal processes(Vol. 3). New York etc.: Wiley.

Volume 4, Issue 1 (2016) 129-135 ISSN 2347 - 3258
International Journal of Advance Research and Innovation

Thermodynamic (Energy-Exergy) Analysis of Solar Assisted Power-Cooling Combined Generation Systems

Kaushalendra Kumar Dubey, R. S. Mishra *
Department of Mechanical Engineering, Delhi Technological University, Delhi, India

Article Info
Article history:
Received 20 January 2016
Received in revised form
10 February 2016
Accepted 28 February 2016
Available online 15 March 2016

Keywords
Energy-Exergy Analysis,
Cogeneration,
Combined Power Cycle,
Organic Rankine Cycle

Abstract
Novel concept to produce power and cooling with the energy contained in low-temperature (< 200° C), thermal resources is presented in this paper . These resources can be obtained from concentrating solar thermal energy, and from waste heat sources. The concept uses thermal energy in a low-temperature boiler to partially boil an organic type working fluid mixture. This produces rich vapor that drives an expander. The expander's output is mechanical power; however, under certain operating conditions its exhaust can be cold enough to use for cooling. An analytical study is identified expander efficiency, expander inlet conditions for determining exhaust temperature, consideration of the operating conditions of integrated solar combined power /cooling cycle . The present research provides simulated performance for improving system efficiency.

1. Introduction

Nowadays due to 40% predicted increase in energy consumption of the world, more environmental concerns and less dependency on fossil fuels, demand for sophisticated power supply options is greatly increased. Environmental concerns will be in form of global warming, acid rains, air, water and soil pollution, ozone depletion, forest devastation and radioactive substances emissions. Utilizing waste heats along with attempts to derive energy out of renewable resources as low grade thermal heat sources have motivated the use of advanced energy recovery systems. The present research issue provides new concept and development of low GWP and ODP refrigerants based utilities for an industrial application. The simulated performance is discussed and relate to improving future modeling and system design efforts.

Cogeneration or combined heat and power (CHP) is the use of a heat engine or power station to generate electricity and useful heat at the same time. .Cogeneration is a thermodynamically efficient use of fuel. In separate production of electricity, some energy must be discarded as waste heat, but in cogeneration this thermal energy is put to use. All thermal power plants emit heat during electricity, which can be released into the natural environment through cooling towers, flue gas, or by other means. By-product heat at moderate temperatures (100–180 °C, 212–356 °F) can also be used in absorption refrigerators for cooling. Requirements of cogeneration may be met in many ways ranging from steam and gas turbines to fuel cells and Sterling engines.

Maidment and Tozer [1] have reviewed a number of combined energy production plants operating in supermarkets. They analyzed different schemes of combined energy production including different cooling and engine technologies.

The thermodynamic cycle of the basic combined cycle consists of two power plant cycles shown in figure of combined power cycle. One is the Joule or Brayton cycle which is a gas turbine cycle and the other is Rankine cycle which is a steam turbine cycle. The cycle 1-2-3-4-1 which is the gas turbine power plant cycle is the topping cycle. It depicts the heat and work transfer process taking place in high temperature region. As shown in Fig-1.

The cycle a-b-c-d-e-f-a which is the Rankine steam cycle takes place at a low temperature and is known as the bottoming cycle. Transfer of heat energy from high temperature exhaust gas to water and steam takes place by a waste heat recovery boiler in the bottoming cycle. During the constant pressure process 4-1 the exhaust gases in the gas turbine reject heat. The feed water, wet and super heated steam absorb some of this heat in the process a-b, b-c and c-d. Cogeneration systems are normally classified according to the sequence of energy use and the operating schemes adopted. A cogeneration system can be classified as either a topping or a bottoming cycle on the basis of the sequence of energy use. In a topping cycle, the fuel supplied is used to first produce power and then thermal energy, which is the by-product of the cycle and is used to satisfy process heat or other thermal requirements. Topping cycle cogeneration is widely used and is the most popular method of cogeneration.

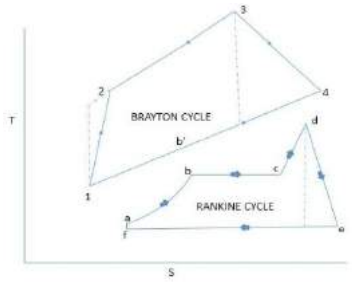

Fig: 1. Combined Power Cycle [1]

2. Topping Cycle

The four types of topping cycle cogeneration systems are briefly explained.

A gas turbine or diesel engine producing electrical or mechanical power followed by a heat recovery boiler to

Corresponding Author,
E-mail address: professor_rsmishra@yahoo.co.in
All rights reserved: http://www.ijari.org

create steam to drive a secondary steam turbine. This is called a combined-cycle topping system.

The second type of system burns fuel (any type) to produce high-pressure steam that then passes through a steam turbine to produce power with the exhaust provides low-pressure process steam. This is a steam-turbine topping system.

A third type employs heat recovery from an engine exhaust and/or jacket cooling system flowing to a heat recovery boiler, where it is converted to process steam / hot water for further use.

The fourth type is a gas-turbine topping system. A natural gas turbine drives a generator. The exhaust gas goes to a heat recovery boiler that makes process steam and process heat.

3. Bottoming Cycle

In a bottoming cycle, the primary fuel produces high temperature thermal energy and the heat rejected from the process is used to generate power through a recovery boiler and a turbine generator. Bottoming cycles are suitable for manufacturing processes that require heat at high temperature in furnaces and kilns, and reject heat at significantly high temperatures. Typical areas of application include cement, steel, ceramic, gas and petrochemical industries. Bottoming cycle plants are much less common than topping cycle plants. The waste gases coming out of the furnace is utilized in a boiler to generate steam, which drives the turbine to produce electricity

4. Tri-generation

Tri-generation technology is a technology that can provide simultaneously three forms of output energy; electrical power, heating and cooling. Tri-generation is also known as CCHP (Combined Cooling, Heating and Power) or CHRP (Combined Heating, Refrigeration and Power). In essence, tri-generation systems are CHP (Combined Heat and Power) or co-generation systems, integrated with a thermally driven refrigeration system to provide cooling as well as electrical power and heating. CHP systems consist of a power system which can be an internal combustion engine driven by a fossil fuel or a biofuel, an external combustion engine or other thermally or chemically driven systems coupled to a generator which produces electricity. A heat recovery system recovers heat from the power system and exhaust gases to be used for heating applications. Effective operation of CHP systems requires maximum utilization of both electrical power and heat. Where there are seasonal variations in heat demand, the efficiency of CHP systems can be increased if the excess heat is used to power thermally driven refrigeration technologies. Tri-generation systems have overall efficiencies as high as 90% compared to 33%-35% for electricity generated in central power plants.

4.1. Organic Rankine Cycle (ORC) for Energy Recovery

The ORC applies the principle of the steam Rankine cycle, but uses organic working fluid with low boiling points, instead of steam, to recover heat from a lower temperature source. The cycle consists of an expansion turbine, condenser, a pump, a boiler and a superheated (provide superheat is needed). [2]

4.2. Organic Rankine Cycle

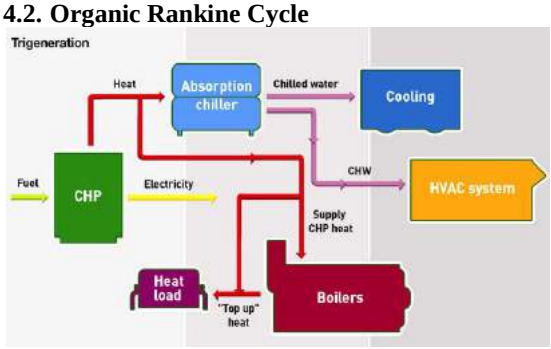

Fig: 2. Tri-generation System Layout [1]

Different form of combined with ORC as a bottoming cycle, ORC with different working fluid for power plants, cement industry, desalination, process industry, furniture manufacturing industry, etc. and Wastage heat recovery

4.3. ORC Working Fluids

The working fluid of an organic Rankine cycle is very important. Pure working fluids such as HCFC123 ($CHCl_2CF_3$), PF5050 ($CF_3(CF_2)_3CF_3$), HFC-245fa ($CH_3CH_2CHF_2$), HFC-245ca (CF_3CHFCH_2F), isobutene ($(CH_3)_2C=CH_2$), n-pentane and aromatic hydrocarbons, have been studied for organic Rankine cycles. The slope of the saturation curve (ds/dt slope) of a working fluid in a Temperature-Entropy diagram .Working fluid classified as a Dry fluid, wet fluid or isentropic fluid, it is defined by. If J=ds/dt, J.>0 for dry fluid (pentane),J=0 for isentropic fluid (R11) and J<0 for wet fluid (water).[3-4].Isentropic or dry fluid was suggested for ORC to avoid liquid droplet impingement in turbine blade during the expansion. If the fluid is too dry the expanded vapor will leave the turbine with substantial superheat, which is a waste and add to the cooling load in the condenser. The cycle efficiency can be increased using this superheat to preheat the liquid after it leaves the feed pump and before it enters the boilers. All components of ORC shown in fig-ORC components [4]

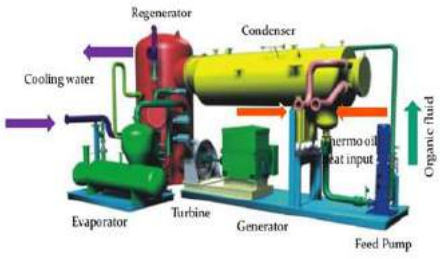

Fig: 3. ORC components [2]

Chen et al. [3] summarized heat-transfer properties of the working fluids are of great importance. Desirable properties are: low viscosity and surface tension, low specific heat of the liquid, high thermal conductivity, high latent heat of vaporization. The evaporator enthalpy ratio i.e. the ratio of enthalpy of vaporization to the sensible enthalpy required to raise the temperature of the compressed liquid should have a high value.

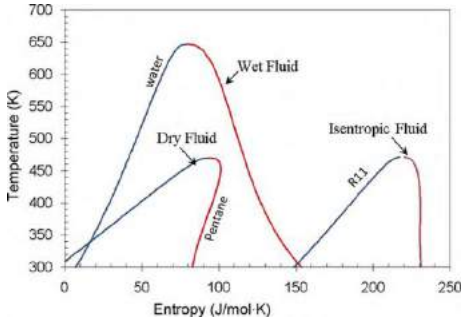

Fig: 4. Tempetrture-Entropy diagram of fluids [4]

4.4. Binary Fluid (Nh_3-H_2o) Thermal System [1]

The Binary fluid (NH_3-H_2O) Thermal System was 1st developed by Aleksander Kalina in the late 1970 and early 1980 for generating electricity using low to medium temperature resources. Kalina system uses ammonia-water (Binary fluid) mixture as working fluid. This mixture is used as source for power and cooling. In this cycle ammonia is the refrigerant and water as is the absorbent due to the high difference in their boiling point and high enthalpy.

In the Kalina system, used binary fluid mixture results in a good thermal match in the boiler due to the non-isothermal boiling created by the shifting mixture composition. Several studies have shown that the Kalina cycle performs substantially better than a steam Rankine cycle system. A second law analysis showed that by using a binary fluid, the Kalina cycle reduced irreversibility in the boiler, resulting in improved efficiency of the cycle.

Table: 1(a). Commercialized Working fluids [4]

S. No	Chemicals	Physical Data			
		Molecular Mass (Kg/K mol)	Normal Boiling Point Temp (T_{bp}) in ^0C	Critical Temp (T_{criti}) in ^0C	Critical Pressure (P_{criti}) in MPa
1	RC118	200.03	-6.0	115.2	2.778
2	R600a	58.12	-11.7	135	3.647
3	R114	170.92	3.6	145.7	3.289
4	R600	58.12	-0.5	152	3.796
5	R601	72.15	36.1	196.5	3.364
6	R113	187.38	47.6	214.1	3.439
7	Cyclohexane`	84.16	80.7	280.5	4.075
8	R290	44.10	-42.1	96.68	4.247
9	R407C	86.20	-43.6	86.79	4.597
10	R32	52.02	-51.7	78.11	5.784
11	R500	99.30	-33.0	105.5	4.455
12	R152a	66.05	-24.0	113.3	4.520
13	R717	17.03	-33.3	132.3	11.333
14	Ethanol	46.07	78.4	240.8	6.148
15	Methanol	32.04	64.4	240.2	8.104
16	R718	10.2	100	374	22.064
17	R134a	102.03	-26.1	101	4.059
18	R12	120.91	-29.8	112	4.114
19	R123	152.93	27.8	183.7	3.668
20	R141b	116.95	32.0	204.2	4.249
21	R245fa	134.05	15.3	154.1	3.64
22	R236fa	152.0	-1.5	124.0	3.20
23	R227ea	170.0	-17.5	102.0	2.95
24	R1234yf	114.02	-29.45	94.7	3.382

Table: 1(b). Commercialized Working fluids [4]

S. No	Chemicals	Environmental Data		
		Atmospheric Life Time (ALT) in years	Ozone Depletion potential (ODP)	Global Warming Potential (GWP) of 100 years
1	RC118	3200	0	10225
2	R600a	0.017	0	20
3	R114	300	1.00	10040
4	R600	0.018	0	20
5	R601	0.01	0	20
6	R113	85	1.000	6130
7	Cyclohexane`	NA	NA	NA
8	R290	0.041	0	20
9	R407C	NA	0	1800
10	R32	4.9	0	675
11	R500	NA	0.738	8100
12	R152a	1.40	0	124
13	R717	0.1	0	<1
14	Ethanol	NA	NA	NA
15	Methanol	NA	NA	NA
16	R718	NA	0	<1
17	R134a	14.0	0	1430
18	R12	100	1.000	10890
19	R123	1.3	0.02	77
20	R141b	9.3	0.120	725
21	R245fa	8.8	0	820
22	R236fa	209	0	6300
23	R227ea	36.5	0	2900
24	R1234yf	NA	~0	4

One drawback of the Kalina system is the fact that high vapor fraction is needed in the boiler, however, the heat exchanger surface is easy to dry out at high vapor fraction as, resulting in lower overall heat transfer coefficients and a larger heat exchange area. Another drawback relates to the corrosives is ammonia. Impurities in liquid ammonia such as air or carbon dioxide can cause stress corrosion cracking of mild steel and also ammonia is highly corrosive towards copper and zinc.

The pump pressurized the saturated liquid (5) which is leaving from the condenser and it is sent in to the high temperature re-cuperator (6). The liquid takes off the heat from the two phases dead vapor (3). The pressurized hot liquid (sub-cooled state) enters (1) into the vaporizer where the liquid is converted in to vapor (2) by utilizing the latent or sensible heat of the hot source (1s-2s). The saturated vapor (2) from the vaporizer is expanded in the turbine up to its condenser pressure. The two phase mixture after giving a part of its latent heat to the incoming liquid (4) enters in to the condenser, where cooling water enters (1w), takes away all the heat available in the two-phase mixture, and leaves at higher temperature (2w).The saturated liquid is pressurized in the pump and the cycle repeats.

5. Combined Rankine and Refrigeration Cooling Cycle-[1]

Mezza [4] proposed novel thermodynamic cycle that uses binary mixture to produce power and refrigeration simultaneously in one loop. This cycle is a combination of Rankine power and absorption cooling cycle. Its advantages include the production of power and cooling in the same cycle, the design flexibility to produce any combination of power and refrigeration, the efficient conversion of moderate temperature heat source and the possibility of improved resource utilization compared to separate power and cooling system. The binary mixture first used was ammonia-water and later on new binary fluids were proposed and studied**.**

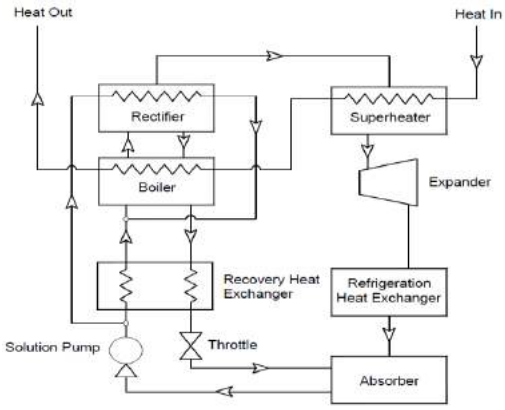

Fig: 6. Binary fluid (NH_3-H_2O) Thermal System [1]

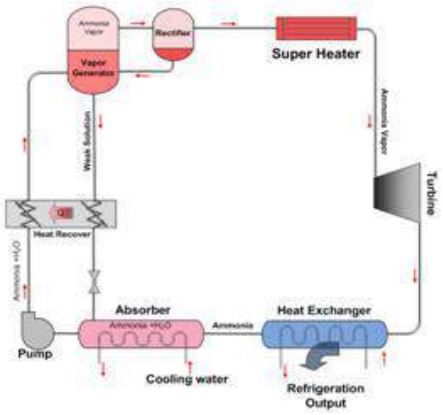

Fig: 7. Combined Rankine and Refrigeration cooling cycle-[1]

5.1. Energy Recovery (High-Low Grade) Technology. [3]

Three categories of wastage heat sources are distinguished with respect to the temperature level, low (<230^{0}C), medium (230-650^{0}C) and high (>650^{0}C).Waste heat sites and thermal levels are listed in table of energy recovery and its sources.

5.2. Status of Energy Recovery Technology in India [3]

(a) Cement Industry

Some studies shown in Table-4 for Indian industries for 2,500 ton per day plant of cement can be used to set up a 1.6 MW waste heat recovery plant using the Organic Rankine Cycle. Based on this assumption and projected manufacturing capacity of cement industry in India, a rough potential of the electricity production from waste heat by ORC technology is estimated to be 574 MW.

Table: 3. Grade of Energy and its sources [3]

Heat Categories	Heat Sources	Temperature in ^{0}C	Suggested recovery technology
High Grade (>650^{0}C)	Solid waste	650-1000	Air preheating
	Nickel refining furnace	1370-1650	Steam generation for heating
	Copper reverberatory furnace	760-815	Thermoelectric and thermal PV
	Glass melting furnace	1000-1550	Heat exchanger for preheating
	Hydrogen plant	650-1000	Thermal PV
Medium Grade (230-650^{0}C)	Steam boiler exhaust	230-480	Steam Rankine cycle
	Gas turbine exhaust	370-540	Organic Rankine cycle
	Drying and baking ovens	230-600	Thermal PV
	Catalytic crackers	425-650	Thermal PV
	Reciprocating engine exhaust	315-600	Thermoelectric
Low Grade (>230^{0}C)	Welding and injection molding	32-88	Kalina cycle
	Hot processed liquids and solids	32-233	Organic Rankine cycle
	Drying, Baking and Curing ovens	93-230	Absorption and adsorption cooling
	Bearing	32-88	Piezoelectric

(b) Glass Industry

Typically, a 500 ton per day glass manufacturing plant will have potential for a 1 MW Organic Rankine Cycle waste heat recovery plant. The projected waste heat recovery potential through ORC in the glass industry in India is total potential estimated at around 36 MW by 2017.

(c) Iron and Steel Industry

Typically, a 6,000 ton per day steel rolling mill has a potential of generating 2.4 MW of electricity through an Organic Rankine Cycle waste heat recovery plant. The projected waste heat recovery potential through ORC in the Iron and Steel sector is total potential estimated to be around 148.4 MW by 2017.

6. Thermodynamic Analysis

Renewable energy sources, such as solar thermal and geothermal, biomass, municipal solid waste (MSW) and vast amounts of industrial waste heat are potentially

promising energy sources capable, to meet the world electricity demand. However, the low grade heat from these sources cannot be converted efficiently to electrical power by using the conventional power generation methods. In this context, research on how to convert these low-grade

Table: 4. ORC Development in India [3]

Sector	Capacity (MW)
1. Wastage Heat Recovery In Major Industry	
a. Cement	574.2
b. Glass	35.7
c. Iron and steel	148.4
Total	758.3
2. Renewable Energy	
a. Solar thermal energy storage	1440
b. Biogas plant	2208
c. Geothermal	NA
Total	3648
Grand Total	4406.3

temperature heat sources into electrical power is of great significance.. The organic Rankine cycle (ORC), whose most important feature is the possibility of using different low temperature heat sources for small and medium power generation, has been studied by many authors. Present Literature review focus on ORC based wastage energy recovery systems, working fluid and their technological development. Hong Gao et al. [5] estimated exergy efficiencies like, 0.35, 0.40, 0.45, 0.50 and 0.55 under different critical temperature (450 to 500^0C) and critical pressure (5 to 10 MPa) respectively for butane based supercritical ORC thermal system. Maria T Johansson et al [6] studied three different engines (Thermo-Electric generator, Organic Rankine cycle engine and Phase Change Material based engine) for wastage energy recovery for steel industry, and estimate conversion efficiency like 1-5%, 7.5-16% and 2.5% respectively under different temperature sources. Wang et al [7] calculated heat recovery efficiency and thermal efficiency of R123 & Tolune based ORC as 0.12% -0.10% and 0.08-0.1% respectively and conclude thermal efficiency is increased with the increase of heat recovery temperature. Omendra et al [8] estimated exergy destruction cost and capital cost of Brayton-Rankine-Kalina combine triple power system such as 40,663 to 37,416 rs and total cost decreased by 4041 ϕ /h as compare with conventional power generation system by using SPECO techno-economic analysis approach and showed the effect of relative humidity on inlet air for exergy destruction from 30-100% of RH value. Abdul Khaliq [9] showed effect of inlet pressure and temperature on 1st and 2nd law efficiency of gas turbine tri-generation system, and discussed 1st law efficiency of cogeneration and tri-generation decreases with increases in pressure ratio but 2nd law efficiency, thermal to electrical energy ratio is increases. Bertrand F. Tchanche, et al [10] estimated 82% of overall efficiency of ocean thermal energy based ORC system with 2765 ε /KW of installation cost and 9-14 ε /KW of electrical power cost. Na Zang et al [11] proposed design of combined refrigeration and binary fluid power cycle and estimate energy and exergy efficiency 26-28 % and 55-60% respectively at temperature level of 450 ^{0}C and that performance compare with nuclear power plant exhaust used as a topping gas turbine power plant. Y Chen et al [12] compared CO_2 transcritical power cycle with R123 based ORC when utilizing low grade of heat source at 150^0C and 0.4kg/s of mass flow rate. The expander isentropic efficiency of both system has been estimated 80% and 70% respectively. Chen et al [3] investigated thermal performance of zeotropic mixture (70% of R134a + 30% of R32) based supercritical rankine cycle and R134a based ORC and achieved 10.77%-13.35% & 88.6%-81.64% of thermal and exergy efficiency at same temperature level of 393-453 ^{0}C respectively. The overall efficiency of both systems estimated 38.1%and 24.2%. R Shankar et al [14] performed analysis of solar integrated combined vapor power and cooling cycle for domestic and industrial level and compare both systems from high pressure and low pressure turbine are 58.75 & 91.57 KW respectively at the atmospheric and separator temperature of 30^OC & 120^0C. Javier Rodriguiz Martin et al [15] estimated 70% and 0.469 of thermal and exergy efficiency of solar parabolic collector based ORC at 238^0C and 311.11 bar of temperature and pressure value. Dincer et al studied [16] the energy efficiency increases while exergy efficiency and electrical to thermal energy ratio decrease with increasing exhaust gas inlet temperature. and effect of increasing process steam pressure, energy efficiency decreases while exergy efficiency and electrical to thermal energy ratio increase. Deepak et al [17] conclude energy and exergy efficiency of different commercial fluid for wastage energy recovery system and examined 7% of theoretical thermal efficiency of new trend of refrigerants like R1234yf with the 30-90 ^{0}C range of temperature. Vijayaraghavan, et al [18] calculated 95, 96.5, 89% of thermal efficiency of Kalina thermal system with 556.5, 511, 141^0C and 19.5, 3.11 & 0.572 bar of inlet turbine temperature and pressure respectively. Nobru et al. [19] Studied ,First Law efficiency on HFO-1234yf driven ORC for low to medium temperature range and found that it is potential working substance having negligible ozone depletion potential, global warming potential and found highest thermal efficiency 8.8-11.4% for expander inlet temperature range of (180-160^0C) in Supercritical Organic Rankine cycle. Padilla et al [20] noticed that turbine exit quality decreases when the absorber temperature decreases in analysis of power and cooling cogeneration using ammonia-water system.

Although lot of work have been presented by various investigators [1-20] but still some problems are still to be analyzed in detail are as follow

The technological implementations of low-temperature ORC in an industry still awaits the arrival of a low GWP replacement fluid exiting fluid to maintain the cost advantage that can be realized by using equipment for ORC duty. The newly developed fluid 1233zd (E) could be that fluid. The medium pressure new refrigerants R1234yf and R1234ze (E) approach R134a and R245fa.. Till now there is no study about solar based combined heating, power and cooling system analysis using HFO-1234yf as working substance in Organic Rankine cycle for food process industry in India. Integrated Solar based Trilateral Flash power ORC cycle and Cogeneration Bottoming ORC cycle is most applicable in ceremics ,rice mill and sugar mill type Indian industry for low grade wastage energy recovery.

6. Research Methodology

A general methodology is proposed here. It comprises three steps. (1) data collection, (2) data analysis and (3) Result Analysis. At the first step, the operating conditions are set and all the data: thermo physical, safety, environmental and calculated properties concerning different candidates are collected. The data are then analyzed at the second step. At this phase, the criteria are classified starting from the most critical ones and the process is done sequentially. At each sub-step, all the fluids are screened using the criterion and before going to the next criterion, the fluids are put in two groups: those which fulfil the criteria (These criteria include good heat transfer properties, non-toxicity, non-flammability, high efficiency, availability and low cost, low vapor specific volume) and those which do not. At the last step, the best thermodynamic systems should come out followed by some alternatives.

The main objective of research work to perform Energy-Exergy analysis of integrated solar energy based wastage heat recovery system (low and medium temperature) using combined heating-power and cooling system for industrial application and following energy systems are considered for above objectives in present investigations

1) Energy-Exergy analysis of ORC system (Sub critical, Trans-critical and Supercritical ORC systems)
2) Energy-Exergy analysis of Integrated solar combined (Heating-Power system) power energy recovery system, Topping and Bottoming type both.
3) Energy-Exergy analysis of ORC with reheating.
4) Energy-Exergy analysis of ORC with regenerative.
5) Energy-Exergy analysis of ORC Tri-generation system.
6) Energy-Exergy analysis of trilateral flash type ORC system.

7. Conclusions

In general conventional steam cycle operates in medium to high temperature and cannot be cost effective at smaller scale or low temperature resources. In The low medium temperature range Organic Rankine, Kalina, Chen, and Transcritical cycles have demonstrated.

From the literature, it is evident that an integrated approach towards operational efficiency improvements of existing systems, reduction of losses in operational mechanisms, end-use efficiency and also making use of waste heat recovery technologies are very much essential for energy conservation.

The organic Rankine cycle applications in waste heat recovery. Working fluid properties and selection (including pure fluids and mixtures) was reviewed. Also some important physical properties of the working fluids for ORC and the performance of the system were introduced. Different applications of ORC systems including solar thermal, biomass ORC, solar thermal reverse osmosis desalination, geothermal application, and waste heat recover from industrial process were intensively investigated. The paper also presented the different employed expander in the ORC system and introduced many factors which should be considered such as the power capacity, isentropic efficiency, cost and complexity their application range. Environmental concern over climate change as well as energy price is reasons supporting application of the waste heat recover by the ORC technology. Different Waste Heat Recovery Systems (WHRS) have been experimented to analyze the effect of various parameters of energy savings. Mathematical modeling by using MATLAB and fluid properties and thermodynamic property estimation using NIST REFPROF 8.0/Modelica software are used in the present investigation.

References

[1] G. G. Maidment, R. M. Tozer, Combined cooling heat and power in supermarkets, Applied Thermal Engineering, 22, 2002, 653–665
[2] www.orccycle.be (Last checked May 2013)
[3] Turboden,www.turboden.eu/en/products/products-hr. php. (Last Accessed August 2014).
[4] V. Maizza, A. Maizza, Working fluids in non-steady flows for waste energy recovery systems, Applied Thermal Energy, 16, 1996, 579-590
[5] Hong Gao, Chao Liu, Chao He, Performance analysis and working fluid selection of a supercritical ORC for low grade wastage heat recovery, Energies, 23, 2012, 3233-3247
[6] Maria T Johanssan, Mats Soderstrom, Electricity generation from low grade temperature industrial excess heat an opportunity for steel industry, proceeding of Int, Conference, Sweden, 2013, 1-18.
[7] EH Wang, HG Zhang, BY Fan, MG Ouyang, Y Zhao, QH. Mu, Study of working fluid selection of organic Rankine cycle (ORC) for engine waste heat recovery. Journal of Energy, Elsevier, 36, 2011, 3406–18.
[8] Omendra Singh, SC Kaushik, Thermodynamic evaluation and optitimization of a Brayton-Rankine-Kalina combined triple power cycle, Journal of energy conversion and management, 71, 2013, 32-42
[9] Abdul Khaliq, Exergy analysis of gas turbine trigeneration system for combined production of power heat and refrigeration. Int. Journal of Refrigeration, Elsevier, 32, 2009, 534-545
[10] Bertrand F. Tchanche, Gr Lambrinos, Low grade heat conversion into power using ORC-A Review of various application, Journal of renewable and sustainable energy reviews, Elsevier, 15, 2011, 3963-3979
[11] Na Zang,Noam Lior, Methodoligy for thermal design of novel combined refrigeration / power binary fluid systems, Journal of refrigeration, Elsevier, 30, 2007, 1072-1085.
[12] Y Chen, P Lundqvist, A Johanssan, A comparative study of the CO_2 transcritical power cycle compared with an ORC with R123 as working fluid in waste recovery, Journal of applied thermal energy, 26, 2006, 2142-2147.
[13] H Chen, DY Goswami, EK. Stefanakos, A supercritical rankine cycle using zeotropic mixture working fluids for the conversion of low-grade heat into power, Journal of energy, Elsevier, 36, 2011, 549-55
[14] R Shankar, T Srinivas, Parametric optimization of vapor power and cooling cycle, 4th Int. Conference on advances in energy reesrach, Elsevier, 54, 2014, 135-141

[15] J. R. Martin, E B. Rodriguez, Thermodynamic evaluation of integrated solar combined cycle systems. Journal of Entropy, 16, 2014, 4246-4259
[16] I Dincer, A. Khaliq, R. Kumar, Performance Analysis Of An Industrial Waste Heat-Based Trigeneration System, International Journal Of Energy Research, Wiley Interscience, 33, 2009, 737–744.
[17] Deepak Tiwari, Akhilesh Arora, Naushad Ahmad Ansari, A. F. Sherwani, Energy and Exergy Analysis of Organic Rankine Cycle Using Alternative Working Fluids, IOSR Journal of Mechanical and Civil Engineering (IOSR-JMCE), 12, 2015, 85-92 .
[18] S. Vijayaraghavan, D.Y. Goswami, A combined power and cooling cycle modified to improve resource utilization efficiency using distillation stage, Energy, 31(8), 2006, 1177-1196.
[19] Yamada Noboru, Mohamad Md Nor Anuar,Trinh Trung Kien, study on Thermal Efficiency of low to medium organic Rankine cycle using HFO-1234yf.Renewable Energy 41 (2012) 368-375.cycle.Applied Thermal Engineering, 51, 2013, 781-786
[20] R.V. Padilla, G. Demirkaya, D. Y. Goswami, E. Stefanakos, M. M. Rahman, Analysis of power and cooling cogeneration using ammonia-water mixture, Energy, 35(12), 2010, 4649-4657